supernovae

Les Houches 1990

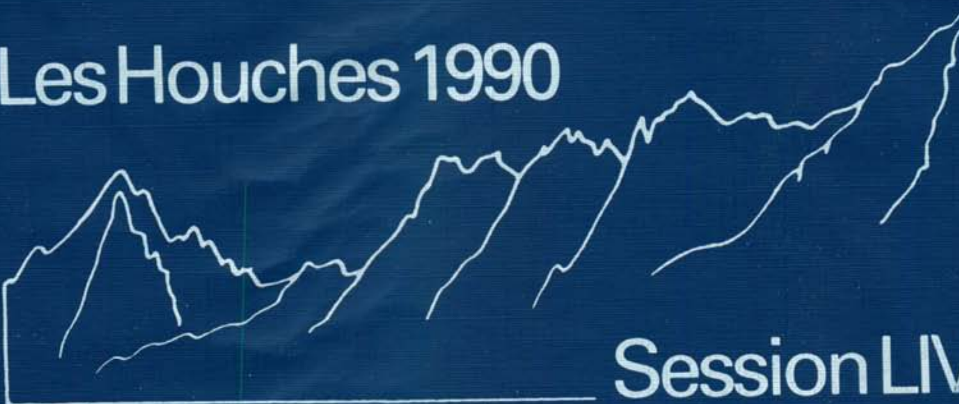

Session LIV

supernovae

S. A. Bludman
R. Mochkovitch
and J. Zinn-Justin

Editors

North-Holland

UJFG NATO ASI

LES HOUCHES

Session LIV

1990

SUPERNOVAE

CONFÉRENCIERS

Z. Barkat
S.A. Bludman
D. Branch
R. Canal
M. Cassé
R.A. Chevalier
C. Fransson
W. Hillebrandt
R.P. Kirshmer
E. Müller
D.K. Nadyozhin
K. Nomoto
C. Pollas
P.J. Schinder
R. Schaeffer
G.A. Tammann
F.-K. Thielemann
D. Vautherin
S.E. Woosley

UJFG NATO ASI

LES HOUCHES

SESSION LIV

31 Juillet – 1 Septembre 1990

SUPERNOVAE

édité par

S.A. BLUDMAN, R. MOCHKOVITCH
et J. ZINN-JUSTIN

1994

NORTH-HOLLAND

AMSTERDAM · LONDON · NEW YORK · TOKYO

ELSEVIER SCIENCE B.V.
Sara Burgerhartstraat 25
P.O. Box 211, 1000 AE Amsterdam, The Netherlands

ISBN: 0 444 81474 4

Printed in the Netherlands

Printed on acid-free paper

LES HOUCHES
ÉCOLE D'ÉTÉ DE PHYSIQUE THÉORIQUE

ORGANISME D'INTÉRÊT COMMUN DE
L'UNIVERSITÉ JOSEPH FOURIER DE GRENOBLE ET DE
L'INSTITUT NATIONAL POLYTECHNIQUE DE GRENOBLE
AIDÉ PAR
LE COMMISSARIAT À L'ÉNERGIE ATOMIQUE

SESSION LIV

INSTITUT D'ÉTUDES AVANCÉES DE L'OTAN
NATO ADVANCED STUDY INSTITUTE

31 Juillet–1 Septembre 1990

Directeurs scientifiques de la session: S.A. Bludman, *Department of Physics, University of Pennsylvania, Philadelphia PA 19104, USA* et R. Mochkovitch, *Centre National de la Recherche Scientifique, Institut d'Astrophysique, 98 Bis Boulevard Arago, 75014, Paris France*

SESSIONS PRÉCÉDENTES

I	1951	Mécanique quantique. Théorie quantique des champs
II	1952	Quantum mechanics. Mécanique statistique. Physique nucléaire
III	1953	Quantum mechanics. Etat solide. Mécanique statistique. Elementary particles
IV	1954	Mécanique quantique. Théorie des collisions; two-nucleon interaction. Electrodynamique quantique
V	1955	Quantum mechanics. Non-equilibrium phenomena. Réactions nucléaires. Interaction of a nucleus with atomic and molecular fields
VI	1956	Quantum perturbation theory. Low temperature physics. Quantum theory of solids; dislocations and plastic properties. Magnetism; ferromagnetism
VII	1957	Théorie de la diffusion; recent developments in field theory. Interaction nucléaire; interactions fortes. Electrons de hauté énergie. Experiments in high energy nuclear physics
VIII	1958	Le problème à N corps (Dunod, Wiley, Methuen)
IX	1959	La théorie des gaz neutres et ionisés (Hermann, Wiley)*
X	1960	Relations de dispersion et particules élémentaires (Hermann, Wiley)*
XI	1961	La physique des basses températures. Low-temperature physics (Gordon and Breach, Presses Universitaires)*
XII	1962	Géophysique extérieure. Geophysics: the earth's environment (Gordon and Breach)*
XIII	1963	Relativité, groupes et topologie. Relativity, groups and topology (Gordon and Breach)*
XIV	1964	Optique et électronique quantiques. Quantum optics and electronics (Gordon and Breach)*
XV	1965	Physique des hautes énergies. High energy physics (Gordon and Breach)*
XVI	1966	Hautes énergies en astrophysique. High energy astrophysics (Gordon and Breach)*
XVII	1967	Problème à N corps. Many-body physics (Gordon and Breach)*
XVIII	1968	Physique nucléaire. Nuclear physics (Gordon and Breach)*
XIX	1969	Aspects physiques de quelques problèmes biologiques. Physical problems in biology (Gordon and Breach)*
XX	1970	Mécanique statistique et théorie quantique des champs. Statistical mechanics and quantum field theory (Gordon and Breach)*
XXI	1971	Physique des particules. Particle physics (Gordon and Breach)*
XXII	1972	Physique des plasmas. Plasma physics (Gordon and Breach)*
XXIII	1972	Les astres occlus. Black holes (Gordon and Breach)*
XXIV	1973	Dynamique des fluides. Fluid dynamics (Gordon and Breach)*
XXV	1973	Fluides moléculaires. Molecular fluids (Gordon and Breach)*
XXVI	1974	Physique atomique et moléculaire et matière interstellaire. Atomic and molecular physics and the interstellar matter (North-Holland)*
June Inst.	1975	Structural analysis of collision amplitudes (North-Holland)
XXVII	1975	Aux frontières de la spectroscopie laser. Frontiers in laser spectroscopy (North-Holland)*
XXVIII	1975	Méthodes en théorie des champs. Methods in field theory (North-Holland)*
XXIX	1976	Interactions électromagnétiques et faibles à haute énergie. Weak and electromagnetic interactions at high energy (North-Holland)*

XXX	1977	Ions lourds et mésons en physique nucléaire. Nuclear physics with mesons and heavy ions (North-Holland)*
XXXI	1978	La matière mal condensée. Ill-condensed matter (North-Holland)*
XXXII	1979	Cosmologie physique. Physical cosmology (North-Holland)*
XXXIII	1979	Membranes et communication intercellulaire. Membranes and intercellular communication (North-Holland)*
XXXIV	1980	Interaction laser-plasma. Laser-plasma interaction (North-Holland)
XXXV	1980	Physique des défauts. Physics of defects (North-Holland)*
XXXVI	1981	Comportement chaotique des systèmes déterministes. Chaotic behaviour of deterministic systems (North-Holland)*
XXXVII	1981	Théories de jauge en physique des hautes énergies. Gauge theories in high energy physics (North-Holland)*
XXXVIII	1982	Tendances actuelles en physique atomique. New trends in atomic physics (North-Holland)*
XXXIX	1982	Développements récents en théorie des champs et mécanique statistique. Recent advances in field theory and statistical mechanics (North-Holland)*
XL	1983	Relativité, groupes et topologie II. Relativity, groups and topology II (North-Holland)*
XLI	1983	Naissance et enfance des étoiles. Birth and infancy of stars (North-Holland)*
XLII	1984	Aspects cellulaires et moléculaires de la biologie du développement. Cellular and molecular aspects of developmental biology (North-Holland)*
XLIII	1984	Phénomènes critiques, systèmes aléatoires, théories de jauge. Critical phenomena, random systems, gauge theories (North-Holland)*
XLIV	1985	Architecture des interactions fondamentales à courte distance. Architecture of fundamental interactions at short distances (North-Holland)*
XLV	1985	Traitement du signal. Signal processing (North-Holland)*
XLVI	1986	Le hasard et la matière. Chance and matter (North-Holland)*
XLVII	1987	Dynamique des fluides astrophysiques. Astrophysical fluid dynamics (North-Holland)*
XLVIII	1988	Liquides en interfaces. Liquids at interfaces (North-Holland)*
XLIX	1988	Champs, cordes et phénomènes critiques. Fields, strings and critical phenomena (North-Holland)*
L	1988	Tomographie océanographique et géophysique. Oceanographic and geophysical tomography (North-Holland)*
LI	1989	Liquides, cristallisation et transition vitreuse. Liquids, freezing and glass transition (North-Holland)
LII	1989	Chaos et physique quantique. Chaos and quantum physics (North-Holland)*
LIII	1990	Systèmes fondamentaux en optique quantique. Fundamental systems in quantum optics (North-Holland)*

* Sessions ayant reçu l'appui du Comité Scientifique de l'OTAN

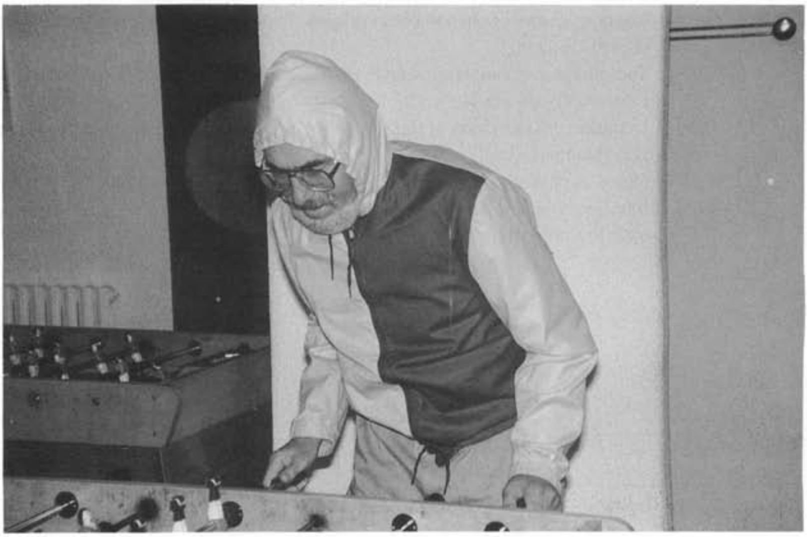

LECTURERS

Z. Barkat Racah Institute of Physics, Hebrew University, Jerusalem, Israel

S.A. Bludman Department of Physics, University of Pennsylvania, Philadelphia PA 19104, USA

D. Branch Department of Physics and Astronomy, University of Oklahoma, Norman OK 73019, USA

R. Canal Departament d'Astronomia i Meterologia, Universitat de Barcelona, 08028 Barcelona, Spain

M. Cassé CEN-Saclay, DAPNIA, Service d'Astrophysique, F-91191 Gif-sur-Yvette Cedex, France

R.A. Chevalier Department of Astronomy, University of Virginia, Charlottesville VA 22903, USA

C. Fransson Stockholm Observatory, S-133 36 Saltsjöbaden, Sweden

W. Hillebrandt Max-Planck-Institut für Physik und Astrophysik, Institut für Astrophysik, Karl-Schwarzschild-Strasse 1, 8046 Garching bei München, Germany

R.P. Kirshner Center for Astrophysics, 60 Garden St., Cambridge MA 02138, USA

E. Müller Max-Planck-Institut für Physik und Astrophysik, Institut für Astrophysik, Karl-Schwarzschild-Strasse 1, 8046 Garching bei München, Germany

D.K. Nadyozhin Institute of Theoretical and Experimental Physics, 117259 Moscow, Russia

K. Nomoto Department of Astronomy, Faculty of Science, University of Tokyo, Bunkyo-ku, Tokyo 113, Japan

C. Pollas Observatoire de la Côte d'Azur, CERGA, F-06460 St Vallier de Thiey, France

P.J. Schinder Department of Astronomy, Cornell University, Ithaca NY 14853, USA

R. Schaeffer Service de Physique Théorique, CEN-Saclay, F-91191 Gif-sur-Yvette Cedex, France

G.A. Tammann Astronomisches Institut der Universität Basel, European Southern Observatory, Garching, Germany

F.-K. Thielemann Harvard-Smithsonian Center for Astrophysics, 60 Garden Street, Cambridge MA 02138, USA

D. Vautherin Division de Physique Théorique, Institut de Physique Nucléaire, Université Paris-Sud, F-91406 Orsay Cedex, France

S.E. Woosley Board of Studies in Astronomy and Astrophysics, University of California at Santa Cruz, Santa Cruz CA 95064, USA

PARTICIPANTS

Benetti, Stefano Dipartimento di Astronomia dell' Università di Padova, Osservatorio Astrofisico di Asiago, Asiago (VI), Italy

Benvenuto, Omar Facultad de Ciencias Astronomicas y Geofisicas, Universidad Nacional de La Plata, Paseo del Bosque S/N (1900) La Plata, Argentina

Blottiau, Patrick Centre d'Etudes de Limeil-Valenton, 94195 Villeneuve-St Georges Cedex, France

Boffin, Henri Institut d'Astronomie d'Astrophysique et de Géophysique, C.P. 165, Université Libre de Bruxelles, 50, av. F.D. Roosevelt, B-1050 Brussels, Belgium

Dgani, Ruth CHEAF, P.O. Box 41882, 1009 DB Amsterdam, Holland

Dominguez, Inma CEAB, C/Sta. Barbara, 17300 Blanes (Gerona), Spain

Dupraz, Christophe Laboratoire de Radioastronomie Millimétrique, Ecole Normale Supérieure, 24 rue Lhomond, F-75231 Paris Cedex 05, France

Emmering, Robert Theoretical Astrophysics, Caltech 130–33, Pasadena CA 91125, USA

Font Roda, José Antonio Departamento de Fisica Teorica, Facultad de Fisica, Universitat de Valencia, Burjassot 46100 Valencia, Spain

Gabi, Silvia Stockholms Observatorium, Institution för Astronomi, S-13300 Saltjöbaden, Sweden

Glasner, Shimon Ami Racah Institute of Physics, The Hebrew University, Jerusalem, Israel

Gomez, Gabriel Instituto de Astrofisica de Canarias, Via Lactea S/N 38200 La Laguna Tenerife, Spain

Gourgoulhon, Eric D.A.R.C.–L.A.M., Observatoire de Paris-Meudon, 92195 Meudon Cedex, France

Hamuy, Mario Cerro Tololo Inter-American Observatory, Casilla 603, La Serena, Chile

Hix, William Raphael Center for Astrophysics (MS-10), 60 Garden St., Cambridge MA 02138, USA

Houck, John Dept. of Astronomy, University of Virginia, Box 3818, University Station, Charlottesville VA 22903-0818, USA

Huguet, Eric D.A.S.G.A.L. Observatoire de Paris-Meudon, F-92195 Meudon Cedex, France
Janka, Hans-Thomas Max-Planck-Institut für Astrophysik, Karl-Schwarzschild-Str. 1, 8046 Garching, Fed. Rep. of Germany
Jeffery, David Dept. of Physics and Astronomy, University of Oklahoma, 440 West Brooks, Rm 131, Norman OK 73019, USA
Jose, Jordi Dept. de Fisica i Enginyeria Nuclear, Facultat d'Informatica de Barcelona, Universitat Politecnica de Catalunya, c/Pau Gargallo 5, E-08028 Barcelona, Spain
Liu, Weihong Center for Astrophysics (MS-14), 60 Garden St., Cambridge MA 02138, USA
Livne, Eli Racah Institute of Physics, Hebrew University, Jerusalem, Israel
Loxen, Johannes Universitätssternwarte Göttingen, Geismar Landstrasse 11, 3400 Göttingen, Fed. Rep. of Germany
Miller, Douglas Dept. of Physics and Astronomy, University of Oklahoma, 440 West Brooks, Rm 131, Norman OK 73019, USA
Mimouni, Jamal Institut de Physique, Université de Constantine, Constantine, Algérie
Mohan Rao, Desaraju Indian Institute of Astrophysics, Bangalore 560 034, India
Montes, Marcos Stanford Physics Department, Stanford University, Stanford CA 94305, USA
Neuforge, Corinne Institut d'Astrophysique, Université de Liège, 5 avenue de Cointe, 4200 Ougrée–Liège, Belgium
Paulus, Guy Institut d'Astronomie et d' Astrophysique, CP-165, Université Libre de Bruxelles, 50, av. F.D. Roosevelt, B-1050 Brussels, Belgium
Pichon, Bernard D.A.R.C./L.A.M., Observatoire de Paris-Meudon, F-92195 Meudon Cedex, France
Pistinner, Shlomi Physics Department, Technion, Haifa, Israel
Romero Bauset, José Vicente Departamento de Fisica Teorica, Facultad de Fisica, Universidad de Valencia, Burjassot 46100 Valencia, Spain
Ruiz Lapuente, Pilar Dpto. de Fisica de la Atmosfera, Astronomia y Astrofisica, Facultad de Fisica, Diagonal 647, Barcelona 08028, Spain
Sabalisck, Nanci Instituto Astronomico e Geofisico, U.S.P., Caixa Postal 30627, Sao Paulo S.P., Brazil
Salinas, Ener Fysikum, Vanadisvägen 9, S-113 46 Stockholm, Sweden
Schmidt, Brian Center for Astrophysics (MS-10), 60 Garden St., Cambridge MA 02138, USA
Serino, Deneyse Janet Lick Observatory, Dept. of Astronomy and Astrophysics, UCSC, Santa Cruz CA 95064, USA
Shigeyama, Toshikazu Dept. of Astronomy, Faculty of Sciences, University of Tokyo, Bunkyo-ku Tokyo 113, Japan

Widlund, Lennart Dept. of Physics, Vanadisvägen 9, S-113 46 Stockholm, Sweden
Yildiz, Mutlu Middle East Technical University, Physics Dept., 06531 Ankara, Turkey
Young, Tim Dept. of Physics and Astronomy, University of Oklahoma, 440 West Brooks, Rm 131, Norman OK 73019, USA

PRÉFACE

La cinquante-quatrième session de l'Ecole d'Eté de Physique Théorique qui s'est tenue aux Houches du 31 Juillet au 1 Septembre 1990 a été consacrée aux progrès récents de la physique des supernovae. Un intérêt particulier a bien sûr été porté aux résultats fascinants obtenus sur la supernova 1987A du Grand Nuage de Magellan.

Les supernovae sont parmi les manifestations lumineuses les plus spectaculaires de l'astronomie et les évènements les plus énergiques depuis le Big-Bang. Ces explosions sont la marque de la mort d'étoiles massives ou d'étoiles dégénérées appartenant à des systèmes binaires. Elles synthétisent des éléments lourds et leurs débris, en se propageant dans le milieu interstellaire, induisent la formation de nouvelles générations d'étoiles. Bien que la supernova 1987A du Grand Nuage de Magellan ait eu un retentissement considérable, tant scientifique que grand public, ce cours de cinq semaines aux Houches est à notre connaissance la première présentation adaptée à des étudiants voulant se spécialiser en physique des supernovae. Dans cette préface, nous donnons la liste des cours et conférences de l'Ecole et cela même dans les cas où ils n'ont pas donné lieu à une contribution écrite dans cet ouvrage.

L'Ecole a débuté par une introduction à la classification spectroscopique et photométrique des supernovae (Kirshner, Branch, Pollas). Le but ultime de ces classifications est de relier les propriétés observationnelles des supernovae aux caractéristiques des étoiles parentes (nature du coeur et de l'enveloppe, environnement circumstellaire) et aux mécanismes d'explosion. Les SN II-P et II-L proviennent sans doute de l'effondrement gravitationnel du coeur dégénéré d'étoiles massives (composé de fer ou d'un mélange O/Ne/Mg). Les SN Ia sont apparemment le résultat de l'allumage des réactions nucléaires au centre d'une naine blanche en accrétion. La classe nouvelle des SN Ib et Ic (dénommées conjointement SN Ibc) peut trouver son origine dans l'effondrement du coeur de fer d'étoiles d'hélium dans des binaires et/ou dans l'allumage thermonucléaire hors du centre dans des naines blanches en accrétion.

En particulier, après la séparation d'avec les SN Ibc, les SN Ia émergent comme une sous-classe homogène de chandelles standards, utiles en cosmologie pour la mesure des champs de vitesse et en tant qu'indicateurs de distance pour H_0 et q_0.

Tammann discute la statistique des supernovae. La fréquence et la fonction de luminosité sont des paramètres importants pour l'étude de la nucléosynthèse et de l'évolution galactique ainsi que pour les perspectives de détection de neutrinos ou d'ondes gravitationnelles lors d'effondrements stellaires (Lagage, Saavedra, Yvert). Plusieurs questions restent posées: le nombre des supernovae sous-lumineuses comme SN 1987A ou celles appartenant à la nouvelle classe des SN Ibc a-t-il été sous-estimé? Quelle est la connexion statistique entre les supernovae d'une part, les restes de supernovae et les pulsars d'autre part?

Les stades avancés de l'évolution stellaire, avec dans les systèmes binaires l'allumage thermonucléaire conduisant à une déflagration ou une détonation sont détaillés par Barkat, Canal, Nomoto et Müller. Le modèle de déflagration du carbone dans une naine blanche en accrétion rend assez bien compte du spectre des SN Ia, et peut-être aussi de celui des SN Ibc (Nomoto, Canal, Woosley et Weaver).

Les SN II, ainsi qu'éventuellement certaines SN Ibc, sont issues de l'effondrement du coeur dégénéré d'étoiles massives isolées, suivi d'une explosion (Hillebrandt, Nadyozhin, Woosley et Weaver). Bien que pour obtenir l'explosion il suffise de déposer à peine 1% de l'énergie des neutrinos à la base de l'enveloppe de la presupernova, les modèles théoriques ont beaucoup de peine à parvenir à ce résultat. Les calculs dépendent de l'équation d'état nucléaire (Vautherin), des techniques de simulation hydrodynamique (Müller), et sont particulièrement sensibles aux détails du transport des neutrinos en raison du faible couplage de ceux-ci avec la matière (Bludman, Nadyozhin, Schinder).

La supernova 1987A est maintenant bien interprétée comme une type II-P dont la luminosité a été faible car son étoile parente avait évolué en une supergéante bleue de relatif petit rayon dans un environnement de faible métallicité. Les caractéristiques de l'explosion sont discutés en grand détail par Nomoto. La courbe de lumière tardive est alimentée en énergie par les photons X durs et gamma provenant de la désintégration du ^{56}Ni (Cassé et Lehoucq, Fransson).

Chevalier (et Ballet) présentent l'évolution des restes de supernovae et leur effet sur le milieu interstellaire. La nucléosynthèse est traitée par Thielemann, Nomoto et Hashimoto et par Woosley et Weaver. Particulièrement intéressante apparaît la possibilité de nucléosynthèse induite par neutrinos. Enfin, l'évolution chimique de notre Galaxie est abordée par Schaeffer.

Ces cours et séminaires ont été complétés par une conférence sur l'intérêt des mesures récentes du flux de neutrinos solaires (Bludman), par une excitante visite au détecteur de neutrinos du tunnel du Mont-Blanc, par plusieurs films et par des soirées d'observation du ciel de montagne avec un petit télescope de 13 cm.

Lors de cette session nous avons eu ainsi l'opportunité de rassembler aux Houches quinze actifs professeurs venant d'Europe, des USA, de Russie, d'Israel et du Japon, présents aux Houches pendant plusieurs semaines et interagissant avec bonheur avec les étudiants. Ceux-ci, femmes et hommes des cinq continents, organisèrent de nombreuses discussions de groupe desquelles vont certainement émerger amitiés et collaborations futures. Nous espérons que cette école a encouragé une nouvelle génération de jeunes astronomes à travailler dans le domaine excitant et en pleine évolution qu'est la physique des supernovae.

Remerciements

La session LIV de l'Ecole d'Eté des Houches et la publication de ce volume de notes de cours ont été rendues possibles grâce:
– au soutien financier de l'Université Joseph Fourier de Grenoble, du Comissariat à l'Energie Atomique, de la division scientifique de l'OTAN et de la NSF;
– aux réflexions et avis du Conseil d'Administration de l'Ecole;
– à la réalisation de nombreuses figures par Anne Placenti et à la frappe efficace de manuscrits par Brigitte Raban;
– à l'aide déterminante de Brigitte Rousset et de Danielle Choupin dans la préparation et l'administration de la session, et à toute l'équipe qui a essayé de rendre la vie à l'Ecole aussi agréable que possible.

S.A. Bludman
R. Mochkovitch
J. Zinn-Justin

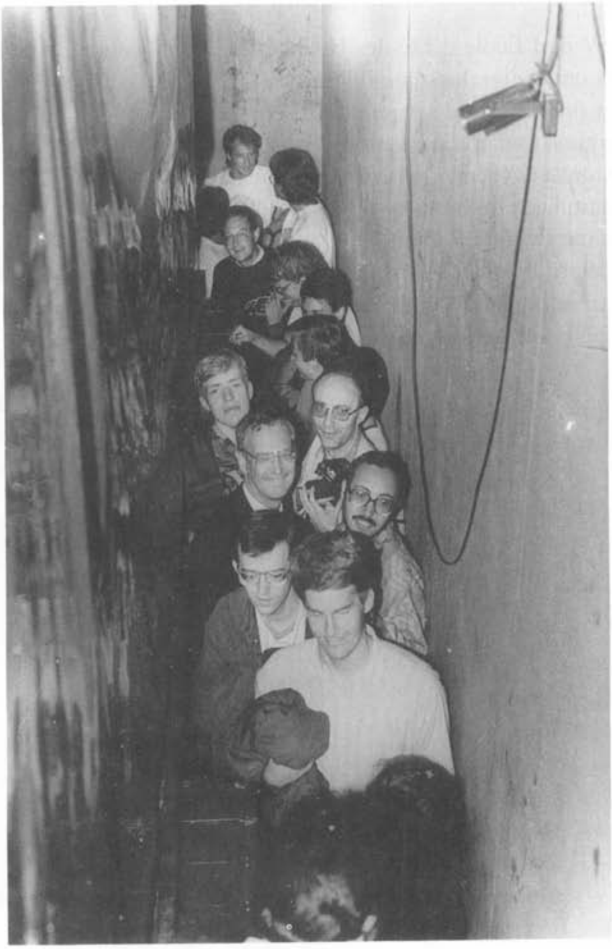

PREFACE

The fifty-fourth session of the Summer School in Theoretical Physics, which took place in Les Houches from July 31 to September 1, 1990, has been devoted to the recent advances in the phycics of supernovae. A special emphasis has naturally been given to the fascinating results obtained from supernova 1987A in the Large Magellanic Cloud.

Supernovae are the most dramatic optical display in astronomy and the most energetic events in the Universe since the Big Bang. These explosions are the cataclysmic deaths of massive stars or of degenerate stars in binaries. Their debris explosively synthesizes the heavy elements and, propagating through the interstellar medium, is reprocessed into later generations of stars. Although supernova 1987A in the nearby Large Magellanic Cloud stimulated tremendous scientific and popular interest, this five-week course at Les Houches is the first comprehensive presentation for advanced students of which we are aware. In this preface, we summarize the institute lectures, parenthetically referring to the lecturers, whether or not their written contributions could appear in this volume.

Our advanced study institute began with the spectroscopic and photometric classification of supernovae (Kirshner, Branch, Pollas). The ultimate aim is to relate these observational classifications to progenitor characteristics (stellar core and envelope, circumstellar environment) and to explosion mechanisms. SN II-P and II-L apparently arise from the gravitational collapse of Fe and O/Ne/Mg degenerate cores of single star progenitors. SN Ia are believed to arise from the accretion-induced central ignition of an accreting white dwarf. The emerging class of SN Ib and Ic (which we discuss together as SN Ibc) may originate in Fe core collapse in binary helium stars and/or by off-center ignition in accretion-induced thermonuclear explosions.

Particularly after SN Ibc are removed, SN Ia emerge as a relatively homogeneous sub-class of standard bombs, cosmologically useful as probes of the nearby peculiar velocity field and as distance indicators for H_0 and q_0.

Tammann discusses supernova statistics. The supernova rates and luminosity functions are important to nucleosynthesis and galactic evolution and for the prospects for neutrino and gravitational wave detection of stellar collapses (Lagage, Saavedra, Yvert). Questions remaining here include: are low-luminosity supernovae, such as SN 1987A and the new sub-class of SN Ibc, being undercounted? Can anything be established statistically relating supernovae to supernova remnants or to pulsars?

Late stages of stellar evolution, culminating in binary star accretion-induced thermal runaway, deflagration or detonation, are discussed (Barkat, Canal, Nomoto, Müller). A model for a centrally ignited carbon deflagration in accreting white dwarfs fits the spectra of SN Ia, and perhaps those of SN Ibc (Nomoto, Canal, Woosley and Weaver).

Type II, and possibly at least some Ibc supernovae, originate in the collapse of the degenerate cores of massive single stars by a neutrino-driven explosion (Hillebrandt, Nadyozhin, Woosley and Weaver). Although only 1% of the neutrino energy needs to be deposited at the base of the presupernova envelope, theoretical models have not yet produced a consistently strong explosion. The calculations are sensitive to nuclear equation of state (Vautherin) and numerical hydrodynamics (Müller) and, because of the weak coupling between neutrinos and matter, especially sensitive to neutrino transport (Bludman, Nadyozhin, Schinder).

Supernova 1987A is now well understood as a type II-P supernova whose luminosity is low because its progenitor evolved as a small-radius blue supergiant in a low-metallicity environment. The explosion parameters are discussed by Nomoto and by others. Its late light curve is driven by hard X-rays and gamma rays from ^{56}Co decay (Cassé and Lehoucq, Fransson).

The evolution of supernova remnants and their effects on the interstellar medium are considered by Chevalier (and Ballet). Nucleosynthesis is discussed by Thielemann, Nomoto and Hashimoto and by Woosley and Weaver. Especially interesting are the possibilities of neutrino-induced nucleosynthesis. Chemical evolution of our galaxy is treated by Schaeffer.

These formal lectures were augmented by a talk on the significance of recent solar neutrino observations (Bludman), by an exciting visit to the neutrino observatory inside the Mont-Blanc tunnel, by several films, and by evenings of observations of the clear mountain sky with a 5 in. refractor telescope at the school.

We were fortunate enough to assemble fifteen active professors from Europe, USA, Russia, Israel and Japan, who came to Les Houches for several weeks, interacting productively with the students, who were women and men from five continents, with all levels of graduate preparation. These students organized several discussion groups from which friendships and collaborations will probably emerge. We hope that the institute stimulated a new generation of young astronomers to work in the exciting, fast-moving field of supernova astrophysics.

Acknowledgements

The LIVth session of Les Houches Summer School and this volume of lectures would not have been possible without:

– the financial support from the Université Joseph Fourier of Grenoble, the Commissariat à l'Energie Atomique, the NATO Scientific Division and the NSF;
– the guidance of the Board of Trustees of the School;
– the preparation of figures by Anne Placenti and the typing of manuscripts by Brigitte Raban;
– the essential role played by Brigitte Rousset and Danielle Choupin in the preparation and administration of the session.

S.A. Bludman
R. Mochkovitch
J. Zinn-Justin

CONTENTS

Lecturers ix

Participants xi

Préface xv

Preface xix

Contents xxiii

Course 1. The frequency of supernovae, by G.A. Tammann *1*

1. Introduction 4
2. The data 5
   2.1. The sample of galaxies 5
   2.2. The sample of SNe 6
3. Relative SN rates 8
   3.1. The radial distance effect 8
   3.2. The inclination effect 9
   3.3. SN rates as function of galaxian blue luminosity 10
   3.4. SN rates as function of galaxian far-infrared luminosity 11
   3.5. SN rates as function of galaxian Hα flux 12
   3.6. Are there fast supernova producers? 13
   3.7. Relative SN frequencies 14
4. Absolute SN frequencies 18
   4.1. The Asagio search 19
   4.2. The search by the Rev. Evans 20
   4.3. The adopted SN frequencies 21
   4.4. The frequency of core collapse SNe as function of the FIR flux 23
   4.5. The frequency of core collapse SNe as function of the Hα flux 23

5. Supernova frequencies in the Local Group 25
5.1. Our Galaxy 25
5.2. Other Local Group galaxies 26
References 28

Course 2. Late stages of stellar evolution, by Zalman Barkat *31*

1. Introduction 34
2. Core–envelope separation 34
3. Evolution of carbon–oxygen stars 35
3.1. Region I 37
3.2. Region II 38
3.3. Region III 47
3.4. Region IV 48
4. Growing stellar cores – intermediate mass stars 49
References 60

Course 3. Massive stars, supernovae, and nucleosynthesis, by S.E. Woosley and T.A. Weaver *63*

1. The evolution of massive stars 66
1.1. The physics of the calculation 66
1.2. A brief overview of massive stellar evolution 73
1.3. Stars in the mass range 15 to 80 $M_{\odot}$ 77
1.4. The path to instability and neutron-star masses 83
2. Type II supernovae 88
2.1. Core collapse and bounce 88
2.2. "Delayed" explosions 90
2.2.1. An overview and some general comments 90
2.2.2. Energy absorbing and emitting processes 95
2.3. Shock propagation and break out 102
2.4. Light curves of type II supernovae 102
2.5. X-ray and γ-ray emission 103
3. Type I supernovae 106
3.1. Type Ia 106
3.1.1. Some general considerations 108
3.1.2. Deflagration flame physics 110
3.1.3. Attempts to improve on the standard model 113
3.2. Accretion-induced collapse 120
3.3. Type Ib supernovae 122

4. Explosive nucleosynthesis in supernovae of type II and Ib 127
4.1. Parameterized explosive nucleosynthesis 128
4.2. The neutrino-nucleosynthesis process 135
4.3. Nucleosynthesis of ^{26}Al 139
4.4. The α-rich freeze-out and the r-process 144
References 151

Course 4. Type Ia supernovae, white dwarfs and neutron stars, by R. Canal *155*

1. Introduction 158
2. The progenitors of type Ia supernovae 159
2.1. Observational constraints 159
2.2. SN Ia rates and progenitor population 160
2.3. Progenitor evolution: mass-accreting C+O white dwarfs 161
2.3.1. H-accreting white dwarfs 163
2.3.2. He-accreting white dwarfs 166
2.3.3. C+O-accreting white dwarfs 166
2.4. Galactic evolution of SN Ia progenitors 168
3. White dwarf physics and type Ia supernovae 169
3.1. The cooling of white dwarfs 169
3.2. The physics of phase transition in white dwarf interiors 170
3.3. Nuclear reaction rates 173
3.4. Mass accretion and core heating 175
3.5. Core ignition and burning propagation 178
3.6. Electron captures and mixing 181
4. Neutron stars in binary systems 185
4.1. X-ray binaries 185
4.1.1. High-mass X-ray binaries 185
4.1.2. Low-mass X-ray binaries 186
4.2. Binary and millisecond pulsars 186
4.3. Formation mechanisms 187
4.3.1. Core collapse of massive stars 187
4.3.2. Capture mechanisms 187
4.3.3. Accretion-induced collapse of white dwarfs 189
4.4. The origin of neutron stars in binaries 189
4.4.1. High-mass X-ray binaries 189
4.4.2. Low-mass X-ray binaries 190
4.4.3. Binary and millisecond pulsars 192

5. Summary 194
References 195

Course 5. *Type I supernovae and evolution of interacting binaries, by K. Nomoto, H. Yamaoka, T. Shigeyama, S. Kumagai and T. Tsujimoto* *199*

1. Type I supernovae and related events 202
2. Evolution of accreting white dwarfs 204
   2.1. Hydrogen shell flashes 205
   2.2. Helium shell flashes 210
   2.3. Merging C+O white dwarfs 212
3. Type Ia supernovae 213
   3.1. Carbon deflagration model 213
   3.2. Deflagration/detonation hybrid models 215
   3.3. Carbon detonation in smaller-mass white dwarfs 218
   3.4. Light curves 219
   3.5. Spectra 223
4. Accretion-induced collapse of white dwarfs 225
   4.1. Low-mass X-ray binaries and binary pulsars 225
   4.2. Solid C+O white dwarfs 226
   4.3. O+Ne+Mg white dwarfs 227
   4.4. Conditions for accretion-induced collapse 230
5. Type Ib/Ic supernovae 232
   5.1. Evolution of interacting binaries 233
   5.2. Nucleosynthesis 234
   5.3. Rayleigh–Taylor instabilities and mixing 235
   5.4. Light curves 238
6. Evolutionary origin of binary pulsars 241
7. Concluding remarks 245

References 246

Course 6. *Models of type II supernovae: an introduction, by Wolfgang Hillebrandt* *251*

1. Introduction and statement of the problem 254
2. Observations of type II supernovae 255

3. Input physics 261
3.1. The basic equations 262
3.2. Initial models 263
3.3. The equation of state of supernova matter 264
3.3.1. The "low" density EOS 265
3.3.2. Self-consistent single-particle models 269
3.4. Weak interaction rates and neutrino transport 275
4. Hydrodynamics (one-dimensional) 281
4.1. Newtonian physics 281
4.2. General relativistic hydrodynamics 286
5. Core collapse supernova models and their problems 287
5.1. An analytic description of core collapse 287
5.2. Numerical simulations and their main results 290
6. Summary, conclusions, and outlook 295
References 297

Course 7. The neutrino signal from a collapsing star, by D.K. Nadyozhin *301*

1. The neutrino signal from a collapsing star 304
1.1. Introduction 304
1.2. The neutrino radiation immediately before the beginning of the collapse 304
1.3. Simple estimates of the neutrino signal properties 307
1.4. Detailed calculations of the neutrino signal 313
1.5. The neutrino signal from Supernova 1987A 320
1.6. Conclusions 322
2. The neutrino heat conduction theory 325
2.1. Introduction 325
2.2. The neutrino transfer equation, stimulated absorption and the neutrino Kirchhoff law 326
2.3. The elements of neutrino hydrodynamics 331
2.4. The neutrino heat conduction approximation 335
2.5. The kinetics of beta-processes and lepton charge diffusion 337
2.6. Conclusions 341

Course 8. Nuclear physics of hot dense matter, by D. Vautherin *345*

1. Introduction 348

2. The phase diagram of hot nuclear matter 349
2.1. Effective nucleon–nucleon interactions 349
2.2. A simplified Skyrme interaction 350
2.3. Mean-field equations at finite temperature 351
2.4. Solution for hot nuclear matter 352
2.5. Cold nuclear matter 353
2.6. High-temperature limit 354
2.7. Phase diagram of nuclear matter 355
2.8. The compound nucleus model of Bonche and Levit 356
2.9. An approximate calculation of the limiting temperature 357
3. Equation of state at subnuclear densities 360
3.1. Introduction 360
3.2. Macroscopic approaches 360
3.3. Microscopic methods: the Wigner–Seitz approximation 362
3.4. The bulk matter approximation 363
3.5. Approximate solution of the equilibrium equations 364
3.6. The compressible liquid drop model 368
3.7. Thomas–Fermi calculations 370
3.8. Hartree–Fock calculations 371
3.9. Sub-saturation phases of nuclear matter 372
4. Beyond nuclear density 375
4.1. Non-relativistic many-body calculations 375
4.2. Relativistic mean-field calculations 377
4.3. Density dependent relativistic corrections 381
4.4. Relativistic Brueckner–Hartree–Fock calculations 382
4.5. Many-body calculations with relativistic corrections 383
4.6. Experimental studies of the equation of state 385
5. Discussion 388
References 389

Course 9. Multidimensional hydrodynamical simulations of supernova explosions, by Ewald Müller *393*

1. Introduction 397
2. Numerical methods 398
2.1. Lagrangian and Eulerian methods 399
2.2. Explicit and implicit methods 400
2.3. Accuracy and efficiency 401
2.4. Conservative difference schemes 403
2.5. Operator splitting or fractional-step coupling 408
2.6. Godunov-type difference methods 411

3. Core collapse with rotation 415
3.1. Overview of expected effects 416
3.2. Equilibrium sequences 420
3.3. Hydrodynamical simulations 424
3.4. Gravitational radiation from collapsing rotating cores 428
4. Instabilities and mixing in type II supernova explosions 432
4.1. Observational evidence from SN 1987A 432
4.2. Rayleigh–Taylor instability 433
4.3. RT instabilities in supernova explosions 434
4.4. Simulations of RT instabilities in polytropes 435
4.5. Simulations of RT instabilities in realistic stellar models 435
4.5.1. Numerical methods 436
4.5.2. Initial models 438
4.5.3. Linear stability analysis 439
4.5.4. Results of two-dimensional simulations 441
4.5.5. Results of three-dimensional simulations 444
4.5.6. Mixing 446
4.5.7. Implications 447
5. Thermonuclear burning fronts and type Ia supernovae 450
5.1. General considerations 450
5.2. Shock waves 452
5.3. Simple theory of steady plane detonations and deflagrations 455
5.4. Detonations and type I supernova models 457
5.5. Deflagrations and type I supernova models 461
5.6. Hydrodynamics and nuclear burning 464
5.7. Hydrodynamic simulations of detonations 468
5.7.1. Detonations caused by numerical errors 469
5.7.2. Detonations with single exothermic reaction 473
5.7.3. Detonation with α-network 476
References 484

Course 10. Supernova 1987A: from progenitor to remnant, by K. Nomoto, T. Shigeyama, S. Kumagai, H. Yamaoka and T. Suzuki *489*

1. Introduction 493

2. Progenitor of SN 1987A 494
2.1. Observations 494
2.2. Blue to red evolution and mass loss 494
2.3. Red to blue evolution and mixing 496
2.4. Lifetime in the HR diagram 500
2.5. Presupernova evolution of the core 501
2.5.1. Quasi-static nuclear burning 502
2.5.2. Presupernova composition structure 502
3. Explosive nucleosynthesis 504
3.1. Explosive nuclear burning 504
3.2. Isotopic ratios and radioactive elements 508
3.3. Comparison to the observed abundances in SN 1987A 509
4. Optical light curve 511
4.1. Shock propagation and hydrodynamical structure 511
4.2. Early light curve 515
4.3. Hydrogen recombination front 519
4.4. Radioactive decays, mixing of ^{56}Ni, and Bochum event 521
4.5. Plateau-like peak and hydrogen recombination 525
4.6. Constraints on explosion energy 527
5. X-ray light curve and clumpy mixing 528
5.1. X-ray light curves at $t < 300$ d 529
5.2. X-ray light curve at $t > 300$ d and effects of clumps 529
5.3. Gamma-ray light curves 531
5.4. X-ray and γ-ray spectra 531
6. Rayleigh–Taylor instabilities and mixing 535
6.1. Linear stability analysis 535
6.2. Two-dimensional hydrodynamic calculation 537
6.3. Mixing 538
6.4. Comparison with observations 541
7. Dust formation 542
8. Pulsar and other radioactive elements 546
8.1. Contributions of ^{57}Co and ^{44}Ti 546
8.2. Predicted line γ-rays 549
8.3. Contribution of the pulsar 549
8.4. Predicted hard radiation from the pulsar 551
8.5. X-rays from the neutron star surface 554

9. Soft X-ray emission and circumstellar matter 555
9.1. Structure of circumstellar matter 555
9.2. Soft X-ray flare and collision with a circumstellar cloud 558
9.3. Collision with the red supergiant shell 559
9.4. Collision with the ring 561
References 564

Course 11. The shock wave breakout and the early supernova hydrodynamics, by D.K. Nadyozhin 569

1. The shock wave breakout and early supernova hydrodynamics 572
1.1. Introduction 572
1.2. Shock wave propagation through the stellar envelope 573
1.3. The self-similar solution 575
1.4. The peak parameters of the shock wave breakout 576
1.5. The beginning of supernova envelope expansion and the transition to inertial outflow 579
1.6. Cooling-and-recombination wave in supernova envelopes 582
1.7. Conclusions 586

Course 12. High energy emission of supernovae and some additional remarks on supernova statistics, by M. Cassé and R. Lehoucq 589

1. Theoretical tools 592
1.1. Historical background 592
1.2. Decay and production of radioactive nuclei 593
1.3. Gamma ray–matter interaction 597
1.3.1. Elementary processes 597
1.3.2. Simple analytic treatment of the problem 599
1.3.3. Observed spectrum 605
1.4. Monte Carlo simulations 607
2. Applications 608
2.1. The case of SN 1987a 609
2.1.1. Fit of the light curve 613
2.1.2. Astrophysical consequences 618
2.1.3. What about a central source? 619
2.2. Gamma ray lines from other supernovae 620
3. Conclusion 623

4. Appendix 625
4.1. Notation 625
4.2. Fundamental constants and units 625
References 626

Course 13. Nucleosynthesis in supernovae, by Friedrich-Karl Thielemann, Ken'ichi Nomoto and Masaaki Hashimoto *629*

1. Introduction 632
2. Thermonuclear rates and reaction networks 632
2.1. Thermonuclear reaction rates 632
2.2. Nuclear reaction networks 635
3. Nucleosynthesis 637
3.1. Hydrostatic burning stages in presupernova evolution 637
3.2. Explosive burning 639
3.2.1. Explosive Si-burning 639
3.2.2. Explosive O-burning 640
3.2.3. Explosive Ne, C, and He-burning 641
3.2.4. r-Process 641
3.2.5. Explosive H-burning 642
3.3. Nucleosynthesis in supernovae 642
4. Type Ia supernovae (SNe Ia) 643
4.1. Explosive burning conditions 643
4.2. Abundances in ejecta 645
5. Type II supernovae (SNe II) 646
5.1. Basic features 648
5.2. Detailed calculations 651
5.2.1. SN 1987A – a 20 $M_\odot$ star 651
5.2.2. 13, 15, and 25 $M_\odot$ models 659
5.3. Gross properties of ejecta 660
6. Averaged SN II abundance yields 667
7. SN I and SN II contributions to nucleosynthesis 671
References 673

Course 14. The late emission from supernovae, by Claes Fransson *677*

1. Introduction 680
2. Hydrodynamical and chemical structure 681

3. Gamma-ray thermalization 685
3.1. Radioactive input 685
3.2. The gamma-ray spectrum 685
3.3. Gamma-ray thermalization 686
3.4. Electron thermalization 688
3.5. Positrons 695
4. Thermal and ionization equilibrium 696
5. Line formation 700
6. Plasma diagnostics 707
7. The spectra of type II supernovae 710
7.1. The hydrogen envelope 710
7.2. The helium mantle 716
7.3. The oxygen core 717
7.4. The iron core 724
8. Type Ia supernovae 726
9. Mixing 726
10. Formation of molecules 727
11. Dust formation in supernovae 729
12. Effects of a neutron star 731
13. Circumstellar excitation 734
14. Conclusions 738
References 739

Course 15. Supernovae and the interstellar medium, by Roger A. Chevalier *743*

1. Introduction 746
2. Supernovae 746
3. The interstellar medium 748
4. Circumstellar environments 750
5. Hydrodynamic evolution 752
6. Circumstellar interaction 756
7. X-ray and infrared emission from hot gas 759
8. Shock wave emission and stability 762
9. Future prospects 764
References 765

Seminar 1. The search for supernovae at the Observatoire de la Côte d'Azur, by Christian Pollas *769*

1. Presentation 772
2. The SN search 772

3. The OCA Schmidt results 776
3.1. What is my method? 776
3.2. Some advice 779
4. Must we continue? 784
References 786

Seminar 2. General relativistic neutrino hydrodynamics: the physics of and numerical techniques for modeling stellar collapse and the early cooling of neutron stars, by Paul J. Schinder *785*

1. Introduction 789
2. General relativistic hydrodynamics 791
2.1. Preliminaries 792
2.2. The equations of polar sliced neutrino hydrodynamics 793
2.3. Numerical techniques 795
2.4. Summary 796
3. General relativistic neutrino transport 796
3.1. The role of neutrinos 796
3.2. The neutrino transport equations 798
3.3. The variable Eddington factor method 800
3.4. Other transport treatments 802
4. Neutrino interactions with the gas 803
4.1. The basic neutrino interactions 803
4.2. The interaction functions G and L 805
5. Conclusion 806
References 806

Seminar 3. The chemical evolution of the galaxy, by R. Schaeffer *809*

1. Introduction 812
2. Modelling galactic chemical evolution 814
2.1. Star formation 814
2.2. Supernova rate 814
2.3. Evolution equation 815
3. The sources of metals 816
3.1. Mass ejection by winds 816
3.2. Type I supernovae 816
3.3. Type II supernovae 817
3.4. Peculiar types of supernovae 817

4. History of galactic evolution modelling. Role of the supernovae 820
References 823

Seminar 4. Solar neutrinos: physics beyond the standard model?, by Sidney A. Bludman *823*

1. Standard solar models: is there a solar neutrino problem? 826
   1.1. Predicted solar neutrino detection rates 826
   1.2. Time variation? 827
2. Distinguishing new neutrino physics from solar model questions 828
   2.1. Neutrino oscillations 828
   2.2. Parke formula for ν_e persistence probability 831
   2.3. Neutrino spectral shape observed at Kamiokande II 833
   2.4. Total rates observed at Kamiokande II, Homestake and Sage 834
3. Physics beyond the standard model 834
   3.1. Neutrino flavor mixing 835
   3.2. See-saw formula for light neutrino masses 836
   3.3. Extrapolation for the τ neutrino mass 837
4. Terrestrial searches for neutrino oscillations 837
5. Conclusions 838

References 839

COURSE I

THE FREQUENCY OF SUPERNOVAE

G. A. TAMMANN

Astronomisches Institut der Universität Basel, Basel, Switzerland, and
European Southern Observatory, Garching, Germany

S. Bludman, R. Mochkovitch and J. Zinn-Justin, eds.
Les Houches, Session LIV, 1990
Supernovae

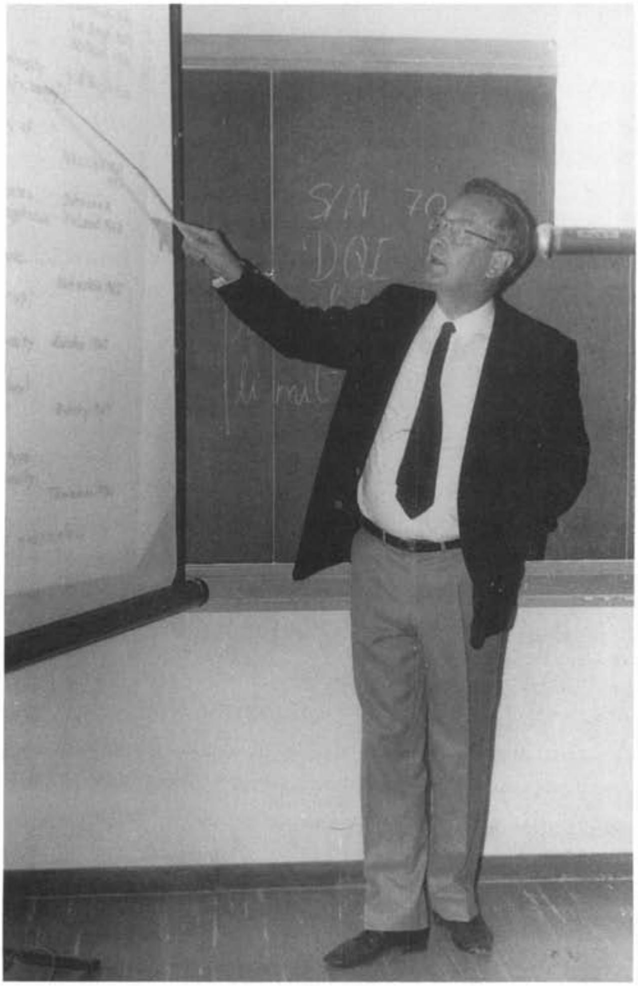

Contents

1. Introduction 4
2. The data 5
   2.1. The sample of galaxies 5
   2.2. The sample of SNe 6
3. Relative SN rates 8
   3.1. The radial distance effect 8
   3.2. The inclination effect 9
   3.3. SN rates in function of galaxian blue luminosity 10
   3.4. SN rates in function of galaxian far-infrared luminosity 11
   3.5. SN rates in function of galaxian Hα flux 12
   3.6. Are there fast supernova producers? 13
   3.7. Relative SN frequencies 14
4. Absolute SN frequencies 18
   4.1. The Asagio search 19
   4.2. The search by the Rev. Evans 20
   4.3. The adopted SN frequencies 21
   4.4. The frequency of core collapse SNe in function of the FIR flux . . . 23
   4.5. The frequency of core collapse SNe in function of the Hα flux . . . 23
5. Supernova frequencies in the Local Group 25
   5.1. Our Galaxy 25
   5.2. Other Local Group galaxies 26
References 28

1. Introduction

The present remarks on supernova[1] frequencies draw heavily on three recent papers (Schröder, Schwengeler, and Tammann, 1991, hereafter SST; van den Bergh and Tammann, 1991, hereafter vdBT; Tammann and Schröder, 1991, hereafter TS). For additional details the reader is referred to these sources.

SN frequencies are an important input parameter for stellar and galaxian evolution. The basic statistics of SNe are very simple. The difficulty lies, as in all fields of astronomy, in the definition of fair samples of SNe and galaxies. In addition, even an optimist can define, in the case of SNe and their parent galaxies, only a badly restricted sample. One stands therefore typically against the pitfalls of small-number statistics.

SN frequency determinations began with Zwicky (1938) and contended themselves for almost forty years with frequencies per "average galaxy". The ensuing controversy of "average" frequencies was caused by the lack of detailed data of the parent galaxies. As Hubble types of a sufficient sample of parent galaxies and at least their *relative* luminosities (from recession velocities) became available, it became clear that different types of SNe have quite different rates in galaxies of different Hubble type and of different luminosity. It became also increasingly clear (Tammann, 1974) that existing SN catalogues suffer severe systematic selection effects, which must be taken into account if physically meaningful SN frequencies are to be determined. In addition the different peak luminosities of SNe of different type have an important effect on their detection probability (Cappellaro and Turatto, 1988; Evans et al., 1989).

In the following it is assumed that only three types of SNe exist, viz. Ia, Ib, and II. SNe Ic are included in Ib; SNe IIℓ and IIp are not distinguished. SNe Ia occur in E and S0 galaxies; in spirals they belong to the old disc population (not halo population! (Tammann, 1977)). SNe Ib are assumed to have massive progenitors, like SNe II, and therefore to belong to the young population.

[1] In the following: supernova = SN, supernovae = SNe.

It is reasonable to assume that the SN rate of a galaxy is proportional to its mass. However, total masses of galaxies are poorly known. On the assumption that the mass-to-light ratio of a given type of galaxy is nearly constant, the mass of a galaxy can be substituted by its luminosity. Indeed one can show that the SN rate scales with the luminosity of a galaxy (section 3.4). One wants therefore not the number of SNe per "average galaxy", but the number of SNe per unit luminosity L (here in solar luminosities $L_{B\odot}$ with $M_{B\odot} = 5^m.48$ assumed). Hence the frequency ν (in years^{-1}) per unit luminosity ($10^{10} L_{B\odot}$) becomes

$$\nu = \frac{N_{SN}}{\Sigma_n (L_i \Delta t_i)}$$

where N_{SN} is the number of SNe that n galaxies have produced, of which the ith galaxy has the luminosity L_i and has been controlled during Δt_i years.

The control time Δt is the sum of the time intervals during which a SN in a given galaxy could not have escaped detection. Δt depends on the apparent magnitude limit m_L of the search, on the epoch of observations, on the distance of the parent galaxy, on the maximum luminosity of the SN and on the shape of its light curve before and after maximum. Δt must therefore be calculated separately for each galaxy and each type of SN.

It has become customary to express SN frequencies ν in "supernova units" = SNu. One SNu corresponds to 1 SN per 100 years per $10^{10} L_{\odot}$. Note that the luminosity scales with the Hubble constant like H_0^{-2}. $H_0 = 50$ km s^{-1} Mpc^{-1} is assumed throughout this paper. For other values of H_0 the SNu values scale therefore with $(H_0/50)^2$.

Only for a minority of all known SNe can the control times be calculated. Most SNe have been found more or less serendipitously. Therefore, to minimize the effects of small-number statistics, the following strategy is used to determine SN frequencies: only *relative* SN rates are derived from a relatively large sample of galaxies (section 3), and then these relative rates are *absolutely* calibrated using two rather restricted SN searches with good control times (section 4).

2. The data

2.1. The sample of galaxies

It is very important to define *objectively*, i.e., independently of SN productivity, a sample of galaxies from which SN frequencies are to be determined. Otherwise it is not possible to decide how many bright, fainter, and faintest galaxies in the field of a detected SN have *potentially* contributed to the discovery.

The galaxy sample should be as large as possible, but on the other hand the galaxies should be nearby and reliable parameters, such as Hubble type, recession velocity, magnitude, etc., should be known. In distant galaxies the discrimination against intrinsically faint SNe becomes severe and SNe in the inner parts of the parent galaxies are lost (cf. section 3.1).

The best compromise seems to be to consider galaxies of the Shapley–Ames Catalog (Sandage and Tammann, 1987) with distances smaller than or equal to the Virgo cluster. Relative distances are determined from recession velocities (corrected for a self-consistent Virgocentric infall model). Luminosities are calculated, as stated before, by assuming H_o = 50 km s^{-1} Mpc^{-1} (Sandage and Tammann, 1990), except for the nearest galaxies for which Cepheid distances are used. Galaxy luminosities are corrected for Galactic and internal absorption.

The choice leads to what is called the "fiducial sample" (for a galaxy listing see SST), consisting of 342 galaxies. This all-sky sample is not necessarily homogeneously searched for SNe. The northern hemisphere has been under scrutiny longer than the southern one. But as long as it is used only to derive *relative* SN rates equal control times are not required. The control times may even be distance-dependent. It is important only that the intensity of the search not be a function of Hubble type and be independent of the specific SN productivity of a sample galaxy.

2.2. *The sample of SNe*

The galaxies of the fiducial sample have produced 97 SNe as of March 1, 1990. The SNe are taken from the list of Barbon, Cappellaro, and Turatto (1989) for the period up to December 31, 1988, and thereafter from the IAU Circulars. The types of the SNe are taken from the same sources; this somewhat arbitrary policy dissolves some contradictions in the literature. Note, however, that for 35% of all SNe of the sample no type is available or they are classified only as "Type I" (Ia of Ib?)! Contrary to Barbon et al. (1989) variable n° 16 in NGC 2403 (Tammann and Sandage, 1968) was not accepted as a SN.

For calculating the control times of different SN types some assumptions must be adopted as to their photometric properties.

SNe Ia are assumed to be perfect standard candles, i.e., they have a uniform absolute magnitude at maximum (Tammann, 1982; Cadonau et al., 1985;

Leibundgut, 1990; Branch and Tammann, 1991). $M_{\max} = -19.79$ is adopted (Leibundgut and Tammann, 1990). The shape of the standard light curve is taken from Cadonau et al. (1985).

The presently available photometric data on SNe Ib do still not allow firm conclusions as to their maximum absolute magnitude $M_{\max}$ and the intrinsic scatter σ_M about this value. $M_{\max} = -18.2$ and $\sigma_M = 0^{\mathrm{m}}$ is adopted here, although there is some evidence that SNe Ib are a less homogeneous class than SNe Ia. The shape of the Ib light curve is assumed to be the same as that of Type Ia (Wheeler and Harkness, 1990).

SNe II are on average considerably fainter than SNe Ia, and even fainter than SNe Ib. Following Tammann and Schröder (1990) for $M_{\max}$ I adopt a broad Gaussian distribution with $\langle M_{\max} \rangle = -17.18$ and $\sigma_M = 1.^{\mathrm{m}}2$ (fig. 1). This luminosity function allows for the strongly underluminous SN 1987A in LMC, but it would be a rather rare event. Miller and Branch (1990) have argued, that similarly faint SNe II are quite frequent objects, but that they are systematically discriminated against in existing searches. More extreme yet is the proposal of Schmitz and Gaskell (1988) that underluminous SNe like SN 1987A dominate the SN population. This conclusion, however, is based on the so-called $V/V_{\max}$ test, which is applicable only if the discovery chance is independent of distance out to a limiting distance $r_{\max}$. But parent galaxies are situated at discrete distances, and even if a background galaxy occasionally lies in the line of sight, the discovery of a SN out there is extremely unlikely. I believe one can set quite stringent limits on the number of SNe with $M_{\max} \sim -15$ from nearby galaxies which have been searched for Cepheids and other variables over extended periods. But this does not preclude that there may be a new, populous type of SNe of only $M_{\max} > -12$. Some theories in fact consider the possibility of "dark" SNe. This possibility introduces the largest uncertainty into present SN statistics. It should be borne in mind that the following SN frequencies allow for only a decreasing number of SNe fainter than $M_{\max} = -17.18$.

The absolute magnitudes shown in fig. 1 are corrected for absorption in our Galaxy, but not for intrinsic absorption in the parent galaxies. This correction is in principle not justified because the discovery chance of a SN is governed by its apparent luminosity, not by its intrinsic luminosity. Strictly speaking no correction for Galactic absorption should be applied to SNe either. But it would be cumbersome to calculate control times for all galaxies according to their individual front absorption. With a mean front absorption of only $A_{\mathrm{B}} \sim 0.15$ for the galaxies of the fiducial sample, the Galactic absorption introduces only a second-order effect.

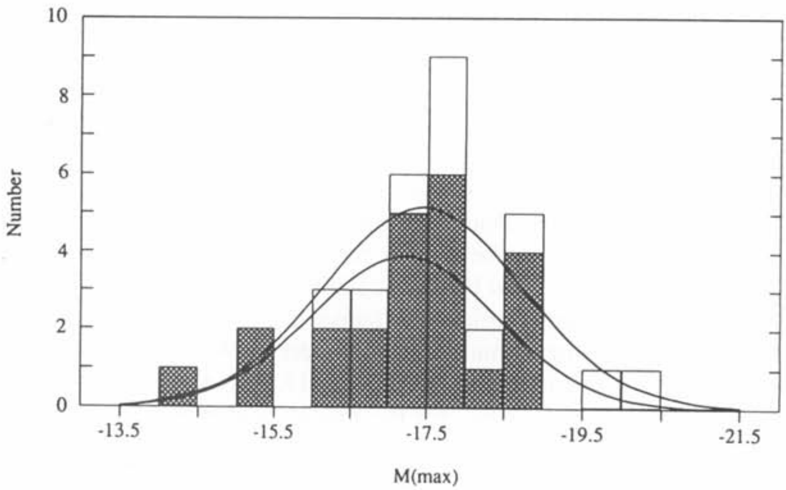

Fig. 1. The distribution in absolute magnitude of a minimum bias sample of SNe II with known maximum brightness. Shaded squares are SNe II nearer than the Virgo cluster. The narrower Gauss function is a fit to the nearer sample; the wider curve represents the combined sample.

3. Relative SN rates

Observed SN numbers are subject to several selection effects, which are explained in this section. In addition the fiducial sample is used to test the basic assumption that the SN productivity is proportional to the galaxian luminosity (in blue as well as in far-infrared (FIR) and Hα light). Also Zwicky's notion of the existence of "fast producers" is investigated. The section is concluded with an investigation of the *relative* frequencies of SNe of different types in galaxies of different bins of the Hubble sequence.

3.1. The radial distance effect

If one plots the projected distances of a SN from the center of its parent galaxy versus the recession velocity of that galaxy, one notices that the radial distance of SNe increases with increasing distance from the observer. In fact the data reveal a distance-dependent lower cutoff, below which no SNe have been found. At a recession velocity of 5000 km s^{-1} the cutoff already conceals the inner 50% of all SNe, assuming that the radial distribution of SNe is everywhere the same. This effect, which was described by Shaw

(1979), can only be due to the high surface brightness in the inner parts of galaxies, which impairs the discovery chance of SNe.

The bias introduced by the Shaw effect seems to be very small for nearby galaxies out to the Virgo cluster. For the fiducial sample the effect is therefore neglected. For SN statistics involving more distant galaxies the effect is expected, however, to be of major importance.

3.2. The inclination effect

The discovery rate of SNe in face-on spirals is considerably higher than in edge-on galaxies (Tammann, 1974, 1982). The reality of the effect has been questioned for a long time, but is now well confirmed (Cappellaro and Turatto, 1988; van den Bergh and McClure, 1990). The best evidence comes from the fiducial sample (SST) and is shown in table 1.

Table 1, columns 3 and 4, show the total blue and FIR (cf. 3.4) luminosities of the relevant galaxies of the fiducial sample. (Individual luminosities are listed in SST.) The number of galaxies involved from column 2 is not the same for blue and FIR luminosities, because FIR magnitudes are missing for a few sample galaxies. For the same reason the number of SNe from column 5 is not the same for the two different colors.

Columns 6 and 7 show the importance of the inclination effect. The number of SNe per unit luminosity, regardless whether blue or FIR luminosities are considered, is about *four* times lower in inclined spirals than in edge-on objects. From this it is clear that SN frequencies would be grossly underestimated if the inclination effect were neglected.

A more detailed analysis shows that the inclination effect sets in quite abruptly at $i \sim 30°$ (SST; cf. also van den Bergh and McClure, 1990). Neither the cause for this nor the cause for the inclination effect is, in general, well understood. It seems reasonable to consider absorption in the parent galaxy *and* the increased surface brightness of inclined galaxies (Tammann, 1974, 1982; SST; cf. however, van den Bergh and McClure, 1990). The discriminating effect of high surface brightness is also revealed by the radial-distance effect (section 3.1).

Table 1
Relative SN rates in spiral galaxies (SO/a–Im) of different inclination

Inclination (1)	$n_{\rm Gal}$ (2)	$\Sigma L_{\rm B}$ (3)	$SL_{\rm FIR}$ (4)	$n_{\rm SN}$ (5)	$n_{\rm SN}/\Sigma L_{\rm B}$ (6)	$n_{\rm SN}/\Sigma L_{\rm FIR}$ (7)
$i \leq 30°$	42/41	114.83	24.42	35	0.30	1.43
$i > 30°$	210/201	604.56	128.26	47/46	0.078	0.359
face-on/inclined					3.8 ± 0.9	4.0 ± 0.9

One may suspect that the inclination effect in spiral galaxies is more severe for SNe from massive progenitors (Type II and Ib) than for SNe of the old population, because the former are expected to be embedded more deeply into the interstellar dust. A corresponding test (SST) can use only SNe of known type and carries correspondingly rather high statistical errors. The inclination factors become 5.0 ± 1.6, 3.7 ± 4.0, and 1.5 ± 1.0 for Type II, Ib, and Ia, respectively. These values point into the expected direction.

The inclination effect may also be a function of galaxy type, because the dust content and the surface brightness vary through the Hubble sequence. Indeed SST have found inclination factors of about 4, 2.5, and 1.2 for Sbc–Sd, Sab–Sb, and S0/a–Sa galaxies respectively. For the rather transparent Sdm–Im galaxies these authors assume the inclination effect to be negligible. These galaxy-type-dependent inclination factors are also adopted in the present paper. The additional dependence on SN type must be neglected here, because the fiducial sample contains a large fraction of SNe of unknown type.

A word of caution is in order. The inclination effect may well depend on the search technique employed. For instance, if the inclination effect is partially caused by surface brightness, it should depend on the focal length of the telescope. Indeed the SN search by the Rev. Evans (section 3.2), whose *visual* search technique is particularly insensitive to surface brightness, is apparently free of any inclination bias.

3.3. SN rates in function of galaxian blue luminosity

As stated above, one expects SN rates to be proportional to galaxy mass and hence to galaxy luminosity. Yet this expectation must be tested, for which goal an unparalleled wealth of data is now available. The test must be restricted to Sbc–Sd galaxies, because other types of galaxies have systematically different SN rates (section 3.7). In fact within the fiducial sample only Sbc–Sd galaxies have produced enough SNe for a stringent test.

The Sbc–Sd galaxies of the fiducial sample are binned according to blue absolute magnitude $M_{\mathrm{B}}^{o,i}$ (corrected for Galactic and intrinsic absorption) in table 2, column 1. Their individual luminosities (in 10^{10} solar units) are summed up in column 2. Here a special trick is applied to allow for the inclination effect. For test galaxies with $i > 30^{\circ}$ the luminosity is divided by the appropriate inclination factor (here $4\times$) as discussed in section 3.2. In this way each galaxy enters with the weight that corresponds to its *observable* SN rate. The notation L^{i} is used in the following to remind the reader that the luminosity L is reduced, where appropriate, by the galaxy type-specific inclination factor. It is clear that the *true* SN rate, including SNe hidden by the inclination effect, should not be related to L^i, but rather to the true luminosity L.

Column 3 of table 2 lists the known number of SNe of all types per luminosity bin. The relative SN rates per unit luminosity are shown in column 4. Within the statistical errors the values scatter about the mean value of 0.37 SNe per $10^{10} L_\odot$. This result verifies the claim that the SN productivity is proportional to the galaxian luminosity.

Table 2
Relative SN rates per unit B luminosity for Sbc–Sd galaxies in function of their absolute B magnitude

$M^{o,i}$ (1)	ΣL^i_B (2)	n_{SN} (3)	$n_{SN}/\Sigma L^i_B$ (4)
−16 ... − 18	.33	0	¡3.03
−18 ... − 19	3.21	1	0.31
−19 ... − 20	24.81	7	0.28
−20 ... − 21	47.74	26	0.54
−21 ... − 22	62.76	20	0.32
−22 ... − 23	26.22	7	0.27
Total	165.06	61	0.37

As stated before, the test cannot be extended to other Hubble types because of the small number of SNe known. However, it seems natural to assume that if SN rates are proportional to blue luminosity in the case of Sbc–Sd galaxies, the relation holds for *all* types of galaxies.

3.4. SN rates in function of galaxian far-infrared luminosity

The rate of SNe from *massive* progenitors should be proportional to the number of massive, i.e., hot stars in a galaxy. The total blue luminosity of a galaxy is not a particularly good indicator of that number. One wonders therefore whether there is a more specific indicator for the massive population of a galaxy. The color (B–V) may have some merit, and indeed SN frequencies do correlate with the galaxian color (Tammann, 1977; Oemler and Tinsley, 1979), but again this color is not specific for the young population. (U–B) colors would be more promising, but this color is known for only an insufficient number of galaxies.

The proposal of Jørgensen (1990) to correlate the SN rate with the far-infrared (FIR) fluxes (at 60 and 100 μm) of galaxies measured by the IRAS satellite is very interesting because FIR luminosities reflect the heating of the interstellar disk by massive stars. The proposal by Jørgensen has been followed up by SST. These authors have compiled for (almost) all galaxies of the fiducial sample FIR luminosities L_{IR}. In order to compare these luminosities with the *observed* number of SNe they must be reduced by the appropriate inclination factor (section 3.2). After subdividing the resulting luminosities L^i_{IR} into five bins of increasing luminosity, SST have found the relative SN rate per unit FIR luminosity to *decrease* with increasing luminosity. The SN rate is therefore *not* proportional to the FIR luminosity. Instead SST have found the SN rate to be proportional to $(L^i_{\mathrm{IR}})^{0.8}$. This power law is not so surprising because L_{IR} does not measure the *number* of massive stars, but rather the *temperature* of the interstellar dust heated by massive stars.

The above analysis should be restricted to Type II and Ib SNe. However, this restriction would invite additional problems of small-number statistics. SST have therefore considered all SNe irrespective of type. Yet, it seems unlikely that this (necessary) inaccuracy could have a qualitative effect on their conclusion.

While in the case of blue luminosities SN rates depend on L_{B} *and* the Hubble type, one may hope that the rate of SNe (of Type II and Ib) can be well predicted by the single parameter L_{IR}. The FIR luminosities are therefore potentially a more powerful indicator of SN rates. SST have checked whether the relative SN rate per unit FIR luminosity is indeed independent of the Hubble type. Unfortunately the hope is not borne out; the dependence on galaxy type seems to persist. I will return to this question in section 4.4.

Even with the dependence on Hubble type, the FIR luminosities are probably equally good indicators of the rates of Type II and Ib SNe as blue luminosities.

3.5. SN rates in function of galaxian Hα flux

Another indicator of the number of massive stars in a galaxy is its Hα flux. Hydrogen atoms are ionized by Lyman continuum photons that come essentially only from stars with more than 10 $M_{\odot}$. Therefore there must be a correlation between Hα flux and the rate of SNe of Type II and Ib, but none is expected for SNe Ia.

Unfortunately Hα observations are available for only a fraction of the galaxies of the fiducial sample. However, Kennicutt and Kent (1983) have provided good Hα fluxes for 126 galaxies of type S0/a–Im, many of which lie beyond the fiducial sample. This sample of galaxies was subjectively selected and one can but assume that the selection was done *independently* of the presence of known SNe.

In an excellent paper Kennicutt (1984) has shown that the *known* SNe of Type II, that have occurred in his Hα sample, lie preferentially in galaxies of high absolute Hα flux. The correlation of SN rate and Hα luminosity is in fact highly significant and is well fit by a direct proportionality. No such correlation was found for SNe I.

The SN sample available to Kennicutt (1984) was quite restricted and necessarily affected by various selection effects. Moreover, SNe Ia and SNe Ib could not yet be distinguished in 1984. Therefore, in order to test Kennicutt's (1984) result, TS have determined the Hα luminosities of the 126 sample galaxies, using their adopted distance scale. In addition they have calculated the hypothetical number of Type II and Ib SNe from the *blue* luminosity of each galaxy by means of the Hubble type-dependent, absolute SN frequencies from table 4. Then breaking the sample down into different bins of Hα luminosity, shows that the SN rate per *unit* Hα luminosity is indeed constant over the whole luminosity range. If instead the sample is broken down into different Hubble types, no variation of the SN rate per unit Hα luminosity is found within statistics. This means that the Hα luminosity is a powerful indicator of the SNe II and SNe Ib rate, without the need of a second parameter (e.g., Hubble type).

3.6. Are there fast supernova producers?

There is the notion that there are some galaxies that have an intrinsic overproduction of SNe. There are indeed some galaxies with multiple SN occurrences. The most extreme cases are NGC 6946 with six SNe and NGC 5236 with five SNe. An ad hoc explanation of this is to assume that these galaxies have experienced a star formation burst in the recent past and that they contain an excess number of massive stars that die now as SNe of Type II or Ib (see, e.g. Rosa and Richter, 1988).

An alternative possibility is that the multiple SN events are just fluctuations caused by chance. This is to say that the number of (known) SNe is *only* a function of (inclination-corrected) blue luminosity L_B^i and of galaxian type, and that deviations from the calculated frequency are simply the consequence of small-number statistics of single events.

It is possible to apply a decisive test to distinguish between the two possibilities, i.e., true overproducers versus statistical fluctuations. If namely the multiple SN events are caused by chance, their observed number must be reproduced (statistically) by Monte Carlo trials, for which the probability to produce a SN is governed only by luminosity L_B^i and galaxian type. Because the trials calculations are to be compared with the actually observed number of SNe, which is affected by the inclination effect of spirals (section 3.2.), it is evident that the inclination-adjusted luminosities L_B^i must be used for the test.

Exclusion of 12 amorphous or peculiar galaxies from the fiducial sample leaves 330 galaxies. Their types and L_B^i values are listed by SST. There are 96 SNe known in these galaxies. These SNe can be statistically distributed over the 330 galaxies, using their probabilities to produce a SN. The probability of each galaxy is simply the product of its appropriate type-dependent *relative* SN frequency and its L_B^i luminosity. Here the relative SN frequencies for different Hubble types have been taken from Tammann (1982, table 2, column 2); these old values are sufficiently close to those derived in table 4 that they do not change the present conclusions.

In table 3 the *predicted* number of galaxies that should have produced 0, 1, 2, ..., 7 SNe (of the total sample of 96 SNe) are listed; the numbers are averages of 1000 Monte Carlo trials. Also shown in table 3 are the *observed* numbers of galaxies that have produced a given number of SNe. The agreement between the predicted and observed number is excellent; this strongly proves in favor of the assumption that SN frequencies depend *only* on Hubble type and L_B^i. This conclusion is further strengthened by the fact that SST found an equally good agreement between SN numbers predicted from infrared luminosities $(L_{IR}^i)^{0.8}$ and the actually observed numbers.

Table 3
Calculated and observed SN occurrences in the sample galaxies (for B probabilities).

	Number of SNe							
	0	1	2	3	4	5	6	7
MC 1000 trials	263.84	48.28	11.27	3.66	1.59	0.75	0.34	0.17
observed	264	50	8	5	1	1	1	0

These results show unambiguously that there is no reason whatsoever to invoke star formation bursts or other peculiarities in some galaxies in order to explain the observed multiple SN occurrences. *Fast SN producers are simply nearby, face-on, overluminous, late-type spirals* (Tammann, 1974; cf. also van den Bergh and McClure, 1990; van den Bergh, 1990). (In section 5.2, I will return briefly to fast SN producers.)

3.7. Relative SN frequencies

The distance-limited fiducial sample of SST lends itself to the determination of *relative* frequencies of SNe of different types and in different types of galaxies. No open samples (Oemler and Tinsley, 1979) should be used for this purpose, because they must contain an undue number of the exceptionally luminous Type Ia SNe.

Table 4
The relative rates of supernovae of different types in different types of galaxies.

Supernovae	E–S0	S0/a–Sa	Sab–Sb	Sbc–Sd	Sdm–Im
all types	0.07	0.05	0.15	0.37	0.40
Type Ia	0.07	0.035	0.035	0.035	0.035
Type Ib	—	0.003	0.019	0.06	0.06
Type II	—	0.012	0.096	0.275	0.30

The galaxies of the fiducial sample are subdivided into five Hubble-type bins in table 4. The first line of the table gives the relative SN frequencies, i.e., the number of SNe (of all types) divided by the total blue, inclination-adjusted luminosity L_B^i in that type bin. Because we have not specified the search time that corresponds to the SNe of the sample, these rates differ from the true absolute rates (in SNu's) by a yet unknown multiplication factor, but the rates, based on a (nearly) unbiased sample of maximum size, should represent the best *relative* rates available.

The statistical errors of the relative rates are negligible for Sbc–Sd galaxies (n_{SN} = 61); they amount to 25% for E–S0 and Sab–Sb galaxies with n_{SN} = 14 and 16, respectively, and they are large for S0/a–Sa and Sdm–Im galaxies with only n_{SN} = 3 and 2, respectively. The somewhat low rate for S0/a–Sa galaxies is therefore not significant. For Sdm–Im galaxies the formal rate is 0.35; but we have assumed a rate of 0.40 to make it slightly larger than the rate of Sbc–Sd spirals. In any case there is a strong variation of the SN rate over different Hubble types. This variation is a factor of 5–6 between early-type and late-type galaxies.

Table 4 does not show the amorphous (Am) galaxies, formerly called IrrII or I0. Oemler and Tinsley (1979) and Thompson (1981) have suggested that the known SNe in these galaxies indicated a quite high frequency per unit luminosity and hence a high star formation rate. However, they could not correct the galaxian luminosities for internal absorption, which must be particularly high in these galaxies. In fact, if one adopts an unrealistically small average internal absorption of $0.^{m}13$, the relative frequency becomes the same as for Im galaxies. With a more realistic average internal absorption of $2.^{m}0$ the SN rate of Am galaxies becomes the same as that of E, S0 galaxies! The available data therefore do not support the notion of Am galaxies being fast SN producers.

The small Am galaxy NGC 5253 has produced two SNe. Of these, SN 1972E was of Type Ia. The close similarity of $V(\max)$ for both SNe suggests that also SN 1895B was of the same type. Because this type of SN comes from the old population, the double occurrence can certainly not be taken as evidence for a star formation burst. The two SNe in an Am galaxy must therefore be considered a statistical fluke.

The only evidence for Am galaxies having a high rate of SNe comes from M82. From the decay of SN radio remnants Kronberg and Sramek (1985) have estimated the SN frequency *in the nucleus* of this galaxy to be $\sim$ 20–30 SNe per century! But none of these SNe have been observed optically. The present *optical* sample of SNe is therefore unsuitable for drawing any final conclusions on the intrinsic SN frequency of Am galaxies.

Not only is the overall SN rate a strong function of Hubble type, as is the relative contribution of different types of SNe. The next step to derive the best SN frequencies must be an evaluation to which extent do the different types of SNe contribute to the relative rates in table 4. This evaluation must be guided by the following considerations.

(1) All SNe in E–S0 galaxies are assumed to be of Type Ia. The evidence for this is not overwhelming. Of 80 SNe known in these galaxies (Barbon et al., 1989) only 8 are classified as Ia or Ia:, but there is no (compelling) evidence that any of the remaining SNe are of a different type. The conclusion is consistent with our belief that SNe Ia come from an old population, which is also the principal constituent of E/S0 galaxies.

(2) Table 4 shows that the observed rate of SNe in early-type spirals (S0/a–Sa) is marginally lower than it is in E–S0 galaxies. For Type Ia alone this becomes more significant by the observation, that *some* of the SNe in early-type spirals are of Type II. Of 47 such SNe, Barbon et al. (1989) list five of Type II (none of which belong to the fiducial sample). The observed 10% contribution of Type II supernova must in fact be higher because all selection effects discriminate against this type, and their contribution must presumably be further increased by some Type Ib SNe.

(3) The ratio of Type II to Type I (i.e., Ia + Ib) SNe in Sbc–Sd galaxies was formerly believed to be $\sim 1:1$ (Tammann, 1982; Cappellaro and Turatto, 1988). However, this conclusion was based on the assumption that the discovery chance of SNe was not sensitive to the SN type. Actually the control times Δt of Type II SNe are considerably shorter than that of Ib and particularly that of Ia SNe. The true frequency of SNe II has therefore been underestimated in the past. Detailed allowance for the different control times does indeed give higher SNe II rates, viz. $2.1:1$ from the revised rates of Cappellaro and Turatto (1988) (section 4.1) as well as from the revised rates

of Evans et al. (1989) (section 4.2). The subsample of *face-on* Sbc–Sd galaxies in the fiducial sample, which suffers minimum bias from inclination and distance effects, yields a ratio of (3.7$\pm$2.0) : 1 (SST). In the following a ratio $n_{\mathrm{II}} : n_{\mathrm{Ia+Ib}} = 3 : 1$ is adopted for Sbc–Sd galaxies. This high value should be sufficient for full allowance for all selection effects (luminosity, inclination, and dust in star forming regions) that discriminate against Type II.

(4) Only 15 certain or probable SNe of the relatively new Type Ib are listed by Barbon et al. (1989). Their statistic is therefore still uncertain. Branch (1986), van den Bergh et al. (1987), and TS have concluded that their frequency in spirals is approximately the same as that of Type Ia. However, that may still represent an underestimate of the true SN Ib frequency, because these objects are intrinsically less luminous than SNe Ia. Furthermore SNe Ib are presumably more strongly concentrated in dusty star forming regions, and they are expected to be more strongly affected by the inclination effect (cf. section 2.1). Finally one suspects that a larger fraction of SNe Ib remains unclassified, as compared to SNe Ia, simply because spectroscopists are less attracted by the fainter SNe Ib. The SN sample of Evans et al. (1989), for which all types are known, corresponds to a revised number ratio in Sbc–Sd galaxies of $n_{\mathrm{Ib}} : n_{\mathrm{Ia}} = 2.7 : 1$ (section 4.2.), but the result rests only on four SNe. Additional support for a relatively high frequency of SNe Ib comes from the fact that all three SNe of "Type I" of the fiducial sample that have occurred in Sbc–Sd galaxies since 1980, belong to Type Ib. A true ratio of $n_{\mathrm{Ib}} : n_{\mathrm{Ia}} = 1.5 : 1$ is adopted in the following, – a value that should be improved in the future. The adopted ratio together with the above $n_{\mathrm{II}} : n_{\mathrm{Ia+Ib}}$ ratio implies that $n_{\mathrm{II}} : n_{\mathrm{Ib}} = 5 : 1$ in Sbc–Sd galaxies. *If* O stars become SNe Ib and early B stars SNe II (van den Bergh, 1988), and *if* the mass function of star formation does not vary from galaxy to galaxy, it is reasonable to assume that this frequency ratio of 5 : 1 applies for all galaxy types from S0/a to Im. This invariant ratio is adopted as the best guess. (This assumption of a Hubble-type-invariant ratio $n_{\mathrm{II}} : n_{\mathrm{Ib}}$ will hardly survive in the future, because the ratio of very massive to massive stars should depend on metallicity and hence on Hubble type. SNe Ib should be relatively more frequent in early-type spirals [Maeder, 1991]).

(5) Because galaxian B magnitudes are a measure of the total intermediate-age population of a galaxy, it is reasonable to assume in first approximation that SNe Ia, which belong to the (old) disc population, have the same frequency per unit B luminosity for all galaxies (S0/a to Im).

The frequency ratios adopted under points (1)–(5) not only suffice to break down the overall SN frequencies for different Hubble types (table 4) into the individual relative rates of the three different types of SNe, but they actually overdetermine the problem. Best-compromise solutions are shown in the lower part of table 4.

The question arises whether the reliability of the relative frequencies of SNe of different types in galaxies of different Hubble type can be tested. The answer is yes. The 96 SNe of the fiducial sample (excluding Am and peculiar galaxies) are in very good statistical agreement with the relative rates in table 4 (SST). The test is, however, not as stringent as one would like. The reason is that the type information is insufficient for 35% of the SN sample, and their type distribution is obviously not the same as that of the 65% with known types. This is the principal reason why general assumptions about the relative type frequencies as adopted under points (1)–(5) cannot be avoided and will remain necessary for a long time. If one wanted instead to determine each entry in table 4 to within an accuracy of $\sim$ 10% from a set of actually counted SNe, one would need $\sim$ 100 SNe of each type in each Hubble bin. The rarer types of SNe would then require a total *unbiased* sample of more than 10 000 SNe! An assumption-free determination of Type Ib SNe in S0/a–Sa galaxies, for instance, will keep the observers busy for several centuries.

4. Absolute SN frequencies

The transformation of the *relative* supernova rates in table 4 into *absolute* frequencies ν in SNu = number of SNe per $10^{10} L_{B\odot}$ per 100 years requires reliable control times. Lacking these, Tammann (1974, 1977, 1982) had to assume that *all* supernovae in a nearby sample of galaxies were known. He could buttress this assumption with a subsample for which approximate survey times were available from the Palomar supernova search. These survey times were never published, and they left open the possibility that other parts of his total sample were systematically undersampled. Tammann's published supernova frequencies are therefore, in fact, lower limits to the true frequencies.

This unsatisfactory situation has been much improved in recent years by two supernova search programs for which all the search dates are known and which lead to realistic control times of the respective sample galaxies. These searches were conducted at Asagio (Cappellaro and Turatto, *1988) and* by the Rev. Evans (van den Bergh et al., 1987; Evans et al., 1989). These data samples are briefly reviewed in the following sections. Automated search programs, which have recently been started by various groups, should provide valuable new information on absolute supernova rates within a few years.

4.1. The Asagio search

Instigated by Professor L. Rosino, a supernova search was begun at the Asagio Observatory in 1959 and continues unto the present. For 376 galaxies surveyed, which have produced 51 supernovae, Cappellaro and Turatto (1988) have calculated control times, making allowance for an inclination effect quite similar to the one adopted here, and for the Shaw effect (sections 3.1 and 3.2). For SN Ia they assumed an absolute magnitude at maximum and a light curve quite similar to the one adopted in section 2.2. Their sample does not contain a confirmed supernova of Type Ib; they have therefore lumped together all supernovae of Type I. This automatically results in an overestimate of the absolute magnitude of SN Ib, but the net effect of this on the calculated frequencies is small. A magnitude correction cannot be applied here anyway, because one does not know which of their supernovae classified as I should be treated as a SN Ib. A more serious problem is that they assumed SNe II to be quite luminous, viz. $M_{\rm B}(\max) = -18.05$ (H_o = 50), which is 0.85 mag. brighter than the mean value adopted in section 2.2. Trial calculations show that a reduction of the maximum luminosity by this amount decreases the control times by a factor of 1.75 on average, and *increases* the SN II frequencies by the same amount. That this correction is indeed justified also follows from their improbable result that $n_{\rm II} : n_{\rm Ia+Ib} = 1 : 1$. After application of the correction to the control time calculations above this ratio takes a more reasonable value of about 2 : 1.

Applying the magnitude correction discussed above to the supernova frequencies of Cappellaro and Turatto (1988), and re-binning their galaxy types to those used here, one obtains the corrected supernova frequencies as given in detail by SST and vdBT.

The overall supernova frequency, corrected in this way, should be quite realistic for the specific Hubble-type mix of the Asiago search. It is based on 51 SNe and the statistical error should therefore be only 14%. But the frequencies for individual SN types in different parent galaxies must be dominated entirely by small-number statistics. The data must therefore be smoothed by means of the relative rates in table 4, which apply to the specific Hubble-type mix of the fiducial sample. For the smoothing one must procede as follows. Taking the individual Asiago frequencies at face value, one calculates the total number of SNe that one expects for the fiducial sample. One finds 0.87 SNu on average. If the same calculation is executed with the *relative* rates in table 4, then the average rate becomes 0.22 SNu, which is 3.95 times lower. All values listed in table 4 can therefore be transformed into absolute frequencies (in SNu) by multiplying them by a factor of 3.95.

4.2. The search by the Rev. Evans

The Rev. Robert Evans has surveyed 855 Shapley–Ames galaxies during the period 1980–1988 (van den Bergh et al., 1987, Evans et al., 1989). Twenty-four supernovae occurred in this sample which were either discovered by Evans, or would have been discovered by him if they had not first been noticed by others. Evans used two telescopes for his survey, the limiting magnitudes of which he estimated to be 14.5 and 15.4 mag. On the basis of these values Evans et al. (1989) calculated control times for SN Ia, SN Ib, and SN II in different galaxy type bins.

It is, perhaps, surprising that most of Evans' SNe were quite bright at the time of discovery. Only three SNe lie within 0.5 mag. of his nominal limiting magnitudes. This suggests strongly that his *effective* limiting magnitude is brighter than his adopted values by $\sim$ 0.5 mag. From the distribution of observing times in Evans' survey it is found that a change in his limiting magnitude by this amount reduces the control times for SN Ia and SN Ib by factors of 1.18 and 1.64, respectively, and increases their frequencies accordingly.

For SNe II Evans et al. (1989) have used a somewhat questionable luminosity function. Using the actual observing dates, SST have therefore recalculated the control times on the basis of the brighter limiting magnitude *and* the luminosity function of TS (fig. 1). This results in a reduction of the original control times by a factor of 1.95 and increase of the frequencies by the same factor.

On the other hand, Evans et al. (1989) have adopted $M_{B\odot} = 5.37$ to transform galaxian B magnitudes into units of solar luminosity (van den Bergh, 1990, private communication), whereas $M_{B\odot} = 5.48$ was adopted throughout this paper. To obtain uniformity all SNu values of Evans et al. (1989) should therefore be *reduced* by a factor of 1.11.

The corrected SN frequencies of Evans et al. (1989) are detailed elsewhere (SST; vdBT). As in the case of the Asagio frequencies, they can be used to calculate the corresponding frequencies for the fiducial sample. One obtains 0.673 SNu per "average" galaxy of that sample. This is 3.06 times higher than the value of 0.22 SNu derived from the relative rates of table 4 for the fiducial sample. All entries in table 4 can therefore be transformed into absolute frequencies (in SNu) by multiplying them by a scale factor of 3.06.

It should be stressed that the Evans sample has *not* been corrected for inclination effects. If our adopted inclination correction of a factor of 4 were applied to Evans' SNe Ib and SNe II in Sbc–Sd galaxies, then their corrected frequency would become 3.1 SNu. This would imply, for instance, for M101, an Sc galaxy with $5.2 \times 10^{10} L_{B\odot}$, one core collapse SN every six years, which is clearly impossible. The Evans sample is definitely much less affected by inclination than other searches. As discussed earlier, it is not surprising because of the *visual* search method of Evans, which is quite insensitive to the underlying galaxian light. The 24 SNe of the sample are, of course, not sufficient to make a meaningful independent determination of the inclination effect. Lacking such data it is assumed that the effect is vanishingly small. This is conservative in the sense that one obtains a lower limit to the true frequencies.

4.3. The adopted SN frequencies

In the two previous subsections it was argued that the relative SN rates in table 4 can be transformed into absolute frequencies by multiplying them by 3.95 and 3.06, respectively. The agreement of these two factors is as good as one can expect from the number of SNe, on which they are based (51 and 24 SNe, respectively). Because the factors carry remaining systematic errors of unknown size, it is probably best to adopt an unweighted *mean* scaling factor of 3.51. Then the relative rates in table 4 translate into the final SN frequencies of table 5.

How good are the values in table 5? The most reliable entry is the one for E–S0's. These galaxies are believed to produce only the particularly bright and presumably (nearly) dust-free Type Ia SNe. The relative rate of E–S0's in table 4 is based on 14 SNe out of a total of 96; its statistical error is therefore ±29%. The absolute calibration that leads to table 5 is based on a total of 75 SNe and carries therefore an additional statistical error of ±12%. This brings the error of $\nu(\mathrm{E} - \mathrm{S0})$ to ±31%. The error of ν for Sbc–Sd galaxies is hardly larger, in spite of the inclination problem, because most of the plentiful sample SNe lie in face-on galaxies ($i < 30°$) anyway. The overall frequency of SNe in the remaining Hubble-type bins can then hardly be changed by more than ±50% without questioning the continuity of the Hubble sequence.

Table 5
The absolute frequencies (in SNu) of SNe of different types in different types of galaxies.

Supernovae	E–S0	S0/a–Sa	Sab–Sb	Sbc–Sd	Sdm–Im
all types	0.25	0.17	0.53	1.29	1.40
Type Ia	0.25	0.12	0.12	0.12	0.12
Type Ib	—	0.01	0.07	0.19	0.23
Type II	—	0.04	0.34	0.98	1.05

The most severe systematic errors stem from uncertainties of the limiting search magnitude and from the possibility that the number of intrinsically faint SNe (of type II or a new type) has been underestimated. An error in the adopted search limit by 1 mag. affects the control times Δt by almost a factor of 2. The possible existence of large numbers of underluminous SNe has been discussed in section 2.2. In addition there is the danger that some SNe remain hidden in H II regions or dust clouds. The systematic errors all tend to increase the frequencies given in table 5. This holds also for the limiting search magnitude, because SN searchers show a tendency to quote optimistic, i.e., too faint magnitude limits.

The separate frequencies for the three types of SNe in table 5 depend essentially on the assumptions introduced in section 3.7 under points (1)–(5). They carry therefore no additional statistical errors, but they are affected, of course, by systematic errors. A severe error could be introduced by the assumption that SNe Ib come from the most massive stars. If they originate instead from old double stars, then the assumption that the ratio $\nu_{\mathrm{Ib}} : \nu_{\mathrm{II}}$ should be constant over the whole range of S0/a to Im galaxies would be meaningless. There are several other error sources, but it is unlikely that the frequencies for individual SN types will need revisions by more than a factor of 2.

Considerable comfort lies in the fact that the overall SN frequencies have hardly moved during the last 15 years. The values in table 5 agree all within 20% with the frequencies available then (Tammann, 1974). There is, however, no such comfort for the separate frequencies of the three SN types. While 53% of all SNe in Sbc–Sd galaxies appeared, then, to belong to Type Ia, a fraction that increased to even 77% (Tammann, 1982) their contribution in this type of galaxies is now down to 9%! This drastic change is caused about equally by two effects: (1) The calculation of realistic control times Δt has shown that the frequency of the exceptionally bright SNe Ia has been overestimated relative to SNe II; (2) What was formerly believed to be Type I SNe has been split into two distinct types, SNe Ia and SNe Ib, of which the former account for only $\sim 40\%$ of the Type I SNe in Sbc–Sd galaxies.

The Shapley–Ames galaxies within the Virgo circle, i.e., the "fiducial sample" has a mean SN rate of 0.77 SNu and a total luminosity of $916 \times 10^{10} L_{\mathrm{B}\odot}$. The 342 galaxies in the sample are therefore expected to produce 7.1 SNe per year. If one considers the galaxies of the sample to be "typical" cases, then the mean interval between SN events in an average galaxy becomes 49 years. It is clear that this number says less about the frequency of SNe than it does about the relatively high mean luminosity ($\langle M_{\mathrm{B}} \rangle = -20.6$) of the galaxies of this primarily flux-limited sample. The number of *observable* SNe is expected, however, to be only 4.2 SNe per year because of the inclination effect ($\Sigma L_B^i = 540 \times 10^{10} L_{B\odot}$). Of this expected number, 2.8 SNe per year have been found on average during the last five years. About 60% of the expected SNe should be brighter than $m_B = 14.5$ at maximum.

A possible problem is presented by the apparently low SN frequencies in distant clusters of galaxies. A survey of 65 clusters with $0.2 < z < 0.4$, presumably containing mainly E and S0 galaxies, has produced only one SN (Hansen et al., 1989; Nørgaard–Nielsen et al., 1989). From the estimated total cluster luminosity (Hansen et al., 1989; Jørgensen, 1990), and with 0.25 SNu from table 5, $\sim$ 10 SNe would have been predicted. This prediction is based on control times derived from an adopted limiting magnitude of $V(\mathrm{lim}) = 24$. The prediction also allows for the $K(z)$ correction, which *brightens* SN Ia at $V(\mathrm{max})$ for $z = 0.3$ and compresses their light curves due to their dependence on color and hence on epoch, as well as for the time dilation $(1 + z)$ (see Leibundgut, 1990). It would be premature, however, to draw any far-reaching conclusions from this apparent lack of distant SNe.

4.4. The frequency of core collapse SNe in function of the FIR flux

In section 3.4, it was found that the frequency of SNe from massive progenitors (Type Ib and II) correlates with the FIR flux like $\nu \propto L_{IR}^{0.8}$. The relation can now be calibrated in the following way. For nearly all galaxies of the fiducial sample, SST have compiled the FIR fluxes. By means of the individual B luminosities of these galaxies, their specific Hubble types, and table 5 one can also calculate $n_{\mathrm{Ib+II}}(100)$, i.e., the probable number of SNe of Types Ib and II per 100 years of a particular galaxy. Adding these numbers within each Hubble-type bin and dividing it by the appropriate sum $\Sigma([L_{IR}^{0.8}])$ then yields the frequency for that Hubble type in $\mathrm{SNu_{IR}}$ (1 $\mathrm{SNu_{IR}}$ = 1 SN of Type Ib or II per FIR unit luminosity $[(10^{10}\ \mathrm{erg} \times \mathrm{s}^{-1})^{0.8}]$ per 100 years).

The relevant data are set out in table 6. (It is irrelevant here whether the observed values L_{IR} are used or the inclination-adjusted values L_{IR}^i, as long as they are used consistently. I have chosen here the latter).

Table 6
The frequency of SNe of type Ib and II per unit FIR flux

	S0/a–Sa	Sab–Sb	Sbc–Sd	Sdm–Im
$\Sigma L_B^{i\,*}$	61.8	108.8	165.1	5.8
$n_{\mathrm{Ib+II}}(100)$	3.3	44.2	194.2	7.4
$\Sigma([L_{IR}^i]^{0.8})$	4.41	18.51	47.68	2.01
$\mathrm{SNu_{IR}}$	0.75	2.39	4.07	3.68

* in $10^{10} L_\odot$

4.5. The frequency of core collapse SNe in function of the Hα flux

In section 3.5, it was described how the expected rates of SNe of Type Ib and II were calculated for a sample of 126 S0/a–Im galaxies with known $H\alpha$ fluxes. The results are here set out in table 7.

As stated before, the data are fully consistent with the assumption that the rate of SNe Ib and II per unit $H\alpha$ flux is independent of the Hubble type of the parent galaxy. The best frequency is 0.18 SNu_α, i.e., 1 SNu_α = 1 SN of Type Ib or II per 100 years per an $H\alpha$ flux of 10^{40} erg $\times$ s^{-1}.

The result is equivalent to 1 core collapse SN per year per 5.6×10^{42} erg s^{-1} in $H\alpha$. Kennicutt (1984) has shown how this value can be used to determine the minimum main-sequence mass M_L of the progenitors of these SNe.

Table 7
The frequency of SNe of type Ib and II per unit $H\alpha$ flux

	S0/a – Im	Sab – Sb	Sbc – Sd
nGal	126	19	96
ΣF_α*	3261	347	2911
$n_{\mathrm{Ib+II}}$**	586.6	52.9	528.7
$SNu\alpha$	0.18	0.15	0.18

* Sum of the $H\alpha$ flux in 10^{40} erg $\cdot$ s^{-1}
** Expected number of SNe Ib and II per 100 years calculated from L_B.

The required $H\alpha$ flux per SN is used to calibrate the initial mass function (IMF) $N(M) \propto M^\beta dM$. The value of M_L is then found by integrating the calibrated IMF from $M_{\max}$ to M_L such that one obtains one stellar death per year, allowing for the appropriate life-times of different mass intervals. The result is insensitive to the choice of $M_{\max}$ because of the paucity of the most massive stars. Kennicutt adopted a SN frequency for Sbc–Sd galaxies of 1.40 SNu_B and considered an IMF with $\beta = -2.5$ as well as the IMF of Miller and Scalo (1979); he found M_L = 7.7 and 12.3 $M_\odot$, respectively. With a frequency of 1.17 SNu_B for SNe Ib + II from table 5 one finds M_L = 8.1 and 12.7 $M_\odot$. The latter value depends again on the IMF of Miller and Scalo, which has since been revised by Scalo (1986) by a factor of $\sim$ 4 downwards for the most massive stars! This brings M_L to $\sim$ 7.3 $M_\odot$, in reasonable agreement with the value of 8.1 $M_\odot$ from the assumption of $\beta = -2.5$.

From this it follows that the best value of M_L is 7.7 $M_\odot$, in fortuitously close agreement with Kennicutt (1984). The error of this determination is estimated to be ± 1 $M_\odot$.

5. Supernova frequencies in the Local Group

5.1. Our Galaxy

(1) *Evidence from historical SNe.* In the last millennium six SNe are known in our Galaxy. They occupy a wedge-shaped sector of the Galactic disk with an apex angle of 50°, they therefore represent $\sim 1/7$ of the total Galactic supernova population. Allowing for one possible additional supernova within the historical sample and for an incompleteness factor of 1.2 at the innermost and outermost regions of the sector, one finds 5.8 ± 2.4 (statistical error) Galactic SNe per century (for details see Tammann, 1982). The historical SNe corresponds to a surface density of 6.3×10^{-11} SNe pc^{-2} yr^{-1} in the Solar neighborhood.

However, the sample of historical SNe has a very puzzling property, i.e., their high scale height above the plane of $\beta = 214$ pc (Tammann, 1982). If the majority of the objects came from normal O and B stars their scale height should not be larger than 90 pc. One cannot explain this discrepancy by postulating that many SNe were missed at small distances z from the Galactic plane, because they would not have sufficiently young SN radio remnants. As long as one cannot understand the z-distribution of the historical SNe, no firm conclusions should be drawn from them.

(2) *The death rate of massive stars.* The death rate of stars more massive than $M_L = 7.7\ M_\odot$ (cf. section 4.5) in the Solar neighborhood follows from data given by Scalo (1986) to be $\sim 1.2\ 10^{-11}$ pc^{-2} yr^{-1} with an estimated error factor of 2. Taken at face value this surface density is a factor of ~ 5 lower than the result from the previous point. Is this discrepancy significant (cf. van den Bergh in vdBT), or is it due to an accumulation of errors? Or is it indicative of untypically high contribution of SNe from low-mass stars within the historical sample (above the $\sim 9\%$ [Sbc–Im] to 23% [Sab–Sb] contribution), which would be consistent with the high z-values of the historical SNe?

(3) *Radio SN remnants.* Three historical SNe of the last millennium lie at Galactic longitudes $100° < 1 < 260°$, a region that contains four radio SNRs of high surface brightness (Clark and Caswell, 1976). These authors list 46 SNRs above the same surface brightness threshold for the entire Galaxy. This suggests, if the evolution of radio SNRs is independent of Galactocentric distance, that the Galaxy has produced $3(46/4) = 34.5$ SNe during the last 1000 years, or 3.5 SNe per century (vdBT). This result is in perfect statistical agreement with the above evidence from historical SNe.

SNe frequencies cannot be derived directly from radio SNRs, even if their evolution with time is assumed to be known, because their lifetimes obviously depend strongly on the interstellar gas density and hence on the distance from the Galactic plane. This is evidenced by their small scale height of $\beta = 60$ pc (Clark and Caswell, 1976), which is even less than that of their massive progenitors.

(4) *External evidence.* With a total luminosity of $L_B = 2.3 \times 10^{10} L_\odot$ (van der Kruit, 1989; scaled here from $M_{B\odot} = 5.25$ to 5.48) the Galaxy should produce 1.2 SNe per century if it is of type Sab–Sb, or, more likely, 3.0 SNe per century if it belongs into the type bin Sbc–Sd (cf. table 5).

Other routes to the Galactic SN frequency are described by vdBT. All methods are inflicted by errors of at least a factor of 2. The most direct evidence comes from the six historical SNe (method 1), corresponding to $\tau = 17(+12, -5)$ years. As a safe compromise value I adopt for all types of SNe combined $\tau = 30$ years within a factor of 2. This value may be compared to the birth rate of pulsars of 1 Galactic pulsar per $\geqslant 50$ years (Narayan and Ostriker, 1990; for a revision by Narayan see vdBT).

5.2. Other Local Group galaxies

The SN frequencies of four additional members of the Local Group (SMC, LMC, M33, and M31) can be calculated using their B, FIR *and* Hα luminosity and the (Hubble-type-specific) SNu values from tables 5–7, respectively. While the B luminosities can be used to calculate the SN frequency of Type Ib + II and Type Ia separately, the FIR and Hα luminosity can predict only the frequency of SNe Ib + II. The relevant numbers are set out in table 8. In the last line the average intervals τ between SN events are calculated to include *all* types of SNe. The ratio $n_{\rm Ia} : n_{\rm Ib+II}$ has here been assumed to be the same as in table 5.

Because the ratios between L_B, $L_{\rm FIR}$, ans $L_{\rm H\alpha}$ vary from galaxy to galaxy, the predicted SN frequencies for a given galaxy vary considerably. The total *range* of frequencies is a factor of 3–4 for a single galaxy. A typical example is M31, for which L_B predicts $\tau_{\rm Ib+II} = 76$ years, while $L_{\rm FIR}$ requires $\tau_{\rm Ib+II} =$ 323 years, with $L_{\rm H\alpha}$ giving an intermediate interval. The low Hα luminosity and very low FIR luminosity of M31, as compared to its B luminosity, must be due to the fact that its recent star formation was lower than that of a typical Sb galaxy. In this sense there seem to exist "slow" and "fast" SN producers. But there is no evidence that this effect causes deviation from the mean SN frequency (per unit B luminosity) by more than a factor of 2 (cf. section 3.6).

The adopted τ-values in table 8 are fully consistent with the historical evidence. In SMC any SN during the last 300 years would probably have

Table 8
SN frequencies in local group galaxies

Galaxy Type	SMC Im	LMC Sm	M33 Sc	M31 Sb
$L_B(10^{10}L_\odot)$	0.052	0.27	0.62	3.19
$n_{\text{Ib+II}}{}^*$	0.067	0.35	0.73	1.31
n_{Ia}	0.006	0.03	0.07	0.38
$(L_{\text{IR}})^{0.8}$ **	0.0013†	0.069†	0.12†	0.13†
$n_{\text{Ib+II}}{}^{\ddagger}$	0.051	0.27	0.47	0.31
$F\alpha(10^{40}\ \text{erg}\cdot\text{s}^{-1})$	1.1¶	4.1¶	3.6¶¶	4.8¶¶
$n_{\text{Ib+II}}{}^{\S}$	0.20	0.74	0.65	0.86
$n_{\text{Ib+II}}$ (adopted)	0.11	0.45	0.62	0.83
n_{Ia} (adopted)	0.01	0.04	0.06	0.38
$\langle\tau\rangle$ (years)	833	204	147	83

* Number of SNe (of specific type) per 100 years, calculated from L_B and table 5.
** L_{IR} in 10^{10} $L_\odot$.
† From SST.
‡ Number of SNe of Type Ib and II per 100 years, calculated from L_{IR} and table 6.
¶ From Kennicutt and Hodge (1986).
¶¶ From Berkhuijsen (1984).
§ Number of SNe of Types Ib and II per 100 years, calculated from $F\alpha$ and table 7.

been detected; the absence of any detection suggest a very low rate. During the same interval one SN was detected in LMC (SN 1987A) which should be compared with τ = 204 years. Kirshner et al. (1989) estimate the age of the second youngest SNR in LMC to be less than 800 years, which give a formal, but very uncertain value of $\tau \sim 400$ years. M33 has been surveyed for SNe for roughly 100 years with no success; this is explained by τ (adopted) = 147 years. From the ratio of known radio SNRs in LMC and M33, vdBT have concluded that M33 should have a SN frequency 1.56 times higher than LMC, which is well borne out by the predicted frequencies in table 8. Also M31 has been surveyed for $\sim$ 100 years; table 8 predicts 1.2 SNe for this interval in almost perfect agreement with the one event known (SN 1885A).

In the previous paragraph I have descended into the shallows of the statistics of very small numbers. But they still allow a firm conclusion. If $H_0 = 100$ (instead of 50 as adopted throughout this paper) all SNu values in tables 5–7 would be increased by a factor of 4, and the τ-values in table 8 would be decreased by the same factor. This would imply that one of the four Local Group galaxies should produce a SN every 11 years. This is in blatant contradiction with observations! A similar discrepancy would also arise for the Galactic rate as calculated from external evidence, requiring τ = 8 (for type Sbc–Sd). It is perhaps surprising that a value of $H_0 = 100$ can be excluded by simply counting SNe in external and in Local Group galaxies.

Acknowledgments

Financial support from the Swiss National Science Foundation is gratefully acknowledged. I have profited from many discussions particularly with Profs. S. van den Bergh, D. Branch, R. Kirshner, and Miss A. Schröder. Many thanks go also to Mrs. M. Saladin for typing the manuscript.

References

Barbon, R., E. Cappellaro, and M. Turatto, 1989, Astron. Astrophys. Suppl. 81, 421.
Berkhuijsen, E.M. 1984, Astron. Astrophys. 140, 431.
Branch, D. 1986, Ap. J. Lett. 300, L5.
Branch, D., and G.A. Tammann, 1991, Ann. Rev. Astron. Astrophys., in press.
Cadonau, R., A. Sandage, and G.A. Tammann, 1985, Supernovae as Distance Indicators, ed. N. Bartel, Berlin: Springer, p. 151.
Cappellaro, E., and M. Turatto, 1988, Astron. Astrophys. 190, 10.
Clark, D.H., and J.L. Caswell, 1976, MNRAS 174, 267.
Evans, R., S. van den Bergh, and R.E. McClure, 1989, Ap.J. 345, 752.
Hansen, L., H.E. Jørgensen, H.U. Nørgaard–Nielsen, R.S. Ellis, and W.J. Couch, 1989, Astron. Astrophys. 211, L9.
Jørgensen, H.E. 1990, in: IXth ERAM Proc. IAU, in press.
Kennicutt, R.C. 1984, Ap.J. 277, 361.
Kennicutt, R.C., and P.W. Hodge, 1986, Ap.J. 306, 130.
Kennicutt, R.C., and S.M. Kent, 1983, A.J. 88, 1094.
Kirshner, R.P., J.A. Morse, P.F. Winkler, and W.P. Blair, 1989, Ap.J. 342, 260.
Kronberg, P.P., and R.A. Sramek, 1985, Science 227, 28.
Leibundgut, B. 1990, in: Supernovae, ed. S. Woosley, in press.
Leibundgut, B., and G.A. Tammann, 1990, Astron. Astrophys. 230, 81.
Maeder, A. 1991, preprint.
Miller, D.L., and Branch, D., 1990, A.J. 100, 530.
Miller, G.E., and J.M. Scalo, 1979, Ap.J. Suppl. 41, 513.
Narayan, R., and J.P. Ostriker, 1990, Ap.J. 352, 222.
Nørgaard–Nielsen, H.U., L. Hansen, H.E. Jørgensen, A.A. Salamanca, R.S. Ellis, and W.J. Couch, 1989, Nature 339, 523.
Oemler, A., and B.M. Tinsley, 1979, Astron. J. 84, 985.
Rosa, M., and Richter, O.-G., 1988, Astron. Astrophys. 192, 57.
Sandage, A., and G.A. Tammann, 1987, A Revised Shapley–Ames Catalog, 2nd Edition. Washington, D.C.: Carnegie Institution.
Sandage, A., and G.A. Tammann, 1990, Ap.J. 365, 1.
Scalo, J.M. 1986, Fundamentals of Cosmic Physics, 11, 1.

Schmitz, M.R., and C.M. Gaskell, 1988, in: Supernova 1987 A in the Large Magellanic Cloud, ed. M. Kafatos and A.G. Michalitsianos, p. 112, Cambridge: Cambridge University Press.
Schröder, A., H. Schwengeler, and G.A. Tammann, 1991, to be published (SST).
Shaw, R.L. 1979, Astron. Astrophys. 76, 188.
Tammann, G.A. 1974, in: Supernovae and Supernova Remnants, ed. C.B. Cosmovici, p. 155, Dordrecht: Reidel.
Tammann, G.A., 1977, in: Supernovae, ed. D.N. Schramm, p. 95, Dordrecht: Reidel.
Tammann, G.A. 1982, in: Supernovae, A Survey of Current Research, ed. M.J. Rees, R.J. Stonehouse, p. 371, Dordrecht: Reidel.
Tammann, G.A., and A. Sandage, 1968, Ap.J. 151, 825.
Tammann, G.A., and A. Schröder, 1990, Astron. Astrophys. 236, 149.
Tammann, G.A., and A. Schröder, 1991, to be published (TS).
Thompson, L.A., 1981, PASP 93, 176.
van den Bergh, S. 1988, Comments Astrophys. 12, 131.
van den Bergh, S. 1990, Astron. Astrophys. Lett. 231, L27.
van den Bergh, S., R.D. McClure, and R. Evans, 1987, Ap.J. 323, 44.
van den Bergh, S., and R.D. McClure, 1990, Ap.J. 359, 277.
van den Bergh, S., and G.A. Tammann, 1991, Ann. Rev. Astron. Astrophys., in press (vdBT).
van der Kruit, P. 1989, in: The Milky Way as a Galaxy, eds. R. Buser and I. King, 19th Saas-Fee Course, Geneva Observatory, p. 342.
Wheeler, J.C., and R.P. Harkness, 1990, preprint.
Zwicky, F. 1938, Ap.J. 88, 529.

COURSE II

LATE STAGES OF STELLAR EVOLUTION

ZALMAN BARKAT

Racah Institute of Physics, Hebrew University
Jerusalem, Israel

S. Bludman, R. Mochkovitch and J. Zinn-Justin, eds.
Les Houches, Session LIV, 1990
Supernovae

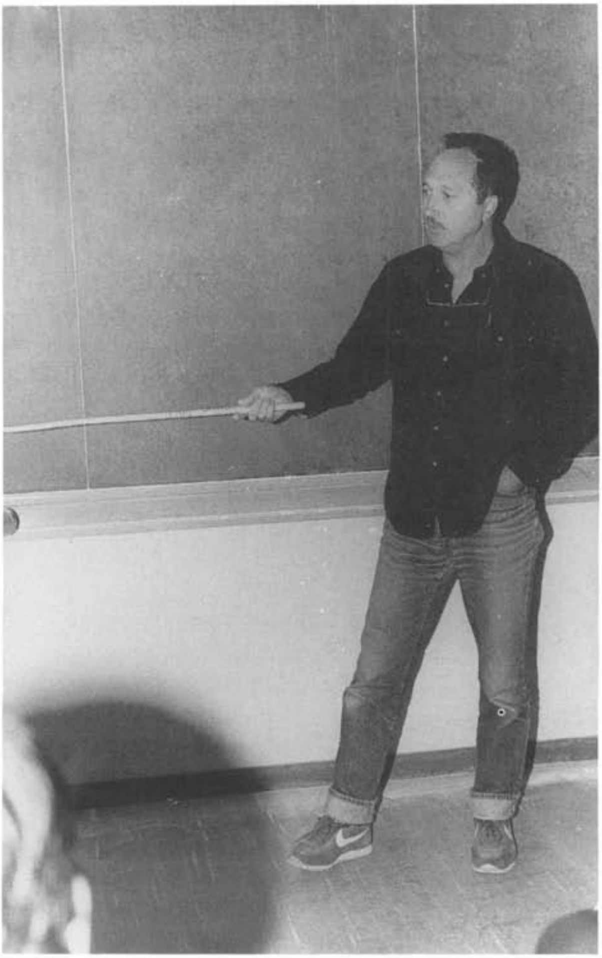

Contents

1. Introduction 34
2. Core-envelope separation 34
3. Evolution of carbon-oxygen stars 35
   3.1. Region I 37
   3.2. Region II 38
   3.3. Region III 47
   3.4. Region IV 48
4. Growing stellar cores–intermediate mass stars 49
References 60

1. Introduction

We define "late stages of evolution" as the epoch in stellar evolution where the rate of energy loss due to escaping neutrinos (q_ν), emitted by thermal processes, is the dominating term (disregarding nuclear energy generation) in the energy conservation equation. This means that $|q_\nu|$ must be larger than the local rate of energy deposition or removal by the heat flux carried by photons. It can be shown that this definition requires a density (ρ) and temperature (T) combination such that:

$$\rho \gtrsim 10^5 \text{ g·cm}^{-3}, \qquad T \geq 10^8 \text{ K} \tag{1.1}$$

We shall see below how the realization of these conditions depends on the stellar mass. Note that in the following discussions mass and luminosity are all in solar units unless otherwise specified.

2. Core-envelope separation

The dominance of neutrino losses dependent only on local conditions only (unlike the heat flux which involves gradients) sets up the stage for core envelope separation. The presence of a burning shell (e.g. helium) where energy generation is an entropy source, keeps the entropy density at that location from decreasing, and the criterion for convective mixing ensures that the entropy above the shell is not lower. Below the shell neutrino losses are free to decrease the entropy. The typical entropy "profile" (mass distribution) develops an "entropy well," which in turn induces (via the condition of hydrostatic equilibrium) very sharp pressure and density gradients near the burning shell. Note that even when burning is extinguished (say due to expansion), the entropy profile and thus the pressure profile does not react quickly enough to change the following arguments. The presence of such a sharp pressure gradient (say at mass point m_c) allows us to treat the *core inner to* m_c, as an *independent star* – that is, to ignore the presence of the stellar mass above it ("*envelope*"). A zero-pressure outer boundary condition at m_c is barely distinguishable from the real one. We still must consider the question of whether the rate of change of the entropy at the edge of the core, when treated as an independent star, may be seriously different from that in the real case and whether this has a significant effect on the core's evolution. Most authors who chose to model the evolution of stellar cores as stars (e.g. helium stars) implicitly assume that the answer to this question is negative. We are not sure that this answer is indeed *always* negative and are currently attempting to study the problem for helium cores. However, it does however appear that for carbon-oxygen cores, one can safely assume that core-envelope separation is a very good approximation.

In any case an important question is whether the core's mass remains constant. In principle a core mass can either increase due to the advance of the burning shell, or decrease due to the mixing of outer layers with the envelope or because of excessive mass loss. We shall discuss these possibilities later. At this stage note that for carbon-oxygen cores there is hardly a danger of mass decrease, but core growth is a distinct and important possibility.

3. Evolution of carbon-oxygen stars

The evolution of a carbon-oxygen star is determined by its mass and by the initial carbon mass fraction (X_c), where the oxygen mass fraction is usually $1 - X_c$. One may add some magnesium and neon but this does not significantly change anything. Note that it is assumed that the initial composition is homogeneous, that is, that it does not depend on location. This is probably a very good approximation since the helium burning that gives rise to such a star is always convective.

As we shall see later some of the details of the evolution may critically depend on X_c, but it is mainly the mass that determines the fate of the star, that is, the type of instability that it will eventually encounter.

Over the years, many authors have published evolutionary tracks of stellar cores. We shall not give here a full list of references but shall later quote some of the most recent works. At this stage, to make a most general classification, we show in fig. 1 old results that describe the evolution of pure oxygen stars (Barkat 1977). The evolution is described by showing the tracks of the stellar centers as full lines on the ρ-T plane. The tracks are labelled by their corresponding mass. Also shown are hatched regions where the adiabatic index γ ($\gamma \equiv (\frac{dlnp}{dln\rho})_{s,x}$) is lower than 4/3,

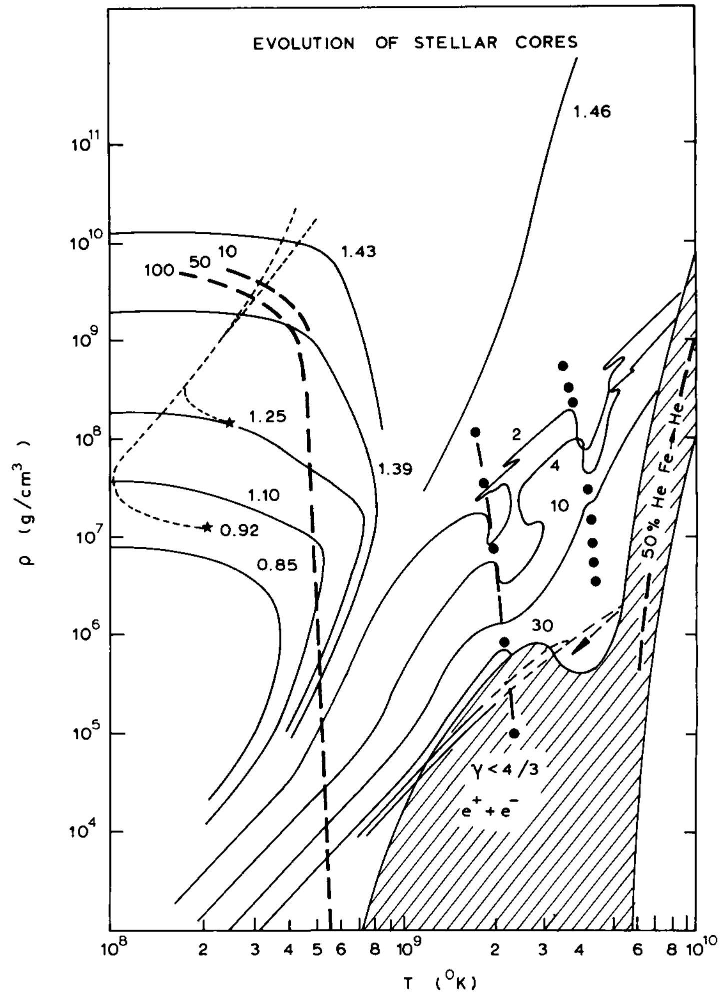

Fig. 1. Evolutionary tracks of ^{16}O stars. Masses label tracks are indicated by the solid lines. Stars at end of tracks represent dynamical instability. Heavy dashed lines show ignition lines of carbon (left), oxygen (middle), and silicon (right). Dashed lines (upper left) represent the evolution of growing cores.

which is where stars' dynamical stability may be lost and therefore can be considered to be stellar "mine fields." The heavy dashed line is the "ignition line" of carbon, commonly defined as the locus of points where energy generation by carbon burning is equal to neutrino energy losses. Note that the tracks in fig. 1 belong to stars that do not contain carbon. The dash-dotted and dotted lines are the oxygen and silicon ignition lines, respectively.

The main point introduced by this figure is a classification of stars' fate by their mass into four mass regions.

We shall now give a short review of current understanding of the important features characterizing these mass regions.

3.1. Region I

The lower limit of this region is at about $m_c \sim 30$. Barkat, Rakavy and Sack (1969), Frayley (1968) – see also Arnett (1977), Ober, El Eid, and Fricke (1983) – have shown that for $m_c > 30$, stars become dynamically unstable just before oxygen ignition. Following the onset of instability, these stars contract at an increasing rate and ignite oxygen explosively. As long as m_c is not too large, that is, not much above 100, one finds that contraction reverses into expansion, but not before enough nuclear energy is liberated to unbind the star. The result is total disruption except for a relatively narrow mass range ($\Delta m_c \approx 5$) just above the lower limit of $m_c \sim 30$. In this latter sub-region, a massive remnant consisting of a few solar masses of the burning products of oxygen remains. This remnant must undergo a second dynamical event but very little has been done to clarify the behavior and astrophysic relevance of this case. The very massive stars mentioned above (i.e. $m_c \gtrsim 100$) form black holes but otherwise the explosion of these stars ("pair-formation supernovae") is found to be quite simple from both the physical as well as the numerical point of view. The problem is that it is still not clear whether stars which give rise to these massive cores ever exist. A recent discussion of this problem is given by Wheeler (1990), and we only mention here that difficulties arise both as to the existence of such stars and whether they would survive the processes of mass loss without reducing their carbon-oxygen core mass below the relevant limit. Note that the answer to these questions may depend on the initial metalicity. If it turns out that for low metalicity, the formation of such stars is favorable, it may have an important impact on our perception of galactic history. We also note that formation of such stars and their subsequent explosion may occur as a result of a merger of colliding stars in dense clusters (Colgate 1967).

3.2. Region II

Stars in this region ($2 \lesssim m_c \lesssim 30$) eventually develop iron cores which collapse due to iron photodecomposition at a temperature of about $6 * 10^9$ K. It is widely believed that the collapse of the iron core must in some way be followed by an explosion of the outer layers giving rise to a supernova of Type II. SN 1987A is a distinct example.

The most important quantitative products of evolutionary calculations in this context are: the mass of the iron core at collapse (which is found to be a crucial parameter in the theory of collapse) and the composition (mass distribution of nuclei) of the outer layers, which are expected to be shock ejected. Several detailed papers describing the evolution of relevant stars have been published; some of the most recent ones are: Woosley and Weaver (1986a, 1986b,1988), Wilson et al. (1986), Nomoto and Hashimoto (1986). Examining the results in the literature, one sees that the values of the final iron cores' mass (m_{F_e}) turn out to be rather scattered in the range $1.20 \lesssim m_{F_c} \lesssim 2.4$, and are sensitive to various physical uncertainties, such as the $^{12}C(\alpha;\gamma)^{16}O$ reaction rate, convection algorithm, beta decay rates, etc.

We (Marom 1990, Barkat and Marom 1990, Marom and Barkat 1993) have carried out an extensive survey of the evolution of carbon-oxygen cores more massive than $m_c = 2$. We believe that the main results of this work will help to clarify the picture of evolution. As mentioned above we use two parameters to characterize the core – (treated as star): m_c (mass) and X_c (carbon mass fraction which is taken to be initially homogeneous). A very important point concerning the dependence of the end result (i.e., iron core mass) on the initial (mainsequence) mass will be made when we analyze the systematics of carbon burning, which is as follows. We find that two cases arise – in the first case, carbon burning occurs in a central convective core which extends up to mass point $m_{tc}^{(1)}$ (where the subscript tc stands for: top of the convective zone). In the second case, carbon begins to burn around the center radiatively and proceeds as a radiative burning shell which travels outwards until at mass point $m_{bc}^{(1)}$, (where the subscript bc stands for: base of the convective zone), burning becomes convective and a convective shell which extends from the base $m_{bc}^{(1)}$ up to $m_{tc}^{(2)}$ is formed. In fig. 2, we show the dependence of $m_{tc}^{(1)}$ and $m_{bc}^{(1)}$ on m_c and X_c. The general behavior is seen to be such that for any X_c, there is a maximal core mass m_c^c below which the first case is realized (i.e., convection around the center) and above which the second case occurs. m_c^c is a function of X_c and is larger for higher values of X_c. At a given m_c, the convective core $m_{tc}^{(1)}$ is *larger* and the base of the convective shell $m_{bc}^{(1)}$ is *lower* for higher values of X_c.

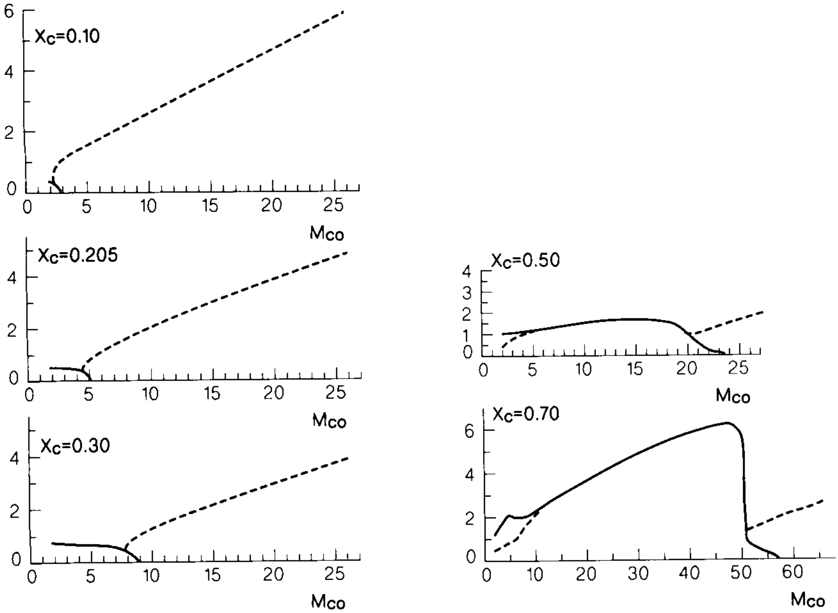

Fig. 2. Convection during central carbon burning as a function of X_c. Solid lines represent the extent of the convection core. Dashed lines represent the base of the first convective shell when it is not situated at the maximum extent of the convective core. (a) $X_C = 0.10$, (b) $X_c = 0.205$, (c) $X_c = 0.30$, (d) $X_c = 0.50$.

Before describing the significance of this behavior, we wish to show how it can be easily understood.

A necessary condition for onset of convection is a local increase in the entropy density (s) such that formation of a negative entropy gradient is promoted. Neglecting the flux carried by photons, we can write this condition as

$$\dot{s} = \frac{1}{T}(q_n - q_\nu) = \frac{q_\nu}{T}\left(\frac{q_n}{q_\nu} - 1\right) > 0 \tag{3.1}$$

where T is the temperature, q_n is the rate of energy generation by nuclear reactions, and q_ν is the rate of energy losses due to escaping neutrinos.

It is well known that for these rates one can write

$$q_n \sim X_c^2 \rho T^{n_1} \tag{3.2}$$

$$q_\nu \sim \frac{T^{n_2}}{\rho^{n_3}} \tag{3.3}$$

where n_1, n_2, n_3 are appropriate constants which for carbon burning are $n_1 \sim 23$, $n_2 \sim 12$, $n_3 \sim 1$.

Also, for massive stars

$$\frac{T^3}{\rho} = B(s)m^2 \tag{3.4}$$

where T, ρ are the temperature and density close to the center, B is a constant that depends on the entropy s, and m is the stellar mass.

We can combine eqs. 3.2, 3.3, 3.4 to get

$$\psi \equiv \frac{q_n}{q_\nu} \sim X_c^2 \rho^{1+n_3} T^{n_1-n_2} \sim \frac{X_c^2 T^{n_1-n_2+3(n_3+1)}}{m^{2(n_3+1)} B^{n_3+1}} \tag{3.5}$$

Remembering that the change of composition is related to the reaction rate

$$dX_c \sim -q_n dt = -q_n dT \left(\frac{dt}{dT}\right) \tag{3.6}$$

Clearly $\dot{T} \equiv \frac{dT}{dt}$ depends on $\dot{S}$ but *not* just on the local value. Rather, it depends on the structural changes of the entire core. For our purposes we assume that $\dot{T}$ does not change appreciably during fuel burning. Thus, using eq. (3.2)

$$dX_c \sim -\left(\frac{1}{\dot{T}}\right) \frac{X_c^2 T^{n_1+3}}{Bm_c^2} dT \tag{3.7}$$

or

$$d\left(\frac{1}{X_c}\right) \sim \frac{d(T^{n_1+4})}{\dot{T} B m_c^2} \tag{3.8}$$

from which

$$\frac{1}{X_c} = \frac{1}{X_c(0)} + \alpha \frac{T^{n_1+4} - T_0^{n_1+4}}{\dot{T} B m_c^2} \tag{3.9}$$

and here $X_c(0), T_0$ are the carbon mass fraction and temperature when the burning starts, α = suitable constant.

One can safely neglect $T_0^{n_1+4}$ as compared to T^{n_1+4} so that

$$X_c = X_c(0)\frac{1}{1+\alpha\frac{X_c(0)T^{n_1+4}}{\dot{T}Bm_c^2}} \tag{3.10}$$

which can be inserted into eq. (3.5) to get

$$\psi \sim \frac{X_c^2(0)T^{n_1-n_2+3(n_3+1)}}{m_c^{2(n_3+1)}B^{n_3+1}(1+\alpha\frac{X_c(0)T^{n_1+4}}{\dot{T}Bm_c^2})^2} \tag{3.11}$$

ψ is seen to have a maximum (ψ_{max}) with respect to T, which can be shown to be

$$\psi_{max} \sim \frac{X_c^2(0)}{m_c^{2(n_3+1)}B^{n_3+1}}\left\{\frac{\dot{T}Bm_c^2}{X_c(0)}\right\}^{\frac{n_1-n_2+3(n_3+1)}{n_1+4}} \tag{3.12}$$

which finally, using the numerical values of n_1, n_2, n_3, becomes

$$\psi_{max} \sim \frac{X_c^{1.4}(0)\dot{T}^{0.6}}{B^{1.4}m_c^{2.8}} \tag{3.13}$$

To satisfy our necessary condition for onset of convection-equation (3.1), we clearly need:

$$\psi > 1 \tag{3.14}$$

and thus, if from eq. (3.13) one finds that $\psi_{max} < 1$, it is clear that convection *cannot* form.

For given $X_c(0), \dot{T}$, and B, one sees that ψ_{max} decreases when m_c increaases. Indeed it can be shown that for $m_c = m_c^c$, ψ_{max} becomes smaller than unity and this explains why at m_c^c, there is a transition from a convective core to radiative burning.

Physically, what happens is that above m_c^c, the relevant parameters $(X_c(0), B, \dot{T})$ "conspire" to prevent q_n from matching q_ν by lowering X_c to the point that it overcomes the effect of the increasing temperature.

For given $\dot{T}$ and B, we see that m_c^c must increase when $X_c(0)$ increases, which is what we have found.

It remains of interest to see if we can also explain the fact that above m_c^c, convection sets in not at the center, but at mass point $m_{bc}^{(1)}$. It turns out that as burning advances outwards two things happen: $B = B(s)$ becomes larger (because s is there larger), and at the same time, $\dot{T}$ also becomes larger, mainly due to the accelerated contraction of the (carbon exhausted) core below the point of burning to where only neutrino losses operate. These two effects act in opposite directions as can be seen from eq. (3.13). The increase of B tends to prevent onset of convection but the increase of $\dot{T}$ tends to promote it. It turns out that close to the center, the effect of B dominates while at some distance from the center, $\dot{T}$ becomes dominant. Indeed, when the peak value of ψ as a function of mass for a given core is monitored in actual calculations, it is seen that the peak value of ψ first decreases but later begins to increasse until at around $m_{bc}^{(1)}$ it exceeds unity and convection sets in.

To illustrate our explanation we have shown that artificial scaling of q_ν does change m_c^c as well as $m_{tc}^{(1)}$ and in just the right way.

Let us now return to the discussion of the significance of the behavior of $m_{tc}^{(1)}$ and $m_{bc}^{(1)}$. Due to entropy losses a carbon exhausted core evolves, toward generally higher density and temperature until the next available fuel is ignited. A measure of the speed of evolution or typical timescale (τ) is given by

$$\tau = \frac{s}{\dot{s}} = \frac{Ts}{q_\nu} \tag{3.15}$$

using eqs. 2.3 and 2.4, we obtain

$$\tau = \frac{s}{T^8 B m^2} \tag{3.16}$$

Now through the condition of hydrostatic equilibrium of the entire star T is an implicit function of s and m. It is apparent that even without writing down an explicit relationship, $T(s, m)$ (which is not easy to do), that τ must be quite sensitive to s and m. In fig. 3 we show $\tau(s, m)$, which we have obtained numerically by modeling cores by artificially suppressing nuclear burning. One can see that the sensitivity is really there such that, at $s = 1$, $\tau \sim \frac{1}{m'^0}$ and at $s = 2$, $\tau \sim \frac{1}{m^6}$.

To appreciate the relevance of this sensitivity, remember that at any stage beyond carbon exhaustion in the inner core, we have a convective burning shell (whose width in mass is, say, Δm_{cc}) above such a core. This burning shell has a finite lifetime (t_{bs}) which lasts until the fuel is consumed and burning is extinguished. This burning depends on several parameters (e.g.: Δm_{cc}, $X_c(0)$, location ...) and as long as

$$t_{bs} << \tau(s, m) \tag{3.17}$$

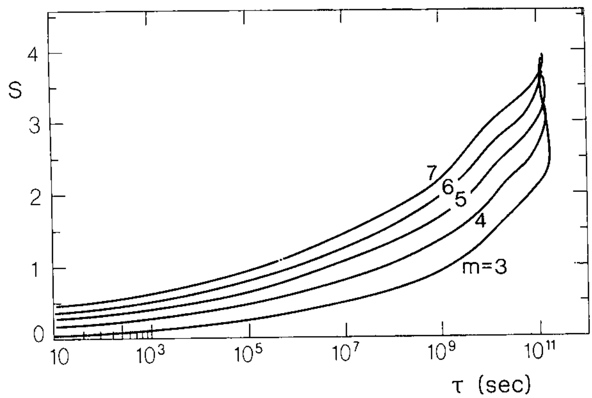

Fig. 3. The entropy, S, in units of kT is plotted as a function of the logarithm of the evolutionary time scale $\tau \equiv S/\dot{S}$ for models of a variety of masses ($M_\odot$) in which the nuclear reactions are suppressed such that the evolution is driven solely by the neutrino losses.

we should expect that the burning shell will be able to consume its fuel well before the core beneath it can evolve in a significant way. Once this happens, the core's mass grows by Δm_{cc} "suddenly" (it does take some time for neutrino losses to reduce the entropy but it is relatively short). A new convective burning shell of finite and usually larger size is then formed above it. To be precise we note that in some cases just before exhaustion of the fuel, the boundary of the convective zone recedes, leaving behind a composition gradient. In this case the new convective zone base is somewhat below the former's maximum extent. To see what happens next we go back to examine eq. (3.17). Typically, it is found that t_{bs} for the new shell becomes *longer* while τ becomes *shorter*. Eventually we should get

$$t_{bs} > \tau \tag{3.18}$$

which implies that the core can evolve without "waiting" for the burning shell. The core mass that is relevant for the next stages of burning all the way through to core collapse is frozen from then on and it is termed "final carbon exhausted core." Due to the sensitivity of the dependence of τ on m, it is found that the transition from inequality (3.17) to inequality (3.18) occurs rather abruptly at around $m^* \cong 1.6$. A "clean" explanation for the physical determination of m^* is still lacking. Without elaborating on this problem here we mention only that we believe that it is *not* simply a manifestation of the Chandrasekhar mass. For now we take the existence of m^* as an empirical fact. We shall call m^* the "critical transition mass" (CTM).

The next step in our analysis is to note that the width (in mass) of convective burning shells (Δm_{cc}) is larger when their base is located further out in the star. This is mainly a result of the relative flatness of the entropy gradient there.

Figure 4 presents the evolutionary picture of a few carbon-oxygen stars with $X_c = 0.30$. (Note that the horizontal axis is related to but not equivalent to time.) The shaded zones are convective zones and the dashed lines describe radiative burning shells. Most of the features that we have described thus far are shown in this figure. In addition one can see that the mass of the final carbon exhausted core below the outer large shaded zone is *not* monotonic in the stars' mass.

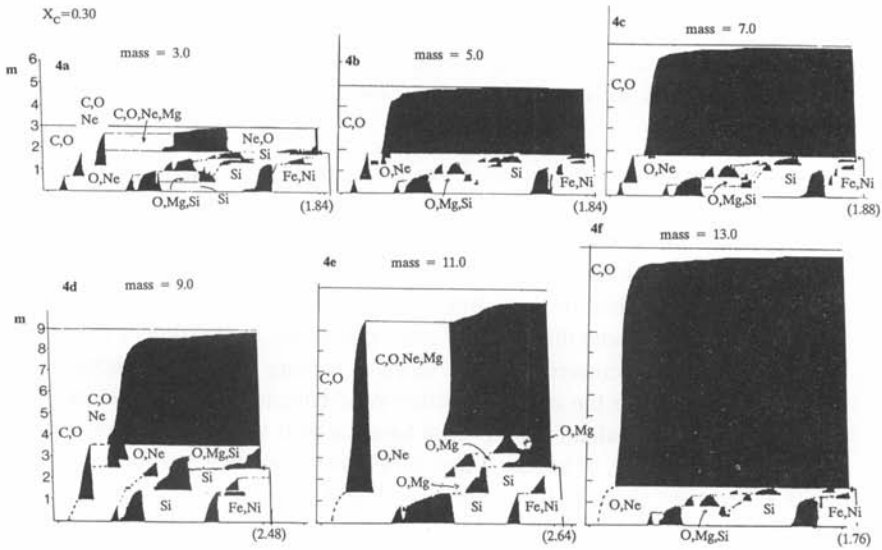

Fig. 4. The evolution of carbon-oxygen cores for $X_c = 0.30$. Shaded regions show convective zones. Horizontal axis is schematic time.

According to our line of argument presented above, this is a result of the fact that *the mass of this final core is bounded by the first convective shell whose base is above m^**. Thus, if we compare two stars whose masses are almost the same and where the top of the *last* convective zone whose *base is below m^** is in one of them just above m^* ($m = m^* + \Delta$) and in the other just below m^* ($m = m^* - \Delta$), we should expect that the final carbon exhausted core's mass will be in the first case $m^* + \Delta$, and in the other it will be $m^* - \Delta + \Delta m_{cc}$. Since Δm_{ce} can be much larger than Δ, we can find a large difference between the final core masses even though the star masses were very close to each other. Further, the core mass of the lighter star can be larger than the core mass of the slightly more massive star. Figure 5 illustrates how the carbon-exhausted final core mass is determined for carbon-oxygen stars in the mass range $2 \leq m_{co} \leq 25$, in the case where $X_c = 0.30$. The horizontal axis is m_{co} and the vertical axis shows the mass boundaries in the stars of successive convective shells. The dash-dotted line (labeled 1′) is the base of the first convective zone. Up to $m_{co} \sim 9$, it coincides with the horizontal axis (center), and from $m_{co} \sim 9$ it increases discontinuously to the point where the radiative shell burning becomes convective as described earlier. The full line (labeled 1) is (as in fig. 2) the upper boundary of the first convective zone. It increases discontinuously at $m_{co} \sim 9$ and quickly extends almost to the star's surface. However, between $m_{co} \sim 9$ and $m_{co} \sim 12.5$, the upper boundary recedes before the entire fuel is consumed and only a composition gradient remains. The dashed line (labeled 2′) is the base of the second convective zone and it is seen to coincide with the former upper boundary of the first zone (i.e., the line labeled 1) up to $m_{co} \sim 7.5$; from there up to $m_{co} \sim 9$ it coincides with the extension of the line 1′ – because this is the point at which radiative burning becomes convective. From $m_{co} \sim 9$, line 2′ jumps to a relatively high value where the receding convection left enough fuel for convective burning. The dash-cross line (labeled 2) is the upper boundary of the second convective zone. From $m_{co} \sim 7.5$ it rises quickly almost to the star's surface. The full circles' line (labeled 3′) is the base of the third convective zone. It is somewhat lower than the upper boundary of the former zone for $m_{co} \leq 6$ and coincides with it above $m_{co} \approx 6$. The crosses (labeled 3) show the upper boundary of the third convective zone which is essentially the stars' surface. For $m_{co} \leq 4$ a fourth convective zone appears (open circles labeled 4′) and extends up to the stars' surface. The horizontal dashed line represents the critical transition mass, m^*.

The final mass of the carbon exhausted core (m_{Fce}) is shown in fig. 6. The value of (m_{Fce}) can be derived from fig. 5 by joining the parts of the various lines representing the bases of convective zones which are above m^*. The nonmonotonic dependence of this core on the star's mass is evident. Similar results are derived for other values of X_c. The basic principles are identical but the quantitative values are different as have been shown in fig. 2.

In reality, since X_c depends on m_{co}, the true final carbon exhausted core should be derived by a proper interpolation; but this would not change the basic picture.

We will not describe here in any detail the stages of evolution beyond the formation of the final carbon exhausted core (i.e. neon, oxygen, silicon and

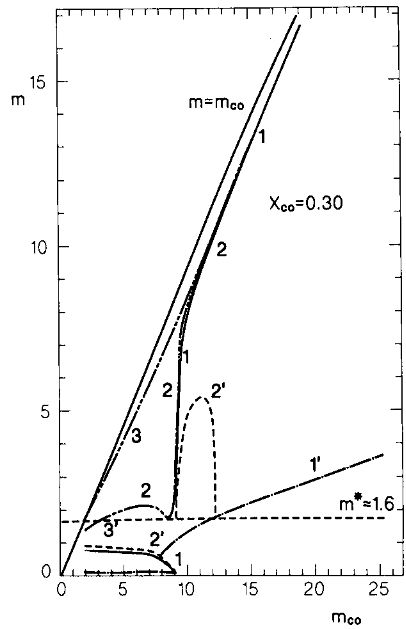

Fig. 5. Boundaries of convective zones for carbon oxygen cores, for $X_c = 0.30$, as function of core mass.

nickel burnings). We mention only that the same factors used in comparing the lifetime of a burning shell with the evolutionary lifetime of the core beneath it be used there as well. The nonmonotonicity just introduced is further complicated in the later stages. However, the actual amplitude of the nonmonotonic variations is however decreasing because the absolute size of later cores is progressively smaller.

The conclusion of this work is that from physical arguments, one should expect and should find a certain nonmonotonic dependence on both the collapsing iron core's mass and on the composition distribution within the outer layers on the mass of the carbon-oxygen core (which may on the other hand be a monotonic function of the main sequence mass, at least if mass loss itself is not too large). The role played by m^* and the dependence of the width and lifetime of convective burning shells on various parameters such as composition, reaction rates, or convective algorithm, guarantee a high level sensitivity on even small changes in these (and other) parameters. This explains the inconsistency of results published and should raise a warning flag against the simple interpolations of results.

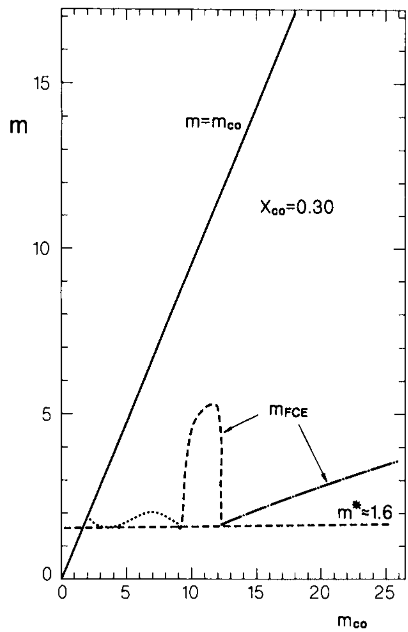

Fig. 6. Dependence of the mass of the final carbon-exhausted core (m_{Fce}) on core mass for $X_c = 0.30$.

3.3. Region III

The characteristic feature defining this region is the onset of electron capture at high Fermi energy due to a high density and relatively low temperature combination well before iron core collapse.

The width of this region in terms of the mass of the carbon-oxygen core is rather narrow ($1.40 \lesssim m_{co} \lesssim 2.0$), yet this should be still of interest in terms of populating stars because of the relative high abundance of parent stars. It is difficult to give a comprehensive picture of evolution in this region due to many complications that arise here, such as temperature inversion that promotes off-center ignition of fuels. The resulting burning shell which develops a convective zone may or may not (Nomoto 1987, Miyaji and Nomoto 1987) advance inwards and reach the center. If it does not we may find heavy, burnt out material (say Ne/Mg, Si) overlaying lighter unburned matter (say $^{16}O, ^{12}C$). The difference in composition may be crucial to the question of when and how electron capture begins. All these features are highly dependent on the star's mass as well as on physical uncertainties such as electron capture rates, heat conductivity, and on numerical algorithms, particularly in the case of convection. We shall not discuss any of these problems further here. We conclude by noting that electron capture soon leads to collapse at relatively low core mass (compared to iron core collapse), low entropy, and at least some neutron enrichment, all of which could be important for the dynamics of collapse.

3.4. Region IV

The stars in this region, bounded from above by the Chandrasekhar mass (approximately 1.40), finally evolve as classically cooling white dwarfs, at an almost constant density. Some of them, those at $m_{co} \lesssim 1.00$ (this limit as well as the others mentioned below are only approximate) do not ever burn carbon. Stars somewhat more massive than this limit do ignite carbon but do so off center. More massive stars than $m_{co} \sim 1.15$ ignite carbon centrally. Oxygen burning occurs only for $m_{co} \gtrsim 1.39$. These results are due to the nature of the evolutionary tracks which attain a maximum temperature and then evolve towards lower temperatures. It should be noted that the physical mechanism responsible for this behavior is the onset of degeneracy. The fact that there exists a minimal star mass for carbon ignition also means that there is a maximum density at which carbon can ever burn (that is, $\leq 10^7\ \mathrm{g \cdot cm^{-3}}$). Even at this density, where the electrons are partially degenerate, carbon ignition is not explosive. Finally, the rate of evolution in this region is such that up to a certain combination of density and temperature, evolution monotonically accelerates since neutrino losses become higher and higher but beyond this point, evolution quickly slows down. Note that the most important neutrino losses in this range are the plasma and/or bremsstrahlung type.

This concludes the discussion of the character of evolution in the four regions of carbon oxygen mass space. As mentioned earlier, for all but the last region, the timescale of the evolution of the carbon-oxygen core in a real star is significantly shorter than the timescale for the burning of the helium shell which may be located above it. However, this is not the case in the $m_{co} \lesssim 1.4$ region. In this region, due to the previously mentioned slowing down of evolution along the white-dwarf cooling track, the presence of a burning shell above the core may become crucial. We discuss this issue in the next section.

4. Growing stellar cores–intermediate mass stars

We have seen that carbon-oxygen cores whose mass is less than approximately 1.40 will eventually "remember" that they are actually surrounded by an envelope. The presence of this envelope may lead to the core mass growth due to the advance of the burning shell which is located above it. We shall discuss later the evolution of such growing cores. At this point we wish to define as "intermediate mass stars" those main-sequence stars which are the parents of carbon-oxygen cores that are relevant to our present discussion, that is, cores whose mass is less than approximately 1.40. This definition is equivalent to the condition that these stars develop degenerate carbon-oxygen cores.

Let us review some of the important characteristic features of the evolution of intermediate mass stars (IMS). Just beyond helium core burning, the structure of these stars shows a rather small ($m_{co} \lesssim 0.5$) carbon oxygen core, surrounded by a helium burning shell just above the core, and a hydrogen burning shell significantly higher, at m_x. The helium burning shell is at first broad, but becomes thin and travels outwards, increasing its luminosity and the core mass behind it. As this occurs the layers above this shell expand due to the absorption of energy (entropy) from the flowing radiation. This expansion lowers the temperature at the hydrogen burning shell, and eventually, this burning is extinguished. An interface consisting of a composition discontinuity (or at least a sharp gradient) is left at the location of the former burning shell, separating the helium core from the envelope. Evolutionary calculations (Kippenhahn et al. 1965, Paczynski 1970a, and Becker and Iben 1979) show that somewhat later, a convective zone which is formed at the stellar surface and becomes gradually deeper, is finally able to penetrate into the helium core through the composition interface. The results of this penetration are both the mixing of helium into the convective envelope which should show up as helium (and CNO nuclei) enrichment of the stellar surface, and the reduction of the helium core mass. In fact, the reduction of the helium core mass can be very large. Figure 7 which is given by Becker and Iben (1979) shows their results relating the core mass just before penetration (or "second dredge up" as Becker and Iben refer to this process) to core mass just after the penetration has reduced it to its minimal size as a function of stellar mass (horizontal axis) and metalicity for $0.001 \lesssim z \lesssim 0.03$. An in depth discussion of the phenomenon of this penetration will be given elsewhere. Here we only point out that as can actually be recognized even by a quick look at fig. 7, we can reinterpret this figure by plotting fig. 8, which shows that the core mass reduction (ΔmHe) depends only on the initial core

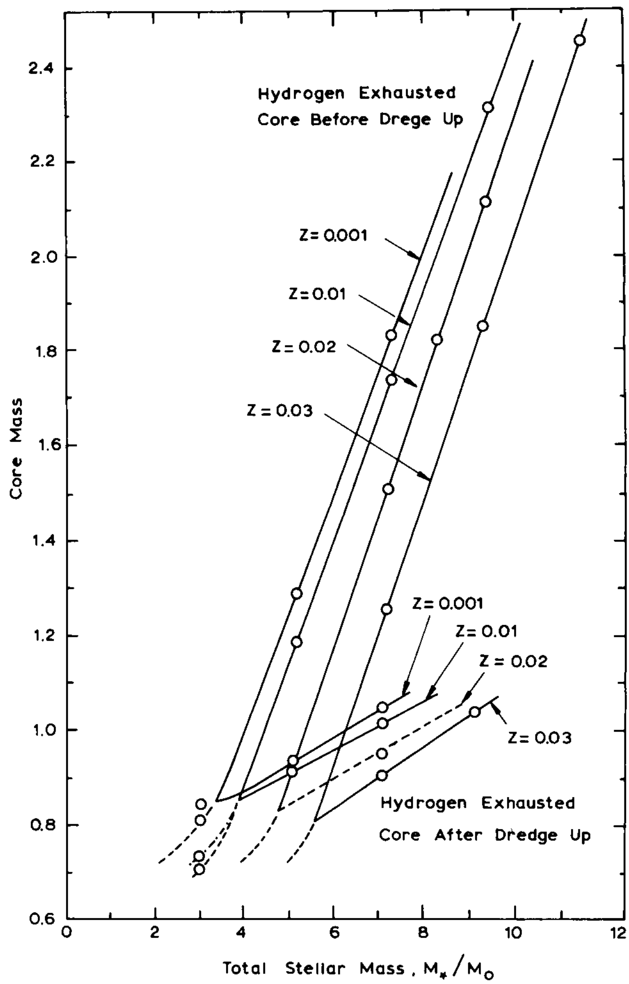

Fig. 7. The size of the hydrogen-exhausted core as a function of the total stellar mass, both before and after the second dredge-up phase. In this figure, $Y = 0.28$ and Z is allowed to vary. From Becker and Iben (1979).

mass (m_{He_i}) and does not depend on stellar mass and/or metalicity. The occurrence of penetration has an important quantitative effect on the delineation of the mass boundary of IMS; we shall come back to discuss this later.

It is found that penetration stops very close to the helium burning shell so that the mass of the helium zone becomes very small (< 0.1). This also

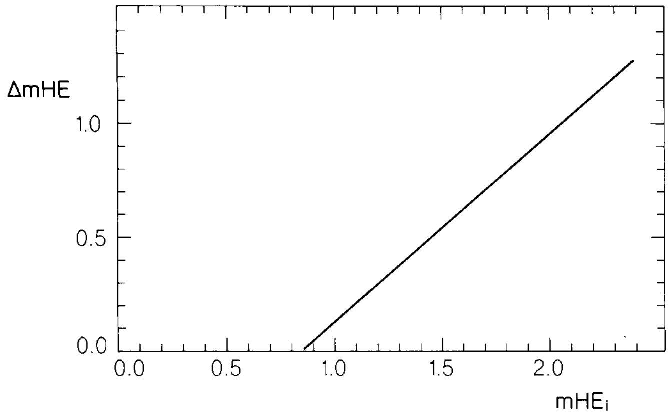

Fig. 8. Dependence of helium-core-mass reduction (ΔmHe) due to second dredge-up on initial helium core mass ($m\mathrm{He}_i$).

means that hydrogen is now present very close to the helium burning shell. It is obvious that hydrogen soon should be re-ignited. Published evolutionary calculations show that hydrogen ignition occurs radiatively and marks the beginning of the famous phase known as "double shell thermal relaxation oscillations" (first noted by Schwarzschild and Harm, 1965, and many others – see for example, Iben 1974, Becker and Iben 1980, Sackman 1977). This phase is characterized by a repeated succession of stages where a "slow and quiet" hydrogen shell burning with no helium burning is followed by a "violent" eruption of helium burning, which extinguishes hydrogen burning and consumes much of the helium accumulated by the former hydrogen burning. After the decay of helium burning, hydrogen reignites and a new and similar (but not necessarily quantitatively identical) cycle starts. We will not discuss this interesting phase of evolution here but will only remark that we feel that the details of the first reignition of the hydrogen shell have not yet been adequately studied and the possibility remains that at some subregion this ignition can be convective, which would lead to a very different sequence of events.

In any case the carbon-oxygen core beneath the helium burning shell must grow as the shells move outwards. The growth of the core mass actually only occurs when the helium shell flash consumes the helium mass layer which has been accumulated during the period of hydrogen shell burning ("interflash period"). The duration of the helium shell flash is much shorter than the interflash period, and both become exponentially shorter as the core mass grows toward $m_{co} \approx 1.40$ (Paczynski 1975). It is customary to describe the rate of core growth as a continuous process and it is then equated to the rate of helium production by the hydrogen burning shell. The luminosity of the latter burning is known to satisfy the "luminosity-core mass relation" (Paczynski 1970, 1971; Uus 1970) which has the form

$$\ell = 59250(m_{co} - 0.522) \tag{4.1}$$

We note that a theoretical explanation of this computationally derived relationship is given by Tuchman, Glasner and Barkat (1983) where the dependence of the constants in equation 4.1 on composition is also discussed, see also Kippenhahn (1981).

Writing

$$\dot{m}_{co} = \frac{\ell}{QX} \tag{4.2}$$

where Q is the Q-value of hydrogen burning ($= 6.4 \times 10^{18}$ erg $\cdot$ gr^{-1}) and X is the hydrogen mass fraction in the envelope.

One gets:

$$\dot{m}_{co} \sim 7.5(m_{co} - 0.522) * 10^{-7} M_{\odot}.\mathrm{yr}^{-1} \tag{4.3}$$

This is the rate at which the core mass grows. As discussed earlier, it only becomes relevant when the core evolution slows down along the white-dwarf-cooling-track. As it turns out at this stage, the combination of core growth which promotes evolution along isentropes, with the cooling which promotes evolution towards a lower temperature, leads to a convergence of evolutionary tracks in such a way that the evolution proceeds along a unique track which does not depend on the initial core mass (see Paczynski 1970, Barkat 1971). This track does depend on the core growth rate and on the rate of energy loss by neutrinos. Figure 9, which is taken from Couch and Arnett (1975), shows how the track can be shifted by these factors as well as how neutrino losses due to thermal Urca processes (see later) introduce certain factors. We note that most of the present discussion is also relevant to the case where a carbon-oxygen star is accreting mass from a binary companion. The only difference is that the cores mass growth rate is, in this case, a "free" parameter determined by the binary's structure and evolution. Also in this case, it is relevant to discuss the possibility that before the onset of accretion, the core may cool down to the point of solidification.

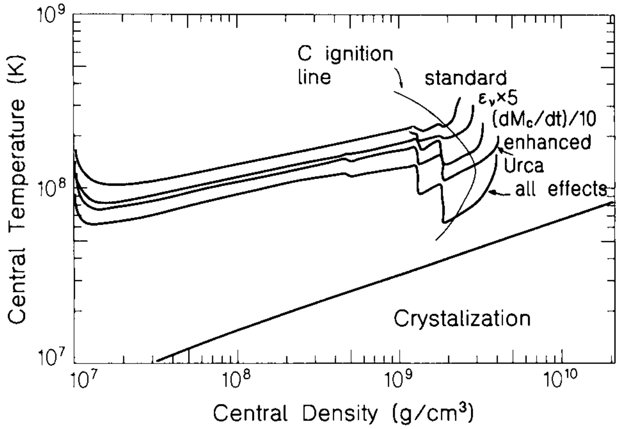

Fig. 9. Effect of uncertainties in neutrino losses, rate of core growth, and thermal Urca loss on evolution of growing carbon cores.

In any case the evolution along the common track leads, as shown in fig. 9, to a point where carbon burning is ignited at $m_c \approx 1.38$ and $\rho \gtrsim 2 \times 10^9$ g$\cdot$cm^{-3}; $T \simeq 3 \times 10^8$ K. We note that in this case the burning rate is boosted (by many orders of magnitude) by "strong screening" promoted by the high density (Salpeter and Van Horn 1969, Graboske et al. 1973). Also note that if and when carbon is absent (because of earlier exhaustion, which is the case for initial core mass $\gtrsim 1.15$) the track leads to oxygen ignition which then occurs at an even higher density $\gtrsim 10^{10}$ g $\cdot$ cm^{-3}. We will see later the significance of this fact.

Before continuing on to discuss the evolution beyond carbon ignition, we would like to stress that this evolution depends on the ability of the core to grow. Clearly, in a single star, growth happens only if the envelope is retained throughout the relevant phase of evolution; that is, up to a core mass of approximately 1.38. It is by no means clear that stars can retain their envelopes that long. Indeed, it is widely believed that well before this stage, the envelope becomes unstable and is eventually ejected forming a "planetary nebula." We will not discuss here either the observational evidence or the theoretical models for this phase. For our purpose it is sufficient to be aware of the fact that most single stars may not evolve to the kind of carbon ignition which we are about to discuss and that it is likely that if such ignition does occur, it is limited to the more massive stars.

The ignition of carbon in growing cores occurs when $\rho \sim 2 \times 10^9$ g $\cdot$ cm^{-3}, $T \sim 3 \times 10^8$ K and the Fermi energy of the electrons E_f is then a few

MeV. At such high degeneracy, ignition is expected to be explosive due to the insensitivity of pressure to temperature increase. As we will see the actual sequence of events is complicated and rather uncertain. Soon after ignition a convective zone begins to grow around the center, spreading the liberated energy over a larger mass and thus slowing the rate at which the temperature and reaction rate would otherwise increase. However, this is not too significant and unless "Urca neutrino losses," which we will discuss later, can control burning, it will indeed eventually proceed on a dynamic timescale. In this case it is clear that a burning front will form and travel through almost the entire core. The matter just behind the front is expected to be in "nuclear statistical equilibrium" at a temperature of approximately 8×10^9 K. The dominant nucleus in this case is ^{56}Ni, and since the total liberated energy is larger than the binding energy, the star explodes producing large amounts of ^{56}Ni. This is currently believed to be the mechanism for a Type I supernova. It can be shown that the burning front may be either a "deflagration" or a "detonation." For a full discussion of the general nature of such fronts, the reader is referred to a number of sources: Courant and Friedrichs (1948), Landau and Lifshitz (1959), Zeldovich and Raizer (1966), and Mazurek and Wheeler (1980).

Several recent papers discuss the question of whether the front in our case is a detonation or a deflagration (e.g., Khokhlov 1991, Woosley and Weaver 1986a, Barkat et al. 1990). We will not discuss the issue here beyond the following remarks.

a. A major difference between a detonation and a deflagration is that the former travels supersonically with respect to the matter ahead of it, while the latter in the same aspects travels subsonically. The significance of this difference in the present context is rather significant as we will see later.

b. Both fronts can be shown to continue to propagate as long as the density is larger than approximately $10^7\ \mathrm{g \cdot cm^{-3}}$. In the present case this means that almost the entire core is incinerated to ^{56}Ni since very little mass (≤ 0.1 at the very edge) is at a lower density. Observationally, this raises a difficult contradiction since in supernovae of Type I, one sees significant amounts of only partially burnt carbon (e.g., Branch et al. 1982, 1983). It appears that the only way to resolve this problem is to "convince" the star to expand such that before the front arrives at the surface, the density is lower than $10^7\ \mathrm{g \cdot cm^{-3}}$ over a significant part of the star. Such pre-expansion can be naturally promoted by a deflagration, which as was already mentioned moves subsonically and can be shown to necessarily push a shock ahead of it. In contrast, in the case of a detonation, one needs an independent mechanism to induce pre-expansion. It is possible that in reality, a combination of a deflagration and a detonation occurs – see Khokhlov 1991, Barkat et al. 1990, Woosley and Weaver 1986a. It is important to note that there are at least some numerical simulations of the explosions that are quite successful in reproducing observational spectra, such as the deflagration model of Nomoto, Thielemann, and Yokoi (1984). Yet, we will immediately see that things might actually be more complex.

Let us return to the discussion of evolution from just after carbon ignition in the core up to the time where burning occurs on a dynamic timescale. Note that most of the following discussion is taken from Barkat and Wheeler (1990). We have already seen that a convective zone grows around the center, spreading the entropy produced and mixing the composition over a larger and larger mass. At first (Arnett 1969) it was believed that nothing can prevent burning from evolving into a thermal runaway.

However, a crucial new ingredient was added when Paczyński (1972) suggested that an adaptation of the "*pulsational Urca process*" (Tsuruta and Cameron 1970) to the case of *convection* could act as a restraining mechanism against the thermal runaway. The basic ideas are very simple:

1. A nucleus ("daughter") may (i.e., has a finite chance to) capture an electron and transform itself into another nucleus ("mother") if the sum of its rest mass and the energy of the electron (rest mass plus kinetic energy) is higher than the rest mass of the mother. Equivalently, the energy of the electron must be greater than the difference between the rest masses of mother and daughter, which is called the "threshhold energy." A "mother" nucleus may emit an electron and transform itself into a "daughter" if the sum of energies of the electron and daughter can be less than the rest-mass energy of the mother. In *both* cases – electron capture or emission – the difference between the energies of the initial and final states is carried away by a neutrino (or antineutrino, as the case may require; in the following we shall use "neutrino" for both). These processes are schematically illustrated by the energy-level diagrams in fig. 10.

2. The matter, which originally contains either suitable mother or daughter nuclei, is subjected to a cycle where the condition for capture is fulfilled in one half of the cycle and the condition for emission is fulfilled in the other half. In this case it should be expected that energy be continuously lost from the system because of the neutrino flux. The probability for the capture (emission) events per nucleus can be shown (Tsuruta and Cameron 1970) to be only a function of the difference between the energy of the electrons and the threshold energy. If successive cycles are identical, we should then expect that a steady state must sooner or later be established where the abundances of mother and/or daughter nuclei will be (to first order) fixed at any phase of the cycle.

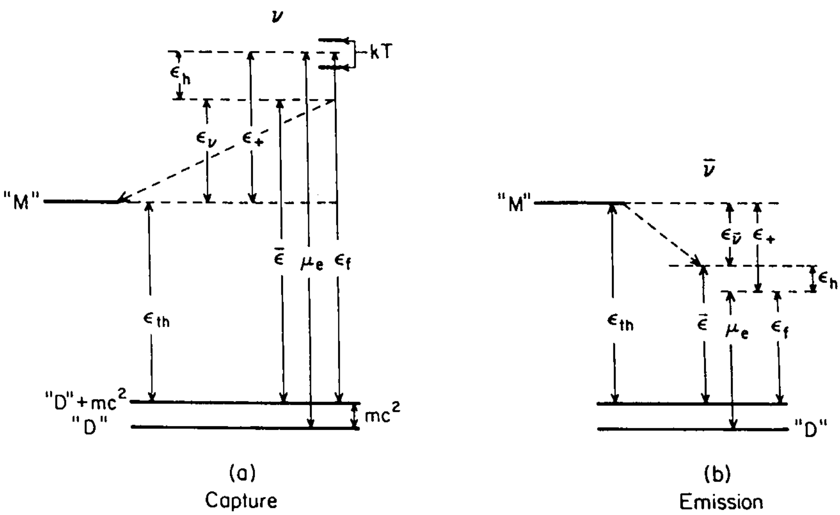

Fig. 10. Schematic energy-level diagram illustrating the relevant energies for electrons, neutrinos, and nuclei for (a) the capture of an electron on a "daughter" nucleus with the associated emission of a neutrino and (b) the decay of the "mother" nucleus with the associated emission of an antineutrino. See text for definition of symbols and associated discussion.

The original Urca process was suggested by Gamow and Schoenberg (1941), and the role of the "cycle" was actually played by the thermal smearing ($\sim KT$) around the Fermi energy which allows both captures and emission at any time the Fermi energy is equal to the relevant threshold energy. Tsuruta and Cameron (1970) applied the same idea to the case of a vibrating high-density star. Matter, which is located at a density for which the Fermi energy is close to the threshold energy of a suitable Urca nucleus (e.g., ^{23}Na at 4.4 MeV or $\rho = 1.714 \times 10^9$ g cm^{-3}), may find itself repeatedly above and below the threshold because of the vibration.

Paczyński (1972) realized that an Urca process should be set up when a convective zone can carry "mother" and/or "daughter nuclei" back and forth across the location in the star where the Fermi energy of the electrons equals their threshold energy. This location in mass coordinates, m_U, where the Fermi energy is equal to the threshold energy, will be denoted as an "Urca shell," and the corresponding radius will be called the "Urca radius." The formalism developed by Tsuruta and Cameron (1970) (see also Paczyński 1973) was used by Paczyński (1972) as the basis for his quantitative estimates.

Paczyński (1972) showed that the rate of energy loss by escaping Urca neutrinos ("Urca losses") would become equal to the energy generation by carbon burning while the extension of the convective zone beyond the Urca radius is still rather small, $\Delta r/r \ll 1$. The central temperature determines the thermonuclear burning rates directly and determines the Urca losses indirectly throughout the extent of the convective core. Paczyński showed that the responsiveness to the increase in central temperature is such that Urca losses ($\propto T^{170}$) are far more sensitive than the thermonuclear rates ($\propto T^{20}$). It follows that Urca losses are easily capable of controlling carbon burning and thus preventing thermal runaway. Paczyński went on to discuss the possible outcome, concluding that a collapse due to electron captures on O and Mg (Finzi and Wolf 1967; Wheeler and Hansen 1971) might be the end result. On the basis of these ideas, Ergma and Paczyński (1974) computed the evolution of carbon-oxygen cores. They found that the result depended on the initial carbon abundance, X_C, but for $X_C < 0.5$, convective Urca losses were able to control carbon burning, so that in a convective core of $0.4\,M_\odot$, carbon was almost completely exhausted before a runaway occurred (see fig. 11).

It was soon pointed out by Bruenn (1973) that the basic electron capture (emission) process actually *heats* matter in spite of the neutrino energy loss. If this were the case, the convective Urca process would not really affect the thermal runaway, and in any case would render the convective Urca mechanism altogether uninteresting.

Couch and Arnett (1975) argued that Bruenn's heating must be offset by work done by convection in carrying the relevant nuclei around a cycle. They evolved cores in which the convective Urca losses were *assumed* to balance thermally the nuclear burning. The evolution to higher density is driven by the continuous contraction of the core; this is due to both the growth of the core in mass and to the decrease in Z/A which accompanies electron capture on some products of carbon burning. Couch and Arnett found that thermal balance is maintained under conditions with monotonically increasing central temperature and hence, the nuclear reaction rates. They found that eventually the evolution became too fast for the Urca process to be important, so that the runaway would then be revived. Contrary to Ergma and Paczyński (1974), they found that at the time of runaway, carbon was far from being exhausted. The runaway point was estimated to be postponed from approximately 2×10^9 up to approximately $6 \times 10^9\ \mathrm{g \cdot cm^{-3}}$ (fig. 11). While this is a substantial change in central density which would result in a considerable increase in the resulting neutronization of the ejecta (Sutherland and Wheeler

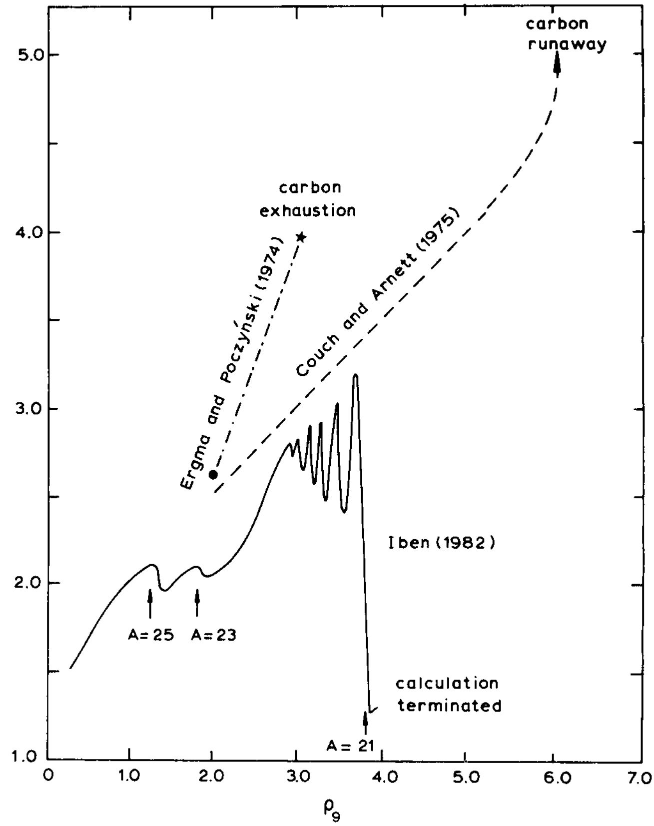

Fig. 11. The results of previous studies of the effect of convective Urca process on the evolution of degenerate carbon-oxygen white dwarfs subsequent to carbon ignition are shown in the central temperature-central density plane, where $\rho_9 \equiv \rho_c/10^9$ g · cm^{-3} and $T_8 \equiv T_c/10^8$ K. Ergma and Paczyński (1974) found that for initial carbon abundance, $X_C < 0.5$, carbon was almost completely exhausted before dynamic thermal runaway occurred. Couch and Arnett (1975) assumed that convective Urca cooling balanced heating and found the core to evolve to approximately 6×10^9 g · cm^{-3} before dynamic thermal runaway. Iben (1982) did the most complete study and found "thermal Urca" cooling on $A = 25$ and $A = 23$ pairs, followed by convective Urca cooling as the core grew in density to exceed the threshold for a convective Urca shell due to the $A = 21$ pair, at which point the calculation was terminated.

1984; Woosley, Axelrod, and Weaver 1984), it is nevertheless not too relevant to the basic dynamic conclusion that detonation or deflagration would still develop, disrupting the star.

Rather than assume that heating is unimportant, Iben (1978, 1982) attacked the problem by compiling in his evolutionary code all relevant equations and physical data. He analyzed his evolutionary calculations in great detail and found that the control temperature went through strong oscillations during the phase when the first Urca pair, ^{23}Na-^{23}Ne, controlled the burning. In the hot state the neutrino cooling exceeded the heating, and in the cool state the heating exceeded the Urca neutrino losses. Iben found that the Urca zone divided into two pieces when a second Urca-active pair, ^{21}Ne-^{21}F, crossed the density threshold at $\rho_c \simeq 3.8 \times 10^9$ g $\cdot$ cm^{-3}. This new central Urca zone was essentially in local equilibrium and strongly cooled the center. This caused the base as well as the outer edge of the outer convective Urca shell to be fixed. Since the convective shell could not expand to increase the Urca cooling, the nuclear heating dominated, and temperature in the convective shell began to increase. Iben concluded that a thermal runaway probably takes place at $\rho \simeq 4 \times 10^9$ g $\cdot$ cm^{-3}, a density high enough to cause problems with the neutronization of the ejecta. This behavior is quite different from that predicted by Couch and Arnett (1975) or by Ergma and Paczyński (1974) (see fig. 11). We will return to a discussion of these results. For now it is enough to say that Iben's calculations are complex and have not been fully assimilated by the community. Most subsequent calculations of degenerate carbon runaway have ignored the convective Urca process and assumed thermal runaway at moderate central densities ($\lesssim 2 \times 10^9$ g$\cdot$cm^{-3}), whereas for a white dwarf that has cooled prior to accretion, the runaway could occur at considerably higher densities (Iben 1982).

Barkat and Wheeler (1990) have recently re-analysed the problem and concluded that while one may wish to check some of the quantitative predictions of Iben's work, it is inappropriate to ignore his main conclusions; so runaway at $\rho \sim 2 \times 10^9$ g $\cdot$ cm^{-3} is highly questionable.

We note that if the thermal runaway occurs at a density which is higher than approximately 10^{10} g$\cdot$cm^{-3} (e.g., this will be the case if and when carbon has been exhausted), one finds that the temperature density combination of the matter behind a burning front (of either type) induces the onset of nuclear statistical equilibrium. The composition in this case promotes very high electron capture rates (as well as neutrino losses) which lower the pressure on a dynamic timescale such that a severe rarefaction wave forms. It is expected that in this case the explosion may turn into an implosion (see Colgate 1971, Barkat et al. 1970, Bruenn 1972, Buchler et al. 1974, Mazurek et al. 1974), and this could be a scenario for formation of neutron stars, with or without a supernova. Returning to the "standard" carbon explosion case, we conclude that to obtain a theoretical model that agrees reasonably well with observations of Type I supernovae, one must avoid the onset of "convective Urca." We estimate that this might be achieved if ignition occurs at a density lower than approximately 10^9 g $\cdot$ cm^{-3}. A rough estimate (based on fig. 9) shows that for this to happen, we need the relevant rate of neutrino losses to be *scaled down* by about an order of magnitude. We are currently checking to see if this is permitted on physical grounds.

References

Arnett, W.D. 1969. Ap. Space Sci. 5, 180
Arnett, W.D. 1977. Ap. J. (Suppl) 35, 145.
Barkat, Z. 1971. Ap. J. 163, 433.
Barkat, Z. 1977. Proc. IAU. Session on supernovae Grenoble, Eds Schramm, D.N.D., Reidel publishing company, Dorrect-Holland, 131.
Barkat, Z., G. Rakavy, and N. Sack. 1967. Phys. Rev. (Letters) 18, 379.
Barkat, Z., J.R. Buchler, and J.C. Wheeler. 1970. Ap. Lett. 6, 117.
Barkat, Z. and A. Marom. 1990. in Supernovae, Jerusalem Winter School, Eds. Wheeler, J.C., Piran, T. and Weinberg, S., Vol 6., 95.
Barkat, Z., E. Livne, D.A. Swartz, and J.C. Wheeler. 1990. in Supernovae, Jerusalem Winter School, Eds. Wheeler, J.C., Piran, T. and Weinberg, S., Vol 6., 133.
Barkat, Z. and J.C. Wheeler. 1990. Ap. J. 355, 602.
Becker, S.A. and I. Iben Jr. 1979. Ap. J. 232, 831.
Becker, S.A. and I. Iben Jr. 1980. Ap. J. 237, 111.
Branch, D., R. Buta, S.W. Falk, M.L. McCall, P.G. Sutherland, A.K. Uomoto, J.C. Wheeler, and B.J. Wills. 1982. Ap. J. (Letters) 252, L61.
Branch, D., C.H. Lacy, M.L. McCall, P.G. Sutherland, A. Uomoto, J.C. Wheeler, and B.J. Wills. 1983. Ap. J. 270, 123.
Bruenn, S.W. 1972. Ap. J. 177, 459.
Bruenn, S.W. 1973. Ap. J. (Letters) 183, L125.
Buchler, J.R., J.C. Wheeler, and Z. Barkat. 1974. Ap. Space Sci. 26, 391.
Colgate, S.A. 1967. Ap. J. 150, 163.
Colgate, S.A. 1971. Ap. J. 163, 221.
Couch, R.G., and W.D. Arnett. 1975. Ap. J. 196, 791.
Courant, R. and K.O. Friedrichs. 1948. Supersonic Flow and Shock Waves (New York; Interscience).
Ergma, E., and B. Paczyński. 1974. Acta Astr. 24, 1.
Finzi, A., and R.A. Wolf. 1967. Ap. J. 150, 115.
Frayley, G.S. 1968. Astrophys. Space Sci. 2, 96.
Gamow, G., and M. Schoenberg. 1941. Phys. Rev. 59, 539.
Graboske, H.C., H.E. DeWitt, A.S. Grossman, and M.S. Cooper. 1973. Ap. J. 183, 177.
Iben, I., Jr. 1974. Ann. Rev. Astr. Ap. 12, 215.
Iben, I., Jr. 1978. Ap. J. 219, 213.
Iben, I., Jr. 1982. Ap. J. 253, 248.

Kippenhahn, R. 1981. Astr. Ap. 102, 293.
Kippenhahn, R., H.C. Thomas, and A. Weigert. 1965. Zs. f. Ap. 61, 241.
Khokhlov, A.M. 1991. Astr. Ap. 245, 114.
Landau, L.D. and E.M. Lifshitz. 1959. Fluid Mechanics Reading: Addison-Wesley.
Marom, A. 1990. Thesis (Hebrew University of Jerusalem).
Marom, A., and Z. Barkat. 1993. In preparation.
Mazurek, T.J., J.W. Truran, and A.G.W. Cameron. 1974. Ap. Space Sci. 27, 261.
Mazurek, T.J., and J.C. Wheeler. 1980. Fundamental of Cosmic Physics 5, 193.
Miyaji, S. and K. Nomoto. 1987. Ap. J. 318, 307.
Nomoto, K. 1987. Ap. J. 322, 206.
Nomoto, K., F.-K. Thielemenn, and K. Yoki. 1984. Ap. J. 286, 644.
Nomoto, K. and K. Hashimoto. 1986. Prog. Part. Nuc. Phys. 17, 267.
Ober, W.W., M.F. El Eid, and K.J. Fricke. 1983. Astr. and Ap. 119, 61.
Paczynski, B. 1970. Acta Astron. 20, 195.
Paczynski, B. 1971a. Acta Astron. 21, 221.
Paczynski, B. 1971b. Acta Astron. 21, 417.
Paczynski, B. 1972. Ap. Letters 11, 53.
Paczynski, B. 1973. Acta Ast. 23, 1.
Paczynski, B. 1975. Ap. J. 202, 558.
Sackman, I.-J. 1977. Ap. J. 212, 159.
Salpeter, E.E. and H.M. Van Horn. 1969. Ap. J. 155, 183.
Schwarzschild, M. and R. Harm. 1965. Ap. J. 159, 903.
Sutherland, P.G., and J.C. Wheeler. 1984. Ap. J. 280, 282.
Tsuruta, S., and A.G.W. Cameron. 1970. Ap. Space Sci. 7, 374.
Tuchman, Y., A. Glasner, and Z. Barkat. 1983. Ap. J. 268, 356.
Uus, U. 1970. Nauch. Inform. Akad. Nauk USSR, 17, 30.
Wheeler, J.C. 1977. Astrophys. Space Sci. 50, 125.
Wheeler, J.C. 1990. in Supernovae, Jerusalem Winter School, Eds. Wheeler, J.C., Piran, T. and Weinberg, S., Vol 6., 1.
Wheeler, J.C., and C.J. Hansen. 1971. Ap. Space Sci. 11, 373.
Wilson, J.R., R. Mayle, S.E. Woosley, and T.A. Weaver. 1986. Proc. of the Twelfth Texas Symp. Ann. N.Y. Acad. Sci.
Woosley, S.E., T.S. Axelrod, and T.A. Weaver. 1984. in Stellar Nucleosynthesis, ed. C. Chiosi and A. Renzini (Dordrecht: Reidel), p. 263.
Woosley, S.E., and T.A. Weaver. 1986a. *in* Radiation Hydrodynamics in stars and compact objects, eds. D. Michalas and K.-H.A. Winkler (Berlin; New York; Springer-Verlag), 91.
Woosley, S.E., and T.A. Weaver. 1986b. Ann. Rev. Astr. Ap. 24, 205.
Zeldovich Y.B. and Y.P. Raizer. 1966. Physics of Shock Waves and High Temperature Hydrodynamic Phenomena (New York; London; Academic Press).

COURSE III

MASSIVE STARS, SUPERNOVAE, AND NUCLEOSYNTHESIS

S. E. WOOSLEY

Board of Studies in Astronomy and Astrophysics
University of California at Santa Cruz
Santa Cruz CA 95064, USA

and

General Studies Group, Physics Department
Lawrence Livermore National Laboratory
Livermore CA 94550, USA

and

T. A. WEAVER

General Studies Group, Physics Department
Lawrence Livermore National Laboratory
Livermore CA 94550, USA

S. Bludman, R. Mochkovitch and J. Zinn-Justin, eds.
Les Houches, Session LIV 1990
Supernovae

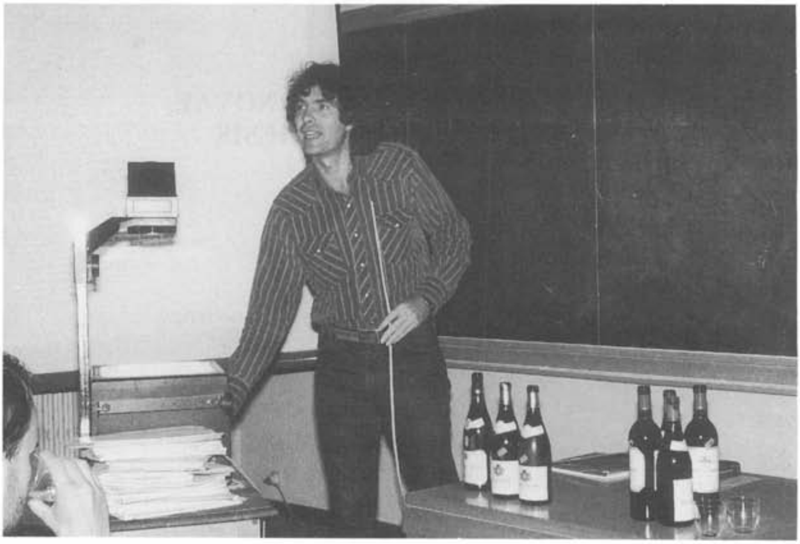

Contents

1. The evolution of massive stars 66
   1.1. The physics of the calculation 66
   1.2. A brief overview of massive stellar evolution 73
   1.3. Stars in the mass range 15 to 80 $M_\odot$ 77
   1.4. The path to instability and neutron star masses 83
2. Type II supernovae 88
   2.1. Core collapse and bounce 88
   2.2. "Delayed" explosions 90
      2.2.1. An overview and some general comments 90
      2.2.2. Energy absorbing and emitting processes 95
   2.3. Shock propagation and break out 102
   2.4. Light curves of Type II supernovae 102
   2.5. X-ray and γ-ray emission 103
3. Type I supernovae 106
   3.1. Type Ia 106
      3.1.1. Some general considerations 108
      3.1.2. Deflagration flame physics 110
      3.1.3. Attempts to improve on the standard model 113
   3.2. Accretion-induced collapse 120
   3.3. Type Ib supernovae 122
4. Explosive nucleosynthesis in supernovae of Type II and Ib 127
   4.1. Parameterized explosive nucleosynthesis 128
   4.2. The neutrino-nucleosynthesis process 135
   4.3. Nucleosynthesis of ^{26}Al 139
   4.4. The α-rich freeze-out and the r-process 144

References 151

1. The evolution of massive stars

1.1. The physics of the calculation

We first consider the evolution of massive stars as determined by the construction of computer models. The basic physics included in our calculations was discussed by Weaver et al. (1978), but there have been many changes since and it is worth reviewing the current situation (see also Woosley and Weaver 1988).

We begin with the equations of momentum and energy conservation written in Lagrangian coordinates:

$$\frac{\mathrm{d}v}{\mathrm{d}t} = -4\pi r^2 \frac{\partial P}{\partial m} - \frac{Gm}{r^2} + \frac{4\pi}{r}\frac{\partial Q}{\partial m} \tag{1.1}$$

and

$$\frac{\mathrm{d}\epsilon}{\mathrm{d}t} = -4\pi P \frac{\partial}{\partial m}(vr^2) - 4\pi Q \frac{\partial}{\partial m}\left(\frac{v}{r}\right) - \frac{\partial L}{\partial m} + \dot{S}. \tag{1.2}$$

Although these might appear complicated, they contain terms that should be familiar. In the first equation, if the acceleration is zero and the term containing the artificial viscosity is set to zero, one recovers the usual condition of hydrostatic equilibrium. In the second equation there are terms for the work that compression (or expansion) does, the energy transported by radiative diffusion or convection, the energy generated by nuclear reactions (less neutrino losses), and, again, a term for the viscosity. The viscosity is given by

$$Q = \tfrac{4}{3}\eta_v r^4 \tfrac{\partial}{\partial r}\left(\tfrac{v}{r}\right), \tag{1.3}$$

where

$$\eta_v = \eta_R + \tfrac{3}{4} l_1 \rho c_s + \tfrac{3}{4} l_2^2 \rho \max(0, -\nabla v), \tag{1.4}$$

and η_R, the *real* viscosity, is taken equal to zero, $l_1 \approx 0.1\Delta r$, and $l_2 \approx 2\Delta r$, where Δr is the zone size. The advantage of solving the hydrodynamic equations rather than just the stellar structure equations (eqs. (1.1) and (1.2), but with no acceleration term and no viscosity) is that it removes the need to make an abrupt transition from one code to another when the star decides to do something dynamic. Such transitions are difficult to accomplish while maintaining near equilibrium, where it exists, and conserving energy. One disadvantage, occasionally, is that we might not want to study *everything* that the star does along the way that is dynamic (e.g., Cepheid oscillations of the outer envelope), but usually such occurrences can be handled with only minor annoyance.

It is essential, however, that these equations be forward differenced and solved implicitly, which is to say the derivatives of all quantities must be included in the calculation and a matrix (which is tri-diagonal since each zone speaks only to the one above and beneath) must be inverted in each iteration. Explicitly differenced hydrodynamics, while easier numerically, suffers from the requirement that time steps be a small fraction of the sound crossing time for any zone (Courant condition). One could never evolve a star with such a severe constraint, and even if one could, energy conservation would become a problem. While the implicit solution is straightforward in one dimension, no one has yet extended the method to a stellar evolution code in two or three dimensions. To preserve composition boundaries, such a code would need to be Lagrangian (mass zoned) rather than Eulerian (space zoned) or else use a moving finite mesh. Nonradial motions would result in "bow-ties" without some clever scheme for rezoning. So far no such code exists.

One must also specify an equation of state (EOS). This too is straightforward although tedious. Since the code will be used under conditions ranging from a collapsing hydrogen cloud (or exploding supernova) to a neutron star, the EOS must be correct in regions where the electrons have an arbitrary degree of degeneracy and a speed arbitrarily close to the speed of light. The radiation is simple, always a black body, and the ions are always Maxwellian, except deep in neutron stars. In making excursions to density in the vicinity of the atomic nucleus, which we hardly ever do, terms must be included for the nuclear force. So far, we have not done this.

One must also compute the ionization state correctly in order to get both the pressure and opacity. We assume thermal equilibrium and solve a Saha equation with terms included to approximate pressure ionization. As an option, usually employed only for the study of supernova light-curve calculations, the Saha equation may be solved for all the ionization states of up to 14 elements as heavy as nickel ($Z = 28$).

Just as one must include modifications to the ideal gas equation when the strong force becomes important, one must also correct for the electrical interaction that occurs because the ions and electrons have charge. These are loosely known as the "Coulomb corrections." They lead to a decrement in the pressure and internal energy. The pressure decrement is approximately (Clayton 1968)

$$\begin{aligned} P_{\text{coul}} &= -0.3\left(\frac{4\pi}{3}\right)^{1/3} N_A^{4/3}\, e^2\, Y_e^{1/3} \rho^{4/3} \sum \frac{Z_i^{5/3} X_i}{A_i} \\ &\approx -5.7 \times 10^{12}\, Y_e^2\, \bar{A}^{2/3}\, \rho^{4/3} \text{ dyne cm}^{-2} \end{aligned} \tag{1.5}$$

where $\bar{A}$ is the mean atomic weight and Y_e is the electron number density divided by ρN_A. Of some relevance is the correction to the (zero-temperature) Chandrasekhar mass implied by these terms

$$M_{\text{ch}} \approx M_{\text{ch}}^0\, [1 - 0.0226\,(Z/6)^{2/3}]. \tag{1.6}$$

Next one must consider how to treat convection. This is the greatest source of variety in the results obtained by several groups studying massive stellar evolution. There is no accurate theory of convection, but everyone today uses some variation of "mixing length" theory (see Clayton 1968 for a simple discussion). Convection transports energy and changes the composition, and both effects are very important. So long as one is interested only in energy transport in a region where the entropy gradient is clearly superadiabatic, and so long as the time scale for mixing is not close to other physically relevant time scales (nuclear, Kelvin Helmholtz, etc.), then the results are not sensitive to the convective formulation employed. The difficulty comes in how to treat convective boundaries, how to treat regions that are semiconvective (see below), and whether to believe the results when mixing and nuclear time scales become comparable.

A historical split in the way convection is treated comes about because the adiabatic condition can be written two ways

$$\begin{aligned} \frac{\mathrm{d}P}{P} - \Gamma_1 \frac{\mathrm{d}\rho}{\rho} &= 0, \\ \frac{\mathrm{d}P}{P} + \frac{\Gamma_2}{1-\Gamma_2}\frac{\mathrm{d}T}{T} &= 0. \end{aligned} \tag{1.7}$$

For convective instability, $A > 0$ or $B > 0$, where

$$\begin{aligned} A &= \frac{1}{\rho}\frac{\mathrm{d}\rho}{\mathrm{d}r} - \frac{1}{\Gamma_1 P}\frac{\mathrm{d}P}{\mathrm{d}r}, \\ B &= \frac{\Gamma_2 - 1}{\Gamma_2}\frac{1}{P}\frac{\mathrm{d}P}{\mathrm{d}r} - \frac{1}{T}\frac{\mathrm{d}T}{\mathrm{d}r}. \end{aligned} \tag{1.8}$$

Here A is known as the *Ledoux* condition for instability, and B is the *Schwarzschild* condition. These two conditions are equivalent except when there are gradients in composition or when radiation pressure is important. Then the Ledoux criterion is more restrictive since

$$A = \frac{4 - 3\beta}{\beta} B + \frac{1}{\mu}\frac{\mathrm{d}\mu}{\mathrm{d}r}, \tag{1.9}$$

where β is the ratio of gas pressure to total pressure. Expressions for Γ are given in Woosley and Weaver (1988).

In our zoned numerical model two dimensionless quantities are calculated

$$\begin{aligned} W_A &= \ln\left(\frac{\rho_1}{\rho_o}\right) - \frac{2}{\Gamma_1^{(1)} + \Gamma_1^{(o)}} \ln\left(\frac{P_1}{P_o}\right) \\ W_B &= \frac{F_o + F_1}{2} \ln\left(\frac{P_1}{P_o}\right) - \ln\left(\frac{T_1}{T_o}\right), \end{aligned} \tag{1.10}$$

where $F = (\Gamma_2 - 1)/\Gamma_2$ and the superscripts and subscripts "0" and "1" refer to the inner and outer zone, respectively. Obviously $W_A > 0$ corresponds to Ledoux convection and $W_B > 0$ corresponds to Schwarzschild convection.

The convective velocity is then computed (e.g., Clayton 1968)

$$V_C = \frac{1}{2}\left(\frac{GM}{\rho r^2} \Delta \nabla \rho\right)^{1/2} l, \tag{1.11}$$

using $W_A = (\Delta \nabla \rho / \rho) \Delta r$.

The "mixing length" l is the pressure scale height:

$$l = \frac{P_o + P_1}{\rho_o + \rho_1} \frac{r_o^2}{GM(r_o)}, \tag{1.12}$$

and operationally Δr is given by $(\Delta M_o + \Delta M_1)/(4\pi r^2(\rho_o + \rho_1))$. A semiconvective velocity can be calculated in an analogous fashion using $W_B = (\Delta \nabla T/T)\Delta r$. The diffusion coefficient for compositional mixing, D_B, is

$$D_B = \tfrac{1}{3} V_C\, l \tag{1.13}$$

and the radiative diffusion coefficient is

$$D_r = \frac{1}{3} \frac{acT^3}{\kappa \rho^2} \left(\frac{\partial \epsilon}{\partial T}\right)_\rho^{-1}. \tag{1.14}$$

The semiconvective diffusion coefficient is

$$D_S = \frac{F D_r D_B}{F D_r + D_B}, \tag{1.15}$$

where F is an arbitrary parameter.

Once the diffusion coefficient is known, convective mixing in either case A or case B is calculated from the diffusion equation

$$\left(\frac{\partial Y_i}{\partial t}\right)_{\text{conv}} = \frac{\partial}{M_r}\left[(4\pi r^2 \rho)^2 D \frac{\partial Y_i}{\partial M_r}\right] \tag{1.16}$$

and added to the purely nuclear terms for $(\mathrm{d}Y_i/\mathrm{d}t)$.

In our studies during the last 3 years, since shortly before SN 1987A, we have generally carried out our calculations with two choices for F in eq. (1.15). In the cases we shall call "unrestricted semiconvection" or sometimes "semiconvection on," F is 0.1. This basically amounts to using a diffusion coefficient for the composition in semiconvective regions equal to 10% that of the radiation diffusion coefficient. The other standard choice, which we call "restricted semiconvection," is $F = 10^{-4}$. This is not exactly the same as using the strict Ledoux criterion; mixing time scales and evolution time scales near the end of hydrogen exhaustion are still comparable. But, as we shall see, it makes a big difference to the evolution of the star what one chooses for F. We have never been able, for example, to get a blue progenitor for SN 1987A, even using the LMC composition, unless $F \lesssim 10^{-3}$.

Note that none of our calculations ever correspond exactly to the case of Schwarzschild convection (as, for example, Nomoto and his colleagues and many others employ). Even if F were taken arbitrarily large, we still do not (so far) transport energy in semiconvective regions by means other than radiation diffusion. Of course, once the composition is mixed, a semiconvective region will usually become convective, so maybe the distinction is not great. Still, $F = 0.1$ is not the same as Schwarzschild convection. The limit $F = 0$ is, however, the strict Ledoux case. We suspect that these distinctions are the cause of (relatively minor) differences between our calculations and those of Nomoto's group. The distinction is particularly important during silicon burning where a decrease in Y_e, the electron mole number, owing to electron capture should, and in the LeDoux case does inhibit mixing between layers where electron capture has not occurred. Naively one would expect such a restriction on convection to result in smaller iron cores, but in fact just the opposite can occur. More efficient convection can cause the silicon core to grow to a critical mass and collapse at just that point where, in the LeDoux case, additional convective shell burning might have occurred.

Which choice for F, if any, is right? A lot of work remains to be done, but a very interesting study of semiconvection has recently been carried out by Spruit (1990). He claims, based upon laboratory experiments, that semiconvection is a "double diffusive" phenomenon, with the region breaking down into cells. Inside a cell there is no composition gradient and convection proceeds as normal. In the zone boundaries, however, the composition gradients are expressed and energy and mass only crosses these boundaries by diffusion. He obtains for the semiconvective diffusion coefficient

$$D_{\mathrm{S}} = (D_r D_{\mathrm{ion}})^{1/2} \left(\frac{4}{\beta} - 3\right) \frac{\nabla_r - \nabla_a}{\nabla_\mu} \tag{1.17}$$

where D_r is given by eq. (1.14), D_{ion} is the ionic diffusion coefficient, β is the ratio of gas pressure to total pressure, ∇_r is the logarithmic derivative of the radiation temperature with respect to radius, ∇_μ is a similar derivative of the composition, and ∇_a is the adiabatic gradient. In typical circumstances the ionic diffusion coefficient is about 10^6 times smaller than the radiative diffusion coefficient and the logarithmic derivative terms give a number less than unity. This suggests a choice $D_{\mathrm{S}} \sim 10^{-4} D_r$ may not be too bad, but the dependence on composition (especially ionic charge) and thermodynamic conditions is much more complex than eq. (1.15) would indicate. We are in the process of implementing this new procedure, but note so far the indication that our "restricted semiconvection" calculations with $F = 10^{-4}$ may be the more physical.

Certainly the part of the computer calculation that takes most of the time and requires the greatest attention is the nuclear physics. This gives both the energy generation rate and the nucleosynthesis. For computational efficiency and clarity, we use different methods for calculating the nuclear reaction network at different stages of the stars evolution. It is scarcely necessary to carry a 150 isotope network to get the energy generation in hydrogen burning correct (although it *is* necessary for silicon burning). The workhorse of the code is the "19 Isotope Approximation Network." This is mostly an "α-chain" from ^{4}He through ^{56}Ni, but includes dummy links to the odd-mass nuclei, e.g., ^{24}Mg(α, p)^{27}Al(p,γ) ^{28}Si which are assumed to be in steady state, i.e., $dY(^{27}\mathrm{Al})/dt = 0$. The inverses of these links are also included for a total of 80 reactions. The "real nuclei" included, those for which matrix elements are actually computed and inverted, are the neutron and proton (hydrogen), ^{3,4}He, ^{12}C, ^{14}N, ^{16}O, ^{20}Ne, and α-particle nuclei up through ^{56}Ni, and ^{54}Fe. Steady-state links of one form or another pass through the nuclei ^{2}H, ^{13}C, ^{13,15}N, ^{14,15,18}O, ^{23}Na, ^{27}Al, ^{31}P, and all the α-particle-minus-one-proton nuclei through ^{55}Co. Also included are the heavy-ion reactions ^{12}C + ^{12}C, ^{12}C + ^{16}O, and ^{16}O + ^{16}O. This network is used from hydrogen burning through oxygen burning until $X(^{16}\mathrm{O}) = 0.04$.

After oxygen depletion one needs additional nuclei in the network in order to follow the electron capture and positron decay (and at *very* late times, β decay) reactions that alter the stellar structure. This is where the going gets tough. Computation through oxygen shell burning and silicon burning take about 80% of the total calculation time. In those zones where oxygen has been (nearly) depleted we use a "quasiequilibrium network" composed of 125 isotopes from magnesium through mass 60. This should be good for $Y_e \gtrsim 0.43$. Efforts are currently underway by Aufderheide, Fushiki, and Hartmann to extend this network to lower Y_e and higher mass numbers. Photodisintegration flow downwards from magnesium to α's is coded explicitly (Bodansky et al. 1968). Two groups of equilibrium isotopes are assumed to be coupled by nonequilibrated link at mass 45 (Woosley et al. 1973).

When there are two groups not in mutual equilibrium, one must specify five independent parameters: T, ρ, η, $X(^{28}\mathrm{Si})$, and $X(^{56}\mathrm{Ni})$, for example, to determine all the abundances. When the two groups melt into one, four parameters specify all abundances (drop $X(^{56}\mathrm{Ni})$). When silicon disappears, true nuclear statistical equilibrium is achieved and three parameters specify all abundances. For reasons of stability, we do not convect individual isotopes in regions that are in quasi- or nuclear-statistical equilibrium. The code would take very small time steps watching the individual nuclei adjust to their new temperature. Instead we convect the parameters of the equilibrium, η and $X(^{28}\mathrm{Si})$. This mixing is *not* implicitly coupled to the stellar structure calculation. Rather one does alternate cycles of "mix and burn" for each time step.

In order to verify that the approximation and equilibrium networks are functioning properly and in order to calculate detailed isotopic nucleosynthesis, an arbitrary implicitly coupled network of any size (currently 150 isotopes) can be carried along in each calculation. This network is selected from a nuclear library of over 500 isotopes. The matrix is inverted in every zone where any substantial nuclear activity is going on and the abundances are convectively mixed. There exists a version of the code in which the large network is coupled to the structure equations, but this is rarely used. Also included in this network are the reactions necessary to study light isotope nucleosynthesis and neutrino-induced reactions (charged and neutral current on all isotopes). References for the reaction rates in the current code are given in Woosley et al. (1990a,b). Tables of reaction rates evaluated at several temperatures are available for a limited time and for those with a serious "need to know" from Robert Hoffman at UCSC.

The greatest uncertainty in the nuclear physics presently employed in the study of massive stellar evolution is the reaction rate for $^{12}C(\alpha, \gamma)^{16}O$. Current estimates range from zero (disallowed since we must breathe) to as much as five times the currently favored value (Caughlan and Fowler 1988). As we shall see, a value roughly twice that of Caughlan and Fowler (1988) seems to be preferred on nucleosynthetic grounds and values more than three and less than one times this standard rate cause nucleosynthetic difficulty.

1.2. A brief overview of massive stellar evolution

The general characteristics of massive stellar evolution and nucleosynthesis have been reviewed many times. See, for example, Arnett (1978); Nomoto and Hashimoto (1986); Chiosi and Maeder (1986); Woosley and Weaver (1986); Woosley (1986); Maeder and Meynet (1988, 1989); Barkat and Marom (1990), and references in all of these.

It is helpful, however, to keep in mind some general characteristics and fiducial numbers (see also Arnett 1978; Nomoto 1984; Nomoto and Hashimoto 1986). From the equation of hydrostatic equilibrium (eq. (1.1) after dropping appropriate terms in acceleration and viscosity) and assuming constant density, it follows that $P_c/\rho_c \propto M/R \propto M^{2/3}\rho^{1/3}$, or $P_c^3/\rho_c^4 \propto M^2$. In fact, one obtains the same proportionality (see, e.g. Clayton 1968; p. 162) in the more general case of a polytrope of index n, in which it can be shown

$$\frac{P_c^3}{\rho_c^4} = 4\pi G \left(\frac{M}{\phi}\right)^2 \tag{1.18}$$

where $\phi = (n+1)^{3/2}\zeta_1^2(d\phi/d\zeta)_{\zeta_1}$, or 10.73 in the case of an n = 3 polytrope.

The pressure may take several forms – ideal gas, radiation, and degeneracy dominate in various situations, but consider as is appropriate, two limiting cases when either ideal gas pressure dominates (or β, the ratio of ideal gas pressure to total pressure, is constant) or electron degeneracy. In the former, since $P_c \propto \rho_c T_c$ (or to T_c^4), the centers of spheres of constant mass will evolve along lines of constant T_c^3/ρ_c. As the star contracts, it heats up and $T \propto \rho^{1/3}$. Eventually, however, either nuclear reactions occur or the core becomes degenerate. If it becomes degenerate, the pressure is no longer sensitive to the temperature. A limiting density is reached (if the electrons do not become fully relativistic) and the core ceases contraction. Along the way, between these two limits, the center of the star of given mass passes through a maximum temperature. If this is sufficient to ignite a given fuel, the star does so, spends some time at approximately those conditions, and then contracts again.

This simple behavior is complicated by several effects: (1) degenerate flashes – sometimes ignition of the fuel significantly changes the structure of the star including the relation between T_c and ρ_c; (2) neutrino losses, which may create temperature inversions; (3) nuclear burning, which affects the abundances of key nuclear fuels; and (4) convection, which affects the extent of various compositional shells, beyond what is already determined by the reaction rates and EOS.

Since complexity is easy to find in stellar evolution, we instead start simply. We construct spheres of constant mass and composition in hydrostatic equilibrium at a density sufficiently low that both degeneracy and nuclear reactions are negligible. As will be appropriate, we consider cores of 0.30, 0.40, and 0.50 $M_\odot$ composed of pure helium, 0.75 and 1.00 $M_\odot$ cores of half carbon and half oxygen, and 1.25, 1.35, 1.40, and 2.0 $M_\odot$ cores of 75% oxygen and 25% neon. These cores are allowed to contract, heat up, reach some maximum temperature before encountering degeneracy, and then cool off. The results are given in fig. 1 and table 1.

Table 1
Conditions at maximum temperature for contracting cores

Mass ($M_\odot$)	Age (yr)	T (K)	ρ (g cm^{-3})	L (erg s^{-1})
0.30	1.3(7)	8.60(7)	1.0(5)	5.3(33)
0.40	1.1(7)	1.27(8)	2.0(5)	1.9(34)
0.50	5.2(6)	1.74(8)	3.4(5)	4.9(34)
0.75	1.2(6)	4.66(8)	1.6(6)	6.9(35)
1.00	9.0(5)	7.61(8)	5.3(6)	2.0(36)
1.25	7.4(5)	1.32(9)	2.6(7)	4.9(36)
1.25$^\nu$	1.6(5)	6.63(8)	6.5(6)	4.9(37)
1.35	8.1(5)	1.65(9)	6.8(7)	5.7(36)
1.40	9.1(5)	1.88(9)	1.4(8)	6.0(36)

Table 1 shows the conditions near maximum central temperature for these cores. In one case, 1.25 $M_\odot$, neutrino losses were included. These had the effect of shifting the maximum to an earlier time when the temperature and density were both lower. When neutrino losses are important, however, it

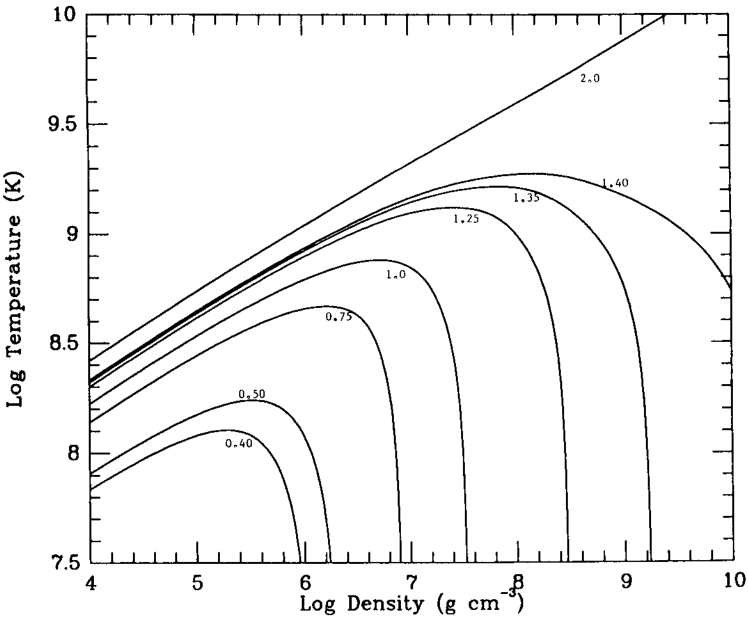

Fig. 1. Central temperature and density for contracting spheres of various masses and appropriate composition (see text). A maximum temperature is reached that depends on the mass, then the core becomes degenerate and cools. Curves are for core masses of (from bottom to top) 0.4, 0.5, 0.75, 1.0, 1.25, 1.35, 1.40, and 2.0 $M_{\odot}$. Neutrino losses and nuclear reactions were ignored in this simple study.

can be misleading to examine only the central conditions. In the case of the 1.25 $M_{\odot}$ core, for example, the actual temperature maximum occurred well off center (fig. 2) at a later time and was twice the central temperature at that time. An obvious consequence of this is that some stars, particularly those near the borderline, may ignite their nuclear burning off center. Inverted compositions may develop with, for example, neon-burning ashes on top of unburned neon. Further burning of central material must await the depletion of fuel in overlaying shells and/or the inefficient propagation of burning inwards by conduction. This makes the studies of such stars very time consuming and complex.

Because of the extreme temperature sensitivity of nuclear energy generation in stars, there is a well-defined ignition temperature for a given fuel. For hydrogen burning it is around 10^7 K and for helium burning about 10^8 K (depending on the density). For heavier fuels the ignition condition can

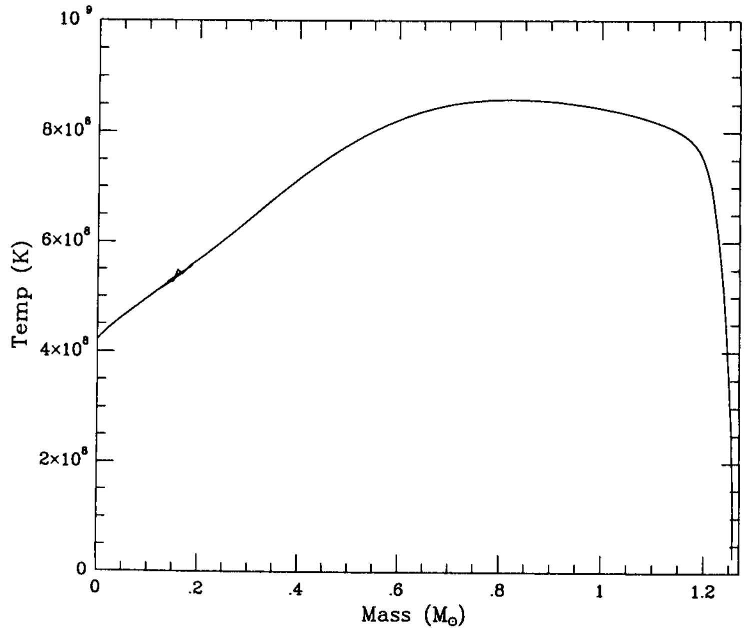

Fig. 2. Temperature distribution in a neon oxygen core of 1.25 $M_\odot$ at a time when maximum temperature (8.6×10^8 K) is reached in the star. This maximum occurs later than peak central temperature and well off center.

be determined from balanced power considerations, equating nuclear energy generation to neutrino losses, leading to an ignition temperature of about 0.74, 1.3, and 1.8, and 3.0 billion K for carbon, neon, oxygen, and silicon, respectively. Table 1 then suggests critical masses of about 0.3 $M_\odot$ for helium ignition, 1.0 $M_\odot$ for carbon ignition, 1.3 $M_\odot$ for neon ignition, and 1.4 $M_\odot$ for oxygen ignition. As mentioned previously, there are modifications for neutrino losses. Calculations that include neutrino losses and burning are straightforward and have been carried out by a number of groups (see summary in Nomoto 1984) with the result that the actual critical masses for helium, carbon, and neon are 0.31 $M_\odot$, 1.06 $M_\odot$, and 1.37 $M_\odot$, respectively.

Equating these critical core masses to their corresponding main sequence masses can be misleading because of the dependence upon initial helium abundance, which affects the size of the helium core; semiconvection, which affects, for a given helium core size, the mass of the carbon-oxygen core; and the reaction rate for $^{12}C(\alpha, \gamma)^{16}O$. Generally speaking however, one needs main sequence masses heavier than about 8 $M_\odot$ to ignite carbon.

Complicated effects of off-center ignition and burning shells continue to about 13 $M_\odot$, although with restricted semiconvection and a small rate for $^{12}C(\alpha,\gamma)^{16}O$, even a 15 $M_\odot$ star may ignite neon burning off center. By 18 $M_\odot$ and beyond though, all burning stages, hydrogen through silicon, ignite at the center of the star.

1.3. Stars in the mass range 15 to 80 $M_\odot$

Historically these are the stars deemed most likely to give the common Type II events, especially Type IIp. SN 1987A is a member of this set and, at least in ways not specifically related to the blue nature of the progenitor star, Sk 202-69, is typical of the evolution expected in this mass range. Mass loss may be important for the circumstellar environment in which the supernova explodes and for nucleosynthesis, but the late stages of evolution for single stars lighter than about 35 $M_\odot$ is uniquely determined by the mass of the helium core at the end of carbon burning. The mass of this core ranges from roughly 1/4 to 1/3 as one moves from the light to heavy ends of the range – a 15 $M_\odot$ star has a helium core of 4 $M_\odot$; a 35 $M_\odot$ star has a core of 14 $M_\odot$.

Above $\sim$35 $M_\odot$ mass loss may be so efficient as to uncover the helium core during the red giant stage and produce a Wolf–Rayet (WR) star (cf. Chiosi and Maeder 1986). Mass loss rates for WR stars may be very large and mass dependent, Langer (1989) suggests, for example, a value for WNE, WC, and WO stars (those showing large surface enhancements of nitrogen, carbon, and oxygen respectively) of

$$\dot{M}_{WR} = (0.6\text{–}1.0) \times 10^{-7} \left(\frac{M_{WR}}{M_\odot}\right)^{2.5} M_\odot\ y^{-1}. \qquad (1.19)$$

Such rates imply that a very massive star, say 65 $M_\odot$, may evaporate all the way down to 5 $M_\odot$ during its evolution. Such a 5 $M_\odot$ residual of a very massive star has, at the time it explodes as a supernova, a very different structure and composition than is obtained either from evolving a 5 $M_\odot$ helium core without mass loss or taking the inner 5 $M_\odot$ of a 65 $M_\odot$ star evolved without mass loss. In particular the carbon-oxygen core is a much larger fraction of the helium core than in the constant mass case (sometimes 100%) and the entropy is higher. Both these effects have important consequences for models of Type Ib supernovae, a subject to which we shall return in section 3.3.

Table 2
25 $M_\odot$ presupernova properties

Model	25S1	25S3	25N1	25N3
$^{12}C(\alpha,\gamma)^{16}O$*	1	3	1	3
Semiconv.	high**	high	low**	low
Metals	solar	solar	solar	solar
^{1}H	9.38	9.33	10.12	10.10
^{4}He	8.61	8.51	10.24	10.28
^{12}C	0.75	0.21	0.65	0.38
^{14}N	8.2(−2)	8.0(−2)	8.7(−2)	9.4(−2)
^{16}O	3.0	2.7	1.3	2.0
^{20}Ne	1.2	0.12	0.70	0.14
^{24}Mg	0.12	2.2(−2)	0.11	5.0(−2)
^{28}Si	0.34	1.1	0.32	0.28
^{32}S	0.14	1.0	0.16	0.16
^{36}Ar	2.1(−2)	0.26	2.2(−2)	3.7(−2)
^{40}Ca	7.7(−3)	0.29	1.1(−2)	2.3(−2)
^{22}Na	3.8(−6)	4.8(−8)	1.5(−6)	1.2(−8)
^{26}Al	4.6(−5)	3.8(−5)	6.8(−6)	2.6(−5)
M_{Fe}	1.45	1.51	1.37	1.53
M_{3500}	1.73	1.58	1.59	1.90
M_{4500}	1.83	1.65	1.67	2.02
M_{He}	9.2	9.3	9.2	9.3
M_{Z}	6.7	6.8	4.5	4.5
R_{12}	59	60	55	55
L_{38}	10	11	8.7	8.8

*Compared to the most recent tabulated experimental value by Caughlan and Fowler (1988).
**High means a semiconvective diffusion limited by $F = 0.1$ in eq. (1.15) the radiative diffusion coefficient. "Low" is 1000 times smaller.

Tables 2 through 7 and figs. 3 and 4 present the results of some recent models (Weaver and Woosley 1991) employing varying prescriptions for semiconvection (see section 1.1) and values for the uncertain $^{12}C(\alpha,\gamma)^{16}O$ reaction rate.

These tables show a number of interesting properties of massive stellar evolution. First we note the dependence of nucleosynthesis on the reaction rate for $^{12}C(\alpha,\gamma)^{16}O$. To the extent that a 25 $M_\odot$ star is representative, tables 2 and 3 show that the nucleosynthesis becomes unacceptable, one way or another, if the reaction rate is much less than that of Caughlan and Fowler (1988) (e.g. Models 25S1 and 25N1) or more than three times larger (Models 25S3 and 25N3). For the small capture rate neon, a carbon burning

Table 3
15, 25, and 35 $M_\odot$ presupernova properties

Model	15S2	15N2	25S2	25N2	35S2	35N2
$^{12}C(\alpha,\gamma)^{16}O$	2	2	2	2	2	2
Semiconv.	high	low	high	low	high	low
Metals	solar	solar	solar	solar	solar	solar
^{1}H	6.90	7.30	9.38	10.10	11.07	12.54
^{4}He	5.18	5.77	8.44	10.27	12.39	14.16
^{12}C	0.16	0.10	0.28	0.48	0.32	0.83
^{14}N	5.2(−2)	6.0(−2)	8.0(−2)	9.2(−2)	0.13	0.11
^{16}O	0.80	0.25	3.91	1.88	6.73	4.45
^{20}Ne	0.20	8.6(−2)	0.14	0.13	0.94	0.48
^{24}Mg	3.0(−2)	1.6(−2)	5.1(−2)	4.38(−2)	0.45	0.32
^{28}Si	0.21	0.14	0.56	0.39	0.62	0.39
^{32}S	0.14	7.3(−2)	0.25	0.17	0.34	0.13
^{36}Ar	3.0(−2)	1.8(−2)	5.7(−2)	3.3(−2)	7.3(−2)	2.8(−2)
^{40}Ca	1.6(−2)	5.5(−3)	2.8(−2)	1.2(−2)	5.9(−2)	1.4(−2)
^{22}Na	2.2(−7)	6.9(−8)	6.4(−8)	4.2(−8)	9.2(−7)	2.0(−7)
^{26}Al	1.1(−5)	1.0(−5)	4.6(−5)	2.1(−5)	3.4(−4)	1.7(−4)
M_{Fe}	1.35	1.23	1.95	1.49	2.03	1.63
M_{3500}	1.58	1.40	2.24	1.80	2.17	2.06
M_{4500}	1.66	1.43	2.48	1.89	2.45	2.21
M_{He}	4.45	4.25	9.19	9.20	14.0	14.6
M_Z	2.72	1.72	6.88	4.30	11.1	7.17
R_{12}	34.9	34.6	61.4	56.9	79.4	81.4
L_{38}	3.45	2.05	10.6	8.68	18.5	18.0

product, is overproduced by more than a factor of two relative to oxygen in the sun. For the large rates, not only are neon and magnesium greatly *underproduced*, but at least in the case of efficient semiconvection, the high entropy associated with a star that skips carbon and neon burning leads to a vast convective oxygen burning shell where silicon and sulfur are greatly *overproduced*. It would be impossible to hide all this silicon and sulfur in the neutron star without making a black hole. It is also interesting that the convective oxygen shell in 25S3 devours most of the carbon oxygen core. There would be very little helium burning s-process ejected from such a star. From this study, a value of about twice the $^{12}C(\alpha,\gamma)^{16}O$ rate of Caughlan and Fowler would be favored on the basis of nucleosynthesis (models 25N2 and 25S2).

One may, of course, question any conclusions based upon a single stellar mass. Tables 3 and 6 show, however, that 15 and 35 $M_\odot$ stars are unlikely to repair the deficiencies of the 25 $M_\odot$ models. If a small alpha-capture rate is considered (15S1), the neon production is still large in a lower mass star (although 15N1 remains to be calculated). If the large rate is employed, neon and magnesium are too small and silicon again too big, although this latter problem is not so severe in the very massive stars. Given all the uncertainties in explosion mechanism, convective theory, and the abundances themselves, it would be premature to claim a particular value for $^{12}C(\alpha, \gamma)^{16}O$ based upon stellar nucleosynthesis, but for now we note a significant preference for a value twice that of Caughlan and Fowler (1988). The ^{22}Na and ^{26}Al synthesis in these models also depend on, among other things, the rate for $^{12}C(\alpha, \gamma)^{16}O$ and will be discussed further in section 4.3.

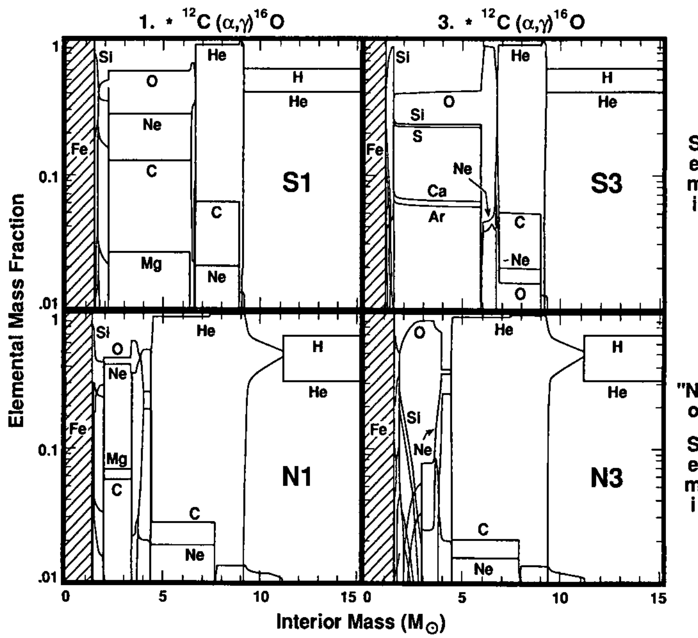

Fig. 3. Core and envelope compositions for four 25 $M_\odot$ stars in which semiconvection and the $^{12}C(\alpha, \gamma)^{16}O$ reaction rate were varied. The bottom two employed a small value for the semiconvective mixing coefficient ($F = 10^{-4}$); the upper two used a larger one ($F = 0.1$). Note the larger CO-core and different structure at the base of the hydrogen envelope in the latter case.

Table 4
25 $M_\odot$ metallicity study

Model	25TS1	25TS3	25TN1	25TN3
$^{12}C(\alpha, \gamma)^{16}O$	1	3	1	3
Semiconv.	high	high	low	low
Metals	0.01 $Z_\odot$	0.01 $Z_\odot$	0.01 $Z_\odot$	0.01 $Z_\odot$
^1H	9.33	9.34	10.35	10.32
^4He	8.71	8.67	10.62	10.69
^{12}C	0.75	0.17	0.64	0.37
^{14}N	1.0(−3)	1.0(−3)	1.2(−3)	1.2(−3)
^{16}O	2.9	3.1	1.1	1.8
^{20}Ne	1.6	0.12	0.56	1.5(−2)
^{24}Mg	0.19	2.9(−2)	0.13	1.2(−2)
^{28}Si	2.5(−2)	1.0	0.18	0.25
^{32}S	3.1(−4)	0.81	4.5(−2)	0.15
^{36}Ar	1.5(−5)	0.18	5.3(−3)	3.9(−2)
^{40}Ca	1.0(−5)	0.17	1.4(−3)	2.1(−2)
^{22}Na	8.2(−6)	3.0(−8)	2.7(−6)	3.3(−8)
^{26}Al	3.1(−6)	3.2(−7)	7.3(−6)	1.6(−6)
M_{Fe}	(1.65)*	1.56	1.47	1.49
M_{3500}	1.69	1.67	1.78	1.79
M_{4500}	1.78	1.75	1.86	1.90
M_{He}	9.2	9.1	9.2	9.2
M_Z	6.7	6.6	4.2	4.2
R_{12}**	52	64	2.9	2.7
L_{38}**	10	10	~9**	~9**

* Implosive oxygen burning in progress. Core poorly defined.
** Pulsating.

The sensitivity of results to the semiconvective diffusion coefficient is also apparent. Most of the differences can be traced to the smaller CO-core obtained when semiconvection is restricted (fig. 2). This gives less heavy-element production and, generally speaking, smaller iron cores. The envelope of the supernova progenitor can also be greatly affected, especially if the metallicity is low (see table 4). There comes a metallicity, however, when even stars with full semiconvection end their lives as blue supergiants (tables 5 and 6).

Finally, we note (table 7) the possibility that very massive stars endowed with mass loss rates as large as suggested by (1.19) may lose, not only all of their hydrogen envelope, but a portion of their helium and carbon–oxygen

Table 5
25 $M_\odot$ Very low metallicity

Model	25ZS1	25ZS3	25US3	25ZN1	25ZN3
$^{12}C(\alpha,\gamma)^{16}O$	1	3	3	1	3
Semiconv.	high	high	high	low	low
Metals	zero	zero	10^{-4} $Z_\odot$	zero	zero
^1H	10.19	10.20	9.79	11.01	11.01
^4He	7.61	7.57	8.66	9.92	10.02
^{12}C	0.49	0.32	0.34	0.55	0.34
^{14}N	1.9(−7)	1.4(−2)	1.4(−5)	1.4(−7)	1.6(−7)
^{16}O	3.4	3.5	3.4	1.1	1.8
^{20}Ne	0.72	0.19	0.11	0.66	1.1(−2)
^{24}Mg	0.40	1.8(−2)	8.4(−2)	0.12	4.3(−3)
^{28}Si	0.37	0.65	0.36	0.23	0.24
^{32}S	8.4(−2)	0.55	0.21	0.10	0.16
^{36}Ar	1.2(−2)	0.13	4.8(−2)	2.4(−2)	4.5(−2)
^{40}Ca	4.3(−3)	0.16	2.7(−2)	5.5(−3)	2.2(−2)
^{22}Na	1.5(−6)	8.7(−7)	1.7(−7)	2.4(−6)	5.4(−9)
^{26}Al	7.9(−5)	4.7(−6)	7.5(−5)	7.8(−8)	4.0(−8)
M_{Fe}	1.90	1.83	2.05	(1.33)*	1.49
M_{3500}	2.13	2.03	2.27	1.56	1.83
M_{4500}	2.30	2.24	2.53	1.63	1.95
M_{He}	8.4	8.1	8.6	7.5	7.5
M_Z	7.1	6.4	6.4	4.1	4.1
R_{12}**	1.2	1.1	1.1	0.71	0.69
L_{38}**	~10**	~8**	~10**	~9**	~7**

* Implosive oxygen burning in progress. Core poorly defined.
** Pulsating.

core as well. The final structure of stars such as 60WRA does not closely resemble what one would obtain from the evolution of an isolated helium core of any mass evolved without mass loss. That is the 4.25 $M_\odot$ residual of Model 60WRA is very different from the end of the evolution of a 4.25 $M_\odot$ bare helium core. Part of the difference is that the carbon–oxygen core in the mass losing calculation is much larger, roughly all of the star in Model 60WRA, although the surface abundance of helium remains nontrivial. The entropies are also higher since the late stages of evolution proceed so quickly that the star retains memory of its previous large size. Thus the density gradients around the iron core and the size of the iron core itself are very different from those of a lower mass star. We shall return to discuss these differences further when we consider the possible origin of Type Ib supernovae (section 3.3) from such stars.

Table 6
Other presupernova models

Model	15S1	15S3*	15T3	15Z3	35S3
Mass/$M_\odot$	15	15	15	15	35
$^{12}C(\alpha,\gamma)^{16}O$*	1	3	3	3	3
Semiconv.	high	high	high	high	high
Metals	solar	solar	0.01 $Z_\odot$	zero	solar
^1H	6.92	6.88	6.86	7.33	11.0
^4He	5.24	5.15	5.27	4.98	12.2
^{12}C	0.18	0.13	0.14	0.15	0.27
^{14}N	5.6(−2)	5.2(−2)	6.0(−4)	4.4(−8)	0.13
^{16}O	0.52	0.92	0.96	0.83	6.75
^{20}Ne	0.44	4.9(−2)	7.3(−3)	7.0(−2)	0.22
^{24}Mg	9.9(−2)	3.4(−2)	7.9(−3)	2.7(−2)	6.6(−2)
^{28}Si	0.14	0.28	0.24	5.1(−2)	0.98
^{32}S	4.9(−2)	0.15	0.14	3.7(−2)	0.96
^{36}Ar	5.2(−3)	4.2(−2)	3.7(−2)	8.0(−3)	0.33
^{40}Ca	2.6(−3)	1.9(−2)	1.8(−2)	7.6(−3)	0.23
^{22}Na	5.2(−7)	4.3(−9)	7.5(−10)	2.4(−7)	1.7(−7)
^{26}Al	1.2(−5)	1.2(−5)	4.6(−8)	1.0(−5)	8.5(−5)
M_{Fe}	1.41	1.33	1.39	1.56	1.92
M_{3500}	1.50	1.60	1.67	1.75	2.12
M_{4500}	1.55	1.66	1.75	1.85	2.23
M_{He}	4.4	4.5	4.7	3.8	14.2
M_Z	2.7	2.8	2.9	2.8	11.2
R_{12}	35	35	26	0.61	78
L_{38}	3.5	3.5	2.2	2.4	19

1.4. The path to instability and neutron star masses

One frequently reads the simplistic statement in the literature that the iron core of a massive star collapses because it: (a) exceeds the Chandrasekhar mass, and; (b) can no longer generate nuclear energy. Some people even go so far as to claim that this explains why neutron stars should have gravitational masses near 1.4 $M_\odot$. While all these statements are truein an approximate, general sense, they obscure some very interesting physics. Consider the traditional Chandrasekhar mass

$$M_{\mathrm{ch}} = 5.83\ Y_e^2 \tag{1.20}$$

which is 1.457 $M_\odot$ for $Y_e = 0.50$. There are numerous corrections that must be added (and subtracted) from this when considering a real stellar core, which after all is not an isolated white dwarf.

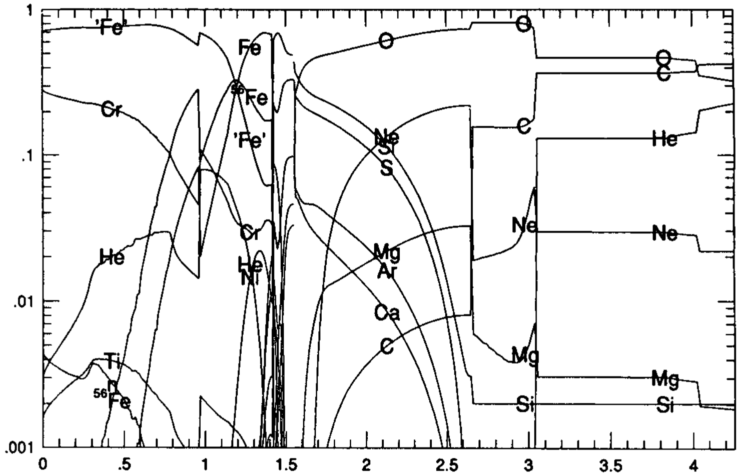

Fig. 4. Composition of Model 60WRA at the time its iron core collapsed. Extensive mass loss as a Wolf–Rayet star has reduced the star's mass to 4.25 $M_\odot$. Central temperature at this point is 8.07×10^9 K and the central density is 6.12×10^9 g cm^{-3}. The luminosity is 4.4×10^{38} erg s^{-1} and the radius 3.9×10^{10} cm. The model contains 400 zones and about 27 000 models have been calculated since carbon ignition. The material external to the iron core is almost entirely carbon and oxygen although the surface abundance of helium is nontrivial. Shallow density gradients near the iron core bode well for producing ^{56}Ni (see section 3.3).

First, the central density is not infinite when the white dwarf becomes unstable to general relativistic gravity (Shapiro and Teukolsky 1983). A structural adiabatic index somewhat greater than $\frac{4}{3}$ is unstable when the post-Newtonian corrections are added to gravity, so real instability sets in at a central density of $\rho = 2.65 \times 10^{10}$ g cm^{-3}. Also at this point, not all of the electrons are (special) relativistic, especially in outer layers. Taken together these corrections imply a 2.7% reduction in $M_{\rm ch}$ so that 1.457 $M_\odot$ becomes 1.418 $M_\odot$.

Second, as discussed earlier, the gas is not ideal. The pressure is reduced by the Coulomb corrections. Recall eq. (1.6)

$$M_{\rm ch} \approx M_{\rm ch}^0 \left[1 \;-\; 0.0226(Z/6)^{2/3}\right],$$

which reduces 1.42 $M_\odot$ to 1.39 $M_\odot$ for a carbon white dwarf. For ^{56}Fe the Coulomb correction is larger and, moreover, $Y_e = 0.464$, so $M_{\rm ch}(^{56}{\rm Fe}) =$ 1.15 $M_\odot$.

Table 7
Massive stars with mass loss

Model	35WR	40WR	60WRA	60WRB	85WRA	85WRB
Initial M	35	40	60	60	85	85
Final M	15.2	11.1	4.25	6.65	8.34	9.71
$^{12}C(\alpha,\gamma)^{16}O$	2.7	3	2.7	1	2.7	1
Semiconv.	low	low	low	low	low	low
Metals	solar	solar	solar	solar	solar	solar
^{1}H	1.45	—	—	—	—	—
^{4}He	8.05	5.1	0.18	0.14	6.7(−2)	7.1(−2)
^{12}C	1.10	1.5	0.53	1.10	0.51	1.29
^{14}N	7.3(−2)	2.3(−2)	—	—	—	—
^{16}O	2.39	2.42	1.51	2.02	4.51	3.96
^{20}Ne	0.15	0.15	0.18	1.29	0.27	1.70
^{24}Mg	9.3(−2)	3.6(−2)	2.8(−2)	0.27	0.18	0.44
^{28}Si	0.26	0.24	0.22	0.27	0.47	0.52
^{32}S	0.13	0.15	0.15	8.0(−2)	0.26	0.12
^{36}Ar	2.9(−2)	3.7(−2)	3.2(−2)	9.0(−3)	6.5(−2)	1.3(−2)
^{40}Ca	1.8(−2)	2.3(−2)	1.7(−2)	3.5(−3)	6.5(−2)	3.8(−3)
$M_{\rm Fe}$	1.45	1.42	1.40	1.46	1.90	1.59
M_{3500}	1.77	1.67	1.66	1.77	2.18	1.96
M_{4500}	1.88	1.76	1.73	1.89	2.48	2.11
R^{c}_{12}	68	0.12	3.92(−2)	2.63(−2)	2.50(−2)	2.40(−2)
L^{c}_{38}	13	—*	4.4	~7.5	—*	~10

* Difficult to determine. Surface was oscillating.

Third, the surface boundary pressure plays a very important role. This decreases the effective Chandrasekhar mass, but the effect varies as silicon and oxygen burning shells are ignited. Frequently a core may begin to collapse, but as it contracts, an overlaying shell of unburned fuel is ignited. This generates energy which raises the overlaying material to larger radii relieving the boundary pressure on the core. At this point the core ceases contracting and may even expand.

Fourth, and probably most important for the core of a massive star is the fact that such cores have finite entropy, i.e., they are not completely degenerate. To rough approximation (Chandrasekhar 1938; Hoyle and Fowler 1960; Baron and Cooperstein 1990)

$$M_{\rm ch} \approx M^{0}_{\rm ch}\left(1 + \left(\frac{\pi^2 k^2 T^2}{\epsilon_{\rm F}^2}\right)\right), \tag{1.21}$$

where $\epsilon_{\rm F}$ is the Fermi energy for relativistic degenerate electrons,

$$\epsilon_{\rm F} = 1.11\,(\rho_7 Y_{\rm e})^{1/3}\ {\rm MeV}. \tag{1.22}$$

The distinction between ϵ_F and the chemical potential μ_e is important in deriving the above equation. To a first approximation (Baron and Cooperstein 1990),

$$\mu_e \approx \epsilon_F \left(1 - \frac{1}{3}\left(\frac{\pi k_B T}{\epsilon_F}\right)^2\right). \tag{1.23}$$

The Chandrasekhar mass may also be expressed in terms of the electronic entropy per baryon

$$M_{ch} \approx M_{ch}^0 \left(1 + \left(\frac{s_e}{\pi Y_e}\right)^2\right), \tag{1.24}$$

where s_e in units of Boltzmann's constant, k, is (Cooperstein and Baron 1990)

$$\begin{aligned} s_e = \frac{S_e}{N_A k} &= \frac{\pi^2 T Y_e}{\epsilon_F} \\ &\approx 0.50\rho_{10}^{-1/3}\left(\frac{Y_e}{0.42}\right)^{2/3} T_{MeV} \end{aligned} \tag{1.25}$$

when near complete relativistic degeneracy is assumed. For typical conditions during silicon burning in a massive star ($\rho_{10} = 0.01$, $Y_e = 0.46$, $T_{MeV} = 0.3$) this correction can increase the "Chandrasekhar mass" by 26%. At collapse the correction is smaller, typically 10%. The core must lose entropy to collapse.

Finally there are minor corrections for the ion and radiation pressure. The star is not entirely supported by electrons. These corrections are small and can be neglected. Perhaps more important, but totally uncertain, is whether a correction should be made for rotation.

Note that in all these correction terms, composition, Y_e, and entropy must be properly averaged over the whole stellar core. Typically in the presupernova models Y_e is 0.42 in the center and 0.48 at the edge, thus an average value is 0.45. The composition is mostly iron ($Z = 26$). Thus the *minimum* core mass capable of collapse, assuming, unrealistically, that the entropy is zero, is $M_{min} \approx 1.09 M_\odot$. The mass that collapses must be reduced by the neutrinos that are lost, that is the binding energy of the neutron star must be subtracted. This mass decrement is reasonably independent of the equation of state so long as a black hole is not formed and is roughly independent of equation of state (Burrows 1990; Lattimer, private communication),

$$\Delta M \approx 0.084 \left(\frac{M_{grav}}{M_\odot}\right)^2, \tag{1.26}$$

or about a 15% reduction depending upon the mass. Thus one could, in principle, have neutron stars with gravitational masses as light as 1.0 $M_\odot$. In nature this never happens.

Including realistic entropy and surface boundary pressure corrections, i.e., using the stellar models themselves, the iron core that collapses is typically between 1.25 and 2.05 $M_\odot$ with 1.3–1.6 being most typical of all but the rarest (most massive) stars (tables 2–7). However, even corrected for neutrino losses, the iron core mass is *not* the neutron star mass. The prompt explosion mechanism does not work (section 2.1). The delayed explosion mechanism takes roughly a second to develop during which time mass accretes. A realistic upper bound on the final mass (in a successful explosion) is to take the mass where the free fall time is about 1 second. This gives roughly 4000 km. Typically masses there are 1.6 $M_\odot$, which when corrected for neutrino losses gives a gravitational mass near 1.4 $M_\odot$. Actual delayed explosion models tend to give mass cuts corresponding to 2500 to 3500 km in the presupernova star (Mayle and Wilson, 1991). For values of $^{12}C(\alpha, \gamma)^{16}O$ that best fit the solar abundances (about twice that of Caughlan and Fowler 1988); for restricted semiconvection, which seems to be required to replicate the evolution of the progenitor star of SN 1987A; and for stars in the mass range 15 to 60 $M_\odot$, the range of masses interior to 3500 km is 1.40 to 2.05 baryon mass corresponding to gravitational masses between 1.27 and 1.78 $M_\odot$ which we think is an appropriate range so long as a black hole does not form. Of course no estimate can be considered reliable until the explosion has been realistically modeled.

And the story may not end even there. For Type II supernovae, there is a "reverse shock" that occurs when the exploding helium core runs into the hydrogen envelope. The sudden increase in ρr^3 leads to a reflection (Weaver and Woosley 1980; Bethe 1990) that communicates the signal to the underlying material to slow down. In the moving material this appears as a shock. For SN 1987A and other Type II's, this shock arrives back at the center of the star after about an hour (Woosley 1988) and leads to an unknown amount of material being decelerated below the escape velocity. Chevalier (1989) estimates the mass in SN 1987A to be $\sim$0.1 $M_\odot$, but the actual value is uncertain and may be much smaller. Woosley (1988) finds that if the explosion energy is less than about 3×10^{50} erg, solar mass quantities of material may fall back onto the core. This did not happen in SN 1987A because we know the explosion energy there to have been much greater than 3×10^{50} erg, but it could, depending on details of the delayed explosion mechanism (section 2.2), happen in other supernovae. Thus it is possible to make a substantial black hole in the middle of an optically brilliant supernova.

All of the radioactivity would be lost, however, which is another reason we know that this did not happen in SN 1987A.

For lighter stars in the 8 to 12 $M_\odot$ range, even though the explosion mechanism is uncertain, the range of iron core masses is more tightly constrained, 1.25–1.38 $M_\odot$ (gravitational mass). This is because of the abrupt density decline outside the iron core that decreases the amount of accretion that can occur during the explosion and because neutron-rich nucleosynthesis precludes the ejection of much of the iron core (section 4.4).

For the accretion-induced collapse of a white dwarf one obtains a nearly unique value. The baryon mass at collapse is white dwarf mass having a central density of about 10^{10} g cm^{-3} (Nomoto and Kondo 1990; Isern et al. 1990; Canal et al. 1990), i.e., about 1.38 $M_\odot$, implying a final neutron star mass of 1.25 $M_\odot$.

2. Type II supernovae

In this section we shall be concerned with the physical processes currently held responsible for the explosion and radiation of Type II supernovae. Discussions of a broader nature appear elsewhere (Woosley and Weaver 1986; Arnett et al. 1989; Petschek 1990; Bethe 1990; Woosley, 1986). Of special importance is the status of the "delayed explosion mode" of Wilson and Mayle which presently is the only one giving credible explosions.

2.1. Core collapse and bounce

For many years it was hoped that a simple, purely hydrodynamical solution to the Type II explosion mechanism could be found. This would reduce reliance upon more intricate calculations of radiation (neutrino) transport and explain a common natural phenomenon in a simple, physically appealing fashion. Unfortunately, nature appears not to have taken this simple path. For the realistic equations of state of the day and presupernova models calculated carefully by at least four independent groups, it appears that the so-called "prompt mechanism" does not work. Nevertheless, the events during the first 20 ms (sound crossing time for the core) following maximum compression remain exceedingly important because, just as the presupernova model set the conditions for the collapse, the propagation and initial death of the shock set the stage for what follows. We shall be skimpy on detail here and refer the interested reader to excellent reviews of the subject by Bethe (1990) and Cooperstein and Baron (1990).

Prior to achieving nuclear density, pressure continues to come predominantly from relativistic electrons, hence $\Gamma_1 \sim 4/3$. At a density $\rho \sim 3 \times 10^{11}$ g cm^{-3}, depending somewhat on their energy, neutrinos become trapped within the collapsing core; i.e., their diffusion time outwards exceeds the collapse time scale, a few milliseconds. From this point on, the total number of neutrinos plus electrons does not vary greatly though the two may exchange identity via the weak interaction. Typically the lepton number density, $n_l \approx 0.40 \rho N_A$ cm^{-3} at trapping with N_A Avogadro's number. The dynamics of collapse naturally segregate the imploding core into two regions: an inner core which collapses homologously ($v \propto r$), with its outer extremity falling at about the sound speed, and an outer core, whose supersonic infall velocity ($v \propto r^{-1/2}$) is roughly 1/2 of the free fall velocity. At maximum, the collapse velocity reaches about 70 000 km s^{-1}. Homology can be preserved only in that inner portion that remains in sound communication. The mass of this inner core is sensitive to a variety of thermodynamic conditions: the pressure decrement compared to that required for hydrostatic equilibrium; the adiabatic index of the gas; and how much electron capture has occurred, but for typical conditions it ranges from 0.5 $M_\odot$ to 0.7 $M_\odot$. As the central regions approach and exceed nuclear density, the equation of state suddenly stiffens (Γ_1 becomes much greater than 4/3) and that portion of the core that was collapsing homologously comes to an abrupt halt. Peak temperature here is $\sim$ 10–15 MeV and peak density, about 7×10^{14} g cm^{-3}, (i.e., several times the nuclear density). Pressure waves propagating outwards accumulate where the Mach number equals one and build into a shock wave that begins to move out. Thus the shock is not born at the center of the star, but out around 0.7 to 0.8 $M_\odot$, i.e., roughly 0.2 $M_\odot$ beyond the homologous core.

Analytic arguments (Lattimer et al. 1985) suggest that the shock wave is born with an energy approximately equal to the gravitational binding energy of the homologous (unshocked) core after it comes to rest, $\sim$(4–7) $\times 10^{51}$ erg, as corrected for nuclear force and energy stored in the excited states of those nuclei that have not merged or evaporated. This energy would be ample to power the supernova if it could all be used, but unfortunately considerable degradation occurs as the shock now attempts to beat its way out through the remainder of the infalling core. Chief among the losses it suffers are neutrino emission, especially when moving into a region where neutrinos from electron capture can diffuse ahead of the shock ($\rho \lesssim 10^{11}$ g cm^{-3}), and photodisintegration. The temperatures of the shocked material are so high that complete stripping of iron down to free nucleons is implied, an energy $\sim 1.5 \times 10^{51}$ erg being required for each 0.1 $M_\odot$ so disintegrated. The shock cannot long endure such prodigious losses and, unless it quickly reaches the edge of the dense core and moves into a region where the low density and high heat capacity give post-shock temperatures too low to disintegrate iron and less efficient in producing neutrinos, it will die. Thus an important criterion for the success of the core bounce mechanism is that the total mass of the collapsing iron core not be too large, one obvious limit being that the difference between the homologous and total core masses not be so great as to consume the entire shock in photodisintegration losses. Unfortunately, as noted above, *all* modern presupernova models have iron cores that are too large.

2.2. "Delayed" explosions

2.2.1. An overview and some general comments

Consequently the shock moves out to some radius, typically ~ 300 km where it stalls, loses all outward velocity and becomes a standing accretion shock. A nearly stationary "neutrinosphere" (surface of near unit optical depth for neutrinos) initially develops at about 50 km where the density $\rho \sim 10^{11}$ g cm^{-3} and the effective neutrino emission temperature is ~ 5 MeV (somewhat of an oversimplification of the actual calculation; the neutrinos actually have an optical depth that depends on their energy and the distribution function is never fully thermalized). As time passes, the neutron star and its neutrinosphere shrink until the radius is only 10 km or so. It is the interaction of the neutrinos from this shrinking core, typically 3×10^{53} ergs of them, with the almost optically thin material above the neutrinosphere that ultimately slows the accretion and turns material around again. The turnaround develops on a time scale comparable to that required for the neutron star to release a fraction of its binding energy, which is ~ 1 second. Since this is so much longer than the hydrodynamic time scale, the model is usually referred to as the "delayed mechanism" (Wilson 1985; Mayle 1985; Bethe and Wilson 1985; Wilson et al. 1986; Mayle and Wilson 1988ab; Mayle 1990; Mayle and Wilson 1991; Bethe 1990, 1993).

Obviously if only 0.5% of the neutron star binding energy could be put in the right place at the right time, an energetic supernova would result. This coupling, however, has been *the* outstanding theoretical problem in the study of supernovae for a very long time (Baade and Zwicky 1934; Colgate and White 1966). It is our opinion and that of at least several others (Colgate 1991; Bethe 1990, 1993) that Wilson and Mayle's model is qualitatively correct. This is not to preclude the possibility that new physics may ultimately be required to obtain agreement with observations, but the general idea of a slowly developing explosion powered by neutrino absorption is appealing for many reasons. It explains in a natural fashion the fact that the mass cut occurs outside of the neutronized core and not within, where the nucleosynthesis would be unacceptable. It may explain the origin of the r-process (section 4.4). It provides the long slow push that is essential to avoid mass reimplosion (Colgate 1991). Finally there is the simple fact that it appears to *work*, at least in some computer calculations, which is more than one can say for any other model at the present time. The delayed mechanism also employs some fascinating physics and it is worth taking some time to discuss some of it.

The explosion of the infalling mantle is essentially a study in accretion physics. Matter passes through an accretion shock, is abruptly slowed, though not stopped, and "settles" rapidly onto the neutron star. A rough schematic is given in fig. 5.

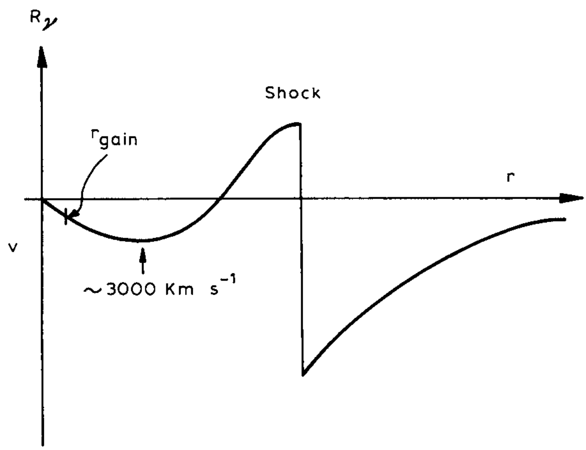

Fig. 5. Qualitative velocity structure at an early epoch in the delayed explosion mechanism.

The rate at which material arrives at the shock can be estimated (Cooperstein et al. 1984) by assuming that material in the mantle has a density distribution

$$\rho(r > R_s) = \frac{H}{r_o^3} \tag{2.1}$$

which experiences an acceleration $\alpha^2 g = \alpha^2[GM(r)/r^2]$. Neglecting pressure, which basically has the effect of making $\alpha < 1$, the velocity at radius r will, after some time, be a fraction of the local escape velocity, i.e.,

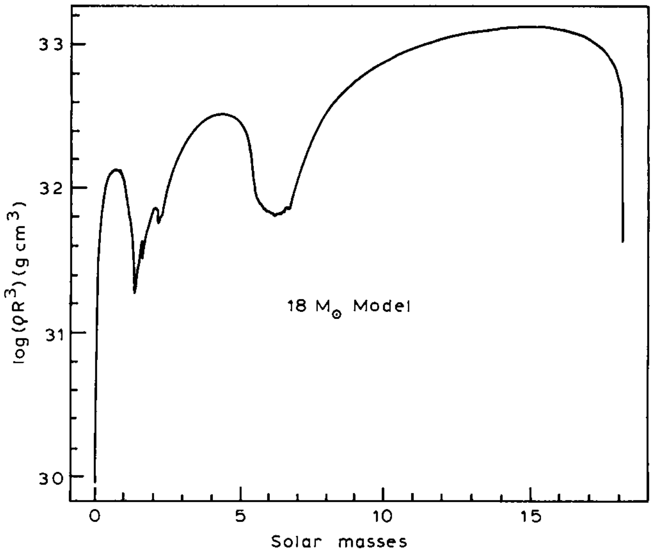

Fig. 6. Product of density and radius-cubed for an 18 M$_\odot$ presupernova star. Overall this quantity is roughly constant but note abrupt changes just outside the iron core and at the hydrogen-helium interface. Regions of abrupt increase in ρr^3 give rise to reflections of the shock wave (Bethe 1990).

$v(r) = -\alpha v_{\rm esc}(r)$. This implies a density structure

$$\rho(r,t) = \frac{2}{3}\frac{H}{\alpha(2GM(r))^{1/2}}\, t^{-1} r^{-3/2}. \tag{2.2}$$

Hence the accretion rate, $4\pi r^2 \rho v$, is

$$\dot{M}(r) = \frac{8\pi}{3} H t^{-1}, \tag{2.3}$$

which, interestingly, is independent of α. For $H \sim 10^{32}$ g (for example, in the inner mantle of an 18 $M_\odot$ star; fig. 6) and $\alpha \sim 1/2$, the accretion rate at the shock is a few tenths of a solar mass per second at time one second. As time passes, H increases so the accretion rate, including the t^{-1} dependence, stays near this value, at least until a black hole is formed. Numerically this is consistent with the results of Woosley and Weaver (1982a) who followed the failed explosion of a 25 $M_\odot$ star for 6 seconds. During that period, 1.8 $M_\odot$ accreted through the shock.

Most interesting for the delayed mechanism is what happens to this material after it passes through the shock and, in particular, the competition between energy absorption from neutrinos flowing out from the neutron star and emission of neutrinos by electron (and positron) capture. In order to merge smoothly with the neutron star, net dissipation (corrected for energy absorption) must carry away energy at a rate equal to the gravitational binding energy of the accreted material, i.e., $L_{\rm dis} = \dot{M}GM_{\rm n}/R_{\rm n} \approx 2.4 \times 10^{52}$ (50 km/R_n) erg s^{-1} where R_n here is the radius of the neutron star, here assumed to be equivalent to the neutrinosphere radius, and M_n is its mass, about 1.5 $M_\odot$. Here we have also assumed $\dot{M} = 0.3\ M_\odot$ s^{-1}, although that will obviously vary from star to star and from time to time. The dissipation is composed of two parts, photodisintegration and neutrino loss. The photodisintegration loss is $\dot{M}Q$ where $Q = 1.7 \times 10^{52}$ erg per solar mass (complete disintegration to nucleons is presumed; 8.8 MeV/nucleon), so the neutrinos must carry off something like 2×10^{52} erg s^{-1} in steady state. If they do not, then the neutron star will begin to "resist" the accretion. Loosely speaking, the sink would back up and the shock consequently move outwards in radius. This does not necessarily imply that any *mass* moves outwards, although it certainly may do so *with or without any additional energy input.* An interesting case was considered in our 1982 paper mentioned above. When all dissipation was turned off, the accretion shock moved rapidly out in radius to several thousand kilometers in 1.3 seconds (note an error in the labeling of the axes in Woosley and Weaver (1982a); in their fig. 11 it should be "R*10", not "R/10"). Positive velocities of roughly 1000 km s^{-1} were also observed behind the shock. While it is certainly not physical to set $L_{\rm dis} = 0$, this calculation demonstrates the important role of dissipation in the accretion process.

The electron and positron capture on nucleons occurs in a narrow region above the neutrinosphere. So another condition for the sink not to back up is that the accretion rate into the loss region must equal that at the shock. If sufficient power is absorbed between the shock and the loss region to slow $\dot{M}$, material may begin to move out. Bethe (1990, 1993) suggests that only energy deposited outside the loss region can be effectively utilized in the explosion. We do not agree because decreasing the losses, even in a region where the net energy generation retains a negative sign, must be useful to explosion. However, it is very important that not too much of the energy absorbed in the "gain region" be advected into the loss region. Slowing this matter, however, takes far less than the 2×10^{52} erg s^{-1} being lost in steady state to electron capture. The kinetic energy of the inward moving material is very small compared to gravity though the thermal energy is comparable. That is what the shock plus gravitational compression after the shock accomplished. Thus the farther out the energy is deposited beyond the loss region, the less work is required to reduce $\dot{M}$. Typically the internal energy of the matter is a few times 10^{18} erg g^{-1} in the region of interest. Absorption of energy comparable to this *in the time that it takes the matter to move to the loss region* will begin to reverse the flow. Since the matter enters the loss region at a few thousand km s^{-1} and the region where it might gain energy by neutrino capture is only ~ 100 km in extent, the available time is short, a few hundredths of a second. Thus the energy absorbed from neutrinos must be $\sim 10^{20}$ erg g^{-1}. As we shall see in the next subsection, this implies neutrino luminosities (in each flavor) of several times 10^{52} erg s^{-1}. Values comparable to this are observed in the Wilson and Mayle models during the first second or so. It is this coincidence that allows the explosion to develop.

Clearly it is to the star's advantage to slow the accretion at the earliest possible moment. The less energy advected into the loss region, the more useful energy will be available for the explosion. The best way to halt the accretion is to increase the neutrino luminosity and so the most successful models of Wilson and Mayle are those that amplify the early luminosity by considering convection in the neutron star. Convection outside the neutrinosphere also plays an important role, in part by cooling the loss region and reducing $L_{\rm dis}$ (Wilson, private communication), but also by allowing energy that would have been advected into the loss region to stay out of it (Bethe 1990, 1993). Convection is probably an essential aspect of the delayed mechanism and the fact that others have not included it may account for the fact that no one, so far, has replicated the successful explosions of Wilson and Mayle.

Once the accretion is halted, a mass separation begins to develop as material actually begins to move outwards. This decreases the efficiency for neutrino capture on nucleons and a second stage of heating commences where the bulk of the final supernova energy is developed. Scattering of neutrinos on pairs and, possibly, neutrino annihilation (Goodman et al. 1987) play an important role here. The density becomes too low, except in a very narrow region near the neutron star, for capture on baryons to be important. Whether or not a full 10^{51} erg of final kinetic energy is finally developed in the delayed explosion model is presently a point of some contention (Hillebrandt, this volume, but see also Mayle and Wilson 1991). Given the large sums of energies involved and sensitivity to the simulation of convection and the angular integration of the neutrino annihilation energy input, it may be that we should be content for now simply to have a mechanism that provides mass ejection.

2.2.2. Energy absorbing and emitting processes

In order to go into more quantitative detail, it is useful to consider some of the physics involved in the delayed mechanism. Some of the formulae developed here were previously presented by Bethe (1993).

All energy absorbing and liberating processes involving the neutrinos have at their heart the basic weak interaction cross section:

$$\sigma_o = \frac{4G_f m_e^2 \hbar^2}{\pi c^2} = 1.7 \times 10^{-44}\ \mathrm{cm}^2. \tag{2.4}$$

This implies, for example, for the electron capture reaction, $e^- + p \rightarrow n + \nu_e$,

$$\begin{aligned} s_o &= \frac{(1+3g_A^2)}{8}\left(\frac{\epsilon_\nu}{m_e c^2}\right)^2 \sigma_o \\ &= 4.5 \times 10^{-44} \epsilon_{\mathrm{MeV}}^2\ \mathrm{cm}^2, \end{aligned} \tag{2.5}$$

where ϵ_{MeV} is the energy of the outgoing neutrino in MeV. The most important heating process, at least at relatively early times is the capture, by nucleons, of electron-flavored neutrinos streaming out from the core,

$$\begin{aligned} n + \nu_e &\rightarrow p + e^- \\ p + \bar{\nu}_e &\rightarrow n + e^+. \end{aligned}$$

Owing to helicity arguments, the cross section for neutrino capture is twice that of the electron, $s_\nu = 2s_o$, and for a relativistic Fermi distribution in which

$$\begin{aligned} \langle \epsilon_\nu^2 \rangle &= \frac{F_5(0)}{F_3(0)} T_\nu^2(\mathrm{MeV}) \\ &\approx 20.8\, T_\nu^2(\mathrm{MeV}) \\ &\approx 250\ \mathrm{MeV}^2, \end{aligned} \tag{2.6}$$

$s_o \approx 1.2 \times 10^{-41}$ cm^2. The energy deposition rate is

$$\begin{aligned} \dot{q}_{\nu\mathrm{cap}} &= \phi_{e\nu}\, 2s_o N_A \rho \frac{X_{\mathrm{nuc}}}{2} \\ &= 2 \times \frac{7}{16}\frac{acR_\nu^2 T_\nu^4}{4r^2}\, 2s_o N_A \rho \frac{X_{nuc}}{2} \\ &\approx 1.0 \times 10^{25}\, \rho_7 \frac{X_{\mathrm{nuc}}}{2} T_\nu^6 \left(\frac{R_\nu}{r}\right)^2\ \mathrm{erg\,cm^{-3}\,s^{-1}} \qquad (2.7) \\ &\approx 1.05 \times 10^{27}\, F_{52}\, \rho_7 \frac{X_{\mathrm{nuc}}}{2} r_7^{-2}\ \mathrm{erg\,cm^{-3}\,s^{-1}} \\ &\approx 1.05 \times 10^{20}\, F_{52} \frac{X_{\mathrm{nuc}}}{2} r_7^{-2}\ \mathrm{erg\,g^{-1}\,s^{-1}}, \end{aligned}$$

where F_{52} is the luminosity of ν_e *and* $\bar{\nu}_e$ divided by 10^{52} erg s^{-1} and it is assumed that the nucleons are roughly half protons and half neutrons (i.e., $Y_e \sim 0.5$). If the fluxes of the two types of neutrinos are different then an obvious redefinition of F_{52} is required.

On the other hand, the inverse reactions lead to an energy *loss*

$$\begin{aligned} n + e^+ &\rightarrow p + \bar{\nu}_e \\ p + e^- &\rightarrow n + \nu_e. \end{aligned}$$

For a relativistic gas of pairs (Mayle 1985; Bethe 1993):

$$\begin{aligned} \dot{q}_{\text{ecap}} &\approx 2 \times \tfrac{7}{8}\, aT^4 s_o N_A \rho \frac{X_{\text{nuc}}}{2} \frac{\langle \epsilon_e^2 \rangle}{\langle \epsilon_\nu^2 \rangle} c \\ &\approx 2.0 \times 10^{25}\, \rho_7 X_{\text{nuc}} T^6 \quad \text{erg cm}^{-3}\text{s}^{-1} \\ &\approx 2.0 \times 10^{18}\, X_{\text{nuc}}\, T^6 \quad \text{erg g}^{-1}\ \text{s}^{-1}. \end{aligned} \tag{2.8}$$

Again the factor of 2 out front recalls the fact that an electron or positron can capture on one-half of the nucleons present and we have used the fact that $\langle \epsilon^2 \rangle \approx 21\, T^2$ for *both* neutrinos and pairs. Equating energy losses and gains implies a relation between temperature and radius at the point of balanced power (Bethe and Wilson 1985; Mayle 1985):

$$T = T_\nu \left(\frac{R_\nu}{2r} \right)^{1/3} . \tag{2.9}$$

In the terminology of Bethe, r here is the "gain radius,"

$$T_{r_7}^3 \approx 5 F_{52}^{1/2}, \tag{2.10}$$

or about 5 to 11 for F_{52} = 1 to 5 (here F_{52} is the flux of electron neutrinos and anti-neutrinos).

The flux, F_{52}, at late times is roughly 1/3 the binding energy of the neutron star divided by the time scale over which most of the neutrino emission occurs, about 2 seconds:

$$F_{52} \approx \frac{BE}{3\tau} \approx 5. \tag{2.11}$$

Behind the shock and above the neutrinosphere the material is nearly in hydrostatic equilibrium. It may be settling at speeds of $\sim$1000 km s^{-1}, but this is far short of the escape velocity, $\sim 10^{10}$ cm s^{-1}. The pressure from relativistic pairs and radiation is very nearly aT^4, but there is an important contribution from the nucleons. At early times, $P_{\rm ion}/aT^4 \sim \frac{1}{2}$, but the ratio later becomes smaller. Assuming radiation dominance, the pressure scale height is

$$\begin{aligned} l_P &\approx \frac{aT^4 r^2}{GM\rho} \\ &\approx 7 \times 10^6 \, \frac{r_7^2 T_{\rm MeV}^4}{\rho_7} \ \ \text{cm}. \end{aligned} \tag{2.12}$$

A successful explosion will require appreciable optical depth beyond the gain radius. If the entropy is roughly constant, the density scale height will be a little longer than the pressure scale height (distance for T^4 to decline by e). Averaged over the entire event we need an neutrino trapping efficiency, or average optical depth $\tau_\nu \sim 0.01$, or

$$\begin{aligned} \tau_\nu = 0.01 &= \int_r^\infty \kappa_\nu \, \rho \, \mathrm{d}r \\ &\approx \kappa_\nu \rho \, l_P \\ &= s_o N_{\rm A} \rho X_{\rm nuc} \, l_P \\ &\approx 4.6 \times 10^{-4} r_7^2 T_{\rm MeV}^4, \end{aligned} \tag{2.13}$$

implying at the gain radius,

$$r_7^2 T_{\rm MeV}^4 = 21 \frac{\tau_\nu}{0.01}. \tag{2.14}$$

Thus in order to gain energy and not lose it we need $r_7 T^3 \lesssim 7$ but in order to gain a significant amount of energy we need $r_7^2 T^4 \gtrsim 20$. Combining the above we obtain, at the gain radius for 1% efficiency $r_7 = 1$ and $T = 2.2$ MeV which is approximately the actual situation at moderately late (roughly 0.5 s) times, confirming that efficiencies ~1% are achieved. For the scale height not to exceed the radius the density must be greater than 10^8 g cm^{-3} at this point, but as heating proceeds and as the neutrinosphere sharpens up, the density at 100 km will decline.

The actual run of temperature and radius is determined by the hydrostatic equilibrium condition and the distribution of density beneath the shock. If the density obeys a power law, $\rho = \rho_0(r_0/r)^n$, then, continuing to assume radiation dominance, the temperature will also obey a power law, $T = T_0(r_0/r)^{(n+1)/4}$. Typically n is 2 to 3 and $T \propto r^{-0.75 \text{ to } -1}$. Thus rT^3 and r^2T^4 both decrease radially outwards and the above conditions are each satisfied at some radius. The trick is getting $r_{\rm min}$ to be less than $r_{\rm max}$.

At least at early times in the models of Wilson and Mayle, these conditions are satisfied, that is the temperature is nearly 2 MeV at 100 km. As time passes however, the density gradient gets steeper near the neutrinosphere and the density declines in what is now the "bubble." A gain radius can still be found but the efficiency for absorption beyond this gain radius decreases. Moreover as the material expands and cools, nucleons reassemble into α-particles thus shutting off energy deposition by capture, as well as cooling by capture. Usually not enough energy has been deposited at this point to blow up the star and, were nothing else to happen, material would begin to fall back in again increasing the density, perhaps giving rise to oscillations (Wilson et al. 1986). Thus more energy deposition is required in a second stage of heating. This occurs by at least two mechanisms, scattering off of electron–positron pairs in the low-density bubble and energy deposition due to neutrino–antineutrino annihilation.

The energy input by neutrino annihilation is (Goodman, Dar, and Nussinov 1986; Cooperstein et al. 1986, 1987), i.e.,

$$\bar{\nu}_{e\mu\tau} + \nu_{e\mu\tau} \rightarrow e^+ + e^-,$$

is

$$\dot{q}_{\nu\bar{\nu}}(r) = \frac{G_F^2 D\Phi(x)}{72\pi^3 c R_\nu^4} L_\nu L_{\bar{\nu}} \left(\frac{\langle\epsilon_{\bar{\nu}}^2\rangle}{\langle\epsilon_{\bar{\nu}}\rangle} + \frac{\langle\epsilon_\nu^2\rangle}{\langle\epsilon_\nu\rangle} \right) \tag{2.15}$$

$$\Phi(x) = (1-x)^4(x^2+4x+5), \tag{2.16}$$

$$x = (1-(R_\nu/r)^2)^{1/2} \tag{2.17}$$

where $G_F^2 = 5.29 \times 10^{-44}$ MeV^{-2} and $D = 2.34$ for electron neutrinos and 0.503 for ν_μ and ν_τ. The total energy deposited external to the neutrinosphere is

$$\begin{aligned} \dot{Q}_{\nu\bar{\nu}} &= \frac{G_F^2 D}{54\pi^2 c R_\nu} L_\nu L_{\bar{\nu}} \left(\frac{\langle\epsilon_{\bar{\nu}}^2\rangle}{\langle\epsilon_{\bar{\nu}}\rangle} + \frac{\langle\epsilon_\nu^2\rangle}{\langle\epsilon_\nu\rangle} \right) \\ &\approx A \left(\frac{50\ \mathrm{km}}{R_\nu} \right) \left(\frac{L_\nu}{10^{53}\ \mathrm{erg\,s^{-1}}} \right)^2 \ \mathrm{erg\,cm^{-3}\,s^{-1}} \end{aligned} \tag{2.18}$$

where $A = 6.2 \times 10^{49}\,\mathrm{erg\,s^{-1}}$ for μ- and τ-neutrinos individually and $2.9 \times 10^{50}\ \mathrm{erg\,s^{-1}}$ for electron neutrinos. For radii several times that of the neutrinosphere

$$\dot{q}_{\nu\bar{\nu}}(r) \approx 9 \times 10^{30} \frac{L_{\mathrm{tot},53}^2}{R_{\nu 6}^4} \left(\frac{R_{\nu 6}}{r_6} \right)^8 \ \mathrm{erg\,cm^{-3}\,s^{-1}}. \tag{2.19}$$

In these equations L_ν is the luminosity of a given flavor of neutrino, typically one or two times 10^{52} erg s^{-1} when R_ν is 20 km, thus contrary to some claims in the literature, we expect the contribution from this process to be rather small, although not negligible. However, it should be noted that the equations used here assume a precise neutrinosphere when calculating the angular integral and the actual situation is likely to be much more complicated. In particular, in a realistic "grey" atmosphere, there may be many more high-angle collisions between neutrons than a sharp photosphere would imply. This effect boosts the efficiency of neutrino annihilation as an energy source at late times (Wilson, private communication).

The remaining (known) process of importance is scattering on electrons and positrons

$$\mathrm{e}^- + \nu_{\mathrm{e},\mu\tau} \rightarrow \mathrm{e}^- + \nu'_{\mathrm{e},\mu\tau}$$
$$\mathrm{e}^+ + \nu_{\mathrm{e},\mu\tau} \rightarrow \mathrm{e}^+ + \nu'_{\mathrm{e},\mu\tau},$$

and the corresponding reactions for $\bar{\nu}_{\mathrm{e},\mu\tau}$. Both these processes and neutrino annihilation have the appealing attribute of continuing to provide energy to a (hot) region even when the baryon density has declined (owing to the expansion that must accompany a successful explosion). The cross section for a neutrino to scatter on a relativistic electron is (Tubbs and Schramm 1975; Mayle 1985; Burrows and Lattimer 1986; Cooperstein, et al. 1986)

$$\begin{aligned}\sigma_e &= A\sigma_o \left(\frac{\epsilon_\nu kT}{(m_e c^2)^2}\right) \\ &\approx 6.5A \times 10^{-44}\, \epsilon_\nu\, T_{\mathrm{MeV}}\ \mathrm{cm}^2\end{aligned} \tag{2.20}$$

where $A = \frac{7}{8}$ for electron neutrinos, $\frac{3}{8}$ for anti-electron neutrinos, and $\frac{1}{8}$ each for μ- and τ-neutrinos and their antiparticles. The number density of pairs, again assuming relativistic, nondegenerate particles, is (Mayle 1985)

$$\begin{aligned}n_{\mathrm{pair}} = n_{\mathrm{e}^+} &= \frac{2}{\pi^2}\left(\frac{m_{\mathrm{e}}c}{\hbar}\right)^3 \left(\frac{k_{\mathrm{B}}T}{m_{\mathrm{e}}c^2}\right)^3 e^{-\eta} \\ &\approx \frac{3}{2\pi^2}\frac{1.2021}{(\hbar c)^3} T^3 \\ &\approx \frac{7}{8}\frac{aT^3}{3k_{\mathrm{B}}}\end{aligned} \tag{2.21}$$

where η is the chemical potential, μ_e, divided by $k_{\mathrm{B}}T$. Taking the chemical potential equal to zero, which gives the second form of the equation, implies $n_{\mathrm{pair}} \approx 2.4 \times 10^{31} T^3_{\mathrm{MeV}}$, leading to an absorption coefficient

$$\lambda_e = 3.09A \times 10^{-12}\, \epsilon_\nu\, T^4_{\mathrm{MeV}}\ \ \mathrm{cm}^{-1}, \tag{2.22}$$

for positron *and* electron scattering. In the limiting case that all neutrinos (μ-, τ-, e-neutrinos, and their antiparticles) are present in equal abundances (approximately so at late times), then $\lambda_e = 9.0 \times 10^{-13} \epsilon_{\mathrm{MeV}} T_{\mathrm{MeV}}^4\ \mathrm{cm}^{-1}$ which is to be used with the *total* neutrino luminosity in all flavors. In each scattering the neutrino deposits a fraction

$$\frac{\Delta E}{E} \approx \frac{1}{2}\left(1 - 4\left(\frac{k_{\mathrm{B}}T}{\epsilon_\nu}\right)\right), \tag{2.23}$$

or very nearly half its energy. Using our earlier formula for the scale height (2.12), and evaluating for the optical depth to total neutrino luminosity at late times external to the gain radius, (2.10), we find

$$\dot{q}_{\mathrm{escat}} \approx 3.6 \times 10^{18} \frac{L_{53,\mathrm{tot}}}{\rho_7 r_7^2} \epsilon_\nu T_{\mathrm{MeV}}^4\ \mathrm{erg\,g^{-1}\,s^{-1}} \tag{2.24}$$

and

$$\tau_e \sim 0.005 \frac{T_{\mathrm{MeV}}^2}{\rho_7}. \tag{2.25}$$

This shows that substantial optical depth to neutrinos can be developed even at late times and that deposition is even favored by lower density at the gain radius (because of the larger pressure scale height). This energy deposition is to be compared, at low density to losses by pair annihilation

$$\mathrm{e}^- + \mathrm{e}^+ \to \nu + \bar{\nu},$$

$$\dot{q}_{\mathrm{pair}} \approx 1.0 \times 10^{25} T^9\ \ \mathrm{erg\,cm^{-3}} \tag{2.26}$$

which is generally negligible.

Finally we apply these semianalytic approximations to an edit of a recent calculation by Mayle and Wilson (1991) of a 20 $M_\odot$ star. At 0.608 s, the temperature and density structure are shown in fig. 7.

At this point the neutrinosphere is located at 21 km and the luminosities are 1.4, 1.6, and 6.4 $\times 10^{52}$ erg s^{-1} in ν_e, $\bar{\nu}_e$, and all the μ- and τ-neutrinos, respectively. Neutrino annihilation is, according to eq. (2.18), contributing 2×10^{49} erg s^{-1} and almost all of this is interior to the gain radius. This process has yet to become important. Exterior to the gain radius, neutrino capture on nucleons, eq. (2.7), and pair capture on nucleons, eq. (2.8), are contributing a net gain of 2.4×10^{50} erg s^{-1} and electron scattering, eq. (2.22), is contributing an additional 5.7×10^{49} erg s^{-1} for a total of 3.0×10^{50} erg s^{-1}.

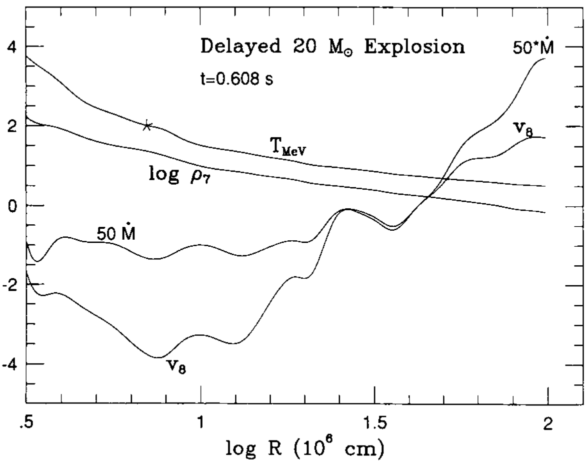

Fig. 7. Temperature, density, velocity, and accretion rate as a function of radius in a 20 $M_\odot$ model calculated by Mayle and Wilson at 0.608 s. The neutrinosphere and gain radius are indicated. The accretion shock is situated at about 2000 km. The gain radius, indicated by a star, is at 50 km where the temperature is 2.4 MeV. The y-axis is in appropriate units and $\dot{M}$ is in solar masses per second. The total mass contained in this region is 0.02 $M_\odot$, mostly at the lower densities.

While this is a bit on the small side (energy is still being advected into the loss region and one might have preferred 5×10^{50} erg s^{-1}), the equations used here are very approximate. It also is not correct to neglect *all* the energy deposited internal to the gain radius. Although most of it is radiated away, the equilibrium temperature is higher when energy is being deposited than when it is not and thus the pressure scale height is larger. Certainly if all material external to the gain radius were to be removed, material would flow from beneath to take its place, doing work in the process. Thus we differ with Bethe (1993) who states that energy deposited interior to the gain radius is irrelevant. Finally we have only examined one arbitrary time point. At any rate, it is encouraging that the numbers are in the right ball park and it suggests that, in the future, meaningful models might be constructed that include only physics of the optically thin region (plus an inner boundary adapted from a realistic neutron star cooling calculation). This would alleviate the need to do high-density physics and neutrino transport in the same code where the explosion is simulated. We look forward to trying it.

2.3. Shock propagation and break out

Once a strong outbound shock is formed, it moves through the mantle and envelope, arriving at the surface of the red or blue supergiant in a time given approximately by the Sedov equation

$$R_s \approx \left(\frac{E_o}{\rho}\right)^{1/5} t^{2/5}, \tag{2.27}$$

or

$$\begin{aligned} t_\mathrm{b} &\approx \left(\frac{3M_\mathrm{H}}{4\pi E_o}\right)^{1/2} R, \\ &\approx 700 \left(\frac{M_\mathrm{H}}{E_{51}}\right)^{1/2} R_{12} \text{ s.} \end{aligned} \tag{2.28}$$

when M_H is the mass *of the hydrogen envelope* in solar masses and R_{12} its radius in units of 10^{12} cm.

As the shock breaks through the surface a bright hard ultraviolet flash occurs, but that is discussed elsewhere in this volume by Nadyozhin and need not be treated in much detail here. The duration, luminosity, and hardness of this flash are all very sensitive to the initial radius of the star. Approximate relations are (Woosley 1990a) $L_\mathrm{peak} \sim 10^{41.5} R_{10}$ erg s^{-1}, $T_\mathrm{peak} \sim 10^{6.3}/R_{10}^{1/4}$ K, and $\tau \sim R_{10}$ s, but all these quantities really need to be calculated in a code in which the detailed effects of the line opacity are considered. In particular, one may expect a large amount of ultraviolet line blanketing from the high velocity metal lines in the outer envelope. This wavelength dependent absorptive opacity is difficult to model in a thermal calculation. Several groups are working on the synthetic spectrum necessary to proper (non-lte) calculation.

2.4. Light curves of Type II supernovae

The key physical parameters that determine the light curve are: (1) the total energy deposited by core processes in the overlaying mantle; (2) the density distribution and composition of the presupernova star, including any previously ejected circumstellar material; and (3) energy input from radioactive material produced and ejected in the explosion. Fortunately, due to the very large differences in scale between the portion of the star that undergoes collapse (radius $\sim 10^8$ cm) and the radii of typical (Type II) presupernova stars

(10^{12} to 10^{14} cm), the still uncertain details of the core phenomena tend to be almost completely averaged out in the ensuing explosion. In most cases, it is an excellent approximation for the purposes of calculating light curves to treat the core as a point mass and energy source (cf. Zel'dovich and Raizer 1966).

Following shock break out, the supernova's luminosity falls rapidly as its surface cools by expansion and radiative emission. Meanwhile, the rest of the star's material is cooled and accelerated by adiabatic expansion. The bulk of the star remains sufficiently optically thick during this acceleration that $\sim 99\%$ of the total supernova energy is converted to kinetic energy in the expanding debris. Only about 1% (typically about 10^{49} ergs) thus remains to be radiated when the star finally starts to become optically thin after expanding to about 10^{15} cm.

For a red supergiant star that has not lost most of its envelope mass, a two- to three-month-long plateau in emission then follows as a cooling wave associated with the transparency induced by hydrogen recombination propagates inwards through the star's exploding envelope (see, for example, Weaver and Woosley 1980). This has been discussed in detail by Woosley and Weaver (1986) and Arnett et al., (1989) and references therein. The light curve of SN 1987A, which may be considered typical of what happens when the explosion occurs in a *blue* supergiant is also covered in that same reference (see also Woosley 1988).

The physics and progenitors of Type II-L supernovae and other peculiar subclasses of Type II are not nearly so well understood. The Type II-L may represent massive stars that have lost most, but not all, of their hydrogen envelopes (Chevalier, 1984) and thus exhibit only very short and difficult to observe plateau phases (Litvinova and Nadyozhin 1983). Alternatively or additionally, these supernovae may be powered mostly by the decay of ^{56}Ni (Doggett and Branch, 1985), with the break in the rate of decline at 100 days being due to the transition from optically thick to optically thin emission, as is clearly seen in Type I supernovae.

A relevant model is shown in fig. 8, but the resemblance to Type II-L observations is not very good (though see Swartz et al. 1990).

2.5. X-ray and γ-ray emission

At late times, after three months in a Type IIp and one month in SN 1987A, the supernova light curve is powered by the decay of ^{56}Co (and at very late times by ^{57}Co and ^{44}Ti). As the supernova expands and thins, the γ-rays from radioactive decay can begin to escape the supernova and be seen. The subject

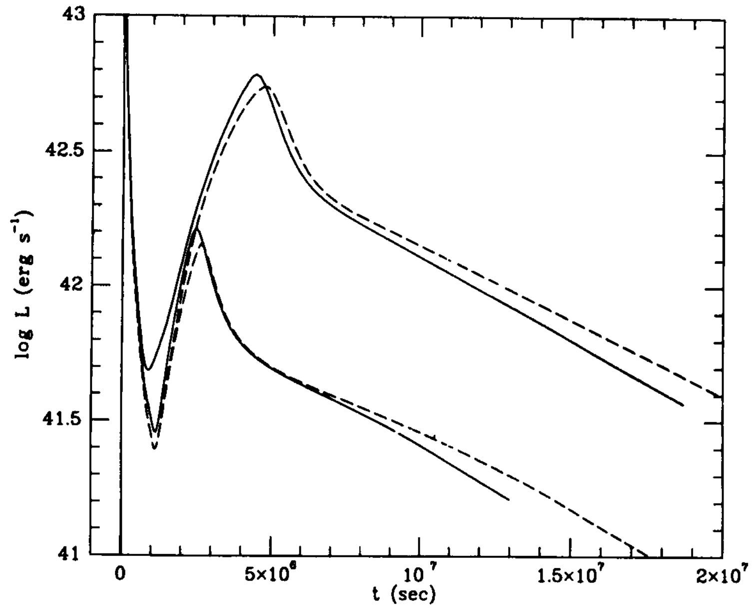

Fig. 8. Light curve resulting from the 1.3×10^{51} erg explosion of a 6 $M_\odot$ helium core (comparable to SN 1987A) capped by a 1 $M_\odot$ envelope of hydrogen and helium having a radius of 1.4×10^{13} cm. The dashed lines are an unmixed version while the solid line shows a model which was mixed comparable to SN 1987A. The top curve was an explosion that made 0.42 $M_\odot$ of ^{56}Ni. The bottom made 0.07 $M_\odot$.

of γ-ray astronomy of supernova is reviewed elsewhere in this volume by Cassé, so here we present just a few equations and numbers

The unscattered flux of γ-rays from a mass, M_{56} of ^{56}Co in solar masses normalized to a distance of 50 kpc (i.e., SN 1987A) is (Woosley 1988; Woosley et al. 1988a)

$$F = 0.81 \left(\frac{M_{56}}{0.1 M_\odot} \right) \exp\left(-t/111.3\,\mathrm{d} \; - \kappa_\gamma \, \phi_o \, (t_o/t)^2\right) \;\mathrm{cm}^{-2}\;\mathrm{s}^{-1}, \tag{2.29}$$

where t is the elapsed time since the explosion, t_o some fiducial time at which the column depth to the edge of the ^{56}Co layer, ϕ_o, is to be determined, and κ_γ is the opacity to 1 MeV γ-rays. Here F is the flux of some line, such as 847 keV, through which all decays proceed and homologous expansion has been assumed. An appropriate value of κ_γ is 0.06 cm^2 g^{-1} and a reasonable time to evaluate the column depth is $t_o = 10^6$ s. This flux will have a maximum at time

$$t_{\max} = (2\tau_{\rm Co}\,\kappa_\gamma\,\phi_o\,t_o^2)^{1/3} = 263\,(\phi_o/10^4)^{1/3}\ \text{days}. \tag{2.30}$$

The maximum flux is easily obtained by evaluating (2.29) at time $t_{\max}$,

$$\begin{aligned} F_{\max} &= 0.602\left(\frac{M_{56}}{0.10 M_\odot}\right)\exp\left[3\left(\frac{\kappa_\gamma\,t_o^2\,\phi_o}{4\tau_{\rm Co}^2}\right)^{1/3}\right] \\ &= 0.602\left(\frac{M_{56}}{0.10\,M_\odot}\right)\exp\left(-0.161\,\phi_o^{1/3}\right)\ \text{cm}^{-2}\ \text{s}^{-1}, \end{aligned} \tag{2.31}$$

a result which is extremely sensitive to the column depth at t_o, i.e., to the expansion rate. Models appropriate to SN 1987A had ϕ_o in the range $(5-7)\times 10^4$ g cm^{-2} at 10^6 s *provided that the* ^{56}Co *remains concentrated at the center of the supernova.* The γ-ray optical depth at maximum emission is 1.4 $(\phi_o/10^4$ g cm$^{-2})^{1/3}$, which is in the range 2–3 for any reasonable model. Thus there is a pronounced continuum even when the γ-rays are at their peak luminosity.

The widths and energy profiles of the γ-ray lines reflect the velocity distribution of the ^{56}Co as modified by optical depth effects. At late times one sees a FWHM roughly twice the average velocity of the ^{56}Co. Early on cobalt on the far side of the supernova will be optically thick and one will see narrower, blue-shifted lines. The technology of 1987 was just barely adequate to detect the supernova and some of the other interesting diagnostics that come from line shapes at early times may not have been obtained.

Type Ia supernova, because they expand faster and have less mass to begin with, have column depths about 100 times less than SN 1987A (e.g. Weaver et al. 1980) and thus peak at a time roughly $(100)^{1/3} = 4.6$ times earlier and have a flux per gram of ^{56}Ni produced $\exp(-0.161(50\,000^{1/3} - 500^{1/3}))$ or 100 times brighter. They also make ten times as much ^{56}Ni and are thus 1000 times brighter in γ-rays. Type Ib's and II-L's are intermediate between these two limits. Table 8 shows the results of Monte Carlo calculations (Pinto and Woosley 1991; Woosley and Pinto 1988; Pinto, private communication) for models of Type Ia, Ib, and IIp supernovae. The numbers given for II-L are interpolated between Ib and IIp assuming that II-L supernovae are a consequence of massive stars that have lost most, but not all of their hydrogen envelope. The line labeled "AIC" is for the accretion-induced collapse of a white dwarf star. The 0.002 $M_\odot$ of ^{56}Ni is based upon a very specific calculation (Mayle and Wilson, 1988a) that may not be applicable in the general case. For the time being, it should be considered an upper bound.

Table 8
Gamma ray emission from several types of supernovae

Type	M_{56} ($M_{\odot}$)	t_{peak} (days)	$\phi_{\max}$ ($\mathrm{cm}^{-2}\ \mathrm{s}^{-1}$) 10 kpc	$\phi_{\max}$ ($\mathrm{cm}^{-2}\ \mathrm{s}^{-1}$) 20 Mpc
Ia	1.0	100	50	1(−5)
Ib	0.3	250	4	8(−7)
IIp	0.1	400	0.04	9(−9)
II-L	0.2	~300	~1	~2(−7)
AIC	0.002?	3	~1	~2(−7)

One important point from table 8 is that *no* Galactic supernova of any type could go undiscovered provided a γ-ray spectrometer of only modest sensitivity is continually on line (SMM and previous balloon-borne detectors have had sensitivities somewhat greater than $10^{-4}\ \mathrm{cm}^{-2}\ \mathrm{s}^{-1}$). Exceptions can be found to all other types of supernova searches, be they optical, radio, infrared, or neutrino.

3. Type I supernovae

3.1. Type Ia

By now you have read and heard a great deal about observations of and models for Type Ia supernovae (see lectures by Branch, Nomoto, Barkat, and Thielemann, this volume). These supernovae are the brightest, the ones having no hydrogen in their spectra and showing indications of being from a low-mass population. Many of the observational properties are in agreement with a basic model, now some thirty years old (Hoyle and Fowler 1960), in which a highly degenerate white dwarf experiences a thermonuclear runaway and is totally disrupted. Since a white dwarf, by itself, is quite stable, the white dwarf must grow by accretion to an unstable mass, therefore it must be in a binary system undergoing mass exchange.

Today there is broad agreement in the community that this type of model is qualitatively correct. There is even a "standard model" based upon the deflagration of carbon (more about this term shortly) in a white dwarf approaching the Chandrasekhar mass (1.38 $M_{\odot}$, to be precise) which explains reasonably well the light curve, late time spectrum, peak light spectrum, and, to some extent, the nucleosynthesis expected of Type Ia supernovae. Presumably this model has been adequately described elsewhere in this volume and a working knowledge will be presumed in what follows (see also Woosley and Weaver 1986; Woosley 1990b).

Yet there remain vexing problems with the standard model – things that either just are not quite right or, at least, are not sufficiently well modeled. Foremost is the problem of nucleosynthesis. If our measurements in nature were only of elements, there would be no problem. Type Ia supernovae make the iron group (chromium through nickel), and a minor portion of the silicon through calcium, and that is about all. From theory we may note that Type Ia supernovae must produce at least 0.6 $M_\odot$ of iron (see below), and quite probably more in order to explain their light curves and velocities, while Type II supernovae produce typically a tenth of a solar mass or so (e.g., SN 1987A; 0.08 $M_\odot$). Thus, unless the event rate of Type Ia, averaged over Galactic history, is less than one-seventh that of Type II and Ib, most of the iron is made in Type Ia.

With earlier statistics suggesting that Type Ia occurred just about as frequently as other supernovae (e.g. Tammann 1982), the dominance of SN Ia in producing iron was clear. More recently, van den Bergh et al., (1987) and Evans et al., (1989) have estimated that the ratio is more like one SN Ia for every four or five SN II and Ib and van den Bergh and Tammann (1990 and this volume) have suggested an even lower rate for Type Ia's, possibly one-sixth or one-seventh that of the II and Ib. Even so, it might prove difficult to reconcile a model in which most of the iron was made in SN II and Ib with the overabundance of O/Fe in metal deficient stars (see Wheeler et al. 1989 for a review) and chemical evolution models still find the SN Ia contribution is important even with the small rates (Rocca-Volmerange and Schaeffer 1990).

The chief problem, however, is that we have *isotopic* measurements of iron in the solar system, which presumably samples the Population I component of the Galaxy, and those isotopic ratios are quite inconsistent, at the factor of 5 level, with what is made in the standard model. Even if only half of the iron in the Galaxy was from Type Ia, we would still have a fundamental difficulty. Since the overabundant isotopes are a consequence of having too many neutrons in the nse distribution, in turn a result of electron capture at high density, this difficulty is sometimes called "the electron capture problem."

While presently the most severe, electron capture may not be the only problem facing the standard model. The light curve is not all that great. One has to push the burning speed to the point where a very large fraction of the star is consumed, which means that the flame must move at an appreciable fraction of the sound speed (why almost sonic yet not quite sonic?). Agreement with observations can then be achieved, although this may reflect a sparse data set of premaximum data points (e.g. Woosley 1990b) and because the flame physics is sufficiently uncertain as to be essentially a free parameter. In fact, the light curve of the carbon *detonation* model, in which the entire white dwarf burns to iron and expands more rapidly, is superior. But that model has had its own problems: too much electron capture; too little intermediate mass elements; and a poor spectrum both at early and late times.

The spectrum of the standard model also poses some interesting problems. One great strength of the model is that it produces large quantities of silicon and calcium that are required for the peak light spectrum. Still a good fit is achieved only if the outer layers are mixed in a prescribed manner that may or may not be realistic (Branch et al. 1985). The late time spectrum also needs more study. Early calculations by Axelrod (1980) included only iron group elements and obtained good agreement, essentially because the expansion speed was right. First attempts at including other elements show strong oxygen emission lines in the model (Pinto 1988) that are not present in Type Ia supernovae (but are there in Type Ib). More work is needed, but there may be difficulties if radioactive ^{56}Ni and ^{56}Co are in too close proximity to oxygen, a strong coolant.

Finally, a general problem with all these white dwarf models is lack of adequate numbers of identified progenitors. We can look at certain stars, Betelgeuse and Sk-203-69 (a twin to the progenitor of SN 1987A) for example, and say there, someday, will be a Type II supernova. For Type Ia we have no such secure identity. The nova instability and accretion-induced collapse severely limit the acceptable accretion rates and, so far at least, there is no compelling observational evidence for a large population of merging white dwarfs.

There have been a number of attempts lately to improve on the standard model (see, e.g. Livne 1990; Livne and Glasner 1990; Khoklov 1990a,b), but before discussing them it will be useful to consider in greater detail the physics that underlies it.

3.1.1. Some general considerations

For a CO dwarf accreting matter at the specified rate ($(0.5$ to $30) \times 10^{-7}\ M_\odot$ y^{-1}), ignition will occur when carbon burning begins to provide an excess of nuclear energy over that which can be carried away by plasma neutrino losses. The exact value of the central density when this occurs varies with the accretion rate and may increase substantially after balanced power is achieved. A typical value is about 3×10^9 g cm^{-3} and the temperature is about 2.5×10^8 K. The white dwarf mass at this point is 1.38 $M_\odot$ although the exact value depends upon Coulomb corrections to the equation of state and other corrections due to special and general relativity. The net binding energy of the star is 5.1×10^{50} erg and its radius is 1600 km. Since the burning of a composition of carbon and oxygen (30% ^{12}C, for example) releases 7.3×10^{17} erg g^{-1}, it is clear that *at least* 0.35 $M_{\odot}$ of iron will ultimately have to be produced in order to disrupt the white dwarf. To give the ejecta an average velocity of 5000 km s^{-1}, this mass is raised to 0.59 $M_{\odot}$. Thus given only the general validity of the carbon deflagration scenario, the iron synthesized in the explosion is rather rigidly constrained.

It is also relevant that the equation of state for this highly degenerate dwarf is characterized by Γ very nearly equal to 4/3. This means that small perturbations in net energy can cause large excursions in radius. For example, although the binding energy is 5.1×10^{50} erg, the addition of only 7.3×10^{49} erg of energy to the star, as would be released by the burning of 0.05 $M_{\odot}$ of the interior to ^{56}Ni, is sufficient to cause the central density to decline (in hydrostatic equilibrium) by a factor of 3.6. Because the density in the central regions is so critical in determining the amount of electron capture that occurs during the explosion and therefore the isotopic nucleosynthesis of the iron group, the possibility that a small amount of burning at a slow rate, $\sim$1 s (after high temperatures $T_9 \sim 5$, are achieved anywhere in the white dwarf), may alter the pre-explosive density structure must be seriously considered (Woosley and Weaver 1986; Woosley 1990b; section 3.1.3).

Once the runaway has begun in earnest, it is virtually impossible to stop by any means other than expansion. As the temperature starts to climb following ignition, the reaction rate accelerates but the pressure rises only imperceptibly. At first, conduction, and then convection is able to transport the excess energy. But as the temperature continues to rise, the rate at which nuclear energy generation is able to change the temperature eventually becomes comparable to and then faster than the time for a convective blob to execute one cycle. This occurs at a temperature of (6–7) $\times 10^8$ K when both are about 10–100 seconds. Beyond this point the theoretician attempting to calculate energy transport is in unknown territory. Critical to these considerations are the events that transpire as the temperature rises from 6×10^8 K to 1.0×10^9 K. At this latter temperature the burning time ($\sim$0.01 s) becomes much shorter than the time required for sound, at 9500 km s^{-1}, to go one pressure scale height, 450 km.

Energy transport by convection may also be influenced by the URCA process (see, e.g. Iben 1978a,b; 1982) and, if the accretion rate is very low, by crystallization and/or phase separation in the core (Lopez, et al. 1986a,b). Such effects make an already hard problem even more difficult and will not be treated here except to note that the general tendency is to suppress the runaway until higher densities.

The condition that burning occurs faster than the convective cycle time (for $T_8 \geqslant 6$) also signals a situation in which nuclear burning may appreciably increase the entropy of a convective blob as it rises. If adiabatic expansion does not truncate the burning, a runaway in velocity may occur as the blob becomes increasingly buoyant. Provided that the blob is too large to cool by conduction, its velocity will increase until either turbulent dissipation leads to fragmentation into pieces small enough to cool by conduction or else the bubble explodes. A likely result, although by no means demonstrated so far, is a runaway ignited at many discrete points throughout a substantial volume. Roughly this volume might be thought to encompass a fraction of a pressure scale height (as did the pre-explosive convection zone).

Following all this in proper detail would take a 3D-Lagrangian hydrodynamics code capable of very fine mass resolution (or moving mesh). Even with the recent advances in computer technology this lies quite a ways down stream from here, so let's begin simple.

3.1.2. Deflagration flame physics

Consider the simplest, but physically unreasonable initial condition of a runaway igniting precisely at a point at the center of a white dwarf of given mass and composition. As mentioned above, it may ignite at many points, but for now consider them individually. The normal flame speed (the microscopic velocity of the flame front, which may be deformed when viewed on a larger scale) can be uniquely determined either analytically or numerically by a variety of techniques (Woosley 1986, 1990b; Woosley and Weaver 1986, 1991). The results of these studies can be summarized

$$v_{\rm cond} \approx 50 \left(\frac{\rho}{2 \times 10^9 \text{ g cm}^{-3}} \right)^{0.8} \left(\frac{X_{12}}{0.5} \right) \text{ km s}^{-1} \tag{3.1}$$

with ρ the density and X_{12} the carbon mass fraction. The width of the flame front is also determined by these same calculations to be $\sim 10^{-3}$ cm. These values are in approximate agreement with those obtainable by simpler means, essentially dimensional analysis: $v_{\rm cond} \sim (\sigma / C_V \, \tau_{\rm nuc})^{1/2}$ with σ, the conductivity, C_V, the heat capacity, and $\epsilon_{\rm nuc}$, the nuclear energy generation, providing that an appropriate temperature, $T \sim 5 \times 10^9$ K, is chosen for when carbon begins to burn appreciably as the flame crosses. Expressions for σ, C_V, and $\epsilon_{\rm nuc}$ are given by Woosley and Weaver (1991).

Obeying the one-dimensional restriction and excluding deformation, a flame of these properties initiated at a single point would slowly ($\gtrsim 30$ s) make its way through the white dwarf, decreasing in speed as regions of lower density were reached. Because the speed is so subsonic, the white dwarf would continually adjust its structure, probably by a series of flashes and oscillations until a highly extended structure developed. If it became unbound at all, the star would do so at very low velocities (see also Nomoto et al. 1976). In short, the observed phenomenon would not at all resemble a Type Ia supernova.

Of course, when considered in more than one dimension, the plane flame front is unstable to deformation. Burning behind a subsonic front in which pressure remains approximately constant raises the temperature and lowers the density. Crossed gravity and density gradients result in Rayleigh–Taylor (RT) instability. Initially the slow normal speed of the conductive flame (eq. (3.1)) prohibits the growth of small scale deformations and large scale deformations cannot exist until a region of the star has been burned out that is comparable to the scale size. An incipient instability having wavelength smaller than

$$\lambda_{\rm min} = \frac{4\pi v_{\rm cond}^2}{g_{\rm eff}} \tag{3.2}$$

with $g_{\rm eff} = g(r)(\Delta\rho/\rho) \approx \left(\frac{4}{3}\right)\pi G r\rho(\Delta\rho/\rho)$ will not grow before the flame has already passed over it. For the time being we restrict ourselves to regions located sufficiently central that density is approximately constant. Burning at $2 \times 10^9 \mathrm{g\,cm^{-3}}$ gives a density reduction of typically 30%. Thus $g_{\rm eff} \approx 10^9\, r_7$ cm s^{-2} with r_7 the distance to the center of the star in units of 100 km and a typical value at 100 km for $\lambda_{\rm min}$ is a few km. At larger radii $g_{\rm eff}$ initially increases and $\lambda_{\rm min}$ consequently becomes smaller. Later, as the star expands appreciably, $g_{\rm eff}$ declines, but $v_{\rm cond}^2$ decreases faster and so does $\lambda_{\rm min}$.

There also exists a maximum deformation that can develop. This is given by the "event horizon," which we shall note here as $r_{\rm b}$, the average radius of the burned out region. Henceforth we shall use the terms "maximum wavelength" and $r_{\rm b}$ interchangeably although there exists some constant on the order of unity relating the two. Until $r_{\rm b} > \lambda_{\rm min}$ no deformations will develop and the flame will proceed slowly at a speed given by simple conduction (eq. 3.1). This happens only for a very small region, $\sim$ 20 km or $3 \times 10^{-5} M_\odot$, near the center of the star. Beyond this point the flame front begins to deform and the range of allowable unstable wavelengths, $\lambda_{\rm min}$ to $r_{\rm b}$, grows rapidly, in fact as r^2 and the problem becomes increasingly complicated. Owing to the discrepant time scales associated with the growth of RT instability for $\lambda_{\rm min}$ and $r_{\rm b}$, ($\tau_{\rm RT} \approx (4\pi\lambda/g_{\rm eff})^{1/2}$), instabilities of smaller wavelength may grow into a nonlinear stage, perhaps even break off and detach, while the longer wavelength deformations are still developing (see next section).

We are interested chiefly in an effective flame speed, $v_{\rm eff}$, such that $\dot{M}_{\rm b} = 4\pi r_{\rm b}^2 v_{\rm eff}\rho$. This is certainly what is needed by those who must map the problem into a one-dimensional computer program. It also gives the rate at which nuclear energy is being released, $q_{\rm nuc}\dot{M}_{\rm b}$ (with $q_{\rm nuc} \approx 7 \times 10^{17}$ erg g^{-1}), which determines the dynamic response of the star which in turn specifies nucleosynthesis and, by way of the ^{56}Ni production, the light curve and spectrum. Because the conductive flame is so thin, the rate at which mass crosses the flame can also be written $\dot{M}_{\rm b} = v_{\rm cond}\rho A$ where A is the area of the arbitrarily deformed (and perhaps not simply connected) flame front. Obviously $v_{\rm eff} = (A/4\pi r_{\rm b}^2)v_{\rm cond}$, i.e., if we knew the ratio of the actual area of the flame front to that of a sphere having a radius such that it encompasses an equivalent mass the desired solution would have been found.

In the present problem $\lambda_{\rm min}$ sets a natural minimum scale at which we are to measure the area of the turbulent flame front (the "tile size"). Smaller surfaces are presumably smooth. The starting point is the undeformed sphere of area $4\pi r_{\rm b}^2$ which in the general case is deformed to a surface having area $4\pi r_{\rm b}^2\,(r_{\rm b}/\lambda_{\rm min})^{(D-2)} \approx 4\pi r_{\rm b}^2\,(\lambda_{\rm max}/\lambda_{\rm min})^{(D-2)}$ where D is the *fractal dimension* of the burning surface. The effective turbulent velocity we seek is then given by

$$v_{\rm eff} = v_{\rm cond}\,(\lambda_{\rm max}/\lambda_{\rm min})^{(D-2)} = v_{\rm cond}(r_{\rm b}/\lambda_{\rm min})^{D-2}. \tag{3.3}$$

Fundamentally (Mandelbrot 1983), $2 < D < 3$, which gives some restrictions on $v_{\rm eff}$. Since $\lambda_{\rm min} \propto r^{-1}$ (at least for small r) and $\lambda_{\rm max} \propto r$, eq. (3.3) shows that the flame will accelerate rapidly as its radius increases. Actually the situation is even better than that. The fractal dimension, D, is not likely to be very close either to 2 or to 3. Observations of fully developed turbulence in many different situations suggest $D \sim 2.5$–2.7 (Mandelbrot 1983, see especially plates 10 and 11 and Chapters 10 and 30). Thus asymptotically we expect the effective flame velocity to be proportional to $(r_{\rm b}/\lambda_{\rm min})^n$ with $n \sim 0.5$ to 0.7 and, for small $r_{\rm b}$,

$$v_{\rm eff} = v_{\rm cond}(r_{\rm b}/\lambda_{\rm min})^n = F X_{12}^{(1-2n)} \rho^{(0.8-0.6n)} r_{\rm b}^{2n}. \tag{3.4}$$

For $\rho = 2 \times 10^9$ g cm^{-3} and $X_{12} = 0.5$ a reasonable range in effective turbulent velocities is from 250 r_7 to 480 $r_7^{1.4}$ km s^{-1} with r_7 the radius, $r_{\rm b}$, in units of 100 km. These expressions are valid only so long as the density, fractal dimension, and the fractional decrease in density across the flame remain constant.

3.1.3. Attempts to improve on the standard model

Incorporation of this prescription into the computer model has brought interesting insights but, in its simplest form, fails to resolve the electron-capture problem. One interesting result, however, which we believe will characterize any realistic solution, is that slow initial propagation of the flame will lead to more electron capture in a small region of the white dwarf than might have been anticipated. Table 9 shows the distribution of Y_e in the inner 0.01 $M_\odot$ of a model in which the fractal dimension, D, was taken to be 2.3. This material all achieved nuclear statistical equilibrium at a temperature of about 9×10^9 K. At the center Y_e is only 0.43, implying that nuclei as neutron-rich as ^{48}Ca and ^{64,66}Ni will be produced in abundance. For a long time the origin of the neutron-rich nuclear statistical equilibrium component of nucleosynthesis has been thought to lie at the inner mass cut of Type II supernovae (Hartmann et al., 1985). That may still occur, but it now seems that realistic models for Type Ia supernovae will produce neutron-rich iron group isotopes as well. This will be interesting not only for those interested in the origin of these isotopes and those who try to understand isotopic abundance anomalies in meteorites, but also γ-ray astronomers.

That is because the nucleus ^{60}Fe is also produced under these same conditions (table 9). At $Y_e = 0.4311$, the mass fraction of ^{60}Fe in the final frozen out abundances is about 9%; for $Y_e = 0.4375$, it is 11%. The exact amount produced in the supernova depends sensitively upon the density at which the carbon runs away, but for our standard model ($\rho_i = 3.7 \times 10^9$ g cm^{-3} we estimate an ^{60}Fe yield of roughly

Table 9
Electron mole number in delayed detonation model

Y_e	η	Mass ($M_\odot$)	ΔM ($M_\odot$)	Nuclei
0.43 – 0.44	0.12 – 0.14	0.0022	0.0022	^{64,66}Ni, ^{60}Fe, ^{48}Ca
0.44 – 0.45	0.10 – 0.12	0.0095	0.0073	^{54}Cr, ^{58}Fe
0.45 – 0.46	0.08 – 0.10	0.026	0.016	^{56,58}Fe
0.46 – 0.47	0.06 – 0.08	0.054	0.029	^{56}Fe
0.47 – 0.48	0.04 – 0.06	0.085	0.031	^{54,56}Fe
0.48 – 0.49	0.02 – 0.04	0.122	0.037	^{54}Fe
0.49 – 0.50	0.00 – 0.02	1.38	1.26	^{56}Ni, ^{28}Si, etc.

10^{-4} $M_\odot$. If one Type Ia supernova occurred in our Galaxy every 200 years (a compromise between the longer interval suggested in this book by Tammann and shorter values elsewhere), a steady concentration of roughly one $M_\odot$ would accumulate in the 2×10^6 year mean life of ^{60}Fe. This would give a signal about an order of magnitude weaker than that of ^{26}Al and should definitely be sought by the Gamma-Ray Observatory and future missions. Because the ^{60}Fe is produced in the innermost layers, its velocity is low $\lesssim 10^8$ cm s^{-1}. The strong emission lines are at 59 keV and 1.17 and 1.33 MeV (equal strengths). If detected, this line would teach us a lot about Type Ia supernovae, especially their Galactic distribution, frequency, and, indirectly, the density at which carbon ignites. It would also be powerful positive evidence for the slow initial flame propagation we favor. Interestingly the seven year integrated spectrum of the Galaxy taken by SMM (Harris et al. 1990) shows lines at 1.17 and 1.33 MeV comparable in strength to ^{26}Al, but the lines are attributed to an on board ^{60}Co calibration source. The upper limit set by SMM is several times greater than the present prediction.

So far as this particular model is concerned, like others with constant fractal dimension, continued evolution leads to an explosion rather typical of previous deflagration models. The ^{54}Fe/^{56}Fe ratio was still far too great, about 5 times solar. The basic problem is that it is difficult for any continuously accelerating flame speed *of constant fractal dimension*, both to move so slowly early on that the white dwarf expands appreciably before burning, and yet still move so fast at late times that a large amount of ^{56}Ni is made at low density. Slow flames die early without making enough ^{56}Ni and fast flames move through the star making too much ^{54}Fe before the star expands. Thus while the above prescription has put the standard model on a more physical basis (the word convection no longer appears), some of the same deficiencies have carried over. Our parameter survey is incomplete, but some other ingredient seems to be required. If the carbon deflagration model is to remain viable, an explanation for the extremely rapid acceleration of the flame at late times must be found.

We now believe that the explanation lies in: (1) the fact that the deflagration is *not* initiated at only one point (section 3.1.1); and (2) the nonlinear nature of the RT instability *and a consequent increase in the fractal dimension of the flame as it propagates*. The discussion of the previous section was based upon a linear analysis of the RT instability. Regions of size greater than $\lambda_{\min}$ will deform before the flame sweeps over them and this sets the "tile size" for a geometry of presumed constant fractal dimension. In reality, however, scales lying well between $\lambda_{\min}$ and r_b (and close to neither) will have time not only to develop, but to progress into a nonlinear growth stage during which they may detach, float away from the main burning region, and seed the development of other islands of burning. As noted before this phenomenon actually commences during the transition from convection to localized burning, but it becomes even more important during the explosion. In terms of our mapping of the burning area onto an equivalent sphere, the effect is to increase the fractal dimension of the flame as the (real) surface becomes increasingly convoluted and noncontiguous. Since the fractal dimension gives the *power* to which the dependence on the radius is raised, a small change in D, say from 2.5 to 2.7, can radically accelerate the flame raising it quickly to very high speeds. In fact, as we have noted previously, within a short time the effective speed may become supersonic (Woosley 1990b). While it is possible, in principle, to have a supersonic effective speed with no shock wave present, after all the effective speed is not a material velocity but a mapping of $\mathrm{d}M/\mathrm{d}t$ onto a sphere, we have modified our earlier view and now believe that a transition to detonation will occur. This is certainly what we have discovered happens when a supersonic effective speed is employed in the code. We now feel that it has physical basis as well.

When the convolution of the surface inside some radius, r_b, becomes sufficient that the rate at which mass is burned substantially augments the internal energy inside r_b in less than the sound crossing time, $r_\mathrm{b}/c_\mathrm{s}$, pressure waves (i.e., sound waves), which travel much faster than the microscopic flame speed, will accumulate outside of some region where the burning is especially efficient and merge into a detonation wave. Once born, the detonation wave travels through the entire white dwarf.

We have now computed six such models. Two of them assumed an initial fractal dimension $D = 2.5$. Burning in these was so rapid from the very beginning that inadequate expansion occurred to solve the electron capture problem. Detonation happened too soon (when D was turned up as we shall describe) and the results were very much like the classical carbon detonation model, which is to say, not good. The other four used $D = 2.3$ initially and are summarized in tables 10 and 11 and figs. 9–11. Two of these assumed Population I abundances and, because of this, still ended up with a ^{54}Fe problem for the same reasons as described in Thielemann et al., (1986). Metallicity is converted to ^{22}Ne during helium burning in the star that originally became the white dwarf and the excess neutrons are later incorporated into ^{54}Fe during the explosion. As Thielemann et al. noted, however, a Population II white dwarf helps with this problem. In the present case, when coupled with the expansion during the slow initial propagation at $D = 2.3$, the ^{54}Fe problem goes away. That is, the iron group isotopes are now well

Table 10
Delayed detonation model summary

Model	DD1	DD2	DD3	DD4
$KE_\infty/10^{51}$ erg	1.56	1.44	1.37	1.22
$M^*(^{12}C)$	1.1(−3)	2.8(−3)	1.9(−3)	3.3(−3)
$M(^{16}O)$	1.9(−2)	3.9(−2)	3.6(−2)	1.0(−1)
$M(^{20}Ne)$	3.0(−4)	6.8(−4)	7.0(−4)	1.2(−3)
$M(^{24}Mg)$	1.4(−3)	2.2(−3)	2.2(−3)	9.0(−3)
$M(^{28}Si)$	6.6(−2)	1.2(−1)	1.4(−1)	2.6(−1)
$M(^{32}S)$	3.9(−2)	6.8(−2)	8.3(−2)	1.6(−1)
$M(^{36}Ar)$	5.7(−3)	9.5(−3)	1.8(−2)	3.5(−2)
$M(^{40}Ca)$	7.9(−3)	1.3(−2)	1.9(−2)	3.7(−2)
$M(^{54}Fe)^{**}$	2.0(−1)	1.9(−1)	7.1(−2)	7.0(−2)
$M(^{56}Ni)$	9.7(−1)	8.7(−1)	9.3(−1)	6.3(−1)
$M(\text{"Fe"})^\dagger$	7.2(−2)	7.1(−2)	7.1(−2)	8.9(−2)

* Solar masses of ejecta.
** Includes some component of ^{58}Ni produced in the α-rich freeze-out.
† All other iron group isotopes; mostly ^{56}Fe.

represented. Note though that it takes both. Thielemann did not get an acceptable solution just by turning the metallicity down. His white dwarf still blew up too quickly. And we do not get an acceptable solution if the white dwarf is Population I.

In each of the models summarized in tables 10 and 11, a flame was born in the center of the white dwarf. The small initial value of D is reasonable since until the flame has moved several tens of kilometers, D is identically 2.0 (section 3.1.3). Beyond this, D begins to grow, but does so slowly since nonradial mixing is not very efficient. Buoyancy is only in the radial

Table 11
Some details of model DD3

Time (sec)	Mass ($M_\odot$)	r_b (10^8 cm)	D	g_{eff} (10^8 cm s^{-2})	λ_{min} (10^3 cm)	v_{eff} (10^8 cm s^{-1})	c_s (10^8 cm s^{-1})	ρ_c (10^7 g cm^{-3})
0.201	0.0162	0.142	2.3	31.8	165	0.246	9.74	303
0.530	0.0665	0.262	2.3	35.7	78.2	0.269	9.32	228
0.698	0.106	0.354	2.3	33.5	40.4	0.251	8.86	157
0.964	0.161	0.572	2.3	19.6	14.6	0.181	7.55	63.8
1.350	0.232	1.15	2.4	6.99	3.24	0.281	5.67	14.0
1.478	0.269	1.46	2.5	5.05	2.66	0.765	5.62	8.70
1.499	0.319	1.58	2.6	5.07	4.02	2.30	6.10	8.12
1.505*	0.385	1.66	2.7	5.54	2.36	7.99	5.66	7.95

* Shortly after this, conduction was terminated. A detonation wave had formed.

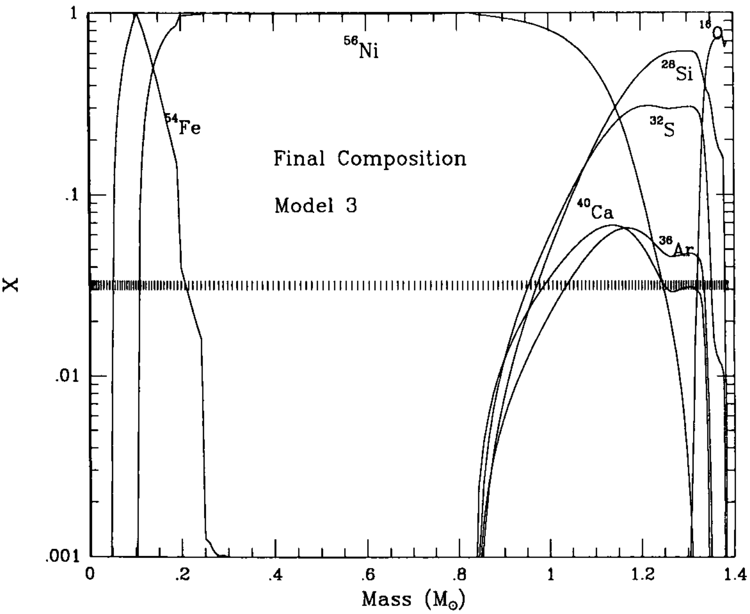

Fig. 9. Final composition of Model DD3.

direction. So long as the range of wavelengths between λ_{min} and r_b is not large, the RT-instability will not have time to develop into a nonlinear regime.

For example, 0.201 s into the evolution of Model DD3 (table 11), 0.0162 $M_\odot$ of carbon and oxygen have burned to iron. The effective flame speed is about 250 km s^{-1} and r_b is about 150 km. There is then less than a factor of ten difference between the growth times of λ_{min} and the largest possible instabilities and only the smallest instabilities can become nonlinear. The net acceleration due to gravity (roughly 0.3 $GM(r)/r^2$) is about 3×10^9 cm s^{-2}, implying that an accelerating blob might move at most $\frac{1}{2}g_{eff}t^2$ ~600 km in 0.2 s (g_{eff} is smaller earlier on). But this ensemble of small blobs would then have to grow to macroscopic size, similar in total area to the burned out core, before affecting the net overall burn rate. That would take another few tenths of a second. So the rate of mass consumption is not greatly affected by the nonlinear RT instability at this early time.

Circumstances have changed markedly by the time 0.2 $M_\odot$ has been burned and one second has passed (table 11). Now the range of unstable wavelengths is much larger; r_b itself is 10 times bigger. Pieces tens of kilometers in size can now detach and accelerate. Moreover, in the longer time, greater

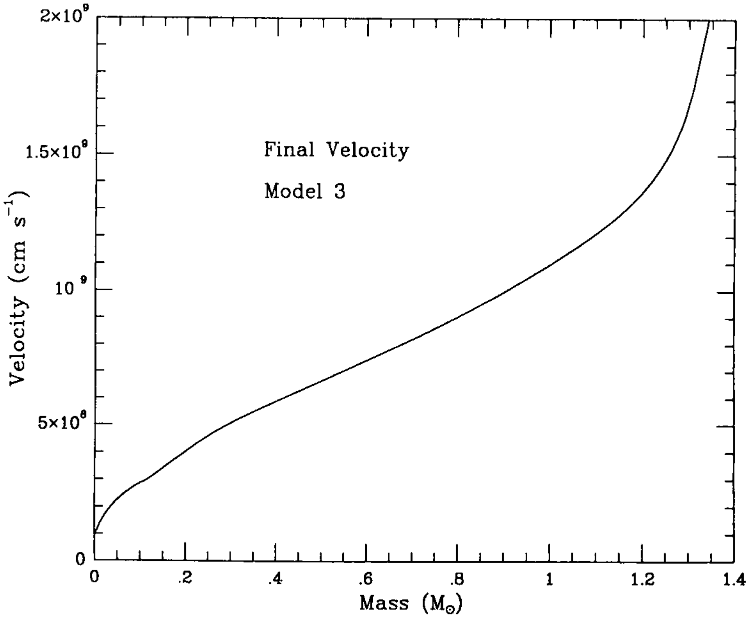

Fig. 10. Final velocity of Model DD3.

velocities have developed for the detached blobs – $v = g_{\mathrm{eff}}t$ would in fact imply supersonic motion. Actually the blobs experience drag and do not move that fast, but they might "float" at an appreciable fraction of the sound speed. By now the smaller blobs detached at an earlier epoch have also grown to appreciable size. In short one may expect that somewhere between a few hundredths and a few tenths of a solar mass the flame surface gets a lot more complicated or, in our terms, its fractal dimension increases, probably to the full turbulent value 2.7. [The extreme limit $D = 3.0$ is not physical as it would correspond to a supernova constructed entirely of *foam* having cell size λ_{min}.] A physical picture we carry is one of an exploding fireworks "bomb" with very many radial streamers coming out, almost at the sound speed. As time passes, burning between the streamers leads to a very rapid rate of mass consumption, eventually implying a supersonic v_{eff}.

Shortly after the dimension is increased to 2.7 in the calculation the flame becomes supersonic and merges smoothly into a detonation wave. By this time the white dwarf has expanded to the point that its central density is only 8×10^7 g cm^{-3}. No more electron capture happens. The detonation continues to the surface. Because of the low density the explosive burning in

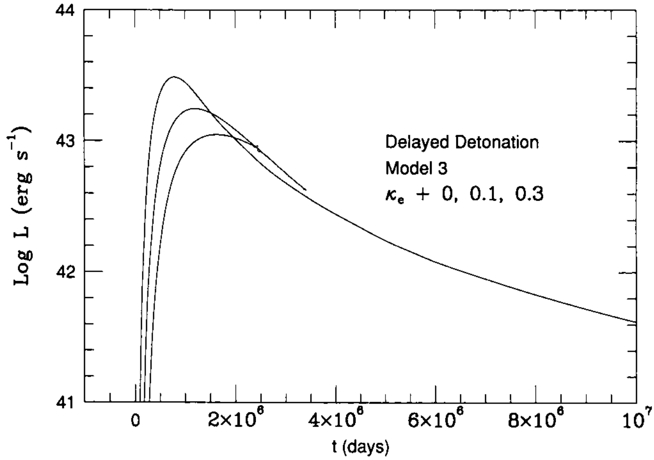

Fig. 11. Light curve from Model DD3. The brightest curve used electron scattering opacity solely. The other models included an arbitrary additive opacity of 0.03, 0.1, and 0.3 cm^2 g^{-1} to represent the effect of Doppler broadened lines. Real Type Ia supernovae probably peak around 15 to 20 days after explosion.

the outer layers produces not iron, but silicon, sulfur, and other intermediate mass elements. In models DD4 even some unburned oxygen was ejected.

By now the reader may have reasonably concluded that the history we assume for the fractal dimension, including the initial and final values and the time and rate at which the transition is made, is annoyingly artificial. We agree, but the multidimensional calculations to test it are probably a long way off. Nevertheless, we believe that our assumptions are reasonable and may be tuned to satisfy all observational constraints, which is more than can be said for any previous model. The composition and final velocity for Model DD3 are shown in figs. 9 and 10. The light curve, calculated using several values of optical opacity, is shown in fig. 11. Use of Type Ia models, delayed detonation or otherwise, as "standard candles" will clearly require more work on the optical radiation transport. However, we note, as did Weaver et al., (1980) and Arnett et al., (1985), a correlation between the time the supernova peaks and its brightness. Models that peak between 15 and 20 days will have a peak luminosity between 1×10^{43} erg s^{-1} and 2×10^{43} erg s^{-1}.

Although our description of what causes the transition to detonation is different, cast as it is in the language of fractal geometry, the outcome, delayed detonation, is much the same as recently suggested by Khoklov (1990a,b). Indeed, although we have long championed the need for expanding the star and then burning rapidly, our examination of the possibility of a late transition to detonation had as its immediate motivation these two preprints. Khoklov also assumes a period of prolonged burning at slow flame velocity that initially expands the white dwarf. He conjectures, however, that then an abrupt transition to detonation occurs. Such transitions are seen to occur in terrestrial explosions and Khoklov attributes the occurrence in the white dwarf to turbulence and the existence of a spectrum of temperature fluctuations in the material that is running away. We instead emphasize the role of the nonlinear RT instability and the initial conditions set up as burning becomes faster than convection. Whatever the cause for the transition, it is clear that "delayed detonation" (Khoklov's term) does help with a number of problems. First, it allows the discontinuous acceleration of flame speed that seems to be required if pre-expansion is to solve the electron capture problem. Second, it produces large quantities of silicon and calcium at a broader range of velocities than in the standard deflagration model. Artificial mixing may no longer be required. Third, the light curve is improved. Finally, because the combustion of the white dwarf to iron and intermediate mass elements is complete, less oxygen remains to (possibly) poison the late time spectrum.

Many more calculations remain to be done – of spectra and detailed nucleosynthesis in particular – but we feel that if Type Ia supernovae are the explosion of carbon–oxygen white dwarfs near the Chandrasekhar mass that this is how it must happen.

3.2. Accretion-induced collapse

Under certain circumstances an accreting white dwarf, be it carbon and oxygen or neon and oxygen, can forestall ignition to a central density of about $10^{10}\,\mathrm{g\,cm^{-3}}$ (Canal et al. 1990; Isern et al. 1990; Nomoto and Kondo 1990). These same works show that whether the white dwarf then explodes or collapses directly to a neutron star is sensitive to the flame speed.

There can be a considerable change between $\rho_{\mathrm{ig}} \approx 3 \times 10^9\,\mathrm{g\,cm^{-3}}$ and $10^{10}\,\mathrm{g\,cm^{-3}}$ because of the extreme sensitivity of electron capture rates to the density. If sufficient electron capture occurs, the density inversion behind the flame will be suppressed because, at constant pressure, material having a smaller value of Y_{e} has greater density. Woosley and Timmes (work in preparation) have determined the conductive flame speed, the equivalent of eq. (3.1), for a mixture of 60% oxygen, 20% neon, and 10% magnesium. It is 85 km s^{-1} times $\rho_{10}^{0.8}$. A similar result has been obtained for a carbon–oxygen mixture by Garcia et al. (1990). Woosley and Timmes have additionally

Table 12
Electron capture behind a conductive flame at 1.05×10^{10} K

t (ms)	Y_e	ρ_{10}	t (ms)	Y_e	ρ_{10}
0.649	0.4945	0.900	17.2	0.4569	0.948
1.02	0.4927	0.902	23.9	0.4504	0.959
1.40	0.4908	0.904	32.5	0.4441	0.971
1.81	0.4890	0.906	43.5	0.4378	0.984
2.69	0.4854	0.909	57.7	0.4316	0.998
5.31	0.4767	0.919	76.0	0.4255	1.011
8.28	0.4700	0.927	99.8	0.4195	1.025
12.1	0.4634	0.937			

studied electron capture behind the flame using a large reaction network. The flame initially raises the temperature to 10^{10} K very abruptly since the flame is only 10^{-5} cm thick. This raise in temperature, at constant pressure, decreases the density at $Y_e = 0.50$ by 10% to 9×10^9 g cm^{-3}. The subsequent evolution in Y_e and density is given in table 12. Most of the electron capture occurs on free protons.

What this means is that in the burning white dwarf, the region of density inversion behind the flame will be limited to a distance $\sim v_{\rm cond}\tau_{\rm cap} \sim$ 85 km s^{-1} times 0.05 s, or a few kilometers. This gives a *maximum* wavelength of Rayleigh–Taylor instability that can develop. On the other hand, one still has a minimum wavelength given by eq. (3.2) such that smaller wavelengths will be annealed by the flame. Unless $\lambda_{\rm min}$ is smaller than a few kilometers the conductive flame will be stable and will receive no acceleration by the Rayleigh–Taylor instability. For the assumed density $\lambda_{\rm min} \approx 1$ km/r_7 with r_7 the radius of the burned out region in hundreds of kilometers.

Once the flame has moved several kilometers, the density in the center begins to rise owing to electron capture and thus the white dwarf begins to collapse. By the time the flame has moved to several hundred kilometers, the infall velocity is faster than the flame and the white dwarf is committed to collapse. At 300 km, the range of wavelengths that can grow unstable is about 0.3 km to 3 km, but values at both extremes are almost stable (a few per cent density inversion hardly suffices for a vigorous overturn) and there is inadequate time for the instability to become terribly nonlinear. Thus, in terms of the previous section, the fractal dimension is not likely to increase well above 2. Say for example, it became 2.3. Then the effective flame speed would be $v_{\rm cond}(3\text{ km}/0.3\text{ km})^{2.3-2.0}$ or about 170 km s^{-1}. This is less than 2% of the sound speed.

It would seem that for ignition densities around 10^{10} g cm^{-3} and greater the white dwarf would have to collapse to a neutron star.

3.3. Type Ib supernovae

Over the last decade increasing evidence, principally spectroscopic in nature, has accumulated that Type I supernova may not be quite so regular and homogeneous a class as they were once considered. Of particular interest is the category of supernovae called Type Ib. The signature of Type Ib is absence of the $\lambda = 6130$ absorption feature in the spectrum taken at peak light, a feature generally attributed to Si II, and the presence instead of an unidentified "doublet" at $\lambda = 6300$ and 6500. Many members of this class now exist and are discussed elsewhere in this volume by Kirshner, Branch, and Nomoto. Additional characteristics of the class include a light curve that is, at peak light, roughly a factor of 4 dimmer than a Type Ia while having a width not less than, and perhaps slightly slower on the rise than average; a luminosity on the tail that declines more slowly than Type Ia (possibly indicating a greater column depth to γ-ray deposition); and a spectrum dominated at late times by emission lines of oxygen. Many Type Ib supernova seem to be located in HII regions and SN 1983N, a prototypical Ib, was the first Type I to be detected in radio. Remarkably no Type Ib has been discovered in an elliptical galaxy. Thus there is compelling evidence that, unlike ordinary Type Ia, Type Ib be associated with massive stars.

There are at least two generic ways of getting a supernova that observers would call Ib (or Ic). The actual frequency depends upon which path nature has favored. First there is the explosion of the stripped down cores of massive stars, commonly called Wolf–Rayet stars. Studies by Ensman and Woosley (1988) indicate, however, that the mass range of the presupernova star is severely restricted. The exploding core cannot be more massive than about 6 $M_\odot$. Essentially this follows from the fact that the explosion energies of Type Ia and Type II supernovae (as exemplified by SN 1987A) are very similar, both near 1×10^{51} erg. For Ib's not to be enormously fainter than Ia's at peak light it also follows that they must produce at least 1/4 to 1/2 as much ^{56}Ni as a carbon deflagration/detonation, i.e., a few tenths of a solar mass. If the light curve peak of the Ib is not to be enormously broader than Ia, and observationally it is not, it follows that the column depth, and hence mass, of the Ib's cannot be much greater than 1.4 $M_\odot$. Subtracting 1.5 $M_\odot$ for the neutron star, this implies a presupernova star of roughly 3 $M_\odot$. Four $M_\odot$ is also not too bad but 6 $M_\odot$ is pushing it unless the Type II supernova explosion energy is frequently an order of magnitude greater than in SN 1987A (Ensman and Woosley 1988). Nomoto and colleagues have recently suggested that the mass constraint on Type Ib progenitors is reduced somewhat when one considers mixing. We do not find this to be a large effect and will discuss it more a little later.

Stripped-down stars can, according to current lore, be obtained in one of two different ways. A lower mass star, e.g. 15 $M_\odot$ might lose its hydrogen envelope due to mass exchange in a binary system becoming a helium core of several solar masses (Uomoto 1986; Ensman and Woosley 1988; Shigeyama et al. 1990) or a single star more massive than about 35 $M_\odot$ could lose so much mass both as a giant and while a WR star that it ended up with only a few solar masses. Neither observations nor theory preclude this, although it does admittedly seem a great deal of mass loss. Both these pictures have strengths and weaknesses. As massive stars, the progenitors would be associated with spiral galaxies and HII regions. The explosion might produce radio emission because there has recently been a lot of mass loss (or exchange). Depending upon the specific model, oxygen would be abundant and silicon might not be, explaining the spectroscopic peculiarities. A somewhat larger mass would account for the slow decline on the tail and a smaller ^{56}Ni mass synthesized would make the display fainter. Yet the models also have problems. Why, in either case, should the star that explodes always end up near 3 or 4 $M_\odot$? Why not 2 or occasionally 6 or 10 $M_\odot$? Maybe it happens and we just do not have a big enough sample yet. Will the explosion produce enough ^{56}Ni? How much fainter than Type Ia are the Ib anyway? If the progenitor is in a binary system then why do we not see an abundant population of WR stars in binaries having low masses?

Examples of this class of model based upon the 3, 4, and 6 $M_\odot$ helium cores of massive stars that lost their hydrogen envelopes (but not much else) have been given by Ensman and Woosley, (1988) and by Shigeyama et al., (1990). Here I present a model of the other type. This model is based upon a 60 $M_\odot$ star studied by Norbert Langer and ourselves. The star endured extensive mass loss, especially after becoming a WR star, and ended up as a 4.25 $M_\odot$ WO star. It is to be emphasized that this residual is quite different both in composition and structure from the 4 $M_\odot$ core of a 15 $M_\odot$ star that lost only its hydrogen envelope. Among other things the entropy is higher as the star remembers its past history as a massive star, thus the star is less centrally condensed and the density gradients are shallower. As a result, explosion (simulated by placing a piston at the edge of the iron core), produces a large amount of ^{56}Ni by explosive nucleosynthesis (figs. 12 and 13). Because the density gradient is shallower a larger mass of ejected material experiences temperatures in excess of 5×10^9 K. For an explosion of 1.7×10^{51} ergs, a ^{56}Ni mass of 0.3 $M_\odot$ is made. This gives the light curve in fig. 14. Actually the figure shows three light curves in which the composition

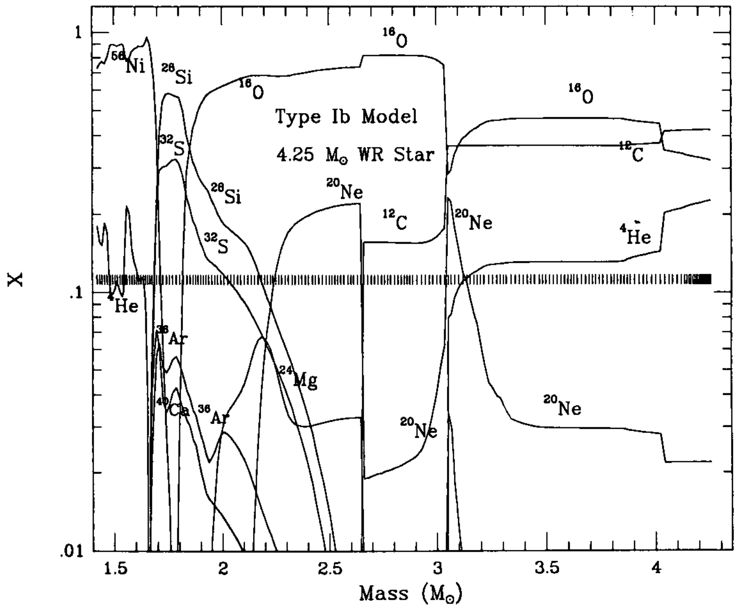

Fig. 12. Final composition of an exploded Wolf–Rayet star model for a Type Ib supernova (Woosley et al. 1991).

has been (a) unmixed; (b) mixed a lot; and (c) almost homogenized. The point is that mixing changes the width of our calculated maximum very little. More mixing causes the light curve to decline earlier but also causes it to rise earlier. There is also a more subtle effect in that radioactivity keeps the gas hot, hence more fully ionized. Therefore mixing increases the optical opacity which is mostly due to electron scattering.

Compared to observation (see, e.g. Ensman and Woosley 1988), none of these light curves is particularly appealing. They are all still too broad even for this large nickel mass and small presupernova mass. In particular they decline too slowly after maximum. Figure 15 takes another tack and arbitrarily varies the electron scattering opacity by a large factor. As has been known for a long time (Weaver et al. 1980), decreasing this opacity leads to a brighter supernova that peaks at an earlier time. This makes the overall peak narrower in better agreement with the observations. It is unclear just why the electron scattering opacity would be so reduced, but one may speculate that clumping would lead to regions of higher density and lower ionization than calculated in the simple 1D homogeneous model. Also clumping would provide voids

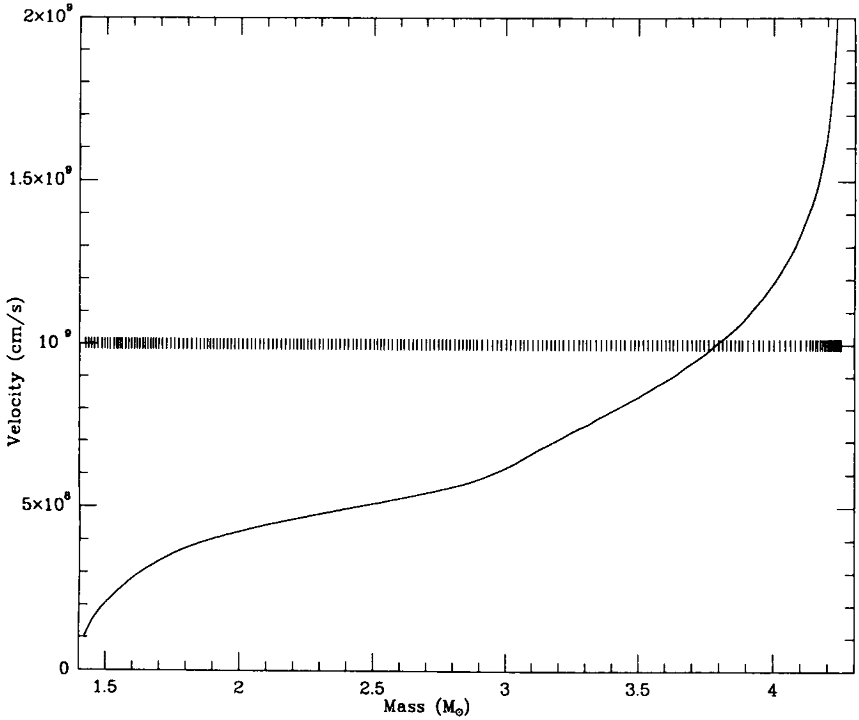

Fig. 13. Final velocity of the model in the previous figure.

where radiation might more effectively leak out. Until more detailed multidimensional calculations are done, this remains, as labeled, sheer speculation.

Another important modification to the bolometric light curve of these models which has not yet been properly calculated is the time-dependent modification from Doppler broadened lines. Early on the photosphere is just beneath very rapidly moving material in which the line opacity may be very large. Later the Doppler shear is less in the material above the photosphere. When the opacity is large, more energy is lost to expansion. Thus the effect would be to reduce emission at early times relative to emission at the peak. This might "sculpt" a narrower light curve out of the one we have calculated using simple electron scattering opacity. In short, a proper light curve can only be determined by doing the time dependent spectrum. This is, in fact, true of *all* supernovae. A number of groups are working on this but no results have been presented so far.

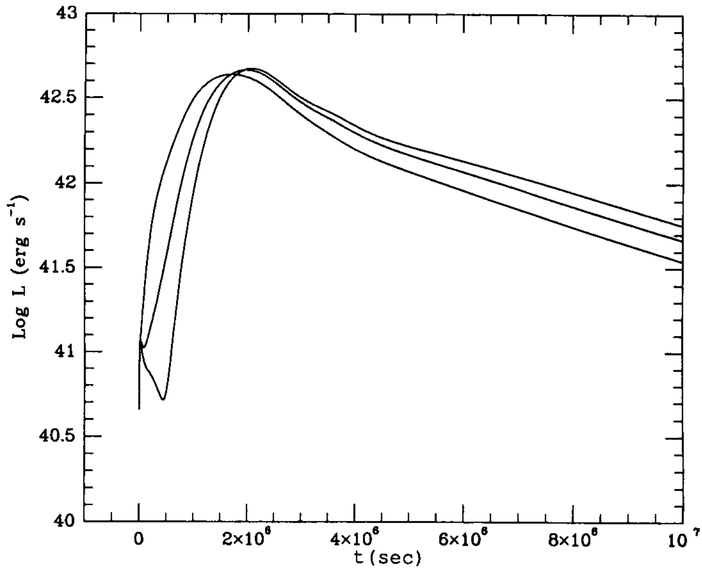

Fig. 14. Light curve from the model in the previous figures. The star has been mixed to various extents, in the most extreme case, almost thoroughly homogenized. The peak and width of the light curve are not greatly affected.

There is a second way of making Type Ib that also has some appeal. In section 3.1 we discussed models for Type Ia based upon carbon deflagration. Looking at the spectra and light curves of Ia and Ib side by side, we are more impressed with the similarites than with the differences. Might the Ib also be some variation of carbon deflagration?

The answer seems to be yes, at least in theory. Suppose the delayed detonation model is indeed the correct one for Type Ia. Then there might also be occasions when the deflagration goes out without igniting a detonation. These would produce less ^{56}Ni (but still a lot compared to massive stars) and thus be fainter. They would expand more slowly, hence the light curve would be broader. There would be a layer of silicon and calcium but it would be very thin (perhaps extended in velocity space by the distortion of the burning surface, but small in mass). There would be a lot of oxygen, hence oxygen lines at late times in the spectrum. All in all, a lot of the observations would be explained. On the other hand, unfortunately, there is no known compelling reason why such fizzled detonations would find themselves in HII regions and never in elliptical galaxies.

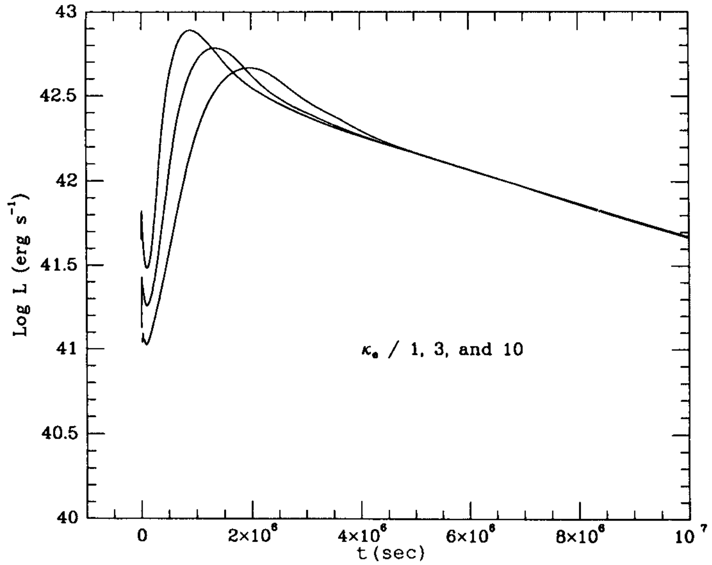

Fig. 15. Light curve from the model in the previous figures. The star has been mixed and the electron scattering opacity multiplied by 1, 1/3, and 1/10 to simulate the effect of clumping. This very artificial and speculative operation leads to a narrower and brighter light curve that may agree better with observations (however, the data set of bolometric observations of SN Ib is very limited).

One might also expect situations in which detonation did occur but very little silicon and calcium were made because the star did not expand enough during the first stage of burning. Such an overly successful detonation would produce iron and little else. There would be little silicon and calcium, but also no oxygen. Whether such objects have been observed is not clear.

4. Explosive nucleosynthesis in supernovae of Type II and Ib

Many aspects of nucleosynthesis have been reviewed, both in a parameterized fashion and in terms of the current supernova models, in the Saas–Fee Lecture Notes (Woosley 1986). Here we update some of those results, especially with regard to explosive nucleosynthesis, and present two new major nucleosynthetic processes – the neutrino, or ν-process and the r-process in the context of an α-rich freeze-out of the high entropy bubble in a delayed supernova explosion (section 2.2). For other recent developments in nucleosynthesis, see section 3 on the delayed detonation model for Type Ia supernovae, especially the neutron-rich isotopes produced in the central regions, and section 1 on massive stellar evolution, especially the sensitivity of hydrostatic nucleosynthesis to semiconvection and the reaction rate for $^{12}C(\alpha, \gamma)^{16}O$. See also the reviews by Thielemann and by Nomoto in this volume.

4.1. Parameterized explosive nucleosynthesis

As the shock, however generated, moves outwards through a massive star whose core has collapsed, pressure inside the shocked region is nearly constant (Weaver and Woosley 1980; Bethe 1990, 1993). Since radiation pressure dominates, one has

$$E_{\text{tot}} \approx 10^{51}\ \text{erg}\ \approx \tfrac{4}{3}\pi r_s^3 a T_s^4 \tag{4.1}$$

where T_s is the temperature behind the shock and r_s, its location. This equation can be solved to give the shock temperature,

$$T_s \approx \frac{1.3 \times 10^{10}}{(r_s/10^8\ \text{cm})^{3/4}}\ \text{K}. \tag{4.2}$$

Energy generated by the nuclear burning is small compared to that imparted by the shock, so the expansion is nearly adiabatic, i.e. $\rho(t)$, the density, is proportional to $T^3(t)$. Moreover, the material expands at approximately the escape velocity, so the density time history for $t \lesssim \tau_{\text{HD}}$ is

$$\begin{aligned} \rho(t) &= \rho_s \exp(-t/\tau_{\text{HD}}) \\ \tau_{\text{HD}} &= \frac{446}{\rho_s^{1/2}}. \end{aligned} \tag{4.3}$$

At later times one needs to use $\rho(t)$ in the equation for τ_{HD} and solve in a self-consistent manner. Because the shock is not particularly strong, the density, at least in the mantle and helium core, is not increased by the customary factor of 7, but by a smaller factor, typically two or three. Using the adiabatic relation and eqs. (4.2) and (4.3), the temperature and density history of an arbitrary point in the presupernova star is specified. If the temperature is high enough to stimulate extensive nuclear burning, the final composition too will be specified by these equations and hence uniquely determined by the presupernova structure of the star. Extensive burning of a given fuel will occur (Woosley 1986) if the characteristic burning time scale is a fraction, F, of the hydrodynamic time scale at that temperature (density) where $F \sim 3/j$ and the characteristic burning reaction is proportional to T^j. Thus if T_s is above 2.5×10^9 K, explosive neon burning will occur; above 3.3×10^9 K explosive oxygen burning will occur; above 4×10^9 K, explosive silicon burning occurs; and above 5×10^9 K, nuclear statistical equilibrium is achieved.

While one must be cautious about using these equations near the region where the shock first begins to move out (though see Bethe 1993), they imply an easy way of estimating iron nucleosynthesis. All material heated to temperatures greater than 5×10^9 K in the explosion process will achieve nuclear statistical equilibrium, i.e. it will be iron. Temperatures this high are achieved for radii less than 4000 km. Thus material between the mass cut (which must be determined by a realistic model) and 4000 km in the presupernova star will be ejected in the form of iron. By examining the neutron excess η of this material in the presupernova model one can also determine the dominant iron group isotope. As long as $\eta \lesssim 0.02$, as it always is this far out in the star, the ejected material will be mostly ^{56}Ni. Stated another way, if one has an accurate measure of the ^{56}Ni created in an explosion (0.075 $M_\odot$ in SN 1987A, for example), the mass cut in a successful model should lie that many solar masses interior to 4000 km. This reasoning is altered if the explosion takes so long to develop that material at 4000 km has already moved in a good fraction of the radius (this takes a second or so), but the argument does show why ^{56}Ni synthesis is larger in stars of high mass where the density gradient near 4000 km is shallower.

The isotopic composition of this iron, and especially the ^{57}Ni/^{56}Ni ratio can be estimated if the neutron excess and nature of the freeze-out are known. Typically the value of η in the silicon shell outside the collapsing core is 0.004 owing to electron capture that went on during and after oxygen burning. Even if there is no silicon shell, or if the silicon shell falls into the neutron star, the base of the oxygen shell is not less than 0.002 for any but the most metal deficient stars (Woosley and Weaver 1982b), nor greater than 0.006. Table 13 shows the ratio of ^{57}Ni/^{56}Ni and several other isotopes resulting from a normal freeze-out from nuclear statistical equilibrium for various values of η. We see that it is virtually impossible for the final iron isotopic ratio, ^{57}Fe/^{56}Fe, to exceed its solar value, 0.024, by more than a factor of 2.5 unless the dominant iron isotope is not ^{56}Ni, but ^{54}Fe. This would not only be unacceptable in terms of nucleosynthesis but, for SN 1987A, would lead to a fainter light curve than was observed. A reasonable range of η, say less than 0.004 restricts the ^{57}Fe/^{56}Fe ratio to less than 0.7.

Table 13
Ordinary freeze-out from NSE

T_9	5.5	5.5	5.5	5.5	5.5	5.5	5.5	5.5
ρ	10^8	10^8	10^8	10^8	10^8	10^8	10^8	10^8
η_i	0	0.001	0.002	0.004	0.007	0.01	0.02	0.03
η_f	1.2(−4)	1.1(−3)	2.1(−3)	4.1(−3)	7.1(−3)	1.0(−2)	2.0(−2)	3.0(−2)
$X(^{44}\mathrm{Ti})$	2.3(−5)	2.1(−5)	2.0(−5)	1.9(−5)	1.7(−5)	1.3(−5)	9.8(−6)	3.7(−6)
$X(^{54}\mathrm{Fe})$	9.8(−4)	2.0(−2)	4.0(−2)	8.3(−2)	1.5(−1)	2.1(−1)	4.3(−1)	6.2(−1)
$X(^{56}\mathrm{Ni})$	8.9(−1)	8.6(−1)	8.3(−1)	7.8(−1)	7.1(−1)	6.3(−1)	3.9(−1)	1.5(−1)
$X(^{57}\mathrm{Ni})$	3.3(−5)	6.5(−3)	9.3(−3)	1.3(−2)	1.7(−2)	1.9(−2)	2.3(−2)	2.0(−2)
$X(^{58}\mathrm{Ni})$	5.5(−5)	2.6(−3)	5.8(−3)	1.3(−3)	2.4(−2)	3.7(−2)	8.8(−2)	1.8(−1)
P_{44}	0.021	0.020	0.019	0.019	0.020	0.020	0.020	0.020
P_{54}	0.018	0.379	0.794	1.73	3.42	5.52	18.2	67.6
P_{56}	1	1	1	1	1	1	1	1
P_{57}	0.112	0.313	0.457	0.685	0.977	1.25	2.45	5.50
P_{58}	0.003	0.075	0.169	0.398	0.839	1.43	5.58	19.2

This simple result from nuclear statistical equilibrium is substantially altered, however, by the the α-rich freeze-out (table 14) which is chiefly responsible for making ^{57}Fe in nature (Woosley et al. 1973; Woosley 1986). If free α-particles are present during the cool down from nuclear statistical equilibrium, as they are in the deeper layers ejected in SN 1987A (Woosley et al. 1988b; Hashimoto et al. 1989), the abundance of ^{57}Ni is enhanced relative to ^{56}Ni. Table 14 shows the iron isotope ratios as modified by both a moderate and a strong α-rich freeze-out. A ^{57}Ni abundance implying ^{57}Fe/^{56}Fe greater than four times solar is disallowed. Also a value less than 0.5 times solar seems difficult to achieve in any circumstances. Values less than solar would suggest little or no component from the α-rich freeze-out is present in the ejecta of SN 1987A.

This range, 0.5 to 2.5, is consistent with recent infrared measurements (Varani et al., 1990) and γ-ray upper limits (Sunyaev et al. 1990) placing the ^{57}Co abundance at a level that would imply one to two times the solar value of ^{57}Fe/^{56}Fe and is also consistent with model supernova calculations by Hashimoto et al. (1989) and Woosley et al. (1988) that suggest a similar range. It is quite inconsistent with some of the values sometimes invoked by those studying the late time light curve. Whatever the observational limit ultimately becomes, it may have more to say about the existence of the α-rich freeze-out in Type II supernovae than about the neutron excess (although both are obviously important). As an aside we note that it is very unlikely that the ^{44}Ti synthesized by SN 1987A exceeds twice that implied by the solar ratio for ^{44}Ca/^{56}Fe.

Table 14
Alpha-rich freeze-out

T_9	5.5	5.5	5.5	5.5	5.5	5.5	5.5	5.5
ρ	10^7	10^7	10^7	10^7	10^7	10^7	10^7	10^7
η_i	0	0.001	0.002	0.004	0.007	0.01	0.02	0.03
η_f	3.5(−4)	1.0(−3)	2.0(−3)	4.0(−3)	7.0(−3)	1.0(−2)	2.0(−2)	3.0(−2)
X_α	6.3(−2)	6.2(−2)	6.1(−2)	5.9(−2)	5.5(−2)	5.1(−2)	3.9(−2)	2.7(−2)
$X(^{44}\mathrm{Ti})$	1.6(−4)	1.5(−4)	1.4(−4)	1.2(−4)	1.0(−4)	8.3(−5)	3.8(−5)	1.2(−5)
$X(^{56}\mathrm{Ni})$	8.9(−1)	8.7(−1)	8.4(−1)	7.9(−1)	7.0(−1)	6.2(−1)	3.5(−1)	8.5(−2)
$X(^{57}\mathrm{Ni})$	8.3(−3)	2.6(−2)	3.0(−2)	3.6(−2)	4.2(−2)	4.6(−2)	4.8(−2)	2.9(−2)
$X(^{58}\mathrm{Ni})$	7.2(−3)	1.3(−2)	3.8(−2)	8.7(−2)	1.6(−1)	2.4(−1)	5.2(−1)	8.1(−1)
P_{44}^*	0.144	0.138	0.136	0.126	0.117	0.107	0.087	0.117
P_{56}	1	1	1	1	1	1	1	1
P_{57}	0.384	1.24	1.45	1.87	2.46	3.06	5.58	13.8
P_{58}	0.199	0.373	0.910	2.72	5.70	9.53	36.1	234

T_9	5.5	5.5	5.5	5.5	5.5	5.5	5.5	5.5
ρ	10^6	10^6	10^6	10^6	10^6	10^6	10^6	10^6
η_i	0	0.001	0.002	0.004	0.007	0.01	0.02	0.03
η_f	4.2(−4)	1.1(−3)	2.1(−3)	4.0(−3)	7.0(−3)	1.0(−2)	2.0(−2)	3.0(−2)
X_α	3.5(−1)	3.5(−1)	3.5(−1)	3.5(−1)	3.4(−1)	3.4(−1)	3.2(−1)	2.9(−1)
$X(^{44}\mathrm{Ti})$	7.7(−4)	7.5(−4)	7.3(−4)	7.1(−4)	6.7(−4)	6.3(−4)	5.1(−4)	6.9(−5)
$X(^{56}\mathrm{Ni})$	5.9(−1)	5.7(−1)	5.5(−1)	5.0(−1)	4.2(−1)	3.4(−1)	8.3(−2)	1.1(−3)
$X(^{57}\mathrm{Ni})$	1.1(−2)	2.7(−2)	2.9(−2)	3.1(−2)	3.3(−2)	3.3(−2)	2.2(−2)	1.2(−3)
$X(^{58}\mathrm{Ni})$	9.2(−3)	1.1(−2)	3.7(−2)	9.0(−2)	1.7(−1)	2.5(−1)	5.2(−1)	4.7(−1)
P_{44}	1.06	1.07	1.09	1.15	1.29	1.51	4.90	49.0
P_{56}	1	1	1	1	1	1	1	1
P_{57}	0.772	1.96	2.14	2.54	3.21	4.05	10.7	41.7
P_{58}	0.385	0.489	1.68	4.44	9.89	18.2	155	1.0(4)

*The production factor here is defined relative to solar mass fractions of $^{56}\mathrm{Fe}$ and the final decay product of the given isotope.

Returning to our discussion of explosive nucleosynthesis in general, we seek a way in which parameterized calculations carried out for a grid of peak *temperatures* and densities and expanded on a hydrodynamic time scale can be mapped into a realistic stellar model (see also Woosley 1986). That mapping is provided by eq. (4.2). An ejected mass, M, initially located between radii r_1 and r_2 will experience a range of shock temperatures given by that equation. The mass of a particular species i in that ejecta is given by

$$\begin{aligned} M_i &= \langle X_i \rangle M_{ej} = \int_{r_1}^{r_2} 4\pi r^2 \rho(r) X_i(r)\, \mathrm{d}r \\ &= \frac{16\pi}{3} \int_{T_2}^{T_1} (\rho r^3) X_i(T)\, \mathrm{d}\ln(T) \end{aligned} \tag{4.4}$$

where, in the general case, ρr^3 varies with T. As we showed in fig. 6, however, ρr^3 is almost a constant. So the ejected masses of species produced explosively are approximately weighted by the logarithm of the temperature interval in which they are synthesized. Empirically $\rho r^{2.5}$ is even closer to a constant than ρr^3. In a 25 $M_\odot$ star, $\rho r^{2.5}$ in the region where explosive nucleosynthesis occurs is roughly 10^{28} cgs units (corresponding to several times 10^{32} g cm^3 for ρr^3 compared to the considerably smaller value for the 18 $M_\odot$ star shown in fig. 17). Thus one should compute $\rho(T)$ from the radial dependencies of both ρ and T and then the average mass fraction

$$\langle X_i \rangle = \frac{\Sigma\, \rho(T) X_i(T)\, (\Delta T / T^5)}{\Sigma\, \rho(T)\, (\Delta T / T^5)} \tag{4.5}$$

where ΔT is the temperature interval of the grid of nucleosynthesis calculations and the sum runs from the lowest temperature where explosive nucleosynthesis might occur (roughly $T_9 = 2$) to the highest temperature matter ejected. In practice, as discussed earlier, it is not physical to use any of these relations for radii so small (about two thousand kilometers) that one is sensitive to details of the explosion mechanism. Thus one should not go much over $T_9 \approx 5$. The iron produced at higher temperatures and the hydrostatic nucleosynthesis that is ejected without explosive modification must come from a stellar model. It is very interesting to note, however, that to the extent that $\rho \propto r^n$, with n a constant, in stars of various mass, *the relative mass fractions (although not the total yield) of nuclei produced by explosive nucleosynthesis will be roughly constant in stars of various masses.* The total mass depends on the actual value of ρr^3, or more generally ρr^n, but this will scale approximately as the mass of the carbon–oxygen core, or even more roughly as the helium core mass, in both cases 1.5 $M_\odot$ should be subtracted for the neutron star. Thus in an 18 $M_\odot$ star ($M_\alpha \approx 5\ M_\odot$), ρr^3 is about 5×10^{31} g cm^3 (fig. 6) whereas in a 25 $M_\odot$ star ($M_\alpha \approx 9\ M_\odot$) it is about 2×10^{32} g cm^3.

The mass independence of the elemental and isotopic ratios coming out of explosive nucleosynthesis in massive stars motivated a parameterized study of the nuclei from magnesium to iron. Rob Hoffman has carried out such a study using the above parameterization and an initial composition characteristic of complete carbon burning in a Pop I star, i.e., a composition consisting initially of oxygen, neon, magnesium, and other trace elements. The range of shock temperatures considered was $T_9 = 2$ to 6 and the grid size, 0.2 billion K. The network size was 329 isotopes and the reaction rate for $^{12}C(\alpha,\gamma)^{16}O$ was that of Caughlan et al., (1985), that is the larger value. The results

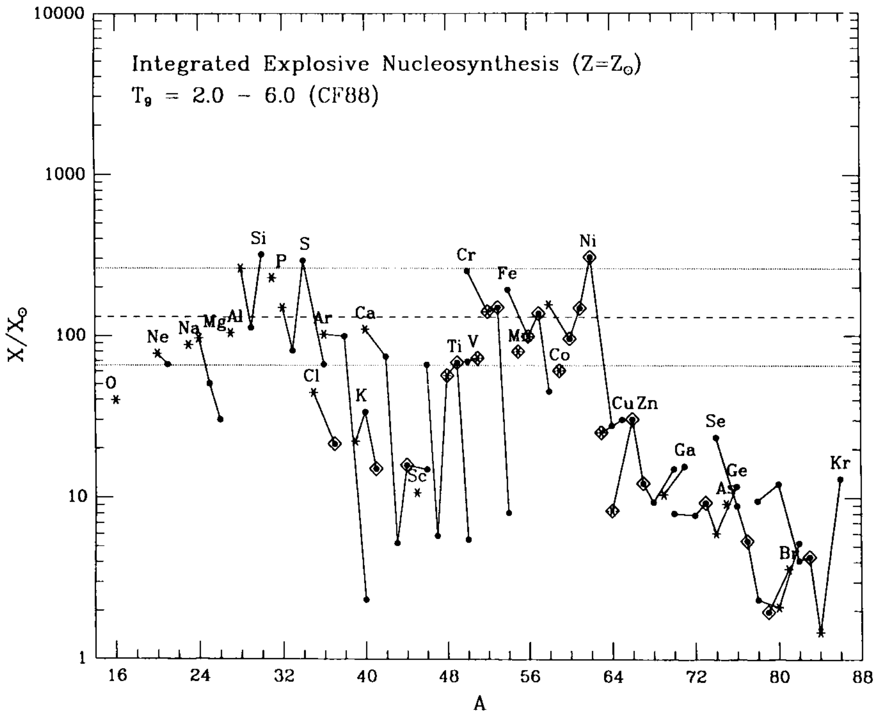

Fig. 16. Composite of parameterized explosive nucleosynthesis calculations for a range of peak explosion temperatures between 2 and 6 billion K. The "Production Factor" is the ratio of final mass fraction produced in the (mass-averaged) ejecta divided by its value in the sun. Dashed lines show a range of a factor of two about a typical value for major species.

shown in fig. 16 are useful for indicating which isotopes probably are and are not products of explosive nucleosynthesis in this temperature range (see also Woosley 1986). The abundance of iron group isotopes to lighter ones is sensitive to the arbitrary choice of the peak temperature considered in the integral (here 6 billion K). The interpretation of the scale is that if roughly one gram in 100 of the Galaxy has been through conditions like these, the solar abundance set of species in the band will have been produced.

The overall fit is remarkably good. Thirty-six of the 56 stable isotopes between ^{16}O and ^{62}Ni are produced within roughly a factor of two of their solar value (and in the sun these abundances scale five orders of magnitude). Carbon and oxygen isotopes are all low or absent, which is not surprising since they come mostly from cooler shells that are not explosively processed (i.e., T_s less than 2 billion K) and in some cases (e.g., ^{13}C) from low mass stars. The species ^{22}Ne is absent since it is made in the helium shell (from α-capture on ^{14}N). Fluorine will be made by the neutrino process (not included in this calculation). Chlorine and potassium are both low, and yet should be products of explosive oxygen burning in this temperature range. Their low production is a puzzle and may indicate some problem either with the solar abundance set of Cameron (1982) and Anders and Grevesse (1989), poorly determined reaction rates, or an enhancement by the s- or ν-processes. Certainly ^{40}K is produced elsewhere by the s-process in the helium shell. The solar abundance of ^{40}Ar is very uncertain and its "low" production here of little concern.

There are a number of problems just beyond the closed neutron and proton shells at calcium. The rare isotope ^{46}Ca would have been much more abundant in the calculation if the initial composition had contained carbon. Perhaps it is made in carbon deflagration supernovae or by hydrostatic carbon burning further out in the star. ^{48}Ca must be made in a very neutron-rich region either deeper in the supernova than considered here or maybe in Type Ia supernovae (section 3). The three nuclei ^{43}Ca, ^{45}Sc, and ^{47}Ti are not made here and are real mysteries. They probably are *not* produced in Type II supernovae. In fact, the only site that seems to provide adequate amounts is high-temperature explosive helium burning as might occur in a helium detonation model for Type I (Woosley 1986). Here ^{44}Ca is underproduced but this may reflect an inadequate inclusion of higher temperature material that experiences the α-rich freeze-out (table 14). In Type II and Ib supernovae, this nucleus is produced as the radioactive progenitor ^{44}Ti in the very bottom-most layers to be ejected. It is also made in helium detonation.

Nuclei of the iron group are well reproduced save for the neutron-rich isotopes ^{50}Ti, ^{54}Cr, ^{58}Fe, and ^{64}Ni. These might owe their origin to electron capture in Type Ia supernovae, as discussed in section 3. One may wonder, since the relative proportions of iron and intermediate mass elements are so well represented here whether one really wants to invoke an alternate synthesis site for iron, namely Type Ia supernovae. If the Type Ia rate is to be as low as Tammann and Van den Bergh suggest, the Type II contribution to present day iron becomes very important. Still we note that, even though solar in isotopic composition, the total yield of iron in Type II's is very sensitive to where one draws the mass cut, how the explosion is simulated, and how much iron falls back in the reverse shock.

In figs. 17 and 18 isotopic nucleosynthesis from entire 18 $M_\odot$ and 20 $M_\odot$ explosions are given for certain choices of $^{12}C(\alpha,\gamma)^{16}O$ and semiconvection.

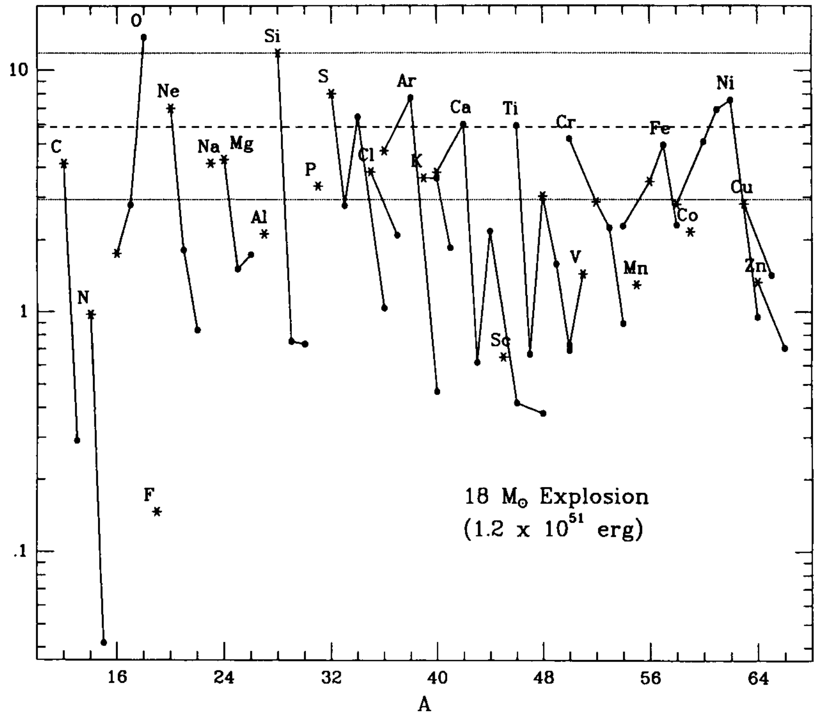

Fig. 17. Final isotopic nucleosynthesis from an 18 $M_{\odot}$ star with restricted semi-convection (F = 10^{-4}), a small value for $^{12}C(\alpha, \gamma)^{16}O$, and an explosion energy of 1.3×10^{51} erg (Woosley et al. 1988b).

Overall there is considerable similarity to the parameterized results. The α-rich freeze-out was very strong in these models with a consequent increase in ^{44}Ca and heavy nickel isotope production and a decrease in ^{54}Fe production (table 14).

4.2. The neutrino-nucleosynthesis process

The neutrino burst generated by core collapse has a typical duration of roughly three seconds (although substantial flux may continue for 10 seconds as in the case of SN 1987A), a time short compared to that required for the overlaying mantle of heavy elements to be ejected. It takes the shock wave a minute or so to reach the edge of the helium core. Thus during its ejection, both before and, in the deeper layers, after shock passage, material

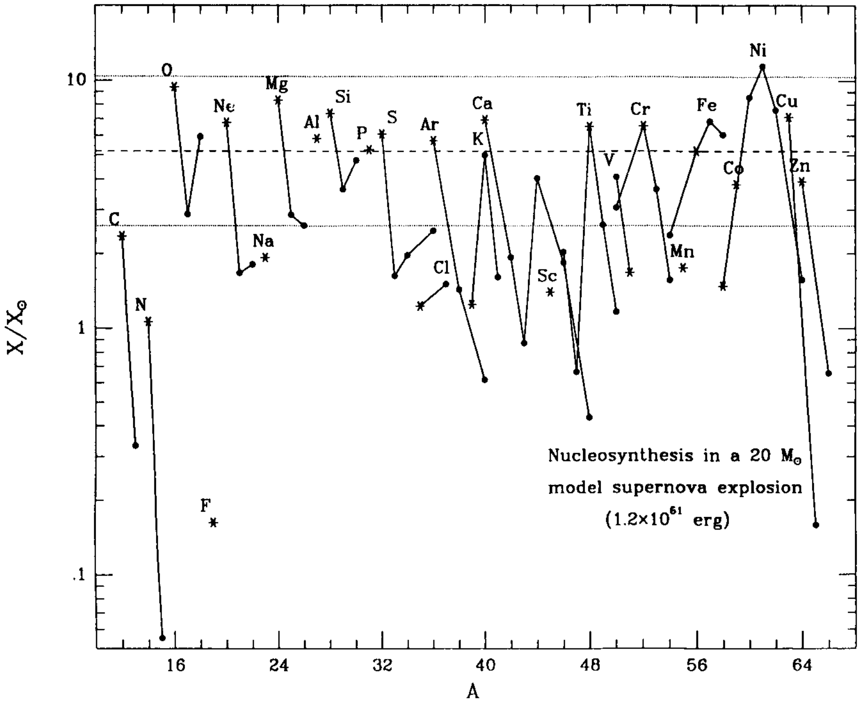

Fig. 18. Final isotopic nucleosynthesis from a 20 $M_\odot$ star with substantial semi-convection (F = 0.1), a large value for $^{12}C(\alpha, \gamma)^{16}O$, and an explosion energy of 1.3×10^{51} erg (Woosley et al. 1988).

will be subject to an intense irradiation of neutrinos. Although the interaction cross section is obviously small, a sufficient number of nuclei will interact to be of importance to the nucleosynthesis, especially of rare nuclei too fragile to be made other ways.

The idea of neutrino nucleosynthesis was first discussed in detail by Domogatskii, Nadyozhin, and colleagues (Nadyozhin and Otroschenko 1980; Domogatskii et al. 1977, 1978; Domogatskii and Nadyozhin 1977, 1978, 1980a,b; Domogatskii and Imshennik 1982), but both the stellar models and cross sections employed in these early studies were very approximate. In general, more consequences were suggested than actually occur in the modern models. More recently neutrino-nucleosynthesis has been studied in detail by Woosley et al., (1990) using a large reaction network and with specific attention to the nuclear processing both before and after shock passage in the hydrogen, helium carbon, neon, oxygen, and silicon shells. The required cross sections were calculated by Haxton and are partly tabulated in that paper.

Although a very large number of weak interactions were included in the network study: $(\nu_e, e^-\gamma)$, (ν_e, e^-p), (ν_e, e^-n), $(\nu_e, e^-\alpha)$, $(\bar{\nu}_e, e^+\gamma)$, $(\bar{\nu}_e, e^+n)$, $(\bar{\nu}_e, e^+p)$, $(\bar{\nu}_e, e^+\alpha)$, $(\nu, \nu'\gamma)$, $(\nu, \nu'n)$, $(\nu, \nu'p)$, $(\nu, \nu'\alpha)$, and several spallation channels of neutrinos interacting with ^{12}C, the most important reactions were those involving the neutral current excitation of the compound nucleus and with a subsequent emission of a neutron or proton. Because of their greater number, higher temperature, and the quadratic dependence of cross section on the energy (minus the threshold Q-value for particle separation), μ- and τ-neutrinos are most important. Supernova models suggest temperatures of 6 to 8 MeV for these neutrinos (although the high energy tail is somewhat depleted compared to a thermal distribution), and an average energy around 20 to 25 MeV. Those states most populated are in the giant electric dipole resonance of the compound nucleus. A representative example are the reactions $^{20}Ne(\nu, \nu'p)^{19}F$ and $^{20}Ne(\nu, \nu'n)^{19}Ne(e^+\nu_e)^{19}F$ both of which make fluorine in the neon shell. At a distance of $\sim 10^9$ cm, the neutrino flux (μ- and τ-neutrinos) would be about 10^{38} cm^{-2} s^{-1} for 3 seconds. The cross section for neutrino ejection of a neutron or proton is (averaged over flavor and antiparticle and assuming equal amounts of each), at 8 MeV, 8.3×10^{-42} cm^2 (Woosley et al. 1990). The product of flux, time, and cross section is then ~ 0.002. Only 0.2% of the neon nuclei in the neon shell will interact. However, in the sun the abundance ratio of neon to fluorine ($^{20}Ne/^{19}F$) is 3000. Thus one will make more than enough ^{19}F to satisfy the solar requirements. Actually the calculation is more complicated because some ^{19}F gets destroyed in shock passage, not all the neon is at the same radius, etc., but the example shows that the process might be important. Detailed calculations by Woosley et al., (1990) show that the abundances of roughly a dozen isotopes may be substantially altered by the neutrino process.

However, those calculations were carried out in a parameterized fashion using conditions from a few select zones in a particular presupernova model (20 $M_\odot$). Adiabatic expansion on a hydrodynamic time scale was assumed. More recently Woosley et al., (1990b) have considered neutrino nucleosynthesis coupled to a complete stellar model of a 25 $M_\odot$ supernova explosion. The star (Pop I) was evolved from the main sequence to core collapse and the composition in each zone was followed using a network of 150 isotopes from carbon through zinc. The large network was not used to provide energy generation rates; that came from a smaller network. However, the large network was updated (in each of roughly 400 zones) each time substantial burning occurred and convective mixing was included for all zones every cycle. At the end of the evolution, the iron core was removed and an explosion simulated using a piston. The explosion energy (kinetic energy of the ejecta at infinity) was 7×10^{50} erg, perhaps a little on the low side. As the shock passed through the star explosive nucleosynthesis was calculated using the large network which also included all appropriate neutrino interactions (see above). The neutrino source was simulated as a black body of total energy 3×10^{53} erg and duration of 3 seconds (e-folding time). The μ- and τ- neutrinos were assumed to constitute 2/3 of this burst, and the electron neutrinos constitute the rest. The electron neutrino temperature was 4 MeV (or zero for the calibration case); the μ- and τ-neutrino temperature was varied. Results are given in tables 15 and 16. Comparison here is to the solar abundances tabulated by Anders and Grevesse (1989) which, in the case of boron especially, differs substantially from Cameron (1982).

Several important results emerge. First, we note that the element lithium is substantially produced. This occurs in the helium shell by the reaction sequence ${}^4\mathrm{He}(\nu, \nu'\mathrm{n}){}^3\mathrm{He}(\alpha, \gamma){}^7\mathrm{Be}(\mathrm{e}^-, \nu){}^7\mathrm{Li}$ as discussed by Woosley et al. (1990a,b). Production in the silicon shell is much less than estimated in the earlier work, because the inner zones expanded at a slower rate after

Table 15
Neutrino nucleosynthesis summary; 25 $M_\odot$– 7.0×10^{50} erg

Species	No ν	$T_\mu = 4$	$T_\mu = 6$	$T_\mu = 8$	$E_{53} = 6., T_\mu = 4$
^{2}H	8.1(−6)	8.8(−6)	8.8(−6)	8.8(−6)	9.1(−6)
^{7}Li	2.7(−8)	2.0(−7)	4.7(−7)	1.2(−6)	2.0(−6)
^{11}B	5.6(−9)	9.6(−7)	1.8(−6)	4.0(−6)	6.3(−6)
^{19}F	2.3(−5)	7.7(−5)	1.4(−4)	2.3(−4)	3.7(−4)
^{22}Na	5.3(−6)	6.3(−6)	7.1(−6)	8.4(−6)	1.1(−5)
^{26}Al	4.8(−5)	5.5(−5)	6.0(−5)	6.8(−5)	8.1(−5)
^{35}Cl	2.8(−4)	3.2(−4)	3.7(−4)	4.4(−4)	5.4(−4)

Table 16
Normalized to ^{16}O In the Sun*

Species	No ν	$T_\mu = 4$	$T_\mu = 6$	$T_\mu = 8$	$E_{53} + 6., T_\mu = 4$
^{7}Li	0.01	0.08	0.19	0.5	0.8
^{11}B	0.004	0.8	1.4	3.2	5.1
^{19}F	0.2	0.7	1.3	2.2	3.5
^{35}Cl	0.4	0.5	0.6	0.7	0.8

*Anders and Grevesse (1989); compared to 2.5 $M_\odot$ of ^{16}O ejected.

the density had declined (eq. (4.3)) and the ^{7}Be was burned up. The solar abundance of lithium is very uncertain since it has been depleted in the sun's outer layers by nuclear reactions, but it is possible that all the lithium in Pop I stars has been made by the ν-process. There may be a supernova contribution to Pop II as well which complicates the use of lithium as a big-bang nucleosynthesis diagnostic. Boron is produced in the carbon shell in considerable abundance although only the more abundant isotope, ^{11}B, is given a solar abundance. In the past a special low-energy component of cosmic rays was invoked to synthesize ^{11}B by spallation of carbon in the interstellar medium. This is no longer necessary. Fluorine, which has traditionally been difficult to produce anywhere, is now made adequately by neutrino interactions in the neon shell. The important radioactive tracers of nucleosynthesis, ^{22}Na and ^{26}Al, also are substantially enhanced. There are also minor contributions to many other isotopes lighter than nickel. Heavier nuclei have not been included in the calculation, but they too may be affected.

It is also gratifying to see that the best agreement with solar values is achieved for μ- and τ-neutrino temperatures in the range 6 to 8 MeV, just the range that those who model the core physics say is realized. While much more work is needed to determine the sensitivity of these results to variations in the stellar mass, explosion energy, neutrino energy spectrum, and rate for $^{12}\mathrm{C}(\alpha, \gamma)^{16}$, it is encouraging that we may someday be able to read the temperature of the neutrinos emitted in the collapse of a massive stellar core from the present abundances of the elements. In particular μ- and τ-neutrino temperatures cooler than about 5 MeV already seem to be excluded.

4.3. Nucleosynthesis of ^{26}Al

The current situation with regard to ^{26}Al synthesis must be regarded as very uncertain, but in our opinion, it remains possible, even likely that Type II and Ib supernovae are the major source of the $\sim 2\ M_\odot$ of ^{26}Al inferred for the present abundance in the Milky Way Galaxy (see also Signore and Dupraz 1990). I say 2 $M_\odot$ and not 3 $M_\odot$ because the distance to the center of the Galaxy may be more like 8 kpc than 10 kpc which was assumed in deriving the traditional mass of ^{26}Al implied by the observations. The mass of ^{26}Al might be reduced even more, although not by much, if the ^{26}Al were not concentrated in the center of the Galaxy, but in a ring farther out.

^{26}Al ($\tau_{1/2} = 7.3 \times 10^5$ years) is produced by a number of processes in massive stars: hydrogen burning in the envelope (where the ^{26}Al can be ejected either in the supernova itself or in the wind preceding the formation of a Wolf–Rayet star); explosive neon burning between temperatures of about 2×10^9 and 3×10^9 K; and by the neutrino process (Woosley et al. 1990a,b). In all cases, however, production occurs by the ^{25}Mg(p,γ)^{26}Al reaction and ^{26}Al will be sensitive to, although not necessarily linear in changes in this reaction rate. The recent downward revision of the rate (Iliadis et al. 1990) at temperatures appropriate to hydrogen shell burning is therefore highly relevant. At a temperature of 30 to 50 million K, for example, the rate has declined from the value tabulated by Caughlan and Fowler (1988) by a factor of 4.5. On the other hand, at higher temperatures appropriate to neon burning and the ν-process the rate has not decreased. Thus only production in the hydrogen shell is changed.

The numbers given in table 17 for ^{26}Al synthesis in 15, 20, 25, and 35 $M_\odot$ stars (Woosley and Weaver 1991, see also tables 2–7) include the hydrogen shell component and may now be altered, especially in the lower mass stars, but in cases where substantial ^{26}Al is produced, most of it comes from the heavy element core. The naming of models in the table follows the convention of section 1, giving first the stellar mass in solar masses, then an indication of convective algorithm with "S" meaning a large amount of semiconvection and "N" meaning very little, and finally a number indicating the factor by which the ^{12}C(α, γ)^{16}O reaction rate (as tabulated by Caughlan and Fowler 1988) was multiplied.

The first striking thing about the ^{26}Al synthesis reported in table 17 is that it is highly variable, not even monotonic with stellar mass. Model 20S2 produces a lot more ^{26}Al than either 15S2 or 25S2. The production has a lot to do with the amount of magnesium in the star and this depends on, in addition to the carbon abundance that comes out of helium burning (and thus ^{12}C(α, γ)^{16}O), the location of various convective carbon, neon, and oxygen burning shells (see also Barkat and Marom (1990) for a discussion of nonmonotonic behavior in massive star evolution). There are general trends however. More massive stars, especially 35 $M_\odot$ stars make more ^{26}Al. The production does not appear to be too sensitive to the ^{12}C(α, γ)^{16}O reaction rate itself, but this can be deceiving. Less carbon (from a larger rate for this reaction) means less magnesium and therefore less aluminum synthesis. But a large value for this rate also implies higher entropy in the stellar core and more extensive convective shells – a larger region where ^{26}Al is produced. Extra semiconvection, which means larger carbon–oxygen cores for a given helium core mass, also favors ^{26}Al synthesis.

In two of the models, 25N2 and 35N2, explosion was simulated. A piston was situated at 2500 km in the presupernova model, well outside the iron core, and at a typical distance for which delayed explosions develop (Wilson, 1985;

Table 17
^{26}Al nucleosynthesis ($M_\odot$) in massive stars

Model	15S1	15S2	15S3	15N2	20S2	20N2
Mass	15	15	15	15	20	20
$^{12}C(\alpha,\gamma)^{16}O$	1	2	3	2	2	2
Semiconv.	high	high	high	low	high	low
$10^5 * M(^{26}Al)$	1.2	1.2	1.1	1.0	13.3	2.0

Model	25S1	25S2	25S3	25N1	25N2	25N3
Mass	25	25	25	25	25	25
$^{12}C(\alpha,\gamma)^{16}O$	1	2	3	1	2	3
Semiconv.	high	high	high	low	low	low
$10^5 * M(^{26}Al)$	4.6	4.6	3.8	0.68	2.1	2.6

Model	35S2	35N2	25N2X	25N2Xν	35N2X	35N2Xν
Mass	35	35	25	25	35	35
$^{12}C(\alpha,\gamma)^{16}O$	2	2	2	2	2	2
Semiconv.	high	low	...	...	...	...
$KE_\infty/10^{51}$	...	...	1.5	1.5	1.5	1.5
$10^5 * M(^{26}Al)$	34	17	2.4	4.4	13	18
$M(^{56}Ni)$	...	...	0.08	0.08	0.31	0.31

Mayle 1985, 1990; Wilson et al. 1986; Mayle and Wilson 1991), and given a trajectory such as to produce the ejection of all exterior mass and a total kinetic energy at infinity of 1.5×10^{51} erg. The shock wave was followed through the star and explosive nucleosynthesis determined in each of the stellar zones. An identical calculation was then carried out that included the nucleosynthesis induced by irradiation from neutrinos from the forming neutron star (Woosley et al. 1990a,b). A total neutrino energy (all flavors) of 4×10^{53} erg was assumed. The baryon masses interior to the mass cuts in the 25 $M_\odot$ and 35 $M_\odot$ models were 1.72 and 1.86 $M_\odot$. The neutrino burst was assumed to e-fold with a 2-second characteristic time scale, the electron neutrino temperature was 4 MeV and the μ- and τ-neutrino temperatures were 8 MeV. The high-energy tails of the neutrino distribution function, to which the neutrino process is sensitive, may not be well represented by a thermal distribution. The parameters adopted here tend to maximize the effect and neutrino-induced nucleosynthesis could, in general, be about a factor of two less efficient than reported. However, the neutrino spectrum tends to get harder at late times. For now we retain the specified parameterization.

It is interesting that the explosion does not always enhance ^{26}Al synthesis. In Model 35N2X, for example, an explosion without neutrino irradiation, the total ^{26}Al production declined from its presupernova value. The shock heated some portion of the ^{26}Al containing material to such high temperature that it was destroyed. In Model 25N2X, on the other hand, the explosion enhanced the ^{26}Al production. In both the 25 and 35 $M_\odot$ models, even those including neutrino irradiation, most of the final abundance of ^{26}Al was created before the explosion in a superheated oxygen–neon shell during the last hour of the star's life. As the iron core begins to contract, even as silicon shell burning is still in progress, this region of the star also contracts to higher temperature and becomes vigorously convective. In a phase that is almost "implosive neon burning" copious ^{26}Al is produced. Obviously the details are sensitive to how time dependent convection is handled and all the other factors affecting the late stages of stellar evolution and the (carbon and) neon abundances. A factor of two error bar on all the numbers in table 17, either up or down, would not be overly generous.

Figure 19 shows the final ^{26}Al distribution in Models 25N2Xν and 35N2Xν. The production in the hydrogen envelope is obviously negligible compared to that made in the core. With the new rate for ^{25}Mg(p,γ)^{26}Al, it may be even smaller. We expect this to be a general characteristic of very massive stars ($M \gtrsim 20\ M_\odot$) and, unless such stars fail to explode, the ^{26}Al ejected in the supernova event should greatly predominate over any component ejected in the stellar wind, say while the star was becoming a Wolf–Rayet star. The ^{26}Al distribution in the 25 and 35 $M_\odot$ supernova cores largely parallels the distribution of magnesium in these objects. In the 35 $M_\odot$ model (fig. 19), the sharp peak at 3.2 $M_\odot$ is a result of explosive neon burning and the tail from 4 to 6 $M_\odot$ is a mixture of ^{26}Al made before the explosion and by the neutrino process in comparable amounts.

Many more models remain to be done, including stars of 20, 30, 40, and 60 $M_\odot$, but the following preliminary conclusions are offered. A reasonable prescription for ^{26}Al synthesis in Type II supernovae might be, in units of $10^{-5}\ M_\odot$: 0.5, 1, 4, 5, and 15 for stars of 12, 15, 20, 25, and 35 $M_\odot$, respectively (although again note the nonmonotonic behavior in table 17). For stars bigger than 35 $M_\odot$, including the Ib progenitors that may result from such stars, also use $1.5 \times 10^{-4}\ M_\odot$. Note that the Type Ib, if they come from massive stellar cores (section 5), will be very important and might contribute, per event, substantially more ^{26}Al than the Type II. As remarked previously, all these numbers have an error bar of at least a factor of two.

Next the rates for Type II and Ib supernovae are critical. Van den Bergh and Tammann (1990) have discussed the Galactic supernova rate concluding that a likely value for core collapse events is two per century. However, as they point out, this is very much less than inferred from the 6 historical supernovae in the last 1000 years (all within 3 or 4 kpc of the Earth and

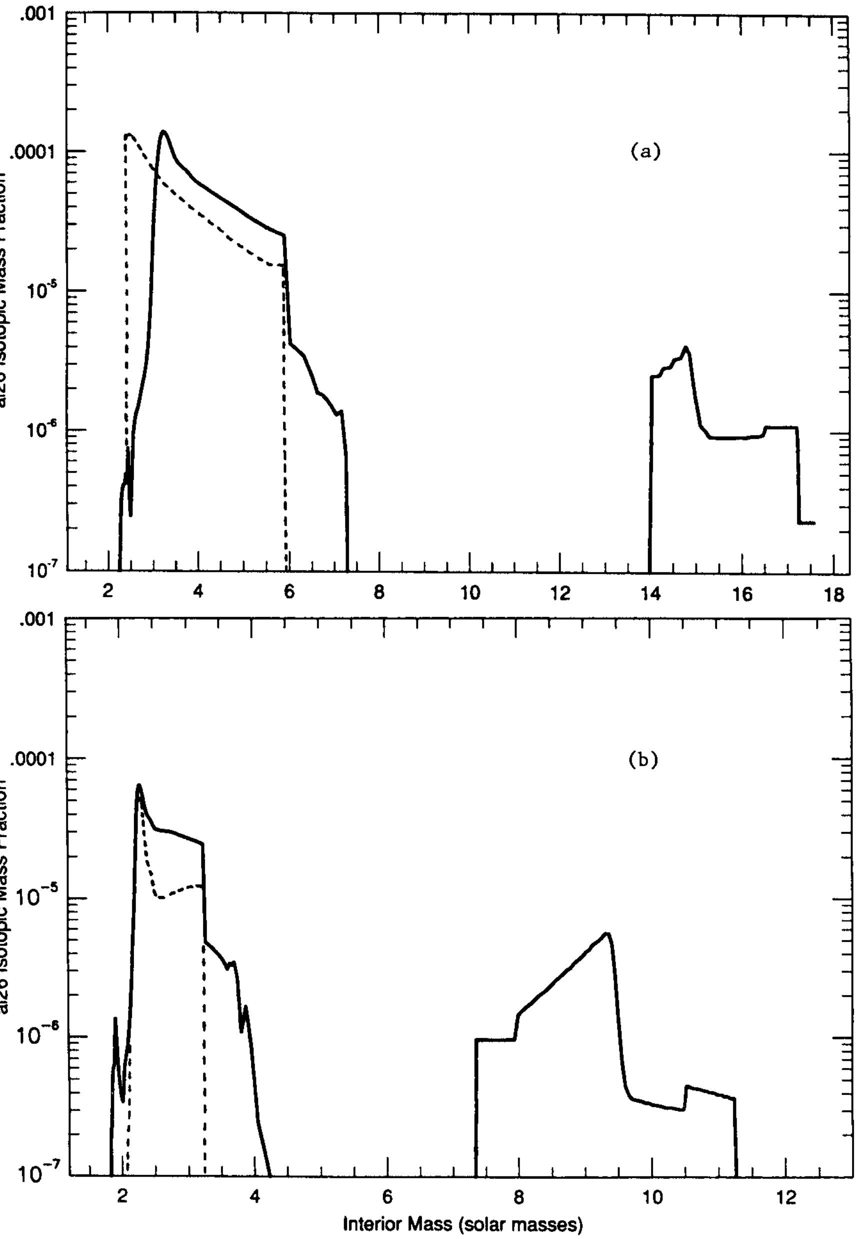

Fig. 19. Distribution of ^{26}Al by mass fraction in: (a) 35 and; (b) 25 $M_{\odot}$ model supernovae. The mass of the helium core in the 25 and 35 $M_{\odot}$ models is 9.2 and 14.6 $M_{\odot}$ respectively. The CO-cores were 4.3 and 7.2 $M_{\odot}$. The dashed line shows the abundance before the explosion, the solid line, after.

within a 50 degree pie slice of the Galactic disk) from which they infer the rate *could* be as frequent as one every 10 years (this will shortly be limited by neutrino and γ-ray detectors, the 7 year lifetime of SMM already placing an interesting upper bound). Perhaps our Galaxy, or our region of the Galaxy, is undergoing a burst of star formation. Let us adopt a rate of 4 core collapse supernovae per century as a reasonable compromise between the arguments of Tammann and Van den Bergh and the observed local Galactic rate. One Type Ib (derived from a massive Wolf–Rayet star) once a century (or any other 35 + $M_\odot$ supernova) plus two or three explosions per century around 15–25 $M_\odot$ could provide all the ^{26}Al necessary to explain the observations. On the other hand, the present error bars are large enough that some other source could dominate.

If the ^{26}Al does come from supernovae (rather than novae or AGB stars), then these calculations suggest that the most massive stars will predominate. One then expects the ^{26}Al to have a distribution in the Galaxy that resembles not only Pop I, but extreme Pop I, i.e., like the O-stars in HII regions and molecular cloud complexes.

4.4. *The α-rich freeze-out and the r-process*

Continuing our discussion of explosive nucleosynthesis and moving deeper within the star, we consider a mixture of iron group nuclei and α-particles cooling from a temperature substantially in excess of 5×10^9 K. If the expansion is quick enough, a portion of the α-particles will persist at low temperature owing to the relative inefficiency of the critical reactions that convert helium into carbon. For temperatures hotter than 10^9 K the triple-alpha reaction rate declines slowly with increasing temperature, remaining roughly constant at a few times 10^{-10} (cm^3 mole^{-1})^2 s^{-1} (Caughlan and Fowler 1988). If the available time is that for hydrodynamic expansion, eq. (4.3), then for densities lower than about 10^8 g cm^{-3}, the α-particles in nse will not all have time to reassemble. As the material continues to cool, it will do so in the presence of an anomalously large flux of light particles (the α-particles will also generate neutrons and protons by their interactions with bound nuclei) and the final composition will differ from what would be calculated in nse. This is the α-rich freeze-out (Woosley et al. 1973; table 14).

Previous calculations have shown, for small values of the neutron excess, that the modification to the most abundant isotope in nse is not very great. A composition that is predominantly ^{56}Ni stays ^{56}Ni although the abundances of trace constituents such as ^{54}Fe and ^{58}Ni change by orders of magnitude. It has long been a curiosity what keeps the process from going farther. At most one finds (see, e.g. Woosley 1986) a trace of zinc and germanium isotopes produced (which later become isotopes of nickel and zinc, respectively), but essentially the nuclear flows stop one or two α-particles beyond ^{56}Ni, even if the α-particle abundance is very large.

We now understand that this happens, not because of the Coulomb barrier, in which case one would expect quite different results for various temperature histories and α-particle mass fractions, but because of *photodisintegration*. Just above the iron group the valley of beta stability (location of stable isotopes) deviates sharply to the neutron-rich side of the $Z = N$ line as a consequence of passing the magic proton shell at $Z = 28$ and the maximum packing fraction in the iron group. Thus protons and α-particles are easily removed for nuclei $A \gtrsim 60$ having small neutron excesses. The small particle separation energies translate into large reaction rates for (γ, p), (n, p), (p, α), (γ, α), and (n, α) reactions which impede the buildup of heavier elements until such low temperatures that the Coulomb barrier *does* stop the build up of heavy nuclei.

This nuclear systematic suggests that heavier nuclei could be assembled in an α-rich freeze-out if the neutron excess were larger. Recently Woosley and Hoffman (1991) have begun to explore the α-rich freeze-out for values of neutron excesses, η, in the range 0.03 to 0.23 and have found the creation of heavier elements all the way up to $A \gtrsim 110$, even when most of the ejecta is in the form of heavy elements. In the limit of an extremely large fraction of unassembled α-particles, they have found that the α-rich freeze-out merges smoothly into the classical r-process.

A promising site for this occurrence is the low-density, high-entropy bubble that forms in the "delayed mechanism" model for the explosion of Type II supernovae (section 2). Material in this bubble has previously been at high density and experienced electron capture (Mayle and Wilson 1988b; see especially their fig. 2). The neutron excess may be quite large; values of η of 0.2 and even more are typical (Mayle and Wilson 1988a).

From the study of Woosley and Hoffman (1991), a number of interesting conclusions has already emerged. First, in material that experiences a high-η, α-rich freeze-out but which has too low an entropy to produce a r-process, they find production of a number of isotopes from the iron group up through $a \sim 100$, whose synthesis has previously been attributed to the r-, s-, and p-processes. Some of these nuclei are summarized in table 18 and include ^{66,68}Zn, ^{70,72}Ge, ^{74,76}Se, ^{78,80,86}Kr, ^{87}Rb, ^{88}Sr, ^{89}Y, ^{90,91,92,94,96}Zr, ^{93}Nb, ^{95,97,98,100}Mo, ^{101,102,104}Ru, ^{103}Rh, ^{105,106,108,110}Pd, and ^{107}Ag. For lower values of neutron excess, Woosley and Hoffman confirm the production by the

Table 18
Sample α-process production factors*

η_i	8.00(−2)	9.00(−2)	1.00(−1)	1.10(−1)	1.20(−1)	1.30(−1)	1.40(−1)	1.50(−1)
η_f	5.95(−2)	6.89(−2)	7.82(−2)	8.76(−2)	9.69(−2)	1.07(−1)	1.16(−1)	1.25(−1)
$X_f(\alpha)$	3.57(−1)	3.26(−1)	3.01(−1)	2.83(−1)	2.66(−1)	2.63(−1)	2.72(−1)	2.68(−1)
^{66}Zn	2.6(5)	2.3(5)	...	...	...	...	...	...
^{70}Ge	7.3(5)	5.3(5)	2.7(5)	...	...	...	...	...
^{72}Ge	...	2.2(5)	2.8(5)	2.1(5)	...	...	...	...
^{74}Se	1.0(6)	4.3(5)	...	...	...	...	...	...
^{76}Se	5.4(5)	5.3(5)	3.8(5)	1.7(5)	...	...	...	...
^{80}Kr	2.7(5)	...	...	...	...	...	...	...
^{86}Kr	...	...	...	...	...	7.6(6)	2.1(7)	1.2(7)
^{85}Rb	...	...	...	...	...	...	7.1(5)	2.1(6)
^{87}Rb	...	...	...	...	...	1.4(7)	1.3(7)	2.2(6)
^{88}Sr	1.6(5)	1.0(6)	3.7(6)	8.1(6)	1.4(7)	1.0(7)	7.6(5)	1.6(6)
^{89}Y	8.4(5)	2.9(6)	5.5(6)	6.7(6)	5.3(6)	3.2(6)	1.6(6)	5.0(6)
^{90}Zr	1.4(7)	2.0(7)	1.9(7)	1.4(7)	4.7(6)	4.4(6)	1.6(7)	3.1(6)
^{91}Zr	4.8(5)	5.6(5)	5.6(5)	5.2(5)	4.3(5)	1.6(6)	1.9(6)	4.1(6)
^{92}Zr	...	...	...	...	...	1.5(5)	2.1(6)	5.5(7)
^{94}Zr	...	...	...	...	...	3.1(5)	...	1.1(6)
^{96}Zr	...	...	...	...	...	4.9(5)	9.2(6)	2.7(7)
^{93}Nb	...	...	...	...	...	2.5(5)	2.5(6)	2.9(6)
^{92}Mo	2.9(5)	...	...	...	...	...	...	...
^{95}Mo	...	...	...	...	...	1.7(5)	3.7(5)	8.2(6)
^{97}Mo	...	...	...	...	...	...	...	7.4(5)
^{104}Ru	...	...	...	...	...	...	...	5.4(5)

* Ratio of final mass fraction to solar mass fraction where greater than 1% of the maximum production. $T_{9p} = 10$, $\rho_p = 5 \times 10^6$ g cm^{-3}.

α-rich freeze-out of ^{44}Ca, ^{57}Fe, ^{59}Co, ^{58,60,61,62}Ni, ^{63}Cu, and ^{64}Zn. These species are all *primary* in the sense that they will be produced in the same quantities by a star of either Population I or II. Neutron excesses this large are the result of electron capture and are independent of the initial metallicity of the star.

All of these species have very low abundances in nature and their synthesis imposes severe constraints upon the frequency with which the conditions for this sort of freeze-out can be realized. In particular the amount of mass ejected, the neutron-excess, and the existence of the α-rich freeze-out in the 9 $M_\odot$ model studied by Mayle and Wilson (1988a) are inconsistent with the requirements of Galactic chemical evolution unless such supernovae happen only once every 10 000 years. We believe it more likely that the thermodynamic or electron-capture history of the ejecta in that particular model is in error or at least does not reflect the typical event. Alternatively these deep layers might reimplode after hydrodynamic interaction with the overlaying mantle and envelope, the so-called "reverse shock" (see, e.g. Weaver and Woosley 1980). More careful modeling of the complete explosion is necessary, but the nucleosynthesis will clearly be a powerful constraint on the supernova explosion mechanism.

Nevertheless, we envision the most likely natural circumstances for the α-process *and the r-process* to be provided by the high entropy bubble that forms at late times in the delayed neutrino transport model for Type II and Ib supernovae. The most recent model for a delayed explosion of a 20 $M_\odot$ star (Mayle and Wilson 1991) provides a tantalizing example. At late times the neutron-rich ($Y_e \lesssim 0.45$) ejecta have entropies near 100 in a few times 10^{-5} $M_\odot$ of ejecta with $Y_e \sim 0.40$ to 0.45 (fig. 19). The value of Y_e is not so critical as the entropy. At higher entropy the α-particle abundance in nse is larger and, at the lower density, is less efficient at assembling into heavy elements. Since the number of neutrons per heavy seed is about $100(1 - 2Y_e)/X_H$, where X_H is the mass-fraction of heavies (for which an average mass of 100 is assumed), decreasing the amount of α-particles that reassemble strengthens the r-process.

The freeze-out of material followed along this path (Woosley and Hoffman, 1991) and having an initial value of $Y_e = 0.45$ ($\eta = 0.10$) shows first the photodisintegration of any initial composition into a nuclear statistical equilibrium comprised almost entirely of free nucleons. Thus all memory of the initial composition, save Y_e, is lost. As expansion and cooling occurs, the nucleons assemble to α-particles and then about 10% of the α-particles into heavy nuclei. After a few tenths of a second material has reached the end of the network at $A \approx 110$, being carried there mostly by (α, n) reactions. The neutron mass fraction at this point is still 8% or about 100 neutrons for each heavy nucleus.

Table 19
Temperature-density trajectory for material expanding in the wind of a delayed 20 $M_\odot$ explosion.

$t(s)$	T_9	ρ_4	$t(s)$	T_9	ρ_4
0	10.	254	0.20	2.87	5.93
0.01	9.36	200	0.40	2.37	4.15
0.02	7.42	88.8	0.60	2.20	2.66
0.03	6.59	62.9	0.80	2.13	1.89
0.04	5.94	44.5	1.0	2.09	1.69
0.05	5.41	32.1	2.0	2.01	1.46
0.075	4.36	16.2	3.0	1.97	1.77
0.10	3.76	11.4			

Table 20
Key evolutionary quantities 20 $M_\odot$ explosion.

t(sec)	T_9	ρ_5	X_n	X_p	X_α	^AZ	$X(^AZ)$	^AZ	$X(^AZ)$
1.0(−18)	10.00	25.36	1.00(−1)	⋯	9.00(−1)	⋯	⋯	⋯	⋯
8.0(−10)	10.00	25.36	1.04(−1)	3.68(−3)	8.93(−1)	^{12}C	8.40(−6)	^{15}N	1.22(−6)
3.25(−7)	10.00	25.36	5.03(−1)	4.03(−1)	9.38(−1)	^{2}H	9.13(−5)	^{3}H	5.66(−7)
0.0157	8.00	11.83	2.73(−1)	1.76(−1)	5.51(−1)	^{2}H	2.67(−5)	^{3}H	3.05(−7)
0.0381	6.07	4.80	9.85(−2)	2.09(−3)	8.99(−1)	^{50}Ti	7.44(−5)	^{54}Cr	5.85(−5)
0.0447	5.69	3.86	9.58(−2)	4.23(−4)	8.96(−1)	^{54}Cr	1.27(−3)	^{60}Fe	7.80(−4)
0.0566	5.14	2.66	9.20(−2)	4.14(−5)	8.82(−1)	^{66}Ni	4.79(−3)	^{86}Kr	4.21(−3)
0.0613	4.95	2.30	9.04(−2)	1.51(−5)	8.75(−1)	^{86}Kr	1.02(−2)	^{84}Se	6.79(−3)
0.0667	4.72	1.96	8.94(−2)	2.53(−6)	8.72(−1)	^{84}Se	1.50(−2)	^{85}Br	7.11(−3)
0.0764	4.34	1.59	8.81(−2)	1.11(−7)	8.68(−1)	^{84}Se	1.80(−2)	^{88}Kr	5.60(−3)
0.0925	4.00	1.21	8.62(−2)	8.90(−9)	8.62(−1)	^{94}Sr	1.02(−2)	^{84}Se	7.95(−3)
0.1071	3.70	1.01	8.44(−2)	2.23(−9)	8.58(−1)	^{94}Sr	1.13(−2)	^{90}Kr	9.99(−3)
0.1257	3.44	0.84	8.25(−2)	⋯	8.54(−1)	^{96}Sr	1.00(−2)	^{100}Sr	6.22(−3)
0.1412	3.25	0.70	8.08(−2)	⋯	8.52(−1)	^{100}Sr	1.81(−2)	^{92}Kr	1.00(−2)
0.1747	3.05	0.54	7.91(−2)	⋯	8.50(−1)	^{102}Sr	1.07(−2)	^{100}Sr	1.02(−2)
0.2421	2.72	0.55	7.49(−2)	⋯	8.45(−1)	^{105}Y	9.53(−3)	^{96}Kr	9.32(−3)
0.2923	2.56	0.48	7.21(−2)	⋯	8.41(−1)	^{107}Y	8.84(−3)	^{104}Sr	8.78(−3)
0.3585	2.43	0.44	6.82(−2)	⋯	8.37(−1)	^{124}Mo	1.07(−2)	^{107}Y	7.20(−3)
0.8317	2.12	0.19	5.35(−2)	⋯	8.27(−1)	^{124}Mo	7.89(−2)	^{72}Ni	7.68(−3)
2.1798	2.00	0.16	4.63(−2)	⋯	8.19(−1)	^{124}Mo	9.36(−2)	^{72}Ni	1.18(−2)
3.4243	1.95	0.40	3.82(−2)	⋯	8.05(−1)	^{124}Mo	9.92(−2)	^{60}Cr	1.69(−2)

Further evolution, had the network been adequate to contain it, would definitely have seen the production of the r-process nuclei. The conditions, $\rho N_A X_n \sim 10^{27}$ cm^{-3} at 2×10^9 K are precisely those determined by Kratz et al. (1988) as appropriate for the r-process. The time scale, a second or two, is also what they determine from an analysis of waiting points. However, the actual time scale may be a little shorter because (α, n) reactions now carry the flow beyond the $N = 50$ closed shell, one of the principal waiting points, and at two billion degrees, the beta-decay rates may be quicker than Kratz et al. estimated. Finally the amount of mass ejected is appropriate. The mass loss rate in the wind here is about 10^{-4} $M_\odot$ s^{-1}, but 80 to 90% of that is α-particles. The duration of the event is a few seconds. Hence the production of r-process nuclei is $\sim 10^{-5}$ to perhaps as much as 10^{-4} $M_\odot$ per event. This is much smaller than some previous estimates of r-process yield in supernovae (see, e.g., Hillebrandt 1978), chiefly because the ejection is not hydrodynamic but a wind.

Given that the r-process occurs in the fashion we have described, some major alterations to traditional thinking may be in order. First *charged particles*, not neutrons may carry the flow to mass 100. The r-process does not commence with iron, but at heavier nuclei possibly in the vicinity of strontium. In any case the closed neutron shell at $N = 50$ is bypassed and the required time for the r-process to occur is shortened. Given the natural spread in Y_e, entropy, and expansion rate that will exist in the various ejected strata of one (and many) supernovae, there will be a continuum of exposure strengths. The r-process abundances will not reflect any one particular set of physical conditions but a combination. Whether good agreement with the solar abundance set can be achieved remains to be seen. We believe that the major abundance peaks reflecting closed neutron shells ($N = 82$ and 126) will persist in the final solution. The good agreement of conditions depicted in figs. 19 and 20 with those derived by Kratz et al. (1988) as appropriate for the r-process is encouraging.

Obviously the r-process in this model will be primary, consistent with recent analysis of metal-deficient stars (see review by Cowan et al. 1991). Although one can think of physical reasons for variations (efficiency of the reverse shock, importance of ram pressure during the explosion), until demonstrated otherwise there is no reason to presume that different masses of supernovae will give different masses of r-process nucleosynthesis. In order to get a dip in Eu/Fe vs. Fe/H at very early times, Mathews and Cowan (1990) conclude that the data can be best fit in a model where the r-process is preferentially made in lower mass supernovae – $\sim 10\ M_\odot$. We feel that the data could also be consistent with a model in which every Type II and Ib super-

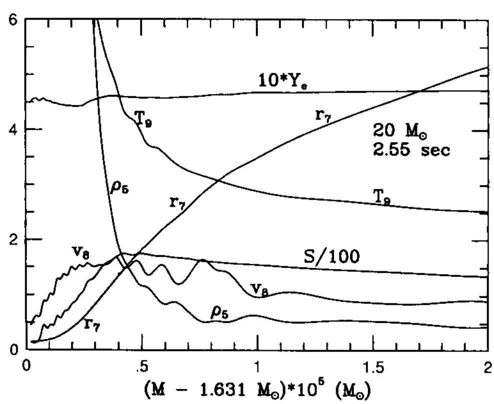

Fig. 20. Conditions at late times in the wind being driven from the surface of the protoneutron star in a delayed supernova explosion of a 20 $M_\odot$ star (adapted from Mayle and Wilson 1991).

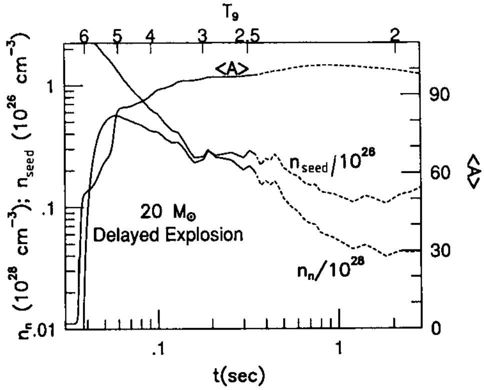

Fig. 21. Evolution of the mean atomic mass number, neutron mass fraction, temperature, and density with time for material in the wind depicted in the previous figure (from Woosley and Hoffman 1991). Once the average mass number approaches 100 the network becomes inadequate to contain the nuclear flows. Thus lines are dashed for times later than 0.3 s.

nova made about the same amount of r-process, but the more massive stars made more iron (a 25 $M_\odot$ supernova might make 0.2 $M_\odot$ of ^{56}Fe (Weaver and Woosley 1980) whereas a 10 $M_\odot$ supernova makes less than 0.01 $M_\odot$ (Mayle and Wilson, 1988a). The more massive stars would explode first and temporarily make a reduced amount of r-process elements, like europium, compared to iron. Mathews (private communication) has studied models of this sort and finds them compatible with observations for certain choices of model parameters.

Since the r-process and α-process occur in the deepest layers to be ejected, they will be subject to an intense irradiation of neutrinos from the cooling neutron star. The effect of the neutrinos on the final composition is likely to be important. During the first second or two, conditions for the r-process are generated – the high-entropy bubble. As the r-process assembles and moves outwards from the neutron star, however, a substantial flux of neutrinos continues. At a distance of $\sim$ 1000 km where the ejecta might stay for 0.1 s, the neutrino flux will be $\sim 10^{40}$ cm^{-2} s^{-1}. The cross section for the evaporation by neutral current scattering will be $\sim 10^{-40}$ cm^2 (Woosley et al. 1990a,b). Thus roughly 10% of the nuclei will lose a neutron at late times (at early times the (ν, ν' n) reaction only contributes negligibly to the (γ, n) reaction). The effect of this will be to smooth out some of the pairing effects in the r-process. In the past, β-delayed neutron ejection has been assigned this role. It may be that the neutrino-induced reaction is more important. Calculations that include all this in a realistic dynamical model are obviously needed.

Acknowledgement

We are grateful to many people who have helped with the calculations and models reported here. Some provided critical unpublished results. We would like particularly to thank Ron Mayle and Ed Baron for their help in developing our understanding, such as it is, of the delayed explosion mechanism. Ron Mayle also provided invaluable computer edits of a recent 20 $M_\odot$ model. Rob Hoffman performed most of the parameterized calculations reported in section 4. Frank Timmes aided with calculations of the flame speed used in section 3.2. The organizers of the meeting are also due some gratitude, both for an excellent school, and for allowing us an unusually large space in these proceedings to express our views.

This work has been supported by the National Science Foundation (AST 88-13649), by the NASA Theory Program (NAGW 1273), and by the Department of Energy (W-7405-ENG-48).

References

Anders, E., and Grevesse, N., 1989, Geochim. Cosmochim. Acta. **53**, 197.

Arnett, W.D., 1978, in: Physics and Astrophysics of Neutron Stars and Black Holes, Proc. of Enrico Fermi Course LXV, Varenna, July, 1975, eds. R. Giaconni and R. Ruffini, (North-Holland, Amsterdam), 356.

Arnett, W.D., D. Branch, and J.C. Wheeler, 1985, Nature **314**, 337.

Arnett, W.D., J.N. Bahcall, R.P. Kirshner, and S.E. Woosley, 1989, Ann. Rev. Astron. and Ap. **27**, 629.

Axelrod, T.A., 1980, Ph.D. thesis, (Univ. Calif., Santa Cruz, also UCRL-52994, Lawrence Livermore National Lab).

Baade, W., and F. Zwicky, 1934, Proc. U. S. National Acad. Sci. **20**, 254.

Barkat, Z., and A. Marom, 1990, in: Supernovae, Jerusalem Winter School for Theoretical Physics, Vol. 6, eds. J.C. Wheeler, T. Piran, and S. Weinberg (World Scientific, Singapore), 95.

Baron, E., and J. Cooperstein, 1990, Ap. J. **353**, 597.

Bethe, H.A., 1990, Rev. Mod. Phys., **62**, 801.

Bethe, H.A., 1993, Ap. J. **412**, 192.

Bethe, H.A., and J.R. Wilson, 1985, Ap. J. **295**, 14.

Bodansky, D., D.D. Clayton, and W.A. Fowler, 1968, Ap. J. Suppl. **16**, 299.

Branch, D., J.B. Dogget, K. Nomoto, and F.-K. Thielemann, 1985, Ap. J. **294**, 619.

Burrows, A.S., 1990, in: Supernovae, ed. A. Petschek, (Springer Verlag, Berlin) p. 159.

Burrows, A., and J.M. Lattimer, 1986, Ap. J. **307**, 178.

Cameron, A.G.W., 1982, in: Essays in Nuclear Astrophysics, eds. C.A. Barnes, D.D. Clayton, and D.N. Schramm, (Cambridge Univ. Press, Cambridge) p. 23.

Canal, R., Isern, and J. Labay, 1990, Ann. Rev. Astron. and Ap. **28**, 183.

Caughlan, G.R., and W.A. Fowler, 1988, Atomic Data and Nuclear Data Tables **40**, 238.

Caughlan, G.R., W.A. Fowler, M. Harris, and B.J. Zimmerman, 1985, Atomic and Nuclear Data Tables **32**, 197.

Chandrasekhar, S., 1938, in: Stellar Structure (Dover, New York) p. 392.
Chevalier, R.A., 1984, Ann. N. Y. Acad. Sci. **422**, 215.
Chevalier, R.A., 1989, Ap. J. **346**, 847.
Chiosi, C., and A. Maeder, 1986, Ann. Rev. Astron. and Ap. **24**, 329.
Clayton, D.D., 1968, Principles of Stellar Evolution and Nucleosynthesis (McGraw-Hill, New York).
Colgate, S.A., 1991, in: Supernovae, Proc. of the Tenth Santa Cruz Summer Workshop, ed. S.E. Woosley (Springer Verlag, New York) 352.
Colgate, S.A., and R.H. White, 1966, Ap. J. **143**, 626.
Cooperstein, J.H., H.A. Bethe, and G.E. Brown, 1984, Nuc. Phys. A **429**, 527.
Cooperstein, J., and E. Baron, 1990, in: Supernovae, ed. A.G. Petschek, (Springer Verlag, New York) p. 213.
Cooperstein, J., L.J. van den Horn, and E. Baron, 1986, Ap. J. **309**, 653.
Cooperstein, J., L.J. van den Horn, and E. Baron, 1987, Ap. J. Lettr. **321**, L129.
Cowan, J.J., F.-K. Thielemann, and J.W. Truran, 1991, Physics Reports, **208**, 267.
Dogget, J.B., and D. Branch, 1985, Astron. J. **90**, 2303.
Domogatskii, G.V., and S.V. Imshennik, 1982, Sov. Astr. Letters **8** (3), 190.
Domogatskii, G.V., and D.K. Nadyozhin, 1977, M.N.R.A.S. **178**, 33P.
Domogatskii, G.V., and D.K. Nadyozhin, 1978, Sov. Astr. **22** (3), 297.
Domogatskii, G.V., and D.K. Nadyozhin, 1980a, Sov. Astr. Letters **6** (2), 127.
Domogatskii, G.V., and D.K. Nadyozhin, 1980b, Ap. Space Sci. **70**, 33.
Domogatskii, G.V., R.A. Eramzhyan, and D.K. Nadyozhin, 1977, in: Neutrino 77, Proc. of the Int. Conf. on Neutrino Physics and Neutrino Astrophysics, Baksan Valley, 18–24 June, 1977, p. 115.
Domogatskii, G.V., R.A. Eramzhyan, and D.K. Nadyozhin, 1978, Ap. Space Sci. **58**, 273.
Ensman, L.M., and S.E. Woosley, 1988, Ap. J. **333**, 754.
Evans, R., S. van den Bergh, and R.D. McClure, 1989, Ap. J. **345**, 752.
Garcia, D., J. Labay, R. Canal, and J. Isern, 1990, in: Proc. of the Int. Symp. on Nuclear Astrophysics, Baden, Austria, eds. H. Oberhummer and W. Hillebrandt, in press.
Goodman, J., A. Dar, and S. Nussinov, 1987, Ap. J. Lettr. **314**, L7.
Harris, M.J., G.H. Share, M.D. Leising, R.L. Kinzer and D.C. Messina, 1990, Ap. J. **362**, 135.
Hartmann, D.H., S.E. Woosley and M. El Eid, 1985, Ap. J. **297**, 837.
Hashimoto, M., K. Nomoto and T. Shigeyama, 1989, Astron. Ap. **210**, L5.
Hillebrandt, W., 1978, Space Sci. Rev. **21**, 639.
Hoyle, F. and W.A. Fowler, 1960, Ap. J. **132**, 565.
Iben, I., 1978a, Ap. J. **219**, 213.
Iben, I., 1978b, Ap. J. **226**, 996.
Iben, I., 1982, Ap. J. **253**, 248.
Iliadis, C., T. Schange, C. Rolfs, U. Schröder, E. Somorjai, H.P. Trautvetter, K. Wolke, P.M. Endt, S.W. Kikstra, A.E. Champagne, M. Arnould, and G. Paulus, 1990, Nucl. Phys. A. **512**, 509.
Isern, J., R. Canal, and J. Labay, 1990, preprint submitted to Ap. J.
Khoklov, A.M., 1990a, Max Planc Inst. für Astophysik preprint 513, Astron. and Ap., in press.
Khoklov, A.M., 1990b, Max Planck Inst. für Astophysik preprint 528, Astron. and Ap., in press.
Kratz, K.-L., F.-K. Thielemann, W. Hillebrandt, P. Möller, V.Harms, A. Wöhr, and J.W. Truran, 1988, in: Sixth Int. Symp. on Capture Gamma-Ray Spectroscopy, J. Phys. G. **24**, S331.
Langer, N., 1989, Astron. and Ap. **220**, 135.
Lattimer, J.M., A. Burrows and A. Yahil, 1985, Ap. J. **288**, 644.

Litvinova, I.Yu., and D.K. Nadyozhin, 1983, Ap. and Spac. Sci. **89**, 89.
Livne, E., 1990a, Racah Inst. of Physics preprint 8, (Hebrew Univ., Jerusalem), Ap. J., in press.
Livne, E., and A.S. Glasner, 1990b, Racah Inst. of Physics preprint 9, (Hebrew Univ., Jerusalem), submitted to Ap. J.
Lopez, R., J. Isern, R. Canal, and J. Labay, 1986a, Astron. and Ap. **155**, 1.
Lopez, R., J. Isern, J. Labay, and R. Canal, 1986b, Rev. Mex. Astron. **13**, 41.
Maeder, A., and G. Meynet, 1988, Astron. and Ap. Suppl. **76**, 411.
Maeder, A., and G. Meynet, 1989, Astron. and Ap. **210**, 155.
Mandelbrot, B., 1983, The Fractal Geometry of Nature, (Freeman, New York).
Mathews, G.J., and J.J. Cowan, 1990, Nature **345**, 491.
Mayle, R.W., 1985, Ph.D. thesis, Lawrence Livermore National Laboratory reprint, UCRL−53713.
Mayle, R.W., 1990, in: Supernovae, ed. A.G. Petsheck (Springer Verlag, New York) p. 267.
Mayle, R.W., and J.R. Wilson, 1988a, Ap. J. **334**, 909.
Mayle, R.W., and J.R. Wilson, 1988b, in: Origin and Distribution of the Elements, ed. G. Mathews (World Scientific, Singapore) p. 433.
Mayle, R.W., and J.R. Wilson, 1991, in: Supernovae, Proc. of the Tenth Santa Cruz Summer Workshop, ed. S.E. Woosley (Springer Verlag, New York) p. 333.
Nadyozhin, D.K., and I.V. Otroschenko, 1980, Soviet Astron. **24** (1), 47.
Nomoto, K., 1984, Ap. J. **277**, 791.
Nomoto, K., and M. Hashimoto 1986, Progress in nuclear and particle physics **17**, 267.
Nomoto, K., and Y. Kondo, 1990, preprint submitted to Ap. J.
Nomoto, K., D. Sugimoto and S. Neo, 1976, Ap. and Spac. Sci. **39**, L37.
Petschek, A.G., ed., 1990, Supernovae (Springer Verlag, Berlin).
Pinto, P.A., 1988, Ph.D. thesis, (Univ. Calif., Santa Cruz).
Pinto, P.A., and S.E. Woosley, 1991, in preparation.
Rocca-Volmerange, B., and R. Schaeffer, 1990, Astron. and Ap. **233**, 427.
Shapiro, S.L., and S.A. Teukolsky, 1983, in: Black Holes, White Dwarfs, and Neutron Stars (John Wiley, New York) p. 156.
Shigeyama, T., K. Nomoto, T. Tsujimoto and M. Hashimoto, 1990, Ap. J. Lettr. **361**, L23.
Signore, M., and C. Dupraz, 1990, Astron. and Ap. **234**, L15.
Spruit, H., 1990, Max Planck Inst. Munich, preprint MPA 541, submitted to Astron. and Ap.
Sunyaev, R.A., A.S. Kaniovsky, V.V. Efremov, S.A. Grebenev, A.V. Kuznetsov, J. Englhauser, S.W. Doebereiner, C. Pietsch, J. Reppin, E. Trümper, E. Kendziorra, M. Maisack, B. Mony and R. Staubert, 1991, in: Supernovae, Proc. of the Tenth Santa Cruz Summer Workshop, ed. S.E. Woosley (Springer Verlag, New York) p. 767, see also Soviet Astron. Lettr. **16** (5) 403.
Swartz, D., R. Harkness, and J.C. Wheeler, 1990, preprint submitted to Ap. J.
Tammann, G., 1982, in: Supernovae: A Survey of Current Research, eds. M.J. Rees and R.J. Stoneham, (D. Reidel, Dordrecht) p. 371.
Thielemann, F.-K., K. Nomoto, and K. Yokoi, 1986, Astron. and Ap. **158**, 17.
Tubbs, D.L., and D.N. Schramm, 1975, Ap. J. **201**, 467.
Uomoto, A., 1986, Ap. J. Lettr. **310**, L35.
Van den Bergh, S., and G.A. Tammann, 1990, preprint in prep. for Ann. Rev. of Astron. and Ap.
Van den Bergh, S., R.D. McClure and R. Evans, 1987, Ap. J. **323**, 44.
Varani, G.-F., W.P.S. Meikle, J. Spyromilio, and D.A. Allen, 1990, MNRAS, in press.
Weaver, T.A. and S.E. Woosley, 1980, Ninth Texas Symp. on Rel. Ap., in: Ann. N.Y. Acad. Sci. **336**, 335.
Weaver, T.A. and S.E. Woosley, 1991, in prep. for Ap. J.

Weaver, T.A., Z.B. Zimmerman, and S.E. Woosley, 1978, Ap. J. **225**, 1021.

Weaver, T.A., T.S. Axelrod and S.E. Woosley, 1980, in: Type I Supernovae, ed. J.C. Wheeler (Univ. of Texas Press, Austin) p. 113.

Wheeler, J.C., C. Sneeden and J.W. Truran, 1989, Ann. Rev. of Astron. and Ap. **27**, 278.

Wilson, J.R., 1985, in: Numerical Astrophysics, ed. J.M. Centrella, J.M. LeBlanc, and R.L. Bowers (Jones and Bartlett, Boston) p. 422.

Wilson, J.R., R. Mayle, S.E. Woosley and T.A. Weaver, 1986, Ann. N.Y. Acad. Sci. **470**, 267.

Woosley, S.E., 1986, Saas-fee lecture notes, in Nucleosynthesis and Chemical Evolution, 16th Advanced Course of the Swiss Soc. of Astron. and Ap., ed. B. Hauck, A. Maeder, and G. Meynet (Geneva Observatory, Geneva), 1.

Woosley, S.E., 1988, Ap. J. **330**, 218.

Woosley, S.E., 1990a, in: Astrophysics from the Moon, eds. M.J. Mumma and H.J. Smith, AIP Conf. Proc. No. 207, 188.

Woosley, S.E., 1990b, in: Supernovae, ed. A. Petschek (Springer Verlag, Berlin) p. 182.

Woosley, S.E., and R.D. Hoffman, 1991, in preparation for Ap. J.

Woosley, S.E., and P.A. Pinto, 1988, in: Nuclear Spectroscopy of Astrophysical Sources, AIP Conf. Proc. 170, eds. N. Gehrels and G. Share (AIP, New York) p. 98.

Woosley, S.E., and T.A. Weaver, 1982a, in: Supernovae: A Survey of Current Research, eds. M.J. Rees and R.J. Stoneham (D. Reidel, Dordrecht) p. 79.

Woosley, S.E., and T.A. Weaver, 1982b, in: Essays in Nuclear Astrophysics, ed. C.A. Barnes, D.D. Clayton, and D.N. Schramm (Cambridge Univ. Press, Cambridge) p. 377.

Woosley, S.E., and T.A. Weaver, 1986, Ann. Rev. Astron. and Ap. **24**, 205.

Woosley, S.E., and T.A. Weaver, 1988, Physics Reports **163**, 79.

Woosley, S.E., and T.A. Weaver, 1991, in preparation.

Woosley, S.E., W.D. Arnett, and D.D. Clayton, 1973, Ap. J. Suppl. **26**, 231.

Woosley, S.E., P.A. Pinto and L.M. Ensman, 1988a, Ap. J. **324**, 466.

Woosley, S.E., P.A. Pinto and T.A. Weaver, 1988b, Proc. Astron. Soc. of Australia **7** (4), 355.

Woosley, S.E., D. Hartmann, W. Haxton, and R. Hoffman, 1990a, Ap. J. **356**, 272.

Woosley, S.E., W. Haxton, and T.A. Weaver, 1990b, Bull. Am. Astron. Soc. **21**, (4), 1095 (and in preparation).

Woosley, S.E., N. Langer, and T.A. Weaver, 1991, in preparation for Ap. J.

Zel'dovich, Ya. B., and Yu. P. Raizer, 1966, in: Physics of Shock Waves and High Temperature Hydrodynamic Phenomena (Academic Press, New York) p. 93.

COURSE IV

TYPE IA SUPERNOVAE
WHITE DWARFS AND NEUTRON STARS

R. CANAL

Departament d'Astronomia i Meteorologia
Universitat de Barcelona, 08028 Barcelona, Spain

S. Bludman, R. Mochkovitch and J. Zinn-Justin, eds.
Les Houches, Session LIV, 1990
Supernovae

Contents

1. Introduction 158
2. The progenitors of Type Ia supernovae 159
   2.1. Observational constraints 159
   2.2. SN Ia rates and progenitor population 160
   2.3. Progenitor evolution: mass-accreting C+O white dwarfs 161
      2.3.1. H-accreting white dwarfs 163
      2.3.2. He-accreting white dwarfs 166
      2.3.3. C+O-accreting white dwarfs 166
   2.4. Galactic evolution of SN Ia progenitors 168
3. White dwarf physics and Type Ia supernovae 169
   3.1. The cooling of white dwarfs 169
   3.2. The physics of phase transition in white dwarf interiors 170
   3.3. Nuclear reaction rates 173
   3.4. Mass accretion and core heating 175
   3.5. Core ignition and burning propagation 178
   3.6. Electron captures and mixing 181
4. Neutron stars in binary systems 185
   4.1. X-ray binaries 185
      4.1.1. High-mass x-ray binaries 185
      4.1.2. Low-mass x-ray binaries 186
   4.2. Binary and millisecond pulsars 186
   4.3. Formation mechanisms 187
      4.3.1. Core collapse of massive stars 187
      4.3.2. Capture mechanisms 187
      4.3.3. Accretion-induced collapse of white dwarfs 189
   4.4. The origin of neutron stars in binaries 189
      4.4.1. High-mass x-ray binaries 189
      4.4.2. Low-mass x-ray binaries 190
      4.4.3. Binary and millisecond pulsars 192
5. Summary 194

References 195

1. Introduction

In these three lectures we mainly deal with two problems: *Type Ia supernovae* and the possible *formation of neutron stars by gravitational collapse of white dwarfs*. Both kinds of events are currently thought to take place in close binary systems where a white dwarf has previously formed, and, after a period of essentially undisturbed cooling, the neutron stars are grown in mass by accreting matter from its companion. Thus, white dwarf physics and close binary evolution are at the core of the two problems. We focus upon the former, since white dwarf physics sets the basis on which different scenarios for the two processes can be developed. As we see in chap. 2, no scenario for bringing a white dwarf to an explosive condition that fulfills all the constraints derived from observations of SN Ia has yet been devised. The same is true for the (more hypothetical) accretion-induced collapse (AIC) of white dwarfs.

SN Ia outbursts and AIC into a neutron star appear as opposite outcomes of the growth of the a white dwarf up to the Chandrasekhar limit (or very close to it). What determines whether the white dwarf collapses or explodes? One possible answer might be chemical composition: C+O white dwarfs explode, whereas O+Ne+Mg white dwarfs collapse. We see however, in sec. 3.6 that for the last composition explosive burning starts at densities too low for collapse to begin. Thus, the answer should instead be sought in the detailed evolution of the white dwarf: its initial mass, cooling, and mass-accretion history.

One salient feature of SN Ia outbursts is their overall homogeneity. This is in accordance with their being produced by the explosions of white dwarfs with very similar masses. They seem nonetheless to show some range of variation in their light curves and expansion velocities, and that might well reflect differences in the physical state of the interiors when explosion is initiated. Precise knowledge of the physics of white dwarf cores at the start of explosive burning is also required to solve problems posed by the dynamics of burning and the associated nucleosynthesis (see lectures by Barkat, Müller, Nomoto, and Woosley, in this volume, and sec. 3.5 below). The effects of previous cooling (as modified by the heating due to mass accretion) determine the physical state of the core (whether it is fluid or solid, and possibly its chemical composition profile as well), and this in turn determines the rates of nuclear fusion reactions, and the mode and speed of burning propagation. Little can be said as to the particular history of the progenitor of any given SN Ia, but we do know that those of the SN Ia observed in elliptical galaxies must have been cooling for several Gyr and thus that their cores should have experienced a phase transition from *fluid* to *solid* state. Accordingly, such initially cold, partially solid white dwarfs should be regarded as prototypes for the objects giving rise to SN Ia outburts. The same objects appear to be the most promising candidates for AIC. Thus we devote most of chap. 3 to the study of the physics associated with cooling and reheating of white dwarf cores.

The presence of neutron stars in close binary systems (and also the possible origin of some isolated neutron stars in such systems) can give extra insights regarding the evolution leading both to SN Ia explosions and to AIC. We discuss in chap. 4 the problem of the origin of neutron stars in binaries, with the primary aim of showing whether the AIC mechanism is ever required to account for neutron star formation. The answer is rather in the affirmative, but the question can not yet be regarded as settled.

2. The progenitors of Type Ia supernovae

2.1. Observational constraints

The progenitors of Type Ia (or "classical Type I") supernovae must satisfy a number of constraints:

(1) Their surfaces must be devoid of H at the time of explosion. The upper limit to the H content is about one percent by mass (see Branch, this volume).

(2) They must be long-lived (ages up to several Gyr), to account for the occurrence of SN Ia in elliptical galaxies, and also to account for the lack of association of the events with HII regions in spiral galaxies (Maza and van den Bergh 1976).

(3) Their explosion has to produce a Ni mass $M_{\rm Ni} \geq 0.5 M_{\odot}$, to account for both the light curves (Arnett 1982; Arnett, Branch, and Wheeler 1985) and late-time spectra (Woosley, Axelrod, and Weaver 1984).

(4) As deduced from the spectra at maximum light, intermediate-mass elements (O, Mg, Si, S, Ca) must be present in their outer layers, (Branch et al. 1982; Wheeler and Harkness 1990).
(5) The explosions must produce events that are very homogeneous in their peak magnitudes ($\sigma \leq 0.4$ mag: Miller and Branch 1990, and Branch, this volume) whereas the light curve shapes and the photospheric expansion velocities may show some range of variability (Phillips et al. 1987; Branch 1987).
(6) The death rates of the progenitors must agree with the observational estimates of the frequency of SN Ia events (see Tammann, this volume, and the discussion below).
(7) Abundance ratios of Fe and Ni isotopes (of which SN Ia appear to be the main producers) must agree with solar system values (see Woosley, this volume).

2.2. *SN Ia rates and progenitor population*

The rate of occurrence of SN Ia events in our galaxy should give some insight as to the nature of their progenitors. This rate is mostly inferred from the observation of external galaxies of various morphological types. The extragalactic rates are usually normalized to B-luminosity (which involves dependence on h^2, h being the value of the Hubble constant H_0 in units of 100 km s^{-1} Mpc^{-1}) on basis of a small sample of face-on Sc spirals. After that, the galactic rate is obtained by interpolation to the assumed type of our galaxy (with an extra uncertainty as to its B-luminosity). There has been discussion as to whether far-infrared (FIR) luminosity could be more directly related to star formation rate (SFR) than B-luminosity, but on the other hand, it is unclear that SN Ia frequency should reflect at all current SFR (Wheeler 1990). As for the data from historical galactic supernovae, they are ambiguous at best. Out of about 7 events, 2 or 3 might have been SN Ia: SN 1006, SN 1572 (Tycho), and SN 1604 (Kepler). But this is disputable for every one of them: SN 1006 might have been a SN II-L (Wheeler and Harkness 1990), while Tycho and Kepler arguably might not be SN Ia (Strom 1988; Bandiera 1987). Thus, the locally determined local SN Ia rate may be consistent with zero!

Let us now outline the problem of converting local rates, surface, and volume densities of potential progenitors into global SN Ia rates and vice versa (see Wheeler 1990). We must first adopt an "effective area" $A_{\rm eff}$ for the galaxy, as required to convert global rates into rates per unit area. $A_{\rm eff}$ is the area that the galaxy would have if the total number of stars in the disk were spread out uniformly at the surface density of the solar neighbourhood (note that this already involves an assumption as to the radial distribution of SN Ia events). The standard exponential model of the galactic disk gives $A_{\rm eff} \sim 10^9$ pc^2 (Ratnatunga and van den Bergh 1989 obtain $A_{\rm eff} \simeq 850$ kpc^2). The effects of the radial distribution could show up as an inclination effect in the frequency of detected events: Tammann (1982) finds it and concludes that SN Ia progenitors do not belong to the extreme halo population; whereas van den Bergh, McClure, and Evans (1987), and Maza and van den Bergh (1976) do not find such an effect. A compromise has thus been reached that the progenitors are part of the *old disk population.* To further illustrate the problem, let us assume that SN Ia progenitors were *novae.* We know that in M31 novae are *bulge* rather than *disk* populations (Ciardullo et al. 1987). This is indicated by the fact that within $30'$ of the galactic center, where the bulge contributes with 60% of the light, more than 96% of the novae are found. In that case, the assumption of a thin exponential disk would overestimate the *local* space density of SN Ia events for a given *global* rate. Thus, while working with local *surface density* rates avoids the problem of choosing a *scale height* for SN Ia, the local rate will be overestimated if the population resembles a *bulge* population. According to the latest estimates (van den Bergh and Tammann 1991; see also Tammann, this volume), we have:

$$r_{\rm SN\ Ia} \simeq 2 \times 10^{-12} A_{\rm eff,9}^{-1}\ \rm pc^{-2}\ yr^{-1} \tag{2.2.1}$$

This rate is compared in the following to the death rates of possible progenitors.

2.3. Progenitor evolution: mass-accreting C+O white dwarfs

Mainly from observational constraints (1) and (2), it is generally thought that SN Ia events are due to the explosion of *white dwarfs* (WDs). An early scenario (Finzi and Wolf 1967) involved *single* WDs. Two possible kinds of WDs were suggested: either WDs of masses $M \simeq 1.40 M_\odot$ with contents of $\sim 10\%$ ^{24}Mg, or WDs of masses $M \simeq 1.20 M_\odot$ consisting of ^{56}Fe cores and intermediate shells with small concentrations of ^{40}Ca. Such WDs should live for $\sim 10^{10}$ yr before becoming SN Ia to comply with constraint (2), and this would correspond to the half-lives of ^{24}Mg and ^{40}Ca against 3rd and 4th forbidden inverse β transitions (electron captures). Such captures would progressively lower the Chandrasekar mass (proportional to Y_e^2, Y_e being the mass-averaged electron mole number). On its mass becoming lower than the actual mass of the WD, the object should start collapsing due to gravitation, but the initial stages of compression and heating would already induce explosive ignition at the center in the first case, and in the intermediate shells in the second case. WDs of the first kind would previously have undergone carbon burning as red-giant cores, while those of the second kind would come from stars that had experienced large mass loss after the start of silicon burning. Both types of evolution seem now very unlikely. Current scenarios are no longer based on single WDs but on *mass-accreting* WDs in *close binary systems* (CBSs).

The mass-accreting WD scenario looks very promising at first. There are large numbers of WDs: their birthrate is estimated to be $\sim 1\ \mathrm{yr}^{-1}$ in the whole galaxy. More than 50% of all stars are in binary systems, and in about half of these systems, the separation between components is of the same order of magnitude as their radii (they are CBSs). It must be noted, however, that most of these are low-mass systems ($M_1+M_2 \simeq 0.8$ to $1.5M_{\odot}$) where mass transfer cannot make either of the two components grow up to the Chandrasekhar mass after becoming a WD.

According to current ideas, three different chemical compositions are possible for WDs in CBSs: He, C+O, and O+Ne+Mg. Since the most successful models up to now (mainly due to observational constraint 4) are based on explosive thermonuclear ignition of C+O WDs, we first consider CBSs containing WDs with this composition (although, as we have already mentioned in the introduction, no satisfactory evolutionary path to bring a C+O WD to explosive carbon ignition has yet been found!).

C+O WDs can be members both of *initially close binaries* or of *initially wide binaries*. In the first case, the WD can form by Roche lobe overflow either just before or just after central helium ignition. In the second case, a WD can form by Roche lobe overflow also, but either in the *asymptotic giant branch* (AGB) phase or in the *thermally pulsing* AGB phase (see fig. 5 in Iben 1974). Roche lobe overflow in initially wide binaries should lead to formation of a *common envelope* engulfing the two components of the system. Friction with the envelope would induce its ejection, and also loss of angular momentum by the system. The latter would change the wide binary into a close binary.

An important question is that of the typical mass range and the upper mass limit for C+O WDs formed in any of the preceding scenarios. Well known CBSs containing white dwarfs are *novae* and *cataclysmic variables* (CVs). Mean masses of CVs are: $\langle M_{\mathrm{CV}}\rangle \simeq 0.79M_{\odot}$. Those of classical novae: $\langle M_{\mathrm{nova}}\rangle \simeq 1.23M_{\odot}$ (Ritter 1989, private communication). A recent model for the recurrent nova U Sco gives $M \simeq 1.38M_{\odot}$ (Starrfield, Sparks, and Shaviv 1989). In this last case, however, the WD might have a O+Ne+Mg composition instead of a C+O one.

Once a C+O WD with a given mass is formed in a CBS, it must accrete material from its companion to grow close to the Chandrasekhar mass and explosively ignite carbon at its center. Depending on the nature of its companion, this material can be either *hydrogen-rich*, *helium-rich*, or even a *carbon-oxygen mixture*. There are problems with all three possibilities; we will examine them in turn.

2.3.1. H-accreting white dwarfs

(i) Theoretical constraints on $\dot{M}_H$. There are, in fact, objections to any rate from zero to infinity! A very general argument has been given by Paczyński (1985). It starts from the known mean mass of single WDs:

$$\langle M_{\rm WD}\rangle \simeq 0.7 M_{\odot} \qquad (2.3.1.1)$$

From this it follows that, to bring a star to the Chandrasekhar mass, $\simeq 0.7 M_{\odot}$ of H must first be accreted and burnt per SN Ia event, which means a release of $\sim 10^{52}$ erg per event. For a rate (in the whole galaxy):

$$r^{*}_{\rm SN\ Ia} \simeq 2 \times 10^{-3}\ {\rm yr}^{-1}, \qquad (2.3.1.2)$$

a global luminosity

$$L \simeq 6 \times 10^{41}\ {\rm erg\ s}^{-1} \qquad (2.3.1.3)$$

is obtained. Then, since

$$L^{*} \leq L_{\rm Edd} \sim 2 \times 10^{38}\ {\rm erg\ s}^{-1}, \qquad (2.3.1.4)$$

(where $L_{\rm Edd}$ is the Eddington luminosity), the total number of active progenitors at any time (in steady state) should be:

$$N^{*} \geq 3000. \qquad (2.3.1.5)$$

Thus, with an effective area of the galactic disk:

$$A_{\rm eff} = 10^{9}\ {\rm pc}^{2} = 10^{3}{\rm kpc}^{2} \qquad (2.3.1.6)$$

there should be $n \geq 9$ such objects emitting at $L \leq L_{\rm Edd}$ within 1 kpc from the Sun. Their effective temperatures being $T_{\rm eff} \sim 10^{6} K$, they should appear as strong EUV sources. No obvious candidates are seen. It is nonetheless possible that they are "hidden" in some way (as symbiotic stars or emission-line variables). In the case they were long-period variables, selection effects would work against their detection. Another way to explain observed data could be to have more numerous and less conspicuous progenitors, accreting mass at rates well below the Eddington limit. There are other difficulties associated with this.

Starting from the lowest accretion rates, we have that accretion at $\dot{M}_{\rm H} \leq 10^{-9} M_{\odot}\ {\rm yr}^{-1}$ is mostly thought to induce nova explosions (Fujimoto and Taam 1982). This would, in general, *reduce* rather than *increase* the mass of the WD. At best, it should make *effective accretion* marginal: $\dot{M}_{\rm eff} \leq 0.1 \dot{M}_{\rm H}$ (Truran 1989, private communication). A case that seems to contradict this hypothesis is SS Cyg. The WD in this system has a mass $M_{\rm WD} \simeq 1.2 M_{\odot}$. This might be an indication that *massive* WDs do effectively grow in mass instead of losing it.

It must be noted, however, that the calculations predicting nova explosions for those rates are based on the assumption of radially-symmetric and "soft" accretion (the last means that the material is deposited at zero velocity on the star surface and that it has the same specific entropy as the layers into which it is incorporated). In fact, *observed* typical accretion rates in novae are $\sim 10^{-8} M_{\odot}\ {\rm yr}^{-1}$ (Patterson 1984; Warner 1987). For such rates, theory predicts that H does not become degenerate enough to produce explosion, even if the accreted matter were substantially enriched in C and O by mixing with deeper layers (Starrfield, Truran, and Sparks 1978; Prialnik, Shara, and Shaviv 1978; Kutter and Sparks 1980; MacDonald 1983). Also, in theoretical models, when the "soft" accretion hypothesis is relaxed (with inclusion of angular momentum and/or with kinetic energy dissipation in the accretion process) it becomes hard to obtain nova explosions (Shaviv and Starrfield 1987; Sparks and Kutter 1987). This is due to boundary-layer heating in the first case, and to partial support from centrifugal force in the second case.

Radial, "soft" accretion at rates $10^{-9} M_{\odot} {\rm yr}^{-1} \leq \dot{M}_H \leq 10^{-6} M_{\odot} {\rm yr}^{-1}$ would burn H steadily or in weak flashes, but this again raises the problem of where the luminous progenitors are that should result from it. Besides, either steady or flashing burning of H into He at $\dot{M}_{\rm H}$ would be equivalent to "soft" accretion of He at $\dot{M}_{\rm He} = \dot{M}_{\rm H}$, and this should lead to *helium detonation* for $10^{-9} M_{\odot}\ {\rm yr}^{-1} \leq \dot{M}_{\rm H} \leq 5 \times 10^{-8} M_{\odot}\ {\rm yr}^{-1}$ (however, this holds only for $M \leq 1.13 M_{\odot}$). Inclusion of the interaction between the H and He-burning layers might nonetheless change this picture.

(ii) Cataclysmic variables and SN Ia. Keeping all those uncertainties in mind, let us now consider the possible relationship between SN Ia and *cataclysmic variables* (CVs). An argument against such a relationship comes from the fact that in M31 the *galactic bulge* is ~ 20 times more efficient than the disk in producing novae, whereas galactic disks in general seem more efficient

than bulges in producing SN Ia (Renzini 1989, private communication). But *radial selection effects* might account for the apparent deficiency of SN Ia in the bulges. Another argument concerns the birthrate of CVs in the solar neighbourhood, which would be $\sim$ 1 order of magnitude lower than the local SN Ia rate (Ritter 1989, private communication). "*Hibernation*" of novae (Shara et al. 1986) might nonetheless mean that large numbers of CVs go undetected (see also Wheeler 1990); this would lead to an underestimate of their birthrates. On this topic, Shara (1990) has recently reported the existence of large numbers of dim stars resembling CVs in their spectral properties, which might be such "hibernating" novae. Their local density would be $N \sim 10^{-4}$ pc^{-3}. Estimates of the birthrate of CVs by various authors significantly differ from each other. Bath and Shaviv (1978) adopt a local density of 2 to 7×10^{-11} pc^{-3} leading to:

$$r_{\rm CV} = 3 - 10 \times 10^{-10} (T_{\rm CN,8})^{-1}\ {\rm pc}^{-2}\ {\rm yr}^{-1}, \qquad (2.3.1.7)$$

where $T_{\rm CN}$ is the lifetime of classical novae (all CVs are here assumed to become novae). Patterson (1984), from a local density of 6×10^{-6} pc^{-3} derives instead:

$$r_{\rm CV} = 9 \times 10^{-12} (T_{\rm CN,8})^{-1}\ {\rm pc}^{-2}\ {\rm yr}^{-1}, \qquad (2.3.1.8)$$

(in both cases, surface densities are calculated assuming a scale height of $\sim$ 150 pc). Including the effects of "hibernation", Wheeler (1990) proposes:

$$r_{\rm CV} \sim \frac{9 \times 10^{-12} \eta_{\rm H}\ {\rm pc}^{-2}\ {\rm yr}^{-1}}{T_{\rm CV,8}}, \qquad (2.3.1.9)$$

$\eta_{\rm H}$ being the "hibernation factor" ($\eta_{\rm H} \geq 1$). If all CVs become novae, $T_{\rm CV} = T_{\rm CN} \sim 10^8$ yr. This would make CV birthrates and SN Ia rates comparable, but does not yet solve the problem, since only a fraction of CVs could evolve into a catastrophic endpoint (a minimal necessary condition is that $M_{\rm tot} > M_{\rm Ch}$).

(iii) Symbiotic stars and SN Ia. Considering now higher mass-accretion rates, we have that steady hydrogen burning should produce a luminosity:

$$L = 2.4 \times 10^{38}\ {\rm erg\ s}^{-1} (M_{\rm core}/M_\odot - 0.52), \qquad (2.3.1.10)$$

(Paczyński 1971). This would give a few bright progenitors within 1 kpc of the Sun (that are not observed). One possibility, as has been pointed out above, is that the progenitors were *symbiotic variables*. Symbiotics made of WD-red giant pairs should have a death rate of $\sim 0.002\,\mathrm{yr}^{-1}$ in the galaxy (Iben and Tutukov 1984a). According to Allen (1980), 27 such systems are known within 3.5 kpc of the Sun. This would correspond to a surface density $\sigma = 7 \times 10^{-7}$ pc^{-2}. A typical liftime would be: $t_{\mathrm{sym}} = 10^6$ yr. From that:

$$r_{\mathrm{sym}} = 7 \times 10^{-13} (t_{\mathrm{sym},6})^{-1}\ \mathrm{pc}^{-2}\ \mathrm{yr}^{-1}. \qquad (2.3.1.11)$$

There is always the question, however, of which fraction of the symbiotics is recognizable (they can be enshrouded in a thick H blanket).

Accretion of H at rates of $10^{-6} M_\odot \leq \dot{M}_{\mathrm{H}} \leq \dot{M}_{\mathrm{Edd}}$ should lead to formation of a red-giant envelope on top of a H-burning shell that, in expanding, fills the Roche lobe of the WD and inhibits further mass accretion. Nonetheless, Hachisu, Kato, and Saio (1989) present a model in which the back pressure from a filled Roche lobe allows accretion at the rate:

$$\dot{M}_{\mathrm{H}} = 7.5 \times 10^{-7} M_\odot\ \mathrm{yr}^{-1}{}_\odot \qquad (2.3.1.12)$$

The object would appear to be a B star and there should be several of them within ~ 1 kpc from the Sun. None are seen. Finally, accretion at $\dot{M}_{\mathrm{H}} \sim \dot{M}_{\mathrm{Edd}} \sim 10^{-5} M_\odot\ \mathrm{yr}^{-1}$ would directly produce a common envelope and suppress accretion.

2.3.2. He-accreting white dwarfs

(i) Theoretical constraints on $\dot{M}_{\mathrm{He}}$. We have already indicated that accretion of He by a WD at rates $10^{-9} M_\odot\ \mathrm{yr}^{-1} \leq \dot{M}_{\mathrm{He}} \leq 5 \times 10^{-8} M_\odot\ \mathrm{yr}^{-1}$. (for $M_{\mathrm{WD}} \leq 1.13 M_\odot$) would give rise to *He detonation.* But in the case of direct accretion from a companion (either a nondegenerate or a degenerate He star) this would again correspond to "soft" accretion only. However, it must be noted that while He detonation inhibits growth of the C+O WD towards the Chandrasekhar mass, it might itself provide a viable model of SN Ia outburst (see Livne and Glassner, this volume).

(ii) Possible companions. Concerning possible candidates, three or four systems made of a WD plus a nondegenerate He star are known, but the mass of the later component seems to be exceedingly low in all of them. Systems consisting of a C+O WD plus a He WD would have very short lifetimes, and this could hardly fit SN Ia statistics.

2.3.3. C+O-accreting white dwarfs

Accretion of material made of a C+O mixture by a C+O WD is possible if it has another C+O WD as its companion in a CBS. Mass transfer would happen through Roche lobe overflow due to decrease in the orbital separation resulting from gravitational wave radiation (Webbink 1984).

(i) Theoretical constraints on $\dot{M}_{C+O}$. The only constraint for this composition is that accretion at $\dot{M}_{\mathrm{C+O}} \geq 5 \times 10^{-6} M_{\odot}\ \mathrm{yr}^{-1}$ induces C ignition close to the surface which leads to quasi-hydrostatic burning of the whole WD into O+Ne+Mg (Nomoto and Iben 1985). According to these authors, the WD should later collapse into a neutron star rather than explode. We see in the next chapter that thermonuclear explosion would appear to be a more likely result.

(ii) Evolution of double degenerate systems. Out of the six possible combinations of He, C+O, and O+Ne+Mg WDs in double degenerate systems, the most probable are CO+CO and He+He. Evolutionary scenarios leading to the formation of such binaries are extensively discussed by Iben and Tutukov (1984a) (see also Webbink 1984).

(iii) Mass-transfer dynamics. Since the radius of a WD increases when its mass decreases, it is the component with lower mass that starts filling its Roche lobe; mass loss self-accelerates and should, in general, have a runaway character. Formation of a massive disk (or torus) around the mass-accreting WD is likely. The effective $\dot{M}_{\mathrm{C+O}}$ then depends on viscous dissipation in the disk, and rather fine tuning is required to avoid nonexplosive off-center carbon ignition (Mochkovitch and Livio 1989). Another possibility is the formation of a common envelope from which roughly radially-symmetric accretion of matter results. It has been speculated that very fast infall of this material might generate a shock wave that would explosively ignite carbon at the center of the WD, but numerical simulations by Benz et al. (1990) do not support this.

(iv) The population of double degenerates. Robinson and Shafter (1989) found no double degenerate systems with $P < 3^{\mathrm{h}}$ among 44 WDs, and concluded at the 90% confidence level that the space density of such systems is lower than that required to account for the SN Ia rate in the galaxy. Foss, Wade, and Green (1990) examined 26 hot WDs with $3^{\mathrm{h}} < P < 10^{h}$ and found, also at the 90% confidence level, that the fraction of double degenerates was < 0.18. If we assume that the initial period distribution is more strongly weighted towards long periods, we can derive:

$$r_{\mathrm{DD}} < 6.3 \times 10^{-12} (h/250\ \mathrm{pc})\ \mathrm{pc}^{-2}\ \mathrm{yr}^{-1}, \qquad (2.3.3.1)$$

where h is the scale height of the population. This could still be consistent with the SN Ia rate eq. (2.2.1), but only if the actual fraction were close to the upper limit and most double degenerates had enough mass to explode

(Wheeler 1990). Iben (1990), and Iben and Tutukov (1990) have recently reanalyzed their predicted rate of formation of double degenerates and conclude that an appreciable fraction of systems should be born with $P > 3^h$, and that only 1/240 to 1/280 of all systems would be in the period range searched by Robinson and Shafter (1989). The survey of Foss, Wade, and Green (1990), however, gives an upper limit that is already close to the value expected for more slowly evolving systems, with longer periods.

Bragaglia et al. (1989, 1991) have found one double degenerate in their own survey. It is most likely made of two He WDs, and it would need more than a Hubble time to merge. Taking their survey and that of Robinson and Shafter (1989) together (thus making a total of 90 WDs), they conclude at the 99% confidence level that the space density of double degenerates with $P < 3^h$ is lower than the minimum required to account for SN Ia. However, they note that non-DA (H-poor) WDs remain essentially unsurveyed (86 out of 90 were DAs), and that evolutionary arguments favour C+O WDs formed in close binaries being totally deprived of their H-rich envelopes, thus showing a non-DA spectral type.

2.4. *Galactic evolution of SN Ia progenitors*

Since SN Ia should be the primary producers of Fe through most of the history of the galaxy while other elements such as O come mainly from the explosion of massive stars (Type II and probably also Type Ib/c supernovae), the [O/Fe] versus [Fe/H] relationship can provide a clue to the nature of SN Ia progenitors. Results on O abundance in extremely metal-poor dwarfs belonging to old disk and halo populations have recently become available (Abia and Rebolo 1989). They show that the [O/Fe] ratio grows monotonically for decreasing metallicity, from [O/Fe] $\simeq 0.0$ at [Fe/H] $\simeq 0.0$ until [O/Fe] $\simeq 1.1$ at [Fe/H] $\simeq -2.0$. The results are compatible with a constant value of [O/Fe] $\simeq 1.1$ for [Fe/H] ≤ -2.0. This can be interpreted in the framework of a fairly standard galactic evolution model (Abia, Canal, and Isern 1991). Best fit to the observed [O/Fe] versus [Fe/H] relationship is obtained when adopting the double degenerate scenario for progenitors of SN Ia.

3. White dwarf physics and Type Ia supernovae

3.1. The cooling of white dwarfs

The theory of WD cooling started with the works of Mestel (1952) and Schatzman (1953). Later contributions include those of Van Horn (1968), Koester (1972), Lamb and Van Horn (1975), Shaviv and Kovetz (1976), Kovetz and Shaviv (1976), Sweeney (1976), D'Antona and Mazzitelli (1978), Mochkovitch (1983), Iben and Tutukov (1984b), Garcia-Berro et al. (1988), and Mochkovitch et al. (1990).

In a WD, the total (photon plus neutrino) luminosity is the sum of different contributions from the release of thermal, gravitational, and nuclear energies respectively:

$$L + L_\nu = L_{\rm th} + L_{\rm grav} + L_{\rm nuc}, \tag{3.1.1}$$

(where L stands for the photon luminosity). For $L \leq 10^{-1} L_\odot$, we have that $L_{\rm nuc} \simeq L_\nu \simeq 0$ (the former if the WD has a He-rich envelope–see Iben and Tutukov 1984). The internal temperature of the WD is closely approximated as uniform and we can derive a relationship:

$$L/L_\odot = \mathcal{L}(T) M_{\rm WD}/M_\odot, \tag{3.1.2}$$

where $\mathcal{L}(T)$ is mainly determined by the physics of the envelope (Van Horn 1968). A "classical" expression for $\mathcal{L}(T)$ is given by Schwarzschild (1965):

$$\mathcal{L}(T) = 4.6 \times 10^{-4} \left(\frac{\mu_i}{\mu_e^2}\right) \left[\frac{1}{Z(1+X)}\right] T_7^{3.5}, \tag{3.1.3}$$

where μ_i and μ_e are the mean masses per ion and electron, respectively, and X and Z stand for the hydrogen and metal mass fractions.

For the thermal luminosity we have:

$$L_{\rm th} = -\frac{dE_{\rm th}}{dt} = -\left[\int_0^{M_{\rm WD}} c_V dM\right] \frac{dT}{dt} + \frac{dm_{\rm sol}}{dt} l, \tag{3.1.4}$$

where $E_{\rm th}$ is the thermal energy contents, c_V the specific heat at constant volume, and the last term corresponds to the release of latent heat at crystallization (l is the specific latent heat and $m_{\rm sol}$ the solid mass).

3.2. The physics of phase transition in white dwarf interiors

Crystallization of a Coulomb plasma is a first-order phase transition predicted by Kirzhnits (1960), Abrikosov (1960), and Salpeter (1961). It was first included in the study of the cooling process of WDs by Mestel and Ruderman (1967). The crystallization process in the *one-component plasma* (OCP) has been studied by Monte Carlo simulations, starting with the work of Brush, Sahlin, and Teller (1966). Further simulations have been performed by Pollock and Hansen (1973); Slattery, Doolen, and DeWitt (1980); and Ogata and Ichimaru (1987). The basic parameter is the *plasma coupling constant*, Γ, representing the ratio of Coulomb to thermal energy:

$$\Gamma = \frac{Z^2 e^2}{kTa}, \tag{3.2.1}$$

where $a = [3/(4\pi n)]^{1/3}$ is the *ion-sphere radius*: the radius of a sphere containing, on average, one ion. Phase transition takes place when $\Gamma \geq \Gamma_{\rm crit}$. Values for the latter range from $\Gamma_{\rm crit} \simeq 171 \pm 5$ (Slattery, Doolen, and DeWitt 1980) to $\Gamma_{\rm crit} \simeq 180 \pm 1$ (Ogata and Ichimaru 1987). For the former value and a pure ^{12}C plasma, we have:

$$T_{\rm crit} = 2.3 \times 10^4 \rho^{1/3}. \tag{3.2.2}$$

The crystal structure is a *body-centered cubic lattice* (bcc), and the latent heat released is $q \simeq kT$ per ion. Thus

$$l \simeq \mathcal{R}T/\mu_i, \tag{3.2.3}$$

$\mathcal{R}$ being the gas constant. For c_V, the Debye expression (Landau and Lifshitz 1958) must be used in solid phase. In the "Coulomb liquid" phase, the expression given by Hansen, Torrie, and Vieillefosse (1977) can be adopted. Cooling times until the start of crystallization are a function of stellar mass. This can be seen in table 1.

Table 1

$M_{WD}/M_\odot$	0.6	1.0	1.2
t_{cryst} (Gyr)	1.9	1.3	1.1

The numbers in table 1 show that most WDs with ages above $\simeq 2$ Gyr should be at least partially solid. In particular, this is always the case for the WD progenitors of SN Ia in *elliptical galaxies*. This indicates the need to include the effects of crystallization in dealing with explosive ignition of C+O WDs, but also poses a further problem since the interiors of such stars are not OCPs but *binary ion mixtures* (BIMs).

We already see, from the expression for Γ, that in a C+O plasma cooling at constant density $\Gamma_{\rm crit}$ is reached first for O ($T_{\rm crit}(^{16}O) > T_{\rm crit}(^{12}C)$). This raises the question of the *miscibility* of C/O mixtures. The two ions are completely miscible in the *fluid* phase (Stevenson 1976); what occurs in the *solid* phase is still a matter of debate. A direct Monte Carlo simulation (Loumos and Hubbard 1973) seemed to indicate that C and O were miscible in any proportion in solid phase. The critical point would be given by:

$$\overline{Z^{5/3}}\Gamma_e = \Gamma_{\rm crit}, \tag{3.2.4}$$

where $\Gamma_{\rm crit}$ is the value found for the OCP and

$$\overline{Z^{5/3}} = \sum_i X_i Z_i^{5/3}, \tag{3.2.5}$$

and

$$\Gamma_e = \frac{e^2}{a_e kT}, \tag{3.2.6}$$

where $a_e = [3/(4\pi n_e)]^{1/3}$ is the *electron-sphere radius* (n_e, the number density of the electrons, replaces n_i, the number density of the ions). Thus, we have for $X_C = X_O = 0.50$, that $T_{\rm crit} = 1.26\, T_{{\rm crit},C}$, the latter being the critical temperature for a pure ^{12}C plasma at the same density.

In contrast with the previous result, Stevenson (1980) proposed a model (based on the *random mixing* hypothesis for calculating free energy in the solid phase) which predicts an *eutectic* phase diagram. C and O would be inmiscible in solid phase and the phase diagram would show a temperature minimum for the *eutectic composition*, $X_C^e \simeq 0.6$. This diagram can be approximated by:

$$\begin{array}{ll} T/T_c = 0.925X_C^l + 0.075 & (X_C^l \geq X_C^e) \\ T/T_C = 1.615 - 1.642X_C^l & (X_C^l \leq X_C^e) \end{array}, \tag{3.2.7}$$

where X_C^l is the C mass fraction in the "liquid" phase (Mochkovitch 1983). Thus, for a composition $X_C = X_O = 0.50$, oxygen "snowflakes" would form first. Being denser than the surrounding fluid, they should fall to the center, and a central solid core of pure O would start to grow. Carbon concentration would steadily increase in the fluid, and for $X_C^l \geq X_C^e$, C crystals would also form. Being lighter than the still-mixed fluid, they should towards the surface to melt again at lower densities. "Salt-finger"-like instabilities would rehomogenize the fluid (Stevenson 1980; Mochkovitch 1983). There should be a contribution from phase separation to $L_{\rm grav}$:

$$L_{\rm grav} = e_{\rm grav} \frac{dm_{\rm Ox}}{dt} \tag{3.2.8}$$

where the specific energy release has been evaluated by Mochkovitch (1983) and by Garcia-Berro et al. (1988) as being: $e_{\rm grav} \sim 10^{14}$ erg g^{-1}. The delay in the cooling process (as compared with the case of complete miscibility) amounts to $\Delta t \simeq 1$ Gyr per $0.1 M_{\odot}$ of deposited O. The total amount that could be deposited depends on the chemical composition profile resulting from previous evolution (Mazzitelli and D'Antona 1986, 1987).

The problem has been more recently reconsidered by Barrat, Hansen, and Mochkovitch (1988) and by Ichimaru, Iyetomi, and Ogata (1988). The first group, adopting a density function approach to calculate the free energy, finds a phase diagram of the *spindle* form: there is only partial depletion of carbon in the solid phase. The gravitational energy release is reduced by $\simeq 1/3$ as compared with the eutectic case (the delay in the cooling process is further reduced by the release taking place at higher temperature and thus at higher luminosity). The solid that crystallizes is a *random alloy* (C and O sites are distributed at random in the lattice), but transition to an *ordered alloy* (a bcc lattice with C and O forming simple cubic sublattices, the structure of the crystals of ClCs) is predicted for lower temperatures. The second group concludes from Monte Carlo simulations that *linear mixing* formulae are more accurate for calculating the free energies of solid alloys than the *random mixing* hypothesis adopted by Stevenson (1980). They deduce an *azeotropic* phase diagram for the C/O mixture. This also means that carbon will be partially depleted in the solid phase. Crystallization takes place (for a given composition) at lower temperatures than for the spindle diagram, and thus the delay in the cooling process is somewhat longer. Unpublished calculations of Hansen's group now give a very deep azeotrope instead of the spindle diagram previously found. On the other hand, Godon et al. (1989) have also recently approached the problem using solid state techniques (linear Muffin-Tin orbitals) and they conclude that, within $\sim 1\%$ accuracy, chemical separation involves no change in energy, and thus that the question can not be reliably answered.

An additional problem is posed by the presence of other nuclear species besides C and O, such as ^{22}Ne (Isern et al. 1991). The phase diagrams for the ^{22}Ne/^{12}C and ^{22}Ne/^{16}O BIMs indicate that there is very little miscibility in solid phase. This is important not only from the point of view of the delay in the cooling process (depending on the mass of the progenitor, ^{22}Ne can amount up to 1 to 2% of the stellar mass and to this could introduce an extra delay $\Delta t \sim 2$ Gyr), but it would also concentrate the most abundanat neutron-rich species at the center of the star. The difference between this and having a uniformly spread ^{22}Ne would help to solve the problem of the ^{54}Fe and ^{58}Ni overabundances predicted by current models of the thermonuclear explosion of WDs (in contrast with the observational constraint 7 above; see also Woosley, this volume).

Summarizing the current situation concerning crystallization in C+O WDs:

(1) Formation of a central solid pure O core seems unlikely.
(2) Most probably, a central C-poor core forms. It is still unclear whether the C/O alloy is a *random* or an *ordered* alloy.
(3) A ^{22}Ne-rich central region very likely forms inside a C-poor core.

3.3. Nuclear reaction rates

In WD interiors, the nuclear fusion rates are enhanced by screening effects. *Electron screening* was first considered by Schatzman (1948) and later by Salpeter (1954). At comparatively low densities, the screening effect of electrons on fields produced by the ions can be treated in the Debye-Hückel approximation: this is the *weak screening* regime. At higher densities, one has to take into account the screening effect of degenerate electrons plus the effects of ion correlations. The latter affect both the pair-distribution function (distribution of turning radii) and the evaluation of effective potential in classically forbidden regions (WKB integrals): this is the *strong screening regime*. The enhancement factors in this last regime are very large. For instance, the rate of the $^{12}\mathrm{C} + ^{12}\mathrm{C}$ reaction in a pure C plasma at density $\rho = 10^9$ g cm^{-3} is enhanced by a factor of 3×10^{30} at $T = 10^7 K$, and by a factor of 3×10^{16} at $T = 10^8 K$, in comparison with the unscreened rate. We have, for the one-component plasma:

$$r^{\mathrm{scr}} = r^{\mathrm{uns}} \times exp[\tau - Q(\rho_0)], \tag{3.3.1}$$

where

$$\tau - Q(\rho_0) = 1.25\,\Gamma - 0.11\tau \left(\frac{3\Gamma}{\tau}\right)^2, \tag{3.3.2}$$

Γ being the plasma coupling constant and

$$\tau \equiv \left[\frac{27\pi^2}{4} \frac{M(Ze)^4}{kT\hbar^2}\right]^{1/3}, \tag{3.3.3}$$

(Itoh et al. 1979). This can be generalized to binary ion mixtures.

For values $\Gamma \geq \Gamma_{\text{crit}}$, this is the *pycnonuclear regime*. The nuclei form a lattice and only reactions between neighboring nuclei are possible (see Salpeter and Van Horn 1969). In the "zero-temperature regime", even the two reacting nuclei are in the lattice ground state. In calculating 3-dimensional WKB integrals, two different approximations can be introduced. In the "fully static" approximation, the nonreacting nuclei are "frozen" at their equilibrium positions ("static lattice"). In contrast, in the "fully relaxed" approximation, the radius $\vec{r}$ of the classical turning point is fixed and the remaining lattice points are allowed to polarize into fully relaxed positions appropriate to it. In the zero-temperature regime,

$$r_0 = \left(\frac{\rho}{A}\right) A^2 Z^4 S \begin{pmatrix} 3.90 \\ 4.76 \end{pmatrix} 10^{46} \lambda^{7/4} \times \exp\left[-\lambda^{-1/2} \begin{pmatrix} 2.638 \\ 2.516 \end{pmatrix}\right] \text{reacts cm}^{-3}\text{s}^{-1}, \tag{3.3.4}$$

where S is the cross-section factor in MeV barns, λ is a characteristic length that depends on ρ, A, and Z, and the upper and lower figures within parentheses correspond to the static and relaxed approximations, respectively. In the nonzero-temperature regime, there is a contribution from nuclei in excited states of the lattice to the pycnonuclear rates:

$$r(T)/r_0 = 1 + \begin{pmatrix} 0.0430 \\ 0.0485 \end{pmatrix} \lambda^{-1/2} \left[1 + \begin{pmatrix} 1.2624 \\ 2.9314 \end{pmatrix} e^{-8.7833\beta^{3/2}}\right]^{-1/2} \times \exp\left\{-7.272\beta^{3/2} + \lambda^{-1/2} \begin{pmatrix} 1.2231 \\ 1.4331 \end{pmatrix} e^{-8.7833\beta^{3/2}} \times \left[1 - \begin{pmatrix} 0.6310 \\ 1.4654 \end{pmatrix} e^{-8.7833\beta^{3/2}}\right]\right\}, \tag{3.3.5}$$

with $\beta = 0.0322334\,\lambda\tau^2$. The upper and lower figures within the parentheses have the same meaning as in the zero-temperature expression. When $\beta \leq 1$, it is accurate enough to include only the first correction term to the zero-temperature rates (Salpeter and Van Horn 1969). More recent investigations of the zero-temperature regime, (Schramm and Koonin 1990) indicate that the effects of lattice polarization on both adiabatic potential and effective tunneling mass almost cancel, and therefore the *static approximation* should give the most realistic results.

3.4. Mass accretion and core heating

We have seen that if the *detached phase* following the formation of a C+O WD in a CBS lasts for more than a couple of Gyr, the core will be partially solid. At the end of the detached phase, however, when the companion starts to transfer mass to the WD, compression of the core increases its temperature and may induce partial or even total melting before carbon ignition takes place at the center of the WD. Besides *homologous compression* of the central layers, both *nonhomologous compression* (Nomoto 1982) and possible burning shells additionally heat the core by conduction from the surface layers. As discussed in Hernanz et al. (1988), the outcome depends on competition between thermal conduction into the center of heat generated at the surface, radiative and neutrino cooling, and density increase due to compression. The time required for a thermal signal to travel over distance l is (Henyey and L'Ecuyer 1969):

$$\tau_{\rm th} = [(3\kappa\rho^2 c_p)(64\sigma T^3)]l^2, \qquad (3.4.1)$$

where κ, ρ, T, σ, and c_p have their usual meanings. The time scale for increase of the central density, when the mass approaches the Chandrasekhar limit, can be expressed (Canal and Schatzman 1976) as:

$$\tau_\rho = (M/\dot{M})(10.08/y_0^3 - 8.3 \times 10^{-4})\, y_0/3, \qquad (3.4.2)$$

where $\dot{M}$ is the mass-accretion rate, and $y_0 = (1+x_F^2)^{1/2}$, with $x_{\rm F} = p_{\rm F}/m_e c$ representing the dimensionless Fermi momentum. The effects of compression can be divided into two terms (Nomoto 1982). The first term is due to the increase in density at a fixed mass-fraction as the star's mass increases, and its effects are quite uniform throughout the whole star. The second term corresponds to compression as matter moves inward in mass-fraction space. It is negligible in the innermost, strongly electron-degenerate layers of the star, but it is large in the semidegenerate outer layers. Thus a thermal wave is generated in these layers and diffuses inwards. Such a "compressional luminosity" can be approximated by:

$$L_g^{\rm NH}/L_\odot = 1.4 \times 10^{-3} T_7\, \dot{M}_{10}, \qquad (3.4.3)$$

T_7 being the temperature in units of $10^7 K$ and $\dot{M}_{10}$ being the mass-accretion rate in units of $10^{-10} M_\odot$ yr^{-1}.

The effect of the thermal wave on the physical state of the WD interior at C ignition depends on the time required for the wave to reach the center of the star as compared to the time required for the WD to reach the Chandrasekhar mass. The latter depends on both its initial mass of the WD and on its mass-accretion rate. As discussed in Hernanz et al. (1988), for every initial mass there is a value of $\dot{M}$ above which the Chandrasekhar mass is attained before the thermal wave has reached the center. This value decreases for increasing masses. Thus, for sufficiently large accretion rates, a fraction of the initial solid core (in case it had formed previously) remains when C ignition occurs. On the other hand, for low enough accretion rates ($10^{-12} M_\odot$ yr$^{-1} \leq \dot{M} \leq 3 \times 10^{-10} M_\odot$ yr^{-1}), radiative cooling dominates. For intermediate mass-accretion rates ($3 \times 10^{-10} M_\odot$ yr$^{-1} \leq \dot{M} \leq 5 \times 10^{-8} M_\odot$ yr^{-1}, if the initial masses are in the range 1.2–1.4$M_\odot$), any initial solid core is completely melted before C ignition. That remains valid if the accretion of C+O by the core takes place through a He-burning shell, but it might be significantly modified if activation of Urca shells (by oscillations induced in the accretion process) produces localized heat sinks (or sources) in the corresponding layers of the core (Isern et al. 1991, in preparation).

The implications of the preceding for ignition of ^{12}C+^{12}C reactions depend on the phase diagram adopted for C/O mixtures.

(1) For the phase diagram of Stevenson (1980), central pure ^{16}O cores would form. Later melting during the accretion process would not change the composition stratification. Depending on the size of the O core (and also on the mass-accretion rate), either *central O ignition* or *off-center C ignition* would occur: the first, for large enough O cores plus moderate or low accretion rates; the second, for smaller O cores and/or large accretion rates (Hernanz et al. 1988). O ignition would be triggered by the formation of ^{16}C at $\rho_c \simeq 2 \times 10^{10}$g cm^{-3} through a sequence of electron captures:

$$\begin{aligned} {}^{16}\mathrm{O} + e^- &\longrightarrow {}^{16}\mathrm{N} + \nu_e \\ {}^{16}\mathrm{N} + e^- &\longrightarrow {}^{16}\mathrm{C} + \nu_e \end{aligned} \tag{3.4.4}$$

Due to the very high density, subsequent electron captures on the incinerated material should then lead to gravitational collapse of the WD (Canal, Isern, and Labay 1980). On the other hand, the off-center C ignitions would produce a range of peak luminosities and rates of postpeak decline in the light curves, plus differences in the expansion velocities (Canal, Isern, and Lopez 1988). However, from the discussion above, complete phase separation now appears unlikely. This would agree with the fact that intrinsic differences in peak luminosity among SN Ia should be minimal, which excludes off-center C ignitions covering a large range in depth from one explosion to another.

(2) A possibility not discarded by the most recent results on the phase diagram of C/O mixtures is the formation of an *ordered alloy*. In that case, $^{12}C + ^{12}C$ reactions would be inhibited in the solid phase. Progressive melting of the core by heat transport from the surface layers would induce *off-center ignitions* (at the bottom of the fluid layers) at different depths, depending on initial mass, initial solid core size, and mass-accretion rate (Canal, Isern, and Labay 1987). Nonetheless, ignition depth would cover a narrower range than in the case of complete C/O separation and this might still be compatible with the homogeneity in peak luminosity of the SN Ia.

(3) Formation of a *random alloy* would always lead (as in cases where the WD remains fluid all the time) to *central* C ignition (except for very high accretion rates). Depending again on initial mass, initial solid core size, and mass-accretion rate, ignition can take place either in the solid or in the fluid phase (before or after complete melting of the core, respectively). Central ignition densities cover the whole range 2 to 3×10^9 g cm^{-3} $\leq \rho_c^{\rm ign} \leq 1.5 \times 10^{10}$ g cm^{-3}. The range 2 to 3×10^9 g cm^{-3} $\leq \rho_c^{\rm ign} \leq 9.5 \times 10^9$ g cm^{-3} corresponds to ignition in *fluid phase*, while the range 9.5×10^9 g cm^{-3} $\leq \rho_c^{\rm ign} \leq 1.5 \times 10^{10}$ g cm^{-3} corresponds to ignition in *solid phase*. The possibility of igniting C explosively at densities significantly larger than $\rho_c^{\rm ign} \simeq 2$ to 3×10^9 g cm^{-3} (the value corresponding to a WD that had remained fluid since its formation, through the detached phase and the mass-accretion stage) could have important implications both for the physics of SN Ia and for the formation of *neutron stars* by gravitational collapse of WDs. Concerning the physics of SN Ia, for instance, ignition at densities $\rho_c^{\rm ign} \geq 4 \times 10^9$g cm^{-3} would avoid the difficulties that arise from *convective Urca cooling* (see Barkat, this volume), since it eliminates the Urca shells corresponding to the ^{23}Na $-^{23}$ Ne pair ($E_{\rm thr} = 4.4$MeV, $\rho_{\rm thr} \simeq 1.7 \times 10^9$ g cm^{-3}) and to the ^{21}Ne $-^{21}$ F pair ($E_{\rm thr} = 5.7$MeV, $\rho_{\rm thr} \simeq 3.8 \times 10^9$ g cm^{-3}). As for neutron star formation, ignition at densities $\rho \geq 10^{10}$ g cm^{-3} is likely to induce collapse, rather than explosion, of the WD. This, as we will see later, could explain the presence of neutron stars in several kinds of binary systems (and also the formation of single *millisecond pulsars*). It may be noted here that in some of those systems (the *low-mass x-ray binaries*, LMXRBs), in contrast with the case of the SN Ia, we actually see companions of the neutron stars (the mass-donors), and they are low-mass stars with H-rich surfaces. This would be evidence (if neutron stars actually form by accretion-induced collapse–see discussion in the next

chapter) that WDs can grow up to the Chandrasekhar mass by accretion of H from a close companion.

3.5. Core ignition and burning propagation

When thermonuclear fuel is explosively ignited (either centrally or off-center) in a white dwarf core, the burning propagates into the surrounding material. There are four possible mechanisms to propagate the burning.

(i) Spontaneous burning. In a contracting core, the condition for explosive burning can be reached quasi-simultaneously in neighboring points. Burning then spreads through a certain fraction of the core without an intervening transport mechanism (ignition in successive points occurs within time intervals shorter than those required by any physical process to propagate the burning). The occurrence of spontaneous burning depends on the temperature profile of the core at ignition, which also determines the size of the spontaneously burned region. The role of this mechanism in determining the ulterior mode of burning propagation has been discussed by Wheeler et al. (1986), Blinnikov and Khokhlov (1986), Barkat et al. (1990), and Woosley (1990) (see also Woosley, this volume).

(ii) Conductive burning. In the absence of any faster mechanism, conduction by degenerate electrons heats up the material surrounding any point where explosive burning has started and bring it in turn to a condition of explosive burning. Conductive burning front velocities for C+O mixtures at various densities have been calculated by Woosley (1990) and by Garcia et al. (1990). Typical values are of the order of a few thousandths of the local sound speed. For a density $\rho \simeq 2 \times 10^9$ g cm^{-3}, the width of the flame front is $\sim 10^{-3}$ cm and the speed of the conductive flame can be approximated by:

$$v_{\rm cond} \simeq 50 \left(\frac{\rho}{2 \times 10^9 \ {\rm g\ cm^{-3}}} \right)^{0.8} \left(\frac{X_{12}}{0.5} \right) \ {\rm km\ s^{-1}}, \qquad (3.5.1)$$

as deduced from numerical simulations of the conductive front done with a zone width of $\sim 10^{-5}$ cm (Woosley 1990). At higher densities, $8 \times 10^9 {\rm g\ cm^{-3}} \le \rho \le 1.5 \times 10^{10} {\rm g\ cm^{-3}}$, the width of the front becomes $\simeq 8 \times 10^{-5}$cm and the conductive velocity is given by:

$$v_{\rm cond} \simeq 84 \left(\frac{\rho}{10^{10} \ {\rm g\ cm^{-3}}} \right)^{0.9} \ {\rm km\ s^{-1}}, \qquad (3.5.2)$$

(Garcia et al 1990).

(iii) Subsonic Hydrodynamic Burning. Heating and expansion of the material as it explosively burns produces both convective and Rayleigh-Taylor instabilities. In turn, these induce mixing of the high-temperature "ashes" with the comparatively cool, unburned fuel, thus spreading burning. Woosley (1990, and this volume) discusses how an initially laminar conductive flame develops into a turbulent burning front. Hydrodynamic burning fronts accelerate while propagating outwards through the core (Müller and Arnett 1982, 1986). Typical average velocities values are of the order of one tenth of the local sound speed. Both conductive and subsonic hydrodynamic burning are designated by the generic name of *deflagrations*. Deflagrations allow the material in outer layers to expand before the arrival of the burning front. This leads to partial burning beyond some (model-dependent) point and even to complete extinction of burning before the outermost layers of the core are reached (Nomoto, Thielemann, and Yokoi 1984; Sutherland and Wheeler 1984).

(iv) Detonation. When the shock waves generated by explosive burning are strong enough to induce explosive ignition of the material they sweep, burning propagates supersonically as a *detonation.* This means that the material in outer layers does not start expanding before arrival of the burning front. Accordingly, there is no quenching of the burning by cooling due to expansion. Partial burning occurs, however, at low densities ($\rho \leq 3 \times 10^7$ g cm^{-3} in the case of a C+O WD), when the thickness of the wave becomes comparable to the density-scale height (Khokhlov 1989). It is currently a matter of debate as to whether spontaneous burning of a large enough fraction of the core directly induces a detonation or, that the burning starts subsonically (in a deflagration) and then later accelerates into a detonation (Khokhlov 1990; see also Barkat and Woosley, both in this volume). The last possibility allows *preexpansion* of the core during the phase of slow burning and in turn, should alleviate the problem of excessive neutronization of the inner core. This ensures that a sizeable fraction of the outer layers are at low enough densities for the detonation to induce only partial burning when it reaches them.

Crystallization of the (C+O) WD core during the detached phase of the CBS, whether or not followed by partial or even total melting in the mass-accretion stage, should have implications relevant to both the mode of ignition and to the propagation of burning. We give a brief summary of these implications.

(1) If the solid phase were a *random C+O alloy* with the same composition as the fluid phase. *Complete melting* of the core prior to C ignition would give a range of ignition densities: 2 to 3 $\times$ 10^9 g cm^{-3} $\leq$

$\rho_{\text{ign}} \leq 9.5 \times 10^9$ g cm^{-3}. As pointed out above, ignition at densities $\rho_{\text{ign}} \geq 4 \times 10^9$g cm^{-3} avoids quenching the burning by convective Urca cooling. The quoted range of ignition densities allows for variation in both the photospheric expansion velocities, and in the rate of post-peak decline of the light curves in the models for SN Ia outbursts, but nonetheless produces *unique peak luminosities* (Bravo 1990; Canal et al. 1991). The implications for the problem of detonation induced by spontaneous burning and for the transition from detonation to deflagration, are currently being explored.

When ignition takes place inside a *residual solid core*, ignition densities are in the range: 9.5×10^9 g cm^{-3} $\leq \rho_{\text{ign}} \leq 1.5 \times 10^{10}$ g cm^{-3}. However, there is the possibility that the presence of impurities and/or crystal defects might induce ignition at lower densities (Hernanz et al. 1990). Ignition in solid phase affects the problem of spontaneous burning, since the dependence of the *pycnonuclear reaction rates* for weekly screened regimes on temperature and density differs from that of the *strongly screened* regimes. Moreover, propagation through solid layers should stabilize the conductive flame and thus allow *preexpansion* before the deflagration can turn into a detonation. This would mean more mass in layers with $\rho \leq 10^7$ g cm^{-3}, where detonation induces only partial burning. The extra mass, in turn, should show in light curves and spectra of the corresponding SN Ia events.

Ignition at densities $\rho_{\text{ign}} \geq 10^{10}$ g cm^{-3}, for burning front velocities below a few hundredths of the local sound speed, induces implosion of the core due to very fast electron captures on the incinerated material (Canal and Isern 1979; Canal et al. 1990; Canal, Isern, and Labay 1990). *Accretion-induced collapse* (AIC) of the C+O WD into a *neutron star* would occur. As stated above, propagation through solid layers should inhibit the growth of hydrodynamic instabilities, and thus keep the burning front conductive, with velocities below the limits just quoted. The neutrino flux produced by electron captures in the incinerated layers would, however, melt the solid ahead of the front after $\sim$ 1 s (Canal et al. 1990). The problem then becomes a question of how fast hydrodynamic instabilities would grow. Woosley (1990, private communication) suggests that at such high densities the width of the unstable, low-density region behind the front is smaller than the minimum wavelength instability that can grow before being consumed by the flame. But the issue is very sensitive with respect to the values of the conductive velocities. AIC of a WD into a neutron star has hardly been modeled. Baron et al. (1987), on basis of a highly disputable initial model, predicted very small mass ejection ($\sim 0.1 M_{\odot}$). This, nonetheless, resulted basically from the high entropy of the initial model, a characteristic that more-realistic models should share. Most likely, the outburst would not resemble a SN Ia (see, however, Colgate 1990).

(2) If the solid phase were a *C-poor random C+O alloy*, crystallization, in this case (most likely in view of current results), would enhance the effects of previous stratification of the chemical composition (Mazzitelli and D'Antona 1986, 1987). The stratification decreases with increasing WD progenitor mass; it is unclear, however, that this "purification" might ever lead to off-center C ignitions.

(3) If the solid phase were an *ordered C+O alloy* (either from start or after further cooling), depending on the size of the solid core initially formed, either AIC (ignition at $\rho_{\rm ign} \simeq 2 \times 10^{10}$g cm^{-3}), off-center, or central C ignition would occur.

(4) If *C and O would completely separate* in the solid phase, in this case (almost discarded by current calculations), AIC would ensue for initial solid cores which were large enough (even with later melting), and off-center ignition would occur for smaller ones. The appreciable range of variation in peak luminosities that the last would produce gives an additional argument against the occurrence of complete phase separation.

(5) If *^{22}Ne is not miscible* with C and O in the solid phase (or if there is a very large enhancement of its abundance when crystallizing), the main effect of the concentration at the center of a large fraction of the ^{22}Ne initially present in the core would be to alleviate the problem of overproduction of ^{54}Fe and ^{58}Ni by the SN Ia (Bravo et al. 1991). This appears most likely from recent calculations (Isern et at. 1991).

3.6. Electron captures and mixing

O+Ne+Mg cores form after nondegenerate C-burning in stars with masses $M \geq 8M_\odot$. Those with masses $M \geq 12M_\odot$ nondegenerately ignite Ne and continue their thermonuclear evolution up to Si burning and the formation of degenerate cores in nuclear statistical equilibrium (NSE). In the mass interval $10M_\odot \leq M \leq 12M_\odot$, Ne burning proceeds through flashes, but the star equally makes it all the way to grow a NSE core (Woosley and Weaver 1986). In contrast, stars with masses $8M_\odot \leq M \leq 10M_\odot$ grow strongly degenerate O+Ne+Mg cores during the C-shell burning phase (Miyaji et al. 1980). The Fermi energy of the electrons at the center eventually becomes larger than the thresholds for electron capture on ^{24}Mg, then shortly afterwards on ^{24}Na, and later on ^{20}Ne (and thus also on ^{20}F). WDs formed in CBSs by loss of the envelope of stars in the above mass range, will also have a 0+Ne+Mg compostiion at some point during the C-shell burning stage. Later, mass transfer from the companion can make the WD grow up to the point where electron captures start at the center.

The electron captures have a double effect. First, they heat up the plasma through both distortion of the Fermi distribution and the γ-rays produced by decay of the daughter nuclei. Second, they lower the electron mole number Y_e and thus lower the Chandrasekhar mass (which is proportional to Y_e^2). The first effect promotes explosive thermonuclear ignition of Ne and O. The second effect leads to gravitational collapse. Earliest calculations of the mass growth of degenerate O+Ne+Mg cores (Miyaji et al. 1980) used electron-capture rates derived from the *gross theory of β-decay*, and adopted the Schwarzschild criterion for stability against convective motions. Central explosive Ne-O ignition was delayed up to $\rho_c \simeq 2\times 10^{10}$ g cm^{-3}. Subsequent electron captures on the incinerated (NSE) material induced gravitational collapse. Burning was propagated (in mass fraction) just by the density increase due to accelerated contraction. Similar results were later obtained by Nomoto (1987) using the same electron-capture rates and adopting the same stability criterion.

Nonetheless, as pointed out by Mochkovitch (1984), the electron captures not only produced a *negative entropy gradient* and the overall decrease of Y_e, but they also create a *positive Y_e gradient.* The latter has a stabilizing effect. In chemically inhomogeneous regions, the Ledoux criterion applies. It gives, for the start of convective motions

$$\nabla_T > \nabla_L, \tag{3.6.1}$$

where

$$\nabla_L \equiv \nabla_{ad} + \left[\left(\frac{\partial ln P}{\partial ln Y_e} \right)_T \Big/ \left(\frac{\partial ln P}{\partial ln T} \right)_{Y_e} \right] \nabla_{Y_e}, \tag{3.6.2}$$

with

$$\nabla_{Y_e} \equiv -\frac{d ln Y_e}{d ln P}, \tag{3.6.3}$$

∇_{ad} being the adiabatic temperature gradient. When the Ledoux criterion is adopted, convection is inhibited until explosive Ne-O ignition. As compared with the case where convection develops as soon as the entropy gradient becomes negative, this means less efficient transport (conduction) of heat generated by the captures, slower decrease of Y_e, and captured electrons with energies closer to the corresponding thresholds (there is no resupply of "mother" nuclei in the higher density regions which would result from mixing material from farther out in the core).

There are two main heating episodes (Miyaji and Nomoto 1987; Canal et al. 1991, in preparation). The first one is due to the sequence of capture

$$\begin{aligned} {}^{24}\mathrm{Mg} + e^- &\longrightarrow {}^{24}\mathrm{Na} + \nu_e \\ {}^{24}\mathrm{Na} + e^- &\longrightarrow {}^{24}\mathrm{Ne} + \nu_e \end{aligned}, \tag{3.6.4}$$

which take place at $\rho \simeq 4 \times 10^9$ g cm^{-3}. These reactions produce a temperature peak that is too low to explosively ignite Ne and O (the temperature decreases afterwards due to thermal neutrino emission).

The second heating episode is due to the sequence:

$$\begin{aligned} {}^{20}\mathrm{Ne} + e^- &\longrightarrow {}^{20}\mathrm{F} + \nu_e \\ {}^{20}\mathrm{F} + e^- &\longrightarrow {}^{20}\mathrm{O} + \nu_e, \end{aligned} \tag{3.6.5}$$

and induces explosive Ne-O ignition. For electron-capture rates derived from the gross theory of β-decay, this happens at $\rho \simeq 9.5 \times 10^9$g cm^{-3}. New rates, based on shell-model calculations (Takahara et al. 1989), are now available. With these rates, explosive ignition takes place at lower density, $\rho \simeq 8.5 \times 10^9$g cm^{-3} (Canal et al. 1991, in preparation).

Central explosive Ne-O ignition at $\rho_c \simeq 9.5 \times 10^9$g cm^{-3} was treated by Miyaji and Nomoto (1987) by suppressing any mode of burning propagation. Gravitational collapse began when electron captures made the Chandrasekhar mass lower than the actual mass of the core. However, it is clear that a conductive burning front should propagate from the center, and that the development of hydrodynamic instabilities would accelerate it. This has been studied by Isern, Canal, and Labay (1991), using the parameterization of the velocity of a turbulent burning front proposed by Woosley (1986) (more recently revised to a power law based on the fractal dimension of the flame–see Woosley 1990, and in this volume)

$$v_{\text{turb}} = F c_s \left(1 - e^{-r/R_0}\right) \tag{3.6.6}$$

where c_s is the local sound speed, r is the distance to the center, and F and R_0 are the adjustable parameters. The authors find that only a extremely slow deflagration ($F = 0.15$ and $R_0 = 10^8$ cm) would cause a neutron star to collapse. Somewhat faster deflagrations would eject only a minor fraction of the core and change its composition to the "Fe-peak" type. Explosions seem most likely: they would give rise to SN II outbursts if they took place in the cores of stars which have retained a H-rich envelope. In the case of mass-accreting O+Ne+Mg WDs (or of stars, either single or in binaries, which have lost their H envelopes), they would produce SN I outbursts (SN Ia or maybe SN Ib/c). It must be noted, however, as has already been pointed out in the case of explosive C ignition at similar densities (see the preceding subsection), that it is not clear that a turbulent burning front should develop such high densities (Woosley 1990, private communication). Nonetheless, explosion will be the outcome if Ne and O are ignited at $\rho \simeq 8.5 \times 10^9 \mathrm{g\ cm}^{-3}$, as happens in the models with no mixing for the most recent electron-capture rates (Canal et al. 1991, in preparation).

Thus, mixing during electron-captures plays a crucial role in determining the fate of the O+Ne+Mg cores, both of single stars and of mass-accreting WDs. A chemically nonhomogeneous region that is unstable according to the Schwarzschild criterion and stable according to the Ledoux criterion is usually called *semiconvective*. It has been claimed (Miyaji and Nomoto 1987) that in such layers *secular overstability* should grow (see also Langer, Sugimoto, and Fricke 1983). On the other hand, Mochkovitch (1984) suggests that a double diffusive interface should form at the level where the electron Fermi energy equals the threshold energy for the corresponding capture. It would separate two thoroughly mixed regions with different values of Y_e. The degree to which extent electron degeneracy would inhibit mixing has not yet been considered.

Mixing, on the other hand, might either *increase* or *decrease* the density required for explosive ignition. It indeed has two opposite effects: mixing of composition, by allowing electron captures far above threshold energy, increases local heating, while entropy mixing counters it. Thus, the treatment of Langer, Sugimoto, and Fricke (1983), which yields appreciable diffusion of chemical composition with little heat diffusion (Langer 1991, private communication), should lower the ignition density. On the contrary, the treatments of convective mixing by Miyaji et al. (1980) and Nomoto (1987) significantly increase ignition density. All this also depends on the electron capture rates. For instance, those of Takahara et al. (1989) are significantly higher than those of Miyaji et al. (1989) for captures on ^{24}Na, at energies well above threshold, which enhances the heating effect of mixing.

4. Neutron stars in binary systems

Neutron stars form by gravitational collapse of the fuel-exhausted cores of massive stars (see Hillebrandt, this volume), and perhaps also (as discussed in the preceding chapter) by AIC of WDs. Single NS are detected by their emission of radio pulses, following the discovery of Hewish et al. (1968). It is also likely that single NS are involved in the emission of *γ-ray bursts*, but this still remains a matter of debate. A significant fraction of NS are members of binary systems. They were first detected as emitters of high-energy photons: binary x-ray pulsars (Giacconi et al. 1971) and x-ray burst sources (Belian et al. 1976). Later, radio pulsars were also observed in binaries. Binary evolution could also be the origin of some isolated pulsars (as it is often claimed in the case of *single millisecond pulsars*).

The presence of NS in binary systems poses the problem of whether the core collapse of massive stars (with its corresponding SN outburst) is always compatible with observed characteristics of these systems; or, if on the contrary, another formation mechanism such as AIC of WDs is required in some cases. Thus, we first briefly review the different types of binary systems containing NS, as well as the kinds of single NS that are thought to have originated in binary systems (see Canal, Isern, and Labay 1990, for a more extensive review).

4.1. X-ray binaries

There are two major groups of binary systems containing x-ray emitting NS: the *high-mass x-ray binaries* (HMXRBs) and the *low-mass x-ray binaries* (LMXRBs).

4.1.1. High-mass x-ray binaries

There are approximately 40 known objects in our galaxy belonging to this group. They have normal *early-type* stars as their optical counterparts. This group includes most of the *x-ray pulsars*. Among them, Cen X-3, by being an eclipsing source, gave the first clue to the binary nature of XRBs. Nonetheless, about a half of the sources in this group do not show pulsations. The periods of the pulsing sources range from fractions of a second up to almost 10^3 s. Strong magnetic fields ($\sim 10^{12}$ G) are inferred from cyclotron lines in the hard x-ray spectra of some of them. The optical companions of the NS are either of spectral type earlier than B2 (and luminosity classes I, II, or III) or Be stars. In the last case, the x-ray sources are transient or at least highly variable. This is is attributed to motion of the NS in an eccentric orbit through a circumstellar shell. HMXRBs are only found along the galactic plane, in accordance with the rest of their Population I characteristics.

4.1.2. Low-mass x-ray binaries

There are approximatly 40 sources in this group. Their optical counterparts are *faint* stars. They have softer x-ray spectra than the HMXRBs, and only three of them show pulsations. Some emit X-ray bursts; no source shows both pulsations and bursts. The absence of pulsations is interpreted as evidence of comparatively weak magnetic fields. About 30 LMXRBs are located within 30′ from the galactic center and they are referred to as "galactic bulge sources." Eight of them are strong sources ($L_X \sim 10^{38}$ erg s^{-1}), while the other 22 are weak sources ($L_X \sim 10^{36}$ to 10^{37}erg s^{-1}). A large fraction of the galactic bulge sources show quasi-periodic oscillations (QPO). Eleven bright x-ray sources are in globular clusters, and ten of them produce bursts. Optical identification is very difficult in globular cluster sources, but overall similarity has led us to group them with the galactic bulge sources in a single class, which encompasses Population II and the old disk population.

4.2. Binary and millisecond pulsars

Only a dozen out of the approximately 500 radio pulsars presently known are in binaries. Four of these binaries are in globular clusters. Binary pulsars can be divided into two groups (see van den Heuvel 1988).

The first group includes three systems, the prototype being PSR 1913+16. They have relatively short orbital periods, and the companions of the pulsars are relatively massive ($M \sim 1.0$ to $1.4 M_\odot$). Two of them have eccentric orbits.

The second group includes nine systems, among them the four *binary millisecond pulsars*. The prototype is PSR 1953+29. They have circular orbits, relatively long orbital periods, and the companions of the pulsars have low or even very-low masses ($M \sim 0.02$ to $0.4 M_\odot$).

Pulsars in the first group seem to be related to the HMXRBs, while those in the second group would be related to the LMXRBs.

Single millisecond radio pulsars would be neutron stars that have been spun up by mass accretion from a disk in a CBS, the companion being later destroyed either by coalescence with the NS or by "evaporation" (see van den Heuvel 1989).

4.3. Formation mechanisms

4.3.1. Core collapse of massive stars

Core collapse in a massive star at the end of its thermonuclear evolution is the "canonical" mechanism to form NS. A supernova explosion must simultaneously eject the mass above the stability limit for a NS ($M_{\rm NS}^{\rm lim} \simeq 2.0$ to $2.5 M_\odot$). Thus, most of the star's mass must be ejected; a stellar black hole would otherwise result. If NS in binaries have been formed by this mechanism in the same binary where they are presently observed, the system must have managed to survive the supernova explosion. It has long been known that the condition for the system to remain bound after the explosion is $M_{\rm ej}/M_{\rm tot} < 1/2$, where $M_{\rm ej}$ is the ejected mass and $M_{\rm tot}$ the total mass of the system (for instance, see Shapiro and Teukolsky 1984). Therefore, if the exploding star were the most massive component of the binary, the system would be disrupted. However, in massive binaries the star that explodes may have become the less massive component of the system, due to a previous large-scale mass transfer (van den Heuvel and Heise 1972; Tutukov and Yungelson 1973; van den Heuvel 1974). Mass transfer, with conservation of the total mass and with conservation of the total angular momentum of the system, satisfactorily explains the formation of HMXRBs (van den Heuvel 1989). Systems containing two NS (such as PSR 1913+16 and PSR 2303+46) or a NS plus a massive WD (such as PSR 0655+64) would result from further evolution of the HMXRB with formation of a common envelope and mass loss by the system.

Triple star evolution has been suggested as an explanation of NS formation by core collapse of a massive star in systems where the companion is a low-mass star (Eggleton and Verbunt 1986). A close pair of massive stars with a distant low-mass companion would first evolve up to the HMXRB stage. Further evolution (with formation of a common envelope) would then make the NS spiral into the center of the companion (which by then would be a red giant). Long-term expansion of the envelope would finally lead to a new common-envelope phase, this time with the low-mass star. This last would spiral in, the envelope would be lost, and a close binary consisting of a NS plus a low-mass companion might finally result.

4.3.2. Capture mechanisms

A binary system containing a NS can also be formed by coupling a previously formed *single* NS with a companion in a *tidal capture* process. In close encounters between two stars, tidal forces produce deformations. The energy required comes from the relative kinetic energy of the two stars, and if this energy is rapidly dissipated, the stars can become bound. The condition for tidal capture (Verbunt 1988) is that the distance of closest approach, d, be

$$d \leq 3R \left(\frac{k}{0.14} \frac{m}{M} \frac{m+M}{2M_\odot} \frac{R_\odot}{R} \right)^{1/6} \left(\frac{10 \text{ km s}^{-1}}{v} \right)^{1/3}, \tag{4.3.2.1}$$

where m is the mass of the NS, M and R are the mass and radius, respectively, of the colliding star, k is the apsidal motion constant, v is relative velocity, and in this case, the normalization constants are typical for globular clusters (where such a process has the best chance to work). Capture occurs if the compact star approaches to within two to three times the radius of the other star. The cross section for passage of the two stars within distance d is given by

$$\sigma = \pi d^2 \left(1 + \frac{2G(m+M)}{v^2 d} \right) \simeq \pi d \frac{2G(m+M)}{v^2}, \tag{4.3.2.2}$$

with the last approximation being valid for small relative velocities, which are appropriate for globular clusters. Thus the capture rate per unit volume is

$$\Gamma = n_c n v \sigma \simeq 6 \times 10^{-11} \frac{n_c}{10^2 \text{ pc}^{-3}} \frac{n}{10^4 \text{ pc}^{-3}} \times \frac{m+M}{M_\odot} \frac{3R}{R_\odot} \frac{10 \text{ km s}^{-1}}{v} \text{ yr}^{-1} \text{ pc}^{-3}, \tag{4.3.2.3}$$

where n_c and n are the number densities of compact stars and of target stars, respectively.

A second capture mechanism involves exchange encounters of NS with binaries. The interaction occurs primarily through formation of a temporary triple system–a process known as resonance scattering. Its rate, for the case of three equal point-masses, has been calculated by Hut and Bahcall (1983):

$$\Gamma_{\text{bin}} \simeq 5 \times 10^{-10} \frac{n_c}{10^2 \text{ pc}^{-3}} \frac{n_{\text{bin}}}{10^2 \text{pc}^{-3}} \frac{m}{M_\odot} \frac{a}{1\,AU} \frac{10 \text{ km s}^{-1}}{v} \text{ yr}^{-1} \text{pc}^{-3}, \tag{4.3.2.4}$$

where n_c and n_{bin} are the number densities of compact objects and of binaries, respectively, and a is the binary separation. As before, values are normalized to typical globular cluster values. For equal masses, the incoming neutron star remains in the binary in two thirds of the encounters. By comparing eqs. (4.3.2.3) and (4.3.2.4) it can be seen that resonance scattering has a larger cross section than tidal capture (a rather than $3R$), but this is more than compensated for by $n_{\rm bin}$ being smaller than n (the density of single stars).

4.3.3. Accretion-induced collapse of white dwarfs

We have already dealt with this mechanism in Sections 3.4 to 3.6. The best candidates for AIC into NS are massive ($M \geq 1.2M_{\odot}$) C+O WDs which, after partially crystallizing, undergo mass accretion at rather high rates ($\dot{M} \geq 5 \times 10^{-8} M_{\odot}$ yr^{-1}) and end up explosively igniting C at densities $\rho \sim 10^{10}$ g cm^{-3}. O+Ne+Mg WDs are much less likely candidates for AIC, since they ignite Ne and O at lower density: $\rho \leq 8.5 \times 10^{9}$ g cm^{-3} (see sec. 3.6 above, and also Canal et al. 1990; Canal, Isern, and Labay 1990; Isern, Canal, and Labay 1991, and references therein).

4.4. The origin of neutron stars in binaries

We now discuss the possible relevance of these formation mechanisms to the origin of different types of binaries containing NS considered in secs. 4.1 and 4.2.

4.4.1. High-mass x-ray binaries

As pointed out in sec. 4.3.1, the origin of the HMXRBs is satisfactorily explained by core collapse in a massive star. Most frequently, mass transfer from the initially more massive component of the binary system will start after the end of core H-burning, and before He ignition. Mass transfer takes place on a thermal time scale, and reduces the primary star to its He core only (the whole H envelope is accreted by the secondary). A second stage of mass transfer can take place if $M_{\rm He} < 3.5M_{\odot}$ owing to expansion of the star during shell C-burning. However, if $M_{\rm He} > 2.2M_{\odot}$, core collapse to a NS will eventually occur. This would correspond to initial masses $M >$ 10–12$M_{\odot}$ of the primary. If mass transfer starts only after core He burning, this lower limit is decreased to $M >$ 8–9$M_{\odot}$ (van den Heuvel 1983).

These evolutionary scenarios account for both early-type and Be-type HMXRBs.

Given the number of HMXRBs known (~ 40) and if we assume that they are the whole population in the galaxy, we can derive a birthrate

$$r_{\rm HMXRB} \simeq 4 \times 10^{-13} (t_{\rm HMXRB,5})^{-1} A_{\rm eff,9}^{-1} \ {\rm pc}^{-2} \ {\rm yr}^{-1}. \qquad (4.4.1.1)$$

It can be interesting to compare this rate with the rate of SN of Types Ib and Ic, since it has been suggested that these arise from the explosion of massive stars which have lost their H-rich envelopes (and in the case of the SN Ic, also most of their He-rich layers) in the course of close binary evolution (see Nomoto, this volume). For a global rate in the galaxy $\sim 0.004\ \mathrm{yr}^{-1}$ (see Tammann, this volume), we have:

$$r_{SN\ Ib+c} \simeq 4 \times 10^{-12} A_{\mathrm{eff},9}^{-1}\ \mathrm{pc}^{-2}\ \mathrm{yr}^{-1}. \qquad (4.4.1.2)$$

The lifetimes attributed to the HMXRBs $\left(t_{\mathrm{HMXRB},5} \sim 0.1 \text{ to } 1.0\right)$, would yield good agreement between the two rates.

4.4.2. Low-mass x-ray binaries

We first consider the globular cluster sources and then the galactic bulge sources, since in some of the scenarios that have been proposed, the latter systems originate from the former.

(i) Globular cluster sources Globular clusters account for only approximately 10^{-4} of the mass of the galaxy, but they contain approximately 10^{-1} of the galactic LMXRBs. Such high efficiency in producing these objects is most likely due to the favorable conditions for tidal capture, that is the high densities of stars and their comparatively low relative velocities. To evaluate the total number of captures in a globular cluster, eq. (4.3.2.3) must be integrated over the cluster volume. Most of the captures occur within a few core radii, since both n_c and n are much higher there than outside this region. The number of x-ray sources in globular clusters is compatible (within appreciable uncertainty) to the formation rate expected from eq. (4.3.2.3): in the core of a globular cluster, n can be $\sim 10^5\ \mathrm{pc}^{-3}$. Compact star density n_c is poorly known. From the models of Verbunt and Meylan (1988), the total number of NS in cluster cores is approximately 10^2, which would give a tidal capture rate ~ 1 every 10^9 yr. To compare this with the observed numbers of bright x-ray sources, the typical lifetime of LMXRBs must also be known. There is a large uncertainty in this last value. If it were approximately 10^9 yr, the expected number would be about one bright x-ray source per dense cluster, as is observed. But combining the two main uncertainties–the uncertainty on n_c and the uncertainty on the lifetime–the final uncertainty is on the order of $\geq 10^2$ (Verbunt 1989).

Alternatively, NS in globular cluster x-ray sources could also be formed by AIC of WDs (Grindlay 1987; van den Heuvel 1988). According to Lightman and Grindlay (1982), the ratio of the number of WDs to the number of NS in globular cluster cores should be ≥ 100. Thus the rate of tidal captures of WDs by main sequence stars should be high. Low-luminosity globular cluster x-ray sources, which form a separate class from the high-luminosity ones, might be mass-accreting WDs in the low accretion-rate regime ($\dot{M} \leq 10^{-9} M_{\odot}\ \mathrm{yr}^{-1}$) (Hertz and Grindlay 1983). Arguments in favor of the AIC mechanism are based on the idea that most NS formed by core collapse of massive stars would escape the cluster due to their high kick velocities, and thus the total number of SN explosions required would be approximately 10^3 rather than approximately 10^2. In turn, this might be in conflict with the observed central condensation and metal enrichment of the clusters containing high-luminosity x-ray sources (see, however, Verbunt, Lewin, and van Paradijs 1989).

(ii) Galactic bulge sources As we have already pointed out in sec. 4.3.1, given the observed characteristics of galactic bulge sources, it seems unlikely that most of them would have formed by core collapse of a massive star that was a member of the present system. The triple-star scenario described at the end of the sec. 4.3.1., although not completely excluded by its low probability alone, would not explain the concentration of LMXRBs toward the galactic bulge regions. Tidal capture is also unlikely since relative velocities of stars in the bulge are ≥ 100 km s^{-1}, which is more than one order of magnitude higher than in globular clusters. According to eq. (4.3.2.3), this lowers the capture rate by the same factor. Besides, n is much lower, and so n_c should be lower, which also decreases the rate. In addition, the kinetic energy to be dissipated in forming a bound system is larger than the binding energy of a dwarf star; thus the encounter would completely disrupt the noncompact object (Finzi 1978).

Alternative nonlocal mechanisms assume the prior formation of the systems in globular clusters, followed by either escape from the cluster or evaporation or disruption of the cluster itself. Ejection seems unlikely. Evaporation of globular clusters might be induced by formation of a single, strongly bound central binary (Heggie 1977). Tidal interactions of the clusters with the galactic field can lead to their disruption (Spitzer 1958). However, the radial distribution of LMXRBs in the bulge does not seem compatible with the cluster disruption hypothesis (Lewin 1977; Eggleton and Verbunt 1986), and the luminosity distributions of LMXRBs in the galactic disk and in globular clusters are different (Lewin and van Paradijs 1985). The evidence from the radial distribution of LMXRBs and globular clusters in M31 would be compatible with a globular cluster origin for the sources located approximately 400 *pc* from the center of the galaxy (Long and van Speybroeck 1983). In that region, the sources also resemble globular cluster sources, since they are more than twice as bright as the rest of the bulge sources. But on the contrary, beyond the approximately 400 *pc* radius hardly any globular cluster seems to have merged with the bulge. Also, in M31 the distributions of novae and of bulge x-ray sources are similar. All this points to AIC as the most likely origin for the majority of the LMXRBs located in the bulge and in the galactic disk.

Evolutionary scenarios for the production of galactic bulge sources by AIC collapse of WDs to NS have been proposed by van den Heuvel (1983, 1989), and by Taam and van den Heuvel (1986). According to theory, a red main-sequence star of $\simeq 1M_\odot$ would fill its Roche lobe and transfer mass to a $\simeq 1.4M_\odot$ WD. A shell with mass $\simeq 0.2M_\odot$ would be ejected after collapse and bounce off the compact object with a velocity about 10^4 km s^{-1}. This should change the binary into a detached pair for a period of approximately 10^9 yr, until angular momentum loss by gravitational radiation and/or magnetic braking would again lead to Roche lobe overflow. Less mass ejection and smaller companion mass might shorten the detached phase down to about 10^8 yr. Long detached phases would be consistent with a low magnetic field in the NS and thus with production of x-ray bursts. Mass transfer driven by gravitational radiation losses or magnetic braking should produce accretion rates of 10^{-10} to $10^{-9}M_\odot$ yr^{-1} (Rappaport, Joss, and Webbink 1982). The strong sources in the bulge require higher mass-transfer rates of $\sim 10^{-8}M_\odot$ yr^{-1}. In these cases, the companion would be an evolved, low-mass subgiant, as in Sco X-1, Cyg X-2, or 2S 0291–63 (van den Heuvel 1989).

The rate of formation of the LMXRBs, according to van den Heuvel (1983), would be 10^{-4} to 10^{-3} times that of the HMXRBs. From the number of known LMXRBs in the bulge (approximately 30), we would have

$$r_{\rm LMXRB} \simeq 3 \times 10^{-16} (t_{\rm LMXRB,8})^{-1} A_{\rm eff,9}^{-1}\, {\rm pc}^{-2} {\rm yr}^{-1} \qquad (4.4.2.1)$$

By comparing this with eq. (4.4.1.1) we see that the above estimate is based on a lifetime of 10^8 to 10^9yr. If we now compare this rate with the SN Ia rate of eq. (2.2.1), we can guess that as an outcome of the growth of a WD towards the Chandrasekhar mass, an AIC should be much rarer than thermonuclear explosion.

4.4.3. Binary and millisecond pulsars

Binary pulsars in the PSR 1913+16 group (see sec. 4.2) seem to be related to the HMXRBs. After formation of such sources, Roche-lobe overflow by the massive star should lead to a common-envelope phase, with a spiraling-in of the NS and eventual loss of the envelope. Then, if the companion of the NS has a mass $\geq 8M_\odot$, its core evolves up to collapse and supernova explosion. This should produce either two NS in a very eccentric orbit (such as PSR 1913+16 and PSR 2303+46), or two runaway pulsars. For lower companion masses ($3M_\odot \leq M \leq 8M_\odot$), the core evolves into a massive WD, and a closed system with a circular orbit form (such as PSR 0655+64).

In contrast, the PSR 1953+29 group of binary pulsars appears to be related to the LMXRBs. Systems like the strong bulge sources should be fed by mass-transfer driven by thermonuclear evolution of the companion star. At the end, only the He core of the companion is left, and the NS has spiraled out. Thus, systems like PSR 1953+29 would be the descendants of wide LMXRBs. Their NS were likely formed by AIC of a WD. PSR 0820+02, a member of this group, provides strong evidence of the latter. Its magnetic field implies an age $\leq 10^7$ to 10^8yr, while the companion is a WD with mass $M = 0.2$ to $0.4 M_\odot$. Formation of such a star requires over 5×10^9yr. The paradox of an old binary that contains a young NS can be solved by assuming that the latter was created in a recent episode of mass accretion, less than about 10^7yr ago. That mass transfer terminated recently is also inferred from the cooling age ($\leq 10^7$yr) of the companion, a still very hot white dwarf (Kulkarni 1986). Nevertheless the number of recently discovered binary pulsars with low-mass companions both in the galactic disk and in globular clusters is so large that their birthrate is now estimated to be about 100 times larger than the one given above for the LMXRBs (Kulkarni and Narayan 1988; Narayan et al. 1990; Kulkarni, Narayan, and Romani 1990; Romani 1990). Shortening of the LMXRB stage due to partial "evaporation" of the companion of the NS has been proposed to solve this paradox (Tavani 1990).

PSR 1953+29 is a millisecond pulsar. The total number of currently active binary millisecond pulsars in the galaxy would be about 10^4 if selection effects are taken into account (Stokes, Taylor, and Dewey 1985). Spin up, due to mass accretion from a disk, would allow them to reach those very short periods when the magnetic field of the NS has reached its "bottom" value of approximately $10^9 G$ (Alpar et al. 1982).

Single millisecond pulsars also seem to be NS previously spun up by accretion in a CBS (van den Heuvel 1989). They might result from coalescence of the NS with a WD in short-period systems such as PSR 0655+64. Another possible origin would be total "evaporation" of the companion by the large energy flux from the millisecond pulsar itself. This seems to be happening in PSR 1957+20 (Fruchter, Stinebring, and Taylor 1989). Thus, in the galactic disk, the NS would have been produced by AIC. In globular clusters, single millisecond pulsars might also form either by direct collision of a NS with a field star, or by a catastrophic encounter between a globular cluster x-ray binary and a field star. In both cases, the result would be a single NS with a disk around it. Accretion of the disk would spin up the NS to millisecond periods. Alternatively, a binary millisecond pulsar could be disrupted by interaction with other cluster stars.

5. Summary

From the discussion in chap. 2, it is clear that the evolution leading to SN Ia outbursts remains obscure. The double C+O WD scenario has no observational evidence to support it, but it cannot be excluded on the basis of surveys which have been made up to now. If this scenario is adopted, the dynamics of mass accretion must still be clarified. On the other hand, if the x-ray sources in the galactic bulge have formed by AIC of a WD to a NS, this would prove that accretion of H can make a WD grow to Chandrasekhar mass. But with the birthrate of LMXRBs (even revised in view of the large numbers of binary radio pulsars with low-mass companions) being much lower than the SN Ia rate, the preceding does not necessarily mean that the SN Ia progenitors must have followed the same evolution.

The dynamics of the SN Ia explosions is still largely unknown. The explosions should burn a large fraction of a massive C+O WD, but such basic points as whether the ignition is central or off-center, the ignition densities, whether the burning propagates subsonically (deflagration) or supersonically (detonation), and whether there is transition from the former mode to the latter, remain unsettled. The physical state of the WD core enters in all these issues, as we saw in sec. 3. Thus the effects of crystallization of the C+O plasma must be taken into account when studying those problems (and might even help to solve some of them), since at least initially, the progenitors of SN Ia in elliptical galaxies should be very cold.

The AIC issue also remains open. Recent results rather exclude O+Ne+Mg WDs as candidates for AIC. Therefore, cold, massive C+O WDs would be the preferred candidates, but the range of initial conditions leading to collapse currently appears to be very narrow. Astronomical evidence on the other hand, as discussed in sec. 4, favors this mechanism as the possible origin of the NS in objects such as the LMXRBs in the galactic bulge, the binary radio pulsars with low-mass companions, and even the single millisecond pulsars.

Acknowledgements. I would first like to thank Prof. Evry Schatzman, whose pioneering contributions to the topics covered in the present lectures have been a constant source of inspiration. I also thank the organizers and all the participants at the Les Houches School for providing a most stimulating environment. This paper has been supported in part by CICYT grants PB87-0147 and PB87-0150.

References

Abia, C., and R. Rebolo 1989. Ap. J. 347, 186.
Abia, C., R. Canal and J. Isern 1991. Ap. J. 366, 198.
Abrikosov, A.A. 1960. Sov. Phys. JETP 12, 1254.
Allen, D.A. 1980. M.N.R.A.S. 192, 521.
Alpar, M.A., A.F. Cheng, M.A. Ruderman, and J. Shaham. 1982. Nature 303, 597.
Arnett, W.D. 1982. Ap. J. 253, 785.
Arnett, W.D., D. Branch, and J.C. Wheeler. 1985. Nature 314, 337.
Bandiera, R. 1987. Ap. J. 319, 885.
Barkat, Z., E. Livne, D. Swartz, and J.C. Wheeler. 1990. *In:* Supernovae, ed. J.C. Wheeler, T. Piran, and S. Weinberg (Singapore: World Scientific), p. 133.
Baron, E., J. Cooperstein, S.H. Kahana, and K. Nomoto. 1987. Ap. J. 320, 304.
Barrat, J.L., J.P. Hansen, and R. Mochkovitch. 1988. Astr. Ap. 199 L15.
Bath, G.T., and G. Shaviv. 1978. M.N.R.A.S. 183, 515.
Belian, R.D., J.P. Conner, and W.D. Evans. 1976. Ap. J. (Letters) 206, L135.
Benz, W., R.I. Bowers, A.G.W. Cameron, and W.H. Press. 1990. Ap. J. 348, 647.
Blinnikov, S.I., and A.M. Khokhlov. 1986. Sov. Astr. Lett. 12, 131.
Bragaglia, A., L. Greggio, A. Renzini, and S. D'Odorico. 1990. *In:* Supernovae, ed. S.E. Woosley (Berlin: Springer-Verlag), p. 599.
Bragaglia, A., L. Greggio, A. Renzini, and S. D'Odorico. 1991. Preprint.
Branch, D. 1987. Ap. J. (Letters) 316, L81.
Branch, D., R. Buta, S.W. Falk, M.L. McCall, P.G.P. Sutherland, A.K. Uomoto, J.C. Wheeler, and B.J. Wills. 1982. Ap. J. (Letters) 252, L61.
Bravo, E. 1990. Ph.D. Thesis (Barcelona: Serv. Publ. UB).
Bravo, E., J. Isern, R. Canal, and J. Labay. 1991. *In:* 1987A and Other Supernovae, ed. J. Danziger, W. Hillebrandt, and L. Lucy (Garching b. München: ESO), p. 167.
Brush, S.G., H.L. Sahlin, and E. Teller. 1966. J. Chem. Phys. 45, 2102.
Canal, R., and E. Schatzman. 1976. Astr. Ap. 46, 229.
Canal, R., and J. Isern. 1979. *In:* White Dwarfs and Variable Degenerate Stars, ed H.M. Van Horn and V. Weidemann (Rochester: Univ. Rochester Press), p. 52.
Canal, R., J. Isern, and J. Labay. 1980. Ap. J. (Letters) 241, L33.
Canal, R., J. Isern, and R. Labay. 1987. Rev. Mex. Astr. Ap. 14, 245.
Canal, R., J. Isern, and R. Lopez. 1988. Ap. J. (Letters) 330, L113.
Canal, R., J. Isern, and J. Labay. 1990. Ann. Rev. Astr. Ap. 28, 183.
Canal, R., D. Garcia, J. Isern, and J. Labay. 1990. Ap. J. (Letters) 356, L51.
Canal, R., J. Isern, E. Bravo, and J. Labay. 1991. *In:* 1987A and Other Supernovae, ed. J. Danziger, W. Hillebrandt, and L. Lucy (Garching b. München: ESO), p. 153.
Ciardullo, R., H.C. Ford, J.D. Neill, G.H. Jacoby, and A.W. Shafter. 1987. Ap. J. 318, 520.
Colgate, S.A. 1990. *In:* Supernovae, ed. S.E. Woosley (Berlin: Springer-Verlag), p. 585.
D'Antona, F., and I. Mazzitelli. 1978. Astr. Ap. 66, 453.
Eggleton, P.P., and F. Verbunt. 1986. M.N.R.A.S. 220, 138.
Finzi, A. 1978. Astr. Ap. 62, 149.
Finzi, A., and R.A. Wolf. 1967. Ap. J. 150, 115.
Foss, D., R.A. Wade, and R.F. Green. 1990. preprint.
Fruchter, A.S., D.R. Stinebring, and J.H. Taylor. 1989. Nature, 333, 237.

Garcia, D., J. Labay, R. Canal, and J. Isern. 1990. *In:* Nuclear Astrophysics: Nuclei in the Cosmos, ed. H. Oberhummer and W. Hillebrandt (Garching b. München: MPI f. Astrophysik), p. 97.

Giacconi, R., H. Gursky, H. Kellogg, E. Schreier, and H. Tananbaum. 1971. Ap. J. (Letters) 167, L67.

Garcia-Berro, E., M. Hernanz, R. Mochkovitch, and J. Isern. 1988. Astr. Ap. 193, 141.

Godon, P., G. Shaviv, J. Ashkenazi, and A. Kovetz. 1989. *In:* White Dwarfs, ed. G. Wegner (Berlin: Springer-Verlag), p. 85.

Grindlay, J.E. 1987. *In:* The Origin and Evolution of Neutron Stars, ed. D.J. Helfand and J.-H. Huang (Dordrecht: Reidel), p. 173.

Hachisu, I., M. Kato, and H. Saio. 1989. Ap. J. (Letters) 342, L19.

Hansen, J.P., G.M. Torrie, and G.P. Vieillefosse. 1977. Phys. Rev. A 16, 2153.

Heggie, D.C. 1977. Comm. Ap. Space Phys., 7, 43.

Henyey, L., and L'Ecuyer, J. 1969. Ap. J. 156, 549.

Hernanz, M., J. Isern, R. Canal, J. Labay, and R. Mochkovitch. 1988. Ap. J., 324, 331.

Hernanz, M., J. Isern, R. Canal, and J. Labay. 1990. Ap. Space Sci. 169, 171.

Hertz, P., and J.E. Grindlay. 1983. Ap. J. 275, 105.

Hewish, A., S.J. Bell, J.D.M. Pilkington, P.F. Scott, and R.A. Collins. 1968. Nature 217, 709.

Hut, P., and J.N. Bahcall. 1983. Ap. J. 268, 319.

Iben, I. 1974. Ann. Rev. Astr. Ap. 12, 215.

Iben, I. 1990. Ap. J. in press.

Iben, I., and A.V. Tutukov. 1984a, Ap. J. Suppl. 54, 335.

Iben, I., and A.V. Tutukov. 1984b, Ap. J. 282, 615.

Iben, I., and A.V. Tutukov. 1990. *In:* Frontiers of Stellar Evolution, ed. D.L. Lambert (Provo: Astr. Soc. Pacific), in press.

Ichimaru, S., H. Iyetomi, and S. Ogata. 1988. Ap. J. (Letters) 334, L17.

Isern, J., R. Mochkovitch, Garcia-Berro, and M. Hernanz. 1991. Astr. Ap. 241, L29.

Isern, J., R. Canal, and J. Labay. 1991. Ap. J. (Letters) 372, L83.

Itoh, N., H. Totsuji, S. Ichimaru, and H.E. DeWitt. 1979. Ap. J. 234, 1079; erratum 1980. Ap. J. 220, 742.

Khokhlov, A.M. 1989. M.N.R.A.S. 239, 785.

Khokhlov, A.M. 1990. MPI preprint.

Kirzhnits, D.A. 1960. Sov. Phys. JETP 11, 356.

Koester, D. 1972. Astr. Ap. 16, 459.

Kovetz, A., and G. Shaviv. 1976. Astr. Ap. 52, 403.

Kulkarni, S.R. 1986. IAU Circ. N^o4160.

Kulkarni, S.R., and R. Narayan. 1988. Ap. J. 335, 775.

Kulkarni, S.R., R. Narayan, and R.W. Romani. 1990. Ap. J. 356, 174.

Kutter, G.S., and W.M. Sparks. 1980. Ap. J. 239, 988.

Lamb, D.Q., and H.M. Van Horn. 1975. Ap. J. 200, 306.

Landau, L.D., and E.M. Lifshitz. 1958. Statistical Physics (Oxford: Pergamon).

Langer, N., D. Sugimoto, and K.J. Fricke. 1983. Astr. Ap. 126, 207.

Lewin, W.H.G. 1977. Ann. NY Acad. Sci. 310, 210.

Lewin, W.H.G., and J. van Paradijs. 1985. Astr. Ap. 142, 361.

Lightman, A.P., and J.E. Grindlay. 1982. Ap. J. 262, 145.

Long, K.S., and L.P. van Speybroek. 1983. *In:* Accretion-Driven Stellar X-Ray Sources, ed. W.H.G. Lewin and E.P.J. van den Heuvel (Cambridge: Cambridge Univ. Press), p. 117.

Loumos, G.L., and W.B. Hubbard. 1973. Ap. J. 180, 199.

Maza, J., and S. van den Bergh. 1976. Ap. J. 204, 519.
MacDonald, J. 1983. Ap. J. 267, 732.
Mazzitelli, I., and F. D'Antona. 1986. Ap. J. 308, 706.
Mazzitelli, I., and F. D'Antona. 1987. *In:* The Second Conference on Faint Blue Stars, ed. A.G.D. Philip, D.S. Hayes, and J.W. Liebert (Schenectady: Davis Press), p. 351.
Mestel, L. 1952. M.N.R.A.S. 112, 583.
Mestel, L., and M.A. Ruderman. 1967. M.N.R.A.S. 136, 27.
Miller, D.L., and D. Branch. 1990. Astr. J., 100, 530.
Miyaji, S., K. Nomoto, K. Yokoi, and D. Sugimoto. 1980. Publ. Astr. Soc. Japan, 32, 303.
Miyaji, S., and K. Nomoto. 1987. Ap. J. 318, 307.
Mochkovitch, R. 1983. Astr. Ap. 122, 212.
Mochkovitch, R. 1984. *In:* Problems of Collapse and Numerical Relativity, ed. D. Banzel and M. Signore (Dordrecht: Reidel), p. 125.
Mochkovitch, R., and M. Livio. 1989. Astr. Ap. 209, 110.
Mochkovitch, R., E. Garcia-Berro, M. Hernanz, J. Isern, and J.F. Panis. 1990. Astr. Ap. 233, 456.
Müller, E., and W.D. Arnett. 1982. Ap. J. (Letters) 261, L107.
Müller, E., and W.D. Arnett. 1986. Ap. J. 307, 619.
Narayan, R., A.S. Fruchter, S.R. Kulkarni, and R.W. Romani. 1990. in Accretion-Powered Compact Binaries, ed. C.W. Mauche (Cambridge: Cambridge Univ. Press), p. 451.
Nomoto, K. 1982. Ap. J. 253, 798.
Nomoto, K. 1987. Ap. J. 322, 206.
Nomoto, K., F.-K. Thielemann, and K. Yokoi. 1984. Ap. J. 286, 644.
Nomoto, K., and I. Iben. 1985. Ap. J. 297, 531.
Ogata, S., and S. Ichimaru. 1987. Phys. Rev. A, 36, 5451.
Paczyński, B.E. 1971. Acta Astr. 21, 271.
Paczyński, B.E. 1985. *In:* Cataclysmic Variables and Low Mass X-Ray Binaries, ed. D.Q. Lamb and J. Patterson (Dordrecht: Reidel), p. 1.
Patterson, J. 1984. Ap. J. Suppl. 54, 443.
Phillips, M.M., et al. 1987. Publ. Astr. Soc. Pacific 99, 592.
Prialnik, D., M.M. Shara, and G. Shaviv. 1978. Astr. Ap. 62, 339.
Pollock, E.L., and J.P. Hansen. 1973. Phys. Rev. A, 8, 3110.
Rappaport, S.A., P.C. Joss, and R.E. Webbink. 1982. Ap. J. 254, 616.
Ratnatunga, K.U., and S. van den Bergh. 1989. Ap. J. 343, 713.
Robinson, E.L., and A.W. Shafter. 1987. Ap. J. 322, 296.
Romani, R.W. 1990. Ap. J. 357, 493.
Salpeter, E.E. 1954. Austral. J. Phys., 7, 373.
Salpeter, E.E. 1961. Ap. J. 134, 669.
Salpeter, E.E., and H.M. Van Horn. 1969. Ap. J. 155, 183.
Schatzman, E. 1948. J. Phys. Radium, 9, 46.
Schatzman, E. 1953. Ann. d'Ap., 16, 162.
Schramm, S., and S.E. Koonin. 1990. Ap. J. in press.
Schwarzschild, M. 1965. Structure and Evolution of the Stars (New York: Dover).
Shapiro, S.L., and S.S. Teukolsky. 1984. Black Holes, White Dwarfs, and Neutron Stars (New York: Wiley).
Shara, M.M., 1990. *In:* Cataclysmic Variables and Low Mass X-Ray Binaries, ed. C. Mauche (Cambridge: Cambridge University Press), in press.
Shara, M.M., M. Livio, A.F.J. Moffat, and M. Orio. 1986. Ap. J. 311, 163.

Shaviv, G., and A. Kovetz. 1976. Astr. Ap. 51, 383.
Shaviv, G., and S. Starrfield. 1987. Ap. J. (Letters) 321, L51.
Slattery, W.L., G.D. Doolen, and H.E. DeWitt 1981. Phys. Rev. A 21, 2087.
Sparks, W.M., and G.S. Kutter. 1987. Ap. J. 321, 394.
Spitzer, L. 1958. Ap. J. 127, 17.
Starrfield, S., J.W. Truran, and W.M. Sparks. 1978. Ap. J. 226, 186.
Starrfield, S., W.M. Sparks, and G. Shaviv. 1989. Ap. J. (Letters) 325, L235.
Stevenson, D.J. 1976. Phys. Lett, 58A, 282.
Stevenson, D.J. 1980. J. Phys. Suppl. $N^o 3$, 41, C2–61.
Stokes, G.H., J.H. Taylor, and R.J. Dewey. 1985. Ap. J. (Letters) 294, L21.
Strom, R.G. 1988. M.N.R.A.S. 230, 331.
Sutherland, P., and J.C. Wheeler. 1984. Ap. J. 280, 282.
Sweeney, M.A. 1976. Astr. Ap. 49, 375.
Taam, R.E., and E.P.J. van den Heuvel, 1986. Ap. J. 305, 235.
Takahara, M., M. Hino, T. Oda, K. Muto, A. Wolters, P.W.M. Glaudemans, and K. Sato. 1989. Nucl. Phys. A 504, 167.
Tammann, G.A. 1982. *In:* Supernovae: A Survey of Current Research, ed. M.J. Rees and R.J. Stoneham (Dordrecht: Reidel), p. 371.
Tavani, M. 1990. Ap. J. in press.
Tutukov, A.V., and L.R. Yungelson. 1973. Nauk. Inf. 27, 58.
van den S. Bergh, R.D. McClure, and R. Evans. 1987. Ap. J. 323, 44.
van den S. Bergh, and G.A. Tammann. 1991. Ann. Rev. Astron. Ap. in press.
van den Heuvel, E.P.J. 1974. *In:* Proc. Solvay Conf. Phys., 16th (Brussels: Univ. Brussels Press), p. 119.
van den Heuvel, E.P.J. 1983. *In:* Accretion-Driven Stellar X-Ray Sources, ed. W.H.G. Lewin, and E.P.J. van den Heuvel (Cambridge: Cambridge Univ. Press), p. 303.
van den Heuvel, E.P.J. 1988. Adv. Space Res. 8(2), 355.
van den Heuvel, E.P.J. 1989. *In:* Timing Neutron Stars, ed. H. Ögelman and E.P.J. van den Heuvel (Dordrecht: Kluwer), p. 523.
van den Heuvel, E.P.J., and J. Heise. 1972. Nature 239, 67.
Van Horn, H.M. 1968. Ap. J. 151, 227.
Verbunt, F. 1988. Adv. Space Res. 8(2), 529.
Verbunt, F. 1989. *In:* Timing Neutron Stars, ed. H. Ögelman and E.P.J. van den Heuvel (Dordrecht: Kluwer), p. 593.
Verbunt, F., and G. Meylan. 1988. Astr. Ap. 203, 297.
Verbunt, F., W.H.G. Lewin, and J. van Paradijs. 1989. M.N.R.A.S. 241, 51.
Warner, B. 1987. M.N.R.A.S. 227, 23.
Webbink, R.F. 1984. Ap. J. (Letters) 277, 355.
Wheeler, J.C. 1990. *In:* Frontiers of Stellar Evolution, ed. D.L. Lambert (Provo: Astr. Soc. Pacific), in press.
Wheeler, J.C., R.P. Harkness, Z. Barkat, and D. Swartz. 1986. Publ. Astr. Soc. Pacific 98, 1018.
Wheeler, J.C., and R.P. Harkness. 1990. Rep. Prog. Phys. 53, 1467.
Woosley, S.E. 1986. *In:* Nucleosynthesis and Chemical Evolution, ed. B. Hauck, A. Maeder, and G. Meynet (Geneva: Saas Fee Courses), p. 1.
Woosley, S.E. 1990. *In:* Supernovae, ed. A. Petschek (Berlin: Springer-Verlag), p. 182.
Woosley, S.E., T.A. Axelrod, and T.A. Weaver. 1984. *In:* Stellar Nucleosynthesis, ed. C. Chiosi and A. Renzini (Dordrecht: Reidel), p. 263.
Woosley, S.E., and T.A. Weaver. 1986. Ann. Rev. Astr. Ap. 24, 205.

COURSE V

TYPE I SUPERNOVAE AND EVOLUTION OF INTERACTING BINARIES

K. NOMOTO, H. YAMAOKA, T. SHIGEYAMA
S. KUMAGAI, AND T. TSUJIMOTO

Department of Astronomy, Faculty of Science
University of Tokyo
Bunkyo-ku, Tokyo 113, Japan

S. Bludman, R. Mochkovitch and J. Zinn-Justin, eds.
Les Houches, Session LIV 1990
Supernovae

Contents

1. Type I supernovae and related events 202

2. Evolution of accreting white dwarfs 204
   - 2.1. Hydrogen shell flashes 205
   - 2.2. Helium shell flashes 210
   - 2.3. Merging C+O white dwarfs 212

3. Type Ia supernovae 213
   - 3.1. Carbon deflagration model 213
   - 3.2. Deflagration/detonation hybrid models 215
   - 3.3. Carbon detonation in smaller mass white dwarfs 218
   - 3.4. Light curves 219
   - 3.5. Spectra 223

4. Accretion–induced collapse of white dwarfs 225
   - 4.1. Low mass x-ray binaries and binary pulsars 225
   - 4.2. Solid C+O white dwarfs 226
   - 4.3. O+Ne+Mg white dwarfs 227
   - 4.4. Conditions for accretion-induced collapse 230

5. Type Ib/Ic supernovae 232
   - 5.1. Evolution of interacting binaries 233
   - 5.2. Nucleosynthesis 234
   - 5.3. Rayleigh-Taylor instabilities and mixing 235
   - 5.4. Light curves 238

6. Evolutionary origin of binary pulsars 241

7. Concluding remarks 245

References 246

1. Type I supernovae and related events

Supernovae have been spectroscopically classified into Type I and Type II according to the absence and presence of hydrogen in their optical spectra. Type I supernovae (SNe I) are further subclassified into Ia, Ib, and Ic. As shown in fig. 1 (Branch et al. 1991), the early-time ($t \sim 1$ month past maximum) photospheric spectra of SNe I define such subtypes. SNe Ia are characterized by the presence of a deep absorption trough near 6150 Å, produced by blueshifted Si II λ6355. SNe Ib and Ic, by contrast, do not show this line. Moderately strong He I lines, especially He I λ5876, distinguish SNe Ib from SNe Ic at early times; i.e., SNe Ib exhibit absorption lines of [He I], whereas these lines are absent in SNe Ic (see Harkness and Wheeler 1990 for a review). Type II supernovae (SNe II) are subclassified into SNe II-P (*plateau*), SNe II-L (*linear*), and SNe II-BL (*bright linear*) according to the light curve shape (Branch et al. 1991).

The late-time ($t \sim 5$–10 months) optical spectra of SNe provide additional constraints on the classification scheme (fig. 2, Branch et al. 1991). SNe Ia show strong blends of Fe emission lines. SNe Ib and Ic, on the other hand, are dominated by emission lines of intermediate-mass elements such as [O I], [Ca II], and Ca II. SNe II are dominated by the strong Hα emission line.

Supernova classification has become more complicated since the discovery of SN 1987K, whose spectral classification changed from Type II to Type Ib/Ic as it aged; it has since been referred to as SN IIb (Filippenko 1988). Hydrogen feature has also been identified in the early time spectrum of SNe Ic 1987M (fig. 3, Jeffery et al. 1991) and 1991A (Filippenko 1991). Interestingly, the early time spectra of SN 1987K are very similar to SNe Ic (1983V and 87M) (fig. 4, Filippenko et al. 1990; Wheeler and Harkness 1990).

The lack of strong hydrogen lines implies that the progenitors of SNe I have lost most of their hydrogen-rich envelope at the time of explosion. Two cases are possible: (1) mass lost to the companion star during the evolution of a close binary system, and (2) stellar-wind type mass loss from a single star. For these cases, we basically have three candidates for the progenitors

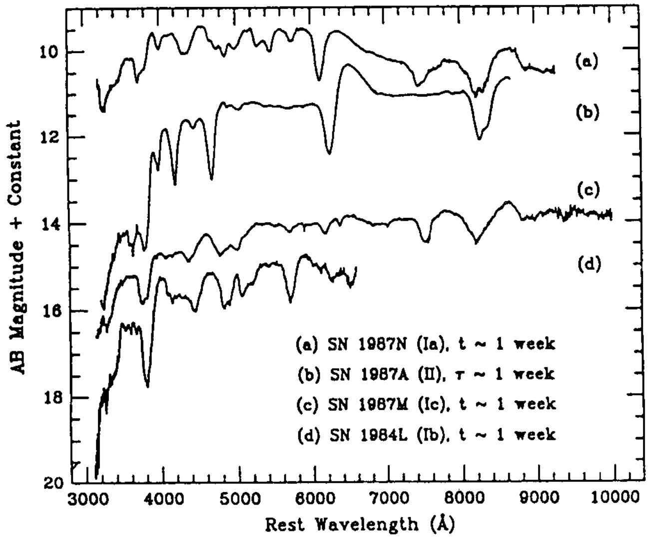

Fig. 1. Spectra of supernovae, showing the early-time distinctions between the four major types and subtypes (Branch et al. 1991). The variable t is taken to indicate time after observed visual maximum, whereas τ represents time after core collapse. AB magnitude $= -2.5 \log f_{\nu} - 48.6$, where the units of f_{ν} are ergs s^{-1} cm^{-2} Hz^{-1}.

of SNe I: (1) white dwarfs, (2) helium stars in binaries, and (3) single Wolf-Rayet stars. Because of complicated mass-loss processes, it has not been easy to identify the exact evolutionary origin of SNe I.

For SNe Ia, accreting white dwarfs have been considered promising candidates of their progenitors. The explosion mechanism originally suggested by Hoyle and Fowler (1960), that is, thermonuclear explosion of electron-degenerate cores, has been basically confirmed by extensive numerical modeling, and by comparison with observations (Nomoto 1986a; Woosley and Weaver 1986b). However, the exact evolution that leads to SNe Ia and the detailed process of thermonuclear explosion need further studies as discussed in sections 2 and 3.

In some binary systems, the white dwarf may undergo accretion-induced collapse (AIC) rather than explosion. The conditions for AIC are examined in section 4 in relation to the origin of binary millisecond pulsars.

For SNe Ib/Ic, models of low-mass helium star explosion in close binaries are presented in section 5. As a related topic, the formation of double neutron star systems is discussed in section 6.

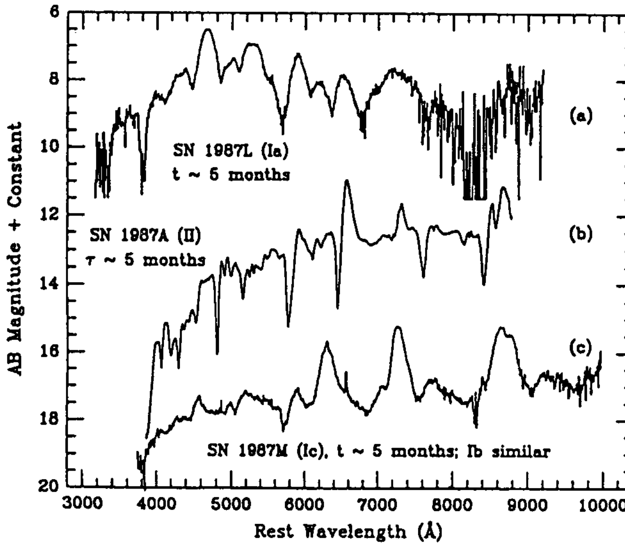

Fig. 2. Spectra of supernovae, showing late time distinctions between different types and subtypes (Branch et al. 1991). Notation is the same as in fig. 1. The SN Ia 1987N (fig. 1) was spectroscopically similar to SN 1987L, shown above. At even later phases, SN 1987A was dominated by strong emission lines of Hα, [O I], [Ca II], and the Ca II near-infrared triplet, with only a weak continuum.

2. Evolution of accreting white dwarfs

Isolated white dwarfs are simply cooling stars that eventually end up as invisible frigid stars. The white dwarf in a close binary system evolves differently because the companion star expands and transfers matter over to the white dwarf at a certain stage of its evolution. Mass accretion can *rejuvenate* the cold white dwarf (e.g., Nomoto and Sugimoto 1977), which in some cases could lead to a SNe Ia or AIC.

The scenario that possibly brings a close binary system to a SN Ia or AIC is as follows (although the exact evolutionary origin is not understood). Initially, the close binary system consists of two intermediate mass stars ($M \lesssim 8\ M_\odot$). As a result of Roche lobe overflow, the primary star of this system becomes a white dwarf composed of carbon and oxygen (C+O). When the secondary star evolves, it begins to transfer hydrogen-rich matter over to the white dwarf.

Mass accretion onto the white dwarf releases gravitational energy at the white dwarf surface. Most of the released energy is radiated away from

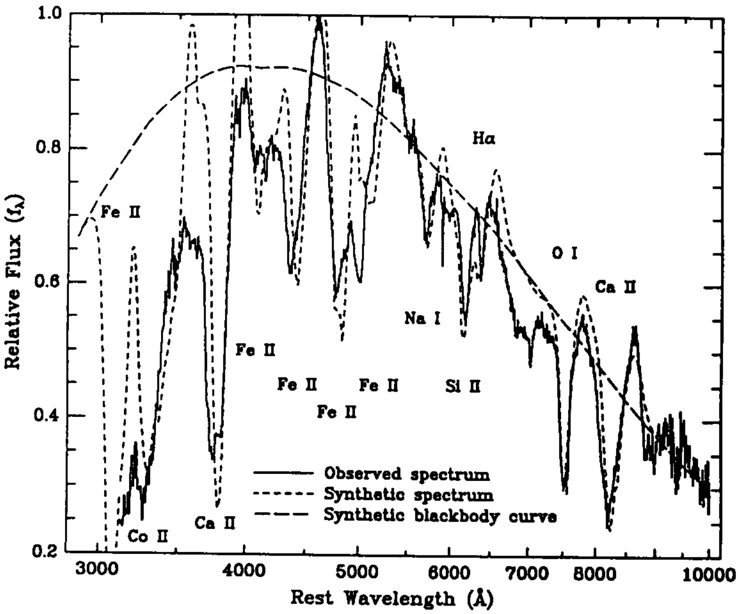

Fig. 3. The observed spectrum of SN Ic 1987M compared to a synthetic spectrum (Jeffery et al. 1991).

the shocked region as UV, and does not contribute much to heating the white dwarf interior. Continuing accretion compresses the previously accreted matter and releases gravitational energy in the interior. A part of this energy is transported to the surface and radiated away from the surface (*radiative cooling*), but the rest goes into thermal energy of the interior matter (*compressional heating*). Thus, the interior temperature of the white dwarf is determined by competition between compressional heating and radiative cooling; i.e., the white dwarf is hotter if the mass accretion rate $\dot{M}$ is larger, and vice versa (e.g., Nomoto and Hashimoto 1987).

2.1. Hydrogen shell flashes

When a certain amount of hydrogen $\Delta M_{\rm H}$ accumulates at the white dwarf surface, hydrogen shell burning is ignited. Figure 5 shows $\Delta M_{\rm H}$ at ignition as a function of $\dot{M}$ and M; $\Delta M_{\rm H}$ is smaller for larger $\dot{M}$ and larger M due to higher temperatures and higher pressures (eq. 2) in the accreted envelope. Here, compressional heating due to accretion is just balanced with cooling due to heat conduction (Nariai and Nomoto 1979; Nomoto 1982a). The type

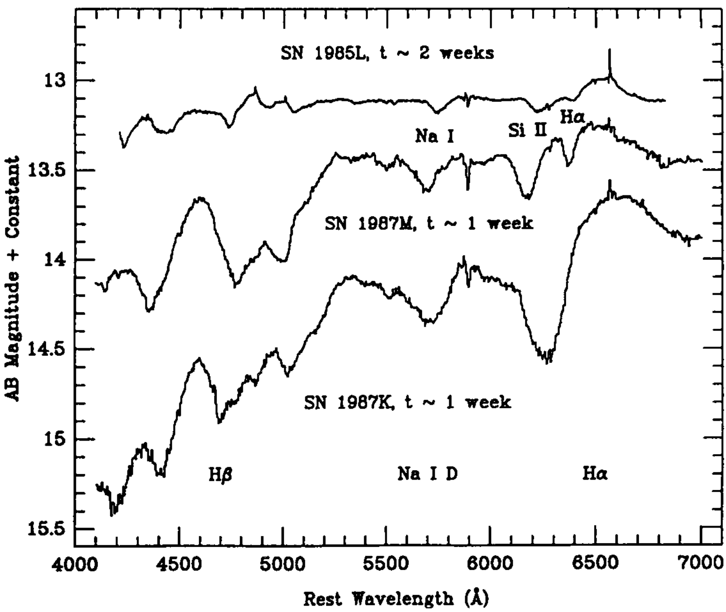

Fig. 4. Comparison of the observed spectra of SN Ic 1987M, SN IIb 1987K, and SN II 1985L (Filippenko et al. 1990; Jeffery et al. 1991).

and strength of hydrogen shell burning depends sensitively on $\dot{M}$ as follows.

(1) *Rapid accretion forming a red-giant-like envelope.* When accretion is rapid, and $\dot{M} \gtrsim \dot{M}_{\rm RH}$, the accreted matter is too hot to be swallowed by the white dwarf, and forms a red-giant-like envelope (fig. 6, Nomoto et al. 1979b). The critical rate, $\dot{M}_{\rm RH}$, corresponds to the growth rate of a degenerate core in red giant stars, due to hydrogen shell burning. Paczynski's (1970) relation of core mass to luminosity, assuming hydrogen abundance of $X = 0.7$, gives

$$(\dot{M})_{\rm RH} = 8.5 \times 10^{-7}(M/M_\odot - 0.52) \quad M_\odot{\rm yr}^{-1} \tag{1}$$

for $0.60 \leq M/M_\odot \leq 1.39$, where the core mass is replaced by the white dwarf mass M.

The matter would form a common envelope, which is eventually lost from the system. As a result of mass and angular momentum losses from the system, some binaries would form a pair of white dwarfs. Further evolution of such a double white dwarf system is driven by gravitational wave radiation, and leads to a Roche lobe overflow of the smaller mass white dwarf (Iben

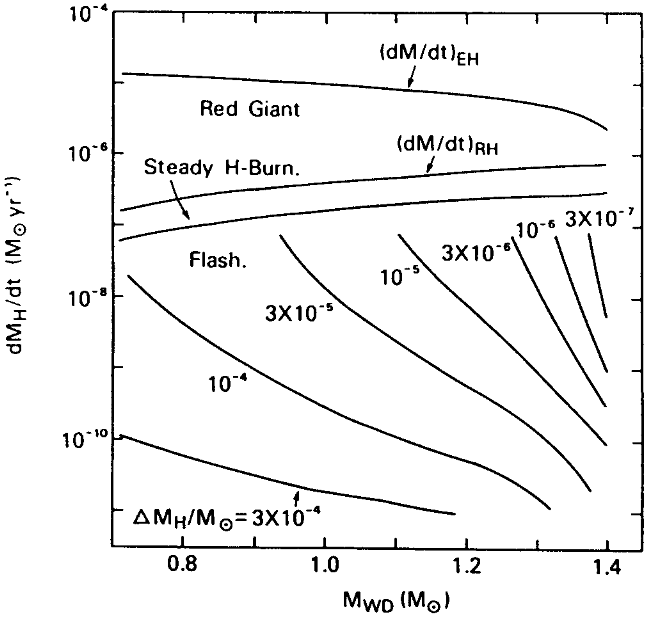

Fig. 5. Types and strength of hydrogen shell burning as a function of accretion rate and the white dwarf mass (Nomoto 1982).

and Tutukov 1984; Webbink 1984). Subsequent merging of the white dwarfs is discussed in section 2.3.

(2) *Steady burning.* For accretion rates in the range of 0.4 $\dot{M}_{\rm RH} \lesssim \dot{M} \lesssim \dot{M}_{\rm RH}$, hydrogen shell burning is stable (e.g., Sienkiewicz 1980). The radius depends very sensitively on $\dot{M}$, ranging from red-supergiant size to white dwarf size. Such hydrogen burning processes accreted matter into helium at a rate of $\dot{M}$.

(3) *Recurrence of flashes.* When the accretion rate is lower than 0.4 $\dot{M}_{\rm RH}$, hydrogen shell burning becomes unstable and flashes. The progress and the strength of the flashes is determined by two parameters (P^*, Ω^*),

$$P^* = \frac{GM\Delta M_{\rm H}}{4\pi r^4} \qquad \Omega^* = \frac{GM}{r} \tag{2}$$

i.e., by pressure and potential at the burning shell corresponding to a completely *flat* configuration (Sugimoto and Fujimoto 1978; Sugimoto et al. 1979). A set of (P^*, Ω^*) can be transformed into $(M, \Delta M_{\rm H})$ since the radius r at the burning shell is well approximated by the radius of the white dwarf, which is determined only by M.

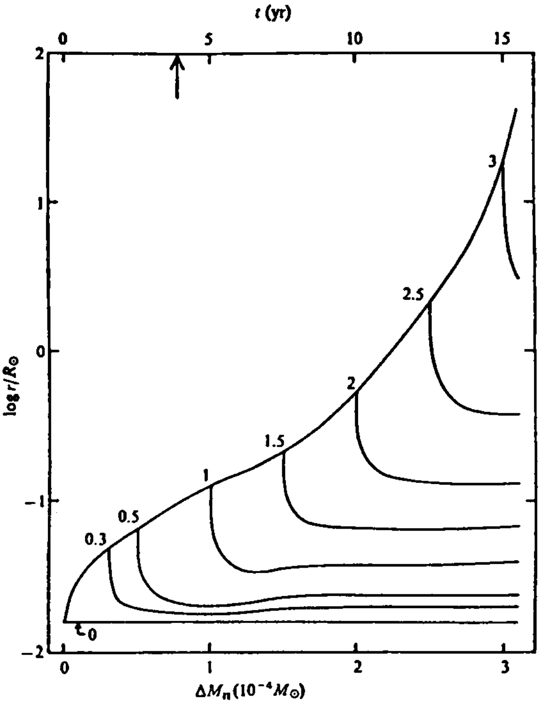

Fig. 6. Increase in the radius of an accreting white dwarf upon rapid accretion (Nomoto et al. 1979a).

Progress of the shell flash can be treated semi-analytically. Initially, the temperature at the burning shell increases along $P = P^*$. As nuclear energy is released, the pressure decreases as a result of expansion described by $P = fP^*$. Here, the flatness parameter f is unity for plane-parallel configuration, and $f < 1$ for more spherical configurations. This is expressed as

$$\frac{1}{f(V,N)} = \sum_{k=0}^{\infty} b_k \qquad b_0 = 1 \qquad b_k = b_{k-1}\frac{k+3}{N+k+1}\frac{N+1}{V} \tag{3}$$

$$V = r/H_p$$

where N and H_p denote the polytropic index for the convective envelope and the scale height of pressure, respectively (Sugimoto and Fujimoto 1978). As specific entropy s in the hydrogen-burning shell increases, f decreases due to increasing H_p, that is, expansion of the accreted envelope. (This corresponds to the change in configuration of the burning shell from plane-parallel to spherical.) Then the temperature reaches its maximum T_H^{max}, which is higher for higher P^* and thus for higher M (smaller r) and larger $\Delta M_{\rm H}$ (eq. 2). Such a relation between $T_{\rm H}^{\rm max}$ and $\Delta M_{\rm H}$ for several M obtained from eq. (3) is shown in fig. 7 (Sugimoto et al. 1979). Results of hydrodynamical calculations (X-mark) are in excellent agreement with the corresponding analytical predictions (filled circles). (Some discrepancies are likely to be caused by a coarse zoning in numerical calculations).

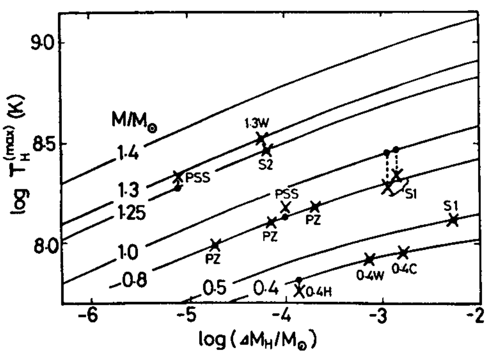

Fig. 7. Maximum temperature attained during the hydrogen shell flash as a function of accreted mass $\Delta M_{\rm H}$ and white dwarf mass M. Analytical values (solid curves) are compared with values obtained by hydrodynamical calculations (X-mark) (see Sugimoto et al. 1979 for details).

The results in figs. 5 and 7 show that generally smaller M and higher $\dot{M}$ lead to a weaker flash, because of the lower pressure at the flashing shell. The flash would induce little mass ejection so a large portion of the accreted matter could be processed into helium for $\dot{M} \approx 2 \times 10^{-7} - 10^{-8}$ $M_\odot$ yr^{-1}.

For slow accretion ($\dot{M} \lesssim 1 \times 10^{-9}$ $M_\odot$ yr^{-1}), hydrogen shell flash is strong enough to grow into a *nova* explosion, which leads to ejection of most of the accreted matter from the white dwarf (e.g, Nariai et al. 1980 and references therein). For these cases, the white dwarf does not become a *supernova*, since its mass hardly grows. However, if white dwarfs are close to the Chandrasekhar mass, novae could grow into AIC of SN Ia because the ejected mass from nova explosions is found to be significantly smaller than the accreted mass (Starrfield et al. 1991).

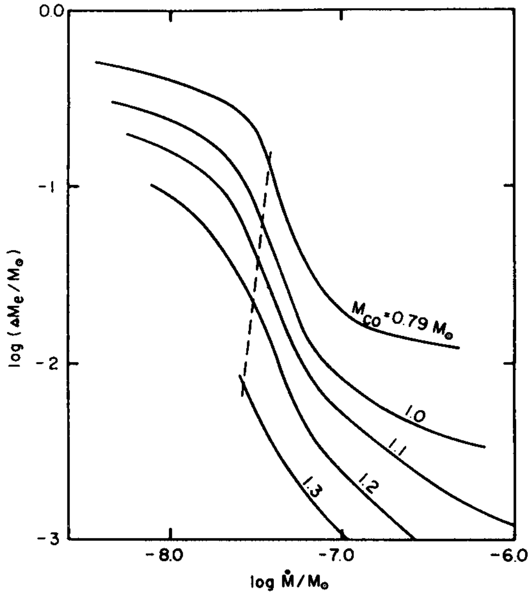

Fig. 8. The mass of accreted helium envelope, $\Delta M_{\rm He}$, at the helium ignition as a function of $\dot{M}$ and the mass of underlying C+O core, $M_{\rm CO}$ (Kawai et al. 1987).

2.2. Helium shell flashes

Suppose that a helium layer grows on the white dwarf as a result of hydrogen shell burning or (if the companion is a helium star) by direct transfer of helium (e.g., Iben et al. 1987). When a certain mass $\Delta M_{\rm He}$ is accumulated, helium shell burning is ignited; the solid lines in fig. 8 show $\Delta M_{\rm He}$ as a function of $\dot{M}$ and the white dwarf masses M (Kawai et al. 1987). The maximum temperature attained during the helium shell flash depends on $\Delta M_{\rm He}$ and M (fig. 9; Fujimoto and Sugimoto 1982) as discussed for hydrogen in section 2.1. The strength of the helium flash depends mainly on $\dot{M}$ as follows.

If the accretion of helium is as slow as $\dot{M} \lesssim 1 \times 10^{-9}$ $M_\odot$ yr^{-1}, the material is too cold to ignite helium burning, so the white dwarf mass is increased. Cases where $M_{\rm CO} \lesssim 1.1$ $M_\odot$ are an exception if pycnonuclear helium burning is ignited (Nomoto 1982a,b).

For $\dot{M}_{\rm det} \gtrsim \dot{M} \gtrsim 10^{-9}$ $M_\odot$ yr^{-1}, helium shell flash is strong enough to initiate an off-center helium detonation, which prevents the white dwarf mass from growing (e.g., Nomoto 1982b; Woosley et al. 1986; Iben and Tutukov 1991). Here we adopt $\dot{M}_{\rm det}$ $\sim 1 \times 10^{-8}$ $M_\odot$ yr^{-1}, since the ^{14}N(e$^-$,

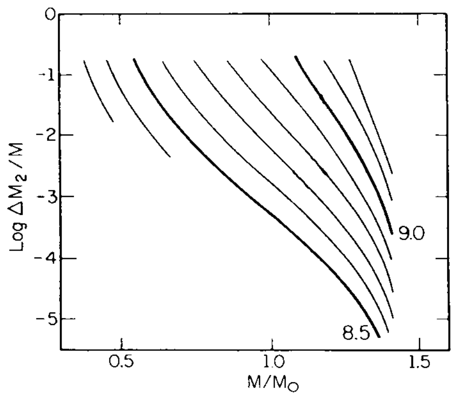

Fig. 9. Maximum temperature log T (K) attained during the helium shell flash as a function of the accreted mass ΔM_2 and the white dwarf mass M (Fujimoto and Sugimoto 1982).

$\nu)^{14}$C$(\alpha, \gamma)^{18}$O (NCO) reaction ignites weak helium flashes (Hashimoto et al. 1986; Limongi and Tornambe 1991) if the mass fraction of CNO elements in the accreting material exceeds 0.005. For smaller CNO abundances, the NCO reaction is not effective and thus $\dot{M}_{\rm det} \sim 4 \times 10^{-8}$ $M_\odot$ yr^{-1} (Nomoto 1982a). Two dimensional hydrodynamical simulations after the initiation of helium detonation have recently been performed by Dgani and Livio (1990) and Livne and Glasner (1991).

For intermediate accretion rates (3×10^{-6} $M_\odot$ yr^{-1} $\gtrsim \dot{M} \gtrsim 1 \times 10^{-8}$ $M_\odot$ yr^{-1}), helium flashes are of moderate strength, thereby recurring many times increasing the white dwarf mass (Taam 1980; Fujimoto and Sugimoto 1982). When the white dwarf mass becomes close to the Chandrasekhar mass, either collapse or thermonuclear explosion would occur.

For C+O white dwarfs, whether they explode or collapse depends not only on $\dot{M}$ but also on the initial mass $M_{\rm CO}$. For $M_{\rm CO} < 1.2$ $M_\odot$, substantial heat inflow from the surface layer into the central region ignites carbon at relatively low central density ($\rho_{\rm c} \sim 3 \times 10^9$ g cm^{-3}), which make SNe Ia, as will be discussed in section 3 (Nomoto et al. 1984). On the other hand, if the white dwarf is sufficiently massive and cold at the onset of accretion, the central region is compressed only adiabatically, thereby being cold (and solid) when carbon is ignited in the center of density, which can be as high as 10^{10} g cm^{-3}. The fate of the white dwarf after ignition at high densities is discussed in section 4.

2.3. Merging C+O white dwarfs

Merging of double C+O white dwarfs is estimated to take place as frequently as SNe Ia (Iben and Tutukov 1984; Webbink 1984). After the smaller mass white dwarf fills its Roche lobe, mass transfer of carbon onto the more massive white dwarf would be very rapid (Iben 1988). This ignites off-center carbon burning if $\dot{M} \gtrsim 2.7 \times 10^{-6}$ $M_\odot$ yr^{-1} in spherical accretion models (Nomoto and Iben 1985). In a steady accretion approximation (Kawai et al. 1987), the mass of the C+O white dwarf M, and the mass overlying carbon-burning shell ΔM_e are determined by $\dot{M}$, as seen in fig. 10. For $\dot{M} \sim \dot{M}_{\rm Edd}$, that is, carbon ignition takes place for the white dwarf with $M \sim 1.06 M_\odot$.

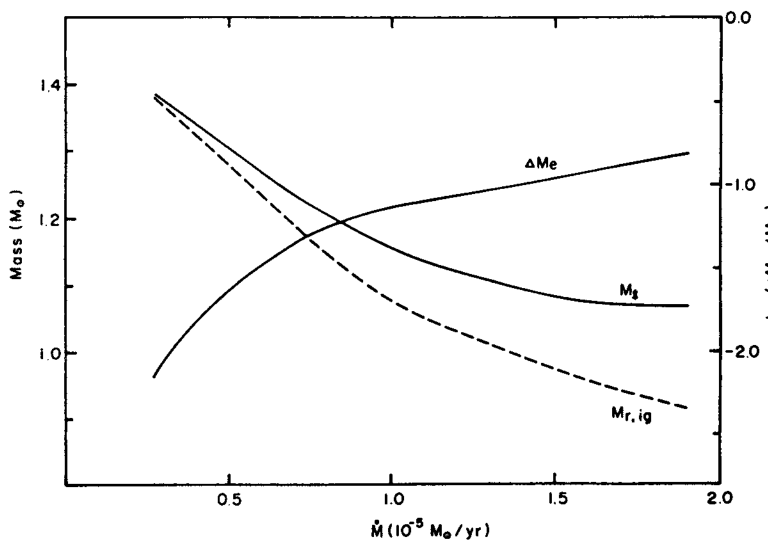

Fig. 10. The white dwarf mass (M), the location of the carbon ignition shell ($M_{r,ig}$), and $\Delta M_e = M - M_{r,ig}$ at the carbon ignition as a function of $\dot{M}$ (10^{-5} $M_\odot$ yr^{-1}) (Kawai et al. 1987).

The actual merging process would be more complicated and its fate is not clear yet. For the possible models of SNe Ia see section 3.3, and for AIC see section 4.4.

3. Type Ia supernovae

3.1. Carbon deflagration model

When carbon is ignited at the center of a white dwarf whose mass is close to the Chandrasekhar mass, carbon burning is so explosive as to incinerate the material into iron-peak elements and the central temperature reaches $\sim 10^{10}$ K. At a high central density such as $\gtrsim 10^9$ g cm^{-3}, nuclear energy release is only $\sim$ 20 % of the Fermi energy of degenerate electrons. Therefore, the resulting shock wave is not strong enough to directly ignite carbon in the adjacent layer. In other words, a *detonation* wave that propagates at supersonic speed does not form.

Instead, the interface between the burned and unburned layers becomes convectively unstable. As a result of mixing with the hot material, fresh carbon is ignited. In this way, a carbon-burning front propagates outward on the time scale for convective heat transport (Nomoto et al. 1976, 1984; Woosley and Weaver 1986a, 1986b). This kind of explosive burning front that propagates at a subsonic speed is called *a convective deflagration* wave. In the model W7 (Nomoto et al. 1984), propagation speed of the convective deflagration wave is on the average about one-fifth of the sound speed. It takes about one second for the front to reach the surface region, significantly slower than the supersonic detonation wave. Hence, the white dwarf expands during the propagation of the deflagration wave (fig. 11).

Behind the deflagration wave, the material undergoes the explosive burning of silicon, oxygen, neon, and carbon, depending on the peak temperatures (fig. 12). In the inner layer, nuclear reactions are rapid enough to incinerate the material into iron-peak elements, mostly ^{56}Ni. When the deflagration wave arrives at the outer layers, the density it encounters has already decreased due to expansion of the white dwarf. At such low densities, the peak temperature is too low to complete silicon burning, and thus only Ca, Ar, S, and Si are produced from oxygen burning. In the intermediate layers, explosive burning of carbon and neon synthesizes S, Si, and Mg. In the outermost layers, the deflagration wave dies and C+O remain unburned. The composition structure after freeze-out is shown as a function of M_r and the expansion velocity $v_{\rm exp}$ in figs. 13 (Thielemann et al. 1986) and 14 (Wheeler and Harkness 1990).

In the carbon deflagration model W7, the amount of ^{56}Ni produced is $M_{\rm Ni} = 0.58\ M_\odot$, and the explosion energy is $E = 1.3 \times 10^{51}$ erg. (Nuclear energy release – Binding energy of the white dwarf). The nuclear energy release is large enough to disrupt the white dwarf completely, and no compact star is left behind.

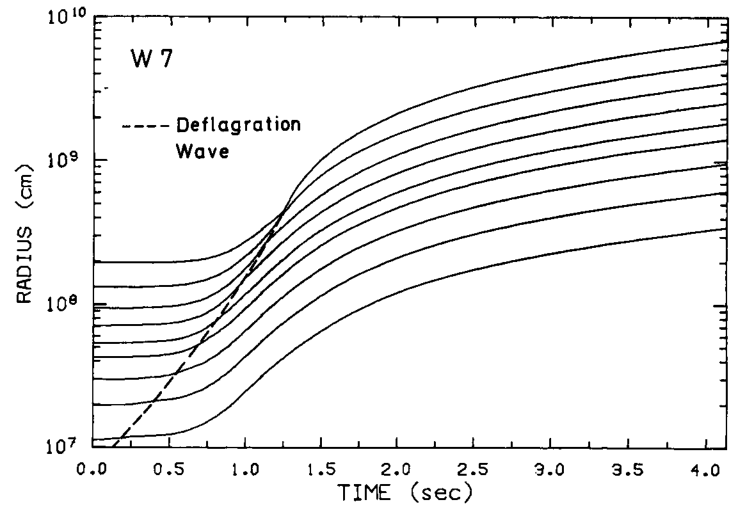

Fig. 11. Propagation of the carbon deflagration wave (dashed line) and associated expansion of the white dwarf (model W7) (Nomoto et al. 1984). The solid lines correspond to $M_r/M_\odot$ = 0.007, 0.03, 0.10, 0.25, 0.41, 0.70, 1.00, 1.28, 1.378, respectively.

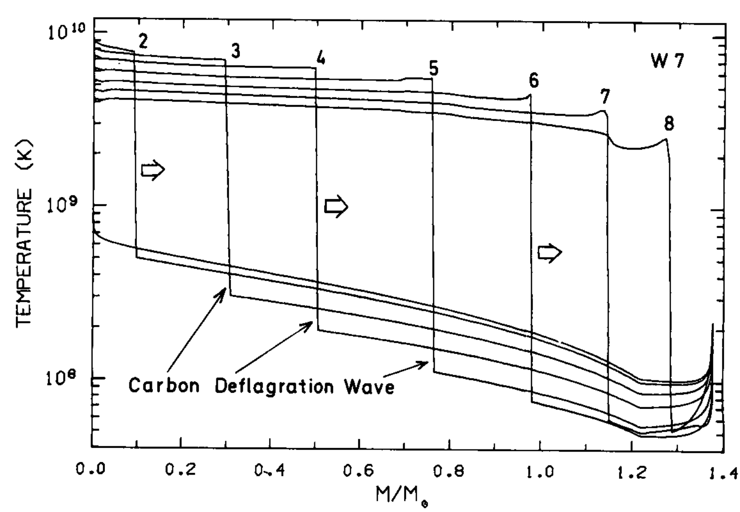

Fig. 12. Change in the temperature distribution during the propagation of the carbon deflagration wave (W7) (Nomoto et al. 1984).

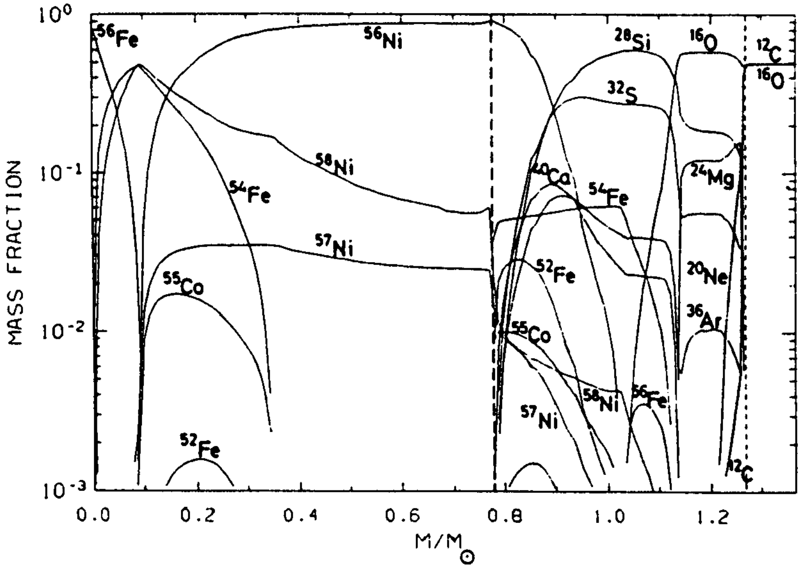

Fig. 13. Composition of a carbon deflagration model W7 for Type Ia supernovae as a function of interior mass (Thielemann et al. 1986).

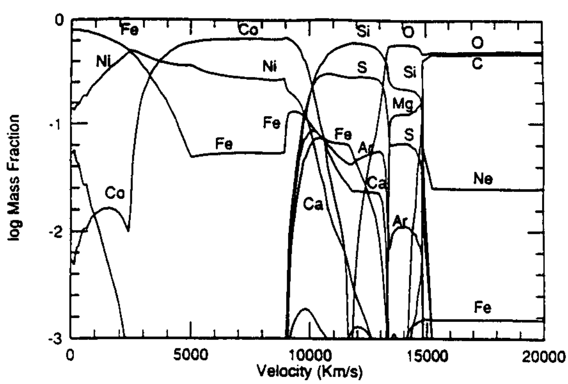

Fig. 14. Same as Fig. 13 but with respect to the expansion velocity (Wheeler and Harkness 1990).

3.2. Deflagration/detonation hybrid models

The outcome of carbon deflagration depends on its propagation speed, which is highly uncertain and involves parameters such as the mixing length of convection (see Müller and Arnett 1986 for 2D simulation). The preceding standard model W7 has been chosen because it accounts well for the observed light curve and spectra at both early and late times in SN Ia. In view of uncertainties involved in presupernova evolution, initiation of carbon detonation/deflagration (Barkat 1991), and propagation of the burning front, it would be necessary to explore other possible models of thermonuclear explosion to compare with the observed spectra and light curves of SNe Ia (sections 3.4–3.5).

If the propagation speed of the deflagration wave is much slower than in W7, the hydrodynamical behavior is very different. Figures 15 and 16 show the expansion and oscillation of the white dwarf for propagation speeds 20 times smaller than in W7, that is, about 1/100 of the sound speed, on the average (Nomoto et al. 1976). The white dwarf expands to quench nuclear burning at stage 6, where the total energy is still negative. Then the star contracts to burn more material, although the densities in fig. 16 are too low to produce additional ^{56}Ni. This makes the total energy positive ($\sim 5 \times 10^{49}$ erg s^{-1}). Eventually the white dwarf is completely disrupted with $M_{\rm Fe} \sim 0.15\ M_{\odot}$.

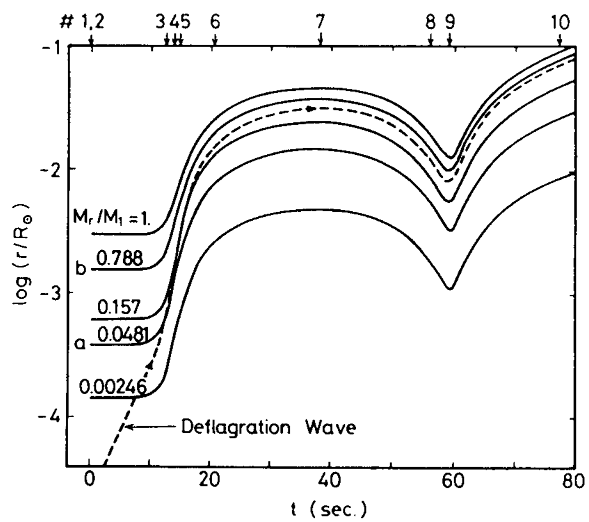

Fig. 15. Expansion and oscillation of the white dwarf induced by a slow carbon deflagration (Nomoto et al. 1976); the deflagration speed is about 1/20 of W7 in figs. 11–14. Eventually it is disrupted completely with no compact star remnant.

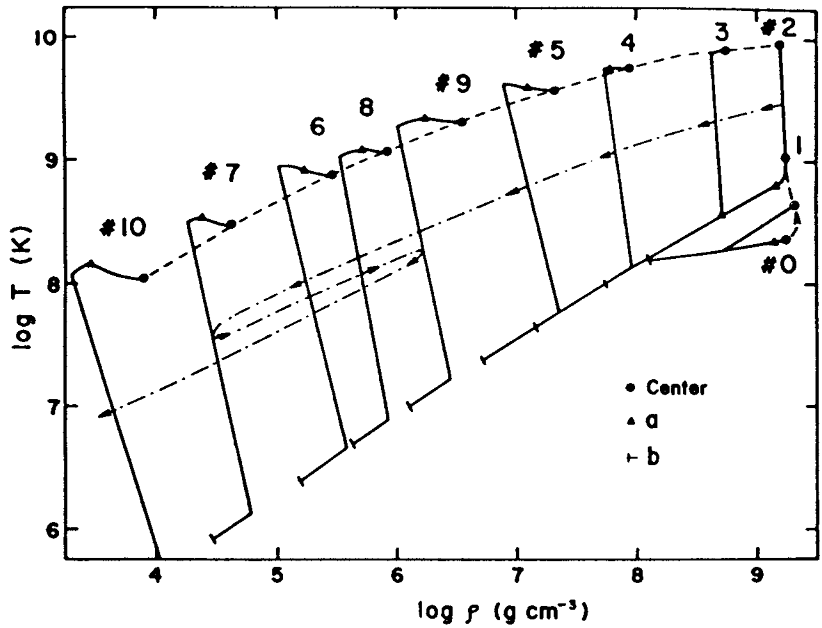

Fig. 16. Changes in the structure line in a density–temperature diagram for the same model shown in fig. 15. The dash-dotted curve shows the propagation of the deflagration wave.

Such a slow propagation model with oscillation produces too little kinetic energy of explosion to account for SN Ia. However, the deflagration wave might be changed into a detonation at low density layers during expansion or contraction (*delayed detonation model*; Khokhlov 1991a, 1991b; Woosley and Weaver 1991). Figure 17 shows a composition structure of such a delayed detonation model as a function of expansion velocity and M_r; here, the transition from deflagration to detonation is assumed to occur when the density at $M_r = 0.6\ M_\odot$ decreases to 3×10^7 g cm^{-3} (Shigeyama et al. 1991b; Nomoto et al. 1991). The composition structure with respect to M_r is not so different from W7 (including some unburned C and O), but Si and Ca layers extend to expansion velocities higher than 15,000 km s^{-1}.

Note, however, that this hybrid model introduces an additional parameter, the deflagration/detonation transition, and has a rather strong constraint on the initial central density of the white dwarf ($\lesssim 2 \times 10^9$ g cm^{-3}) to avoid overproduction of ^{64}Cr (Khokhlov 1991b).

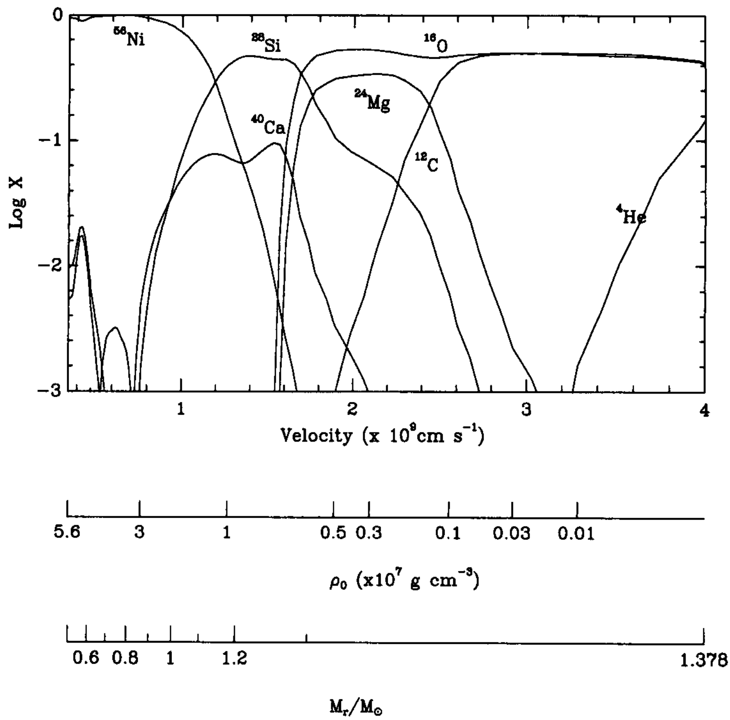

Fig. 17. Composition of a delayed detonation model as functions of the expansion velocity, M_r, and the initial density (Shigeyama et al. 1991b).

3.3. Carbon detonation in smaller mass white dwarfs

The above models assume that white dwarf mass increases to $\sim$ 1.4 $M_\odot$ when carbon ignites at the center. There is a possibility that an explosive carbon ignition occurs in smaller mass C+O white dwarfs. In the merging scenario, the initial mass of the white dwarf is likely to be around 1.0 $M_\odot$ if it is formed from BB binary evolution. In this case, a star with an initial mass of 5 to 8 $M_\odot$ becomes a helium star of 1.5 to 2 $M_\odot$, which greatly expands to undergo the Roche lobe overflow when its degenerate C+O core grows to $\sim$ 1 $M_\odot$ (see Sugimoto and Nomoto 1980; Nomoto 1982c; and references therein). Suppose that a merging of double white dwarfs ignites an off-center carbon flash which produces a shock wave. (This could happen if convective energy transport during the carbon flash is much less efficient than in the previous calculations, or if dynamic effects during merging are rather large (see Iben 1988, and Wheeler and Harkness

1990). The shock wave might propagate toward the central region and increase its strength because of decreasing area at the shock front. Then in the central region it might become strong enough to ignite explosive carbon burning, which would form either a deflagration or detonation. For stronger shock and lower central density, a detonation would be more likely the case.

This scenario, although highly hypothetical, could lead to the formation of a carbon detonation wave for white dwarfs of masses as small as $\sim$ 1 to 1.2 $M_\odot$ with the central densities as low as 2 to 6 $\times$ 10^7 g cm^{-3}. For example, white dwarf with M = 1.03, 1.05, and 1.07 $M_\odot$ have central densities of 2.5, 3, and 4 $\times$ 10^7 g cm^{-3}, respectively. For these white dwarfs, carbon detonation produces 0.49, 0.56, and 0.68 $M_\odot$ ^{56}Ni, and kinetic energies of 1.22, 1.26, and 1.33 $\times$ 10^{51} ergs, respectively (Shigeyama et al.1991a). Because of low central densities, nucleosynthesis in the detonation wave should produce a significant quantity of intermediate mass elements. Figure 18 shows composition distribution as a function of M_r and the expansion velocity for carbon detonation in the 1.05 $M_\odot$ white dwarf (see Shigeyama et al.1991a for $M = 1.03$ $M_\odot$). The outer layers are Si-rich, which is similar to W7, but Si and Ca layers extend to expansion velocities higher than 15,000 km s^{-1}, which are common to the delayed detonation models (fig. 17).

The above nucleosynthesis is different from almost complete incineration by carbon detonation in a white dwarf near the Chandrasekhar limit (Arnett 1969), and helium detonation in helium white dwarfs (Nomoto and Sugimoto 1977; Woosley et al. 1986). The absence of an outer helium layer leads to a Si-rich surface layer; this is different from the carbon detonation induced by off-center helium detonation, which produces ^{56}Ni at velocities which are too high to be compatible with observations (Livne 1990; Livne and Glasner 1991).

The isotopic ratios of integrated abundances of ejecta after decay of unstable nuclei are shown with respect to solar abundances in fig. 19 for M = 1.05 $M_\odot$ (Shigeyama et al.1991b). Because of low neutron excess in the central region, overproductions of ^{54}Fe, ^{58}Ni, and ^{64}Cr are not observed, and the isotopic ratios of iron peak elements are within a factor of 2 relative to the solar ratios. This is an important difference from the carbon deflagration/detonation models with $M \sim 1.4$ $M_\odot$.

3.4. Light curves

In the exploding white dwarf, released nuclear energy (minus initial binding energy of the white dwarf) is transformed into kinetic energy of expansion, and without a late-time energy source the star could not be as bright as a

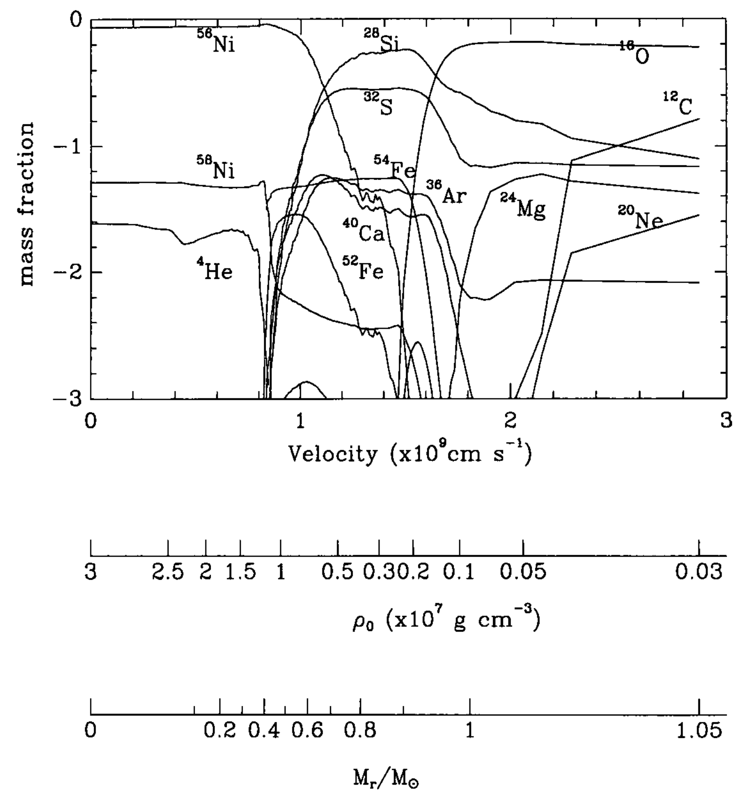

Fig. 18. Composition of a carbon detonation model of the 1.05 $M_\odot$ white dwarf as functions of the expansion velocity, M_r, and the initial density of the white dwarf.

supernova. However, during the expansion phase, ^{56}Ni decays into ^{56}Co with a half-life of 6.6 days, and ^{56}Co decays into ^{56}Fe with a half-life of 77 days. These radioactive decays produce γ-rays and positrons whose energies power the light curve as follows.

Gamma-rays originating from radioactive decays are degraded into X-rays by multiple Compton scatterings. Photoelectric absorption of x-rays and collisional ionization due to energetic electrons eventually heats up the expanding materials and produce optical light as clearly observed in SN 1987A (e.g., Kumagai et al. 1989; Shigeyama et al. 1988; Shigeyama and Nomoto 1990).

The calculated bolometric light curves for W7 and the carbon detonation model M = 1.03 $M_\odot$ (CDT3) are shown in figs. 20a and 20b, respectively,

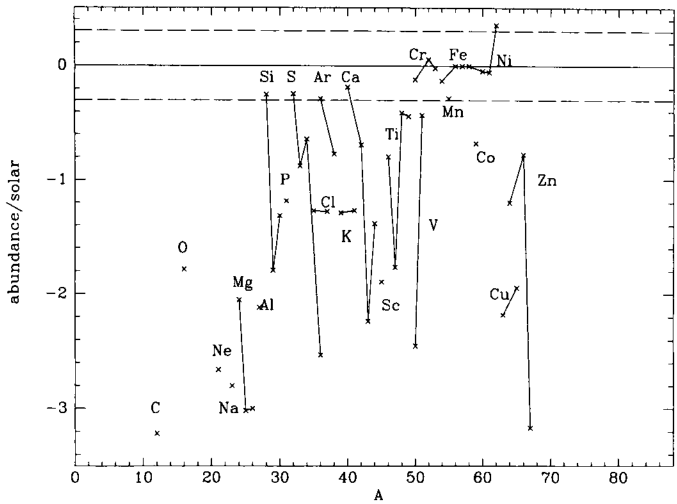

Fig. 19. The ratios of integrated abundances of the carbon detonation model with $M = 1.05\ M_\odot$ after decay of unstable nuclei, normalized to ^{56}Fe, relative to solar abundances.

by the solid curves for three cases of optical opacity (κ = 0.1, 0.2, and 0.3 cm^2 g^{-1}). Maximum brightness is reached when the expansion time scale becomes comparable to that of heat diffusion from the radioactive source. The light curve shape thus depends on the effective diffusion time $(\kappa M/v_{\rm exp}c)^{1/2}$ (Arnett 1982). Therefore, the date of the maximum $t_{\rm max}$ is earlier, and thus the maximum luminosity $L_{\rm max}$ is higher for smaller κ and higher $v_{\rm exp}$.

The calculated curves are compared with observed visual light curves of SN 1972E, SN 1981B, and SN 1990N in figs. 20a and 20b (Leibundgut et al. 1991a, 1991b; IAU Circ. 5039, 5040), where the observed maximum brightness is arbitrarily shifted to the calculated $L_{\rm max}$. It is seen that the light curves of CDT3 and W7 with $\kappa = 0.3$ cm^2 g^{-1} are both in reasonable agreement with the slow rise of SN 1990N. Since the bolometric light curve is regarded as close to the visual one, this agreement is encouraging for further study, whether the explosion model has actually an expansion opacity as large as κ = 0.3 cm^2 g^{-1} on the average (Harkness 1991; Höflich et al.1991; Khokhlov et al.1991).

After the peak, the bolometric luminosity gets closer to the energy deposition rate, which decreases because of the increasing transparency of the ejecta to γ-rays as well as the decreasing number of radioactive elements (dashed lines in fig. 20). The calculated curve of the decline phase for W7

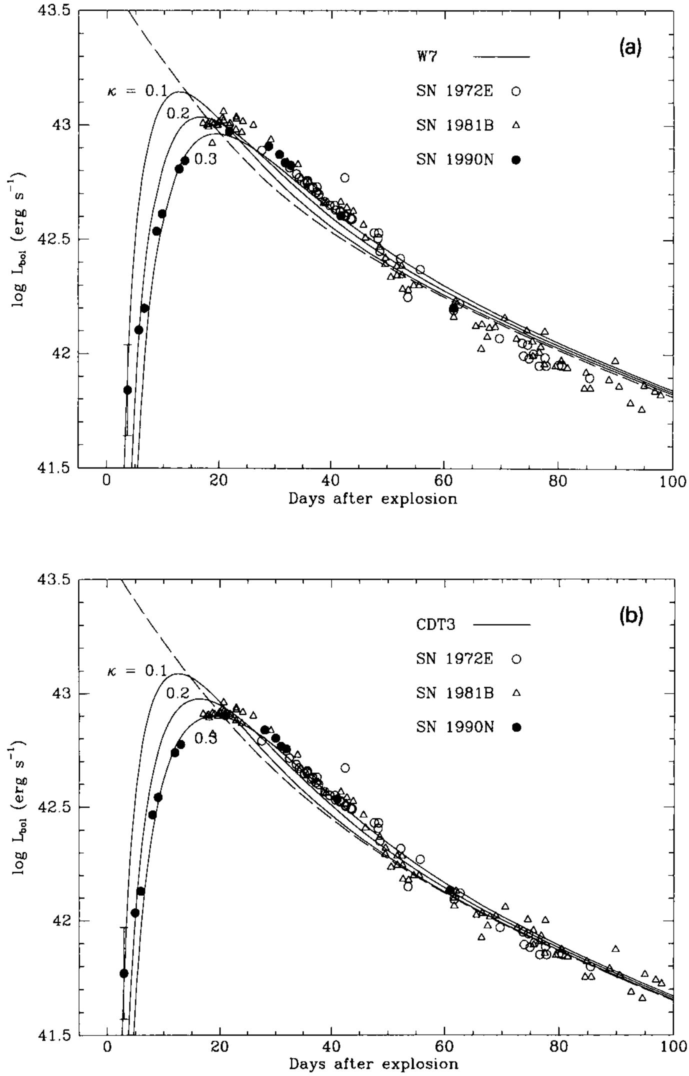

Fig. 20. The calculated bolometric light curve for the carbon deflagration model W7 (a) and the carbon detonation model CDT3 (b) for κ = 0.1, 0.2, and 0.3 cm^2 g^{-1}, as compared with the observed visual light curves of SN 1972E, SN 1981B, and SN 1990N (Leibundgut et al. 1991a, 1991b). Dashed lines refer to a decreasing number of radioactive elements.

and CDT3 are in reasonable agreement with observed visual light curves of SN 1972E, SN 1981B, and SN 1990N (fig. 20).

The maximum brightness L_{max} of SNe Ia when explained with radioactive decay models has been used to estimate the Hubble constant H_0 (in units of km s^{-1} Mpc^{-1} hereafter). From the well-observed six SNe Ia, Arnett et al.(1985) derived $L_{max} \sim 1.9 \pm 0.3 \times 10^{43}$ $(H_0/50)^{-2}$ erg s^{-1}.

As seen from figs. 20a and 20b, the maximum brightness obtained from radioactive decay models depends on the date of maximum light t_{max}. If t_{max} $\sim$ 20 d is common to most of SNe Ia, the theoretical L_{max} is lower than previous estimates, which would give a larger H_0. For $\kappa = 0.1$, 0.2, and 0.3 cm^2 g^{-1}, respectively, t_{max} = 13, 16, and 20 d and L_{max} = 1.4, 1.1, and 0.93 $\times$ 10^{43} erg s^{-1} for W7; and t_{max} = 12, 16, and 19 d and L_{max} = 1.2, 0.93, and 0.79 $\times$ 10^{43} erg s^{-1} for CDT3. These values, respectively, give H_0 ($\pm$ 6) = 58, 66, and 72 for W7, and H_0 ($\pm$ 6) = 63, 71, and 77 for CDT3.

The mass of ^{56}Ni may be constrained from the minimum expansion velocities of Ca and Si, which is estimated to be $\sim$ 8000 km s^{-1} for SN 1981B (Branch et al. 1983; Harkness 1991). This velocity in model CDT3 is $\sim$ 7500 km s^{-1}, so that $M_{Ni} \sim 0.5$ $M_\odot$ would be the minimum among the carbon detonation models.

If $t_{max} \sim 20$ d would be common to most of SNe Ia, $H_0 \sim 60$ to 83 is inferred from the models, with M_{Ni} = 0.49 to 0.68 $M_\odot$ considered here. For larger M models with larger M_{Ni}, H_0 may be roughly scaled as $M_{Ni}^{-1/2}$. Note, however, that the above estimate of H_0 is subject to uncertainties involved in (1) the expansion opacity, which needs to be used in future SN Ia models, and (2) the determination of M_{Ni}, which needs detailed comparisons between the calculated and observed spectra and light curves.

3.5. Spectra

Because SNe Ia do not have a thick hydrogen-rich envelope, elements newly synthesized during the explosion can be observed in the spectra, which enables us to diagnose the internal hydrodynamics and nucleosynthesis in SNe Ia.

Synthetic spectra are calculated based on the abundance distribution and expansion velocities of the carbon deflagration model W7, and are found to be in excellent agreement with the observed optical spectra of SN 1981B (Branch et al. 1985) and SN 1989B (fig. 21; Harkness 1991). In fig. 21, the calculated spectrum for stratified composition is in better agreement than for mixed composition. The material velocity at the photosphere near maximum light is $\sim$ 10,000 km s^{-1}, and the spectral features are identified as P-Cygni profiles of Fe, Ca, S, Si, Mg, and O.

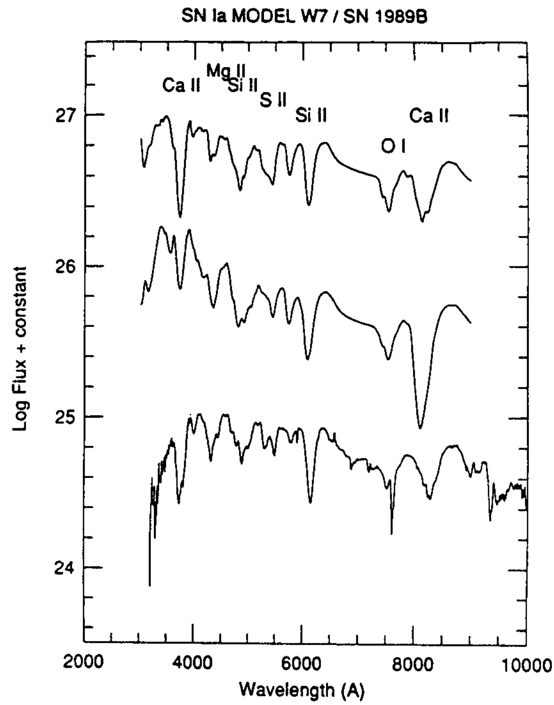

Fig. 21. The maximum light spectrum of SN Ia 1989B (bottom) is compared to a synthetic spectrum for the carbon deflagration model W7, with no mixing (top), and mixing for $v > 11{,}000$ km s^{-1} (middle) (Harkness 1991).

At late times, the spectra are dominated by emission lines of Fe and Co. The outer layers are transparent, and the inner Ni-Co-Fe core is exposed. Synthetic spectra of emission lines of [Fe II] and [Co I] for the carbon deflagration model agree quite well with the spectra observed at such a phase (Axelrod 1980; Woosley and Weaver 1986b).

Good agreement between the calculated and observed spectra (especially near maximum light) implies that the composition structure as a function of velocity for SNe Ia must be similar to W7 in spite of serious remaining uncertainties associated with presupernova evolution of binary systems, initiation of deflagration rather than detonation, and propagation of the burning front. To discriminate between the deflagration, detonation, and hybrid models, comparison between the synthetic spectra and the pre-maximum spectra of SN Ia would be important. Recent examples include SN 1990N (Leibundgut et al. 1991) and SN 1991T (Hamuy and Phillips 1991).

The new spectral features of SN 1990N are that the expansion velocities of Si and Ca extend to $v_{\rm exp} \sim 20{,}000$ km s^{-1}, and that the Fe and Co lines are present two weeks before the maximum. Possible explanations of these features with the deflagration model are:

(1) The observed lines of Si, Ca, Fe, and Co originate from the unprocessed materials at the outermost layers of the white dwarf.

(2) The high velocity heavy elements are synthesized by a deflagration in the inner layers and mixed with outer layers (Branch et al. 1985).

Other possibilities are that those high velocity heavy elements are produced by:

(3) a detonation in the hybrid model (Khokhlov et al. 1991), or

(4) the carbon detonation in low mass white dwarfs (Shigeyama et al. 1991a).

4. Accretion–induced collapse of white dwarfs

4.1. Low mass x-ray binaries and binary pulsars

An unexpectedly large number of low mass binary pulsars (LMBPs) have recently been discovered. The birth rate of LMBPs is now estimated to be about 100 times higher than that of low mass x-ray binaries (LMXBs) in both the Galactic disk (Kulkarni and Narayan 1988; Narayan et al. 1990) and the globular clusters (Kulkarni et al. 1990; Romani 1990). Since LMXBs have been thought to be the progenitors of LMBPs, this birth rate discrepancy has raised a serious question about the evolutionary origin of LMBPs. Two scenarios have been proposed to resolve this problem: (1) accretion-induced collapse (AIC) of white dwarfs in close binaries (Michel 1987; Chanmugam and Brecher 1987; Bailyn and Grindlay 1990; Romani 1990; Ray and Kluzniak 1990), and (2) shortening of the LMXB phase due to evaporation of the companion star (e.g., Tavani 1991 and references therein). Further, combinations of AIC and tidal capture of neutron stars have been suggested as an explanation for the very high incidence of LMBPs in globular clusters (Romani 1990; Ray and Kluzniak 1990).

Possible models for AIC advanced previously include solid C+O white dwarfs (Canal et al. 1980; Isern et al. 1983) and O+Ne+Mg white dwarfs (Nomoto et al. 1979a), whose masses could grow to the Chandrasekhar mass limit for a white dwarf. In the AIC models, collapse of a white dwarf is induced by electron capture that effectively reduces the Chandrasekhar mass limit (Fig. 22)

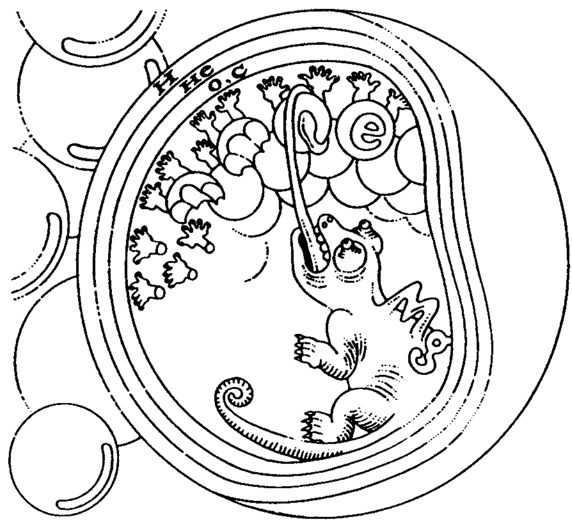

Fig. 22. Collapse of an O+Ne+Mg core is induced by electron capture (H. Nomoto 1989).

However, since the white dwarf contains nuclear fuel, whether the white dwarf undergoes collapse or explosion depends on whether nuclear energy release or electron capture is faster behind the deflagration wave. The energy generation rate is determined mainly by the propagation velocity of the deflagration wave, $v_{\rm def}$, while the electron capture rate depends on the density. If $v_{\rm def}$ is lower than a certain critical speed, electron capture induces collapse. If, on the other hand, $v_{\rm def}$ is sufficiently high, complete disruption results. It is important to determine the critical velocity that divides collapse and explosion.

4.2. Solid C+O white dwarfs

It is possible that accreting C+O white dwarfs could collapse rather than explode, depending on conditions in the white dwarfs. As described above, compression of a white dwarf by accreted matter first heats up a surface layer because of the small pressure scale height there. Later, heat diffuses inward (Nomoto et al. 1984). The diffusion timescale depends on $\dot{M}$, and is short for larger $\dot{M}$ because of the large heat flux and steep temperature gradient generated by rapid accretion. For example, the time it takes for the heat wave to reach the central region is $\sim 2 \times 10^5$ yr for $\dot{M} \sim 10^{-6}$ $M_\odot$ yr^{-1}

(Nomoto and Iben 1985) and 5×10^6 yr for $\dot{M} \sim 4 \times 10^{-8}$ $M_\odot$ yr^{-1} (Nomoto et al. 1984). If the initial mass of the white dwarf, $M_{\rm CO}$, is smaller than 1.2 $M_\odot$, entropy in the center increases substantially due to heat inflow and thus carbon ignites at relatively low central density ($\rho_c \sim 3 \times 10^9$ g cm^{-3}). On the other hand, if the white dwarf is initially more massive than 1.2 $M_\odot$ and cold at the onset of accretion, the central region is compressed only adiabatically, and thus is cold when carbon is ignited in the center. In the latter case, ignition density is as high as 10^{10} g cm^{-3} (e.g., Isern et al. 1983), and the white dwarf may well have a solid core. For such a case, it is necessary to determine the critical condition for which a carbon deflagration induces collapse rather than explosion.

For solid C+O white dwarfs, recent work finds that no significant separation of carbon and oxygen occurs during solidification (Barrata et al. 1988; Ichimaru et al. 1988). This, in turn, leads to the ignition of explosive carbon burning at much lower densities than the densities specified in models which postulate chemical separation (Isern et al. 1983).

In solid cores, carbon ignition takes place in the pycnonuclear reaction regime (Ogata et al. 1991) and develops into explosive burning at $\rho_c \sim 1 \times 10^{10}$ g cm^{-3}. After a thermal runaway of carbon burning, it is likely that a conductive deflagration wave propagates in the solid core. A detonation wave would not form due to the steep temperature gradient in the central solid region. Convection would not be effective unless the solid core is melted by heating from nuclear burning or neutrinos (Canal et al. 1990a).

The conductive deflagration in a solid C+O white dwarf is calculated assuming a constant ratio of $v_{\rm def}/v_s$ for the conductive deflagration wave (Nomoto 1986b, 1987b; Nomoto and Kondo 1991; Canal et al. 1990b).

Figure 23 shows the change in central density associated with propagation of the deflagration wave. Three cases with $v_{\rm def}/v_s = 0.05$, 0.03, and 0.01 are calculated, and the latter two slow cases undergo collapse. This implies that the critical velocity, $v_{\rm crit}$, dividing collapse and explosion is $v_{\rm crit} \sim 0.04\ v_s$ for $\rho_c \sim 10^{10}$ g cm^{-3}. Since the realistic value of conductive deflagration speed is $v_{\rm def} \sim 0.01\ v_s$ (Woosley and Weaver 1986a), the collapse is the most likely outcome for the solid white dwarf.

4.3. O+Ne+Mg white dwarfs

O+Ne+Mg white dwarfs are formed from stars of main-sequence masses of 8 to 12 $M_\odot$, in close binaries with initial masses as large as 1.1 to 1.37 $M_\odot$ (Nomoto et al. 1979a; Nomoto 1984a, 1987a). After mass accretion from the companion star, the mass of the white dwarf increases toward the

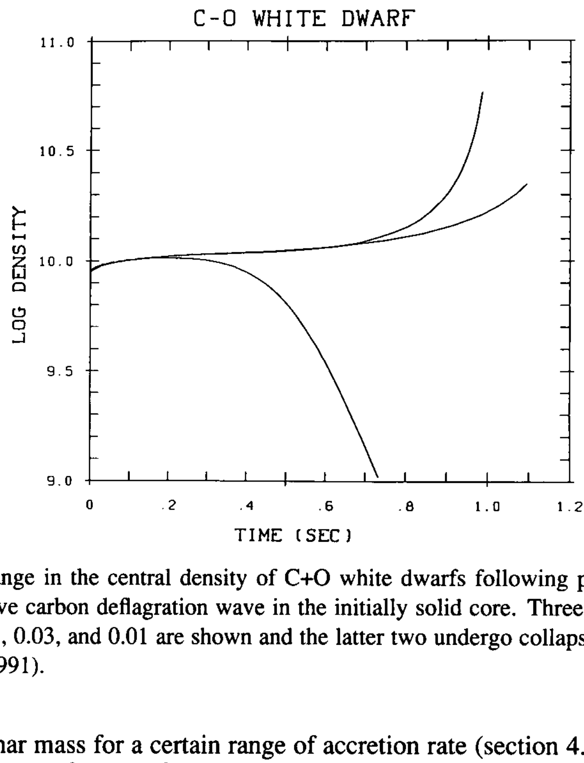

Fig. 23. Change in the central density of C+O white dwarfs following propagation of a conductive carbon deflagration wave in the initially solid core. Three cases with $v_{\rm def}/v_{\rm s}$ = 0.05, 0.03, and 0.01 are shown and the latter two undergo collapse (Nomoto and Kondo 1991).

Chandrasekhar mass for a certain range of accretion rate (section 4.4). When $\rho_{\rm c}$ exceeds 4×10^9 g cm^{-3}, the O+Ne+Mg white dwarf undergoes electron captures: ^{24}Mg (e$^-$, ν) ^{24}Na (e$^-$, ν) ^{20}Ne and ^{20}Ne (e$^-$, ν) ^{20}F (e$^-$, ν) ^{20}O (fig. 22; H. Nomoto 1989). Electron capture not only reduces the effective Chandrasekhar mass but also releases heat due to γ-ray emission, which eventually ignites oxygen deflagration at a certain central density.

In previous AIC models (Nomoto et al. 1979a), oxygen is ignited at $\rho_{\rm ig} \sim 2.5 \times 10^{10}$ g cm^{-3} after the initiation of collapse (Miyaji et al. 1980). At such central densities, electron capture is much faster than burning, thus promoting further collapse. However, $\rho_{\rm ig}$ has been found to depend on the timescale of semiconvective mixing in the electron capture region (Nomoto 1984b; Mochkovitch 1984; Miyaji and Nomoto 1987). If semiconvective mixing is negligible and heating due to γ-ray emission is confined to the very center, oxygen burning is ignited at $\rho_{\rm ig} \sim 9.5 \times 10^9$ g cm^{-3} before collapse occurs (Miyaji and Nomoto 1987). Hydrodynamic calculations are carried out to see whether this model leads to collapse or explosion (Nomoto and Kondo 1991).

The heat released by electron capture on ^{24}Mg results in the formation of a liquid core even if the white dwarf initially had a solid core (Mochkovitch 1984; Miyaji and Nomoto 1987; Canal *et al.* 1990a). When γ-rays resulting from electron capture on ^{20}Ne ignite explosive oxygen burning, there are several possible modes of subsequent propagation of the explosive burning front. In the present case the formation of a detonation wave is very unlikely because negligible semiconvective mixing forms a very steep temperature gradient when explosive oxygen burning starts.

Therefore, it is likely that an oxygen deflagration wave forms and propagates at a subsonic velocity. The propagation velocity, $v_{\rm def}$, depends on which mode of heat transport is faster, conductive or convective. For conductive deflagration, we apply $v_{\rm def} = 0.01\ v_{\rm s} \sim 100$ km s^{-1}, where $v_{\rm s}$ denotes the local sound velocity, which is a good approximation of $v_{\rm def}$ obtained by numerical calculations (Woosley and Weaver 1986a). For the convective deflagration wave, we apply a time dependent mixing length prescription, using the ratio between the mixing length and the pressure scale height (or radial distance) $\alpha = \ell/\min\,(H_p, r) = 0.7$, 1.4, and 2 (Nomoto et al. 1984). For small α, the deflagration speed in the very central region is slower than the conductive deflagration, because of a small buoyancy force across the burning front. The minimum $v_{\rm def}$ is then set to be 0.01 $v_{\rm s}$.

Whether this leads to collapse or explosion depends on which is faster behind the deflagration wave, nuclear energy release or electron capture. The energy generation rate is determined mainly by the propagation velocity of the deflagration wave, $v_{\rm def}$, while the electron capture rate depends on density. If $v_{\rm def}$ is lower than a certain critical speed, electron capture induces collapse. If, on the other hand, $v_{\rm def}$ is sufficiently high, complete disruption results.

Figure 24 shows changes in central density associated with the propagating deflagration front for three cases. It is seen that the slowest case of $\alpha = 0.7$ leads to increasing $\rho_{\rm c}$, that is, collapse, while the propagation with $\alpha = 2$ results in explosion. The intermediate case with $\alpha = 1.4$ is marginal. The fate of the convective deflagration wave depends mainly on whether $v_{\rm def}$ exceeds $\sim 0.03\ v_{\rm s}$ in the central region at $M_r \lesssim 0.1$ to 0.2 $M_\odot$.

Though determination of $v_{\rm def}$ may require multi-dimensional calculations, the carbon deflagration model for Type Ia supernovae favors $\alpha = 0.7$. The model with $\alpha = 0.7$ can nicely account for many of the observed features of Type Ia supernovae, while the propagation with $\alpha = 0.8$ is a little too fast to be consistent with spectral features of SN Ia (Nomoto et al. 1984). For oxygen deflagration, $\alpha < 1$ may also be the case for the same prescription of deflagration. Then, the collapse of O+Ne+Mg white dwarfs would be the most likely outcome since $\alpha \sim 1.4$ is marginal between collapse and explosion.

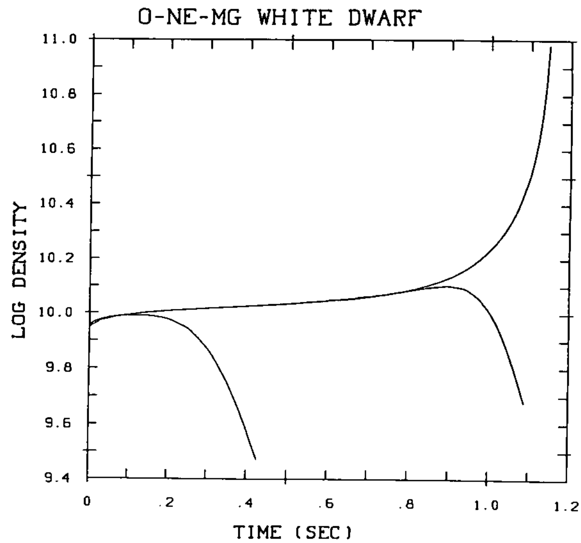

Fig. 24. Same as fig. 23 but for the O+Ne+Mg white dwarfs following the propagation of the oxygen deflagration wave for three cases with $\ell/\min(H_p, r) = 1.4$, 1.0, and 0.7. For the slowest case of $\ell/H_p = 0.7$, the central density increases, that is, white dwarf undergoes collapse. Faster propagation induces an explosion of the white dwarf (Nomoto and Kondo 1991).

If total disruption results from the white dwarf with a central density of $\sim 10^{10}$ g cm^{-3} (Isern et al.1991), such an explosion should be extremely rare since the ejection of too much neutron-rich iron-peak elements would not be compatible with solar isotopic ratios. In addition, explosions with such low energy as approximately a few times 10^{50} ergs, due to large neutrino losses does not match any frequently observed subclass of SN I.

4.4. Conditions for accretion-induced collapse

With results from sections 2–4, we draw boundaries for SNe Ia and AIC in a diagram showing mass accretion rate ($\dot{M}$) *versus* mass of the white dwarf at the onset of accretion (M_{CO} and M_{ONeMg}) in figs. 25 and 26 (Nomoto 1986b; Nomoto and Kondo 1991). We note that boundaries for the growth of white dwarfs must be regarded as relatively optimistic since wind-type mass loss associated with shell flashes of hydrogen and helium are not fully taken into account (see Kato and Hachisu 1989).

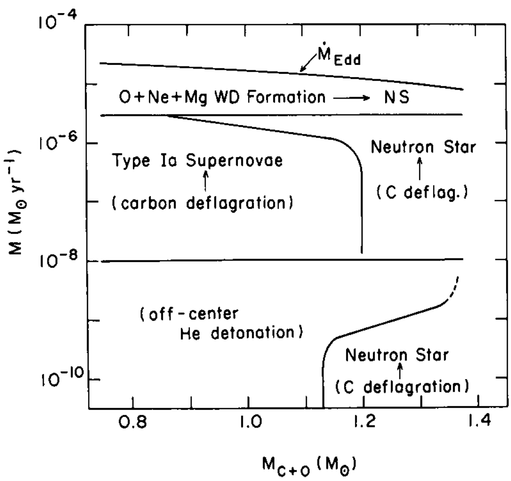

Fig. 25. The final fate of accreting C+O white dwarfs expected for their initial mass and accretion rate $\dot{M}$ (Nomoto and Kondo 1991).

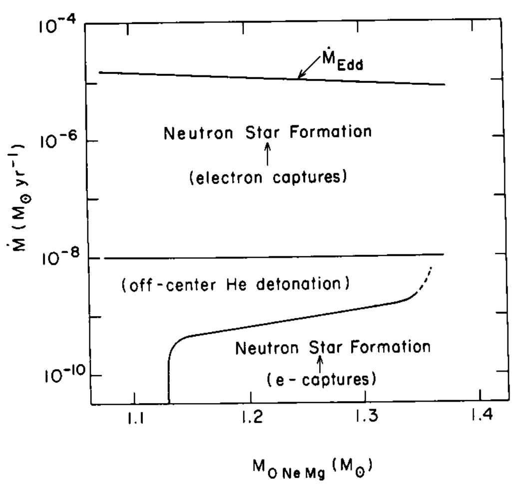

Fig. 26. Same as fig. 25 but for O+Ne+Mg white dwarfs. Collapse is triggered by electron capture on ^{24}Mg and ^{20}Ne (Nomoto and Kondo 1991).

For $\dot{M} \gtrsim 3 \times 10^{-6}$ $M_\odot$ yr^{-1}, we adopt the following scenario as an optimistic view for AIC. First, merging of double C+O white dwarfs forms a thick disk around more massive component (Benz et al. 1990). Then, subsequent heat generation at the boundary layer ignites off-center carbon burning (Mochkovitch and Livio 1990), which quietly burns the entire C+O white dwarf into O+Ne+Mg (Nomoto and Iben 1985; Saio and Nomoto 1985). Eventually the O+Ne+Mg white dwarf collapses.

Figure 26 shows that for a relatively wide parameter range, the O+Ne+Mg white dwarf can increase its mass. Since M_{ONM} can be very close to the Chandrasekhar mass, only a small increase in mass is enough to trigger a collapse. Such very massive O+Ne+Mg white dwarfs would give rise to recurrent novae (Nariai and Nomoto 1979).

Figures 25 and 26 clearly show that close binaries with relatively high $\dot{M}$ and high initial white dwarf mass are favored for AIC. This leads to the possibility that LMBPs with relatively long orbital periods may originate from AIC (Nomoto 1987b; Romani 1990; Ray and Kluzniak 1990), since the mass transfer rate from giant stars may be relatively high. On the other hand, Wheeler (1990) suggested that many of the white dwarfs in cataclysmic variables could possibly increase their masses toward the Chandrasekhar mass, ending up with $\dot{M} \sim 10^{-9}$ $M_\odot$ yr^{-1} at the lower-right hand corners of Figures 25 and 26. Resultant systems could be short orbital period LMBPs. Also, if we consider various types of helium star companions (helium main-sequence, helium subgiants, helium white dwarfs, etc.; Iben et al. 1987) as well as companions surrounded by a common envelope (Hachisu et al. 1989), LMBPs with relatively short orbital periods could be formed from AIC.

5. Type Ib/Ic supernovae

Wolf-Rayet stars with a wide range of masses have been proposed for the progenitors of SNe Ib and Ic, since most SNe Ib/Ic are associated with star-forming regions (see Wheeler and Harkness 1990 for a review). Recently Shigeyama et al. (1990), Hachisu et al. (1991), Nomoto et al. (1990), and Yamaoka and Nomoto (1991) have calculated the evolution, nucleosynthesis, Rayleigh-Taylor instabilities, and optical light curves of the progenitors of exploding helium stars. They have suggested that the helium stars of 3 to 5 $M_\odot$ (which form from stars with initial masses $M_{\mathrm{i}} \sim 12$ to 18 $M_\odot$ in binary systems) are the most likely progenitors of typical SNe Ib/Ic, and that SNe Ic progenitors may be slightly less massive than those of SNe Ib. Such low-mass helium star models can account for the observations that: (1) the light curves of SNe Ic decline faster than SNe Ib, and (2) the early time spectra of SNe Ic show the presence of hydrogen (Jeffery et al. 1991), while hydrogen is absent in SNe Ib. It remains an open question as to how the presence of hydrogen causes the difference between SNe Ib and Ic in their early time spectra (Lucy 1991).

5.1. Evolution of interacting binaries

The difference in spectral features between SNe Ic and Ib may be due to the presence of a thin envelope of hydrogen in SNe Ic immediately prior to the explosion. By modeling evolving massive stars in close binary systems, we examine whether hydrogen can be left on helium stars after mass exchange and wind-type mass loss. Following are some preliminary results for two cases, 13A and 18A, where the initial masses of the primary stars are $M_{\rm i} = 13\ M_\odot$ (13A) and $18\ M_\odot$ (18A), and their Roche lobe radii are $50\ R_\odot$ (Yamaoka and Nomoto 1991).

After hydrogen exhaustion, the star undergoes Roche lobe overflows forming a helium star of $\sim 3.4\ M_\odot$ (13A) and $\sim 5\ M_\odot$ (18A). Figure 27 (upper), shows the composition structure at the onset of mass transfer during core helium burning (upper), and after the Roche lobe overflow (lower). It is seen that significant amounts of hydrogen remain in a relatively thick layer below the surface ($0.5\ M_\odot$ for 13A, and $1\ M_\odot$ for 18A).

Whether such a hydrogen layer will be further lost from the helium-rich star depends on the Roche lobe radius and wind mass loss rate. If the helium star is detached from its Roche lobe during helium burning, the star loses its masses in a wind. If the mass loss rate depends on mass such as $\dot{M} \propto M^{2.5}$ (Langer 1989), it may lead to different surface abundances between 13A and 18A. For case 13A, hydrogen still may remain in the layer down to $\sim 0.2\ M_\odot$ below the surface, whereas for case 18A, all hydrogen may be lost in a wind (Yamaoka and Nomoto 1991). If a common envelope forms or the Roche lobe radius has become small enough for mass and angular momentum to be lost from the system, then all hydrogen will be lost from the star.

Although more parameter study is needed, the present results suggest that more hydrogen may remain on the stellar surface if the helium star has an initially smaller main-sequence mass. Also, more compact binary systems may lose more hydrogen through common envelope evolution.

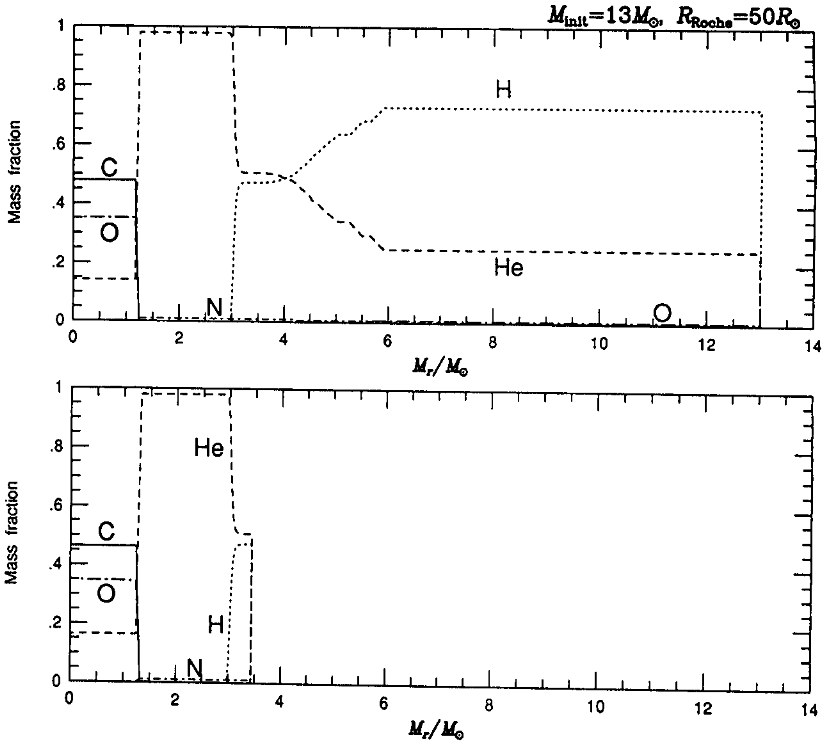

Fig. 27. Change in the composition structure during the binary evolution for the star with M_i = 13 $M_\odot$ (Yamaoka and Nomoto 1991).

5.2. Nucleosynthesis

Assuming that the helium star progenitors of SNe Ib/Ic are formed in close binary systems as described above, Shigeyama et al. (1990) performed hydrodynamic calculations of the explosion of helium stars with masses M_α = 3.3, 4, 6, and 8 $M_\odot$. These are presumed to form from the main-sequence stars of masses M_i $\sim$ 13, 15, 20, and 25 $M_\odot$, respectively. These stars eventually undergo iron core collapse, as in SNe II. A shock wave is then formed at the mass cut which divides the neutron star and the ejecta.

Behind the outward propagating shock wave, materials are processed into nuclear statistical equilibrium (NSE) composition, mostly ^{56}Ni, if the maximum temperature exceeds 5×10^9 K (Hashimoto et al. 1989; Thielemann et al. 1990). As derived from the approximate relation $E = 4\pi r^3/3\ aT^4$ with

E being the final kinetic energy of explosion (Thielemann et al. 1991), such a high temperature is realized in a sphere of radius $\sim$ 3700 $(E/10^{51}\ \mathrm{erg})^{1/3}$ km. With $E = 1 \times 10^{51}$ erg, this region contains a mass M_{NSE} ($\sim$ 1.44 – 1.46 $M_\odot$ for M_α = 3.3 and 4 $M_\odot$). Then the mass of ^{56}Ni plus neutron-rich iron peak elements is given by $M_{\mathrm{NSE}} - M_{\mathrm{NS}}$.

The adopted presupernova models (Nomoto and Hashimoto 1988) have iron core masses as small as 1.18 $M_\odot$ and 1.28 $M_\odot$ for M_α = 3.3 $M_\odot$ and M_α = 4 $M_\odot$, respectively, the mass being significantly smaller than 1.4 $M_\odot$ in the 6 $M_\odot$ star due to the larger effect of Coulomb interactions during the progenitor's evolution. If M_{NS} is approximately equal to the iron core mass, the *upper limit* to the possible ^{56}Ni masses are obtained as 0.26 and 0.15 $M_\odot$, for M_α = 3.3 and 4 $M_\odot$, respectively.

Figure 28 shows the abundance distribution after explosive burning for M_α = 4 $M_\odot$ (Shigeyama et al. 1990). The masses of oxygen produced in the outer layers are 0.21 and 0.43 $M_\odot$ for M_α = 3.3 and M_α 4 $M_\odot$, respectively. These masses could be consistent with those inferred from the late time spectra of SNe Ib/Ic in view of the strong dependence of oxygen mass on the temperature of the ejecta (Uomoto 1986).

5.3. Rayleigh-Taylor instabilities and mixing

As will be shown in section 5.4, helium star models are in good agreement with the observed SNe Ib light curves only if extensive mixing of ^{56}Ni takes place. Mixing and clumpiness in SNe Ib are also inferred from late time emission line features (Fransson and Chevalier 1989; Filippenko and Sargent 1989).

Rayleigh-Taylor instabilities in helium stars develop as follows. When the shock wave hits the helium envelope, expansion of the inner core is largely decelerated, which forms a reverse shock. Then a pressure inversion appears (i.e., the pressure increases outward) in the layer between the forward shock and the reverse shock. The interface between the core and the helium envelope becomes most strongly Rayleigh-Taylor unstable, because the density decreases steeply outward and thus $(dP/dr)(d\rho/dr) < 0$. The instability continues to grow until the forward shock reaches the low density surface; then a rarefaction wave propagates inward from the surface to stabilize the interior. Note that in the 20 $M_\odot$ model of SN 1987A by Hachisu et al. (1990), the most unstable point is the hydrogen/helium interface, due to a massive hydrogen-rich envelope.

For helium stars of M_α = 3.3, 4, and 6 $M_\odot$, Hachisu et al. (1991) have carried out 2D hydrodynamic calculations to follow the Rayleigh-Taylor instability. As seen in fig. 29a–c, the instability leads only to limited mixing

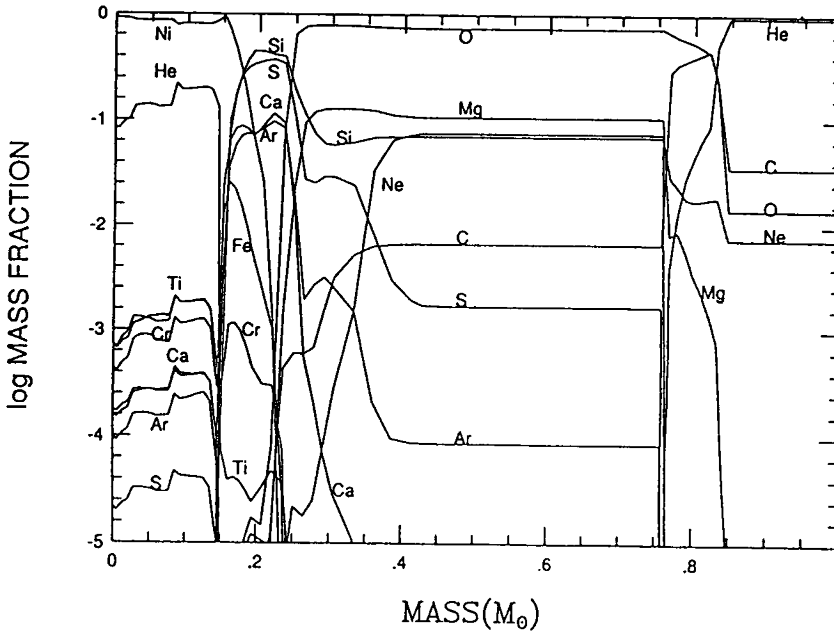

Fig. 28. Explosive nucleosynthesis in the 4 $M_\odot$ helium star (Shigeyama et al. 1990). Composition of the innermost 1 $M_\odot$ of the ejecta is shown. (The outermost 1.72 $M_\odot$ helium layer and the 1.28 $M_\odot$ neutron star are not included in the figure.) About 0.15 $M_\odot$ ^{56}Ni and 0.43 $M_\odot$ oxygen are produced.

and clump formation for $M_\alpha = 6\ M_\odot$, while it does induce a large scale mixing for M_α = 3.3 and 4 $M_\odot$. For $M_\alpha = 3.3\ M_\odot$, ^{56}Ni is mixed to the layer 0.4 $M_\odot$ beneath the surface (Fig. 30; Hachisu et al.1991), which is close to the extent of mixing as required from the light curves.

Such mass dependence of the Rayleigh-Taylor instability can be understood from differences in the stellar structure as follows.

(1) For smaller M_α the mass ratio between the helium envelope and the core (excluding the neutron star) is larger (i.e., 2.5, 2.7, 1.0, and 0.45 for M_α = 3.3, 4, 6, and 8 $M_\odot$, respectively), so that the deceleration of the core and the pressure inversion are larger.

(2) Smaller mass stars have a steeper density gradient near the composition interface.

(3) The stellar radius is larger for smaller M_α, so that more time is required for the shock wave to reach the stellar surface; thus the instability grows for a longer time.

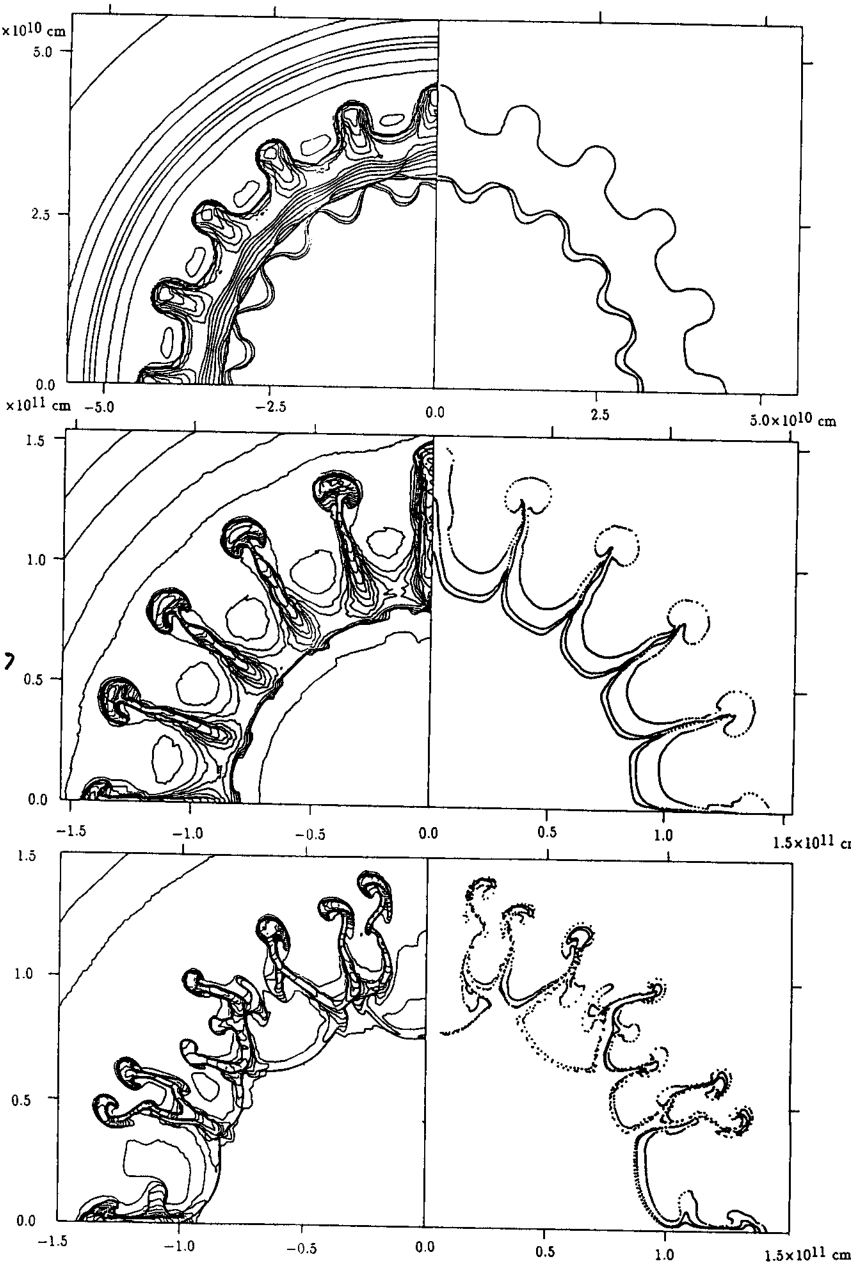

Fig. 29. Rayleigh-Taylor instabilities in the exploding helium star of $M_\alpha = 3.3\ M_\odot$ ($t = 180$ s). Shown are the density contour map (*left*) and the marker particles at the composition interfaces, He/C+O, O/Si, and Ni/Si from the outer layer (*right*) (Hachisu et al. 1991).

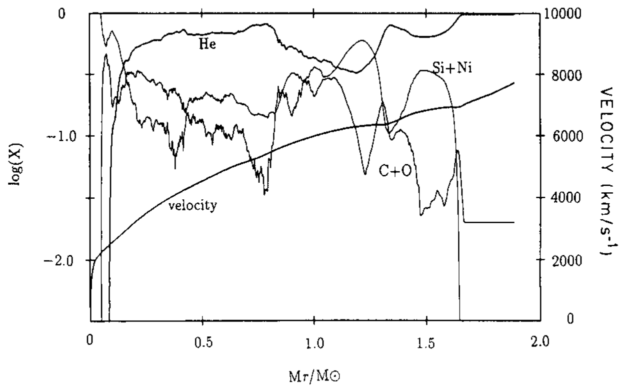

Fig. 30. Chemical composition for $M_\alpha = 3.3\ M_\odot$ at $t = 180$ s is plotted against the radial mass coordinate, M_r. Mass fractions of He, C+O, and Si+Ni are shown by thick, intermediate, and thin lines, respectively. The mean radial velocity is also shown (thick solid line). ^{56}Ni is mixed to the layer at $M_r = 1.7 M_\odot$, that is, 0.4 $M_\odot$ beneath the surface.

We should emphasize the importance of the density structure rather than stellar mass. For example, a single Wolf-Rayet star which reduces its mass down to 4 to 5 $M_\odot$ by wind could be a SNe Ib/Ic progenitor (Langer 1989). However, such a star would not undergo extensive mixing despite the small mass, because its helium envelope would be too small to decelerate the core to any significant extent.

5.4. Light curves

Figure 31 shows the observed bolometric light curves of SNe Ia 1972E and 1981B (Graham 1987), SN Ib 1983N (Panagia 1987), and the approximate bolometric light curve of SN Ic 1987M constructed from flux-calibrated spectra (Filippenko et al. 1990; Nomoto et al. 1990). In each case, the observed light curve has been shifted along the abscissa to match the corresponding theoretical curve. The peak bolometric luminosities assume $H_0 = 60$ km s^{-1} Mpc^{-1}.

The previous Wolf-Rayet star models have some difficulties (1) in reproducing the light curves of typical SNe Ib, which decline as fast as SNe Ia (Panagia 1987), and (2) in producing enough ^{56}Ni to attain the maximum luminosities of SNe Ib in relatively low mass helium star models (Ensman and Woosley 1988). In particular, fig. 31 demonstrates an important feature of SN Ic 1987M, that is, its brightness fell somewhat more rapidly than that

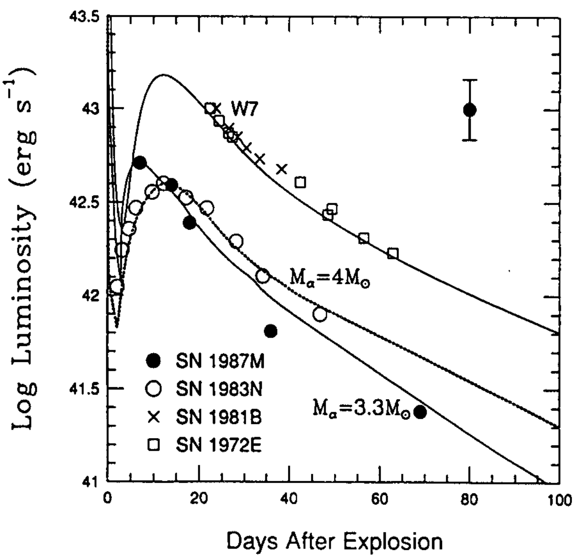

Fig. 31. Approximate bolometric light curve of SN Ic 1987M, and the bolometric light curves of SNe Ia 1972E and 1981B and of SN Ib 1983N. The predicted curves of the 3.3 $M_\odot$ model for SN 1987M, the 4 $M_\odot$ model for SN Ib, and the W7 model for SN Ia are indicated by solid and dotted lines. The error bar illustrates the 2σ photometric uncertainty in the SN 1987M points (Nomoto et al. 1990).

of SNe Ia and SN Ib 1983N (it also fell more rapidly than SN Ic 1983I reported by Tsvetkov 1985). Maximum brightness of 1987M is not significantly different from that of SNe Ib if we take the extinction estimated by Jeffery et al. (1991).

Figure 31 also shows the calculated bolometric light curves of the exploding helium star models with M_α = 3.3 $M_\odot$ for SN Ic and M_α = 4 $M_\odot$ for SN Ib, as well as the white dwarf model W7 for SNe Ia (Nomoto et al. 1984). The amount of ^{56}Ni is 0.58 $M_\odot$ (W7), 0.15 $M_\odot$ (SN Ic), and 0.15 $M_\odot$ (SN Ib). The helium star models assume a uniformly mixed distribution of elements from the center through the layer at 0.2 $M_\odot$ beneath the surface for both cases. Such mixing may be due to Rayleigh-Taylor instability during the explosion (Fig. 29; Hachisu et al. 1991).

The calculated bolometric light curves of helium stars are powered by radioactive decay of ^{56}Ni and ^{56}Co. Maximum brightness is higher if the ^{56}Ni mass is larger and the date of maximum is earlier. After the peak, the light curve declines at a rate that depends on how fast γ-rays from radioactive decay escape from the star without being thermalized; decline is faster if the ejected mass is smaller and if ^{56}Ni is mixed closer to the surface.

Significant effects of mixing on the light curve have been noted in Shigeyama et al. (1990). Figures 32 and 33 compare light curves with and without mixing by assuming 0.15 $M_{\odot}$ of ^{56}Ni mass for all models to clarify the stellar mass dependence. Figure 32 shows that the tails of the calculated light curves for unmixed models decline much more slowly than those of SN 1983N and 83I after $\sim$ day 40. For the mixed models shown in fig. 33, the light curve shape is different from the unmixed cases as follows:

(1) Maximum luminosity is reached $\sim$ 10 days earlier, and is thereby higher than in the unmixed cases because of earlier radioactive heating of the surface layers.

(2) Decline of the tail is much faster than the unmixed cases.

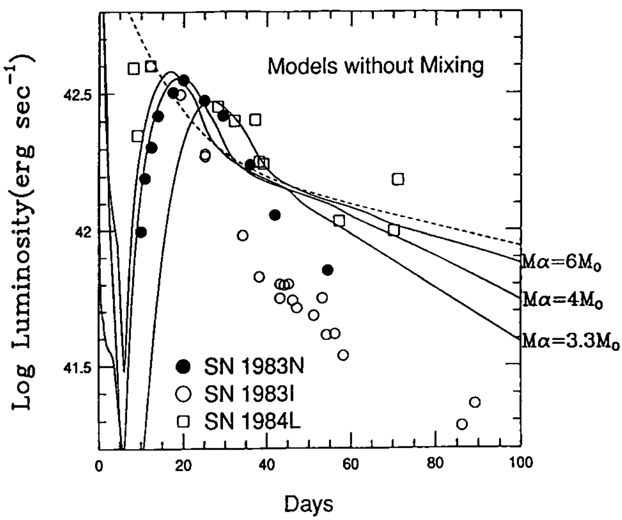

Fig. 32. Calculated light curves of exploding helium stars of M_α = 3.3, 4, and 6 $M_{\odot}$ (Shigeyama et al.1990). All the models assume the production of 0.15 $M_{\odot}$ ^{56}Ni, kinetic energy of explosion E = 1 $\times 10^{51}$ erg, and no mixing (i.e., stratified composition structure). Filled and open circles are the observed light curves of SN Ib 1984L (visual), 1983N (bolometric), and 1983I (visual). The dotted curve is the energy generation rate of the ^{56}Ni–^{56}Co decays.

The resulting bolometric light curves of M_α = 3.3 $M_{\odot}$ and 4 $M_{\odot}$ are in good agreement with SN Ic 1987M and SN Ib 1983N, respectively. Compared with

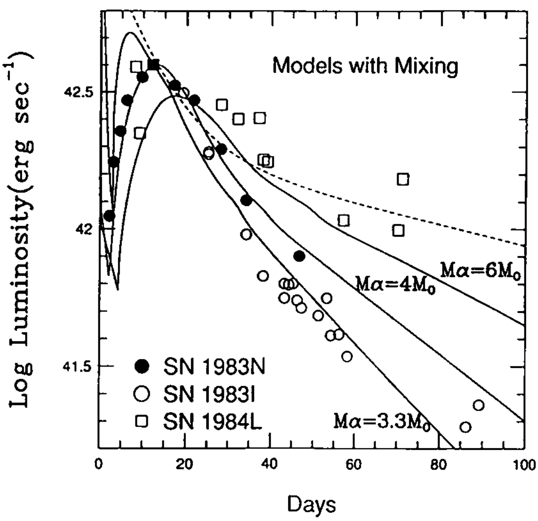

Fig. 33. Same as fig. 32 but with *mixed* abundance distribution.

the 4 $M_\odot$ model, the light curve of the 3.3 $M_\odot$ model declines faster due to less mass being ejected, just as observed in SN Ic 1987M.

It is interesting to compare SNe Ib/Ic with SN 1987K, whose spectral classification changed from Type II to Type Ib/Ic as it aged, thereby being called as SNe IIb (Filippenko 1988). The decline of the SN 1987K light curve is as fast as that of a SNe Ia (and thus SNe Ic) (Turatto et al. 1990). The early time spectra of SN 1987K are very similar to SNe Ic (1983V and 1987M) and, conversely, the hydrogen feature has been identified in the early time spectrum of SN Ic 1987M (Jeffery et al. 1990). This strongly suggests that the difference in spectral features between SNe Ic and Ib is due to the presence of a thin envelope of hydrogen in SNe Ic immediately prior to the explosion. More hydrogen can be left on the smaller mass helium stars after mass exchange and wind-type mass loss (section 5.1).

6. Evolutionary origin of binary pulsars

The low mass helium stars considered for the progenitors of SNe Ib/Ic would mostly occur in close binaries, because 12–18 $M_\odot$ stars would not lose their entire hydrogen-rich envelope by wind mass loss. Meurs and van den Heuvel (1989) predicted that more than 70 percent of massive star explosions would occur in close binaries. This estimate predicts that the frequencies of occurrence of SNe Ib/Ic are higher than SN II, which might be consistent with the increasing number of SNe Ic which have been recently discovered.

The binary scenario suggests that SNe Ib/Ic might be closely related to the formation of binary pulsars and x-ray binaries. If a binary system is not disrupted by supernova mass ejection, a neutron star is left to orbit around a companion star of various types (a main-sequence star or a helium star). Many of them would become Be x-ray binaries.

Recently, the masses of the component stars in the binary pulsar system 1532+12 have been determined, which strongly suggests a neutron star companion (Wolszczan 1991). Their masses, eccentricity, semi-major axis, and orbital period are summarized in table 1, together with those of the first binary pulsar 1913+16 (Taylor 1991). A possible evolutionary scenario for such systems is as follows (e.g., van den Heuvel 1991): (1) Two main-sequence stars exist, 1 and 2; (2) Roche lobe overflow of star 1, which becomes a helium star 1; (3) the first supernova explosion of the helium star 1 to form a neutron star 1; (4) Roche lobe overflow of star 2, which leads to a spiral-in of the neutron star 1 into star 2 and thus to considerable shrink of the system due to losses of angular momentum and mass from the system. The system now consists of the recycled neutron star 1 and a helium star 2; (5) the second supernova explosion of the helium star 2. This forms a two neutron star system in an eccentric orbit.

Given the observed orbital parameters in table 1 and the assumption of a circular orbit for the pre-explosion helium star 2–neutron star 1 system, the mass of the helium star 2 M_α and the possible kick velocity $v_{\rm kick}$ at the explosion can be calculated. If the explosion is spherical (i.e., $v_{\rm kick} = 0$), $M_\alpha \sim 2.1\ M_\odot$ (Wolszczan 1991). This is smaller than the minimum mass of helium star that can form a neutron star [$\sim 2.5\ M_\odot$ (Nomoto 1984a) – $\sim 2.2\ M_\odot$ (Habets 1986) depending on the treatment of overshooting and semi-convection]. This suggests that either the explosion is not spherical or the exploding star had lost even its helium layer before the explosion.

If we assume that the neutron star gets a finite kick velocity $v_{\rm kick}$ within the orbital plane of the explosion of helium star 2, the kick velocity and its direction can be calculated as functions of assumed M_α and the initial orbital radius a_0 before the explosion where $a_{\rm f}(1-e) < a_0 < a_{\rm f}(1+e)$ (fig. 34; Yamaoka et al. 1991; Nomoto et al. 1991). For the kick in other directions, the corresponding value of $v_{\rm kick}$ is larger. It should be noted that smaller helium stars have larger radii at the collapse; $\sim 3\ R_\odot$ for $M_\alpha \sim 3.3\ M_\odot$ (Nomoto and Hashimoto 1988). For the solid line in figs. 34 and 35, the

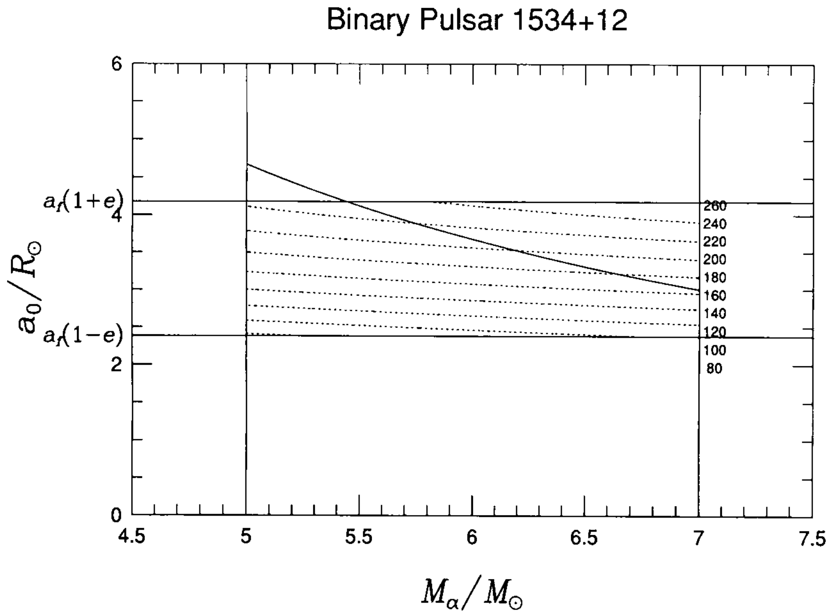

Fig. 34. Kick velocity imparted to the neutron star at the explosion of helium star 2 of mass M_α as a function of M_α and the initial orbital radius a_0 before the explosion (Yamaoka et al. 1991). Here $a_f(1-e) < a_0 < a_f(1+e)$. For the solid line, the radius of the helium star is equal to its Roche lobe radius, so that only the upper-right part of the parameter space is allowed. For PSR 1534+12, $v_{\rm kick} \sim 180$ to 240 km s^{-1} is necessary to avoid disruption of the binary system.

radius of the helium star is equal to its Roche lobe radius. Since star 2 is a helium star, M_α should be larger than 5 $M_\odot$ to underfill the Roche lobe. If this is the case, a kick velocity of $v_{\rm kick} \sim 180$ to 240 km s^{-1} is necessary to avoid disruption of the binary system. The same relation is obtained for 1913 + 16 in fig. 35, where $v_{\rm kick} \sim 340$ to 420 km s^{-1} is necessary (see also Burrows and Woosley 1986).

Two possible extreme cases are: (1) star 2 is a helium star more massive than ~ 5 $M_\odot$, for which the explosion produces a large kick velocity, and (2) star 2, being initially a helium star of smaller than 5 $M_\odot$, loses its helium envelope to become an almost bare C+O star. The masses of C+O stars are: 6.0, 3.8, 2.1, 1.8 $M_\odot$ for M_α = 8, 6, 4, 3.3 $M_\odot$, respectively (Nomoto and Hashimoto 1988). For $M_\alpha \lesssim 4$ $M_\odot$, therefore, the explosion of star 2 could be spherical with $v_{\rm kick} = 0$.

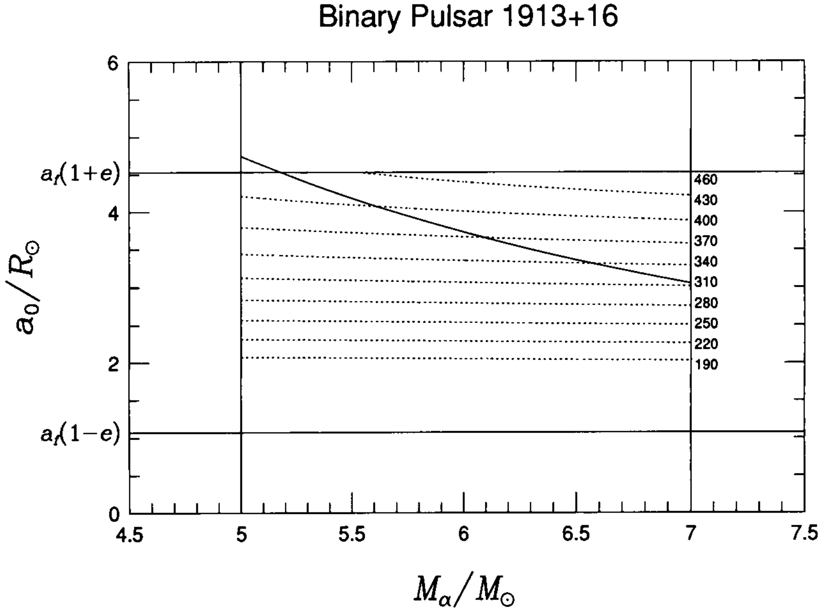

Fig. 35. Same as fig. 34 but for PSR 1913 + 16, where $v_{\rm kick} \sim 340 - 420$ km s^{-1} is necessary (Yamaoka et al. 1991).

Table 1. Binary Pulsars

PSR	M_p ($M_\odot$)	M_c ($M_\odot$)	e	a_f ($R_\odot$)	P_b (hours)	$P_b/\dot{P}_b$ (years)
1913+16	1.4421 $\pm$0.0012	1.3875 $\pm$0.0012	0.617127	2.8	7.752	3×10^8
1532+12	1.32 $\pm$0.03	1.36 $\pm$0.03	0.274	3.28	10.1	$\sim 1 \times 10^9$

If the main difference between SNe Ib and Ic are the absence and presence of a hydrogen-rich envelope, the first explosion could be SN Ic because of the possible presence of hydrogen, while the second explosion might be SN Ib if star 2 loses even its helium envelope. These dual binary scenarios also suggest that SNe Ic occur more frequently than SNe Ib.

7. Concluding remarks

Figure 36 summarizes the initial masses M_i of the progenitors for the various types of supernovae currently proposed by several groups (e.g., Branch et al. 1991). The upper and lower rows, respectively, show the cases of single stars and helium stars of masses M_α (or white dwarfs) in close binary stars. Masses of ^{56}Ni produced are inferred from light curves based on the radioactive decay model.

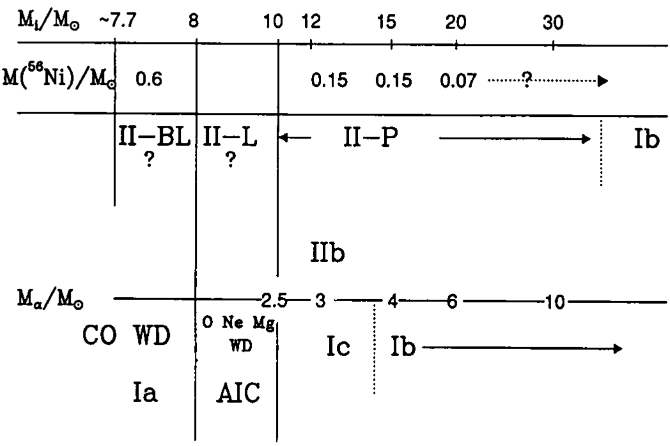

Fig. 36. Hypothetical connection between supernova types and their progenitors for single stars (upper) and close binary stars (lower). M_i and M_α represent the initial mass and the helium star mass, respectively. AIC stands for Accretion-Induced Collapse of white dwarfs.

Single stars more massive than $\sim 8\ M_\odot$ would retain their hydrogen-rich envelope, thereby ending their lives as SNe II. Among them, SNe II-BL and SNe II-L are tentatively assumed to be explosions of AGB stars having degenerate C+O cores (carbon deflagration) and O+Ne+Mg cores (electron capture induced collapse), respectively (Swartz et al. 1991). Interacting binaries are the likely progenitors of SNe I, as has been discussed in the preceding sections. It must be emphasized that the supernova types versus progenitor's mass relation presented in fig. 36 is still highly hypothetical and will be tested by future observations of light curve tails and good spectra (Branch et al. 1991).

We would like to thank M. Hashimoto, F.-K. Thielemann, A.V. Filippenko, D. Branch, D. Jeffery, and Y. Kondo for collaborative work on the subjects discussed in this paper. This work has been supported in part by Grants-in-Aid for Scientific Research (01540216, 01790169, 02234202, 02302024, 03218202) of the Ministry of Education, Science, and Culture in Japan.

References

Arnett, W.D., 1969. *Astr. Ap.* **5**, 180.

Arnett, W.D., 1982. *Ap. J.* **253**, 785.

Arnett, W.D., D. Branch, and J.C. Wheeler 1985. *Nature* **314**, 337.

Axelrod, T. 1980. in *Type I Supernovae*, ed. J.C. Wheeler (Univ. of Texas), p. 80.

Bailyn, C.D., and J.E. Grindlay. 1990. *Ap. J.* **353**, 159.

Barkat, Z. 1992. in this volume.

Barrat, J.L., J.P. Hansen, and R. Mochkovitch 1988. *Astr. Ap.* **199**, L15.

Benz, W., R.L. Bowers, A.G.W. Cameron, and W. Press 1990. *Ap. J.* **348**, 647.

Branch, D., J.B. Doggett, K. Nomoto, and F.-K. Thielemann 1985. *Ap. J.* **294**, 619.

Branch, D., C.H. Lacy, M.L. McCall, P.G. Sutherland, A. Uomoto, J.C. Wheeler, and B.J. Wills 1983. *Ap. J.* **270**, 123.

Branch, D., K. Nomoto, and A.V. Filippenko 1991. *Comments on Astrophysics*, **XV**, 221.

Burrows, A., and S.E. Woosley 1986. *Ap. J.* **308**, 680.

Canal, R., D. Garcia, J. Isern, and J. Labay 1990b. *Ap. J. (Letters)* **356**, L51.

Canal, R., J. Isern, and J. Labay 1980. *Ap. J. (Letters)* **241**, L33.

Canal, R., J. Isern, and J. Labay 1990a. *Ann. Rev. Astr. Ap.* **28**, 183.

Chanmugam, G., and K. Brecher 1987. *Nature* **329**, 696.

Dgani, R., and M. Livio 1990. *Ap. J.* **361**, 540.

Ensman, L., and S.E. Woosley 1988. *Ap. J.* **333**, 754.

Filippenko, A.V. 1988. *A. J.* **96**, 1941.

Filippenko, A.V. 1991. *IAU Cir.* No. 5169.

Filippenko, A.V., A.C. Porter, and W.L.W. Sargent 1990. *A. J.* **100**, 1575.

Filippenko, A.V., and W.L.W. Sargent 1989. *Ap. J. (Letters)* **345**, L43.

Fransson, C., and R.A. Chevalier 1989. *Ap. J.* **343**, 323.

Fujimoto, M.Y., and D. Sugimoto 1982. *Ap. J.* **257**, 291.

Graham, J.R. 1987. *Ap. J.* **315**, 588.

Habets, G.M.H.J. 1986. *Astr. Ap.* **167**, 61.

Hachisu, I., Y. Eriguchi, and K. Nomoto 1986. *Ap. J.* **308**, 161.

Hachisu, I., M. Kato and H. Saio 1989. *Ap. J. (Letters)* **342**, L19.

Hachisu, I., T. Matsuda, K. Nomoto, and T. Shigeyama 1990. *Ap. J. (Letters)* **358**, L57.

Hachisu, I., T. Matsuda, K. Nomoto, and T. Shigeyama 1991. *Ap. J. (Letters)* **368**, L27.

Hamuy, M., and M.M. Phillips 1991. *IAU Cir.* No. 5251.

Harkness, R.P. 1991. in *SN 1987A and Other Supernovae* ed. I.J. Danziger (Garching: ESO), in press.

Harkness, R.P., and J.C. Wheeler 1990. in *Supernovae*, ed. A. Petschek (Springer-Verlag), p. 1.

Hashimoto, M., K. Nomoto, K. Arai, and K. Kaminisi 1986. *Ap. J.* **307**, 687.

Hashimoto, M., K. Nomoto, and T. Shigeyama 1989. *Astr. Ap.* **210**, L5.

Höflich, P., A.M. Khokhlov, and E. Müller 1991. *Astr. Ap.*, in press.

Hoyle, F., and W.A. Fowler 1960. *Ap. J.* **132**, 565.

Iben, I.Jr. 1988. *Ap. J.* **324**, 355.
Iben, I.Jr., K. Nomoto, A. Tornambe, and A. Tutukov 1987. *Ap. J.* **317**, 717.
Iben, I.Jr., and A. Tutukov 1984. *Ap. J. Suppl.* **55**, 335.
Iben, I.Jr., and A. Tutukov 1991. *Ap. J.* **370**, 615.
Ichimaru, S., H. Iyetomi, and S. Ogata 1988. *Ap. J. (Letters)* **334**, L17.
Isern, J., R. Canal, and J. Labay 1991. *Ap. J. (Letters)* **372**, L83.
Isern, J., Labay, J., Hernanz, M., and Canal, R. 1983. *Ap. J.* **273**, 320.
Jeffery, D., D. Branch, A.V. Filippenko, and K. Nomoto 1991. *Ap. J. (Letters)* **377**, L89.
Kato, M., and I. Hachisu 1989. *Ap. J.* **346**, 424.
Kawai, Y., H. Saio, and K. Nomoto 1987. *Ap. J.* **315**, 229.
Khokhlov, A.M. 1991a. *Astr. Ap.* **245**, 114.
Khokhlov, A.M. 1991b. *Astr. Ap.* **245**, L25.
Khokhlov, A.M., E. Müller, and P. Höflich 1991. *Astr. Ap.*, submitted.
Kumagai, S., T. Shigeyama, K. Nomoto, M. Itoh, J. Nishimura, and S. Tsuruta 1989. *Ap. J.* **345**, 412.
Kulkarni, S.R., and R. Narayan 1988. *Ap. J.* **335**, 755.
Kulkarni, S.R., R. Narayan, and R.W. Romani 1990. *Ap. J.* **356**, 174.
Langer, N. 1989. *Astr. Ap.* **220**, 135.
Leibundgut, B., R.P. Kirshner, A.V. Filippenko, J.C. Shields, C.B. Foltz, M.M. Phillips, and G. Sonneborn 1991a. *Ap. J. (Letters)* **371**, L23.
Leibundgut, B., G.A. Tammann, R. Cadonau, and D. Cerrito 1991b. *Astr. Ap. Suppl.*, in press.
Limongi, M., and A. Tornambe 1991. *Ap. J.* **371**, 317.
Livne, E. 1990. *Ap. J. (Letters)* **354**, L53.
Livne, E., and A.S. Glasner 1991. *Ap. J.* **370**, 272.
Lucy, L.B. 1991. *Ap. J.*, submitted.
Meurs, E.J.A., and E.P.J. van den Heuvel 1989. *Astr. Ap.* **226**, 88.
Michel, F.C. 1987. *Nature* **329**, 310.
Miyaji, S., and K. Nomoto 1987. *Ap. J.* **318**, 307.
Miyaji, S., K. Nomoto, K. Yokoi, and D. Sugimoto 1980. *Pub. Astr. Soc. Japan* **32**, 303.
Mochkovitch, R. 1984. *Problems of Collapse and Numerical Relativity*, ed. D. Bancel and M. Signore (Dordrecht: Reidel), p. 125.
Mochkovitch, R., and M. Livio 1990. *Astr. Ap.* **236**, 378.
Müller, E., and W.D. Arnett 1986. *Ap. J.* **307**, 619.
Narayan, R., A.S. Fruchter, S.R. Kulkarni, and R.W. Romani 1990. in *Accretion-Powered Compact Binaries*, ed. C.W. Mauche (Cambridge University Press), p. 451.
Nariai, K., and K. Nomoto 1979. in *IAU Colloquium 53, White Dwarfs and Variable Degenerate Stars*, ed. H.M. Van Horn and V. Weidemann (Univ. of Rochester), p.525.
Nariai, K., K. Nomoto, and D. Sugimoto 1980. *Pub. Astr. Soc. Japan* **32**, 473.
Nomoto, H. 1989. *Exploring SN 1987A* (in Japanese), (Tokyo: Kodansha).
Nomoto, K. 1982a. *Ap. J.* **253**, 798.
Nomoto, K. 1982b. *Ap. J.* **257**, 780.
Nomoto, K. 1982c. in *Supernovae: A Survey of Current Research*, ed. M.J. Rees and R.J. Stoneham (Dordrecht: Reidel), p. 210.
Nomoto, K. 1984a. *Ap. J.* **277**, 791.
Nomoto, K. 1984b. *Problems of Collapse and Numerical Relativity*, ed. D. Bancel and M. Signore (Dordrecht: Reidel), p. 89.
Nomoto, K. 1986a. *Ann. NY Acad. Sci.*, **470**, 294.
Nomoto, K. 1986b. *Prog. Part. Nucl. Phys.*, **17**, 249.

Nomoto, K. 1987a. *Ap. J.* **322**, 206.

Nomoto, K. 1987b. in *IAU Symposium 125, The Origin and Evolution of Neutron Stars*, ed. D.J. Helfand and J.-H. Huang (Dordrecht: Reidel), p. 281.

Nomoto, K., A.V. Filippenko, and T. Shigeyama 1990. *Astr. Ap.* **240**, L1.

Nomoto, K., and M. Hashimoto 1987. *Ap. Space Sci.* **131**, 395.

Nomoto, K., and M. Hashimoto 1988. *Physics Reports*, **163**, 13.

Nomoto, K., and I. Iben Jr. 1985. *Ap. J.* **297**, 531.

Nomoto, K., and Y. Kondo 1991. *Ap. J. (Letters)* **367**, L19.

Nomoto, K., S. Miyaji, D. Sugimoto, and K. Yokoi 1979a. in *IAU Colloquium 53, White Dwarfs and Variable Degenerate Stars*, ed. H.M. Van Horn and V. Weidemann (Univ. of Rochester), p.56.

Nomoto, K., K. Nariai, and D. Sugimoto 1979b. *Pub. Astr. Soc. Japan* **31**, 287.

Nomoto, K., and T. Shigeyama 1991. in *Supernovae*, ed. S.E. Woosley (Berlin: Springer), p. 572.

Nomoto, K., and D. Sugimoto 1977. *Pub. Astr. Soc. Japan* **29**, 765.

Nomoto, K., D. Sugimoto, and S. Neo 1976. *Ap. Space Sci.* **39**, L37.

Nomoto, K., F.-K. Thielemann, and K. Yokoi 1984. *Ap. J.* **286**, 644.

Nomoto, K., H. Yamaoka, T. Shigeyama, S. Kumagai, and T. Tsujimoto 1991. in *Neutron Stars: Observations and Theory*, ed. J. Ventura and D. Pines (Kluwer; NATO ASI), in press.

Ogata, S., H. Iyetomi, and S. Ichimaru 1991. *Ap. J.* **372**, 259.

Paczyński, B. 1970. *Acta Astr.*, **21**, 1.

Panagia, N. 1987. in *High Energy Phenomena Around Collapsed Stars*, ed. F. Pacini (D. Reidel), p. 33.

Ray, A., and W. Kluzniak 1990. *Nature* **344**, 415.

Romani, R.W. 1990. *Ap. J.* **357**, 493.

Saio, H. and K. Nomoto 1985. *Astr. Ap.* **150**, L21.

Shigeyama, T., and K. Nomoto 1990. *Ap. J.* **360**, 242.

Shigeyama, T., K. Nomoto, and M. Hashimoto 1988. *Astr. Ap.* **196**, 141.

Shigeyama, T., K. Nomoto, T. Tsujimoto, and M. Hashimoto 1990. *Ap. J. (Letters)* **361**, L23.

Shigeyama, T., K. Nomoto, H. Yamaoka, and F.-K. Thielemann 1991a. *Ap. J. (Letters)*, submitted.

Shigeyama, T., K. Nomoto, H. Yamaoka, and F.-K. Thielemann 1991b. in preparation.

Sienkiewicz, R. 1980. *Astr. Ap.* **85**, 295.

Starrfield, S., W.M. Sparks, J.W. Truran, and G. Shaviv 1991. in *Supernovae*, ed. S.E. Woosley (Berlin: Springer), p. 602.

Sugimoto, D. and M.Y. Fujimoto 1978. *Pub. Astr. Soc. Japan* **30**, 467.

Sugimoto, D., M.Y. Fujimoto, K. Nariai, and K. Nomoto 1979. in *IAU Colloquium 53, White Dwarfs and Variable Degenerate Stars*, ed. H.M. Van Horn and V. Weidemann (Univ. of Rochester), p. 280.

Sugimoto, D., and K. Nomoto 1980. *Space Sci. Rev.*, **25**, 155.

Swartz, D.A., J.C. Wheeler, and R.P. Harkness, 1991. *Ap. J.* **374**, 266.

Taam, R.E. 1980. *Ap. J.* **237**, 142.

Tavani, M. 1991. *Ap. J.*, in press.

Taylor, J. 1991. in *X-Ray Binaries and the Formation of Binary and Millisecond Radio Pulsars*, ed. E.P.J. van den Heuvel (Kluwer; NATO ARW), in press.

Thielemann, F.-K., M. Hashimoto, and K. Nomoto 1990. *Ap. J.* **349**, 222.

Thielemann, F.-K., K. Nomoto, and M. Hashimoto 1991. in this volume.

Thielemann, F.-K., K. Nomoto, and K. Yokoi 1986. *Astr. Ap.* **158**, 17.

Tsvetkov, D.Yu. 1985. *Sov. Astr.*, **29**, 211.

Uomoto, A. 1986. *Ap. J. (Letters)* **310**, L35.

Van den Heuvel, E.P.J. 1991. in *Neutron Stars: Observations and Theory*, ed. J. Ventura and D. Pines (Kluwer; NATO ASI), in press.

Webbink, R. 1984. *Ap. J.* **277**, 355.

Wheeler, J.C. 1990. in *Frontiers of Stellar Evolution*, ed. D.L. Lambert (San Francisco: Astron. Soc. of Pacific), in press.

Wheeler, J.C., and R. Harkness 1990. *Rep. Prog. Phys.*, **53**, 1467.

Wolszczan, A. 1991. *Nature* **350**, 688.

Woosley, S.E., R.E. Taam, and T.A. Weaver 1986. *Ap. J.* **301**, 601.

Woosley, S.E., and T.A. Weaver 1986a. *Lecture Notes in Physics*, **255**, 91.

Woosley, S.E., and T.A. Weaver 1986b. *Ann. Rev. Astr. Ap.* **24**, 205.

Woosley, S.E., and T.A. Weaver 1991. in this volume.

Yamaoka, H., and K. Nomoto 1991. in *SN 1987A and Other Supernovae* ed. I.J. Danziger (Garching: ESO), in press.

Yamaoka, H., T. Shigeyama, and K. Nomoto 1991. in preparation.

COURSE VI

MODELS OF TYPE II SUPERNOVAE: AN INTRODUCTION

WOLFGANG HILLEBRANDT

Max-Planck-Institut für Physik und Astrophysik
Institut für Astrophysik
Karl-Schwarzschild-Str. 1
D-8046 Garching b. München, FRG

S. Bludman, R. Mochkovitch and J. Zinn-Justin, eds.
Les Houches, Session LIV 1990
Supernovae

Contents

1. Introduction and statement of the problem 254
2. Observations of Type II supernovae 255
3. Input physics 261
   3.1. The basic equations 262
   3.2. Initial models 263
   3.3. The equation of state of supernova matter 264
      3.3.1. The "low" density EOS 265
      3.3.2. Self-consistent single-particle models 269
   3.4. Weak interaction rates and neutrino transport 275
4. Hydrodynamics (1-dimensional) 281
   4.1. Newtonian physics 281
   4.2. General relativistic hydrodynamics 286
5. Core collapse supernova models and their problems 287
   5.1. An analytic description of core collapse 287
   5.2. Numerical simulations and their main results 290
6. Summary, conclusions, and outlook 295
References 297

1. Introduction and statement of the problem

Supernovae of Type II, that is, explosions of stars which show strong Balmer lines (hydrogen) in their spectra, are now generally believed to originate from massive stars ($M \gtrsim 8\ M_\odot$, where $M_\odot \simeq 2\ 10^{33}$g is the mass of the sun), at the end of their quiet hydrostatic evolution. If this interpretation is correct, they cannot be powered directly by thermonuclear burning and must get their energy, at least partially, from another source. It is therefore intriguing to relate the Type II phenomenon to the formation of neutron stars, an idea that goes back to Baade and Zwicky (1934) and is supported by the fact that several supernova remnants, including the Crab Nebula, do indeed contain neutron stars. In this picture the energy observed in the explosion must ultimately come from a gain in gravitational binding of the core and/or from the binding energy of the newly born neutron star.

Two mechanisms are presently discussed which are potentially able to transform a small fraction of the gravitational energy into outward momentum of the stellar envelope. Neither, however, so far gives a satisfactory explanation of the entire phenomenon. In one class of models the stellar envelope is ejected by a hydrodynamic shock wave generated by a rebounding core near nuclear matter density, but this mechanism seems to work only for a very limited range of precollapse stellar models. Alternatively, neutrino emission from a hot neutron star may heat some outer layers of the core sufficiently to cause an explosion, but it has still not been confirmed that this mechanism works at all.

The question therefore arises whether the apparent problems of various supernova models are due to our incomplete knowledge of certain physical input data, such as the equation of state for hot and dense matter, or whether something fundamental is missing in the models. In the following sections we will address both aspects in some detail. We will start with a brief review of the observational facts relevant to our discussion; in particular, the information available from Supernova 1987A in the Large Magellanic Cloud will be discussed. We then will present an overview of the basic physical input that is needed if supernova models are to be computed. This includes initial models, the equation of state, weak interaction rates, and neutrino transport schemes. Section 4 is devoted to very simple ways to solve the hydrodynamic equations for a spherically symmetric stellar core, and in section 5 the results of several numerical studies will be discussed. The course concludes with a section entitled "Summary, conclusions, and outlook."

2. Observations of Type II supernovae

According to Zwicky's classification, supernovae are called Type II if they show strong hydrogen emission lines in their spectra, and Type I otherwise. Since, in particular, Type Ia events are thought to be caused by thermonuclear disruptions of white dwarfs, we shall consider only Type II supernovae here, although certain other classes of Type I supernovae may also be the result of a core collapse (e.g., K. Nomoto, this volume). At maximum light their luminosity is typically around 10^{43} erg s^{-1}; the total energy in the outburst is found to be on the order of 10^{51} erg, but only a percent or less of this energy is emitted in form of optical radiation. Most of the energy appears to be in the kinetic energy of the ejected matter, which has velocities on the order of 10^4 km s^{-1}. From the spectra one obtains photospheric temperatures near maximum light of about 15 000 K or larger. The light curves stay near maximum for a few days, and in many cases a plateau is observed that lasts for about 100 days. Besides showing strong Balmer lines, indicating hydrogen, the overall abundances of elements seem to be approximately solar.

All these findings, together with the fact that Type II supernovae are only found in spiral arms of galaxies with young populations of stars, indicate that the progenitor stars are quite massive and have extended hydrogen-rich envelopes. Similar conclusions are reached from x-ray observations of some young supernova remnants, that is, CasA, and Puppis A. Also the observed rate of about one per 50 to 100 years in giant spiral galaxies (Tammann 1982; van den Bergh et al. 1987; see also G. Tammann, this volume) is consistent with the assumption that all stars more massive than about 8 $M_{\odot}$ explode as Type II supernovae. Moreover, one can conclude that the progenitors of most Type II supernovae will be in the mass range from 8 to 15 $M_{\odot}$, because those are much more frequently born than more massive ones (Salpeter 1955; Miller and Scalo 1979).

Next one can ask whether there is observational evidence that our basic hypothesis – namely that Type II supernovae are directly related to the formation of neutron stars – is indeed correct. In fact, several young supernova remnants (Crab, Vela, SNR 0540–693, and others) do contain pulsars or X-ray point sources (RCW 103, 3C58, and others), but other remnants do not (CasA, SN 1006, Tycho, and others), and in none of the positive detections is it certain beyond doubt that the explosions were indeed of Type II. Moreover, Manchester et al. (1983) have analyzed 85 supernova remnants in the galaxy, the Large Magellanic Cloud (LMC) and the Small Magellanic Cloud (SMC), and found only 5 radio pulsars nearby. Because the frequency of both types of supernovae is approximately equal, this result is surprising if one believes that all Type II events leave neutron stars behind. Furthermore, not all of the identified pulsars are related to the nearby supernova remnants. On the other hand, there is no obvious contradiction, since many neutron stars may not possess strong magnetic fields or the radio radiation may not be beamed towards us. In this respect only CasA presents a problem, because the neutron star should manifest itself as a x-ray point source, but the upper limit obtained for the x-ray flux is far below the values expected from standard neutron star cooling (Tsuruta 1979).

One may also hope to obtain some information on the explosion mechanism from observations of element abundances in supernova ejecta, because they are sensitive to the strength of the shock wave and to the position of the mass cut between the newly born neutron star and the ejected material; but again only weak constraints can be obtained. The Crab nebula, for example, has been observed at various wavelengths (Davidson et al. 1982; Henry and McAlpine 1982; Henry et al. 1984), but with the exception of a large overabundance of helium relative to hydrogen, possible overabundance of nickel, and a significant underabundance of oxygen, all other elements seem rather normal. In CasA, on the other hand, optical data obtained from fast moving knots (Chevalier and Kirshner 1979) show large abundance inhomogeneities, but virtually no hydrogen, helium, carbon, or nitrogen.

The knots are also depleted in neon and magnesium, but relative to oxygen, some are enriched in sulphur, argon, and calcium. These results have been confirmed by X-ray observations (Pravdo and Smith 1979; Becker et al. 1979; Holt 1983; Pravdo and Nugent 1983; Jansen et al. 1985). They indicate that the exploding star has undergone at least oxygen burning, which means that it was a massive star. Moreover, the abundances in the fast moving knots closely match the products of explosive oxygen burning (El Eid and Langer 1986), indicating that at least part of the explosion energy came from nuclear burning.

An object similar to CasA has recently been observed (SN 1985f in NGC 4618 – Fillipenko and Sargent 1985). This supernova showed strong oxygen emission lines, indicating more than 5 $M_{\odot}$ of oxygen in the ejecta, very little hydrogen and apparently no helium. The most straightforward explanation of this event is that we have seen the explosion of a very massive star ($M \simeq 50\ M_\odot$ on the main sequence) which lost most of its hydrogen-rich envelope prior to the explosion. An even stranger supernova (SN 1961v) has been observed in NGC 1058. In this case the progenitor star was observed for about 30 years before the outburst, the velocity of the ejected material was very low, and the optical light curve declined very slowly on timescales longer than about 6 years. The remnant is now a very strong radio source, comparable to CasA (if the estimated distance of about 12 Mpc is correct). By modelling the light curve, Utrobin (1984) has concluded that the exploding star may have had a mass of about 2000 $M_\odot$.

Thus, it is obvious that Type II supernovae do not form a homogeneous class of objects, and that observations alone do not give us a clear answer as to what the mass of the progenitor stars was and what the right explosion mechanism is. When on February 23, 1987, a supernova explosion was observed in the LMC at a distance of only roughly 50 kpc, this event caused a lot of excitement in the astronomical community, because never since Kepler's supernova in 1604 has a supernova been so close. There was some hope, therefore, that most of the open questions in supernova theory could now be answered. However, it soon became clear that this was not the case. Moreover, SN 1987A raised new problems, which we will discuss in some detail now.

Spectra taken during the second night showed Balmer lines (hydrogen), indicating that the supernova was of Type II (Catchpole et al. 1987; Fosbury et al. 1987; Tyson and Boeshaar 1987). Its position coincided with that of a blue supergiant, Sanduleak (Sk)-69^{o}202 (Walborn et al. 1987; West et al. 1987). When the UV-radiation from the supernova weakened a few weeks after the explosion it became obvious that this star had indeed disappeared (Gilmozzi et al. 1987; Walborn et al 1987). From its spectral class (B3) and its luminosity class (Ia) (Rousseau et al. 1978; Isserstedt 1975; West et al. 1987) one could conclude that the main sequence mass of the progenitor had been close to 20 $M_\odot$ (Arnett 1987; Hillebrandt et al. 1987; Nomoto et al. 1987; Truran and Weiss 1987).

The first big surprise was that, in contrast to theoretical expectations, the progenitor was a blue rather than a red supergiant. Moreover, the presence of low-velocity circumstellar material indicates that the progenitor was a red supergiant some 7000 years ago (Fransson et al. 1989; Wampler and Richichi 1989). One possible way to explain this rather complicated evolution is to assume that helium has been mixed more or less homogeneously throughout most of the hydrogen-rich envelope (Nomoto and Hashimoto 1988; Saio et al. 1988). Additional evidence for strong mixing prior to the explosion comes from the interpretation of the optical spectra (Cassatella 1987; Blades et al. 1987; Williams 1987; Höflich 1988). The reason for these mixing processes is simply not known but may indicate that Sk-69^{o}202 has been a rapidly rotating star (Weiss et al. 1988). In any case, the first nearby supernova has demonstrated that stellar evolution models are still rather uncertain, and one has to keep these uncertainties in mind if attempts are made to model the final explosions.

The light curve of SN 1987A was significantly different from "standard" Type II supernovae (fig. 1). While, however, the very rapid decline during the first few days as well as the slow increase to maximum light can easily be explained from the rather compact structure of the progenitor star (Arnett 1988a; Shigeyama et al. 1988; Utrobin 1988; Woosley et al. 1988), if an explosion energy of $(1.5 \pm 0.5)\ 10^{51}$ erg is assumed, the flat maximum requires mixing of processed material into hydrogen-rich layers during the explosion (Arnett 1988b; Woosley 1988; Fu 1988; Nomoto et al. 1989). In fact, this conclusion is not only based on the interpretation of the light curve but also on direct observations. Already in August 1987, γ-ray lines from the radioactive decay of ^{56}Co were discovered (Matz et al. 1988) and at about the same time hard x-rays were detected. The hard x-ray flux remained nearly constant for over one year and then dropped below the detection limit of existing x-ray satellites (Dotani et al. 1987; Sunyaev et al. 1987; Tanaka 1988). Moreover, strong IR-lines of Ni, Co, and Fe were seen from November 1987 on with velocities up to 3000 km s^{-1}, corresponding to the matter velocity at the photosphere in April 1987 (Rank et al. 1988; Erickson et al. 1988; Witteborn et al. 1988). However, no evidence for Fe or Co enhancements was found in the early optical spectra. The only reasonable explanation for all these findings is that radioactive Co has been mixed inhomogeneously, far out into the H-rich envelope, and formed clumps there. On the other hand, this is difficult to explain within the framework of spherically symmetric supernova models.

The total amount of radioactive Co produced in SN 1987A can be estimated in two independent ways. First, from fig. 1 it is obvious that the late light curve decays on a timescale identical to the lifetime of ^{56}Co. It is therefore reasonable to assume that the late light curve is powered by radioactive decay energy. The initial amount of ^{56}Ni necessary to fit the observations is then about 0.07 $M_\odot$ (Woosley 1988; Arnett 1988b; Shigeyama et al. 1988). Second, the strength of the IR CoII line at 10.53 μ gives 0.0044 $M_\odot$ at day 280, and 0.0023 $M_\odot$ at day 400, in excellent agreement with the estimate obtained from the light curve (Danziger et al. 1989). Moreover, the estimated amount of iron observed at day 280 ($\simeq$ 0.06 $M_\odot$; Danziger et al. 1989) strengthens the conclusion that the late light curve was indeed powered by radioactive decay. This information sets important constraints on the mass of the neutron star which has presumably formed in SN 1987A. The fact that about 0.1 $M_\odot$ of ^{56}Co has been ejected limits the maximum mass to about 1.7 to 1.8 $M_\odot$, because ^{56}Co is synthesized in the Si-shell and at the inner edge of the O-shell, if the explosion energy is around 10^{51} erg as indicated by the early light curve (Nomoto et al. 1989). Moreover, the mass of the final neutron star cannot be below 1.4 $M_\odot$ because otherwise more iron-group elements than observed would have been ejected. Of course, these conclusions rest on the (reasonable) assumption that the main sequence mass of the progenitor star was about 20 $M_\odot$ and that the iron-core masses predicted by stellar evolution models are approximately correct.

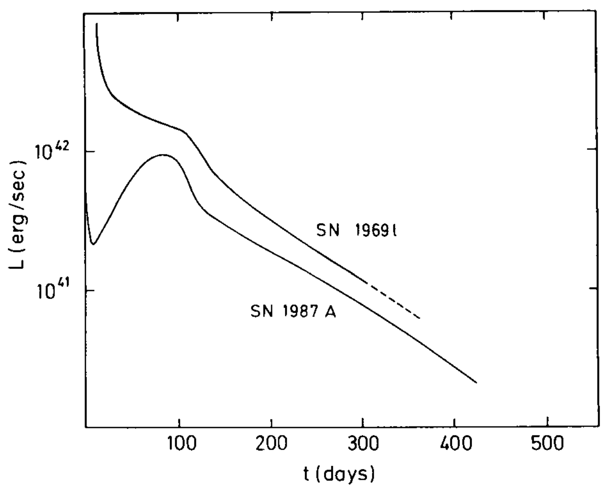

Fig. 1. Light curve of SN 1987A in comparison to a typical Type II light curve. While the late light curves are similar, indicating roughly the same amount of ^{56}Co in both cases, for SN 1987A, lower peak luminosity and presence of a broad maximum reflect the rather compact nature of the progenitor star.

As will be discussed later, the mass of the newly born neutron star is crucial for the explosion mechanism. Therefore it is important to ask whether there are additional observational constraints. Of course, the neutrino burst associated with SN 1987A (Bionta et al. 1987; Hirata et al. 1987) has clearly shown that a compact object, presumably a neutron star, formed during the collapse of the central core of its progenitor star. Because the total energy emitted in the form of neutrinos cannot exceed the binding energy of the final cold neutron star, a lower limit on its mass can be obtained. Unfortunately, the total $\bar{\nu}_e$-energies estimated from the KAMIOKANDE and IMB data are only weakly consistent, leaving uncertainties of about a factor of two (see fig. 2). Moreover, we do not know whether some of the events were caused by (ν, e)-scattering rather than ($\bar{\nu}_e$, p)-reactions or whether some of the events were due to noise in the detectors. Finally, if the progenitor of SN 1987A was a rapidly spinning star, anisotropies of the neutrino emissions would add further uncertainties (Janka and Mönchmeyer 1988). So in conclusion, we can only state that the neutrino data are consistent with the assumption that a neutron star of about 1.5 $M_\odot$ was born in SN 1987A and radiated away a significant fraction of its binding energy in the form of thermal neutrinos during the first few seconds of its life, but neutrino observations do not prove this assumption.

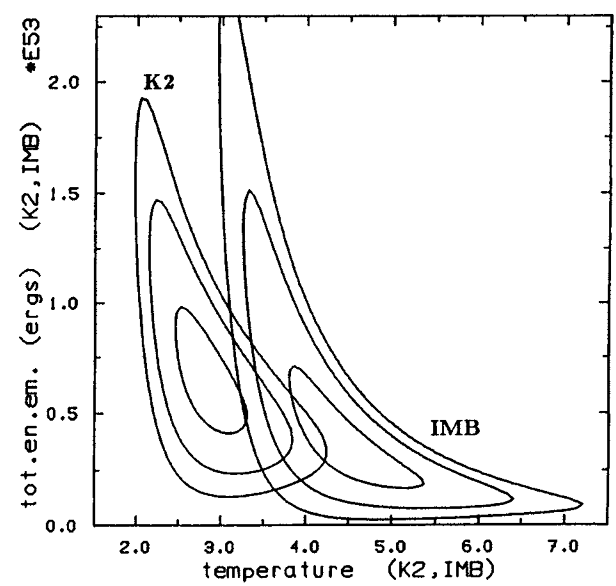

Fig. 2. Maximum likelihood regions in temperature – total energy plane for neutrinos observed by KAMIOKANDE (K2) and IMB detectors for assumed Fermi-Dirac distributions. The contours mark 68%, 95%, and 99% confidence levels (from Janka and Hillebrandt 1989b).

At the time of writing, there is no direct proof for the existence of a neutron star in SN 1987A, the only good test case that we have for our theoretical models. Optical pulses have been searched for but have not been found

(Ögelman et al. 1990). Moreover, there is no indication of an x-ray point source (Trümper, private communication) nor for pulsed radio emmission. However, the light curve shows extra luminosity on the order of 10^{38} erg/sec (Bouchet et al. 1990), which seems to be approximately constant since autumn 1989 (although variations of a factor of two cannot be excluded); the extra luminosity cannot easily be accounted for by radioactive decay models. A possible explanation would be that the compact object in the center of SN 1987A is still surrounded by an accretion disk, and that what we observe is accretion luminosity. In fact, this interpretation would, in a natural way, explain why the luminosity is so close to the Eddington value. It could account for apparent variations in the luminosity by means of disk instabilities similar to those found in dwarf novae (Meyer and Meyer-Hofmeister 1984; Meyer and Meyer-Hofmeister 1991). Such a disk should be the normal case in core collapse, provided that the progenitor star possessed some angular momentum and some matter fell back onto the newly-born compact object. Therefore, roughly constant bolometric light curves with Eddington luminosities over several years should be a common phenomenon for core collapse supernovae. But for the present these speculations do not help answer the questions raised in this article.

We conclude this section with a brief discussion of evidence for significant large-scale anisotropies in SN 1987A. During the first few months after the initial outburst, frequency-dependent linear polarizations were observed by several groups (Barrett 1987; Schwarz 1987; Mendez et al. 1988). It is not clear yet whether these polarizations were caused by prolate or oblate deformations, but deviations from spherical symmetry seem to be on the order of 5 to 20% (Höflich et al. 1989). From their recent Speckle observations at optical wavelengths (Papaliolios et al. 1989) find that the expanding envelope is rather asymmetric, and that the ratio between the minor and major axes is about 2 to 3. It is difficult to imagine a mechanism for such large asymmetries other than a large deformation of the progenitor's envelope. Therefore it is tempting to conclude that Sk–69°202 was in fact a fast rotator; so we would have to revise several of the ideas outlined in the following sections.

3. Input physics

As was mentioned in the introduction, the cores of massive stars will collapse to rather high densities once they have exhausted their nuclear fuel. It is believed, although there is very little direct observational evidence, that at the end of this process, the stellar envelope is ejected in a supernova explosion and a compact neutron star is left behind (see Imshennik and Nadyozhin

1983; or Hillebrandt 1987 for recent reviews). Whether or not this picture is correct must be demonstrated by numerical simulations and, therefore, our first aim should be to compute the dynamics of a collapsing stellar core.

3.1. The basic equations

If we neglect for a moment general relativistic corrections and assume spherical symmetry (e.g. neglect possible effects due to rotation) the basic equations read:

$$\frac{\partial \ln \rho}{\partial t} + \frac{u - u_g}{r} \frac{\partial \ln \rho}{\partial \ln r} + \frac{1}{r^2} \frac{\partial (r^2 u)}{\partial r} = 0, \tag{3.1}$$

$$\frac{\partial u}{\partial t} + (u - u_g) \frac{\partial u}{\partial r} + \frac{p}{\rho} \frac{\partial \ln p}{\partial r} + \frac{\partial \phi}{\partial r} = 0, \tag{3.2}$$

$$\frac{\partial s}{\partial t} + (u - u_g) \frac{\partial s}{\partial r} = \frac{\dot{\varepsilon}}{k_B T}, \tag{3.3}$$

$$\frac{1}{r^2} \frac{\partial}{\partial r} \left(r^2 \frac{\partial \phi}{\partial r} \right) = 4\pi G \rho, \tag{3.4}$$

where $\partial/\partial t$ is the time derivative with respect to a moving system of coordinates, ϕ the gravitational potential, ρ the mass density, p the pressure, s the specific entropy, and $\dot{\varepsilon}$ represent energy sources and sinks. The EOS enters via p and s, which are in general functions of ρ, T and the composition. Moreover, we have written the hydrodynamic equations in terms of logarithmic quantities, because pressure and density vary over several orders of magnitude inside a collapsing star. u_g is the grid velocity. The choice $u \equiv u_g$ leads to co-moving (Lagrange) coordinates, and the variable r can then be replaced by a mass-coordinate

$$m(r) = 4\pi \int_0^r \rho\, r'^2 dr'.$$

$u_g \equiv 0$ means a fixed (Euler) system of coordinates. In general one will work with either Lagrange-coordinates (in the case of a non-rotating star) or with a moving grid, because during collapse more and more matter will be compressed in smaller and smaller volumes.

Equations (3.1) through (3.4) can in principle be solved, provided that initial values ($\rho(r, t_0)$, $p(r, t_0)$, $u(r, t_0)$, and $s(r, t_0)$), an equation of state, and rate equations which determine composition changes, are known. If we denote the concentration of a particular species by x_i, then the latter will be of the general form

$$\dot{x}_i = f(x_j, \rho, T) \tag{3.5}$$

and will also determine the energy generation rate $\dot{\varepsilon}$. Additional complications arise from the fact that neutrinos are not always advected with the matter, therefore transport equations for neutrinos have to be solved together with the rate and hydrodynamic equations. Moreover, general relativity becomes important once the density inside the collapsing core exceeds the density of nuclear matter. Finally, non-spherical effects, such as rotation or large-scale convection, may have to be included. It should be noted that so far in all numerical simulations of stellar collapse certain simplifications are made which make it difficult to compare the results. We will come back to this problem later in section 5.

3.2. *Initial models*

Stars can only collapse if their core mass exceeds the Chandrasekhar mass given by

$$M_{CH} \simeq 5.72 (y_e)^2 M_\odot, \tag{3.6}$$

where y_e is the electron concentration, $y_e = n_{e^-}/n_B$, which is slightly less than 0.5 in the cores of evolved stars. n_{e^-} and n_B denote number densities of electrons and baryons, respectively. In addition, the stellar cores should contain very little or no burnable nuclear fuel (He, C, O) because otherwise the collapse may be stopped by nuclear burning. Finally, the adiabatic index of the core material defined as $\gamma := (\partial \ln p / \partial \ln \rho)_s$ should be smaller than the critical value of 4/3 to guarantee a dynamical instability. Stellar evolution models (Arnett 1977; Nomoto 1984; Weaver et al. 1985; Wilson et al. 1986) predict that all three conditions are fulfilled for stars of mass $50 M_\odot \gtrsim M \gtrsim 8 M_\odot$ on the main sequence. Typical physical conditions near the centers of those stars are densities on the order of 10^{10}g cm^{-3}, temperatures near 10^{10} K, and entropies of about 1 k_B per nucleon. The composition of matter is dominated by iron-group elements (Fe, Ni, ...) and the core mass is approximately 1.5 $M_\odot$ or slightly larger.

From these numbers we can draw a first important conclusion. The pressure of the ions, $p_{\text{ion}} \simeq n_{\text{ion}} k_B T$ is of the order of 10^{26} erg cm^{-3}, and the radiation pressure is about 3×10^{25} erg cm^{-3}. Both contributions to the total pressure are therefore much less than the contribution from the relativistic degenerate electron gas, which contributes about 10^{28} erg cm^{-3}. Consequently, relativistic electrons will dominate the pressure provided that the nucleons remain bound in heavy nuclei, which is the case if the entropy stays low. For a relativistic gas of Fermions, the adiabatic index γ is equal to 4/3 and it will drop below this critical value if the particle concentration decreases. The chemical potential of the electrons inside the stellar core is on the order of 10 MeV and, therefore, some electrons will be captured by free protons and heavy nuclei, leading to the desired result.

We mention in passing that the existence of a Chandrasekhar mass is also responsible for what is called "core convergence." To ignite the central fuel a stellar core has to contract. With increasing central density the electron pressure becomes more and more important. Therefore, in order to contract, the core mass has to be at least the Chandrasekhar mass. The core mass will grow due to burning in a shell surrounding the core. Consequently, the core mass cannot grow significantly beyond the critical mass, at least if the entropy is fairly low. But, of course, these arguments also apply only to stellar cores that are not supported by centrifugal forces. It is possible that rotation induced mixing may destroy the (core mass, main sequence mass)-relation. In particular, observations of SN 1987A indicated that the star underwent considerable mass-loss prior to the explosion, that there were considerable asphericities in the ejecta, and that there was considerable mixing of matter from interior shells into the hydrogen-rich envelope at early times (see Hillebrandt and Höflich 1989 and section 2). These findings indicate that either the progenitor of SN 1987A was a rather peculiar star, or stellar evolution is not yet fully understood.

Stellar evolution models up to the onset of collapse have been computed by Ken'ichi Nomoto and his group and by Stan Woosley and collaborators (see their contributions to this volume). All these models are, of course, non-rotating ones and they implement convection in some version of the mixing-length theory. Whether or not they are realistic is yet to be seen.

3.3. The equation of state of supernova matter

As was mentioned in previous sections, to model stellar collapse and supernova explosions we need an equation of state from, say, 10^{-6} to several times nuclear matter density, and which cover entropies per nucleon of about 0.5 to 10, where the high values may be reached in shock-heated matter. Because this topic is also discussed by Dominique Vautherin in this volume, we can be somewhat brief, but will nevertheless mention the essentials that will enter into most of the numerical models described in this article.

3.3.1. The "low" density EOS

In accord with the discussion presented earlier we will first assume that

(i) matter is in nuclear statistical equilibrium at fixed electron concentration y_e,

(ii) neutrons, protons, and nuclei can be described by an ideal Boltzmann gas,

(iii) electrons, positrons, and neutrions are non-interacting Fermions.

Of course, in particular condition (ii) is only valid if the typical interparticle distance is large compared to particle size and the range of the interaction forces. The applicability of this approach, therefore, is limited to densities below a few times 10^{12}g cm^{-3}. The contributions from the nucleonic components to the free energy can then be written as

$$f_i = -n_i\, k_B T \left\{ 1 + \ln \left[\frac{1}{n_i} \left(\frac{m_i k_B T}{2\pi\hbar^2} \right)^{3/2} \omega_i(T) \right] \right\} \tag{3.7}$$
$$+\, m_i c^2 + \text{(interaction terms)}.$$

Here i denotes neutrons, protons, and nuclei, respectively, $\omega_i(T)$ are the nuclear partition functions, and all other quantities have their usual meaning.

If we define an effective chemical potential μ_i' by the Boltzmann-relation

$$e^{-\mu_i'/k_B T} := \frac{1}{n_i} \left(m_i k_B T / 2\pi\hbar^2 \right)^{3/2}, \tag{3.8}$$

we may write the true chemical potential as

$$\mu_i = \left(\frac{\partial f_i}{\partial n_i} \right)_{T, y_e} = \mu_i' + m_i c^2 + \text{(interaction terms)}. \tag{3.9}$$

At the temperatures of interest here ($T > 5 \times 10^9$K), nuclei will be thermally excited, and we have to take nuclear excited states into consideration. This can be done as follows. We can treat each excited state of a nucleus A as a separate species in equilibrium with free neutrons and protons:

$$A^{(J)}(Z, N) \rightleftarrows N \cdot n + Zp, \tag{3.10}$$

where n denotes a neutron, p a proton, and J labels the excited states.

The equilibrium condition is then

$$\mu_{AZ}^{(J)} = (A - Z)\mu_n + Z\mu_p \tag{3.11}$$

or

$$\mu_{AZ}'^{(J)} = (A - Z)\mu_n' + Z\mu_p' + B_{AZ}^{(J)} + \text{ (interaction terms)}\ , \tag{3.12}$$

where now $B_{AZ}^{(J)} = (A - Z)m_n c^2 + Zm_p c^2 - m_{AZ}^{(J)} c^2$ stands for the binding energy of the nucleus A in the excited state J.

If we define $\beta := 1/k_B T$ and the partition function $\omega(\beta)$ by

$$\begin{aligned}\omega(\beta) : &= \sum_J (2I_J + 1)e^{-\beta\{B_{AZ}^{(0)} - B_{AZ}^{(J)}\}} \\ &= \sum_J (2I_J + 1)e^{-\beta E_J},\end{aligned} \tag{3.13}$$

where I_J is the spin and $B_{AZ}^{(0)}$ is the ground state binding energy, we find from eq. (3.8) for the number density of a given nuclear species

$$n_i = \sum_J n_{AZ}^{(J)} = \omega(\beta)\left(\frac{2\pi m_i^{(0)}}{h^2\beta}\right)^{3/2} e^{\{\beta B_i^{(0)} + (A-Z)\eta_n + Z\eta_p\}} \quad , \tag{3.14}$$

where again the degeneracy parameter η has been introduced by $\eta := \beta\mu'$.

Equation (3.14) contains four unknown quantities. The partition function $\omega(\beta)$ and the ground state binding energy $B_{AZ}^{(0)}$ have to be determined, if possible, from experiments or from nuclear physics models. Otherwise, As was mentioned earlier, nuclei inside a collapsing stellar core tend to be neutron rich and unstable in the laboratory. Consequently we have to rely mainly on theoretical extrapolations from experimental data, which make the determination of the low-density EOS of supernova matter still uncertain (see El Eid and Hillebrandt 1980, Mazurek et al. 1979).

To determine the degeneracy parameters of neutrons and protons two more equations are needed. These are the baryon number conservation

$$n_B = n_n + n_p + \sum_i A_i n_i \tag{3.15}$$

and charge neutrality

$$y_e = (n_p + \sum_i Z_i n_i)/n_B. \tag{3.16}$$

The approach to the EOS outlined so far has completely neglected long-range Coulomb interactions between nuclei. However, because at densities below a few times 10^{12} g cm^{-3} and temperatures corresponding to an entropy of $1k_B$/nucleon, supernova matter behaves like a weakly coupled plasma, the

Debye-Hückel description of Coulomb interactions is a good approximation, and one may add a term

$$f_c = -\frac{2e^3}{3}(\pi/k_BT)^{1/2}(\sum_i n_i Z_i^2)^{3/2} \tag{3.17}$$

(Landau and Lifshitz 1974) to the free energies of eq. (3.7). The main effect of this correction is to increase somewhat the masses of the most abundant nuclei in nuclear statistical equilibrium without changing the overall behaviour of the EOS. On the other hand, the inclusion of the Coulomb correction eq. (3.17) makes the numerical solution much more troublesome, because the number densities (eq. (3.14)) are no longer given explicitly, but require the solution of a coupled non-linear system of stiff equations.

Nucleon-nucleon interactions may also be included in this general scheme by means of an "effective" nuclear two-body force (see El Eid and Hillebrandt 1980). However, because such a treatment is not self-consistent we will not go into details here, but come back to this question later in subsection 3.3.2.

Finally, we have to add the contributions from (relativistic) leptons to obtain the complete EOS. As was discussed earlier, typically the electron Fermi-energy is much larger than the rest mass and, therefore, the EOS can be expressed in terms of the relativistic Fermi integrals

$$F_n := \int_0^\infty \frac{z^n dz}{e^{z-\eta}+1}, \tag{3.18}$$

as

$$n = g\,\frac{4\pi}{c^3h^3}\,(k_BT)^3F_2(\eta), \tag{3.19}$$

$$\varepsilon = g\,\frac{4\pi}{c^3h^3}\,(k_BT)^4F_3(\eta), \tag{3.20}$$

$$p = \frac{1}{3}\varepsilon, \tag{3.21}$$

where the statistical weight g is 2 for electrons and positrons and 1 for neutrinos. If $\eta \gg 1$ holds, the Fermi-integrals can be approximated by $F_2(\eta) \simeq \frac{1}{3}\eta^3$ and $F_3(\eta) \simeq \frac{1}{4}\eta^4$ leading to the well-known expression

$$\varepsilon = \frac{3}{4}\left(\frac{6\pi^2}{g}\right)\hbar c\, n^{4/3} \tag{3.22}$$

for the energy density of relativistic degenerate Fermions.

Some results of the model EOS described here are shown in figs. 3 and 4. Note that the method has been extrapolated to high densities, where some of the approximations become questionable. It can be seen, however, that the most important piece of information is the nuclear partition function. On the other hand, nucleon-nucleon interactions seem to be of minor importance, at least up to densities of about 5×10^{13} g cm^{-3}. It also has turned out that the number of nuclear species included in the equilibrium "network" strongly affects the concentration of free protons, which in turn are of great importance for the electron capture rates and thus the effective adiabatic index. Note that in practice we not only have to determine energy-density and pressure as functions of density, temperature, and composition, but also that the deviation of the adiabatic index from its critical value of 4/3 is important. This fact makes it necessary to consider also minor contributions to the EOS.

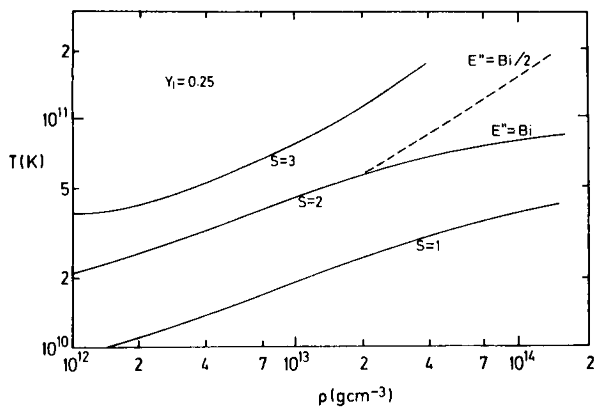

Fig. 3. Isentropes calculated from the El Eid and Hillebrandt (1980) EOS. The S = 2 curve has been computed for two diffent choices of of the nuclear partition function. For a small partition function (dashed curve) free neutrons begin to drip out of the nuclei considerably below nuclear matter density.

In this respect some remarks on the number of "dripped" particles seem to be useful. As we saw earlier the total entropy inside a collapsing stellar core is on the order of $1 k_B$/nucleon. If we make the reasonable assumption that neutrons and protons are not degenerate, then their entropy is given by

$$S_{n,p} = k_B\, n_{n,p} \left\{ \frac{5}{2} - \ln \left[\frac{n_{n,p}}{2} \left(\frac{h^2 \beta}{2\pi m_0} \right)^{3/2} \right] \right\} . \qquad (3.23)$$

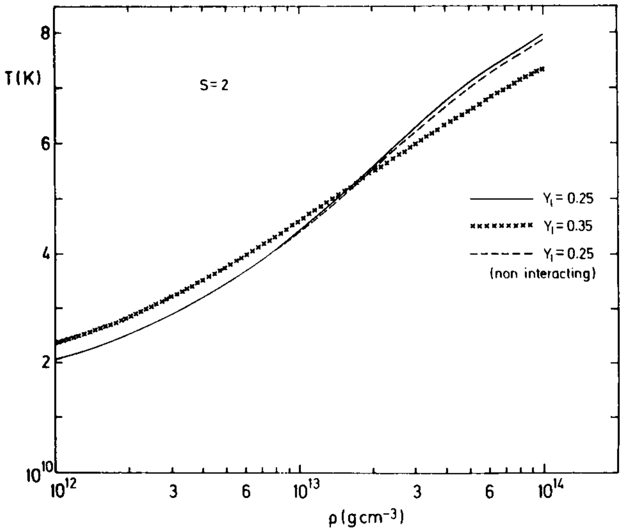

Fig. 4. Effects of nucleon-nucleon interactions and of lepton concentration y_l on the EOS of supernova matter (from El Eid and Hillebrandt 1980).

In general we will find $\frac{n_{n,p}}{2}\left(\frac{h^2\beta}{2\pi m_0}\right)^{3/2} < 1$ and therefore the contribution of a free neutron or proton to the total entropy will be larger than 5/2. Consequently, the concentration of neutrons and protons has to be less than 0.2 in order to keep the total entropy around 1 k_B/nucleon. This in turn means that most nucleons remain bound in nuclei, as was discussed earlier. Thus, the pressure will be dominated by relativistic leptons, and most of the entropy is stored in nuclear excited states. Because entropy is almost conserved during collapse, the nuclear contributions to the EOS cannot be neglected (see fig. 5).

3.3.2. Self-consistent single-particle models

As was discussed in previous sections the Boltzmann-gas approach to the nuclear part of the EOS is no longer valid if the nuclear radius R_N becomes comparable to the Coulomb interaction radius R_c. Phenomenologically one finds $R_N \sim A^{1/3}$ and R_c is roughly proportional to $(A/\rho)^{1/3}$ leading to

$$\frac{R_N}{R_c} \simeq 10^{-5}\rho^{1/3}. \tag{3.24}$$

From eq. (3.24) we can conclude that if we require $R_N/R_c \ll 1$, ρ has to be smaller than 10^{12}g cm^{-3}. Therefore, at high densities a self-consistent model

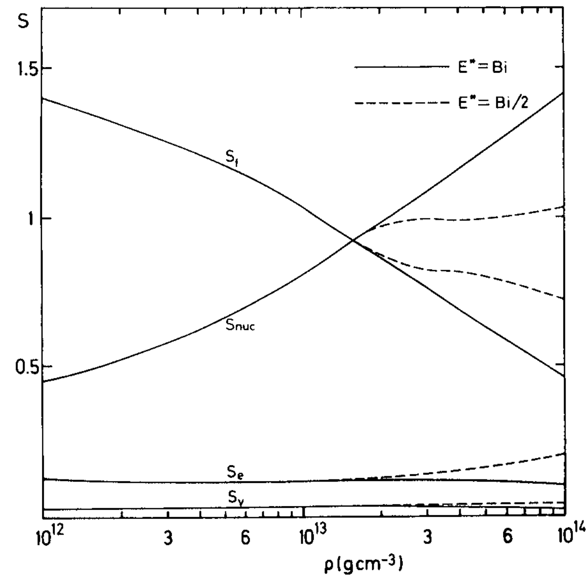

Fig. 5. Contributions from various components to the entropy of supernova matter (from El Eid and Hillebrandt 1980). S_f is the entropy of free nucleons, S_{nuc} that of heavy nuclei. S_e and S_ν denote contributions from electrons and neutrinos, respectively.

has to be invented for the nuclear EOS. At even higher densities, $\rho \gtrsim 0.1\ \rho_0$, similar arguments also show that nucleon-nucleon interactions have to be included self-consistently.

The most advanced method which has been applied to the supernova problem so far is the temperature dependent Hartree-Fock method (Bonche and Vautherin 1981; Hillebrandt and Wolff 1985; see also D. Vautherin, this volume). In this method one starts from a model Hamiltonian which in second quantization reads

$$H = \sum_{i,j} < i|t|j > a_i^+ a_j + \frac{1}{2} \sum_{\substack{i,j\\k,l}} < ij|V|kl > a_i^+ a_j^+ a_k a_l. \qquad (3.25)$$

Here t is the kinetic energy operator, V an effective nucleon-nucleon interaction (including Coulomb interactions), and a^+ and a are nucleon creation and annihilation operators, respectively.

In mean field approximation the one-particle density operator is given by

$$\hat{\rho} = \frac{1}{\hat{Z}} \exp\left\{-\sum_i \alpha_i a_i^+ a_i\right\}, \tag{3.26}$$

where

$$\hat{Z} = \sum_{n_1,n_2,\ldots=0,1} \langle n_1 n_2 \ldots | \exp\left\{-\sum_i \alpha_i a_i^+ a_i\right\} | n_1 n_2 \ldots \rangle \tag{3.27}$$

is the grand partition function, and the sum runs over all completely antisymmetrized states. The α_i are variational parameters which determine the occupation number of a state i. In particular, the occupation probability for a single-particle state i can be obtained from

$$n_i = Tr(\hat{\rho} a_i^+ a_i) = (1 + e^{\alpha_i})^{-1}. \tag{3.28}$$

The grand canonical potential Ω can now be obtained from

$$\Omega = \Omega(T, V_c, \mu_k) = F - \mu_k N_k = E - T \cdot S - \mu_k N_k, \tag{3.29}$$

where $F = F(T, V_c, N_k)$ is the free energy, $E = Tr(\hat{\rho} \cdot H)$ is the energy, $S = -Tr(\hat{\rho} \ln \hat{\rho})$ is the entropy, and $N_k = Tr(\hat{N}_k \hat{\rho})$ the particle number. V_c is the volume of a unit cell and μ_k a Lagrange multiplier, which has the physical meaning of a chemical potential. Finally, the index k stands for neutrons and protons, respectively.

By using eq. (3.26) for the density operator we obtain

$$E = \sum_i \langle i|t|i\rangle n_i + \frac{1}{2}\sum_{i,j} \langle ij|V|ij - ji\rangle n_i n_j, \tag{3.30}$$

$$S = -\sum_i \{n_i \ln n_i + (1 - n_i)\ln(1 - n_i)\}, \tag{3.31}$$

and

$$N_k = \sum_i n_i^k. \tag{3.32}$$

We can now minimize Ω with respect to the α_i and the single-particle wave functions $|i>$. The variation with respect to the single-particle wave functions yields the well-known Hartree-Fock equations

$$W|\phi_m> = \varepsilon_m |\phi_m>, \tag{3.33}$$

where $< i|W|j > = < i|t|j > + \sum_l n_l \{< il|V|jl - lj >\}$ and the ε_m are single-particle energies.

The variation of Ω with respect to the α_i relates occupation probabilities and chemical potentials via

$$n_m = \left(1 + e^{(\varepsilon_m - \mu_k)/k_B T}\right)^{-1} . \tag{3.34}$$

These equations can be solved in the following way. First one has to choose an effective interaction V. Since, by definition, the Hartree-Fock method deals with independent particles, nucleon-nucleon correlations have to be modelled by V. In practical applications, Skyrme-type forces have been used because they are tailored to fit the properties of finite nuclei and also symmetric nuclear matter and neutron matter in the Hartree-Fock model (see Hillebrandt and Wolff 1985 and references therein). It is obvious that a resulting EOS will depend on the particular choice of V, but we have to live with this uncertainty.

Next the Hartree-Fock eqs. (3.33) must be solved, and here a new problem arises. In the deep interior of a collapsing star, the nuclei forms a Coulomb-lattice. Therefore we must solve the Hartree-Fock equations for a unit cell with periodic boundary conditions. This immediately leads to a 3-dimensional problem which cannot be solved for the whole range of temperatures, densities, and lepton concentrations present in a supernova core. One therefore assumes spherical symmetry and applies the Wigner-Seitz method to include Coulomb-lattice effects. However, this means that we cannot impose periodic boundary conditions on the single-particle wave functions. One therefore solves eq. (3.33) with respect to the boundary conditions so that even for angular momentum states, the wave functions should be zero on R_c, whereas for odd ones the derivative should be zero. Whether or not this is a good choice must be checked by 3-dimensional computations and some of the ongoing discussions concerning the geometrical structure of matter near the transition to homogeneous nuclear matter may result from these uncertainties.

Once the Hartree-Fock equations have been solved we can compute E, S, and Ω. The derivative of F with respect to V_c yields the pressure, and finally contributions from leptons and photons have to be added.

As can be seen from fig. 6 for given T, ρ, and y_e the free energy per nucleon may have several minima indicating nuclear shell effects. The most stable solution will then be the one which gives the lowest free enthalpy

$$G = G(P, V_c, T, N_k, \ldots) = F + PV_c = \mu_k N_k \quad , \tag{3.35}$$

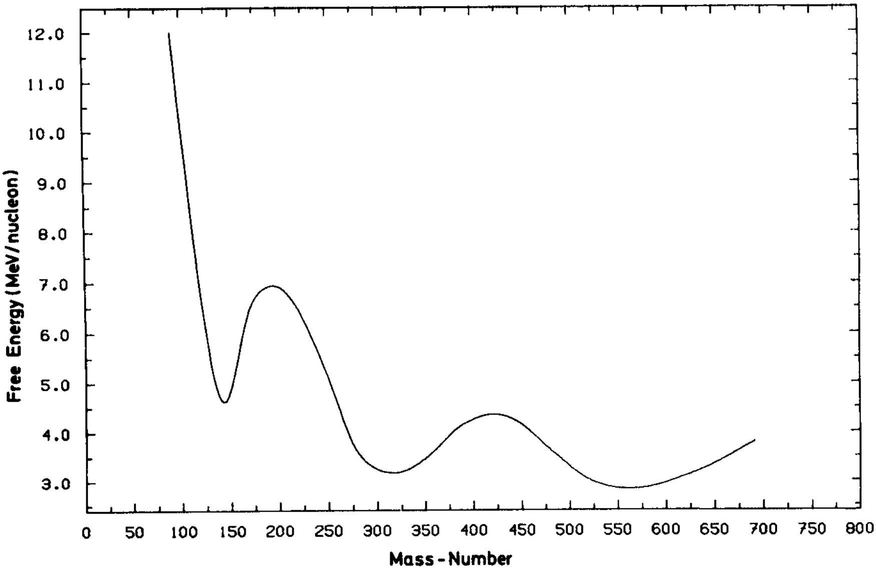

Fig. 6. Free energy per nucleon in Hartree-Fock approximation as a function of nucleon number in a Wigner-Seitz cell (from Hillebrandt et al. 1984). A density of 6×10^{13} g/cm^3, a temperature of 2.5 MeV, and an electron concentration of 0.35 were chosen.

In the example shown in fig. 6, this would correspond to the state with about 560 nucleons in a Wigner-Seitz cell. Note, however, that the minima in the free energy are quite flat and that different minima are separated only by barriers on the order of $k_B T$. Therefore, in reality, the matter of a collapsing star locally will also be a mixture of many nuclear species and the "one nucleus" approximation outlined here is very questionable.

Figures 7 and 8 show some more results for the EOS of supernova matter at high densities. First, it can be seen that in agreement with our earlier discussion for low entropies ($S \simeq 1\ k_B$/nucleon), the adiabatic index is always close to 4/3 up to rougly nuclear saturation density. This means that the collapse proceeds to nuclear matter density unless non-equilibrium processes increase the entropy, or the critical value of γ is increased by rotation. Second, it is apparent that for somewhat higher entropies ($S \gtrsim 2\ k_B$/nucleon), temperature effects become very pronounced, even at densities beyond nuclear-matter density, where the method described can still be applied but gradually loses reliability because the parameters of the effective interaction have been fitted to properties of stable nuclei. Fortunately, the adiabatic index just beyond

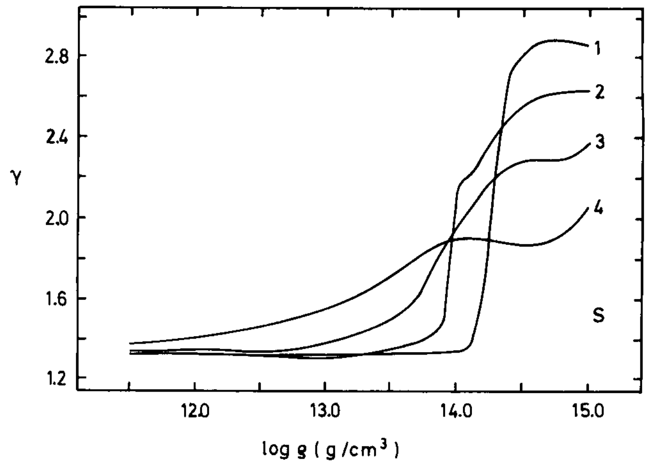

Fig. 7. Adiabatic index versus density for a sequence of isentropes obtained by the Hartree-Fock method. The phase transition to homogenous nuclear matter appears as a jump in γ. The electron fraction was 0.35. Neutrinos were not included.

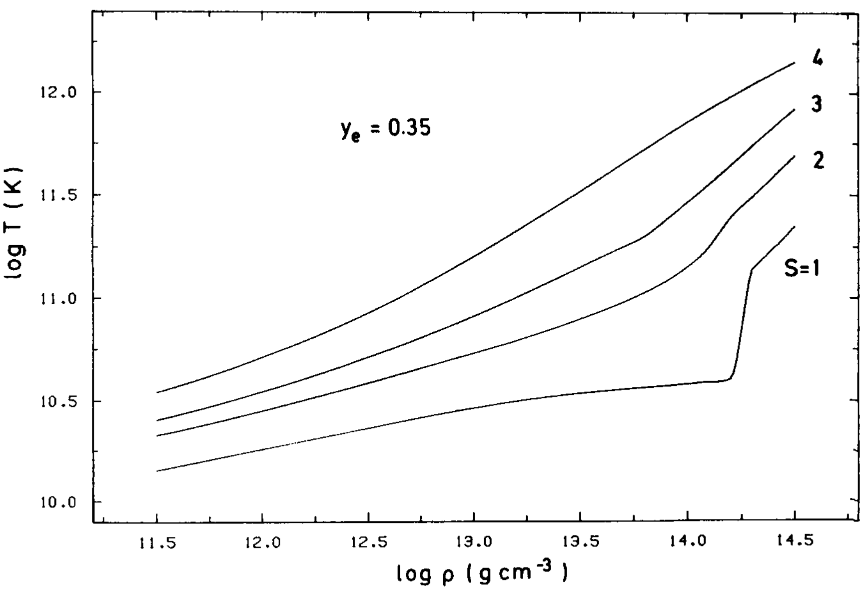

Fig. 8. Isentropes corresponding to fig. 7.

ρ_0 is likely to be of the order of 3 and, therefore, a collapsing core will not overshoot this density by much.

Recently, the difficulties which core-collapse models have in explaining the observed supernova outburst (see also section 5) have caused the initiation of parameter studies to investigate the sensitivity of the hydrodynamic simulation of the EOS near and beyond nuclear matter density. In particular, Baron et al. (1985a, 1985b; 1987), in a series of papers used an analytic model for the nuclear EOS and investigated the impact of the nuclear compressibility on the outcome of core-collapse simulations. Their main result was that a soft EOS near nuclear saturation density increases the chance for a successful explosion, but within reasonable ranges of their parameters they obtained rather different results, indicating the importance of the EOS.

3.4. Weak interaction rates and neutrino transport

In general, in a collapsing star and during the explosion phase, weak interaction reactions such as

$$\begin{aligned} e^- + \left\{ \begin{matrix} p \\ A(Z, N) \end{matrix} \right\} &\rightarrow \left\{ \begin{matrix} n \\ A(Z-1, N+1) \end{matrix} \right\} + \nu_e \\ \nu_e + n &\rightarrow p + e^- \\ \nu_e + e^- &\rightarrow \nu_e + e^-, \quad \text{etc.} \end{aligned} \tag{3.36}$$

are not in equilibrium unless the density exceeds several times 10^{12} g cm^{-3}. Of particular importance are reactions which change the electron concentration y_e, because, as we have seen, electrons dominate the pressure during most of the collapse. The rates for electron captures on free protons can be computed with numeric exactness (see Takahashi et al. 1978), but electron captures on nuclei are much more difficult (see figs. 9 and 10 for a schematic representation).

Present models are probably only accurate to within factors of about five (Fuller et al. 1982; Takahashi et al. 1978; Wambach 1986). Fortunately, most EOS predict a proton concentration which is sufficiently high, such that the change in y_e is mainly due to electron captures on free protons. The same is not true for entropy generation due to non-equilibrium weak interactions, as will be discussed below.

Other important processes include neutrino-absorption by free neutrons, neutrino-electron scattering, neutrino-nucleus coherent scattering and neutrino-neutron scattering. Again, the cross-sections and reaction rates can be computed with numeric exactness (Bruenn 1985), but in most numerical studies approximate values are used.

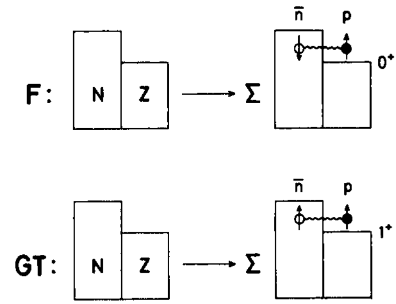

Fig. 9. Schematic representation of Fermi (F) and Gamov-Teller β-transitions.

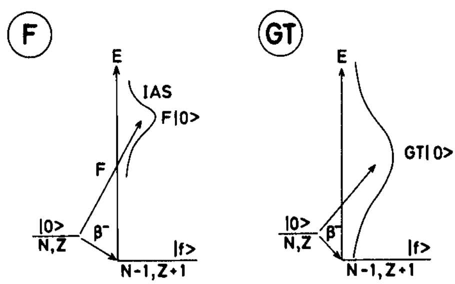

Fig. 10. Schematic representation of the β-strength for both Fermi and Gamov-Teller transitions. In reality, the β-strength function will have significant structure not shown here.

In a collapsing star neutrinos are mainly produced by electron captures because the electrons are degenerate and therefore the positron concentration is extremely low. We find ν_e's only and their energy are on the order of 2/3 of the electron Fermi energy ($\simeq$ 10–20 MeV). Neutrino opacities are dominated by coherent scattering off heavy nuclei, for which the cross section is given approximately by

$$\sigma \simeq 10^{-44}\text{cm}^2\, N^2 \left[\frac{E_\nu}{\text{MeV}}\right]^2, \tag{3.37}$$

where for simplicity we have assumed a Weinberg angle $\sin^2\theta_W = 0.25$ and N is the neutron number of the nucleus.

Neutrinos are predominantly produced at densities between 10^{11} and 10^{12}g cm^{-3}, the "deleptonization shell," where the typical nucleus has about 80 to 100 nucleons and 50 neutrons. The mean free path of the neutrinos is therefore

$$\ell_\nu \simeq \frac{1}{n_A \sigma} \simeq 10^7\text{cm} \left[\frac{\rho}{10^{12}\text{g cm}^{-3}}\right]^{-1} \frac{A}{N^2} \left[\frac{E_\nu}{10\text{MeV}}\right]^{-2}, \tag{3.38}$$

where n_A is the density of an average heavy nucleus with mass number A. Here we have assumed that the concentration of free nucleons is small, which is well justified if the entropies per nucleon are less than about 2 k_B. From eq. (3.38) we find that the matter becomes opaque for neutrinos once the density exceeds $\simeq 5 \times 10^{11}$ g cm^{-3}. The diffusion time

$$\tau_{\text{diff}} \simeq \frac{d^2}{\frac{1}{3}c\ell_\nu}; \quad d \simeq 10^7\text{cm} \tag{3.39}$$

is then on the order of 2 s and thus much longer than the collapse time ($\simeq 10^{-3}$ s). Consequently, neutrinos are trapped and move with the matter. Neutrino-electron scattering, finally, equilibrates the neutrinos' energy distribution, and at densities beyond 10^{12} g cm^{-3}, weak interactions also approach an equilibrium. Therefore, the entropy of stellar matter should be constant above 10^{12} g cm^{-3}, and the collapse should be adiabatic unless shocks heat the matter.

Entropy generation during the equilibration phase can be estimated as follows (Bruenn 1985):

Before neutrino trapping, (ν_e, e)-scattering as well as ν-absorption can be neglected. The change in specific entropy is thus given by

$$k_B T \frac{ds}{dt} = (\mu_e + \mu_p - \mu_n - \langle E_\nu \rangle_{\text{emit}}) \left(-\frac{dy_e}{dt}\right), \tag{3.40}$$

where the μ's denote chemical potentials of the respective particles and $\langle E_\nu \rangle_{\text{emit}}$ is the average neutrino energy in emission processes. For e^--captures on free protons we have $\langle E_\nu \rangle_{\text{emit}} \simeq \frac{5}{6}\mu_e$ (since $\mu_e \gg k_B T$) and e^--captures on heavy nuclei give approximately

$$\langle E_\nu \rangle_{\text{emit}} \simeq \frac{3}{5}(\mu_e + \mu_p - \mu_n - \Delta), \tag{3.41}$$

where Δ is the excitation energy, because part of the decay energy is stored in nuclear excited states. It is clear from eq. (3.40) and eq. (3.41) that the latter process always leads to an increase in entropy, whereas e^--captures on free protons will decrease the entropy. The net-effect is a very small increase.

After neutrino trapping the change of entropy is given by

$$k_B T \frac{ds}{dt} \simeq (\mu_e + \mu_p - \mu_\nu - \mu_n) \left(-\frac{dy_e}{dt} \right), \tag{3.42}$$

which is always positive. From numerical models one obtains typically changes in y_e of at most 0.1, and differences of the chemical potentials of less than 5 k_B T. The increase of the entropy is therefore at most 0.5 k_B and the entropy always stays low (Bethe 1982).

After core-bounce the out-going shockwave increases the entropy to values of about 7 to 9 k_B. Heavy nuclei are dissociated into free neutrons and protons. This means that the neutrino scattering cross sections are significantly reduced and neutrinos can diffuse on timescales on the order of a few ms to the shock front, where they pile up until the shock passes the neutrino sphere. But only those neutrinos which are created in the shocked gas can diffuse, because the diffusion time in the unshocked material is still on the order of several tenths of a second and thus much longer than the shock propagation time. Once the shock has passed the neutrinosphere, most of these neutrinos are emitted on a hydrodynamical timescale ($\sim$ ms) (Hillebrandt and Müller 1984). In the shocked gas the temperature is sufficiently high so that neutrino degeneracy is removed. This leads to an increase of e^--captures on free protons, and the matter becomes more neutron rich. As a result the electron chemical potential drops to values close to $k_B T$. But since the temperature is still high ($k_B T \gtrsim 1$ MeV), electron-positron pairs form in equilibrium and anti-neutrino producing reactions such as $e^+ + n \to \bar{\nu}_e + p$ and $e^+ + e^- \to \bar{\nu}_e + \nu_e$ become important. Moreover, electron-positron pairs will also decay into μ-and τ-neutrinos. Therefore, we expect that most of the energy of the proto-neutron star will be carried away by neutrinos of all flavours (see fig. 11).

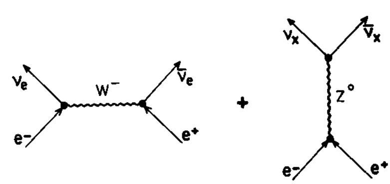

Fig. 11. (e^+, e^-)-decay channels into neutrinos.

We conclude this section with some remarks on the way neutrino transport is usually treated in numerical simulations of stellar collapse and supernova explosions, and how this should be done. During collapse and after core-bounce we will always find regions in the star where neutrinos are either streaming freely or diffusing outwards. So, in principle, we would have to solve the Boltzmann transport equation. This transport equation, however, is a set of complicated partial integro-differential equations (Castor 1972) and therefore has never been used in core-collapse computations – approximations to it are used instead (see also D. Nadyozhin, this volume).

To derive simple transport equations one may replace the Boltzmann equation by moment equations

$$M_\nu^n := \frac{1}{2}\int_{-1}^{1} I_\nu\, \mu^n d\mu, \quad n = 0, 1, 2, \dots\ , \tag{3.43}$$

where $\mu = \cos\theta$ and I_ν is the intensity of neutrinos of energy ϵ_ν. Then one obtains

$$M_\nu^0 = J_\nu =: \frac{1}{4\pi}\, G_\nu \quad \text{(neutrino energy)}, \tag{3.44}$$

$$M_\nu^1 = H_\nu =: \frac{1}{4\pi}\, F_\nu \quad \text{(neutrino energy flux)}, \tag{3.45}$$

$$M_\nu^2 = K_\nu \quad \text{(neutrino pressure)}. \tag{3.46}$$

The diffusion approximation follows if we use the closure conditions

$$M_\nu^3 \equiv 0, \quad K_\nu = J_\nu/3 = p_\nu. \tag{3.47}$$

In Lagrangian coordinates we then get

$$\dot{G}_\nu + \frac{1}{r^2}\,\frac{\partial(r^2 F_\nu)}{\partial r} + \frac{\dot{\rho}}{3\rho}\,\frac{\partial G_\nu}{\partial\, ln\ \epsilon_\nu} = -\ c\Sigma_a^\nu G_\nu + q_\nu, \tag{3.48}$$

$$\frac{1}{c}\dot{F}_\nu + \frac{c}{3}\,\frac{\partial G_\nu}{\partial r} - F_\nu\left[\frac{2v}{cr} + \frac{2}{c}\,\frac{\dot{\rho}}{\rho}\right] - \frac{v}{cr}\,\frac{\partial}{\partial\epsilon_\nu}(\epsilon_\nu F_\nu) = -\Sigma_t^\nu F_\nu, \tag{3.49}$$

where Σ_a^ν is the macroscopic absorption cross section, q_ν is the spectral emissivity, and Σ_t^ν denotes the macroscopic transport cross section, which is equal to $(\lambda_\nu)^{-1}$ (Arnett 1977).

In addition, if we assume a thermal distribution of neutrinos,

$$G_\nu = \text{const.}\epsilon_\nu^3(1 + \exp((\epsilon_\nu - \mu_\nu)/k_B T))^{-1}, \tag{3.50}$$

and drop terms of the order $(\frac{v}{c})^2$ (non-relativistic limit), we obtain

$$F_\nu = -\frac{c}{3\Sigma_t^\nu}\frac{\partial G_\nu}{\partial r} \tag{3.51}$$

and

$$\dot{G}_\nu - \frac{1}{r^2}\frac{\partial}{\partial r}\left[r^2\frac{c}{3\Sigma_t^\nu}\frac{\partial G_\nu}{\partial r}\right] + \frac{\dot{\rho}}{3\rho}\frac{\partial G_\nu}{\partial\, ln\, \epsilon_\nu} = -c\Sigma_a^\nu G_\nu + q_\nu. \tag{3.52}$$

By multiplying eq. (3.52) by ϵ_ν^{-1} and integrating over $d\epsilon_\nu$ we get the usual diffusion approximation

$$\frac{\partial}{\partial t}(\rho y_\nu) - \frac{1}{r^2}\frac{\partial}{\partial r}\left[r^2\frac{c^2}{3\bar{\Sigma}_t}\frac{\partial}{\partial r}(\rho\, y_\nu)\right] = \text{sources and sinks.} \tag{3.53}$$

Here the mean free path is given by

$$(\bar{\Sigma}_t)^{-1} = \int_0^\infty (\Sigma_t^\nu)^{-1} d\epsilon_\nu \Big/ \int_0^\infty d\epsilon_\nu. \tag{3.54}$$

Since in thermal equilibrium the relations $n_\nu \sim T^3 F_2(\mu_\nu/k_B T)$ and $g_\nu \sim T^4 F_3(\mu_\nu/k_B T)$ hold, where the F's denote relativistic Fermi-integrals, the neutrino energy flux can be computed once the particle flux is known.

The approximation described here has two major shortcomings. First, at densities below 10^{12} g cm^{-3} neutrinos are not in thermal equilibrium and, second, the diffusion approximation breaks down at the neutrinosphere, where the mean free path becomes comparable to the stellar radius. The second problem is usually circumvented by introducing a so-called flux-limiter, which guarantees that for $\bar{\lambda} \gg \Delta r$, the free streaming limit is obtained. The first problem can only be solved by non-equilibrium transport models such as "two-fluid models" (Hillebrandt 1987), "flux-limited" diffusion (Arnett 1977; Bowers and Wilson 1982; Bruenn 1985), "variable Eddington-factor" methods (Janka 1990), Monte-Carlo transport (Janka 1987; Janka and Hillebrandt 1989a, 1989b), or direct integrations of the Boltzmann equation (Mayle et al. 1988). However, it should be noted that even the most elaborate transport schemes used in stellar collapse models are based on the diffusion equation, and therefore, may misrepresent the actual neutrino spectra.

4. Hydrodynamics (1-dimensional)

Next, we briefly discuss how one can compute the collapse of a stellar core in a very simple way, provided that all necessary input physics is known. We restrict ourselves to spherically symmetric collapse because the multidimensional case is discussed by Ewald Müller in this volume. We begin with a finite differencing scheme for Newtonian physics; the general relativistic version of this scheme is given in the second subsection.

4.1. Newtonian physics

It is convenient to solve the 1-dimensional problem in Lagrange coordinates (see subsection 3.1) with mass as the appropriate independent variable,

$$r \rightarrow m(r) = 4\pi \int_0^r \varrho\, r^2\, dr. \tag{4.1}$$

The equation of motion then reads

$$\frac{du}{dt} = -4\pi\, r^2 \frac{dp}{dm} - 4\pi\, G\, m(r)\varrho \frac{dr}{dm}. \tag{4.2}$$

Mass conservation is simply

$$\varrho(r) = \frac{3}{4\pi} \frac{dm}{dr^3}, \tag{4.3}$$

and the entropy equation becomes

$$\frac{ds(m,t)}{dt} = \frac{\dot{\varepsilon}}{k_B T}. \tag{4.4}$$

We prefer to work with an entropy equation rather than an equation for the internal energy, because as was discussed earlier, the entropy per mass is rather well conserved during stellar collapse. Of course, eqs. (4.1) through (4.4) have to be supplemented by an EOS, $p = p(\varrho, s, y_e)$ and $s = s(\varrho, T, y_e)$, rate equations for y_e,

$$\dot{y}_e = \frac{dy_e}{dt} = \lambda_{\nu n} y_n - \lambda_{e^- p} y_p - \sum_i \lambda_{e^- i} y_i, \tag{4.5}$$

and neutrino transport equations. Here y_e denotes again the electron concentration, y_i the abundance of nucleus i, and the λ's are reaction rates. In addition, initial values $m(r)$, $p(m)$, $u(m)$, $s(m)$, etc., have to be given at a certain time $t = t_0$. For example, one can take a polytropic model or a "realistic" model from a stellar evolution calculation at the onset of collapse.

We deal here with finite differencing methods only and describe a very simple though still useful numerical scheme to solve the preceding set of equations (for more elaborate techniques see Ewald Müller's contribution in this volume). One begins by dividing the (spherical) star into N concentric mass-zones (see fig. 12). Each zone has a certain mass Δm (or thickness Δr). Figure 13 shows how the discretisation may be done for the dependent variables. That is, for a given function $\varrho(r, t_0)$ and chosen Δm_i, $i = 1, N$; $\Sigma \Delta m_i = M$, one has from the continuity equation (4.7)

$$\Delta r_i^3 = \frac{3}{4\pi \varrho_i} \Delta m_i \tag{4.6}$$

with $\varrho_i = \varrho(r_i - \frac{1}{2} \Delta r_i)$.

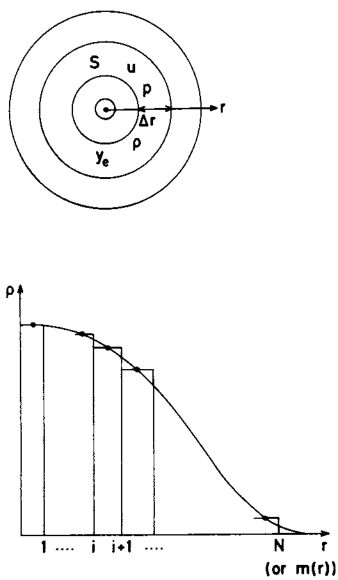

Fig. 12. Schematic discretisation of the density distribution of a model star.

Densities, pressures, etc., are commonly attributed to the centers of a zone, whereas velocities and radii are taken at the zone boundaries. Of course, there is some ambiguity in the choice of the outer boundary conditions. But

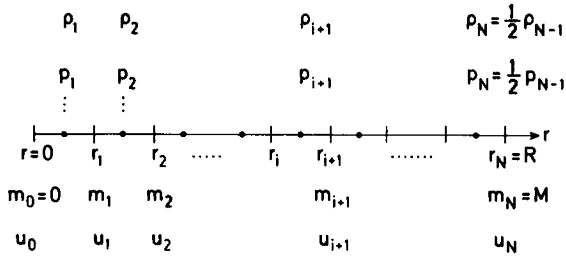

Fig. 13. Centering of the dependent variables in the discretisation scheme described in the text.

in general, because $\varrho(M) \ll \varrho_c$, these boundary layers do not influence the dynamics of the inner core significantly, and the choice of boundary conditions is not crucial, provided that the radius R is sufficiently far out.

Given the preceding discretisation scheme outline, one can write the equation of motion in the form of

$$\begin{aligned} u_i(t_j + \Delta t) - u_i(t_j) = \Bigg(& -4\pi\, r_i^2 \, \frac{p_i - p_{i+1}}{m_{i-1} - m_i} \\ & -4\pi G\, m_i \varrho_i \, \frac{r_{i-1} - r_i}{m_{i-1} - m_i} \Bigg)\Bigg|_{t=?} \cdot \Delta t. \end{aligned} \tag{4.7}$$

where discretisation errors are of the order $O(\Delta m_i/m)$ if a grid not "equidistant" in Δm_i is used. Such a scheme is called "of first order accurate in space."

There remains the question of what time the spatial derivatives have to be taken. Of course, the simplest choice is to adapt $t = t_{\text{old}}$, in which case the code is called explicit because all quantities are extrapolated forward in time. In this case we can proceed as follows. In the first step the new velocities are computed from the equation of motion:

$$\begin{aligned} u_i(t_{j+1}) = u_i(t) - 4\pi \Bigg(& r_i^2(t_j) \, \frac{p_i(t_j) - p_{i+1}(t_j)}{m_{i-1} - m_i} \\ & - G m_i \varrho_i \, \frac{r_{i-1}(t_j) - r_i(t_j)}{m_{i-1} - m_i} \, (t_{j+1} - t_j) \Bigg). \end{aligned} \tag{4.8}$$

Next from the definition of the velocity u, the new radius of each zone is obtained:

$$r_i(t_{j+1}) = r_i(t_j) + \frac{1}{2}(u_i(t_{j+1}) + u_i(t_j))(t_{j+1} - t_j). \tag{4.9}$$

We then solve the continuity equation for the new densities:

$$\varrho_i(t_{j+1}) = \frac{3}{4\pi} \frac{m_{i-1} - m_i}{r_{i-1}^3(t_{j+1}) - r_i^3(t_{j+1})}, \tag{4.10}$$

and finally update the entropies

$$s_i(t_{j+1}) = s_i(t_j) + \left(\frac{ds}{dt}\right) \Delta t, \tag{4.11}$$

pressures, abundances, etc.

Alternatively, one may use $t = t_{\text{new}}$ in which case the discretized hydrodynamic equations resemble an implicit set of non-linear equations which have to be solved iteratively. Certainly the latter choice is numerically much more complex and time-consuming. Moreover, implicit methods tend to have stability problems. On the other hand, implicit techniques can handle various time scales because the only restriction for the time-step Δt is the accuracy requirement. In contrast, explicit methods are simple, fast, and stable, but are required to obey certain time-step constraints such as the so-called Courant-Friedrich-Levy condition which guarantees that in one time-step, information (soundwaves, etc.) cannot cross a mass-zone. More generally speaking, in an explicit code, the time-step always has to be smaller than the shortest intrinsic time-scale, which may lead to severe numerical problems.

Stellar collapse may serve as an example to illustrate these problems. During collapse, matter velocities will be on the order of the velocity of sound and may reach values of about 0.2 c. Δr will typically be on the order of 10^5 to 10^6cm and therefore

$$t_{CFL} := \min_i \frac{\Delta r_i}{u_s^i + |u^i|} \simeq \text{ few } 10^{-5}\text{s} \tag{4.12}$$

In the diffusion regime, ν-transport times are on the order of 1s for particle number and a few seconds for the energy. These are much longer than t_{CFL}. With an explicit code, therefore, neutrino cooling must be computed on hydrodynamical time-scales, and the number of time steps is on the order of several million! In contrast, during collapse free streaming of neutrinos will limit the time step to a fraction of the Courant-Friedrich-Levy time.

We conclude this section with some remarks on shock-heating and pseudo-viscosity. The problem in this type of numerical scheme is that any physical "molecular" viscosity is very small but, because of the discretisation, discontinuities in a shock front cannot be treated exactly nor can they be resolved numerically. There are at least two ways of handling this problem. Either trace the shock and then solve a local Riemann-problem (see E. Müller, this volume), which leads to a non-Lagrangian scheme and concern about conservation laws, or, alternatively, the shock may be smeared over a few (2–3) mass zones by what is called a "pseudo-viscosity." Of course, this pseudo-viscosity should have all properties of a physical viscosity; namely that it should be of the form of Tscharnuter and Winkler (1979):

$$Q := \left\{ \begin{array}{cc} \ell^2 \varrho \operatorname{div}(\mathbf{u}) \{(\nabla \times \mathbf{u}) - \frac{1}{3}\operatorname{div}(\mathbf{u})\mathbf{e}\} & ; \operatorname{div}(\mathbf{u}) < 0 \\ 0 & ; \text{ else} \end{array} \right\}, \tag{4.13}$$

where "×" means the tensor product. This tensor is trace free and is identical to zero if matter is not compressed or is homologously contracting. In spherical symmetry eq. (4.13) reduces to

$$q := Q_r^r = \left\{ \begin{array}{cc} 3\ell^2 \varrho \frac{\partial(r^2 u)}{\partial r^3} \left\{ \frac{\partial u}{\partial r} - \frac{\partial(r^2 u)}{\partial r^3} \right\} & ; \frac{1}{r}\frac{\partial r u}{\partial r} < 0 \\ 0 & ; \text{ else} \end{array} \right\}, \tag{4.14}$$

$$Q_\theta^\theta = 3\ell^2 \varrho \, \frac{\partial(r^2 u)}{\partial r^3} \left\{ \frac{u}{r} - \frac{\partial(r^2 u)}{\partial r^3} \right\} = Q_\phi^\phi, \tag{4.15}$$

where ℓ is a constant on the order of (1–2) $\cdot \Delta r$. In the equation of motion the pressure gradient has now to be replaced by

$$\frac{\partial p}{\partial r} \rightarrow \frac{\partial p}{\partial r} + Q_{r;k}^k = \frac{\partial p}{\partial r} + \frac{3}{r}\frac{\partial r^2 q}{\partial r^3}. \tag{4.16}$$

The entropy equation becomes

$$k_B T \dot{s} = \varepsilon_q = -\frac{9}{2}\ell^2 \frac{\partial(r^2 u)}{\partial r^3} \left(\frac{\partial u}{\partial r} - \frac{\partial(r^2 u)}{\partial r^3} \right)^2. \tag{4.17}$$

Very often in numerical schemes the Richtmyer-viscosity is used, namely

$$q = \left\{ \begin{array}{cc} \ell^2 \varrho \left(\frac{\partial u}{\partial r}\right)^2 & ; \frac{\partial u}{\partial r} < 0 \\ 0 & ; \text{ else} \end{array} \right\}. \tag{4.18}$$

The problem with this form is that it does not vanish during homologous contraction and that it is not possible to implement it in a coordinate invariant way into the equation of motion. However, it is equivalent to the tensor viscosity for planar geometry for which it was originally invented.

4.2. General relativistic hydrodynamics

The basic equations for spherical symmetry can be found in Misner and Sharp (1964, 1965), and a finite differencing scheme extending the one described in section 4.2. was given by Van Riper (1979). Therefore, we repeat only the essential aspects here.

In general relativity and spherical symmetry, the metric can be written in the form

$$ds^2 = e^{2\phi}c^2dt^2 + \left(\frac{\partial r}{\partial m}\right)^2 \Gamma^{-2}dm^2 + r^2 d\Omega^2 \qquad (4.19)$$

where $\Gamma^2 := 1 + \left(\frac{u}{c}\right)^2 - \frac{2G\tilde{m}}{c^2 r}$; $\tilde{m}(m) = \int_0^m \left(1 + \frac{E}{c^2}\right) \Gamma\, dm$ is the gravitating mass, $\partial r/\partial t = e^{\phi}u$ is the velocity, m the rest mass (the Lagrangian coordinate, proportional to the baryon number), r the radial (Schwarzschild-) coordinate, and E the internal energy density.

We can obtain the "potential" ϕ from

$$\frac{\partial\phi}{\partial p} = -\frac{V}{c^2 W} \qquad (4.20)$$

where V is the specific volume, $V = (m_0 n_B)^{-1}$, and $W = 1 + (E + pV)/c^2$ is the dimensionless enthalpy. The boundary condition imposed on ϕ at the surface is

$$\phi_s = \frac{1 - \frac{G\tilde{M}}{c^2 R}}{\sqrt{1 + \left(\frac{u_s}{c}\right)^2 - \frac{2G\tilde{M}}{c^2 R}}}. \qquad (4.21)$$

In all these equations the time t is the proper time in the rest frame of the distant observer.

The equation of motion now reads

$$\frac{\partial u}{\partial t} = e^{\phi}\left[-\frac{4\pi r^2}{W}\frac{\partial p}{\partial m} - \frac{G}{r^2}\left(\tilde{m} + \frac{4\pi r^3 p}{c^2}\right)\right] \qquad (4.22)$$

and the continuity equation becomes

$$V = \frac{1}{\Gamma}\frac{\partial[(4\pi/3)r^3]}{\partial m}. \qquad (4.23)$$

This set of equations looks very similar to its Newtonian counterpart and, consequently, the differencing scheme to solve them is very similar to the one described in section 4.1, the only difference being that we have to integrate eq. (4.20) subject to the boundary condition (4.21) first, before we can update u, obtaining the new values of Γ and finally the new specific volume V. Of course, general relativistic effects become very important when $\varrho_{\rm bounce} \gg \varrho_0$ and also during the early cooling phase of a newly born neutron star. They are less important for models using stiff equations of state; but since they are easy to handle, there is no reason to omit general relativity, and in fact most numerical collapse simulations have been carried out in this framework.

5. Core collapse supernova models and their problems

In the following section the presently favoured models of Type II supernovae will be discussed. We start with a brief account of an analytical approach to the core collapse problem first presented by Goldreich and Webber (1980), and later generallized by Yahil and Lattimer (1982). We then review the results of some recent numerical studies. An outlook on possible future work follows.

5.1. An analytic description of core collapse

We now want to discuss briefly an analytical approach to the core-collapse problem. Of course, detailed models require full solutions of the hydrodynamic equations, the rate equations, etc., but we can also understand the main features from some analytic considerations. The way these are presented here are not fully exact because we neglect boundary terms. However, our results are only meant to indicate certain general properties of a collapsing stellar core.

In Lagrange coordinates the Newtonian hydrodynamic equations read

$$\dot{u} = -4\pi\, r^2 \frac{\partial p}{\partial m} - \frac{Gm}{r^2} \tag{5.1}$$

and

$$\frac{\partial m}{\partial r} = 4\pi\, r^2 \rho . \tag{5.2}$$

As we saw earlier the assumption of an adiabatic collapse with $\gamma = 4/3$ is a fair approximation to the real problem. In addition, if we assume that the stellar structure can be approximated by a so-called polytrope

$$p = K\, \rho^{(1+n)/n}, \tag{5.3}$$

of index $n = 3$, where K is a constant which determines the entropy of the model, the EOS and the stellar structure are consistent and the collapse problem can be solved analytically (Goldreich and Weber 1980). For our present discussion some general properties of the solution are sufficient.

The equation of motion eq. (5.1) can be written as

$$\frac{1}{2}\frac{\partial}{\partial t}(u^2) = -4\pi\, r^2 u \frac{\partial p}{\partial m} - u \frac{Gm}{r^2}, \tag{5.4}$$

or

$$\frac{\partial}{\partial t}\left(\frac{u^2}{2} - \frac{Gm}{r}\right) = -4\pi\, r^2 u \frac{\partial p}{\partial m}, \tag{5.5}$$

because of the identity

$$\frac{\partial}{\partial t}\left(\frac{1}{r}\right) = -\frac{1}{r^2}\frac{\partial r}{\partial t} = -\frac{1}{r^2} u. \tag{5.6}$$

The right-hand side of eq. (5.5) can be replaced by

$$\begin{aligned} 4\pi\, r^2 u \frac{\partial p}{\partial m} &= \frac{\partial}{\partial m}(pu\, 4\pi\, r^2) - p\frac{\partial(4\pi\, u\, r^2)}{\partial m} \\ &= \frac{\partial}{\partial m}(pu\, 4\pi\, r^2) + \frac{p}{\rho^2}\frac{\partial \rho}{\partial t} \\ &= \frac{\partial}{\partial m}(pu\, 4\pi\, r^2) + \frac{\partial(\varepsilon/\rho)}{\partial t}, \end{aligned} \tag{5.7}$$

where we have used the thermodynamic relation $dE = -p\, dV$ and $\varepsilon = E/V$ to give

$$\frac{\partial \varepsilon}{\partial t} = \frac{p+\varepsilon}{\rho}\frac{\partial \rho}{\partial t}.$$

Now, by combining eqs. (5.5) and (5.7) we obtain

$$\begin{aligned} \frac{\partial}{\partial t}\left(\frac{u^2}{2} - \frac{Gm}{r} + \frac{\varepsilon}{\rho}\right) &= \frac{\partial}{\partial m}(pu\, 4\pi r^2) \\ &= -\frac{\partial}{\partial m}\left(\frac{4\pi}{3} r^3\, 3p\, \frac{u}{r}\right) \cdot \\ &= -\frac{\partial}{\partial m}\left(3p\, V\, \frac{u}{r}\right) \end{aligned} \tag{5.8}$$

Inserting $\gamma = \frac{4}{3}$ (or $p = \frac{1}{3}\varepsilon$) we finally get

$$\frac{\partial}{\partial t}\left(\frac{u^2}{2} - \frac{Gm}{r} + \frac{\varepsilon}{\rho}\right) = -\frac{\partial}{\partial m}\left(E \cdot \frac{u}{r}\right). \tag{5.9}$$

At $t = 0$, matter can be considered as being almost at rest and the initial conditions are

$$\frac{Gm}{r} = \frac{\varepsilon}{\rho} \quad \text{and} \quad \frac{u^2}{2} = E_{\text{tot}} = 0. \tag{5.10}$$

At later times, $t \neq 0$, for a self-gravitating $\gamma = 4/3$ gas sphere, the total energy per gramme is conserved and therefore

$$\frac{\partial}{\partial m}\left(E \cdot \frac{u}{r}\right) \equiv 0, \tag{5.11}$$

must hold at all times. This in turn means that the velocity $u(m, t)$ can be written as

$$u = a(t) \cdot r(m), \tag{5.12}$$

which is called a homologeous solution because the velocity is proportional to the distance from the star's center at all times.

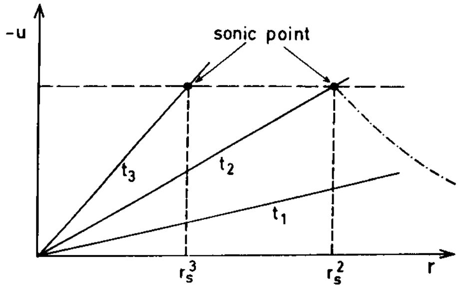

Fig. 14. Schematic representation of infall velocity versus radius for a $\gamma = 4/3$ gas. The dashed horizontal line indicates the sound velocity. The velocity of inner mass zones is proportional to their distance from the star's center. Outside the sonic point r_s, a free fall sollution is approximately valid and is indicated by the dashed-dotted line. t_1, t_2, and t_3 label different snapshots. Of course, in a star the sound velocity will not be constant.

Fig. 14 shows schematically how the collapse will proceed in time. It also indicates a complication. Because a is independent of $m(r)$, a radius r_s must exist at which u exceeds the sound velocity u_s. The matter outside the sonic point cannot communicate via sound waves (compression waves) with the material inside r_s, and homology must be broken at r_s. Goldreich and Weber (1980) have shown that the mass inside r_s is always the Chandrasekhar mass, which in turn is a function of y_e. During collapse, therefore, the mass inside the sonic point decreases with decreasing electron concentration to values of about 0.7 to 0.8 $M_\odot$ (Hillebrandt 1987). Moreover, homology is broken once γ deviates significantly from 4/3 which is the case for $\rho \simeq \rho_0$. Therefore, we expect the "bounce" to occur at $\rho \simeq \rho_0$. This information is brought to r_s on a sound-crossing time and a shock forms at r_s.

5.2. *Numerical simulations and their main results*

Over the years a variety of ideas have been investigated, none of which however, can explain supernova explosions beyond doubt. Generally speaking they can be put into one of three classes depending on the mechanism responsible for energy and momentum transfer from the stellar interior to the envelope. These are a hydrodynamical shock wave, a thermonuclear burning front, or a neutrino flux, or some combination of the three.

At present it seems plausible that only under very special circumstances can a shockwave created by the rebounding inner core lead to the prompt ejection of the stellar envelope. Roughly speaking, the argument is as follows. We can obtain a rough estimate of the energy put into the shockfront from

$$E_s \simeq \left(\frac{GM_{\rm CH}}{r_s} - \frac{\bar{\varepsilon}}{\bar{\varrho}}\right) M_{\rm CH}, \tag{5.13}$$

where $\bar{\varrho}$ and $\bar{\varepsilon}$ are average values of energy density and density inside the sonic radius r_s at bounce and $M_{\rm CH} = M_{\rm CH}(y_e)$ is the Chandrasekhar mass. The first term in eq. (5.13) gives the gravitational binding of the inner core per gramme whereas the second term is the internal energy per gramme. So the energy available to the shock is, roughly speaking, given by the kinetic energy of the inner core (see Yahil and Lattimer 1982). For a polytropic structure and an appropriate equation of state, eq. (5.13) can be written as

$$E_S \simeq (K_1\, M_{\rm CH}^{2/3}\bar{\varrho}^{1/3} - K_2\bar{\varrho}^{\gamma-1})\, M_{\rm CH}, \tag{5.14}$$

From eq. (5.14) it is obvious that the shock energy increases with increasing $\bar{\varrho}$. Therefore, "soft" EOS at densities beyond nuclear matter density favour prompt hydrodynamically driven explosions because the collapse is stopped at higher densities. In addition, because $M_{\rm CH}$ is proportional to y_e^2, a "low" initial entropy leading to a small concentration of free protons and thus to fewer electron captures, also works in favour of an explosion. Finally, a "stiff" EOS at $\varrho \lesssim \varrho_0$, that is, an adiabatic index γ very close to the critical value of 4/3 ensures homology up to ϱ_0 and, therefore, again gives high shock energies. But, even in the most favourable cases, the shock energy does not exceed 8×10^{51}erg, and more typical values are around $(4–5)\times 10^{51}$erg (see Hillebrandt 1987). It then follows that the most energetic shocks at best can dissociate 0.4 $M_\odot$ of heavy elements into free neutrons and protons and, because $M_{\rm CH} < 0.8 M_\odot$ in all recent simulations, the iron core mass must be less than $1.2 M_\odot$. The latter condition is (if at all) fulfilled in stars with main sequence masses of less than 10 or 12 $M_\odot$, but certainly not in the case of the progenitor of SN 1987A (see fig. 15).

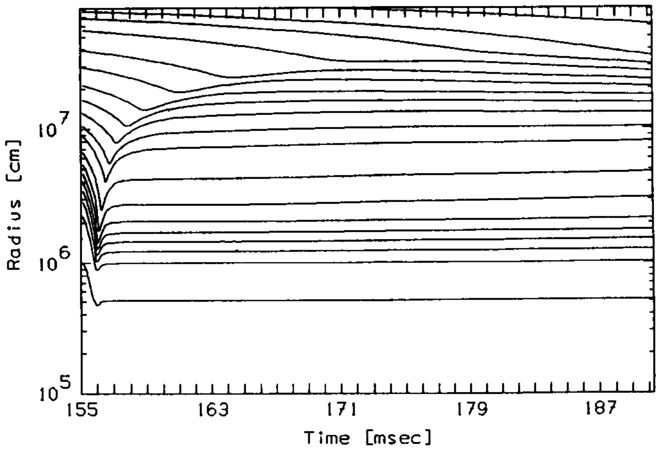

Fig. 15. Radius versus time for various mass zones of a collapsing stellar model of 20 $M_\odot$. It is obvious that the shock stalls at a radius of about 300 km (from Hillebrandt 1987).

Therefore, it seems more likely that neutrinos are needed in one way or another to drive a shock wave out into the stellar envelope. A possibility which has been discussed extensively is the so-called delayed explosion mechanism (Wilson 1985; Bethe and Wilson 1985), the idea being that a few hundred milliseconds after core-bounce, energy transfer by neutrinos may revive a stalled shock. In its original version this explosion mechanism was based on the reactions

$$\begin{aligned} e^- + p &\to n + \nu_e \\ e^+ + n &\to p + \bar{\nu}_e \\ e^+ + e^- &\to \nu_x + \bar{\nu}_x \end{aligned} \tag{5.15}$$

in the hot shocked and dissociated gas. These neutrinos and those diffusing out of the unshocked core can interact with the outer layers via the inverse reactions

$$\begin{aligned} \nu_e + n &\rightarrow e^- + p \\ \bar{\nu}_e + p &\rightarrow e^+ + n \end{aligned} \tag{5.16}$$

and neutrino-electron scattering. The net effect is some heating, proportional to the neutrino energy distribution and the density structure near the neutrinosphere. Moreover, the process is likely to be a self-regulating one since neutrino heating proceeds on a much longer time-scale than the hydrodynamical time-scale. Therefore, once enough heat has been added to lift the layers in the gravitational potential of the proto-neutron star, the density drops and thus heating is turned off. Accordingly, one would expect that at most roughly the binding energy of the stellar mantle can be released which is on the order of a few 10^{50} erg, in agreement with some numerical simulations (Wilson et al. 1986, see fig. 5), but in contrast to the much higher explosion energy observed in SN 1987A (see Hillebrandt and Höflich 1989).

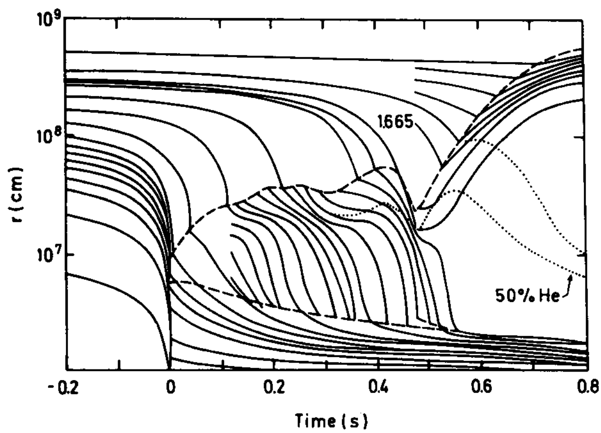

Fig. 16. Same as fig. 15, but for a $25M_\odot$ model (from Wilson 1985). Time is measured from core-bounce. The position of the shock front (upper broken curve) and the neutrinosphere are also shown. The stalled shock is revived by neutrino heating 0.5 s after bounce.

A way out of these problems might be the inclusion of neutrino-antineutrino annihilation radiation in the numerical models, as was first suggested by Goodman, Dar, and Nussinov (1987). The basis of this explosion mechanism is the observation that most of the binding energy of the neutron star is radiated away in all three neutrino flavors on time-scales of several seconds. According to numerical simulations by Wilson and Mayle (1989), this energy may lead to the formation of a hot (high entropy, low density) bubble from the reactions $\nu_x\bar{\nu}_x \rightleftarrows e^+e \rightleftarrows 2\gamma$ and $(\nu_e, \bar{\nu}_e)$ (e^+, e^-)-scattering. It is obvious that the $\nu_x\bar{\nu}_x$-annihilation cross-section is only large for head-on collisions and therefore, the heating is limited to a region very near the proto-neutron star. Moreover, in the mass-zones to be heated the density should be low, $\varrho \lesssim 10^5$g cm^{-3}, to raise the entropy to values above 100 k_B/nucleon, which are necessary to push the matter outwards. So, generally speaking, this explosion mechanism requires a very steep density gradient in the outer layers of the proto-neutron star to be efficient, and in the "delayed explosion" models (Wilson et al. 1986) this seems in fact to be the case.

However, there are several problems which make the results obtained by Wilson and Mayle (1989) uncertain. First, the neutrino spectra obtained from their multi-group flux-limited diffusion scheme seem to overestimate the high-energy part as was first criticized by Janka (1987) and by Janka and Hillebrandt (1989a) (see also fig. 17). Second, their simulations assumed spherical symmetry and therefore, a certain averaging procedure had to be applied to eliminate the angle distribution of the neutrinos. This averaging, however, is crucial because the annihilation rate is proportional to

$$Q \sim \int d\tau(\varepsilon_\nu + \varepsilon_{\bar{\nu}})F_\nu F_{\bar{\nu}}(1 - \hat{\Omega}_\nu\hat{\Omega}_{\bar{\nu}})^2, \tag{5.17}$$

where $d\tau = d\varepsilon_\nu d\varepsilon_\nu d\Omega_\nu d\Omega^*_{\bar{\nu}}/(4\pi)$ is the volume element in energy space, and ε_ν, $\varepsilon_{\bar{\nu}}$ are neutrino energies, F_ν and $F_{\bar{\nu}}$ are the neutrino fluxes, and $\hat{\Omega}_\nu$ and $\hat{\Omega}_{\bar{\nu}}$ are unit vectors in the direction of the neutrino and antineutrino, respectively. Therefore, only head-on collisions contribute significantly to the rate. Janka (1990) has argued that neutrino back-scattering in the semi-transparent layers may increase the effective annihilation rate considerably very near the proto-neutron star, in comparison with the vacuum approximation applied by Goodman et al. (1987). Then, limb-darkening should also be included which, in contrast, reduces the heating by a similar factor of 2 to 3, but in layers further away from the core. Both effects are difficult to treat by flux-limited diffusion schemes, and require more accurate neutrino transport models (Janka 1990). Given these uncertainties and shortcomings of the Wilson and Mayle (1989) simulations, it seems premature to conclude that the "hot bubble" explosion mechanism is the answer to the question how supernovae explode (Colgate 1989, 1990). The explosion mechanism may be even more complicated than anticipated so far. In particular, in the models of Wilson and Mayle (1989) the layers that finally form the hot bubble are Rayleigh-Taylor unstable already a few tenths of a second after core-bounce, and the growth-time of the instability is on the

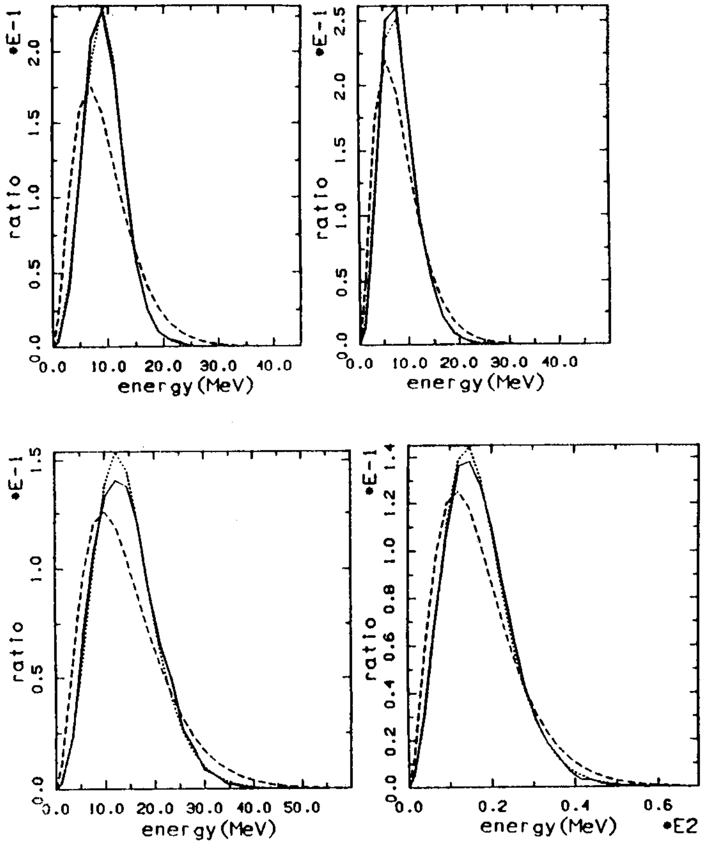

Fig. 17. Typical Monte Carlo spectra (solid lines) for early and late time electron neutrinos, electron antineutrinos and muon neutrinos (from left to right) in comparison with blackbody spectra repesenting the mean neutrino energy correctly (dashed line) and Fermi-Dirac fit distributions with an effective chemical potential (dotted lines). The discrepancies indicate the non-thermal nature of the true spectra, but those fits which reproduce the first three moments of the Monte-Carlo energy distribution are very accurate. (From Janka and Hillebrandt 1989a).

order of or even less than the hydrodynamic time-scale. It is, therefore, likely that there is a considerable transport of energy from the surface of the proto-neutron star to the matter in the forming bubble by macroscopic motions of the matter. Certainly, this effect deserves further attention. One may even speculate, that the rather high velocities of layers containing heavy elements observed in SN 1987A could have resulted from Rayleigh-Taylor instabilities in the innermost layers of the ejecta. But a realistic treatment of these effects will require 3-dimensional rather than spherically symmetric simulations.

6. Summary, conclusions, and outlook

In these lecture notes we have discussed scenarios which may explain Type II supernova outbursts. All models were based on the assumption that the chain of events leading to the optical outburst starts at the end of quiet evolution of a massive stellar core, continues into collapse on a hydrodynamic time-scale, and ends leaving behind a compact object, presumably a neutron star.

Certainly, SN 1987A is the first clear case of a rather massive star that has undergone such a core collapse and ejected its envelope in a Type II supernova explosion. Such behavior was predicted by most theoretical models, but direct observational evidence was not very strong. Moreover, the rather high explosion energy as well as certain properties of the observed neutrino signals indicate that the explosion mechanism is still not yet fully understood. In contrast, the blue nature of the progenitor star and the unusual light curve can be explained by rather standard stellar evolution models, although several details again remain to be explored. Certainly, if a pulsar should show up in SN 1987A, which is expected to happen in the near future, some of the uncertainties in core collapse models will be removed. In particular we would know whether or not rotation played an important role; up to now, it is still an open question. The presence of a neutron star in SN 1987A would also remove ambiguities in the interpretation of neutrino data but unfortunately, at present there is no direct evidence for a pulsar.

Theoretical models developed prior to the explosion of SN 1987A predict that the collapse of a massive star to neutron star densities will manifest itself in a fast burst of ν_e's with energies around 10 to 15 MeV, followed by significant emission of neutrinos and antineutrinos of all flavors over a time-scale of several seconds. However, because the cross section for $(\bar{\nu}_e, p)$-reactions is about a factor of 100 higher than that for (ν_e, e)-scattering at the energies under consideration, only $\bar{\nu}_e$'s were expected to give a clear signal in existing neutrino detectors even if the collapsing star was at a distance greater than about 5 kpc. The calculated neutrino luminosities and spectra are very sensitive to astrophysical models and the physical input data, but the observed neutrino flux from SN 1987A indicates that the basic ideas are essentially correct. The observations have shown, in particular, that massive stars indeed do collapse, thereby emitting most of their gravitational binding energy in form of thermal neutrinos.

Besides being of interest to astrophysics and particle physics, with the exception of neutron stars, supernova cores are the only cosmic objects in which low-entropy matter is compressed to nuclear densities and beyond. It is therefore tempting to use their properties to constrain the equation of state at such high densities. Unfortunately, observations of Type II supernovae as well as supernova models do not impose strong constraints on the nuclear equation of state. First, a surprisingly small number of supernova remnants definitely does contain a neutron star. Moreover, very little observational information on the explosion mechanism is available, and even the best studied case, SN 1987A is not an exception to that rule. We only know for sure that some supernovae leave neutron stars behind and that the kinetic energy of the ejecta is typically around 10^{51} erg. Whether or not this energy is supplied by a hydrodynamic shock wave, as suggested by the prompt explosion models, or comes from neutrino energy deposition, nuclear burning, etc., is a completely open question. It may well be that stars can only explode by the prompt mechanism if they possess a significant amount of initially angular momentum. Nevertheless, there is little doubt that soft equations of state favor prompt explosions (at least for non-rotating models), but this should not be regarded as a proof that these equations of state correctly describe the properties of matter at densities beyond nuclear matter density. In contrast, effects caused by rotation will be larger if the equation of state near nuclear saturation density is stiff.

In conclusion, there is very little hope to extract information on the equation of state from supernova models unless we know more about the explosion mechanism. In this respect, a galactic Type II supernova would certainly help. While in the case of SN 1987A only $\bar{\nu}_e$'s from the early cooling phase of the neutron star have been detected, there is a good chance to see also ν_e's from the deleptonization burst in existing neutrino detectors, provided that the supernova explodes at a distance of less than a few kpc. Luminosity and energies are strongly dependent upon the hydrodynamical evolution of the stellar core. Therefore, if the temporal change of both quantities could be measured, this would impose strong constraints on the theoretical models. Finally, there is a fair chance to detect gravity waves from a galactic supernova, and thus, to probe the importance of rotation and asphericities on the dynamics of the stellar core near bounce.

Other uncertainties in supernova models come from poorly determined stellar evolution models, unknown nuclear reaction rates, inaccurate description of neutrino transport, etc., and it seems worthwhile to search for improvements before trying very elaborate multi-dimensional numerical simulations. On the other hand, SN 1987A has told us that at least sometimes supernovae seem to be non-spherical, a discovery that will make life much more troublesome for supernova theorists in the future.

References

Arnett, W.D., 1977. *Astrophys. J.* **218**, 815.

Arnett, W.D., 1987. *Astrophys. J.* **319**, 136.

Arnett, W.D., 1988a. *Astrophys. J.* **331**, 377.

Arnett, W.D., 1988b. Proc. 4th George Mason Astrophysics Workshop: SN1987A in the LMC, ed. by M. Kafatos and A.G. Michalitsianos, p. 301.

Baade, W., and F. Zwicky, 1934. *Phys. Rev.* **45**, 138.

Baron, E., J. Cooperstein, and S. Kahana, 1985a. *Phys. Rev. Lett.* **55**, 126.

Baron, E., J. Cooperstein, and S. Kahana, 1985b. *Nucl. Phys.* **A440**, 744.

Baron, E., H.A. Bethe, G.E. Brown, J. Cooperstein, and S. Kahana, 1987. *Phys. Rev. Lett.* **59**, 736.

Barrett, P., 1987. in *SN 1987A*, ed. by I.J. Danziger, ESO, Garching, p. 173.

Becker, R.H., S.S. Holt, B.W. Smith, N.E. White, E.A. Bolt, R.F. Mushotzky, and P.J. Serlemitsos, 1979. *Astrophys. J. Lett.* **238**, L73.

Bethe, H.A., G.E. Brown, and J. Cooperstein, 1987. *Astrophys. J.* **322**, 201.

Bethe, H.A., 1982. in Supernovae: A Survey of Current Research, ed. by M.J. Rees and R.J. Stoneham, NATO-ASI **C90**, Reidel, Dordrecht, p. 35.

Bionta, R.M. et al., 1987. *Phys. Rev. Lett.* **58**, 1494.

Blades, J.C., J.M. Wheatley, N. Panagia, M. Grewing, M. Pettini, and W. Wamsteker, 1988. *Astrophys. J.* **334**, 308.

Bonche, P., and D. Vautherin 1981. *Nucl. Phys.* **A372**, 496.

Bouchet, P., I.J. Danziger, and L.B. Lucy, 1990. *Astron. J.*, in press.

Bowers, R.B., and J.R. Wilson, 1982. *Astrophys. J.* **263**, 366.

Bruenn, S.W., 1985. *Astrophys. J. Suppl.* **58**, 771.

Cassatella, A., 1987. in *SN 1987A*, ed. by I.J. Danziger, ESO, Garching, p. 101.

Castor, J.I., 1972. *Astrophys. J.* **178**, 779.

Catchpole, R.M. et al., 1987. *M.N.R.A.S.* **229**, 15p.

Chevalier, R.A., and R.P. Kirshner, 1978. *Astrophys. J.* **219**, 931.

Colgate, S.A., 1989. *Nature* **341**, 489.

Colgate, S.A., 1990. preprint.

Danziger, I.J., P. Bouchet, C. Gouiffes, and F. Rufener , 1989. Big Bang, Active Galactic Nuclei and Supernovae, ed. by S. Hayakawa and K. Sato, Universal Academic Press, Tokyo, p. 429.

Davidson, K. et al., 1982. *Astrophys. J.* **253**, 696.

Dotani, T. et al., 1987. *Nature* **330**, 230.

El Eid, M.F., and N. Langer, 1986. *Astron. Astrophys.* **167**, 274.

El Eid, M.F., and W. Hillebrandt, 1980. *Astron. Astrophys. Suppl.* **42**, 215.

Erickson, E.F., M.R. Haas, S.W.J. Colgan, S.D. Lord, M.G. Burton, J. Wolf, D.J. Hollebach, and M. Werner, 1988. *Astrophys. J.* **330**, L39.

Fillipenko, A.V., and W.L.W. Sargent, 1985. *Nature* **316**, 407.

Fosbury, R.A.E., I.J. Danziger, L.B. Lucy, C. Gouiffes, and S. Cristiani, 1987. in *SN 1987A*, ed. by I.J. Danziger, ESO, Garching, p. 139.

Wilson, J.R., 1985. in Numerical Astrophysics, ed. by J. Centrella, J. Le Blanc, and R. Bowers, Jones and Bartlett, p. 422.

Wilson, J.R., R.W. Mayle, 1989. in The Nuclear Equation of State, Part A, ed. by W. Greiner and H. Stöcker, Plenum Press, N.Y., p. 731.

Wilson, J.R., R.W. Mayle, S.E. Woosley, and T.A. Weaver, 1986. *Ann. NY Acad. Sci.* **479**, 267.

Witteborn, F., J.D. Bregman, D. Wooden, P.A. Pinto, D.M. Rank, S.E. Woosley, and M. Cohen, 1989. *Astrophys. J. Lett.* **338**, L9.

Woosley, S.E., 1988. *Astrophys. J.* **330**, 218.

Woosley, S.E., P.A. Pinto, and T.A. Weaver, 1988. *Proc. Astron. Soc. Austrl.* **7**, 355.

Yahil, A., and J.M. Lattimer, 1982. in Supernovae: A Survey of Current Research, ed. by M.J. Rees and R.J. Stoneham, NATO-ASI **C90**, Reidel, Dordrecht, p. 53.

ments before trying very elaborate multi-dimensional numerical simulations. On the other hand, SN 1987A has told us that at least sometimes supernovae seem to be non-spherical, a discovery that will make life much more troublesome for supernova theorists in the future.

References

Arnett, W.D., 1977. *Astrophys. J.* **218**, 815.

Arnett, W.D., 1987. *Astrophys. J.* **319**, 136.

Arnett, W.D., 1988a. *Astrophys. J.* **331**, 377.

Arnett, W.D., 1988b. Proc. 4th George Mason Astrophysics Workshop: SN1987A in the LMC, ed. by M. Kafatos and A.G. Michalitsianos, p. 301.

Baade, W., and F. Zwicky, 1934. *Phys. Rev.* **45**, 138.

Baron, E., J. Cooperstein, and S. Kahana, 1985a. *Phys. Rev. Lett.* **55**, 126.

Baron, E., J. Cooperstein, and S. Kahana, 1985b. *Nucl. Phys.* **A440**, 744.

Baron, E., H.A. Bethe, G.E. Brown, J. Cooperstein, and S. Kahana, 1987. *Phys. Rev. Lett.* **59**, 736.

Barrett, P., 1987. in *SN 1987A*, ed. by I.J. Danziger, ESO, Garching, p. 173.

Becker, R.H., S.S. Holt, B.W. Smith, N.E. White, E.A. Bolt, R.F. Mushotzky, and P.J. Serlemitsos, 1979. *Astrophys. J. Lett.* **238**, L73.

Bethe, H.A., G.E. Brown, and J. Cooperstein, 1987. *Astrophys. J.* **322**, 201.

Bethe, H.A., 1982. in Supernovae: A Survey of Current Research, ed. by M.J. Rees and R.J. Stoneham, NATO-ASI **C90**, Reidel, Dordrecht, p. 35.

Bionta, R.M. et al., 1987. *Phys. Rev. Lett.* **58**, 1494.

Blades, J.C., J.M. Wheatley, N. Panagia, M. Grewing, M. Pettini, and W. Wamsteker, 1988. *Astrophys. J.* **334**, 308.

Bonche, P., and D. Vautherin 1981. *Nucl. Phys.* **A372**, 496.

Bouchet, P., I.J. Danziger, and L.B. Lucy, 1990. *Astron. J.*, in press.

Bowers, R.B., and J.R. Wilson, 1982. *Astrophys. J.* **263**, 366.

Bruenn, S.W., 1985. *Astrophys. J. Suppl.* **58**, 771.

Cassatella, A., 1987. in *SN 1987A*, ed. by I.J. Danziger, ESO, Garching, p. 101.

Castor, J.I., 1972. *Astrophys. J.* **178**, 779.

Catchpole, R.M. et al., 1987. *M.N.R.A.S.* **229**, 15p.

Chevalier, R.A., and R.P. Kirshner, 1978. *Astrophys. J.* **219**, 931.

Colgate, S.A., 1989. *Nature* **341**, 489.

Colgate, S.A., 1990. preprint.

Danziger, I.J., P. Bouchet, C. Gouiffes, and F. Rufener , 1989. Big Bang, Active Galactic Nuclei and Supernovae, ed. by S. Hayakawa and K. Sato, Universal Academic Press, Tokyo, p. 429.

Davidson, K. et al., 1982. *Astrophys. J.* **253**, 696.

Dotani, T. et al., 1987. *Nature* **330**, 230.

El Eid, M.F., and N. Langer, 1986. *Astron. Astrophys.* **167**, 274.

El Eid, M.F., and W. Hillebrandt, 1980. *Astron. Astrophys. Suppl.* **42**, 215.

Erickson, E.F., M.R. Haas, S.W.J. Colgan, S.D. Lord, M.G. Burton, J. Wolf, D.J. Hollebach, and M. Werner, 1988. *Astrophys. J.* **330**, L39.

Fillipenko, A.V., and W.L.W. Sargent, 1985. *Nature* **316**, 407.

Fosbury, R.A.E., I.J. Danziger, L.B. Lucy, C. Gouiffes, and S. Cristiani, 1987. in *SN 1987A*, ed. by I.J. Danziger, ESO, Garching, p. 139.

Fransson, C., M. Grewing, A. Cassatella, N. Panagia, and W. Wamsteker, 1987. *Astron. Astrophys.* **177**, L33.

Fu, A., 1988. *Proc. Astron. Soc. Austrl.* **7**, 505.

Fuller, G.M., W.A. Fowler, and M.J. Newman, 1982. *Astrophys. J.* **252**, 715.

Gilmozzi, R., A. Cassatella, J. Clavel, C. Fransson, R. Gonzalez, C. Gry, N. Panagia, A. Talavera, and W. Wamsteker, 1987. *Nature* **328**, 318.

Goodman, J., A. Dar, and S. Nussinov, 1987. *Astrophys. J.* **314**, L7.

Goldreich, P., and S.V. Weber, 1980. *Astrophys. J.* **238**, 991.

Henry, R.B.C., and G.M. McAlpine, 1982. *Astrophys. J.* **258**, 11.

Henry, R.B.C., G.M. McAlpine, and R.P. Kishner, 1984. *Astrophys. J.* **278**, 619.

Hillebrandt, W., 1987. in High Energy Phenomena around Collapsed Stars, ed. by F. Pacini, NATO-ASI **C195**, Reidel, Dordrecht, p. 73.

Hillebrandt, W., and P. Höflich, 1989. *Rep. Prog. Phys.* **52**, 1421.

Hillebrandt, W., and E. Müller, 1984. in *Neutrino Physics and Astrophysics*, ed. by K. Kleinknecht and E.A. Paschos, World Scientific Pub., Singapore, p.229.

Hillebrandt, W., and R.G. Wolff, 1985. in Nucleosynthesis: Challenges and New Developments, ed. by W.D. Arnett, and J.W. Truran, Univ. Chicago Press, Chicago, p. 131.

Hillebrandt, W., K. Nomoto, and R.G. Wolff, 1984. *Astron. Astrophys.* **133**, 175.

Hillebrandt, W., P. Höflich, J.W. Truran, and A. Weiss, 1987. *Nature* **327**, 597.

Hirata, K. et al., 1987. *Phys. Rev. Lett.* **58**, 1490.

Höflich, P., 1988. IAU Symposium 108: Atmospheric Diagnostic of Stellar Evolution, ed. by K. Nomoto, Springer, Heidelberg, p. 388.

Höflich, P., Sharp and Ch.M., J. Zorec, 1989. in Particle Astrophysics Workshop ed. by E.B. Norman, World Scientific, Singapore, p.186.

Holt, S.S., 1983. in IAU Symposium 101: Supernova Remnants and their X-Ray Emission, ed. by J. Danziger and P. Gorenstein, Reidel, Dordrecht, p.17.

Imshennik, V.S., and D.K. Nadyozhin, 1983. *Astrophys. Space Phys. Rev.* **2**, 75.

Isserstedt, J., 1975. *Astron. Astrophys. Suppl.*, **19**, 259.

Janka, H.-T., 1987. *Lecture Notes in Physics* **287**, 319.

Janka, H.-T., 1990. preprint MPA546, *Astron. Astrophys.*, in press.

Janka, H.-T., and W. Hillebrandt, 1989a. *Astron. Astrophys. Suppl.* **78**, 375.

Janka, H.-T., and W. Hillebrandt, 1989b. *Astron. Astrophys.* **224**, 49.

Janka, H.-T., and R. Mönchmeyer, 1989. *Astron. Astrophys.*, **209**, L5.

Jansen, F.A., et al., 1985. in *Astronomy from Space*, ed. by G.G. Fazio et al., Pergamon Press, Oxford, p.49.

Landau, L.D., and E.M. Lifshitz, 1974. *Lehrbuch der Theoretischen Physik*, Bd.IV and V, Akademie-Verlag Berlin.

Lattimer, J.M., 1981. *Ann. Rev. Nucl. Part. Sci.* **31**, 337.

Manchester, R.N., J.R. Tuohy, and N. D'Amico, 1983. in IAU Symposium 101: Supernova Remnants and their X-Ray Emission, ed. by J. Danziger and P. Gorenstein, Reidel, Dordrecht, p. 495.

Matz, S.M., G.H. Share, M.D. Leising, E.L. Chupp, W.T. Vestrand, W.R. Purcell, M.S. Strickman, and C. Reppin, 1988a. *Nature* **331**, 416.

Mayle, R., J.R. Wilson, J. Ellis, K. Olive, D.N. Schramm, and G. Steigman, 1988. *Phys. Lett.* **B203**, 188.

Mazurek, T.J., J.M. Lattimer, and G.E. Brown, 1979. *Astrophys. J.* **229**, 713.

Mendez, M., A. Clocchaiatti, G. Benvenuto, C. Feinstein, and U.G. Marraco, 1988. *Astrophys. J.* **334**, 295.

Meyer, F., and E. Meyer-Hofmeister, 1984. *Astron. Astrophys.* **132**, 143.

Meyer, F., and E. Meyer-Hofmeister, 1991. in preparation.

Miller, G.E., and J.M. Scalo, 1979. *Astrophys. J. Suppl.* **41**, 513.

Misner, C.W., and D.H. Sharp, 1964. *Phys. Rev* **B136**, 571.

Misner, C.W., and D.H. Sharp, 1965. *Phys. Rev. Lett.* **15**, 279.

Nomoto, K., 1984. *Astrophys. J.* **277**, 791.

Nomoto, K., and M. Hashimoto, 1988. *Physics Reports* **163**, 13.

Nomoto, K., T. Shigeyama, and M. Hashimoto, 1987. in *SN 1987A* ed. by I.J. Danziger, ESO, Garching, p. 325.

Nomoto, K., M. Hashimoto, T. Shigeyama, S. Kumagai, H. Yamaoka and H. Saio, 1989. in Big Bang, Active Galactic Nuclei and Supernovae, ed. S. Hayakawa and K. Sato, Universal Academy Press, Tokyo, p. 495.

Ögelmann, H., et al., 1990. preprint MPE188, *Astron. Astrophys. Lett.*, in press.

Papaliolios, et al., 1989. *Nature* **338**, 565.

Pravdo, S.H., and J.J. Nugent, 1983. in IAU Symposium 101: Supernova Remnants and their X-Ray Emission, ed. by J. Danziger and P. Gorenstein, Reidel, Dordrecht, p. 29.

Pravdo, S.H., and B.W. Smith, 1979. *Astrophys. J. Lett.* **234**, L195.

Rank, D.M., P.A. Pinto, S.E. Woosley, J.D. Bregman, F.C. Witteborn, Axelrod T.S., and Cohen M., 1988b. *Nature* **331**, 505.

Rousseau, J., N. Martin, L. Prevout, E. Reheirot, A. Robin, and J.P. Brunet, 1978. *Astron. Astrophys. Suppl.* **31**, 243.

Saio, H., M. Kato, and K. Nomoto, 1988. *Astrophys. J.* **331**, 388.

Salpeter, E.E., 1955. *Astrophys. J.* **121**, 161.

Schwarz, H.E., 1987. in *SN 1987A*, ed. by I.J. Danziger, ESO, Garching, p. 167.

Shigeyama, T., K. Nomoto, and M. Hashimoto, 1988. *Astron. Astrophys.* **196**, 141.

Sunyaev, R. et al., 1987. *Nature* **330**, 327.

Takahashi, K., M.F. El Eid, and W. Hillebrandt, 1978. *Astron. Astrophys.* **103**, 358.

Tammann, G.A., 1982. in Supernovae: A Survey of Current Research, ed. by M.J. Rees and R.J. Stoneham, NATO-ASI **C90**, Reidel, Dordrecht, p. 371.

Tanaka, Y., 1988. IAU Colloquium 108: Atmospheric Diagnostic of Stellar Evolution, ed. by K. Nomoto, Springer, Heidelberg, p. 399.

Truran, J.W., and A. Weiss, 1987. in *SN 1987A*, ed. by I.J. Danziger, ESO, Garching, p. 271.

Tscharnuter, W.M., and K.H. Winkler, 1979. *Comp. Phys. Comm.* **18**, 171.

Tsuruta, S., 1979. *Physics Reports* **56**, 237.

Tyson, J.A., and P.G. Boeshaar, 1987. *PASP* **99**, 905.

Utrobin, V.P., 1984. *Astrophys. Space Sci.* **98**, 115.

Utrobin, V.P., 1988. *Atominform*, p. 20.

Van den Bergh, S., R.D. Mc Clure, and R. Evans, 1987. *Astrophys. J.* **323**, 44.

Van Riper, K.A., 1979. *Astrophys. J.* **232**, 558.

Walborn, N.R., B.M. Lasker, V.G. Laidler, and Y.-H. Chu, 1987. *Astrophys. J.* **321**, L41.

Wambach, J., 1986. in *Weak and Electromagnetic Interactions in Nuclei*, ed. by H.V. Klapdor, Springer, Berlin, p.950.

Wampler, E.J., and A. Richichi, 1989. *Astron. Astrophys.* **217**, 31.

Weaver, T.A., S.E. Woosley, and G.M. Fuller, 1985. in Numerical Astrophysics, eds. J. Centrella, J. LeBlanc and R. Bowers, Jones and Bartlett, Boston, p. 374.

Weiss, A., W. Hillebrandt, and J.W. Truran, 1988. *Astron. Astrophys.* **197**, L11.

West, R.M., A. Lauberts, H.E. Jorgensen, and H.-E. Schuster, 1987. *Astron. Astrophys.* **177**, L1.

Williams, R.E., 1987. *Astrophys. J.* **320**, L117.

Wilson, J.R., 1985. in Numerical Astrophysics, ed. by J. Centrella, J. Le Blanc, and R. Bowers, Jones and Bartlett, p. 422.

Wilson, J.R., R.W. Mayle, 1989. in The Nuclear Equation of State, Part A, ed. by W. Greiner and H. Stöcker, Plenum Press, N.Y., p. 731.

Wilson, J.R., R.W. Mayle, S.E. Woosley, and T.A. Weaver, 1986. *Ann. NY Acad. Sci.* **479**, 267.

Witteborn, F., J.D. Bregman, D. Wooden, P.A. Pinto, D.M. Rank, S.E. Woosley, and M. Cohen, 1989. *Astrophys. J. Lett.* **338**, L9.

Woosley, S.E., 1988. *Astrophys. J.* **330**, 218.

Woosley, S.E., P.A. Pinto, and T.A. Weaver, 1988. *Proc. Astron. Soc. Austrl.* **7**, 355.

Yahil, A., and J.M. Lattimer, 1982. in Supernovae: A Survey of Current Research, ed. by M.J. Rees and R.J. Stoneham, NATO-ASI **C90**, Reidel, Dordrecht, p. 53.

COURSE VII

THE NEUTRINO SIGNAL FROM A COLLAPSING STAR

D.K. NADYOZHIN

Institute of Theoretical and Experimental Physics
117259 Moscow, USSR

S. Bludman, R. Mochkovitch and J. Zinn-Justin, eds.
Les Houches, Session LIV 1990
Supernovae

Contents

Contents *303*

1. The neutrino signal from a collapsing star 304
   1.1. Introduction 304
   1.2. The neutrino radiation immediately before the beginning of the collapse 304
   1.3. Simple estimates of the neutrino signal properties 307
   1.4. Detailed calculations of the neutrino signal 313
   1.5. The neutrino signal from Supernova 1987A 320
   1.6. Conclusions 322
2. The neutrino heat conduction theory 325
   2.1. Introduction 325
   2.2. The neutrino transfer equation, stimulated absorption and the neutrino Kirchhoff law 326
   2.3. The elements of neutrino hydrodynamics 331
   2.4. The neutrino heat conduction approximation 335
   2.5. The kinetics of beta-processes and lepton charge diffusion 337
   2.6. Conclusions 341

1. The neutrino signal from a collapsing star

1.1. Introduction

It is well known that the cores of massive stars undergo hydrodynamic contraction at terminal stages of stellar evolution. The contraction, or gravitational collapse, is initiated by thermal dissociation of the iron-group nuclei into α-particles and free nucleons and also by the electron-nuclear capture processes (neutronization). The most important property of the collapse is a powerful neutrino radiation which eventually takes away nearly all the released energy. The neutrino signals generated by collapsing stellar cores give, in principle, an opportunity to follow the collapse dynamics with the aid of neutrino underground detectors.

We begin this lecture with a discussion of the neutrino radiation for the very final (presupernova) stages of stellar evolution. Then, we dwell on simple estimates of the neutrino signal properties in order to clarify the physical significance of the relevant processes. Finally we discuss results of sophisticated calculations for successive transparent, semi-transparent and opaque stages of the collapse.

1.2. The neutrino radiation immediately before the beginning of the collapse

When a hydrostatic stellar core approaches its final unstable configuration the neutrino luminosity of a star exceeds its common photon luminosity by many orders of magnitude (see, for example, Weaver et al. 1978, Sparks and Endal 1980, Sofia et al. 1979). The neutrino emission stimulates the temperature rise in the central region of the massive stellar core and thereby strongly accelerates the production of the final thermonuclear species, the iron group nuclei.

The neutrinos come mainly from the electron-positron pair annihilation (Chiu and Morrison 1960, Chiu 1961) and the decays of plasmons (Adams et al. 1963)

$$e^- + e^+ \Longrightarrow \nu + \tilde{\nu}\,, \tag{1.1}$$

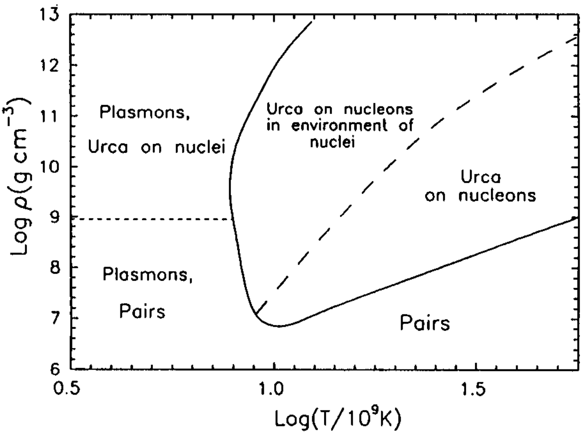

. 1. Temperature-density diagram showing the predominant neutrino emission pro-
ses (Nadyozhin and Chechetkin 1969).

$$pl \Longrightarrow \nu + \tilde{\nu} \,, \tag{1.2}$$

ere ν and $\tilde{\nu}$ denote neutrino and antineutrino of the same type (flavour). e contribution of electron neutrinos and antineutrinos ν_e $\tilde{\nu}_e$ in total emission dominates because they are produced both by charged and neutral currents itrary to μ and τ neutrinos and antineutrinos ν_μ $\tilde{\nu}_\mu$ ν_τ $\tilde{\nu}_\tau$ which are ipled only to neutral currents (temperature is too low for creation of $\mu^-\mu^+$ l $\tau^-\tau^+$ pairs). For high densities, the famous Urca-process (Gamow and iöenberg 1941)

$$(A, Z) + e^- \Longrightarrow (A, Z-1) + \nu_e \,, \tag{1.3}$$

$$(A, Z-1) \Longrightarrow (A, Z) + e^- + \tilde{\nu}_e \,, \tag{1.4}$$

nes into play (fig. 1). For high temperatures, process (1.4) is dominated positron capture (Pinaev 1963)

$$(A, Z-1) + e^+ \Longrightarrow (A, Z) + \tilde{\nu}_e \,. \tag{1.5}$$

s process should be certainly taken into account under physical condi- is in presupernova interiors. Moreover, it can be shown (Nadyozhin and :chetkin 1969), that for $T_9 \gtrsim 7$ the rates of the electron-positron nuclear

interactions (processes 1.3–1.5) turn out to be less than the rates of e^- ar
e^+ interactions with neutrons and protons (or free nucleons) appearing due
thermal dissociation of nuclei under conditions of nuclear statistical equili
rium (NSE). (Here $T_9 \equiv T/10^9 K$.) Thus, we have to allow for the followi
processes,

$$e^- + p \Longrightarrow n + \nu_e \,, \qquad (1.$$

$$e^+ + n \Longrightarrow p + \tilde{\nu}_e \,, \qquad (1.$$

rather than processes (1.3–1.5). The kinetics of e^- and e^+ interactions wi
nuclei and free nucleons as well as the resulting neutrino emission have be
discussed by Imshennik et al. (1966, 1967).

Figure 1 shows the regions where one or two of the above processes dor
inate. When $T_9 \lesssim 8$, the plasmon decays (process 1.2) contribute significant
to neutrino energy losses within a wide range of density variations. Process
(1.3–1.5) are expected to account for the bulk of the total neutrino emissi
rate for densities $\rho \gtrsim 10^9$g cm^{-3} and fairly low temperatures. For high tempe
atures ($T_9 > 8$), the main sources of neutrino emission are pair annihilati
(1.1) (low densities $\rho \lesssim 10^7$–10^8g cm^{-3}) and Urca-processes on free nucleo
(1.6, 1.7) (high densities). Along the inclined dashed line the mass fractio
of free nucleons and nuclei are the same. Above this line, processes (1
1.7) continue to contribute copiously to the total neutrino emission, althou
the mass fraction of free nucleons becomes rather low.

During the presupernova stage and the initial neutrino-transparent sta
of gravitational collapse, the neutrino luminosity can be easily calculated
follows

$$L = 4\pi \int_0^{R_c} \varepsilon_\nu \, \rho r^2 \, dr = \int_0^{M_c} \varepsilon_\nu \, dm, \qquad (1$$

where $\varepsilon_\nu = \varepsilon_\nu(\rho, T)$ is specific rate of total energy losses including all t
relevant neutrino emission processes for all the neutrino types; R_c and
denote the radius and mass of collapsing stellar core. If necessary, one m
consider the contributions of different processes and/or of different neutri
types separately. The function $\varepsilon_\nu(\rho, T)$ has been calculated allowing for a
of other processes such as various neutrino interactions with photons in
Coulomb fields of nuclei and electrons (photo-neutrino processes). For furt
details and innovations see Blinnikov and Rudzskij (1989) (pairs); Di
(1972), Munakata et al. (1985) (pairs, plasmons, photo-neutrino); Fuller
al. (1982,1985) (electron-nuclear weak interactions), and references there

In order to calculate ε_ν, one has first to derive the spectrum of emitted ieutrinos and then to integrate it over neutrino energy:

$$\varepsilon_\nu = \int_0^\infty B(E)\,dE\,. \tag{1.9}$$

Iere, the spectral emissivity $B(E)dE$ represents the energy emitted per unit nass and time in the form of neutrinos with energies between E and $E +$ lE. When processes (1.6) and (1.7) are the main sources of neutrinos and ıntineutrinos, we get

$$B(E) = \frac{1}{m_\mathrm{p}}\frac{\ln 2}{ft}\left(\frac{E}{m_\mathrm{e}c^2}\right)^5\left[\frac{X_\mathrm{p}}{1+\exp(\frac{E-\mu_e}{kT})} + \frac{X_\mathrm{n}}{1+\exp(\frac{E+\mu_e}{kT})}\right], \tag{1.10}$$

vhere X_p and X_n are mass fractions of free protons and neutrons, respecively; μ_e is the electron chemical potential; m_e and m_p denote the electron ınd proton masses, and c is the speed of light. From the neutron lifetime neasurements (Mampe et al. 1989) we have $ft = 1055 \pm 4\ s$. The first and he second terms in square brackets in eq. (1.10) correspond to emission of lectron neutrinos and antineutrinos in processes (1.6) and (1.7) respectively. Equation (1.10) is accurate for fairly high temperatures ($T_9 \gtrsim 10$), when the eutron-proton mass difference becomes insignificant.

Thus, a star manifests its readiness to enter the collapse by a violent enancement in its neutrino radiation. Such a neutrino precursor of the gravational collapse implies a total energy of $\sim 10^{49}$–10^{50}erg radiated for a ımescale about 10^2–10^3s, with characteristic energies of single neutrinos vithin 2–4 MeV. Unfortunately, the neutrino precursor can hardly be oberved by present neutrino detectors, even for the neighbouring collapses xpected at distances of 1–10 kpc in our Galaxy. The reason is because in iis case the energies of single neutrinos appear to be well below the neuino detectors' thresholds and the signal-to-noise ratio is rather low due to ie long timescale of the precursor.

.3. *Simple estimates of the neutrino signal properties*

number of useful conclusions about the neutrino signal can be drawn by omparing the initial stellar core structure on the verge of mechanical stability ith that of the final hydrostatic neutron star. The total energy release must e equal to the neutron star gravitational binding energy $\mathcal{E}_G$. It is generally ccepted now that nearly all $\mathcal{E}_G$ is taken away by neutrinos. Gravitational waves open another channel by which the energy could be transported to in-finity. However, for moderately rotating stellar cores, the gravitational waves are able to remove, at best, only some percents of $\mathcal{E}_G$ (see, for example, Müller 1984).

Using the theory of neutron star structure, one can calculate $\mathcal{E}_G$ for specified stellar core mass M_c before collapse. For our discussion it is sufficient to make use of simple approximate formulae (Lattimer and Yahil 1989) connecting M_c, $\mathcal{E}_G$ and the gravitational neutron star mass M_g measured by a distant observer:

$$\mathcal{E}_G = 1.5 \times 10^{53} M_g^2 \,\text{erg}\,, \tag{1.11}$$

$$M_c = M_g + 0.084 M_g^2\,. \tag{1.12}$$

Here both M_c and M_g are expressed in solar units. For every M_c, we can solve eq. (1.12) with respect to M_g and then find $\mathcal{E}_G$ from eq. (1.11). The results are presented in the first three columns of table 1.

Table 1
Masses and binding energies of the neutron stars.

$M_c/M_\odot$	$M_g/M_\odot$	$\mathcal{E}_G \times 10^{-53}$erg	$N \times 10^{-57}$	$(\mathcal{E}_G/N)$ MeV
1.10	1.01	1.54	1.31	73
1.40	1.27	2.40	1.67	90
1.70	1.51	3.41	2.03	105
2.00	1.74	4.56	2.38	120
2.30	1.97	5.84	2.74	133

According to the modern theory of stellar evolution, stars of masses 10–2 $M_\odot$, at the beginning of their life (at the Main Sequence on the Hertzsprung-Russel diagram) terminate evolution with dense central iron cores of mass M = 1.4–1.7$M_\odot$, surrounded by much more massive but rarefied and extended envelopes, having no influence on the development of the collapse but bein crucial for the onset of the supernova optical emission. It should be men-tioned, however, that one can not exclude the existence of somewhat mor massive cores, such as $M_c \simeq 2M_\odot$ or even still heavier. Three distressin uncertainties inherent in the modern theory of stellar evolution-convectio mass loss, and rotation permit us to vary the presupernova parameters withi somewhat wider ranges than those predicted by detailed calculations.

Thus, we see that the total energy of the neutrino signal $\mathcal{E}_{\nu\bar{\nu}}$ is expecte to be about

$$\mathcal{E}_{\nu\bar{\nu}} \simeq \mathcal{E}_G \simeq (2-5) \times 10^{53}\,\text{erg}. \tag{1.13}$$

What is the timescale of the energy emission? Before answering the ques-
tion, it is useful to look at values of stellar core radius R_c, central density
ρ_c, and temperature T_c predicted by the theory of stellar evolution

$$R_c = (2-5)\times 10^8\,\mathrm{cm}, \tag{1.14}$$
$$\rho_c = 10^9 - 10^{10}\,\mathrm{g\,cm^{-3}}, \tag{1.15}$$
$$T_c \simeq 6\times 10^9 K \simeq 0.5\,\mathrm{MeV}. \tag{1.16}$$

The time required for a spherical layer of radius R_c, enclosing mass M_c
nitially at rest, to fall onto the center in the absence of pressure gradient
free fall) is given by

$$t_{ff} = \frac{\pi}{2}\sqrt{\frac{R_c{}^3}{2GM_c}} = \sqrt{\frac{3\pi}{32G\bar{\rho}}}\,, \tag{1.17}$$

vhere G is the gravitational constant and

$$\bar{\rho} = \frac{3M_c}{4\pi R_c{}^3} \tag{1.18}$$

s the mean density inside radius R_c. Entering eq. (1.17) with R_c from eq.
1.14) and $M_c = 1.4M_\odot$, we get

$$t_{ff} = (0.33 - 1.3)\,\mathrm{s}\,. \tag{1.19}$$

n reality, the pressure gradient is not negligible and according to detailed
alculations the total time of contraction turns out to be 2–3 times longer. As
result, the hot hydrostatic neutron star should form in time t_{ac},

$$t_{ac} = (2-3)t_{ff} \simeq (1-4)\,\mathrm{s}\,. \tag{1.20}$$

he neutrino emission continues for $t > t_{ac}$ since a lot of energy is still stored
the form of heat inside the nascent neutron star. The dependence of the
eutrino luminosity L on time (the neutrino "light curve") is schematically
iown in fig. 2. The collapse proceeds in a highly non-homogeneous manner.
irst, an internal part of the core (an inner core) of mass $\sim (0.8-1)M_\odot$
egins to collapse. At the beginning of the collapse, the density throughout
e inner core does not differ appreciably from the central density ρ_c. As a
sult, the contraction of the inner core appears to be nearly homogeneous.
he timescale of the inner core contraction, t_{ffic}, can be found from eq.
.17) by substituting ρ_c instead of $\bar{\rho}$. Using eq. (1.15) for ρ_c, we obtain

$$t_{ffic} \simeq (6.6 - 2.1)\times 10^{-2}\,\mathrm{s}\,. \tag{1.21}$$

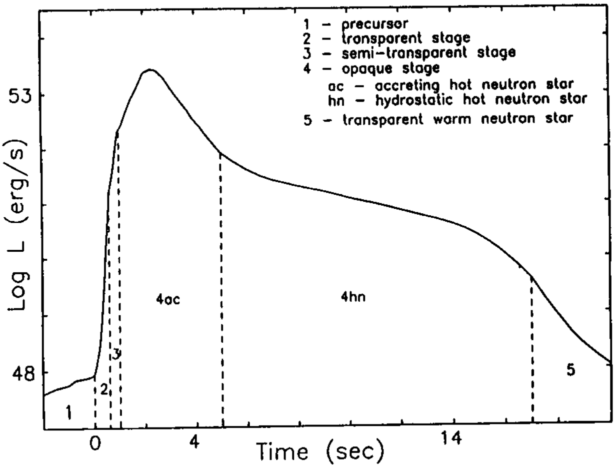

Fig. 2. Schematic neutrino light curve representing the time behaviour of the total ne
trino emission. Different stages of the neutrino emission are indicated. The duratio
of stages 2, 3 and of the beginning of stage 4ac are enlarged for clarity.

The neutrino luminosity increases sharply during the inner core collapse ar reaches its maximum at $t \simeq t_{ffic}$, when the inner core is decelerated co siderably while the rate of energy supply due to accretion of outer layers stellar core appears to be insufficient for stimulating further increase in tl neutrino luminosity. The timescale of the initial sharp rise in L (stages and 3 in fig. 2) is even several times shorter than t_{ffic}. After maximum, falls, since the accretion is gradually exhausted and finally ceases at $t \simeq$ (the end of stage 4ac in fig. 2). The hot hydrostatic neutron star forms ar continues to lose its thermal energy by neutrino radiation (stage 4hn).

To estimate the timescale of neutron star cooling we have to take in account the neutrino opacity, which is also crucial for calculations of t neutrino spectra. On stage 4hn the mean neutrino free path l_ν is much short than the neutron star radius $R_{ns} \simeq 10^6$cm. Therefore, neutrinos have to diffu slowly through the star. The timescale of neutron star cooling is given by

$$t_{cl} \simeq \tau \frac{R_{ns}}{c} \frac{\mathcal{E}_{th}}{\mathcal{E}_{\nu tr}}. \quad (1.2$$

Here τ is the neutrino optical depth of the neutron star:

$$\tau = R_{ns} < \sigma_{\nu\tilde{\nu}} > n, \quad (1.2$$

vhere $<\sigma_{\nu\bar{\nu}}>$ stands for the mean cross section of neutrino interaction with tellar matter and n is the effective number density of the neutrino-interacting articles. $\mathcal{E}_{th}$ in eq. (1.22) is the total thermal energy of the neutron star vhereas $\mathcal{E}_{\nu tr}$ is the energy trapped in the neutron star at a given time in form f neutrinos (do not confuse with $\mathcal{E}_{\nu\bar{\nu}}$). In order to estimate $<\sigma_{\nu\bar{\nu}}>$, we may se a typical expression for the cross section

$$\sigma_\nu \simeq \sigma_0 \left(\frac{E}{m_e c^2}\right)^2 , \qquad (\sigma_0 \equiv 1.7 \times 10^{-44}\,\mathrm{cm}^2) , \tag{1.24}$$

nd insert some characteristic neutrino energy $E = E_{ef}$. Under conditions f high neutrino optical depth, neutrino heat conduction theory applies and major contribution to the diffusion energy flux comes from neutrinos of nergies around

$$E_{ef} \simeq 2\,kT. \tag{1.25}$$

n first approximation, the characteristic temperature $\bar{T}$ in eq. (1.25) may be lentified with the total energy released per nucleon, and can be evaluated as ollows

$$k\bar{T} \simeq \frac{2}{3}\frac{\mathcal{E}_G}{N} \simeq 60\,\mathrm{MeV} , \tag{1.26}$$

here $N \simeq M_c\,/m_\mathrm{n}$ is total number of nucleons in the neutron star (table 1) d m_n denotes the neutron mass. The numerical value in eq. (1.26) corre-onds to $M_c = 1.4 M_\odot$. The energy $\mathcal{E}_{\nu tr}$ stored in the hot neutron star in rm of neutrinos can be approximated by

$$\mathcal{E}_{\nu tr} \simeq 3 \left(\frac{7}{8} a T^4\right)\left(\frac{4\pi}{3} R_\mathrm{ns}^3\right) , \tag{1.27}$$

here the factor 3 accounts for the total number of neutrino types. The term the first parenthesis gives the neutrino-antineutrino energy density per utrino type in a zero chemical potential approximation and the factor $\frac{7}{8}$ counts for the difference between Fermi-Dirac and Bose-Einstein statistics. e thermal energy $\mathcal{E}_{th}$ includes, besides $\mathcal{E}_{\nu tr}$, the kinetic energies of non-lativistic neutrons and protons, relativistic electrons, positrons and photons th admixtures of muons and pions.

Assuming $\mathcal{E}_{th} \simeq \mathcal{E}_G$, $n \simeq 3N/(4\pi R_\mathrm{ns}^3)$, $R_\mathrm{ns} \simeq 10^6$ cm and $M_c = 1.4 M_\odot$, e can easily calculate from eqs. (1.23–1.27)

$$\mathcal{E}_{\nu tr} \simeq 1.9 \times 10^{52}\,\mathrm{erg}, \tag{1.28}$$

$$\mathcal{E}_{th}\,/\mathcal{E}_{\nu tr} \simeq 13, \tag{1.29}$$

$$\tau \simeq 4 \times 10^5, \quad (1.30$$

$$t_{cl} \simeq 140\,\mathrm{s}. \quad (1.31$$

We see that $\mathcal{E}_{\nu tr}$ is about an order of magnitude less than $\mathcal{E}_{th}$ and that th neutrino optical depth of the neutron star is very large. It is precisely thi fact that explains the great excess of t_{cl} above the time $R/c \simeq 3 \times 10^{-4}$ which is required for neutrinos to escape the neutron star in the absence c interaction with matter.

The value of t_{cl}, specified by eq. (1.31), turns out to be 5–7 times greate than that obtained in detailed calculations. This is because we have certainl overestimated the product $< \sigma_{\nu\tilde{\nu}} > n$ in eq. (1.23). In fact, since the cros sections for $\nu_\mu\ \tilde{\nu}_\mu$ and $\nu_\tau\ \tilde{\nu}_\tau$ are less than that for $\nu_e\ \tilde{\nu}_e$ by a factor of 3– it would be better to take for $< \sigma_{\nu\tilde{\nu}} >$ a value which is about 2–3 times le than σ_ν given by eq. (1.24). Moreover, it would be more correct to use for some 2 times smaller value than the total nucleon density since, for exampl ν_e are absorbed only by neutrons whereas $\tilde{\nu}_e$ are absorbed only by proton Finally, the non-dimensional coefficient of proportionality in eq. (1.22) ma be somewhat less than 1. We were concerned with an order of magnitu estimate and we have obtained it.

What we can say about the mean energy $E_{\nu m}$ of emitted neutrinos? It clear that $E_{\nu m}$ must be considerably lower than energies of neutrinos trapp in deep interiors of the hot neutron star. In order to obtain a rough estima we recall that the main absorbers of the electron neutrinos and antineutrin are free nucleons (through processes which are inverse to (1.6) and (1.7 Free nucleons appear copiously at densities $\rho \gtrsim \rho_\mathrm{n} \simeq 10^{12}\ \mathrm{g\ cm^{-3}}$. Belc this density matter is, therefore, much less opaque to neutrino than abo For this reason, the neutrinos (being involved in a slow diffusion from de neutron star interiors to its surface), are expected to decouple from matt at the layer where density decreases to ρ_n. The bulk of the radiated ener must be carried away by those neutrinos whose "optical" depth is about 1 $\rho \simeq \rho_\mathrm{n}$. This condition gives us the following relation to determine $E_{\nu m}$

$$\tau \simeq 1 \simeq R_\mathrm{ns} < \sigma_{\nu\tilde{\nu}} > \frac{\rho_\mathrm{n}}{m_\mathrm{n}} . \quad (1.$$

Solving this equation with respect to $E = E_{\nu m}$ we get

$$E_{\nu m} \simeq m_\mathrm{e} c^2 \sqrt{\frac{m_\mathrm{n}}{q \sigma_0 \rho_\mathrm{n} R_\mathrm{ns}}} \simeq 12\,\mathrm{MeV}, \quad (1.$$

where we have introduced a factor $q \simeq 1/6$ accounting for the above m tioned reduction in $< \sigma_{\nu\tilde{\nu}} > n$.

Thus, in this section we have outlined a general physical picture of the gravitational collapse and obtained an idea of the basic neutrino signal properties such as the total radiated energy (table 1), the time behaviour of the neutrino luminosity (the neutrino light curve, fig. 2), and the characteristic energies of individual neutrinos.

1.4. Detailed calculations of the neutrino signal

Figure 3 shows the total neutrino light curve resulting from calculations of the gravitational collapse with allowance for neutrino opacity. The differences in shape between this curve and that presented in fig. 2 are mainly due to a specific logarithmic scale along the horizontal axis with time measured from the moment when averaged neutrino optical depth of the collapsing core $\tau_\nu = 0.001$. Such a scale permits us to represent in detail a sharp transition between transparent and opaque stages of the collapse which proves most difficult in numerical simulation. During this transition, at the beginning of stage 4ac the central region experiences pulsations (shown by squares and crosses) which are rather of numerical nature but may have also some physical grounds.

Transparent and semi-transparent stages of the collapse (stages 2 and 3). This stage is controlled by the same processes which are responsible for neutrino precursor emission (section 1.2). When the density increases, processes (1.3) and (1.6) become more and more violent and the process of neutronization gathers its strength. The neutronization continues for the semi-transparent stage 3, and at the beginning of the opaque stage 4 too. As a result, ν_e radiation flux proves to be more intensive than fluxes of other neutrino types. Specifying an effective energy $E_{\nu ec}$ (carried away eventually by ν_e per one electron capture), we can easily evaluate energy $\mathcal{E}_{\nu ec}$ radiated owing to the neutronization

$$\mathcal{E}_{\nu ec} \simeq \frac{26}{56} N E_{\nu ec} \simeq 1.2 \times 10^{52}\,\mathrm{erg}. \tag{1.34}$$

Here we have assumed that the core is initially composed of iron. We made use also of N from table 1 (for $M_c = 1.4 M_\odot$) and put $E_{\nu ec} = 10\,\mathrm{MeV}$. The timescale of such a ν_e pulse is $\sim 10^{-2}$ s. Its discovery is one of the most important objectives of future programs aimed at searching for gravitational collapses in our Galaxy. The ν_e pulse is expected to be more distinctive for low M_c, since in this case the neutronization turns out to be non-equilibrium. However, for more massive cores such as $\sim 2 M_\odot$ (fig. 3) this pulse does not

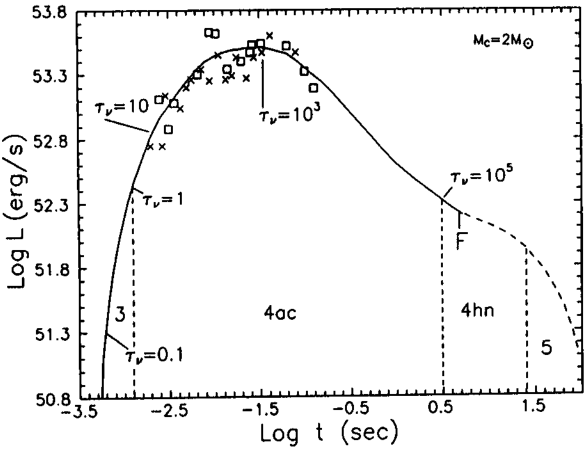

Fig. 3. The total neutrino light curve for the gravitational collapse of a $2M_\odot$ iron-oxygen stellar core calculated with the use of the neutrino heat conduction theory (Nadyozhin 1978). Point F marks the end of the hydrodynamic calculations.

protrude on a steeply rising neutrino light curve because $E_{\nu ec}$ is now as low as $\sim$ (2–3) MeV.

It is worth remembering here an expression for energy density $U(E, r)$ of neutrino radiation which holds for the transparent stage of the collapse:

$$U(E,r) = \frac{1}{2cr} \int_0^{R_c} r' \rho B(E) \ln \left| \frac{r+r'}{r-r'} \right| dr' . \tag{1.35}$$

The spectral emmisivity $B(E)$ depends, of course, on r'–through T, for example, as in eq. (1.10). Equation (1.35) holds both inside and outside the star. At the center ($r = 0$), we get

$$U(E,0) = \frac{1}{c} \int_0^{R_c} \rho B(E) \, dr' , \tag{1.36}$$

whereas at large distances from the stellar core ($r \gg R_c$)

$$U(E,r) = \frac{1}{cr^2} \int_0^{R_c} r'^2 \rho B \, dr' = \frac{S(E)}{4\pi c r^2} , \tag{1.37}$$

where $S(E)$ is the spectral neutrino luminosity connected with total neutrino luminosity L by

$$L = \int_0^\infty S(E)\, dE \, . \tag{1.38}$$

Equations (1.35–1.38) hold for all the neutrino types. Integrating eqs. (1.35–1.37) over E, one can obtain corresponding relations for the total energy density U. For the neutrino spectral number density, we have

$$n(E) = U(E)/E \, . \tag{1.39}$$

Equations (1.8–1.10) and (1.35–1.38) represent the formalism for studying the neutrino emission at the transparent stage of the collapse.

The neutrino opaque stage of the collapse (stages 4ac and 4hn) begins after the appearance of the neutrino opaque ($\tau_\nu > 1$) core. The core is immersed in a transparent accreting envelope whose volume neutrino radiation is much less than the neutrino flux from the neutrinosphere and so we shall concentrate mainly on the latter. The term "neutrinosphere" had been introduced by analogy with the common stellar photosphere.

In the spherically symmetric case, the neutrinosphere is defined as a sphere of radius $R_{\nu\text{ph}}$ at which the neutrino black body energy flux with local values of temperature T and neutrino chemical potential μ is precisely equal to the total neutrino energy flux which the star radiates to infinity. The corresponding values of T and μ are designated as $T_{\nu\text{ph}}$ and $\mu_{\nu\text{ph}}$. The neutrinosphere is usually located at the neutrino optical depth $\tau_{\nu\text{ph}} \approx 0.3$–$1$.

Inside the neutrinosphere, the diffusion of different type neutrinos can be calculated with the aid of the neutrino heat conduction (NHC) theory (Imshennik and Nadyozhin 1972, 1979). According to this theory, the diffusion of neutrino energy is accompanied by the diffusion of the electron, mu and tau lepton charges. The fluxes of energy and lepton charges are proportional to linear combinations of temperature and chemical potential gradients. The coefficients of these combinations are determined by the neutrino mean free paths averaged over the energies of individual neutrinos by a method similar to the well known Rosseland mean for photon opacity.

The solution of the NHC equations has to satisfy the boundary conditions imposed at the neutrinosphere. Physically, these conditions account for the absence of external sources of neutrino emissions in the close vicinity of the collapsing star–so-called free radiating surface conditions. Thus, the NHC theory gives us an effective method to determine both the neutrino fluxes and the neutrino photosphere properties. Neutrino luminosity for any neutrino type can be expressed as

$$L_\nu = 4\pi R_{\nu\mathrm{ph}}^2 A T_{\nu\mathrm{ph}}^4 F_3(\psi_{\nu\mathrm{ph}}) , \quad (\psi_{\nu\mathrm{ph}} \equiv \mu_{\nu\mathrm{ph}}/kT) . \tag{1.40}$$

Here F_3 is the Fermi-Dirac function of index 3 and

$$A = \frac{7}{16}\frac{1}{F_3(0)}\frac{\pi^2 k^4}{15\hbar^3 c^3} = \frac{7}{16}\frac{a}{F_3(0)} , \tag{1.41}$$

where a is the radiation density constant.

In general, the neutrinosphere parameters $R_{\nu\mathrm{ph}}$, $T_{\nu\mathrm{ph}}$, and $\psi_{\nu\mathrm{ph}}$ differ fo[r] different neutrino types. Really, a substantial difference exists only betwee[n] the electron and other type neutrinos. Therefore, in good approximation w[e] may consider only two sets of the neutrinosphere parameters–one for th[e] electron and another for μ and τ neutrinos and antineutrinos. Bearing this i[n] mind, we may represent the total luminosities for ν_e, $\tilde{\nu}_e$ and ν_μ, $\tilde{\nu}_\mu$, ν_τ, $\tilde{\nu}_\tau$ as follows

$$L_{\nu e} = 4\pi R_{\nu e\mathrm{ph}}^2 A T_{\nu e\mathrm{ph}}^4 \Phi_3(\psi_{\nu e\mathrm{ph}}) , \tag{1.42}$$

$$L_{\nu\mu\tau} = 2 \times 4\pi R_{\nu\mu\mathrm{ph}}^2 A T_{\nu\mu\mathrm{ph}}^4 \Phi_3(\psi_{\nu\mu\mathrm{ph}}) , \tag{1.43}$$

where

$$\Phi(x) = F_3(x) + F_3(-x) . \tag{1.44}$$

In eqs. (1.42) and (1.43) we take into account the fact that, in a black bod[y] approximation, chemical potentials of neutrinos and antineutrinos have dif[-]ferent signs. The Fermi-Dirac functions of integer indices have a remarkabl[e] property (Rhodes 1950, Nadyozhin 1974, see also Blinnikov and Rudzsk[ii]

1989) resulting in the following analytical representation

$$\Phi(x) = \frac{x^4}{4} + \frac{\pi^2}{2}x + \frac{7\pi^4}{60} . \tag{1.45}$$

Thus, the conception of the neutrinosphere proves to be useful for analyzing the properties of the neutrino energy and lepton fluxes from the collapsing stellar cores. Lack of space does not permit us to discuss the lepton charge fluxes in detail. We shall only mention that they are small enough for the hot neutron star cooling (stage 4hn), since neutrinos and antineutrinos are radiated with nearly equal intensities. When the neutrinosphere parameters are specified, one can approximate the spectral neutrino luminosity $S(E)$ by black body Fermi-Dirac distributions. For example, for the $\tilde{\nu}_e$ -spectrum we get

$$S_{\tilde{\nu}e}(E)\,dE = 4\pi R^2_{\tilde{\nu}\mathrm{eph}} \frac{A}{k^4} \frac{E^3\,dE}{1 + \exp\left(E/kT_{\tilde{\nu}\mathrm{eph}} - \psi_{\tilde{\nu}\mathrm{eph}}\right)} . \tag{1.46}$$

Hydrodynamic modelling of the gravitational collapse implies that $T_{\nu\mathrm{eph}} \approx T_{\tilde{\nu}\mathrm{eph}} \approx$ (3–4) MeV while the chemical potentials $\psi_{\nu\mathrm{eph}} = -\psi_{\tilde{\nu}\mathrm{eph}}$ prove to be less than 1, for a $2M_\odot$-core at least (Nadyozhin 1978).

Unfortunately, a black body approximation for the neutrino spectra becomes inadequate when one deals with such spectrum-sensitive problems as neutrino signal registration by underground detectors and elucidation of the effects of neutrino nucleosynthesis. Both problems are very sensitive to the high-energy tail of the spectrum. For $E \gg kT_{\nu\mathrm{eph}}$ the spectra must decay faster than one would expect from black body distribution. In this connection, there appears necessity to calculate the neutrino spectra at much greater length with the use of the neutrino transfer equations. Such calculations are indispensable to investigations of the initial steep front of the neutrino signal (stages 2, 3 and the beginning of stage 4ac) when the NHC theory is not yet applicable.

The sophisticated spectral calculations deal with a set of transfer equations describing all the neutrino types and allowing for a number of interactions between neutrinos and stellar matter. The most important interactions are

$$\nu_e + n \rightleftarrows p + e^-, \tag{1.47}$$

$$\tilde{\nu}_e + p \rightleftarrows n + e^+, \tag{1.48}$$

$$\nu + \tilde{\nu} \rightleftarrows e^- + e^+, \tag{1.49}$$

$$\nu + \tilde{\nu} \rightleftarrows pl, \tag{1.50}$$

$$\nu + e^- \rightleftarrows e^{-\prime} + \nu', \tag{1.51}$$

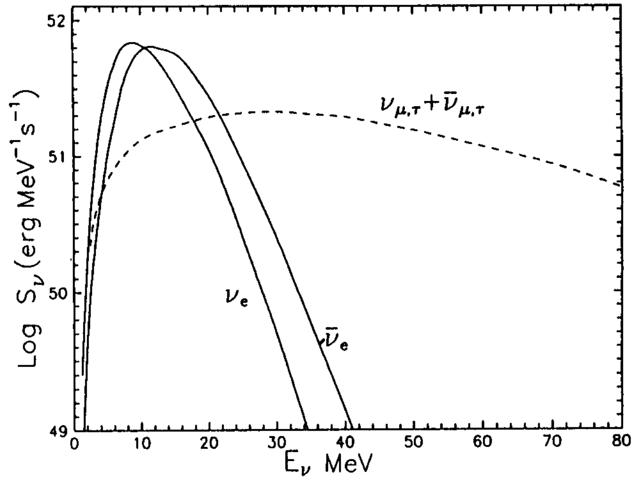

Fig. 4. The spectral neutrino luminosities (ν_e,$\bar{\nu}_e$: Nadyozhin and Otroshenko 1980
$\nu_{\mu\tau}$ + $\bar{\nu}_{\mu\tau}$: Schinder and Shapiro 1983).

$$\nu \ + e^+ \rightleftarrows \ e^{+'} + \nu', \qquad (1.52$$

$$\nu \ + p \rightleftarrows \ p' + \nu', \qquad (1.53$$

$$\nu \ + n \rightleftarrows \ n' + \nu', \qquad (1.54$$

$$\nu \ + (A, Z) \rightleftarrows \ (A, Z)' + \nu'. \qquad (1.55$$

These processes proceed in both directions; ν and $\tilde{\nu}$ in processes (1.49 and (1.50) refer to all three types of neutrino and the corresponding an tineutrino, in processes (1.51–1.55), describing the neutrino scattering of electrons, positrons, protons, neutrons, and nuclei ν denotes any neutrin or antineutrino species. The cross section of processes (1.47) and (1.48) i at least, several times greater than that of other processes. This is why th properties of the ν_e $\tilde{\nu}_e$ signal differ from those of the ν_μ $\tilde{\nu}_\mu$ and ν_τ $\tilde{\nu}_\tau$ sig nals. The process (1.55) describes a coherent neutrino scattering off nucle that occurs because the Compton wavelength λ_c for neutrinos of energie $E \approx$ (10–20) MeV is comparable with or even greater than the nuclear ra dius: $\lambda_c = hc/E \sim 10^{-12}$ cm. Figure 4 shows an example of the neutrin spectra calculated with the use of the transfer equations. The ν_e and $\tilde{\nu}_e$ spec tra are taken from Nadyozhin and Otroshenko (1980) and a joint ν_μ $\tilde{\nu}_\mu$ ı

$\tilde{\nu}_\tau$ spectrum from Schinder and Shapiro (1983). The maxima of the ν_e and $\tilde{\nu}_e$ spectra are about $E_m \simeq (10\text{–}12)$ MeV. Hence the corresponding neutrinosphere temperature must be about $E_m/3 \simeq 4$ MeV. For $\nu_{\mu\tau}$-spectrum we have $E_m \approx (25\text{–}30)$ MeV. The corresponding $\nu_{\mu\tau}$-neutrinosphere temperature turns out to be a factor of 2 greater than that of the ν_e-neutrinosphere. Similar results had been obtained by Bowers and Wilson (1982) and Giovanoni et al. (1989).

The important point is the distribution of the total energy flux over the neutrino types. There exists a consensus at present that after the neutrino light curve maximum (when more than 90 percent of the total energy is radiated), the energy flux is distributed almost equally over all the neutrino and antineutrino types–each of the neutrino species takes away about 1/6 of the neutron star binding energy. This assumption is supported by detailed calculations (Wilson 1980, Schinder and Shapiro 1983). The equipartition certainly does not hold for pre-maximum stages of the collapse (stages 1–3, fig. 2, 3), when the emission of electron neutrinos and antineutrinos dominates the total energy flux.

Let us compare now the parameters of the $\nu_e\tilde{\nu}_e$-neutrinosphere with that of the $\nu_{\mu\tau}$-neutrinosphere. Assuming in accordance with the equipartition $L_{\nu e} = \frac{1}{2} L_{\nu\mu\tau}$, we can obtain from eqs. (1.42) and (1.43) in zero chemical potential approximation

$$R_{\nu\mu\mathrm{ph}} = \left(\frac{T_{\nu e\mathrm{ph}}}{T_{\nu\mu\mathrm{ph}}}\right)^2 R_{\nu e\mathrm{ph}} \approx \frac{1}{4} R_{\nu e\mathrm{ph}} \,. \tag{1.56}$$

This result disagrees with the physical structure of a hot neutron star. In fact, the neutrino optical depth $\tau_{\nu\mu}$ must increase sharply inside the neutron star, and the inequality $\tau_{\nu\mu} \lesssim 1$ can therefore hold only in an outermost layer with a radius that does not substantially differ from both the neutron star radius and $R_{\nu e\mathrm{ph}}$. On the other hand, the shape of the $\nu_{\mu\tau}$-spectrum is close to that of a black body, and we conclude that the ν_μ ν_τ-neutrino flux is described by nearly thermal in shape but diluted spectrum. This means that we have to modify eq. (1.43) by inserting in the right hand side an additional factor of ~1/16. From the physical point of view, this occurs owing to the lack of ν_μ and ν_τ for the truly absorptive processes like (1.47) and (1.48) for ν_e and $\tilde{\nu}_e$.

Another important point is necessity to take into consideration the effects of general relativity such as the red shift in gravitational field of the collapsing star and gravitational time dilation. For ν_e and $\tilde{\nu}_e$ spectra presented in fig. 4, these effects were taken into account by the introduction of appropriate corrections to the Newtonian solution. However, this problem deserves more consistent treatment. An approach to numerical modelling of the general relativistic neutrino transport has recently been developed by Schinder (1988) and Schinder and Bludman (1989).

1.5. The neutrino signal from Supernova 1987A

The burst of neutrino radiation detected from SN 1987A has opened a new epoch in the investigation of supernovae in general and gravitational collapse in particular. Many papers are devoted to this great event in our understanding of stellar evolution. So we present below only a short account of how the theoretical considerations above help us understand two dozen of those really brilliant-for-science neutrinos that were captured by underground neutrino detectors on 23 February 1987. For details and references we recommend, to begin with, the reviews of Schramm and Truran (1990), Hillebrandt and Höflich (1989), Burrows (1990) and Imshennik and Nadyozhin (1989).

From the calculations of gravitational collapse for a $2M_\odot$ stellar core by Nadyozhin (1978), it follows (Nadyozhin and Otroshenko 1980) that the $\tilde{\nu}_e$-spectrum can be approximated by (see also Blinnikov et al. 1988)

$$S_{\tilde{\nu}e}(E) = 4\pi R^2_{\tilde{\nu}\mathrm{eph}} \frac{q}{\beta^2} \frac{\pi}{c^2 h^3} \frac{E^3 \exp\left[-\alpha(E/kT_1)^2\right]}{1 + \exp(E/kT_1)}, \quad (1.57)$$

$$\beta = \sqrt{1 - R_g/R_{\tilde{\nu}\mathrm{eph}}}, \quad (1.58)$$

where R_g is the gravitational radius of the neutrinosphere while α, q and T_1 are the fitting parameters. For electron antineutrinos we have α =0.024, q =0.807 and $T_1 = 1.12\beta T_{\tilde{\nu}\mathrm{eph}}$. These are the values that approximate the $\tilde{\nu}_e$-spectrum presented in fig. 4. In eq. (1.57), E is the energy of $\tilde{\nu}_e$ at the Earth; when escaping the neutrinosphere it has the energy $E_0 = E/\beta$. The spectral luminosity specified by eq. (1.57) is somewhat different from that given by eq. (1.46), since it relates to a distant observer and takes into account an additional cut-off factor for high $\tilde{\nu}_e$ energies.

In view of the poor statistics of detected neutrino events, it is most reliable to compare the general characteristics of the neutrino signal, such as the total number of events recorded in time t, $N(t)$, and the mean neutrino energy $\bar{\epsilon}(t)$, released in the detector at time t. Using the $\tilde{\nu}_e$-spectrum given by eq. (1.57) one can calculate the dependences $N(t)$ and $\bar{\epsilon}(t)$ expected for the IMB and KamiokaNDE II (KII) detectors (for details see Imshennik and Nadyozhin 1989, or Blinnikov et al. 1988). A comparison of calculations with the neutrino signal recorded by the IMB and KII detectors is presented in figs. 5 and 6, respectively. The full smooth lines in figs. 5a and 6a correspond to $N(t)$ calculated for the $\tilde{\nu}_e$-spectrum shown in fig. 4, while the step-like

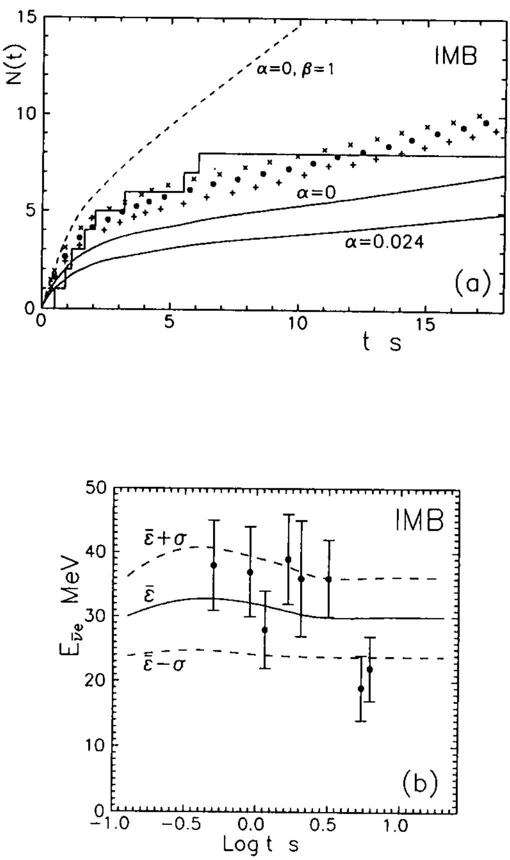

Fig. 5. A comparison of theoretical predictions with the neutrino signal from SN 1987A registered by the IMB detector. (See text for further explanations.) (a) The data for the step-like curve from Bionta et al. (1987). The time has been synchronized so that the first event in the detector coincides with the moment when $N(t)=1$. (b) The energies of neutrino events with the experimental uncertainties (bars) from LoSecco et al. (1988). A curve in the middle of $\pm 1\sigma$ confidence band gives the dependence of $\bar{\epsilon}(t)$.

curves represent the responses of the IMB and KII detectors to the SN 1987A neutrino signal. The regions bound by the dashed lines in figs. 5b and 6b are the theoretical $\pm 1\,\sigma$ confidence limits. The coincidence between theory and experiment can be considered fairly good, taking into account the fact that no special fitting of this 10 year old theoretical prediction to the experiment was done. Better agreement would be achieved if the $\tilde{\nu}_e$-flux were somewhat greater. There are certain reasons for such an increase. First, the neutrino opacity in the calculations in question must have been overestimated. Second, a probable enhancement in the neutrino flux due to non-stationary convection in the outermost layers of the collapsing core (Burrows and Lattimer 1988, Wilson and Mayle 1988) was not taken into account. The crosses and filled circles in figs. 5a and 6a correspond to a 1.5-fold increase in the neutrino flux due to either an increase in $T_{\tilde{\nu}\mathrm{eph}}$ (shown by $\times$) by a factor of $\sqrt[4]{1.5}$ (11 percent increment), or in $R_{\tilde{\nu}\mathrm{eph}}$ (shown by $+$) by $\sqrt{1.5}$ times (22 percent), or in both $T_{\tilde{\nu}\mathrm{eph}}$ and $R_{\tilde{\nu}\mathrm{eph}}$ (filled circles) by factors of $\sqrt[8]{1.5}$ and $\sqrt[4]{1.5}$, respectively. These corrected results demonstrate a remarkable agreement with experiment. Note that these modifications have almost no influence on the theoretical curves $\bar{\epsilon}(t)$ in figs. 5b and 6b.

Figures 5a and 5b show also that the sensitivity of the results to the parameter α is not very high. However, the effects of general relativity are of crucial importance: compare the full lines $\alpha = 0$ with the dashed lines calculated for the case when these effects are neglected ($\beta = 1$).

Thus, we conclude that the neutrino signal from SN 1987A has certainly confirmed the basic theoretical prediction about the diffusive nature of the bulk of the neutrino emission expected from collapsing stellar cores.

1.6. Conclusions

Summarizing the above discussion, we shall first formulate theoretical predictions for the main properties of the neutrino signal from collapsing stellar cores.

(i) The signal has a shape of a (10–20) s pulse consisting of a mixture of all three neutrino and antineutrino types (ν_e $\tilde{\nu}_e$ ν_μ $\tilde{\nu}_\mu$ ν_τ $\tilde{\nu}_\tau$). The total energy of the pulse is virtually equal to the binding energy of the neutron star (2–5) $\times$ 10^{53} erg.

(ii) The signal begins with a very steep jump ($\Delta t \approx 0.03\,s$) of the total neutrino luminosity from $\sim 10^{48}$ erg/s characteristic of the preceding presupernova evolution (stage 1 in fig. 2) up to the maximum value of $\sim 3 \times 10^{5}$ erg/s. At the luminosity maximum the neutrino optical depth of the collapsed

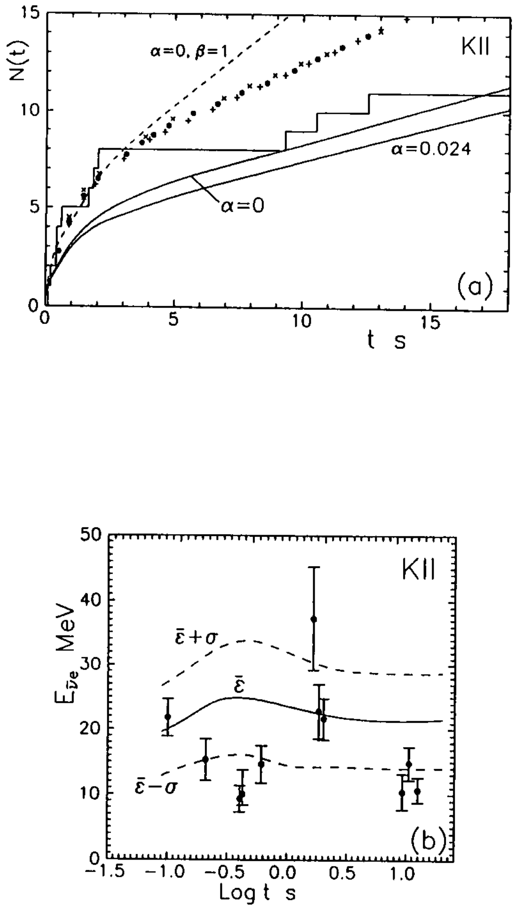

Fig. 6. Same as Fig. 5, but for the KII detector. Both the step-like curve (a) and the energies and uncertainties (b) come from Hirata et al. (1987, 1988).

inner core is $\sim 10^2$–10^3. Within the jump there is a transition from the neutrino-transparent to the neutrino-opaque stage of the collapse.

(iii) The neutrino-opaque stage begins with a non-stationary accretion of the outer envelope onto the hot opaque inner core (stage 4ac in figs. 2 and 3) which crawls for $\sim (1$–$4)\,s$.

(iv) The neutrino signal ends with a prolonged tail (stage 4hn) with lifetime of (10–20) s which is related to the cooling of a hot nascent neutron star.

(v) The bulk of the neutrino pulse energy is radiated during stages 4ac and 4hn. The total energies radiated for stages 2+3, 4ac, and 4hc relate in order of magnitude as 1 :20 :20. For the collapse of a low mass stellar core (1.2–1.3) $M_{\odot}$, a short pulse of 10 MeV ν_e is expected owing to a non-equilibrium neutronization with the total energy of $\sim 10^{52}$ erg, reducing the above ratios to 1 :10 :10.

(vi) The total radiated energy is nearly equally distributed over all the six neutrino and antineutrino species. However, for stages 2 and 3, the electron neutrinos and antineutrinos dominate the total neutrino flux.

(vii) The mean energies of the individual neutrinos are (10–12) MeV for ν_e and $\tilde{\nu}_e$ and ~ 25 MeV for $\nu_\mu\ \tilde{\nu}_\mu\ \nu_\tau\ \tilde{\nu}_\tau$.

(viii) The $\nu_e\ \tilde{\nu}_e$-spectra are close to the thermal Fermi-Dirac distributions with somewhat suppressed high-energy tails, whereas $\nu_\mu\ \tilde{\nu}_\mu\ \nu_\tau\ \tilde{\nu}_\tau$ are described by nearly thermal distributions, diluted by a factor of 0.05–0.1.

(ix) The bulk of the total neutrino pulse energy is radiated under conditions of high neutrino opacity and has a diffusive nature.

The neutrino signal from SN 1987A does not contradict these predictions. However, the pulsar expected inside the SN 1987A remnant has not yet been discovered. It is not excluded that SN 1987A has given rise to a black hole. Nearly all the above predictions also remain qualitatively true for black hole formation, except for the absence of a prolonged stage of neutron star cooling. Nevertheless, if the black hole mass is about 5–10 $M_{\odot}$, the lifetime of the neutrino radiation can reach about $\sim 10\,$s as a result of both the deceleration of accretion (due either to the nearly Eddington photon flux or to fast rotation) and the general relativistic time dilation effect.

Further progress in our understanding of the neutrino signal from the collapsing stellar cores and the mechanism of the supernova outburst is expected, first of all from the investigation of collapsing rotating stellar cores (see Hillebrandt et al. 1990 and references therein). The neutrino transparent and semi-transparent stages of collapse deserve considerably deeper insight, since they bear a lot of information about the dynamics of stellar core contraction and the physical processes involved. There is even hope to see a bounce shock wave in neutrino 'light' (Giovanoni et al. 1989). We ought to be ready for the registration of neutrino burst from a nearby collapse in our Galaxy. If it occurred, for example, at the site of the Crab pulsar ($\simeq$ 1.7 kpc distant), more than ten thousand neutrinos would be captured by the underground neutrino detectors; among them nearly 1000 neutrinos would come from the transparent and semi-transparent regions of the star.

2. The neutrino heat conduction theory

2.1. Introduction

An extensive investigation of gravitational collapse carried out in the last decade by numerous researchers has led to an unambiguous conclusion that the bulk of the resulting neutrino burst energy comes from the collapsing neutrino-opaque central core and from the subsequent cooling of a hot nascent neutron star, whose neutrino optical depth turns out to be initially as high as $\sim 10^5$. Hence, all three neutrino types are forced to diffuse slowly through the neutron star before escaping from the neutrinosphere. Under such conditions, one obviously has to treat neutrino transport in stellar interiors with an adequate theory based on the diffusive nature of the neutrino flux, rather than with the neutrino transfer equation in its the most general form. However, the latter should certainly be used in the outermost layers of the collapsing stellar core for calculating detailed spectra of the radiated neutrinos and for elucidating mechanisms of supernova explosions.

The aim of this lecture is to describe in a consistent way the neutrino heat conduction (NHC) theory formulated by Imshennik and Nadyozhin (1972). First attempts to include the NHC in gravitational collapse hydrodynamics were taken by Arnett (1966) and Schwartz (1967). These authors used the equations based on a rough analogy with radiative (photon) heat conduction; the energy density of neutrinos in stellar interiors was assumed to be equal to that of antineutrinos. (A zero neutrino chemical potential was arbitrarily postulated.) Therefore, important effects such as lepton charge diffusion and the contribution of the neutrino chemical potential gradient to the total energy flux were omitted. Historically, their results were, however, the first important attempts to incorporate neutrino diffusion into gravitational collapse hydrodynamics.

For simplicity we confine ourselves mostly to discussion of electron neutrinos. The results can be easily generalized by allowing for μ and τ neutrinos (Imshennik and Nadyozhin 1979). In this case, one meets, however, with a delicate point deserving further investigation: the main sources of the μ and τ neutrino opacity are due to an inelastic scattering off electrons, positrons, and nucleons; whereas for electron neutrinos absorption by free neutrons and protons dominates the neutrino opacity. At present there is a really good basis for developing a complete NHC theory owing to recent experimental evidence for the existence of only three of the light neutrino families (Aarnio et al. 1990, Decamp et al. 1990).

2.2. The neutrino transfer equation, stimulated absorption and the neutrino Kirchhoff law

A consistent derivation of the NHC equations is based on the equation of neutrino transfer, involving interactions, between neutrino radiation and matter in relative motion. This equation is analogous in many ways to that derived by Thomas (1930) for photons and subjected to further extensive investigation (see Imshennik and Morozov 1981 and references therein). For simplicity, we mostly consider the case when true neutrino absorption dominates the neutrino scattering off matter, and give brief comments concerning incorporation of the scattering in the NHC theory. In the absence of scattering, the neutrino transfer equation in a fixed (laboratory) reference frame in a spherically symmetric case is

$$\frac{1}{c}\frac{\partial I_\nu}{\partial t} + \mu\frac{\partial I_\nu}{\partial r} + \frac{1-\mu^2}{r}\frac{\partial I_\nu}{\partial \mu} = -\frac{I_\nu}{l_\nu} + \mathcal{E}_\nu \ , \tag{2.1}$$

where $I_\nu = I_\nu\ (\varepsilon_\nu\ , \mu, r, t)$ is the intensity of the neutrino radiation, the index ν denotes any neutrino and antineutrino species, and μ is the cosine of the angle between the direction of neutrino motion and the radius vector (a direction cosine). The intensity I_ν , the neutrino mean free path l_ν , and the emissivity $\mathcal{E}_\nu$ are connected with the corresponding quantities $I_{\nu 0}$, $l_{\nu 0}$, and $\mathcal{E}_{\nu 0}$ in the co-moving reference frame (where matter is at rest at the point considered) by the following relations

$$\frac{I_{\nu 0}}{\varepsilon_{\nu 0}^3} = \frac{I_\nu}{\varepsilon_\nu^3}, \tag{2.2}$$

$$l_{\nu 0} = L\, l_\nu, \tag{2.3}$$

$$\mathcal{E}_{\nu 0} = L^2\, \mathcal{E}_\nu. \tag{2.4}$$

The values of neutrino energy $\varepsilon_{\nu 0}$ and the directional cosine μ_0 in a co-moving reference frame are expressed through the values ε_ν and μ in the fixed reference frame as

$$\varepsilon_{\nu 0} = L\, \varepsilon_\nu, \tag{2.5}$$

$$\mu_0 = \frac{1}{L}\frac{\mu - u/c}{\sqrt{1-(u/c)^2}}. \tag{2.6}$$

The factor L is given by

$$L = \frac{1-\mu u/c}{\sqrt{1-(u/c)^2}} = \frac{\sqrt{1-(u/c)^2}}{1+\mu_0 u/c}. \tag{2.7}$$

One should keep in mind that $l_{\nu 0}$ and $\mathcal{E}_{\nu 0}$ depend only on one variable $\varepsilon_{\nu 0}$ (apart from a trivial dependence on r), whereas $I_{\nu 0}$ depends both on $\varepsilon_{\nu 0}$ and μ_0. For subsequent calculations, it is useful to present the relations between the differentials of the neutrino energy and the directional solid angle Ω in both the reference frames in question:

$$d\varepsilon_{\nu 0} = L\, d\varepsilon_\nu, \tag{2.8}$$

$$d\Omega_0 = \frac{d\Omega}{L^2}, \qquad (d\Omega = 2\pi d\mu,\ d\Omega_0 = 2\pi d\mu_0). \tag{2.9}$$

Equations (2.2–2.9) account for abberation and the Doppler effect, and assure invariance of the transfer equation (2.1) under Lorentz transformations.

When the terms of order of $(u/c)^2$ are small enough, eq. (2.7) is reduced to

$$L = 1 - \mu u/c. \tag{2.10}$$

We shall continue our discussion with this approximation, although there are no principal difficulties in accounting for the relativistic velocities.

Integrating I_ν over ε_ν, we get

$$\mathbf{I}_\nu = \mathbf{I}_\nu\ (\mu, r, t) = \int_0^\infty I_\nu\ (\varepsilon_\nu\ , \mu, r, t)\, d\varepsilon_\nu. \tag{2.11}$$

The total neutrino intensity $\mathbf{I}_\nu$ is coupled with matter through hydrodynamic equations in which it enters through the angular moments K_ν, S_ν, and U_ν:

$$K_\nu = K_\nu\ (r,t) = \frac{2\pi}{c}\int_{-1}^{1} \mu^2 \mathbf{I}_\nu\, d\mu, \tag{2.12}$$

$$S_\nu = S_\nu\ (r,t) = 2\pi \int_{-1}^{1} \mu \mathbf{I}_\nu\, d\mu, \tag{2.13}$$

$$U_\nu = U_\nu\ (r,t) = \frac{2\pi}{c}\int_{-1}^{1} \mathbf{I}_\nu\, d\mu. \tag{2.14}$$

Physically, K_ν and S_ν represent fluxes of neutrino momentum (the neutrino pressure) and the neutrino energy, respectively, while U_ν specifies the neutrino energy density.

Let us now consider the properties of neutrino emissivity. Since the neutrinos obey Fermi-Dirac statistics, due to the Pauli principle, their emissivity has to be scaled down with increasing phase space occupancy. Thus, instead of stimulated emission in case of photons, stimulated absorption arises in case of neutrinos. The number of neutrinos dn_ν in the volume element dV propagating inside the solid angle $d\Omega$ with energies within ε_ν and $\varepsilon_\nu + d\varepsilon_\nu$ is expressed through I_ν by

$$dn_\nu = \frac{I_\nu}{c\varepsilon_\nu}\, dV d\Omega\, d\varepsilon_\nu. \tag{2.15}$$

For the total number of accessible quantum states, dn_q, we get

$$dn_q = \frac{p_\nu^2}{h^3}\, dV d\Omega\, dp_\nu = \frac{\varepsilon_\nu^2}{(ch)^3}\, dV d\Omega\, d\varepsilon_\nu. \tag{2.16}$$

Hence, the occupancy of the phase space is

$$\frac{dn_\nu}{dn_q} = c^2 h^3 \frac{I_\nu}{\varepsilon_\nu^3} \equiv f_\nu, \tag{2.17}$$

and, in accordance with eq. (2.2), proves to be independent of the chosen reference frame. Neutrino emissivity has to be scaled with the number of free quantum states, and so must be proportional to the blocking factor $(1 - f_\nu)$. Thus, in the co-moving reference frame

$$\mathcal{E}_{\nu 0} = (1 - f_\nu)\, B_{\nu 0}, \tag{2.18}$$

where $B_{\nu 0}$ already does not depend on the neutrino radiation field and is determined only by emission properties of the medium.

This is the point where true emission differs crucially from scattering. For the latter, $B_{\nu 0}$ retains dependence on the neutrino radiation field through the input channel of the reaction; the greater the neutrino density, the greater $B_{\nu 0}$. In other words, in true emission and absorption processes, neutrinos are created and disappear; whereas for scattering they only change momentum and energy. The output channel in the scattering processes always 'remembers' the input one. The dependence of $B_{\nu 0}$ on the neutrino radiation field also takes place for all those processes that involve more than one the neutrino species, such as the electron-positron and the neutrino-antineutrino annihilation and plasma-neutrino interactions.

The most important processes of pure emission and absorption for electron neutrinos, ν_e, and antineutrinos, $\tilde{\nu}_e$, are their interactions with free neutrons and protons

$$n + e^+ \rightleftarrows p + \tilde{\nu}_e, \tag{2.19}$$

$$p + e^- \rightleftarrows n + \nu_e, \tag{2.20}$$

$$n \rightleftarrows p + e^- + \tilde{\nu}_e. \tag{2.21}$$

If the temperature were high enough for copious production of μ and τ mesons, similar processes with μ and τ leptons and antileptons (instead of e^- and e^+) would be the sources of pure emission and absorption for μ and τ neutrinos and antineutrinos.

Since for true emission-absorption processes both $B_{\nu 0}$ and the neutrino mean free path $l_{\nu 0}$ do not depend on the neutrino radiation field, one can derive a universal relation between $B_{\nu 0}$ and $l_{\nu 0}$, generalizing the well known Kirchhoff law for the case of neutrino radiation. To obtain this relation, consider the state of total thermodynamic equilibrium when the neutrino radiation and matter at rest have the same temperature. Then, the neutrino intensity must be isotropic and distributed over energies in accordance with the Fermi-Dirac statistics:

$$I_{\nu 0} = I_{\nu 0e} = \frac{\varepsilon_{\nu 0}^3}{c^2 h^3} \frac{1}{1 + \exp\left(\frac{\varepsilon_{\nu 0} - \mu_\nu}{kT}\right)} = \frac{\varepsilon_{\nu 0}^3}{c^2 h^3} f_{\nu e}, \tag{2.22}$$

where μ_ν is the neutrino chemical potential. Under conditions of thermodynamic equilibrium, for matter at rest, the right hand side of eq. (2.1) must equal zero:

$$-\frac{I_{\nu 0}}{l_{\nu 0}} + \mathcal{E}_{\nu 0} = 0. \tag{2.23}$$

Inserting in eq. (2.23) $I_{\nu 0} = I_{\nu 0e}$ from eq. (2.22) and using eq. (2.18), one obtains Kirchhoff's Law for the neutrino radiation in the form

$$\tilde{l}_{\nu 0} B_{\nu 0} = I_{\nu 0e}, \tag{2.24}$$

where $\tilde{l}_{\nu 0}$ is the mean free path corrected for stimulated absorption

$$\tilde{l}_{\nu 0} = (1 - f_{\nu e}) \, l_{\nu 0} = \frac{l_{\nu 0}}{1 + \exp\left(\frac{\mu_\nu - \varepsilon_{\nu 0}}{kT}\right)}. \tag{2.25}$$

The relations given by eqs. (2.24) and (2.25) are universal: they hold whether or not the neutrino radiation is in equilibrium with matter. However, matter itself *must be* in local thermodynamical equilibrium. When neutrinos and matter are not in equilibrium, one should mean by μ_ν in eq. (2.22) and (2.25) that value of the chemical potential which the neutrinos would have if they were in equilibrium.

With the aid of eqs. (2.3), (2.4), (2.18), (2.24), and (2.25), the neutrino transfer equation (2.1) can be written in a more suitable form

$$\frac{1}{c}\frac{\partial I_\nu}{\partial t} + \mu\frac{\partial I_\nu}{\partial r} + \frac{1-\mu^2}{r}\frac{\partial I_\nu}{\partial \mu} = -\frac{I_\nu - I_{\nu e}}{\tilde{l}_\nu}, \tag{2.26}$$

where

$$\tilde{l}_\nu = \frac{\tilde{l}_{\nu 0}}{L}, \tag{2.27}$$

$$I_{\nu e} = L^{-3} I_{\nu 0 e} = \frac{\varepsilon_\nu^3}{c^2 h^3}\frac{1}{1+\exp\left(\frac{L\varepsilon_\nu - \mu_\nu}{kT}\right)}. \tag{2.28}$$

Hence, in the fixed reference frame $\tilde{l}_\nu$ and $I_{\nu e}$ turn out to be non-isotropic.

Let us now write expressions for U_ν,K_ν, and S_ν in the fixed reference frame, when the neutrino radiation and matter are in equilibrium. The neutrino energy density is given by

$$\begin{aligned} U_{\nu e} &= \frac{2\pi}{c}\int_{-1}^{1} \mathrm{I}_{\nu e}\, d\mu = \frac{2\pi}{c}\int_{-1}^{1}\frac{d\mu}{L^4}\int_0^\infty \frac{\varepsilon_{\nu 0}^3}{c^2h^3}\frac{d\varepsilon_{\nu 0}}{1+\exp\left(\frac{\varepsilon_{\nu 0}-\mu_\nu}{kT}\right)} \\ &= \frac{15aT^4}{2\pi^4} F_3\left(\frac{\mu_\nu}{kT}\right), \left(a = \frac{\pi^2 k^4}{15\hbar^3 c^3}\right), \end{aligned} \tag{2.29}$$

where F_3 is the Fermi-Dirac function of index 3. The final expression for $U_{\nu e}$ in eq. (2.29) is obtained by neglecting terms of the order $(u/c)^2$ and integrating over μ:

$$\int_{-1}^{1}\frac{d\mu}{L^4} \approx \int_{-1}^{1}\left(1+4\frac{u}{c}\mu\right) d\mu = 2. \tag{2.30}$$

Continuing the analogous calculations, we get

$$K_{\nu e} = \frac{1}{3} U_{\nu e}, \tag{2.31}$$

$$S_{\nu e} = \frac{4}{3}\frac{u}{c} U_{\nu e}. \tag{2.32}$$

Likewise, the neutrino number density is determined as

$$n_{\nu e} = \frac{4\pi}{c} \int_0^\infty \frac{I_{\nu 0e}}{\varepsilon_{\nu 0}} \, d\varepsilon_{\nu 0} = \frac{15}{2\pi^4} \frac{a}{k} T^3 F_2\left(\frac{\mu_\nu}{kT}\right) . \tag{2.33}$$

So, in the limit $(u/c)^2 \ll 1$, the neutrino equilibrium energy density $U_{\nu e}$, the neutrino pressure $K_{\nu e}$, and the neutrino number density $n_{\nu e}$ are indistinguishable in the fixed and co-moving reference frames; whereas the neutrino energy flux $S_{\nu e}$ differs from $S_{\nu 0e} = 0$, owing to anisotropy in the $I_{\nu e}$ distribution.

Differentiating $K_{\nu e}$ by T at the fixed μ_ν (Landau and Lifshitz 1980), one can obtain the expression for the neutrino entropy $\mathcal{S}_{\nu e}$:

$$\mathcal{S}_{\nu e} = \frac{4}{3} \frac{U_{\nu e}}{T} - \frac{\mu_\nu}{T} n_{\nu e}. \tag{2.34}$$

Making use of properties of the Fermi-Dirac functions and assuming $\mu_\nu = -\mu_{\tilde{\nu}}$, one can obtain a simple analytical expression for the total neutrino and antineutrino entropy

$$\mathcal{S}_{\nu\tilde{\nu}e} = \mathcal{S}_{\nu e} + \mathcal{S}_{\tilde{\nu}e} = \frac{7}{6} aT^3 \left[1 + \frac{15}{7\pi^2} \left(\frac{\mu_\nu}{kT}\right)^2\right], \tag{2.35}$$

which holds for both the non-degenerate ($\mu_\nu = 0$) and extreme degenerate ($\mu_\nu \gg kT$) cases. A similar expression can be derived also for the total neutrino and antineutrino energy density $U_{\nu\tilde{\nu}e}$.

2.3. *The elements of neutrino hydrodynamics*

The laws of energy and momentum conservation for a system consisting of neutrino radiation and matter can be written as

$$\frac{\partial}{\partial x_k} \left(T_{jk} + W_{jk}\right) = f_j\,, \quad (j,\, k = 1, 2, 3, 4), \tag{2.36}$$

where W_{jk} and T_{jk} denote neutrino and matter energy-momentum tensors respectively, while f_j are components of the external 4-force. The components of the symmetric tensor W_{jk} are given by

$$W_{\alpha\beta} = K_{\nu\alpha\beta} = \frac{1}{c} \int e_\alpha e_\beta \, \mathbf{I}_\nu \, d\Omega, \tag{2.37}$$

$$W_{\alpha 4} = \frac{i}{c} S_{\nu\alpha} = \frac{i}{c} \int e_\alpha \, \mathbf{I}_\nu \, d\Omega\,, \quad (i = \sqrt{-1}), \tag{2.38}$$

$$W_{44} = -U_\nu = -\frac{1}{c} \int \mathbf{I}_\nu \, d\Omega, \tag{2.39}$$

where e_α and e_β $(\alpha, \beta = 1, 2, 3)$ stand for direction cosines of the neutrino propagation. In further considerations, we shall neglect terms of the order of $(u/c)^2$. Inserting in eq. (2.36) W_{jk} from eqs. (2.37–2.39) and the standard expressions (Landau and Lifshitz 1976) for T_{jk}, and using the baryon conservation law in the form

$$\frac{\partial \rho}{\partial t} + \frac{\partial}{\partial x_\alpha}(\rho u_\alpha) = 0, \tag{2.40}$$

where ρ is the density of matter or, more precisely, the number density of nucleons multiplied by the proton mass, one obtains the equations describing the motion of matter in the neutrino radiation field as

$$\rho \frac{d}{dt}\left[u_\alpha\left(1 + \frac{P + E\rho}{\rho c^2}\right)\right] = -\frac{\partial P}{\partial x_\alpha} - (\mathrm{div}\ K_\nu)_\alpha - \frac{1}{c^2}\frac{\partial S_{\nu\alpha}}{\partial t} + f_\alpha, \tag{2.41}$$

$$\rho\left[\frac{dE}{dt} + P\frac{d}{dt}\left(\frac{1}{\rho}\right)\right] = u_\alpha\,(\mathrm{div}\ K_\nu)_\alpha + \frac{u_\alpha}{c^2}\frac{\partial S_{\nu\alpha}}{\partial t} - \frac{\partial S_{\nu\alpha}}{\partial x_\alpha} - \frac{\partial U_\nu}{\partial t}. \tag{2.42}$$

Here the α-component of the $K_{\nu\alpha\beta}$-tensor divergence is given by

$$(\mathrm{div}\ K_\nu)_\alpha = \frac{\partial K_{\nu\alpha\beta}}{\partial x_\beta}. \tag{2.43}$$

The pressure and the specific energy of matter are denoted by P and E, respectively.

To simplify further discussion and to make it more understandable from the physical point of view, we shall restrict ourselves to spherically symmetric motion. Using the rules of tensor differentiation, we get

$$(\mathrm{div}\ K_\nu)_r = \frac{1}{r^2}\frac{\partial}{\partial r}\left(r^2 K_{\nu rr}\right) - \frac{K_{\nu\theta\theta}}{r} - \frac{K_{\nu\phi\phi}}{r}, \tag{2.44}$$

$$\mathrm{div}\ \mathbf{S}_\nu = \frac{\partial S_{\nu\alpha}}{\partial x_\alpha} = \frac{1}{r^2}\frac{\partial}{\partial r}\left(r^2 S_{\nu r}\right). \tag{2.45}$$

Let $\mathbf{i}_r$, $\mathbf{i}_\theta$, and $\mathbf{i}_\phi$ be the spherical unit basis vectors while $\mathbf{i}_\nu$ is the unit vector pointing to the direction of the neutrino propagation. Then, taking into account the obvious relations

$$e_r^2 = (\mathbf{i}_\nu \mathbf{i}_r)^2 = \mu^2,$$

$$\begin{aligned} e_\theta^2 &= (\mathbf{i}_\nu \mathbf{i}_\theta)^2 = (1-\mu^2)\cos^2\phi', \\ e_\phi^2 &= (\mathbf{i}_\nu \mathbf{i}_\phi)^2 = (1-\mu^2)\sin^2\phi', \\ d\Omega &= \sin\theta'\, d\theta'\, d\phi' = -d\mu'\, d\phi', \end{aligned}$$

where θ' is the angle between $\mathbf{i}_\nu$ and $\mathbf{i}_r$, ϕ' stands for the angle between $\mathbf{i}_\theta$ and the projection of $\mathbf{i}_\nu$ on the plain containing vectors $\mathbf{i}_\theta$ and $\mathbf{i}_\phi$. Then if I_ν is independent of ϕ', we can verify that eqs. (2.37–2.39) for $K_{\nu rr}$, $S_{\nu r}$, and U_ν reduce to eqs. (2.12–2.14), while for $K_{\nu\theta\theta}$ and $K_{\nu\phi\phi}$ they give

$$K_{\nu\theta\theta} = K_{\nu\phi\phi} = \frac{\pi}{c}\int_{-1}^{1}\left(1-\mu^2\right)\mathbf{I}_\nu\, d\mu = \frac{1}{2}\left(U_\nu - K_{\nu rr}\right). \tag{2.46}$$

In the spherically symmetric case, only the radial components of all the vectors in the triple ($\alpha = 1,2,3$) remain different from zero eq. (2.41). Hence, the five neutrino hydrodynamics eqs. (2.40–2.42) reduce to only three equations

$$\begin{aligned} \rho\frac{d}{dt}\left[u\left(1+\frac{P+E\rho}{\rho c^2}\right)\right] &= -\frac{\partial P}{\partial r} - \rho\frac{Gm}{r^2} \\ &\quad - \left\{\frac{1}{c^2}\frac{\partial S_\nu}{\partial t} + \frac{\partial K_\nu}{\partial r} + \frac{1}{r}(3K_\nu - U_\nu)\right\}, \qquad (2.47) \\ \rho\left[\frac{dE}{dt} + P\frac{d}{dt}\left(\frac{1}{\rho}\right)\right] &= u\left\{\frac{1}{c^2}\frac{\partial S_\nu}{\partial t} + \frac{\partial K_\nu}{\partial r} + \frac{1}{r}(3K_\nu - U_\nu)\right\} \\ &\quad - \left\{\frac{\partial U_\nu}{\partial t} + \frac{1}{r^2}\frac{\partial}{\partial r}\left(r^2 S_\nu\right)\right\}, \qquad (2.48) \\ \frac{\partial\rho}{\partial t} + \frac{1}{r^2}\frac{\partial}{\partial r}\left(r^2\rho u\right) &= 0, \qquad (2.49) \end{aligned}$$

where the index r is omitted. We have here substituted the Newtonian force of gravity for f_α. Thus, neutrino radiation is coupled to matter by the two differential combinations enclosed in braces in eqs. (2.47) and (2.48). In the absence of neutrino radiation, these terms disappear and eqs. (2.47–2.49) reduce to the usual equations of spherically symmetric hydrodynamics. To clarify the physical sense of the neutrino terms, we multiply eq. (2.26) by 2π and integrate over μ and ε_ν. Repeating this procedure after multiplying eq. (2.26) by $2\pi\mu/c$, we finally get

$$\frac{\partial U_\nu}{\partial t} + \frac{1}{r^2}\frac{\partial}{\partial r}\left(r^2 S_\nu\right) = 2\pi\int_{-1}^{1}\int_{0}^{\infty}\left(-\frac{I_\nu - I_{\nu e}}{\tilde{l}_\nu}\right) d\varepsilon_\nu\, d\mu, \tag{2.50}$$

$$\frac{1}{c^2}\frac{\partial S_\nu}{\partial t} + \frac{\partial K_\nu}{\partial r} + \frac{1}{r}(3K_\nu - U_\nu) = \frac{2\pi}{c}\int_{-1}^{1}\mu\int_{0}^{\infty}\left(-\frac{I_\nu - I_{\nu e}}{\tilde{l}_\nu}\right) d\varepsilon_\nu \, d\mu. \tag{2.51}$$

The right hand sides of eqs. (2.50) and (2.51) represent rates of the energy and momentum transport from matter to neutrino radiation. Therefore the braced term on the right hand side of eq. (2.47), taken with the opposite sign, gives the force by neutrino radiation on the matter, whereas the first braced term in the right hand side of eq. (2.48), multiplied by u, represents the work done by matter on neutrino radiation per unit time.

For astrophysical implications, it is useful to rewrite eqs. (2.47–2.49) in the Lagrangian independent variables t (time) and m (the mass enclosed by radius r). The equation of continuity can be used in two equivalent forms

$$\frac{d}{dt}\left(\frac{1}{\rho}\right) = 4\pi\frac{\partial(r^2 u)}{\partial m} \quad \text{or} \quad \frac{1}{\rho} = \frac{4\pi}{3}\frac{\partial r^3}{\partial m}. \tag{2.52}$$

Taking eq. (2.52) into account and neglecting terms of the order of $(u/c)^2$, one can reduce eqs. (2.47) and (2.48) to

$$\frac{du}{dt} = -4\pi r^2\frac{\partial}{\partial m}(P + K_\nu) - \frac{Gm}{r^2} - \frac{1}{\rho}\left[\frac{1}{c^2}\frac{\partial S_\nu}{\partial t} + \frac{1}{r}(3K_\nu - U_\nu)\right] + \frac{u}{\rho c^2}\left[\frac{\partial U_\nu}{\partial t} + 4\pi\rho\frac{\partial}{\partial m}\left(r^2 S_\nu\right)\right], \tag{2.53}$$

$$\frac{d}{dt}\left(E + \frac{U_\nu}{\rho}\right) + (P + K_\nu)\frac{d}{dt}\left(\frac{1}{\rho}\right) = -4\pi\frac{\partial}{\partial m}\left(r^2 H_\nu\right) + \frac{u}{\rho}\left[\frac{1}{c^2}\frac{\partial S_\nu}{\partial t} + \frac{1}{r}(3K_\nu - U_\nu)\right]. \tag{2.54}$$

In deriving eqs. (2.53) and (2.54), we have neglected the term $(P + E\rho)/\rho c^2 \sim (a_s/c)^2$ and have introduced a new designation

$$H_\nu \equiv S_\nu - u(U_\nu + K_\nu). \tag{2.55}$$

Here, a_s is the velocity of sound. It can be shown that H_ν is the neutrino energy flux $S_{\nu 0}$ in the co-moving reference frame. Neglecting the $(u/c)^2$ terms we get

$$S_{\nu 0} = \int\int \mu_0 I_{\nu 0}\, d\varepsilon_{\nu 0}\, d\Omega_0 \approx \int\int \left[\mu - \frac{u}{c}\left(1 + \mu^2\right)\right] I_\nu\, d\varepsilon_\nu\, d\Omega = S_\nu - u(U_\nu + K_\nu) = H_\nu. \tag{2.56}$$

All the results obtained in this section relate to any neutrino and antineutrino types. In order to take into account several types of neutrinos or antineutrinos simultaneously, one should simply summarize the corresponding values of U_ν ,K_ν ,S_ν , and H_ν. Moreover, these results hold whether or not the star is transparent to neutrinos.

2.4. The neutrino heat conduction approximation

In this section we concentrate on the neutrino-opaque case when the neutrino mean free path $\tilde{l}_\nu$ becomes much less than the characteristic length over which physical quantities (such as pressure, density, temperature) vary appreciably. Under such conditions, the neutrino intensity I_ν must be close to its equilibrium value $I_{\nu e}$. This permits us to make use of successive approximations for determining the diffusion corrections to the equilibrium isotropic neutrino intensity.

For this purpose, it is useful to rewrite eq. (2.26) as

$$\mathcal{D}I_\nu \; = \; -\frac{I_\nu \; - I_{\nu e}}{\tilde{l}_\nu}, \tag{2.57}$$

where $\mathcal{D}$ denotes the linear differential operator

$$\mathcal{D} \equiv \frac{1}{c}\frac{\partial}{\partial t} + \mu\frac{\partial}{\partial r} + \frac{1-\mu^2}{r}\frac{\partial}{\partial \mu}, \tag{2.58}$$

which acts on I_ν at the fixed ε_ν . Inserting in the left hand side of eq. (2.57) the equilibrium intensity $I_{\nu e}$ given by eq. (2.28), we obtain the first order approximation

$$I_\nu^{(1)} \; = \; I_{\nu e} \; - \; \tilde{l}_\nu \mathcal{D} I_{\nu e}. \tag{2.59}$$

To derive the NHC equations, we also need the second approximation $I_\nu^{(2)}$ which results from the substitution of $I_\nu^{(1)}$ in the left hand side of eq. (2.57)

$$I_\nu^{(2)} \; = \; I_{\nu e} \; - \; \tilde{l}_\nu \mathcal{D} I_\nu^{(1)} = I_\nu^{(1)} \; + \; \tilde{l}_\nu \mathcal{D}\left(\tilde{l}_\nu \mathcal{D} I_{\nu e} \; \right). \tag{2.60}$$

Entering eqs. (2.50) and (2.51) with $I_\nu \; = \; I_\nu^{(2)}$, one obtains for the neutrino differential combinations

$$\frac{\partial U_\nu}{\partial t} + \frac{1}{r^2}\frac{\partial}{\partial r}\left(r^2 S_\nu \; \right) = 2\pi \int\limits_{-1}^{1}\int\limits_{0}^{\infty} \mathcal{D} I_\nu^{(1)} \, d\varepsilon_\nu \, d\mu, \tag{2.61}$$

$$\frac{1}{c^2}\frac{\partial S_\nu}{\partial t} + \frac{\partial K_\nu}{\partial r} + \frac{1}{r}(3K_\nu \; - U_\nu \;) = \frac{2\pi}{c}\int\limits_{-1}^{1} \mu \int\limits_{0}^{\infty} \mathcal{D} I_\nu^{(1)} \, d\varepsilon_\nu \, d\mu. \tag{2.62}$$

Straightforward calculations of the integrals in eqs. (2.61) and (2.62) result in

$$\frac{\partial U_\nu}{\partial t} + \frac{1}{r^2}\frac{\partial}{\partial r}\left(r^2 S_\nu\right) = \frac{\partial U_{\nu 0e}}{\partial t} + \frac{1}{r^2}\frac{\partial}{\partial r}\left[r^2\left(\frac{4}{3}uU_{\nu 0e} - \frac{4\pi}{3}\int_0^\infty \tilde{l}_{\nu 0}\frac{\partial I_{\nu 0e}}{\partial r}\, d\varepsilon_{\nu 0}\right)\right], \tag{2.63}$$

$$\frac{1}{c^2}\frac{\partial S_\nu}{\partial t} + \frac{\partial K_\nu}{\partial r} + \frac{1}{r}(3K_\nu - U_\nu) = \frac{\partial K_{\nu 0e}}{\partial r}. \tag{2.64}$$

When deriving eqs. (2.63) and (2.64), we have, as usual, neglected terms of order $(u/c)^2$, such as those containing $uc^{-2}\partial/\partial t$. The terms including the combinations $(u/c)\tilde{l}_\nu\partial/\partial r$ and $\left(\tilde{l}_\nu/c\right)\partial/\partial t$ were also omitted since they are small compared to terms of order u/c and $\tilde{l}_\nu\partial/\partial r$. These terms, proportional to $u\tilde{l}_\nu$, determine the viscosity of neutrino radiation (van den Horn and van Weert 1984). Summarizing eqs. (2.63) and (2.64) with the same equations for antineutrinos, derived by substituting $-\mu_\nu$ in place of μ_ν, and inserting the results in eqs. (2.53) and (2.54), we obtain the NHC equations in the final form

$$\frac{dr}{dt} = u, \tag{2.65}$$

$$\frac{du}{dt} = -4\pi r^2\frac{\partial}{\partial m}(P + K) - \frac{Gm}{r^2}, \tag{2.66}$$

$$\frac{d}{dt}\left(\frac{1}{\rho}\right) = 4\pi\frac{\partial(r^2u)}{\partial m} \quad \text{or} \quad \frac{1}{\rho} = \frac{4\pi}{3}\frac{\partial r^3}{\partial m}, \tag{2.67}$$

$$\frac{d}{dt}\left(E + \frac{U}{\rho}\right) + (P + K)\frac{d}{dt}\left(\frac{1}{\rho}\right) = -4\pi\frac{\partial}{\partial m}\left(r^2 H\right), \tag{2.68}$$

$$K = \frac{1}{3}U = \frac{1}{3}(U_{\nu 0e} + U_{\tilde{\nu}0e}) = \frac{5aT^4}{8\pi^4}\left(\psi_\nu^4 + 2\pi^2\psi_\nu^2 + \frac{7\pi^4}{15}\right), \tag{2.69}$$

$$H = -\frac{7}{8}\frac{4acT^3}{3}4\pi r^2\rho\left(l_T\frac{\partial T}{\partial m} + Tl_\psi\frac{\partial\psi_\nu}{\partial m}\right), \tag{2.70}$$

$$l_T = l_{T\nu} + l_{T\tilde{\nu}}, \quad l_\psi = l_{\psi\nu} - l_{\psi\tilde{\nu}}, \tag{2.71}$$

$$l_{T\nu} = \frac{15}{7\pi^4}\int_0^\infty l_{\nu 0}\frac{x^4 e^{2(x-\psi_\nu)}}{\left(1 + e^{x-\psi_\nu}\right)^3}dx, \tag{2.72}$$

$$l_{\psi\nu} = \frac{15}{7\pi^4}\int_0^\infty l_{\nu 0}\,\frac{x^3 e^{2(x-\psi_\nu)}}{\left(1+e^{x-\psi_\nu}\right)^3}dx, \tag{2.73}$$

$$\psi_\nu \equiv \frac{\mu_\nu}{kT}. \tag{2.74}$$

Here K and U denote the total neutrino and antineutrino pressure and energy densities. The quantities $l_{T\tilde{\nu}}$ and $l_{\psi\tilde{\nu}}$ can be found from eqs. (2.72) and (2.73) by the change of $l_{\nu 0}$ and ψ_ν on $l_{\tilde{\nu}0}$ and $-\psi_\nu$, respectively.

The most important property of the NHC theory is that not only the temperature gradient contributes but also that the neutrino chemical potential contributes to the total energy flux.

2.5. *The kinetics of beta-processes and lepton charge diffusion*

Because of the new independent variable ψ_ν, the system of eqs. (2.65–2.74) is incomplete. In order to close the system, one has to take into account the kinetics of *beta-processes*. By beta-processes we mean those weak interactions which are responsible for true neutrino emission and absorption. For the electron neutrinos and antineutrinos, the complete list of these processes implies processes (2.19)–(2.21) and

$$e^{\pm} + (A,Z) \rightleftarrows (A, Z\pm 1) + (\tilde{\nu}_e \text{ or } \nu_e), \tag{2.75}$$

$$(A,Z) \rightleftarrows (A, Z\pm 1) + e^{\mp} + (\tilde{\nu}_e \text{ or } \nu_e). \tag{2.76}$$

Processes (2.19–2.21), (2.75), and (2.76) change the total numbers of neutrons, N_n, and protons, N_p, (either free or bounded in nuclei) in stellar matter. Since there are no other processes capable of producing such transmutations, the equation controlling the time behavior of the ratio $\Theta = N_n/N_p$ reads

$$\begin{aligned}\frac{\rho}{m_p}\frac{1}{(1+\Theta)^2}\frac{d\Theta}{dt} = \sum_{A,Z}\Big\{&[n(A,Z)W_{e^-} - n(A,Z-1)W_\nu]\\ &-[n(A,Z)W_{e^+} - n(A,Z+1)W_{\tilde{\nu}}]\\ &-[n(A,Z)D_{e^-\tilde{\nu}} - n(A,Z+1)W_{e^-\tilde{\nu}}]\\ &+[n(A,Z)D_{e^+\nu} - n(A,Z-1)W_{e^+\nu}]\Big\},\end{aligned} \tag{2.77}$$

where the summation is taken over all values of A and Z. (For neutrons $A = 1$, $Z = 0$, and for protons $A = 1$, $Z = 0$.) The rates of the e^-, e^+, ν_e, and $\tilde{\nu}_e$ captures are designated by W, whereas D stands for the $e^\pm$ decays. Every pair of the brackets in eq. (2.77) contains the rates of the direct and corresponding inverse processes. The rates W and D include the blocking factors accounting for the phase space occupancy of ν_e,$\tilde{\nu}_e$, and $e^{\pm}$. Using expressions for W and D from the weak interaction theory and the principle of detailed equilibrium, which connects the rates of the direct and inverse processes, one can convert eq. (2.77) to the form

$$\frac{\rho}{m_p}\frac{1}{(1+\Theta)^2}\frac{d\Theta}{dt}$$
$$=\frac{2\pi}{h^3c^2}\int_0^\infty\int_{-1}^{1}\frac{\varepsilon_{\nu 0}^2}{l_{\nu 0}^\beta}\left[(1-f_\nu)\exp\left(\frac{\mu_\nu-\varepsilon_{\nu 0}}{kT}\right)-f_\nu\right]d\mu_0\, d\varepsilon_{\nu 0}$$
$$-\frac{2\pi}{h^3c^2}\int_0^\infty\int_{-1}^{1}\frac{\varepsilon_{\tilde{\nu}0}^2}{l_{\tilde{\nu}0}^\beta}\left[(1-f_{\tilde{\nu}})\exp\left(\frac{-\mu_\nu-\varepsilon_{\tilde{\nu}0}}{kT}\right)-f_{\tilde{\nu}}\right]d\mu_0 d\varepsilon_{\tilde{\nu}0}. \quad (2.78)$$

Here all the beta-processes rates are expressed through the total mean free paths $l_{\nu 0}^\beta$ and $l_{\tilde{\nu}0}^\beta$ of neutrinos and antineutrinos

$$\frac{1}{l_{\nu 0}^\beta}=\sum_{A,Z}\left(\frac{1}{l_{\nu 0}^{(1)}}+\frac{1}{l_{\nu 0}^{(2)}}\right), \quad (2.79)$$

$$\frac{1}{l_{\tilde{\nu}0}^\beta}=\sum_{A,Z}\left(\frac{1}{l_{\tilde{\nu}0}^{(1)}}+\frac{1}{l_{\tilde{\nu}0}^{(2)}}\right), \quad (2.80)$$

where $l^{(1)}$ and $l^{(2)}$ stand for neutrino and antineutrino captures in processes (2.75) and (2.76) respectively.

It should be emphasized that we have made only a single assumption in deriving eq. (2.78): matter was assumed to be in a state of total thermodynamic equilibrium. This enables us to use Fermi-Dirac distributions for the electrons and positrons, and to express all nuclear number densities, $n(A, Z)$, through free neutrons (n_n) and protons (n_p), in accordance with the nuclear statistical equilibrium (see W. Hillebrandt's lectures in this volume). At the same time no constraints were imposed on the neutrino radiation entering eq. (2.78) (in the form of only two quantities f_ν and $f_{\tilde{\nu}}$ given by eq. (2.17)): the neutrino energy and momentum distributions are, in general, arbitrary. In case f_ν = $f_{\tilde{\nu}}$ = 0, for example, eq. (2.78) describes the kinetics of beta-processes under neutrino-transparent conditions. The quantity μ_ν in eq. (2.78) is defined by

$$\mu_\nu = \mu_e - Q_n - kT\ln\left(\frac{n_n}{n_p}\right), \quad (2.81)$$

where μ_e is the electron chemical potential and Q_n = 1.29 MeV is the neutron-proton mass difference. Here μ_ν is simply a convenient designation for the combination in the right hand side of eq. (2.81). This combination comes from the properties of matter rather than from neutrino radiation.

Suppose now that the beta-processes are in local equilibrium, that is, they do not change the neutrino (antineutrino) and electron (positron) numbers in every element $d\Omega_0\, d\varepsilon_0$ of phase space. Then, from eq. (2.78) it immediately follows that $d\Theta/dt = 0$ and that the neutrinos and antineutrinos should be described by Fermi-Dirac distributions (see eq. 2.22) with the neutrino chemical potential defined by eq. (2.81), while the antineutrino chemical potential must have the opposite sign

$$\mu_{\tilde{\nu}} = -\mu_{\nu}. \tag{2.82}$$

Thus, we have derived the expressions (2.81) and (2.82).

To derive the kinetic equation of the beta-processes in the framework of the NHC approximation, one has to insert in eq. (2.78) the second order approximations for f_ν and $f_{\tilde{\nu}}$

$$f_{\nu,\tilde{\nu}} = f^{(2)}_{\nu,\tilde{\nu}} = \frac{c^2 h^3}{\varepsilon^3_{\nu,\tilde{\nu}}}\, I^{(2)}_{\nu,\tilde{\nu}}. \tag{2.83}$$

After time consuming calculations (which are nevertheless simple in principle), eq. (2.78) can be reduced to the equation of lepton charge diffusion

$$\frac{d\Lambda_e}{dt} + 4\pi \frac{\partial}{\partial m}\left(r^2 F\right) = 0, \tag{2.84}$$

where the specific lepton charge is defined as the difference between lepton and antilepton numbers per nucleon

$$\Lambda_e = \frac{m_p}{\rho}\left(n_{e^-} - n_{e^+} + n_{\nu e} - n_{\tilde{\nu} e}\right). \tag{2.85}$$

For the lepton charge flux, F, we get

$$F = -\frac{7}{8}\frac{4acT^3}{3k}\, 4\pi r^2 \rho \left(\frac{\lambda_T}{T}\frac{\partial T}{\partial m} + \lambda_\psi \frac{\partial \psi_\nu}{\partial m}\right), \tag{2.86}$$

$$\lambda_T = \lambda_{T\nu} - \lambda_{T\tilde{\nu}}\,,\quad \lambda_\psi = \lambda_{\psi\nu} + \lambda_{\psi\tilde{\nu}}, \tag{2.87}$$

$$\lambda_{T\nu} = \frac{15}{7\pi^4}\int_0^\infty l_{\nu 0}\, \frac{x^3 e^{2(x-\psi_\nu)}}{\left(1+e^{x-\psi_\nu}\right)^3}\, dx, \tag{2.88}$$

$$\lambda_{\psi\nu} = \frac{15}{7\pi^4}\int_0^\infty l_{\nu 0}\, \frac{x^2 e^{2(x-\psi_\nu)}}{\left(1+e^{x-\psi_\nu}\right)^3}\, dx. \tag{2.89}$$

The expressions for $\lambda_{T\bar{\nu}}$ and $\lambda_{\psi\bar{\nu}}$ are obtained when substituting $-\psi_\nu$ for ψ_ν in eqs. (2.88) and (2.89). From the comparison of these equations with eqs. (2.72) and (2.73) it follows that

$$l_{\psi\nu} = \lambda_{T\nu}\,, \quad l_{\psi\bar{\nu}} = \lambda_{T\bar{\nu}}\,, \quad l_\psi = \lambda_T\,. \tag{2.90}$$

Equations (2.90) represent the Onsager principle of symmetry for the kinetic coefficients (Landau and Lifshitz 1980) of neutrino radiation.

Equation (2.84) describing lepton charge diffusion closes the system of neutrino hydrodynamics equations in the NHC approximation.

The calculation of the neutrino mean free paths l_T, l_ψ, λ_T, and λ_ψ as functions of temperature, density and the neutrino chemical potential ψ_ν proves to be, in general, a difficult problem, since one has to take into account neutrino interactions with all the nuclear species in both the ground state and in numerous excited states (Kolb and Mazurek 1979). For free nucleon gas heated to high temperatures ($kT \gg m_e c^2$), the following analytical expressions result (Imshennik and Nadyozhin 1972, Bludman and Van Riper 1978):

$$\lambda_\psi = \frac{15}{14\pi^4}\,\frac{m_p}{\sigma_n}\,\frac{1}{\rho}\left(\frac{m_e c^2}{kT}\right)^2\frac{(1+\theta)^2}{\theta}, \tag{2.91}$$

$$l_T = \lambda_\psi\left(\psi_\nu^2 - 2\,\frac{\theta-1}{\theta+1}\,\psi_\nu + \frac{\pi^2}{3}\right), \tag{2.92}$$

$$l_\psi = \lambda_T = \lambda_\psi\left(\psi_\nu - \frac{\theta-1}{\theta+1}\right), \tag{2.93}$$

where $\theta = n_n/n_p$ and $\sigma_n \simeq 2.5\times10^{-44}\mathrm{cm}^2$ is a typical cross-section of neutrino interactions with free nucleons.

Thus, we have obtained two equations for the diffusion of energy and lepton charge which require four extra boundary conditions. Two of them may be taken in the center of the star,

$$\frac{\partial T}{\partial r} = 0\,, \quad \frac{\partial\psi_\nu}{\partial r} = 0\,, \quad (m=0), \tag{2.94}$$

accounting for the absence of central point sources of neutrino energy and lepton charge. The other two boundary conditions may be imposed at the surface of the neutrino-opaque stellar core:

$$-\frac{c}{4}U + \frac{1}{2}H = 0\,, \quad (m = M_c), \tag{2.95}$$

$$-\frac{c}{4}(n_\nu - n_{\bar{\nu}}) + \frac{1}{2}F = 0\,, \quad (m = M_c), \tag{2.96}$$

which express the absence of external neutrino sources near the neutrino-opaque core. (M_c is the mass of the core.)

2.6. Conclusions

Electron neutrino and antineutrino interactions with atomic nuclei (and especially with free neutrons and protons) produce strong sources of true neutrino and antineutrino absorption and emission. As a result, the NHC theory works well for electron neutrinos, even at the initial stages of collapse, as soon as the neutrino-opaque core forms. By means of this theory, it is possible to explain the properties of the neutrinosphere and to obtain the general characteristics of electron neutrino and antineutrino spectra, which turn out to be close to the equilibrium Fermi-Dirac distributions. The central temperature for the massive ($\sim 2M_\odot$) stellar cores attains about 50–100 MeV, thereby giving rise to thermal production of μ and π mesons which interact with free nucleons, producing true emission and absorption for muon neutrinos (Domogatskii 1969). Therefore, the NHC theory may account for the muon neutrino transport, at least in the near-central regions of collapsing massive stellar cores.

The Supernova 1987A has confirmed theoretical predictions of the neutrino signal properties expected from collapsing stars, and revealed an urgent need for further developments in neutrino transport theory. The most difficult problem is to properly account for neutrino scattering processes in energy and momentum transport. In the neutrino-opaque case, NHC theory may be generalized to account for scattering in the approximation of "Comptonized" neutrino transport (Imshennik and Nadyozhin 1979), where the neutrino and antineutrino chemical potentials are not coupled by the equality $\mu_\nu = -\mu_{\bar{\nu}}$. (If l_a and l_s are the effective mean free paths for absorption and scattering, respectively, $\mu_\nu = -\mu_{\bar{\nu}}$ holds only when $l_a \ll l_s$.) One may also treat neutrino scattering in the transport cross section approximation (Bludman and Van Riper 1978). However, in the external layers of collapsing stellar cores with moderate values of neutrino optical depth, one has to handle the neutrino transport as thoroughly as possible. Neutrino scattering may be of crucial importance for elucidating the mechanism of supernova explosion (e.g. Myra and Bludman 1989) which is not completely understood so far. Moreover, the high sensitivity of neutrino detectors and of neutrino nucleosynthesis yields on the high energy tails of the neutrino spectra requires sophisticated calculations of the neutrino transport in the collapsing core mantles, such as the angular moments methods (e.g. Fu 1987), the Monte Carlo simulation technique (Janka and Hillebrandt 1989) and others, or straightforward integration of the neutrino transfer equation (Schinder and Shapiro 1983). These methods, however, still require time-dependent values of the total neutrino energy and lepton charge fluxes as boundary conditions at a certain intermediate layer. Therefore, they fail to describe the neutrino transport through deep stellar interiors, especially in hot nascent neutron stars. The boundary fluxes may be calculated in the framework of the NHC theory.

We have attempted to describe the physical basis of neutrino energy and momentum transport under conditions of high neutrino opacity. We hope that this compressed account will help those who will study the difficult problem of neutrino contributions to gravitational collapse dynamics and the mechanism of the supernova outburst.

References

Lecture 1: The neutrino signal from a collapsing star

Adams, J.B., M.A. Ruderman and C.H. Woo. 1963. Phys. Rev., 129, 1383.
Blinnikov, S.I. and M.A. Rudzskij. 1989. Astron. Zh., 66, 730 (Sov. Astron., 1990, 33(4), 377)
Blinnikov, S.I., V.S. Imshennik and D.K. Nadyozhin. 1988. Astrophys. Space Sci., 150, 273.
Bionta, R.M., G. Blewitt, C.B. Bratton et al. 1987. Phys. Rev. Letters, 58, 1494.
Bowers, R. and J.R. Wilson. 1982. Astrophys. J., 263, 366.
Burrows, A. 1990. in Supernovae, ed. A.G. Petschek (Springer-Verlag, New-York).
Burrows, A. and J.M. Lattimer. 1988. Phys. Reports, 163, 51.
Chiu, H.Y. 1961. Phys. Rev., 123, 1040.
Chiu, H.Y. and P. Morrison. 1960. Phys. Rev. Letters, 5, 573.
Dicus, D.A. 1972. Phys. Rev., D6, 941.
Fuller, G., W.A. Fowler and M. Newman. 1982. Astrophys. J., 252, 715.
Fuller, G., W.A. Fowler and M. Newman. 1985. Astrophys. J., 293, 11.
Gamov, G. and M. Schönberg. 1941. Phys. Rev., 59, 539.
Giovanoni, P.M., D.C. Ellison and S.W. Bruenn. 1989. Astrophys. J., 342, 416.
Hillebrandt, W. and P. Höflich. 1989. Rep. Prog. Phys., 52. 1421.
Hillebrandt, W., E. Müller and R. Mönchmeyer. 1990. in NATO ASI on 'The Nucleon Equation of State.'
Hirata, K., T. Kajita, M. Koshiba et al. 1987. Phys. Rev. Letters, 58, 1490.
Hirata, K., T. Kajita, M. Koshiba et al. 1988. Phys. Rev., D38, 448.
Imshennik, V.S. and D.K. Nadyozhin. 1972. Zh. Eksp. Teor. Fiz., 63, 1548. (Soviet Phys. JETP 1973, 36, 821).
Imshennik, V.S. and D.K. Nadyozhin. 1979. Astrophys. Space Sci., 62, 309.
Imshennik, V.S. and D.K. Nadyozhin. 1989. Soviet Sci. Rev., Sec. E, 8, part 1, 1.
Imshennik, V.S. D.K. Nadyozhin and V.S. Pinaev. 1966. Astron. Zh., 43, 1215.
Imshennik, V.S., D.K. Nadyozhin and V.S. Pinaev. 1967. Astron. Zh., 44, 768.
Lattimer, J.M. and A. Yahil. 1989. Astrophys. J., 340, 426.

LoSecco, J.M., Z.J. Ajaltouni, J. Annis et al. 1988. Talk at Topical Workshop 'Supernova 1987A. One Year Later,' La Thuile, Italy.
Mampe, W., P. Ageron, C. Bates, J.M. Pendlebury, and A. Steyerl. 1989. Phys. Rev. Letters, 63. 593.
Müller, E. 1984. in Problems of Collapse and Numerical Relativity. Proceed. NATO Adv. Res. Workshop, Toulouse, France 7–11 Nov. 1983. (Dordrecht, Netherlands: Reidel 1984).
Munkata, H., Y. Kohyama and N. Itoh. 1985. Astrophys. J., 296, 197.
Nadyozhin, D.K. 1974. Nauchn. Inform. Astron. Sov. Akad. Nauk SSSR No. 32, 3.
Nadyozhin, D.K. 1978. Astrophys. Space Sci., 53, 131.
Nadyozhin, D.K. and V.M. Chechetkin. 1969. Astron. Zh., 46, 270.
Nadyozhin, D.K. and I.V. Otroshenko. 1980. Astron. Zh., 57, 78.(Sov. Astron., 1980, 24(1), 47).
Pinaev, V.S. 1963. Zh. Eks. Theor. Phys., 45, 548.
Rhodes, P. 1950. Proc. Roy. Soc., A204, 396.
Schinder, P.J. 1988. Phys. Rev., D38, 1673.
Schinder, P.J. and S.A. Bludman. 1989. Astrophys. J., 346, 350.
Schinder, P.J. and S.L. Shapiro. 1983. Astrophys. J., 273, 330.
Schramm, D.N. and J.W. Truran. 1990. Phys. Reports, 189, 90.
Sofia, S., W.M. Sparks and A.S. Endal. 1979. Nature, 277, 456.
Sparks, W.M. and A.S. Endal. 1980. Astrophys. J., 237, 130.
Weaver, T.A., G.B. Zimmerman and S.E. Woosley. 1978. Astrophys. J., 225, 1021.
Wilson, J.R. 1980. in 9th Texas Symposium on Relativistic Astrophysics. Proceedings NY Acad. Sci., 336, 358.
Wilson, J.R. and R.W. Mayle. 1988. Phys. Reports, 163, 63.

Lecture 2: The neutrino heat conduction theory

Aarnio, P., et al. (DLPHI Collaboration). 1990. Phys. Letters, B241, 425.
Arnett, W.D. 1966. Canadian J. Phys., 45, 1621.
Bludman, S.A., and K.A. Van Riper. 1978. Astrophys. J., 224, 631.
Decamp, D., et al. (ALEPH Collaboration). 1990. Phys. Letters, B235, 399.
Domogatskii, G.V.. 1969. Nauch. Inform. Astron. Sov. Akad. Nauk SSSR No. 13, 94. Preprint Inst. Nuclear Researches Acad. Sci. USSR, No. 96, 1973.
Fu. A. 1987. Astrophys. J, 323, 211.
Imshennik, V.S. and D.K. Nadyozhin. 1972. Zh. Eksp. Teor. Fiz., 63, 1548. (Soviet Phys. JETP, 1973, 36, 821).
Imshennik, V.S. and D.K. Nadyozhin. 1979. Astrophys. Space Sci., 62, 309.
Imshennik, V.S., and Yu.I. Morozov. 1981. Radiative Relativistic Gas Dynamics of High-Temperature Phenomena (In Russian). Atomizdat, Moscow.
Janka, H.-T. and W. Hillebrandt. 1989. Astron. Astrophys. Suppl., 78, 375.
Kolb, E.W. and T.J. Mazurek. 1979. Astrophys. J., 234, 1085.
Landau, L.D. and E.M. Lifshitz. 1976. Fluid Mechanics, Pergamon Press.
Landau, L.D. and E.M. Lifshitz. 1980. Statistical Physics, Pergamon Press.
Myra, E.S. and S.A. Bludman. 1989. Astrophys. J., 340, 384.
Schinder, P.J. and S.L. Shapiro. 1983. Astrophys. J., 273, 330.
Schwartz, R.A. 1967. Annals Phys., 43, 42.
Thomas, L.H. 1930. Quart. J. of Math. (Oxford), 1, 239.
van den Horn, L.J. and C.G. van Weert. 1984. Astron. Astrophys., 136, 74.

COURSE VIII

NUCLEAR PHYSICS OF HOT DENSE MATTER

D. VAUTHERIN

Division de Physique Théorique
Institut de Physique Nucléaire
91406, Orsay Cedex, France

S. Bludman, R. Mochkovitch and J. Zinn-Justin, eds.
Les Houches, Session LIV 1990
Supernovae

Contents

Contents *347*

1. Introduction 348
2. The phase diagram of hot nuclear matter 349
   2.1. Effective nucleon-nucleon interactions 349
   2.2. A simplified Skyrme interaction 350
   2.3. Mean-field equations at finite temperature 351
   2.4. Solution for hot nuclear matter 352
   2.5. Cold nuclear matter 353
   2.6. High temperature limit 354
   2.7. Phase diagram of nuclear matter 355
   2.8. The compound nucleus model of Bonche and Levit 356
   2.9. An approximate calculation of the limiting temperature 357
3. Equation of state at subnuclear densities 360
   3.1. Introduction 360
   3.2. Macroscopic approaches 360
   3.3. Microscopic methods: the Wigner-Seitz approximation 362
   3.4. The bulk matter approximation 363
   3.5. Approximate solution of the equilibrium equations 364
   3.6. The compressible liquid drop model 368
   3.7. Thomas-Fermi calculations 370
   3.8. Hartree-Fock calculations 371
   3.9. Sub-saturation phases of nuclear matter 372
4. Beyond nuclear density 375
   4.1. Non-relativistic many-body calculations 375
   4.2. Relativistic mean field calculations 377
   4.3. Density dependent relativistic corrections 381
   4.4. Relativistic Brueckner-Hartree-Fock calculations 382
   4.5. Many-body calculations with relativistic corrections 383
   4.6. Experimental studies of the equation of state 385
5. Discussion 388

References 389

1. Introduction

The equation of state of hot dense matter $P(\rho, T)$ is an essential ingredient in the description of the gravitational contraction of massive stars. This gravitational contraction is believed to be the origin of Type II supernovae explosions and of neutron star formation. It is important for both prompt [1] and delayed [2, 3] explosion mechanisms because, in both cases, it sets the initial conditions of the evolution. The equation of state is required for up to several (typically five) times the nuclear density and for temperatures on the order of ten MeV. Calculating the equation of state in this domain requires the determination of the most stable configuration of a system of neutrons, protons, nuclei, electrons, and neutrinos. This is a difficult problem, both below and above nuclear density. Below nuclear density, one is faced with the nuclear physics of very unusual nuclei, namely hot, superheavy, exotic nuclei immersed in a neutron vapor. Indeed, because of electron screening, the mass of these nuclei can easily reach $A = 1000$, that is, about four times the mass of the heaviest elements observed on earth. It is important to determine the vaporisation temperature of such nuclei. Indeed, below the boiling temperature, nucleons are bound in nuclei and do not contribute to the pressure, whereas above this temperature their contribution stiffens significantly the equation of state. Above nuclear density, one has to deal eventually with the many-body physics of overlapping (or nearly overlapping) bags of quarks and gluons. Since no solution to this problem is presently available, most approaches use effective theories in which structureless nucleons interact via meson fields.

Two important simplifications can be used in the construction of equations of state needed in studies of stellar collapse. The simplifications greatly reduce the amount of numerical calculation. As pointed out by Bethe et al. [1], they are justified by the trapping of neutrinos when the density is greater than 10^{11} g/cm^3. First, the entropy per baryon S/A is almost constant during the collapse and its value is close to one. This is because creation of entropy (or disorder) by beta transitions to nuclear excited states is forbidden by the Pauli blocking of neutrinos. Second, the electron fraction $Y_e = Z/A$ remains nearly constant at a value close to 0.30.

This article is organized as follows. Section 2 presents a calculation of the properties of hot nuclear matter in the mean field approximation. Because nuclear forces are attractive at long range and repulsive at short range, the phase diagram of nuclear matter is expected to be that of a Van der Waals fluid, with an equilibrium between a dense (nucleus) phase and a dilute (vapor) phase. A critical temperature T_c also exists. In actual nuclei the phase equilibrium equations are complicated by the presence of Coulomb and surface effects. These effects make nuclei unstable at a limiting temperature T_L which is well below the critical temperature T_c. We show that a useful approximation for study of the phase equilibrium equations is to consider low temperature expansions for the nucleus, and high temperature expansions for the vapor. As an application we derive a simple formula for the limiting temperature T_L beyond which nuclei no longer exist.

These results are used in section 3 to discuss the equation of state at subnuclear density. After a brief sketch of macroscopic methods, we review the bulk matter approximation in which dense matter is modeled as drops of asymmetric nuclear matter in equilibrium with a nucleon vapor. In this case we show that low and high temperature expansions provide useful approximation formulas for a discussion of the properties of dense matter and its equation of state. More elaborate methods, such as the compressible liquid drop model, the Thomas-Fermi, and Hartree-Fock methods are also presented.

Section 4 deals with the difficult problem of calculating the equation of state in the domain of densities greater than the nuclear saturation density. We present the standard methods of non-relativistic many-body theory as well as relativistic mean-field and Dirac-Brueckner approaches.

A summary of our main conclusions is given in section 5.

2. The phase diagram of hot nuclear matter

2.1. *Effective nucleon-nucleon interactions*

To discuss the equation of state of dense matter at subnuclear density, it is convenient to examine first the properties of hot nuclear matter. Nuclear matter is an ideal, macroscopic system of neutrons and protons, which interact only via nuclear forces. Its density ρ is spatially uniform, as is its proton fraction $Y_p = Z/(N+Z)$. This system does not exist on earth because nuclei with more than about hundred protons are destroyed by the Coulomb repulsion. However, it is produced (with $Y_p \sim 1/3$) during the collapse of massive stars, because the electron background, which ensures the electric neutrality of the star, almost completely screens the Coulomb forces. This system is also believed to be present (with $Y_p \simeq 0$) in neutron stars. From an extrapolation to large A of the observed properties of actual nuclei, one finds that the equilibrium density of this ideal system of symmetric nuclear matter would be $\rho_0 = 0.17$ nucleons/fm^3 (which corresponds to 2.8×10^{14} g/cm^3), and that it would have a binding energy per nucleon E_0/A close to -16 MeV [4]. The density ρ_0 and the ratio E_0/A are generally referred to as saturation density and saturation energy, respectively.

To calculate properties of nuclei and nuclear matter, two distinct approaches have been used. The most fundamental starts from a realistic nucleon-nucleon force such as the Orsay [5], Bonn [6], or Argonne [7] potential, to reproduce as well as possible, two-body scattering data, and to derive nuclear properties from standard many-body techniques. Such techniques include variational methods as well as Brueckner type calculations of the effective nucleon-nucleon force used in mean field calculations [8]. These techniques require large amounts of numerical work. For this reason an alternative approach has been developed in which the effective nuclear interaction is parameterized directly. This approach loses contact with two-body scattering data but it is simple to use and produces accurate predictive results. With only a few parameters, it can give excellent descriptions of masses, radii, charge distributions, single particle energies, deformation, and fission barriers of nuclei throughout the periodic table. This is the approach adopted in the present section, in which we use the simple and remarkably successful effective interaction proposed by Skyrme [4, 8].

2.2. A simplified Skyrme interaction

For pedagogical reasons, we consider a schematic version of the Skyrme force containing only a zero-range two-body attraction and a zero-range three-body repulsion

$$v = t_0\delta(\mathbf{r}_1 - \mathbf{r}_2) + t_3\delta(\mathbf{r}_1 - \mathbf{r}_2)\delta(\mathbf{r}_2 - \mathbf{r}_3). \tag{2.1}$$

The values of the two parameters t_0 and t_3 are adjusted to reproduce the binding energy per nucleon and the saturation density of nuclear matter. The formulas derived in the following sections lead to

$$t_0 = -983.4 \text{ MeV} \times \text{fm}^3, \quad t_3 = 13105.8 \text{ MeV} \times \text{fm}^6. \tag{2.2}$$

With these values, the t_3 term (as shown below) becomes dominant at densities larger than saturation density. The dominance of the repulsive term at large density reflects the repulsive character of the nucleon-nucleon force at short distances, while the t_0 term (although zero ranged) simulates the long range nuclear attraction, due to one- and two-pion exchanges.

2.3. Mean-field equations at finite temperature

A great merit of the Skyrme force is that it leads to simple mean field equations. As an illustration, consider the case of a symmetric $N = Z$ nucleus at finite temperature T. In the mean field approximation, this nucleus is described as a set of independent nucleons in a potential $U(\mathbf{r})$, which results from the interaction of one nucleon with all the others. For instance, the average potential acting on a nucleon with spin σ and isospin τ, generated by the t_0 term, is given by

$$U(\mathbf{r}, \sigma, \tau) = \sum_{\sigma', \tau'} \int \rho(\mathbf{r}', \sigma', \tau') t_0 \delta(\mathbf{r} - \mathbf{r}')(1 - \delta_{\sigma\sigma'}\delta_{\tau\tau'}) d\mathbf{r}', \tag{2.3}$$

where $\rho(\mathbf{r}, \sigma, \tau)$ is the probability density of nucleons with spin σ and isospin τ. Note that eq. (2.3) contains a factor $(1 - \delta_{\sigma\sigma'}\delta_{\tau\tau'})$ due to the Pauli principle which forbids, at the same point $\mathbf{r}$, the presence of two nucleons with identical quantum numbers. For a spin saturated and symmetric nucleus, eq. (2.3) leads to $U = 3t_0\rho(\mathbf{r})/4$. A similar calculation for the t_3 term gives

$$U(\mathbf{r}) = \frac{3}{4} t_0 \rho(\mathbf{r}) + \frac{3}{16} t_3 \rho^2(\mathbf{r}). \tag{2.4}$$

To construct a system of independent nucleons at temperature T, we occupy the single nucleon orbitals $\varphi_i(\mathbf{r})$

$$\left(-\frac{\hbar^2}{2m}\Delta + U(\mathbf{r})\right)\varphi_i(\mathbf{r}) = e_i \varphi_i(\mathbf{r}), \tag{2.5}$$

with the usual Fermi occupation numbers

$$f_i = \frac{1}{1 + \exp((e_i - \mu)/kT)}. \tag{2.6}$$

In the previous equation, i denotes the set of space, spin, and isospin quantum numbers. The value of the chemical potential μ in eq. (2.6) is fixed by the condition

$$\sum_i f_i = A. \tag{2.7}$$

The self-consistent nucleon density is then given in terms of the single particle wave functions and occupations numbers by

$$\rho(\mathbf{r}) = \sum_i f_i |\varphi_i(\mathbf{r})|^2. \tag{2.8}$$

This equation completes the set of mean-field eqs. (2.4–2.8) at finite temperature T. It is non-linear since it involves the solution of Schrödinger equations whose potentials depend on both eigenfunctions and eigenvalues through eqs. 4, 6 and 8. Once the orbitals φ_i and their occupation numbers f_i have been determined, the energy E of the nucleus is obtained from

$$E = \frac{1}{2} t_0 \sum_{\sigma\sigma'\tau\tau'} \int d\mathbf{r} \rho(\mathbf{r}, \sigma, \tau) \rho(\mathbf{r}, \sigma', \tau')(1 - \delta_{\sigma\sigma'}\delta_{\tau\tau'}) + t_3 \text{ term} \tag{2.9}$$

For a symmetric nucleus, the corresponding energy density is

$$\epsilon = \frac{\hbar^2}{2m}\tau + \frac{3}{8} t_0 \rho^2 + \frac{1}{16} t_3 \rho^3, \tag{2.10}$$

where τ is the kinetic energy density

$$\tau(\mathbf{r}) = \sum_i f_i |\nabla \varphi_i(\mathbf{r})|^2. \tag{2.11}$$

The entropy of the nucleus is given by the usual formula for independent fermions

$$S = -k \sum_i \{ f_i \log f_i + (1 - f_i) \log(1 - f_i) \}. \tag{2.12}$$

2.4. *Solution for hot nuclear matter*

Now consider these equations for uniform nuclear matter. The potential U is a constant and the space parts of the single particle wave functions are plane waves $\varphi_i(\mathbf{r}) = \Omega^{-1/2} \exp(i\mathbf{k}.\mathbf{r})$, where Ω is the quantization volume. The single particle energies e_i are given by

$$e_i = \frac{\hbar^2}{2m} k^2 + U. \tag{2.13}$$

Inserting these values into eqs. (2.6, 2.8, 2.11) gives

$$\rho = g \lambda^{-3} F_{3/2}(\beta U - \alpha), \tag{2.14a}$$

$$\tau = 4\pi g \lambda^{-5} F_{5/2}(\beta U - \alpha), \tag{2.14b}$$

where $g = 4$ is the spin-isospin degeneracy factor, λ the thermal wave length

$$\lambda = \left(\frac{2\pi\hbar^2}{mkT}\right)^{1/2}, \tag{2.15}$$

$\beta = 1/kT$, $\alpha = \beta\mu$ and F_n is the Fermi integral

$$F_n(x) = (2/\sqrt{\pi}) \int_0^\infty u^{n-1}(1 + e^{u+x})^{-1} du. \tag{2.16}$$

For given values of density ρ and temperature T, eq. (2.14*a*) determines the argument $\beta U - \alpha$ of the Fermi function which in turn fixes the kinetic energy density τ of the system, and its entropy density

$$\mathcal{S} = \frac{5}{3}\frac{\hbar^2}{2m}\beta\tau + (U - \mu)\beta\rho. \tag{2.17}$$

The pressure $P(\rho, T)$ is the opposite of the grand potential per unit volume, that is,

$$\begin{aligned} P(\rho, t) &= -\epsilon + T\mathcal{S} + \mu\rho, \\ &= \frac{2}{3}\frac{\hbar^2}{2m}\tau + \frac{3}{8}t_0\rho^2 + \frac{1}{8}t_3\rho^3. \end{aligned} \tag{2.18}$$

Finally, we also give the free-energy density $f(\rho, T)$, an important tool in the discussion of the statistical phase equilibrium

$$f(\rho, T) = -\frac{2}{3}\frac{\hbar^2}{2m}\tau - \frac{3}{8}t_0\rho^2 - \frac{1}{8}t_3\rho^2 + \mu\rho. \tag{2.19}$$

2.5. *Cold nuclear matter*

At zero temperature, the non-relativistic kinetic energy density τ is

$$\tau = \frac{3}{5}\rho k_F^2, \tag{2.20}$$

where k_F is the Fermi momentum $k_F = (6\pi^2\rho/g)^{1/3}$. To determine the equilibrium density ρ_0, we minimize the energy per nucleon

$$\frac{E}{A} = \frac{\epsilon}{\rho} = \frac{3}{5}T_F + \frac{3}{8}t_0\rho + \frac{1}{16}t_3\rho^2, \tag{2.21}$$

where $T_F = \hbar^2 k_F^2/2m$, with respect to ρ. This leads to

$$0 = \frac{2}{5}T_F + \frac{3}{8}t_0\rho_0 + \frac{1}{8}t_3\rho_0^2. \tag{2.22}$$

By inverting eqs. (2.21–2.22), one finds the values of t_0 and t_3 corresponding to given values of E/A and ρ_0

$$\frac{1}{16}t_3\rho_0^2 = \frac{1}{5}T_F - \frac{E}{A}, \qquad \frac{3}{16}t_0\rho_0 = \frac{E}{A} - \frac{2}{5}T_F. \tag{2.23}$$

For $\rho_0 = 0.17$ fm^{-3} and $E/A = -16$ MeV, one obtains the values given in eq. (2.2). Another interesting quantity is the compression modulus of nuclear matter

$$K = k_F^2 \frac{\partial^2 E/A}{\partial k_F^2} = \frac{6}{5}T_F + \frac{9}{4}t_0\rho + \frac{15}{8}t_3\rho^2. \tag{2.24}$$

For the values shown in eq. (2.2), one finds K= 380 MeV which is somewhat higher than the value K = 220 MeV extracted from the observed energies of monopole vibrations (see ref. [9] and the discussion in section 4.6). The discrepancy is due to the oversimplified version of the Skyrme force we have used. More elaborate versions such as SkM [10] do reproduce the observed value.

2.6. High temperature limit

When the thermal wavelength λ is much smaller than the average distance between nucleons, that is, when

$$\rho(2\pi\hbar^2/mkT)^{3/2} \ll 1, \tag{2.25}$$

one can derive an explicit expression for the pressure. Indeed, in such a case the argument $x = \beta U - \alpha$ of the Fermi function is large (see eq. 2.14) so that the Fermi function can be approximated by

$$F_n(x) \simeq \frac{2}{\sqrt{\pi}}\Gamma(n)\left\{e^{-x} - e^{-2x}\frac{1}{2n} + \cdots\right\}.$$

This leads to the following expansions for the kinetic energy density

$$\tau = 6\pi\rho\lambda^{-2}(1 + \rho\lambda^3/4g\sqrt{2} + \cdots),$$

and for the pressure [11]

$$P = \rho kT\left(1 + \frac{\rho\lambda^3}{4g\sqrt{2}} + \cdots\right) + \frac{3}{8}t_0\rho^2 + \frac{1}{8}t_3\rho^3. \tag{2.26}$$

Note that the second term in P, which is a quantum correction to the classical pressure ρkT, is small when eq. (2.25) holds. Note also that near nuclear density, the contribution of the t_3 term is comparable in magnitude to the t_0 term.

2.7. *Phase diagram of nuclear matter*

Isothermal lines defined by eq. (2.26) are plotted in fig. 1. At low density, the classical term ρkT dominates. If the temperature T is not too high, the attractive t_0 term produces a decrease in the pressure. As density increases, P rises again due to the t_3 term. As the temperature is increased, the local minimum in P due to the nuclear attraction becomes less pronounced and eventually disappears as T becomes equal to the critical value T_c:

$$kT_c = \frac{3}{8t_3}(t_0 + \sqrt{2}kT_c\lambda^3/3g)^2. \tag{2.27}$$

Using the values from eq. (2.2) of the parameters, one obtains $T_c = 22.0$ MeV which corresponds to a critical density $\rho_c = (8T_c/3t_3)^{1/2} = 0.067\ \text{fm}^{-3}$. At the critical point, the parameter $\rho\lambda^3/4g\sqrt{2}$ is 0.12 which a posteriori justifies the use of the high temperature expansion given in eq. (2.26).

In fig. 1, one notes that for some densities, $dP/d\rho < 0$. This indicates an instability and shows that a constant density configuration does not correspond to the lowest value of the free energy anymore. In fact, it becomes more favorable to uniformly occupy a volume fraction $u\Omega = \Omega_1$ by A_1 nucleons

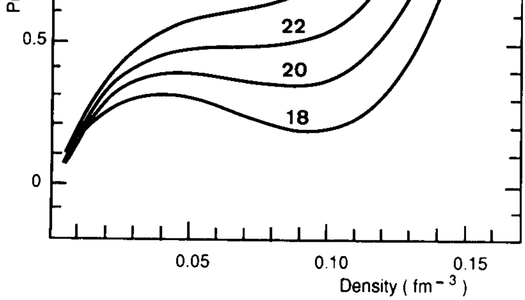

Fig. 1. Isothermal lines calculated from eq. (2.26) for several values of the temperature T in MeV.

with a density $\rho_1 = A_1/\Omega_1$, and the rest of the volume with the remaining $A_2 = A - A_1$ nucleons with another constant density $\rho_2 = A_2/(\Omega - \Omega_1)$. Then, a minimization of the free energy

$$F = F(\Omega_1, A_1, T) + F(\Omega - \Omega_1, A - A_1, T)$$

with respect to the two parameters, A_1 and Ω_1 leads to the following equations which define phase equilibrium

$$\mu(\rho_1, T) = \mu(\rho_2, T) \ , \quad P(\rho_1, T) = P(\rho_2, T) \ . \tag{2.28}$$

When $dP/d\rho$ is negative, the solution of these equations yields a mixed configuration distinct from the two phases. The densities ρ_1 and ρ_2 of the phases are obtained by the Maxwell graphical construction. This construction stipulates that in the (P, v) plane, $(v = 1/\rho)$, the two areas delimited by the line $P = P_1$ and the isotherm $P(v, T)$ be equal. This requirement is justified by the Gibbs-Duhem relation $\rho \partial\mu(\rho, T)/\partial\rho = \partial P(\rho, T)/\partial\rho$ which allows one to rewrite eq. (2.28) as

$$0 = \mu_2 - \mu_1 = (P_2/\rho_2 - P_1/\rho_1) + \int_{\rho_1}^{\rho_2} P(\rho, T) d\rho/\rho^2 .$$

2.8. *The compound nucleus model of Bonche and Levit*

The previous calculation of phase equilibrium ignores two effects which are important for nuclei. They are finite size (or surface) effects and Coulomb interactions. Can a nucleus survive temperatures of about 20 MeV, when these effects are included? To answer this question, Bonche and Levit [12, 13] have considered the following model. They describe the nucleus as a homogeneous system of A nucleons (N neutrons, Z protons) inside a sphere of volume $\Omega = 4\pi R^3/3$. Therefore, its density is $\rho_N = A/\Omega$ and its free energy F_N can be written as the sum of volume, surface, and Coulomb contributions

$$F_N = \Omega f(\rho_N, T) + \alpha(T) 4\pi R^2 + 3Z^2 e^2/5R, \tag{2.29}$$

where the nuclear surface tension is parameterized as [12]:

$$\alpha(T) = \alpha_0 (1 + 3T/2T_c)(1 - T/T_c)^{3/2}, \quad \alpha_0 = 1.14\text{MeV} \times \text{fm}^{-2}. \tag{2.30}$$

Bonche and Levit assumed this nucleus to be in equilibrium with an external vapor whose Coulomb energy is neglected (in a more realistic model, the external vapor is a nearly pure neutron gas because of the Coulomb barrier).

Thus, the free energy of the vapor is $F_v = \Omega_v f(\rho_v, T)$ where Ω_v and ρ_v denote the volume and the density of the vapor, respectively. The two parameters of the model, the radius R and the density of the external vapor ρ_v, are determined by two equilibrium conditions

$$
\begin{aligned}
P(\rho_N, T) + \frac{1}{R}\left(\frac{Z^2 e^2}{5A}\rho_N - 2\alpha(T)\right) &= P(\rho_v, T), \\
\mu(\rho_N, T) + \frac{6}{5}\frac{Z^2}{A}\frac{e^2}{R} &= \mu(\rho_v, T).
\end{aligned}
\tag{2.31}
$$

As expected, the Coulomb interaction increases the pressure of the nucleus phase, while the surface tension decreases it. Bonche and Levit solved the previous equations for various mass numbers A. They found that there is a limiting temperature T_L beyond which no solutions to eqs. (2.31) can be found. For the Skyrme interaction, eq. (2.2), T_L ranges from 12 MeV in light nuclei to about 7 MeV in heavy nuclei. We now describe an approximation scheme to solve eqs. (2.31) that provides a good qualitative description of the results of Bonche and Levit.

2.9. *An approximate calculation of the limiting temperature*

Our approximation scheme is based on the observation that a temperature of about 7 MeV is high for the dilute (vapor) phase, but at the same time it is low for the dense (nucleus) phase. Thus, we use high temperature expansions for pressure P_v and chemical potential μ_v in the right hand sides of eqs. (2.31)

$$
\begin{aligned}
P_v(\rho, T) &= \rho kT\left(1 + \frac{\rho\lambda^3}{4g\sqrt{2}} + \cdots\right) + \frac{3}{8}t_0\rho^2 + \frac{1}{16}t_3\rho^3, \\
\mu_v(\rho, T) &= kT\left(\log\frac{\rho\lambda^3}{g} + \frac{1}{2g\sqrt{2}}\rho\lambda^3 + \cdots\right) + \frac{3}{4}t_0\rho + \frac{3}{16}t_3\rho^2,
\end{aligned}
\tag{2.32}
$$

and low temperature expansions for pressure P_N and chemical potential μ_N in the nucleus phase

$$
\begin{aligned}
\frac{1}{\rho^2}P_N(\rho, T) &= \frac{1}{9\rho_0^2}(\rho - \rho_0)\left(K - 5\frac{\pi^2}{2}\frac{(kT)^2}{T_F}\right) + \frac{\pi^2}{6}\frac{(kT)^2}{\rho_0 T_F} + \cdots \\
\mu_N(\rho, T) &= \frac{E_0}{A} + \frac{1}{9}\left(\frac{\rho - \rho_0}{\rho_0}\right)\left(K - 5\frac{\pi^2}{2}\frac{(kT)^2}{T_F}\right) - \frac{\pi^2}{12}\frac{(kT)^2}{T_F} + \cdots
\end{aligned}
\tag{2.33}
$$

In this equation, T_F is the Fermi energy, ρ_0 the saturation density, K the compression modulus, and E_0 the total energy at saturation. Note that we have also performed an expansion in the difference $(\rho - \rho_0)$, and that the Gibbs-Duhem relation $\rho\partial\mu/\partial\rho = \partial P/\partial\rho$ is satisfied exactly by eq. (2.32) and to the lowest order in $\delta\rho = \rho - \rho_0$ by eqs. (2.33). Let us now evaluate the change $\delta\rho = \rho - \rho_0$ of the density inside the nucleus. With a good approximation, the external pressure in eq. (2.31) can be ignored which gives

$$\frac{1}{9}\left(K - 5\frac{\pi^2}{2}\frac{(kT)^2}{T_F}\right)\frac{\delta\rho}{\rho_0} = \frac{1}{R}\left(2\frac{\alpha(T)}{\rho_0} - \frac{Z^2e^2}{5A}\right) - \frac{\pi^2}{6}\frac{(kT)^2}{T_F}. \tag{2.34}$$

As expected, the density inside the nucleus is decreased by both Coulomb and thermal effects, while the surface tension tends to increase it. Due to the large value of the compression modulus K of nuclear matter (380 MeV) the resulting change in the density given by eq. (2.34) remains small, typically on the order of a few percent. For this reason, the Coulomb and surface terms in the left hand sides of eqs. (2.31) can be safely estimated by setting $\rho = \rho_0$ and $R = R_0 = (3/4\pi\rho_0)^{1/3}$ in these formulas.

Now, we can eliminate the density of the nucleus phase in eqs. (2.31). This is easily realized if one notes that the Gibbs-Duhem relation $\rho\partial\mu/\partial\rho = \partial P/\partial\rho$ requires that the coefficients of $\delta\rho$ in eqs. (2.33) to be equal. The result is

$$\frac{E_0}{A} - \frac{\pi^2}{4}\frac{(kT)^2}{T_F} + \frac{1}{R_0}\left(\frac{2\alpha(T)}{\rho_0} + \frac{Z^2e^2}{A}\right) = \mu(\rho_v, T). \tag{2.35}$$

In deriving eq. (2.35) we have dropped the term $P(\rho_v, T)/\rho_0$ which is negligible in comparison to μ_N since ρ_v/ρ_0 is small.

For a given value of T, this equation determines the density of the external vapor ρ_v. Let us now show that there is a limiting temperature T_L beyond which eq. (2.35) has no solution. Indeed, for a fixed T, the chemical potential $\mu(\rho_v, T)$ cannot exceed a value μ_M which corresponds to the lowest root ρ_M of the equation $\partial\mu/\partial\rho_v = 0$. Ignoring the t_3 term in μ, which is small, one finds

$$\begin{aligned} \rho_M(T) &= 1/(3|t_0|/4kT - \lambda^3/2g\sqrt{2}), \\ \mu_M(T) &= -kT(1 + \log(g/\rho_M\lambda^3)). \end{aligned} \tag{2.36}$$

Note that the maximum exists only when ρ_M is positive, that is, when the temperature is greater than $2(2\pi\hbar^2/m)^3/9t_0^2g^2 = 0.254$ MeV. When temperature increases, the left hand side of eq. (2.35) decreases from

$$\mu_0 = \frac{E_0}{A} + \frac{1}{R_0}\left(2\frac{\alpha(0)}{\rho_0} + \frac{Z^2e^2}{A}\right),$$

to minus infinity. In the range of interest, this decrease is slow (typically $T < 15MeV$) since the Fermi energy T_F is large. In contrast, $\mu_M(T)$ decreases very rapidly. A limiting temperature T_L is then reached when

$$kT_L = \frac{-E_0/A + \pi^2(kT_L)^2/4T_F - (2\alpha(T_L)/\rho_0 + Z^2e^2/A)/R_0}{1 + \log(g/\rho_M\lambda^3)}. \qquad (2.37)$$

To solve this equation, we substitute the approximation $T_L = -E_0/A$ in the right hand side of eq. (2.37) and iterate until convergence. The values obtained from eq. (2.37) for nuclei along the stability line

$$Z = A/2 - 0.003 \times A^{5/3}$$

are shown in fig. 2. Agreement with the results of Bonche and Levit is good, especially for heavy nuclei for which the approximation $T_L \ll T_F$ is well justified.

It is instructive to examine the difference between the critical temperature T_c and the limiting temperature T_L. When $T = T_c$ the nucleus and vapor densities are equal. In contrast $T = T_L$ corresponds to a Coulomb instability (this can be checked by evaluating the various terms in eq. (2.37)) that occurs when the vapor density is small (0.012 fm^{-3} in lead 208) while the density in the nucleus is still close to ρ_0. This is precisely a situation for which our approximation scheme is well suited.

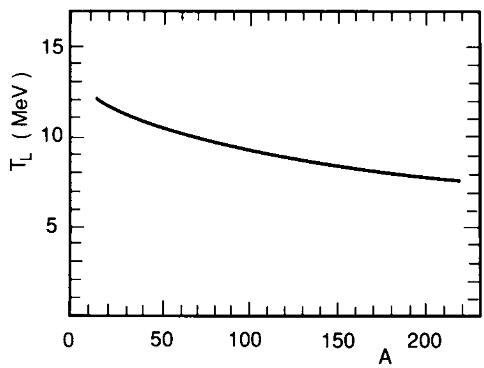

Fig. 2. Limiting temperature (in MeV) of nuclei along the stability line, as a function of their mass number A, calculated from eq. (2.37).

3. Equation of state at subnuclear densities

3.1. Introduction

We now turn to the problem of calculating the pressure of a mixture of hot nuclei surrounded by a nucleon vapor. Two different approaches have been used to investigate this problem. The first is the so called macroscopic approach, which uses semi-empirical expressions for nuclear masses and classical partition functions for the nucleon vapor. This is legitimate as long as the vapor is not dense enough to modify nuclear properties. This is true up to roughly one tenth of nuclear density. Beyond this density it is no longer justified to make a distinction between nucleons in nuclei and nucleons in the vapor. The second approach is a microscopic description of all nucleons present and thus is necessary for this problem. Several methods have been developed for this purpose. In the following, we describe the bulk equilibrium approximation (sections 3.4, 3.5), the compressible liquid drop model (section 3.6), Thomas-Fermi and Hartree-Fock calculations (sections 3.7 and 3.8).

3.2. Macroscopic approaches

In this approach, hot dense matter is described as a statistical mixture of Boltzmann gases of various nuclei. Let us label by a single index i, both the mass A and the charge Z of a nucleus. With this notation the density ρ_i of a given species i is obtained from a formula analogous to eq. (2.14a) namely

$$\rho_i = g_i \lambda_i^{-3} \exp(\alpha_i - \beta E_i) \tilde{Z}_i(\beta) , \tag{3.1}$$

where $\lambda_i = (2\pi\hbar^2/m_i kT)^{1/2}$ is the thermal wavelength associated with the mass m_i of the nucleus, $g_i = (2J_i + 1)$ is the degeneracy of the ground state and E_i its energy.

The main formal difference between this eq. (3.1) and eq. (2.14) is the factor $\tilde{Z}$, that is, the internal partition function of the nucleus $\tilde{Z}(\beta) = Z_i(\beta)\exp(\beta E_i)$, which accounts for the internal excitations of the nuclear species i. In addition, the so called degeneracy parameter α must be modified

$$\alpha_i = N\beta(\mu_n - U_n) + Z\beta(\mu_p - U_p), \tag{3.2}$$

where μ_n and μ_p are the chemical potentials in the neutron and proton vapors, and U_n and U_p are their average (mean-field) nuclear potentials. For the simplified Skyrme force eq. (2.1) one obtains

$$U_n(\mathbf{r}) = t_0\left(\rho(\mathbf{r}) - \frac{1}{2}\rho_n(\mathbf{r})\right) + \frac{t_3}{4}(\rho^2(\mathbf{r}) - \rho_n^2(\mathbf{r})), \tag{3.3}$$

where ρ_n is the density of the neutron vapor. In principle ρ_n should be calculated by setting $N = 1$, $Z = 0$ in eq. (3.2) and by solving eqs. (3.1–3.3) self-consistently. In practice, it is a good approximation to neglect U_n in eq. (3.2).

For given values of μ_n, μ_p and T, the previous set of equations allows one to calculate the baryon density ρ, the proton fraction $Y_p = \rho_p/\rho$ and the entropy per baryon S/A. The values of μ_n, μ_p, and kT have to be adjusted iteratively to obtain the desired values of ρ, Y_p and S/A. The equation of state is then obtained by adding the partial pressures $\rho_i kT$, which arise from all the nuclear species, to the electron and vapor contributions.

To perform actual calculations of eqs. (3.1–3.3), two important ingredients are needed: first, the nuclear ground state energies E_i (or binding energies B_i) which are generally taken from semi-empirical formulas; and second, the nuclear partition functions which are usually extracted from Fermi gas type formulas for nuclear level densities. The quality of these ingredients determines the range of applicability of the present approach. Indeed, semi-empirical mass formulas are not expected to be accurate for extremely exotic nuclei. In addition, Fermi gas type level densities may provide poor approximations at high temperatures [14]. Still, this approach is very useful below approximately $\rho_0/10$. To illustrate, let us review the results of El Eid and Hillebrandt [15]. These authors find that in the density range of $\rho_0/100 - \rho_0/10$, a nearly constant adiabatic index

$$\gamma = \frac{\partial \log P}{\partial \log \rho}, \tag{3.4}$$

along the adiabat $S/A = 1$, with a value $\gamma \simeq 1.35$, and a slowly rising temperature (from 1 MeV to about 2.5 MeV). The small difference between the calculated γ and the relativistic Fermi gas value $\gamma = 4/3$ shows that the pressure is generated almost entirely by relativistic electrons. The mass of the most abundant nuclear species (including alpha particles), is close to $A \simeq 70$ and nearly constant as a function of density. Similar results were obtained by other groups; for example, Sato [16], Arnett [17], Mazurek, Lattimer, and Brown [18].

3.3. Microscopic methods: the Wigner-Seitz approximation

Beyond $\rho_0/10$, one introduces microscopic methods which take into account the fact that nuclei arrange themselves on the lattice sites of a crystal. Indeed, in this density range, the electron screening becomes important. In turn, this favors a configuration with heavy nuclei, such that the restoring forces, which result from a displacement away from the equilibrium positions, are large (see below). Under such conditions, one can further simplify the calculation by evaluating the grand potential with the Wigner-Seitz approximation [19]. In this approximation, the crystal is divided into cells delimited by the equidistant planes between nearest neighbours. The interactions between different cells are neglected and the grand potential of each cell is calculated independently. Further, when the density of the medium does not vary rapidly in the vicinity of the cell edge, the Wigner-Seitz cell can be replaced by a sphere so that the numerical solution is reduced to that of a one dimensional radial problem. The calculations of Rüdiger Wolff, who analyzed in detail the case of non-spherical cells [20], have shown that this latter approximation is rather satisfactory. For the Wigner-Seitz approximation to be accurate, it is also necessary that the plasma parameter $\Gamma = Z^2e^2/RkT$ be greater than 155 [21] (Z is nucleus charge, R the cell size). This condition is indeed satisfied in the range $\rho_0/10 - \rho_0$.

The problem is now reduced to the determination of the grand potential $-P\Omega$ of a system of Z protons, N neutrons, and Z electrons at temperature T, inside a sphere of radius R. For a given baryon density ρ, N and Z are determined by imposing $Z/(N+Z) = Y_p$, $\rho = 3(N+Z)/4\pi R^3$. The optimal cell radius, which is now a variational quantity, is determined by a minimizing of the grand potential per nucleon. The value of the temperature T is fixed by the value of the entropy per nucleon $S/A \simeq 1$.

For the contribution of the electrons to the pressure, one can safely take that of an ultrarelativistic Fermi gas, that is,

$$\rho = Y_p \rho k \theta_F \frac{1}{4} + \frac{\pi^2}{6}\left(\frac{T}{\theta_F}\right)^2 + \cdots, \tag{3.5}$$

where θ_F is the electron Fermi temperature. Finally, the difference between the uniform electron density and the proton density generates an additional contribution to the grand potential; the Coulomb lattice energy

$$E_L = \frac{1}{2}\int \rho_e(\mathbf{r}_1)(\rho_e(\mathbf{r}_2) - \rho_p(\mathbf{r}_2))\frac{e^2}{r_{12}} d\mathbf{r}_1 d\mathbf{r}_2. \tag{3.6}$$

3.4. *The bulk matter approximation*

With the simplest microscopic method, one can ignore the Coulomb and surface effects in the calculation of the contribution of nucleons to the grand potential. In analogy with the model of section 2.7, nuclei are described as a drop of nuclear matter in equilibrium with a vapor inside a Wigner-Seitz cell [22, 23] (see fig. 3).

Compared to section 2.7, more parameters must be determined since the proton fractions in the nucleus and in the vapor may be different. Let us denote Ω_N as the volume occupied by the nucleus, Ω as the cell volume, and N_N and Z_N as the neutron and proton numbers of the nucleus, respectively. The free energy of the Wigner-Seitz cell is

$$F = F_0(T, N_N, Z_N, \Omega_N) + F_0(T, N - N_N, Z - Z_N, \Omega - \Omega_N). \quad (3.7)$$

where F_0 is the free energy calculated for uniform nuclear matter. By minimizing F with respect to N_N, Z_N, and Ω_N we find the following equations

$$\mu_{Nn} = \mu_{vn} \ , \qquad \mu_{Np} = \mu_{vp} \ , \qquad P_N = P_v \ , \quad (3.8)$$

where the indices N and v refer to the nucleus and the vapor, respectively, while the indices n and p refer to neutrons and protons.

Note that since eq. (3.7) does not include Coulomb and surface terms, the present approach leaves undetermined the size of nuclei (and the size of the

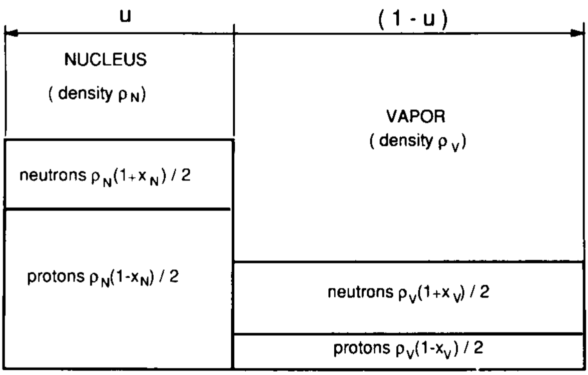

Fig. 3. Schematic representation of the Wigner-Seitz cell in the bulk matter approximation.

Wigner-Seitz cell). Solutions of eqs. (3.8) have been obtained numerically by Barranco and Buchler [22], and by Lamb, Lattimer, Pethick and Ravenhall [23]. The main result of these calculations is that, just below nuclear density, there is a softening of the equation of state arising from the nucleon-nucleon attraction. To understand this result, we present an approximate solution of the phase equilibrium equations (along the lines of section 2.9), which leads to simple and transparent analytic formulas.

3.5. Approximate solution of the equilibrium equations

As in section 2.9, we perform low-temperature expansions for the pressure and chemical potential in the nucleus phase, while the vapor phase is described in the high temperature limit. To solve the equilibrium equations we still consider a simplified Skyrme force of the form of eq. (2.1). However, since we now wish to describe nuclei with different neutron and proton numbers, this force must be modified to reproduce the symmetry energy coefficient $a_\tau((N-Z)/A)^2$ in the mass formula. This can be achieved by considering an interaction of the form

$$v = t_0(1+x_0P_\sigma)\delta(\mathbf{r}_1-\mathbf{r}_2)+t_3\delta(\mathbf{r}_1-\mathbf{r}_2)\delta(\mathbf{r}_2-\mathbf{r}_3). \tag{3.9}$$

With this interaction, the energy density in nuclear matter becomes

$$\epsilon = \frac{\hbar^2}{2m}\tau+\frac{3}{8}t_0\rho^2-\frac{1}{4}t_0\left(x_0+\frac{1}{2}\right)(\rho_n-\rho_p)^2+\frac{1}{4}t_3\rho_n\rho_p\rho, \tag{3.10}$$

yielding the following value of the symmetry energy coefficient

$$a_\tau = \frac{1}{3}T_F-\frac{1}{4}t_0\left(x_0+\frac{1}{2}\right)\rho-\frac{1}{16}t_3\rho^2. \tag{3.11}$$

Adjusting a_τ to the observed value of 30 MeV [4] leads to

$$x_0 = 0.48. \tag{3.12}$$

Let us now write explicitly the equilibrium eqs. (3.8). If we denote x_N as the asymmetry $(N-Z)/A$ of the nucleus, x_v as the asymmetry of the vapor, and x as the total asymmetry $1-2Y_p$, we find that these quantities are related by

$$u = \frac{(x_v-x)\rho_v}{(x_v-x)\rho_v+(x-x_N)\rho_N}, \tag{3.13}$$

where ρ_N and ρ_v are the densities of the nucleus and of the vapor respectively, and where u is the fraction of the total volume occupied by the nucleus phase. In terms of u, ρ_N, ρ_v the total density ρ is

$$\rho = u\rho_N+(1-u)\rho_v. \tag{3.14}$$

For the neutron and proton chemical potentials of the vapor μ_{vn} and μ_{vp}, we keep only the lowest order terms of the high temperature expansion

$$\begin{aligned}\mu_{vn} &= kT\log\{(1+x_v)\rho_v\lambda^3/g\},\\ \mu_{vp} &= kT\log\{(1-x_v)\rho_v\lambda^3/g\}.\end{aligned}\tag{3.15}$$

where we have adopted the notations of eqs. (2.14) and (2.15). In contrast, for the neutron and proton chemical potentials μ_{Nn} and μ_{Np} in the nucleus, we consider the low temperature formulas

$$\begin{aligned}\mu_{Nn} &= U_n + T_N(1+x_N)^{2/3} - (\pi^2T^2/12T_N)(1+x_N)^{-2/3},\\ \mu_{Np} &= U_p + T_N(1-x_N)^{2/3} - (\pi^2T^2/12T_N)(1-x_N)^{-2/3},\end{aligned}\tag{3.16}$$

where $T_N = \hbar^2k_N^2/2m$, $k_N = (6\pi^2\rho_N/g)^{1/3}$. The neutron potential U_n is given by

$$U_n = \frac{3}{4}t_0\rho_N - \frac{1}{2}t_0x_0\rho_Nx_N + \frac{1}{16}t_3\rho_N^2(1-x_N)(3+x_N),$$

with a similar formula for U_p. To lowest order in x_N, the formulas in eq. (3.16) provide the following relation between the chemical potentials

$$\mu_{Nn} - \mu_{Np} = 4a_\tau(T)x_N,\tag{3.17}$$

where $2a_\tau(T)$ is the second derivative of the free energy with respect to x_N

$$a_\tau(T) = \frac{1}{3}T_N - \frac{1}{4}t_0\left(x_0+\frac{1}{2}\right)\rho_N - \frac{1}{16}t_3\rho_N^2 + \frac{\pi^2}{36}\frac{(kT)^2}{T_N}.\tag{3.18}$$

Since the chemical potentials are identical in the nucleus and vapor phases, we find from eqs. (3.15) and (3.17), the asymmetry and density of the vapor

$$\begin{aligned}x_v &= \tanh(2a_\tau x_N/kT),\\ \rho_v &= g\lambda^{-3}(1-x_v^2)^{-1/2}\exp(\mu_N/kT),\end{aligned}\tag{3.19}$$

where μ_N is the average chemical potential $(\mu_{Nn}+\mu_{Np})/2$. When $N \simeq Z$, μ_N can be approximated to first order in x_N by the relation (2.33), that is,

$$\mu_N = \frac{E_0}{A} + \frac{1}{9}\left(\frac{\rho_N-\rho_0}{\rho_0}\right)\left(K - 5\frac{\pi^2}{2}\frac{(kT)^2}{T_F}\right) - \frac{\pi^2}{12}\frac{(kT)^2}{T_F}.\tag{3.20}$$

However, for large values of the asymmetry x_N, it will be necessary to return to the exact expression given by eqs. (3.16).

We can write the equality of the pressures in the nucleus and vapor phases. A straightforward generalization of eqs. (2.32) and (2.33) leads to

$$\begin{aligned} P_N = \; & \frac{1}{5}\{(1+x_N)^{5/3} + (1-x_N)^{5/3}\}\rho_N T_N \\ & + \frac{\pi^2}{12}\{(1+x_N)^{1/3} + (1-x_N)^{1/3}\}\rho_N \frac{T^2}{T_N} \\ & + \frac{1}{8} t_0 \rho_N^2 (3 - x_N^2(2x_0+1)) + \frac{t_3}{8}\rho_N^3(1-x_N^2), \end{aligned} \tag{3.21}$$

for the pressure in the nucleus and

$$\begin{aligned} P_v = \; & \rho_v T(1 + \frac{\rho_v \lambda^3}{4g\sqrt{2}}(1+x_v^2) + \cdots) \\ & + \frac{1}{8} t_0 \rho_v^2 (3 - x_v^2(2x_0+1)) + \frac{1}{8} t_3 \rho_v^3 (1 - x_v^2), \end{aligned} \tag{3.22}$$

for the pressure in the vapor. In first approximation, the equality $P_N = P_v$ can be replaced by $P_N \simeq 0$ because of the large value of the compression modulus K. The linearization of eq. (3.21) in $(\rho_N - \rho_0)$ and x_N^2 gives the following approximate equation for the density ρ_N of the nucleus

$$\begin{aligned} \frac{1}{9}\left(\frac{\rho_N - \rho_0}{\rho_0}\right)\left\{K - 5\frac{\pi^2}{2}\frac{(kT)^2}{T_F}\left(1 + \frac{x_N^2}{45}\right) + Mx_N^2\right\} \\ = -\frac{\pi^2}{6}\frac{(kT)^2}{T_F}\left(1 - \frac{x_N^2}{9}\right) - Lx_N^2. \end{aligned} \tag{3.23}$$

In this formula the quantities L and M are given by

$$\begin{aligned} L &= \frac{2}{9}T_F - \frac{1}{8}t_0(2x_0+1)\rho_0 - \frac{1}{8}t_3\rho_0^2 = 2.15 \text{ MeV}, \\ M &= \frac{10}{3}T_F - \frac{9}{4}t_0(2x_0+1)\rho_0 - \frac{27}{8}t_3\rho_0^2 = -413.06 \text{ MeV}. \end{aligned} \tag{3.24}$$

From the relation, $L = \rho\partial a_\tau(0)/\partial\rho$, one can check that the difference between ρ_N and ρ_0, induced by the asymmetry x_N of the nucleus in eq. (3.23), has very little effect on the value of the symmetry energy coefficient. Since the dependence of this coefficient on temperature is also weak, it is a good approximation to replace a_τ in equation (3.19) by its value at zero temperature and normal density, that is, 30 MeV. We can now construct a simple approximation of the equation of state in the region of phase equilibrium. For given values of $x = 1-2Y_p$, T and x_v, eq. (3.19), with $\mu_N = E_0/A - \pi^2(kT)^2/4T_F$, provides the value of the density ρ_v of the vapor, while eq. (3.19) gives the asymmetry x_N

$$x_N = \frac{kT}{4a_\tau} \log \frac{1+x_v}{1-x_v}. \tag{3.25}$$

From the eqs. (3.13) and (3.14), one obtains the fraction u of the volume occupied by the nucleus, the value of the total density, and finally, the equation of state by means of eq. (3.22). This procedure is approximate but can easily be improved if one uses the exact expressions, eqs. (3.21) and (3.22) and iterates the preceding procedure until the desired accuracy is reached in the solution of the equilibrium equation $P_N = P_v$.

The result for the isotherm T= 10 MeV, $Y_P = 1/3$ are shown in fig. 4. When the density reaches the value

$$\rho_{min} = g\lambda^{-3}(1-x^2)^{-1/2}\exp(\mu_N/kT), \tag{3.26}$$

the nucleus phase appears. As a result, the growth of the pressure with density is abruptly reduced. In the region of phase equilibrium, the vapor and nucleus asymmetries $(N-Z)/A$ both increase with density. However the eq. (3.19) shows that the vapor asymmetry x_v is much larger than the nucleus asymmetry. This varies from $x_v = 1/3$ to about unity while x_N goes from $kT\log 2/4a_\tau = 0.058$ to $1/3$.

Note that in the region of phase equilibrium, pressure is not constant as a function of density because of the extra degree of freedom associated with the neutron-proton asymmetry [23]. In contrast, if one imposes the constraint $x_v = x_N = x$, then the volume fraction occupied by the nucleus is no longer determined by eq. (3.13), and the pressure remains constant.

When the average density ρ reaches the density ρ_N of the nucleus calculated for an asymmetry x and a temperature T (about 0.14 fm^{-3} for $x = 1/3, T = 10$ MeV), all the matter goes into the nucleus phase. This generates a rapid increase in the pressure. For comparison, we have graphed in fig. 4 the electron pressure given by eq. (3.5).

The approximation scheme developed in the present section can also be used to calculate adiabats. The entropies per nucleon of the nucleus and of the vapor, estimated respectively in the low and high temperature limits, are given by the simple formulas

$$\begin{aligned} S_N/A &= \pi^2 T(1-x_N^2/9)/(2T_F)+\cdots \\ S_v/A &= -\log(\rho\lambda^3/g)+5/2+3\rho\lambda^3/(8g\sqrt{2})+\cdots \end{aligned} \tag{3.27}$$

From these formulas, combined with eqs. (2.32) and (3.14), one checks that entropy conservation prevents nuclei from becoming very hot. For instance

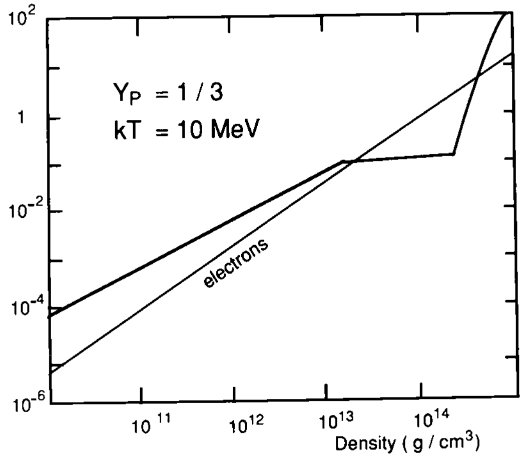

Fig. 4. Pressure (in MeV/fm^3) versus density along the isotherm $T = 10$ MeV for a proton fraction $Y_p = 1/3$. Scales are logarithmic for both pressure and density.

along the adiabat $S/A = 1$, $Y_p = 0.5$, one finds (using $T_F = 38.4$ MeV and $\mu_v = E/A = -16$ MeV) that the temperature reaches 4 MeV at a density close to $\rho_0/75$ and 7.8 MeV only at nuclear density. At $T = 4$ MeV nuclei occupy 0.9 percent of the total volume, but carry 46 percent of the total entropy. As density increases adiabatically, there is a transfer of entropy from the vapor to nuclei and consequently temperature increases rather slowly, as noted in [24].

An attractive feature of the bulk matter approximation is that, while maintaining the calculations at a level of great simplicity, it still allows one to understand the important aspects of the nuclear physics of hot dense matter. In particular, it emphasizes the essential role of the nuclear attraction, which leads to phase equilibrium, thereby producing a significant softening of the equation of state as discussed by Lamb et al. [23].

3.6. The compressible liquid drop model

This approach has been developed and exploited by the Illinois group [24, 25]. It is an improvement of the bulk matter approximation, which includes two important additional ingredients, namely Coulomb and surface effects. These generate two additional terms, F_{coul} and F_{surf} in the free energy of the

Wigner-Seitz cell. As compared to the expression given in section 2.8, the expression of F_{surf} must be modified to allow for the fact that the neutron excess x_N is no longer zero. As a result the critical temperature now depends on the neutron excess x_N. From eqs. (2.27) and (3.22), one finds

$$T_c = \frac{3}{8t_3(x_N)}(t_0(x_N) + \frac{\sqrt{2}}{3g}T_c\lambda^3(1 + x_N^2))^2,$$

where

$$\begin{aligned} t_0(x_N) &= t_0(1 - x_N^2(2x_0 + 1)/3), \\ t_3(x_N) &= t_3(1 - x_N^2). \end{aligned} \tag{3.28}$$

For the values given by eqs. (2.2) and (3.12) of the parameters, T_c is seen to decrease when x_N increases. In the calculations of [25], a Skyrme II interaction was chosen. These authors use the following parameterization of T_c

$$T_c(x_N) = T_c(0)(1 - 3.3x_N^2 - 7.3x_N^4)^{1/2}, \tag{3.29}$$

and the following expression for the surface tension

$$\alpha(x_N, T) = \frac{\alpha(0,T)}{1 + ax_N^2}\left(\frac{T_c^2 - T^2}{T_c^2 + bT^2}\right)^{5/4}. \tag{3.30}$$

In this equation, $\alpha(0, T)$ is given by eq. (2.30) while $a = 7.87$ and $b = .93 - 5.1x_N^2 - 1.1x_N^4$.

In contrast to section 2.8, a second modification must be made because the Coulomb energy E_c now includes screening of the nucleus charge by the electrons. At zero temperature, E_c is given by

$$E_c = \frac{3}{5}\frac{Z^2e^2}{R_N}\left\{1 - \frac{3}{2}\frac{R_N}{R_c} + \frac{1}{2}\left(\frac{R_N}{R_c}\right)^3\right\} \tag{3.31}$$

where R_N is the radius of the nucleus and R_c the cell radius. Note that there is total screening for $R_N = R_c$. At non-zero temperatures, corrections must be made to the previous formula because nuclei are no longer localized.

With the above formulas the minimization of the free energy with respect to the variational parameters $x_N, x_v, \rho_N, \rho_v, u$ and R_c can still be performed in a sufficiently simple way to allow systematic calculations of adiabats and isotherms with wide ranges of proton fractions. The main result of such calculations [24, 25] is that, although nuclear temperatures can become close to 10 Mev near saturation density along the adiabat $S/A = 1$, nuclei do survive all the way to approximately ρ_0. This is a surprising result since limiting temperatures of only 8 MeV were found in section 2.9 for heavy nuclei. However, one should keep in mind that such low limiting temperatures arise in nuclei because of the strong Coulomb repulsion. This repulsion is largely screened in hot dense matter as was just noted in the discussion of eq. (3.31).

In numerical calculations of stellar collapse, simplified equations of state are convenient because they lead to significant reductions of the amount of computer time required. Such equations of state have been constructed in ref. [26] and are discussed in the review article by Bethe [27].

3.7. Thomas-Fermi calculations

This approach was developed by Marcos, Barranco, Buchler [28] Ogasawara and Sato [29]. A detailed review can be found in the article by Barranco, Garcias, Pi and Suraud [30]. In contrast to the previous model, it is a microscopic approach in which the free energy F in the Wigner-Seitz cell is a function of the neutron and proton density profiles $\rho_n(\mathbf{r})$ and $\rho_p(\mathbf{r})$. Thus, nucleons in the nucleus, vapor, or surface are described in a consistent microscopic way. For a general Skyrme interaction and a symmetric nucleus $N = Z$ (i.e., $x = 0$), F reads

$$F = \int \{\epsilon(\rho, \nabla\rho) - T\mathcal{S}(\rho)\} d\vec{r}, \tag{3.32}$$

where ρ is the total density $\rho_n + \rho_p$, and ϵ is the energy density given by

$$\epsilon = \frac{\hbar^2}{2m^*}\tau + \frac{3}{8}t_0\rho^2 + \frac{t_3}{8}\rho^{1+\sigma} + \frac{1}{64}(9t_1 - 5t_2)(\nabla\rho)^2. \tag{3.33}$$

In this equation, t_0, t_1, t_2, t_3, σ are the parameters of the force and m^* is the effective mass satisfying

$$\frac{\hbar^2}{2m^*} = \frac{\hbar^2}{2m} + \frac{1}{16}(3t_2 + 5t_2)\rho. \tag{3.34}$$

The kinetic energy density τ is a function of ρ defined by eqs. (2.14) and (2.15) with the mass m replaced by m^*, and the entropy density $\mathcal{S}$ defined by eqs. (2.17) and (2.14). The minimization of the grand potential with respect to the density can be performed by the gradient method or imaginary time method which was developed in ref. [30–32]. The main advantage of the Thomas-Fermi method is that it is a microscopic but nevertheless numerically tractable method. It is particularly useful for the calculation of the exotic phases of hot dense matter that occur just below saturation density, for which the sperical symmetry in the Wigner-Seitz cell is spontaneously broken (see section 3.9).

3.8. Hartree-Fock calculations

This is the most detailed description presently available of the properties of hot dense matter [20, 34]. In this approach the mean-field equations at finite temperature given by eqs. (2.4–2.8) are solved for the nucleons present in the Wigner-Seitz cell. For a given radius R_c of the unit cell, knowledge of the density ρ and the proton fraction Y_p determines the number of neutrons and protons. The cell radius is adjusted to minimize the free energy per baryon for a fixed value of the temperature T. Ultimately, the temperature T is adjusted in order to have an entropy per baryon S/A equal to unity. Each of the previous steps requires a series of mean-field calculations with large numbers of nucleons, which means that the method is computationally cumbersome. An illustration of the method is shown in fig. 5, which displays the free energy per baryon in the Wigner-Seitz cell, calculated for various values of the number of nucleons in the unit cell. One finds a broad minimum at a large value of the mass number $A \simeq 600$. This large number is explained by the screening of Coulomb forces by the electrons. Compared with normal nuclei,

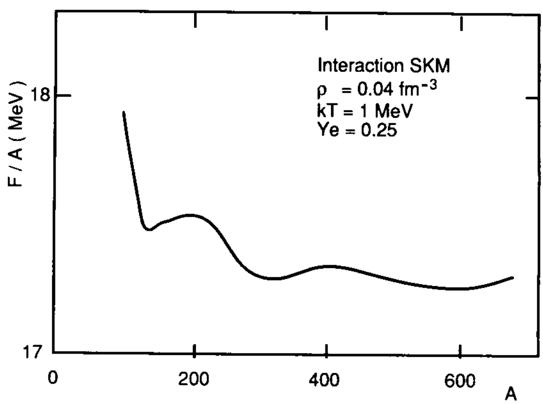

Fig. 5. Free energy per baryon in the Wigner-Seitz cell as a function of the nucleon number in the cell.

the surface tension plays a larger role and therefore favors the existence of heavy nuclei. The plasma parameter associated with such a large values of A is large ($\Gamma = 2000$) so that the system is a good crystal. Note that shell effects are visible in fig. 5 because the temperature ($T = 1$ MeV) is smaller than the spacing between nuclear shells.

The structure of the crystal obtained in the Hartree-Fock calculations of ref. [34] is represented in fig. 6, which shows neutron and proton density distributions along the line joining the centers of neighbouring cells for various densities along the adiabat $S/A = 1$.

For $\rho = 0.07$ fm^{-3}, the number of nucleons is $A \simeq 1000$ and the temperature $T = 5.53$ MeV. Note that although T and A are large, nuclei do survive. As a result, pressure is due mainly from the relativistic electrons and the adiabatic index is close to 1.30. The main interest of the Hartree-Fock approach is that it includes a detailed microscopic description of nuclei. Therefore, it is a useful reference for testing the validity of other simpler approaches. However, because of the large numerical work that it involves, systematic calculations can only be envisaged when the complexity of the situation justifies a detailed microscopic description.

3.9. *Sub-saturation phases of nuclear matter*

At about half saturation density, Lamb et al. [24] found that nuclei turn inside out to become bubbles so that the matter looks like spherical cavities arranged into a regular lattice. This is the so called "swiss-cheese" or bubble configuration. The main reason for this transition is that bubbles have about the same volume and Coulomb energies as nuclei, but have a lower surface energy. However, the location of the transition point is also sensitive to the curvature energy [35]. The transition occurs abruptly in calculations imposing a spherically symmetric Wigner-Seitz cell. However, a reliable description can be obtained only by using three-dimensional Thomas Fermi calculations which relax the spherical symmetry. An example is shown in fig. 7, which displays some of the results of the Thomas-Fermi calculations of Lassaut et al. [36, 37]. This figure shows (for a face centered cubic lattice) density contours in the planes $z = 0$ and $z = R_c/2$ (labelled I and II in the figure) with x and y ranging from 0 to R_c, that is, from the center to the cell boundary.

The graphs labelled a, b, c, d, e correspond to increasing values of density ranging from 0.01 fm^{-3} to 0.07 fm^{-3}. From this figure, one can see that nuclei grow to the point where bridges develop between them, which leads to the formation of cavities. In fact, it has been found by various authors [36, 38, 39] that many more exotic phases occur before the nuclei merge

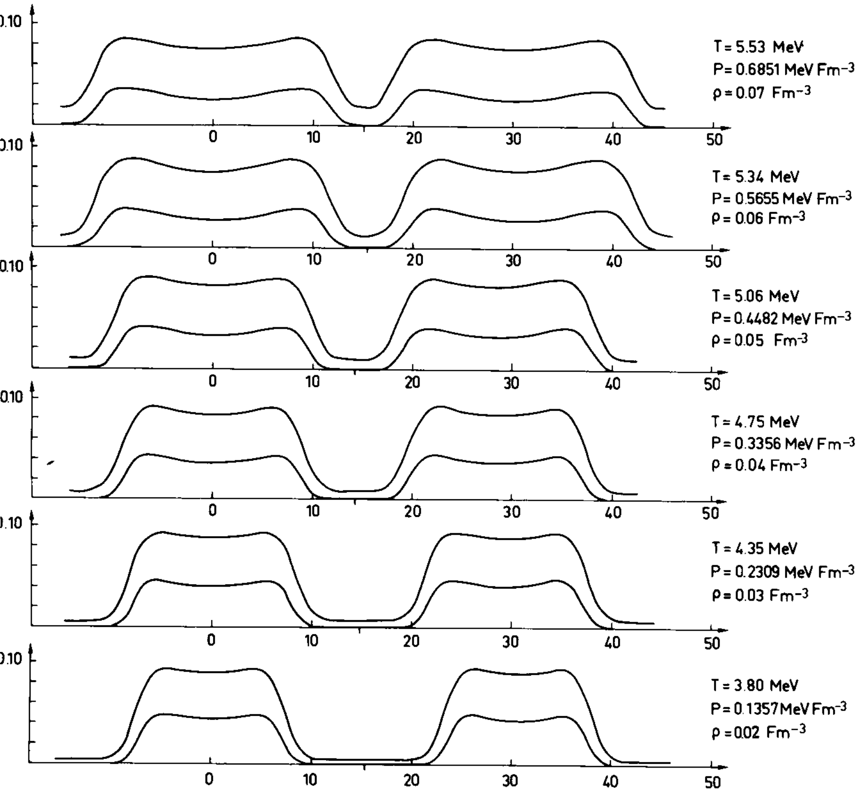

Fig. 6. Neutron and proton density profiles along the line joining the centers of neighbouring cells.

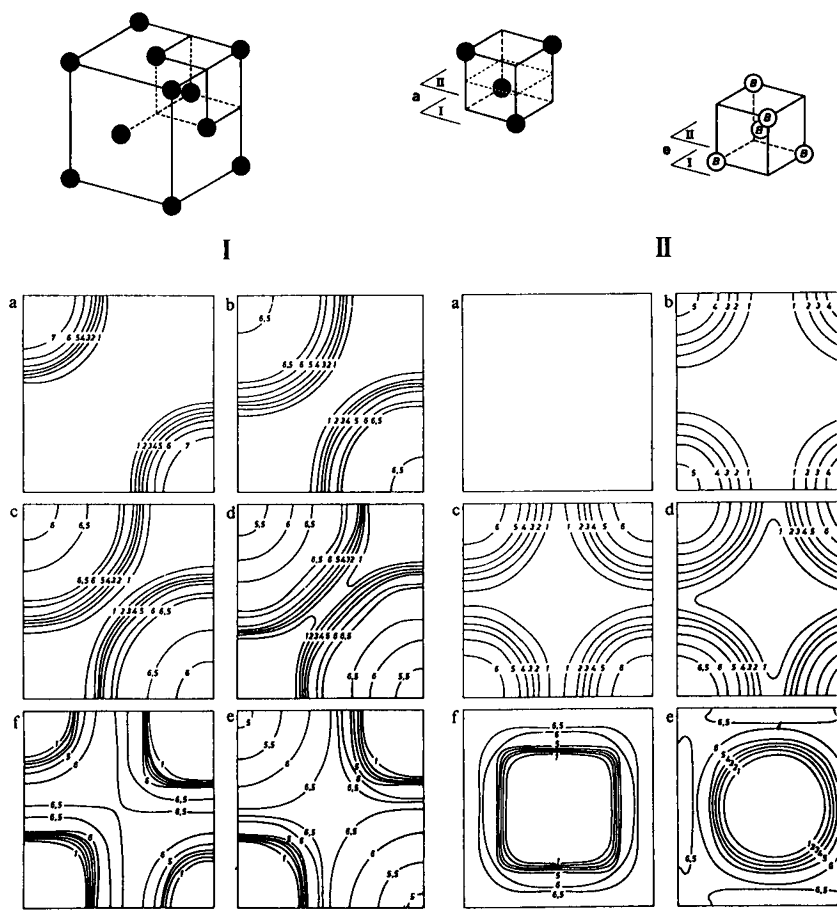

Fig. 7. Density contours in sections I and II of the Wigner-Seitz cell, obtained in the calculations of Lassaut et al. [36], for various values of baryon density. The graph (f) shows the density contours of a metastable configuration with the same average density as graph (d).

into nuclear matter. The sequence of phases obtained in [36, 39] is: nuclei, nuclear rods, slabs, tubes, bubbles, and uniform matter. These phases are of great interest from the point of view of the many-body theory. However, they seem to have only minor effects on the equation of state.

4. Beyond nuclear density

4.1. Non-relativistic many-body calculations

Beyond saturation density, it is no longer possible to use phenomenological forces valid only at low relative momenta. Therefore, it is necessary to return to more fundamental techniques mentioned in section 2.1, namely the variational method or the Brueckner Hartree-Fock method using realistic nucleon-nucleon forces such as the Orsay [5], Bonn [6], or Argonne [7] potentials. A detailed description of these methods is beyond the scope of this article, and we outline them only for the particular case of infinite nuclear matter.

Variational methods in nuclear matter became popular with the work of Robert Jastrow [40] who suggested minimizing the expectation value of the nuclear hamiltonian with a correlated wave function of the form

$$\Psi(\mathbf{r}_1, \mathbf{r}_2, \ldots, \mathbf{r}_A) = \prod_{i<j} F(|\mathbf{r}_i - \mathbf{r}_j|)\Phi(\mathbf{r}_1, \mathbf{r}_2, \ldots, \mathbf{r}_A), \tag{4.1}$$

where Φ is a determinant of plane waves and F a correlation factor determined variationally. However, because of the complexity of the nucleon-nucleon force, the form given in eq. 4.1 has been found to be too simple. Recent calculations use correlation factors depending on spin and isospin [41]

$$\begin{aligned} F = \;& f_c(r) + f_\tau(r)\vec{\tau}_1.\vec{\tau}_2 + f_\sigma(r)\vec{\sigma}_1.\vec{\sigma}_2 \\ & + f_{\sigma\tau}(r)(\vec{\sigma}_1.\vec{\sigma}_2)(\vec{\tau}_1.\vec{\tau}_2) + f_t(r)S_{12} + f_{t\tau}(r)S_{12}\vec{\tau}_1.\vec{\tau}_2 \\ & + f_b(r)\vec{L}.\vec{S} + f_{b\tau}\vec{L}.\vec{S}(\vec{\tau}_1.\vec{\tau}_2). \end{aligned} \tag{4.2}$$

The evaluation of the expectation value of the energy, $\langle\Psi|H|\Psi\rangle$ is a rather elaborate step. In the calculations of ref. [41], it is performed by the so called Fermi hypernetted chain single operator summation techniques. Minimization of the energy involves a set of 29 coupled integral equations, which were solved in the case of the Argonne potential.

Brueckner-Hartree-Fock calculations of nuclear matter also imply large amounts of numerical work. In a first step, one constructs the so-called reaction matrix, or G-matrix, which sums the ladder diagrams of the perturbation expansion. Its matrix elements satisfy

$$\langle ij|G(E)|k\ell\rangle = \langle ij|V|k\ell\rangle + \sum_{mn>F} \frac{\langle ij|V|mn > \langle mn|G(E)|k\ell\rangle}{E - e_m - e_n}, \quad (4.3)$$

where the indices $i, j, \ldots$ stand for the quantum numbers $\mathbf{k}_i$ (momentum), σ_i (spin), and τ_i (isospin) of the state i. This equation is usually written symbolically as

$$G = V - V\frac{Q}{e}G = V - V\frac{Q}{e}V\frac{Q}{e}V + \cdots \quad (4.4)$$

where the Pauli operator Q eliminates the intermediate states m, n in eq. (4.3) belonging to the set F of occupied orbits, and where e denotes the energy denominator. The argument E of the G-matrix in eq. (4.3) is often referred to as the starting energy.

The single particle energies e_i in eq. (4.3) are defined self-consistently by the relation

$$e_i = \frac{k_i^2}{2m} + \sum_{j<F}\langle ij|G(E = e_i + e_j)|ij\rangle. \quad (4.5)$$

The total energy of nuclear matter takes the same form as in the Hartree-Fock approximation, but the two-body interaction V is replaced by the reaction matrix G

$$E = \sum_i \frac{k_i^2}{2m} + \frac{1}{2}\sum_{ij<F}\langle ij|G(E = e_i + e_j)|ij\rangle. \quad (4.6)$$

This expression is the lowest order contribution in the reaction matrix to the energy. For realistic interactions, this is insufficient to achieve a reasonable convergence of the perturbation expansion. In the work of Day and Wiringa [42], the contributions of third-order terms (the so-called ring diagram) and fifth-order terms (three-body cluster diagram) to the energy have been calculated. There are no contributions from terms with two reaction matrix insertions since these are already included in eq. (4.4) .

The previous equations can be generalized (and solved) at finite temperatures [43]. Such generalizations are important since they provide thermal properties of dense nuclear matter. In addition, they give some information on the temperature dependence of the effective nucleon-nucleon force. In the range of temperatures from zero to ten MeV, this dependence was found to be small [43, 44]. This result justifies the calculations presented in sections 2 and 3, which used temperature independent effective interactions.

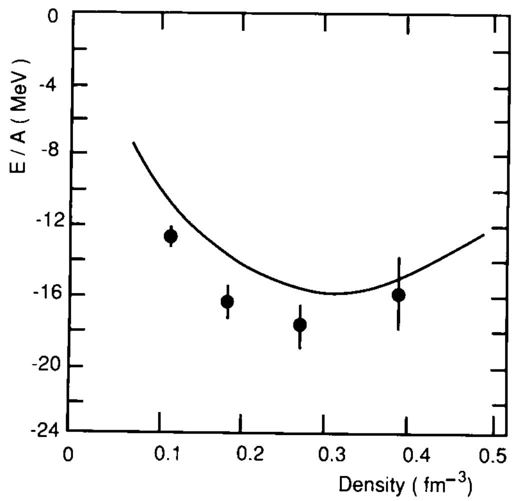

Fig. 8. Comparison between the results of Brueckner calculations (data points) and variational calculations (solid line) [42].

As can be seen in fig. 8, the results of variational calculations agree well with those of Brueckner-Hartree-Fock calculations (including ring and three-body cluster graphs). It can also be noted in this figure that saturation of nuclear matter occurs at a density which is too high (about twice the observed value), while the binding energy is only slightly too large. Although in the previous approaches, it is difficult to check to see that full convergence has been reached, there is a general and well motivated belief that the discrepancies be attributed to three-body nuclear forces and to relativistic corrections. We now describe relativistic mean-field calculations which are of interest in the identification of the role of relativistic corrections in nuclear saturation.

4.2. Relativistic mean field calculations

Relativistic mean-field theory was initiated by the work of Walecka [45]. It is an *effective* theory which ignores (as in non-relativistic Hartree-Fock) the effects of short range nucleon-nucleon correlations (i.e., the factors F in eq. (4.1)). Also meson exchanges are restricted to sigma and omega mesons.

Other mesonic degrees of freedom such as pi and rho degrees of freedom are left out (see, however, [46]). Further, antisymmetry (or Fock terms) are ignored, as is the structure of nucleons. These limitations certainly make extrapolations to high densities questionable. However, relativistic mean-field calculations are of interest in several respects. First, they provide a satisfactory description of a wide range of nuclear properties [47, 48]. Second, they allow recognition of the importance of relativistic effects, regarding such effects as nuclear saturation or the strength of the one-body spin-orbit potential in nuclei [47].

As in the non-relativistic case, it is assumed that nucleons are independent particles moving in an average potential generated by mutual interactions. However, a major difference is that now the motion of the nucleons is described relativistically. The wave functions ψ_i, $i = 1, 2, \ldots, A$ of the occupied nucleon orbitals satisfy the Dirac eq. (we adopt the usual convention $\hbar = c = 1$ throughout this section)

$$(\alpha.\mathbf{p} + \beta m + U_0 + \beta U_s)\psi_i = e_i \psi_i \ . \tag{4.7}$$

In eq. (4.7), α and β are the usual Dirac matrices, m is the nucleon mass, U_s is the scalar potential, and U_0 is the fourth component of the vector potential. We have retained U_0 only because we wish to describe stationary states of the nucleus. For non-stationary states, U_0 should be replaced by $U_0 - \alpha \cdot \mathbf{U}$ in the Dirac Hamiltonian.

In the work of Walecka, nucleons interact via the exchange of a scalar meson (with a mass μ and a coupling constant g_S) and a vector meson (with mass M and a coupling constant g_V). As in the non-relativistic case, we calculate the average nuclear field as the sum of interactions weighted by adequate probabilities. Ignoring the dynamics of the meson fields, we find

$$\begin{aligned} U_s(\mathbf{r}) &= -\frac{g_S^2}{4\pi} \int \frac{e^{-\mu|\mathbf{r}-\mathbf{r}'|}}{|\mathbf{r}-\mathbf{r}'|} \rho_S(\mathbf{r}') d\mathbf{r}', \\ U_0(\mathbf{r}) &= \frac{g_V^2}{4\pi} \int \frac{e^{-M|\mathbf{r}-\mathbf{r}'|}}{|\mathbf{r}-\mathbf{r}'|} \rho_B(\mathbf{r}') d\mathbf{r}', \end{aligned} \tag{4.8}$$

where ρ_S and ρ_B are, respectively, the scalar density and the baryon density of the nucleus.

$$\begin{aligned} \rho_B(\mathbf{r}) &= \sum_{i<F} \psi_i^+(\mathbf{r})\psi_i(\mathbf{r}), \\ \rho_S(\mathbf{r}) &= \sum_{i<F} \psi_i^+(\mathbf{r})\beta\psi_i(\mathbf{r}). \end{aligned} \tag{4.9}$$

Equation (4.8), which does not take into account exchange (or Fock) terms, corresponds, in fact, to the Hartree approximation.

The total energy density ϵ of the nucleus is the sum of kinetic and potential energy contributions

$$\epsilon = \sum_{i<F} \psi_i^+(\alpha.\mathbf{p} + \beta m)\psi_i + \frac{1}{2}U_s(\mathbf{r})\rho_S(\mathbf{r}) + \frac{1}{2}U_0(\mathbf{r})\rho_B(\mathbf{r}). \qquad (4.10)$$

In the case of uniform nuclear matter, plane waves are solutions of eqs. 4.7–4.9

$$\psi_i(\mathbf{r}) = \left(\frac{E^* + m^*}{2E^*}\right)^{1/2} \left[\begin{array}{c} \chi \\ \frac{\sigma.\mathbf{k}}{E^*+m^*}\chi \end{array} \right] \exp(i\mathbf{k}.\mathbf{r})\frac{1}{\sqrt{\Omega}}, \qquad (4.11)$$

where $\chi = \begin{pmatrix} 1 \\ 0 \end{pmatrix}$ or $\begin{pmatrix} 0 \\ 1 \end{pmatrix}$ for spin up or down nucleons, respectively, and where

$$m^* = m + U_s \qquad E^* = (k_i^2 + m^{*2})^{1/2} = e_i - U_0. \qquad (4.12)$$

Inserting eq. (4.11) into eq. (4.9) one finds the values of the scalar and baryon densities

$$\rho_S = \frac{1}{\Omega}\sum_{i<F} m^*/(k_i^2 + m^{*2})^{1/2}, \qquad (4.13)$$

$$\rho_B = gk_F^3/6\pi^2 \quad g = 2 \text{ (neutron matter)}, \quad 4 \text{ (nuclear matter)},$$

and from eq. (4.8), the values of the scalar and vector potentials

$$U_S = -g_S^2\rho_S/\mu^2, \qquad U_0 = g_V^2\rho_B/M^2. \qquad (4.14)$$

Equation (4.14) is the self-consistency relation, which for a given baryon density ρ_B, defines the optimal value of the effective mass m^*, and thus the value of the scalar density ρ_S. To perform the integration in eq. (4.13) it is convenient to introduce a variable x such that $\sinh x = k/m^*$, and to define a dimensionless quantity y by the relation

$$\sinh y = k_F/m^*. \qquad (4.15)$$

Then the expression for the scalar density (4.13) can be written as

$$\rho_S = g\frac{1}{8\pi^2}m^{*3}(\sinh 2y - 2y), \qquad (4.16)$$

and the self-consistency eq. (4.14) becomes

$$1 - \frac{m^*}{m} = gg_S^2\frac{1}{8\pi^2}\frac{m^{*3}}{m\mu^2}(\sinh 2y - 2y). \qquad (4.17)$$

For a given value of the ratio m^*/m, this equation unambiguously defines the value of y and the value of the Fermi momentum k_F through eq. (4.15). To obtain the energy density (at zero temperature) one inserts the solution of eqs. (4.7), (4.12), and (4.14) into eq. (4.10). The result is

$$\epsilon = \frac{1}{\Omega}\sum_i (k_i^2 + m^{*2})^{1/2} + \frac{1}{2} g_S^2 \frac{\rho_S^2}{\mu^2} + \frac{1}{2} g_V^2 \frac{\rho_B^2}{M^2}. \tag{4.18}$$

The sum (integration) in the first term is again performed in terms of the variable x. The result is

$$\epsilon = g\frac{m^{*4}}{64\pi^2}(\sinh 4y - 4y) + \frac{1}{2} g_S^2 \frac{\rho_S^2}{\mu^2} + \frac{1}{2} g_V^2 \frac{\rho_B^2}{M^2}. \tag{4.19}$$

It is worthwhile to examine the high and low density limits of this expression. At low density, eq. (4.13) shows that $\rho_S \simeq \rho_B$, while $m^* \simeq m - g_S^2\rho_B/\mu^2$ from eq. (4.12) and eq. (4.14). The energy density becomes

$$\begin{aligned} \epsilon &\simeq m^*\rho_B + \frac{3}{5}\rho_B \frac{\hbar^2}{2m} k_F^2 + \frac{1}{2} g_S^2 \frac{\rho_S^2}{\mu^2} + \frac{1}{2} g_V^2 \frac{\rho_B^2}{M^2}, \\ &\simeq m\rho_B + \frac{3}{5}\rho_B \frac{\hbar^2}{2m} k_F^2 + \frac{g_V^2}{2M^2}\rho_B^2 - \frac{g_S^2}{2\mu^2}\rho_B^2. \end{aligned} \tag{4.20}$$

Thus, we see from eq. (4.20) that scalar meson exchanges correspond to an attractive term at low density, while the vector meson leads to a repulsion. At high density, one has $\rho_S \simeq \mu^2 m/g_S^2$ and the term ρ_B becomes dominant so that

$$\epsilon \simeq \frac{g_V^2}{2M^2}\rho_B^2 + \cdots \tag{4.21}$$

The pressure $P = \rho^2\partial(\epsilon/\rho)/\partial\rho$ is just $P = \epsilon$ and the sound velocity at high density ($v = c(\partial P/\partial\epsilon)^{1/2}$) approaches c from below, in agreement with the requirement of causality.

From the low and high density expressions of the energy density given in eq. (4.20) and eq. (4.21) one learns an important fact: it is possible to produce nuclear saturation with a simple, relativistic Hartree calculation. This possibility must be attributed to relativistic effects since a non-relativistic treatment with the same ingredients just gives the quadratic dependence of eq. (4.20), and thus no saturation. This is an interesting feature of relativistic approaches which will be discussed further in the next section.

In the work of Walecka, the two dimensionless parameters of the model

$$C_S^2 = g_S^2 m^2/\mu^2, \qquad C_V = g_V^2 m^2/M^2, \tag{4.22}$$

were adjusted to obtain saturation at $E/A = -15.75$ MeV and $k_F = 1.42\ \mathrm{fm}^{-1}$. This gives $C_S^2 = 266.9$ and $C_V^2 = 195.7$. The resulting saturation curve is stiff with a compression modulus, $K = 480$ MeV. For neutron matter (i.e., $g = 2$ in eq. (4.19)) one finds a dip in the energy per neutron near $k_F = 1.4\ \mathrm{fm}^{-1}$ with a positive value $E/N = +2$ MeV. This is at variance with the neutron matter calculations of Siemens and Phandaripande [49]. However, it should be noted that there is no reason to expect good symmetry properties from the Walecka model in view of the absence of rho meson exchanges.

4.3. Density dependent relativistic corrections

As compared to non-relativistic methods, this relativistic model differs in that it involves not only the baryon density ρ_B, but also the scalar density ρ_S defined by expression (4.13). It can be expanded as

$$\rho_S = \rho_B - \frac{3}{10}\left(\frac{k_F}{m^*}\right)^2 \rho_B + \cdots \tag{4.23}$$

In the non-relativistic limit, ρ_S reduces to ρ_B. Relativistic corrections are seen to depend on m^*, and thus on ρ_B, since $m^* \simeq m - g_S^2\rho_B/\mu^2$. Calculating the difference $\rho_S(m^*) - \rho_S(m)$, we find that $\rho_S(m^*)$ can be written as $\rho_S(m)$ plus a relativistic correction

$$\rho_S(m^*) = \rho_S(m) - \frac{3}{5}\frac{g_S^2\rho_B^2 k_F^2}{\mu^2 m^3} + \cdots \tag{4.24}$$

A similar decomposition can be performed for the energy density $\epsilon(m^*, k_F)$, which can be expressed as $\epsilon(m, k_F)$ plus a relativistic correction. Using the following formula, valid to second order in $m^* - m$

$$\begin{aligned} &\tfrac{1}{\Omega}\textstyle\sum_i (k_i^2 + m^{*2})^{1/2} \\ &= \tfrac{1}{\Omega}\textstyle\sum_i (k_i^2 + m^2)^{1/2} + \tfrac{1}{2}(m^* - m)(\rho_S(m) + \rho_S(m^*)) + \cdots \end{aligned} \tag{4.25}$$

one finds an expansion of the eq. (4.18) to energy density

$$\epsilon(m^*, k_F) = \epsilon(m, k_F) + \frac{3}{10}\frac{k_F^2}{m}\rho_B\left(\frac{g_S^2\rho_B}{m\mu^2}\right)^2 + \cdots \tag{4.26}$$

From the previous calculation, we thus learn that the self-consistent dependence of m^* on the baryon density induces a density dependent relativistic correction to the binding energy per nucleon $\Delta E/A = \Delta\epsilon/\rho$, which varies as $\rho_B^{8/3}$. Taking the values of the coupling constant g_S from eq. (4.22) one obtains

$$\frac{\Delta E}{A} = 4.6 \text{ MeV } (\rho_B/\rho_0)^{8/3}. \tag{4.27}$$

Such a density dependent relativistic correction has been the subject of several studies and discussions [50]–[52]. In particular it has been emphasized by previous authors that the high power of ρ_B occurring in eq. (4.27) is important to cure the tendency of nuclear matter to saturate at too high a density.

4.4. Relativistic Brueckner-Hartree-Fock calculations

The most obvious limitations of the relativistic Hartree calculations described in section (4.2) are neglect of short range correlations, exchange or Fock terms; and the omission of pionic (and other) degrees of freedom. For this reason several authors have attempted to improve these calculations by including some of the previous effects [53]–[56]. This has been carried out within the framework of the relativistic Brueckner-Hartree-Fock method. As in non-relativistic calculations, one defines a reaction matrix $G(E)$ related to the bare interaction V via the usual integral equation

$$G = V - V(Q/e)G. \tag{4.28}$$

However, the difference is that single particle energies occurring in the denominator of eq. (4.28) (see eqs. (4.3) and (4.4)) are now obtained by solving the Dirac equation

$$\{\alpha.\mathbf{k} + \beta m + \Sigma(\mathbf{k})\}u(\mathbf{k}) = e_\mathbf{k} u(\mathbf{k}), \tag{4.29}$$

where Σ is the mass operator

$$\Sigma(\mathbf{k}) = \sum_{k'<k_F} \{\langle\mathbf{kk}'|G(E)|\mathbf{kk}'\rangle - \langle\mathbf{kk}'|G(E)|\mathbf{k}'\mathbf{k}\rangle\}, \tag{4.30}$$

calculated with a starting energy $E = e_\mathbf{k} + e_{\mathbf{k}'}$. Here again there is a double self-consistency: the calculation of G requires the single particle energies $e_\mathbf{k}$ and vice-versa. The equations are solved with an iteration procedure performed for each value of the Fermi momentum k_F. At convergence the energy density is given by the following generalization of eq. (4.10)

$$\epsilon = \sum_{k<k_F} u(\mathbf{k})\{\alpha.\mathbf{k} + \beta m + \frac{1}{2}\Sigma(\mathbf{k})\}u(k), \tag{4.31}$$

which allows the calculation of the pressure $P = \rho^2\partial(\epsilon/\rho)/\partial\rho$.

Solutions of the above equations for rather realistic boson exchange potentials, including π, σ, ω, ρ, η, and δ exchanges have been reported in the literature for both nuclear and neutron matter, at zero temperature as well as at finite temperature. We now briefly summarize the results of the Groningen group. Similar results were obtained by the Bonn group [55].

A first achievement of Dirac-Brueckner calculations is that saturation of nuclear matter occurs at a reasonable value of the density, with only a small underbinding. In contrast, non-relativistic calculations with the *same* interaction give a saturation density that is about twice as large. Part of the difference is due to the density dependent relativistic corrections discussed in the previous section. Another achievement of the Dirac-Brueckner approach is that it leads to a reasonable value of the compression modulus of nuclear matter, K = 250 MeV. However, the predicted equation of state is rather stiff at densities above nuclear density.

For asymmetric nuclear matter, relativistic Brueckner calculations predict a symmetry energy coefficient a_τ of 26 MeV, which is in good agreement with experimental data (27 to 30 MeV). The compression modulus of nuclear matter decreases with asymmetry. While K = 250 MeV for $Z/A = 1/2$, it is only K = 210 MeV for $Z/A = 1/3$, and K = 110 MeV for $Z/A = 1/5$. However, the stiffness of the equation of state just above nuclear density appears to be nearly independent of Z/A. Equations of state with various values of Z/A are, in fact, nearly parallel in this region.

Altogether, the Dirac-Brueckner approach is rather promising since it starts from a realistic nucleon-nucleon force, and is able to reproduce the properties of nuclear matter including the saturation density. In fact, from the experience acquired in non-relativistic many-body calculations, this agreement appears almost too good, since one can expect ring diagrams, three-body cluster diagrams, and three-body forces to significantly modify the saturation curve. Therefore, an evaluation of these contributions is of crucial interest.

4.5. Many-body calculations with relativistic corrections

In view of the difficulties encountered in the calculation of higher order corrections to Dirac-Brueckner theory, several authors have suggested a different approach, which is simpler and somewhat more phenomenological.

Rather than improving Dirac-Brueckner results, which appears too difficult, they add the relativistic corrections described in section 4.3 to the results of the complete many-body calculations outlined in section 4.1. In a first step, Ainsworth, Baron, Brown, Cooperstein, and Prakash [51] parameterize these results for the binding energy per nucleon

$$\frac{E_2}{A} = \frac{E_0}{A} + \frac{K}{18}\left(\frac{\rho - 2\rho_0}{2\rho_0}\right)^2, \tag{4.32}$$

with $K = (230 \text{ to } 300)$ MeV, $E_0/A = -(16.6 \text{ to } 17.8)$ MeV. Then, to account for relativistic corrections, they add a term of the form discussed above

$$\frac{E_R}{A} = B(\rho/\rho_0)^{8/3}, \tag{4.33}$$

with $B = 4.4$ MeV. Adding eqs. (4.32) and (4.33) is still not sufficient to obtain a reasonable equation of state because there is one ingredient still missing, which is the contribution E_3 of three-body forces. Ainsworth et al. [51] use the parameterized form

$$\frac{E_3}{A} = C(\rho/\rho_0)^{1.4}, \tag{4.34}$$

with a coefficient C equal to -3.9 MeV. Their zero-temperature equation of state is then obtained by calculating

$$P = \rho^2 \frac{\partial}{\partial\rho}(E_2 + E_R + E_3)/A. \tag{4.35}$$

From this zero-temperature formula, it is easy to construct the equation of state at finite temperature by using low temperature correction formulas described in section 8 of the review article by Bethe [27].

More elaborate evaluations of the contribution of three-body forces have been made by Grangé, Lejeune, Martzolff, and Mathiot [52]. These authors used the framework of meson exchange currents to establish new consistency requirements between the initial two-body force and the residual three-body force. Starting from the Orsay-Paris potential [5], they first solved the Brueckner-Bethe equations. Adding relativistic and three-body corrections, as well as contributions from the nucleon excited states, they obtain the graph of binding energy per nucleon versus density curve shown in fig. 9. The results are quite satisfactory in that there is qualitative agreement with empirical results. Given the approximations made in treating the many-body problem, the small discrepancy that still persists with saturation data is probably not significant.

4.6. Experimental studies of the equation of state

The experimental determination of the equation of state of (symmetric) nuclear matter is one of the major motivations for the study of nuclear collisions in the range of relativistic energies. This range was first explored at the BEVALAC, with bombarding energies of about 0.2 to 2 GeV per nucleon. Hydrodynamic and cascade models of such reactions predict the existence of a compression phase, in which the total density reaches typically 2 to 3 times nuclear density, for an incident energy of 0.5 to 1 GeV per nucleon [51, 57]. During this phase the temperature of the system (assuming that this concept is still meaningful) can become as high as 50 to 100 MeV (see fig. 9 of Ainsworth et al. [51]).

The maximum value of the density during collision is related to the compressibility of the medium and to the equation of state. However, in the absence of a detailed quantum mechanical description of the reaction, it is

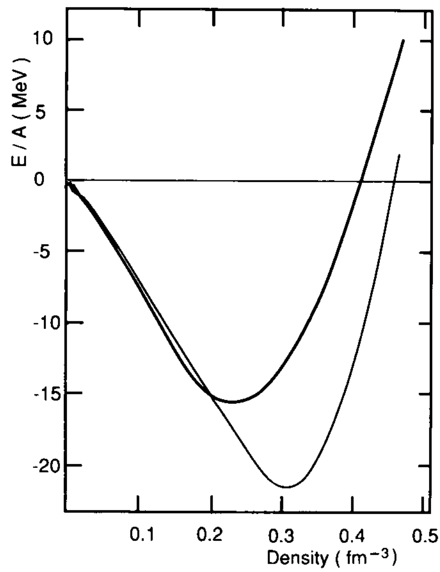

Fig. 9. Energy of nuclear matter versus density obtained in the calculations of Grangé et al. [52], indicated by the heavy solid line. The results of Brueckner-Hartree-Fock calculations are indicated by the thin line.

difficult to extract the equation of state. Indeed, the information about the compression phase is partially lost during the expansion phase because of final state interactions.

With one line of approach, Boltzmann-like equations are used, namely the Vlasov-Nordheim or Boltzmann-Uehling-Uhlenbeck equation. This equation is known to be adequate for near equilibrium situations [58]. There is also some indication that it reasonably describes nuclear collisions. It contains two ingredients: the equation of state and the effective scattering cross section σ_{eff} of two nucleons in the medium. An analysis of collision data may therefore provide information on these two quantities. This has been the subject of a large number of investigations, both experimental and theoretical, [59]–[61]. An important issue is the determination of the observables of the reaction which are most sensitive to the equation of state. It has been argued that one such observable is the flow tensor, or more precisely, the flow angle θ_F of the reaction products with respect to the incident beam. Analyses focusing on this observable have suggested a stiff equation of state, with $K = 400$ MeV and an adiabatic index $\gamma = 3$ at high density.

However, there are some uncertainties in these results. In particular one should first keep in mind the assumptions of the Boltzmann-Uehling-Uhlenbeck approach, which retains only mean-field and two-body collisions. Further, it assumes that cross-sections are local functions of the Wigner distributions $f(\mathbf{r}, \mathbf{p}, t)$. The Wigner distributions are required to be positive definite in order to interpret them as phase space probabilities [58]. Another source of uncertainty, studied by several authors, is the effect of momentum dependent interactions [62]. Finally, Pandharipande and Schlagel have pointed out that collisions are very sensitive to effective cross-sections in the medium and much less sensitive to the compression modulus K. These authors conclude that the accuracy of simulations based on mean-field approximations should be significantly improved in order to study the equation of state [58].

A second line of approach has been initiated by the work of Stock et al. [57]. These authors have proposed using the total multiplicity of produced pions as an observable that is characteristic of the high density stage of the collisions. This suggestion is attractive in several respects. First of all, it is based on a simple and convincing physical picture. Indeed, a stiff equation of state means that more energy is stored as compressional energy, and that less thermal energy is available to create pions. Also, a significant advantage of this observable is that cascade calculations [63] suggest that the total number of pions and delta resonances, and therefore the eventual pion yield, remains nearly constant during the expansion phase. This makes analyses much simpler since it is no longer necessary to incorporate the expansion phase. The calculation of the pion multiplicity is reduced to the determination of a statistical equilibrium between nucleons, pions, and delta resonances at the density ρ_M and temperature T_M reached in the collision. These two ingredients can be obtained from the equation of state by means of hydrodynamic models. Simple, one-dimensional constructions of ρ_M and T_M can be obtained from in the article by Ainsworth et al. [51].

Analyses based on pion multiplicities also suggest a rather stiff equation of state which agrees well with that obtained from sideways flow analyses (see fig. 7 of reference [51]). Uncertainties in this approach have been discussed by several authors, and are reviewed in the Les Houches lectures by D. Lhôte [64]. They arise, in particular, because of our imperfect knowledge of nucleon and delta effective masses in nuclear matter.

To conclude this section we briefly mention the revision of the compression modulus of nuclear matter which has been suggested recently by the Groningen group [65]. This group has performed measurements of the energy of the giant monopole resonance in a large set of tin isotopes whose masses are 112, 114, 116, 120, 124, 144, 148, 150, and 152. In analogy with the hydrodynamic model, one can define from the data, the compression modulus of the nucleus with Z protons and mass A by

$$E(O^+) = \hbar (K(A,Z)/m \langle r^2 \rangle)^{1/2}, \tag{4.36}$$

This quantity can be decomposed into volume, surface, symmetry, and Coulomb terms

$$K = K_\infty + K_S A^{-1/3} + K_\tau \left(\frac{N-Z}{A}\right)^2 + K_c Z^2 A^{-4/3}. \tag{4.37}$$

By using estimates of K_c and performing a least squares fit of the quantities K_∞, K_S, K_τ, the authors of reference [65] have obtained the following values

$$\begin{aligned} K_\infty &= 300 \pm 25 \text{ MeV}, \\ K_S &= -750 \pm 86 \text{ MeV}, \\ K_\tau &= -320 \pm 180 \text{ MeV}. \end{aligned} \tag{4.38}$$

These values agree with the analysis of the earlier Grenoble data performed by Treiner et al. [66] using the same procedure. In contrast, analyses based on random phase approximation, using momentum dependent zero-range forces [66] or gaussian finite range forces [9], lead to a couple (K, K_S) on the order of (220 MeV, -250 MeV). However, these calculations tend to predict monopole energies larger than those experimentally observed in medium size nuclei. Several aspects should be examined before a definite conclusion about the value of the compression modulus can be reached. First, one expects surface effects to be sensitive to the radial dependance of the nucleon-nucleon interaction. Hence, microscopic calculations using more realistic (Yukawa type) profiles should be performed. Second, the energy weighted sum rules are not saturated in medium and light nuclei, pointing to some missing strength in these nuclei. Finally, it may be that the quantity K_∞ should not be identified with the compression modulus K_{nm} of nuclear matter. This question was discussed in ref. [66], where it was shown that K_∞ and K_{nm} are equal in a scaling model (which was adopted in the analysis of the Groningen group) using Skyrme forces. Whether the same conclusion holds for a more realistic finite range interaction remains to be established.

5. Discussion

In the present review we have discussed some of the nuclear physics problems which occur in determination of the equation of state of hot dense matter. This is a particularly rich domain of nuclear physics. It deals with very unusual nuclei, whose mass numbers can sometimes be as large as a thousand, whose existence becomes possible in dense matter because of the screening of Coulomb forces.

We have seen that below nuclear density, most properties of dense matter can be understood, at least qualitatively, by means of the bulk matter approximation, which focuses on the equilibrium between drops of nuclear matter and an external vapor. Accurate solutions of the equilibrium equations can be found by using a low-temperature expansion for the nuclei and a high-temperature expansion for the vapor. In this density domain, reliable determinations of the equation of state are available via microscopic methods. The only uncertainty is in the level density parameter $a = S/2T$, where S is the entropy of a nucleus at temperature T. At low temperature, the empirical value of this parameter for a nucleus of mass number A is $A/8$ MeV^{-1}, while mean-field values are $A/16$ MeV^{-1}. The difference is generally attributed to the collective effects, which are not included in the mean-field approximation [67, 68]. Does this mean that mean-field calculations of hot dense matter are inadequate for estimating the temperatures reached during stellar collapse? In fact, there is some indication that the answer to this question is no. The reason is that the value $A/8$ MeV^{-1} has been found to be adequate only in the vicinity of the ground state, that is, in the domain of low temperatures. In contrast, for temperature of about 4 MeV (which is in the range of interest for stellar collapse), the value of the level density parameter has been found to be close to $A/16$ MeV^{-1} [69]. This result is not unexpected. Indeed, the relative importance of collective states on level densities should decrease with temperature because of the limited number of such states.

Beyond nuclear density, the situation regarding the equation of state is not yet satisfactory, although significant progress has been achieved in recent years. The most important advance was recognition of the importance of density dependent relativistic corrections. Combinations of such correction terms with the results of non-relativistic many-body calculations provide estimates of the equation of state which may be reasonable up to about 3 to 4 times nuclear density [51, 52].

We have not discussed the regime of densities above four times the nuclear density. Reviews of this question can be found in refs. [27, 51, 70]. We have also not discussed the influence of the equation of state on supernovae models. The interested reader is referred to the recent review by E. Mueller [71].

Acknowledgements

A large fraction of the material presented in this article is the result of long standing collaborations with P. Bonche, S. Levit, and E. Suraud. I wish also to thank J. Treiner for discussions regarding the compression modulus of nuclear matter, and J.F. Mathiot for discussions about the equation of state at high density. Special thanks are due to H. Flocard for his continuous constructive criticism and for his numerous suggestions throughout the preparation of these lecture notes. And finally, I am grateful to Agnes Fercoq for TEX-typing the manuscript with care and patience.

References

[1] H.A. Bethe, G.E. Brown, J. Applegate and J.M. Lattimer, Nucl. Phys. **A324** (1979) 487.
[2] H.A. Bethe and J.R. Wilson, Ap. J. **295**(1985) 14.
[3] J.R. Wilson and R. Mayle, Phys. Rep. **163** (1988) 63.
[4] P. Ring and P. Schuck, The nuclear many-body problem, Springer, Berlin, 1980.
[5] M. Lacombe et al., Phys. Rev. **C21** (1980) 861.
[6] R. Machleidt, Adv. Nucl. Phys. **19** (1989) 189.
[7] R.B. Wiringa, R.A. Smith and A.L. Ainsworth, Phys. Rev. **C29** (1984) 1207.
[8] D. Vautherin and D.M. Brink, Phys. Rev. **C5** (1972) 626.
[9] J.P. Blaizot, Phys. Rep. **64** (1980) 171.
[10] H. Krivine, J. Treiner and O. Bohigas, Nucl. Phys. **A336** (1980) 155.
[11] H. Jaqaman, A.Z. Mekjian and L. Zamick, Phys. Rev. **C27** (1983) 2782.
[12] S. Levit and P. Bonche, Nucl. Phys. **A347** (1985) 426.
[13] J. Besprosvany and S. Levit, Phys. Lett. **217B** (1989) 1.
[14] D.L. Tubbs and S.E. Koonin, Ap. J 232 (1979) L59.

[15] M.F. El Eid and W. Hillebrandt, Astron. Astrophys. **42** (1980) 215.
[16] K. Sato, Prog. Theor. Phys. **54** (1975) 1325.
[17] W.D. Arnett, Ap. J. 218 (1977) 815.
[18] T.J. Mazurek, J.M. Lattimer and G.E. Brown, Ap. J. 229 (1979) 713.
[19] E.P. Wigner and F. Seitz, Phys. Rev. **46** (1934) 509
[20] R. Wolff, Thesis, Technische Universität Munchen, 1983, W. Hillebrandt, K. Nomoto and R.G. Wolff, Astron. Astrophys. **133** (1984) 175.
[21] J.P. Hansen, Phys. Rev. **A8** (1973)3096.
[22] M. Barranco and J.R. Buchler, Phys. Rev. **C22** (1980) 1729.
[23] D.Q. Lamb, J.M. Lattimer, C. Pethick and D.G. Ravenhall, Nucl. Phys. **A360** (1981) 459.
[24] D.Q. Lamb, J.M. Lattimer, C. Pethick and D.G. Ravenhall, Phys. Rev. Lett. **41** (1978) 1623.
[25] J.M. Lattimer, C.J. Pethick, D.G. Ravenhall and D.Q Lamb, Nucl. Phys. **A432** (1985) 646.
[26] H.A. Bethe, G.E. Brown, J. Cooperstein and J.R. Wilson, Nucl. Phys. **A403** (1983) 625.
[27] H.A. Bethe, Ann. Rev. Nucl. Part. Sci. **33** (1988) 1.
[28] S. Marcos, M. Barranco and J.R. Buchler, Nucl. Phys. **A381** (1982) 507.
[29] R. Ogazawara and K. Sato, Prog. Theor. Phys. **68** (1982) 222.
[30] M. Barranco, F. Garcias, M. Pi and E. Suraud, in "Proceedings of the La Rabida Summer School," M. Lozano, M.L. Gallardo and J.M. Arias eds. Springer, Hamburg, 1989.
[31] K.T.R. Davies, H. Flocard, S.J. Krieger and M.S. Weiss, Nucl. Phys. **A342** (1980) 111.
[32] S. Levit, Phys. Lett. **139B** (1984) 147.
[33] E. Suraud and D. Vautherin, Phys. Lett. **138B** (1984) 325; E. Suraud, Astron. Astrophys. **143** (1985) 844.
[34] P. Bonche and D. Vautherin, Nucl. Phys. **A372** (1981) 496 ; Astron. Astrophys. **12** (1982) 268.
[35] C.J. Pethick, D.G. Ravenhall and J.M. Lattimer, Phys. Lett. **128B** (1983) 137.
[36] M. Lassaut, H. Flocard, P. Bonche, P.H. Heenen and E. Suraud, Astron. Astrophys. **183** (1987) L3.
[37] P. Bonche and D. Vautherin, Le Courrier du C.N.R.S., Suppl. Images de la Physique, **65** (1986) 83.
[38] R.D. Williams and S.E. Koonin, Nucl. Phys. **A435** (1985) 844.
[39] D.G. Ravenhall, C.J. Pethick and J.R. Wilson, Phys. Rev. Lett. **50** (1983) 2066.
[40] R. Jastrow, Phys. Rev. **79** (1950) 389; **81** (1951) 165.
[41] R.B. Wiringa, V. Fiks and A. Fabrocini, Phys. Rev. **C38** (1988) 1010.
[42] B.D. Day and R.B. Wiringa, Phys. Rev. **C32** (1985) 1057.
[43] A. Lejeune, P. Grangé, M. Martzolff and J. Cugnon, Nucl. Phys. **A453** (1986) 189.
[44] J.R. Buchler and B. Datta, Phys. Rev. **C19** (1979) 494.
[45] J.D. Walecka, Ann. Phys. **83** (1974) 491.
[46] J. Diaz Alonso, Phys. Rev. **D31** (1985) 1315.
[47] B.D. Serot and J.D. Walecka, Adv. Nucl. Phys. **16** (1986) 1.
[48] Y.K. Gambhir, P. Ring and A. Thimet , Ann. Phys. **198** (1990) 132.
[49] P.J. Siemens and V.R. Pandharipande, Nucl. Phys. **A173** (1971) 561.
[50] M.R. Anastasio, L.S. Celenza, W.S. Pong and C.M. Shakin, Phys. Rep.**100** (1983) 328.
[51] T.L. Ainsworth, E. Baron, G.E. Brown, J. Cooperstein and M. Prakash, Nucl. Phys. **A464** (1987) 740.
[52] P. Grangé, A. Lejeune, M. Martzolff and J.F. Mathiot, Phys. Rev. **C40** (1989) 1040.
[53] M.R. Anastasio, L.S. Celenza and C.M. Shakin, Phys. Rev. **C23** (1981) 2273.
[54] C.J. Horowitz and B.D. Serot, Nucl. Phys. **A464** (1987) 613.

[55] R. Brockmann and R. Machleidt, Phys. Rev. **C42** (1990) 1965.
[56] B. ter Haar and R. Malfliet, Phys. Rev. Lett. **56** (1986) 1237 ; **59** (1987) 1652.
[57] R. Stock et al., Phys. Rev. Lett. **49** (1982) 1236.
[58] V.R. Pandharipande and T.J. Schlagel, Nucl. Phys. **A519** (1990) 157c.
[59] K.H. Kampert, Les Houches Lectures, M. Soyeur, H. Flocard, B. Tamain and M. Porneuf, eds., Plenum New-York 1989.
[60] H. Stöcker and W. Greiner, Phys. Rep.**137** (1986) 278.
[61] G.F. Bertsch and S. das Gupta, Phys. Rep.**160** (1988) 189.
[62] C. Gale, G.M. Welke, M. Prakash, S.J. Lee and S. das Gupta, Phys. Rev. **C41** (1990) 1545.
[63] J. Cugnon et al., Nucl. Phys. **A352** (1981) 505 ; **A379** 553.
[64] D. Lhôte, Les Houches Lectures, M. Soyeur, H. Flocard, B. Tamain and M. Porneuf, eds., Plenum, New-York, 1989.
[65] M.M. Sharma et al., Phys. Rev. **C38** (1988) 2562.
[66] J. Treiner, H. Krivine, O. Bohigas and J. Martorell, Nucl. Phys. **A371** (1981) 253.
[67] G.F. Bertsch and T.T.S. Kuo, Nucl. Phys. **A112** (1968) 204.
[68] N. Vinh Mau and D. Vautherin, Nucl. Phys. **A445** (1985) 245.
[69] G. Nebbia et al., Phys. Lett. **176B** (1986) 20; M. Gonin et al., Phys. Lett. **217B** (1989) 406.
[70] G. Baym, Les Houches Lectures, 1977, North Holland, Amsterdam, 1978.
[71] E. Müller, J. Phys. **G16** (1990) 1571.

COURSE IX

MULTIDIMENSIONAL HYDRODYNAMICAL SIMULATIONS OF SUPERNOVA EXPLOSIONS

EWALD MÜLLER

Max-Planck-Institut für Physik und Astrophysik
Institut für Astrophysik
Karl-Schwarzschild-Str. 1
D-8046 Garching b. München, FRG

S. Bludman, R. Mochkovitch and J. Zinn-Justin, eds.
Les Houches, Session LIV 1990
Supernovae

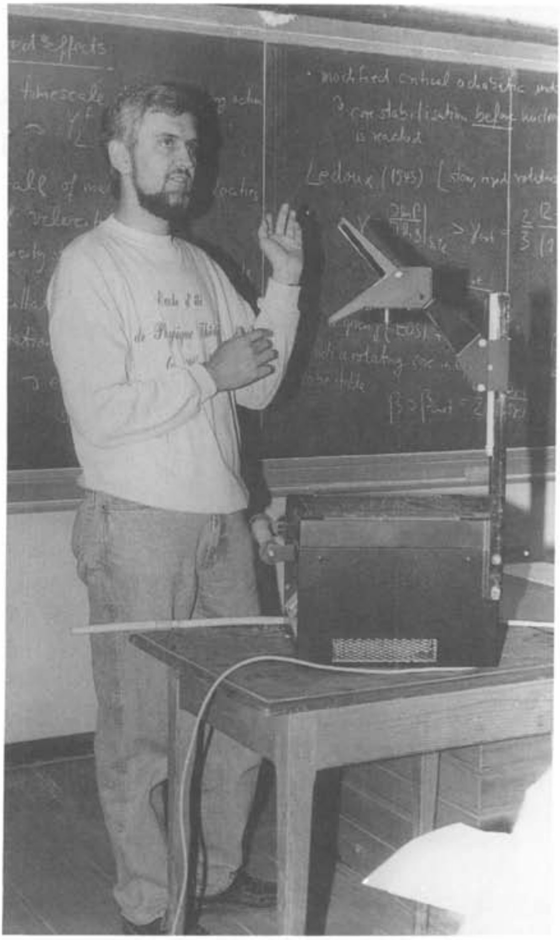
Ledoux (1945)

Contents

1. Introduction 397
2. Numerical methods 398
   2.1. Lagrangian and Eulerian methods 399
   2.2. Explicit and implicit methods 400
   2.3. Accuracy and efficiency 401
   2.4. Conservative difference schemes 403
   2.5. Operator splitting or fractional-step coupling 408
   2.6. Godunov-type difference methods 411
3. Core collapse with rotation 415
   3.1. Overview of expected effects 416
   3.2. Equilibrium sequences 420
   3.3. Hydrodynamical simulations 424
   3.4. Gravitational radiation from collapsing rotating cores 428
4. Instabilities and mixing in Type II supernova explosions 432
   4.1. Observational evidence from SN 1987A 432
   4.2. Rayleigh-Taylor instability 433
   4.3. RT instabilities in supernova explosions 434
   4.4. Simulations of RT instabilities in polytropes 435
   4.5. Simulations of RT instabilities in realistic stellar models 435
      4.5.1. Numerical methods 436
      4.5.2. Initial models 438
      4.5.3. Linear stability analysis 439
      4.5.4. Results of two-dimensional simulations 441
      4.5.5. Results of three-dimensional simulations 444
      4.5.6. Mixing 446
      4.5.7. Implications 447
5. Thermonuclear burning fronts and Type Ia supernovae 450
   5.1. General considerations 450
   5.2. Shock waves 452
   5.3. Simple theory of steady plane detonations and deflagrations 455
   5.4. Detonations and Type I supernova models 457
   5.5. Deflagrations and Type I supernova models 461
   5.6. Hydrodynamics and nuclear burning 464
   5.7. Hydrodynamic simulations of detonations 468
      5.7.1. Detonations caused by numerical errors 469

5.7.2. Detonations with single exothermic reaction 473
5.7.3. Detonation with α-network 476
References 484

1. Introduction

Ever since supernova explosions have been studied, hydrodynamical simulations have played an important if not sometimes crucial role (e.g., in the case of delayed explosions), together with observations and basic physical and analytical investigations. The problem is so hopelessly complex and non-linear, involving very different areas of macro and micro physics (hydrodynamics, gravity, equation of state, transport processes, strong and weak interactions, nucleosynthesis), that one cannot expect to solve the supernova problem without numerical simulations.

In view of all the complex physics which is to be included in a simulation, and in view of the computer resources available ten or even twenty years ago, it is immediately obvious that the first simulations performed in this field were one-dimensional, that is, spherically symmetric simulations (Colgate and Johnson 1960; Colgate and White 1966; Arnett 1966, 1967, 1968, 1969; Wilson 1971). But only a few years after the first one-dimensional simulations, some pioneers began exploring multi-dimensional models. LeBlanc and Wilson (1970) performed the first 2D (i.e., axisymmetric) hydrodynamical and magneto-hydrodynamical simulations of Type II supernova explosions, while Mahaffy and Hansen (1975) calculated the first non-spherical Type I supernova explosions.

With the growing power of computers, multi-dimensional supernova simulations became more common, although still remaining a small fraction of all simulations. This is due to the fact that besides modern supercomputers, multi-dimensional simulations also require a long-term commitment of a researcher's (or sometimes a group of researcher's) time and effort, which in most cases leads to a lower publication rate. Unfortunately such "low output" engagements (when only counting the number of publications) are not always honoured properly by the astrophysics community. This opinion will hopefully change in a few years, because the development of highly accurate and efficient finite difference schemes within the last ten years will allow for sophisticated multi-dimensional supernova simulations which will have a significant impact on the field.

When first asked to give this lecture series on multi-dimensional hydrodynamical simulations of supernova explosions, I was somewhat uncertain how to attack this enormously wide field. Obviously, there are three more or less distinct parts to this topic: the numerical methods, the physics of supernova explosions, and the simulations themselves. Because the school was intended for students in astrophysics rather than in computational fluid dynamics, I decided to keep the numerical part quite short and general. Thus the first lecture, devoted to numerics, contains a personally biased compendium of sub-problems which are of importance in any multi-dimensional hydrodynamical simulation.

Each of the remaining three lectures deals with one specific aspect of supernova simulations, namely the influence of rotation on the dynamics of core collapse (chapter 3), Rayleigh-Taylor instabilities and mixing processes which occur in expanding supernova envelopes (chapter 4), and thermonuclear burning fronts in Type Ia supernovae (chapter 5). Each lecture contains a discussion of the underlying physics and models, together with a presentation of the results of the simulations. Because a detailed and thorough discussion of the physics is far beyond the scope of the three lectures, and because it can also be found in the contributions of the other lecturers, no comprehensive presentation of the physics of supernova explosions is intended. Thus, the second and third lectures depend heavily on the lecture series of Hillebrandt and Nadyozhin on the theory of Type II supernovae, while the final lecture requires a study of the lectures of Barkat, Canal, Nomoto, and Woosley for full understanding of the theory of Type I supernovae.

2. Numerical methods

The first lecture deals both with some general and some specific numerical topics of multi-dimensional hydrodynamical simulations. The topics which have been selected for the lecture are merely thought to serve as a (by no means complete) guide to and a personally biased view of key aspects of the subject. A comprehensive discussion of this rapidly evolving field is far beyond the scope of this lecture series. Thus, no attempt is made to discuss the basic concepts of finite difference methods (i.e., the discretization and approximation of partial differential operators) which underlie all of the hydrodynamical simulations discussed below. A detailed and comprehensive introduction to finite difference methods can be found in the textbooks of Roache (1972), Potter (1973), Anderson, Tannehill, and Pletcher (1984), Oran and Boris (1987), and in a recent review article by Benz (1991). More mathematically oriented readers may also wish to consult the classical textbook of Richtmyer and Morton (1967).

2.1. Lagrangian and Eulerian methods

The hydrodynamical equations can be formulated with respect to two distinct classes of coordinate systems, called Lagrangian and Eulerian coordinates, respectively (see Potter 1973).

Lagrangian hydro-codes integrate the hydrodynamical equations using *comoving* coordinates, that is, time derivatives are calculated with respect to a coordinate system attached to and moving with the fluid. The Lagrangian formulation guarantees that no numerical, that is, unphysical diffusion of momentum, heat, nor composition occurs during a simulation, because the nonlinear advection terms responsible for the occurrence of numerical diffusion are not present in the Lagrangian formulation of hydrodynamical equations (see also section 2.4). Numerical diffusion causes especially difficult problems with attempts to model (thermonuclear) burning fronts (see chapter 5). The advantage of the Lagrangian formulation breaks down, however, and severe numerical difficulties arise when multi-dimensional problems are attempted. The comoving grid in general becomes very distorted, leading to grid tangling in the case of shear or vortex flow, for example. Then one is forced to *rezone* the grid. Even when the rezoning is done carefully, which is not as easy and straightforward as one might think (note, e.g., that the conservation of mass, linear, and angular momentum, and of energy should not be violated by the rezoning algorithm), a significant amount of numerical diffusion of the various quantities is introduced. Thus the major advantage of the Lagrangian approach is lost.

For multi-dimensional problems, therefore, Eulerian hydro-codes using time-independent spatial coordinates are preferred, since the grid remains regular. Obviously, special efforts then have to be used to minimize the inevitable numerical diffusion. This can be achieved using more accurate, higher-order schemes (see chapter 5).

Within the last fifteen years, a new type of Lagrangian hydrodynamics method has been developed, the so-called *Smooth Particle Hydrodynamics* (SPH) method (Lucy 1977; Gingold and Monaghan 1977; Monaghan 1982). SPH is a free-Lagrange method, in which spatial gradients are evaluated without the use of any grid. Thus the method does not suffer from the problems caused by grid tangling and subsequent rezoning. For a detailed review of the SPH-method see Monaghan (1985) and Benz (1989, 1991).

2.2. Explicit and implicit methods

Following Potter (1973) let us consider a system defined by the state vector $\vec{u}(\vec{r}, t)$, in the space domain $R = R(\vec{r})$. If $\vec{u} = \vec{u}^0$ is defined at time $t = 0$, and if $\vec{u}$ is defined on the surface S of R for all time t, we wish to determine $\vec{u}$ for all time t in R. The state of the system may be obtained for all time t as solutions to the initial value equation

$$\frac{\partial \vec{u}}{\partial t} = L\vec{u} \,. \tag{2.2.1}$$

In general, L is a nonlinear operator which is algebraic for ordinary differential equations, and is a spatial differential operator for eq. (2.2.1) a partial differential equation.

Neglecting higher than second order terms, the most general discretization of eq. (2.2.1) with respect to time is given by (Potter 1973)

$$\vec{u}^{n+1} = \vec{u}^n + L\vec{u}^n(1-\varepsilon)\Delta t + L\vec{u}^{n+1}\varepsilon\Delta t, \tag{2.2.2}$$

where $\vec{u}^n$ and $\vec{u}^{n+1}$ are the state vectors of the system at adjacent time points t^n and $t^{n+1} = t^n + \Delta t$. Here ε is an interpolation parameter, $0 \le \varepsilon \le 1$, and second order accuracy is only maintained when $\varepsilon = 1/2$. In the special case when $\varepsilon = 0$, the new state $\vec{u}^{n+1}$ is defined explicitly by the known state $\vec{u}^n$ at the previous time step. In this event the method is called *explicit*, while otherwise if $\varepsilon \neq 0$ the method is called *implicit*.

Explicit schemes are only stable if the size of the time step is restricted by the well known Courant-Friedrichs-Levy condition (CFL, Potter 1973), given (on a 2D Cartesian grid) by

$$\Delta t \le \Delta t_{\mathrm{CFL}} = \mathrm{Min}_{ij} \left\{ \frac{|u_i|}{\Delta x_i} + \frac{|v_j|}{\Delta y_j} + c_{ij}\sqrt{\left(\frac{1}{\Delta x_i}\right)^2 + \left(\frac{1}{\Delta y_j}\right)^2} \right\}^{-1} . \tag{2.2.3}$$

The minimum in eq. (2.2.3) is computed with respect to all zones (i, j), and Δx_i, Δy_j, u_i, v_j and c_{ij} are the grid spacing and flow velocities in the x- and y-directions, and the local sound speed, respectively.

In general, implicit schemes allow for larger time steps, but at the expense of solving a system of nonlinear algebraic equations. This is achieved by linearizing the system and iterating the solution (e.g., with the Newton-Raphson method). Thus, implicit schemes require in each timestep several (typically 3 to 5) times the solution of a linear system, that is, several matrix inversions. Obviously, implicit schemes become prohibitive time and storage consumers when used directly for two- or even three-dimensional problems, because the order of the matrix to be inverted is given by the product of the number of variables times the number of zones in each spatial direction, that is, $NV \cdot N1 \cdot N2 \cdot N3$.

Although operator-splitting techniques can help to significantly reduce this problem (see section 2.5), implicit schemes have not been widely used in astrophysics because of two further difficulties. First, the evaluation of the Jacobian required for an iterative solution of the nonlinear system is a problematic task, since some variables may only be given in tabular form (equation of state, opacities, etc.). In addition, experience shows that errors made in the evaluation and in programming of the numerous derivatives are difficult to locate (as they only manifest themselves as a non-convergence of the iteration), and thus, their removal may take a significant amount of the code development time. Second, when features are present in the flow across which one or several variables vary sharply and which are neither stationary in the Lagrangian nor in the Eulerian reference frame (e.g., shocks and in particular accretion shocks), the advantage of the implicit approach can be greatly reduced. As convergence is only obtained in all zones if none of the iterated variables vary by more than about 10 to 30% from time step to time step; sharp, non-stationary features in the flow lead to a more or less severe time step restriction. This restriction can only be overcome with an adaptive grid: this, however, poses other, sometimes even more challenging, problems concerning the stability of the numerical scheme and the stiffness of the algebraic system (see Winkler and Norman 1986; Mönchmeyer and Müller 1989b).

2.3. Accuracy and efficiency

Because multi-dimensional calculations place such a demand on resources and time, one should expend considerable effort in finding the best procedure. Accuracy, determined by testing problems with known solutions, and efficiency, getting maximum performance from existing hardware, should be the main concerns.

The computational expense of a given calculation is proportional to the number of zones calculated and the number of time steps taken. Thus, in 3D,

$$\text{Load} \sim (l/\Delta x)^3\,(\tau/\delta t)\,, \tag{2.3.1}$$

where l is a characteristic length, Δx is the (equidistant) zone size, τ is the time the calculation is to be run, and δt is the average size of a time step. For an explicit method, the size of the time step is limited by the CFL condition $\delta t \leq \Delta x / c_s$ (c_s is the local sound speed; see previous section), so that

$$\text{Load} \sim l^3 \, \tau \, c_s \, / \, (\Delta x)^4 \, . \tag{2.3.2}$$

If one method (A) can produce equally accurate results, but uses n times the number of zones needed by another method (B), then the ratio of expense is

$$\text{Load(A)} \, / \, \text{Load(B)} \; = \; n^4 \, . \tag{2.3.3}$$

The memory requirement scales as n^3; in practice this is often the inflexible limit. One may argue for more computer time, but the memory size is difficult to change.

Estimating n for different pairs of codes is not trivial, but depends upon the problem to some extent. An important problem of interest is the preservation of temperature or heat differences (when modeling burning fronts; see chapter 5) and of compositional differences (when modeling mixing processes; see chapter 4). A useful test problem is one which propagates a compositional step-function through the mesh, with no pressure gradients (alternatively one may use compensating steps in density and temperature). The result should simply be a translation of the step to new positions. Numerical errors tend to broaden the step into a "ramp" which spreads over several zones. Plotting the width of the ramp in zones, as a function of the number of zones propagated through, is a useful way to compare quality of numerical methods; this is shown in fig. 1 (see Fryxell, Müller and Arnett 1989).

Fryxell, Müller, and Arnett (1989) have tested a number of popular methods in multi-dimensional numerical hydrodynamics: Lax-Wendroff, donor cell; Godunov's method, a flux-vector splitting method (SADIE); and the piecewise parabolic method (PPM) of Colella and Woodward (1984). A brief description of these codes and the relevant references can be found in the work of Fryxell, Müller, and Arnett (1989).

Let us consider a grid of 400 zones per dimension (which is at least required for the simulations discussed in chapters 4 and 5), where a contact discontinuity has been propagated through half the grid, that is, through 200 zones. Figure 1 then shows that a version of PPM, without special software for detection of such contact discontinuities, has a ramp width of about 6 zones. Lax-Wendroff gives a ramp about 12 zones wide. PPM, with contact detection, gives a ramp only 2 zones wide. SADIE, which does shocks very

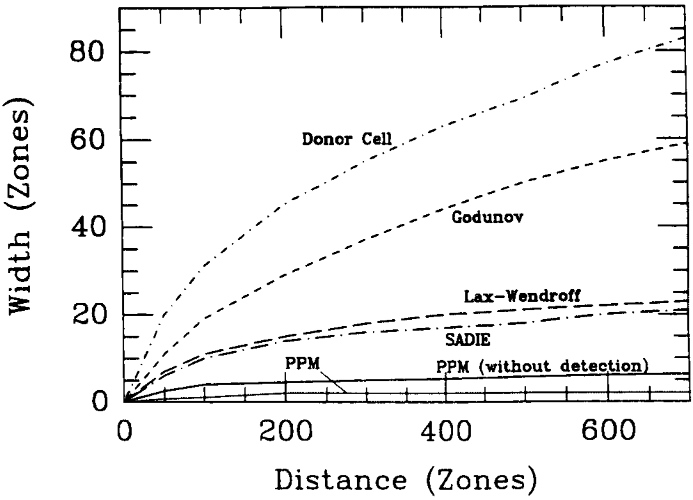

Fig. 1. Comparison of several numerical methods for the translational motion of a contact discontinuity (see Fryxell, Müller and Arnett 1989).

well, is as bad as Lax-Wendroff for this test. For both of these methods, $n \simeq 6$. First order methods, such as donor cell and Godunov, are much worse ($n \simeq 20$ and $n \simeq 15$).

The computational load for a given accuracy of SADIE or Lax-Wendroff ($n \simeq 6$, which is second best after PPM on the step test problem) relative to PPM (with contact detection switched on) are 216 (in 2D) and 1296 (in 3D). Here, it is assumed that each grid point requires the same effort, which is not the case, but this is not a major error for problems which have significant microphysics. If n is as much as 2, this implies a significant difference in performance on problems in which compositional differences are important. Note that the ratio of speed for a supercomputer ($\simeq$ 1000 mflops) and a typical workstation ($\simeq$ few mflops) is $\simeq 10^3$, which is comparable to the difference in 3D performance for a resolution ratio of $n \simeq 6$.

2.4. Conservative difference schemes

The hydrodynamical equations express the conservation of mass, momentum and energy (see Potter 1973). For a viscous free fluid, the Eulerian form of the equations including gravity and energy sink or source terms, is given by mass conservation:

$$\frac{\partial \varrho}{\partial t} + \operatorname{div}\,(\varrho \vec{v}) = 0 \tag{2.4.1}$$

momentum conservation:

$$\frac{\partial \varrho \vec{v}}{\partial t} + \operatorname{div}\,(\varrho \vec{v}\,\vec{v}) + \operatorname{grad} p = \varrho \operatorname{grad} \Phi \tag{2.4.2}$$

energy conservation:

$$\frac{\partial e}{\partial t} + \operatorname{div}\,\left[(e + p)\,\vec{v}\right] = \varrho\,\vec{v} \operatorname{grad} \Phi + q \tag{2.4.3}$$

Here

$$e = \frac{1}{2}\varrho\,|\vec{v}|^2 + \varepsilon \tag{2.4.4}$$

is the sum of the kinetic and the internal energy ε, while ϱ, $\vec{v}$, p, Φ and q are the mass density, velocity, pressure, gravitational potential, and energy sink/source terms, respectively.

The hydrodynamical equations must be supplemented by an equation of state

$$p = f(\varrho, \varepsilon) \tag{2.4.5}$$

and by an equation for the gravitational potential Φ, which for a self-gravitating fluid is Poisson's equation.

Many analytically equivalent forms of the hydrodynamical equations exist. Some of these forms are better suited for discretization than others. Let us consider for example the continuity equation (eq. 2.4.1), which can also be written as

$$\frac{\partial \varrho}{\partial t} + \vec{v} \operatorname{grad} \varrho + \varrho \operatorname{div} \vec{u} = 0\,. \tag{2.4.6}$$

The second term in eq. (2.4.6) describes the change of ϱ due to the advection of the density distribution by the flow; note that this term is not present in Lagrangian schemes. Although eq. (2.4.6) is analytically equivalent to eq. (2.4.1), the latter form of the continuity equation is to be preferred for discretization, because it directly expresses the underlying conservation property. Obviously the conservation of mass should also hold for the corresponding difference equation, which is not easily guaranteed when starting off from eq. (2.4.6) but which becomes straightforward when eq. (2.4.1) is used as a starting point (see following discussion).

Among the discretized hydrodynamical equations, which in general do not necessarily conserve mass, momentum and energy, there exists a class of discretized equations which guarantees the conservation laws. This class of difference equations is called *conservative.*

To derive a class of *conservative difference schemes*, the hydrodynamical equations are integrated over an Eulerian finite volume element V enclosed by the surface ∂V. Then mass conservation takes the form

$$\frac{\partial}{\partial t}\int_V \varrho \, dV + \int_V \operatorname{div}(\varrho\vec{v})\, dV = 0 . \qquad (2.4.7)$$

Using Gauss' theorem one obtains

$$\frac{\partial}{\partial t}\int_V \varrho \, dV + \iint_{\partial V} \varrho\vec{v}\, d\vec{f} = 0 , \qquad (2.4.8)$$

where $d\vec{f}$ is an outwards-pointing element on the surface ∂V. By analogy one can derive the momentum and energy conservation equations

$$\frac{\partial}{\partial t}\int_V \varrho\vec{v}\, dV + \iint_{\partial V} \varrho\vec{v}\,(\vec{v}\, d\vec{f}) = \int_V (\varrho \operatorname{grad}\Phi - \operatorname{grad} p)\, dV, \qquad (2.4.9)$$

and

$$\frac{\partial}{\partial t}\int_V e\, dV + \iint_{\partial V} (e + p)\,\vec{v}\, d\vec{f} = \int_V (\varrho\vec{v} \operatorname{grad}\Phi + q)\, dV. \qquad (2.4.10)$$

The finite volume formulation of the hydrodynamical equations has a further advantage. Besides reflecting the underlying physics, it also allows for a treatment of discontinuities in the flow.

To generalize the finite volume formulation to moving coordinate systems (see Winkler, Mihalas and Norman, 1984), we first define three kinds of time derivatives: (1) the *moving grid time derivative* (d/dt), which is taken with respect to fixed values of the moving coordinates; (2) the *Lagrangian time derivative* (D/Dt), which is taken with respect to a definite fluid element; (3) the *Eulerian time derivative* $(\partial/\partial t)$, which is taken with respect to fixed coordinates in the laboratory frame.

Further, let $\vec{r}_g$ be the position of a definite set of grid coordinates of the moving grid, and $\vec{r}_e$ be the position of a definite point ("element") in the fluid; then the *grid velocity* is given by

$$\vec{v}_g = \frac{d}{dt}\vec{r}_g , \qquad (2.4.11)$$

the *fluid velocity* by

$$\vec{v} = \frac{D}{Dt}\vec{r}_e\,, \tag{2.4.12}$$

and the *relative velocity* by

$$\vec{v}_{\rm rel} = \vec{v} - \vec{v}_g\,. \tag{2.4.13}$$

Note that Lagrangian coordinates correspond to the special case of $\vec{v}_g = \vec{v}$, while $\vec{v}_g = 0$ for Eulerian coordinates.

The different time derivatives of any quantity f are then related by

$$\frac{Df}{Dt} = \frac{\partial f}{\partial t} + \vec{v}\,\mathrm{grad}\, f\,, \tag{2.4.14}$$

and

$$\frac{df}{dt} = \frac{\partial f}{\partial t} + \vec{v}_g\,\mathrm{grad}\, f\,, \tag{2.4.15}$$

where the gradient in both equations is taken with respect to Eulerian coordinates.

If J denotes the Jacobian (or functional determinant) of the transformation between the coordinates of a moving grid volume dV^0 at time t_0, and its volume $dV = J\,dV^0$ at some later time t, one can derive with

$$\frac{dV}{dt} = \frac{dJ}{dt}\,dV^0 = \frac{d\ln J}{dt}\,dV \tag{2.4.16}$$

and

$$\begin{aligned}\frac{d}{dt}J &= \frac{d}{dt}\frac{\partial(x,y,z)}{\partial(x^0,y^0,z^0)}\\ &= \frac{\partial\left(\frac{\partial x}{\partial t},y,z\right)}{\partial(x^0,y^0,z^0)} + \frac{\partial\left(x,\frac{\partial y}{\partial t},z\right)}{\partial(x^0,y^0,z^0)} + \frac{\partial\left(x,y,\frac{\partial z}{\partial t}\right)}{\partial(x^0,y^0,z^0)}\end{aligned} \tag{2.4.17}$$

and

$$\frac{1}{J}\frac{dJ}{dt} = \frac{\partial(u_g,y,z)}{\partial(x,y,z)} + \frac{\partial(x,v_g,z)}{\partial(x,y,z)} + \frac{\partial(x,y,w_g)}{\partial(x,y,z)} \tag{2.4.18}$$

the *moving grid expansion formula* (see Winkler, Mihalas and Norman, 1984)

$$\frac{d\ln J}{dt} = \mathrm{div}\,\vec{v}_g\,. \tag{2.4.19}$$

To obtain the so-called *moving grid transport theorem* (see Winkler, Mihalas and Norman, 1984) start from the relation

$$\frac{d}{dt}(\xi\, dV) = \frac{d\xi}{dt}\, dV \;+\; \xi\, \frac{dV}{dt}\,, \tag{2.4.20}$$

where ξ is an extensive quantity, that is, the density, the energy, or the entropy. Using Eqs. (2.4.16) and (2.4.19) this equation becomes

$$\frac{d}{dt}(\xi\, dV) = \frac{d\xi}{dt}\, dV + \xi\, \mathrm{div}\, \vec{v}_g\, dV, \tag{2.4.21}$$

which can be rewritten utilizing eq. (2.4.14) as

$$\frac{d}{dt}(\xi\, dV) = \frac{\partial \xi}{\partial t}\, dV + \vec{v}_g\, \mathrm{grad}\, \xi\, dV + \xi\, \mathrm{div}\, \vec{v}_g\, dV, \tag{2.4.22}$$

or

$$\frac{d}{dt}(\xi\, dV) = \frac{\partial \xi}{\partial t}\, dV + \mathrm{div}\, (\xi\, \vec{v}_g)\, dV. \tag{2.4.23}$$

Integrating eq. (2.4.23) over a finite volume V_g corresponding to fixed values of the moving coordinates, and noting that the time derivative d/dt and the integration over V_g can be interchanged, one obtains the moving grid transport theorem

$$\frac{d}{dt}\int_{V_g} (\xi\, dV) \;=\; \int_{V_g} \frac{\partial \xi}{\partial t}\, dV \;+\; \int_{V_g} \mathrm{div}\, (\xi\, \vec{v}_g)\, dV. \tag{2.4.24}$$

When this transport theorem is applied to the equation of mass conservation (eq. (2.4.7)) one obtains

$$\frac{d}{dt}\int_{V_g} \varrho\, dV = \int_{V_g} \frac{\partial \varrho}{\partial t}\, dV + \int_{V_g} \mathrm{div}\, (\varrho\, \vec{v}_g)\, dV. \tag{2.4.25}$$

Using eq. (2.4.1) the integrand of the first integral on the right hand side of eq. (2.4.25) can be rewritten as

$$\frac{d}{dt}\int_{V_g} \varrho\, dV = -\int_{V_g} \mathrm{div}\, (\varrho\, \vec{v})\, dV + \int_{V_g} \mathrm{div}\, (\varrho\, \vec{v}_g)\, dV, \tag{2.4.26}$$

from which

$$\frac{d}{dt}\int_{V_g} \varrho\, dV + \int_{V_g} \mathrm{div}\, \left[\varrho\, (\vec{v} - \vec{v}_g)\right]\, dV = 0. \tag{2.4.27}$$

follows. Finally this equation can be reformulated applying Gauss' theorem and the definition of relative velocity (eq. (2.4.13)):

$$\frac{d}{dt}\int_{V_g} \varrho \, dV + \iint_{\partial V_g} \varrho \, \vec{v}_{\text{rel}} \, d\vec{f} = 0. \tag{2.4.28}$$

This is the continuity equation in finite volume formulation for a moving grid. The momentum and energy conservation equations can be obtained similarly.

Let V_t be the total volume of the computational grid, N the number of grid cells of volume V_c, that is, $V_t = N\, V_c$, and $\vec{j}_\xi$ the current density of a quantity ξ (i.e., $\vec{j}_\xi = \xi\, \vec{v}$). Then a scheme is called conservative, if

$$\sum_{i=1}^{N}\left[\int_{V_c(i)} \varrho\, \xi \, dV\right]^{n+1} = \sum_{i=1}^{N}\left[\int_{V_c(i)} \varrho\, \xi \, dV\right]^{n} + \left[\Delta t \iint_{\partial V_t} \vec{j}_\xi \, d\vec{f}\right]^{n} \tag{2.4.29}$$

holds. The superscripts denote that the respective terms are to be evaluated at time t^n and $t^{n+1} = t^n + \Delta t$, respectively. Because the surface integral in eq. (2.4.29) extends across the surface of the computational volume, eq. (2.4.29) says that advection *must not* change the sum of the volume integrals (with time), if the current density $\vec{j}_\xi$ is zero across the surface ∂V_t of the grid.

From eq. (2.4.29), a *sufficient* condition for any conservative difference scheme can be derived. The (approximate) evaluation of the surface integrals in eq. (2.4.29) has to be done in such a way that the flux leaving a three-dimensional computational cell (i, j, k) in the positive x-direction is identical to the flux entering the neighboring cell $(i+1, j, k)$ from the negative x-direction, and that analogous conditions hold for all other cell interfaces. Although this condition may sound trivial, it is not fulfilled, for example, when in the equation of mass conservation written in non-conservation form (eq. 2.41) the divergence operator is approximated by a centered difference operator (see Roache 1972, section III-A-3), that is, in 1D Cartesian coordinates

$$\left.\frac{\partial \varrho u}{\partial x}\right|_i \approx \frac{(\varrho u)_{i+1} - (\varrho u)_{i-1}}{x_{i+1} - x_{i-1}}\,. \tag{2.4.30}$$

2.5. Operator splitting or fractional-step coupling

A widely used technique in multi-dimensional hydrodynamics is the so-called *alternating direction implicit* or *explicit* (ADI or ADE) technique (see

Roache 1972, Beam and Warming 1978), which allows the splitting of the multi-dimensional problem into a set of one dimensional sub-problems. The ADI/E technique is a special case of the more general operator splitting or fractional-step coupling technique, described in detail by Yanenko (1971). In the following paragraphs, the main idea of this technique is discussed (see Oran and Boris 1987, sections 4–6).

The nonlinear set of coupled partial differential equations describing hydrodynamical flows can be written

$$\frac{\partial}{\partial t}\vec{U}(\vec{r},t) = \vec{G}(\vec{U},\nabla\vec{U},\nabla^2\vec{U},\vec{r},t) \tag{2.5.1}$$

where $\vec{U} = (\varrho, \varrho u, \varrho v, \varrho w, \varrho e)^T$ is the hydrodynamical state vector (u, v, and w are the three velocity components). Consider writing eq. (2.5.1) in the form

$$\frac{\partial}{\partial t}\vec{U}(\vec{r},t) = \vec{G}_1 + \vec{G}_2 + \vec{G}_3 \ldots , \tag{2.5.2}$$

where $\vec{G}$ has been broken into its constituent processes,

$$\vec{G} = \vec{G}_1 + \vec{G}_2 + \vec{G}_3 \ldots . \tag{2.5.3}$$

Each of the functions $\{\vec{G}_i\}$ contributes a part of the overall change in $\vec{U}$ during a timestep. Thus eq. (2.5.1) can be solved by successive operations, that is, $\vec{U}$ is advanced in time in several fractional steps, the first due to all processes noted $\vec{G}_1$, the second due to all processes called $\vec{G}_2$, etc. For example, $\vec{G}_1$ might contain the advection terms, $\vec{G}_2$ the gravity terms, $\vec{G}_3$ the heat diffusion term, $\vec{G}_4$ a energy source arising from a nuclear reaction network, and so forth.

The advantage of operator splitting is obvious. The processes and their interactions can be treated independently by analytic, implicit, explicit, or other techniques using the best method available for each type of term. Operator splitting further allows for and encourages modular program design. Each module (e.g., a reaction network solver, or a 1D advection solver) can be programmed and tested independently. If a new technique becomes available, the respective modules can often be modified without changing the entire structure of the code.

In general the method of splitting is often based not on a rigorous mathematical analysis but merely on numerical experiments and physical guidelines. The qualitative criterion for its validity is that the values of the physical variables must not change too rapidly over a timestep from any of the individual processes. Therefore a *warning* has to be issued here. It is by no means obvious that operator splitting is justified, nor that a solution obtained in this way is identical to the one obtained solving the original equations.

How to split the equations is a kind of art, which relies on numerical experiments and experience. However, there exists a rule of thumb, that one should avoid splitting terms which nearly cancel each other, that is, pressure gradient and gravity force terms, or terms describing the emission and absorption of photons.

Operator splitting can be used to partition multi-dimensional hydrodynamical problems into a set of one-dimensional problems. In this approach, sometimes called "dimension-splitting" and first introduced by Godunov (1959), the multi-dimensional hydrodynamical equations are integrated by means of so-called one-dimensional "sweeps." In two-dimensional Cartesian coordinates (x, y), for example, in one sweep only the advection in the x-direction is computed, followed by a sweep in the y-direction. According to Strang (1968) the order of the sweep directions should be reversed from timestep to timestep, that is, a timestep with xy-sweeps should be followed by one with yx-sweeps. This procedure guarantees that the total scheme remains second order accurate in time, if each sweep is computed with that accuracy in time, because the second order error generated in using second order one-dimensional finite difference operators $D_x D_y$ in place of second-order two-dimensional difference operators $D_{xy} = D_x + D_y$ is canceled by the error in using $D_y D_x$ subsequently. Note that here, as Woodward (1986) has shown, the sweeps must be two-dimensional in nature, if more than second order accuracy is required. Thus, operator splitting allows for a convenient modular structure of the hydro-code consisting of a 1D kernel. Once a 1D version of the code has been programmed and tested, it is quite easy to extend the code to a 2D or 3D version.

The performance of a code can be significantly improved by operator splitting. For example, consider a diffusion term which in some applications has to be treated implicitly to avoid a too-restrictive timestep limitation. On a two-dimensional Cartesian grid consisting of $NX \times NY$ grid points, the fully implicit treatment requires the inversion of a matrix of order $NX \times NY$. However, when splitting the diffusion operator into two parts which describe one-dimensional diffusion in x- and y-directions, the computational load can be reduced to the inversion of NX matrices of order NY, and NY matrices of order NX. Thus, the computational load is reduced from $(NX \cdot NY)^3$ to $NX \cdot NY^3 + NY \cdot NX^3$ operations. For $NX = NY = 100$ this translates into a speed-up factor of 5000 (2×10^8 vs. 10^{12} operations).

2.6. *Godunov-type difference methods*

Since van Leer (1979) published a second order extension of a first order difference scheme proposed by Godunov (1959) to compute hydrodynamical flows involving discontinuities, higher order schemes based on Godunov's approach have become increasingly popular (see Harten, Lax and van Leer 1983; Einfeldt and Munz 1987). Godunov's scheme is a so-called *"shock-capturing" scheme*, that is, discontinuities in the flow (shocks and contact discontinuities) do not have to be treated by special means, but are correctly described by the difference scheme itself without grid-dependent parameters (as required for artificial viscosity methods).

Godunov-type schemes belong to the class of so-called *upwind difference schemes*, where the partial differential operators are approximated by one-sided instead of centered difference operators. The direction of the one-sided differences is not fixed globally, but is locally determined by the direction of the hydrodynamical waves. This approach guarantees that the correct region of dependence of the hyperbolic hydrodynamical equations is taken into account (e.g., disturbances cannot travel upwind in a supersonic flow). The well known and widely used *donor cell method* (Gentry, Martin and Daly 1966) is an example of such an upwind scheme.

First order upwind difference schemes are robust and *monotonic* (i.e., a monotonic initial-value distribution is numerically advected such that the resulting distribution is monotonic again; van Leer 1977), but very diffusive (fig. 1). Two approaches have been proposed to reduce the numerical diffusion. In their flux-corrected transport (FCT) scheme, Boris and Book (1973) add an anti-diffusive flux to the numerical flux obtained by the upwind scheme. The anti-diffusive flux is limited in such a way that the superior properties of the upwind scheme of handling discontinuities is not lost. A second approach is due to van Leer (1979), who (as already mentioned) developed the basis for less diffusive higher-order Godunov schemes.

In Godunov-type schemes the flux difference (of the fluxes entering and leaving a computational zone) at zone interfaces is split in a right and left part, and approximated in a suitable way. Thus these schemes are also called *flux-difference splitting* schemes, and are not to be confused with the *flux-vector splitting* schemes (Steger and Warming 1981; van Leer 1982; see also Müller 1988) where the fluxes are split directly. The essential part of any Godunov-type scheme is the exact or approximate solution of a *Riemann problem* at each zone interface (see fig. 2). The following discussion of Godunov's method is taken from Einfeldt and Munz (1987).

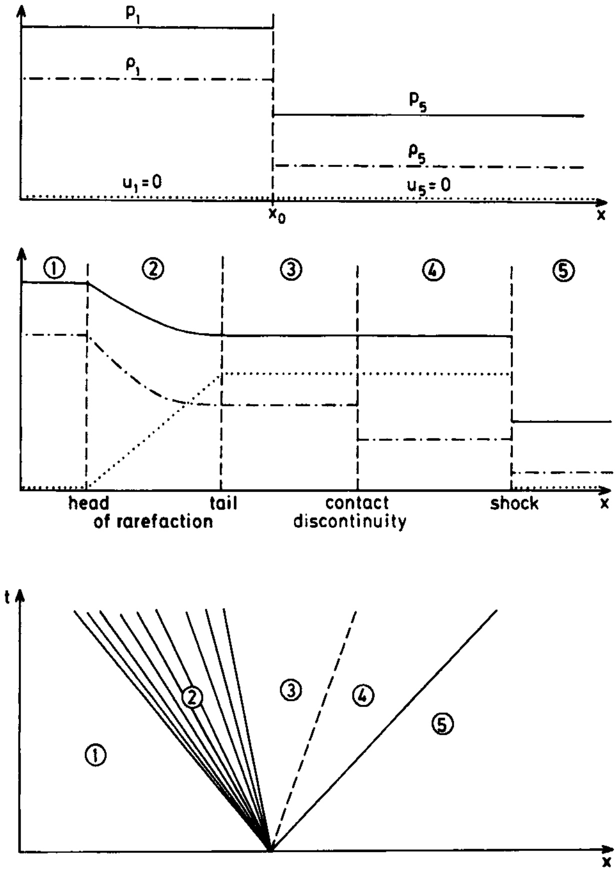

Fig. 2. Schematic solution of a Riemann problem. The initial state at $t = 0$ (top figure) consists of two constant states (1) and (5) with $p_1 > p_5$, $\rho_1 > \rho_5$, and $u_1 = u_5 = 0$ separated by a diaphragm at x_0. The time-space diagram (bottom figure) shows that after the diaphragm is removed, a shock wave (solid line) and a contact discontinuity (dashed line) move to the right, while a rarefaction (bundle of solid lines) moves to the left. Thus five distinct states occur in the flow for $t > 0$ (middle figure).

A Riemann problem is a Cauchy problem with piecewise constant *initial* data

$$\frac{\partial U}{\partial t} + \frac{\partial F(u)}{\partial x} = 0 \tag{2.6.1}$$

with

$$U(x,0) = \begin{cases} w_e & x < 0 \\ w_r & x > 0 \end{cases} . \tag{2.6.2}$$

The solution of the Riemann problem only depends on the states w_e and w_r, and on the ratio x/t, that is, $U = U(x/t; w_e, w_r)$. It consists of constant states separated by simple waves, that is, by shocks, contact discontinuities and rarefaction waves (see Courant and Friedrichs 1948).

In the original Godunov difference scheme the distributions at time t^n are approximated by piecewise constant functions (see fig. 3)

$$V(x,t^n) = V_i^n \qquad x \in I_i = [(i-1/2)\Delta x,\ (i+1/2)\Delta x]. \tag{2.6.3}$$

To obtain a numerical approximation at the next time level $t^{n+1} = t^n + \Delta t$, first solve exactly the initial value problem

$$\frac{\partial U}{\partial t} + \frac{\partial F(U)}{\partial x} = 0, \qquad U(x,t^n) = V(x,t^n), \tag{2.6.4}$$

for $t^n \leq t \leq t^{n+1}$. The solution of this initial value problem is called $U^n(x,t)$.

Each discontinuity in $V(x,t^n)$ defines a local Riemann problem. Note that there is no interaction between neighbouring Riemann problems as long as

$$\lambda A^n_{\max} \leq 1/2, \quad \lambda \equiv \frac{\Delta t}{\Delta x}, \tag{2.6.5}$$

where $A^n_{\max}$ is the maximum propagation speed at $t = t^n$. Thus $U^n(x,t)$ can be expressed by the local Riemann problems:

$$U^n(x,t) = U\left(\frac{x-(i+1/2)\Delta x}{t-t^n};\ V_i^n,\ V_{i+1}^n\right) \tag{2.6.6}$$

with $i\Delta x < x < (i+1)\Delta x$ and $t^n \leq t \leq t^{n+1}$.

V_i^{n+1}, the piecewise constant approximation of $V(x,t^{n+1})$ at $t = t^{n+1}$, is obtained by averaging $U^n(x,t^{n+1})$:

$$V_i^{n+1} = \frac{1}{\Delta x}\int_{I_i} U^n(x, t^n+\Delta t)\,dx. \tag{2.6.7}$$

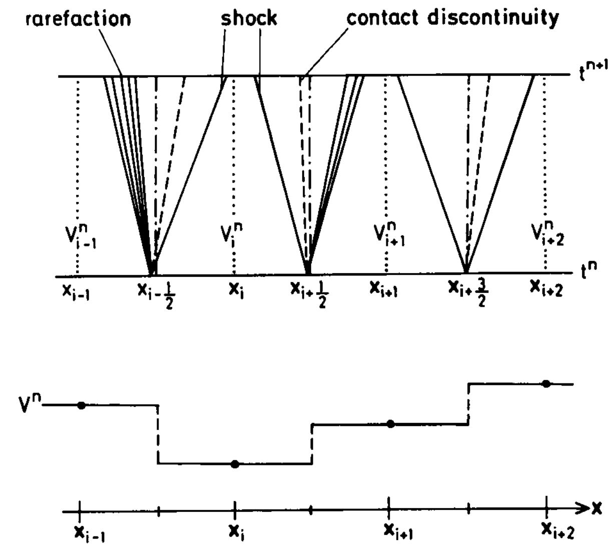

Fig. 3. Illustration of Godunov's method. The distribution at $t = t^n$ is approximated by piecewise constant states V_i^n separated by discontinuities at zone interfaces (bottom figure). The solution at the new time level $t = t^{n+1}$ is obtained by averaging over the solutions of the local Riemann problems defined by the discontinuities (top figure). The dotted and dashed-dotted lines in the top figure denote the position of the zone centers and zone interfaces, respectively.

V_i^{n+1}, like $U^n(x,t)$ (eq. (2.6.6)), can be written in terms of the local Riemann problems

$$\begin{aligned} V_i^{n+1} =& \frac{1}{\Delta x}\int_0^{\frac{\Delta x}{2}} U\left(\frac{x}{\Delta t};\ V_{i-1}^n,\ V_i^n\right) dx + \\ & \frac{1}{\Delta x}\int_{-\frac{\Delta x}{2}}^0 U\left(\frac{x}{\Delta t};\ V_i^n,\ V_{i+1}^n\right) dx. \end{aligned} \tag{2.6.8}$$

Using the integral formulation of the hydrodynamical equations in conservation form (see section 2.4) eq. (2.6.8) can be transformed into

$$V_i^{n+1} = V_i^n - \lambda\left[F(V_{i+1/2}^n) - F(V_{i-1/2}^n)\right] \tag{2.6.9}$$

with

$$\begin{aligned} V_{i+1/2}^n &= U(0;\ V_j^n,\ V_{j+1}^n) \\ V_{i-1/2}^n &= U(0;\ V_{j-1}^n,\ V_{i-1}^n). \end{aligned} \tag{2.6.10}$$

This shows that eq. (2.6.8) is in conservation form. Note also that eq. (2.6.9) gives the correct description as long as the waves emerging from the interface at $(i+1/2)\Delta x$ do not reach those emerging from the interface at $(i-1/2)\Delta x$ (see fig. 3), that is, it is sufficient to demand that

$$\lambda A^n_{\max} < 1 . \tag{2.6.11}$$

instead of eq. (2.6.5), which is the CFL condition (see eq. (2.2.3)).

Obviously Godunov-type methods require the solution of a Riemann problem (i.e., of a nonlinear algebraic system) at each zone interface. The computational effort involved has often been used as a counter argument against this class of difference methods. However, with higher-order Godunov-like schemes, such as those with the piecewise parabolic method (PPM) of Colella and Woodward (1984), the gain in accuracy more than compensates for the extra computations per zone in the case of multi-dimensional simulations (see section 2.3). For completeness note also that Godunov-type schemes have been proposed which use approximate Riemann solvers, requiring less computations per timestep compared with exact Riemann solvers (see Roe 1981, Osher 1984). These schemes are also less accurate, however.

3. Core collapse with rotation

Up until now, only a few attempts have been made to relax the assumption of spherical symmetry and to perform axisymmetric, that is, two-dimensional Type II supernova simulations, which allow the study of effects due to rotation (LeBlanc and Wilson 1970; Müller, Różyczka and Hillebrandt 1980; Tohline, Schombert and Boss 1980; Müller and Hillebrandt 1981; Bodenheimer and Woosley 1983; Symbalisty 1984; Mönchmeyer and Müller 1989a; Mönchmeyer 1989, 1991; see also Hillebrandt, Müller and Mönchmeyer 1990; Mönchmeyer et al. 1991).

It is obvious that the simulation of rotational core collapse is computationally more difficult and more expensive than a spherical collapse calculation. However, it is still surprising that only a few simulations have been performed in the past, because (i) stars and especially massive stars rotate in general (see Tassoul 1978), and because (ii) angular momentum conservation and increasing centrifugal forces allow small initial rotational energies to change the standard collapse picture completely. Therefore the inclusion of rotation may be crucial for the correct modeling of a Type II supernova explosion.

3.1. Overview of expected effects

Core stabilization. The collapse of stellar iron cores is initiated by electron captures on nuclei and free protons, and by nuclear photodisintegration processes. Both effects lower the pressure and the index $\Gamma = (D \ln P / D \ln \rho)|_M$ defined for a mass element M along its trajectory. In the absence of rotation, the core becomes dynamically unstable if $\Gamma < 4/3$.

The collapse of a non-rotating core is characterized by the formation of a subsonically and homologously (i.e., $v \propto r$) contracting inner core (IC) and a supersonically falling outer core. During collapse, the mass of the IC is roughly equal to the Chandrasekhar mass, which itself depends on the mean diminishing lepton concentration of the IC. The collapse of the IC cannot be stopped before nuclear matter densities are reached. At this stage, the adiabatic index rises sharply, which leads to "bounce" of the inner core. A shock wave is formed near the edge of the IC, and propagates outwards through the iron core. The shock wave either turns into an accretion shock inside the iron core, or reaches the stellar mantle, causing a supernova explosion. In massive iron cores, the shock suffers from severe energy losses, mainly due to the photodisintegration of nuclei, and stalls inside the core about ten milliseconds after core bounce (for a review see Cooperstein and Baron 1990; Müller 1990).

The most important difference between the collapse of rotating and non-rotating cores is that centrifugal forces in rotating cores may stop the collapse *before* nuclear matter densities are reached. This possibility was pointed out by Shapiro and Lightman (1976), and discussed in more detail by Tohline (1984), and by Eriguchi and Müller (1985; see also section 3.2). Numerical examples of such a low-density bounce have been given by Müller, Różyczka and Hillebrandt (1980), Symbalisty (1984), and by Mönchmeyer and Müller (1989a).

A theoretical argument for the stabilizing influence of rotation on (pseudo-) radial modes of stars was derived by Ledoux (1945; eq. 77). To guarantee the stability of a configuration in rotational equilibrium, the adiabatic index (at fixed entropy S and fixed electron concentration Y_e) defined as

$$\gamma = \left. \frac{\partial \ln P}{\partial \ln \rho} \right|_{S, Y_e}, \qquad (3.1.1)$$

should fulfill the condition

$$\gamma > \gamma_{\rm crit} = \frac{2}{3} \frac{(2 - 5\beta)}{(1 - 2\beta)}, \qquad (3.1.2)$$

with

$$\beta = \frac{E_{\rm rot}}{|E_{\rm pot}|} \,. \tag{3.1.3}$$

Here $E_{\rm rot}$ and $E_{\rm pot}$ are the rotational and potential energy, respectively. Although eq. (3.1.2) is only derived for slow rigid rotators with γ independent of density, numerical calculations show (see Tassoul 1978) that eq. (3.1.2) also holds under more general conditions. Equation (3.1.2) has also been used by Tohline (1984) to distinguish between stable and unstable collapsed cores.

For a given average γ, the critical value of β that a rotating core in equilibrium must exceed to be stable against pseudo-radial modes is

$$\beta \; > \; \beta_{\rm crit} = \frac{1}{2}\frac{(4-3\gamma)}{(5-3\gamma)} \,. \tag{3.1.4}$$

However, this is only a necessary condition for a core bounce at subnuclear densities (see Tohline 1984; Mönchmeyer 1991).

The stability and hydrodynamical evolution of a collapsing iron core is not determined by the adiabatic index defined in eq. (3.1.1) but instead by an *effective* index

$$\begin{aligned} \Gamma = \left.\frac{D\ln P}{D\ln\rho}\right|_M = \gamma &+ \left.\frac{\partial\ln P}{\partial\ln Y_e}\right|_{\rho,S}\left.\frac{\delta\ln Y_e}{\delta\ln\rho}\right|_M + \left.\frac{\partial\ln P}{\partial\ln Y_\nu}\right|_{\rho,S}\left.\frac{\delta\ln Y_\nu}{\delta\ln\rho}\right|_M \\ &+ \left.\frac{\partial\ln P}{\partial S}\right|_{\rho,Y_e}\left.\frac{\delta S}{\delta\ln\rho}\right|_M \end{aligned} \tag{3.1.5}$$

calculated along a collapse trajectory of a given Lagrangian mass element M (van Riper and Lattimer 1981; Cooperstein and Baron 1990; Mönchmeyer 1991). Accordingly, Γ must be used in the Ledoux-formula (eq. (3.1.2)) in place of γ, that is, the stability of the core is influenced by electron captures and non-adiabatic processes. It can be shown (Mönchmeyer 1991; Cooperstein and Baron 1990) that in realistic cores, the last two terms in eq. (3.1.5) significantly reduce Γ below the value of γ until neutrinos become trapped and weak reactions come into equilibrium at densities $\rho \gtrsim 3 \times 10^{12}$ g cm^{-3}.

Eq. (3.1.2) further shows that even a small amount of initial rotational energy can be sufficient to stabilize a core at densities less than nuclear matter density, provided that angular momentum is conserved during the collapse and that Γ has a value close to 4/3.

Collapse timescale. Due to conservation of angular momentum and the resulting increase of centrifugal forces matter does not fall in on radial trajectories. In addition, matter in the equatorial plane does not fall towards the center as fast as matter at the polar axis. This last effect especially leads to a progressive flattening of the core. In comparison to a spherically symmetric configuration, the collapse time scale is longer in rotating models.

Core oscillations. In contrast to spherically symmetric cores, which come to rest soon after bounce, the kinetic infall energy of a rotating core bouncing due to centrifugal forces is converted into oscillations, which are damped by non-spherical pressure waves. Therefore, after bounce a rotating core oscillates with a superposition of various axisymmetric radial and surface modes. The frequency of these modes is determined by the average density of the inner core. Simulations and analytical considerations show that the radial oscillations become large and nonlinear if the collapse is stopped just before nuclear matter densities are reached (Mönchmeyer 1991; see also Mönchmeyer et al., 1991).

Convective mixing. From 1D-calculations, one knows that a negative entropy gradient is established behind the shock after photodisintegration losses have weakened it significantly. This region of decreasing entropy is unstable against convection, provided that the stabilizing lepton gradient is not too large (Epstein 1979). Arnett (1985) has first pointed out the possible importance of convection for the Type II supernova mechanism. However, whether convection indeed helps or even harms the propagation of the shock is debated (Burrows 1987; Bethe, Brown and Cooperstein, 1987; Mönchmeyer 1991). Note that for rotating cores, mixing of high and low entropy matter may be enhanced if convectional currents are supported by vortices which result from rotation in regions where deformed surfaces of constant pressure do not coincide with isopycnic surfaces. On the other hand, it has been argued that rotation may have a stabilizing effect on certain types of convective instability modes (see Tassoul 1978). However, especially for centrally condensed and differentially rotating objects, the interaction of rotation and convection is not yet understood.

Shock propagation. The propagation of the shock wave is influenced by rotation because of several effects (Mönchmeyer 1989, 1991; Mönchmeyer and Müller 1989a; Müller 1990):

1. Rotation can lead to a bounce at lower densities than in the non-rotating case, which implies that the kinetic infall energy of the inner core and consequently the initial shock energy of rotating cores is reduced.

2. Rotation on the other side tends to enlarge the mass of the inner core, because it changes the velocity profile and stops the collapse due to electron captures before the mass of the inner core can shrink to values found for spherical models at bounce. Numerical results show that the mass of the inner core increases by roughly 10–20% for initial values of $0.01 \lesssim \beta \lesssim 0.02$.
3. In the outer core, the binding energy gained during collapse is transferred both into rotational *and* kinetic infall energy. According to the virial theorem, rotation acts like a $\gamma = 5/3$ gas. It therefore helps to stabilize the shock-heated matter in the gravitational potential, that is, a larger part of the dissipated kinetic infall energy can support the expansion of the heated matter behind the shock front until equilibrium is achieved, at larger radii and at lower potential energy. The resulting compressional work adds up to the work of the expanding inner core, and strengthens the shock.
4. Centrifugal forces considerably reduce the ram pressure of the supersonic flow in comparison to 1-D models.
5. The asymmetry of the supersonic flow gives rise to an angular dependent propagation speed of the shock wave. This effect is evident in the dissipation rates of kinetic energy, and in the maximum entropy values obtained behind the shock front.

Whether the combined action of these effects strengthens or weakens the propagation of the shock wave depends on the amount and distribution of the angular momentum of the core.

Tri-axial instabilities. Due to conservation of angular momentum, it cannot be excluded that configurations may form during core collapse, which are unstable against tri-axial deformations on secular or even dynamical time scales (Tohline 1984; Eriguchi and Müller, 1985), if $\beta \geq 0.14$ and $\beta \geq 0.27$, respectively (see Tassoul 1978). Whether these instabilities indeed do occur is a non-trivial question, since the equation of state at sub-nuclear densities is stiff, that is, if the adiabatic index is very close to 4/3, the core may be stabilized before its rotational energy exceeds the critical value. If, on the other hand, the initial amount of rotation is small enough for the collapse to proceed to nuclear densities, $\beta > 0.14$ may not be reached before bounce.

Observations. Finally, two effects of rotation should be mentioned which are of importance for observations of SNe. First, during the collapse of rotating cores gravitational waves are emitted (see section 3.4). Second, the non-spherical density-stratification of a rotating core before and after bounce modifies the neutrino signal in a characteristic way, and leads to a directional dependence of the ν-signal (Janka and Mönchmeyer 1989a, 1989b).

3.2. Equilibrium sequences

The idea that the properties of the core at the endpoint of its collapse can be estimated without performing a detailed collapse calculation is attributed to Shapiro and Lightman (1976). They used a virial relation to determine global properties of rotating equilibria, and examined these properties over a wide range of parameters so that guidelines could be established for more detailed hydrodynamical simulations, which have to be restricted in parameter space. This approach was later extended by Tohline (1984), and by Eriguchi and Müller (1985).

To explain the idea, let us follow Tohline (1984) and consider a *nearly spherical, adiabatic* collapse during which J, the total angular momentum, is conserved. Then define two dimensionless quantities α and β, which are the absolute value of the ratio of thermal energy to gravitational potential energy, and the absolute value of the ratio of rotational energy to gravitational energy in the core, respectively. For a spherical core of mass M and radius R,

$$\alpha \equiv \left| \frac{E_{\rm th}}{E_{\rm pot}} \right| = \frac{c^2 R}{GM} f_\alpha \,, \tag{3.2.1}$$

and

$$\beta \equiv \left| \frac{E_{\rm rot}}{E_{\rm pot}} \right| = \frac{V^2 R}{GM} f_\beta \,, \tag{3.2.2}$$

where c is the average sound speed in the core and V is the rotational velocity at the surface of the core. The quantities f_α and f_β are dimensionless structure factors of order unity, and depend on the specific structure of the rotating core.

Assuming that the pressure p is related to the density ϱ through an effective adiabatic index γ (which is allowed to vary during the collapse), Tohline (1984) then considers a homologous collapse of the rotating core. During such a collapse (which indeed occurs according to spherical collapse simulations) the factors f_α and f_β do not change. Thus at any stage during collapse

$$\alpha = \alpha_0 \left(\frac{c}{c_0} \right)^2 \left(\frac{R}{R_0} \right) = \alpha_0 \left(\frac{R}{R_0} \right)^{4-3\gamma} \,, \tag{3.2.3}$$

where the quantities denoted by subscript zero refer to the initial conditions in the core. By conservation of angular momentum (J = const. and thus $V \sim R$)

$$\beta = \beta_0 \left(\frac{v}{v_0} \right)^2 \left(\frac{R}{R_0} \right) = \beta_0 \cdot \left(\frac{R}{R_0} \right)^{-1} \,. \tag{3.2.4}$$

Combining eqs. (3.2.3) and (3.2.4) one finds

$$\alpha\beta^{4-3\gamma} = \text{ const. } = \alpha_0\beta_0^{4-3\gamma}. \tag{3.2.5}$$

For equilibrium configurations, a second condition must be fulfilled, namely the virial equilibrium condition (without surface terms):

$$E_{\rm th} + E_{\rm pot} + E_{\rm rot} = \frac{3\gamma - 4}{3(\gamma - 1)}\, E_{\rm pot}\,. \tag{3.2.6}$$

Thus

$$\alpha + \beta = \frac{1}{3(\gamma - 1)}\,, \tag{3.2.7}$$

Note that Tohline (1984) only considered the case $\gamma = 5/3$. Combining eqs. (3.2.5) and (3.2.7) one derives the relation

$$\left[\frac{1}{3(\gamma - 1)} - \beta\right] \beta^{4-3\gamma} = \alpha_0\, \beta_0^{4-3\gamma}. \tag{3.2.8}$$

Equation (3.2.8) specifies what the core's global β must be, if the core is to be in virial equilibrium following a phase of contraction.

Tohline (1984) then defines a function $F(\beta, \gamma)$, which is just the left hand side of eq. (3.2.8) for $\gamma = 5/3$. This function is very useful for a qualitative discussion of rotational core collapse. But instead of discussing $F(\beta, \gamma)$, which was derived assuming spherical adiabatic contraction, let us consider the function

$$F_{\rm EM} = \alpha\, \beta^{4-3\gamma} / \left(f_\alpha\, f_\beta^{4-3\gamma}\, f_M^{14-10\gamma}\, f_J^{6\gamma-8}\right), \tag{3.2.9}$$

of Eriguchi and Müller (1985), equivalent to $F(\beta, \gamma)$ in eq. (3.2.8), except for the additional numerically determined dimensionless factors f_α, f_β, f_M and f_J, depending on the details of structure of the rigidly and differentially rotating polytropes considered by the latter authors.

Figure 4 shows F_{EM} as a function of β for various values of the adiabatic index. Note that in fig. 4, the collapse must proceed along a horizontal line since F_{EM} is constant during collapse, if as assumed, the mass and the total angular momentum of the core are conserved during collapse. From fig. 4 it is immediately obvious that there exists only one equilibrium state for $\gamma \geq 4/3$, because F_{EM} is a monotonic function of β in this case. For $\gamma < 4/3$, however, there exist two equilibrium states with the same mass and

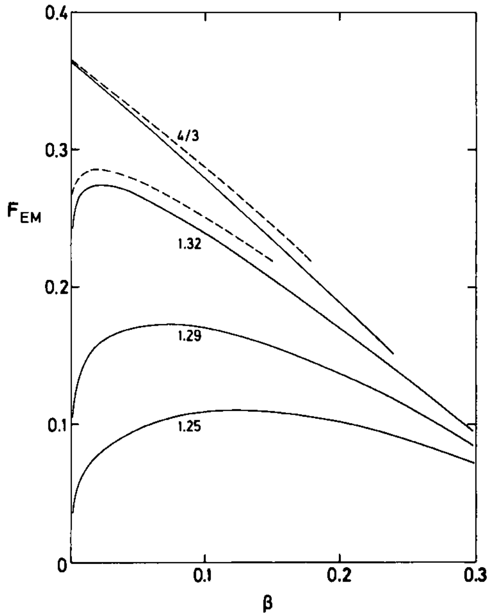

Fig. 4. Equilibrium parameter F_{EM} as a function of the (absolute) value of the ratio of rotational to gravitational energy β. The number attached to each curve is the adiabatic index γ, determined by the equation of state. The solid and dashed curves represent different rotation laws. See text for further information (from Eriguchi and Müller 1985).

the same angular momentum, one that is dynamically unstable, and the other that is dynamically stable against radial modes (i.e., collapse). For a given adiabatic index, the unstable (stable) equilibria correspond to all points to the left (right) of the maximum of $F_{EM}(\beta)$ at $\beta = \beta_{\max}$ (see Tohline 1984). Figure 4 further shows that the dependence of F_{EM} on the rotation law is very weak.

Following Tohline (1984), assume that the adiabatic index of a rotating core (with $\beta = \beta_i$) in a stable equilibrium condition suddenly decreases to a certain value smaller than 4/3, due to electron capture processes, and due to photodisintegration of heavy nuclei. In fig. 4, the drop in the adiabatic index can be envisaged by a shift down a vertical line, that is, F_{EM} decreases with $\beta = \beta_i$ being constant. If β_i is smaller than $\beta_{\max}$, defined above, the core is in an unstable equilibrium condition and must start to collapse (along a horizontal line in fig. 4) on a dynamical time scale. Eventually the core reaches a stable equilibrium configuration with the same value of F_{EM} but with a different value of β, say β_f.

Two further constraints on the core's evolution must be taken into account to predict the outcome of the collapse. The first constraint has to do with the fact that stellar cores typically start collapsing from a density of a few times 10^9 g cm^{-3}, and that therefore a density change of a factor of 10^5 will lead to neutron star densities in the core. Consequently, the basic assumption that γ is roughly constant and smaller than 4/3 is no longer valid, because the equation of state drastically stiffens ($\gamma > 2$) beyond nuclear matter density. The second constraint follows from stability considerations. It is well known that MacLaurin spheroids are secularly and dynamically stable with respect to non-axisymmetric perturbations with angular dependence $e^{im\Phi}$ and $m = 2$, if β does not exceed values of about 0.14 and 0.27, respectively (see Shapiro and Teukolsky 1983). It has been further shown that for $m = 2$ modes, the critical β's change only slightly if differentially rotating polytropes are considered (Ostriker and Tassoul 1969; Ostriker and Bodenheimer 1973; Durisen and Imamura 1981). Later Imamura et al. (1985) and Managan (1985) showed for instabilities caused by gravitational radiation reaction, that in contrast to the $m = 2$ bar mode, the secular stability limits for higher modes ($m > 2$) are quite sensitive to the compressibility and angular momentum distribution of the polytrope. In particular they found that the critical values for higher modes ($m > 2$) decrease. However, in the presence of viscosity, these gravitational radiation reaction modes are more strongly damped (Lindblom and Detweiler 1977; see also Managan 1986).

Gathering all the previous pieces of information, Eriguchi and Müller (1985) were able to predict the fate of a collapsing, rotating stellar core as a function of both the initial state, represented by β_i, and the equation of state, represented by γ. Possible evolutionary scenarios are shown in fig. 5. Initial models in the upper right part of the diagram (i.e., above the upper hatched curve) cannot collapse at all, while for those situated below the lower hatched curve, the increase in density is more than a factor of 10^5 during collapse. Thus, only initial models with parameters between these two critical curves are able to reach a final equilibrium state which is stable against radial modes (i.e., further collapse), and which has a density intermediate to white dwarf and neutron star densities. These equilibrium states can be divided into three categories: (i) states which are secularly and dynamically stable against non-axisymmetric perturbations; (ii) states which are dynamically stable, but secularly unstable, against non-axisymmetric per-

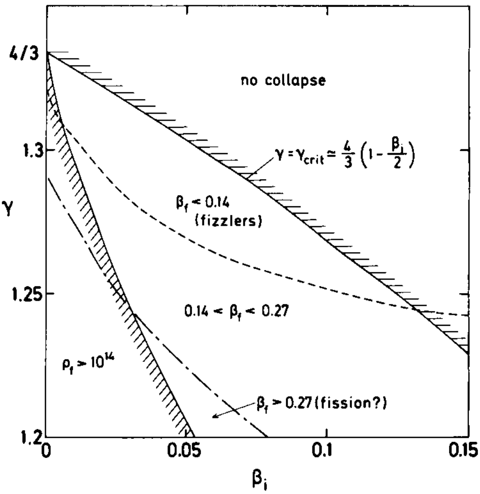

Fig. 5. Possible evolutionary scenarios of collapsing rotating polytropes as a function of the initial (absolute) value of the ratio of rotational to gravitational energy, β_i, and of the adiabatic index γ determined by the equation of state. See text for further information (from Eriguchi and Müller 1985).

turbations; and finally (iii) states which are both dynamically and secularly unstable against non-axisymmetric perturbations. Initial models belonging to the last category will probably fission, whereas initial models belonging to category (ii) and probably to category (i) will become so-called fizzlers, and collapse to neutron star densities on a secular time scale only.

3.3. Hydrodynamical simulations

The most recent and elaborate axisymmetric simulations have been performed by Mönchmeyer and Müller (henceforth MM; see Mönchmeyer 1989, 1991; Mönchmeyer and Müller 1989a; Mönchmeyer et al. 1991; see also Müller 1990). Since a review of all previous simulations is beyond the scope of this lecture, only the results of MM are discussed in the following.

MM performed four two-dimensional numerical simulations of the hydrodynamical evolution of axisymmetrically collapsing rotating $1.36\,M_\odot$ stellar iron cores. They have taken into account (i) equation of state (EOS) data based on nuclear statistical equilibrium (NSE), and Hartree–Fock calculations performed by Wolff (see Hillebrandt and Wolff 1985) in the density regime 10^6 g cm^{-3} $\leq \rho \leq 4 \cdot 10^{14}$ g cm^{-3}, (ii) electron captures on free protons, and neutrino captures on free neutrons, (iii) neutrino trapping at densities $\rho \gtrsim 3 \cdot 10^{11}$ g cm^{-3}, and (iv) local angular momentum conservation. Thus, the influence of increasing centrifugal forces, the influence of a kinetic equilibrium of the considered weak reactions at densities $\rho \gtrsim 5 \cdot 10^{12}$ g cm^{-3}, and the influence of a steep pressure rise at nuclear densities on the collapse of a stellar iron core could be studied.

The hydrodynamical equations are solved using a conservative, explicit numerical code of second order accuracy differencing (Mönchmeyer and Müller 1989b). The code is an improved version of the numerical scheme of Różyczka (1985), substantially modified to guarantee 2nd order accuracy and monotonicity constraints on moving, non-equidistant grids in curvilinear coordinates. A numerically stable and sufficiently accurate treatment of shocks is achieved by the implementation of a tensor pseudo-viscosity formalism taken from Tscharnuter and Winkler (1979).

Before discussing the properties of the rotating models of MM, it has to pointed out that the concept of homology cannot be used for rotating cores. Yet there exists a surface, which separates subsonically falling matter from supersonically falling matter, and the inner core (IC; see section 3.1) can be defined as the matter inside a surface of constant density for which the (absolute) value of the angle-averaged radial infall velocity has a maximum.

Common to all models of MM is the formation of a subsonically falling IC during collapse. About 10–20 msec before bounce, this IC begins contracting rapidly, whereby it significantly flattens due to angular momentum conservation. At bounce, the ratio of its polar to equatorial radius is roughly 1/2 in each model. The profile of the infall velocity is asymmetric during collapse, especially in the supersonic flow region. At bounce, the ratio of the maximum polar infall velocity to the maximum equatorial infall velocity typically ranges from 1.8 to 2.5, and the maximum compression of the IC in the polar direction occurs before the equatorial contraction is stopped completely.

In one model (Model B of MM) with an initial value of $\beta_i = 0.02$, centrifugal forces stop the collapse already at a central (sub-nuclear!) density of 2×10^{13} g cm^{-3}, that is, this model is a fizzler (see section 3.2 and fig. 5). Behind a rather weak shock front, a secularly stable rotating equilibrium configuration is formed in agreement with the simple equilibrium model discussed in the previous section. The further secular evolution of this configuration, which occurs due to neutrino cooling on a timescale on the order of 0.1 sec, has not yet been investigated.

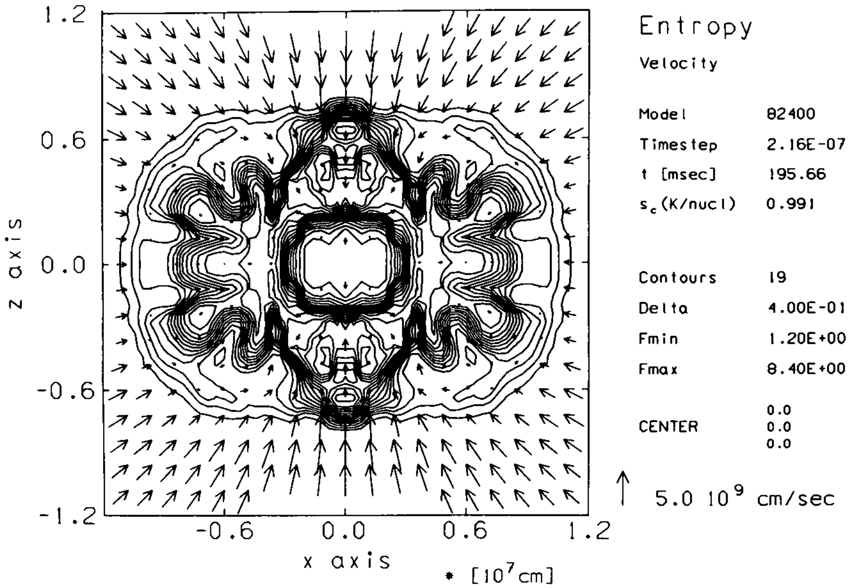

Fig. 6. Profiles of the specific entropy and flow pattern 6.5 msec after bounce, showing the instability at the edges of the high entropy region. The contours cover a range from F_{min} to F_{max} with a spacing of delta. The time, the central entropy and the velocity scale are given in the legends of the figure (from Mönchmeyer and Müller 1989a).

In a second, initially more slowly rotating model (Model A of MM; $\beta_i = 0.005$), core bounce is caused by the stiffness of the equation of state beyond nuclear saturation density (similar to non-rotating models). As a consequence, most of the kinetic infall energy of the IC is transferred to the shock within 0.3 msec after bounce. Therefore, due to the stiffness of the NEOS, the amplitudes of oscillations of the IC are small. Despite a rather small initial shock energy of only 3.6×10^{51} erg, the shock reaches a mass coordinate of $\approx 1.3\ M_\odot$ before it stalls, because of the stabilizing effect of rotation on the shocked matter. In contrast to one-dimensional models, a Rayleigh-Taylor instability develops behind the shock front (fig. 6). However, as discussed by Bethe, Brown and Cooperstein (1987), and as found in the simulation, the decrease in entropy gradient caused by the instability weakens the shock (see also section 3.1).

In a third model (Model D of MM) with $\beta_i = 0.01$, that is, intermediate to the two previously discussed models, and with an initially more differential rotation law, bounce occurs due to centrifugal forces at a sub-nuclear central density of 1.5×10^{14} g cm^{-3}. Therefore the kinetic infall energy of the IC is only 1.6×10^{51} erg. But due to the small adiabatic index of matter at sub-nuclear densities, the IC can be compressed more easily. In this model the kinetic infall energy of the IC is not directly transferred to the shock, but instead powers a large scale post-bounce expansion of the IC, which pushes the shock like an expanding piston. In addition, centrifugal forces support the expansion of the shocked matter (see section 3.1), and by the resulting adiabatic cooling of the matter part of the disintegration energy can be regained. Due to these favourable effects the shock reaches and even penetrates the silicon shell with a positive (radial) velocity, indicating a weak explosion. When the calculation is stopped, the mass surrounded by the shock surface is 1.42 $M_\odot$ (fig. 7).

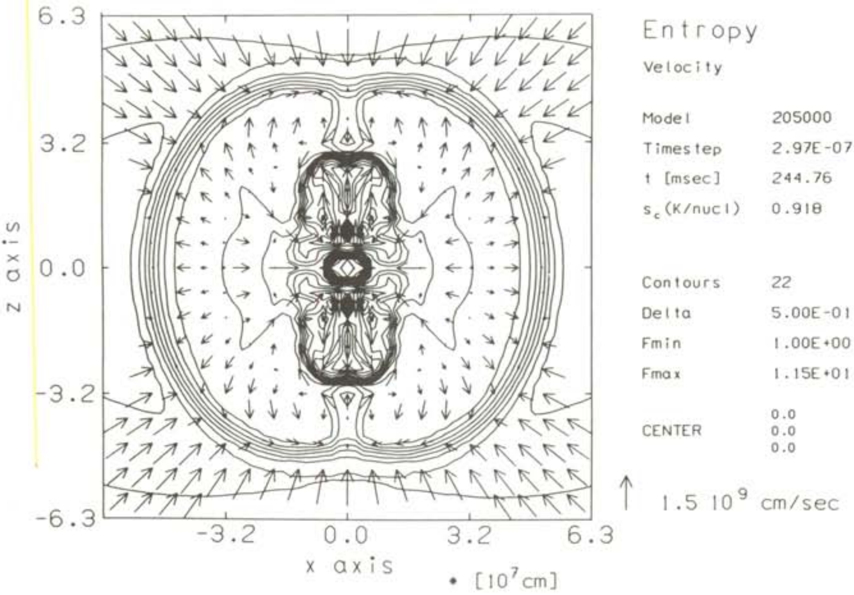

Fig. 7. Model bouncing due to centrifugal forces about 45 msec after (the first) bounce. Note the shock front, which has already penetrated the silicon shell, and the 'jet,' which rapidly expands into a polar direction (from Mönchmeyer 1989).

3.4. Gravitational radiation from collapsing rotating cores

At present, the only published gravitational-radiation data based on two-dimensional *iron core collapse* calculations are due to Müller (1982); Finn and Evans (1990); and Mönchmeyer et al. (1991). Müller (1982) has analyzed the core collapse models of Müller and Hillebrandt (1981), which were computed using a realistic equation of state and non-uniform rotation. However, the neutrino pressure was neglected in these calculations. Finn and Evans (1990) have simulated and analyzed the collapse of core models using a simplified equation of state, without any explicit treatment of the microphysics. Mönchmeyer et al. (1991) analyzed the significantly improved (in comparison with Müller and Hillebrandt 1981) axisymmetric iron core collapse models computed recently by MM (see previous section).

Before discussing the signals computed by Mönchmeyer et al. (1991), let me point out a general aspect important for any method which extracts gravitational wave data from hydrodynamical simulations. Optimal design of gravitational-wave detectors and their future application to "gravitational-wave astronomy" requires a knowledge of the expected waveforms, the corresponding frequency spectra, and the total energy emitted by possible radiation sources (for a review see Thorne 1987). Thus, any extraction method should introduce as little numerical noise as possible. The standard formulas used (e.g., by Müller 1982) for the emitted quadrupole radiation require the use of numerical approximations to the second (for the waveform; see eq. (3.4.3) below) and third (for the emitted energy and the spectrum) time derivatives of the quadrupole moment. Unfortunately, most numerical differentiation methods lead to an amplification of numerical noise inherent in the quadrupole data of a core collapse simulation. However, recent analytical work by Finn (1989), Nakamura and Oohara (1989), Oohara and Nakamura (1989), Finn and Evans (1990), and Blanchet, Damour, and Schäfer (1990) offers a significant improvement over the standard formulae for the extraction of waveforms, spectra, and emitted energy from numerical simulations. According to this work, the quadrupole signal can be expressed in terms of a volume integral over a compact region, depending only on the density and velocity as well as the gradients of gravitational potential. These quantities are accurately known because they are evaluated as part of the numerical solution of the continuity and Euler equations.

We have also developed and applied a method for obtaining smooth estimates of derivatives of a noisy signal using fast Fourier transforms. This method significantly reduces the amount of noise as compared to standard finite differences and allows the extraction of the amplitudes of the currentoctupole and the mass-hexadecapole radiation, as well as to obtain estimates of the energy emitted in these modes.

For the numerical calculation of the gravitational quadrupole radiation field, h^{TT}, Mönchmeyer et al. (1991) used an expression derived independently by Nakamura and Oohara (1989), and by Blanchet, Damour and Schäfer (1990):

$$\begin{aligned} h_{ij}^{TT}(\vec{X},t) = \frac{4G}{c^4 R} P_{ijkl}(\vec{N}) \int d^3x \Big[\rho v_k v_l &+ \frac{1}{2} x^k (f_l^{vis} - \rho \partial_l \Phi) \\ &+ \frac{1}{2} x^l (f_k^{vis} - \rho \partial_k \Phi) \Big] , \end{aligned} \tag{3.4.1}$$

where $R = |\vec{X}|$ is the distance between the observer and the source, Φ is the Newtonian gravitational potential, ρ is the mass-density, $\vec{v}$ is the velocity, and $\vec{f}^{visc}$ is the force density due to viscosity. The other quantities have their usual meaning except for $P_{ijkl}(N)$ (with $\vec{N} = \vec{X}/R$) which denotes the transverse-traceless (TT) projection operator onto the plane orthogonal to the outgoing wave direction $\vec{N}$, acting on symmetric Cartesian tensors according to

$$\begin{aligned} P_{ijkl}(\vec{N}) &= (\delta_{ik} - N_i N_k)(\delta_{jl} - N_j N_l) \\ &\quad - \frac{1}{2}(\delta_{ij} - N_i N_j)(\delta_{kl} - N_k N_l) . \end{aligned} \tag{3.4.2}$$

∂_i represents the partial derivative with respect to the x^i-coordinate. The integrand in eq. (3.4.1) is defined on a compact manifold and is known to the 2nd-order accuracy level of the numerical algorithm of the hydro-code. Eq. (3.4.1) can be shown to be equivalent to the standard representation

$$h_{ij}^{TT}(\vec{X},t) = \frac{2G}{c^4 R} P_{ijkl}(\vec{N}) \frac{\partial^2}{\partial t^2} Q_{kl}\left(t - \frac{R}{c}\right), \tag{3.4.3}$$

where the mass-quadrupole tensor of the matter distribution is given by

$$Q_{ij}(t) = \int d^3x\, \rho(\vec{x},t) \left(x^i x^j - \frac{1}{3}\delta_{ij}\vec{x}^2 \right). \tag{3.4.4}$$

It can easily be shown that evaluating the integral in eq. (3.4.1) by an integration scheme (of at least 2nd-order) is by one order of accuracy, superior to twice applying numerical time-differentiation methods to quadrupole-data which are given at discrete points of time (see Mönchmeyer et al. 1991).

The gravitational radiation field gives direct information about the second time derivative of the mass-quadrupole tensor (see eq. 3.4.4). In case of axisymmetry, the quadrupole moment, Q, is the only independent component of the quadrupole tensor. Its relations to the Cartesian components, Q_{ij}, and to the pure-spin, tensor-harmonic components, M^{E2}_{2m}, of the radiative mass-quadrupole tensor, are

$$Q \equiv \frac{3}{4}\sqrt{\frac{5}{\pi}}\, Q_{zz} \equiv \frac{c^4}{G}\frac{5\sqrt{3}}{16\pi}\, M^{E2}_{20}\,. \tag{3.4.5}$$

The wave amplitudes which result from the four MM models are shown in fig. 8; the dimensionless amplitudes h^{TT} are given by

$$h^{TT}_{\theta\theta} = \frac{1}{8}\sqrt{\frac{15}{\pi}}\sin^2\theta\,\frac{\ddot{M}^{E2}_{20}}{R}\,, \qquad h^{TT}_{\phi\phi} = -h^{TT}_{\theta\theta}\,, \tag{3.4.6}$$

and zero otherwise. θ denotes the polar angle and ϕ the azimuth angle.

The differences in hydrodynamics among the four models are reflected in characteristic features of the temporal structure of the gravitational wave signals (see fig. 8). Note in particular the different post bounce oscillation timescales, and the pronounced spike like structures with different half-widths and different amplitudes, indicating bounce events with different deceleration and acceleration time scales.

According to Mönchmeyer et al. (1991) the maximum values of the dimensionless amplitude h^{TT} for a detector-source distance of 10 Mpc range from 4×10^{-24} to 2×10^{-23}. The frequencies at maximum spectral energy density have values of 100–700 Hz, and the total energy emitted in quadrupole waves is in the range $(0.2\text{–}8.0) \times 10^{-8}\ M_\odot c^2$. Due to the very small acceleration time scale at bounce, Model A generates the strongest signal. However, compared to current detector abilities the signal is rather weak (see Hough et al. 1989, and references therein).

Concerning the temporal structure of the signals, the signal of Model A (see fig. 8) is representative of a standard type of signal. "Standard" signals with their typical *precursor–main burst–ringing down tail* pattern were already predicted for collapse processes many years ago (Ruffini 1978), and were later found by explicit simulations of different collapse processes, such as, the collapse of neutron star like configurations to rotating black holes (Stark and Piran 1985), and the collapse of stellar iron cores to neutron stars (Müller 1982).

A very remarkable outcome of the calculations of Mönchmeyer et al. (1991) is the fact that the signal structure of Model D differs qualitatively from the "standard" signal structure of Model A concerning post-bounce

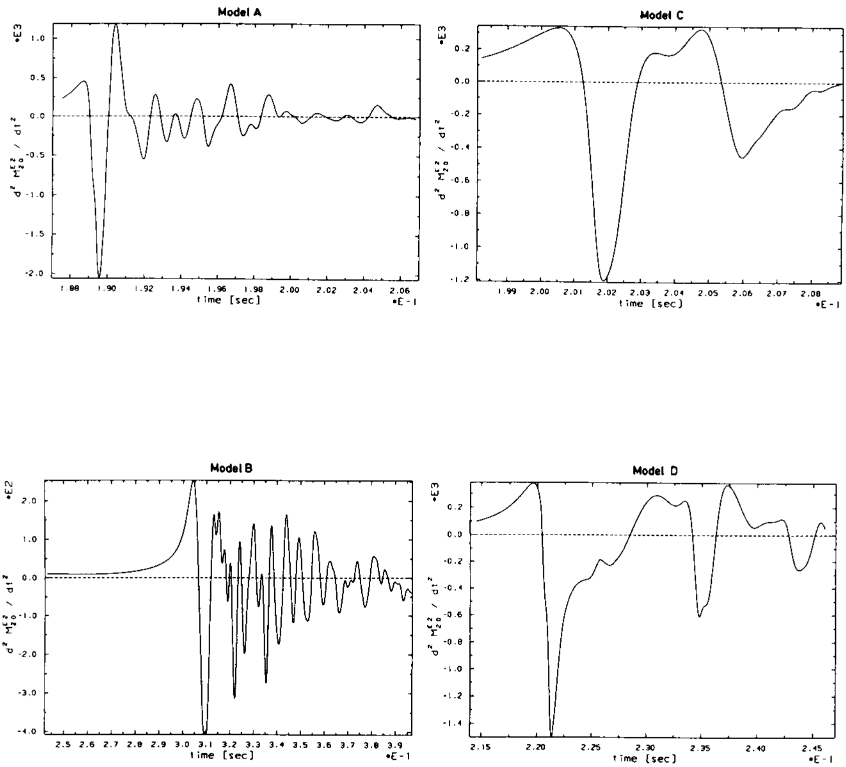

Fig. 8. Quadrupole wave amplitude (in cm) of four axisymmetric core collapse models versus time (from Mönchmeyer et al. 1991).

behaviour. The signal of Model D, whose inner core is expanding and contracting coherently, shows *two* very pronounced spikes caused by the first and the second bounce (see fig. 8). Obviously the *non-linearity* of the only weakly damped large-scale oscillation of the inner core prevents the appearance of the standard ring down of the signal, which is found for strongly damped small scale oscillations of cores collapsed to nuclear densities such as Model A (see Mönchmeyer et al. 1991). However, for times later than the computed times, the ring-down tail should eventually appear in Model D, too.

The signal of Model B is similar to a standard signal, but with a more complicated sub-structure due to the superposition of different 2D-oscillation modes. One requirement for a large scale oscillation, namely a sufficiently large excitation energy, is not fulfilled in this model. The signal of Model C shows a pattern intermediate to the signals of Models A and D (see fig. 8). This is a consequence of the fact that the dynamics of Model C shows similarities both to the dynamics of Model A *and* Model D.

4. Instabilities and mixing in Type II supernova explosions

The idea that nonradial motion occurs in the envelopes of Type II supernovae was first discussed by Falk and Arnett (1973). Some years later Chevalier (1976) used the stability analysis of Chandrasekhar (1961) to show that in the idealized case of a blast wave propagating down a power law density gradient, Rayleigh-Taylor (henceforth RT) instabilities (see section 4.2) could develop for a range of power law indices. The criterion for gas behind the shock front becoming unstable was that the density and pressure gradients should be in opposite directions (see section 4.3). The recent observations of mixing in SN 1987A (see section 4.1) have caused renewed theoretical interest in this problem. A number of multi-dimensional hydrodynamical simulations have been performed during the last two years, to determine if RT instabilities do occur in supernovae and, if they do, how much mixing would result. Some of these simulations are discussed in the remaining two sections (4.4 and 4.5) of this lecture.

4.1. Observational evidence from SN 1987A

Independent observational evidence exists that substantial nonradial motion and mixing has occurred during the explosion of SN 1987A. This evidence includes the early detection of x-rays (e.g., Dotani et al. 1987; Sunyaev et al. 1987; Wilson et al. 1988) and γ-rays (Matz et al. 1988; Mahoney et al. 1988; Sandie et al. 1988; Cook et al. 1988; Gehrels, Leventhal and MacCullum 1988; Teegarden et al. 1989), both of which can most easily be explained if radioactive ^{56}Co had been mixed from the interior regions of the star into the envelope, where the optical depth was much smaller. Assuming that the radioactive ^{56}Co is homogeneously mixed over a certain interior region of the star, Arnett (1988) found that the radius of that region has to be on the order of 20 to 30% of the stellar radius to explain the time behavior of the observed x- and γ-ray flux from SN 1987A.

Moreover, the expansion velocities inferred from the line width of infrared spectral lines of Fe II (Erickson et al. 1988; Haas et al. 1990) and of Ni II, Ar II, and Co II (Rank et al. 1988; Barthelmy et al. 1989; Witteborn et al. 1989) indicate that these elements were mixed from the slower moving inner regions of the supernova into the faster moving outer layers. According to Haas et al. (1990), the inferred expansion velocity of the bulk of the Fe II is about 2000 km/sec, and up to 4000 km/sec for a significant fraction (8 to 30%) of the iron mass. The bulk velocity is about equal to that of the supernova photosphere in April 1987, when there was no evidence for Fe and Co overabundances in the optical spectra (Höflich 1987, 1988). The observed line widths and the spectral synthesis thus imply that Fe and Co must have been mixed outward inhomogeneoulsy (i.e., in the form of clumps).

The smoothness of the light curve is also indirect evidence of a need for mixing to occur (Arnett 1988; Woosley 1988; Shigeyama, Nomoto and Hashimoto 1988). Mixing of hydrogen into the center of the star allows for a time spread in the liberation of the recombination energy, and thus helps to model the rather smooth and broad maximum observed in the light curve of SN 1987A (Shigeyama and Nomoto 1990). On the other side, mixing of heavies into the hydrogen rich envelope leads to a homogenizing of the opacity, which again smooths the light curve (see Arnett et al. 1989, and references therein).

4.2. *Rayleigh-Taylor instability*

As stated by Chandrasekhar (1961),

> The Rayleigh-Taylor instability derives from the character of the equilibrium of an incompressible heavy fluid of variable density. An important special case in this connexion is that of two fluids of different densities superposed one over the other (or accelerated towards each other).

To gain some insight into Rayleigh-Taylor (henceforth RT) instability, I will discuss two special cases in some detail.

Following Chandrasekhar (1961), consider the static case of two uniform fluids of constant density, ϱ_1 and ϱ_2, separated by a horizontal boundary at $z = 0$. The fluids are subject to an acceleration g (e.g., due to gravity) acting in a negative z-direction, and the interface between the fluids is subject to forces arising from surface tension T. Suppose further that this system is slightly perturbed. Then by a normal mode analysis of the disturbance, that is, seeking solutions of the form $\exp(ik_x x + ik_y y + nt)$, where k_x, k_y and n are constants, the following dispersion relation can be derived (Chandrasekhar 1961)

$$\tau^{-2} = gk \left\{ \frac{\varrho_2 - \varrho_1}{\varrho_2 + \varrho_1} - \frac{k^2 T}{g(\varrho_2 + \varrho_1)} \right\} . \tag{4.2.1}$$

Here the growth rate $\tau = n^{-1}$, and the absolute value of the wave vector of the perturbation $k = \sqrt{k_x^2 + k_y^2}$. According to eq. (4.2.1)

(i) if $\varrho_2 < \varrho_1$ (i.e., the lighter fluid is on top of the heavier fluid), the arrangement of fluids is *stable*, because $n^2 < 0$, while

(ii) if $\varrho_2 > \varrho_1$, the arrangement of fluids is *unstable* for all wave numbers in the range $0 < k < k_c$, where $k_c = \sqrt{(\varrho_2 - \varrho_1)\, g/T}$, but is stable for wavenumbers $k > k_c$, because surface tension succeeds in stabilizing short wavelength perturbations.

Consider a second simple case, namely that of a fluid confined between two rigid planes at $z = 0$ and $z = d$, which has an exponentially varying density $\varrho = \varrho_0 \exp(\beta z)$ with a typical (constant) density scale height β^{-1}. The corresponding dispersion relation is (Chandrasekhar 1961)

$$\tau^{-2} = g\beta \left[1 + \frac{\frac{1}{4}\beta^2 d^2 + m^2 \pi^2}{k^2 d^2} \right] , \tag{4.2.2}$$

where m is an integer ≥ 1. Obviously, the stratification is *stable if β is negative*, while it is *unstable if β is positive.* Note that the modes with shortest growth time have $m = 1$, and that if d, k, and m are given, τ is smallest if $\frac{1}{4}\beta^2 d^2 = k^2 d^2 + m^2 \pi^2$.

4.3. RT instabilities in supernova explosions

Since the energy given to the shock wave in a supernova explosion is much larger than the binding energy of the mass outside the collapsed core, gravity is dynamically unimportant for the propagation of the shock wave through the stellar envelope. Thus, as first pointed out by Chevalier, the only way to drive a RT instability is by *pressure and density gradients of opposite signs*, the *"effective acceleration"* being the (negative) pressure gradient, that is,

$$g \Longrightarrow -\frac{1}{\varrho} \frac{\partial p}{\partial r} . \tag{4.3.1}$$

To be of any consequence for the supernova explosion, the RT instability growth time, τ_{RT}, obviously must be shorter than the hydrodynamical timescale, $\tau_{\mathrm{hydro}} \equiv r_{sh}/v_{sh}$, where r_{sh} and v_{sh} are the radius and the velocity of the shock wave. Substituting g in eq. (4.2.2) according to relation (4.3.1), Chevalier (1976) derived the following RT instability criterion for power-law density distributions:

$$\left[\left(\frac{H_1}{r_{sh}}\right) \cdot \min\left\{\left(\frac{H_1}{r_{sh}}\right), \left(\frac{H_2}{r_{sh}}\right)\right\}\right]^{-1/2} \cdot \frac{c_s}{v_{sh}} > 1\,, \tag{4.3.2}$$

where $H_1 \equiv \left|(\partial \ln P/\partial r)^{-1}\right|$ and $H_2 \equiv \left|(\partial \ln \varrho/\partial r)^{-1}\right|$ are the (absolute) pressure and density scale heights, and where c_s is the local sound speed.

4.4. Simulations of RT instabilities in polytropes

Soon after the first observational evidence was obtained that instabilities and mixing had occured in SN 1987A (see section 4.1), several groups began to perform simulations of these processes. In these first studies, the density distribution of the progenitor star of SN 1987A was approximated by either a polytropic or a power-law density distribution, both of which are not appropriate, however, for a blue supergiant star (see next section).

The first of these calculations was performed by Nagasawa, Nakamura and Miyama (1989), using a three-dimensional smooth particle hydrodynamics (SPH) code for the idealized case of a shock propagating through a polytropic density distribution. They found that a small amount of mixing occurred, but probably not enough to explain the observations. However, Benz and Thielemann (1990) repeated their calculations, also using SPH, and found that the development of the instability depended very sensitively on how the explosion was initiated. They concluded that the instability found by Nagasawa, Nakamura and Miyama (1989) was probably a numerical artifact. The same conclusion was reached by Müller et al. (1989b), who repeated their calculations using several different finite difference codes in both two and three dimensions. The results for a polytropic density distribution showed no instability. However, a power-law density distribution with a power-law index in the range which was predicted to be unstable by Chevalier (1976) did show signs of a RT instability.

4.5. Simulations of RT instabilities in realistic stellar models

Realistic presupernova models have a density structure very different from that of a polytrope (see fig. 10). Thus, it was not clear whether the results obtained for polytropic and power-law density distributions could be generalized. Hence, numerical simulations with realistic stellar models had to be performed (Arnett, Fryxell, and Müller 1989; Müller, Fryxell, and Arnett 1989; Benz and Thielemann 1990; Den, Yoshida, and Yamada 1990; Hachisu et al. 1990; Yamada, Nakamura, and Oohara 1990; Fryxell, Müller, and Arnett 1991; Hachisu et al. 1991; Herant and Benz 1991; Müller, Fryxell, and Arnett 1991). Because a comprehensive presentation of this rapidly growing field is beyond the scope of the lecture, I shall concentrate on my own simulations, which were performed in collaboration with Dave Arnett and Bruce Fryxell. The most recent collection of papers on the subject can be found in Danziger et al. (1991).

4.5.1. Numerical methods

As already pointed out in section 2.3, using a highly accurate method pays for itself in multi-dimensional simulations. Thus, we performed the calculations described below with a state-of-the-art hydro-code called PROMETHEUS (see Fryxell, Müller and Arnett 1989). The code solves Euler's equations of hydrodynamics using the piecewise-parabolic method (PPM) of Colella and Woodward (1984). The method was extended to include an arbitrary number of separate fluids used to keep track of the amount of mixing of various nuclear species. Ten different elements were included in the calculations presented below, and modifications were made to handle an arbitrary, that is, non gamma-law, equation of state (Colella and Glaz 1985). The code uses sophisticated techniques to obtain very high resolution and resolve fine structure (for more details see Fryxell, Müller, and Arnett 1989).

The superior resolution capabilities of our code are illustrated in fig. 9. It shows density contours from a calculation done with PROMETHEUS using 167^2 zones in the active region (i.e., inside 1/3 of the initial stellar radius): this should be compared to fig. 2 of Hachisu et al. (1990), which has a zoning of 1025^2 in a quadrant. Although it used one-sixth the number of zones per dimension (one thirty-sixth in total), PROMETHEUS gives slightly better resolution than the Lax-Wendroff code of Hachisu et al. (1990). We do not expect that this ratio in resolution power is significantly biased by the fact that the two calculations used different initial stellar models and differed by a factor of two in seed amplitude. The calculation shown in fig. 9 required approximately 15 minutes of Cray-2 time, while the calculation of Hachisu et al. (1990) required 2 hours on a VP-200, even with their simplified physics (gamma-law equation of state; marker particles to estimate the amount of mixing).

PROMETHEUS can also handle moving grids, which is crucial for many problems and in particular, for the simulation of RT-instabilities in supernovae. For a given amount of resources (i.e., CPU and memory), moving grids allow one to obtain an effective resolution to be obtained far beyond the

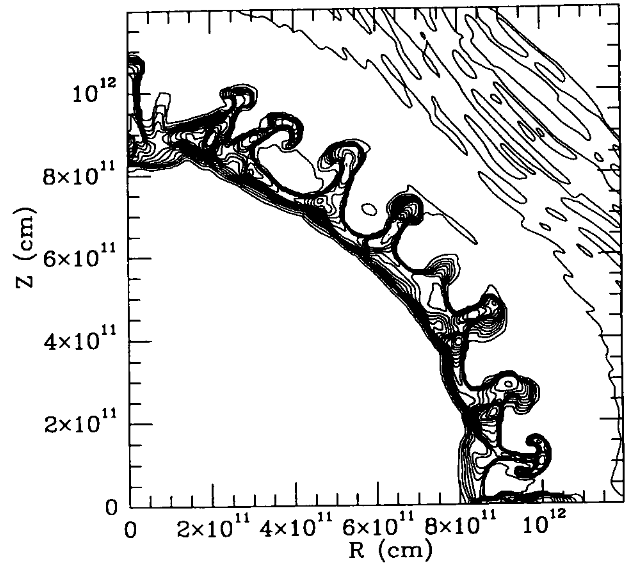

Fig. 9. Density contours from an axisymmetric model obtained with PROMETHEUS using 167^2 (equidistant) zones in the active region ($r = 10^{12}$ cm), to be compared to fig. 2 of Hachisu et al. (1990), which has a zoning of 1025^2 in a quadrant. PROMETHEUS obtained similar results with 1/6 as many zones per dimension (1/36 total) because of inherently better resolution, especially of contact discontinuities (from Fryxell, Müller, and Arnett 1991).

scope of fixed Eulerian grids. For example, a two-dimensional calculation carried out by us on a non-equidistant moving cylindrical grid of 700×700 zones achieved a resolution equivalent to 3500 equidistant (cylindrical) zones per dimension, while another two-dimensional calculation performed on a moving grid in spherical coordinates (r, θ) of 800 radial zones achieved a resolution equivalent to 4000 equidistant (radial) zones. In all two-dimensional simulations, we assume axial symmetry about the vertical axis, and equatorial symmetry, that is, in all cases the flow is calculated in one quadrant only.

The three-dimensional simulation is performed in equidistant spherical polar coordinates (r, θ, ϕ) using a $200 \times 20 \times 20$ Eulerian grid with periodic boundary conditions in angular direction at $\theta = \pi/2 \pm \pi/20$ and $\phi = \pm\pi/20$, respectively. Therefore, the angular resolution is 0.9 degrees corresponding to 100 equidistant angular zones in one quadrant.

In all simulations, the equation of state consists of contributions from radiation and the 10 Boltzmann gases (H, ^{4}He, ^{12}C, ^{16}O, ^{20}Ne, ^{24}Mg, ^{28}Si,

^{56}Fe, ^{56}Co, and ^{56}Ni), assumed to be completely ionized, and which are used to keep track of the amount of mixing of nuclear species. Both contributions (i.e., radiation and gas pressure) are important, because the effective adiabatic index varies from 4/3 to over 3/2. The variation is especially pronounced in the structures that form the instability.

4.5.2. Initial models

The initial model used in all calculations discussed in this lecture is a 15 $M_\odot$ star near the end of core carbon exhaustion, having a 4 $M_\odot$ He-core and a metallicity $z = z_\odot/4$ (fig. 10; Arnett 1987; see also Arnett, Fryxell, and Müller 1991). Using such an "early" pre-collapse model is justified, because (i) the density structure outside the oxygen core does not change significantly until the arrival of the shock wave, and (ii) the propagation of the shock inside the oxygen core cannot be correctly modeled without knowing the explosion mechanism (see also section 4.5.7).

After mapping the initial model onto a uniformly fine-zoned Eulerian grid ($\Delta r = 5\ 10^7$ cm) the explosion is artificially initiated by instantly depositing a mixture of internal (50%) and kinetic (50%) energy into the inner few zones. Note that this procedure implicitly assumes that neither the way the explosion is started (i.e., by the prompt or delayed explosion mechanism), nor possible initial asymmetries (due to the presence of rotation) influence shock propagation and the growth of the RT instability. Unfortunately, this assumption, which greatly simplifies the simulations, may have to be abandoned (see section 4.5.7).

The propagation of the shock through the central regions of the model is followed using a one-dimensional version of PROMETHEUS. This enabled us to obtain a very accurate representation of the flow behind the shock. Following the initial propagation with a one-dimensional code has an important advantage. After the initial explosion energy is put into the star, the central temperature is extremely high. As a result, the timestep required for stability is very small. Simulating the evolution of this stage with a multi-dimensional code requires enormous amounts of computer time, most of which would be wasted, since it takes some time before any multi-dimensional effects become important. Finally, a few hundred seconds after the explosion, the flow begins to become unstable and the one-dimensional results are mapped onto the multi-dimensional grid. At this point (in all models presented below at $t = 300$ sec), a random perturbation of 10% amplitude is added to the radial velocity of each zone to get the instability started. The further propagation of the shock and the development of the instability is then followed on the multi-dimensional grid using PROMETHEUS. The shock is allowed to propagate off the grid; the grid is not expanded to follow the expansion of the outer layers of the star. This allows us to keep more zones (and therefore higher resolution) in the region of the instability.

4.5.3. Linear stability analysis

According to the density and pressure profiles at 300 sec (see fig. 2 in Fryxell, Müller, and Arnett 1991) the flow is RT unstable in the mass range $0.9\ M_\odot \lesssim m(r) \lesssim 1.6\ M_\odot$ (i.e., at the He/C-O interface) and in the mass range $3.2\ M_\odot \lesssim m(r) \lesssim 4.2\ M_\odot$ (i.e., at the H/He interface). In both regions, the initial density distribution varies strongly (see fig. 10), resulting in a non-uniform shock propagation, which in turn gives rise to the unstable profiles.

To obtain a more quantitative measure of the instability, we have performed a linear stability analysis calculating the propagation of the shock wave on a fine zoned one-dimensional moving grid (1000 zones inside the He-core; 400 zones in the H-envelope).

As pointed out by Bandiera (1984), who performed a local linear stability analysis in a plane-parallel geometry, and re-emphasized by Benz and Thielemann (1990) the RT growth rate

$$\sigma_{RT} = \frac{c}{\gamma} \sqrt{-\gamma \mathcal{P} \mathcal{R}}, \tag{4.5.1}$$

Density (top) and chemical composition (bottom) vs. mass for derived for an incompressible fluid, only gives a lower limit to the actual "convective" growth rate

$$\sigma_C = \frac{c_s}{\gamma} \sqrt{\mathcal{P}^2 - \gamma \mathcal{P} \mathcal{R}}. \tag{4.5.2}$$

Here $c_s, \gamma, \mathcal{P} = d \ln P/dr$, and $\mathcal{R} = d \ln \rho/dr$ are the sound speed, the adiabatic index, and the reciprocals of the pressure and density scale height, respectively. The integrated growth rates

$$\Sigma_{RT} = \int_0^t \sigma_{RT}\, dt' \quad \text{and} \quad \Sigma_C = \int_0^t \sigma_C\, dt', \tag{4.5.3}$$

are shown as a function of interior mass in fig. 11 at different times. The growth of any perturbation ξ_0 over a time t can then be estimated from $\xi/\xi_0 = \exp(\Sigma_{RT})$, and from $\xi/\xi_0 = \exp(\Sigma_C)$, respectively.

Two prominent peaks centered at $m(r) \approx 1.3\ M_\odot$ and at $m(r) \approx 4.0\ M_\odot$ are already clearly visible in fig. 11 at $t = 600$ sec. Between the peaks, a narrow stable layer exists, extending from about $1.7\ M_\odot$ to $2.3\ M_\odot$. The convective growth rates are found to be about one order of magnitude larger than the corresponding RT growth rates, that is, RT stable mass layers are moderately unstable if the less restrictive convective (Schwarzschild) criterion

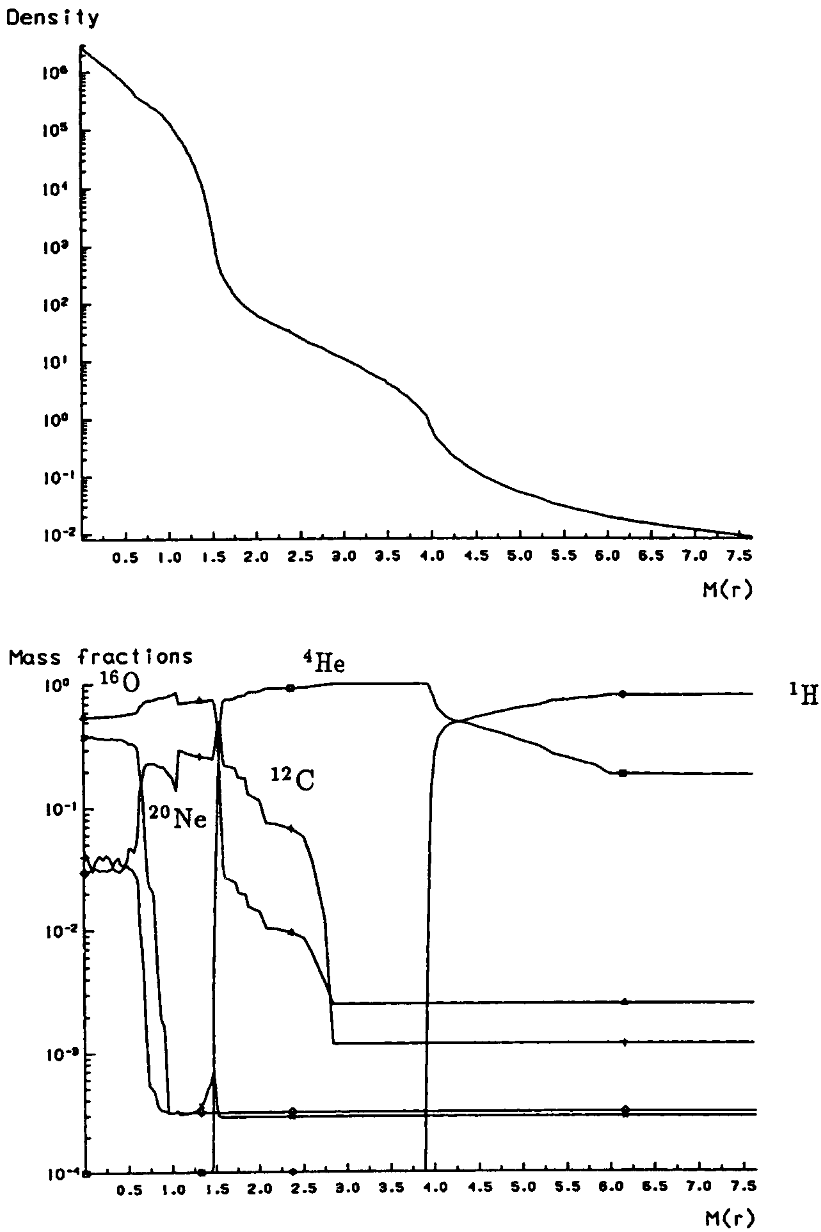

Fig. 10. Density (top) and chemical composition (bottom) vs. mass for the innermost 7.5 $M_\odot$ of the 15 $M_\odot$ stellar model of Arnett (1987). The model has a 4 $M_\odot$ helium core, a 1.5 $M_\odot$ oxygen core, and a metallicity $z = z_\odot/4$. The density profile shows two steep drops, occurring at the H/He and He/C-O interfaces. These regions become unstable due to the passage of the shock (from Müller, Fryxell, and Arnett 1991).

is used. Figure 11 further shows that the instability at the He/C-O interface is much more pronounced than at the H/He interface, and that the ratio of the maximum growth rates at both interfaces increases if effects due to compressibility are taken into account.

4.5.4. Results of two-dimensional simulations

According to the results of the linear stability analysis, the 15 $M_\odot$ model should show pronounced instabilities, both at the H/He interface and at the He/C-O interface. Our previous calculations (Fryxell, Müller, and Arnett 1991), which used up to 500 × 500 equidistant zones, are not decisive in this respect. Early snapshots of the evolution figs. 12a (t = 3433 sec) and 12b (t = 5405 sec) clearly show the growth of the RT instability at the outer edge of the He-shell, that is, at the H/He interface. However, whether the instability also grows at the He/C-O interface (its position corresponds to the concentration of contour lines at the trailing edge of the expanding mass shell in fig. 12a) is less obvious, although a careful inspection of figs. 12a and 12b suggests the growth of the second instability.

To clarify this point, we performed an additional simulation using 1000 × 1000 equidistant zones. All other parameters were identical to the 500^2 simulation, that is, the explosion energy was 10^{51} erg, and a random perturbation of the (radial) velocity of 10% amplitude was imposed at t = 300 sec. Figs. 12c (t = 3039 sec) and 12d (t = 5534 sec) show snapshots of the density distribution obtained on the 1000^2 grid at roughly the same time as those displayed in figs. 12a and 12b, respectively. The higher resolution run shows without doubt that two separate RT instabilities occur in the 15 $M_\odot$ stellar model, and that both reach the nonlinear stage characterized by narrow finger-like structures which are topped by "mushroom caps." These "caps" actually develop as a result of the Kelvin-Helmholtz instability, that is, due to the instability of shear flow at the edge of the fingers, inside of which matter flows faster than outside. Both instabilities are already far into the nonlinear regime one hour after the beginning of the explosion, but they are still spatially separated at this stage (fig. 12c). Roughly half an hour later the instabilities have begun to interact, producing "mushrooms inside mushrooms" (fig. 12d).

Having resolved both instabilities on the 1000^2 grid is a substantial improvement compared to our previous calculations, but the question remains, whether the improvement is sufficient to obtain a converged solution. For obvious reasons, another doubling of the grid size (i.e., 2000 zones per dimension, 4 times more memory and most importantly 8 times more CPU time) was not practical, since the 1000^2 run already took 180 CPU-hours on a Cray-2. Instead PROMETHEUS was modified to handle moving grids,

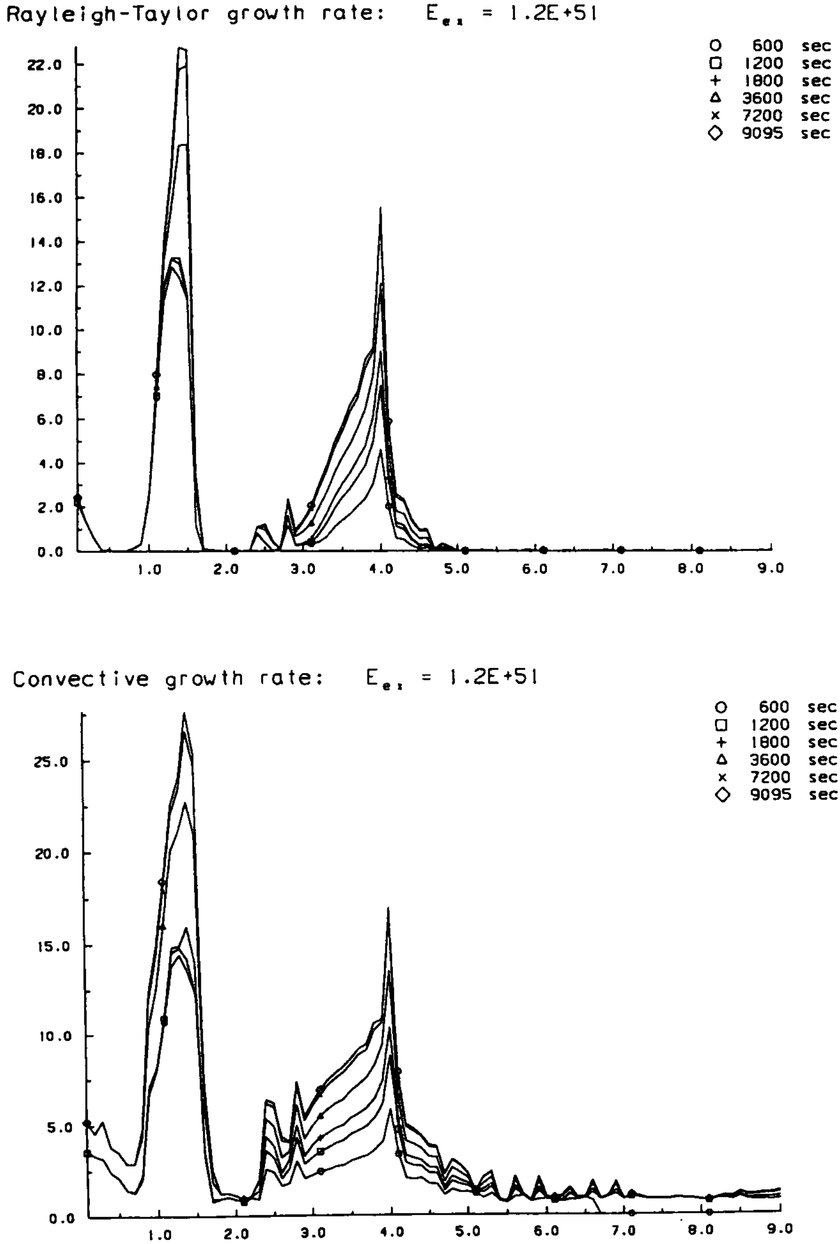

Fig. 11. Integrated RT (top) and convective (bottom) growth rates vs. mass at different times for the 15 $M_\odot$ stellar model of Arnett (1987). Obviously, a strong instability is predicted by the local linear stability analysis, both at the H/He and at the He/C-O interface (from Müller, Fryxell, and Arnett 1991).

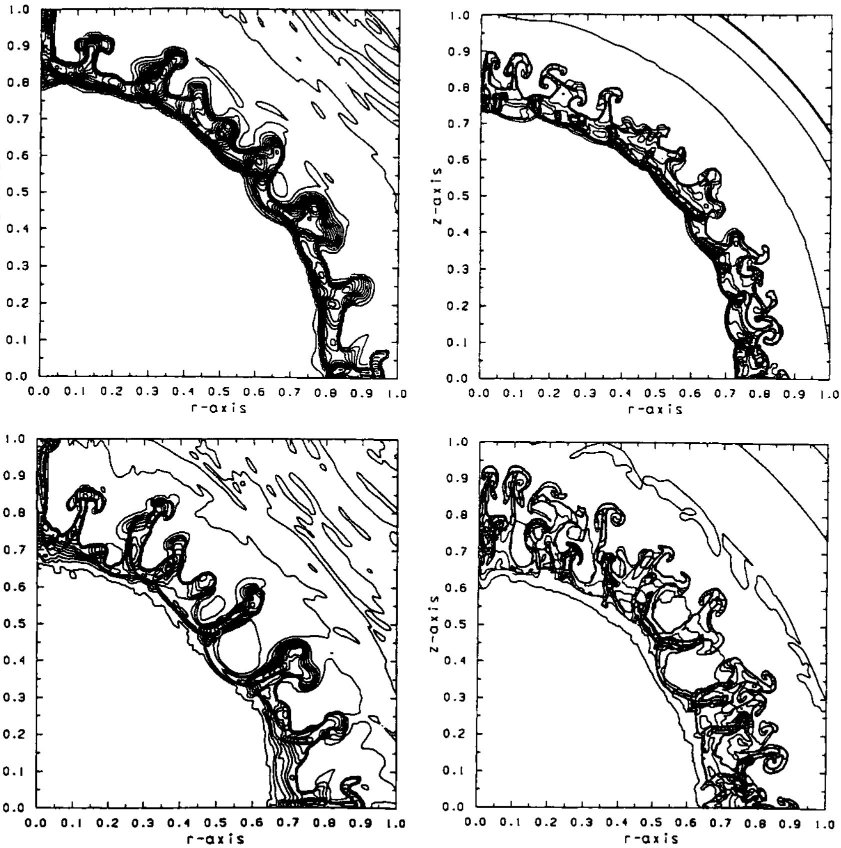

Fig. 12. Density contours (equally spaced on a linear scale) showing the evolution of the RT instability at different numerical resolutions for an explosion energy of 10^{51} erg and an initial random perturbation of 10% amplitude. The two figures on the left (12a, top; 12b, bottom) are from a calculation using 500×500 zones, while the figures on the right (12c, top; 12d, bottom) are from a calculation using 1000×1000 zones. There is rotational symmetry about the vertical axis, and equatorial symmetry about the horizontal axis. The axes are labeled in units of 1.0×10^{12} cm (12a and 12c) and of 1.5×10^{12} cm (12b and 12d), respectively (from Müller, Fryxell, and Arnett 1991).

which are also essential when trying to follow the evolution into the epoch of ^{56}Ni-decay. The grid is moved in such a way that 500 zones always remain inside the unstable region (in the radial direction), resulting in a resolution equivalent to up to 4000 equidistant (radial) zones for the whole star.

Figure 13 shows three snapshots of the evolution obtained with a moving grid of 800 × 400 zones in spherical coordinates 3.09×10^3 (fig. 13a), 5.04×10^3 (fig. 13b), and 1.72×10^4 (fig. 13c) seconds after the onset of the explosion. One sees both instabilities grow (fig. 13a) and then interact (fig. 13b). In the final model (fig. 13c), the He-shell is shredded into clumpy fragments, and the density contrast exceeds a value of five. Note that even five hours after the explosion, the instabilities are still distinguishable. The interaction produced dense blobs of matter (red in fig. 13c) originally located at the He/C-O interface, which almost reached the outer edge of less dense structures (yellow in fig. 13c) which formed as a consequence of the RT instability at the H/He interface. The shredding of the He-shell becomes more obvious from fig. 13d, which shows the spatial distribution of the helium mass-fraction in the final model.

We have obtained quantitatively quite similar results using a moving grid of 700 × 180 zones in spherical coordinates. Comparing the results of both calculations indicates that a radial grid of 500 zones inside (and 200 to 300 zones outside) the helium core is sufficient to resolve the instability in the 15 $M_\odot$ stellar model, because the preferred scale of the RT instability given by the density scale height of the unstable layer can then be resolved. The comparison further indicates that in the angular direction, at least 150 to 200 zones are required for an adequate description of the instability.

Taken together, the new results strongly suggest that we have resolved all main features of the instabilities caused by shock passage through the 15 $M_\odot$ stellar model, insofar as we can speak of a converged solution. However, there are still significant differences as far as specific details of the structure of the "turbulent" layer and the amount and extent of mixing are concerned (see section 4.5.6).

4.5.5. Results of three-dimensional simulations

What happens to the instability when the restriction of axial symmetry is relaxed? To answer this question, we have performed a preliminary three-dimensional calculation using periodic boundary conditions in angular direction (Müller, Fryxell, and Arnett 1989). The angular periodicity is introduced, because (i) in 2-D calculations, the amplitude, frequency, and radial position of the instability show no significant dependence on angle, and (ii) fewer computer resources are required. Of course, the dependence of the solution on the extension of the angular grid must be studied while keeping the angular and radial zone size fixed. In addition, one has to use a moving grid in the radial direction to improve resolution as discussed above. We are currently investigating these questions.

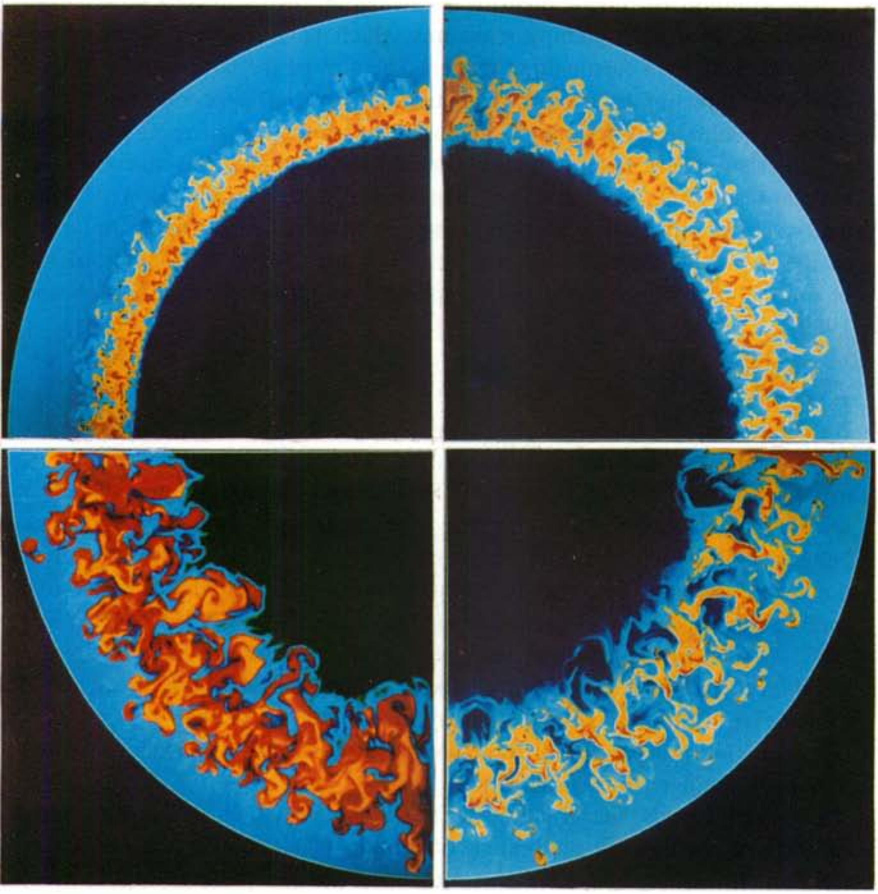

Fig. 13. Color-coded density plots (decreasing from red via yellow and light blue to dark blue), plots showing the evolution of the RT instability on a moving grid of 800×400 zones, in spherical coordinates, for an explosion energy of 10^{51} erg, and an initial random perturbation of 10% amplitude. The snapshots are taken at $t = 3.09 \times 10^3$ sec (13a; top left), $t = 5.04 \times 10^3$ sec (13b; top right), and $t = 1.72 \times 10^4$ sec (13c; bottom right), respectively. The plots show only a part of the (moving) computational grid up to a radius of 1.0×10^{12} cm (13a), 1.4×10^{12} cm (13b), and 3.0×10^{12} cm (13c), respectively. Fig. 13d (bottom left) shows the distribution of the helium mass fraction corresponding to the density in fig. 13c. The helium shell (yellow and red) has been shredded by RT instabilities (from Müller, Fryxell, and Arnett 1991).

The preliminary three-dimensional calculation also shows a pronounced instability, producing clumpy structures which have up to a factor of ten higher density than surrounding matter. The size of the structures is limited in angular direction by the grid resolution. The overall appearance of the instability qualitatively resembles the coarse two-dimensional results obtained on Eulerian spherical grids with 200 equidistant radial zones and a similar angular resolution. Note, however, that without the assumption of axial symmetry, genuine three-dimensional clumpy structures form. This "similarity" of the two- and three-dimensional results is also found when the amount of mixing in different models is compared (see Müller, Fryxell, and Arnett 1989).

4.5.6. Mixing

By computing the advection of several separate fluids, each of which represents a different nuclear species, it is possible to determine the amount of mixing which occurs in each model. Both our previous simulations and our new high resolution simulations show that the material outside (inside) the helium shell, which is mostly hydrogen (heavy elements), has been pushed downward (upward) into the inner (outer) layers of the expanding supernova shell. This is consistent with the spectral analysis of SN 1987A (Höflich 1987, 1988). In like manner, helium is mixed inward and outward by the instability. This is a macroscopic mixing process in which large fragments of material of different composition are mixed together, rather than a microscopic mixing process in which the composition is mixed together to form a region of homogeneous composition.

On coarser grids, the instability is less resolved, which leads to an overestimate of the amount and extent of mixing. This can be understood as follows. In our lower resolution simulations, the morphology of RT instability is characterized by a few relatively straight finger-like structures, the length of these fingers determining the extent (in radius or velocity) of mixing (see Fryxell, Müller, and Arnett 1991). When the resolution is increased, the fingers are no longer straight, because of the Kelvin-Helmholtz instability, which was not resolved before. Due to the Kelvin-Helmholtz instability, the fingers become bent, and thus extend less far out in radius (see fig. 13c). As can be seen from fig. 14, the extent of mixing in the calculation using an equidistant cylindrical grid of 1000×1000 zones is overestimated by about 5% in velocity space as compared to a simulation using a moving spherical grid of 700×180 zones. This difference is much less than that between the 1000×1000 run and the old 500×500 calculation, which gave an about 30% larger maximum velocity of the "metals" (see fig. 18 in Fryxell, Müller, and

Arnett 1991). The three results, taken together, suggest that our latest two-dimensional simulations have sufficient resolution to determine the extent of mixing with an error of a few percent only.

4.5.7. Implications

Column densities. The (local) density contrast produced by the RT instability can be up to a factor of 10 in some places. The variation in column density (i.e., the angular variation in radially integrated density) is about a factor of 1.5 in the highest resolution run (800×400 zones) for the 15 $M_\odot$ stellar model. This is somewhat less than the variation in the calculation done on the 1000^2 grid, but almost a factor of two less than the variation in our older calculations, performed on a grid of 500^2 zones (see Fryxell, Müller, and Arnett 1991). This dependence of the variation in column density on grid resolution supports our previous statement that our latest simulations have reached a numerical resolution adequate to the problem. Density variations (clumping) of the order mentioned above would decrease the diffusion time for escaping gammas and thermal photons. Mass estimates from diffusion times would be less than the actual masses. Such an error could be significant for SNIb's.

Dependence on stellar model. We have demonstrated that in the 15 $M_\odot$ stellar model of Arnett (1987), the RT instability caused by the propagation of the shock wave through the star is pronounced and gives rise to a significant amount of mixing. However, several important questions remain open. Does the instability also occur in other stellar models, and if so, is the amount and the extent of mixing comparable or very different? The first question has been positively answered by the two-dimensional calculations of Hachisu et al. (1990, 1991), who investigated a 20 $M_\odot$ stellar model (with a 6 $M_\odot$ helium core) for SN 1987A, and three helium star models of 3.3, 4.0, and 6.0 $M_\odot$ as Type Ib/Ic supernova progenitors, and also found pronounced RT instabilities. Their results qualitatively show that mixing of the ejected material seems to be more extensive for smaller mass stars. However, further high resolution two-dimensional and three-dimensional calculations are definitely required to quantitatively determine the dependence of the extent of mixing on the stellar model.

As a step in this direction, we have begun to examine a 20 $M_\odot$ star at the onset of collapse with a 6 $M_\odot$ He-core and a metallicity $z = z_\odot/3$ (Arnett 1987; see also Arnett, Fryxell, and Müller 1991). According to the linear stability analysis, significant growth rates are predicted, both at the H/He, and at the He/C-O interface, the latter, however, being significantly less than in the 15 $M_\odot$ model. First and still preliminary (because of the coarse grid)

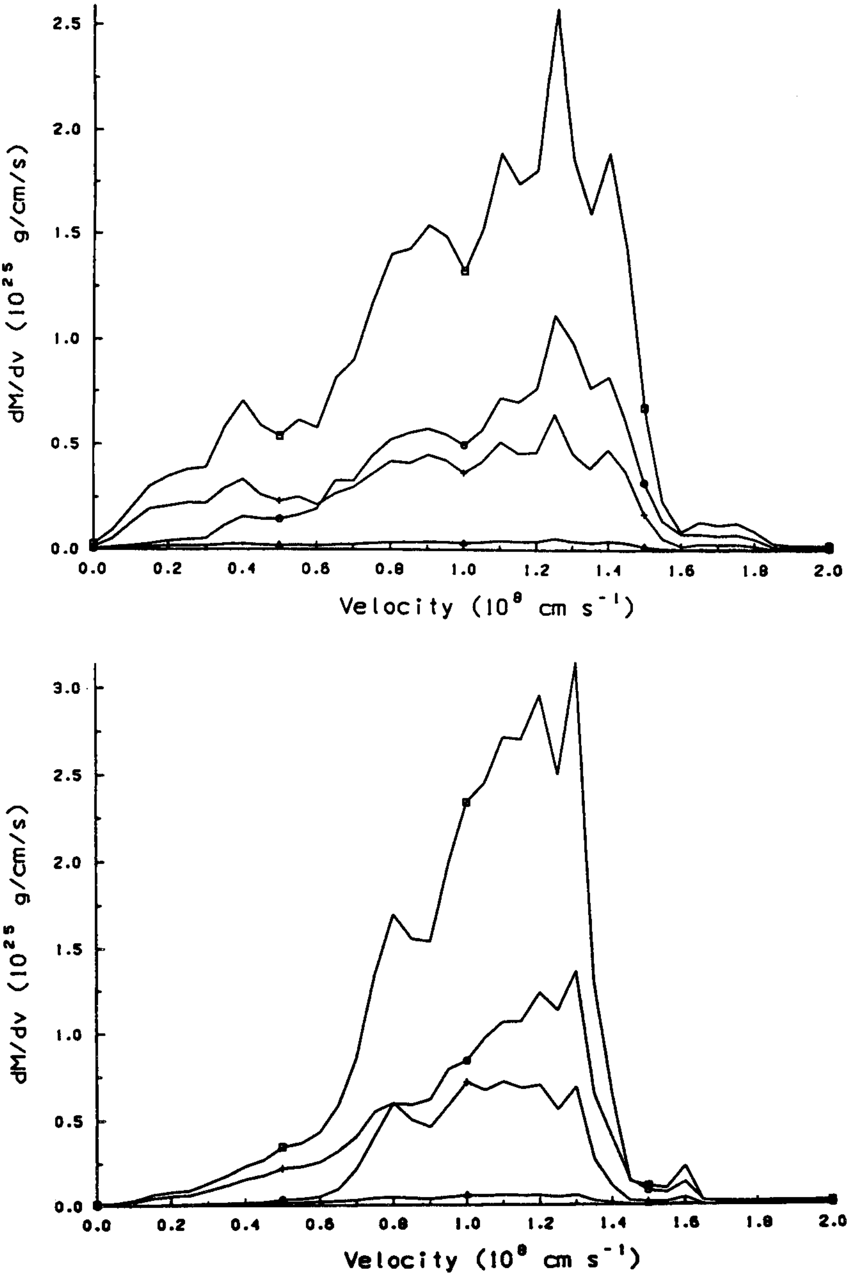

Fig. 14. Abundances of four nuclei (^{12}C, ^{16}O, ^{20}Ne, and ^{24}Mg; from top to bottom) in terms of the mass per unit velocity interval dM/dv versus radial velocity, for an explosion energy of 10^{51} erg, and an initial random perturbation of 10% amplitude. Figure 14a (top) shows the results obtained on an equidistant cylindrical grid of 1000 × 1000 zones, while the results given in fig. 14b (bottom) are obtained on a moving spherical grid of 700 × 180 zones (from Müller, Fryxell, and Arnett 1991).

two-dimensional calculations show a pronounced instability at the H/He interface, and a weak instability at the He/C-O interface. Furthermore, due to the more massive He-core of the 20 $M_\odot$ model (6 $M_\odot$ instead of 4 $M_\odot$), the stable mass layer between the unstable interfaces (the so-called "stability gap") has a mass almost twice as large for the 20 $M_\odot$ model (1.1 $M_\odot$) as for the 15 $M_\odot$ star (0.6 $M_\odot$). In the preliminary calculations, an interaction of both instabilities could not be observed, and thus a smaller extent of radial mixing is found, which is consistent with the result of Hachisu et al. (1991) that less massive stars show more extensive mixing. Most interestingly, however, the strength of the instability at the He/C-O interface seems to be not independent of how the explosion is initiated, i.e., it is sensitive to the explosion mechanism. If confirmed, this would mean that the assumption underlying all RT simulations performed up to now, namely that the formation of the shock wave and its propagation can be studied independently, is not justified. The consequence would obviously be a drastic complication of the problem.

The epoch of ^{56}Ni-*decay.* The amount of mixing, and in particular the amount of mixing of radioactive ^{56}Ni found in the simulations during early phases of the evolution of the supernova, is insufficient to explain the observations. However, the ^{56}Ni, which is formed in the explosion and pre-mixed by early instabilities modeled in the simulations up to now, undergoes radioactive decay on a timescale of about a week. This might have a significant effect on the amount and extent of mixing.

Note that due to the decay of ^{56}Ni and ^{56}Co, a significant amount of energy is released, some of which goes into kinetic energy. Thus, it does not seem unlikely that the material, which initially was inside the helium shell (this includes the radioactive ^{56}Ni), and which was mixed out to a peak velocity of $\approx$ 1500 km s^{-1} (see fig. 14), could be accelerated even further. That this effect indeed works has recently been demonstrated by two-dimensional (SPH) calculations performed by Herant and Benz (1991), who showed that the mixing induced by RT instabilities occurring during the first few hours is substantially modified at later times by the radioactive decay of ^{56}Ni and ^{56}Co, increasing the peak velocity of the nickel and its decay-product, iron, by approximately 30%.

These "boosted" iron velocities are consistent with the velocities deduced from infrared iron lines for the bulk of the observed Fe (Haas et al. 1990). However, they fail to explain the high velocity wings of the lines, which extend to velocities $\gtrsim$ 3000 km/s, and which (according to Haas et al. 1990) represent from 8 to 30% of the iron. The 17.94 and 25.99 μm [FeII] line profiles observed by Haas et al. (1990) also contain an unresolved 3–5σ

emission feature (see their fig. 1), which can be interpreted as a high velocity clump of material, containing $\approx 3\%$ of the total iron mass, and moving with a velocity of about 3900 km/s.

Although three-dimensional calculations of the ^{56}Ni-decay epoch are still missing, and therefore the present results have to be taken with some care, they strongly indicate that the mixing induced by RT instabilities in the envelope is probably not sufficient to quantitatively explain the observations of SN 1987A. This failure again may be taken as evidence that the formation of the shock wave and its propagation cannot be studied independently. A very early mixing already during the epoch of shock formation, that is, mixing induced by the RT unstable hot neutrino bubble created in the late time neutrino explosion scenario (Colgate 1991) may be required to resolve the discrepancy between observations and simulations.

5. Thermonuclear burning fronts and Type Ia supernovae

The numerical simulation of thermonuclear burning fronts lies at the heart of any model of Type Ia supernovae, currently thought to be produced by the thermonuclear explosion of accreting carbon-oxygen white dwarfs (see the lectures of Barkat, Canal, Nomoto, and Woosley). As various models proposed since the pioneering work of Arnett (1969) will be discussed in great detail by other lecturers, I shall focus in this lecture on the physics and numerics of thermonuclear burning fronts, and only refer to astrophysical models where necessary. Recent reviews on Type Ia supernovae can be found in Khokhlov (1989a), Wheeler and Harkness (1990), and Woosley (1990).

5.1. General considerations

Three types of combustion waves have been widely used in astrophysics to date: thermal, detonation, and deflagration waves. In a "thermal" wave, the matter is stationary while a heating wave moves through, and the fuel is consumed at elevated temperatures. This corresponds to "radiative" burning in stellar evolution. Almost all calculations have been carried out with an assumption of spherical symmetry, and hence are one-dimensional. It is important to note that there is no convective transport in such 1-D problems. To allow for convective motion, some prescription for mixing of composition, energy, and momentum must be added. It is usually presumed that the mixing is fast compared to the nuclear consumption of fuel, so that coupling is simple. Thus, we have a sort of "modified thermal" wave, with highly subsonic mixing motions. With reasonable zoning, such an approach seems satisfactory, although the behavior of the boundary of the convective zone may cause some worry. After helium burning, this approach becomes more and more suspect. In particular, in shell burning with neutrino cooling, the flame zone and the edge of the convective zone are unresolved, even within the conceptual simplification of the algorithm.

A detonation wave is one in which the fuel is heated to ignition by compression associated with a shock wave, and the released energy drives the shock in turn. It is the most violent sort of combustion wave. A deflagration wave is one in which the fuel is heated to ignition by the transport of heat from the already-burned matter, and the energy released is transported to heat new fuel to ignition. The nature of the transport makes possible a much more complex set of phenomena. Strictly speaking, we should examine transport by radiative diffusion and by conduction, but not by "convection." Such "convection" is part of the hydrodynamic process, and should not be hidden in a phenomenological description of heat flow; unfortunately that has been done in extensive discussions of the "Carbon Deflagration" supernova mechanism.

There are two separate time scales for burning which must be considered. The first is the *ignition time scale* of the fuel, defined to be the temperature e-folding time

$$\tau_{\mathrm{T}} = \frac{T}{\dot{T}} \approx \frac{C_V T}{\dot{\epsilon}_{\mathrm{nuc}}}, \tag{5.1.1}$$

where $\dot{\epsilon}_{\mathrm{nuc}}$ is the energy release rate of the nuclear processes, and C_V is the specific heat. Because charged-particle reactions are heavily modified by Coulomb barrier penetration, this time scale strongly decreases with increasing temperature. The second important timescale is the *burning time*, that is, the time to significantly reduce the abundance of fuel, which is defined as

$$\tau_i = \frac{X_i}{\dot{X}_i} = \frac{Y_i}{\dot{Y}_i}, \tag{5.1.2}$$

where X_i is the mass faction of species i, and Y_i is the mole number, obtained by dividing the mass-fraction by the atomic weight of the species. In simple cases, this differs from τ_T by the ratio of the thermal energy content to the Q-value for the reaction (per unit mass burned). For example, for ${}^{12}\mathrm{C} + {}^{12}\mathrm{C}$ this ratio is 0.25 T_9, where T_9 is temperature in units of 10^9 K; this is on the order of unity at explosive temperatures. For comparison, the ratio is about 0.005 for hydrostatic hydrogen burning by the CNO cycle. This ratio can also approach zero in explosive situations, if the matter is degenerate. In this case, the specific heat approaches zero, so that consumption of a small amount of fuel gives a large change in temperature.

Finally, two timescales associated with hydrodynamic motion must be considered. The first is the time for a region to react to a pressure imbalance, which is taken to be the *sound travel time*

$$\tau_{\text{hyd}} = \frac{\delta r}{c_s}, \tag{5.1.3}$$

where c_s is the local sound speed, and δr is the size of the region. Finally, there is the time for a convective element to move through the region in which convection occurs (obviously an oversimplification of a complex process). This *convective time scale* is defined by

$$\tau_{\text{conv}} = \frac{\delta r_{\text{conv}}}{v_{\text{conv}}}, \tag{5.1.4}$$

where δr_{conv} is the width of the convective zone and v_{conv} is the typical velocity of a convective blob.

Depending on the relative sizes of the various time scales, very different requirements for numerical treatment arise. If the nuclear time scales τ_i are all large compared to τ_{conv}, the convective zone might be approximated as uniform in abundances, which slowly evolve on the nuclear timescales. If *some* of the τ_i are shorter than τ_{conv}, it is not correct to ignore the abundance gradients that this implies. In particular, these gradients may interact with the burning to modify the convective flow itself. If the nuclear time scales are all small compared to τ_{conv}, the problem simplifies again, and each region is loosely coupled to its neighbors. For more dynamic problems, such as pulses or explosions, the convenient fiction of steady state convection is untenable, and the hydrodynamics must be treated as an equally important aspect of the problem.

5.2. Shock waves

Before discussing detonations and deflagrations, first consider the simpler case of a one-dimensional flow with a shock wave but no burning (fig. 15). From mass conservation one obtains the condition

$$\rho_1 (u_1 - D) = \rho_2 (u_2 - D) \equiv j, \tag{5.2.1}$$

where D is the velocity of the shock front, ρ is the mass density, u is the fluid velocity, and the subscripts 1 and 2 denote the pre-shock and post-shock states, respectively. A second jump condition, which expresses momentum conservation across the front, can be written as

$$\rho_1 u_1 (u_1 - D) - \rho_2 u_2 (u_2 - D) = p_2 - p_1, \tag{5.2.2}$$

or using eq. (5.2.1)

$$\rho_1 (u_1 - D)^2 + p_1 = \rho_2 (u_2 - D)^2 + p_2, \tag{5.2.3}$$

where p is the pressure. The third jump condition, based on energy conservation, is

$$\rho_1 (e_1 + \frac{u_1^2}{2}) (u_1 - D) - \rho_2 (e_2 + \frac{u_2^2}{2}) (u_2 - D) = p_2 u_2 - p_1 u_1 \tag{5.2.4}$$

or using eqs. (5.2.1) and (5.2.3) as

$$\frac{1}{2}(u_1 - D)^2 + e_1 + p_1 V_1 = \frac{1}{2}(u_2 - D)^2 + e_2 + p_2 V_2 , \tag{5.2.5}$$

where e is the specific internal energy, and $V \equiv 1/\rho$ is the specific volume. Equations (5.2.1), (5.2.3) and (5.2.5) are the Rankine-Hugoniot relations. By eliminating the velocity from the first two jump conditions, one derives

$$j^2 = -\frac{p_1 - p_2}{V_1 - V_2}, \tag{5.2.6}$$

which is a *pure mechanical* relation between the pre-shock and post-shock state variables, independent of the equation of state. Note that according to eq. (5.2.6), two different types of processes are compatible with the mechanical conservation laws, namely processes in which either or both pressure and density increase or decrease. However, in non-reacting gases, processes of the second kind are excluded because they would involve a decrease of entropy (see Courant and Friedrichs 1948). Using the definition of j, the equation for the *Rayleigh line* is obtained as

$$\mathcal{R}(V_2, p_2) \equiv \rho_1^2 (u_1 - D)^2 - \frac{p_2 - p_1}{V_1 - V_2} = 0. \tag{5.2.7}$$

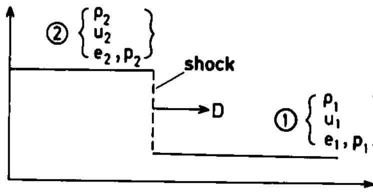

Fig. 15. A plane, one-dimensional shock wave moving with velocity D. The pre-shock (1) and post-shock (2) states are completely characterized by their density ρ, velocity u, and energy e (or pressure p).

Eliminating the relative fluid velocities $(u_1 - D)$ and $(u_2 - D)$ from the energy jump condition, and using the jump conditions for mass and momentum, the equation for the *Hugoniot relation* is obtained

$$\mathcal{H}(V_2, p_2) \equiv e_2 - e_1 + \frac{p_2 + p_1}{2}(V_2 - V_1) = 0, \qquad (5.2.8)$$

which only involves pure thermodynamic quantities ($\mathcal{H}$ is the Hugoniot function). It characterizes all pairs of values (V_2, p_2) for the state on one side of the shock front that is compatible with the three shock relations when the values (V_1, p_1) on the other side are given. Note that for a given equation of state $p = p(\rho, e)$, the intersection of the Rayleigh line and the Hugoniot curve determines the post-shock state (see fig. 16). In other words the pre-shock state (u_1, V_1, p_1) and the shock velocity D determine the complete post-shock state (u_2, V_2, p_2) (see Courant and Friedrichs 1948).

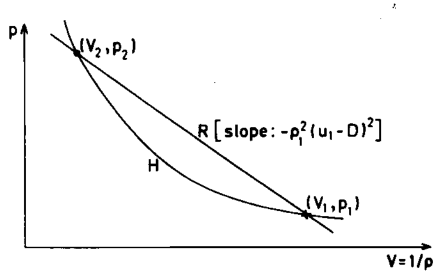

Fig. 16. Hugoniot curve H and Rayleigh line R for shocks. For a given pre-shock state (V_1, p_1, u_1) and shock speed D, the intersection of both curves determines the post-shock state (V_2, p_2, u_2).

5.3. Simple theory of steady plane detonations and deflagrations

Detonations are the most violent form of burning one encounters. Astrophysical detonations generally occur only under degenerate conditions. During the initial stages of a thermonuclear runaway, before the temperature rises significantly, the reaction rate is still relatively small. In nondegenerate matter, the pressure increase produced by the reactions causes the burning region to expand and cool, preventing the runaway from proceeding; in other words, $\tau_T > \tau_{\rm hyd}$. On the other hand, if the matter is degenerate, the temperature increase created by the burning does not create a significant increase in pressure. Thus, the temperature continues to increase until the matter becomes nondegenerate. At this point, the energy generation rate is too large for hydrodynamic motion to stop it, and an explosion results. If the resulting shock is sufficiently strong to raise the fuel above the ignition temperature, a detonation wave propagates outwards from the point of ignition.

As the shock propagates into unburned fuel, it compresses and heats the material beyond the ignition point. Immediately behind the shock is the reaction zone, in which the fuel burns. In its simplest form, detonation theory neglects the width of the reaction zone (i.e., only instantaneous reactions are considered), so that the detonation front is treated as a sharp discontinuity (see Courant and Friedrichs 1948; Fickett and Davis 1979). In this case, jump conditions can be derived for the change in hydrodynamic variables across the front, in much the same way as is done for a simple shock, above. The resulting Rankine-Hugoniot relations are the same as in the case of shocks, except for the energy conservation, which now reads (see Courant and Friedrichs 1948)

$$\frac{1}{2}(u_1 - D)^2 + E_1 + p_1 V_1 = \frac{1}{2}(u_2 - D)^2 + E_2 + p_2 V_2 \,, \tag{5.3.1}$$

where $E \equiv e + B$ is the sum of the internal energy of the gas per unit mass and the binding energy ($B < 0$) per mass. In analogy to the case of a pure shock *Hugoniot function for the burned material* is defined as

$$\mathcal{H}_2(V, p) \equiv E_2(V, p) - E_2(V_1, p_1) + (V - V_1)\,\frac{p + p_1}{2} \,. \tag{5.3.2}$$

Then the *Hugoniot relation* can simply be written in the form (see Courant and Friedrichs 1948)

$$\mathcal{H}_2(V, p) = E_1(V_1, p_1) - E_2(V_1, p_1) \,. \tag{5.3.3}$$

Note that $\mathcal{H}_2 > 0$ for exothermic reactions, and that E_1 and E_2 are different functions!

Suppose the specific volume V_1 and pressure p_1 of the unburnt gas are given, but not the velocity D of the burning front. Then the pressure and specific volume of the burnt gas satisfy eq. (5.3.3) for all reactions compatible with the three conservation laws. However, not all values of p and V satisfying eq. (5.3.3) actually correspond to a reaction process compatible with the conservation laws, because of the condition

$$\frac{p_2 - p_1}{V_2 - V_1} < 0\,, \tag{5.3.4}$$

derived from eq. (5.2.6). The *Hugoniot curve*, that is, the graph of all points in the (p, V)-plane which satisfy eqs. (5.3.3) and (5.3.4) is shown in fig. 17. It consists of two separate branches, called the detonation branch ($p_2 > p_1$ and $V_2 < V_1$), and the deflagration branch ($p_2 < p_1$ and $V_2 > V_1$), which reflects the fact that the conservation laws are compatible with two different types of processes.

As in the case without burning, the intersection of the Rayleigh line (eq. 5.2.7) and the Hugoniot curve (eq. 5.3.3) determines the post-detonation (post-deflagration) state. Note, however, that to obtain the post-detonation (post deflagration) state, a detonation (deflagration) velocity must first be chosen. Unlike the case for simple shocks, the front velocity is not determined

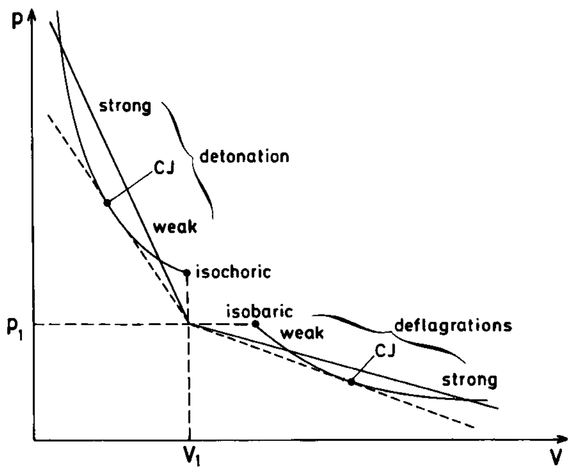

Fig. 17. Hugoniot curve for detonations and deflagrations (see text for details).

from the jump conditions. Depending on the value chosen for the detonation (deflagration) velocity, the Rayleigh line intersects the Hugoniot curve at 0, 1, or 2 points (see fig. 17). If there is no intersection, no detonation (deflagration) wave is possible for that detonation (deflagration) velocity. If there are two points of intersection, there are two possible solutions. These two solutions correspond to *strong* and *weak* detonations (deflagrations). A strong detonation (weak deflagration) propagates at a speed slower than the post-detonation (post-deflagration) sound velocity with respect to the fluid behind the shock, so that disturbances generated behind the front eventually catch up with it. Thus, this solution is unstable. Weak detonations (strong deflagrations) propagate faster than the post-detonation (post deflagration) sound velocity with respect to the fluid behind the shock. Strong deflagrations can never actually occur, and weak detonations are generally considered to be unphysical except under certain special conditions (see Courant and Friedrichs 1948). The detonation which usually occurs in nature is the one corresponding to the speed at which the Rayleigh line and Hugoniot curve have only one point of intersection. This detonation (deflagration) speed, called the *Chapman-Jouguet velocity*, is equal to the sum of the post-detonation (post-deflagration) fluid velocity and sound speed, that is,

$$D_{CJ} = u_2 + c_2. \tag{5.3.5}$$

By assuming that the front propagates with this velocity, the post-detonation (post-deflagration) state is completely determined. Both the pressure and the density increase (decrease) across the front; while in the frame in which the shock is stationary, the fluid velocity decreases (increases).

5.4. Detonations and Type I supernova models

Although the above theory provides a satisfactory explanation for simple detonations, it has significant limitations due to the assumptions that the reaction rate is infinite, and that the reaction zone has zero width. A slightly more complex treatment is used in the Zeldovich-von Neumann-Doering (ZND) model (Zeldovich 1940; von Neumann 1942; Doering 1943). This theory assumes that the shock, which is taken to be infinitely thin, is followed by a reaction zone of finite width. The primary difference from the equations given above is that the term in the Hugoniot curve involving energy generated by the reaction must now be multiplied by the extent of the reaction. Thus, each state within the reaction zone can be determined by the intersection of the Hugoniot curve for the appropriate extent of reaction and the Rayleigh line. The final state obtained after the fuel is completely burned is exactly the same as for the simpler theory described above. As shown in section 5.7.2 a correct numerical treatment of detonations can only be achieved, if the finite width of the reaction zone is taken into account.

Additional complications in the theory arise due to multi-dimensional effects, such as cellular detonations and spinning detonations; and due to non-stationary propagation of the wave, giving rise to oscillatory galloping detonations. The complicated time-dependent three-dimensional cellular structure of the detonation wave is a result of instabilities driven by the strong positive feedback between gas-dynamical fluctuations and the burning rate, which is highly dependent on temperature and more weakly on density. However, the stability and structure questions concerning detonations are far beyond the scope of this discussion (see Fickett and Davis 1979 for a general discussion, and Khokhlov 1989a for astrophysical implications).

Up until now, only a few multi-dimensional simulations of astrophysical detonations have been performed (Mahaffy and Hansen 1975; Müller and Arnett 1986; Denisov et al. 1986; Dgani and Livio 1990; Livne and Glasner 1990; Steinmetz, Müller, and Hillebrandt 1991). However, none of these simulations are concerned with the multi-dimensional internal structure of the detonation wave. In the simulations of Mahaffy and Hansen (1975), Denisov (1986), and of Steinmetz, Müller and Hillebrandt (1991), the propagation of non-spherical detonations in rotating white dwarfs was examined. The non-spherical shape (on scales of the stellar radius) of the detonation front arises because the front propagates through the oblate density stratification of the rotating dwarf. The other two numerical studies addressed the problem of geometrical effects in off-center detonation models of Type Ib supernovae proposed by Branch and Nomoto (1986). In the off-center models, the accreting white dwarf possesses a core composed of a mixture of carbon and oxygen surrounded by a helium layer. The burning is ignited at the base of the helium shell leading in one-dimensional (i.e., spherically symmetric) simulations to both an outward and an inward propagating detonation (see Nomoto 1982; Woosley, Taam and Weaver 1986). However, as He-ignition very likely occurs at a point rather than over an entire spherical shell, Branch and Nomoto (1986) speculated that in such a case, instead of the so-called double detonation, only a single outward propagating He-detonation might occur, if multi-dimensional effects are taken into account. In their two-dimensional simulations Dgani and Livio (1990) found that in those models which give rise to strong double detonations in one-dimensional calculations, off-center point ignition also causes a double detonation, that is, spherical damping does not occur. Livne and Glasner (1990), on the other hand, conclude that both double detonations and single detonations are possible under appropriate conditions.

Concerning detonations in Type Ia supernovae models, astrophysicists in the past have mainly tried to answer two other important questions: (i) under what conditions does a detonation wave form? and (ii) if it forms, will it actually propagate through the star? The second question has been answered positively. Starting with the calculation of Arnett (1969), it has been demonstrated in many numerical simulations, that once a detonation is formed, it propagates self-consistently in a white dwarf composed of either helium or a mixture of carbon and oxygen (for a review see Khokhlov 1989a). Note that in all of these calculations, the detonation was artificially initiated.

The problem of detonation formation is much more difficult. Shock tube analysis in planar geometry (Mazurek, Meier, and Wheeler 1977) indicates that the formation of a detonation in carbon-oxygen white dwarfs is unlikely, unless the white dwarf has an almost isothermal core (see below). Based on energy arguments Nomoto, Sugimoto, and Neo (1976; see also Nomoto, Thielemann, and Yokoi 1984) came to the same conclusion. All these authors only considered constant volume explosions in degenerate C–O mixtures, but it is a common feature of most explosive gaseous mixtures that constant volume explosions generate only weak shock waves, which are unable to trigger a detonation. Nevertheless, self-initiation of a detonation has been observed in numerous laboratory experiments, where a sudden transition from subsonic burning (i.e., from deflagration) to detonation occurs (see Lee and Moen 1980; see also chapter 12-3.4 of Oran and Boris 1987).

In addition, none of the above authors really addressed the question of whether a detonation does or does not form in the conditions actually encountered in the evolutionary calculations, that is, in a strongly driven, convective, turbulent core. Due to convection, the temperature gradient at the time of runaway is adiabatic (Arnett 1969). Under those conditions, a carbon detonation is more likely to form (Mazurek, Meier, and Wheeler 1977), since it is easier to start a detonation in matter that is already on the verge of exploding than in cold fuel (Mazurek, Truran, and Cameron 1974). Calculations by Woosley and Weaver (1986) suggest that the formation of either a detonation or a deflagration is possible. The outcome is critically dependent on both the mass zoning and especially on the temperature at which a mixing-length approximation to the energy transport is relinquished preceding the runaway.

Detonation formation has been studied in great detail by Blinnikov and Khokhlov (1986, 1987), and by Khokhlov (1990a, 1990b). They pointed out the crucial importance of non-simultaneous burning for the initiation of detonations in degenerate carbon-oxygen mixtures. From experiments, it is known that an essential feature for the initiation of a detonation is the existence of a non-uniformly pre-heated region (see Lee and Moen 1980), which can either be produced by adiabatic pre-compression ahead of an accelerating deflagration wave, mixing of hot burnt matter with fresh fuel in the vicinity of a turbulent flame front, or shock heating. Because burning proceeds non-simultaneously throughout the pre-heated region, the generated shock wave eventually reaches detonation strength (Lee and Moen 1980). Note that the exact crucial effect of non-simultaneous burning is neglected in constant volume explosions, where by definition, the whole region burns simultaneously.

Consider two points in the core of a white dwarf having a finite temperature gradient. As the burning time is shorter for higher temperatures, the fuel is first incinerated at the point of higher temperature; that is, non-simultaneous burning occurs. This difference in burning times leads to propagation of the boundary separating burnt from unburnt matter. If the corresponding phase velocity is larger than the local speed of sound, the burning at one point does not influence the burning at another point. The phase velocity, of this so-called spontaneous burning (Zeldovich, 1980), is obviously given by

$$D_{\rm sp} = \left(\frac{d\tau_{\rm nuc}}{dr}\right)^{-1}. \tag{5.4.1}$$

Note that the phase velocity is very sensitive to the initial temperature ($D_{\rm sp} \propto T^{\alpha}(dT/dr)^{-1}$ with $\alpha \approx 21$ for the ${}^{12}{\rm C} + {}^{12}{\rm C}$ rate and $0.6 \lesssim T/10^9 K \lesssim 1.2$; Woosley and Weaver 1986), and that it approaches infinity for an isothermal temperature distribution (Mazurek, Meier, and Wheeler 1977). If the initial temperature gradient is small enough, the phase velocity exceeds the sound speed, and hence the corresponding region of the white dwarf runs away in less than a sound crossing time. This creates a supersonic expansion of the burned volume, which can lead to the detonation of a large fraction of the star.

Blinnikov and Khokhlov (1986, 1987), in particular, studied steady spontaneous burning waves which propagate with velocities $D_{\rm sp} \geq D_{\rm CJ}$ through matter without temperature fluctuations. They found that for a wide range of parameters, the spontaneous wave can transform into a detonation. The possibility of spontaneous burning in Type I supernovae was independently proposed by Woosley and Weaver (1986), who however did not take into account the hydrodynamics of the spontaneous burning wave, and thus overlooked the possibility of detonation formation. Later Khokhlov (1990a) also considered the influence of fluctuations on the initiation of detonations. Using a statistical approach, he could show that the existence of a steady spontaneous wave is not necessary for initiation of a detonation, but that the conditions of detonation formation are mainly determined by initial fluctuations in temperature, density, and fuel concentration.

5.5. Deflagrations and Type I supernova models

Deflagrations represent a much less violent form of burning than detonations, but in many ways are more complex (see chap. 5 of Williams 1985; Zeldovich et al. 1985). They result when the burning is unable to produce sufficient overpressure to create a shock strong enough to ignite the fuel. The motion of the front is usually very subsonic. Burning is initiated by the diffusive transfer of heat from the hot ashes behind the front into the cold fuel. For the case of a thin front, deflagrations must obey the same jump conditions as detonations (see section 5.3), but the propagation velocity now depends on the rate of heat transfer. Another major difference is that the pressure and density decrease behind the deflagration front, and, in the reference frame in which the front is stationary, the velocity increases. In the case of a deflagration which begins at the origin in spherical symmetry, the velocity behind the front must eventually become zero to satisfy the boundary condition at the origin. The only way in which this can happen is if the deflagration is preceded by a compression wave which accelerates material away from the front. The passage of the deflagration then provides exactly the correct jump in velocity so that the material behind the front comes to rest. This can happen since the deflagration velocity is subsonic, and therefore, there is communication by sound waves between the origin and the rest of the flow.

Unlike the case of Chapman-Jouguet detonations, where it is possible to compute the exact propagation velocity, the propagation speed of deflagrations can only be crudely estimated (Landau and Lifshitz 1959; Fryxell and Woosley 1982; Nozakura, Ikeuchi and Fujimoto 1984). For the simplest case of a laminar front propagating as a result of radiative diffusion or conduction, it is fairly easy to obtain an order of magnitude estimate for the velocity of the wave. The width of the deflagration can be approximated by setting the diffusion timescale $\tau_{\rm diff}$ equal to the burning timescale τ_i. Thus, the width of the front is given by

$$\delta \sim \sqrt{\lambda\, c\, \tau_i}\ , \tag{5.5.1}$$

where λ is the mean free path of photons or electrons and c is the speed of light. The velocity D of the deflagration can then be estimated as

$$D \sim \frac{\delta}{\tau_i} \sim \sqrt{\lambda\, c/\tau_i}\ . \tag{5.5.2}$$

For the $^{12}C + ^{12}C$ reaction, Woosley and Weaver (1986) give an estimate of $v_{cond} \approx 30$ km s^{-1} for a density of 2×10^9 g cm^{-3}. In addition to their analytical estimate, they have also determined the conductive speed numerically. At 2×10^9 g cm^{-3}, the steady flame speed is ≈ 50 km s^{-1}, and at 5×10^8 g cm^{-3} it is ≈ 16 km s^{-1} (the width of the burning front in both cases being $\approx 10^{-3}$ cm) (see also the lecture of Woosley).

If the deflagration is propagated by turbulent convection rather than by diffusion, two situations can arise. If the scale of the turbulence is small compared to the width of the front, the deflagration remains laminar, and the above equations still apply if the mean free path of the photons or electrons is replaced by the typical length scale for the turbulence, and if the velocity of the diffusing objects is replaced by the convective velocity. If, on the other hand, the thickness of the front is small compared with the length scale of the turbulence, the front will be wrinkled. In this case, the velocity of the front is increased in comparison with the velocity of the diffusively propagated deflagration, both by the increase in heat transfer rate and by the increase in the surface area of the front. The upper limit to the speed which an extremely wrinkled burning front can obtain is approximately the convective velocity.

Another complication which arises is that many astrophysical deflagrations fronts are Rayleigh-Taylor unstable (Müller and Arnett 1982, 1986; Woosley and Weaver 1986). When a deflagration propagates outwards from the center of a star against the force of gravity, the flow is unstable (see section 4.2) since the density decreases behind the front. The situation that results is a hot low-density bubble that tries to expand outward into a denser medium. Under these conditions, the flame front is almost certainly wrinkled, and the average rate of propagation of the front is determined by the growth rate of the instability (see Müller and Arnett 1986). It is also possible that the distortions could become so extreme that the front might not remain simply-connected (due to Kelvin-Helmholtz instabilities; see section 4.5), and blobs of burning material would be scattered throughout the star ahead of the main deflagration wave.

The fact that the propagation velocity of a laminar deflagration depends upon the width of the front can cause severe computational problems. To calculate the correct structure, it is necessary to resolve the width of the front on the computational grid. In addition, for a wrinkled deflagration, the fuel consumption rate is determined by the laminar conductive velocity (which is normal everywhere to the front) multiplied by the surface area of the front. Since the surface area depends on the amount of wrinkling of the front, that is, on the growth rate of the Rayleigh-Taylor instability, the complicated wrinkled structure has to be resolved numerically, as well. In many cases of interest, the width of the front will be much smaller than a single zone. In this case, the only way to obtain the correct deflagration structure is to use an adaptive grid to obtain very high resolution near the front, or to use a front tracking method. In one-dimensional calculations, this procedure is difficult but probably feasible. However, if the front is severely wrinkled, moving the grid to obtain the required resolution at the front is virtually impossible with current technology.

Up until now, this has been attempted only in the work of Müller and Arnett (1982, 1986) using an explicit axisymmetric Eulerian hydrodynamic code. Although severely hampered by grid resolution issues and, to a lesser extent, by the symmetry restrictions imposed, they were able to show that the front is Rayleigh-Taylor unstable and that the overall propagation speed indeed depends on the amount of wrinkling in the burning front. All other workers in the field have used a more or less sophisticated ad hoc parameterization of the burning velocity within their one-dimensional Lagrangian stellar evolution codes (for details see the lecture by Woosley).

Recently Khokhlov (1990a, 1990b) has proposed a new Type Ia supernova model which includes both the deflagration model and the detonation model as a limiting case. In his so-called *delayed detonation* model, after an epoch of slow subsonic burning, a deflagration to detonation transition occurs when fluctuations in the vicinity of the turbulent flame front reach a certain critical level (see also previous section). For this to happen, the deflagration velocity must exceed a corresponding critical velocity D_{tr}. If the deflagration velocity D_{def} always remains less than the critical velocity D_{tr}, the explosion proceeds as a deflagration, while if D_{def} exceeds D_{tr} during flame acceleration, the explosion turns into a detonation. Unfortunately, for carbon-oxygen white dwarfs, the determination of D_{tr} requires three-dimensional high-resolution hydrodynamic simulations that take into account the interaction of turbulence and nuclear burning. Such calculations are currently not feasible and probably will not be within a foreseeable amount of time. Thus, Khokhlov (1990b) assumed in his model calculations that the transition occurs at a certain stage of the explosion. He could show that the delayed detonation models combine the advantages of the deflagration and detonation models without being hampered by their deficiencies. In particular, as the (delayed) detonation propagates through an already pre-expanded star, intermediate mass elements (Si, S, Ca, etc.) can be synthesized in the outer layers ($\rho \lesssim 10^7$ g/cm^3) of a white dwarf moving with velocities consistent with observations. In addition, delayed detonation models seem to be very promising candidates for solving some long standing nucleosynthesis problems arising in both the deflagration and detonation models (for details see Khokhlov 1990b, 1991 and the lecture of Woosley).

5.6. Hydrodynamics and nuclear burning

With very few exceptions, numerical calculations which couple hydrodynamics and nuclear burning have been performed using Lagrangian hydrodynamics. There is a good reason for this. Lagrangian methods provide no artificial mixing of nuclear species, and thus eliminate one of the major errors present in Eulerian codes. Since most previous calculations have been performed with only one spatial dimension, usually with spherical symmetry, using a Lagrangian method was the natural way to proceed. However, this is no longer true for multi-dimensional flows, because severe difficulties arise in using Lagrangian codes when more than one spatial dimension is required. The formation of vortices in the flow causes large distortions in the Lagrangian grid, and perhaps even grid tangling. Although this can be alleviated by periodic rezoning, the major advantage of the Lagrangian approach is then lost. The sudden mixing of species during rezoning may provide even worse effects than the gradual mixing during the entire Eulerian calculation.

Thus, for two or three-dimensional calculations, Eulerian methods are probably to be preferred, since the grid remains regular. However, the errors associated with the mixing of species must then be considered. The amount of mixing can be controlled to some extent by using an adaptive grid which moves with the species discontinuities, but this can lead to the same grid tangling problems associated with Lagrangian methods. In addition, an implicit method may be required to move the grid correctly, which enormously increases the complexity of the code, as well as the amount of computer time required. Local mesh refinement can help to keep the size of the mixed region small, but can not eliminate the error entirely. If the fluid in the mixed region explodes due to numerical error, the results will still be qualitatively wrong. Multi-fluid calculations, which track the location of the interfaces between the various fluids, can perhaps solve the problem for simple cases, but for flows containing a large number of species, in which every zone may have a different composition due to burning, such methods are impractical.

For this reason, Fryxell, Müller, and Arnett (1989) investigated the errors involved in coupling nuclear burning into Eulerian hydrodynamic codes to examine the feasibility of performing multi-dimensional calculations. Five different Eulerian schemes were used in their test calculations, which indicated that the higher-order Godunov-type piecewise parabolic method (PPM) of Colella and Woodward (1984; see also section 2.6) was superior to all other methods tested. A Lagrangian version of the PPM scheme was also included in the tests so that the effects of artificial mixing could easily be seen. Although all of the tests presented were one-dimensional, they clearly showed the types of errors encountered in performing multi-dimensional calculations.

All of the codes tested by Fryxell, Müller, and Arnett (1989) used zone centered variables and were written in strict conservation form. In most circumstances, this is the best approach, since it guarantees that shock jumps are correct. However, using a conservative energy equation can lead to large errors if the kinetic energy is much larger than the thermal energy. In this case, the resulting pressure and temperature may be very inaccurate. When nuclear burning is included in the calculation, such large temperature errors could be disastrous. Using a nonconservative equation for internal energy only is probably better under these circumstances, but this situation did not occur in any of their test problems (see next section), and thus conservative methods should provide more accurate results. In any case, it is important, as pointed out by Fryxell, Müller, and Arnett (1989), to maintain conservation of the partial density of each species, both globally and locally. When using a conservative formulation for the species equations, global conservation is guaranteed. However, changes to some of the difference methods are required to ensure that the sum of the partial densities equals the total density in each zone (see below).

Several modifications to the standard scheme are required to include the effects of nuclear burning. First, the species equations must be added to the hydrodynamical equations (see eqs. 2.4.1 to 2.4.3), that is, for each species an equation of the (conservation) form

$$\frac{\partial \varrho X_i}{\partial t} + \operatorname{div}(\varrho X_i \vec{v}) = \varrho \dot{X}_i , \tag{5.6.1}$$

has to be solved, where X_i and $\dot{X}_i$ represent the mass-fraction of the i-th species, and its rate of change resulting from nuclear reactions, respectively. The fuel consumption term gives rise to a corresponding rate of change in the internal energy $\dot{e}_{\rm nuc}$, which has to be included in the energy sink/source term q in the energy conservation equation (2.4.3).

When discretizing eq. (5.6.1), the values of the mass-fraction of each species at the zone interfaces are obtained by interpolation. If this interpolation is nonlinear, as for example, in the case of PPM, an additional step is required at this point. Since the parabolic interpolation polynomial used in PPM is subject to a nonlinear monotonicity constraint, that is, the constraint operates on each abundance in a different way, the sum of the resulting interface values of the mass-fractions are not, in general, equal to unity. As a result, the sum of the zone averaged mass-fractions at the new time are also not equal to unity. This local nonconservation error can have serious effects on the results of the calculation, at times even leading to unphysical features in the flow.

One way to guarantee that the sum of the mass-fractions remains unity is to omit one of the species equations. The value of the partial density for that species would then be determined by subtracting the sum of the partial densities of the other species from the total density. This has the undesirable consequence of concentrating the total error in one abundance. If the errors which occur become large (the error can frequently exceed 100%), the value of this last abundance is meaningless. Fortunately, there is a better solution to this problem, as was shown by Fryxell, Müller, and Arnett (1989). When the error in the sum of the mass-fractions at the zone interface, after applying monotonicity, is in error by more than some specified amount, the zone interface values are set equal to the zone average value. This reduces species advection to first-order in that zone, and causes more artificial mixing of species, but these errors are usually less severe than those obtained without the correction. In choosing the maximum amount of error allowed before flattening the zone structure, there is a trade-off between the error in conservation and the amount of mixing. The maximum error allowed in the calculations presented in the next section is 10^{-7}.

Ideally, the reaction network should be coupled directly into the hydrodynamic scheme. This approach is very expensive, and in most cases not necessary. Instead, an operator-split approach may be used (see section 2.5). The value of the state vector $(\varrho, \varrho\vec{v}, \varrho e, \varrho X_i)^T$ at the new time level is first computed, neglecting the effects of the source terms in the energy and species equations (i.e., $\dot{e}_{\rm nuc}$ and $\varrho\dot{X}_i$). The implicit network equations are then solved iteratively using the new (i.e., advected) values of density ϱ, temperature T (obtained from the equation of state), and mass-fractions X_i to obtain $\dot{e}_{\rm nuc}$ and $\dot{X}_i$. The first term is then used to update the energy, and subsequently by means of the equation of state, to update the temperature and pressure. Without significantly greater effort, a stronger and more stable coupling of the reaction network into the hydrodynamic scheme can be achieved when the source term in the energy equation (and hence the temperature) is iteratively updated *together* with the abundances, rather than in an extra step (Müller 1986).

Making an intelligent choice for the value of δt is one of the most critical aspects in efficiently solving problems which couple hydrodynamics and clear burning. Using too small a value requires the computation of an necessarily large number of time steps, whereas using too large a value ds either to unacceptably large errors, or, if an iterative method is used to ve the reaction network, to an unconverged result.

When a reaction network is incorporated into an explicit hydro-code, sev-l restrictions (besides the CFL-condition; see section 2.2) on δt must be posed. First, the temperature and the mass fraction of each nuclear species ıst not be allowed to change by too much during the timestep. Since the n-iterative solution of the network requires linearization of the equations, oo large a change in any variable is permitted, the linear approximation is longer valid, and large errors result. In addition, if an iterative procedure used, the solution does not converge. These restrictions take the form

$$\delta t_T^{n+1} = \alpha_T \; \delta t^n \; \frac{T^{n+1}}{|T^{n+1} - T^n|} \tag{5.6.2}$$

$$\delta t_X^{n+1} = \alpha_X \; \delta t^n \; \frac{X_i^{n+1}}{|X_i^{n+1} - X_i^n|}, \tag{5.6.3}$$

ıere the values of the dimensionless constants α_T and α_X depend on the e of network used for the calculation and the violence of the burning. Typ-lly, allowable changes in the temperature are 3% or less, while abundance anges of 5% to 10% can usually be tolerated. When an iterative method solution is used for the network, another timestep restriction is achieved requiring that the solution converges in a small number of iterations. This triction can be written as

$$\delta t_I^{n+1} = \delta t^n \, \mathrm{Min} \left\{ 1, \left(\frac{3}{I} \right)^2 \right\}, \tag{5.6.4}$$

ıere I is the number of iterations required for convergence on the previ-s solution of the network. This restriction has the effect of reducing δt ıenever the number of iterations required exceeds three.

The value of δt is chosen to be the minimum obtained from each of above equations in the most restrictive zone. There are times when en this value of δt is too large for the network to converge. When this ppens, there is an additional procedure which can be used to continue calculation. The values of temperature, energy, and mass-fraction are red before the network is solved. If the network does not converge, the lue of δt can be reduced and the network recomputed starting from the ginal values. Since a smaller value of δt was used for the network than for the hydrodynamics, the network must be solved several times until the variables have been advanced to the correct time level. Equivalently, one could recalculate the entire hydrodynamics and burning step with the same value of δt, but this requires storing old values of all of the hydrodynamic variables.

5.7. Hydrodynamic simulations of detonations

As a prelude to studying the coupled processes of hydrodynamics and nuclear burning in a general geometry, Fryxell, Müller, and Arnett (1989) have critically examined some of the numerical tools available to the theorist. They have performed an extensive set of test calculations of one-dimensional shock tubes with and without burning using five different Eulerian schemes: a higher-order Godunov scheme (PPM), a flux-vector splitting scheme (SADIE), a first-order Godunov scheme, a Lax-Wendroff scheme, and a Donor Cell scheme. Some of their results will be discussed in this section.

The equation of state used in all of the calculations was chosen to provide the correct qualitative behavior for a realistic astrophysical gas, but yet simple enough to be used for easily reproducible test calculations. Three contributions to the pressure are included – ideal gas, radiation, and a term which simulates a degenerate electron gas as a simple gamma-law. The effects of radiation pressure strongly limits the temperature which the combustion products reach, and the effects of electron degeneracy can determine whether the fuel burns explosively, producing a detonation or deflagration, or quietly, such as in the center of the sun. Thus, the pressure and internal energy density can be expressed in terms of density and temperature by the formulas

$$P = P_g + P_r + P_e \tag{5.7.1}$$

where, for n nuclear species,

$$P_g = \sum_{i=1}^{n} Y_i \varrho RT \tag{5.7.2}$$

$$P_r = \frac{1}{3} a T^4 \tag{5.7.3}$$

$$P_e = K \rho^{\frac{4}{3}} \, . \tag{5.7.4}$$

The constants in eqs. (5.7.2)–(5.7.4) are the ideal gas constant R, the radiation constant a, and a somewhat arbitrary constant $K = 2.384 \times 10^{14}$ (cgs units), which was chosen to provide an appropriate amount of degeneracy pressure. Y_i is the number fraction of the i-th species.

Two separate reaction networks are used by Fryxell, Müller, and Arnett (1989). The first was a very simple network consisting of two species, ^{12}C and ^{56}Ni, and a single exothermic reaction. In reality, carbon does not burn directly to nickel. However, the approximation was made for this network that after the ^{12}C(^{12}C, α)^{20}Ne reaction is complete, the reaction products burn instantly to ^{56}Ni. Thus they used the rate for the initial reaction only, but took the energy release obtained from burning the carbon completely to nickel.

In some of their test problems, they used a second, more complex, reaction network, which contained the 13 species of the complete α-chain up to ^{56}Ni. These nuclei (^{4}He, ^{12}C, ^{16}O, ^{20}Ne, ^{24}Mg, ^{28}Si, ^{32}S, ^{36}Ar, ^{40}Ca, ^{44}Ti, ^{48}Cr, ^{52}Fe, and ^{56}Ni) are linked by 27 reactions, which include the 11 (α, γ) reactions from ^{12}C$(\alpha, \gamma)^{16}$O to ^{52}Fe$(\alpha, \gamma)^{56}$Ni, the corresponding 11 endothermic photo-disintegration reactions, the three heavy-ion reactions ^{12}C(^{12}C,α)^{20}Ne, ^{12}C(^{16}O,α)^{24}Mg, and ^{16}O(^{16}O,α)^{28}Si, and the triple-α reaction and its inverse.

5.7.1. Detonations caused by numerical errors

In one set of test calculations Fryxell, Müller, and Arnett (1989) showed that due to numerical errors, artificial detonations can be obtained. The initial conditions for this set of degenerate shock tube calculations with burning were given by

$$\begin{aligned} \rho_L &= 2 \times 10^9 \text{ g cm}^{-3} & \qquad \rho_R &= 2 \times 10^9 \text{ g cm}^{-3} \\ u_L &= 0 & u_R &= 0 \\ T_L &= 5 \times 10^9 \text{ K} & T_R &= 5 \times 10^8 \text{ K.} \end{aligned}$$

The composition of the material is ^{56}Ni on the left side of the grid and ^{12}C on the right. The simple two-species nuclear reaction network for burning carbon to nickel was included, and the radiation pressure term discarded in the equation of state. The calculations are performed on a grid of length 0.1 cm, with the initial jump located at 0.05 cm.

The solution to the problem obtained using the Eulerian PPM code on a grid of 200 zones at time 5×10^{-11} s is plotted in fig. 18. The ^{12}C to the right of the contact discontinuity is initially at too low a temperature to burn, and the shock is far too weak to raise the temperature to the ignition point. There is no fuel to the left of the contact discontinuity where the temperature is high, so there is no burning in that region either. In fact, if the contact discontinuity remained perfectly sharp, there would be no energy generation from burning during the entire cal-

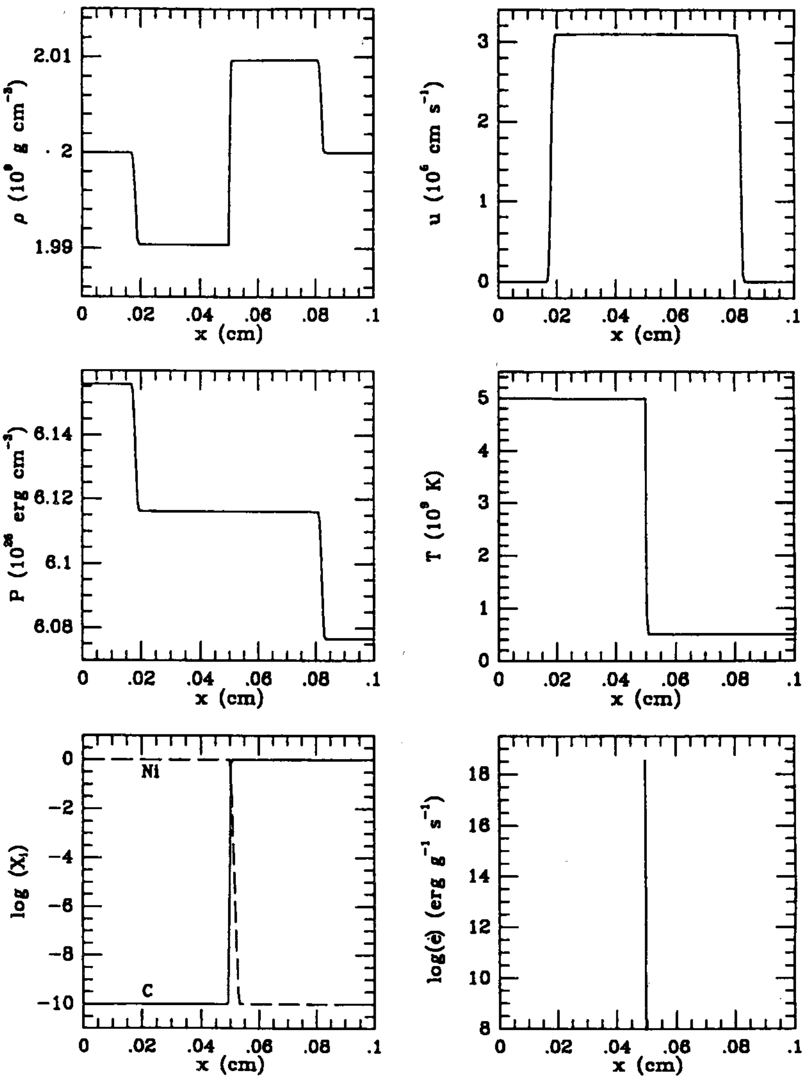

Fig. 18. Solution of the degenerate shock tube, with nuclear burning calculated using Eulerian PPM on a grid of 200 zones at time 5×10^{-11} s. The shock which propagates into the unburned ^{12}C is too weak to raise the temperature above the ignition point. The only burning which takes place is a result of numerical diffusion of heat and composition across the contact discontinuity. Only one zone is burning, and the energy generation rate is dynamically not important on the time scales considered here (from Fryxell, Müller, and Arnett 1989).

culation. However, since the discontinuity is spread slightly by Eulerian difference schemes, a small amount of the fuel is diffused into the region where the temperature is high, and some of the heat is conducted from the hot region into the fuel. Thus, there is a narrow region where nuclear burning occurs, as can be seen in the plot of the energy generation rate (fig. 18). Fortunately, in this case the amount of diffusion is small enough that the energy generation is not dynamically important, and the results are qualitatively correct. The flow never reaches a configuration where the temperature and the abundance of ^{12}C are large in the same zone. In fact, at the end of the calculation, not even one zone has burned completely.

The results obtained with Godunov's method and Lax-Wendroff were qualitatively similar to those shown in fig. 18, the main difference being that the burning region is somewhat wider, due to the larger diffusion in these methods. The rate of burning was not dynamically important, although a few zones burned from ^{12}C to ^{56}Ni during the calculation. The results produced by the Donor Cell code showed oscillations of an amplitude sufficient to cause the ^{12}C to ignite, producing an energy generation rate of 5×10^{28} erg g^{-1} s^{-1}.

The results produced by SADIE are very different from those obtained with PPM. Unlike the other schemes in the comparison, SADIE has the property of rapidly spreading slowly moving (and even stationary) contact discontinuities. Thus, the amount of mixing between the cold fuel and the hot ashes across the contact is much larger than for other codes. Under these conditions, the amount of mixing is sufficient to cause the fuel to detonate, as shown in fig. 19. These results are plotted at an earlier time (1.06×10^{-11} s) since the speed of the detonation front is much greater than that of the simple shock. The temperature of the fuel is raised to more than 4×10^{11} K, producing an energy generation rate of $\approx 10^{34}$ erg g^{-1} s^{-1}. The resulting detonation appears physically correct, traveling at the correct speed and producing the correct post-detonation conditions. However, the origin of the detonation is due completely to a numerical error.

To complicate matters further, Fryxell, Müller, and Arnett (1989) preformed a calculation using Eulerian PPM with slightly modified initial conditions. The fluid in the entire grid is given an initial velocity $u_L = u_R = 10^8$ cm s^{-1}. The results should look exactly the same as fig. 18, except shifted to the right by a distance $u_L\ t$. However, the results, plotted at $t = 3 \times 10^{-11}$ s in fig. 20, look almost identical to those obtained with SADIE. The only reason SADIE gives different results from the other codes is that the contact discontinuity is nearly stationary. When the discontinuity is moved across the grid, every Eulerian code spreads it to some

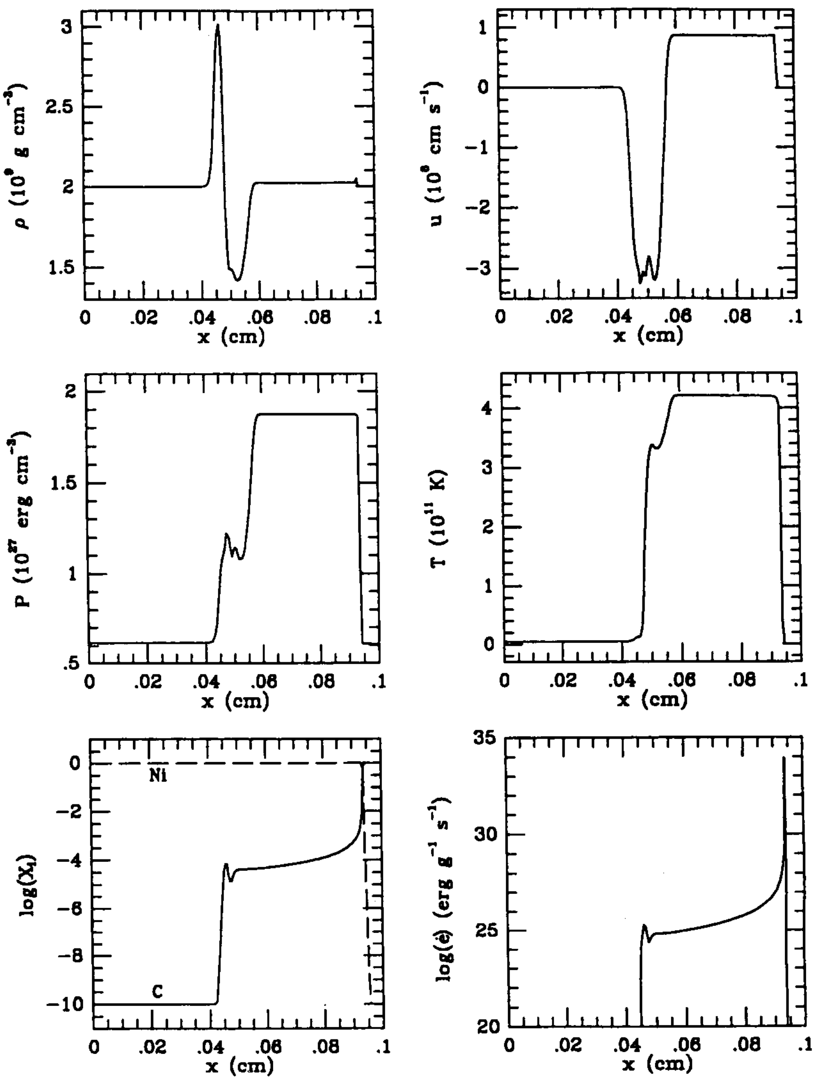

Fig. 19. Solution of the degenerate shock tube with nuclear burning, calculated using SADIE on a 200 zone grid. The amount of artificial spreading of the contact discontinuity provides sufficient diffusion of heat and mixing of composition that the ^{12}C detonates. Although the code treats the detonation correctly after it is formed, its initiation is a numerical artifact. The results are plotted at an earlier time than in fig. 18 ($t = 1.06 \times 10^{-11}$ s), since the detonation speed is much larger than that of the simple shock in fig. 18 (from Fryxell, Müller, and Arnett 1989).

extent. Even with PPM (the code which spreads discontinuities least of those tested here), the spreading is sufficient to cause the ^{12}C to detonate, producing a qualitatively incorrect solution. This shows the degree of caution needed in calculating reactive flows with an Eulerian hydrodynamic code.

5.7.2. Detonations with single exothermic reaction

Another set of test problems that Fryxell, Müller, and Arnett (1989) considered contained a detonation, which, unlike the previous example, is not of numerical origin. The fluid to the left of the interface is given a finite velocity, which produces a sufficiently strong shock to ignite the fuel to the right of the interface. The equation of state for this example includes all three terms (ideal gas, radiation, and simplified electron degeneracy). Nuclear energy generation is provided by a simple reaction network containing only ^{12}C and ^{56}Ni. This is the simplest possible situation to analyze, since there is only a single exothermic reaction to deal with. The initial conditions used for this set of calculations are

$$\begin{aligned} \rho_L &= 1.25 \times 10^9 \text{ g cm}^{-3} & \rho_R &= 1 \times 10^9 \text{ g cm}^{-3} \\ u_L &= 5 \times 10^8 \text{ cm s}^{-1} & u_R &= 0 \\ T_L &= 2 \times 10^{10} \text{ K} & T_R &= 8 \times 10^7 \text{ K}. \end{aligned}$$

The initial composition of the material to the left of the jump is pure ^{56}Ni, with pure ^{12}C to the right. The calculations are performed on grids of length $2, 4, 8$, and 16×10^{-4} cm, with the initial jump always in the middle of the grid.

In this set of calculations, the number of zones in the grid is fixed at 200, while the length of the grid is increased. This provides an indication of the coarsest grid which still produces acceptable results. The density profile obtained on four different grids with Eulerian PPM is plotted in fig. 21. In doubling the grid length from 2×10^{-4} cm to 4×10^{-4} cm, the only noticeable difference in the results is in the resolution of the peak behind the shock. The speed of the front and post-detonation state remain unchanged. However, when the grid length is doubled again, the results change qualitatively. The shock now propagates to the right with a velocity considerably higher than the Chapman-Jouguet velocity, and an additional plateau appears in the profile. The values at the second plateau are still the same as the post-detonation values obtained in the more finely-zoned calculations, as they must be in a conservative scheme. However, because an additional unphysical wave forms, the results are totally unacceptable. If the grid size is doubled again, the situation becomes worse. The speed of the shock front increases further,

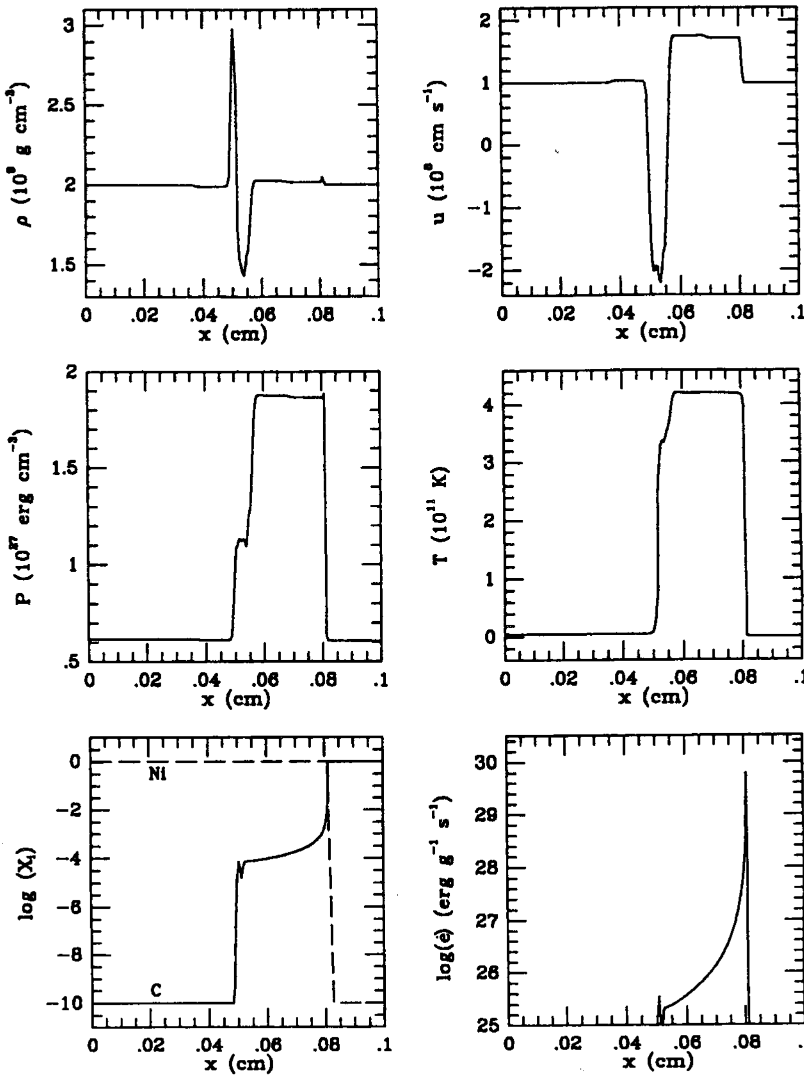

Fig. 20. Solution of the degenerate shock tube with nuclear burning at time 3×10^{-11} s. The solution is obtained using Eulerian PPM, on a grid of 200 zones. This calculation differs from the one shown in fig. 18 in that the fluid in every zone is given an initial velocity $u = 10^8$ cm s^{-1}. The correct solution should look identical to that shown in fig. 18, except shifted to the right by a distance of 0.003 cm. Instead, the additional motion of the contact discontinuity created enough mixing and diffusion that a detonation resulted. This detonation is qualitatively similar to the one obtained by SADIE (fig. 19; from Fryxell, Müller, and Arnett 1989).

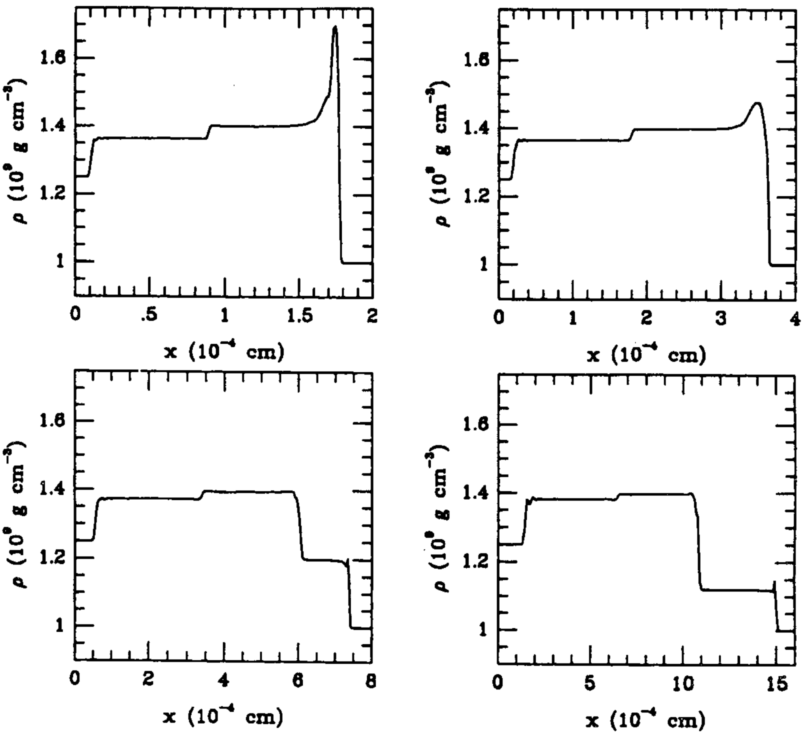

Fig. 21. Density profiles for the single-reaction carbon detonation obtained with Eulerian PPM on 200 zone grids of four different lengths. For grids of lengths 2×10^{-4} cm and 4×10^{-4} cm, the detonation is qualitatively correct and propagates at the Chapman-Jouguet velocity. For larger grid lengths, an unphysical weak detonation is obtained, which propagates faster than the Chapman-Jouguet velocity. The times at which the plots are shown, in order of increasing grid length, are 9.0×10^{-14} s, 1.8×10^{-13} s, 3.2×10^{-13} s, and 5.6×10^{-13} s (from Fryxell, Müller, and Arnett 1989).

and the discrepancy between the post-shock values of the variables and the correct post-detonation values is even larger. Similar behavior was noticed by Colella, Majda, and Roytburd (1986).

This example clearly shows the fallacy of the argument that claims that since jump conditions in a detonation (as in a shock) are based only on conservation laws, detonations can be calculated on any mesh with a conservative difference scheme. In ideal hydrodynamics, the shock front is infinitely thin. Thus, the fuel spends no time within the shock, and does not start to burn until it reaches the post-shock state. The problem arises when the time which the fuel spends within the shock front (given by the width of the shock produced by the difference scheme divided by the velocity of the shock), becomes comparable to or longer than the burning-time of the fuel. When this happens, nearly all of the fuel is burned within the shock front. Thus, when numerical errors become large enough that the physics of the problem is violated, it is not surprising that an unphysical solution is obtained. If the energy production within the lower portion of the shock front is large enough, the pressure in these zones is raised sufficiently to create a bulge in the shock profile. This bulge then propagates to the right ahead of the real front, producing the extra wave.

The grid size at which each code makes the transition to an unphysical solution is different, and depends on shock width and the amount of mixing of fuel and ashes. The two first-order codes and Lax-Wendroff produce correct behavior until a grid length of 4×10^{-4} cm is reached. SADIE and Eulerian PPM work properly until the grid length reaches 8×10^{-4} cm. The Lagrangian PPM method produces unacceptable results only when a grid size of 16×10^{-4} cm or larger is used.

It is possible, however, to obtain acceptable results on large grids by making a small modification to the codes. An incorrect solution was obtained because the burning was occuring within the shock, instead of behind it. This error can be avoided by not allowing the fuel to burn in any zone which contains a shock. Such zones are easily detected in a hydrodynamic code. Any zone which contains a sufficiently large pressure gradient and a negative velocity divergence (to ensure that the zone is compressing) can be considered to be within a shock. The results obtained using this algorithm with the Eulerian PPM code are shown in fig. 22 on a grid of length 8.0×10^{-4} cm. The detonation again moves at the correct velocity and the proper post-detonation state is achieved.

5.7.3. *Detonation with α-network*

The final calculation of Fryxell, Müller, and Arnett (1989) that will be discussed is another shock tube containing a detonation. However, energy generation is now produced by the 13-species 27-reaction α-network described at the beginning of this section. This calculation is presented only as an example of the type of results which can be obtained when using a moderately complex network with an Eulerian hydrodynamic code.

For a detonation with an α-network, it is impossible to obtain a solution which is even close to being converged using the techniques examined in the

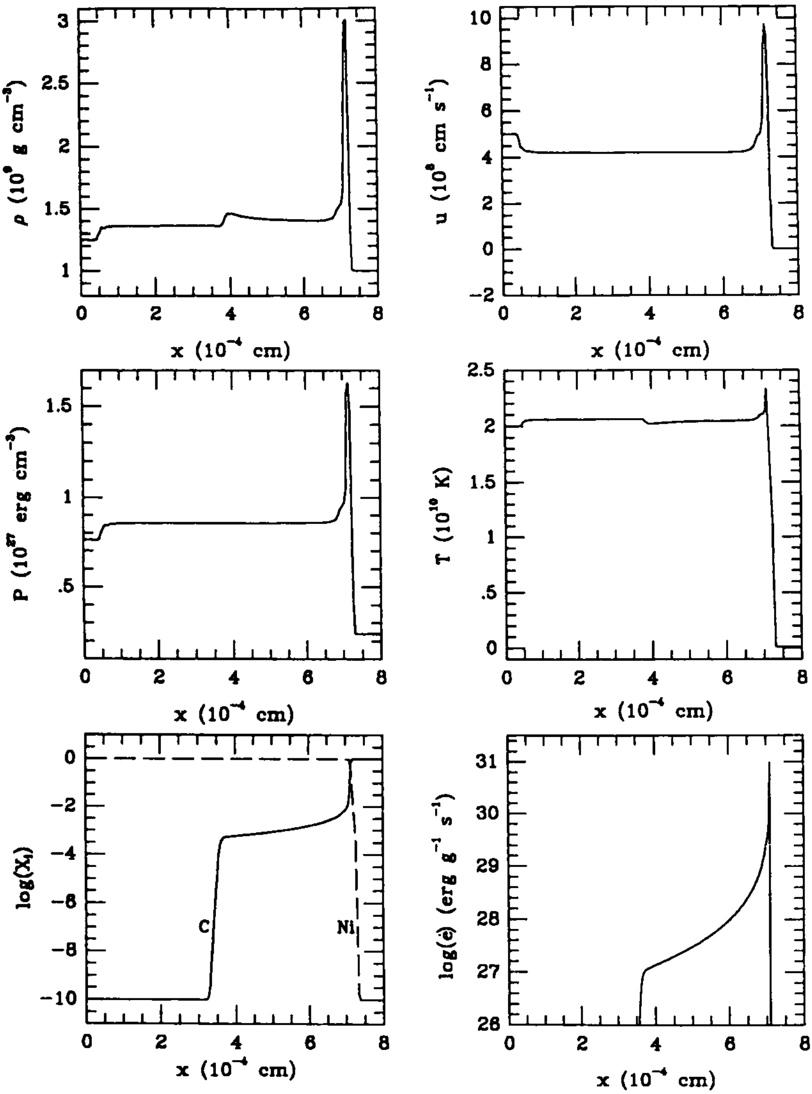

Fig. 22. Results obtained using Eulerian PPM for the single-reaction carbon detonation on a 200-zone grid of length 8×10^{-4} cm. Unlike the result presented in fig. 21, the correct qualitative behavior is obtained by not allowing the fuel to burn in any zone which contains part of the shock front (from Fryxell, Müller, and Arnett 1989).

survey of Fryxell, Müller, and Arnett (1989). Since the burning times for the various reactions differ by several orders of magnitude, there is no way to resolve the time and length scales for each of the burning processes. In this sense, the detonation wave is no longer thin. If one chooses to resolve the structure of the front, as in the previous example, then the calçulation cannot proceed long enough to follow completion of the burning. If, on the other hand, a calculation is performed to see what the final products of the burning are, the structure of the front cannot be resolved. This also makes calculating the correct qualitative behavior easier than with the simple network. Since the front is wider for the α-network, qualitatively correct detonations can be computed on grids large enough that meaningful calculations of stellar size problems can be performed. The initial conditions for this detonation are

$$\begin{aligned} \rho_L &= 2.5 \times 10^9 \text{ g cm}^{-3} & \rho_R &= 1 \times 10^9 \text{ g cm}^{-3} \\ u_L &= 5 \times 10^8 \text{ cm s}^{-1} & u_R &= 0 \\ T_L &= 8 \times 10^9 \text{ K} & T_R &= 8 \times 10^7 \text{ K}. \end{aligned}$$

The initial composition of the material to the left of the jump is pure ^{56}Ni, with pure ^{12}C to the right. All other mass-fractions are set to an initial value of 10^{-10} in each zone, and all three terms in the equation of state are included. Results were obtained on grids of two different lengths, 0.01 cm (jump at $x = 0.005$ cm) and 1 cm (jump at $x = 0.5$ cm), so that the structure of the front can be seen on two different time scales. The results of the smaller grid are shown at 6×10^{-12} s while the results of the larger grid are plotted at 6×10^{-10} s.

The structure of the detonation obtained using Eulerian PPM on a 1 cm grid of 800 zones is shown in fig. 23. There is a small poorly-resolved peak immediately behind the shock front. Behind the peak is a plateau, which is not quite flat, since nuclear burning is still occurring in this region. At the left of the plot is a second plateau. The density and pressure in this region have been reduced slightly by a rarefaction wave which has propagated to the left from the initial discontinuity. The two plateaus are joined by a contact discontinuity. This discontinuity is uncharacteristically wide for PPM because of the nonlinear interaction of the diffusion of species across the discontinuity with the burning processes. The enhanced rate of species diffusion is a result of the flattening of the zone structure required to maintain local conservation of the abundances. The structure of the detonation obtained on the 10^{-2} cm grid is qualitatively similar.

The time evolution of the abundances can be seen in fig. 24 which shows the results obtained on both grids. There are three distinct regions in the post-detonation flow. The region between the shock and the contact discontinuity

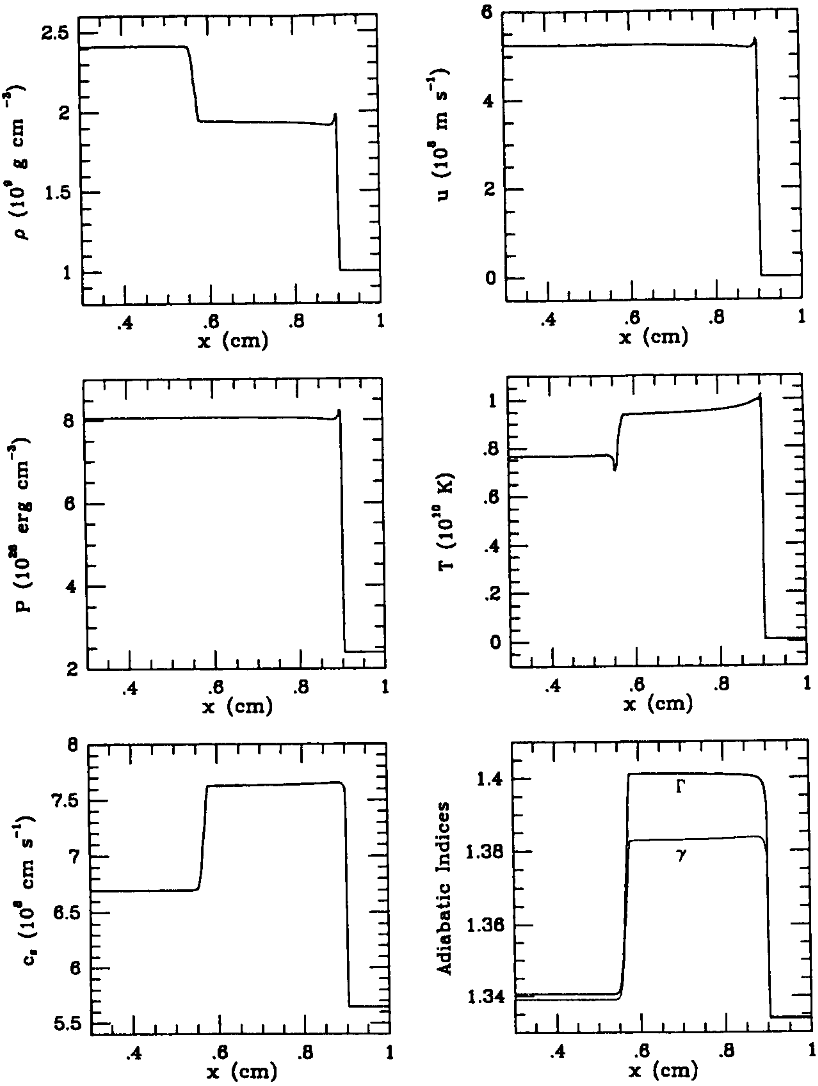

Fig. 23. Results obtained with the Eulerian PPM code for the α-chain network detonation on an 800-zone grid of length 1 cm. The detonation structure is shown at time 6×10^{-10} s (from Fryxell, Müller, and Arnett 1989).

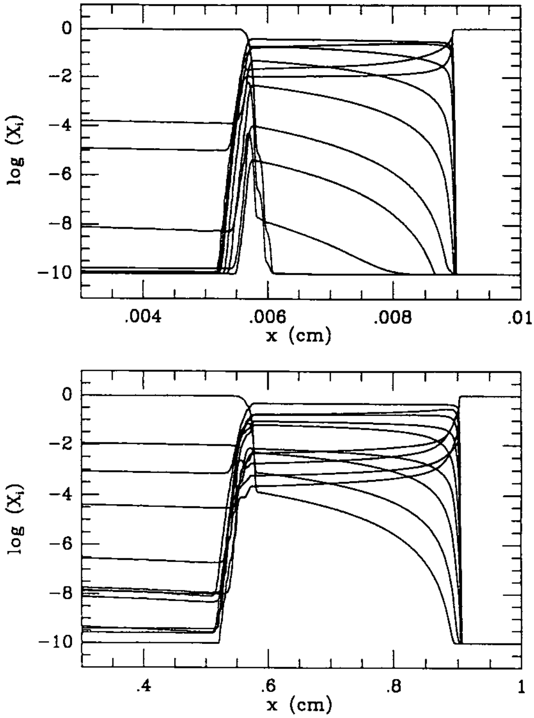

Fig. 24. Composition profiles obtained with Eulerian PPM for the α-chain network detonation on 800-zone grids of two different lengths. The upper graph is plotted at time 6×10^{-12} s, while the lower graph is shown at time 6.0×10^{-10} s. Thus, comparison of the two plots shows the time evolution of nuclear abundances. In the upper graph, the largest abundance near the left side of the grid is Ni, followed by Fe, He, and Cr. Only trace amounts of the other elements are present. In the post-detonation region ($x \approx 0.008$), He is the most abundant species, followed by O, Mg, Si, S, Ne, C, Ar, Ca, and Ti, with only trace amounts of the heavier elements. In the lower graph, the most abundant species at the left of the grid is again Ni, followed by Fe, He, Cr, Ca, Ar, Si, Ti, S, Mg, O, C, and Ne. In the post-detonation region, the most dominant species (in order of abundance) are He, Si, S, Ar, and Ca (from Fryxell, Müller, and Arnett 1989).

contains the early time products of carbon burning. To the left of the contact discontinuity is a region in which the initial composition of almost pure ^{56}Ni is beginning to photo-disintegrate, forming an equilibrium distribution of abundances. At the contact discontinuity, there is a third narrow region which contains a mixture of species from the other two regions. This mixing is unphysically large and results completely from the diffusion present in the Eulerian hydrodynamic method.

The evolution of the abundances proceeds as follows. Since the material ahead of the shock is pure ^{12}C, the only reaction in the network which can operate is ^{12}C(^{12}C,^{4}He)^{20}Ne. Thus, the dominant abundances immediately behind the shock should be ^{4}He and ^{20}Ne. This behavior is just barely detectable on the smaller grid. Further behind the shock, the ^{20}Ne photo-disintegrates into ^{16}O and ^{4}He. With the formation of a significant abundance of ^{16}O, the three heavy-ion reactions become dominant, producing ^{20}Ne, ^{24}Mg, and ^{28}Si. The abundance of ^{32}S, which is produced by the ^{28}Si$(\alpha, \gamma)^{32}$S reaction, also becomes significant near the contact discontinuity on the smaller grid. The remaining (α, γ) reactions are just beginning at this time, producing trace abundances of ^{36}Ar, ^{40}Ca, ^{44}Ti, and ^{48}Cr. The abundances at a somewhat later time, which can be seen in the results obtained on the 1 cm grid, show the depletion of the ^{12}C and ^{16}O, and an increase in the abundances of products of the (α, γ) reactions. The mass-fraction of the heaviest element in the network, ^{56}Ni, has increased to about 10^{-4} near the contact discontinuity at this time.

The evolution of the abundances at the left of the grid is less complicated. At the time plotted for the smaller grid, a small amount of ^{56}Ni has photo-disintegrated into ^{52}Fe and ^{4}He, and the ^{52}Fe has produced a trace of ^{48}Cr. Notice that the abundance curves have a small slope. This is a result of propagation of the rarefaction through this region, which causes different mass elements to have slightly different temperature and density histories. At the later time, the abundance of ^{52}Fe has risen to 10^{-2}, and the abundances of the lighter species are also beginning to increase. This process continues until a state of nuclear statistical equilibrium is reached. The region between the shock and contact discontinuity also eventually reaches a state of equilibrium, but the values of the abundances are different because of the different values of temperature and density.

The abundances obtained on a coarser grid of 200 zones are shown in fig. 25. The results are qualitatively similar to those discussed above. The primary difference is that the region in the center where mixing has taken place is much wider. Fortunately, the mixing in this case does not seem to have a significant effect on the qualitative results of the calculation. Although it is too early at this time to compare these results with the Chapman-Jouguet solution (since the burning is far from complete), the propagation velocity of the detonation front seems to be correct, and the variables behind the detonation appear to be approaching the correct values. However, it should also

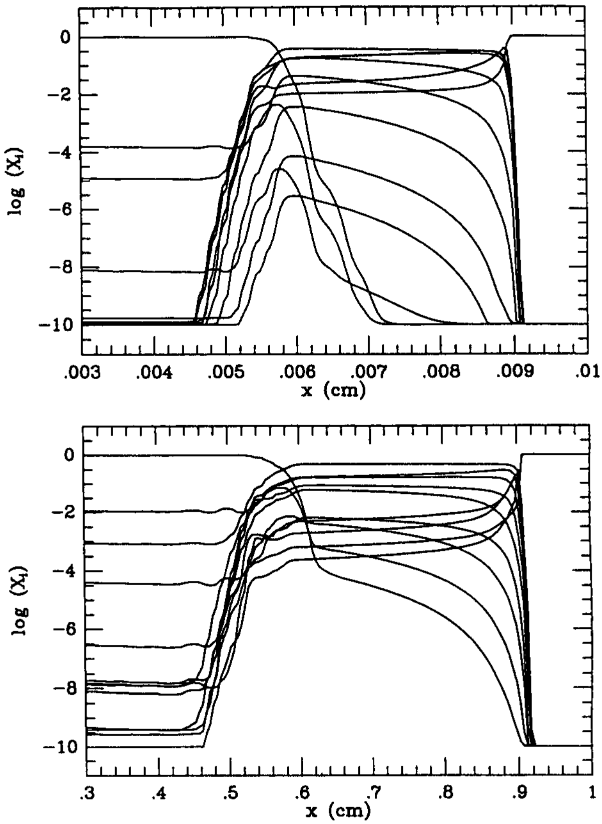

Fig. 25. Same as fig. 24, except that the calculations are performed on a 200-zone grid. The region of numerical mixing of composition near the center of the grid is considerably wider than in fig. 24 (from Fryxell, Müller, and Arnett 1989).

be noted that in similar calculations performed with more diffusive schemes, such as Godunov and the Donor Cell method, the mixing of species dominates the abundance profiles over more than half the region between the shock and contact discontinuity, making it difficult, if not impossible, to follow abundance changes caused by various burning processes *in this part of* the flow.

Finally, for comparison, the abundances profiles are shown, as obtained by Fryxell, Müller, and Arnett (1989) using the Lagrangian PPM code on a grid of 200 zones (fig. 26). The results are much cleaner, since there is no

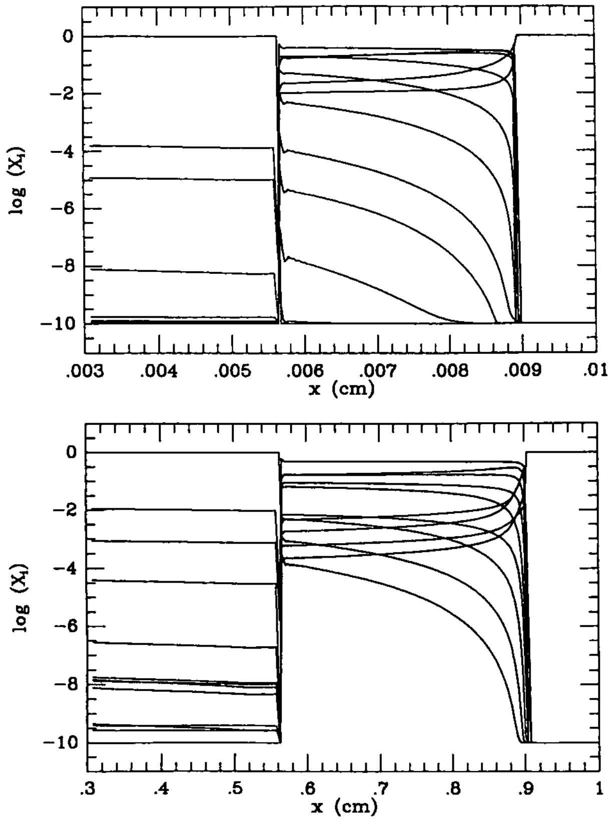

Fig. 26. Same as fig. 24, except that the calculations are performed using Lagrangian PPM on a 200-zone grid. The artificially mixed region in the center of the grid is not present in Lagrangian calculations (from Fryxell, Müller, and Arnett 1989).

mixing region in the center to corrupt the abundance profiles. The boundary between the two burning regions is very sharply defined. Even so, except for this central region, the results obtained by the Eulerian code agree very well with the Lagrangian results. Thus, it appears that even with a network containing many species, a good Eulerian code can produce reasonable results for many problems. For more diffusive Eulerian methods, the mixing in the central region could be so severe that it would corrupt the abundance profiles over the entire grid, making it virtually impossible to observe abundance changes due to the various burning processes.

Acknowledgements

This work benefited from discussions with my colleagues Dave Arnett, Bruce Fryxell, Wolfgang Hillebrandt, Alexei Khokhlov, Ralph Mönchmeyer, and Matthias Steinmetz. The author thanks H.-Thomas Janka for a careful reading of the manuscript, and for suggesting modifications to improve the text.

References

Anderson, D.A., J.C. Tannehill, and R.H. Pletcher. 1984. Computational Fluid Mechanics and Heat Transfer, McGraw-Hill, New York.

Arnett, W.D. 1966. *Canad. J. Phys.* **44**, 2553.

Arnett, W.D. 1967. *Canad. J. Phys.* **45**, 1621.

Arnett, W.D. 1968. *Astrophys. J.* **153**, 341

Arnett, W.D. 1969. *Astrophys. Spac. Sci.* **5**, 180.

Arnett, W.D. 1985. Unpublished.

Arnett, W.D. 1987. *Astrophys. J.* **319**, 136.

Arnett, W.D. 1988. *Astrophys. J.* **331**, 337.

Arnett, W.D., J.N. Bahcall, and R.P. Kirshner, and S.E. Woosley 1989. *Ann. Rev. Astronom. Astrophys.* **27**, 629.

Arnett, W.D., B.A. Fryxell, and E. Müller. 1989. *Astrophys. J. Lett.* **341**, L63.

Arnett, W.D., B.A. Fryxell, and E. Müller. 1991. *In*: Proceedings of The ESO/EIPC Workshop: SN 1987A and Other Supernovae, eds. I.J. Danziger, L.B. Lucy, W. Hillebrandt, ESO, Garching, in press.

Bandiera, R. 1984. *Astron. Astrophys.* **139**, 368.

Barthelmy, S., N. Gehrels, M Leventhal, C.J. MacCullum, B.J. Teegarden, and J. Tueller. 1989. *IAU Circular* **4764**.

Beam, R.M. and R.F. Warming. 1978. *American Inst. of Aeronautics and Astronautics Journal* **16**, 393.

Benz, W. 1989. *In*: Numerical Modeling of Non Radial Stellar Pulsations: Problems and Prospects, ed. J.R. Buchler, Kluwer, Dordrecht.

Benz, W. 1991. *In*: Proceedings of the 2nd European Predoctoral Astrophysics School on Theory and Observation of Late Stages of Stellar Evolution and Computational Methods in Astrophysical Fluid Dynamics, ed. B. de Loore, Lecture Notes in Physics, Springer, Berlin, in press.

Benz, W., F.-K. Thielemann. 1990. *Astrophys. J. Lett.* **348**, L17.

Bethe, H.A., G.E. Brown, and J. Cooperstein. 1987. *Astrophys. J.* **322**, 201.

Blanchet, L., T. Damour, and G. Schäfer. 1990. *Mon. Not. Roy. Astronom. Soc.* **242**, 289.

Blinnikov, S.I. and A.M. Khokhlov. 1986. *Sov. Astron. Lett.* **12**, 131.

Blinnikov, S.I. and A.M. Khokhlov. 1987. *Sov. Astron. Lett.* **13**, 364.

Bodenheimer, P. and S.E. Woosley, 1983. *Astrophys. J.* **269**, 381.

Boris, J.P. and D.L. Book. 1973. *J. Comp. Phys.* **11**, 38.

Branch, D. and K. Nomoto. 1986. *Astron. Astrophys.* **164**, L13.

Burrows, A. 1987. *Astrophys. J. Lett.* **318**, L57.

Chandrasekhar, S. 1961. Hydrodynamic and Hydromagnetic Stability, Oxford: Clarendon Press.

Chevalier, R.A. 1976. *Astrophys. J.* **207**, 872.

Colella, P. and P.R. Woodward. 1984. *J. Comp. Phys.* **54**, 174.

Colella, P. and H.M. Glaz. 1985. *J. Comp. Phys.* **59**, 264.

Colella, P., A. Majda, and V. Roytburd. 1986. *SIAM J. Sci. Stat. Comput.* **7**, 1059.

Colgate, S.A. 1991. *In*: Supernovae, ed. S.E. Woosley, p. 352. New York: Springer.

Colgate, S.A. and H.J. Johnson. 1960. *Phys. Rev. Lett.* **5**, 235.

Colgate, S.A. and R.H. White. 1966. *Astrophys. J.* **143**, 626.

Cook, W.R., et al. 1988. *Astrophys. J. Lett.* **334**, L87.

Cooperstein, J. and E. Baron. 1990. *In*: Supernovae, ed. A. Petschek, p. 213. New York: Springer-Verlag.

Courant, R. and K.O. Friedrichs. 1948. Supersonic Flow and Shock Waves, Interscience, New York.

Danziger, I.J., L.B. Lucy, and W. Hillebrandt. 1991. eds., Proceedings of The ESO/EIPC Workshop: SN 1987A and Other Supernovae, Garching: ESO. In press.

Den, M., T. Yoshida, and Y. Yamada. 1990. KUNS preprint 1004; *KEK Progress Report*, **89**, 173.

Denisov, A.A., A.V. Koldoba, Yu. A. Poveshenko, Yu. P. Popov, and V.M. Chechetkin. 1986. preprint IPM AN SSSR-99.

Dgani, R., M. Livio. 1990. *Astrophys. J.* **361**, 540.

Doering, W. 1943. *Ann. Phys.* **43**, 421.

Dotani, T., et al. 1987. *Nature* **330**, 230.

Durisen, R.H. and J.N. Imamura. 1981. *Astrophys. J.* **243**, 612.

Einfeldt, B. and C.-D. Munz. 1987. *Kernforschungszentrum Karlsruhe Report*, No. **4191**.

Elias, J.H., K. Mathews, G. Neugebauer, and S.E. Persson. 1985. *Astrophys. J.* **296**, 37.

Epstein, R.I. 1979. *Mon. Not. Roy. Astronom. Soc.* **188**, 305.

Erickson, E.F., M.R. Haas, S.W.J. Colgan, S.D. Lord, M.G. Burton, J. Wolf, D.J. Hollebach, and M. Werner. 1988. *Astrophys. J.* **330**, L39.

Eriguchi, Y. and E. Müller. 1985. *Astron. Astrophys.* **147**, 161.

Falk, S.W. and W.D. Arnett. 1973. *Astrophys. J. Lett.* **180**, L65.

Fickett, W. and W.C. Davis. 1979. Detonations, Univ. Berkeley: California Press.

Finn, L.S. 1989. *In*: Frontiers in Numerical Relativity, eds. C.R. Evans, L.S. Finn and D.W. Hobill, Cambridge: Cambridge University Press.

Finn, L.S. and C.R. Evans. 1990. *Astrophys. J.* **351**, 588.

Fryxell, B.A., E. Müller, and W.D. Arnett. 1989. *MPA preprint* **449** (Apr. 1989); and *In*: Numerical Methods in Astrophysics, ed. P.R. Woodward, New York: Academic Press, in press.

Fryxell, B.A., E. Müller, and W.D. Arnett. 1991. *Astrophys. J.* **367**, 619.

Fryxell, B.A. and S.E. Woosley. 1982. *Astrophys. J.* **261**, 332.

Gehrels, N., M. Leventhal, and C.J. MacCallum. 1988. *In*: Nuclear Spectroscopy of Astrophysical Sources, eds. N. Gehrels and G. Share, p. 87. New York: AIP.

Gentry, R.A., R.E. Martin, and B.J. Daly. 1966. *J. Comp. Phys.* **1**, 87.

Gingold, R.A. and J.J. Monaghan. 1977. *Mon. Not. Roy. Astronom. Soc.* **181**, 375.

Godunov, S.K. 1959. *Matematicheskii Sbornik* **47**, 271.

Haas, M.R., S.W.J. Colgan, E.F. Erickson, S.D. Lord, M.G. Burton, and D.J. Hollenbach. 1990. *Astrophys. J.* **360**, 257.

Hachisu, I., T. Matsuda, K. Nomoto, and T. Shigeyama. 1990. *Astrophys. J. Lett.* **358**, L57.

Hachisu, I., T. Matsuda, K. Nomoto, and T. Shigeyama. 1991. *Astrophys. J. Lett.* **368**, L27.

Harten, A., P.D. Lax, and B. van Leer. 1983. *SIAM Rev.* **25**, 35.

Herant, M. and W. Benz. 1991. *Harvard-Smithsonian Center for Astrophysics, Preprint Series, No.* **3169**; and *Astrophys. J. Lett.* in press.

Hillebrandt, W., E. Müller, and R. Mönchmeyer. 1990. *In*: NATO ASI on The Nuclear Equation of State, eds. W. Greiner and H. Stöcker, p. 689. New York: Plenum.

Hillebrandt, W. and R.G. Wolff. 1985. *In*: Nucleosynthesis: Challenges and New Developments, eds. W.D. Arnett and J.W. Truran, p. 131. Univ. Chicago Press.

Höflich, P. 1987. *In*: IAU Colloquium No. **108**, Atmospheric Diagnostic of Stellar Evolution, ed. K. Nomoto, p. 288. Berlin: Springer Verlag.

Höflich, P. 1988. in *Proc. Astron. Soc. Austr.* **7**, 434.

Hough, J. et al. 1989. Proposal for a Joint German-British Interferometric Gravitational Wave Detector, Max-Planck-Institut für Quantenoptik, Report 147, Garching.

Imamura, J.N., J.L. Friedman, and R.H. Durisen. 1985. *Astrophys. J.* **294**, 474.

Janka, H.-T. and R. Mönchmeyer. 1989a. *Astron. Astrophys.* **209**, L5.

Janka, H.-T. and R. Mönchmeyer. 1989b. *Astron. Astrophys.* **226**, 69.

Khokhlov, A.M. 1989a. *Astrophysics and Space Physics Reviews* **8**, 1.

Khokhlov, A.M. 1989b. *Mon. Not. Roy. Astronom. Soc.* **239**, 785.

Khokhlov, A.M. 1990a. *Max-Planck-Institut für Astrophysik, Preprint* **513**; and *Astron. Astrophys.*, in press.

Khokhlov, A.M. 1990b. *Max-Planck-Institut für Astrophysik, Preprint* **528**; and *Astron. Astrophys.*, in press.

Khokhlov, A.M. 1991. *Max-Planck-Institut für Astrophysik, Preprint* **570**; and *Astron. Astrophys.*, in press.

Landau, L.D. and E.M. Lifshitz. 1959. *Fluid Mechanics.*, Oxford: Pergamon. Vol. 6 of Course in Theoretical Physics.

LeBlanc, J.M. and J.R. Wilson. 1970. *Astrophys. J.* **161**, 541.

Ledoux, P. 1945. *Astrophys. J.* **102**, 143.

Lee, J.H.S. and I.O. Moen. 1980. *Progress in Energy and Combustion Sciences* **6**, 359.

Lindblom, L. and S.L. Detweiler. 1977. *Astrophys. J.* **211**, 565.

Livne, E. and A.S. Glasner. 1990. *Astrophys. J.* **361**, 244.

Lucy, L.B. 1977. *Astron. J.* **82**, 1013.

Mahaffy, J.H. and C.J. Hansen. 1975. *Astrophys. J.* **201**, 695.

Mahoney, W.A., et al. 1988. *Astrophys. J. Lett.* **334**, L81.

Managan, R.A. 1985. *Astrophys. J.* **294**, 463.

Managan, R.A. 1986. *Astrophys. J.* **309**, 598.

Matz, S.M., G.H. Share, M.D. Leising, E.L. Chupp, W.T. Vestrand, W.R. Purcell, M.S. Strickman, and C. Reppin. 1988. *Nature* **331**, 416.

Mazurek, T.J., D.L. Meier, and J.C. Wheeler. 1977. *Astrophys. J.* **213**, 518.

Mazurek, T.J., J.W. Truran, and A.G.W. Cameron. 1974. *Astrophys. Spac. Sci.* **27**, 261.

Monaghan, J.J. 1982. *SIAM J. Sci. Stat. Comput.* **3**, 422.

Monaghan, J.J. 1985. *Comput. Phys. Rep.* **3**, 71.

Mönchmeyer, R. 1989. *In*: Proc. 5th Workshop on Nuclear Astrophysics, eds. W. Hillebrandt and E. Müller, p. 92. MPA-P1, Garching.

Mönchmeyer, R. 1991. Ph.D. thesis, Tech. Univ. München, unpublished.

Mönchmeyer, R. and E. Müller. 1989a. *In*: NATO ASI on Timing Neutron Stars, eds. H. Ögelman, and E. van den Heuvel, p. 549. Dordrecht: Kluwer.

Mönchmeyer, R. and E. Müller. 1989b. *Astron. Astrophys.* **271**, 351.

Mönchmeyer, R., G. Schäfer, E. Müller, and R. Kates. 1991. *Max-Planck-Institut für Astrophysik, Preprint* **508**; and *Astron. Astrophys.*, in press.

Müller, E. 1982. *Astron. Astrophys.* **114**, 53.

Müller, E. 1986. *Astron. Astrophys.* **162**, 103.

Müller, E. 1988. *J. Comp. Phys.* **79**, 227.
Müller, E. 1990. *J. Phys. G*, **16**, 1571.
Müller, E. and W.D. Arnett. 1982. *Astrophys. J. Lett.* **261**, L109.
Müller, E. and W.D. Arnett. 1986. *Astrophys. J.* **307**, 619.
Müller, E., B.A. Fryxell, and W.D. Arnett. 1989. *Max-Planck-Institut für Astrophysik, Preprint* **491**; and *In*: Chemical and Dynamical Evolution of Galaxies, eds. F. Ferrini, F. Matteucci and J. Franco, Casa Editrice Giardini, Pisa, in press.
Müller, E., B.A. Fryxell, and W.D. Arnett. 1991. *In*: Proceedings of The ESO/EIPC Workshop: SN 1987A and Other Supernovae, eds. I.J. Danziger, L.B. Lucy, W. Hillebrandt, Garching: ESO, in press.
Müller, E. and W. Hillebrandt. 1981. *Astron. Astrophys.* **103**, 358.
Müller, E., W. Hillebrandt, M. Orio, P. Höflich, R. Mönchmeyer, and B.A. Fryxell. 1989. *Astron. Astrophys.* **220**, 167.
Müller, E., M. Różyczka, and W. Hillebrandt. 1980. *Astron. Astrophys.* **81**, 288.
Nagasawa, M. and T. Nakamura, and S. Miyama. 1989. *Publ. Astron. Soc. Japan* **40**, 691.
Nakamura, T. and K. Oohara. 1989. *In*: Frontiers in Numerical Relativity, eds. C.R. Evans, L.S. Finn, and D.W. Hobill, Cambridge: Cambridge Univ. Press.
Nomoto, K. 1982. *Astrophys. J.* **253**, 798.
Nomoto, K., D. Sugimoto, and S. Neo. 1976. *Astrophys. Spac. Sci.* **39**, 37.
Nomoto, K., F.-K. Thielemann, and K. Yokoi. 1984. *Astrophys. J.* **286**, 644.
Nozakura, T., S. Ikeuchi, and M.Y. Fujimoto. 1984. *Astrophys. J.* **286**, 221.
Oohara, K. and T. Nakamura. 1989. *Prog. Theor. Phys.* **82**, 535.
Oran, E.S. and J.P. Boris. 1987. Numerical Simulations of Reactive Flow, New York: Elsevier.
Osher, S. 1984. *SIAM J. Numer. Anal.* **21**, 217.
Ostriker, J.P. and P. Bodenheimer. 1973. *Astrophys. J.* **180**, 171.
Ostriker, J.P. and J.L. Tassoul. 1969. *Astrophys. J.* **155**, 987.
Potter, D. 1973. Computational Physics, New York: Wiley.
Rank, D.M., et al. 1988. *Nature* **331**, 505.
Richtmyer, R.D. and K.W. Morton. 1967. Difference Methods for Initial-Value Problems, New York: Wiley.
Roache, P.J. 1972. Computational Fluid Dynamics, Albuquerque, New Mexico: Hermosa Publ.
Roe, P.L. 1981. *J. Comp. Phys.* **43**, 357.
Różyczka, M. 1985. *Astron. Astrophys.* **143**, 59.
Ruffini, R. 1978. in Physics and Astrophysics of Neutron Stars and Black Holes, eds. R. Giacconi and R. Ruffini, Amsterdam: North Holland.
Sandie, W.G., et al. 1988. *Astrophys. J. Lett.* **334**, L91.
Shapiro, S.L. and A.P. Lightman. 1976. *Astrophys. J.* **207**, 263.
Shapiro, S.L. and S.A. Teukolsky. 1983. Black Holes, White Dwarfs, and Neutron Stars, p. 173ff. New York: Wiley.
Shigeyama, T. and K. Nomoto. 1990. *Astrophys. J.* **360**, 242.
Shigeyama, T., K. Nomoto, and M. Hashimoto. 1988. *Astron. Astrophys.* **196**, 141.
Stark, R.F. and T. Piran. 1985. *Phys. Rev. Lett.* **55**, 891.
Steger, J.L. and R.F. Warming. 1981. *J. Comp. Phys.* **40**, 263.
Steinmetz, M., E. Müller, and W. Hillebrandt. *Astron. Astrophys.*, to be submitted.
Strang, G. 1968. *SIAM J. Numer. Anal.* **5**, 506.
Sunyaev, R., et al. 1987. *Nature* **330**, 227.
Symbalisty, E. 1984. *Astrophys. J.* **285**, 729.
Tassoul, J.-L. 1978. Theory of Rotating Stars, New Jersey: Princeton Univ. Press.

Teegarden, B.J., S.D. Barthelmy, N. Gehrels, J. Tueller, M. Leventhal, and C.J. MacCallum. 1989. *Nature* **339**, 122.

Thorne, K.S. 1987. *In*: 300 Years of Gravitation, eds. S.W. Hawking and W. Israel, Cambridge: Cambridge Univ. Press.

Tohline, J.E. 1984. *Astrophys. J.* **285**, 721.

Tohline, J.E., J.M. Schombert, and A.P. Boss. 1980. *Space Sci. Rev.* **27**, 555.

Tscharnuter, W.M. and K.-H. Winkler. 1979. *Comp. Phys. Comm.* **18**, 171.

van Leer, B. 1977. *J. Comp. Phys.* **23**, 276.

van Leer, B. 1979. *J. Comp. Phys.* **32**, 101.

van Leer, B. 1982. *Lecture Notes in Physics* **170**, 507.

von Neumann, J. 1942. *In*: John von Neumann, collected works, ed. A.J. Taub, Vol. 6, p. 203.

van Riper, K.A. and J.M. Lattimer. 1981. *Astrophys. J.* **249**, 270.

Wheeler, J.C. and R.P. Harkness. 1990. *Rep. Progress Phys.* **53**, 1467.

Williams, F.A. 1985. Combustion Theory, Menlo Park, California: Benjamin Cummings.

Wilson, J.R. 1971. *Astrophys. J.* **163**, 209.

Wilson, R.B., et al. 1988. *In*: Nuclear Spectroscopy of Astrophysical Sources, eds. N. Gehrels and G. Share, p. 66. New York: AIP.

Winkler, K.-H. and M.L. Norman. 1986. *In*: Astrophysical Radiation Hydrodynamics, eds. K.-H. Winkler and M.L. Norman, p. 71. Dordrecht: Reidel.

Winkler, K.-H., D. Mihalas, and M.L. Norman. 1984. *J. Quant. Spectrosc. Rad. Transf.* **31**, 473.

Witteborn, F., D.M. Rank, J.D. Bregman, P.A. Pinto, D. Wooden, and T.S. Axelrod. 1989. *Astrophys. J. Lett.* **338**, L9.

Woodward, P.R. 1986. *In*: Radiation Hydrodynamics in Stars and Compact Objects., eds. D. Mihalas and K.H. Winkler, IAU Colloquium No. 89, *Lecture Notes in Physics* **255**, p. 245. Berlin: Springer.

Woosley, S.E. 1988. *Astrophys. J.* **330**, 218.

Woosley, S.E. 1990. *In*: Supernovae, ed. A.G. Petschek, p. 182. New York: Springer-Verlag.

Woosley, S.E., R.E. Taam, and T.A. Weaver. 1986. *Astrophys. J.* **301**, 601.

Woosley, S.E. and T.A. Weaver. 1986. *In*: Radiation Hydrodynamics in Stars and Compact Objects., eds. D. Mihalas and K.H. Winkler, IAU Colloquium No. 89, *Lecture Notes in Physics* **255**, p. 91. Berlin: Springer.

Yamada, Y., T. Nakamura, T., and K. Oohara. 1990. KEK Preprint, **90-32**.

Yanenko, N.N. 1971. The Method of Fractional Steps, New York: Springer.

Zeldovich, Ya.B. 1940. *Zh. Eksp. Teor. Fiz.* **10**, 542 (English translation: NACA TM 1261 [1960]).

Zeldovich, Ya.B. 1980. *Arch. Combust.* **1**, 1.

Zeldovich, Ya.B., G.I. Barenblatt, V.B. Librovich, and G.M. Makhviladze. 1985. The Mathematical Theory of Combustion and Explosions, p. 487f. New York: Plenum.

COURSE X

SUPERNOVA 1987A: FROM PROGENITOR TO REMNANT

K. NOMOTO, T. SHIGEYAMA, S. KUMAGAI

H. YAMAOKA, AND T. SUZUKI

Department of Astronomy, Faculty of Science
University of Tokyo
Bunkyo-ku, Tokyo 113, Japan

S. Bludman, R. Mochkovitch and J. Zinn-Justin, eds.
Les Houches, Session LIV 1990
Supernovae

Contents

1. Introduction 493
2. Progenitor of SN 1987A 494
   2.1. Observations 494
   2.2. Blue to red evolution and mass loss 494
   2.3. Red to blue evolution and mixing 496
   2.4. Lifetime in the HR diagram 500
   2.5. Presupernova evolution of the core 501
      2.5.1. Quasi-static nuclear burning 502
      2.5.2. Presupernova composition structure 502
3. Explosive nucleosynthesis 504
   3.1. Explosive nuclear burning 504
   3.2. Isotopic ratios and radioactive elements 508
   3.3. Comparison to the observed abundances in SN 1987A 509
4. Optical light curve 511
   4.1. Shock propagation and hydrodynamical structure 511
   4.2. Early light curve 515
   4.3. Hydrogen recombination front 519
   4.4. Radioactive decays, mixing of ^{56}Ni, and Bochum event 521
   4.5. Plateau-like peak and hydrogen recombination 525
   4.6. Constraints on explosion energy 527
5. X-ray light curve and clumpy mixing 528
   5.1. X-ray light curves at $t < 300$ d 529
   5.2. X-ray light curve at $t > 300$ d and effects of clumps 529
   5.3. Gamma-ray light curves 531
   5.4. X-ray and γ-ray spectra 531
6. Rayleigh-Taylor instabilities and mixing 535
   6.1. Linear stability analysis 535
   6.2. Two dimensional hydrodynamic calculation 537
   6.3. Mixing 538
   6.4. Comparison with observations 541
7. Dust formation 542
8. Pulsar and other radioactive elements 546
   8.1. Contributions of ^{57}Co and ^{44}Ti 546
   8.2. Predicted line γ-rays 549
   8.3. Contribution of the pulsar 549
   8.4. Predicted hard radiation from the pulsar 551
   8.5. X-rays from the neutron star surface 554
9. Soft x-ray emission and circumstellar matter 555
   9.1. Structure of circumstellar matter 555

9.2. Soft x-ray flare and collision with a circumstellar cloud 558
9.3. Collision with the red supergiant shell 559
9.4. Collision with the ring 561
References 564

1. Introduction

The supernova 1987A (SN 1987A) in the Large Magellanic Cloud is providing us with an excellent opportunity to test the theory of massive star evolution, nucleosynthesis, and supernova explosion. Spectral observations showed that SN 1987A is a Type II supernova, that is, an explosion of a massive star. Indeed, a massive blue supergiant star, Sk–69°202, has been identified as the progenitor of SN 1987A. The historic observations of neutrino burst from SN 1987A (Hirata et al. 1987; Bionta et al. 1987) dramatically proved the validity of the current theory of Type II supernovae and opened a new era of neutrino astronomy (Arnett et al. 1989; Hillebrandt and Höflich 1989 for reviews).

SN 1987A has been extensively observed at all wave bands including x-rays and γ-rays. From broadband photometric observations ranging from ultraviolet to far-infrared, the bolometric light curve has been constructed (Menzies et al. 1987; Catchpole et al. 1987, 1988, 1989; Whitelock et al. 1988, 1989; Hamuy et al. 1987; Suntzeff et al. 1988; Suntzeff and Bouchet 1990; Bouchet et al. 1991b). The light curves thus obtained enable us to probe the physical processes occurring in the interior of SN 1987A.

SN 1987A has confirmed the basic prediction of stellar evolution theory and, in addition, provided additional information on the explosion energy E, mass and distribution of ^{56}Ni, and the mass of the hydrogen-rich envelope M_{env}. These are important quantities, because theory of massive star evolution/explosion still contains considerable uncertainties such as (i) the mechanism that tranforms collapse into explosion, (ii) the mass loss, and (iii) convection (material mixing, in general).

SN 1987A has also shown several new and unexpected events discussed in this paper, which include:

(1) the blue-supergiant progenitor rather than a red-supergiant,
(2) the optical light curve of unique shape,
(3) early emergence of the x-rays and γ-rays,
(4) dust formation in the ejecta,
(5) the nature of circumstellar matter.

Consideration of these events leads us to deeper understanding of the mixing, mass loss, and explosion of massive stars.

2. Progenitor of SN 1987A

2.1. Observations

The progenitor of SN 1987A has been identified as a blue supergiant star Sk–69°202. Its effective temperature and luminosity are $\sim$ 13,000 K and $\sim 1.3 \times 10^5\ L_\odot$, respectively, so that its radius is $\sim 3 \times 10^{12}$ cm. The presupernova luminosity is determined by the helium core mass, M_α, as $L = 1.9 \times 10^5$, 1.3×10^5, 6.1×10^4, and $4.0 \times 10^4\ L_\odot$ for $M_\alpha = 8$, 6, 4, and 3.3 $M_\odot$, respectively (Nomoto and Hashimoto 1988; Nomoto et al. 1987; Woosley 1988). From this relation, the helium core mass of the progenitor is estimated as $M_\alpha \approx 6\ M_\odot$ whose main sequence mass is $M_{\rm ms} \approx 20 \pm 2\ M_\odot$.

Why the progenitor was blue at the explosion has been a fundamental question. UV observations have provided important clues to solve this problem. The UV emission lines of CNO elements show that the expansion velocity of the emitting gas was smaller than 30 km s^{-1} and the abundance ratios of N/C and N/O were much larger than the solar values (Panagia et al. 1987; Fransson et al. 1989). This is clear evidence that materials which had been processed by the CNO cycle were lost from the progenitor during its red-supergiant phase. A further implication is that the progenitor had evolved once to a red supergiant stage, lost some fraction of its hydrogen-rich envelope, and then contracted to the size of the blue supergiant. The recent observations of SN 1987A with HST has clearly revealed the presence of a ring around SN 1987A (Jacobsen et al. 1991), which confirmed this evolutionary picture.

2.2. Blue to red evolution and mass loss

The unexpected evolutionary behavior of the progenitor of SN 1987A can be ascribed to the low metallicity of the LMC. Several types of evolution of low metallicity massive stars have been presented (e.g., Weiss 1989 and references therein). Saio et al. (1988a, 1988b) and Yamaoka et al. (1991) adopted the Schwarzschild criterion for convection and modeled the evolution of stars with the initial masses $M_{\rm ms}$ = 21–23 $M_\odot$ and low metallicity Z = 0.005, starting from the main-sequence through neon ignition. Mass loss rate is given as a function of (L, $T_{\rm eff}$) which is 4–6 times the rate given by de Jager et al. (1988).

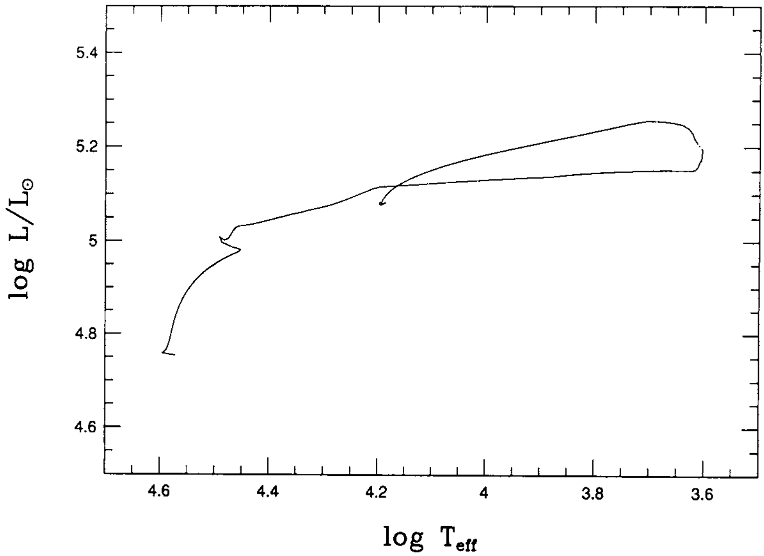

Fig. 1. Evolutionary path in the HR diagram from the main-sequence through carbon ignition for the star with the initial mass of $M_{\rm ms} = 23\ M_\odot$ and metallicity $Z = 0.005$ (Yamaoka et al. 1991).

Figure 1 shows the typical evolutionary path that reaches the blue supergiant progenitor for the star with $M_{\rm ms} = 23\ M_\odot$ (Yamaoka et al. 1991). During the star's evolution from blue supergiant to red, stellar mass decreases from $23\ M_\odot$ to $16\ M_\odot$ and forms a helium core of $M_{\rm core} = 6.7\ M_\odot$. During the red phase, a helium layer of $0.7\ M_\odot$ is mixed into the hydrogen-rich envelope, yielding $M_{\rm core} = 6.0\ M_\odot$ and $M_{\rm env} = 10\ M_\odot$. Dredge-up of the helium layer enhances the surface helium abundance to $Y_{\rm surf} = 0.43$, which is large enough to drive the star to move from the red to the location of Sk–69°202.

Figure 2 shows three types of evolutionary path (A, B, C) depending on mass loss, metallicity, and change in helium abundance Y in the envelope. Evolution from blue to red supergiant is driven by mass loss in the following way. As $M_{\rm env}$ decreases, the surface luminosity $L_{\rm surf}$ that the blue supergiant can radiate gets smaller, while the core luminosity $L_{\rm core}$ does not change appreciably because it depends mainly on $M_{\rm core}$. As a result the envelope starts to expand to absorb the excess luminosity.

Whether the star remains blue or moves to red can be understood also from the existence or non-existence of envelope solutions for blue supergiants. For the envelope to fit to the core for given L, $T_{\rm eff}$, and $M_{\rm core}$, a certain relation

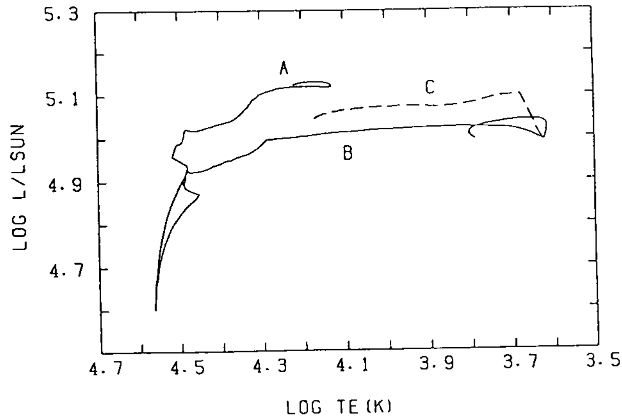

Fig. 2. Evolutionary tracks in the HR diagram of the initially 20 $M_\odot$ star (Saio et al. 1988a). Cases A, B, and C correspond to: (A) models with no mass loss; (C) models with no artificial enhancement of helium in the hydrogen-rich envelope, and (B) models with enhancement of helium up to Y = 0.4.

between M_{env} and the surface helium abundance Y should be satisfied (figs. 3 and 4; Saio et al. 1988a; Barkat and Wheeler 1988). For example, the relations are Y = 0.25 and 0.4 for M_{env} = 16 $M_\odot$ and 10 $M_\odot$, respectively; for $L = 10^5$ $L_\odot$ and Z = 0.005. Accordingly, if M_{env} were as massive as 16 $M_\odot$ (i.e., almost no mass loss) for $Y \sim 0.25$, the star would have remained blue without undergoing extensive redward evolution (case A in fig. 2) as found by Hillebrandt et al. (1987) and Arnett (1987). However, as the star loses a significant fraction of its envelope mass, it moves toward the red becoming a red supergiant star, because M_{env} is too small for the star to remain blue for its L and Y (cases B and C in fig. 2). Thus, mass loss is the driving mechanism of redward evolution.

2.3. Red to blue evolution and mixing

Evolution from red to blue takes place after the C+O core forms and helium shell burning becomes active (Nomoto et al. 1988a, 1989). Whether the star remains red or returns to blue depends on the balance between core luminosity L_{core}, and surface luminosity L_{surf}. Surface luminosity depends on surface abundance, and thus on mixing.

Sequences of envelope models in thermal equilibrium (i.e., $L_{surf} = L_{core}$) are integrated from the surface to the helium burning shell for several helium abundances, Y, as shown in fig. 5 (Nomoto et al. 1991a). Along the line,

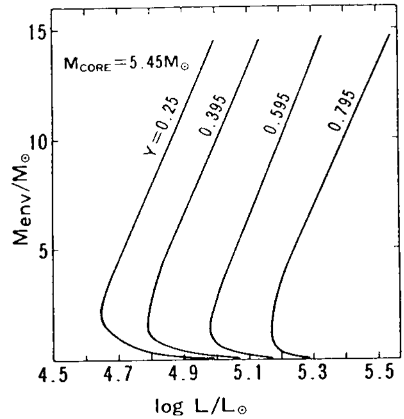

Fig. 3. Envelope solutions with the outer boundary of log $T_{\rm eff}$ = 4.2 and inner boundary conditions that fit to the core at M_r = 5.45 $M_\odot$ and r = 0.6 $R_\odot$ (Saio et al. 1988a). The ordinate is the mass of the hydrogen-rich envelope ($M_{\rm env} = M - 5.45$ $M_\odot$) given as a function of luminosity L and the mass fraction of helium Y.

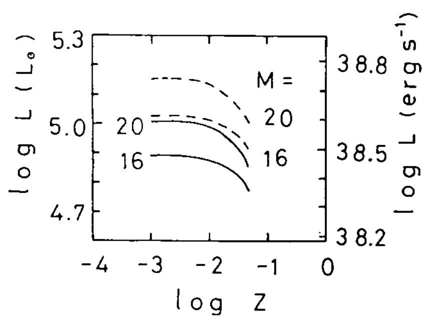

Fig. 4. Envelope solutions for different metallicity (Saio et al. 1988a). For log $T_{\rm eff}$ = 4.2, lines for constant total mass ($M = M_{\rm env} + 5.45$ $M_\odot$ = 20 and 16 $M_\odot$) are given as a function of luminosity L and the mass fraction of heavy elements Z. The solid and dashed lines are for helium abundance $Y = 0.255 - Z$ and $0.4 - Z$, respectively.

the core radius changes. It should be noted that $L_{\rm surf}$ is larger for larger Y (and smaller Z) because of the smaller opacity. If the hydrogen-rich envelope is metal deficient and becomes sufficiently helium-rich by mixing, the resultant decrease in opacity causes an increase in surface luminosity eventually exceeding the core luminosity. To compensate for this luminosity imbalance created by adding the gravitational energy release, the envelope

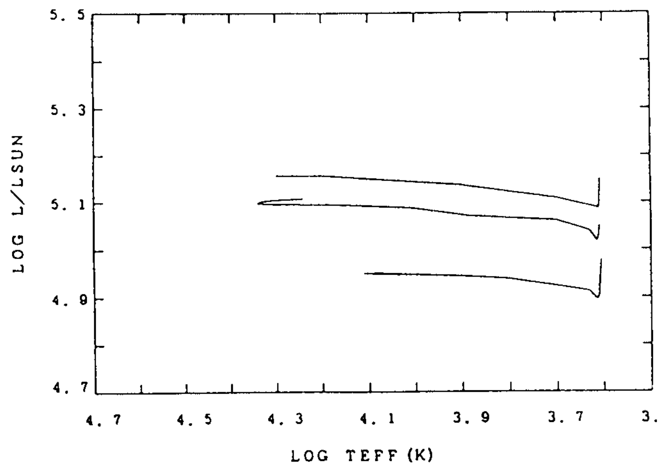

Fig. 5. Red supergiant envelope solutions for the 16 $M_{\odot}$ star having a helium core of $M_{\alpha} = 6\ M_{\odot}$. At the inner boundary, the envelope (including the helium layer) is fitted to the helium burning shell at $M_r = 3.4\ M_{\odot}$. Shown are the three sequences for the surface helium abundance of $Y = 0.50$, 0.43, and 0.25, where the star is more luminous for larger Y (Nomoto et al. 1991a).

starts to contract, undergoing extensive excursion from red back to blue (case C in fig. 2; case B has a value of Y which is too small to become sufficiently compact).

The mechanism for such an enhancement of helium would be convective mixing of the material near the bottom of the hydrogen-rich envelope, including a part of the helium layer. Though the surface convection zone of the current model is not deep enough, the deep mixing model has the advantage that the observed helium enhancement (Allen et al. 1989) and large N/C and N/O ratios over the solar values can be consistently explained.

The N/C ratio at the surface depends on the extent of mixing in the envelope; deeper mixing yields larger N/C and N/O ratios at the surface since the materials in the deeper layers are more nitrogen-rich (fig. 6). If a hydrogen-rich envelope is uniformly mixed, the N/C ratio is consistent with the observation only for $7\ M_{\odot} < M_{\rm env} < 11\ M_{\odot}$ (Saio et al. 1988b). For smaller $M_{\rm env}$, the N/C ratio is too large and vice versa. The N/O ratio is less restrictive. For $M = 16.3\ M_{\odot}$ ($M_{\rm env} = 10.3\ M_{\odot}$), mixing down to at least $M_r = 7\ M_{\odot}$ is required to explain the observed N/C ratio. Complete mixing in the entire hydrogen-rich envelope and a dredge-up of helium layer are consistent with observations. For such deep mixing, the N/O ratio agrees with the ob-

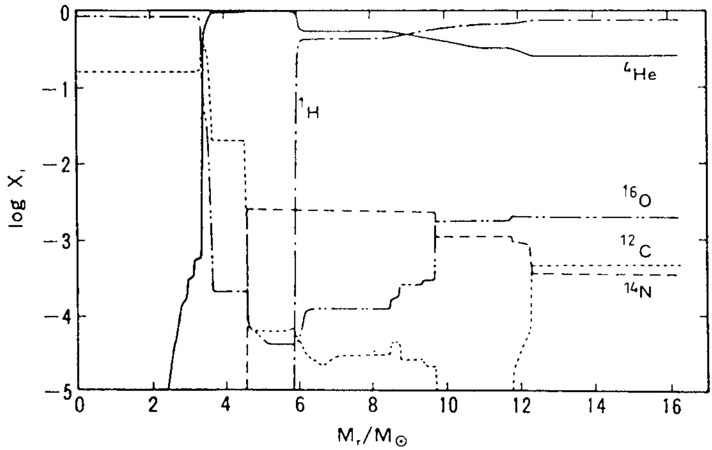

Fig. 6. Composition structure of the star of fig. 2, where X_i denotes the mass fraction and M_r denotes the mass included in a sphere with radius r (Saio et al. 1988b). The stage illustrated is when the C+O core forms and helium shell burning begins. Stellar mass has decreased from $M_I = 21\ M_\odot$ to $16.3\ M_\odot$. Elements shown are ^{1}H (dash-dotted line), ^{4} He (solid), ^{12}C (dotted), ^{14}N (dashed), and ^{16}O (dash-two dotted). Other elements are not shown for clarity.

served ratio, therefore the observed nitrogen overabundance in circumstellar matter can be explained by the evolution of a progenitor that experienced blue-red-blue evolution due to enhanced Y_{surf}.

The composition of a hydrogen-rich envelope after convective mixing is summarized in table 1. Evolution toward blue is more likely to occur for a lower metallicity envelope ($Z < 0.01$) (fig. 4). The envelope with larger Z has larger opacity, thereby requiring a greater enhancement of Y to reduce the opacity for evolution toward blue.

Table 1
Mass fractions in the hydrogen-rich envelope of the progenitor

H	He	^{12}C	^{13}C	^{14}N	^{13}O	heavier
0.565	0.430	1.82×10^{-4}	2.9×10^{-5}	1.42×10^{-3}	1.14×10^{-3}	rest

2.4. Lifetime in the HR diagram

If the Schwarzshild criterion is adopted for convection, the timescale of redward excursion depends on mass loss rate. For larger rates, the star moves redward earlier because of a faster decrease in M_{env}. Figure 7 shows the lifetime of evolution from blue to red in the HR diagram in effective temperature bins normalized to unity (solid) for the mass loss rate of 6 times the rates given by de Jager et al. (1988). The dashed histogram is the number of supergiants with $-8 < M_{bol} < -9$ in the LMC, which is also normalized to unity. This model is qualitatively consistent with the observed histogram (Humphreys and Davidson 1978; Fitzpatrick and Garmany 1990).

If the Ledoux criterion is adopted, the star makes a loop in the HR diagram and eventually returns to red. [We need fine-tuning of the time scale of semi-convective mixing for the star to stay in blue (Woosley et al. 1988a; Langer et al. 1989).] The timescale for the star to move from blue to red seems to be too fast to reproduce the observed histogram (Tuchman and Wheeler 1991).

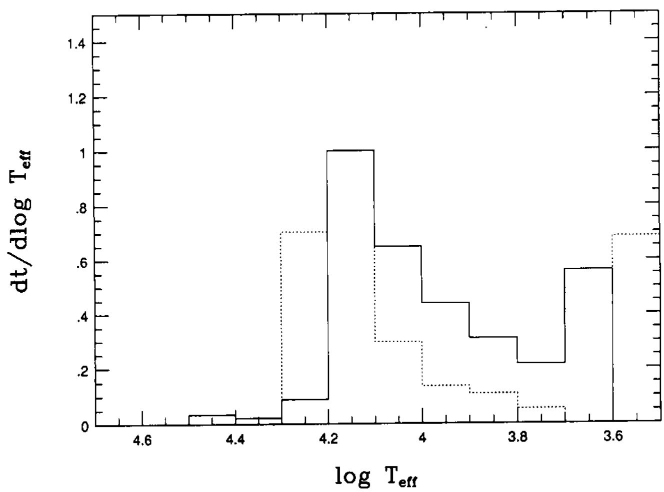

Fig. 7. The lifetime of evolution from blue to red in the HR diagram in effective temperature bins normalized to unity (solid) for a mass loss rate of 6 times that given by de Jager et al. (1988). The dashed histogram represents the number of supergiants with $-8 < M_{bol} < -9$ in the LMC, which is also normalized to unity (Yamaoka et al. 1991).

2.5. Presupernova evolution of the core

After returning from red, the progenitor evolved to form an onion-skin like composition structure. The star eventually collapsed due to photodisintegration of iron nuclei and electron capture. The outcome of collapse and nucleosynthesis is highly sensitive to the iron core mass and a density structure in the heavy element mantle. However, there exist considerable uncertainties in determining the presupernova models, because they depend on carbon abundance after helium burning, which in turn depends on the $^{12}C(\alpha, \gamma)^{16}O$ rate (Fowler 1984) and overshooting at the edge of a convective helium-burning core (e.g., Bertelli et al. 1985). A larger reaction rate and overshooting would yield a smaller carbon abundance but these factors, especially overshooting, involve large uncertainties.

Since no reliable theory of convection exists, it is necessary to explore the various possible evolutionary paths within an uncertain range. Moreover, the mass of the evolved core is close to the Chandrasekhar mass, so that the core structure is sensitive to the electron mole number Y_e and equation of state of strongly degenerate matter. Therefore, inclusion of improved physical input is expected to bring a large effect on the presupernova structure.

Nomoto and Hashimoto (1988) have carried out the calculation of massive star evolution. The important improvements of their models, when compared with those by Woosley and Weaver (1986) are: (i) Coulomb interaction is included in the equation of state (Slattery et al. 1982); (ii) electron capture is included from the beginning of oxygen burning; and (iii) the nuclear reaction rates and electron capture rates for silicon burning are obtained from an extensive network calculation with 250 species. Improvements (i) and (ii) lead to a decrease of the effective Chandrasekhar mass and, hence, to a decrease of the core mass. The behavior of silicon shell burning described in improvement (iii), crucial in the determination of the final presupernova structure, is considerably different from the models by Woosley and Weaver (1986).

The Schwarzschild criterion for convective stability is adopted and overshooting is neglected (see Woosley and Weaver 1988 for effects of semiconvection). A high $^{12}C(\alpha, \gamma)^{16}O$ rate (Caughlan et al. 1988) is adopted. For $M_\alpha = 6\ M_\odot$, carbon abundance is more important for structure than improvements (i) and (ii) mentioned above. As described below, the presence of an active carbon burning shell in our model results in the formation of a smaller iron core and an outer mantle of lower density than in Woosley and Weaver (1986). The helium core of 6 $M_\odot$ evolves as shown in the following section.

2.5.1. Quasi-static nuclear burning

The star undergoes alternating stages of gravitational contraction and central nuclear burning of hydrogen, helium, carbon, neon, oxygen, and silicon. The helium burning stage lasts 6.0×10^5 yr and a C-O core of 3.80 $M_\odot$ forms. The mass fractions of carbon and oxygen are $X(^{12}\mathrm{C}) = 0.22$, and $X(^{16}\mathrm{O}) = 0.76$, respectively. This amount of carbon is large enough for active (i.e., convective) carbon burning to take place in the center and, later, in the outer shell.

Carbon burning starts in the center (1.4×10^4 yr after exhaustion of helium) and lasts only 450 yr. When carbon in the core is almost depleted, the resultant composition is $X(^{16}\mathrm{O}) = 0.66$ and $X(^{20}\mathrm{Ne}) = 0.26$. The carbon burning layer shifts to the outer shell and a convective shell develops at $M_r = 1.67\ M_\odot$.

Neon burning is ignited in the center (40 yr after exhaustion of carbon) and lasts only 0.4 yr. After exhaustion of neon in the center, an oxygen-rich core of $X(^{16}\mathrm{O}) = 0.79$ and $X(^{24}\mathrm{Mg}) = 0.10$ forms.

Oxygen burning synthesizes silicon- and sulfur-rich elements and the product becomes somewhat neutron-rich. The main weak processes involved are electron capture and positron decay. When $X(^{16}\mathrm{O}) = 0.01$, Y_e drops to 0.493 (neutron excess $\eta = 1 - 2\,Y_\mathrm{e} = 0.014$) in the convective core where $X(^{28}\mathrm{Si}) = 0.54$, $X(^{32}\mathrm{S}) = 0.17$, $X(^{34}\mathrm{S}) = 0.12$, and $X(^{38}\mathrm{Ar}) = 0.13$.

During contraction of the Si-S core, electron capture on the products of oxygen burning decreases Y_e down to 0.46, when silicon is ignited. After exhaustion of silicon, a convective silicon-burning shell appears successively. The outer edge of the convective silicon burning zone is limited by an entropy barrier at the oxygen burning shell at $M_r = 1.6\ M_\odot$, where a steep density gradient exists.

2.5.2. Presupernova composition structure

Composition structure at the presupernova stage is as follows. This is based on a density of $\rho_\mathrm{c} = 2 \times 10^{10}$ g cm^{-3}, shown in fig. 8.

(1) Fe core of $M_r \leq 1.40\ M_\odot$, composed of nuclear statistical equilibrium elements, that is, iron peak elements and a trace of ^{4}He, free protons and neutrons.

(2) Fe-Si layer at $1.40\ M_\odot < M_r \leq 1.48\ M_\odot$ is composed of two quasi-statistical equilibrium clusters, that is, a Fe cluster and a Si cluster. The neutron excess is $\eta \equiv 1 - 2\,Y_\mathrm{e} = 0.012$.

(3) Si-rich layer at $1.48\ M_\odot < M_r \leq 1.67\ M_\odot$ is composed of a Si quasi-statistical equilibrium cluster (mainly ^{28}Si, ^{32}S, ^{34}S, ^{38}Ar) where $\eta = 0.012$ for $M_r \leq 1.63\ M_\odot$ and $\eta = 0.0026$ for $1.63\ M_\odot < M_r \leq 1.67\ M_\odot$. The neutron excess in this layer is important for synthesis of neutron-rich iron

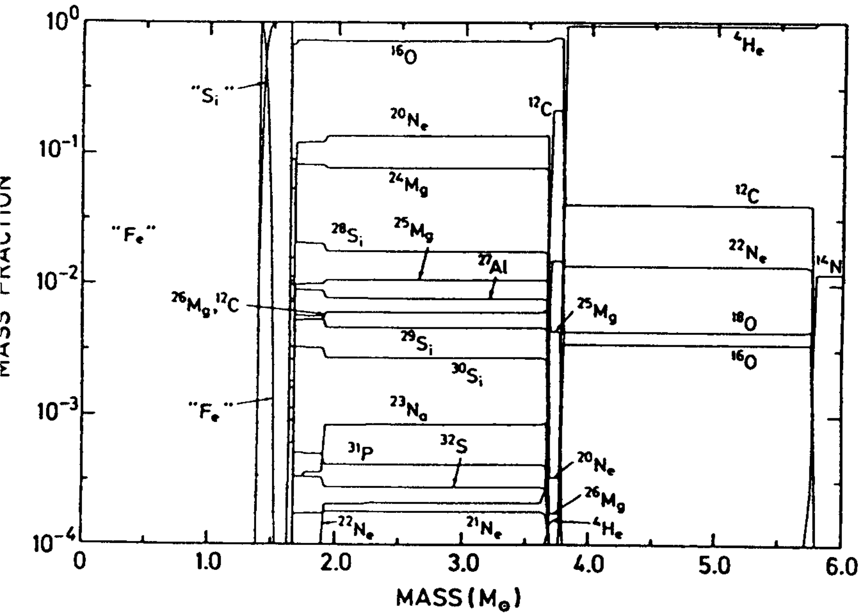

Fig. 8. Abundance distribution at the onset of collapse for the 6 $M_\odot$ helium core of the 20 $M_\odot$ star. "Fe" and "Si" denote iron-peak elements and silicon-peak elements, respectively (Nomoto and Hashimoto 1988).

peak elements, but it is subject to uncertainties involved in electron capture rates and the time scale of mixing for neutron-rich species from the bottom of the convective oxygen and silicon burning layer.

(4) Oxygen-rich layer at 1.67 $M_\odot < M_r \leq 3.66$ $M_\odot$ is composed of ^{16}O, ^{20}Ne, ^{24}Mg, and a trace of Si, Al, Mg, and Na isotopes with $\eta = 0.0016$.

(5) Carbon and oxygen layer at 3.66 $M_\odot < M_r \leq 3.76$ $M_\odot$ which includes a trace of Na, Mg, and Ne isotopes.

(6) Helium-rich layer at 3.76 $M_\odot < M_r \leq 5.71$ $M_\odot$, which includes ^{12}C, ^{16}O, ^{18}O, ^{22}Ne, and ^{25}Mg. These elements are produced from 3 $\alpha \rightarrow$ ^{12}C(α, γ)^{16}O, and ^{14}N(α, γ)^{18}F(β^+)^{18}O(α, γ)^{22}Ne(α, n)^{25}Mg reactions in the convective helium burning layer. Whether the last reaction leads to s-process nucleosynthesis needs more investigation (e.g., Prantzos et al. 1988).

(7) Helium layer at 5.71 $M_\odot < M_r \leq 6.0 M_\odot$, composed of ^{4}He and ^{14}N.

The gradient of entropy and density is relatively small at the iron core edge. The largest jump in these quantities is seen at the oxygen-burning shell. Accordingly, the mass cut that divides the neutron star and the ejecta could be approximately 1.6 $M_\odot$ for 20–25 $M_\odot$ stars.

3. Explosive nucleosynthesis

The initial model for explosion calculation is constructed from the models of pre-collapse $6\,M_\odot$ helium core and the hydrogen-rich envelope described in sec. 2. Since it is highly uncertain how the shock wave forms and what mass cut divides the neutron star residue and ejecta, the inner $1.6\,M_\odot$ is replaced with a point mass neutron star. Energy is then deposited instantaneously at the bottom of the ejecta generating a strong shock wave.

In the following, the name of the hydrodynamical model identifies its ejected mass $M_{\rm ej}$ and the final kinetic energy of explosion E. For example, 14E1 and 11E0.6 denote the models with $M_{\rm ej} = 14.6\,M_\odot$ and $E = 1 \times 10^{51}$ ergs, and $11.4\,M_\odot$ and 0.6×10^{51} erg, respectively. The model 14E1 consists of a heavy element layer of $2.2\,M_\odot$, a helium-rich layer of $2.2\,M_\odot$, and a hydrogen-rich envelope of $10.2\,M_\odot$.

3.1. Explosive nuclear burning

As the shock wave propagates through the Si and O-rich layers, explosive nucleosynthesis takes place behind the shock (Nomoto et al. 1988b; Hashimoto et al. 1989; Thielemann et al. 1990). Nucleosynthesis is determined by the peak temperature T as shown in the following three subsections (Thielemann et al. 1991 for details).

Explosive silicon burning. Explosive Si-burning takes place at $T >$ 4–5 $\times 10^9$ K and can be divided into three different regimes: incomplete Si-burning, and complete Si-burning, with either a normal or α-rich freeze-out.

Complete Si-exhaustion at $T > 5 \times 10^9$ K produces only Fe-group nuclei. The most abundant nucleus in the normal and α-rich freeze-out is ^{56}Ni if $\eta < 2 \times 10^{-2}$ or $Y_e > 0.49$. For less abundant nuclei, the final α-capture plays a dominant role transforming nuclei like ^{56}Ni, ^{57}Ni, and ^{58}Ni into ^{60}Zn, ^{61}Zn, and ^{62}Zn in an α-rich freeze-out where trace abundances of ^{40}Ca, ^{44}Ti, ^{48}Cr, and ^{52}Fe are also obtained. For the 20 $M_\odot$ model only α-rich freeze-out is encountered.

Incomplete Si-burning takes place at $T \approx 4 - 5 \times 10^9$ K. Temperatures are not high enough for an efficient bridging of the bottleneck above the magic proton number Z = 20 by nuclear reactions. Besides the dominant fuel nuclei ^{28}Si and ^{32}S, the α-nuclei ^{36}Ar and ^{40}Ca are most abundant. Partial leakage through the bottleneck above Z = 20 produces ^{56}Ni and ^{54}Fe as dominant abundances in the Fe-group. Smaller amounts of ^{52}Fe, ^{58}Ni, ^{55}Co, and ^{57}Ni are also produced.

Explosive oxygen burning. At $T > 3.3 \times 10^9$ K, a quasi-equilibrium is established among nuclei in the range $28 < A < 45$. The main burning products are ^{28}Si, ^{32}S, ^{36}Ar, ^{40}Ca, ^{38}Ar, and ^{34}S. Also ^{33}S, ^{39}K, ^{35}Cl, ^{42}Ca, and ^{37}Ar are produced with mass fractions less than 10^{-2}. In zones with $T \sim 4 \times 10^9$ K, there still exists contamination by the Fe-group nuclei ^{54}Fe, ^{56}Ni, ^{52}Fe, ^{58}Ni, ^{55}Co, and ^{57}Ni.

Explosive neon and carbon burning. The main burning products are ^{16}O, ^{24}Mg, and ^{28}Si, synthesized via the reaction sequences ^{20}Ne (γ, α) ^{16}O and ^{20}Ne (α, γ) ^{24}Mg (α, γ) ^{28}Si; this is similar to the hydrostatic case. Zones with $T > 2.1 \times 10^9$ K undergo a combined version of explosive Ne and C-burning. Besides the major abundances, Ne-burning also supplies substantial amounts of ^{27}Al, ^{29}Si, ^{32}S, ^{30}Si, and ^{31}P, and in addition, C-burning contributes the nuclei ^{20}Ne, ^{23}Na, ^{24}Mg, ^{25}Mg, and ^{26}Mg.

In the 20 $M_\odot$ star, the maximum temperature T behind the shock is shown in fig. 9, where T is approximated by $E = 4\pi r^3/3\ aT^4$ for a sphere of radius r (e.g., Woosley 1988). The region with $T > 5 \times 10^9$ K, for example,

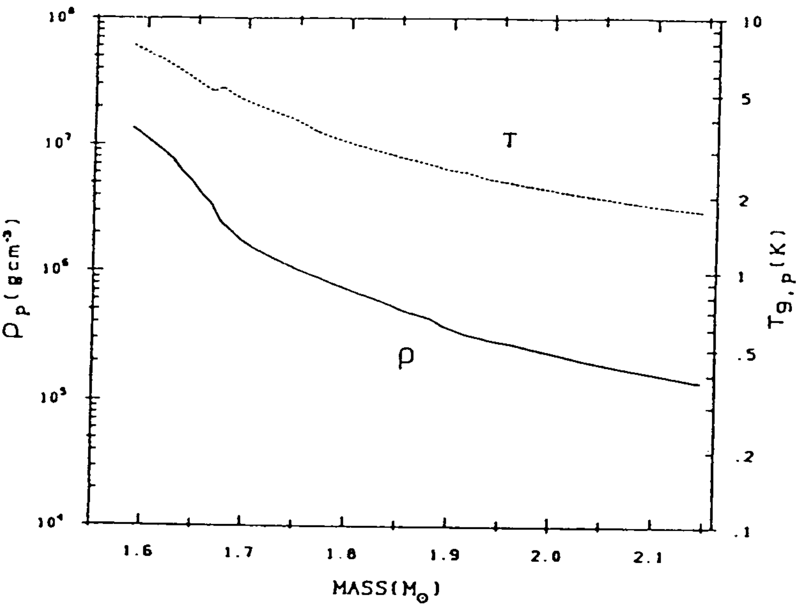

Fig. 9. Peak temperatures and corresponding densities at the passage of the shock wave for $E = 1 \times 10^{51}$ erg (Hashimoto et al. 1989).

corresponds to a sphere of radius approximately 3700 $(E/10^{51}\ \mathrm{erg})^{1/3}$ km which contains 1.7 $M_\odot$.

Explosive nucleosynthesis for $E = 1 \times 10^{51}$ erg takes place as follows:

(1) complete Si-burning extends out to 1.69 $M_\odot$,

(2) incomplete Si-burning starts at 1.69 $M_\odot$ and extends out to 1.74 $M_\odot$,

(3) explosive O-burning occurs up to 1.8 $M_\odot$, and

(4) explosive Ne-burning leads to an ^{16}O-enhancement over its hydrostatic value in mass zones up to 2 $M_\odot$.

The resulting abundance distribution is shown in fig. 10. Figure 11 shows detailed abundance distributions in zones which undergo α-rich freezeout (left), and incomplete Si-burning (M_r < 1.74 $M_\odot$) with explosive O-burning (right). The integrated abundances of stable isotopes relative to the solar values (normalized to ^{28}Si) are shown in fig. 12.

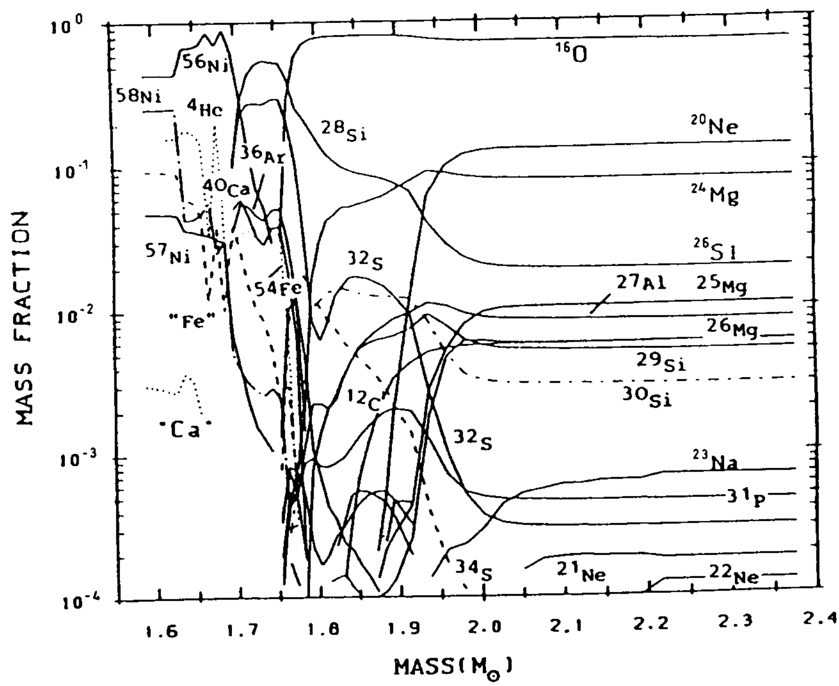

Fig. 10. Abundance distribution after passage of the supernova shock front (Hashimoto et al. 1989). Matter outside 2 M$_\odot$ is essentially unaltered. Mass zones inside or 2 M$_\odot$ experience explosive Si, O, Ne, and C-burning.

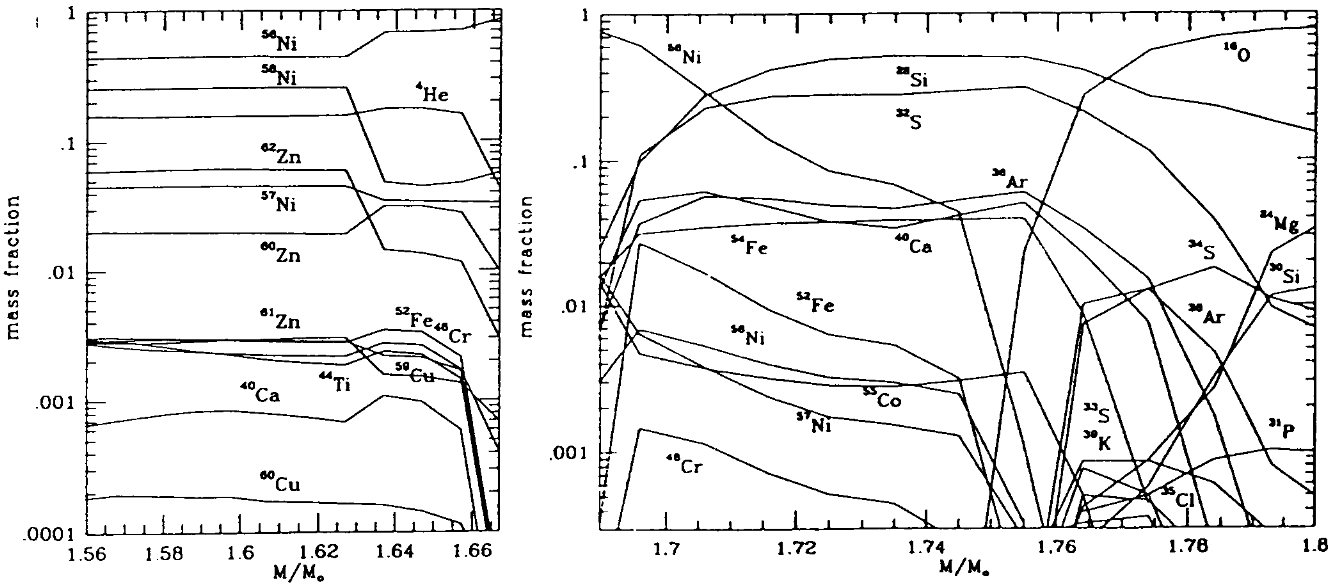

Fig. 11. Detailed abundance distributions in zones which undergo alpha-rich freezeout (left), and incomplete Si-burning at $M_r < 1.74\ M_\odot$ with explosive O-burning at $M_r < 1.8\ M_\odot$ (right) (Thielemann et al. 1990).

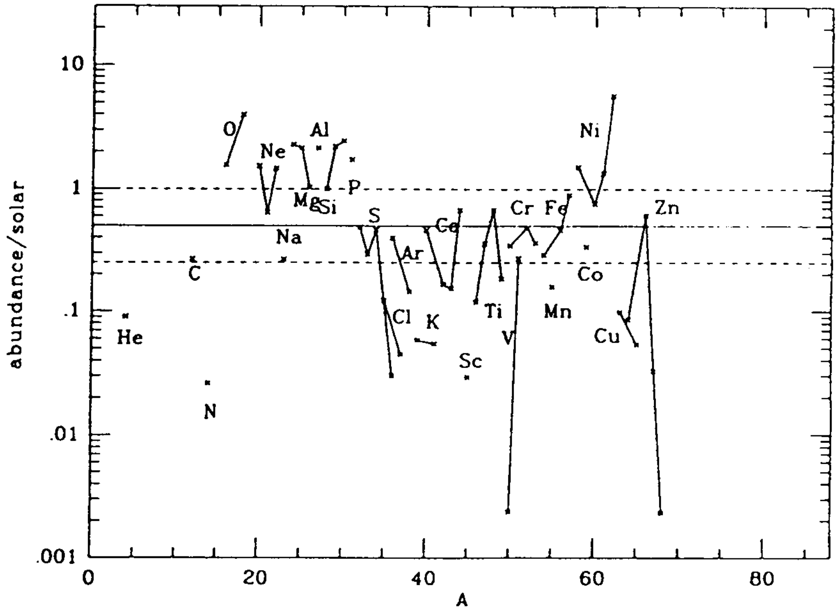

Fig. 12. The abundances of stable isotopes relative to the solar values (normalized to ^{28}Si) (Thielemann et al. 1990).

3.2. Isotopic ratios and radioactive elements

The isotopic ratios among iron-peak elements including ^{57,58}Ni and ^{44}Ti can be compared to observations. These abundances depend on the distribution of Y_e in the Si-rich region. In our presupernova model, Y_e changes from 0.4987 to 0.494 at $M_r = 1.63\ M_\odot$, which corresponds to a change in the neutron excess $\eta = 1 - 2Y_e$ from 2.6×10^{-3} to 1.2×10^{-2}.

In presupernova evolution, this position marks the outer boundary of the O-burning convective shell, which extends from 1.05 to 1.63 $M_\odot$ after exhaustion of oxygen in the central region (Nomoto and Hashimoto 1988). Because of higher densities and larger abundances of silicon-rich products, this layer undergoes more electron captures than the outer layers during oxygen-shell burning and the subsequent contraction of Si-rich core. The outer layers do not experience many electron captures, because of low density.

It should be noted that the outer boundary of the convective layer may not be accurately determined because of a rather flat entropy distribution there. Therefore it is quite possible to have a smaller size convective O-burning shell. To take into account this uncertainty, Nomoto et al. (1991a) examined nucleosynthesis where the region with $Y_e = 0.4987$ extends down to $M_r = 1.60\ M_\odot$. The resulting abundances are shown in table 2.

The isotopic ratios ^{57}Fe/^{56}Fe and ^{44}Ca/^{56}Fe reflect the ratios of ^{57}Ni/^{56}Ni and ^{44}Ti/^{56}Ni after the radioactive decays of $^{57}\mathrm{Ni} \rightarrow {}^{57}\mathrm{Co} \rightarrow {}^{57}\mathrm{Fe}$ and $^{44}\mathrm{Ti} \rightarrow {}^{44}\mathrm{Sc} \rightarrow {}^{44}\mathrm{Ca}$. The ^{58}Ni/^{56}Fe ratio strongly depends on η near the mass cut and is close to the solar value in table 2, while it is about 5 times the solar value in Hashimoto et al. (1989). On the other hand, the ^{57}Fe/^{56}Fe and ^{44}Ca/^{56}Fe ratios are not so different from Hashimoto et al. (1989) and Thielemann et al. (1990), and the ^{57}Fe/^{56}Fe is still 1.7 times the solar value.

3.3. Comparison to the observed abundances in SN 1987A

What can be learned about nucleosynthesis from photometric and spectroscopic observations of SN 1987A? The mass of ^{56}Ni is determined to be approximately 0.07 $M_\odot$ from the optical light curve. This places the mass cut between the ejecta and the remaining neutron star at 1.60 $M_\odot$.

The infrared spectra reveal emission lines of heavy elements such as Ne, S, Ar, Ca, Ni, Co, and Fe (Rank et al. 1988; Erickson et al. 1988; Danziger et al. 1988; Aitken et al. 1988; Terndrup et al. 1988). These are certainly freshly synthesized elements, as seen from their estimated masses. In particular, the observed time change of the masses of Co and Fe is in good agreement with those resulting from the decay of $\sim 0.07 M_\odot$ ^{56}Co (Danziger et al. 1989; Aitken et al. 1988).

The ionic masses estimated from spectroscopic observations are given by Danziger et al. (1991). The sum of Co and Fe is consistent with the ^{56}Ni mass derived from the light curve. The mass of stable nickel (^{58}Ni etc.) has been estimated to be 3–5 $\times 10^{-3}$ $M_\odot$ at day 400 (Witteborn et al. 1989; Danziger et al. 1991). This is in better agreement with table 2 than with Hashimoto et al. (1989).

Observed mass estimates of other elements are approximately consistent with table 2. The crucially important element is oxygen, since oxygen mass is very sensitive to the progenitor's mass as well as the $^{12}\mathrm{C}(\alpha, \gamma)^{16}\mathrm{O}$ rate (Woosley et al. 1988b).

Table 2
Nucleosynthesis products for the model of SN 1987A

Species	Mass[a]	$\langle X_i/X_{16}\rangle^b$	Species	Mass[a]	$\langle X_i/X_{16}\rangle^b$
^{4}He	2.10	0.0580	^{48}Ca	2.41 (−16)	1.13 (−11)
^{12}C	0.114	0.243	^{45}Sc	1.04 (−7)	0.0173
^{13}C	1.17 (−10)	2.07 (−8)	^{46}Ti	6.81 (−6)	0.197
^{14}N	0.00272	0.0159	^{47}Ti	1.73 (−6)	0.0538
^{15}N	6.48 (−10)	9.60 (−7)	^{48}Ti	1.85 (−4)	0.557
^{16}O	1.48	1.0	^{49}Ti	4.89 (−6)	0.193
^{17}O	9.86 (−9)	1.64 (−5)	^{50}Ti	1.12 (−10)	4.39 (−6)
^{18}O	8.68 (−3)	2.59	^{50}V	2.15 (−10)	0.00150
^{19}F	7.84 (−11)	1.25 (−6)	^{51}V	6.40 (−6)	0.110
^{20}Ne	0.229	0.914	^{50}Cr	3.54 (−5)	0.308
^{21}Ne	3.03 (−4)	0.474	^{52}Cr	8.64 (−4)	0.376
^{22}Ne	0.0293	1.46	^{53}Cr	7.12 (−5)	0.268
^{23}Na	0.00115	0.224	^{54}Cr	6.26 (−9)	9.29 (−5)
^{24}Mg	0.147	1.85	^{55}Mn	2.27 (−4)	0.111
^{25}Mg	0.0185	1.77	^{54}Fe	0.00252	0.229
^{26}Mg	0.0174	1.45	^{56}Fe	0.0732	0.405
^{27}Al	0.0155	1.73	^{57}Fe	0.00307	0.696
^{28}Si	0.0850	0.842	^{58}Fe	3.70 (−9)	6.48 (−6)
^{29}Si	0.00980	1.85	^{59}Co	1.31 (−4)	0.253
^{30}Si	0.00719	1.98	^{58}Ni	0.00371	0.485
^{31}P	0.00105	0.833	^{60}Ni	0.00218	0.718
^{32}S	0.0229	0.374	^{61}Ni	1.59 (−4)	1.19
^{33}S	8.84 (−5)	0.177	^{62}Ni	7.26 (−4)	1.69
^{34}S	0.00126	0.437	^{64}Ni	2.06 (−15)	1.83 (−11)
^{36}S	4.23 (−7)	0.0291	^{63}Cu	3.00 (−6)	0.0338
^{35}Cl	6.05 (−5)	0.154	^{65}Cu	7.02 (−7)	0.0172
^{37}Cl	4.96 (−6)	0.0375	^{64}Zn	1.78 (−5)	0.116
^{36}Ar	0.00378	0.316	^{66}Zn	2.08 (−5)	0.229
^{38}Ar	3.25 (−4)	0.137	^{67}Zn	6.39 (−8)	0.00471
^{40}Ar	4.65 (−9)	1.14 (−3)	^{68}Zn	5.33 (−9)	8.48 (−5)
^{39}K	3.24 (−5)	0.0604	^{70}Zn	3.79 (−21)	1.77 (−15)
^{41}K	1.28 (−6)	0.0314	^{69}Ga	2.21 (−12)	3.60 (−7)
^{40}Ca	0.00325	0.351	^{71}Ga	1.54 (−18)	3.67 (−13)
^{42}Ca	9.45 (−6)	0.146	^{70}Ge	1.51 (−14)	2.26 (−9)
^{43}Ca	3.38 (−6)	0.244	^{72}Ge	1.19 (−20)	1.30 (−15)
^{44}Ca	9.15 (−5)	0.417	^{73}Ge	3.91 (−24)	7.20 (−19)
^{46}Ca	1.12 (−11)	2.59 (−5)	^{74}Ge	9.85 (−23)	7.84 (−18)

[a] in $M_\odot$; Mass integrated at $1.60\ M_\odot \le M_r \le 6.0 M_\odot$.
[b] $\langle X_i/X_{16}\rangle \equiv [X_i/X(^{16}O)]/[X_i/X(^{16}O)]_\odot$
(numbers in parenthesis are powers of ten)

4. Optical light curve

SN 1987A was identified with a Type II supernova, yet its light curve is quite unique.

(i) It took only 3 hours for the visual magnitude to reach 6.4 magnitude after a neutrino burst (McNaught 1987; Zoltowski 1987).

(ii) At the subsequent plateau in the V band, the visual magnitude was much dimmer than that of a typical Type II-P supernova.

(iii) Afterwards, the optical luminosity increased until about 84 d, forming a broad peak.

(iv) The supernova declined rapidly at first and then more slowly at 0.01 mag/day, which coincides with the ^{56}Co decay rate.

In the theoretical models, the light curve is powered by two energy sources:

(1) A shock wave initially establishes the radiation field with energy of roughly half the explosion energy. The early light curve up to $t \sim 25$ d can be accounted for by the diffusive release of this energy.

(2) Later radioactive decay of ^{56}Co provides energy for the light curve.

The calculated light curve shape, being sensitive to hydrodynamics, is a useful tool to infer the distribution of elements, mass of ejecta (in particular, mass of hydrogen-rich envelope, $M_{\rm env}$), and explosion energy, E (Nomoto and Shigeyama 1988). For example, the observed features (i) and (ii) impose important constraints on the progenitor's radius and explosion energy. Also, owing to the small contribution of initial shock heating, the later light curve provided unique information on the internal energy source and material distribution. Let us first describe hydrodynamical features which affect the light curve shape (Shigeyama et al. 1988; Shigeyama and Nomoto 1990).

4.1. Shock propagation and hydrodynamical structure

Figures 13a and 13b show the density distribution of the progenitor model from its center to the surface against M_r and r, respectively. As the shock wave propagates through the surface, the shocked layers undergo acceleration and deceleration. As discussed in section 6, the composition interfaces of hydrogen/helium and helium/C+O are strongly Rayleigh-Taylor unstable, which induces mixing of material before shock breakout at the surface. Particularly important for light curve behavior is the mixing of ^{56}Ni into the hydrogen-rich envelope, and mixing of hydrogen down to the central region. In the mixed model of light curve calculations, the abundance distribution given in fig. 14 is adopted. This is inferred from the comparison of the

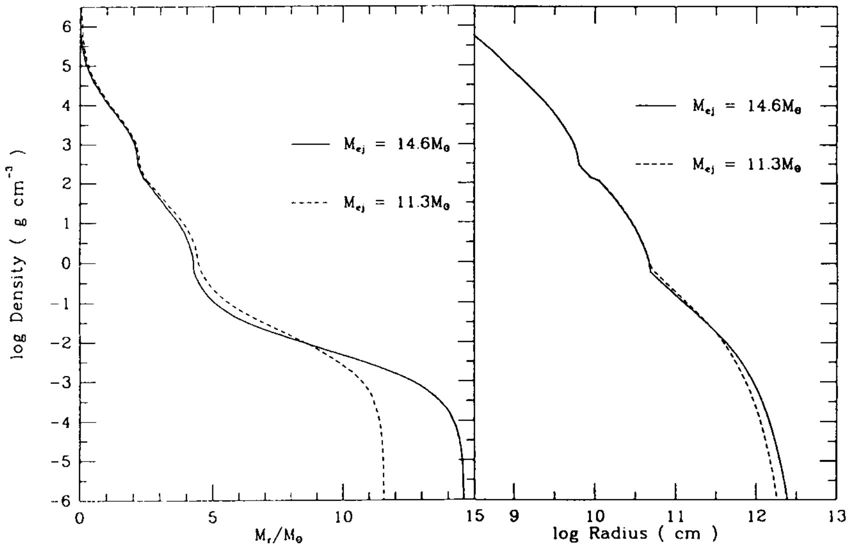

Fig. 13. The initial density distribution against M_r (a) and radius (b) for models 14E1 (solid) and 11E0.6 (dashed) (Shigeyama and Nomoto 1990).

x-ray and γ-ray light curves and spectra with observations (Kumagai et al. 1989).

The shock wave arrives at the surface of the star at $t_{\rm prop}$, which is approximated for different values of the initial radius R_0 and the ejected mass $M_{\rm ej}$, and for different explosion energies E as (Shigeyama et al. 1987):

$$t_{\rm prop} \sim 2^{\rm h} \left(\frac{R_0}{3 \times 10^{12}\rm cm}\right) \left[\left(\frac{M_{\rm ej}}{10 M_\odot}\right) \Big/ \left(\frac{E}{1 \times 10^{51}\rm erg}\right)\right]^{\frac{1}{2}} . \quad (1)$$

After the shock wave reaches the surface, the star starts to expand; soon the expansion becomes homologous as $v \propto r$. Figures 15–16 show the density profile against M_r and r for 14E1. The density distribution in the outermost layers is well approximated by a power law of $r^{-8.6}$. In fig. 17, the velocity distribution for the homologous expansion is shown for 11E0.6 and 14E1. The velocity gradient with respect to enclosed mass M_r is very steep near the surface, while it is almost flat in the helium layer and the heavy element core. This is because the core materials are decelerated and form a dense

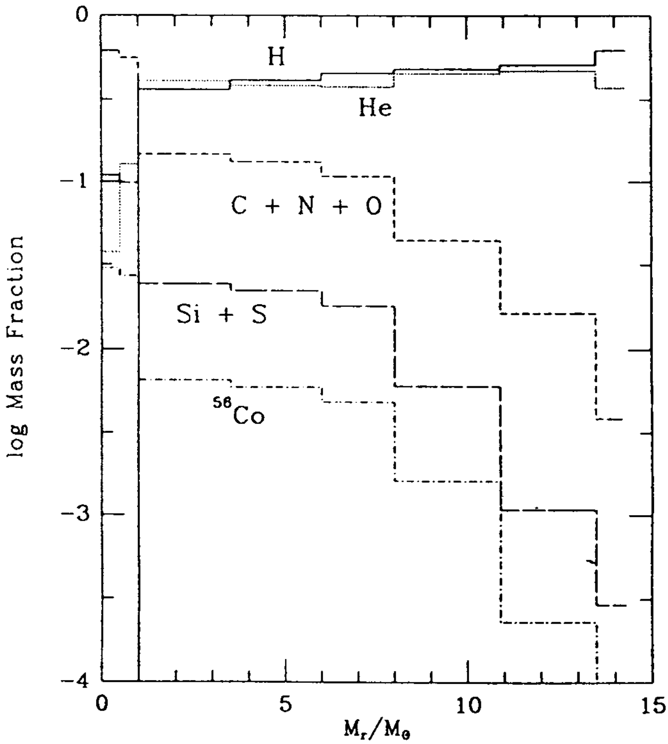

Fig. 14. The abundance distribution of the ejecta with mixing assumed for the models shown in figs. 15–19. Expansion velocities of the ejected materials are indicated (Kumagai et al. 1989).

shell due to reverse shock when the expanding core hits the hydrogen-rich envelope. The kinetic energy of the helium and heavy element layers is only 10% of the total kinetic energy.

As the star expands, the photosphere moves inward in M_r. Because of the steep velocity-gradient near the surface, the velocity of material at the photosphere decreases as seen in fig. 18 (14E1). We compared this time change with $v_{\rm ph} = R_{\rm ph}/t$, where $R_{\rm ph}$ is the radius of the black body surface obtained from the photometric observations (Menzies et al. 1987; Catchpole et al. 1987; Hamuy et al. 1987). Approximate photospheric velocities are obtained from the radial velocities measured for absorption minima of Fe II lines (Phillips 1988). The photospheric velocity of 14E1 is in good agreement with SAAO and CTIO data, but slightly smaller than Fe II line velocities.

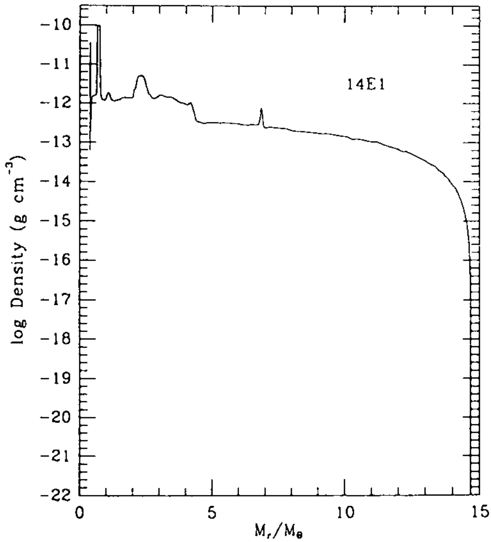

Fig. 15. The density profile against M_r at $t = 100$ d for model 14E1.

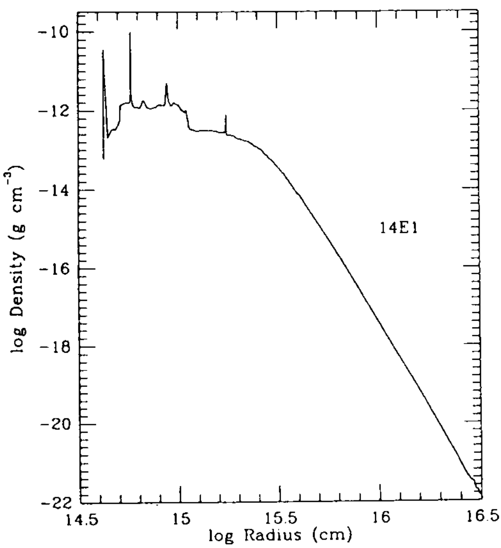

Fig. 16. Same as fig. 15 except for the radius.

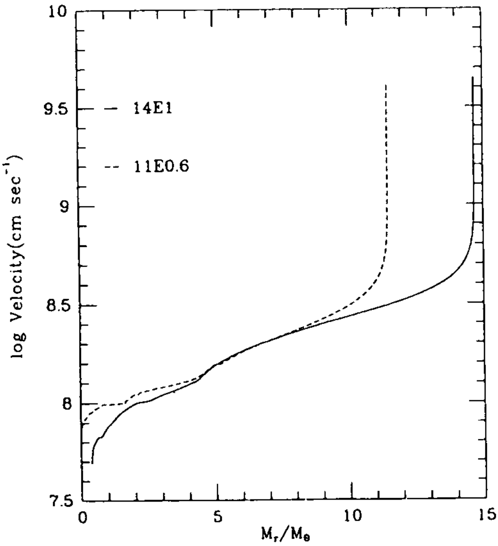

Fig. 17. The velocity profiles at t = 100 d for models 14E1 (solid curve) and 11E0.6 (dashed curve).

This suggests $E/M_{\rm env}$ should not be so different than $\sim 1 \times 10^{50}$ erg $M_\odot^{-1}$ in order for the model to be consistent with observations.

4.2. Early light curve

After the shock breakout at the surface, the supernova shows its brilliant optical display. The early light curve up to $t \sim 25$ d is due to diffusive release of internal energy from the radiation field that is established by the shock wave. Initially the energy of the radiation field is $\sim$ 57% of the explosion energy for 14E1. Figure 19 shows the calculated bolometric light curve for 11E0.6 (dashed) and 14E1 (solid). The bolometric luminosity reaches $L_{\rm bol}$ = 4×10^{44} ergs s^{-1} at its peak, and the effective temperature becomes as high as $T_{\rm eff} = 4 \times 10^5$ K. Hence, most of the radiation is emitted as an UV burst. The total energy of radiation during the first two days amounts to $\sim 10^{47}$ ergs.

UV photons ionize the circumstellar material ejected from the supernova progenitor during the red supergiant stage of its evolution. The UV emission lines from circumstellar N, C, and O are actually observed and, in particular, the N V line was seen to increase almost linearly up to approximately day 400 (Kirshner 1988). This implies that nitrogen was ionized to N VI by

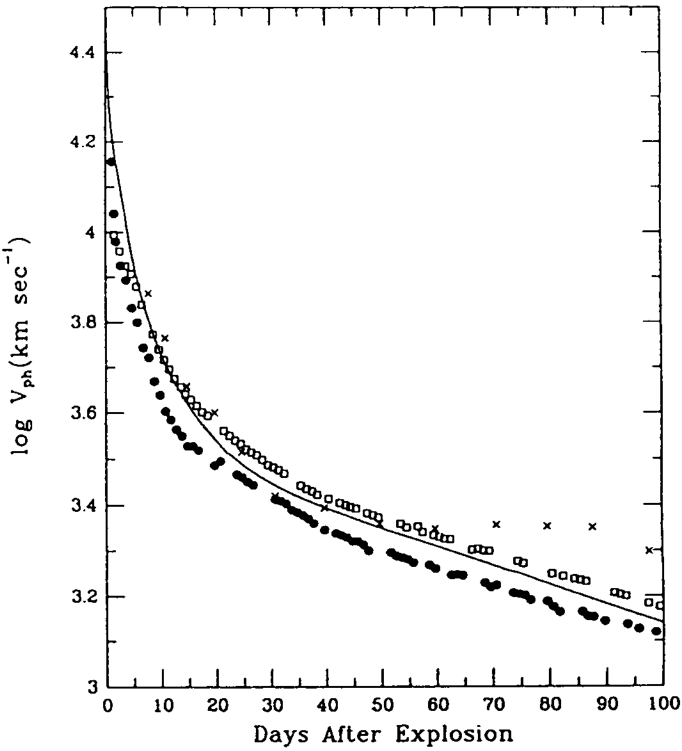

Fig. 18. Changes in the expansion velocity of the material at the photosphere for model 14E1. Observed values are R_{ph}/t obtained at SAAO (open squares; Catchpole et al. 1987) and CTIO (filled circles; Hamuy et al. 1987). Radial velocity measurements for the absorption minimum of FeII 5169 lines are plotted as crosses (Phillips et al. 1987).

the initial UV burst (Fransson et al. 1989). To supply a sufficient number of ionizing photons to the circumstellar matter, the peak temperature of radiation from the supernova must have been 4–8 $\times$ 10^5 K (Fransson and Lundqvist 1989). The effective temperatures of models 14E1 and 11E0.6 satisfy this condition. Moreover, the ejecta is scattering-dominant, so that the color temperature is higher than the effective temperature (see below). In fact, the color temperature obtained by non-LTE atmospheric calculation is as high as 8 $\times$ 10^5 K for 14E1 (Höflich et al. 1991).

After the UV burst, the ejected gas and radiation field expand rapidly so that the interior temperature decreases almost adiabatically as r^{-1}. As a

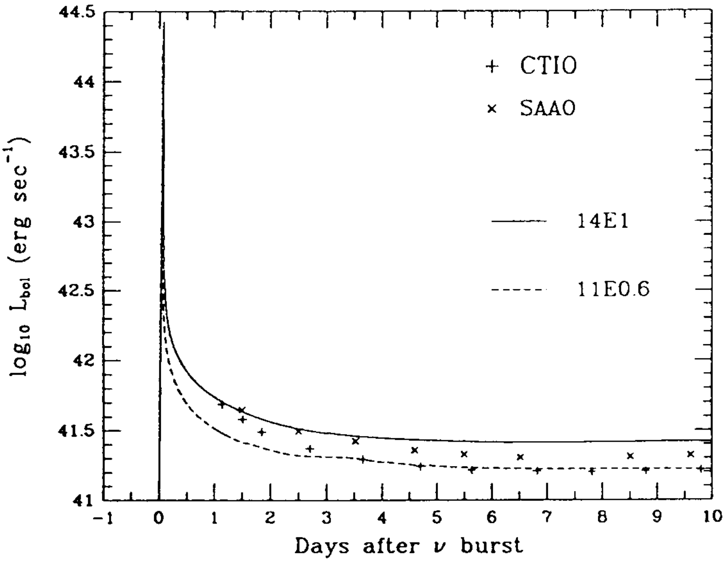

Fig. 19. The calculated bolometric luminosities for models 14E1 (solid curve) and 11E0.6 (dashed) during the first ten days. The observed points are taken from observations at SAAO (Menzies et al 1987; Catchpole et al. 1987) and CTIO (Hamuy et al. 1987).

result, the bolometric luminosity sharply decreases to $L_{\rm bol} \sim$ 2–3 $\times 10^{41}$ erg s^{-1} to form a short plateau phase. The calculated bolometric light curve is in good agreement with observations (fig. 19). The luminosity at this phase is lower than the typical Type II-P supernovae by a factor of 10–20. A small initial radius leads to such low luminosity because a much larger fraction of the radiation field energy is lost by PdV work than in an ordinary Type II-P supernova (Shigeyama et al. 1987; Arnett 1987; Woosley et al. 1988a).

During the first day, visual luminosity increases because the intensity peak is rapidly shifted to the optical wavelength due to a falling photospheric temperature. For the optical flare-up of the supernova to be seen at 6.4 mag at t = 3 h, the condition $t_{\rm prop}$ < 3 h (eq. (1)) should be satisfied, which requires a relatively large $E/M_{\rm env}$ and small R_0 (Shigeyama et al. 1987). Also, the ejected gas and the radiation field should have expanded rapidly, so that the temperature becomes lower and the radius of the photosphere becomes larger at a sufficient rate. Therefore the expansion velocities and thus $E/M_{\rm env}$ should be larger than certain values for the given initial radius.

To satisfy this condition, E should be as large as 0.6–1.5 $\times 10^{51}$ erg for $M_{\rm env}$ = 7–10 $M_\odot$.

Although theoretical models are generally in good agreement with observations in the early phase, uncertainties remain in the theoretical models. The supernova atmosphere is scattering-dominated, so that color temperature is significantly higher than the effective temperature; the resultant spectrum is a superposition of spectra emerging from the layers with different depths and temperatures (Shigeyama et al. 1987; Pizzochero 1990; Höflich et al. 1991). The bolometric correction is sensitive to color temperature because it is as high as $4 - 8 \times 10^4$ K. If we apply the bolometric correction based on color temperature, the theoretical visual luminosity is lower so that larger $E/M_{\rm env}$ and smaller R_0 are required, as found by Shigeyama et al. (1987).

To examine this problem, a non-LTE light curve calculation has been carried out for a given temperature distribution of the present models (Höflich et al. 1991). Figure 20 shows an excellent agreement between observations and the calculated V-light curve for $E = 1.25 \times 10^{51}$ ergs. The earliest part is sensitive to $t_{\rm prop}$, so that the constraint is scaled as $R_0/E^{1/2}$. Thus, the uncertainty of E is about 20%. (Here a distance modulus of 18.5 and an extinction of 0.6 are adopted [West et al. 1987].)

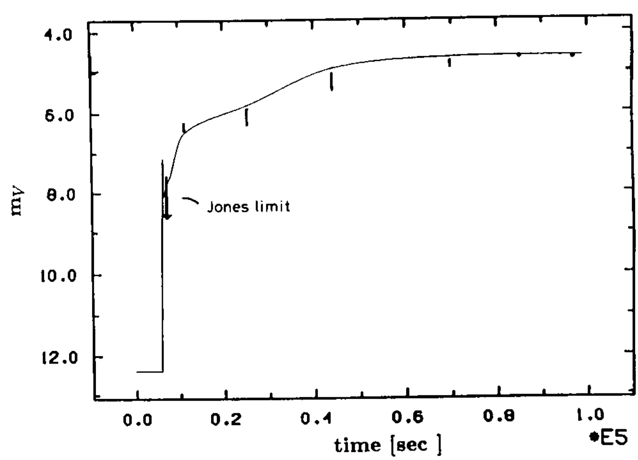

Fig. 20. The visual light curve obtained from non-LTE calculations for 14E1.25, that is, $E = 1.25 \times 10^{51}$ ergs (Höflich et al. 1991). The observed points are taken from SAAO and CTIO, except for two early points measured on plates (McNaught 1987; Zoltowski 1987).

4.3. Hydrogen recombination front

After a minimum at about day 10, the observed bolometric luminosity increases and forms a broad peak. The theoretical light curve for this phase is determined by the hydrogen recombination front and the distribution of hydrogen and ^{56}Ni. The role of the propagating hydrogen recombination front in determining the light curve shape can be understood as follows. Since electron scattering is the dominant opacity source, opacity sharply decreases outward beginning at the recombination front. Consequently the internal energy (mostly from the radiation field) is efficiently transported away, and the temperature drops sharply from 10,000 K to 5500 K at the hydrogen recombination front.

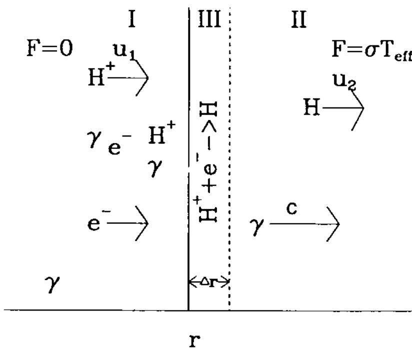

Fig. 21. Schematic structure around the hydrogen recombination front (Shigeyama and Nomoto 1991).

Propagation of the hydrogen recombination front is analyzed as follows (Shigeyama and Nomoto 1991). Let us divide the layers around the front into three regions (I, II, and III) as shown in fig. 21. The front is located at radius r. In region I, hydrogen is fully ionized ($T_1 \geq 10^4$ K). The electron opacity is so large that radiative energy flux is negligible compared to advective energy flux due to matter flow. Region II, where hydrogen is neutral (T_2 <6000 K), is optically thin. Region III is the transition layer where hydrogen is partially ionized and the temperature and opacity decrease sharply from region I to II. If the thickness of region III (Δr) is much smaller than r, three conservation laws (mass, momentum, and energy) must hold between region I and II as

$$\rho_1 u_1 = \rho_2 u_2, \tag{2}$$

$$\rho_1 u_1^2 + \frac{2k\rho_1 T_1}{m_{\mathrm{H}}} + \frac{aT_1^4}{3} = \rho_2 u_2^2 + \frac{\rho_2 T_2}{m_{\mathrm{H}}} + \frac{aT_2^4}{3}, \tag{3}$$

$$\frac{\rho_1 u_1^3}{2} + \rho_1 u_1 \left(\frac{5kT_1}{m_{\mathrm{H}}} + \frac{\epsilon_{\mathrm{H}}}{m_{\mathrm{H}}} + \frac{4aT_1^4}{3\rho_1} \right) =$$

$$\frac{\rho_2 u_2^3}{2} + \rho_2 u_2 \left(\frac{5kT_2}{2m_{\mathrm{H}}} + \frac{4aT_2^4}{3\rho_2} \right) + \sigma T_{\mathrm{eff}}^4 . \tag{4}$$

Here u is the velocity of the matter in the rest frame of the front, and ϵ_H is the ionization energy of hydrogen (=13.6 eV). The subscripts 1 and 2 denote the regions I and II, respectively.

These equations can be approximated since (i) the gas pressure is negligible as compared with the radiation pressure, (ii) $T_2^4 << T_1^4$, (iii) ϵ_{H} is negligibly smaller than the radiation energy, and (iv) v is proportional to r in the rest frame of the front. Then Δr can be written as $\Delta r/r = \Delta u/u$. To satisfy the steady state condition, $\Delta\rho/\rho$ and $\Delta u/u$ are much smaller than unity. Here, $u_1 = u - \Delta u/2$, $\rho_1 = \rho + \Delta\rho/2$, $u_2 = u + \Delta u/2$, $\rho_2 = \rho - \Delta\rho/2$. Using these new variables and neglecting the small terms, the conservation laws are rewritten as

$$\rho_1 u_1 = \rho_2 u_2 = \rho u, \tag{5}$$

$$\frac{\Delta\rho}{\rho} = \frac{\Delta u}{u} \equiv 2\xi, \tag{6}$$

$$-\xi + \frac{aT_1^4}{6\rho u^2} = 0, \tag{7}$$

$$-2\xi - \frac{\epsilon}{m_H u^2} + \frac{4aT_1^4}{3\rho u^2} = 0. \tag{8}$$

The solution gives us the propagation velocity of the front relative to the matter,

$$u = \frac{c}{4}\left(\frac{T_{\mathrm{eff}}}{T_1}\right)^4,$$

$$u = 1.35 \times 10^3 \left(\frac{T_1}{15000K}\right)^{-4} \left(\frac{T_{\mathrm{eff}}}{5500K}\right)^4 \ \mathrm{km\ sec^{-1}}, \tag{9}$$

and the width of the front

$$\frac{\Delta r}{r} = \frac{16aT_{\mathrm{eff}}^4}{3\rho c^2}\left(\frac{T_1}{T_{\mathrm{eff}}}\right)^{12},$$

$$\sim 7 \times 10^{-3} \left(\frac{\rho}{1 \times 10^{-12}\mathrm{g\ cm^{-3}}}\right)^{-1} \left(\frac{T_1}{15000\mathrm{K}}\right)^{12} \left(\frac{T_{\mathrm{eff}}}{5500\mathrm{K}}\right)^{-8} \tag{10}$$

which is typically $\Delta r \sim 7 \times 10^{12}$ cm $(r/10^{15}$ cm). The steady front approximation is justified, since the time scale for the front to become steady is $\Delta r/u \sim 5.2 \times 10^4$ s, which is smaller than the dynamical time scale of the ejecta ($\sim$ 10 d).

This solution suggests that:

(i) If $u > v$, where v is the velocity of the ejecta in the inertial frame at the recombination front, the front does not move appreciably because u is too small to significantly change radius r in about a month. Thus the radius of the photosphere is nearly constant in time. This results in the plateau seen in the light curve of a SN II-P, because the luminosity, L, is written as $L = 4\pi r_{\rm ph}^2 \sigma T_{\rm eff}^4$.

(ii) If $v > u$, the recombination front moves outward in the inertial frame, and results in an increase in the luminosity. Our numerical calculation shows that this occurred from day 20 to 60, because of the high velocity in the outer layers. Before day 20, v is much higher than u, so the recombination front cannot be in steady state.

In the explosion, ejected material expands to pass through this recombination front where its temperature quickly decreases. In other words, the cooling wave propagates inward in mass (fig. 22). The velocity at the photosphere then becomes lower as the photosphere moves inward in mass. For 14E1, the recombination front reaches $M_r = 12.3\ M_\odot$ (at $t = 20$ d), 11.0 $M_\odot$ (25 d), 8.7 $M_\odot$ (30 d), 6.3 $M_\odot$ (40 d), 5.0 $M_\odot$ (60 d), 3.6 $M_\odot$ (80 d), and 2.0 $M_\odot$ (100 d). The radius of the front moves from 6×10^{14} cm to 8×10^{14} cm during the luminosity increase from $t = 20$ d to 60 d. It is almost stationary at 8×10^{14} cm during the plateau around the peak (60–100 d) (fig. 23).

The luminosity during propagation of the recombination front is given as

$$L = 4\pi R_{\rm ph}^2 a T_1^4 u, \tag{11}$$

where u is the matter velocity with respect to the front as given by eq. (8), and $R_{\rm ph}$ the photospheric radius. Since $T_{\rm eff} \sim 5500$ K at the recombination front, the luminosity is primarily determined by $R_{\rm ph}$. It should be noted that $R_{\rm ph}$ and L depend on the distribution of radioactive elements, as discussed below.

4.4. Radioactive decays, mixing of ^{56}Ni, and Bochum event

After approximately day 25, the light curve is powered by radioactive decays as follows (fig. 24). When a ^{56}Co decays to a ^{56}Fe, γ-ray photons are emitted

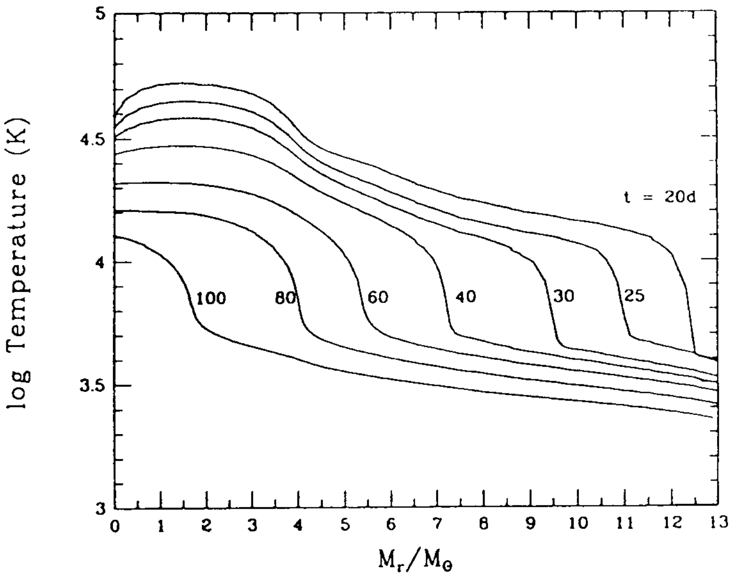

Fig. 22. Change in the temperature profile against M_r for 14E1 (Shigeyama and Nomoto 1990). The hydrogen recombination front propagates inward in M_r as indicated by the date.

with the energy of 847 keV, 1028 keV, 1238 keV, etc. The average energy of photons emitted by ^{56}Co is about 1.28 MeV, and on average the number of these photons is 2.88. These γ-ray photons are degraded into x-rays by Compton scatterings and absorbed by heavy elements. In the first several scatterings, an electron takes about a half of the photon energy per scattering. These high energy electrons collide with ions or atoms to ionize or excite them. The ionized electrons are thermalized through the same processes. In this way, the energy of γ-rays emitted by ^{56}Co decay is deposited in the supernova ejecta and powers optical light.

The effect of radioactive heating on the light curve depends on the distribution of ^{56}Ni. The bolometric light curves for the mixed and unmixed cases are compared in fig. 25. The difference in the light curve shape becomes apparent around day 25, which can be interpreted as follows.

For the unmixed case, the temperature inside the recombination front T_l is lower than in the mixed case at $M_r < 11\ M_\odot$ because of a lack of radioactive heating. Hence u is higher in eq. (9) for $T_\mathrm{eff} \sim 5500$ K; i.e., the recombination front propagates faster in M_r and reaches a deeper layer for a given time

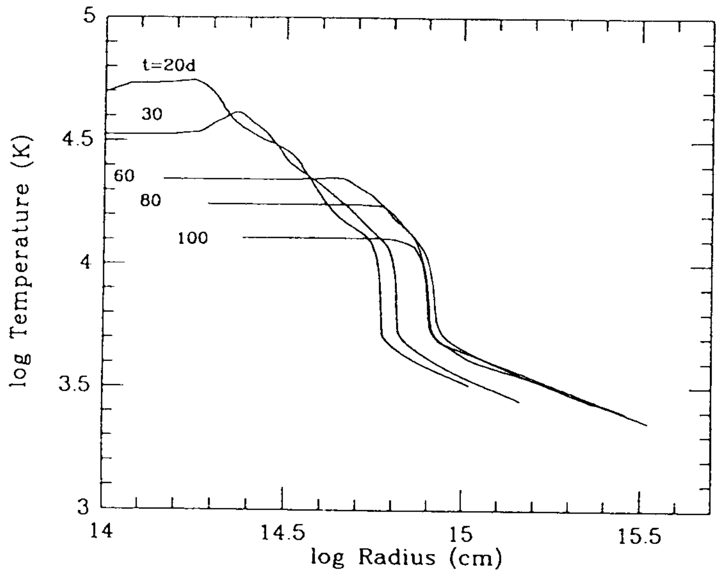

Fig. 23. Change in the temperature profile against r (Shigeyama and Nomoto 1990). The hydrogen recombination front is almost stationary during the plateau-like peak at t = 60–100 d.

than in the mixed model. At the deeper layer, the matter expansion velocity v is lower and the photospheric radius ($R_{ph} = vt$) is smaller accordingly. As a result, because of this rapid decrease of R_{ph}, the calculated bolometric luminosity starts to decrease at approximately day 25. The increase in luminosity due to radioactive heating is delayed to $t = 42$ d, a dip appears in the light curve, and in the rising part of the light curve is steeper than the mixed model (fig. 25); these are clearly incompatible with observation.

On the contrary, for the mixed model with ^{56}Ni closer to the surface, heating of the outer layers due to radioactive decays is significant. Compared with the unmixed model, the propagation speed of the recombination front u with respect to M_r is slower, and hence the photosphere is located at larger M_r and R_{ph} ($= vt$). Its effect starts to appear in the light curve from $t \sim 25$ d and forms a smooth increase in the optical light curve as observed (solid line in fig. 25; Nomoto et al. 1987; M. Itoh et al. 1987). Around this date, the photosphere reaches $M_r \sim 11\ M_\odot$ where the mass fraction of ^{56}Ni exceeds 1×10^{-3} (fig. 14).

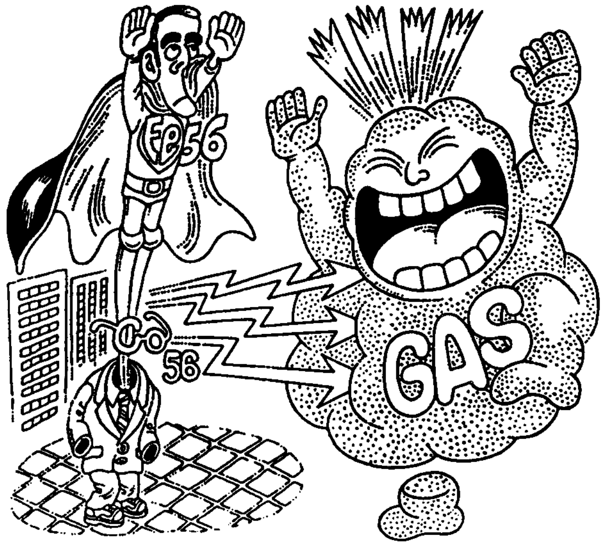

Fig. 24. The expanding supernova gas is excited by the decay of ^{56}Co into ^{56}Fe (H. Nomoto 1989).

From the observational side, Phillips (1988) noted that some color changes started from $t = 25$ d, which may indicate the appearance of heat flux due to radioactive decays. More interestingly, satellite emission bumps appeared in the wings of H_α, starting from day 25 (Hanuschik and Dachs 1988; Blanco et al. 1987). Among the proposed interpretations of this Bochum event is a possibility that x-rays and γ-rays from radioactive decays became an additional source of ionization at the photosphere (Lucy 1988; Phillips and Heathcote 1989). Our model supports this interpretation because a significant amount of mixed ^{56}Ni started to appear at the photosphere around day 25 (fig. 14).

Photometric observations, spectroscopic observations, and theoretical modeling strongly suggest that substantial amounts of ^{56}Ni (larger than $\sim 10^{-3}$ in mass fraction) is mixed into the middle of the hydrogen-rich envelope (i.e., to the layer of $M_r \sim 11\ M_\odot$ where the expansion velocity is ~ 3000 km s^{-1}). The mixing of ^{56}Ni should occur significantly earlier than day 25. Such early mixing would more likely be due to Rayleigh-Taylor instability induced by reverse shock (see section 6) rather than due to the ^{56}Ni bubble, although the time scale of the latter event needs further study.

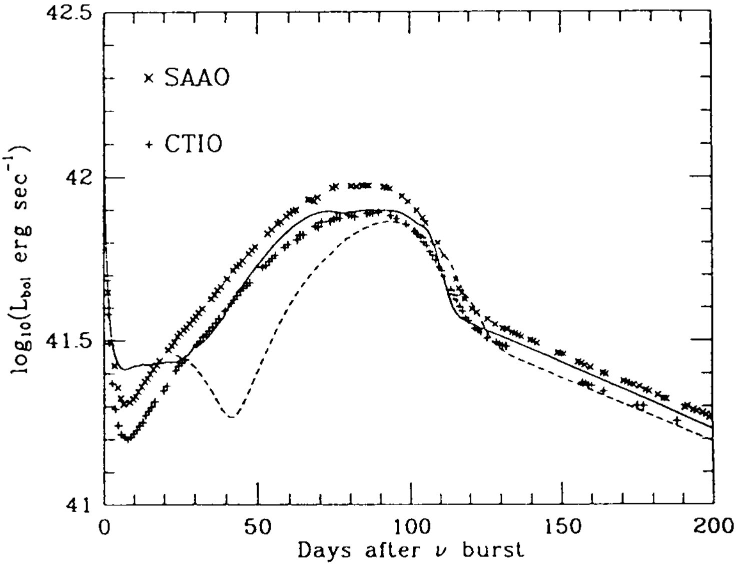

Fig. 25. The dependence of the bolometric light curves on the ^{56}Ni distribution for 14E1. The solid curve assumes the abundance distribution in fig. 14, while the dashed curve assumes the confinement of ^{56}Ni in the innermost layer. Observed points are taken from SAAO (Catchpole et al. 1987) and CTIO (Hamuy et al. 1988).

4.5. Plateau-like peak and hydrogen recombination

After an almost exponential increase up to day $\sim$ 60, the observed bolometric light curve formed a plateau-like broad peak through day $\sim$ 100. After a relatively rapid drop, the luminosity declined slowly for t = 120–400 d at a rate which coincides with the energy generation rate due to the Co-decay

$$L = 1.43 \times 10^{43} M_{\rm Co}/M_{\odot} e^{-t/111.3{\rm d}} \quad {\rm ergs\ s^{-1}}, \tag{12}$$

with $M_{\rm Co} = 0.075 M_{\odot}$ (Catchpole et al. 1987; Suntzeff et al. 1988). Thus the energy source that continually heats up the expanding star is certainly decaying ^{56}Co.

The calculated optical light curve for 14E1 is successful in reproducing the plateau-like peak (fig. 26). Here the stationary nature of the recombination front described in section 4.3 is responsible for forming a peak, which is essentially the same as the peak which occurs in SN II-P.

The width of the plateau depends on the depth of the mixed hydrogen-rich layer. Figure 26 compares the light curves for models with different distri-

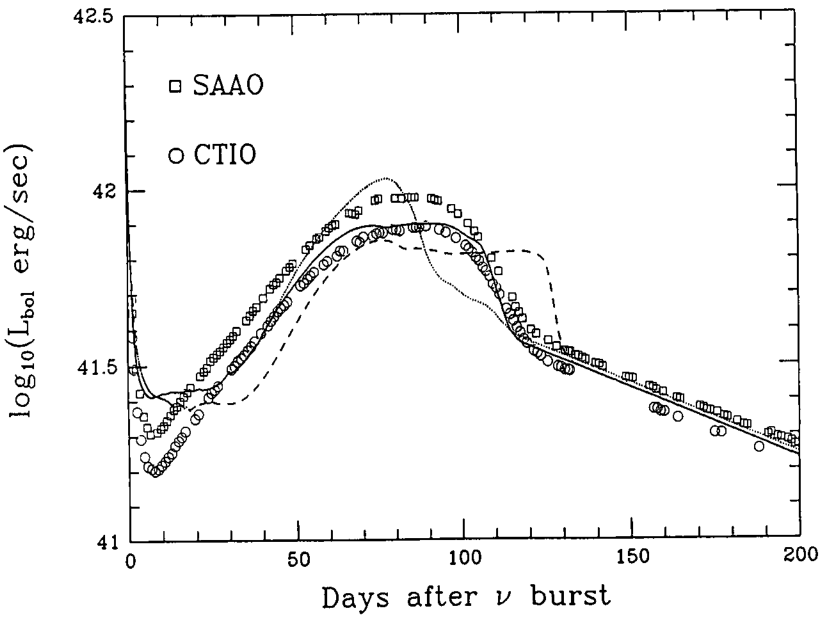

Fig. 26. Dependence of bolometric light curves on the hydrogen distribution for model 14E1 with 0.075 $M_\odot$ ^{56}Ni. The solid curve assumes the abundance distribution in fig. 14, while the dashed and dotted curves assume mixing of hydrogen down to the center and the shell of $M_r = 3\, M_\odot$, respectively.

butions of hydrogen. The solid curve assumes the abundance distribution in fig. 14, while the dashed and dotted curves assume mixing of hydrogen down to the center and the shell of $M_r = 3\ M_\odot$, respectively. For deeper mixing of hydrogen the plateau lasts longer, and vice versa. In our favorite model, shown by the solid line, hydrogen is mixed down to the shell of $M_r = 1\, M_\odot$, where the expansion velocity is as low as $\sim$ 800 km s^{-1} (fig. 14).

The relation between duration of the plateau phase and depth of the hydrogen layer can be given more quantitatively. First of all, let us describe the formation of a plateau in terms of the matter velocity u with respect to the recombination front (eq. (9)), and the matter velocity at the photosphere v with respect to r. Whether the radius at the photosphere increases or decreases is determined by whether u is higher or lower than v. (Here positive values of u and v indicate the inward motion of the front with respect to M_r and the outward motion of the hydrogen-rich layer, respectively.) If $u < v$, the photospheric radius increases to increase the luminosity. If $u \sim v$, the photospheric radius is stationary, keeping the luminosity constant.

For our model, $u \lesssim 2000$ km s^{-1}. Hence luminosity increases when the recombination front (and thus the photosphere) is in the outer hydrogen-rich envelope where $v > 3000$ km s^{-1}. The plateau appears when the front enters into the slowly moving inner layer and v becomes comparable to u. When the photosphere enters into layers which lack a sufficient amount of hydrogen, the hydrogen recombination front disappears and the plateau phase is terminated.

Suppose that hydrogen is mixed down to the shell where the expansion velocity of the hydrogen-rich layer is at its minimum $v^{\mathrm{H}}_{\mathrm{min}}$. Then this minimum hydrogen velocity is related to observed quantities for the plateau phase as

$$v^{\mathrm{H}}_{\mathrm{min}} = R_{\mathrm{ph}}/t_{\mathrm{pl}}, \tag{13}$$

$$R_{\mathrm{ph}} = \left(\frac{L_{\mathrm{pl}}}{4\pi\sigma T^4_{\mathrm{eff}}}\right)^{1/2}. \tag{14}$$

Here t_{pl} is the time t at the end of the plateau (approximately 100 d for SN 1987A), L_{pl} is the luminosity at $t \sim t_{\mathrm{pl}}$, and $T_{\mathrm{eff}} \sim 5500$ K due to the association of the photosphere with the hydrogen recombination front. Then $v^{\mathrm{H}}_{\mathrm{min}}$ can be estimated from the observed L_{pl} and t_{pl} as

$$v^{\mathrm{H}}_{\mathrm{min}} \sim 1 \times 10^3 \text{ km s}^{-1} \left(\frac{L_{\mathrm{pl}}}{8.5 \times 10^{41} \text{ erg s}^{-1}}\right)^{1/2} \left(\frac{t_{\mathrm{pl}}}{100\mathrm{d}}\right)^{-1}, \tag{15}$$

which is consistent with $v^{\mathrm{H}}_{\mathrm{min}} \sim 800$ km s^{-1} required in the present model of SN 1987A.

For the minimum hydrogen velocity, Höflich (1988) analyzed the spectrum at day 221 and obtained $v^{\mathrm{H}}_{\mathrm{min}} \sim 800$ km s^{-1}. This is very close to the value obtained in model 14E1. Meikle et al. (1989) also suggested mixing of hydrogen with oxygen at an expansion velocity of 2000 km s^{-1} or less to account for the narrow OI line in the infrared spectra.

4.6. Constraints on explosion energy

In the above discussion the light curve is used to probe the internal abundance distribution. The light curve shape is also sensitive to hydrodynamics (Shigeyama et al. 1987, 1988; Nomoto et al. 1987; Woosley et al. 1988a; Arnett and Fu 1989). These dependencies are summarized here for the present set of models (Shigeyama and Nomoto 1990).

First, the peak value of the bolometric luminosity and its date depend on E and $M_{\rm env}$ as follows: $L_{\rm pk} = 7.9 \times 10^{41}$ergs s^{-1} at $t = 73$ d for 14E1, 8.5 $\times 10^{41}$ergs s^{-1} at $t = 63$ d for 14E1.4, and 1×10^{42} erg s^{-1} at $t = 50$ d for 11E1. For 11E1 (14E1.4) the luminosity maximum is reached a little too early, compared with observations. For such large $E/M_{\rm env}$, the expansion velocities of the hydrogen-rich envelope are larger than in 14E1. Hence the photospheric radius $R_{\rm ph}$ is larger, which makes the luminosity higher at the same epoch.

Second, the width of the plateau-like peak depends on the explosion energy and envelope mass. The plateau ends at $t_{\rm pl} \sim 90$ d in 14E1.4, earlier than in 14E1, because $v^{\rm H}_{\rm min}$ is $\sim$ 10% larger in 14E1.4 than that in 14E1. The smaller envelope mass in 11E1 also results in a higher $v^{\rm H}_{\rm min}$ due to larger $E/M_{\rm env}$, thereby leading to termination of the plateau as early as $t_{\rm pl} \sim 80$ d. These models are too energetic to be compatible with observations. For 11E0.6, on the other hand, the agreement of the light curve with observation is as good as 14E1. Thus $E/M_{\rm env}$ is as important as hydrogen distribution in determining $t_{\rm pl}$.

To summarize, both the pre-peak light curve and the plateau-like light curve are in good agreement with the observations for the models with $E/M_{\rm env} = (1.1 \pm 0.3) \times 10^{51}$ erg $M_\odot{}^{-1}$. This constraint is consistent with the condition obtained from the photospheric velocity as seen in fig. 18. The constraint on $M_{\rm env}$ is obtained as $M_{\rm env}$ = 7–10 $M_\odot$ (Saio et al. 1988b) in order that the presupernova evolution model be consistent with the observed enhancement of N/C and N/O in circumstellar matter. Therefore, the explosion energy should be in the range of $E = (1.0 \pm 0.4) \times 10^{51}$ erg.

5. X-ray light curve and clumpy mixing

In ^{56}Co decay, the line γ-rays (847 keV, 1238 keV, 2599 keV, 1771 keV, ...) undergo multiple Compton scatterings while being degraded into x-rays. As the column density of the ejecta decreases with expansion, the scattering and photoelectric absorption decreases, so that these hard x-rays and γ-rays appear; those that have been predicted to emerge from the supernova (McCray et al. 1987; Chan and Lingenfelter 1987; Gehrels et al. 1987; Grebenev and Sunyaev 1987; Xu et al. 1988; Ebisuzaki and Shibazaki 1988b). X-rays and γ-rays from SN 1987A have been actually observed by the x-ray satellites *Ginga* and *Kvant* (Dotani et al. 1987; Sunyaev et al. 1987, 1989; Tanaka 1988a, 1988b; Inoue et al. 1991), the *Solar Maximum Mission* satellite (Matz et al. 1988), and balloon-borne detectors (Sandie et al. 1988; Wilson et al. 1988; Cook et al. 1988; Mahoney et al. 1988; Rester et al. 1989; Tueller et al. 1990).

However, these detections of x-rays and γ-rays occurred much earlier than predicted by theory. This problem can be solved if ^{56}Co is mixed into the hydrogen-rich envelope, since the column density to ^{56}Co layer depends on mixing (M. Itoh et al. 1987; Kumagai et al. 1988a, 1988b, 1989; Pinto and Woosley 1988a, 1988b; Ebisuzaki and Shibazaki 1988a; Shibazaki and Ebisuzaki 1988; Sutherland et al. 1988; Arnett 1988; Grebenev and Sunyaev 1988; Leising 1988; Yamada et al. 1989; Fu and Arnett 1989; Lehoucq et al. 1989; Bussard et al. 1989; The et al. 1990).

The dependence of x-ray and γ-ray light curves and spectra on distribution of the heavy elements and ^{56}Co in the ejecta is studied for 14E1 with a distribution of elements given in fig. 14. Here ^{56}Ni is mixed up to M_r = 10 $M_\odot$ where the expansion velocity of the material amounts to 4200 km s^{-1}. The column depth in this layer is 2.4 g cm^{-2} at t = 200 d (Kumagai et al. 1989).

5.1. X-ray light curves at t < 300 d

The effects of mixing on the light curves and spectra of x-rays and γ-rays (e.g., M. Itoh et al. 1987; Kumagai et al. 1988a, 1988b) are summarized as follows: (*a*) the γ-rays and Compton-degraded x-rays emerge early because of the small column depth to the cobalt layer, and (*b*) the photoelectric absorption of x-rays in the hydrogen-rich envelope is larger, which reduces the 10–30 keV x-ray flux at relatively early stages.

Figure 27 shows the calculated light curve for different degrees of clumpiness in the supernova ejecta, that is, *mixing and clumps* (solid curve), *mixing without clumps* (dash-dotted), and *no mixing* (dashed) (Kumagai et al. 1989). These curves are based on hard x-ray data (16–28 KeV). To account for the early emergence of x-rays and γ-rays, ^{56}Ni needs to be mixed up to $\sim$ 3000 km s^{-1} and 4000 km s^{-1}, respectively. For the mixed model, the x-rays in the early stages originate from ^{56}Co at the outermost layers. Later, x-rays from ^{56}Co in the deeper core contribute.

5.2. X-ray light curve at t > 300 d and effects of clumps

Until t reaches approximately 300 d, the dashed curve is in good agreement with the *Ginga* observations. At later phases, however, the observed 16–28 keV X-ray flux declines much more slowly than the calculated x-ray flux, which assumes the homogeneous and spherically symmetric mixing

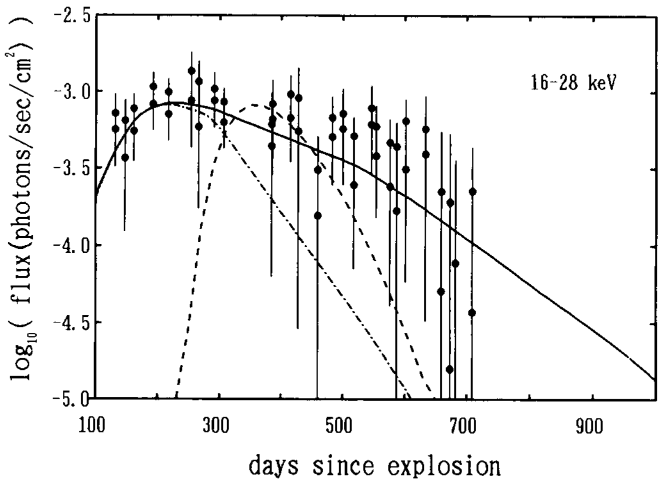

Fig. 27. X-ray (16–28 keV) light curve model 14E1 for SN 1987A with 0.076 $M_\odot$ ^{56}Co and 0.0043 $M_\odot$ ^{57}Co (Kumagai et al. 1989). Three curves show different degrees of clumpiness in the supernova ejecta, that is, cases with *mixing and clumps* (solid curve), *mixing without clumps* (dash-dotted), and *no mixing* (dashed). The x-ray observations by *Ginga* are shown by the filled circles.

(dash-dotted curve in fig. 27). The decrease in the calculated x-ray flux is due to photoelectric absorption in the heavy-element-rich core. Models with different abundance distributions were tested, but the disagreement with observations could not be removed.

We then take into account the effect of clumps on photoelectric absorption in the core. The mixing between core and envelope materials produces a non-spherical distribution of elements, that is, chemically inhomogeneous clumps. It should be noted that the amount of hydrogen and helium at $M_r < 8\ M_\odot$ is comparable to the amount of heavy elements (fig. 14). If the heavy elements are localized in clumps, a large fraction of x-rays could be transported through the hydrogen- and helium-rich regions without suffering much photoelectric absorption. This would effectively reduce the opacity.

In the following models, we assume that the photoelectric opacity is reduced by some factor only in the core. The solid curve in fig. 27 is a light curve for the model in which photoelectric opacity is reduced by a factor of 9 at $M_r < 8\ M_\odot$. This curve shows a much slower decline than the thin solid curve, and is consistent with the *Ginga* observations. [If the opacity in the outer envelope of $M_r > 8\ M_\odot$ is also reduced, the light curve would be too high at $t < 300$ d, while it would not be affected in the later stage. This indicates the importance of photoelectric absorption in the heavy element core, and the clumpiness thereof rather than in the outer envelope.]

The x-ray flux from ^{57}Co decay exceeds that from ^{56}Co decay at $t > 600$ d. However, it is not sufficiently large to slow down the decline of the x-ray flux; the reduction of photoelectric opacity is still necessary to account for the observations for $t > 300$ d.

The observed x-rays might originate from the buried pulsar (Bandeira et al. 1988; Pacini 1988). If so, the pulsar x-ray luminosity should be $\sim 2 \times 10^{38}$ erg s^{-1}, which should have appeared in the bolometric light curve. However, such an effect was not observed.

5.3. Gamma-ray light curves

Figure 28 shows the calculated γ-ray line light curves for 847 and 1238 keV and other lines, which are consistent with the *SMM* observations (Leising and Share 1990). The agreement is reasonably good for 3 lines; in particular, the emergence of γ-rays in the calculation will be as early as observed if ^{56}Co is mixed to the outer layers with expansion velocities as high as $v_{\mathrm{exp}} \sim 4000$ km s^{-1}. Though calculated fluxes are slightly smaller than observed fluxes at t about 200 d, a slightly flatter distribution of mixed elements (than in fig. 14) results in better agreement. Also the effect of clumpiness on γ-ray transport would be significant for the early phase (Yamada et al. 1989; Bussard et al. 1989).

Subsequent light curve changes occur very slowly, as discussed above for x-rays. The flux ratio between the two γ-ray lines at 847 keV and 1238 keV is close to unity at early stages because of the smaller cross section for 1238 keV when compared with 847 keV. The ratio approaches the experimental value of 0.68 as column depth decreases.

5.4. X-ray and γ-ray spectra

Another important comparison is on the emergent spectrum and its evolution. Figures 29 and 30 show hard x-ray and γ-ray spectra for the model with photoelectric opacity reduced by a factor of 9 (fig. 27, solid lines). These spectra are compared with observations by *Ginga* (thin diamonds; Tanaka 1988b; Inoue et al. 1991) and *Kvant* (HEXE, crosses; and Pulsar X-1, thick diamonds – Sunyaev et al. 1987, 1989) at t = 180–600 d and the balloon-borne observation (Wilson et al. 1988) at $t = 240$ d. The calculated spectra for $E > 30$ keV are in good agreement with HEXE and Pulsar X-1 observations.

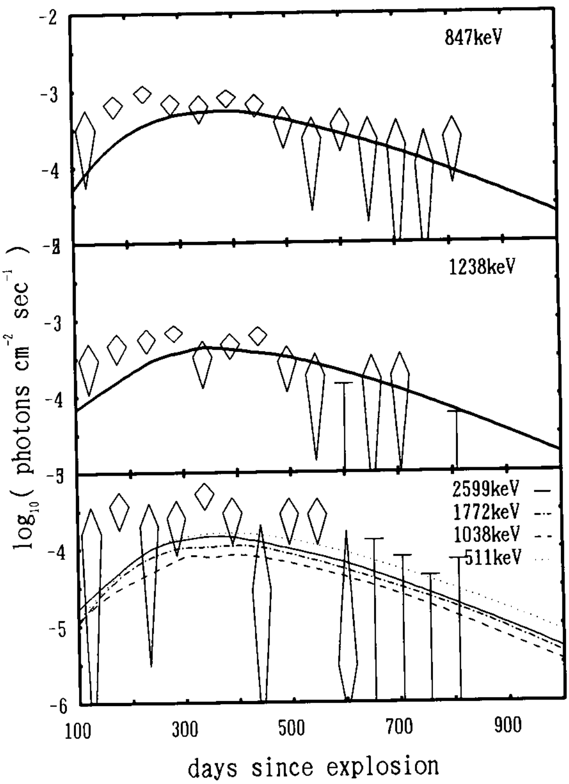

Fig. 28. Calculated γ-ray light curves for 847 keV, 1238 keV, and other lines. The hydrodynamical model 14E1 with abundance distribution in fig. 14 is adopted. For comparison, gamma-ray observations by SMM are shown by the diamonds.

This implies that the downscatterings of γ-rays and hard x-rays in SN 1987A are well modeled by our calculation. The theoretical spectrum does not appreciably change until t is approximately 400 d, and becomes harder as the ejecta expands and the number of Compton scatterings decreases.

For 16–28 keV, the flux observed with HEXE is systematically higher than that observed with *Ginga*; our calculated fluxes for the models 14E1 and 11E1 (Kumagai et al. 1989) are closer to the *Ginga* flux and the *HEXE* flux, respectively. The spectrum for this energy range is very sensitive to photoelectric absorption. At $t < 300$ d, absorption by heavy elements which are mixed into the envelope is dominant, while at later stages absorption in the core is significant. Comparison between the observed and calculated

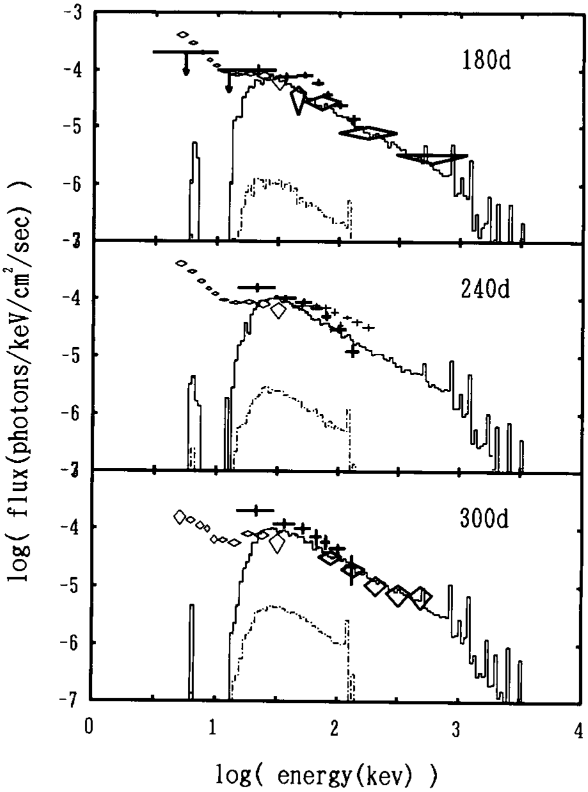

Fig. 29. Calculated hard x-ray and γ-ray spectra due to the decay of ^{56}Co (solid curve) and ^{57}Co (dash-dotted) for the model with reduction of the photoelectric opacity by a factor of 9 at $M_r < 8\ M_\odot$ (i.e., the solid curves in fig. 27) at t = 180 d, 240 d, and 300 d. The thin diamond shows the spectra observed by *Ginga* (Tanaka 1988a, 1988b); the thick diamond and the thick crosses are observations by Pulsar X-1 and HEXE, respectively *Kvant* (Sunyaev et al. 1987, 1989); and the thin crosses are balloon-borne observations (Wilson et al. 1988).

spectra at 16–28 keV thus provides important information on the distribution of heavy elements and clumpiness in both the core and the envelope.

The dash-dotted curves in figs. 29 and 30 show the emergent spectra due to degraded line γ-rays (122 keV and 136 keV) from the ^{57}Co decay (also Lehoucq et al. 1989). Compare these with the curves for ^{56}Co decay. Because of the longer half-life of ^{57}Co (271 d) as compared with ^{56}Co (77 d), the x-rays below 122 keV are dominated by the ^{57}Co component for t > 600

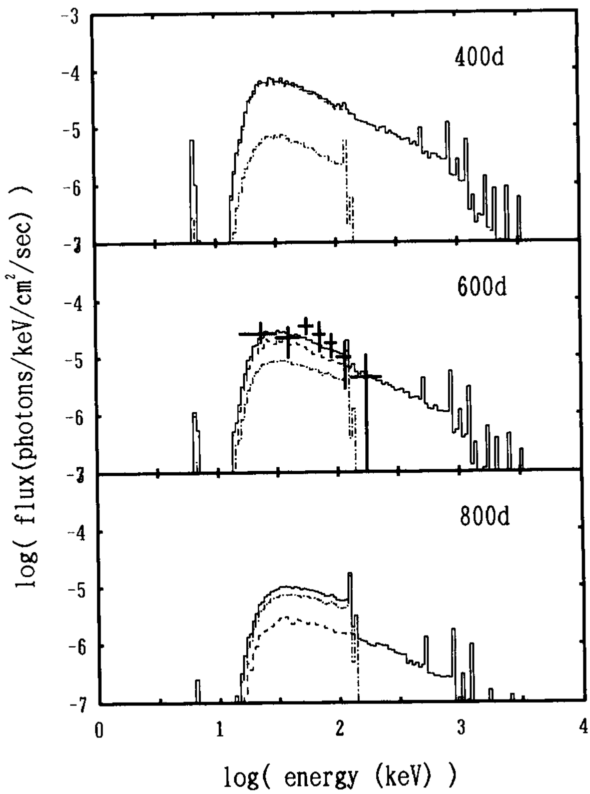

Fig. 30. Same as fig. 29 but for t = 450 d, 600 d, and 800 d. The dash-dotted curves show the emergent spectra due to the degraded line γ-rays (122 keV and 136 keV) from ^{57}Co decay. The solid curves show the sum of contributions from ^{56}Co and ^{57}Co.

d. It is interesting to compare the predicted hard x-ray spectrum at t = 600 d with HEXE observations (Sunyaev et al. 1989). Without contributions from ^{57}Co decay, the theoretical flux below 100 keV is about a factor of 2 smaller than the observed flux. With the adopted abundance of ^{57}Ni, the contributions from decays of ^{56}Co and ^{57}Co are comparable at $t \sim$ 600 d, which leads to a good agreement between the predicted and the observed flux, as seen in fig. 30. This suggests that the abundance ratio of ^{56}Ni/^{57}Ni may be somewhat larger than the solar ratio as calculated by Hashimoto et al. (1989).

The x-rays below 16 keV observed by *Ginga* cannot be accounted for by Compton degraded γ-rays. Instead, the time variations of the intensity and spectrum of this soft component are very well reproduced as thermal emissions from ejecta which are heated by collision with preexisting circumstellar matter (H. Itoh et al. 1987; Masai et al. 1987, 1988). This is described in section 9.

6. Rayleigh-Taylor instabilities and mixing

6.1. Linear stability analysis

As discussed in sections 4–5, the light curves at all wave bands indicate the occurrence of large scale mixing in SN 1987A. The most promising mechanism to mix the ejecta of SN 1987A is Rayleigh-Taylor instability. Although gravity is negligible in the explosion, acceleration of matter effectively acts as gravity and can be responsible for Rayleigh-Taylor instability. The growth rate, G_{RT}, of this instability is estimated as

$$G_{\mathrm{RT}} = \sqrt{-\frac{\rho_+ - \rho_-}{\rho_+ + \rho_-}\frac{1}{\rho}\frac{dP}{dr}k}, \tag{16}$$

where k is the wave number of the perturbation and ρ_+ and ρ_- are the densities of the upper and lower layers. Equation (16) shows that the layer is Rayleigh-Taylor unstable when $(dP/dr)(d\rho/dr) < 0$ (see Bandiera 1984; Benz and Thielemann 1990; and Goodman 1991 for convective criterion).

Ebisuzaki et al. (1989) performed a linear stability analysis of the explosion for model 14E1. Figure 31 shows the evolution of the pressure profile of the exploding star. Dashed lines indicate the H/He interface and He/metal interface. Before the explosion, the pressure gradient is negative, since it is balanced with gravitational attraction (stage 0). After the blast shock passes, the layer expands to decrease the pressure rapidly. When the blast shock is propagating through the hydrogen-rich envelope with a much less steep pressure gradient, an inwardly propagating reverse shock forms (stages 2–4). The layer between the blast wave and the reverse shock is decelerated and thus has a positive pressure gradient. When the blast shock reaches the surface layer with a steep pressure gradient, an inward-moving rarefaction wave forms, and produces a negative pressure gradient that accelerates the matter outward (stage 5). As a result, the H/He interface is first accelerated, then decelerated, and finally accelerated again; that is, the pressure gradient changes its sign twice. The He/metal interface also experiences similar acceleration and deceleration.

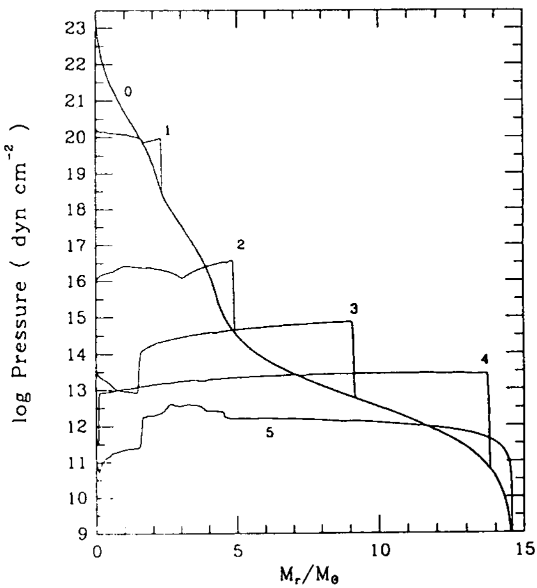

Fig. 31. Change in pressure profile in the ejecta of model 14E1. Stage numbers correspond to: (0) t = 0; (1) 9.0 s; (2) 167 s; (3) 1060 s; (4)3330 s; and (5) 7460 s after the explosion. The pressure gradient is positive between the blast and reverse shocks.

Figure 32 shows the time evolution of the density profile. Near the H/He and the He/metal interfaces (dashed lines), the density steeply decreases with radius because of changes in the mean molecular weight, μ, and the specific entropy, s. During the hydrodynamic stages of explosion near the composition interfaces the sign of the gradients of μ and s and therefore of density, do not change.

Figures 31 and 32 clearly show that the pressure gradient is positive during the deceleration phase (stages 2–4 for the H/He interface), while the density gradient remains negative near the H/He and He/metal interfaces. These layers are Rayleigh-Taylor unstable.

The distribution of the amplification factor ζ/ζ_0 at t = 18,000 s is plotted against M_r in fig. 33 for l = 20 (solid curve). Here the amplification factor is given as

$$\zeta/\zeta_0 = \exp\left(\int_0^t \mathrm{Re}(G_{\mathrm{RT}})dt'\right), \tag{17}$$

and well exceeds 100 near the H/He interface.

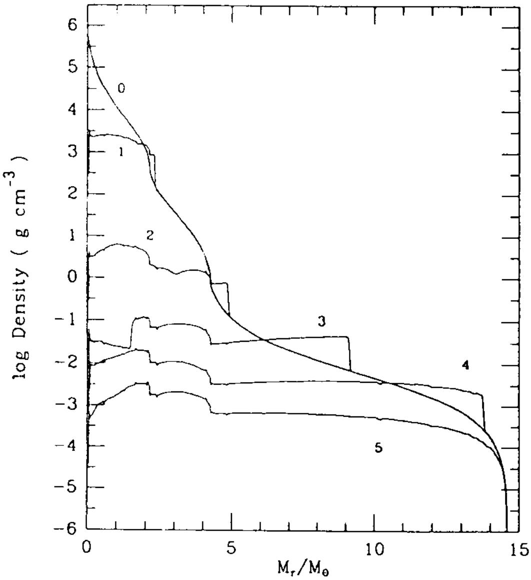

Fig. 32. The same as fig. 31 but for the change in the density profiles. The density steeply decreases outward at the H/He and He/metal interfaces.

Figure 34 shows the time change in amplification factor at the H/He interface for l = 10 and 20; the instability stops growing when the shock breaks out of the surface.

6.2. *Two dimensional hydrodynamic calculation*

In 2-D hydrodynamic simulations, Arnett et al. (1989) found a large nonlinear growth of the Rayleigh-Taylor instability around the He/C+O interface, but only a limited growth around the H/He interface. Hachisu et al. (1990), Den et al. (1990), Yamada et al. (1990), and Herant and Benz (1991) carried out 2-D and 3-D hydrodynamic calculations for model 14E1, and confirmed the nonlinear growth of the Rayleigh-Taylor instability. Hachisu et al. (1990) found that the instability grows much more extensively at the H/He interface rather than at the He/C+O interface, as seen in fig. 35 for sinusoidal perturbation. A possible source of the difference from Arnett et al. (1989) would be the difference in the initial model.

Hachisu et al. (1990) assumed equatorial symmetry and used 1793 × 1793 mesh points to resolve the large-scale mushroom structures. In their 2D calculation, a 5% perturbation is applied to the velocity field just after the

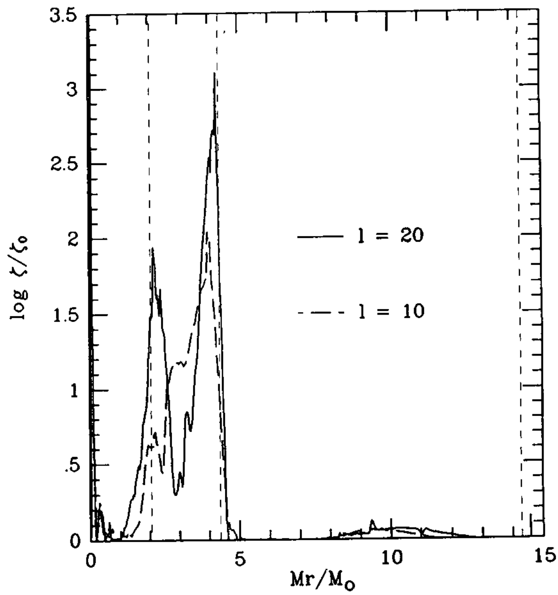

Fig. 33. Amplification factor (ζ/ζ_0) at t = 18,000 s plotted against mass (M_r). The H/He and He/metal interfaces are Rayleigh-Taylor unstable and the amplification factors are well above 100 for both l = 10 and l = 20.

blast shock hits the hydrogen-rich envelope ($\sim$ 100 s after the explosion). The Rayleigh-Taylor instability sets in at the H/He interface, and continues to grow until the blast shock breaks out of the hydrogen-rich envelope. The growth time to nonlinear regime is about 1000 s, and the mushroom structures become apparent at t = 2000 s. Figures 35 and 36, respectively, show the density contour map and the composition interfaces at t = 3109 s for random perturbation (Hachisu et al. 1991; Nomoto et al. 1991b, 1991c).

6.3. Mixing

The Rayleigh-Taylor instability, initiated first at the H/He interface, induces mixing between the core and the envelope. Figure 36 clearly shows that the heavy elements (core material) are mixed to the middle of the hydrogen-rich envelope.

Figure 37 shows abundance distributions after mixing as a function of mass and the expansion velocity (Nomoto et al. 1991b, 1991c). Core materials composed of C+O and silicon-rich elements are mixed to the layers

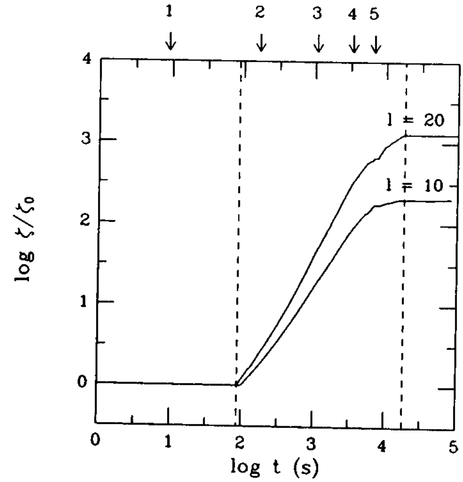

Fig. 34. Time change in the amplification factor at the H/He interface for l = 10 and 20. Stage numbers 1–5 are the same as in figs. 31 and 32. The instability stops growing when the shock breaks out of the surface.

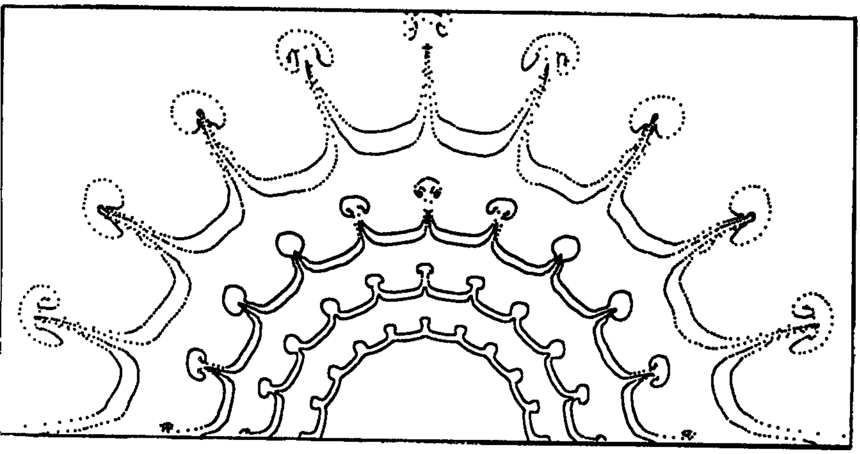

Fig. 35. Nonlinear growth of Rayleigh-Taylor instability for 14E1 with 5% sinusoidal perturbations on velocities (Hachisu et al. 1991; Nomoto et al. 1991b, 1991c).

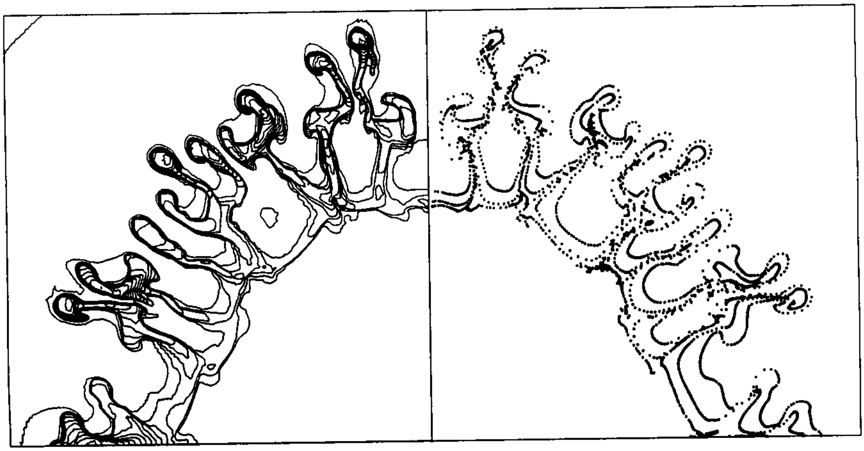

Fig. 36. The same as fig. 35 except for random perturbations. Density contours are shown at left, and positions of the marker particles initially located at the H/He, He/C+O, and C+O/Si interfaces are shown at right. The core material finally reaches the top of the mushroom head (Hachisu et al. 1991; Nomoto et al. 1991b, 1991c).

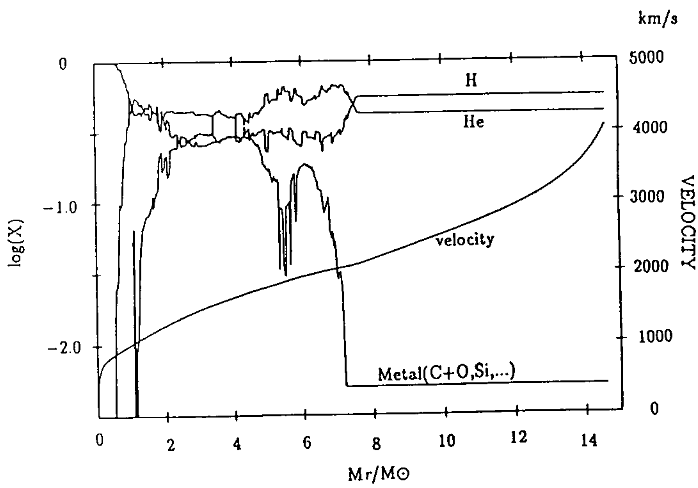

Fig. 37. Abundance distribution (mass fraction) as a result of Rayleigh-Taylor instability. Hydrogen is mixed down to $M_r \sim 1\ M_\odot$. The mean radial velocity is also shown (Hachisu et al. 1991; Nomoto et al. 1991b, 1991c).

having expansion velocities of approximately 2200 km s^{-1}. At the same time, hydrogen is mixed down to the core at expansion velocities as low as about 800 km s^{-1}. These velocities are close to the terminal values, since the shock has already broken out of the hydrogen-rich envelope at this time.

6.4. Comparison with observations

Indications of large-scale mixing are summarized as follows:

(1) The broad infrared lines of heavy elements and the γ-ray lines of ^{56}Co have provided direct evidence that Ar, Ni, Co, and Fe are mixed from the low velocity cores ($v \sim 500$ km s^{-1}) to the high velocity outer envelope ($v = 2000 - 3000$ km s^{-1}) (Erickson et al. 1988; Witteborn et al. 1989; Tueller et al. 1990).

(2) The unexpectedly early emergence of hard x-rays, and the smooth increase in the pre-maximum optical luminosity have shown indirect evidence at the presence of mixed radioactive materials at a velocity of about 3000 km s^{-1} (Kumagai et al. 1989; Pinto and Woosley 1988b; Arnett and Fu 1989; Shigeyama and Nomoto 1990).

(3) Larger scale mixing of radioactive material up to the expansion velocity of about 4000 km s^{-1} is required by an unexpectedly early emergence of γ-rays (see also Chugai 1991).

(4) Conversely, mixing of hydrogen into the metal-rich core down to a low expansion velocity such as 800 km s^{-1} is indicated by the plateau-like peak of the optical light curve. Also, the minimum velocity of hydrogen found to be as low as around 800 km s^{-1}.

(5) Formation of chemically inhomogeneous clumps, in particular, a hydrogen/helium-rich *hole* in the core is suggested from the very slow decline in hard x-rays observed with *Ginga* (Kumagai et al. 1989). Clumps are also indicated from the spectroscopic features (Stathakis et al. 1991; Fransson 1991).

The 2D hydrodynamic calculations clearly show that Rayleigh-Taylor mixing can reproduce most of the observational indications of mixing summarized above. Heavy elements are concentrated into high-density fingers so that the hydrogen- and helium-rich fingers may effectively be *holes* for x-rays because of much smaller photoelectric absorption. Note also that dust can form preferentially in the high-density clumps, which could account for why dust formed in the ejecta has not led to a blackout of the supernova (see sec. 7; Dwek 1988; Lucy et al. 1989; Kozasa et al. 1989a, 1989b).

Regarding the early emergence of gamma-rays, the Rayleigh-Taylor instability alone may not convey ^{56}Ni to the surface layer whose expansion velocity is as large as $\sim 3000 - 4000$ km s^{-1}. Acceleration of the core material by energy input from the decay of ^{56}Ni (Woosley 1988; Arnett 1988) is found to be not so effective (Herant and Benz 1991). The ejecta might be clumpy enough to make the ejecta more transparent to γ-rays.

7. Dust formation

With the increasing fraction of the x-ray and γ-ray luminosity $L_{X\gamma}$ (shown by a dashed curve in fig. 38), the calculated optical bolometric luminosity decreases faster than the energy generation rate of radioactive decays L_{Co}. This prediction is consistent with the observed U to M bolometric luminosity, L_{U-M}, from 260 d to 450 d (Whitelock et al. 1988; Suntzef et al. 1988).

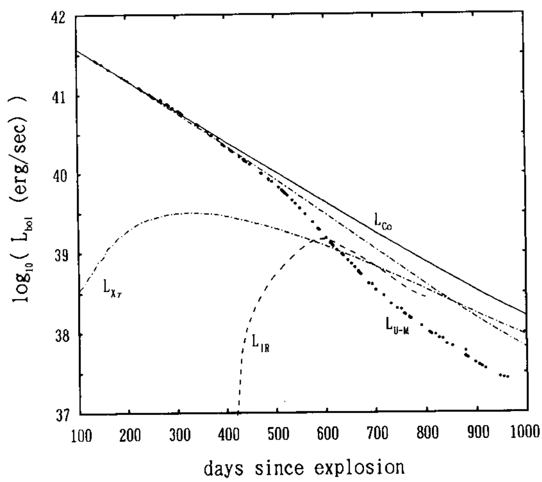

Fig. 38. Observed U to M bolometric luminosity (SAAO: lower filled circles); observed infrared luminosity L_{IR} (dashed); energy generation rate L_{Co} due to the decays of ^{56}Co and ^{57}Co (solid curve); and the calculated x-ray and γ-ray luminosity $L_{X\gamma}$ (dash-dotted). The observed luminosity of $L_{U-M} + L_{IR}$ is almost equal to the predicted luminosity of $L_{Co} - L_{X\gamma}$ (dash-dotted).

Afterwards, however, the observed L_{U-M} decreases faster than our theoretical luminosity, $L_{Co} - L_{X\gamma}$ (Whitelock et al. 1989; Suntzef and Bouchet 1990). During this phase, an increase in the 10–13 μm emission was reported (Roche et al. 1989), as seen from the IR luminosity L_{IR} in fig. 38. Here the observed luminosity of $L_{U-M} + L_{IR}$ is almost equal to the predicted luminosity of $L_{Co} - L_{X\gamma}$ (dash-dotted line.) This agreement strongly supports the idea that the source of the IR flux is from the emission of newly formed dust in the ejecta, not from the circumstellar matter.

Kozasa et al. (1989a, 1989b, 1991) investigated the formation of dust grains for 11E1, 14E1, and nucleosynthesis in fig. 14 by assuming a simple form of temperature decrease, namely, $T(t) \propto t^{-3(\gamma-1)}$. The gas temperatures at condensation are 1800 K for graphite, 1600 K for Al_2O_3, 1400 K for $MgSiO_3$, and 1140 K for Fe_3O_4 grains. The grain species are closely related to the mixing. Without mixing, the helium layer contains more carbon than oxygen, so that graphite grains condense first. On the other hand, if mixing occurs, oxygen is more abundant than carbon for all layers, so that oxidic grains form.

Figure 39 shows the condensation time of dust grains as a function of M_r in the mixed ejecta 14E1 for $\gamma = 1.27$. Each grain species condenses almost simultaneously at $1.7\ M_\odot \lesssim M_r \lesssim 4.0\ M_\odot$; that is, Al_2O_3 grains at

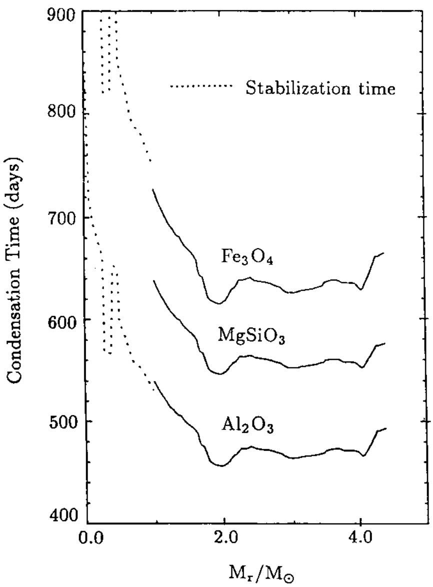

Fig. 39. The condensation time of dust grains as a function of M_r in the ejecta 14E1 for $\gamma = 1.27$. The index γ describes the decrease in temperature as $T(t) \propto t^{-3(\gamma-1)}$ (Kozasa et al. 1991).

approximately day 470, $MgSiO_3$ grains at approximately day 560, and Fe_3O_4 grains at approximately day 630 (Kozasa et al. 1991). Thus, final radii and the total mass of dust grains formed are $\sim$ 10 A (0.009 $M_\odot$) for Al_2O_3, $\sim$ 70 A (0.19 $M_\odot$) for $MgSiO_3$, and $\sim$ 10 A (0.031 $M_\odot$) for Fe_3O_4 as seen in fig. 40.

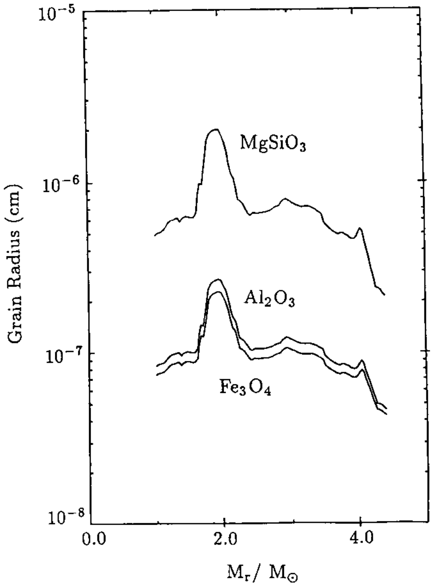

Fig. 40. The radii of dust grains formed at M_r in the ejecta (Kozasa et al. 1991).

The condensation of dust grains starts at around day 460 and continues up to approximately day 730. This formation history is consistent with the IR observations of SN 1987A as follows. The first condensate Al_2O_3 grain is a good emitter around 10 μm and its formation can account for an early rise in the observed IR light curve starting from around day 460. On the other hand, the mass absorption coefficient of Al_2O_3 grains is so small that their formation does not lead to any observable changes in the visual to near-IR region. After approximately day 550 and 630, the optical depths increase due to $MgSiO_3$ and Fe_3O_4 grains, respectively.

The analysis of the blue-shifted lines show that extinction due to dust grains is negligible up to day 530, increases rapidly after day 580, and gradually increases after day 670 (Lucy et al. 1989, 1991). Time evolution of optical depth in the ejecta can be qualitatively accounted for by sequential formation of Al_2O_3, $MgSiO_3$, and Fe_3O_4 grains.

If the grains formed uniformly, the optical depths of $MgSiO_3$ and Fe_3O_4 grains are so large that they would black out the supernova. However, the observed extinction shows very small condensation efficiency (Lucy et al. 1989). The x-ray luminosity is far too small to destroy dust grains. Thus, the low efficiency of extinction is likely to be due to clumpiness in the ejecta (Lucy et al. 1989, 1991).

For the somewhat clumpy ejecta, the thermal radiation from Al_2O_3 and $MgSiO_3$ grains is calculated. Thus, the total infrared light curve that results is shown by open squares in fig. 41. This is in good agreement with the observed curve (filled circles) (Kozasa et al. 1991).

The formation of dust grains in SN 1987A is interesting in view of the origin of the isotopic anomalies of heavy elements in carbonaceous chondrites and the origin of interstellar dust grains in general.

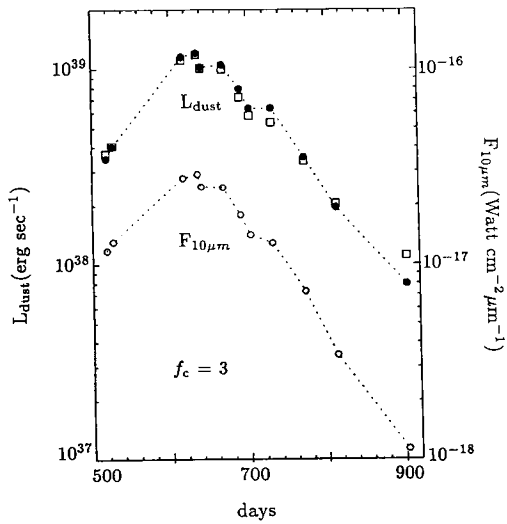

Fig. 41. The calculated total infrared light curve due to thermal radiation from Al_2O_3 and $MgSiO_3$ grains (open squares), compared with the observed curve (filled circles) (Kozasa et al. 1991).

8. Pulsar and other radioactive elements

The bolometric light curve of SN 1987A has recently shown an interesting behavior in its decline (fig. 42). For around the first 800 days, the ESO bolometric light curve (Bouchet et al. 1991a) is in good agreement with the model 14E1 which includes only the decays of ^{56}Co and ^{57}Co (solid line in fig. 42). Afterwards the ESO light curve shows leveling off around during days 900–1070 with a decline following (Bouchet et al. 1991a). The bolometric light curve obtained by CTIO (Suntzeff et al. 1991) is somewhat below the ESO curve, but still its decline rate has been significantly slowed down since around day 900.

Here we examine the two possible sources of heating beyond that of ^{56}Co: (1) radioactive decays of ^{57}Co and ^{44}Ti; and (2) a central magnetized neutron star as either an isolated pulsar or an accreting x-ray pulsar (Kumagai et al. 1991).

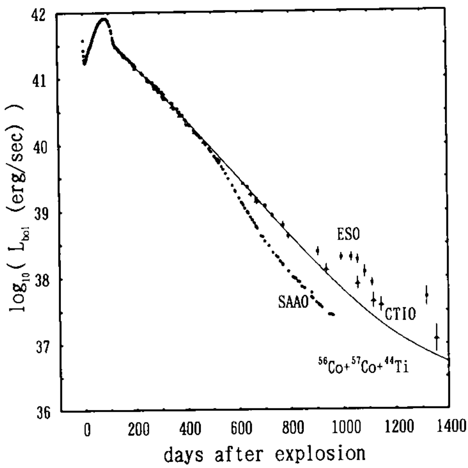

Fig. 42. The calculated UVOIR light curve for the standard abundances of 14E1 (solid line) compared with the U to M SAAO light curve and the UVOIR light curves observed at ESO and CTIO.

8.1. Contributions of ^{57}Co and ^{44}Ti

Explosive nucleosynthesis calculations have shown that radioactive ^{57}Ni and ^{44}Ti are synthesized together with ^{56}Ni by silicon burning and the subsequent α-rich freezeout (e.g., Woosley and Hoffman 1991). The half lives of ^{57}Co and ^{44}Ti are so long (271 d and 47 yr, respectively) that their decays could dominate the late light curve. In ^{44}Ti decay after about 1100 d, the luminosity due to positron emission dominates the light curve.

We first calculate the light curve to see how much ^{57}Co is required to account for the observed light curve. We then examine how the isotopic ratios depend on neutron excess near the bottom of the ejecta, and to what extent these are constrained from observations. Nucleosynthesis products in the ejecta is taken from table 2, which contains 0.073 $M_\odot^{56}$ Ni, 0.0031 $M_\odot^{57}$ Ni, and 9.2 $\times 10^{-5}$ $M_\odot^{44}$ Ti. With respect to the solar isotopic ratios, this standard case has

$$\langle^{57}\mathrm{Co}/^{56}\mathrm{Co}\rangle \equiv [X(^{57}\mathrm{Ni})/X(^{56}\mathrm{Ni})]/[X(^{57}\mathrm{Fe})/X(^{56}\mathrm{Fe})]_\odot = 1.7,$$
$$\langle^{58}\mathrm{Ni}/^{56}\mathrm{Ni}\rangle \equiv [X(^{58}\mathrm{Ni})/X(^{56}\mathrm{Ni})]/[X(^{58}\mathrm{Ni})/X(^{56}\mathrm{Fe})]_\odot = 1.2,$$

and

$$\langle^{44}\mathrm{Ti}/^{56}\mathrm{Ni}\rangle \equiv [X(^{44}\mathrm{Ti})/X(^{56}\mathrm{Ni})]/[X(^{44}\mathrm{Ca})/X(^{56}\mathrm{Fe})]_\odot = 1.0.$$

Figure 43 shows the calculated UVOIR light curve, powered by the decays of ^{56}Co (0.073 $M_\odot$) and ^{57}Co with various $\langle^{57}\mathrm{Co}/^{56}\mathrm{Co}\rangle$ ratios. Here

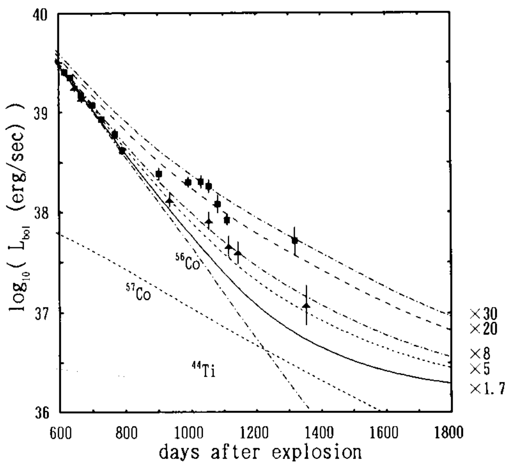

Fig. 43. The calculated UVOIR light curve powered by the decays of ^{56}Co (0.073 $M_\odot$), ^{44}Ti (9.2 $\times 10^{-5}$ $M_\odot$), and ^{57}Co with various $\langle^{57}\mathrm{Co}/^{56}\mathrm{Co}\rangle$ ratios. The dash-dotted (^{56}Co), dashed (^{57}Co), and dotted (^{44}Ti) lines show the individual contribution for the standard abundances.

the solid line is the standard case of $\langle^{57}\mathrm{Co}\ /^{56}\mathrm{Co}\rangle = 1.7$. (The deviation of the ^{57}Co contribution from the line for exp $(-t/91.2\ \mathrm{d})$ is due to the increasing fraction of x-rays and γ-rays, as calculated with the Monte Carlo method.) The decline of CTIO curve is consistent with the decay rate of ^{57}Co if $5 \lesssim \langle^{57}\mathrm{Co}/^{56}\mathrm{Co}\rangle \lesssim 10$ for 14E1 and $8 \lesssim \langle^{57}\mathrm{Co}/^{56}\mathrm{Co}\rangle \lesssim 16$ for 11E1. For 11E1, which is the same as 14E1 except for the 6.7 $M_\odot$ hydrogen-rich envelope (Shigeyama et al. 1988), more γ-rays escape without being thermalized because of larger E/M than in 14E1.

The ^{57}Co/^{56}Co ratio in the ejecta has been variously estimated from the spectroscopic observations as $\langle^{57}\mathrm{Co}/^{56}\mathrm{Co}\rangle \lesssim 1.7$ (Danziger et al. 1991) and 1–2 (Varani et al. 1990). Hard x-rays from Compton degradation of line γ-rays from ^{57}Co decay dominate the flux at $E < 136$ keV for $t > 700$ d. Compared with this prediction, hard x-ray continuum observations with HEXE has given estimates of $\langle^{57}\mathrm{Co}/^{56}\mathrm{Co}\rangle \lesssim 1.5$ at $\sim$ day 800 (Sunyaev et al. 1990).

If we take the constraint $\langle^{57}\mathrm{Co}/^{56}\mathrm{Co}\rangle \lesssim 2$, we can tentatively conclude that excess brightness of the recent light curve could not be accounted for by the decay of ^{57}Co. However, in view of possible uncertainties and the model dependence of the observed $\langle^{57}\mathrm{Co}/^{56}\mathrm{Co}\rangle$, it would be useful to use $\langle^{58}\mathrm{Ni}/^{56}\mathrm{Ni}\rangle$ as a supplementary constraint on $\langle^{57}\mathrm{Co}/^{56}\mathrm{Co}\rangle$. The mass of ^{58}Ni has been estimated to be approximately 0.0022–0.003 $M_\odot$ (Rank et al. 1988; Witterborn et al. 1989; Aitken et al. 1988; Meikle et al. 1989; Danziger et al. 1991), which gives $\langle^{58}\mathrm{Ni}/^{56}\mathrm{Ni}\rangle \sim 0.7$–$1.0$.

Table 3
Isotopic Ratios

$\langle^{57}\mathrm{Co}/^{56}\mathrm{Co}\rangle$...	1.5	1.7	2.0	2.3	4.4
$\langle^{58}\mathrm{Ni}/^{56}\mathrm{Ni}\rangle$ ...	1.0	1.2	3.0	4.4	14.0
$\langle^{44}\mathrm{Ti}/^{56}\mathrm{Ni}\rangle$ ...	0.7	1.0	1.1	1.2	2.1

As mentioned in section. 3.2, the ratios $\langle^{57}\mathrm{Co}/^{56}\mathrm{Co}\rangle$ and $\langle^{58}\mathrm{Ni}/^{56}\mathrm{Ni}\rangle$ depend on the distribution of neutron excess η near the bottom of the ejecta, which consists of approximately two layers with $\eta = 0.0026$ and $\eta = 0.0117$ in model 14E1 (Hashimoto et al. 1989; Thielemann et al. 1990). The location of this change in η is subject to uncertainties since it marks the outer edge of the convective oxygen burning shell (Nomoto and Hashimoto 1988; Thielemann et al. 1990). By varying this location, we obtain the relations between these ratios in the ejecta summarized in table 3 (see also Woosley and Hoffman 1991 for a wider range of parameters). Since ^{58}Ni/^{56}Ni is much more sensitive to η than other isotopic ratios, the observed upper mass limit to ^{58}Ni provides other upper limits as $\langle ^{57}\text{Co}/^{56}\text{Co}\rangle \lesssim 2.0$ and $\langle ^{44}\text{Ti}/^{56}\text{Ni}\rangle \lesssim 1.1$.

If $\langle ^{57}\text{Co}/^{56}\text{Co}\rangle \gtrsim 4$ is assumed, $\langle ^{58}\text{Ni}/^{56}\text{Ni}\rangle \gtrsim 10$ which would be inconsistent with the observed upper limit. Lehoucq et al. (1991) discussed the possible case of $\langle ^{44}\text{Ti}/^{56}\text{Ni}\rangle \gtrsim 10$, but such a large ratio seems unlikely from the above nucleosynthesis constraints.

8.2. *Predicted line γ-rays*

Our nucleosynthesis calculations and the spectroscopic constraints on ^{57}Co and ^{58}Ni suggest $\langle ^{57}\text{Co}/^{56}\text{Co}\rangle \lesssim 1.7$ and $\langle ^{44}\text{Ti}/^{56}\text{Ni}\rangle \lesssim 1.1$. Thus, it is probably less likely that the decay of ^{57}Co alone can supply enough energy to power the recent light curve of SN 1987A. In other words, a buried pulsar would be the more likely energy source, unless the observed luminosity excess is mostly due to infrared echo from circumstellar materials (see Dwek 1991).

However, it is useful to provide a prediction to test ^{57}Co abundance by direct observations of line γ-rays with balloon experiments (Matteson et al. 1991; Kamae and Takahashi 1991). The predicted light curves of line γ-rays from the decays of ^{57}Co and ^{44}Ti are shown in fig. 44 for our standard case. The line γ-rays from ^{57}Co (14 kev, 122 keV and 136 keV) forms a broad peak at t = 800–1000 d. If $\langle ^{57}\text{Co}/^{56}\text{Co}\rangle \gtrsim 5$, the 122 keV line γ-ray flux is predicted to exceed approximately 2×10^{-4} photons cm^{-2} s^{-1} at maximum and 1.5×10^{-4} photons cm^{-2} s^{-1} at t around 1400 d.

The 1159 keV line γ-ray from ^{44}Sc decay forms a light curve shown by the dashed curve in fig. 44. Future γ-ray observations may be able to observe this line.

8.3. *Contribution of the pulsar*

In modeling the energy supply from a central neutron star, we assume that the neutron star emits x-rays and γ-rays with a luminosity $L_{X\gamma}$ and a spectrum similar to that of an isolated pulsar or an x-ray pulsar (see Kumagai et al. 1989 for details; also Woosley et al. 1989). The energy deposited in the ejecta is calculated with the Monte Carlo simulation method.

Figure 45 shows the calculated UVOIR bolometric light curves of 14E1 powered by the pulsar with several $L_{X\gamma}$ in addition to the cobalt decays with $\langle ^{57}\text{Co}/^{56}\text{Co}\rangle = 1.7$. The original pulsar radiation is assumed to have a Crab-like power law spectrum.

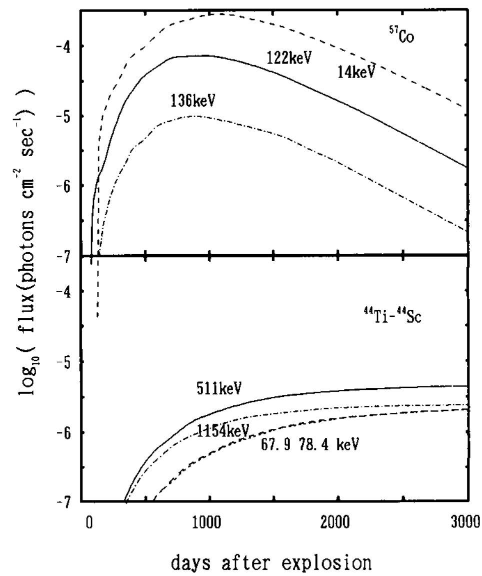

Fig. 44. Light curves of line γ-rays expected from the decays of ^{57}Co and ^{44}Ti for the standard abundances.

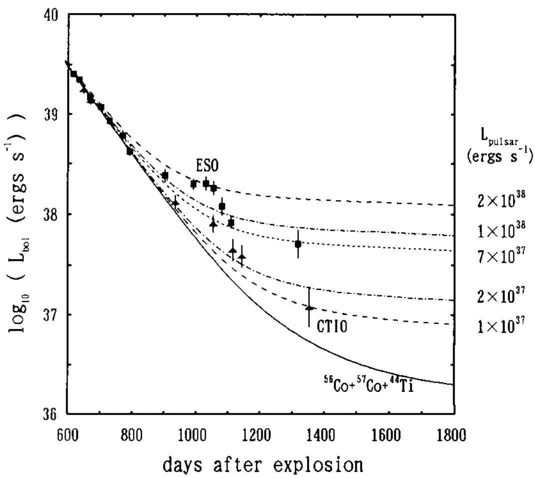

Fig. 45. The calculated UVOIR bolometric light curves of 14E1 powered by the pulsar for several $L_{X\gamma}$ in addition to the cobalt decays with $\langle ^{57}Co/^{56}Co \rangle = 1.7$. The original pulsar radiation is assumed to have a Crab-like power law spectrum.

It is seen that the flat part of the ESO light curve at days 900–1070 can be reproduced if $L_{X\gamma} \sim 2 \times 10^{38}$ erg s^{-1} for 14E1. The subsequent decline corresponds to the decrease in $L_{X\gamma}$ down to around 0.8–1 $\times 10^{38}$ erg s^{-1}. Such a rapid decrease has not been predicted by the simple pulsar model, and might be related to some instabilities in the materials accreting onto the neutron star (Bouchet et al. 1991a; Mineshige et al. 1991).

The CTIO light curve can be approximated through day 1350 with the pulsar of $L_{X\gamma} \sim 2 \times 10^{37}$ erg s^{-1}. Afterwards, the calculated light curve is predicted to level off so that the next observation is crucial to judge the energy source.

The reported color temperature is as low as 160 K (Bouchet et al. 1991a) which suggests that pulsar radiation is absorbed by the dust and reemitted at far IR. From the luminosity, color temperature, and the date of leveling off of the light curve, the expansion velocity at the far IR photosphere is estimated to be about 2300 km s^{-1} (Shigeyama et al. 1991). This means that the dust layer around the pulsar extends into the original hydrogen-rich envelope, which is consistent with the mixing of heavy elements seen in fig. 37. The optical depth of this dust layer is fairly thick, so that the time variation reported by ESO observations requires the dust layer to be highly clumpy (Shigeyama et al. 1991).

8.4. Predicted hard radiation from the pulsar

If the observed UVOIR bolometric luminosity is mostly powered by the central neutron star, it might be possible to observe x-rays from it with current and future x-ray satellites. The optical depth at day 2000 as a function of energy is shown in fig. 46 with the effect of clumpiness (see also section 5).

As expected from fig. 46, the calculated emergent spectrum for the pulsar energy input (see below) shows that the soft component below approximately 10 keV is mostly photoabsorbed, so that the most promising energy range for pulsar radiation detection is approximately 20 keV, which is covered with x-ray satellite *Ginga*. Figure 47 shows the 16–28 keV x-ray light curves with the contributions of x-ray pulsar-like (dash-dotted curve: $L_{X\gamma} = 2 \times 10^{37}$ erg s^{-1}) and power-law radiation (dashed curve: $L_{X\gamma} = 2 \times 10^{37}$ and 1×10^{38} erg s^{-1}). It is seen that whether or not the ejecta becomes sufficiently thin for *Ginga* to detect x-rays would be marginal competition with the life time of *Ginga*.

The nature of the newly born neutron star is highly uncertain. Let us discuss several possible cases (Kumagai et al. 1989; Woosley et al. 1989).

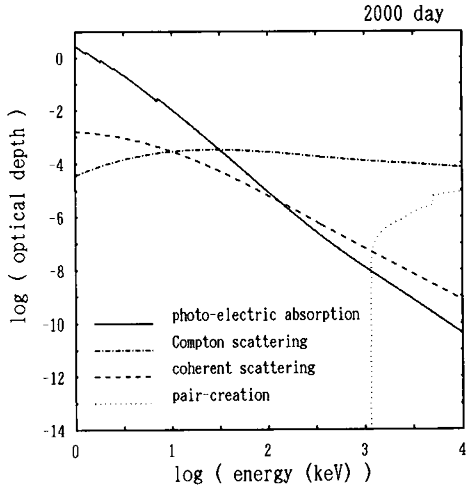

Fig. 46. The optical depth due to various processes for 14E1 at day 2000 as a function of energy.

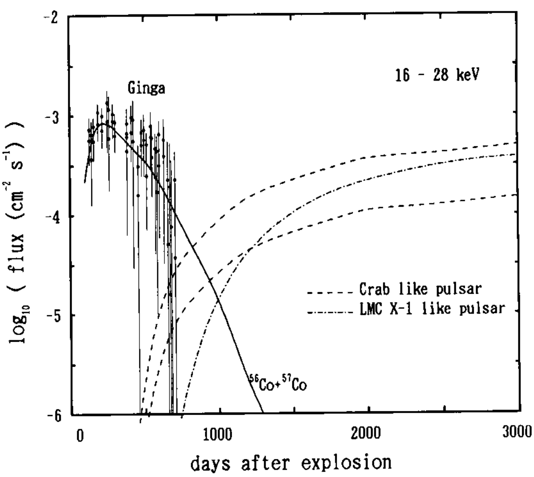

Fig. 47. The light curves of 16–28 keV x-rays expected from the Crab-like pulsar (dash-dotted lines for $L_{X\gamma} = 1 \times 10^{38}$ and 2×10^{37} erg s^{-1}) and the x-ray pulsar (dashed line for $L_{X\gamma} = 2 \times 10^{37}$ erg s^{-1}). The solid line is due to cobalt decays; the filled circles are the observed flux with *Ginga*.

In the presence of strong magnetic fields, the star manifests itself as an isolated pulsar because the nonthermal radiation from the pulsar mechanism dominates over stellar surface radiation. The dash-dotted lines in fig. 48 show the emergent spectrum at t = 800–2000 d for $L_{X\gamma} = 3.5 \times 10^{37}$ erg s^{-1}. Here the soft component below approximately 10 keV is mostly photoabsorbed. *Ginga* detects the emergent x-ray flux at $t > 1200$ d if $L_{X\gamma} \sim 1 \times 10^{38}$ and 1×10^{38} erg s^{-1}, while the flux is too low to be detected by *Ginga* if $L_{X\gamma}$ is lower.

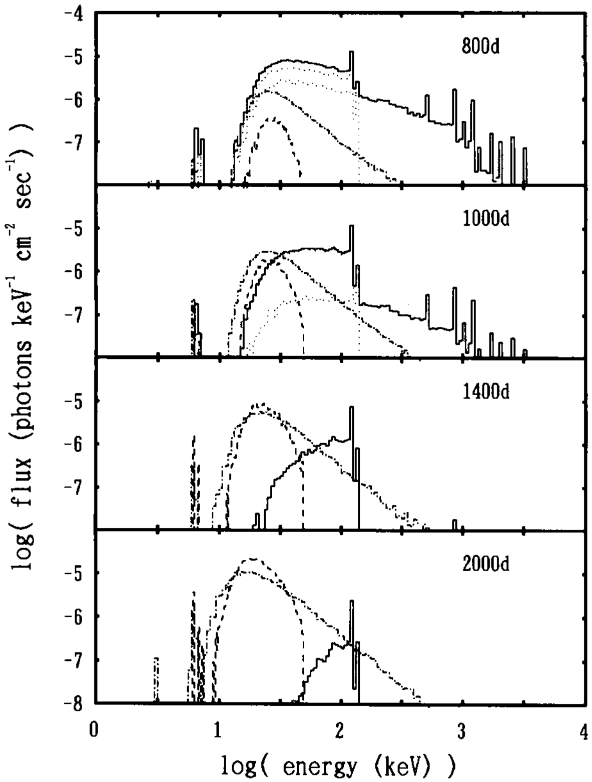

Fig. 48. The spectrum emerging from the supernova at t = 800–2000 d for SMC X-1 like (dash-dotted: $L_{X\gamma} = 3.5 \times 10^{37}$ erg s^{-1}), and power-law spectra (dashed: $L_{X\gamma} = 3.5 \times 10^{37}$ erg s^{-1}).

Next we consider the effect of accretion. If some ejected material falls back (Colgate 1988; Chevalier 1989) and forms an accretion disk (Michel 1988), the neutron star could be heated by accretion for a fairly long period. The spectrum of the resulting radiation depends on the strength of the stellar magnetic field. If it is weak, the accreting star emits blackbody radiation, possibly near the Eddington limit. If the field is stronger than around 10^{11} G, the neutron star appears as an x-ray pulsar.

For the strong field case, assume that the spectrum is similar to SMC X-1. The dash-dotted curves in fig. 48 show the emergent spectra at t = 800–2000 d for $L_{X\gamma} = 3.5 \times 10^{37}$ erg s^{-1}. The 16–28 keV flux is lower at an earlier phase but higher at a later phase than the power law case with the same $L_{X\gamma}$. At the early phase, the high energy cut-off for the x-ray pulsar leads to a smaller contribution to Compton degradation of high energy photons than the power law case. At a later phase, the spectrum becomes close to the original one so that a larger flux is emitted from the x-ray pulsar than in the power law case, as seen in fig. 48.

For very weak magnetic fields, we assume that the neutron star with 1.4 $M_\odot$ and a 10 km radius emits an Eddington luminosity of 3.5×10^{38} erg s^{-1} for hydrogen-depleted material. The corresponding blackbody temperature is 2.3 keV; the spectrum emerging from the supernova at t = 1000 d peaks at $\sim$ 16 keV. For 16–28 keV, the difference in the light curves (compared with the pulsar cases) is due to its softer spectrum, as discussed for the x-ray pulsar. Most of the blackbody radiation is photoabsorbed, and provides an almost constant energy input to the UV-IR bolometric light curve. Thus, the decline of the bolometric light curve becomes significantly slower from $t \sim 600$ d. This possibility has been ruled out from the observed bolometric luminosity.

8.5. X-rays from the neutron star surface

The obvious emission from young neutron stars is thermal radiation from the surface, which would peak in the soft x-ray band. Within the range of a few to 20 days after the explosion, the surface temperature falls to 3×10^6 K due to plasmon neutrino loss near the surface (Nomoto and Tsuruta 1987a, 1987b; Tsuruta and Nomoto 1989). Later cooling depends on whether or not exotic cooling agents like pion condensates are present in the central part of the neutron star. If pion condensates exist, the surface temperature starts to decrease from 3×10^6 K at an age of 20–50 yrs because of the finite time scale of heat conduction (Umeda et al. 1991). With such a surface temperature, surface x-rays and their possible decline due to exotic cooling could be observed by future x-ray astronomy satellites.

To examine when black body radiation of 3×10^6 K from the neutron star surface can emerge from the supernova debris, we performed Monte Carlo simulations for the same model whose optical depth is given in fig. 46. Change in the emergent spectrum is shown in fig. 49. The photons below 1 keV are largely photoabsorbed, thereby requiring more than 1000 yrs before they emerge. However, the total x-ray luminosity reaches 10^{32} erg s^{-1} in 20 yrs, as seen in fig. 50. Therefore, future x-ray satellites whose observational sensitivities are as good as *AXAF* might be able to observe the possible decrease in x-ray flux due to exotic cooling. (This also depends on the degree of clumpiness that reduces the effective photoelectric opacity.) However, the collision of the supernova ejecta with a circumstellar ring may obscure soft x-rays from the neutron star (see below).

Figure 51 summarizes time changes in the predicted x-ray spectrum of SN 1987A due to pulsar emission with a Crab-like power law spectrum (1×10^{37} erg s^{-1} and a black body emission from the neutron star surface of 3×10^6 K ($\sim 1 \times 10^{35}$ erg s^{-1}). For comparison, detectability of current and future x-ray and γ-ray missions (*Ginga, Astro-D, DUET, AXAF, GRANAT, GRO*) is shown. If the pulsar luminosity is higher than 1×10^{36} erg s^{-1}, observation of pulsar radiation at 5–10 keV would be promising.

9. Soft x-ray emission and circumstellar matter

9.1. Structure of circumstellar matter

The presence of circumstellar matter (CSM) around SN 1987A has been shown by radio, soft x-ray, UV, and optical observations (e.g., Turtle et al. 1987; Kirshner 1988; Sonneborn 1991; Panagia and Gilmozzi 1991; Wampler et al. 1990; Crots and Heathcore 1991). The circumstellar shell observed at UV and optical bands is located at a distance of about 5×10^{12} km from the ejecta center and moves at approximately 15 km s^{-1}. Such a slow velocity implies that the dense shell was lost from the progenitor at its red supergiant stage (see section 2). According to the UV echo model (Lundqvist and Fransson 1991), the gas density of this shell is around 3×10^4 cm^{-3}, and the observed mass is ~ 0.03 $M_\odot$. Radio and x-ray observations imply the presence of a blue supergiant wind.

Masai and Nomoto (1991) and Masai et al. (1991) postulated that the circumstellar structure and development is as follows: In the outermost regions where $r > R_s$, the red supergiant wind is slowly expanding with a density distribution of 81 $(r/R_s)^{-2}$ cm^{-3}. This slow red wind is overtaken by a

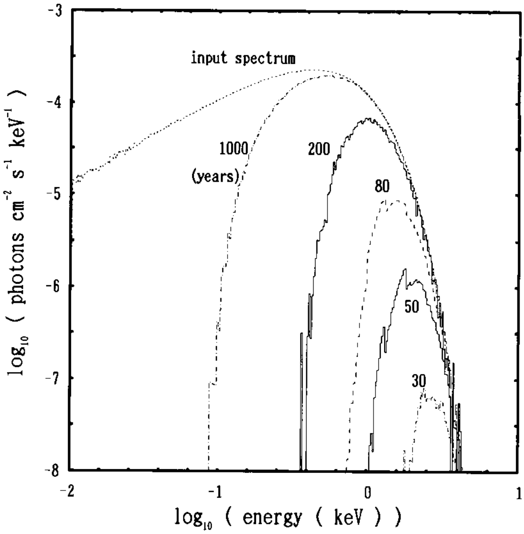

Fig. 49. Change in the emergent spectrum of x-rays from the neutron star surface where the black body temperature is 3×10^6 K.

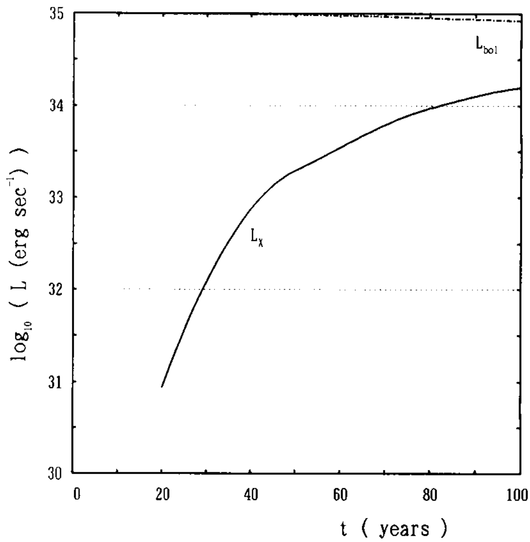

Fig. 50. Change in the total x-ray luminosity from the neutron star surface.

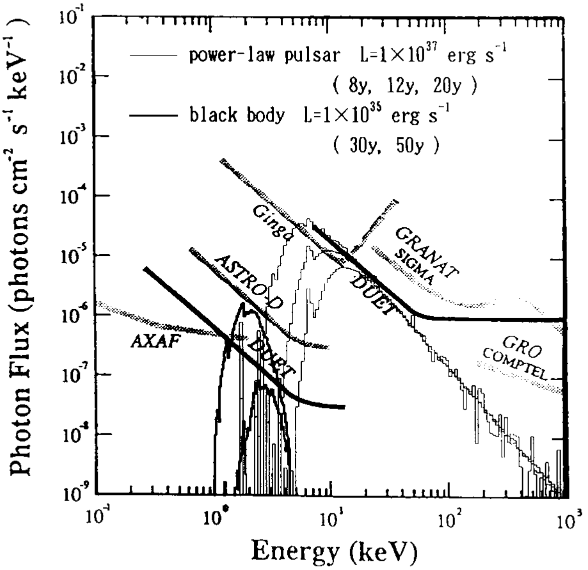

Fig. 51. The emergent spectrum of x-ray emission due to possible pulsar activity and the neutron star surface black body in SN 1987A.

fast blue wind, which produces two shocks, one propagating inward into the blue wind and the other propagating outward into the red wind (Chevalier 1988). The latter shock forms a dense thin shell at $r = R_s \approx 5 \times 10^{12}$ km, with a thickness of about 1×10^{10} km, as found by UV observations. At $R_I < r < R_s$, the blue wind matter exists with a constant density of 9 cm^{-3}. Here $R_I \approx 3 \times 10^{11}$ km represents the radius of the inward shock front which formed a dense shell. The dense shell is located at $r = R_I \sim 3 \times 10^{11}$ km, with a density of 3×10^5 cm^{-3} and a thickness of 9×10^9 km. Interior to this shell, a steady blue giant wind matter exists.

Recently the *Hubble Space Telescope* has revealed that the CSM is in the form of a ring with inclination of about 45 degrees (Jacobsen et al. 1991; Panagia and Gilmozzi 1991). These features are consistent with a slow expansion velocity of the CSM and no detection of UV echo for the first 80 days after explosion.

9.2. *Soft x-ray flare and collision with a circumstellar cloud*

Ginga has been observing soft x-ray emissions from SN 1987A (Dotani et al. 1987). This has been interpreted as thermal emission from the collision of expanding ejecta with preexisting circumstellar matter (H. Itoh et al. 1987; Masai et al. 1987). In January 1988, the soft component flared up (Tanaka 1988a, 1988b; Inoue et al. 1991). This flare was modeled by Masai et al. (1988), assuming a dense shell at $r = R_{\mathrm{I}}$ as described above.

In this model, the ejecta is first heated by the reverse shock that arises from the collision with the inner CSM; the resulting thermal emission of $T \sim 12$ keV dominates the soft x-rays observed since around 70 d. The outwardly propagating blast wave hits the outer dense shell, and enhances the soft x-rays at $t \sim 260$ d. This collision forms the second reverse shock that propagates into the ejecta. Resulting reheating of the ejecta up to about 17 keV in electron temperature produces a large flare at $t \sim 330$ d (January 1988). The calculated light curve and spectra are in good agreement with the observations (fig. 52; Masai et al. 1988).

The dense shell is assumed to cover 16 percent of the spherical area on the *far side.* Then absorption of soft x-ray and radio emissions by intervening matter explains the lack of emissions of radio and x-rays below 2 keV.

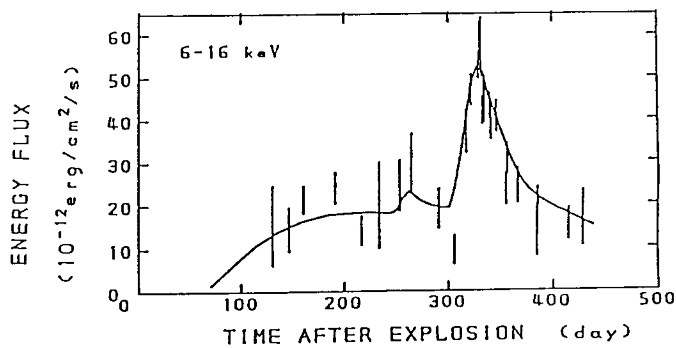

Fig. 52. Light curve in the energy range of 6–16 keV. The bars show the observed data by *Ginga* (Masai et al. 1988).

9.3. *Collision with the red supergiant shell*

The supernova ejecta further expands and collides with the ring in several years. Let us first describe the model of collision with a spherical shell (see also Chevalier and Liang 1990; Chevalier 1991; Luo and McCray 1991a). Masai et al. (1991) and Itoh et al. (1991), assuming the CSM structure described in section 9.1, have calculated the hydrodynamics of collision for 14E1 and predicted the following x-ray emission from this event.

The ejecta is currently interacting with the blue giant wind matter at $R_I < r < R_s$. Shock waves associated with this interaction are heating up the blue wind, which produces soft x-rays. The x-ray luminosity depends on the density of the blue wind matter, but may reach the detection limit of *ROSAT*, 10^{34} erg s^{-1}, as shown in fig. 53 (Itoh et al. 1991).

This shock wave propagates further and strikes the dense red giant wind shell. It heats up the matter of both the ejecta and the dense shell causing a spike-like flare with a duration of a few years (fig. 53, fig. 54); this is dominant at 0.8–2 keV (fig. 54). The x-ray luminosity reaches $\sim 10^{37}$ erg s^{-1}. The blast shock propagating outward hits the red supergiant wind remnant behind the dense shell, and causes an enhancement in soft x-rays at 2–7 keV (fig. 54). This enhancement lasts for about 50 years with a luminosity higher than 10^{36} erg s^{-1}.

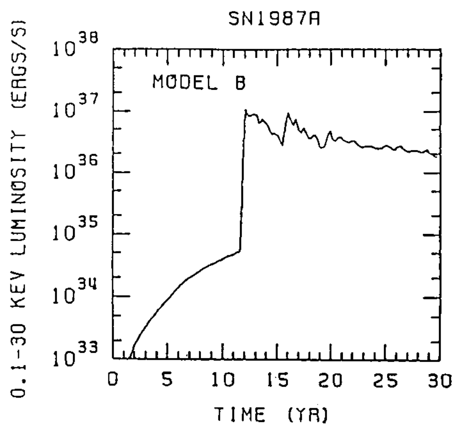

Fig. 53. Time evolution of 0.1–30 keV x-ray luminosity during interactions of the ejecta with the blue giant wind and the red supergiant shell (Itoh et al. 1991).

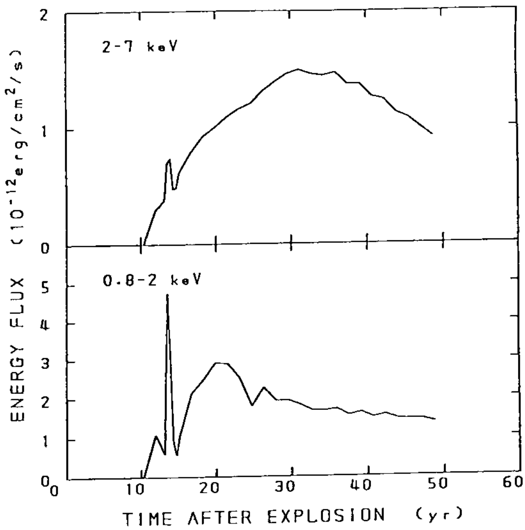

Fig. 54. Time evolution of x-ray flux from the collision of the ejecta with the red supergiant shell, in energy units integrated over photon energies of (a) 0.8–2 keV and (b) 2–7 keV (Masai et al. 1991).

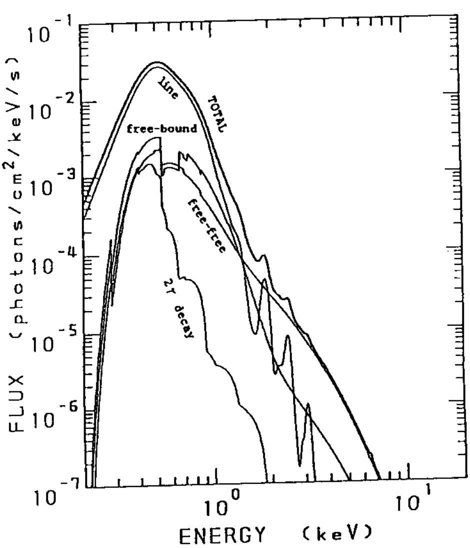

Fig. 55. X-ray spectra expected from collision of the ejecta with the red supergiant shell at 11.6 yr (Masai et al. 1991).

The x-ray spectrum from shocked matter at 11.6 yr is shown in fig. 55. Here free-free, free-bound, two photon decay, and bound-bound transitions are taken into account for 15 elements with nonequilibrium ionization.

9.4. Collision with the ring

For more realistic prediction, we have to model the collision between the ejecta and the ring. In this case, the blue giant wind might have escaped mostly in the polar direction. Without being confined within the red wind shell, the density of the blue wind between the ejecta and the ring is likely to be very low. With this assumption, the direct collision of the ejecta with the ring has been calculated with the 2D SPH code (Suzuki et al. 1991; also Luo and McCray 1991b). The ring is assumed to have a circular cross section with a 10^{11} km radius and uniform density. The red giant wind matter is distributed behind the ring.

Figures 56 and 57 show how the matter distribution changes after collision. Three shock waves are formed: an almost stationary shock wave in the ejecta, a deformed shock inside the ring, and a shock wave that propagates in the red giant wind at approximately 1×10^4 km s^{-1}. The red wind matter behind the shock is accelerated to about 7500 km s^{-1}. The shock fronts which are deformed around the ring collide with each other behind the ring. Eventually the ring is surrounded with the ejecta. The shock wave propagating through the ring arrives at the edge of the opposite side, which forms a peak of x-ray luminosity from the ring.

The x-ray emission due to free-free transitions has two components from the ring and ejecta. The peak luminosity from the ring could reach around 10^{37} erg s^{-1} with an electron temperature of about 2×10^7 K. The ejecta emits harder radiation.

Future x-ray satellites such as *AXAF* and *DUET* will certainly observe this remarkable event, which will be so bright as to dominate the soft x-rays from the neutron star surface. It is also predicted that the shocked ring will emit strong IR radiation due to heated dust (Itoh 1988; Itoh et al. 1991; Luo and McCray 1991a, 1991b).

We would like to thank Drs. H. Saio, M. Kato, M. Hashimoto, F.-K. Thielemann, I. Hachisu, T. Matsuda, T. Kozasa, H. Hasegawa, K. Masai, and H. Itoh for recent collaborative work. This work has been supported in part by Grants-in-Aid for Scientific Research (02302024, 03218202) from the Ministry of Education, Science, and Culture in Japan.

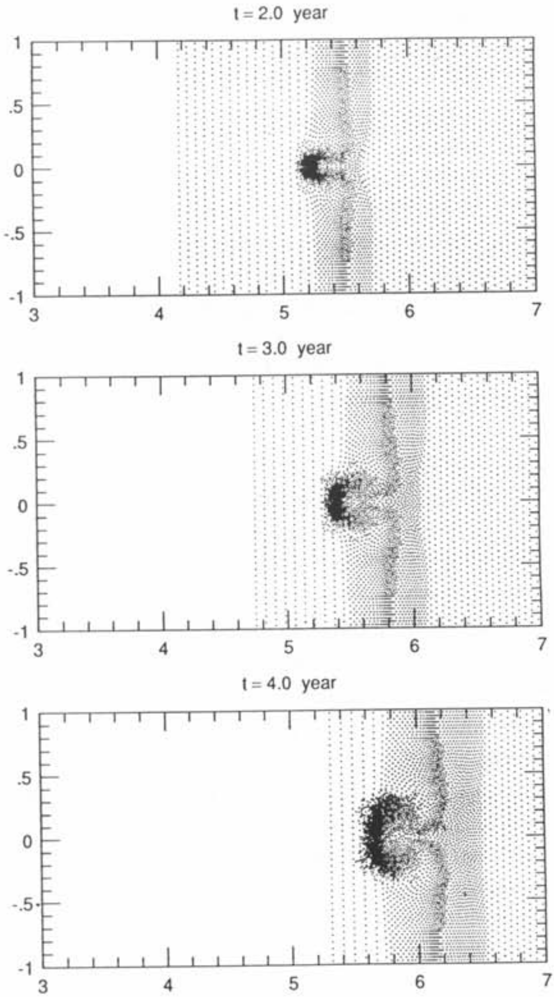

Fig. 56. Change in matter distribution during the collision of the supernova ejecta with the ring.

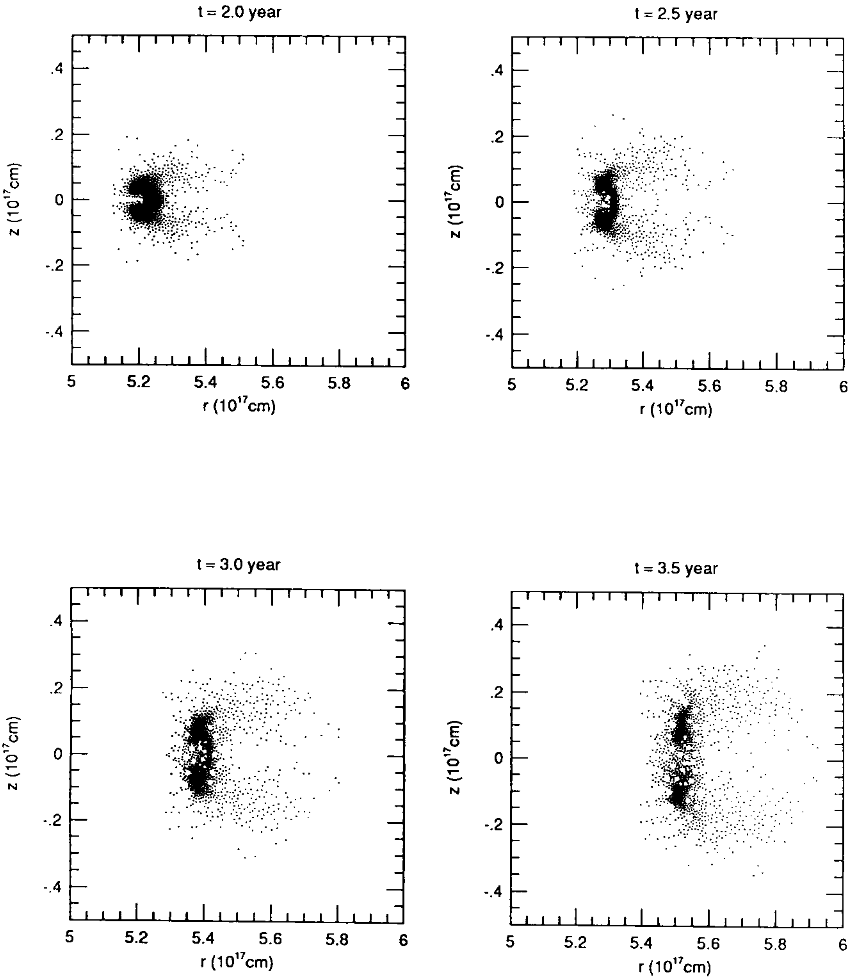

Fig. 57. Same as fig. 56, but for only the matter that originally formed the ring.

References

Aitken, D.K., C.H. Smith, S.D. James, P.F. Roche, A.R. Hyland, and P.J. McGregor, 1988. *M.N.R.A.S.* **235**, 19p.

Allen, D.A., W.P.S. Meikle, and J. Spyromilio, 1989. *Nature* **342**, 403.

Arnett, W.D., 1987. *Ap. J.* **319**, 136.

Arnett, W.D., 1988. *Ap. J.* **334**, 500.

Arnett, W.D., and A. Fu, 1989. *Ap. J.* **340**, 396.

Arnett, W.D., B.A. Fryxel, and E. Müller, 1989. *Ap. J.* **341**, 163.

Arnett, W.D., J.N. Bahcall, R.P. Kirshner, and S.E. Woosley, 1989. *Ann. Rev. Astr.* **27**, 629.

Bandiera, R., 1984. *Astr. Ap.* **139**, 368.

Bandiera, R., F. Pacini, and M. Salvati, 1988. *Nature* **332**, 418.

Barkat, Z., and J.C. Wheeler, 1988. *Ap. J.* **332**, 247.

Benz, W., and F.-K. Thielemann, 1990. *Ap. J. (Letters)* **348**, L17.

Bertelli, G., A.G. Bressan, and C. Chiosi, 1985. *Astr. Ap.* **150**, 33.

Bionta et al., 1987. *Phys. Rev. Lett.* **58**, 1494.

Blanco et al., 1987. *Ap. J.* **320**, 589.

Bouchet, P., I.J. Danziger, and L. Lucy, *A. J.*, submitted.

Bouchet, P., M.M. Phillips, N.B. Suntzeff, C. Gouiffes, R.W. Hanuschik, D.H. Wooden, 1991b. *Astr. Ap.*, in press.

Bussard, R.W., A. Burrows, and L.S. The, 1989. *Ap. J.* **341**, 401.

Catchpole, R. et al., 1987. *M.N.R.A.S.* **229**, 15p.

Catchpole, R. et al., 1988. *M.N.R.A.S.* **231**, 75p.

Catchpole, R. et al., 1989. *M.N.R.A.S.* **237**, 55p.

Caughlan, G.R., W.A. Fowler, M.J. Harris, and B.A. Zimmerman, 1985. *Atomic Data and Nuclear Data Tables* **32**, 197.

Chan, K.W., and R.E. Lingenfelter, 1987. *Ap. J. (Letters)* **318**, L51.

Chevalier, R.A., 1988. *Nature* **332**, 514.

Chevalier, R.A., 1989. *Ap. J.* **346**, 847.

Chevalier, R.A., 1992. In this volume.

Chevalier, R.A., and E.P. Liang, 1989. *Ap. J.* **344**, 332.

Chugai, N.N., 1991. *In*: Supernovae, p. 286.

Colgate, S.A., 1988. *In*: Supernovae 1987A in the LMC, p. 341.

Cook, W.R., D.M. Palmer, T.A. Prince, S.M. Schindler, C.H. Starr, and E.C. Stone, 1988. *Ap. J. (Letters)* **334**, L87.

Crotts, A.P.S., and S.R. Heathcote, 1991. *Nature* **350**, 683.

Danziger, I.J., P. Bouchet, R.A.E. Fosbury, C. Gouiffes, L. Lucy, A.F.M. Moorwood, E. Oliva, and F. Rufener, 1988. *In*: Supernovae 1987A in the LMC, p. 37.

Danziger, I.J., P. Bouchet, C. Gouiffes, and F. Rufener, 1989a. *In:* Big Bang, Active Galactic Nuclei and Supernovae, ed. S. Hayakawa and K. Sato (Tokyo: Universal Academy Press), p. 429.

Danziger, I.J., C. Gouiffes, P. Bouchet, and L.B. Lucy, 1989b. *IAU Cir.*4746.

Danziger, I.J., L.B. Lucy, P. Bouchet, and C. Gouiffes, 1991. *In*: Supernovae, p. 69.

De Jager, C., H. Nieuwenhuijzen, and K.A. van der Hucht, 1988. *Astr. Ap. Suppl.* **72**, 259.

Den, M., T. Yoshida, and Y. Yamada, 1990. *Progr. Theor. Phys.* **83**, 723.

Dotani, T. et al., 1987. *Nature* **330**, 230.

Dwek, E., 1988. *Ap. J.* **329**, 814.

Dwek, E., 1991. *In*: Supernovae, p. 54.

Ebisuzaki, T., and N. Shibazaki, 1988a. *Ap. J. (Letters)* **327**, L5.
Ebisuzaki, T., and N. Shibazaki, 1988b. *Ap. J.* **328**, 699.
Ebisuzaki, T., T. Shigeyama, and K. Nomoto, 1989. *Ap. J. (Letters)* **344**, L65.
Erickson, E. F., M.R. Haas, S.W.J. Colgan, S.D. Lord, M.G. Burton, J. Wolf, D.J. Hollenbach, and M. Werner, 1988. *Ap. J. (Letters)* **330**, L39.
Fowler, W.A., 1984. *Rev. Mod. Phys.* **56**, 149.
Fransson, C., 1992. In this volume.
Fransson, C., A. Cassatella, R. Gilmozzi, R.P. Kirshner, N. Panagia, G. Sonneborn, and W. Wamsteker, 1989. *Ap. J.* **336**, 429.
Fransson, C., and R.A. Chevalier, 1988. *Ap. J.* **343**, 323.
Fransson, C., and P. Lundqvist, 1989. *Ap. J.* **341**, 159.
Fu, A., and W.D. Arnett, 1989. *Ap. J.* **340**, 414.
Gehrels, N., C.J. MacCallum, and M. Leventhal, 1987. *Ap. J. (Letters)* **320**, L19.
Goodman, J., 1990. *Ap. J.* **358**, 214.
Grebenev, S.A., and R.A. Sunyaev, 1987. *Soviet Astr. Letters*, **13**, 945.
Grebenev, S.A., and R.A. Sunyaev, 1988. *Soviet Astr. Letters*, **14**, 675.
Hachisu, I., T. Matsuda, K. Nomoto, and T. Shigeyama, 1990. *Ap. J. (Letters)* **358**, L57.
Hachisu, I., T. Matsuda, K. Nomoto, and T. Shigeyama, *Ap. J.*, submitted.
Hamuy, M., N.B. Suntzeff, R. Gonzalez, and G. Martin, 1987. *A. J.* **95**, 63.
Hanuschik, R.W., and J. Dachs, 1988. *Astr. Ap.* **205**, 135.
Hashimoto, M., K. Nomoto, and T. Shigeyama, 1988. *Astr. Ap.* **210**, L5.
Herant, M., and W. Benz, 1991. *Ap. J.* **370**, L81.
Hillebrandt, W., and P. Höflich, 1989. *Rep. Prog. Phys*, **52**, 1421.
Hillebrandt, W., P. Höflich, J.W. Truran, and A. Weiss, 1987. *Nature* **327**, 597.
Hirata, K., et al., 1987. *Phys. Rev. Lett.* **58**, 1490.
Höflich, P., 1988. *Proc. Astron. Soc. Australia* **7**, p. 434.
Höflich, P., K., Nomoto, and T. Shigeyama, *Astr. Ap.*, submitted.
Humphreys, R.M., and K. Davidson, 1978. *Ap. J.* **232**, 409.
Inoue, H., Hayashida, M. Itoh, and Y. Tanaka, 1991. *Pub. Astr. Soc. Japan*in press.
Itoh, H., 1988. *Pub. Astr. Soc. Japan* **40**, 263.
Itoh, H., S. Hayakawa, K. Masai, and K. Nomoto, 1987. *Pub. Astr. Soc. Japan* **39**, 529.
Itoh, H., K. Masai, and K. Nomoto, 1991. *In: Frontiers of X-ray Astronomy*, ed. Y. Tanaka and K. Koyama (Tokyo: Universal Academy Press), in press.
Itoh, M., S. Kumagai, T. Shigeyama, K. Nomoto, and J. Nishimura, 1987. *Nature* **330**, 233.
Jacobsen, P. et al., 1991. *Ap. J. (Letters)* **369**, L63.
Kamae, T., and T. Takahashi, 1991. Private communication.
Kirshner, R.P., 1988. IAU Colloquium 108, Atmospheric Diagnostics of Stellar Evolution, p. 252.
Kozasa, T., H. Hasegawa, and K. Nomoto, 1989a. *Ap. J.* **344**, 325.
Kozasa, T., H. Hasegawa, and K. Nomoto, 1989b. *Ap. J. (Letters)* **346**, L81.
Kozasa, T., H. Hasegawa, and K. Nomoto, 1991. *Astr. Ap.*, in press.
Kumagai, S., M. Itoh, T. Shigeyama, K. Nomoto, and J. Nishimura, 1988a. *In*: Supernovae 1987A in the LMC, p. 414.
Kumagai, S., M. Itoh, T. Shigeyama, K. Nomoto, and J. Nishimura, 1988b. *Astr. Ap.* **197**, L7.
Kumagai, S., T. Shigeyama, K. Nomoto, M. Itoh, J. Nishimura, and S. Tsuruta, 1989. *Ap. J.* **345**, 412.
Kumagai, S., T. Shigeyama, M. Hashimoto, and K. Nomoto, 1991. *Astr. Ap.* **243**, L13.

Langer, N., M.F. El Eid, and I. Baraffe, 1989. *Astr. Ap.* **224**, L17.
Lehoucq, R., M. Cassé, and C.J. Cesarsky, 1989. *Astr. Ap.* **224**, 117.
Lehoucq, R., C.J. Cesarsky, and M. Cassé, *Astr. Ap.*, submitted.
Leising, M.D., 1988. *Nature* **332**, 516.
Leising, M.D., and G.H. Share, 1990. *Ap. J.* **357**, 638.
Lucy, L.B., 1988. *In*: Supernovae 1987A in the LMC, p. 323.
Lucy, L.B., I.J. Danziger, C. Gouiffes, and P. Bouchet, 1989. Structure and Dynamics of the Interstellar Medium, IAU Colloquium 120, ed. G. Tenorio-Tagle et al. (Springer-Verlag), p. 164.
Lucy, L.B., I.J. Danziger, C. Gouiffes, and P. Bouchet, 1991. *In*: Supernovae, p. 82.
Lundqvist, P., and C. Fransson, 1991. *Ap. J.*, in press.
Luo, D., and R. McCray, 1991a. *Ap. J.* **372**, 194.
Luo, D., and R. McCray, 1991b, *Ap. J.*, in press.
Mahoney, W.A., L.S. Varnell, A.S. Jacobson, J.C. Ling, R.G. Radocinski, and Wm.A. Wheaton, 1988. *Ap. J. (Letters)* **334**, L81.
Masai, K., S. Hayakawa, H. Itoh, and K. Nomoto, 1987. *Nature* **330**, 235.
Masai, K., S. Hayakawa, H. Inoue, H. Itoh, and K. Nomoto, 1988. *Nature* **335**, 804.
Masai, K., K. Itoh, and K. Nomoto, 1991. *SN 1987A and Other Supernovae.*
Masai, K., and K. Nomoto, 1991. *In*: Supernovae, p. 153.
Matteson, J., et al. 1991. *In*: Supernovae, p. 283.
Matz, S.M., G.H. Share, M.D. Leising, E.L. Chupp, W.T. Vestrand, W.R. Purcell, M.S. Strickman, and C. Reppin, 1988. *Nature* **331**, 416.
McCray, R., J.M. Shull, and P. Sutherland, 1987. *Ap. J. (Letters)* **317**, L73.
McNaught, R.N., 1987. *IAU Cir.*4389.
Meikle, W.P.S., D.A. Allen, J. Spyromilio, and G.-F. Varani, 1989. *M.N.R.A.S.* **238**, 193.
Menzies, J.M. et al., 1987. *M.N.R.A.S.* **227**, 39p.
Michel, F.C., 1988. *Nature* **333**, 644.
Mineshige, S., K. Nomoto, and T. Shigeyama, *Astr. Ap.*, submitted.
Nomoto, H., 1989, Exploring SN 1987A (in Japanese), (Tokyo: Kodansha).
Nomoto, K., and M. Hashimoto, 1988. *Physics Report* **163**, 13.
Nomoto, K., M. Hashimoto, T. Shigeyama, S. Kumagai, H. Yamaoka, and H. Saio, 1989. *In: Big Bang, Active Galactic Nuclei and Supernovae*, ed. S. Hayakawa and K. Sato (Tokyo: Universal Acad. Press), p. 495.
Nomoto, K., and T. Shigeyama, 1988. *In*: Supernovae 1987A in the LMC, p. 273.
Nomoto, K., T. Shigeyama, and M. Hashimoto, 1987. *In*: SN 1987A, ed. I.J. Danziger (Garching: ESO), p. 325.
Nomoto, K., T. Shigeyama, and M. Hashimoto, 1988a. *In: IAU Colloquium 108, Atmospheric Diagnostics of Stellar Evolution*, ed. K. Nomoto, *Lecture Notes in Physics*, **305**, 319.
Nomoto, K., T. Shigeyama, S. Kumagai, and M. Hashimoto, 1988b. *In: Proc. Astron. Soc. Australia*, **7**, 490.
Nomoto, K., T. Shigeyama, S. Kumagai, and H. Yamaoka, 1991a. *In*: Supernovae, p. 176.
Nomoto, K., T. Shigeyama, S. Kumagai, and H. Yamaoka, 1991b. *In:* Supernovae and Stellar Evolution, ed. A. Ray and T. Velusamy (World Scientific), p. 116.
Nomoto, K., T. Shigeyama, S. Kumagai, I. Hachisu, and T. Matsuda, 1991c. *SN 1987A and Other Supernovae.*
Nomoto, K., and S. Tsuruta, 1987a. *Ap. J.* **312**, 711.
Nomoto, K., and S. Tsuruta, 1987b. *In*: SN 1987A, ed. I.J. Danziger (Garching: ESO), p. 571.

Pacini, F., 1988. *In:* Physics of Neutron Stars and Black Holes, ed. Y. Tanaka, (Tokyo: Universal Academy Press), p. 461.
Panagia, N., and R. Gilmozzi, 1991. *SN 1987A and Other Supernovae.*
Panagia, N. et al., 1987. *IAU Cir.*4514.
Phillips, M.M., 1988. *In*: Supernovae 1987A in the LMC, p. 16.
Phillips, M.M., and S.R. Heathcote, 1989. *Pub. Astr. Soc. Pacific* **101**, 137.
Pinto, P., and S.E. Woosley, 1988a. *Ap. J.* **329**, 820.
Pinto, P., and S.E. Woosley, 1988b. *Nature* **333**, 534.
Pizzochero, P., 1990. *Ap. J.* **354**, 333.
Prantzos, N., M. Arnould, and M. Cassé, 1988. *Ap. J. (Letters)* **331**, L15.
Rank, D.M. et al. 1988. *Nature* **331**, 505.
Rester, A.C., R.L. Coldwell, F.E. Dunnam, G. Eichhorn, J.I. Trombka, R. Starr, and G.P. Lasche, 1989. *Ap. J. (Letters)* **342**, L71.
Roche, P.F., D.K. Aitken, C.H. Smith, and S.D. James, 1989. *Nature* **337**, 533.
Saio, H., M. Kato, and K. Nomoto, 1988a. *Ap. J.* **331**, 388.
Saio, H., K. Nomoto, and M. Kato, 1988b. *Nature* **334**, 508.
Sandie, W.G., G.H. Nakano, L.F. Chase, Jr., G.J. Fishman, C.A. Meegan, C.A., R.B. Wilson, W.S. Paciesas, and G.P. Lasche, 1988. *Ap. J. (Letters)* **334**, L91.
Shibazaki, N., and T. Ebisuzaki, 1988. *Ap. J. (Letters)* **327**, L9.
Shigeyama, T., T. Kozasa, and K. Nomoto, 1991. *SN 1987A and Other Supernovae.*
Shigeyama, T., and K. Nomoto, 1990. *Ap. J.* **360**, 242.
Shigeyama, T., and K. Nomoto, 1991. *In*: Supernovae, p. 198.
Shigeyama, T., K. Nomoto, and M. Hashimoto, 1988. *Astr. Ap.* **196**, 141.
Shigeyama, T., K. Nomoto, M. Hashimoto, and D. Sugimoto, 1987. *Nature* **328**, 320.
Slattery, W.L., G.D. Doolen, and H.E. De Witt, 1982. *Phys. Rev. A*, **26**, 2255.
Sonneborn, G., 1991, *In*: Supernovae, p. 125.
Stathakis, R.A., M.A. Dopita, R.D. Cannon, and E.M. Sadler, 1991. *In*: Supernovae, p. 95.
Suntzeff, N.B., and P. Bouchet, 1990. *A. J.* **1609**, 650.
Suntzeff, N.B., M. Hamuy, G. Martin, A. Gomez, and R. Gonzalez, 1988. *A. J.* **96**, 1864.
Suntzeff, N.B., M.M. Phillips, D.L. Depoy, J.H. Elias, and A. Walker, *A. J.*, submitted
Sunyaev, R. et al., 1987. *Nature* **330**, 227.
Sunyaev, R. et al., 1989. *Soviet Astr. Letters* **15**, 291.
Sunyaev, R. et al., 1990. *Soviet Astr. Letters* **16** 403.
Sutherland, P., Y. Xu, R. McCray, and R.P. Ross, 1988. IAU Colloquium 108, Atmospheric Diagnostics of Stellar Evolution, 394.
Suzuki, T., T. Shigeyama, and K. Nomoto, 1991. *In:* Frontiers of X-ray Astronomy, ed. Y. Tanaka and K. Koyama (Tokyo: Universal Academy Press), in press.
Tanaka, Y., 1988a. IAU Colloquium 108, Atmospheric Diagnostics of Stellar Evolution, 399.
Tanaka, Y., 1988b. in Physics of Neutron Stars and Black Holes, ed. Y. Tanaka, (Tokyo: Universal Academy Press), p. 431.
Terndrup, D.M., et al. 1988. *Proc. Astron. Soc. Australia* **7**, p. 412.
The, L.-S., A. Burrows, and R.W. Bussard, 1990. *Ap. J.* **352**, 731.
Thielemann, F.-K., M. Hashimoto, and K. Nomoto, 1990. *Ap. J.* **348**, 222.
Thielemann, F.-K., K. Nomoto, and M. Hashimoto, 1992. In this volume.
Tsuruta, S., and K. Nomoto, 1989. *Ap. Letters and Comm.* **27**, 241.
Tuchman, Y., and J.C. Wheeler, 1991. *In*: Supernovae, p. 159.
Tueller, J., S. Barthelmy, N. Gehrels, B.J. Teegarden, M. Leventhal, and C.J. MacCallum, 1990.

Ap. J. (Letters) **351**, L41.
Turtle, A.J. et al. 1987. *Nature* **327**, 38.
Umeda, H., K. Nomoto, S. Tsuruta, T. Muto, and T. Tatsumi, *Ap. J.*, submitted.
Varani, G.-F., W.P.S. Meikle, J. Spyromilio, and D.A. Allen, 1990. *M.N.R.A.S.* **245**, 570.
Wampler, E.J., L. Wang, D. Baade, K. Banse, S. D'Odorico, C. Gouiffes, and M. Tarenghi, 1990. *Ap. J. (Letters)* **362**, L13.
Weiss, A., 1989. *Ap. J.* **339**, 365.
West, R.M., A. Lauberts, H.E. Jorgensen, H.E. Schuster, 1987. *Astr. Ap.* **177**, L1.
Whitelock, C. et al., 1988. *M.N.R.A.S.* **234**, 5.
Whitelock, C. et al., 1989. *M.N.R.A.S.* **240**, 7p.
Wilson, R.B., G.J. Fishman, C.A. Meegan, W.S. Paciesas, and G.N. Pendleton, 1988. *In:* Nuclear Spectroscopy of Astrophysical Sources, ed N. Gehrels and G. Share (New York: AIP), p. 66.
Witteborn, F.C., J.D. Bregman, D.H. Wooden, P.A. Pinto, D.M. Rank, S.E. Woosley, and M. Cohen, 1989. *Ap. J. (Letters)* **338**, L9.
Woosley, S.E., 1988. *Ap. J.* **330**, 218.
Woosley, S.E., and R.D. Hoffman, 1991. *Ap. J. (Letters)* **368**, L31.
Woosley, S.E., P.A. Pinto, and L. Ensman, 1988a. *Ap. J.* **324**, 466.
Woosley, S.E., P.A. Pinto, and D. Hartmann, 1989. *Ap. J.* **346**, 395.
Woosley, S.E., P.A. Pinto, and T.A. Weaver, 1988b. *Proc. Astron. Soc. Australia* **7**, 335.
Woosley, S.E., and T.A. Weaver, 1986. *Ann. Rev. Astron. Ap.* **24**, 205.
Woosley, S.E., and T.A. Weaver, 1988. *Physics Report* **163**, 79.
Xu, Y., P. Sutherland, R. McCray, and R. Ross, 1988. *Ap. J.* **327**, 197.
Yamada, Y., K. Kasahara, and T. Nakamura, 1989. *Progr. Theor. Phys.* **81**, 93.
Yamada, Y., T. Nakamura, and K. Oohara, 1990. *Progr. Theor. Phys.*, in press.
Yamaoka, H., H. Saio, K. Nomoto, and M. Kato, 1991. *In:* IAU Symp. 143, Wolf Rayet Stars and Interrelations with Other Massive Stars in Galaxies, ed. K. Van der Hucht and B. Hidayat (Kluwer), p. 571.
Zoltowski, F., 1987. *IAU Cir.* 4389.

COURSE XI

THE SHOCK WAVE BREAKOUT AND EARLY SUPERNOVA HYDRODYNAMICS

D.K. NADYOZHIN

Institute of Theoretical and Experimental Physics
117259 Moscow, USSR

S. Bludman, R. Mochkovitch and J. Zinn-Justin, eds.
Les Houches, Session LIV 1990
Supernovae

Contents

Contents *571*

1. The shock wave breakout and early supernova hydrodynamics 572
   1.1. Introduction 572
   1.2. Shock wave propagation through the stellar envelope 573
   1.3. The self-similar solution 575
   1.4. The peak parameters of the shock wave breakout 576
   1.5. The beginning of supernova envelope expansion and the transition to inertial outflow 579
   1.6. Cooling-and-recombination wave in supernova envelopes 582
   1.7. Conclusions 586

1. The shock wave breakout and early supernova hydrodynamics

1.1. Introduction

We shall discuss the early stages of supernova hydrodynamics in the case when a presupernova star has a compact structure similar to the Large Magellanic Cloud blue supergiant star *Sk*–69^0202, which gave rise to Supernova 1987A. In the envelopes of compact stars, density is sufficiently high for the shock wave (SW) front to be considered as an interface separating external unperturbed material from internal material already involved in the explosion. In red supergiant stars, progenitors of most supernovae observed in distant galaxies, a powerful thermal wave appears ahead of the SW, preventing the latter from demonstrating a cumulative self-similar approach to the stellar surface. In a blue supergiant progenitor, on the contrary, the SW cumulates and its breakout is followed by a violent expansion, resulting in adiabatic cooling of the outermost stellar layers. A copious recombination of helium and, eventually, hydrogen occurs, which drastically decelerates the further temperature decrease and creates conditions favourable for the appearance of a cooling-and-recombination wave (CW).

At this stage of the expansion, thermal processes have virtually no influence on the dynamics of the supernova envelope which is expelled with highly supersonic velocities in free (inertial) expansion. Thus, one can consider radiation transport from the supernova envelope into a relatively simple and well-established hydrodynamical background. Here we restrict our consideration to the first several weeks of the supernova outburst, when energy release due to ^{56}Co decay is not yet of appreciable importance to the supernova light curve. In case of SN 1987A, this is $\sim$ 40–50 days from the beginning of the outburst when the light curve is still on the way to its maximum (fig. 1). We will closely follow the papers of Imshennik and Nadyozhin (1988, 1989) and Grasberg and Nadyozhin (1976), in which one can find further details.

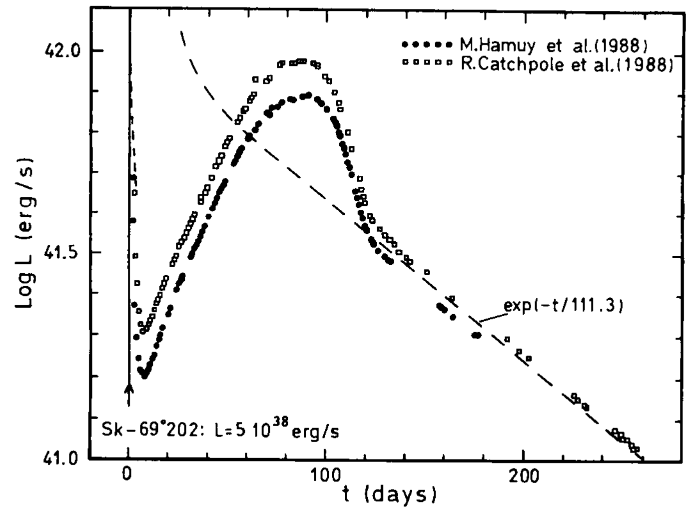

Fig. 1. The SN 1987A luminosity versus time according to the CTIO (Hamuy et al. 1988) and SAAO (Catchpole et al. 1988) observations. The theoretically reconstructed sharp luminosity peak at $t \approx 0$ is generated by a shock wave breakout.

1.2. Shock wave propagation through the stellar envelope

The theory of stellar structure tells us that in the radiative envelopes of massive stars the opacity, κ, is dominated by Thompson scattering-off free electrons and is virtually independent of temperature and density. Under such conditions, the structure of the outer envelope is represented in terms of temperature, $T(r)$, and density, $\rho(r)$, by the following expressions

$$T(r) = \frac{\mu m_u}{4k}\frac{GM}{R_0}\left(1-\frac{L}{L_c}\right)\left(\frac{R_0}{r}-1\right) = 1.1\times 10^6\left(\frac{R_0}{r}-1\right)\mathrm{K}, \quad (1.1)$$

$$\rho(r) = \frac{a\mu m_u}{3k}\left(\frac{L_c}{L}-1\right)T^3 = 1.2\times 10^{-4}\left(\frac{R_0}{r}-1\right)^3 \mathrm{g\,cm^{-3}}, \quad (1.2)$$

where the Eddington critical luminosity L_c is

$$L_c = \frac{4\pi c\, GM}{\kappa} = 6.9\times 10^5\, L_\odot\,. \quad (1.3)$$

Here M and R_0 are the total mass and radius of the star, μ is the molecular weight, and the other designations have their usual meaning. The numerical coefficients in eqs. (1.1–1.3) have been estimated for Presupernova 1987A assuming $L = 1.3 \times 10^5 L_\odot$, $R_0 = 47 R_\odot$, $M = 18 M_\odot$, $\mu = 0.62$, and $\kappa = 0.34\ \mathrm{cm}^2/\mathrm{g}$, which correspond to the standard $X = 0.7$ hydrogen content by mass. Equations (1.1) and (1.2) prove accurate enough down to a radius $r \approx 0.4 R_0$.

Unfortunately, the mechanism of massive star explosions into supernovae is not yet understood in detail. Nevertheless, there is no doubt that the SW is generated in deep stellar interiors at radii quite less than the radius of the presupernova core, which undergoes either gravitational collapse or thermonuclear explosion. Propagating outward, the SW is attenuated to some extent by spherical divergence. Then, breaking through an intermediate region with a steep density gradient, the SW accelerates due to hydrodynamic accumulation. The density profile given by eq. (1.2) turns out to be steep enough for the SW to continue accelerating at radii $r \gtrsim 0.4 R_0$ (Klimishin and Gnatyk 1981; Klimishin 1984).

Entering the outer stellar envelope, the SW becomes more and more radiation-dominated. The radiation pressure and specific energy behind the SW front become much greater than that of matter. As a result, the effective adiabatic index γ approaches 4/3 and the SW compression approaches $\rho_2/\rho_1 = (\gamma + 1)/(\gamma - 1) \approx 7$. A most remarkable property of such a SW consists in the disappearance of viscous discontinuity of density, velocity, pressure, and temperature across its front. This occurs when compression surpasses the critical value $(\rho_2/\rho_1)_{cr} = 6.68$ for which the ratio of radiation pressure P_r to gas pressure P_g behind the SW attains $(P_r/P_g)_{cr} = 8.48$ (Zel'dovich and Raizer 1967, Imshennik and Morozov 1964). The front width of a radiation-dominated SW can be estimated as

$$\Delta\tau_{SW} \simeq \frac{c}{D}\,, \quad \Delta r_{SW} \simeq \frac{c}{\kappa\rho_1 D}\,, \tag{1.4}$$

where $\Delta\tau_{SW}$ and Δr_{SW} are the optical and the Eulerian thickness, while c and D are the velocities of light and the SW respectively. As soon as the SW approaches the stellar surface, accumulation effects build up; when the hydrodynamic flow can be considered plane-parallel, the SW obeys the self-similar solution of Gandel'man and Frank-Kamenetzkii (1956). Below, we shall use the self-similar solution to estimate properties of the initial peak of hard UV-radiation which announces the onset of the supernova light curve.

1.3. The self-similar solution

Near the stellar surface the density law (1.2) can be represented in the form

$$\rho(x) \simeq K_1 x^3 = 1.2 \times 10^{-4} x^3 \ \mathrm{g\,cm^{-3}} , \tag{1.5}$$

where $x \equiv (R_0 - r)/R_0$ is the relative distance to the stellar surface. The self-similar solution holds for the power density distribution $\rho = K_1 x^n$ with an arbitrary (generally non-integer) positive n. According to this solution, the velocity D of the strong SW grows infinitely as

$$D = \frac{dx_{SW}}{dt} = -K_2 \, x_{SW}^{-\lambda} , \tag{1.6}$$

where λ depends only on n and the adiabatic index γ. For density, pressure, and velocity distributions behind the SW front (for $x \geq x_{SW}$) we have

$$\rho = K_1 \, x^n \, h\left(\frac{x}{x_{SW}}\right) , \tag{1.7}$$

$$P = K_1 \, K_2^2 \, x^{n-2\lambda} \, g\left(\frac{x}{x_{SW}}\right) , \tag{1.8}$$

$$u = -K_2 \, x^{-\lambda} \, f\left(\frac{x}{x_{SW}}\right) . \tag{1.9}$$

Solving eq. (1.6), one gets

$$x_{SW} = [-(1+\lambda)K_2 \, t\,]^{\frac{1}{(1+\lambda)}} , \tag{1.10}$$

where time is synchronized so that the SW arrives at the stellar surface at $t = 0$. For SW propagation inside the star $t < 0$, whereas for the subsequent expansion of stellar matter in vacuum $t > 0$. Figure 2 shows time behaviour of the velocity profile for a self-similar SW approach to the stellar surface. When the SW approaches the stellar surface $x_{SW} \to 0$ and $x/x_{SW} \to \infty$ for any fixed x-value, while functions h, g, and f tend to limits h_∞, g_∞, and f_∞. So, at $t = 0$ the density, pressure, and velocity profiles have a power shape shown by the dashed curve in fig. 2. The values of λ and h_∞, g_∞, f_∞ were tabulated by Grasberg (1981) for different n and γ. Here we are interested in the special case

$$\begin{aligned} &n = 3, \quad &&\gamma = 4/3, \quad &&\lambda = 0.5572, \\ &h_\infty = 53.30, \quad &&g_\infty = 1.570, \quad &&f_\infty = 0.645 . \end{aligned} \tag{1.11}$$

Note that owing to additional compression in the flow behind the SW, h_∞ is much higher than the compression at the SW front $\rho_2/\rho_1 \simeq 7$. The constants

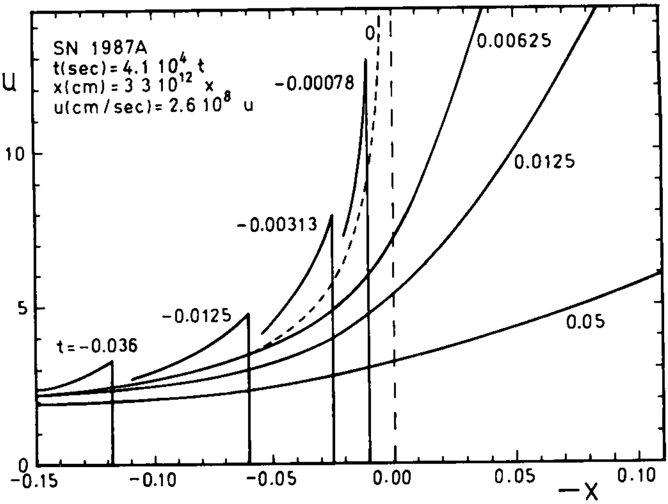

Fig. 2. Self-similar emergence of a shock wave at the stellar surface. Factors of transition to dimensional units are shown for SN 1987A.

K_1 and K_2 are, in general, arbitrary in the self-similar solution. In our case, K_1 is specified by eq. (1.2), while a K_2 value can be determined by fitting the self-similar solution to SN 1987A hydrodynamic models:

$$K_2 \simeq 3 \times 10^8 \sqrt{\frac{\mathcal{E}_{51}}{M_{o16}}} \ \mathrm{cm\,s^{-1}} , \tag{1.12}$$

where $\mathcal{E}_{51}$ is the total explosion energy in 10^{51}erg and M_{o16} is the mass of the ejected envelope in $16M_\odot$ (since one should subtract from the total presupernova mass M about $2M_\odot$ to account for the neutron star remnant).

1.4. The peak parameters of the shock wave breakout

The self-similar solution fails to describe the final stage of the SW arrival at the stellar surface, when the SW front width becomes comparable to the SW distance from the surface, x_{SW}. At this moment, the cumulation saturates and the outward radiative energy losses become significant. So one has to cut off the self-similar solution when the SW reaches the optical depth

$$\tau_{SWc} = \int_{R_c}^{R_0} \kappa\rho\, dr \simeq \frac{c}{D}\,. \tag{1.13}$$

Inserting in eq. (1.13) ρ and D from eqs. (1.5) and (1.6), one can find the cut-off value:

$$x_{SWc} = \frac{R_0 - r_{SWc}}{R_0} = \left(\frac{4c}{\mathrm{K}_1\mathrm{K}_2\,\kappa R_0}\right)^{1/(4-\lambda)}\,. \tag{1.14}$$

Now, besides τ_{SWc} and D_c, we are able to estimate other quantities such as the velocity of matter $u_c = \frac{2}{\gamma+1}D_c$; the shock density $\rho_{2c} = \frac{\gamma+1}{\gamma-1}\rho_{1c}$; and total mass enclosed between the cut-off radius R_c and the stellar surface $\Delta M_c = 4\pi R_0^2\,\tau_{SWc}/\kappa$. The limiting temperature T_c can be found from the Hugoniot condition

$$\frac{1}{3}aT_c^4 = \frac{2}{\gamma+1}\,\rho_{1c}\,D_c^2\,, \tag{1.15}$$

while the maximum energy $\mathcal{E}_{rc}$ emitted during the SW breakout is approximately given by

$$\mathcal{E}_{rc} \simeq 4\pi R_0^2\,\sigma T_c^4\,\frac{\Delta t_c}{\tau_{SWc}}\,, \tag{1.16}$$

where σ is the Stefan-Boltzmann constant and $\Delta t_c = R_0 x_{SWc}/u_c$ is the timescale of the SW breakout. Using numerical values specified by eq. (1.11) and eq. (1.12) with $M_{o16} = 1$, we come to the SW breakout parameters compiled in table 2 for two values of the total explosion energy $\mathcal{E}$.

The quantities T_c, x_{SWc} and u_c depend only weakly on the SW front width. From the physical point of view, however the characteristic temperature T_c proves to be poorly determined, because radiation is coupled with matter mainly by electron scattering, rather then by true absorption and emission. Therefore, the emerging spectrum is expected to differ from the Planckian one. One could treat this problem in the framework of Compton radiative hydrodynamics (Imshennik and Morozov 1981; Imshennik 1976) based on the Bose–Einstein spectrum with the non-zero chemical potential (Zel'dovich and Illarionov 1973; Illarionov and Sunyev 1974; Weaver and Chapline 1974). This gives an even greater value of T_c than obtained above, however, the total radiative energy flux should remain virtually the same. Calculations of the supernova models show that the resulting deficit of photons can reach

Table 1
The shock wave breakout parameters for SN 1987A from Imshennik and Nadyozhin (1988, 1989)

$\mathcal{E}$ (erg)	3×10^{51}	1.5×10^{51}
x_{SWc}	0.0212	0.0234
τ_{SWc}	6.6	9.9
u_c (10^8 cm s^{-1})	40	26
ρ_{2c} (10^{-8} g cm^{-3})	0.83	1.1
ΔM_c (10^{-6} $M_\odot$)	1.3	2.0
Δt_c (s)	18	29
T_c (10^6 K)	1.7	1.5
$\mathcal{E}_{rc}$ (10^{47} erg)	1.6	1.1

a factor of $\sim$ 55, while the temperature may be twice as high as calculated under the radiative heat conduction approximation (Imshennik and Utrobin 1977; see also Klein and Chevalier 1978). Nevertheless, these peculiarities have almost no practical effect on the other quantities in table 1 (except for T_c).

The SW breakout leads to a drastic expansion of the outermost layers in vacuum; high pressure created by the SW produces further acceleration of matter in a rarefaction wave. This stage is described by another self-similar solution (Sakurai 1960; Litvinova and Nadyozhin 1990) which holds for the inner part of the stellar envelope located below the SW breakout zone, with a depth of about 2% of the stellar radius (table 1). The resulting acceleration is estimated to be about a factor of $\beta \approx 1.6$ for $n = 3$ and $\gamma = 4/3$ for every Lagrangian layer (Litvinova and Nadyozhin 1990). The final velocities of Lagrangian layers with different values of the mass coordinate m are determined by

$$u_m = \beta(n, \gamma)\, u_0(m)\,, \tag{1.17}$$

where $u_0(m)$ is the velocity distribution at $t = 0$ shown by the dashed curve in fig. 2.

Thus, the SW breakout elevates surface temperature to $(1\text{–}2)\times 10^6$ K in 20–30 s, accelerating the outermost layer of mass ($\sim 2 \times 10^{-6} M_\odot$) to 30,000–40,000 km/s. Total radiated energy in the hard ultraviolet and soft X-ray wavelengths amounts to $\sim 10^{47}$ ergs. The outermost $\sim 2 \times 10^{-6} M_\odot$ are further accelerated in the rarefaction wave, and acquire a final velocity of

$u_m \sim 50{,}000$ km/s. SW breakout must have lead to the SN 1987A flare, which probably began with a nearly instantaneous jump of about $5^m - 6^m$ in visual stellar magnitude m_v, as a consequence of a much more violent increase in total luminosity (up to $\sim 10^{45}$ erg/s). This sharp luminosity peak lasted $\sim R_0/c \simeq 100$ second. (One should take into account that at this moment optical flux in the far Rayleigh–Jeans spectral region decreases as T rather than as T^4.)

1.5. The beginning of supernova envelope expansion and the transition to inertial outflow

Because of vigorous expansion, the outermost layers cool rapidly and decrease of T^4 overcomes the growth of the radiating area $\sim R^2$. As a result, supernova luminosity falls sharply (as it did during the first week of the SN 1987A's life – (fig. 1)). Finally, helium and hydrogen recombinations succeed in braking the rate of temperature decrease, and the light curve turns up following growth of the radiating area.

As time goes on, pressure forces become negligible in the expanding supernova envelope: all of the thermal energy transforms into kinetic energy of radial motion, and the envelope enters a stage of free inertial expansion. Each Lagrangian layer keeps a constant velocity; velocity and density distribution are controlled by

$$\frac{\partial u}{\partial t} + u\frac{\partial u}{\partial r} = 0\,, \tag{1.18}$$

$$\frac{\partial \rho}{\partial t} + \frac{1}{r^2}\frac{\partial}{\partial r}\left(r^2 u\rho\right) = 0\,. \tag{1.19}$$

One can easily verify that the solution of eqs. (1.18) and (1.19) is given by

$$u = \frac{r}{t}\,, \tag{1.20}$$

$$\rho = \frac{1}{r^3}\, f\left(\frac{r}{t}\right) = \frac{1}{r^3}\, f\,(u) = \frac{1}{t^3}\,\frac{f\,(u)}{u^3}\,, \tag{1.21}$$

where we have assumed that each Lagrangian layer has moved from its initial position r_0 by a distance $r \gg r_0$. The function $f(u)$ is mathematically arbitrary, and is determined by the preceding phases of supernova envelope expulsion. It bears information about both the presupernova structure and the details of the explosive energy release.

The function $f(u)$ determines the velocity-mass spectrum:

$$M(u) = 4\pi \int_{u}^{u_{mc}} \frac{f(u)}{u}\, du + \Delta M_c , \tag{1.22}$$

where $u_{mc} = \beta u_c$, with u_c and ΔM_c presented in table 1. The function $M(u)$ defines the ejected mass whose velocity exceeds u. Using the self-similar distributions of ρ and u from eqs. (1.7) and (1.9) at $t = 0$, one can obtain explicit expressions for $f(u)$ and $M(u)$ in outermost layers subjected to the self-similar acceleration:

$$f(u) = B\, u^{-s} , \quad (u \leq u_{mc}) , \tag{1.23}$$

$$M(u) = \frac{\lambda}{n+1} B \left(u^{-s} - u_{mc}^{-s}\right) + \Delta M_c , \quad (u \leq u_{mc}) , \tag{1.24}$$

where

$$s = \frac{n+1}{\lambda} , \quad B = \frac{4\pi}{\lambda} R_0^3 \mathrm{K}_1 h_\infty (\beta \mathrm{K}_2 f_\infty)^s . \tag{1.25}$$

Equation (1.21) gives

$$\rho = \frac{B}{r^3 u^s} = \frac{B\, t^s}{r^{3+s}} . \tag{1.26}$$

Using the numerical values specified by eq. (1.11), we get for $u < u_{mc}$

$$\rho = B \frac{t^{7.2}}{r^{10.2}} , \tag{1.27}$$

$$M(u) \simeq 0.139\, B\, u^{-7.2} . \tag{1.28}$$

Figure 3 shows $f(u)$ obtained for different hydrodynamic models. The high-velocity ($u \gtrsim$ 10,000 km/s) part of this dependence has a slope very close to the power law given by eq. (1.23). This part contains, however, only $\sim 0.01 M_\odot$. For practical purposes we recommend the following approximation for $\log u \gtrsim 8.8$:

$$\log f = -6 \log u + 85.7 , \tag{1.29}$$

where u is measured in cm/s. Equation (1.29) is a fairly accurate for the outer $\sim 0.3 M_\odot$, and results in a somewhat gentler density gradient ($\rho \sim r^{-9}$) than that specified by eq. (1.27).

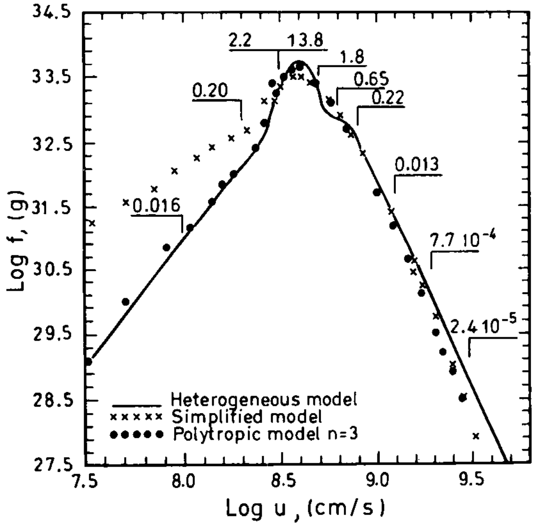

Fig. 3. The time-conserving function $f(u) = r^3\rho$ versus u for the inertial free expansion of SN 1987A hydrodynamic models. The numbers give total masses (in solar units) having velocities greater (at right) or lesser (at left) than the indicated values of u. The total mass of the expelled envelope equals to $16\,M_\odot$ for all the three models.

These theoretical predictions for a steep density gradient in the outermost supernova envelope agree with the density profiles estimated from SN 1987A spectra (Chugai 1987, Branch 1987, Wheeler et al. 1988). Thus, we can conclude from fig. 3 that the structure of the outermost high-velocity SN 1987A envelope with mass $\sim 0.3 M_\odot$ is sensitive neither to the internal presupernova structure nor to the explosion mechanism. By contrast, intermediate layers with velocities of 3000–5000 km/s, which contain the major portion of the supernova envelope mass, mostly reflect the structure of deep presupernova interiors. The dependence of $f(u)$ for inner low-velocity layers ($u \lesssim 2500$ km/s) is also sensitive to the supernova explosion mechanism. Elucidation of $f(u)$ in the low-velocity region would provide important information on the SN 1987A explosion mechanism, and interaction of the envelope with the collapsed stellar remnant.

1.6. Cooling-and-recombination wave in supernova envelopes

When the temperature of the outermost supernova layers falls below $\sim$ 20,000K, copious helium and (somewhat later) hydrogen recombination begins. The opacity of stellar matter strongly decreases when the temperature falls from 20,000K down to 4000K. Such a steep opacity drop leads to specific supernova envelope cooling, called the cooling-and-recombination wave (CW). The CW was discovered during study of the fireball produced by nuclear explosions in Earth's atmosphere. (For detailed description see Zel'dovich and Raizer 1967.)

The first numerical hydrodynamic models of supernovae (Imshennik and Nadyozhin 1964) showed that a CW also may arise in supernova envelopes. However, the supernova CW differs from the atmospheric CW. The former propagates supersonically and is accompanied by copious matter recombination, whereas the latter is subsonic and recombination within its front is not crucially important. To derive the properties of the CW in supernova envelopes, we use the notion of a transparency temperature T_2, defined by Zel'dovich and Raizer as the temperature at which the mean free path for photons is approximately the characteristic length over which physical quantities change appreciably. In supernova envelopes, the transparency temperature can be estimated from the following expression

$$\kappa(\rho, T_2)\,\rho\, R_{CW} \approx 1\,, \tag{1.30}$$

where R_{CW} is the CW radius. The opacity can be approximated by

$$\kappa(\rho, T) \simeq Q(\rho, T)\exp\left(-\frac{\chi}{kT}\right)\,. \tag{1.31}$$

Here $Q(\rho, T)$ weakly depends on ρ and T, and χ is an effective value of the ionization potential. Inserting κ from eq. (1.31) in eq. (1.30), we get

$$T_2 \simeq \frac{\chi}{k\,\ln(\rho Q R_{CW})}\,. \tag{1.32}$$

Thus, we see that T_2 is proportional to the ionization potential χ and depends only weakly (logarithmically) on density and CW radius. The radiative energy flux S_2, generated by the CW, can be estimated as

$$S_2 = 2\sigma T_2^4 = \sigma T_{ef}^4\,. \tag{1.33}$$

The flux S_2 comes from thermal and ionization energy, because the radiative flux S_1 ahead of the CW (at its inner side designated by the index 1 hereafter)

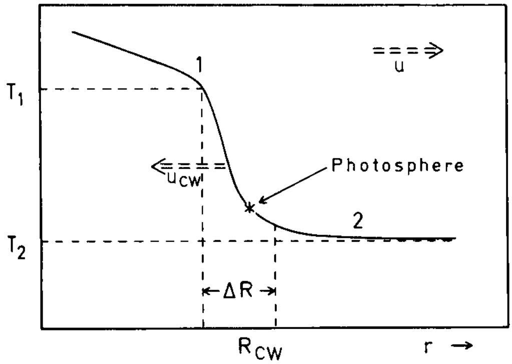

Fig. 4. Schematic structure of the cooling-and-recombination wave.

is negligible. Hence, the CW velocity with respect to matter (in a comoving frame) u_{CW} can be estimated as

$$\rho\, \Delta E\, u_{CW} = 2\sigma T_2^4 \,, \tag{1.34}$$

where $\Delta E = E_1 - E_2$ is the change of the specific internal energy across the CW front. It includes the recombination, thermal, and black body radiation energies. The CW in supernova envelopes is usually strong enough. This means that $E_1 \gg E_2$. For ΔE one can write

$$\Delta E \simeq E_1 \simeq q\, \frac{\chi}{A m_u} \,. \tag{1.35}$$

The factor $q \approx 1.2$–1.5 accounts for the contributions of thermal and black body radiation energies.

Figure 4 shows the schematic structure of the CW front, which can be derived from the laws of energy, momentum and mass conservation (Zel'dovich and Raizer 1967; Imshennik and Nadyozhin 1964).

We only give the final expressions for CW front optical $\Delta\tau_{CW}$ and Eulerian Δr_{CW} thicknesses

$$\Delta\tau_{CW} \approx \left(\frac{T_1}{T_2}\right)^4 \approx 15 - 40 \,, \tag{1.36}$$

$$\frac{\Delta r_{CW}}{R_{CW}} \approx \frac{\kappa_2}{\kappa_1}\left(\frac{T_1}{T_2}\right)^4 \sim 10^{-2} \,. \tag{1.37}$$

Table 2
Characteristics of the cooling-and-recombination wave in matter of differing composition according to Imshennik and Nadyozhin (1989). The first values of T_2 and T_{ef} refer to a density of 10^{-9} g/cm^3; the second to 10^{-12} g/cm^3 (10^{-13} g/cm^3 for H). For intermediate density values, T_2 and T_{ef} can be evaluated by logarithmic interpolation. The last row of temperature values applies to any mixture of Mg, Si, Fe, Co, Ni

Chemical composition	Ionization potential, eV	T_2, K	T_{ef}, K
H	13.60	3800–5000	4500–5900
He	24.59	6800–8100	8100–9600
C	11.26	3500–4100	4200–4900
O	13.62	4200–5000	5000–5900
Mg	7.65		
Si	8.15		
Fe	7.87	2500–3200	3000–3800
Co	7.86		
Ni	7.64		

Here we use typical ratios $T_1/T_2 \simeq 2 - 2.5$ and $\kappa_2/\kappa_1 \sim 10^{-3}$; T_1 is the temperature at which recombination becomes effective, for hydrogen $T_1 \simeq$ 10,000 K. According to eq. (1.37), the CW front is geometrically thin and can be considered as a jump. However, optically, the CW is thick enough to describe energy flux in the radiative heat conduction approximation for which the effective temperature $T_{ef} \simeq \sqrt[4]{2}\,T_2$, as indicated by eq. (1.33). The values of T_{ef} and T_2 are listed in table 2 for a number of chemical species. For hydrogen-enriched material, the typical values of T_{ef} are in the range 4500–5900 K. The observed photospheric temperature fell in this range ~ 10 days after the beginning of the SN 1987A explosion. Nearly the same T_{ef} corresponds to oxygen-enriched material which is found while studying explosions of Wolf–Rayet stars (Schaeffer et al. 1987). Taking into account that the CW forms when a supernova envelope is already in free expansion, one can confirm that the kinematics of the CW front is controlled by the following equation

$$\frac{dR_{CW}}{dt} = u - u_{CW} = \frac{R_{CW}}{t} - \frac{2\sigma T_2^4}{\rho\,\Delta E}\,, \tag{1.38}$$

where we also used eq. (1.34). Assuming further the power law

$$\rho = \frac{B}{t^3}\left(\frac{r}{t}\right)^{-\alpha} \tag{1.39}$$

and the virtual constancy of T_2 and E_1, one can reduce eq. (1.38) to

$$\frac{dR_{CW}}{dt} = \frac{R_{CW}}{t} - b\,t^3\left(\frac{R_{CW}}{t}\right)^{\alpha} . \tag{1.40}$$

In case of self-similar expansion, $\alpha = 3+(n+1)/\lambda$ in eqs. (1.39) and (1.40). Equation (1.40) admits an analytical solution (Grasberg and Nadyozhin 1976) which leads to the following expression for CW luminosity

$$L = 8\pi R_{CW}^2\,\sigma T_2^4 \propto t^{2\frac{\alpha-4}{\alpha-1}} . \tag{1.41}$$

This result is in fair agreement with the time behaviour of SN 1987A's luminosity in the interval $t \simeq$ 10–50 days, when α is expected to vary between ~ 10 and ~ 6.

Hence, one can conclude that the increase in SN 1987A luminosity during this time interval was not powered by ^{56}Co decay, but rather ensued from thermal and recombination energies released in the CW regime. Nevertheless, all models which neglect radioactive energy sources predict that SN 1987A must have faded down by the time $t \sim 50$ days. However, the radioactive energy source generates an extra energy flux below the photosphere and keeps the light curve from decreasing. Then, the radiative energy flux S_1 is not negligible, and the CW does not exist in the strict sense of the word; one has to add S_1 to the left hand side of eq. (1.34). However, physical conditions at the photosphere level can remain for some time close to those at the outer edge of the CW (see the detailed SN 1987A models calculated by Shigeyama and Nomoto, 1990). This occurs because values of T_{ef} from table 2 retain their physical meaning irrespective of the presence of the CW, namely, they give *lower limits* to the photosphere temperature for specified chemical compositions. From this we can conclude that in Presupernova 1987A the helium layer had certainly mixed with the outer hydrogen-enriched layers. Otherwise, the effective temperature would have exceeded $\sim$ 8000K for some time while the photosphere passed through such a helium shell. So, we have further evidence for a large-scale mixing in the SN 1987A envelope, which is crucially important for successful modelling of the SN 1987A light curve (Shigeyama and Nomoto 1990). For further evidence, see Arnett et al. (1989) and references therein.

Suppose now that the macroscopic mixing leads to a chemically nonhomogeneous photosphere. Then a transparency temperature will depend on the solid angles, and the photosphere will recede with different radial speeds in different directions relative to matter. Estimates show that, owing to this effect, the photosphere can acquire a non-spherical shape with asymmetry up to a factor of 2. It should be emphasized that such an asymmetry may occur even for *nearly spherically symmetric* distributions of total density and velocity in the supernova envelope. This effect should be of importance for interpretation of the light polarization observed in the SN 1987A spectra (Cropper et al. 1988, Méndez et al. 1988, Vid'machenko et al. 1988). In particular, the macroscopic chemical clumping of material inside the SN 1987A envelope (Haas et al. 1990) may result in an intricate time-variation of the polarization produced by recession of the photosphere in the interiors of the SN 1987A envelope, which is very non-uniform in time and angle.

1.7. Conclusions

The semianalytical approach demonstrated above is fruitful in elucidating a physical picture of the shock wave breakout and the early phases of those supernovae that come from explosions of the compact presupernovae. It can serve as a basis for deeper physical insight in the numerical modelling, aimed at refining our understanding of radiative transport in a highly time-dependent hydrodynamical background. One of the most important problems is an accurate estimate of the maximum temperature associated with the short luminosity peak which certainly occurred in the SN 1987A outburst. The discovery of narrow UV emission lines originating from circumstellar gas around SN 1987A (Fransson et al. 1989) gives unambiguous evidence for such a high-temperature luminosity peak. According to Fransson and Lundqvist (1989), the properties of the observed UV lines indicate that the maximum temperature attained during the shock wave breakout should have been somewhat less than 10^6K. However, the maximum temperature T_c in table 1 is, at least, 1.5 times greater. To resolve this controversy, more sophisticated calculations of shock wave breakout and presupernova envelope structure are urgently needed.

References

Arnett, W.D., J.N. Bahcall, R.P. Kirshner, and S.E. Woosley. 1989. Ann. Rev. Astron. Astrophys. 27, 629.

Branch, D. 1987. Astrophys. J. Letters 320, L23.

Catchpole, R.M., P.A. Whitelock, M.W. Feast, J.W. Menzies et al, 1988. Mon. Not. R. Astron. Soc. 231, 75.

Chugai, N.N. 1987. Astron. Zirk., No. 1494.
Cropper, M., J. Bailey, J. McCowage, R.D. Cannon, W.J. Couch, J.R. Walsh, J.O. Strade, and F. Freeman. 1988. Mon. Not. R. Astron. Soc, 231, 695.
Fransson, C., and P. Lundquist. 1989. Astrophys. J. Letters 341, L59.
Fransson, C., A. Cassatella, A. Gilmozzi, R. Kirshner, R.P. Panagia, N. Sonneborn, and W. Wamsteker. 1989. Astrophys. J. 336, 429.
Gandel'man, G.M., and D.A. Frank-Kamenetskii. 1956. Dokl. Akad. Nauk. SSSR 107, 811 (Soviet Phys. Dokl. 1, 223).
Grasberg, E.K. 1981. Astr. Zh. 58, 155 (Soviet Astr. 25, 85).
Grasberg, E.K., and D.K. Nadyozhin. 1976. Astrophys. Space Sci. 44, 409.
Haas, M.R., S.W.J. Colgan, E.F. Erickson, S.D. Lord, M.G. Burton, and D.J. Hollenbach. 1990. Astrophys. J. 360, 257.
Hamuy, M., N.B. Suntzeff, R. González, and G. Martin. 1988. Astron. J. 95, 63.
Illarionov, A.F., and R.A. Sunyaev. 1974, Astron. J. 51, 698.
Imshennik, V.S. 1976. Preprint M.V. Keldysh Inst. Appl. Math. No. 86.
Imshennik, V.S., and Yu.I. Morozov. 1964. Pricl. Mech. Tech. Phys., No. 2, 8.
Imshennik, V.S., and Yu.I. Morozov. 1981. Radiative Relativistic Gas Dynamics of High-Temperature Phenomena (In Russian). Atomizdat, Moscow.
Imshennik, V.S., and D.K. Nadyozhin. 1964. Astron. Zh. 41, 829 (Soviet Astron., 8, 664, 1965).
Imshennik, V.S., and D.K. Nadyozhin. 1988. Pis'ma Astron. Zh. 14, 1059 (Soviet Astron. Letters 14(6), 449).
Imshennik, V.S., and D.K. Nadyozhin. 1989. Soviet Sci. Rev., Sec. E, 8, Part 1, 1.
Imshennik, V.S., and V.P. Utrobin. 1977. Pis'ma Astron. Zh., 3, 68 (Soviet Astron. Letters 3, 34).
Klein, R.I., and R.A. Chevalier. 1978. Astrophys. J. Letters 223, L109.
Klimishin, I.A. 1984. The Shock Waves in Stellar Envelopes. Nauka Publishers, Moscow (In Russian).
Klimishin, I.A., and B.I. Gnatyk. 1981. Astrofizika 17, 547.
Litvinova, I.Yu., and D.K. Nadyozhin. 1990. Pis'ma Astron. Zh. 16, 61.
Méndez, M., A. Clocchiatti, O.G. Benvenuto, C. Feinstein, and H.G. Marraco. 1988. Astrophys. J. 334, 295.
Sakurai, A. 1960. Comm. Pure Appl. Math. 13, 353.
Schaeffer, R., M. Cassé, R. Mochkovitch, and S. Cahen. 1987. Astron. Astrophys. Letters 184, 6.
Schigeyama, T., and K. Nomoto. 1990. Astrophys. J. 360, 242.
Vid'machenko, A.P., Yu.N. Gnedin, V.M. Larionov, and L.V. Larionova. 1988. Pis'ma Astron. Zh. 14, 387 (Soviet Astron. Letters 14(3), 163).
Weaver, T.A., and C.F. Chapline. 1974. Astrophys. J. Letters 192, L57.
Wheeler, J.C., R.P. Harkness, and Z. Barkat. 1988. Proceedings G. Mason Univ. Workshop SN1987A, M. Kafatos, ed. Cambridge Univ. Press, 264.
Zel'dovich, Ya.B., and A.F. Illarionov. 1973. JETP, 65, 1294.
Zel'dovich, Ya.B., and Yu.P. Raizer. 1967. Physics of Shock Waves and High-Temperature Hydrodynamic Phenomena, W.D. Hayes and R.F. Probstein, eds. Academic Press. V. II.

COURSE XII

HIGH ENERGY EMISSION OF SUPERNOVAE

M. CASSÉ AND R. LEHOUCQ

CE Saclay, DAPNIA, Service d'Astrophysique
91191 Gif sur Yvette Cedex, France

S. Bludman, R. Mochkovitch and J. Zinn-Justin, eds.
Les Houches, Session LIV, 1990
Supernovae

Contents

1. Theoretical tools 592
   1.1. Historical background 592
   1.2. Decay and production of radioactive nuclei 593
   1.3. Gamma ray–matter interaction 597
      1.3.1. Elementary processes 597
      1.3.2. Simple analytic treatment of the problem 599
      1.3.3. Observed spectrum 605
   1.4. Monte-Carlo simulations 607
2. Applications 608
   2.1. The case of SN 1987a 609
      2.1.1. Fit of the light curve 613
      2.1.2. Astrophysical consequences 618
      2.1.3. What about a central source? 619
   2.2. Gamma ray lines from other supernovæ 620
3. Conclusion 623
4. Appendix 625
   4.1. Notation 625
   4.2. Fundamental constants and units 625
References 626

1. Theoretical tools

1.1. Historical background

Seeing a new star in the sky in 1572, the great Danish astronomer, Tycho Brahé (whose name is borne by a supernova), concluded pertinently that the upper region of the sky, beyond the moon, belongs to the sphere of birth and corruption. A single glance at the sky and solid reason abolished two thousand years of Aristotelian metaphysics. But he made a slight error of sign: it was not one more star but one less.

His pupil Johannes Kepler (whose name is borne by a supernova and also by a computer code) also had the chance to see the appearance of a "new star." And as direct successors of both, we have had the same chances, and even more, since in the meantime telescopes have been invented, notably optical ones (Galileo 1610) but also x, γ and ν (neutrino) telescopes.

What have we learned from neutrinos and high energy photons? Indeed, they have offered a splendid confirmation of theoretical expectations, giving the astrophysical community confidence in its models. This gratification, which is more than welcome, somewhat softens the vexations of solar neutrinos. Two great physical predictions have found their realization through νs and γs. The first prediction, published in 1934, just after the discovery of the neutron is due to Walter Baade and Fred Zwicky: "With all reserve, we advance the view that a supernova represents the transition of an ordinary star to a neutron star." The second prediction, in its more concise form, would say: "Iron is made as Nickel." Suess and Urey (1956) were the first to realize that the doubly magic ^{56}Ni nucleus should be promoted in natural nucleosynthesis: "No property of the ^{56}Fe nucleus is known that could possibly explain its predominance in nature. ^{56}Fe is an isobar of the doubly magic unstable ^{56}Ni, which contains 28 protons and 28 neutrons. The expectation of a correlation of abundances with nuclear properties leads inevitably to the conclusion that ^{56}Ni was the primeval nucleus from which ^{56}Fe was formed and, hence, that the nuclei of this mass region had formed on the neutron deficient side of the energy valley."

Truran, Arnett, and Cameron (1967) and Bodansky, Clayton, and Fowler (1968) demonstrated theoretically that this is indeed the case in explosive conditions. Parameterized models of explosive nuclear reprocessing were developed to follow the genesis of iron-peak nuclei. The influential parameters were singled out: peak temperature; initial composition (through the neutron excess of the shocked material); and the density of the burning zone (through the freeze out of nuclear reactions which can occur in a dense bath of α particles) (Woosley, Arnett and Clayton 1973). Finally, nuclear networks were incorporated into hydrodynamic codes, principally in the US (Woosley, Weaver, and collaborators) and Japan (Nomoto and collaborators). The subject of explosive nucleosynthesis is reviewed in this volume by Woosley and Weaver and in "Nucleosynthesis and chemical evolution" 16^{th} Advanced Saas-Fee Course of Astrophysics and Astronomy by Woosley (1986). This article can be regarded as the New Testament, with respect to the Bible of B^2FH (Burbidge et al. 1957). Nowadays, explosive nucleosynthesis is under systematic study (Thielemann, Nomoto this volume, Thielemann, Hashimoto, and Nomoto 1990, Arnould and Prantzos 1990).

1.2. Decay and production of radioactive nuclei

Isotopic astronomy, a term tailored for the analysis of isotopic anomalies in meteorites, applies equally well to the study of signatures of specific radionuclides by monoenergetic gamma rays induced by their decay. Among the radioactive species synthesized and ejected by supernovæ, the most important by far both in mass and by its consequences is ^{56}Ni, the progenitor of iron through the decay chain $^{56}\mathrm{Ni} \rightarrow {}^{56}\mathrm{Co} \rightarrow {}^{56}\mathrm{Fe}$. The daughter nuclei are produced in excited states and "cool off" by gamma-ray line emission (see table 1). Gamma-ray photons produced by ^{56}Ni decay (mean lifetime of 8.8 days) cannot be observed directly due to a high Compton envelope depth early in core collapse supernovæ. However, interacting with the expanding material, they power the optical light curve near its maximum. On the other hand, the disintegration of ^{56}Co into ^{56}Fe, with a mean lifetime of 111.3 days is perfectly suited to leave its imprint on the electromagnetic manifestations of supernovæ, and indeed it does. Type Ia supernovæ (SN Ia) definitely show radioactive tails (see fig. 1) as do some Type II supernovæ (SN II), among them SN 1987a, which is thought to originate from the explosion of a massive star ($\simeq 18\ M_{\odot}$). This massive star was stripped of a part of its hydrogen-rich envelope (Arnett 1988, Arnett et al. 1989, Schaeffer et al. 1987). As to ^{57}Co and ^{44}Ti, their long mean lifetimes allow them to remain after the decay of ^{56}Ni and ^{56}Co and presumably, to power the bolometric light curve at late times.

Table 1
Characteristics of the gamma-ray line emitters: mean lifetime; mean energy of the positron emitted; branching ratio of β decay; energies of the main γ-ray photons; and their branching ratios.

Decay	τ	$\overline{E}_e$ (keV)	%	E_γ (keV)	%
$^{56}Ni \rightarrow {}^{56}Co$	8.8 days	—	—	158.38	98.80
				269.50	35.57
				480.44	35.57
				749.95	49.89
				811.85	87.44
				1561.8	14.13
$^{56}Co \rightarrow {}^{56}Fe$	111.3 days	β^+, 660	19	847	99.95
				1038	13.99
				1175	2.279
				1238	67.57
				1360	4.328
				1772	15.69
				2015	3.078
				2035	7.886
				2598	16.89
				3202	3.038
				3254	7.406
				3273	1.749
$^{57}Co \rightarrow {}^{57}Fe$	391.0 days	—	—	14	89.00
				122	88.85
				136	11.00
$^{44}Ti \rightarrow {}^{44}Ca$	69.2 years	β^+, 597	94	68	100.0
				78	100.0
				1156	100.0

Indeed, supernovæ can be classified as very radioactive (SN Ia) and moderately radioactive (SN 1987a, SN IIp and SN Ib) just by noting the absolute luminosity at the start of their exponential decline, which is a measure of the amount of ^{56}Co produced. In addition, the gamma-ray line emission of these various objects should depend on the mass of the overlaid envelope, on the explosion energy through the expansion velocity, and on the internal distribution of the gamma-ray emitters. In this game, SN Ia are clearly favored due to the large amount of ^{56}Ni synthesized which is associated with a low mass progenitor (a white dwarf forced to explode by accretion, in all likelihood), as pointed out in the late sixties by Clayton, Colgate, and Fishman (1969). At the other extreme, it is likely that pair production supernovæ, which are the rarest kind due to the extreme mass of their progenitor, would be poor ^{56}Ni and ^{56}Co suppliers and hence weak gamma-ray emitters. Thus, between

Type I supernovae

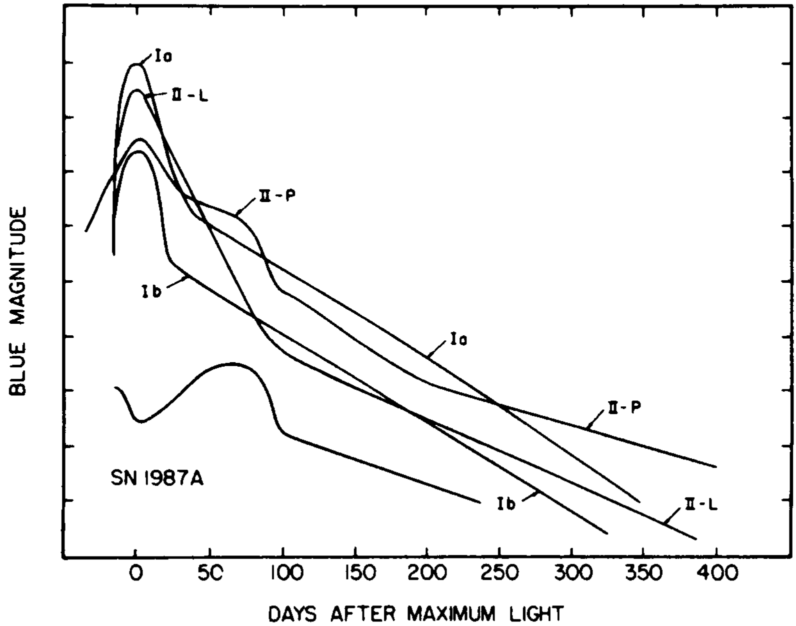

0.6 and 0.01 $M_\odot$ of ^{56}Fe, in the form of its radioactive progenitor (^{56}Ni), was thought to be synthesized and ejected into the surrounding medium by all kinds of supernovæ. The deposit of a significant amount of ^{56}Co and possibly other radionuclides in the interstellar medium could not escape forever to be seen by gamma-ray telescopes. The high energy spectrum of a supernova originating from the explosion of a 25 $M_\odot$ star was even predicted (Weaver and Woosley 1980, Woosley, Axelrod and Weaver 1981).

The case of SN I's was more highly advertised (Clayton, Colgate, and Fishman 1969). However, nature has chosen to confirm the first form of those expectations, that is, that of Woosley and collaborators. Indeed an armada of flying objects has observed the 847 keV line from ^{56}Co decay and sometimes the accompanying 1238 keV line in the spectrum of SN 1987a (SMM: Matz et al. 1988, Leising and Share 1990; balloon experiments: Sandie et al. 1988, Cook et al. 1988, Mahoney et al. 1988, Rester et al. 1989, Teegarden et al. 1989, Tueller et al. 1990; for a review, see Gehrels, McCallum, and Leventhal 1987). Remarkably, the predicted intensity of the 847 keV line, corrected for the distance effect, is only twice the observed intensity, although the emergence time is quite different due to the unexpected occurrence of mixing in the ejects, and *mass loss* in the progenitor, which reduces the envelope mass (e.g. Woosley 1988, Rank et al. 1988).

The role of ^{57}Co as gamma-ray producer was pointed out by Clayton (1974). Originating from ^{57}Ni, it decays with a lifetime of 391 days into excited states of ^{57}Fe by *pure electron capture*. The daughter nucleus de-excites by photon emission at 14, 122, and 136 keV.

Another set of important lines has been emphasized which are those from ^{44}Ti radioactivity. This isotope decays with a mean lifetime of 69.2 years into an excited state of ^{44}Sc, which cascades to its ground state, emitting lines at 68 and 78 keV. ^{44}Sc quickly decays (with a lifetime of 2.9 hours) into the 1156 keV excited state of ^{44}Ca.

Further, positrons from ^{56}Co (0.19 per decay) and/or ^{44}Ti (0.94 per decay) decay, and even if only a small fraction of them escapes, this would explain a substantial part, if not all, of the 511 keV line luminosity of the Galaxy (Ramaty and Lingenfelter 1981; Woosley, Axelrod, and Weaver 1981).

Even before 1987, many astrophysicists were convinced that unique astrophysical information was encoded in line energies, shapes and intensities of supernova photons, and in particular, that the detection of gamma-ray lines from radioactive nuclei produced by explosive nucleosynthesis in supernovæ would make a major contribution to its understanding. (Clayton et al. 1969; Clayton 1973; Lingenfelter and Ramaty 1978; Woosley, Axelrod, and Weaver 1981; Ramaty and Lingenfelter 1981; Clayton 1982). After 1987, this view became more widespread and many models have flourished which consider the transfer of gamma-ray lines in the expanding envelope of the magellanic supernova. The models were of two types. Those that were developed early in the process were without radial mixing of ^{56}Ni (McCray, Shull, and Sutherland 1987; Woosley et al. 1988; Shull and Xu 1987; Chan and Lingenfelter 1987; Xu et al. 1988; Gehrels, McCallum, and Leventhal 1987; Ebisuzaki and Shibazaki 1988a, 1988b). Later on, models with radial mixing were developed under the the constraints of gamma-ray lines that emerged earlier than predicted, and hard x-ray photons originating from their comptonization (Grebenev and Sunyaev 1987; Pinto and Woosley 1988a, 1988b; Leising 1988; Shibazaki and Ebisuzaki 1988; Sutherland et al. 1988; Kumagai et al. 1988, 1989; Fu and Arnett 1989; Lehoucq, Cassé, and Cesarsky 1989, 1991; Bussard, Burrows, and The 1989; The, Burrows, and Bussard 1990). Mixed models were shown to explain the smoothness of the early (< 100 days) light curve (e.g., Shigeyama and Nomoto 1990). Such models were motivated by the likely occurrence of Rayleigh-Taylor instabilities (e.g., Chevalier 1976; Hashisu et al. 1990). Beyond day $\simeq$ 100, gamma-rays and positrons of radioactive origin affect the energetics of the supernova envelope, breaking the adiabaticity of the expansion. Without this supply of energy, SN 1987a would have faded away very shortly. Finally, the long lasting effects of ^{57}Co and ^{44}Ti on the bolometric light curve have been explored (Lehoucq, Cassé, and Cesarsky 1989; Pinto, and Woosley 1988a, 1988b; Grebenev and Sunyaev 1988a, 1988b, Kumagai et al. 1988, 1989). They were then adjusted to explain the observed flattening after day 1000 or 1200 (Bouchet et al. 1990; Lehoucq, Cassé and Cesarsky 1990; Cassé, Lehoucq, and Cesarsky 1991; Nomoto et al. 1991). Satellites observations of the 68, 78, and 1156 keV lines of ^{44}Ti from SN 1987a will be required to settle the question of the feeding of the late light curve by a central object (a pulsar or an accreting object) or by radioactivity mainly (see chapter 2).

1.3. Gamma ray–matter interaction

1.3.1. Elementary processes

(i) The dominant process of interaction between hard x and γ photons emitted by radioactive nuclei and the ejected matter of the envelope is *Compton scattering.* The scatterings occur indifferently on bound and free electrons, due to the high energy of the impinging photons. Indeed, at energies $h\nu > \alpha m_e c^2$ ($\simeq$ 3.7 keV), the wavelength of the incident photon is shorter than the Bohr radius. The scattering of a high energy photon by a neutral atom leads to the ejection of one of the bound electrons. This electron acquires a recoil energy $h\nu(\frac{h\nu}{mc^2})$, greater than the ionization potential, which is of the order $\frac{1}{2}\alpha^2 m_e c^2$. In each scattering event, due to the recoil effect, the photon shifts toward lower frequencies by a quantity $\Delta\nu$, given on the average by $\frac{\overline{\Delta\nu}}{\nu} = 1 - \frac{Ln(1+2x)}{2x}$ where $x = \frac{h\nu}{m_e c^2}$ is the dimensionless energy of the photon. Indeed, ν and ν', the photon frequency before and after scattering are related by

$$\nu' = \frac{\nu}{1 + \frac{h\nu}{mc^2}(1 - \cos\theta)} \tag{1.1}$$

The relative change in frequency is defined by

$$\frac{\Delta\nu}{\nu} = \frac{\nu' - \nu}{\nu} = -\frac{x(1 - \cos\theta)}{1 + x(1 - \cos\theta)}$$

and averaging over the solid angle gives

$$\frac{\overline{\Delta\nu}}{\nu} = -\int_0^\pi \frac{x(1 - \cos\theta)}{1 + x(1 - \cos\theta)} \frac{2\pi \sin\theta \, d\theta}{4\pi}.$$

Using a change of variable, $t = x(1 - \cos\theta)$, this integral becomes

$$\frac{\overline{\Delta\nu}}{\nu} = \int_0^{2x} \frac{t}{1+t} \frac{dt}{2x} = 1 - \frac{1}{2x} Ln(1+2x)$$

When $x \ll 1$ (that is, at low energy), this simplifies to $\frac{\overline{\Delta\nu}}{\nu} \simeq -\frac{h\nu}{mc^2}$. Let us denote by n the mean number of scattering events per unit of time. Then, a crude simplification gives $\frac{d\nu}{\nu} = -\frac{h\nu}{mc^2}\, ndt$ which integrates to $u = \frac{1}{x} - \frac{1}{x_0}$, where $u = nt$ is the number of scattering events required to lower the photon's energy from $h\nu_0 = x_0 mc^2$ to $h\nu = mc^2$. If $x \ll x_0$, then $u \simeq \frac{mc^2}{h\nu}$. In the diffusion problem, the mean number of scatterings $\overline{u}$ can be high enough to ensure that the photons have a wide escape time distribution. In that case, the spectrum formed through comptonization is continuous.

(ii) For energies less than $\simeq$ 30 keV, the escape probability of photons decreases exponentially because of an increase in the *photoionization* cross section for K-shell electrons of heavy elements (C, O, Si, Fe). This probability is equal to $P_{abs}(x) = \exp\Big(-\tau_{abs}(x)\Big)$, where τ_{abs} is the effective absorption depth along the photon trajectory namely,

$$\tau_{abs}(x) = \int_0^t \sigma_{abs}(x') N_e\, c\, dt' \tag{1.2}$$

where $\sigma_{abs}(x)$ is the photoabsorption cross section, and N_e is the electron density. Tables of photoabsorption cross sections can be found in Hayakawa (1969); Veigele (1973); and Morrison and McCammon (1983). This photoabsorption mechanism leads to a sharp low energy cut-off in the supernova x-ray spectrum.

(iii) Gamma-ray photons with energy higher than $2m_ec^2$ may be absorbed by electron-positron *pair formation* in the field of nuclei. However, the probability of this process does not exceed a few per cent of the Compton scattering one and this effect will be neglected.

We first develop the analytical method following ideas presented by Sunyaev and Titarchuk (1980), and Grebenev and Sunyaev (1987) for illustration. Then, we present a widely used numerical method, based on Monte Carlo simulations, which can be used to predict the behavior of the high energy spectrum.

1.3.2. Simple analytic treatment of the problem

The differential cross-section of Compton scattering in given by (Blumenthal and Gould 1970, Akhiezer, and Berestetskiy 1981)

$$d\sigma_c(x \to x') = \pi r_0^2 \left(\frac{x'}{x} + \frac{x}{x'} + (\frac{1}{x'} - \frac{1}{x})^2 - 2(\frac{1}{x'} - \frac{1}{x})\right) \frac{dx'}{x^2} \quad (1.3)$$

where r_0 is the classical radius of the electron, $x = \frac{h\nu}{mc^2}$ and $x' = \frac{h\nu'}{mc^2}$ are the dimensionless energies[1] before and after the scattering event, and are related by

$$x' = \frac{x}{1 + x(1 - \cos\theta)}$$

Another way of writing the Compton differential cross section is to use the (x, θ) variables, which gives

$$\mathrm{d}\sigma_c(x, \theta) = \frac{1}{2} r_0^2 \Big(1 + x(1 - \cos\theta)\Big)^{-2} \left(1 + \cos^2\theta + \frac{x^2(1 - \cos\theta)^2}{1 + x(1 - \cos\theta)}\right) \mathrm{d}\Omega.$$

which is an even function of θ and (as we can see on fig. 2), the scattering direction is increasingly forwardly peaked as energy increases.

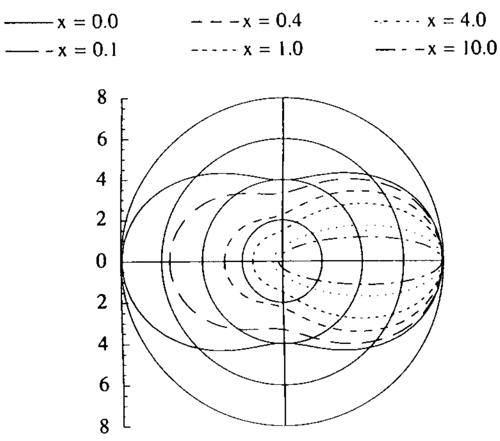

Fig. 2. Compton differential cross section per unit solid angle (number of photons scattered at the angle θ in units of 10^{-26} cm^2/electron for various values of $x = \frac{h\nu}{mc^2}$).

[1] In the following we use the term "energy" to refer to either the dimensionless energy x or the "true" energy xm_ec^2.

The total cross section for Compton scattering is given by

$$\sigma_c(x) = \int_{\frac{x}{1+2x}}^{x} \mathrm{d}\sigma_c(x \to x') = \int_0^{\pi} \frac{\mathrm{d}\sigma_c}{\mathrm{d}\Omega}(x,\theta)\mathrm{d}\Omega \qquad (1.4)$$

We get the well-known Klein-Nishina formula

$$\sigma_c(x) = 2\pi r_0^2 \left[\frac{1+x}{x^2}\left(\frac{2(1+x)}{1+2x} - \frac{Ln(1+2x)}{x}\right) + \frac{1}{2x}Ln(1+2x) - \frac{1+3x}{(1+2x)^2}\right]$$

where $\sigma_c(x)$ is represented on fig. 3.

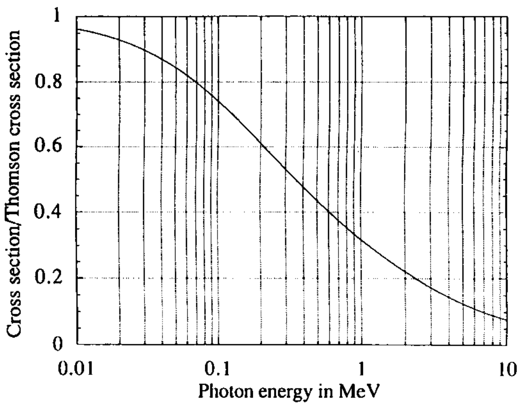

Fig. 3. Compton total cross section in units of Thomson cross section versus photon energy.

In extreme energy limits, the Klein-Nishina formula can be approximated by

$$\sigma_c(x) = \sigma_T\left(1 - 2x + \frac{26}{5}x^2 + O(x^3)\right) \qquad \text{if } x \ll 1 \text{ (i.e., low energies)}$$

and

$$\sigma_c(x) = \frac{3}{8}\sigma_T\frac{1}{x}\left(Ln(2x) + \frac{1}{2}\right) \qquad \text{if } x \gg 1 \text{ (i.e., high energies)}$$

where $\sigma_T = \frac{8\pi}{3}r_0^2$ is the Thomson cross section.

Photon energy evolution as a function of time. Let N_e be the mean electronic density in the envelope. For a single photon, the quantity $N_e c\, d\sigma_c(x \to x')$ represents the number of scatterings per unit of time, shifting the photon energy from x to x'.

Thus, $x(t)$ follows the equation[2]

$$x(t+dt) = x(t) + \left(\int (x'-x) N_e c\, d\sigma_c(x \to x')\right) dt$$

which can be rewritten as

$$\frac{dx}{dt} = N_e c \int_{\frac{x}{1+2x}}^{x} (x'-x)\, d\sigma_c(x \to x') \qquad (1.5)$$

Since the number of diffusions per unit of time is equal to $\sigma_c(x) N_e c$, the energy lost per diffusion is

$$\epsilon(x) = -\frac{1}{\sigma_c(x) N_e c} \frac{dx}{dt} \qquad (1.6)$$

In the extreme limit where $x \ll 1$, $\sigma_c \simeq \sigma_T$ and the number of scatterings per unit time is on the order of $\sigma_T N_e c$, so that the energy lost per diffusion is on the order of

$$\alpha(x) = -\frac{1}{\sigma_T N_e c} \frac{dx}{dt} \simeq x^2\left(1 - \frac{21}{5}x + \frac{147}{10}x^2 + O(x^3)\right)$$

But, in the general case,

$$\epsilon(x) = \frac{\sigma_T}{\sigma_c(x)} \times \left[\frac{3}{8x^2}\left(6x + (x^2 - x - 3) Ln(1+2x) - \frac{2x^2}{1+2x}\left(1 + x - \frac{x^2}{1+2x}\left(\frac{1-\frac{4x}{3}}{1+2x}\right)\right)\right]$$

$\epsilon(x)$ is represented on fig. 4. We note that the relative energy lost per diffusion (i.e. $\frac{\epsilon(x)}{x}$) is an increasing function of the photon energy and varies from 1% at 10 keV to 30% at 10 MeV.

---

[2] We write this as a "continuous" equation instead of a "discrete" equation since we treat the diffusive regime, where the number of scatterings can be much greater than one, as a "continuous" regime.

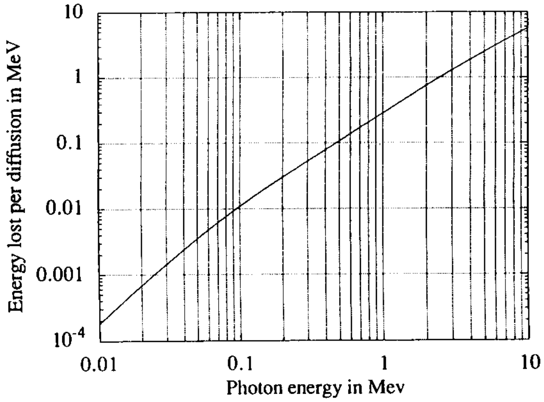

Fig. 4. Energy lost per diffusion (i.e. $\epsilon(x)mc^2$) in MeV versus photon energy.

Note that the relation between, x_0, x, and the escape time t is given by

$$t = \int_x^{x_0} \left(-\frac{dt'}{dx'}\right) dx' = \int_x^{x_0} \frac{dx'}{\sigma_c(x) N_e c\ \epsilon(x')}.$$

Accordingly, the number of scatterings $u(x_0, x)$ that a photon of initial energy $x_0 mc^2$ has to experience to lower its energy to xmc^2 $(x < x_0)$ is given by

$$u(x_0, x) = \int_{x_0}^{x} \left(-\frac{1}{\epsilon(x)}\right) dx = \int_x^{x_0} \frac{dx}{\epsilon(x)} \tag{1.7}$$

(see fig. 5).

Distribution of photons as a function of their escape time. This was obtained by Sunyaev and Titarchuk (1980) for the case of a point source inside a spherical cloud in the Thomson scattering limit (i.e. $x \ll 1$). The probability $P(u)du$ that a photon undergoes a number of scatterings in the range $[u, u + du]$ before escaping the envelope is given by the series

$$P(u)du = \sum_{k=1}^{+\infty} \lambda_k\ \sin(\lambda_k \tau_0)\ \exp\left(-\frac{\lambda_k^2 u}{3}\right)\ du \tag{1.8}$$

where λ_k are solutions of

$$tg(\lambda_k \tau_0) = \frac{\lambda_k \tau_0}{1 - \frac{3}{2}\tau_0}$$

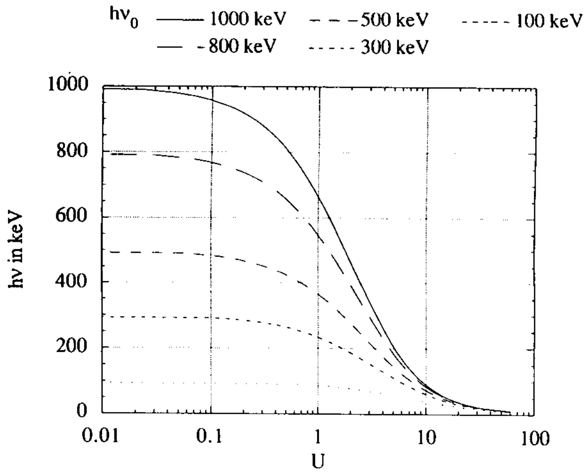

Fig. 5. Number u of diffusions required to decrease the photon energy from its initial value $h\nu_0$ to its final value $h\nu$.

where τ_0 is the Thomson radial optical depth of the envelope and is equal to $\sigma_T N_e R$. The probability density is represented on fig. 6 for various values of τ_0.

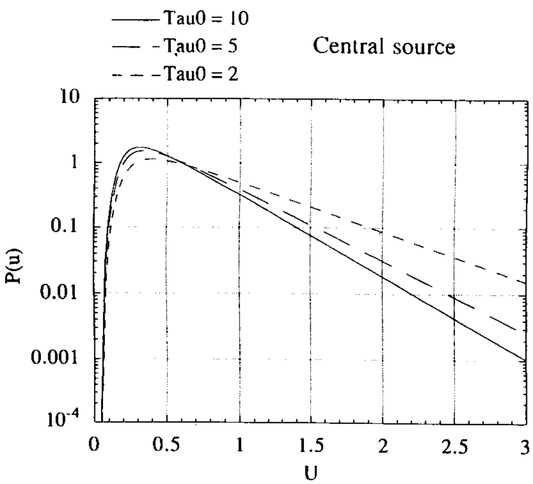

Fig. 6. Density of probability of escape versus the number of diffusions suffered by a photon for various values of τ_0, the Thomson depth, in the case of a central source.

As we can see from eq. (1.8), $P(u)$ is entirely determined by u/τ_0^2. As we are in the Thomson limit u, the number of scatterings is equal to $\sigma_T N_e ct$. Thus

$$\frac{u}{\tau_0^2} = \frac{\sigma_T\ N_e\ c\ t}{(\sigma_T\ N_e\ R)^2} = \frac{c\ t}{\sigma_T\ N_e\ R^2} = \frac{3}{4}\frac{t}{t_d}$$

where t_d is the diffusion time equal to $R^2/4D$ and D is the diffusion coefficient $\frac{c}{3\,\sigma_T\,N_e}$. Thus, from eq. (1.8), we obtain the probability that a photon escapes between time t and $t+dt$.

But in the real problem, the diffusion coefficient as well as the diffusion time depends on x. Thus, u/τ_0^2 had to be replaced by the relevant parameter u_{eff}/τ_0^2, so that

$$\frac{4u_{eff}}{3\tau_0^2} = \int_0^t \frac{dt'}{t_d} \quad \text{and} \quad t_d = \frac{R^2}{4D(x)} \tag{1.9}$$

The diffusion coefficient $D(x)$ is now energy dependent and has the form

$$D(x) = \frac{c}{3N_e\sigma_{tr}(x)}$$

where $\sigma_{tr}(x)$ is the transport cross section defined by

$$\sigma_{tr}(x) = \int_0^\pi (1-\cos\theta)\left(\frac{d\sigma}{d\Omega}\right)(x,\theta)\,d\Omega = \int_{\frac{x}{1+2x}}^x \left(\frac{1}{x'} - \frac{1}{x}\right) d\sigma_c(x \to x')$$

The $(1-\cos\theta)$ factor arises because the "effective" collisions are those with a non-negligible scattering angle θ. Integration of this last equation gives $\sigma_{tr}(x) = \varphi(x)\sigma_T$ and,

$$\frac{8}{3}x^4\varphi(x) = (3+4x-x^2)Ln(1+2x) + \frac{2x^4}{(1+2x)^2} + 2x(x^2-x-3).$$

In the limit where $x \ll 1$, $\varphi(x) = 1 - \frac{14}{5}x + \frac{81}{10}x^2 + O(x^3)$. Thus eq. (1.9) becomes

$$\begin{aligned}\frac{4u_{eff}}{3\tau_0^2} = \int_0^t \frac{dt'}{t_d} &= \frac{4}{3\tau_0^2}\int_x^{x_0} \frac{\sigma_T}{\sigma_{tr}(x')}\sigma_T\ N_e\ c\left(-\frac{dt'}{dx'}\right)dx' \\ &= \frac{4}{3}\tau_0^2\int_x^{x_0}\frac{dx'}{\varphi(x')\alpha(x')}\end{aligned}$$

Taking into account the respective dependences of φ and α on x', and after a numerical integration, we obtain the curve represented in fig. 7.

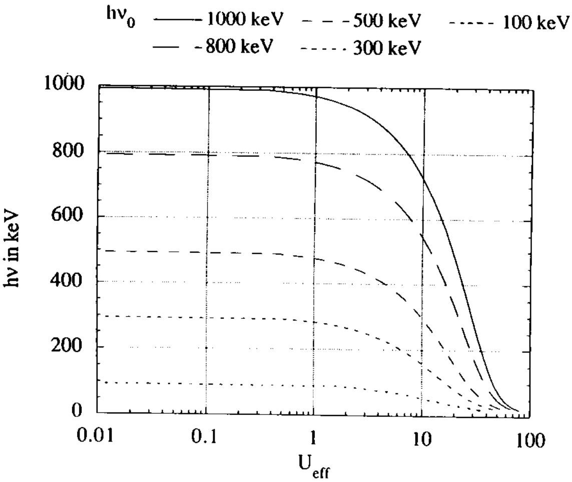

Fig. 7. u_{eff}, time expressed in units of the characteristic diffusion time required to lower the photon energy from $h\nu_0$ to $h\nu$.

Note that $u_{eff}(x_0, x)$ marks the time spent along the photon trajectory in units of the characteristic diffusion time. It is different from $u(x_0, x)$, which is the actual effective number of scatterings suffered by the photon during its travel through the envelope.

If we assume that the escape probability after a number of scatterings in the range $[u, u + du]$ has the same form as in the Thomson limit (eq. (1.8)) then, in this case, dP is given by

$$dP = P(u_{eff}) \left(\frac{du_{eff}}{dx} \right) \left(\frac{dx}{du} \right) du = P(u_{eff}) \frac{\sigma_T}{\sigma_c(x)\, \varphi(x)} du \quad (1.10)$$

The probability density $\frac{dP}{du}$ is illustrated in fig. 8 for an initial energy $x_0 m_e c^2$ of 847 keV, typical of a ^{56}Co source.

1.3.3. Observed spectrum

The spectral density of photons escaping the envelope due to comptonization of a particular γ-ray line is determined by

$$I_x(x)\, dx = I_0\, P_{abs}(x)\, P\Big(u_{eff}(x_0, x)\Big) \left(\frac{d\, u_{eff}}{dx} \right) dx \quad (1.11)$$

where I_0 is source line function (photon cm^{-2} s^{-1}), x_0 is the rest-energy of the line and $P_{abs}(x)$ is the photoabsorption escape probability, see eq. (1.2).

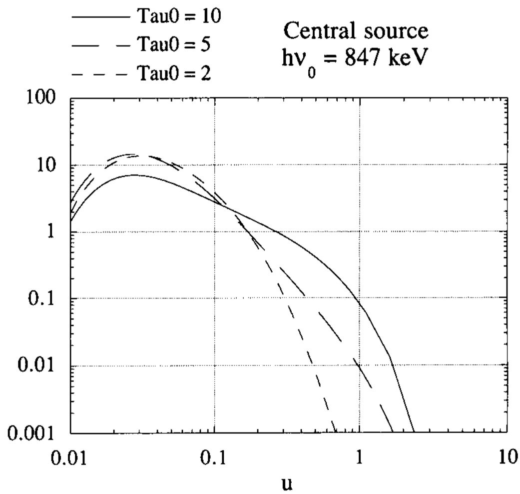

Fig. 8. Probability density $\frac{dP}{du}$ versus the number of scatterings u, for the 847 keV line of a central source of ^{56}Co, and for various values of τ_0, the radial Thomson depth.

Thus,

$$I_x(x) = I_0 \;\; P_{abs}(x) \;\; P\Big(u_{eff}(x_0, x)\Big) \;\; \frac{1}{\alpha(x)\;\varphi(x)} \tag{1.12}$$

Alternately, we can write the spectral density in term of the energy, namely

$$I_\nu(x) = \frac{I_x(x)}{mc^2} \qquad \text{in photon cm}^{-2}\text{s}^{-1}\text{keV}^{-1} \tag{1.13}$$

I_0, as the source line function, is equal to

$$g \, \frac{1}{4\pi d^2} \, \frac{M}{m} \, \frac{1}{\tau_{rad}} \, \exp\left(-\frac{t}{\tau_{rad}}\right)$$

where g is the branching ratio of the line
τ_{rad} is the mean lifetime of the decaying element
M is the total mass of the radioactive element produced
m is the mass of the radioactive nucleus of interest
d is the distance to the supernova.

1.4. Monte-Carlo simulations

Monte-Carlo codes are statistical devices designed to follow individually the fate of a large number of photons (say more than 10^5) interacting with the free and bound electrons of the ejected material through Compton scattering and photoelectric absorption. The spectrum of the emergent photons is calculated at different times, and, in addition, the amount of energy trapped in the expanding remnant is evaluated. The method is straightforward (see below) and gives a transparent representation of the chain of physical events involved, but as with all numerical calculations, it presents the danger of furnishing lists of numbers that can be easily misinterpreted. Thus, it needs to be carefully checked using simple analytical cases. The core of the program, based on a method devised by Pozdnyakov, Sobol, and Sunyaev (1983), is detailed in Ambwani and Sutherland (1988). In the following we paraphrase their description.

The inputs of the model are the masses of radioactive species of interest (i.e. ^{56}Co, ^{57}Co, and ^{44}Ti), with their distribution and with the density, velocity, and composition profiles of the exploded star extracted from separate model. Homologous expansion is assumed, which is in agreement with numerical simulations.

The logical steps are outlined as follows:

1. Emission: Photons are released from radioactive zones in proportion to the zone mass; the rate of disintegration, $\frac{1}{\tau}\exp(-\frac{t}{\tau})$; and branching ratios of the gamma-ray emission. The energy is specified for each photon, together with the radius of the released point, and the initial direction of propagation.

2. Escape/interaction: Each photon is allowed to propagate along a distance s until

$$\exp\left(-\int_0^s (n_e\sigma_c + \sum_a n_a\sigma_a)\mathrm{d}s\right) = x$$

where x is a random number chosen in the interval [0, 1]; n_e and n_a are the number density of free electrons and heavy species; and σ_c and σ_a are Compton and photoabsorption cross sections. If the limit of the envelope is reached, the photon escapes and its escape time and energy are recorded. A new photon is then generated.

If the photon stays within the envelope, it suffers an interaction. Its specific fate is chosen at random in proportion to the ratio of the Compton and photoelectric cross sections. If Compton scattering is its fate, a new polar angle is chosen such that $\frac{\sigma(\theta)}{\sigma_T} = x$, where $\sigma(\theta)$ and σ_T are, respectively, the Klein-Nishina cross section integrated from 0 to θ and the total one. x is fired at random between 0 and 1. The azimuthal angle φ is also chosen randomly between 0 and 2π. For simplicity, the energy transfered to the interacting electron is deposited at the point of interaction. If photoabsorption is its fate, the energy of the photon is again deposited at the point of interaction. In the physical conditions prevailing in the ejecta, positronium forms (Bussard et al. 1979; Brown and Leventhal 1987), and two monoenergetic gamma's (511 keV) are emitted 25% of the time. These 511 keV photons are propagated as the others. The kinetic energy of the positrons resulting from β-decay is also deposited at the point of release.

When the photon under consideration is lost, a new one is generated. Therefore, producing the spectra or the energy deposition function is a simple matter of bookkeeping.

2. Applications

Generally speaking, the x and γ signatures of supernovæ contain important information on:

(i) The kind and quantity of radionuclides synthesized. Masses of 56, 57, and 44 isobars would allow a fine theoretical determination of the mass cut, that is, the dividing line between imploding and ejected zones and a better definition of the physical conditions prevailing in the production layers (Woosley, these proceedings, Hashimoto et al. 1989; Thielemann, Hashimoto, and Nomoto 1990; Thielemann, Nomoto, and Hashimoto 1990).

(ii) The transparency of the envelope at the time of measurement. This is itself a function of ejected mass and explosion energy, or, more precisely of the column depth of the occulting material.

(iii) The velocity profile within the ejecta that provided the radionuclides are radially distributed. This has indeed proven to be the case, and thus determined the extent of internal mixing. Careful observation of line profiles would offer a better understanding of hydrodynamic instabilities leading to mixing and/or fragmentation (Müller, Fryxell, and Arnett 1990; Benz and Thielemann 1990).

The evolution of different gamma-ray line intensities results from a competition between the activity (emission rate $= \lambda f N_0 e^{-\lambda t}$ where λ is the decay constant, f is the branching ratio, and N_0 is the initial number of radionuclides of interest) and the progressive thinning out of the ejecta. In the simple case of a point-like emission located in the center of an homogeneous sphere (mass M and uniform density ρ) in homologous expansion (edge velocity v) driven by an explosion energy E, the optical depth of the ejected envelope

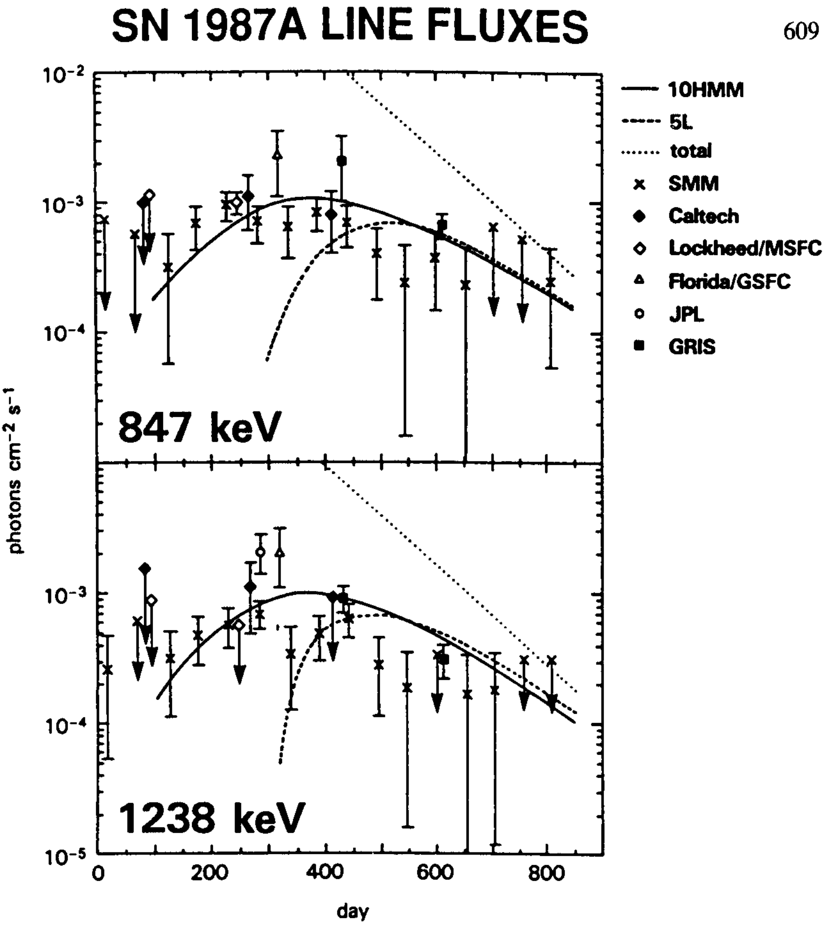

Fig. 9. SN 1987a γ-ray light curves at 847 and 1238 keV (from Tueller et al. 1990 and references therein). Theoretical predictions rely on the models from Pinto and Woosley (1988a, 1988b). The solid line corresponds to 10HMM, the dashed line to 5L without mixing, and the dotted line to complete transparency.

is proportionnal to $(\frac{M^2}{E})\frac{1}{t^2}$ and the luminosity of a particular gamma-ray line is $L_\gamma(t) = (\lambda f N_0 e^{-\lambda t})e^{-\tau(t)}$.

2.1. The case of SN 1987a

The Monte Carlo transfer code presented in sec. 1.4 was quite successfully applied to the Magellanic supernova. Indeed, the comptonization-photoabsorption model rather nicely fits the spectra as observed at different times at x and γ energies, and the light curves in different energy bands: 847 keV line, x-rays, optical, and IR (see figs. 9–12).

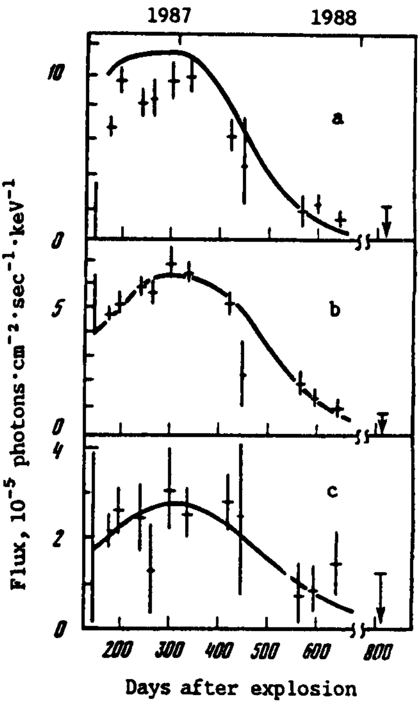

Fig. 10. Light curve in different x-ray bands. The data are from Sunyaev et al. (1990) and the fits are based on the Monte-Carlo calculations of Grebenev and Sunyaev (1988a, 1988b).

However, a weakness of the model is revealed by the shape of the 847 keV line as observed on day 613 by the GRIS experiment (Tueller et al. 1990). Until now, no one has been able to explain the slight red shift and the large width of the line (fig. 13).

This failure probably marks the limits of spherically symmetric models and illustrates the necessity of coupling the transfer code with a three-dimensional simulation of envelope mixing and clumping. Indeed, mixing in the ejecta is

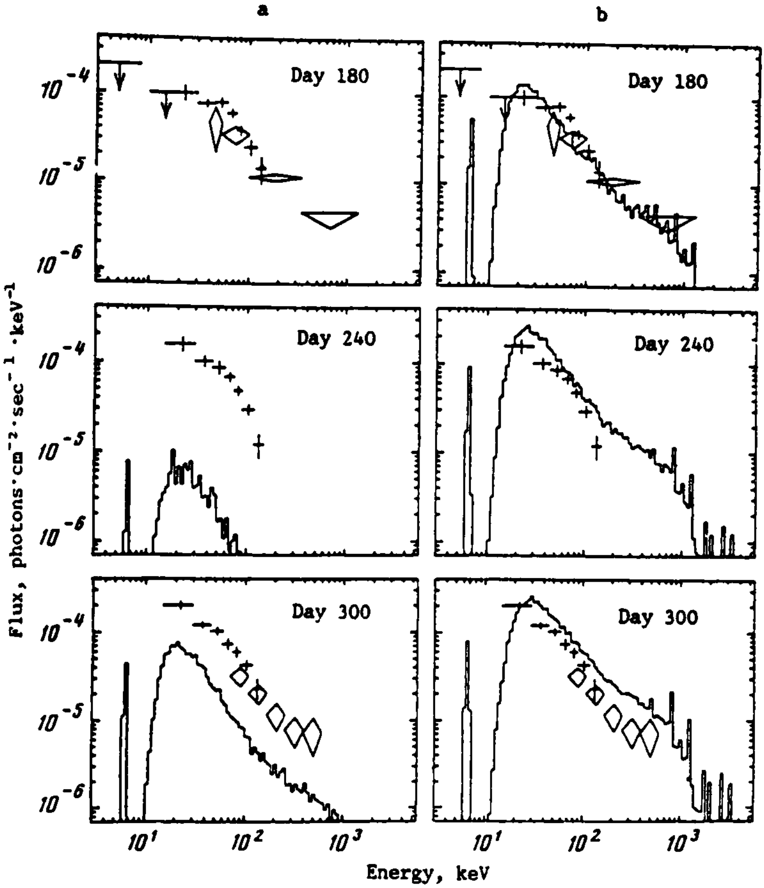

Fig. 11. X-ray spectra at different times without and with internal mixing of ^{56}Co (Sunyaev et al. 1988). This figure clearly illustrates the effect of mixing [a) without, b) with].

conspicuous not only from the early emergence of x-rays (Donati et al. 1987) and γ-ray lines (Matz et al. 1988) (fig. 9) but also from the intensity and the width of the infrared lines (Erikson et al. 1988; Witteborn et al. 1989; Bouchet 1990). It is also implied, in an indirect manner, by the smoothness of the early light curve (Arnett et al. 1989; Shigeyama and Nomoto 1990).

The admixture of ^{56}Co in the outer layers plays a double role:

(i) It serves as a source of hard photons at low optical depth for subsequent comptonization.

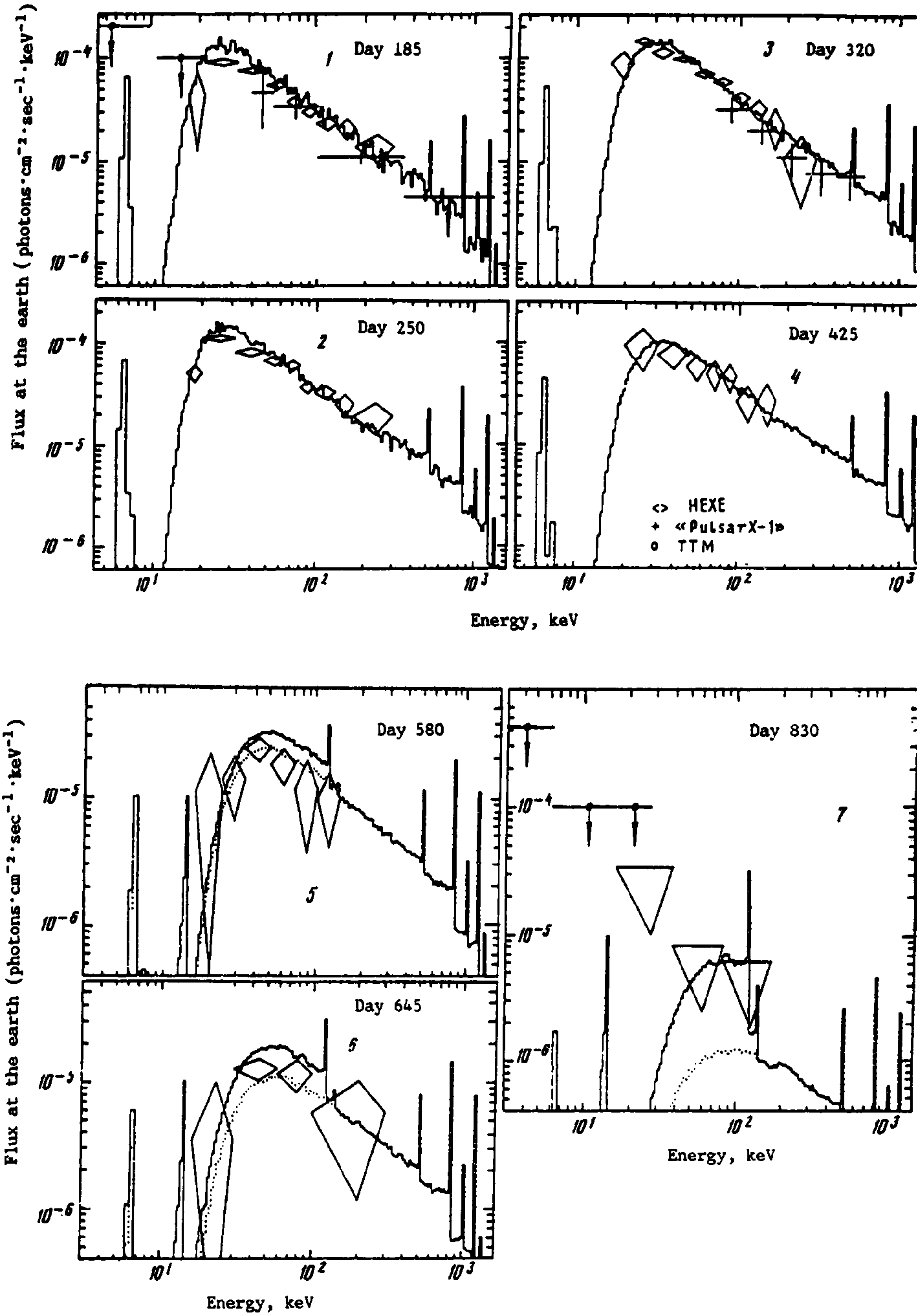

Fig. 12. X-ray spectra at different times (Sunyaev et al. 1990). The data points are from the Roentgen observatory, and the fits are based on the Monte-Carlo calculations of Grebenev and Sunyaev. The ^{56}Co contribution is shown by the dotted line. The 57/56 ratio is taken as twice solar.

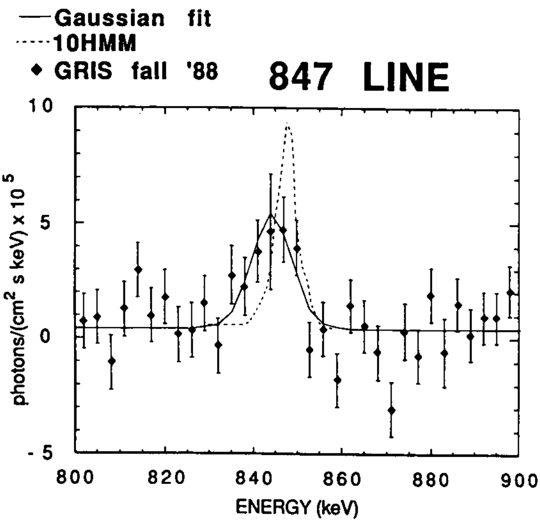

Fig. 13. The 847 keV line profile on day 613 from the GRIS experiment (Tueller et al. 1990). The solid line is a gaussian fit of the data and the dashed line is the predicted profile from the 10HMM model of Woosley and collaborators.

(ii) It significantly increases the envelope metallicity and thus enhances photoabsorption.

Progress in numerical calculations in two or three dimensions is impressive (Arnett, Fryxell, and Müller 1990) but they only cover the very early phases of expansion. Thus, at the moment, the mixing prescriptions used by the various authors have a rather ad-hoc character.

2.1.1. Fit of the light curve

The bolometric light curve is defined as the change of the total luminosity integrated over the whole electromagnetic spectrum. Practically, in our case, it can be split into a low energy part, from radio to UV, and a high energy part, from soft x-rays to γ-rays. The radio and UV flux being unsignificant in the energy budget at the times of interest (Bouchet et al. 1990), thus, the energy output of the supernova is $L_{SN} = L_{IRO} + L_{x,\gamma}$ (IR, O, x, and γ stand for infrared, optical, x and gamma fluxes). The late evolution of L_{IRO} is a clue to the underlying physical processes at work – either radioactivity or electromagnetic emission from a central source, or both.

The brightness decreased by a factor of $\simeq$ 10000 from April 1987 to day $\simeq$ 1000. At peak, it reached $\simeq$ 200000 $L_{\odot}$. L_{IRO} up to day 600 is of exceptional quality due to the high luminosity of the object, and is nicely explained by the radioactive model (e.g. Shigeyama et al. 1988). Pieced together, the various spectral bands lead to the light curve presented on fig. 14.

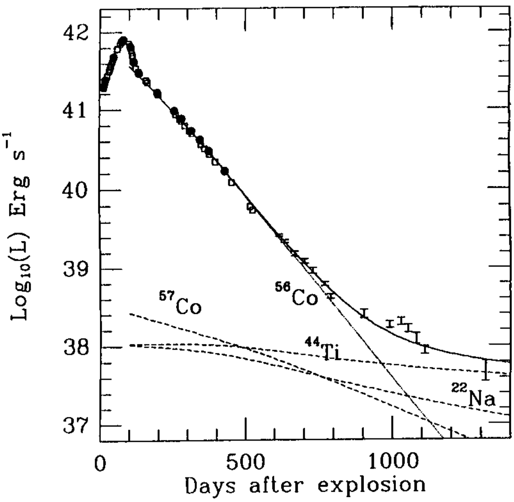

Fig. 14. Bolometric light curve with its radioactive components (Bouchet et al. 1990). The mass of ^{56}Co, ^{57}Co, ^{44}Ti, and ^{22}Na are respectively 0.069, 2.5×10^{-3}, 2×10^{-3}, and $6\times10^{-5}M_\odot$. The theoretical curves are from the model of Woosley, Pinto, and Hartmann (1989).

By day $\simeq$ 500, an important event had occurred: the efficient formation of dust grains (Danziger et al. 1990; Lucy et al. 1989; Bouchet 1990). Beyond this date, infrared emission due to grains is overwhelming. From day $\simeq$ 600 to day 700, the IR contribution to the IRO flux amounts to 80%. Thus, an accurate determination of L_{IRO} requires precise observations in the 5 to 20 micron band, accessible from ground based telescopes; and also a daring extrapolation to the far infrared region (Suntzeff et al. 1990; Bouchet et al. 1990). After day 900, SN 1987a radiates mainly in the IR, but the flux is relatively weak by present standards and achieving good photometry is a difficult task. It is annoying that the fluxes reported from 10 to 19 microns by ESO (Bouchet et al. 1990) are significantly higher than that of CTIO (Suntzeff et al. 1990). The difference between the two sets of data is the more pronounced for days 991 and 1030. In spite of detailed analyses concerning the telescope apertures, the IR echo, and the width of the filters, the difference

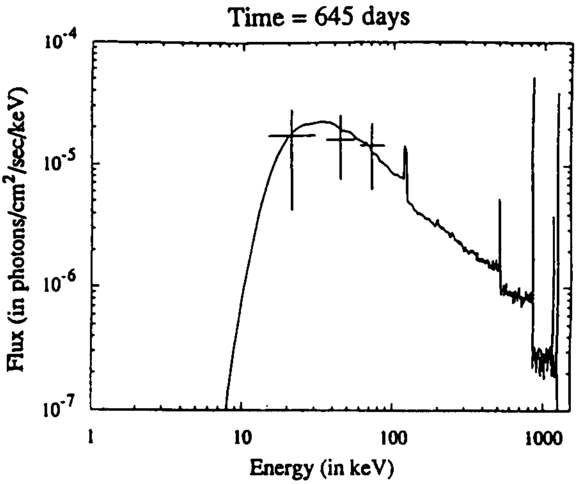

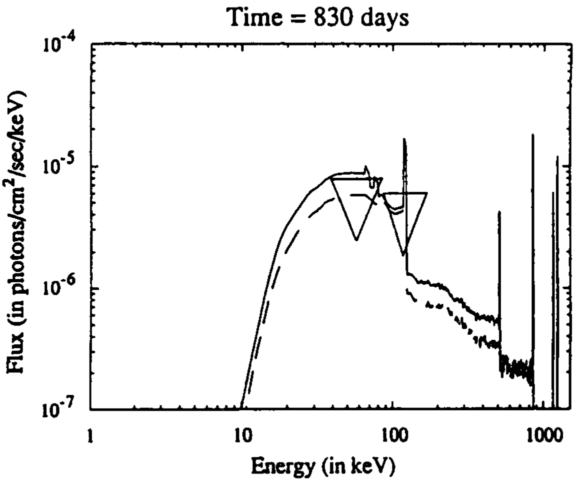

Fig. 16. X-ray spectra obtained with the same set of parameters as those used in fig. 15.

of pure radioactivity. If real, the excess emission would be due to a time varying source embedded within the remnant. The luminosity in its high state would be about 8.5×10^{37} ergs/s (Bouchet et al. 1990), which is close to the Eddington luminosity of a spherically accreting neutron star. However, there is no good reason to believe that a newly born neutron star would be a favorable site of accretion. Certain observers think that the contrary may be true (Bignami, private communication).

2.1.2. Astrophysical consequences

We have seen that the bulk of the light curve can be explained at the expense of a huge production of ^{44}Ti compared with the prediction ($2.8 \times 10^{-3} M_\odot$ instead of $1.4 \times 10^{-4} M_\odot$). Is this solution viable?

This explanation is at variance with theoretical predictions which lead to a quasi-solar production ratio and could lead to a marked overabundance of ^{44}Ca with respect to ^{56}Fe in the solar system material. But this argument is not decisive, since many ways out are still open. One can imagine for instance, that as far as nucleosynthesis is concerned, SN 1987a is not a typical SN II. Alternatively, it could be imagined that in the course of the galactic evolution, type Ia supernovæ would dilute the ^{44}Ti excess originating from SN II. A more serious difficulty comes from the non-detection, up until now, of titanium decay lines in the galactic plane. Indeed, $^{44}\text{Ti} \rightarrow {}^{44}\text{Sc} \rightarrow {}^{44}\text{Ca}$ gamma rays are considered tracers of unknown SN II remnants which could be discovered everywhere in the Milky Way with moderately sensitive detectors, allowing accurate determination of their galactic rate and distribution. If every core collapse supernova (SN II and possibly SN Ib) in the galaxy, with an estimated recurrence time on the order of one per century, produced as much ^{44}Ti as SN 1987a, there should always be at least one strong source of γ-ray lines at 68, 78, and 1156 keV ($\simeq 3 \times 10^{-3}$ photon/cm^2/s for a distance of 10 kpc). No evidence was found for such emission from a point source anywhere in the galactic plane, using a 1σ upper limit of 8.3×10^{-5} photon/cm^2/s (Mahoney et al. 1991). A possible way out is to assume that only massive stars of Type O, like Sanduleak-69202, produce 2 to $3 \times 10^{-3} M_\odot$ of ^{44}Ti; in other words that SN 1987a belongs to an infrequent SN class. For instance, the total number of O stars ($\simeq 2.3 \times 10^4$) and their weighted average age ($\simeq 8 \times 10^6$ years) imply a birth (death) rate of about 0.3 per century. The probability that HEAO 3 would have observed a point source with these characteristics is only on the order of 50% (from fig. 2 of Mahoney et al. 1991).

In conclusion, before deciding that theoretical revisions of the scheme of explosive nucleosynthesis are necessary, and/or that SN 1987a is an atypical supernova, we ought to be certain that some 4×10^{30} g of ^{44}Ti *have been* explosively synthesized and ejected by SN 1987a itself. The best verification would be detection by gamma-ray experiments of an enhanced emission ($\simeq 10^{-4}$ photon/cm^2/s) at 68 and 78 keV from SN 1987a. This is a primary objective of the SIGMA and GRO space missions and for the next generation of gamma-ray spectrometers (integral or NAE).

2.1.3. What about a central source?

The latest optical and infrared observations have been used to obtain an upper limit of 8.5×10^{37} erg/s (with possible variations of $\simeq 10\%$ around this mean value) on the integrated luminosity of a hypothetical central source (Bouchet et al. 1990). Thus, the question remains open: Is the remnant presently powered by ^{44}Ti decay, by the rotation of a magnetized object, or by accretion onto a dense star? This remains a topic for future investigation.

Besides monitoring the FIR light curve, which is a particulary difficult task, decisive observations should be made at energies characteristic of the ^{44}Ti decay lines. If emission is not detected by SIGMA, GRO, and future experiments, the radioactive solution will be abandoned. On the other hand, the search for hard x-rays from the putative remnant star should begin to bear fruit around 50 keV in a few years since it is buried more deeply in the ejecta than the radioactive sources (fig. 17).

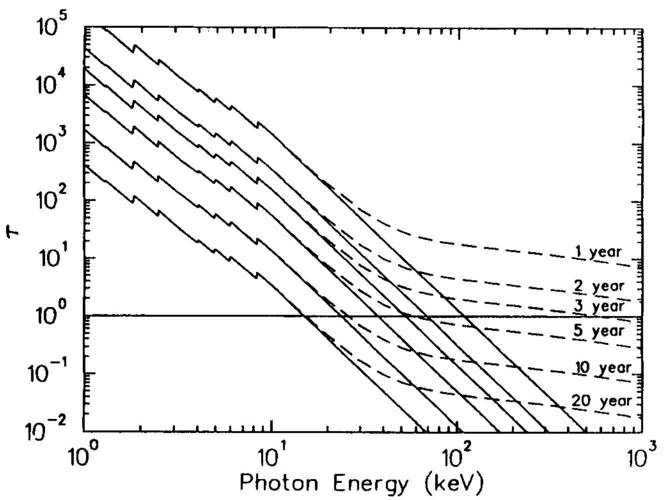

Fig. 17. Optical depth to the center at different energies and various times from The, Burrows, and Bussard 1990 (solid line: photoelectric, dashed line: total). $\tau = 1$ indicates the transparency time at each energy.

In summary, optical and infrared observations are becoming increasingly difficult, and should be supplemented by γ-ray line measurements at 68 and 78 keV in order to qualify or rule out the radioactive hypothesis. Hard x-ray measurements in the 10 to 100 keV band would be most suitable to discover the central source. Attempts have been made to predict the emergent spectrum by setting at the center of the ejecta neutron stars with different types of x-ray emission (Crab pulsar, Her X1, Cyg X1) (Mastichiadis et al. 1988, 1989; Woosley, Pinto and Hartmann 1989).

2.2. Gamma ray lines from other supernovæ

In the exponential battle between activity and transparency, SN Ia (Type Ia supernovae), which have low mass and high expansion velocity are favoured. Burrows and The (1990), using the W7 model of Nomoto et al. (1984), have compared the gamma-ray line luminosity to the typical blue luminosity of a typical SN Ia (see fig. 18). It appears that the total gamma-ray luminosity overcomes the total optical luminosity a dozen days after maximum blue light.

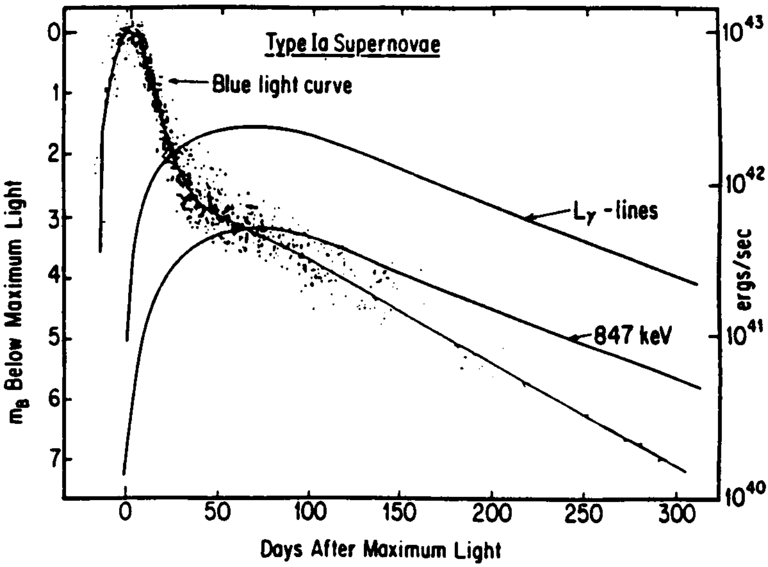

Fig. 18. Blue and gamma light curves of a typical SN Ia.

Due to the rapid thinning out of the object, the ^{56}Ni lines show up at a possible observable level (2 to 5 $\times$ 10^{-4} photon/cm^2/s at 1 Mpc), but rapidly disappear with a mean lifetime of 8.8 days. The exceptional intensity of the 847 keV line emission consecrates these objects as main targets of the gamma-ray emissions. Indeed, the sensitivity of the instruments gives promise of an observation of an SN Ia of up to about 3 Mpc (SIGMA), 4 Mpc (GRO), or 10 Mpc (NAE/INTEGRAL) (Burrows 1991a, 1991b).

The prospects are less favorable concerning the outcome of the Wolf-Rayet explosions. These stars are residues of massive objects that have been victims of heavy mass loss due to stellar wind, or Roche lobe overflow when involved in a close binary system (for a review see Chiosi and Maeder 1986).

Due to its large mass at explosion (say 18 $M_{\odot}$), SN 1987a would appear dimmer than a typical SN Ib, which are considered to be the result of an explosion of light (say 4 $M_{\odot}$) WR stars (Ensman and Woosley 1988; Shigeyama et al. 1990). Once again, the trend is easy to understand: those supernovæ that have lighter envelopes (the lightest progenitors), higher expansion speeds (lower masses at the same explosion energy), and higher radioactive yields are brightest at 847 keV; they peak earlier (80 days for a SN Ia compared with 400 days for SN 1987a and 200 days for a SN Ib), and are considerably brighter. NAE or INTEGRAL would not be sensitive enough to observe supernovæ of this kind at 1 Mpc. In this scheme, SN Ib occupy the middle positions, their intensity is heavily dependent on the extent of internal mixing, as indicated by the different curves shown in fig. 19, which correspond to

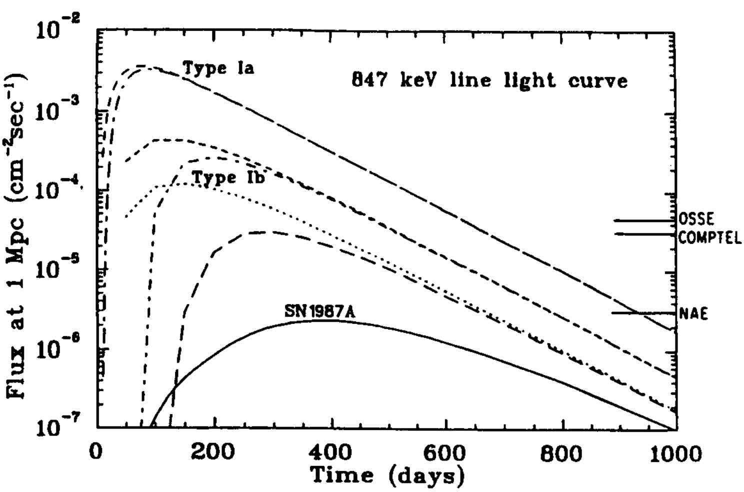

Fig. 19. Calculated gamma-ray emission of a SN Ia (Burrows and The 1990), SN 1987a (The, Burrows and Bussard 1990), and an exploding WR star (The, Clayton, and Burrows 1990) located at 1 Mpc using different mixing procedures.

extreme cases (no mixing at all, or on the contrary, total mixing). More elaborate calculations are underway. For instance, Rayleigh-Taylor instabilities of exploding helium stars (3.3 and 4 $M_{\odot}$) are being explored by Shigeyama et al. (1990).

The interpretation of the hard x-ray spectra of aging supernovæ is more subtle, and in particular that of SN Ia, as shown by Burrows and The (1990). Due to the devastating results of the photoelectric effect, the evolution of the luminosity in the hard x-ray band is very sensitive to composition and density profiles of the outermost layers. This, in turn is conditioned by the damping of the deflagration wave at the end of its path (see fig. 20). The observation of x-ray emissions in the range 10 to 100 keV, if prompt enough, would allow clear distinction of different models of the same object. For instance, on day 10 the predicted continuum flux would differ by several orders of magnitude.

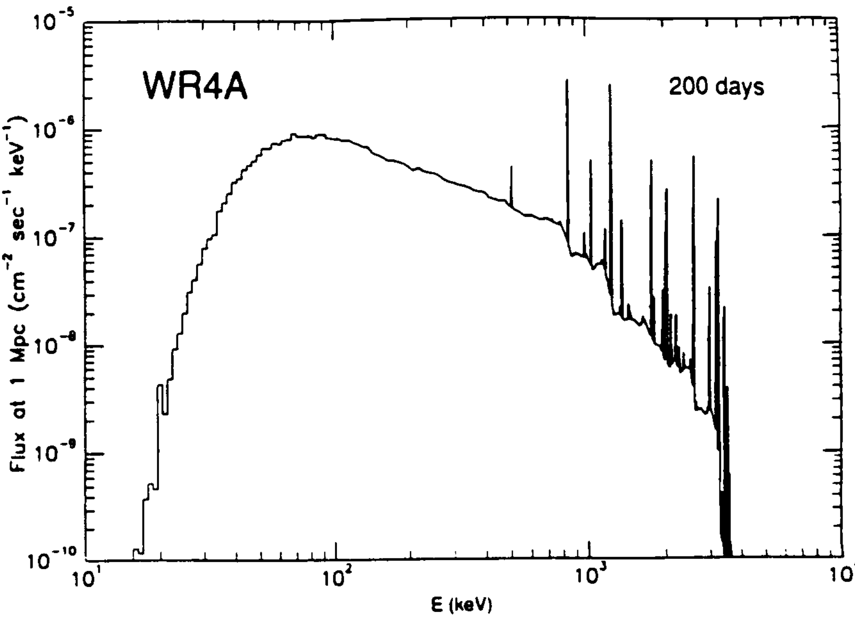

Fig. 20. Predicted spectrum of an exploding WR star located at 1 Mpc at day 200.

3. Conclusion

In Part I of this course, we presented the main theoretical method used to treat gamma-ray transfer in the expanding envelope of supernovæ affected by strong density, velocity, and composition gradients, that is, the Monte-Carlo simulation code.

In Part II, we discussed various applications of this method to SN 1987a, and showed that it offers excellent diagnostics for the autopsy of exploded stars.

SN 1987a, the most spectacular stellar event in several centuries, has received deserved attention by gamma-ray observers. The emergence of its gamma-ray lines is probably the clearest consequence of prompt nuclear evolution within the shocked stellar interior. Thus, the Magellanic supernova has definitively established the power of nuclear gamma-ray line astronomy. Thanks to SN 1987a and the detection of nuclear gamma-ray lines at 847 keV and 1238 keV from radioactive ^{56}Co, explosive nucleosynthesis is leaving the realm of pure speculation and entering the world of observable phenomena. With its light envelope, this supernova of modern time provided us with a unique chance to observe the decay lines of ^{56}Co which carry precise information on the abrupt structural and nuclear changes that occur just before and just after the disruption, as well as an opportunity to observe the position of the frontier which separates the infalling material from the ejected matter. Most astrophysicists in the field, however, would argue that a completely satisfactory theoretical model of the supernova process does not yet exist. Thus, further work is required.

Concerning the late light curve, we still don't know if the weak interaction (primarily β decay of ^{44}Ti) dominates the electromagnetic one due to a central object, like a pulsar or an accreting neutron star. Since the main radioactivity, that of ^{56}Co, is now extinct, it is now time to search for a long lasting radioactive emission (for instance that of ^{44}Ti) since the ejecta is now quasi-transparent to gamma-ray lines, but it is probably still opaque to any lower energy photons which originate from the central source. Is ^{44}Ti the last radioactive chance for the supernova to survive a while? Nucleosynthesis experts do not think so, but the issue is so important that it is worth checking observationally (Cassé, Lehoucq and Cesarsky 1991).

More generally, the radioactivity of supernovæ of different kinds should manifest itself by the shape of their light curves and by a strongly evolving hard photon spectrum (see the beautiful summaries of Sutherland 1990; and Burrows, 1991a, 1991b). The x-ray continuum, together with the discrete features superimposed on it, should provide a wealth of data on the following:

the nature of the progenitor; the mass of the ejecta, its density, velocity and composition profiles; and principally on the explosion energy.

To summarize, the energy, shape, and evolution of gamma-ray lines carry precious information about the physical conditions and processes at work during the brief and dramatic episode that marks the end of the stellar history. High energy diagnostics are becoming a fundamental method for comparing observations to theoretical models. Gamma-ray lines from radioactivity will be a prime target for present and future generations of gamma-ray telescopes. The SIGMA and GRO missions, hopefully followed by the NAE satellite, will open a new era in the understanding of stellar explosions.

Acknowledgements

We express our gratitude to Peter Sutherland, Ken Nomoto and Masa-aki Hashimoto for their generous collaboration. Nicolas Prantzos is acknowledged for his pertinent remarks. This work has been done under the auspices of PICS 18. We thank the members of the Institut d'Astrophysique de Paris for their hospitality.

4. Appendix

4.1. Notation

ν	photon frequency
$x = \frac{h\nu}{mc^2}$	dimensionless energy of the photon
N_e	electron density in the envelope
R	radius of the envelope
σ_T	Compton cross section
$\sigma_c(x)$	Klein-Nishina cross section
$\sigma_{tr}(x)$	transport cross section
τ_0	Thomson radial optical depth
θ	angle of diffusion
$D(x)$	diffusion coefficient
t_d	characteristic diffusion time
$u(x_0, x)$	number of scattering needed to reached energy x starting from an initial energy x_0
$u_{eff}(x_0, x)$	time along photon trajectory in unit of t_d
$\epsilon(x)$	dimensionless energy lost per diffusion
$P(u)$	density of probability of escape
I_0	source line function
$I_\nu(x)$	spectral density of the observed spectrum

4.2. Fundamental constants and units

Planck constant	$h = 6.626 \times 10^{-34}$ J $\cdot$ s^{-1}
Speed of light	$c = 2.99792458 \times 10^8$ m $\cdot$ s^{-1}
Mass of the electron	$m_e = 9.109 \times 10^{-31}$ kg
Fine structure constant	$\alpha = \frac{1}{137.036}$
Classical radius of the electron	$r_e = 2.818 \times 10^{-15}$ m
Thomson cross section	$\sigma_T = \frac{8\pi}{3} {r_e}^2$
Light year	ly $= 9.461 \times 10^{15}$ m
Parsec	pc $= 3.26$ ly
Mass of the Sun	$M_\odot = 1.99 \times 10^{30}$ kg
Luminosity of the Sun	$L_\odot = 3.90 \times 10^{26}$ J $\cdot$ s^{-1}
Electron-volt	eV $= 1.602 \times 10^{-19}$ J
Unit of energy in CGS	erg $= 10^{-7}$ J

References

Akhiezer, A.I. and V.B. Berestetskiy, 1981. "Quantum Electrodynamics," Moscow Nauka.

Ambwani, K. and P. Sutherland. 1988. Ap. J., 325, 820.

Arnett, W.D., 1988. Ap. J., 331, 377.

Arnett, W.D., J.N. Bahcall, S.E. Kirschner, and S.E. Woosley. 1989. Ann. Rev. Astr. Astrophys., 7, 629.

Arnett, W.D., B.A. Fryxell, and E. Müller. 1990. Ap. J. Letters, 341, L63.

Arnould, M. and N. Prantzos. 1990. in "Chemical and Dynamical Evolution of Galaxies," eds F. Ferrine, J. Franco and F. Matteuci.

Benz, W. and F.K. Thielemann. 1990. Ap. J. Letters, 348, L17.

Blumenthal, G.R. and R.J. Gould. 1970. Rev. Mod. Phys., 42, 237.

Bodansky, D., D.D. Clayton, and W.A. Fowler. 1968. Phys. Rev. Letters, 20, 161.

Bouchet, P., I.J. Danziger, and L.B. Lucy. 1990. submitted to Astron. J.

Bouchet, P., 1990. Thesis, Université de Paris VII.

Brown, B.L. and M. Leventhal. 1987. Ap. J., 319, 637.

Burbidge, E.M., G.R. Burbidge, W.A. Fowler, and F. Hoyle. 1957. Rev. Mod. Phys., 29, 547.

Burrows, A. and L.S. The. 1990. Ap. J., 360, 626

Burrows, A., 1991a. in the proceedings of the ESO/EIPC Workshop "SN 1987A and other supernova," Marciana Marina, Isola d'Elba, September 17–22, 1990.

Burrows, A., 1991b. to be published in the proceedings of the International Symposium on "Gamma-Ray Line Astrophysics," Saclay, France, December 10–13, 1990.

Bussard, R.W., R. Ramaty. and R. Drachmann, 1979. Ap. J., 228, 928.

Bussard, R.W., A. Burrows, and L.S. The. 1989. Ap. J., 341, 401.

Cassé, M., R. Lehoucq, and C.J. Cesarsky. 1991. to be published in the proceedings of the International Symposium on "Gamma-Ray Line Astrophysics," Saclay, France, December 10–13, 1990.

Chan, K.W. and R.E. Lingenfelter. 1987. Ap. J. Letters, 318, L51.

Chiosi, C. and A. Maeder. 1986. Ann. Rev. Astron. Astrophys., 24, 329.

Chevalier, R.A., 1976. Ap. J., 207, 872.

Clayton, D.D., S.A. Colgate, and G. Fishmann. 1969. Ap. J., 155, 75.

Clayton, D.D., 1973. in "Gamma Ray Astrophysics," ed. F.W. Stecker and J. Trombka, NASA Spec. Pub. 339, p. 263.

Clayton, D.D., 1974. Ap. J., 188, 155.

Clayton, D.D., 1982. in "Essays in Nuclear Astrophysics," eds C.A. Barnes, D.D. Clayton and D.N. Schramm, Cambridge University Press, p. 401.

Cook, W.R. et al. 1988. Ap. J. Letters, 334, L87.

Danziger, I.J., L.B. Lucy, P. Bouchet, and C. Gouiffes. 1990. in "Supernovæ," Santa-Cruz Workshop, July 10–22, 1989. ed S.E. Woosley, Springer-Verlag.

Donati, T. et al. 1987. Nature, 330, 230.

Ebisuzaki, T. and N. Shibazaki. 1988a. Ap. J., 328, 699.

Ebisuzaki, T. and N. Shibazaki. 1988b. Ap. J. Letters, 327, L5.

Ensmann, L.M. and S.E. Woosley. 1988. Ap. J., 333, 754.

Erikson, E.F. et al. 1988. Ap. J. Letters, 330, L9.

Fu, A. and W.D. Arnett. 1989. Ap. J., 340, 414.

Gehrels, N., C.J. McCallum, and M. Leventhal. 1987. Ap. J. Letters, 320, L19.

Grebenev, S.A. and R.A. Sunyaev. 1987. Sov. Astron. Letters, 13, 397.

Grebenev, S.A. and R.A. Sunyaev. 1988a. Sov. Astron. Letters, 14, 288.

Grebenev, S.A. and R.A. Sunyaev. 1988b. Sov. Astron. Letters, 14, 452.
Hachisu, I., T. Matsuda, K. Nomoto, and T. Shigeyama. 1990. Ap. J. Letters, 358, L57.
Hashimoto, M., K. Nomoto, and T. Shigeyama. 1989. Astron. Astrophys., 210, L5.
Hayakawa, S., 1969. "Cosmic Ray Physics," Wiley Interscience.
Kumagai, S., M. Itoh, T. Shigeyama, K. Nomoto, and J. Nishimura. 1988. Astron. Astrophys., 197, L7.
Kumagai, S., M. Itoh, T. Shigeyama, K. Nomoto, and J. Nishimura. 1989. Ap. J., 345, 412.
Lingenfelter, R.E. and R. Ramaty. 1978. Physics Today, 31, 40.
Lehoucq, R., M. Cassé, and C.J. Cesarsky. 1989. Astron. Astrophys., 224, 117.
Lehoucq, R., M. Cassé, and C.J. Cesarsky. 1991. in the proceedings of the ESO/EIPC Workshop "SN 1987A and other supernova," Marciana Marina, Isola d'Elba, September 17–22, 1990.
Leising, M.D., 1988. Nature, 332, 516.
Leising, M.D. and G.H. Share. 1990. Ap. J., 357, 638.
Lucy, L.B., I.J. Danziger, C. Gouiffes, and P. Bouchet. 1989. in "Lecture Notes in Physics," IAU Colloquium 120, ed. M. Moles and J. Melnick, Springer-Verlag.
McCray, R., J.M. Shull, and P. Sutherland. 1987. Ap. J. Letters, 317, L73.
Mahoney, M.D. et al. 1988. Ap. J. Letters, 334, L81.
Mahoney, W.A., J.C. Ling, W.A. Wheaton, and J.C. Hig published in the proceedings of the International Symposium on "Gamma-Ray Line Astrophysics," Saclay, France, December 10–13, 1990.
Mastichiadis, A., H. Ögelman, and J.G. Kirk. 1988. Astron. Astrophys., 201, L19.
Mastichiadis, A., N. Kyfalis, and J. Ventura. 1989. Astron. Astrophys., 208, L11.
Matz, S.M. et al. 1988. Nature, 331, 416.
Morrison, R.L. and D. McCammon. 1983. Ap. J., 270, 119.
Müller, E., B. Fryxell, and W.D. Arnett. 1989. Astron. Astrophys., 220, 167.
Nomoto, K., F.K. Thielemann, and K. Yokoi. 1984. Ap. J., 286, 664.
Nomoto, K., T. Shigeyama, S. Kumagai, and M. Hashimoto. 1988. Proc. Astr. Soc. Austr., 7, 490.
Nomoto, K. et al. 1991. to be published in the proceedings of the International Symposium on "Gamma-Ray Line Astrophysics," Saclay, France, December 10–13, 1990.
Pinto, P.A. and S.E. Woosley. 1988a. Ap. J., 329, 820.
Pinto, P.A. and S.E. Woosley. 1988b. Nature, 333, 534.
Pozdnyakov, L.A., I.M. Sobol, and R.A. Sunyaev. 1983. Astr. Space Phys. Rev. E, V2,189.
Ramaty, R. and R.E. Lingenfelter. 1981. Phil. Trans. R. Soc. Lond. A, 301, 671.
Rank, D.M. et al. 1988. Nature, 331, 505.
Rester, A.C. et al. 1989. Ap. J. Letters, 342, L71.
Sandie, W.G. et al. 1988. Ap. J. Letters, 334, L91.
Schaeffer, R., M. Cassé, and S. Cahen. 1987. Ap. J. Letters, 316, L31.
Shibazaki, N. and T. Ebisuzaki. 1988. Ap. J. Letters, 327, L9.
Shigeyama, T., K. Nomoto, and M. Hashimoto. 1988. Astron. Astrophys., 196, 141.
Shigeyama, T. and K. Nomoto. 1990. Ap. J., 360, 242.
Shigeyama, T., K. Nomoto, T. Tsujimoto, and M. Hashimoto 1990. Ap. J. Letters, 361, L23.
Shull, J.M. and Y. Xu. 1987. in "Supernova 1987a in the LMC," ed. M. Kafatos and A. Michalitsianos, Cambridge University Press, p. 371.
Suess, H.E. and H.C. Urey. 1956. Rev. Mod. Phys., 28, 53.
Suntzeff, N. B., M.M. Phillips, J.H. Elias, D. Depoy, and A.R. Walker. 1990. IAU Circ. n° 4995.
Sunyaev, R.A. and L.G. Titarchuk. 1980. Astron. Astrophys., 86, 121.
Sunyaev, R.A. et al. 1988. Sov. Astron. Letters, 14, 247.

Sunyaev, R.A. et al. 1990. Sov. Astron. Letters, 16, 403.
Sutherland, P.G., Y. Xu, R. McCray, and R.P. Ross. 1988. in IAU colloquium 108 "Atmospheric Diagnostics of Stellar Evolution," ed. K. Nomoto, Springer Verlag, p. 394.
Sutherland, P.G., 1990. in "Supernovæ," ed. A. Petschek, Springer Verlag.
Teegarden, B.J. et al. 1989. Nature, 339, 122. . The, L.S., A. Burrows, and R. Bussard. 1990. Ap. J., 352, 731.
The, L.S., D.D. Clayton, and A. Burrows. 1991. to be published in "Wolf-Rayet Stars and Interrelations with Other Massive Stars in Galaxies."
Thielemann, F.K., M. Hashimoto, and K. Nomoto. 1990. Ap. J., 349, 222.
Thielemann, F.K., K. Nomoto, and M. Hashimoto. 1990. to appear in "Chemical and Dynamical Evolution of Galaxies," eds F. Ferrini, J. Franco and P. Matteucci.
Truran, J.W., W.D. Arnett, and A.G.W. Cameron. Canadian J. Phys., 1967. 44, 563.
Tueller, J., et al. 1990. Ap. J. Letters, 351, L41.
Varani, G.F., W.P.S. Meikle, J. Spyromilio, and D.A. Allen. 1990. Month. Not. Roy. Astr. Soc., 245, 570.
Veigele, W.J., 1973. Atomic Data Tables, 5, 51.
Weaver, T.A. and S.E. Woosley. 1980. Ann. NY Acad. Sci., 336, 335.
Witteborn, F. et al. 1989. Ap. J. Letters, 339, L9.
Woosley, S.E., W.D. Arnett, and D.D. Clayton D.D. 1973. Ap. J. Suppl., 26, 231.
Woosley, S.E., T. Axelrod, and T.A. Weaver. 1981. Comments in Nucl. Part. Phys., 9, 185.
Woosley, S.E., 1988. Ap. J., 330, 218.
Woosley, S.E., P.A. Pinto, and L. Ensman. 1988. Ap. J., 324, 446.
Woosley, S.E., P.A. Pinto, and D. Hartmann. 1989. Ap. J., 346, 395.
Woosley, S.E. and R.D. Hoffman. 1990. preprint.
Xu, Y., P. Sutherland, R. McCray, and R.R. Ross. 1988. Ap. J., 327, 197.

COURSE XIII

NUCLEOSYNTHESIS IN SUPERNOVAE

FRIEDRICH-KARL THIELEMANN

Harvard-Smithsonian Center for Astrophysics
60 Garden Street
Cambridge MA 02138, USA

KEN'ICHI NOMOTO

Department of Astronomy, Faculty of Science
University of Tokyo
Bunkyo-ku, Tokyo 113, Japan

and

MASAAKI HASHIMOTO

Department of Physics, College of General Education
Kyushu University
Rapponmatsu, Fukuoka 810, Japan

S. Bludman, R. Mochkovitch and J. Zinn-Justin, eds.
Les Houches, Session LIV 1990
Supernovae

Contents

1. Introduction 632
2. Thermonuclear rates and reaction networks 632
   2.1. Thermonuclear reaction rates 632
   2.2. Nuclear reaction networks 635
3. Nucleosynthesis 637
   3.1. Hydrostatic burning stages in presupernova evolution 637
   3.2. Explosive burning 639
      3.2.1. Explosive Si-burning 639
      3.2.2. Explosive O-burning 640
      3.2.3. Explosive Ne, C, and He–burning 641
      3.2.4. r-Process 641
      3.2.5. Explosive H-burning 642
   3.3. Nucleosynthesis in supernovae 642
4. Type Ia supernovae (SNe Ia) 643
   4.1. Explosive burning conditions 643
   4.2. Abundances in ejecta 645
5. Type II supernovae (SNe II) 646
   5.1. Basic features 648
   5.2. Detailed calculations 651
      5.2.1. SN 1987A – a 20 $M_\odot$ star 651
      5.2.2. 13, 15, and 25 $M_\odot$ models 659
   5.3. Gross properties of ejecta 660
6. Averaged SN II abundance yields 667
7. SN I and SN II contributions to nucleosynthesis 671
References 673

1. Introduction

This review concentrates on *nucleosynthesis processes* in supernovae rather than discussing *supernova mechanisms* in general. A brief initial introduction is given to the physics in astrophysical plasmas which governs composition changes. We present the basic equations for thermonuclear reaction rates and nuclear reaction networks. The required nuclear physics input for reaction rates is discussed, that is, cross sections for nuclear reactions, photodisintegrations, electron and positron captures, neutrino captures, inelastic neutrino scattering, and beta decay half lives. After a brief review of hydrostatic burning stages in stellar evolution, we discuss the nucleosynthesis in Type I (SNe I) and Type II (SNe II) supernovae.

Except for SNe Ia, which are explained by exploding white dwarfs in binary systems, all other types (SNe Ib, Ic, II-L and II-P) seem to be linked to the gravitational collapse of massive stars (M>8 $M_\odot$) at the end of their hydrostatic evolution. SN 1987A, the first type II supernova for which the progenitor star was known, is used as an example for nucleosynthesis calculations. Results for 13, 15, 20 and 25 $M_\odot$ stars are presented, as well as the average nucleosynthesis in SNe II, integrated over the progenitor mass range. Finally the complementary role of SNe I and SNe II in galactic nucleosynthesis is discussed.

2. Thermonuclear rates and reaction networks

In this chapter we want to outline the essential features of thermonuclear reaction rates and nuclear reaction networks. This serves the purpose of defining a unified terminology used throughout the review. More detailed discussions can be found in Clayton (1968) and Fowler, Caughlan, Zimmerman (1967).

2.1. Thermonuclear reaction rates

The nuclear cross section for a reaction between target j and projectile k is defined by

$$\sigma = \frac{\text{number of reactions target}^{-1}\text{sec}^{-1}}{\text{flux of incoming projectiles}} = \frac{r/n_j}{n_k v}. \qquad (2.1)$$

The second equality holds for the case that the relative velocity between targets with the number density n_j and projectiles with number density n_k is constant and has the value v. Then r, the number of reactions per cm^3 and sec, can be expressed as $r = \sigma v n_j n_k$. More generally, when targets and projectiles follow specific distributions, r is given by

$$r_{j,k} = \int \sigma |\vec{v}_j - \vec{v}_k| d^3 n_j d^3 n_k. \tag{2.2}$$

The evaluation of this integral depends on the type of particles and distributions which are involved. For nuclei j and k in an astrophysical plasma, obeying a Maxwell-Boltzmann distribution,

$$d^3 n_j = n_j \left(\frac{m_j}{2\pi kT}\right)^{3/2} \exp\left(-\frac{m_j v_j^2}{2kT}\right) d^3 v_j, \tag{2.3}$$

Equation (2.2) simplifies to $r_{j,k} = \langle \sigma v \rangle n_j n_k$. The thermonuclear reaction rates have the form (Fowler, Caughlan, Zimmerman 1967; Clayton 1968)

$$r_{j,k} = \langle \sigma v \rangle_{j,k} n_j n_k$$

$$\langle j, k \rangle := \langle \sigma v \rangle_{j,k} = \left(\frac{8}{\mu \pi}\right)^{1/2} (kT)^{-3/2} \int_0^\infty E \sigma(E) \exp(-E/kT) dE. \tag{2.4}$$

Here μ denotes the reduced mass of the target-projectile system. In astrophysical plasmas with high densities and/or low temperatures, effects of electron screening become highly important. This means that the reacting nuclei, due to the electron background, feel a different Coulomb repulsion than in the case of bare nuclei. Under most conditions (with non-vanishing temperatures) the generalized reaction rate integral can be separated into the traditional expression without screening [eq. (2.4)] and a screening factor (see Salpeter and van Horn 1969; Itoh, Totsuji, Ichimaru 1977; Hansen, Torrie, Veillefosse 1977; Alastuey and Jancovici 1978; Itoh et al. 1979; Ichimaru, Tanaka, Iyetomi 1984; Ichimaru and Utsumi 1984; Thielemann and Truran 1987; Fushiki and Lamb 1987; Itoh et al. 1990; Schramm and Koonin 1990)

$$\langle j, k \rangle^* = f_{scr}(Z_j, Z_k, \rho, T, Y_i) \langle j, k \rangle. \tag{2.5}$$

This screening factor is dependent on the charge of the involved particles, the density, temperature, and the composition of the plasma. Here Y_i denotes the abundance of nucleus i defined by $Y_i = n_i/(\rho N_{\mathrm{A}})$, where n_i is the number density of nuclei per unit volume and N_A is Avogadro's number. At high densities and low temperatures, screening factors can enhance reactions by many orders of magnitude and lead to *pycnonuclear ignition.* In the extreme case of very low temperatures, where reactions are only possible via ground state oscillations of the nuclei in a Coulomb lattice, eq. (2.5) breaks down, because it was derived under the assumption of a Boltzmann distribution (for recent references see Fushiki and Lamb 1987 and Schramm and Koonin 1990).

When in eq. (2.2) particle k is a photon, the relative velocity is always c and quantities in the integral are not dependent on d^3n_j. Thus it simplifies to $r_j = \lambda_{j,\gamma}n_j$, and $\lambda_{j,\gamma}$ results from an integration of the photodisintegration cross section over a Planck distribution for photons of temperature T

$$d^3n_\gamma = \frac{1}{\pi^2(c\hbar)^3}\frac{E_\gamma^2}{\exp(E_\gamma/kT)-1}dE_\gamma$$

$$r_j = \lambda_{j,\gamma}(T)n_j = \frac{\int d^3n_j}{\pi^2(c\hbar)^3}\int_0^\infty \frac{c\sigma(E_\gamma)E_\gamma^2}{\exp(E_\gamma/kT)-1}dE_\gamma. \tag{2.6}$$

There is, however, no direct need to evaluate photodisintegration cross sections, because, due to detailed balance, it can be expressed by the capture cross section for the inverse reaction $l + m \to j + \gamma$ (Fowler, Caughlan, Zimmerman 1967)

$$\lambda_{j,\gamma}(T) = \left(\frac{G_lG_m}{G_j}\right)\left(\frac{A_lA_m}{A_j}\right)^{3/2}\left(\frac{m_ukT}{2\pi\hbar^2}\right)^{3/2}\langle l,m\rangle\exp\left(-Q_{lm}/kT\right). \tag{2.7}$$

This expression depends on the reaction Q-value Q_{lm}, the temperature T, the inverse reaction rate $\langle l,m\rangle$, the partition functions $G = \sum(2J_i + 1)\exp(-E_i/kT)$ and the mass numbers A of the participating nuclei.

A procedure similar to eq. (2.6) is used for electron captures by nuclei. Because the electron is about 2000 times less massive than a nucleon, the velocity of the nucleus is negligible in the center of mass system in comparison to the electron velocity ($|\vec{v} - \vec{v}_e| \approx |\vec{v}_e|$). The electron capture cross section has to be integrated over a Boltzmann, partially degenerate, or Fermi distribution of electrons, dependent on the astrophysical conditions. The electron capture rates are a function of T and $n_e = Y_e\rho N_A$, the electron number density (Fuller, Fowler, Newman 1980, 1982). In a neutral, completely ionized plasma, the electron abundance is equal to the total proton abundance in nuclei $Y_e = \sum_i Z_iY_i$ and

$$r_j = \lambda_{j,e}(T,\rho Y_e)n_j. \tag{2.8}$$

The same authors generalized this treatment for the capture of positrons, which are in a thermal equilibrium with photons, electrons, and nuclei. At high densities ($\rho > 10^{12}$g-cm^{-3}) the size of the neutrino scattering cross section on nuclei ensures that enough scattering events occur to thermalize a neutrino distribution. Then the inverse process to electron capture (neutrino capture) can also occur and the neutrino capture rate can be expressed in a manner similar to eqs. (2.6) or (2.8), integrating over the neutrino distribution (Fuller, Fowler, Newman 1985). Also inelastic neutrino scattering on nuclei can be expressed in this form. The latter can cause particle emission, like that which occurs in photodisintegrations (e.g. Woosley et al. 1990). It is also possible that a thermal equilibrium among neutrinos was established at a different location than at the point where the reaction occurs. In such a case the neutrino distribution can be characterized by a chemical potential and a temperature which is not necessarily equal to the local temperature. Finally, for normal decays, like beta or alpha-decays with half-life $\tau_{1/2}$, we obtain an equation similar to eqs. (2.6) or (2.8) with a decay constant $\lambda_j = ln2/\tau_{1/2}$ and

$$r_j = \lambda_j n_j. \tag{2.9}$$

2.2. Nuclear reaction networks

The time derivative of the number densities of each of the species in an astrophysical plasma (at constant density) is governed by different expressions for r, the number of reactions per cm^3 and sec, as discussed above for different reaction mechanisms which can change nuclear abundances

$$\left(\frac{\partial n_i}{\partial t}\right)_{\rho=const} = \sum_j N_j^i r_j + \sum_{j,k} N_{j,k}^i r_{j,k} + \sum_{j,k,l} N_{j,k,l}^i r_{j,k,l}. \tag{2.10}$$

The reactions listed on the right hand side of the equation belong to the three categories of reactions: (1) decays, photodisintegrations, electron and positron captures, and neutrino induced reactions ($r_j = \lambda_j n_j$); (2) two-particle reactions ($r_{j,k} = \langle j, k\rangle n_j n_k$); and (3) three-particle reactions ($r_{j,k,l} = \langle j, k, l\rangle n_j n_k n_l$), like the triple-alpha process, which can be interpreted as successive captures with an intermediate unstable target (see Nomoto, Thielemann, and Miyaji 1985). The individual N^i's are given by: $N_j^i = N_i$, $N_{j,k}^i = N_i/(N_j!N_k!)$, and $N_{j,k,l}^i = N_i/(N_j!N_k!N_l!)$. The $N_i's$ can be positive or negative numbers and they can specify how many particles of species i are created or destroyed in a reaction. The denominators, including factorials, avoid double counting the number of reactions when identical particles react with each other (for example in the $^{12}C+^{12}C$ or the triple-alpha reaction; for details see Fowler, Caughlan, Zimmerman 1967). To exclude changes in the number densities $\dot{n}_i$, which are due only to expansion or contraction of the gas, the nuclear abundances $Y_i = n_i/(\rho N_A)$ were introduced. For a nucleus with atomic weight A_i, A_iY_i represents the mass fraction of this nucleus; therefore $\sum A_iY_i = 1$. In terms of nuclear abundances Y_i, a reaction network is described by the following set of differential equations

$$\dot{Y}_i = \sum_j N_j^i \lambda_j Y_j + \sum_{j,k} N_{j,k}^i \rho N_A \langle j,k \rangle Y_j Y_k$$
$$+ \sum_{j,k,l} N_{j,k,l}^i \rho^2 N_A^2 \langle j,k,l \rangle Y_j Y_k Y_l. \tag{2.11}$$

Equation (2.11) derives directly from eq. (2.10) when the definition for the $Y_i's$ is introduced. This set of differential equations is solved with a fully implicit treatment. Then the stiff differential equations can be rewritten (see Press et al. 1986, section 15.6) as difference equations of the form $\Delta Y_i/\Delta t = f_i(Y_j(t+\Delta t))$, where $Y_i(t+\Delta t) = Y_i(t) + \Delta Y_i$. In this treatment, all quantities on the right-hand side are evaluated at time $t+\Delta t$. This results in a set of non-linear equations for the new abundances $Y_i(t+\Delta t)$, which can be solved using a multi-dimensional Newton-Raphson iteration procedure. The total energy generation per gram, due to nuclear reactions in time step Δt which changed the abundances by ΔY_i, is expressed in terms of the excess mass $M_{ex,i}c^2$ of participating nuclei (Wapstra, Audi, Hoekstra 1988)

$$\Delta\epsilon = -\sum_i \Delta Y_i N_A M_{ex,i} c^2. \tag{2.12}$$

As noted above, the important ingredients in nucleosynthesis calculations are decay half-lives, electron and positron capture rates, photodisintegrations, neutrino induced reaction rates, and strong interaction cross sections. Beta-decay half-lives for unstable nuclei have been predicted by Takahashi, Yamada, and Kondo (1973); Klapdor, Metzinger, and Oda (1984); Takahashi and Yokoi (1987, also including temperature effects) and more recently with strongly improved quasi-particle RPA calculations (Kratz et al. 1988; Staudt et al. 1989, 1990; Möller and Randrup 1990). Electron and positron capture calculations have been performed by Fuller, Fowler, and Newman (1980, 1982, 1985) for a large variety of nuclei with mass numbers between A=20 and A=60 (they also included neutrino capture rates; for recent revisions see also Takahara et al. 1989 and for heavier nuclei Aufderheide et al. 1990). Rates for inelastic neutrino scattering have been presented by Woosley et al. (1990). Photodisintegration rates can be calculated via detailed balance from the reverse capture rates. Experimental nuclear rates for light nuclei have been discussed in detail in the reviews by Rolfs, Trautvetter, and Rodney (1987), Filippone (1987) and the book by Rolfs and Rodney (1988). The most recent rate compilation is the one by Caughlan and Fowler (1988). Experimental neutron capture cross sections are summarized by Bao and Käppeler (1987). Rates for unstable light nuclei are given by Malaney and Fowler (1988, 1989), Wiescher et al. (1986, 1987, 1988, 1989, 1990) and Thielemann and Wiescher (1990).

For the vast number of medium and heavy nuclei which exhibit a high density of excited states at capture energies, Hauser-Feshbach (statistical model) calculations are applicable. The most recent compilations were provided by Holmes et al. (1975), Woosley et al. (1979), and Thielemann, Arnould, Truran (1987). For a detailed discussion of the methods involved and neutron capture cross sections for heavy unstable nuclei, see section 3.4 and the appendix in Cowan, Thielemann, Truran 1991.

3. Nucleosynthesis

Nucleosynthesis calculations can in general be classified into two categories: (1) nucleosynthesis during hydrostatic burning stages of stellar evolution on long time scales, and (2) nucleosynthesis in explosive events (with different initial fuel compositions, specific to the event). In the following we want to briefly discuss reactions of importance for both conditions and the major burning products.

3.1. Hydrostatic burning stages in presupernova evolution

The main hydrostatic burning stages and most important reactions are:

H-burning. There are two alternative reaction sequences; the different pp-chains which convert ^{1}H into ^{4}He, initiated by ^{1}H(p,e^+)^{2}H, and the CNO cycle which converts ^{1}H into ^{4}He by a sequence of (p,γ) and (p,α) reactions on C, N, and O isotopes and subsequent beta decays. The CNO isotopes are all transformed into ^{14}N, since the reaction ^{14}N$(p,\gamma)^{15}$O is the slowest reaction in the cycle.

He-burning. the main reactions are the triple-alpha reaction ^{4}He$(2\alpha,\gamma)^{12}$C and ^{12}C$(\alpha,\gamma)^{16}$O.

C-burning. ^{12}C(^{12}C, α)^{20}Ne and ^{12}C(^{12}C,p)^{23}Na. Most of the ^{23}Na nuclei will react with free protons via ^{23}Na(p,α)^{20}Ne.

Ne-burning. ^{20}Ne$(\gamma,\alpha)^{16}$O, ^{20}Ne(α,γ) ^{24}Mg and ^{24}Mg$(\alpha,\gamma)^{28}$Si.

O-burning. ^{16}O(^{16}O,α)^{28}Si, ^{16}O(^{16}O,p)^{31}P, and ^{16}O(^{16}O,n)^{31}S(β^+)^{31}P. Similar to carbon burning, most of the ^{31}P is destroyed by a (p,α) reaction to ^{28}Si.

Si-burning. Si-burning is usually initiated by photodisintegration reactions, which then provide particles for capture reactions at temperatures in excess of 3×10^9K. Si-burning ends in an equilibrium abundance distribution around Fe (thermodynamic equilibrium). In such an equilibrium (also denoted nuclear statistical equilibrium, NSE) the abundance of each nucleus is governed only by the temperature T, density ρ, its nuclear binding energy B_i and statistical weight $G_i = \sum_j (2J_j^i + 1)\exp(-E_j^i/kT)$

$$Y_i = (\rho N_A)^{A_i-1}\frac{G_i}{2^{A_i}}A_i^{3/2}\left(\frac{2\pi\hbar^2}{m_u kT}\right)^{\frac{3}{2}(A_i-1)} \exp(B_i/kT)Y_{\rm p}^{Z_i}Y_{\rm n}^{N_i}. \qquad (3.1)$$

This equation is derived from the relation between chemical potentials (Maxwell-Boltzmann distributions) in a thermal equilibrium ($\mu_i = Z_i\mu_p + N_i\mu_n$), where the subscripts n and p stand for neutrons and protons.

s-process. the slow neutron capture process leads to the build-up of heavy elements during core and shell He-burning, where (through a series of neutron captures and beta decays) starting on existing heavy nuclei around Fe, nuclei up to Pb and Bi can be synthesized. The neutrons are provided by a side branch of He-burning, ^{14}N$(\alpha,\gamma)^{18}$F$(\beta^+)^{18}$O(α,γ) ^{22}Ne(α,n)^{25}Mg. An alternative stronger neutron source in He-shell flashes is the reaction ^{13}C(α,n)^{16}O, which requires admixture of hydrogen and the production of ^{13}C via proton capture on ^{12}C and a subsequent beta-decay.

An extensive overview covering the major and minor reaction sequences in all burning stages from helium to silicon burning is given in Arnett and Thielemann (1985), and Thielemann and Arnett (1985). For less massive stars which burn at higher densities, electron captures are already important in O-burning and lead to a smaller Y$_e$ or larger neutron excess $\eta = \sum_i (N_i - Z_i)Y_i = 1 - 2Y_e$. For a general overview of the s-process see Käppeler et al. (1982), Mathews and Ward (1985), and Käppeler, Beer, and Wisshak (1989).

Most reactions in hydrostatic burning stages proceed through stable nuclei. This is simply explained by the long time scales involved. For a 25 $M_\odot$ star, which is relatively massive and therefore experiences quite short burning phases, Weaver and Woosley (1980) quote the following values: H-burning 7×10^6 years, He-burning 5×10^5 y, C-burning 600 y, Ne-burning 1 y, O-burning 180 days, Si-burning 1 d. Because all these burning stages are long compared to beta-decay half-lives, nuclei can decay back to stability before undergoing the next reaction (with a few exceptions of very long-lived unstable nuclei).

3.2. Explosive burning

Extensive calculations of explosive carbon, neon, oxygen, and silicon burning, appropriate for supernova explosions, were performed in the late 1960s and early 1970s, with detailed discussions about the expected abundance patterns (for a general reference see Woosley, Arnett, and Clayton 1973; Truran 1985). Besides minor contributions of ^{22}Ne after He-burning (or nuclei which originate from it in later burning stages), the fuels for explosive nucleosynthesis consist mainly of alpha-particle nuclei like ^{12}C, ^{16}O, ^{20}Ne, ^{24}Mg, or ^{28}Si. Because the timescale of explosive processing is very short (a fraction of a second to several seconds), only few beta decays can occur during the explosive nucleosynthesis event, and heavier nuclei, again with N$\approx$Z, are formed. However, the spread of nuclei around a line of N=Z can be large and many reaction rates on unstable nuclei have to be known. Depending on the temperature, intermediate to heavy nuclei are produced in explosive burning. For $T > 5 \times 10^9$K, essentially all Coulomb barriers can be overcome and the doubly-magic nucleus ^{56}Ni, with the largest binding energy per nucleon for $N = Z$, is formed with a dominant abundance.

3.2.1. Explosive Si-burning

Zones which experience temperatures in excess of 4.0–5.0$\times10^9$K undergo explosive Si-burning. Temperatures beyond 5×10^9K lead to complete Si-exhaustion and produce only Fe-group nuclei. Explosive Si-burning can be divided into three different regimes: incomplete Si-burning, and complete Si-burning with either a normal or an alpha-rich freeze-out. Which of the three regimes is encountered depends on the peak temperatures and densities attained during passage of the shock front (see fig. 20 in Woosley, Arnett, and Clayton 1973; and for applications to supernova calculations fig. 5 in Thielemann, Nomoto, Yokoi 1986, and fig. 5 in Thielemann, Hashimoto, Nomoto 1990). The most abundant nucleus in the normal and alpha-rich freeze-out is ^{56}Ni, in case the neutron excess is smaller than 2×10^{-2}, or Y_e

is larger than 0.49. For the less abundant nuclei final alpha-capture plays a dominant role, transforming nuclei like ^{56}Ni, ^{57}Ni, and ^{58}Ni into ^{60}Zn, ^{61}Zn, and ^{62}Zn in an alpha-rich freeze-out where trace abundances of ^{40}Ca, ^{44}Ti, ^{48}Cr, and ^{52}Fe also remain. At high temperatures in complete Si-burning, before freeze-out or in a normal freeze-out, the abundances are in a full NSE and given by eq. (3.1). An alpha-rich freeze-out occurs generally at low densities when the triple-alpha reaction, transforming ^{4}He into ^{12}C, is not fast enough to keep the He-abundance in equilibrium during fast expansion and cooling in explosive events.

Incomplete Si-burning is characterized by peak temperatures of $4-5\times 10^9$K. Temperatures are not high enough for an efficient bridging of the bottleneck above the proton magic number Z=20 by nuclear reactions. Besides the dominant fuel nuclei ^{28}Si and ^{32}S, we find alpha-nuclei ^{36}Ar and ^{40}Ca most abundant. Partial leakage through the bottleneck above Z=20 produces ^{56}Ni and ^{54}Fe as dominant abundances in the Fe-group. Smaller amounts of ^{52}Fe, ^{58}Ni, ^{55}Co, and ^{57}Ni are also encountered.

3.2.2. Explosive O-burning

Temperatures in excess of roughly 3.3×10^9K lead to a quasi-equilibrium (QSE) in the lower QSE-cluster, which extends over the range 28<A<45 in mass number (Woosley, Arnett, Calyton 1973), but a full NSE with dominant abundances in the Fe-group cannot be attained. The main burning products are ^{28}Si, ^{32}S, ^{36}Ar, ^{40}Ca, ^{38}Ar, and ^{34}S, while ^{33}S, ^{39}K, ^{35}Cl, ^{42}Ca, and ^{37}Ar have mass-fractions of less than 10^{-2}. In zones with temperatures close to 4×10^9K there still exists a contamination by the Fe-group nuclei ^{54}Fe, ^{56}Ni, ^{52}Fe, ^{58}Ni, ^{55}Co, and ^{57}Ni. The abundances in the QSE-cluster are determined by alpha, neutron, and proton abundances. Because electron captures during explosive processing are negligible, the original neutron excess stays unaltered and fixes the neutron to proton ratio (at least for O-burning zones; for exceptions at high densities and temperatures during explosive Si-burning in Type Ia supernovae see chapter 4). Under those conditions the resulting composition is dependent only on the alpha to neutron ratio at freeze-out. Woosley, Arnett, and Clayton (1973) pointed out that with a neutron excess η of 2×10^{-3} the solar ratios of ^{39}K/^{35}Cl, ^{40}Ca/^{36}Ar, ^{36}Ar/^{32}S, ^{37}Cl/^{35}Cl, ^{38}Ar/ ^{34}S, ^{42}Ca/^{38}Ar, ^{41}K/^{39}K, and ^{37}Cl/^{33}S are attained within a factor of 2 for freeze-out temperatures in the range $(3.1-3.9)\times 10^9$K. This is the typical neutron excess resulting from solar CNO-abundances, which are first transformed into ^{14}N in H-burning and then into ^{22}Ne in He-*burning via* $^{14}\mathrm{N}(\alpha,\gamma)^{18}\mathrm{F}(\beta^+)^{18}\mathrm{O}(\alpha,\gamma)^{22}\mathrm{Ne}$. In stars with lower metallicities these ratios will drop accordingly.

3.2.3. *Explosive Ne, C, and He–burning*

The main burning products of explosive neon burning are ^{16}O, ^{24}Mg, and ^{28}Si, synthesized via the reaction sequences ^{20}Ne(γ, α)^{16}O and ^{20}Ne(α, γ) ^{24}Mg(α, γ)^{28}Si, in a manner similar to the hydrostatic case. The mass zones in question have peak temperatures in excess of 2.1×10^9K, and undergo a combined version of explosive neon and carbon burning. Besides the major abundances, mentioned above, explosive neon burning also supplies substantial amounts of ^{27}Al, ^{29}Si, ^{32}S, ^{30}Si, and ^{31}P. In addition, explosive carbon burning contributes in addition the nuclei ^{20}Ne, ^{23}Na, ^{24}Mg, ^{25}Mg, and ^{26}Mg.

Explosive He-burning is characterized by the same reactions as hydrostatic He-burning, producing ^{12}C and ^{16}O. Neutron sources like ^{22}Ne(α, n)^{25}Mg or ^{13}C(α, n)^{16}O, which sustain an s-process neutron flux in hydrostatic burning, were expected to release a large neutron flux under explosive conditions which can even cause an r-process (rapid neutron capture; Truran, Cowan, Cameron 1978; Thielemann, Arnould, Hillebrandt 1979). This did not materialize, however, when employing realistic stellar models (see subsection 3.2.4).

3.2.4. *r-Process*

The operation of an r-process is characterized by the fact that 10 to 100 neutrons per nucleus in the Fe-peak have to be available to form all heavier r-process nuclei by neutron capture. This translates into a neutron excess $\eta = 0.4 - 0.7$. Such a high neutron excess can only by obtained through capture of energetic electrons (on protons or nuclei) which must overcome large negative Q-values. This can be achieved either by degenerate electrons with large Fermi energies, thermal electrons at high temperatures, or a combination thereof. The first requires a compression to densities of 10^{11} to 10^{12}g cm^{-3}, with beta equilibrium between electron captures and β^--decays (Cameron 1989). The second can occur in the "high entropy bubble" beyond the neutrinosphere of delayed SNe II explosions (Woosley and Weaver 1991). Wilson and Mayle (1988) report values of $Y_e = 0.2$, i.e. $\eta = 0.6$ for these mass zones. After the freeze-out of charged particle reactions in matter which expands from an initial high temperature state in NSE, neutron captures will proceed to form heavy nuclei.

A different situation surfaces for maximum temperatures below freeze-out conditions for charged particle reactions with Fe-group nuclei. Then reactions among light nuclei which release neutrons, like (α, n) reactions on ^{13}C and ^{22}Ne, can sustain a neutron flux. The constraint of having 10 to 100 neutrons per heavy nucleus, in order to attain r-process conditions, can then be met by small abundances of Fe-group nuclei. Such conditions are expected when a shock front passes the He-burning shell and enhances the ^{22}Ne(α, n) reaction by orders of magnitude. However, Blake et al. (1981) and Cowan, Cameron and Truran (1983) could show that this neutron source is not strong enough for an r-process in realistic stellar models. Recent research, based on additional neutron release via inelastic neutrino scattering (Epstein, Colgate, and Haxton 1988), also failed to produce neutron densities which are required for such a process to operate (see also Woosley et al. 1990).

The r-process (rapid neutron-capture process) works on principles similar to the s-process by building heavy elements via neutron captures and beta-decays. However, the r-process works on an explosive time scale, with a sudden high density of neutrons. Under these conditions, neutron captures on nuclei are still preferred over beta-decays, even for unstable nuclei out to neutron separation energies of 2.0MeV in each isotopic chain.

3.2.5. Explosive H-burning

There are at least two astrophysical sites where explosive hydrogen burning takes place. Both include compact objects (white dwarfs and neutron stars) and mass transfer of hydrogen-rich material onto their surface. This happens in binary stellar systems with mass overflow from the companion star. The result is that a shell of hydrogen-rich material piles up on the surface of the compact star until the increasing density and temperature at the base of this envelope finally leads to ignition and hydrogen burning, mainly on CNO nuclei. As the ignition happens under degenerate conditions (within the electron gas, where screening of nuclear reactions is highly important), the pressure is dependent only on density and not on temperature. Therefore, energy release from nuclear burning does not result in a pressure increase, which could lead to a stabilizing readjustment of the whole envelope. Instead a thermonuclear runaway occurs, causing explosive ejection of the envelope. Events of this type are observed as novae, when occuring on white dwarfs, and as x-ray bursts, when occuring on neutron stars. We will not discuss explosive hydrogen burning in novae and x-ray bursts in this review but refer to Wallace and Woosley (1981), Wiescher et al. (1986), and Taam (1985).

3.3. Nucleosynthesis in supernovae

In the following chapters we will apply these explosive burning processes to nucleosynthesis calculations in supernovae (SNe) for nuclei with A<70. For a discussion of the explosive production of heavier nuclei in supernovae see Cowan, Thielemann, Truran (1991). There exist many original and review articles about the mechanisms of SNe I and SNe II (e.g. Nomoto, Thielemann, Yokoi 1984; Nomoto 1986; Bruenn 1989; Cooperstein and Baron 1990; Woosley and Weaver 1986ab; Wilson and Mayle 1988; Mayle and Wilson 1990; Bethe 1990; and lectures at this summer school), so that we do not intend to repeat such a discussion here. We rather want to concentrate on the accompanying nucleosynthesis processes. After treating both types of supernova events in chapters 4 and 5, we will concentrate in chapter 6 on SNe II yields, averaged over the mass range of progenitor stars. This is used to understand abundances in low metallicity stars which only experienced SNe II enrichment during early galactic evolution. Chapter 7 includes a comparison of both contributions (SNe I and SNe II) to the enrichment of heavy elements in the galaxy.

One of the major free parameters in stellar evolution, and thus for the presupernova models, is the still uncertain $^{12}C(\alpha, \gamma)^{16}O$ reaction (see Filippone, Humblet, Langanke 1989; Caughlan et al. 1985; Caughlan and Fowler 1988). The calculations, presented in this review, are based on stellar models which employed the rate of Caughlan et al. (1985).

4. Type Ia supernovae (SNe Ia)

4.1. Explosive burning conditions

As discussed in other lectures in this volume, SNe Ia can be explained by central carbon ignition and total disruption of a cold (but not solid) degenerate white dwarf, when such a star exceeds the Chandrasekhar mass via mass transfer in a binary system. This model agrees with the total energetics, light curves and spectra of SNe Ia. The progenitors in the binary system therefore had main sequence masses $M<8M_\odot$ (in order to become white dwarfs during their evolution). In the following sections we want to discuss in detail burning conditions as they occur in SNe Ia. We take the model W7 by Nomoto, Thielemann, and Yokoi (1984) and Thielemann, Nomoto, and Yokoi (1986) as a typical example. There is still considerable uncertainty in the physics of propagating flame fronts (see Woosley and Weaver 1986b, 1991; Müller and Arnett 1986; Zeldovich et al. 1985; Nomoto and Shigeyama 1990; Khoklov 1991a, 1991b; and lectures in this volume), and open questions remain. The propagation of the burning front after central C-ignition has in published calculations been treated only in a parametrized way, fitting the mixing-length parameter in the time-dependent mixing-length theory of Unno (1967) to the observed supernova energy or varying the fractal dimension of the burning front surface, which is not spherical but wrinkled in reality. Both these parameters can be tuned to obtain deflagrations (subsonic), detonations (supersonic burning front propagation), or delayed detonations; see models W6, W7, and W8 in Nomoto, Thielemann, Yokoi 1986.

Temperatures in the burning front are increased by about a factor of 10, in comparison to the initial values, leading to explosive burning of the C-O fuel. Figure 1 displays the mass fractions of a few major nuclei of model W7. We see that the outer zones experience explosive C and Ne-burning, where first carbon fusion produces ^{20}Ne, which photodisintegrates back to ^{16}O. Further towards the center, zones undergo explosive O-burning where ^{16}O is also burned by fusion reactions to ^{28}Si and ^{32}S. Even higher temperatures lead to the burning of Si. In incomplete Si-burning, doubly-magic ^{56}Ni is produced together with intermediate nuclei like ^{40}Ca. Inside 0.8M$_\odot$ only Fe-group nuclei exist with a dominant abundance of ^{56}Ni, which has the highest binding per nucleon for N=Z nuclei. The situation only changes towards the very center, where the densities become high enough to cause Fermi energies (of the electron gas) in excess of several MeV, which enables appreciable amounts of electron captures on free protons (and to a minor extent on heavy

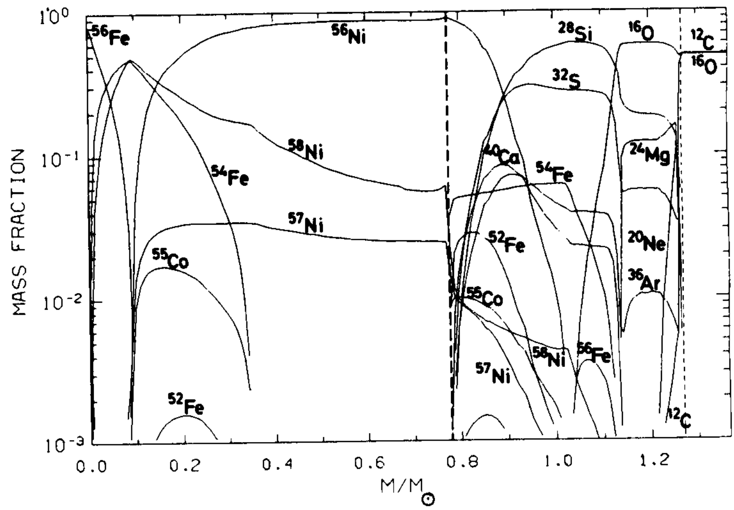

Fig. 1. Major abundances after explosive processing. In the inner 0.8 M$_\odot$ only Fe-group nuclei are produced. The inner dashed line shows the transition to incomplete Si-burning, followed further out by products of explosive O, Ne, and C-burning. The outer dashed line marks quenching of the burning front.

nuclei ≈40%). This changes the total proton-to-neutron ratio and the most abundant nuclei become first ^{54}Fe and ^{58}Ni and finally ^{56}Fe. The region of complete Si-burning is divided into an inner zone of 0.35$M_\odot$ with a normal freeze-out, and an outer region with an alpha-rich freeze-out. We see the strong decline of ^{54}Fe and the dominance of ^{58}Ni in the alpha-rich freeze-out.

4.2. Abundances in ejecta

One of the major aspects of nucleosynthesis calculations is to understand the chemical evolution of galaxies and especially the present abundances in our galaxy, the solar system abundances being a snapshot in time at a specific location. Figure 2 shows the ratio of abundances produced in a SN Ia event to solar abundances. Displayed are abundance ratios after decay of unstable nuclei, normalized to unity for ^{56}Fe. If a SN Ia event always starts from the same configuration (a white dwarf with $M=M_{Ch}$), the same nucleosynthesis products are expected from each event, and the comparison with solar abundances is actually meaningful without averaging over a complete sample. It

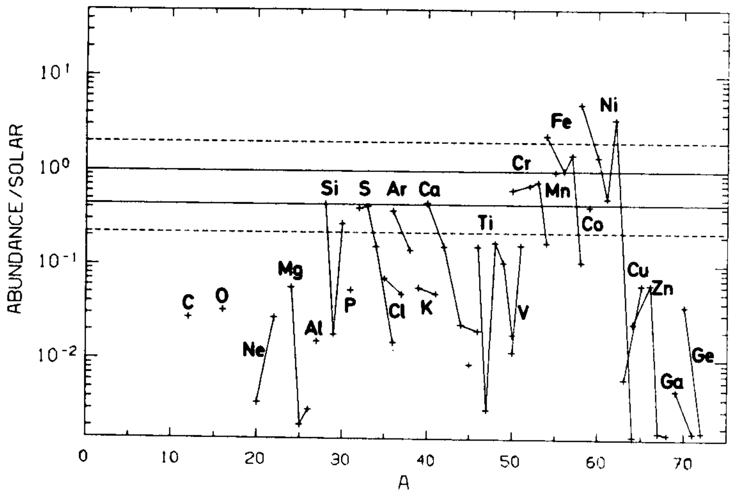

Fig. 2. The abundances of stable isotopes formed in a SN I event are shown relative to their solar values. The ratio is normalized to ^{56}Fe. Note the strong overabundances of ^{58,62}Ni and ^{54}Fe.

is obvious from fig. 2 that the production of Fe-group nuclei in comparison to their solar values is a factor of 2 larger than the production of intermediate nuclei from Si to Ca. This shows that SNe Ia are the dominant production sites of Fe-group nuclei, while SNe II have to fill in the intermediate nuclei.

One undesirable aspect is the large scale of deviations from solar abundances within the Fe-group, when SNe Ia are the main contributors of these nuclei to the interstellar medium. We notice here especially ^{54}Fe, ^{58}Ni, and ^{62}Ni (originating from ^{62}Zn-decay). All these nuclei come from a chain in the nuclear chart which is displaced by two units to the neutron-rich side from the N=Z chain and therefore measures the neutron excess of the material. Outside of $0.3M_{\odot}$, where electron capture is not effective, the neutron excess is only determined by the ^{22}Ne admixture to ^{12}C and ^{16}O in the original white dwarf, coming from ^{14}N in He-burning, which in turn originated from all CNO-nuclei in H-burning, i.e., the metallicity. Using time-averaged metallicities would reduce the overproduction of these nuclei by 25-40%. Probably more important is that the propagation of the burning front is not fully understood yet. A burning front which starts with a small velocity and then accelerates (Woosley and Weaver 1986b, 1991; Khoklov 1991a, 1991b), could reduce the amount of material which is displayed in the mass zones between 0.05 to $0.3M_{\odot}$, where ^{54}Fe, ^{58}Ni, and ^{62}Ni are produced predominantly.

It is not generally a large η or small Y_e (i.e. the amount of electron capture) which is problematic. The inner core, where stable ^{56}Fe rather than ^{56}Ni is produced, has an even larger neutron excess. However, that composition is helpful in obtaining a light curve which agrees very well with observations (Graham 1987) and it does not create very non-solar overproductions. Only zones with $0.02 < \eta < 0.05$ ($0.47 < Y_e < 0.49$) are highly problematic, and need to be reduced in mass by a factor of 2 to 4.

5. Type II supernovae (SNe II)

The most desirable way to perform explosive nucleosynthesis calculations in SNe II would come from a hydrodynamical calculation which follows the Fe-core collapse, the bounce at nuclear densities, and the propagating shock wave through the envelope before ejection. However, open problems still exist with the supernova mechanism of massive stars (see Bruenn 1989a, 1989b; Cooperstein and Baron 1989; Baron and Cooperstein 1990; Myra and Bludman 1989; Wilson and Mayle 1988; Mayle and Wilson 1988, 1990; and Bethe 1990). Here we want to make use of the fact that typical energies of 10^{51} erg are observed and light curve as well as calculations of explosive nucleosynthesis can be performed with an artificially induced shock wave

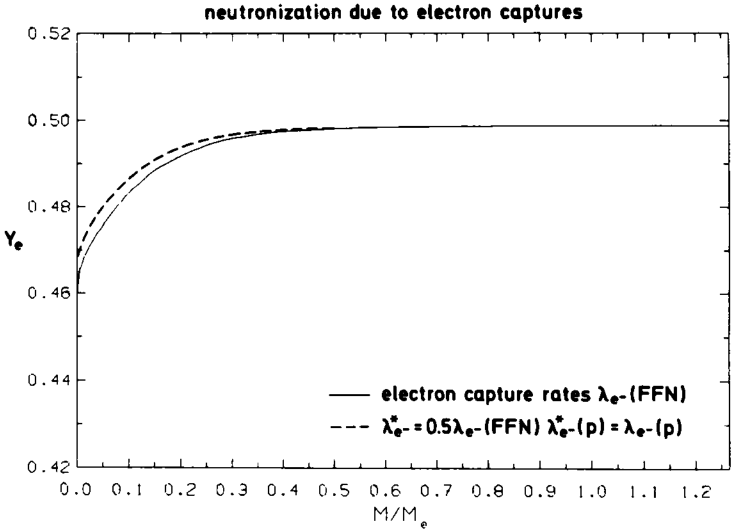

Fig. 3. Y_e as a function of the radial mass coordinate. The small values at the center are due to electron captures on protons and heavy nuclei during the high temperature and density phase of the explosion. The two lines (solid and dashed) result from a sensitivity study, using either the electron capture rates from Fuller, Fowler, Newman (1984), or reducing the rates by a factor of 2 for nuclei (but not for protons).

of appropriate energy applied to the pre-collapse stellar model (see Woosley and Weaver 1986a; Shigeyama, Nomoto, Hashimoto 1988; Woosley 1988; Woosley, Pinto, Weaver 1988; Hashimoto, Nomoto, Shigeyama 1989; Arnett et al. 1989; Thielemann, Hashimoto, Nomoto 1990). There will, of course, be variation of this value with progenitor mass, but only by a small factor. As we will show later, the temperatures obtained during propagation of the shock wave are proportional to $E^{1/3}$. Thus, we expect that this uncertainty introduces negligible errors. Larger uncertainties are expected from missing knowledge of the exact core structure at the time when the shock wave starts propagating outward. The lack of knowledge of the shock structure introduces an additional uncertainty, because different ways of initiating the explosion (piston, thermal bomb, kinetic bomb) can lead to different results. Aufderheide, Baron, and Thielemann (1991) have studied these questions in detail and come to the conclusion that errors in the bulk composition of up to 30% are introduced. While this is not negligible, it is small enough in order to proceed with nucleosynthesis studies before the SN II mechanism is understood completely.

One remaining problem, when performing calculations with initiated shock waves, cannot be avoided. The location of the mass cut between neutron star and ejected envelope is unclear and can only be deduced from observational constraints. In case of SN 1987A the light curve, powered by decaying ^{56}Ni and ^{56}Co, could be utilized to determine the mass of ^{56}Ni produced, which is located in the innermost region of the ejecta and therefore provides information about the mass cut. For progenitors of different mass, where such information is not available, we have to search for other sources of information. In addition we cannot make judgements about the ejection of matter which experienced stronger neutronization via electron captures during core collapse, because this effect was not included in the pre-explosion models.

Haxton (1988), Woosley and Haxton (1988), and Woosley et al. (1990) examined the possible effect of inelastic neutrino scattering on explosive nucleosynthesis, an idea which was introduced earlier by Domogatsky and Nadyozhin (1977).

Inelastic neutrino scattering can populate excited states which are unstable against particle emission and produce neighboring nuclei. Outside the neutrino-sphere, scattering events will be rare and therefore this process will be mostly of importance for nuclei with very small abundances, which are not produced otherwise. We did not include this effect in the present calculations.

5.1. Basic features

As discussed above, the most significant parameter in explosive nucleosynthesis is the temperature, and a good prediction of the composition can already be made by knowing only $T_{\max}$, without having to perform complex nucleosynthesis calculations. Weaver and Woosley (1980) already recognized that matter behind the shock front is strongly radiation-dominated. Assuming an almost homogeneous density and temperature distribution behind the shock (which is approximately correct, see fig. 3 in Shigeyama, Nomoto, and Hashimoto 1988), one can equate the supernova energy with radiation energy inside the radius R of the shock front

$$E_{SN} = \frac{4\pi}{3} R^3 a T^4. \tag{5.1}$$

This equation can be solved for R, and with $T = 5 \times 10^9$K, the lower bound for explosive Si-burning with complete Si-exhaustion and $E_{SN} =$

10^{51}erg, the result is $R \approx 3700$ km (see Woosley 1988). For the evolutionary model by Nomoto and Hashimoto (1988) of a 20 $M_\odot$ star, utilized in this calculation, this radius corresponds to 1.7 $M_\odot$, in excellent agreement with the exact hydrodynamic calculation (see Thielemann, Hashimoto, Nomoto 1990 and section 5.2). Temperatures which characterize the edge of the other explosive burning zones correspond to the following radii: incomplete Si-burning (T_9=4, R=4980km), explosive O-burning (3.3, 6430), and explosive Ne/C-burning (2.1, 11750). This relates to masses of 1.75, 1.81, and 2.05$M_\odot$ in case of the 20$M_\odot$ star. The radii mentioned are model-independent and vary only with the supernova energy.

When applying the same procedure to other SN II progenitor models by Nomoto and Hashimoto (1988), and assuming an average supernova energy of 10^{51}erg, the masses in table 1 result. Table 1 can be understood in the following way. Matter between the mass cut and the mass indicated with ex Si-c undergoes explosive Si-burning with Si-exhaustion. Then a zone follows with incomplete Si-burning until ex Si-i, explosive O-burning until ex O, explosive Ne/C-burning until ex Ne, and unprocessed matter from the C/Ne-core is ejected until C-core. The masses involved (ΔM) are displayed in the intermediate line, which also lists the most abundant elements in these zones. As discussed before, we do not know a priori where the mass cut is located, and therefore cannot predict the total amount of ejected matter which experienced complete Si-burning (Si-c). The zones beyond explosive Ne/C-burning ($T_{max} < 2.1 \times 10^9$K) are essentially unaltered and the composition is almost identical to the pre-explosive one.

Table 1
Masses in explosive and hydrostatic burning

Burning Site	Main Products	13$M_\odot$	15$M_\odot$	20$M_\odot$	25$M_\odot$
Fe-core		1.18	1.28	1.40	1.61
mass cut		?	?	1.60	?
	"Fe", He	?	?	0.10	?
ex Si-c		1.42	1.46	1.70	1.79
	Si, S, Fe, Ar, Ca	0.06	0.06	0.05	0.06
ex Si-i		1.48	1.52	1.75	1.85
	O, Si, S, Ar, Ca	0.06	0.05	0.06	0.07
ex O		1.54	1.57	1.81	1.92
	O, Mg, Si, Ne	0.12	0.16	0.24	0.34
ex Ne		1.66	1.73	2.05	2.26
	O, Ne, Mg, Si	0.09	0.29	1.65	3.49
C-core		1.75	2.02	3.70	5.75

Table 2
Mass Fraction of Elements in Burning Sites

Element	C-core	ex Ne	ex O	ex Si-i	ex Si-c
O	0.72	0.80	0.45		
Ne	0.13	0.04			
Mg	0.09	0.08	0.005		
Si	0.02	0.08	0.30	0.40	
S			0.20	0.25	
Ar			0.025	0.06	
Ca			0.02	0.05	
Fe				0.20	0.70

Thielemann, Nomoto and Hashimoto (1990) gave the average composition for major elements in individual explosive burning stages, based on calculations for SN 1987A. These are displayed in table 2. By taking the masses ΔM from table 1 for the individual burning zones and multiplying them by the mass fractions given in table 2, one can predict abundance yields for this whole mass range of SN II progenitors. The explosive yields should be quite insensitive to this procedure, and quite accurate, because they depend only on peak temperatures, densities, and the neutron excess of matter. The latter should be very similar outside the Fe-core for different stellar masses. An exception might be material which undergoes complete Si-burning, because the mass cut (and with it the neutron excess) will depend on the individual star and the details of the explosion mechanism. This also underlines the major uncertainty hidden in these yields. With the explosion mechanism not completely understood yet, one has to assume a position of the mass cut, and dependent on that position and the compression occurring during collapse (prior to the ejection of these mass zones), matter will have a variety of neutron excess values and might even contain r-process nuclei. An indication is found from observations of r-process abundances as a function of stellar metallicity (timing the formation in galactic evolution) that lower mass SNe II ($\leq 11\ M_\odot$) eject r-process nuclei, but that SNe II with more massive progenitors do not (Mathews and Cowan 1990; Cowan, Thielemann, Truran 1991). Another uncertainty can be found in the zones containing only hydrostatically processed material. Here we expect a changing C to O ratio, reflecting the increasing temperatures in core He-burning of more massive stars. Ne and Mg as products of C-burning could change as well, and thus the C, O, Ne, and Mg abundances are not necessarily represented correctly by those of a 20 $M_\odot$ star.

5.2. Detailed calculations

5.2.1. SN 1987A – a 20 $M_\odot$ star

We want to illustrate this section with the example of a 20 $M_\odot$ star (Nomoto and Hashimoto 1988). The explosion energy used corresponds to a supernova energy of 10^{51}erg. As mentioned before, this treatment cannot predict the position of mass cut between neutron star and ejecta, but the observation of 0.07 ± 0.01 $M_\odot$ of ^{56}Ni in SN 1987A (a 20 $M_\odot$ star) gives an important constraint, because ^{56}Ni is produced in the innermost ejected zones. Explosive nucleosynthesis due to burning in the shock front is shown in fig. 4 for a few major nuclei. Inside 1.7 $M_\odot$ all Fe-group nuclei are produced in *explosive* Si-burning during the SN II event. At 1.63 $M_\odot$, Y_e changes from 0.494 to 0.499 and leads to a smaller ^{56}Ni abundance further inside, where more neutron-rich Ni-isotopes share the abundance with ^{56}Ni.

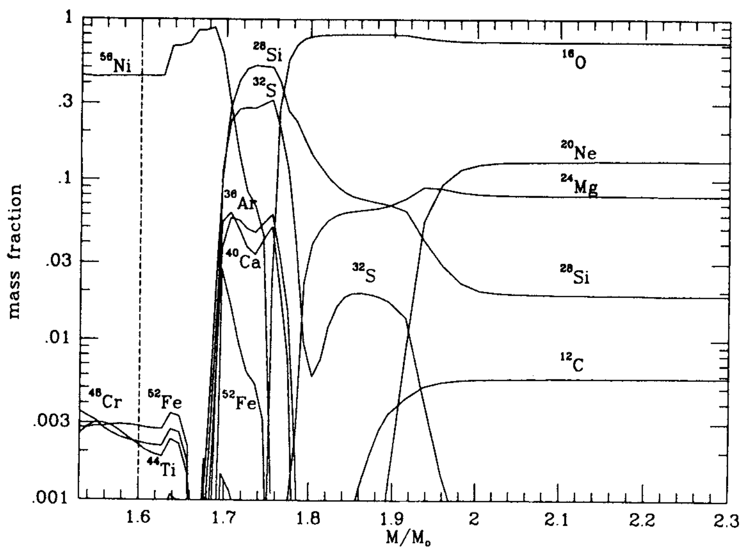

Fig. 4. Mass fractions of a few major nuclei after passage of the supernova shockfront. Matter outside 2 $M_\odot$ is essentially unaltered. Mass zones further in experience explosive Si, O, Ne, and C-burning. In order to eject 0.07 $M_\odot$ of ^{56}Ni the mass cut between neutron star and ejecta is required to be located at 1.6 $M_\odot$.

In this star, only alpha-rich freeze-out and incomplete Si-burning are encountered. Contrary to SNe Ia, densities in excess of 10^8gcm^{-3}, which would result in a normal freeze-out, are not attained in the ejecta of this 20 $M_\odot$ star.

The most abundant nucleus in the alpha-rich freeze-out is ^{56}Ni. For the less abundant nuclei, the final alpha-capture plays a dominant role, transforming nuclei like ^{56}Ni, ^{57}Ni, and ^{58}Ni into ^{60}Zn, ^{61}Zn, and ^{62}Zn (see fig. 5).

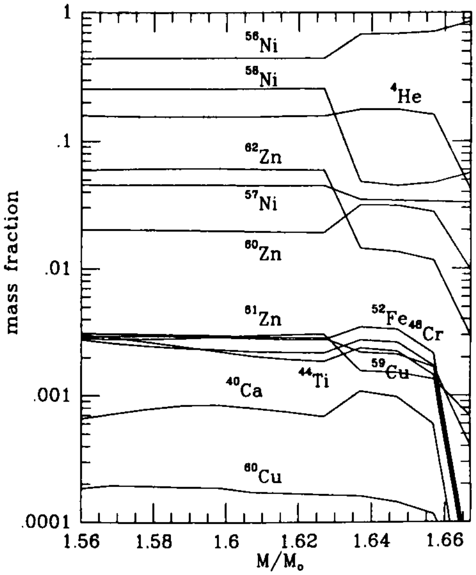

Fig. 5. Mass fractions of the dominant nuclei in zones which experience alpha-rich freeze-out. Notice the relatively large amounts of Zn and Cu nuclei, which originate from alpha-captures on Ni and Co. One can recognize their strong decrease beyond 1.66 M$_\odot$, which goes parallel with the decrease of the ^{4}He-abundance and other alpha-nuclei like ^{40}Ca, ^{44}Ti, ^{48}Cr, and ^{52}Fe. Nuclei which would dominate in a nuclear statistical equilibrium like ^{56,57,58}Ni stay constant or increase even slightly. The increase of all nuclei with N = Z at 1.63 M$_\odot$ and the decrease of nuclei with N > Z is due to the change in Y_e (see fig. 8).

The region which experiences incomplete Si-burning starts at 1.69 M$_\odot$ and extends out to 1.74 M$_\odot$. In the innermost zones with temperatures close to 4×10^9K, there still exists a contamination by the Fe-group nuclei ^{54}Fe, ^{56}Ni, ^{52}Fe, ^{58}Ni, ^{55}Co, and ^{57}Ni. Explosive O-burning occurs in the mass zones up to 1.8 M$_\odot$ (see fig. 6). The main burning products are ^{28}Si, ^{32}S, ^{36}Ar, ^{40}Ca, ^{38}Ar, and ^{34}S. With mass fractions less than 10^{-2}, ^{33}S, ^{39}K, ^{35}Cl, ^{42}Ca, *and* ^{37}Ar are produced. Explosive Ne-burning leads to an ^{16}O-enhancement over its hydrostatic value in the mass zones up to 2 M$_\odot$ (see fig. 7).

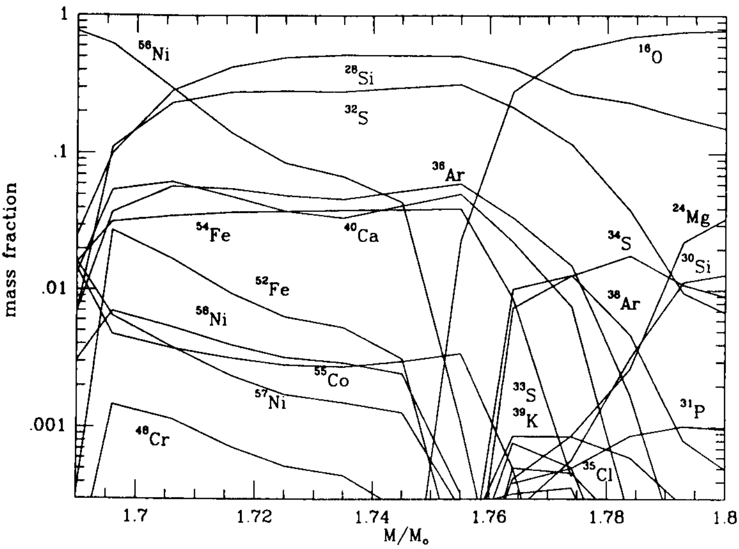

Fig. 6. Mass fractions of nuclei in the zones of incomplete Si-burning M < 1.74 $M_\odot$ and explosive O-burning M < 1.8 $M_\odot$. The Si-burning zones are are characterized by important quantities of Fe-group nuclei besides ^{28}Si, ^{32}S, ^{36}Ar, and ^{40}Ca. Explosive O-burning produces mostly the latter, together with more neutron-rich nuclei like ^{30}Si, ^{34}S, ^{38}Ar etc.

Traditionally the r-process is assumed to occur close to the mass cut between neutron star and ejecta in matter with very high neutron excess. Using the ^{56}Ni constraint and assuming a spherical explosion led to a mass cut at 1.6 $M_\odot$. Tables 3 through 5 display the abundances found for mass cuts at 1.59 and 1.63 $M_\odot$. Both are within the uncertainty limits required by the ^{56}Ni constraint. The most neutron-rich zones of the ejecta are located at the inner boundary with a Y_e of 0.494 (see fig. 8) which corresponds to a neutron excess $\eta = \sum_i (N_i - Z_i) Y_i / \sum_i A_i Y_i = 1 - 2Y_e$ of 1.2×10^{-2}. These zones which experience temperatures in excess of 5×10^9K, produce predominantly nuclei in the mass range 50-60. The quoted value of η therefore indicates that each nucleus has about 0.5 more neutrons than protons. For that mass region this corresponds to a nucleus still being about 1.5 mass units *more* proton-rich than the stability line.

This means that when utilizing induced spherical explosion calculations with a pre-collapse stellar model, no r-process material is contained in these

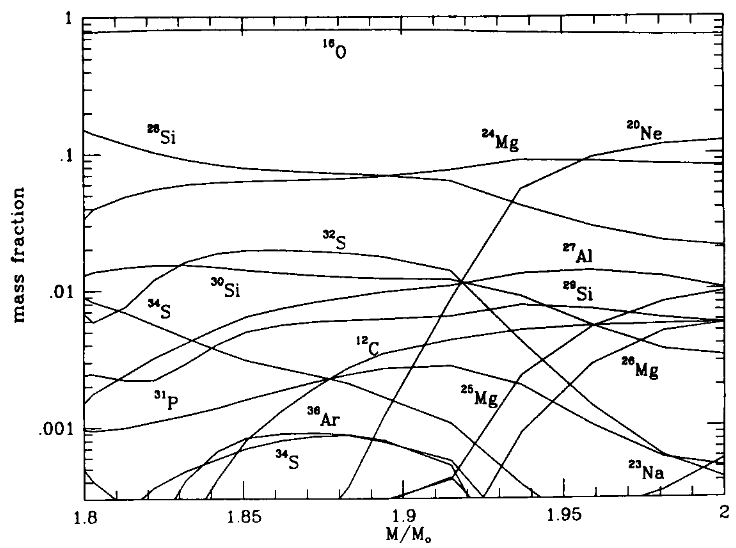

Fig. 7. Composition in mass zones of explosive Ne and C-burning. The dominant products are ^{16}O, ^{24}Mg, and ^{28}Si. Besides the major abundances, mentioned above, explosive neon burning supplies also substantial amounts of ^{27}Al, ^{29}Si, ^{32}S, ^{30}Si, and ^{31}P. Explosive carbon burning contributes in addition the nuclei ^{20}Ne, ^{23}Na, ^{24}Mg, ^{25}Mg, and ^{26}Mg.

zones close to the mass cut between neutron star and ejecta. However, rotation could violate spherical symmetry and cause jet-like ejection from deeper zones (LeBlanc and Wilson 1970; Symbalisty, Schramm, and Wilson 1985). For reasonable ratios of rotational to gravitational energy 1% before collapse (Mönchmeyer and Müller 1989a, 1989b) find small jet-like circulations at the poles when the shock front is still close to the collapsed core, but obtain almost spherical symmetry when the shock front reaches the Si-zone. This indicates that a 20 $M_\odot$ star would not eject r-process nuclei in its final supernova explosion, although SNe II are strongly expected to be the dominant r-process source. SNe II with smaller masses, however, should contribute r-process nuclei (Mathews and Cowan 1990; Cowan, Thielemann, Truran 1991). The present treatment neglects neutronization effects which happen during collapse and until the onset of a delayed explosion (of the order 1 sec after bounce). Wilson and Mayle (1988), Bethe (1990) and Woosley and Weaver (1991) report r-process conditions with a neutron excess η up to 0.6 in the "high entropy bubble," developing in delayed explosions. But

Table 3
Composition of ejecta after explosive processing, mass cut at 1.59 $M_\odot$

$M/M_\odot$	$M/M_\odot$	$M/M_\odot$	$M/M_\odot$	$M/M_\odot$
d 3.40E − 17	t 1.08E − 20	he3 1.35E − 19	he4 2.10E + 00	li6 5.10E − 19
li7 4.42E − 20	be7 7.39E − 22	be9 7.64E − 18	be10 1.46E − 21	b10 2.73E − 17
b11 6.35E − 16	b12 4.86E − 24	c11 1.17E − 17	c12 1.14E − 01	c13 4.46E − 07
c14 7.39E − 09	c15 1.52E − 14	n13 7.90E − 11	n14 2.71E − 03	n15 4.39E − 08
n16 4.49E − 13	n17 1.04E − 18	o14 4.08E − 18	o15 1.79E − 11	o16 1.48E + 00
o17 3.73E − 09	o18 8.68E − 03	o19 7.09E − 10	o20 1.45E − 13	f17 5.24E − 15
f18 2.41E − 08	f19 1.54E − 10	f20 4.65E − 13	f21 9.55E − 16	ne18 3.08E − 23
ne19 5.30E − 16	ne20 2.28E − 01	ne21 3.02E − 04	ne22 2.93E − 02	ne23 1.62E − 07
ne24 1.52E − 12	ne25 2.55E − 18	na21 2.50E − 12	na22 1.01E − 07	na23 1.17E − 03
na24 2.01E − 08	na25 3.21E − 12	na26 1.43E − 18	mg22 1.30E − 16	mg23 4.33E − 07
mg24 1.47E − 01	mg25 1.84E − 02	mg26 1.71E − 02	mg27 8.40E − 09	mg28 3.16E − 12
al24 2.69E − 22	al25 1.73E − 10	al26 6.77E − 06	al27 1.59E − 02	al28 6.33E − 06
al29 1.47E − 08	al30 4.81E − 14	si26 1.09E − 14	si27 2.64E − 07	si28 8.43E − 02
si29 9.70E − 03	si30 7.25E − 03	si31 1.21E − 06	si32 1.89E − 09	si33 1.24E − 17
p28 2.14E − 23	p29 2.66E − 10	p30 5.22E − 05	p31 1.13E − 03	p32 5.59E − 07
p33 3.68E − 07	p34 1.20E − 11	p35 5.54E − 14	s30 1.22E − 14	s31 2.51E − 08
s32 2.49E − 02	s33 1.14E − 04	s34 1.11E − 03	s35 2.49E − 07	s36 2.41E − 07
s37 1.54E − 16	s38 6.04E − 18	cl32 3.02E − 22	cl33 1.33E − 11	cl34 3.81E − 09
cl35 5.13E − 05	cl36 5.42E − 07	cl37 5.75E − 07	cl38 6.90E − 12	cl39 6.09E − 14
cl40 4.48E − 18	ar34 6.96E − 15	ar35 3.45E − 09	ar36 4.10E − 03	ar37 5.66E − 06
ar38 3.08E − 04	ar39 1.59E − 09	ar40 1.77E − 09	ar41 2.07E − 13	ar42 2.43E − 15
ar43 1.79E − 19	ar44 1.11E − 21	k36 1.98E − 19	k37 6.23E − 13	k38 2.52E − 07
k39 2.90E − 05	k40 7.00E − 09	k41 1.98E − 09	k42 7.76E − 12	k43 2.22E − 13
k44 2.29E − 15	k45 6.72E − 17	k46 2.45E − 19	ca38 1.07E − 17	ca39 1.29E − 09
ca40 3.31E − 03	ca41 2.28E − 06	ca42 9.79E − 06	ca43 8.09E − 09	ca44 4.23E − 09
ca45 3.51E − 12	ca46 2.93E − 12	ca47 2.78E − 15	ca48 3.97E − 17	ca49 2.60E − 25
sc40 8.86E − 23	sc41 6.56E − 15	sc42 4.59E − 10	sc43 2.80E − 06	sc44 2.41E − 09
sc45 5.05E − 09	sc46 3.49E − 11	sc47 5.44E − 12	sc48 4.90E − 14	sc49 9.01E − 16
sc50 4.06E − 22	ti42 1.33E − 25	ti43 2.57E − 12	ti44 2.09E − 04	ti45 1.84E − 07
ti46 3.66E − 06	ti47 8.14E − 08	ti48 2.27E − 08	ti49 6.48E − 11	ti50 4.72E − 11
ti51 2.88E − 17	ti52 6.33E − 21	v44 2.37E − 23	v45 2.03E − 13	v46 2.68E − 15
v47 6.92E − 06	v48 3.79E − 08	v49 3.05E − 08	v50 2.26E − 10	v51 1.59E − 09
v52 2.56E − 14	v53 4.03E − 17	v54 5.42E − 25	cr46 1.93E − 20	cr47 5.74E − 10
cr48 2.49E − 04	cr49 3.79E − 06	cr50 2.93E − 05	cr51 4.42E − 07	cr52 4.04E − 06
cr53 8.24E − 10	cr54 2.11E − 11	cr55 1.33E − 18	cr56 8.76E − 22	mn48 2.02E − 22
mn49 2.60E − 14	mn50 1.50E − 13	mn51 1.26E − 05	mn52 4.00E − 07	mn53 3.13E − 06
mn54 1.02E − 08	mn55 3.33E − 09	mn56 1.03E − 14	mn57 7.35E − 18	fe51 2.41E − 15
fe52 9.49E − 04	fe53 7.98E − 05	fe54 2.66E − 03	fe55 9.41E − 06	fe56 2.62E − 05
fe57 2.74E − 09	fe58 1.25E − 10	fe59 3.11E − 17	fe60 6.08E − 20	co53 3.88E − 18
co54 5.80E − 14	co55 2.65E − 04	co56 9.57E − 06	co57 3.92E − 06	co58 3.63E − 09
co59 1.18E − 09	co60 1.59E − 14	co61 1.10E − 16	co62 1.64E − 23	ni55 5.96E − 18
ni56 7.57E − 02	ni57 4.17E − 03	ni58 1.37E − 02	ni59 2.12E − 05	ni60 4.36E − 06
ni61 6.88E − 09	ni62 2.07E − 08	ni63 1.17E − 14	ni64 7.07E − 17	ni65 2.07E − 23
cu57 9.55E − 13	cu58 8.59E − 08	cu59 1.75E − 04	cu60 1.21E − 04	cu61 1.79E − 05
cu62 2.03E − 06	cu63 5.16E − 08	cu64 6.46E − 13	cu65 1.70E − 14	cu66 2.45E − 19
cu67 2.08E − 23	zn59 1.06E − 20	zn60 2.34E − 03	zn61 2.09E − 04	zn62 3.36E − 03
zn63 1.14E − 05	zn64 2.78E − 07	zn65 4.05E − 09	zn66 1.70E − 10	zn67 1.25E − 13
zn68 4.44E − 16	zn69 2.65E − 22	ga61 6.01E − 18	ga62 2.11E − 18	ga63 1.06E − 06
ga64 2.41E − 06	ga65 7.17E − 07	ga66 1.58E − 07	ga67 5.96E − 09	ga68 2.72E − 13
ga69 6.89E − 14	ga70 3.53E − 18	ga71 4.04E − 21	ge63 4.48E − 23	ge64 1.40E − 05
ge65 2.62E − 06	ge66 7.96E − 05	ge67 6.62E − 07	ge68 2.08E − 07	ge69 1.97E − 10
ge70 1.79E − 12	ge71 5.32E − 16	ge72 1.16E − 18	ge73 1.25E − 22	

Table 4
Composition after decay of radioactive species

M/M$_\odot$	M/M$_\odot$	M/M$_\odot$	M/M$_\odot$
d 3.40$E-17$	he3 1.46$E-19$	he4 2.10$E+00$	li6 5.10$E-19$
li7 4.50$E-20$	be9 7.64$E-18$	b10 2.73$E-17$	b11 6.47$E-16$
c12 1.14$E-01$	c13 4.46$E-07$	n14 2.71$E-03$	n15 4.40$E-08$
o16 1.48$E+00$	o17 3.73$E-09$	o18 8.68$E-03$	f19 8.63$E-10$
ne20 2.28$E-01$	ne21 3.02$E-04$	ne22 2.93$E-02$	na23 1.17$E-03$
mg24 1.47$E-01$	mg25 1.84$E-02$	mg26 1.71$E-02$	al27 1.59$E-02$
si28 8.43$E-02$	si29 9.70$E-03$	si30 7.30$E-03$	p31 1.13$E-03$
s32 2.49$E-02$	s33 1.15$E-04$	s34 1.11$E-03$	s36 2.51$E-07$
cl35 5.16$E-05$	cl37 6.24$E-06$	ar36 4.10$E-03$	ar38 3.08$E-04$
ar40 2.54$E-09$	k39 2.91$E-05$	k41 2.28$E-06$	ca40 3.31$E-03$
ca42 9.79$E-06$	ca43 2.81$E-06$	ca44 2.09$E-04$	ca46 3.78$E-11$
ca48 3.97$E-17$	sc45 1.89$E-07$	ti46 3.66$E-06$	ti47 7.00$E-06$
ti48 2.49$E-04$	ti49 3.82$E-06$	ti50 4.72$E-11$	v50 2.26$E-10$
v51 1.30$E-05$	cr50 2.93$E-05$	cr52 9.53$E-04$	cr53 8.30$E-05$
cr54 1.02$E-08$	mn55 2.75$E-04$	fe54 2.66$E-03$	fe56 7.57$E-02$
fe57 4.17$E-03$	fe58 3.75$E-09$	co59 1.96$E-04$	ni58 1.37$E-02$
ni60 2.46$E-03$	ni61 2.27$E-04$	ni62 3.36$E-03$	ni64 8.01$E-13$
cu63 1.25$E-05$	cu65 3.34$E-06$	zn64 1.67$E-05$	zn66 7.98$E-05$
zn67 6.68$E-07$	zn68 2.08$E-07$	ga69 1.97$E-10$	ga71 5.32$E-16$
ge70 1.79$E-12$	ge72 1.16$E-18$	ge73 1.25$E-22$	

again, the question remains which part of that bubble is actually ejected as a function of progenitor mass.

In order to get a general feeling about the nucleosynthesis production in a 20 M$_\odot$ SN II, we display the abundance ratio over solar (normalized to ^{28}Si) in fig. 9. Nuclei heavier than Si and P are on average produced by a factor of 2 to 4 less than ^{28}Si. P, Si, Al, Mg, Na, and Ne, while also produced in explosive burning, have large contributions from the zones of hydrostatic C and Ne-burning, which are unaltered during the explosion. The reason is the existence of an extended shell of combined C and Ne-burning, ranging from 1.8 to 3.7 M$_\odot$ (see fig. 10 in Nomoto and Hashimoto 1988). Essentially in the progenitor star, all heavier elements originate from explosive processing. The products of explosive burning from S to Cu originate mainly from mass zones up to 1.8 M$_\odot$. They fall well along a line of constant overproduction (within reasonable errors). A few nuclei like ^{36}S, ^{37}Cl, ^{40}Ar, ^{58}Fe, and possibly some odd-Z nuclei, which are underabundant in fig. 9, are mainly produced by the weak s-process during core He-burning (Arnett and Thielemann 1985). They were not included in the 30 nuclei network for hydrostatic burning stages, and consequently their s-process contribution is neglected.

Table 5
Composition of ejecta for mass cut at $1.63 M_\odot$

$M/M_\odot$	$M/M_\odot$	$M/M_\odot$	$M/M_\odot$
d $3.40E-17$	he3 $1.46E-19$	he4 $2.10E+00$	li6 $5.10E-19$
li7 $4.50E-20$	be9 $7.64E-18$	b10 $2.73E-17$	b11 $6.47E-16$
c12 $1.14E-01$	c13 $4.46E-07$	n14 $2.71E-03$	n15 $4.40E-08$
o16 $1.48E+00$	o17 $3.73E-09$	o18 $8.68E-03$	f19 $8.63E-10$
ne20 $2.28E-01$	ne21 $3.02E-04$	ne22 $2.93E-02$	na23 $1.17E-03$
mg24 $1.47E-01$	mg25 $1.84E-02$	mg26 $1.71E-02$	al27 $1.59E-02$
si28 $8.43E-02$	si29 $9.70E-03$	si30 $7.30E-03$	p31 $1.13E-03$
s32 $2.49E-02$	s33 $1.15E-04$	s34 $1.11E-03$	s36 $2.51E-07$
cl35 $5.04E-05$	cl37 $6.17E-06$	ar36 $4.09E-03$	ar38 $3.05E-04$
ar40 $2.46E-09$	k39 $2.19E-05$	k41 $1.50E-06$	ca40 $3.28E-03$
ca42 $8.36E-06$	ca43 $1.63E-06$	ca44 $1.09E-04$	ca46 $3.78E-11$
ca48 $3.97E-17$	sc45 $6.97E-08$	ti46 $3.35E-06$	ti47 $2.81E-06$
ti48 $1.55E-04$	ti49 $3.69E-06$	ti50 $4.72E-11$	v50 $2.26E-10$
v51 $9.01E-06$	cr50 $2.90E-05$	cr52 $8.36E-04$	cr53 $8.05E-05$
cr54 $1.02E-08$	mn55 $2.73E-04$	fe54 $2.66E-03$	fe56 $5.88E-02$
fe57 $2.41E-03$	fe58 $3.13E-09$	co59 $8.16E-05$	ni58 $3.84E-03$
ni60 $1.66E-03$	ni61 $1.05E-04$	ni62 $8.83E-04$	ni64 $8.60E-14$
cu63 $2.21E-06$	cu65 $1.10E-06$	zn64 $1.09E-05$	zn66 $1.96E-05$
zn67 $1.07E-07$	zn68 $2.87E-08$	ga69 $2.28E-11$	ga71 $5.45E-17$
ge70 $1.99E-13$	ge72 $1.12E-19$	ge73 $1.12E-23$	

The ratio between elements heavier than Si and P to lighter elements reflects mainly a comparison of the size of hydrostatic zones to explosively processed ones and is a function of stellar mass (and the methods used in stellar evolution calculations). This is evident when comparing to Woosley, Pinto, and Weaver (1988) who use a different treatment of convection (Ledoux vs. Schwarzschild) and have smaller C-burning cores. There exist a number of quantitative comparisons for SN 1987A between nucleosynthesis predictions and observations (see e.g. Table 2 in Danziger et al. 1990 or section IVb in Thielemann, Hashimoto, Nomoto (1990) which give reasonable agreement for C, O, Si, Cl, Ar, Co, and Ni (or Fe). Here we want to concentrate on two crucial aspects, O and stable Ni, that is, Ni isotopes after the decay of ^{56}Ni.

The amount of ^{16}O is closely linked to the "effective" $^{12}C(\alpha,\gamma)^{16}O$ rate during core He-burning. This effective rate is determined by three factors: (1) the actual nuclear rate, (2) the amount of semiconvection and overshooting, mixing fresh He-fuel into the core at late phases of He-burning, when temperatures are relatively high and favor alpha-capture on ^{12}C, and (3) the stellar mass which determines the central temperature during He-burning. Our model calculations predict 1.48 $M_\odot$ of ejected ^{16}O. This is within the ob-

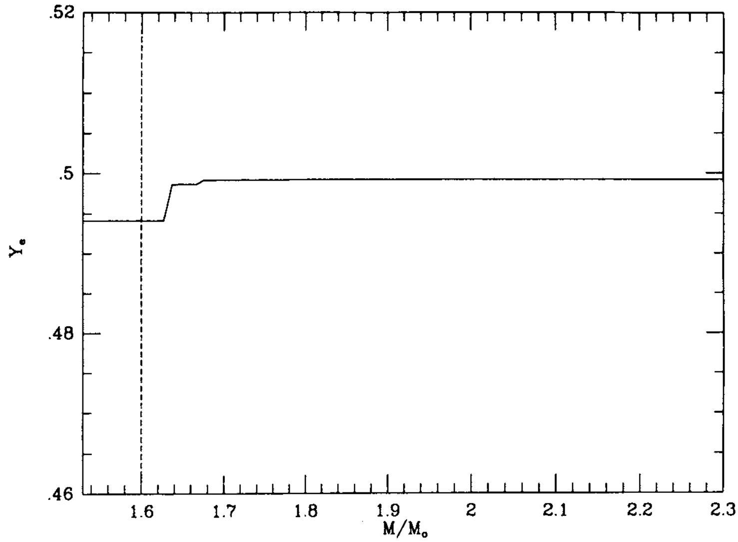

Fig. 8. Electron abundance Y_e as a function of radial mass. The drop at $1.63 M_\odot$ reflects the outer boundary of the Si-zone which experienced core O-burning and admixtures of Si shell-burning during hydrostatic evolution. The position of the mass cut, with respect to this change in Y_e, is crucial for the composition of Fe-group elements.

servational constraints of 0.2–3.0 $M_\odot$ (see table 2 in Danziger et al. 1990), but somewhat unsatisfying. The improved analysis of observations for SN 1987A by Pinto and Spyromilio (1991) helped to put tighter constraints on the pre-collapse models by increasing the lower limit to 0.7 $M_\odot$. Our value lies just at the center of the remaining uncertainty range 0.7–3.0 $M_\odot$.

The nuclei ^{58,61,62}Ni, which show large overabundances, are produced in form of the neutron-rich species ^{58}Ni and ^{61,62}Zn. Their production is strongly dependent on Y_e (see fig. 8) and varies therefore with the position of the mass cut between ejected matter and the remaining neutron star. Especially for Ni-abundances the position of the mass cut is crucial and one could expect lower mass SNe II to eject more of these neutron-rich species as they are expected to also produce r-process elements. This could explain a fraction of the observed very high Ni abundances in some supernova remnants like the Crab (Henry and Fesen 1988), but not the huge overproduction found by these authors. More probably they have to be explained away by atomic or

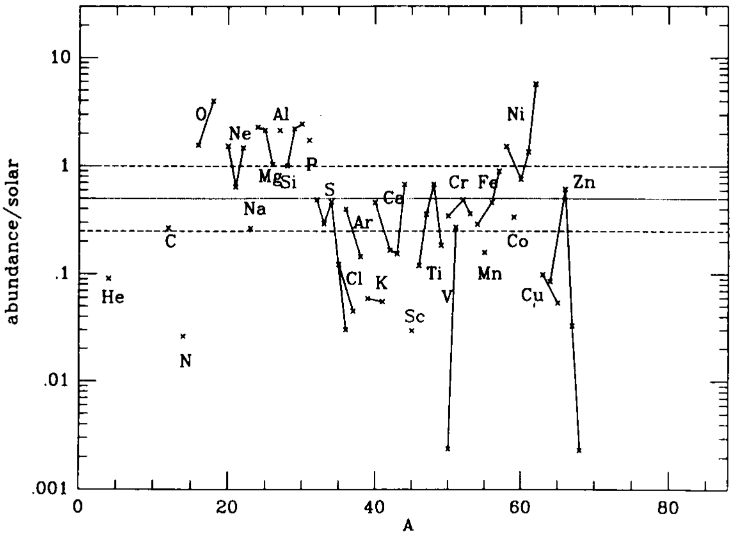

Fig. 9. Composition of the supernova ejecta in comparison to solar abundances, normalized to ^{28}Si. Elements lighter than P have strong contributions from hydrostatic C and Ne-burning. Heavier nuclei originate from explosive processing and show similar ratios within a factor of 2 to 3. The ^{58,61,62}Ni abundances are strongly dependent on the mass cut, i.e., the neutron excess of ejected matter.

other effects. It should be mentioned at this point that the ^{57}Ni/^{56}Ni ratio is correlated with the abundances of stable Ni isotopes, predominantly ^{58}Ni, i.e. ^{58}Ni/^{56}Ni. Recent light curve observations of SN 1987A (Elias et al. 1991, Bouchet et al. 1991) could be interpreted with a high 57/56 ratio of 4 times solar, but this would also require stable Ni abundances not yet substantiated from observations (Witteborn et al. 1989). In order to meet the stable Ni constraints of 3–5$\times 10^{-3}$ $M_\odot$ (Danziger et al. 1990, Witteborn et al. 1989) only an upper limit of 1.4–1.7 times solar is permitted for the 57/56 ratio (see figs. 12b/c in Thielemann, Hashimoto, Nomoto 1990). This also agrees well with observations by Varani et al. (1990).

5.2.2. 13, 15, and 25 $M_\odot$ models

Detailed explosive nucleosynthesis calculations for progenitors of 13, 15, and 25 $M_\odot$ were performed in the same way as in Thielemann, Hashimoto, Nomoto (1990) for the 20 $M_\odot$ star. For first results see Thielemann et al. (1991a). Figures 10, 11, and 12 give an idea how the same types of explosive and hydrostatic burning zones are distributed as a function of the Lagrangian mass coordinate (for comparison see fig. 4). One can recognize how, with increasing progenitor mass, the appropriate explosive and hydrostatic burning zones also appear at larger mass coordinates. Figures 10 through 12 *can* also be compared with the analytical estimates in table 1, and are in good agreement. At present, no proven evidence about the position of the mass cut between neutron star and ejecta exists in these cases. Therefore, we only list in tables 6 through 9 the integrated abundances for matter outside the boundary of incomplete Si-burning, which will be ejected in any case. This underpredicts largely the abundance of Fe-group nuclei, while abundances of nuclei as heavy as Ca are close to their correct values. In order to judge the expected differences compare tables 3 and 8.

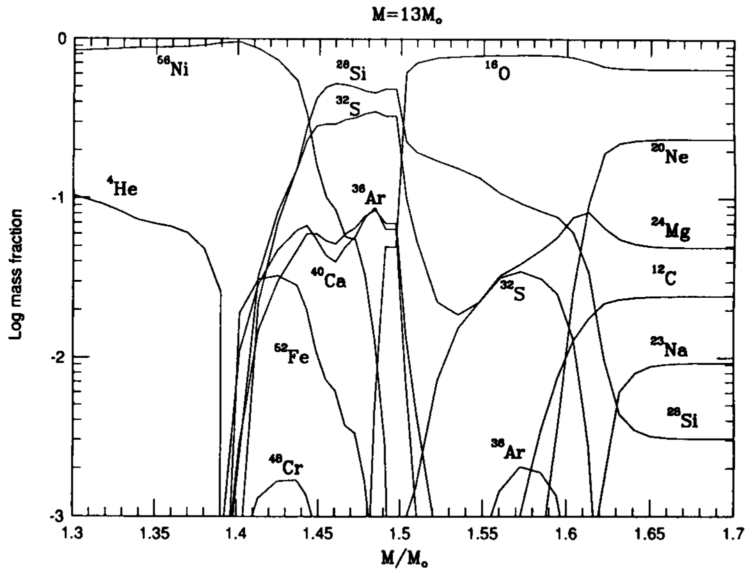

Fig. 10. Mass fractions of a few major nuclei, as they result from explosive processing after the passage of the supernova shock front through a 13 $M_\odot$ star.

5.3. Gross properties of ejecta

In this section we want to concentrate on element abundances and the overall nucleosynthesis behavior in SNe II as a function of progenitor mass. The

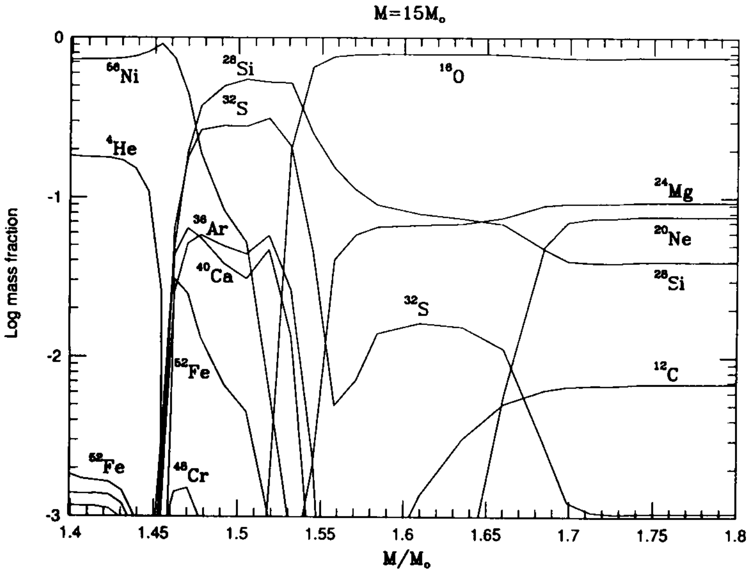

Fig. 11. The same as fig. 10 for a 15 $M_{\odot}$ star.

results are presented in table 10, together with the analytic predictions (second column) following from the utilization of tables 1 and 2 in section 5.1. From the comparison we can see that the agreement between analytical predictions and detailed calculations is quite reasonable; one finds differences of up to 30%. For the lighter elements O, Ne, Mg, which result from hydrostatic burning stages, variation of the hydrostatic yields with the progenitor mass is the reason and the composition of a 20 $M_{\odot}$ star is not necessarily representative. For heavier elements the inaccuracy is due to uncertainties related to the (artificial) initiation of the explosion. Aufderheide, Baron and Thielemann (1991) concluded that all initiated SN II calculations will have such an intrinsic error and one cannot expect the calculations to be more accurate in any case.

The content of table 10 indicates an interesting behavior. While the heavier intermediate mass nuclei originate only from explosive O and Si-burning, which contribute similar amounts for all progenitor masses (see also table 1), the lighter elements, C through Si, have dominant or essential contributions from hydrostatic burning (C/Ne-core) or explosive Ne-burning. For both latter cases we see a tremendous mass dependence in table 1, and a strong reduction of the involved mass zones for less massive stars. The mass cuts

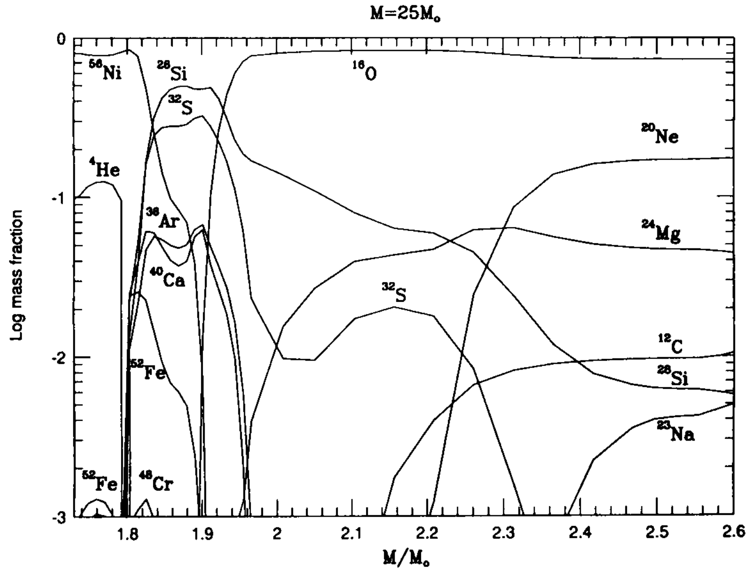

Fig. 12. The same as fig. 10 for a 25 M$_\odot$ star.

between ejecta and neutron stars were taken in such a way that the 0.07 M$_\odot$ of ejected ^{56}Ni for SN 1987A (a 20 M$_\odot$ star) could be reproduced. For 15 and 13 M$_\odot$ stars we follow the arguments by Shigeyama et al. (1990), Nomoto et al. (1990), and Hachisu et al. (1990) that one can reproduce the light curves of SNe Ib and SNe Ic, respectively, when these progenitors lost (almost all) their H-envelope by mass transfer in a binary system. Thus, SN Ib/c events are interpreted as explosions of massive stars in binary systems which lost the complete H-envelope to the binary companion (Ib), or retained a minor amount of the H-envelope (Ic), which is sufficient to suppress spectral He-lines and leads to only minor H -features. The need for relatively low mass progenitors is due to the fact that they also possess small He-cores (3.3 and 4 M$_\odot$, respectively) which result in the steep observed slope of their light curves (Ic is similar to Ia). The early escape of x-rays and gamma-rays from ^{56}Co-decay for small He-cores steepens the light curves in comparison to the pure ^{56}Co exponential decay slope. There is no direct observational reason for low Fe-yields in the case of the 25 M$_\odot$ star. Possible arguements for the choice are given in chapter 6.

Table 6
13 $M_\odot$ – mass cut at incomplete Si-burning

$M/M_\odot$	$M/M_\odot$	$M/M_\odot$	$M/M_\odot$	$M/M_\odot$
t 6.29E − 19	he3 1.00E − 18	he4 1.45E + 00	li7 4.54E − 25	be10 4.78E − 24
b10 4.70E − 23	b11 4.76E − 14	b12 5.36E − 25	c11 5.76E − 17	c12 5.96E − 02
c13 1.12E − 08	c14 8.26E − 09	n13 1.23E − 13	n14 6.09E − 03	n15 2.22E − 08
n16 7.93E − 22	n17 3.65E − 22	o14 1.74E − 11	o15 1.70E − 10	o16 2.07E − 01
o17 5.74E − 08	o18 1.01E − 02	o19 1.03E − 15	o20 1.59E − 17	f17 1.67E − 16
f18 1.17E − 10	f19 8.33E − 10	f20 1.13E − 11	f21 5.30E − 22	ne18 2.53E − 15
ne19 6.84E − 15	ne20 2.64E − 02	ne21 2.58E − 04	ne22 2.09E − 03	ne23 3.78E − 09
ne24 7.05E − 13	ne25 6.38E − 20	na20 3.46E − 21	na21 2.06E − 14	na22 9.41E − 08
na23 8.88E − 04	na24 2.84E − 06	na25 1.24E − 08	na26 2.21E − 12	mg21 2.14E − 23
mg22 2.54E − 12	mg23 9.31E − 07	mg24 9.57E − 03	mg25 1.58E − 03	mg26 1.02E − 03
mg27 1.69E − 07	mg28 9.46E − 10	al24 1.85E − 16	al25 5.96E − 12	al26 1.82E − 06
al27 1.03E − 03	al28 9.21E − 06	al29 1.15E − 07	al30 6.68E − 11	si25 1.91E − 18
si26 3.11E − 09	si27 5.90E − 07	si28 4.51E − 02	si29 6.23E − 04	si30 1.28E − 03
si31 1.13E − 06	si32 6.63E − 09	si33 5.41E − 15	p27 4.71E − 21	p28 4.76E − 15
p29 4.18E − 06	p30 3.53E − 06	p31 2.13E − 04	p32 3.86E − 07	p33 2.99E − 07
p34 6.03E − 11	p35 1.01E − 12	s29 1.27E − 17	s30 7.89E − 06	s31 4.17E − 06
s32 2.49E − 02	s33 9.55E − 05	s34 1.40E − 03	s35 2.07E − 07	s36 2.15E − 07
s37 9.06E − 16	s38 6.11E − 17	cl31 1.39E − 19	cl32 3.60E − 14	cl33 1.43E − 07
cl34 1.22E − 06	cl35 2.50E − 05	cl36 5.25E − 07	cl37 7.65E − 07	cl38 1.21E − 11
cl39 4.15E − 13	cl40 2.59E − 16	ar33 1.12E − 13	ar34 3.11E − 06	ar35 1.91E − 06
ar36 5.15E − 03	ar37 3.41E − 06	ar38 3.19E − 04	ar39 2.48E − 09	ar40 2.75E − 09
ar41 5.89E − 13	ar42 2.46E − 14	ar43 1.97E − 17	ar44 9.60E − 19	k35 1.16E − 20
k36 2.20E − 14	k37 2.33E − 10	k38 6.37E − 08	k39 6.40E − 06	k40 7.09E − 09
k41 2.96E − 09	k42 1.58E − 11	k43 1.16E − 12	k44 1.23E − 13	k45 3.54E − 14
k46 1.24E − 15	ca37 1.88E − 14	ca38 7.55E − 08	ca39 3.40E − 07	ca40 5.25E − 03
ca41 4.20E − 07	ca42 6.05E − 06	ca43 1.30E − 08	ca44 1.39E − 08	ca45 1.44E − 11
ca46 1.48E − 11	ca47 1.76E − 13	ca48 6.21E − 15	ca49 4.63E − 20	sc40 4.01E − 20
sc41 2.44E − 13	sc42 4.74E − 09	sc43 2.77E − 08	sc44 3.02E − 10	sc45 4.01E − 09
sc46 1.46E − 10	sc47 2.75E − 11	sc48 9.61E − 13	sc49 4.91E − 14	sc50 1.83E − 17
ti42 1.41E − 11	ti43 2.59E − 08	ti44 2.50E − 06	ti45 3.15E − 09	ti46 1.29E − 06
ti47 5.43E − 08	ti48 4.97E − 08	ti49 3.38E − 10	ti50 3.22E − 10	ti51 7.66E − 15
ti52 1.45E − 15	v44 1.45E − 16	v45 7.91E − 14	v46 2.90E − 10	v47 8.05E − 09
v48 4.54E − 09	v49 1.43E − 08	v50 5.16E − 10	v51 3.68E − 09	v52 3.33E − 13
v53 5.72E − 14	v54 6.15E − 18	cr46 1.77E − 10	cr47 9.94E − 09	cr48 7.83E − 05
cr49 5.35E − 09	cr50 9.37E − 07	cr51 1.35E − 07	cr52 5.80E − 07	cr53 4.73E − 10
cr54 5.01E − 11	cr55 1.85E − 16	cr56 2.30E − 16	mn48 6.79E − 16	mn49 2.19E − 10
mn50 1.32E − 08	mn51 1.24E − 06	mn52 3.20E − 08	mn53 1.01E − 07	mn54 1.68E − 09
mn55 9.67E − 10	mn56 1.75E − 14	mn57 9.13E − 15	mn58 3.24E − 18	fe50 4.34E − 10
fe51 3.54E − 07	fe52 1.43E − 03	fe53 2.70E − 06	fe54 3.51E − 06	fe55 2.26E − 07
fe56 1.22E − 06	fe57 4.19E − 10	fe58 6.55E − 11	fe59 1.37E − 16	fe60 5.85E − 16
fe61 4.58E − 21	fe62 1.56E − 20	co52 8.64E − 17	co53 3.65E − 11	co54 2.25E − 06
co55 3.02E − 05	co56 6.95E − 08	co57 1.81E − 08	co58 1.65E − 10	co59 1.98E − 10
co60 1.30E − 14	co61 5.61E − 15	co62 1.14E − 18	co63 1.53E − 17	ni54 1.45E − 10
ni55 4.18E − 06	ni56 3.39E − 02	ni57 1.74E − 04	ni58 2.02E − 05	ni59 7.71E − 09
ni60 3.45E − 08	ni61 3.37E − 11	ni62 5.64E − 11	ni63 5.97E − 16	ni64 4.07E − 15
ni65 4.47E − 20	ni66 1.97E − 18	ni67 2.17E − 23	cu57 7.91E − 14	cu58 8.82E − 07
cu59 7.17E − 07	cu60 3.43E − 08	cu61 5.43E − 11	cu62 2.34E − 14	cu63 2.91E − 13
cu64 1.73E − 16	cu65 9.36E − 15	cu66 9.86E − 19	cu67 3.97E − 17	cu68 1.57E − 21
cu69 2.77E − 20	zn59 1.31E − 08	zn60 1.06E − 05	zn61 1.20E − 08	zn62 1.66E − 10
zn63 5.70E − 14	zn64 1.46E − 13	zn65 7.01E − 16	zn66 4.86E − 13	zn67 3.71E − 17
zn68 9.29E − 16	zn69 1.05E − 20	zn70 2.87E − 18	zn71 3.09E − 23	zn72 4.28E − 21
ga61 7.40E − 18	ga62 9.17E − 12	ga63 5.57E − 12	ga64 4.69E − 14	ga65 1.24E − 16
ga66 1.07E − 20	ga67 1.42E − 17	ga68 1.75E − 19	ga69 7.04E − 17	ga70 1.25E − 19
ga71 6.18E − 18	ga72 7.88E − 22	ga73 1.98E − 19	ga74 5.83E − 23	ge63 2.11E − 13
ge64 8.08E − 12	ge65 1.05E − 14	ge66 9.12E − 17	ge67 4.94E − 21	ge68 5.01E − 18
ge69 4.87E − 19	ge70 2.24E − 15	ge71 1.27E − 18	ge72 2.49E − 16	ge73 2.50E − 20
ge74 4.47E − 18	ge75 2.00E − 22	ge76 2.93E − 19	ge77 1.01E − 23	ge78 3.50E − 22

Table 7
15 $M_\odot$ – mass cut at incomplete Si-burning

$M/M_\odot$	$M/M_\odot$	$M/M_\odot$	$M/M_\odot$	$M/M_\odot$
t 1.05E − 20	he3 4.69E − 20	he4 1.81E + 00	be10 1.19E − 24	b10 4.69E − 24
b11 1.44E − 15	c11 1.20E − 17	c12 8.32E − 02	c13 4.70E − 10	c14 1.44E − 10
n13 1.10E − 16	n14 5.37E − 03	n15 1.38E − 10	o14 1.01E − 20	o15 5.72E − 12
o16 4.17E − 01	o17 3.98E − 09	o18 1.35E − 02	o19 3.76E − 19	o20 1.95E − 21
f17 1.09E − 18	f18 2.10E − 11	f19 2.27E − 11	f20 4.24E − 14	f21 1.53E − 22
ne19 9.56E − 17	ne20 2.65E − 02	ne21 4.39E − 05	ne22 1.26E − 02	ne23 1.15E − 10
ne24 8.82E − 16	ne25 3.44E − 24	na21 4.04E − 15	na22 3.44E − 08	na23 1.97E − 04
na24 2.72E − 08	na25 1.48E − 11	na26 2.67E − 16	mg22 2.47E − 17	mg23 5.26E − 07
mg24 4.06E − 02	mg25 3.25E − 03	mg26 2.52E − 03	mg27 1.63E − 08	mg28 1.51E − 11
al24 8.75E − 21	al25 7.31E − 14	al26 2.68E − 06	al27 5.27E − 03	al28 5.98E − 06
al29 1.48E − 08	al30 8.33E − 13	si26 2.99E − 14	si27 8.88E − 07	si28 6.20E − 02
si29 4.24E − 03	si30 4.95E − 03	si31 2.40E − 06	si32 6.75E − 09	si33 2.15E − 16
p28 7.59E − 20	p29 2.19E − 11	p30 1.44E − 06	p31 8.22E − 04	p32 1.01E − 06
p33 6.54E − 07	p34 5.18E − 11	p35 2.35E − 13	s30 7.23E − 14	s31 9.90E − 08
s32 2.16E − 02	s33 8.96E − 05	s34 1.06E − 03	s35 5.25E − 07	s36 5.72E − 07
s37 6.95E − 16	s38 3.86E − 17	cl32 1.38E − 21	cl33 5.93E − 13	cl34 1.52E − 08
cl35 4.59E − 05	cl36 5.66E − 07	cl37 7.92E − 07	cl38 1.76E − 11	cl39 3.03E − 13
cl40 2.61E − 17	ar34 7.09E − 15	ar35 7.43E − 09	ar36 3.58E − 03	ar37 3.75E − 06
ar38 2.49E − 04	ar39 2.79E − 09	ar40 4.73E − 09	ar41 9.18E − 13	ar42 2.55E − 14
ar43 2.80E − 18	ar44 2.95E − 20	k36 1.82E − 22	k37 1.13E − 15	k38 8.09E − 09
k39 9.22E − 06	k40 5.67E − 09	k41 2.89E − 09	k42 3.54E − 11	k43 2.15E − 12
k44 3.79E − 14	k45 2.35E − 15	k46 1.34E − 17	ca38 3.24E − 17	ca39 1.20E − 09
ca40 3.02E − 03	ca41 6.17E − 07	ca42 4.55E − 06	ca43 5.38E − 09	ca44 5.88E − 09
ca45 8.79E − 12	ca46 1.05E − 11	ca47 2.90E − 14	ca48 7.10E − 16	ca49 1.48E − 22
sc41 1.41E − 18	sc42 3.58E − 13	sc43 1.96E − 10	sc44 1.66E − 10	sc45 1.59E − 09
sc46 5.57E − 11	sc47 1.56E − 11	sc48 3.45E − 13	sc49 1.36E − 14	sc50 9.83E − 20
ti42 3.71E − 23	ti43 1.35E − 15	ti44 1.05E − 06	ti45 2.19E − 08	ti46 1.65E − 06
ti47 2.66E − 08	ti48 2.66E − 08	ti49 2.03E − 10	ti50 4.17E − 10	ti51 4.93E − 16
ti52 2.04E − 18	v45 1.44E − 19	v46 2.08E − 11	v47 1.54E − 08	v48 4.01E − 09
v49 1.00E − 08	v50 2.44E − 10	v51 1.86E − 09	v52 9.86E − 14	v53 7.19E − 16
v54 3.33E − 21	cr46 3.40E − 20	cr47 7.25E − 13	cr48 4.17E − 05	cr49 3.32E − 06
cr50 2.22E − 05	cr51 1.96E − 07	cr52 2.24E − 06	cr53 8.22E − 10	cr54 6.72E − 11
cr55 1.94E − 17	cr56 8.08E − 20	mn48 2.24E − 25	mn49 2.82E − 16	mn50 1.04E − 09
mn51 5.07E − 06	mn52 1.05E − 07	mn53 8.88E − 07	mn54 5.89E − 09	mn55 2.46E − 09
mn56 2.26E − 14	mn57 1.37E − 16	mn58 3.62E − 22	fe50 5.50E − 21	fe51 4.07E − 12
fe52 6.23E − 04	fe53 6.26E − 05	fe54 1.92E − 03	fe55 3.28E − 06	fe56 9.73E − 06
fe57 1.50E − 09	fe58 1.51E − 10	fe59 2.00E − 16	fe60 5.75E − 18	fe61 1.21E − 24
fe62 4.31E − 25	co53 4.95E − 17	co54 5.65E − 09	co55 2.10E − 04	co56 8.36E − 07
co57 3.36E − 07	co58 1.03E − 09	co59 5.49E − 10	co60 1.69E − 14	co61 1.34E − 15
co62 1.17E − 20	co63 1.10E − 20	ni54 4.25E − 22	ni55 3.72E − 12	ni56 1.05E − 02
ni57 1.46E − 04	ni58 1.75E − 04	ni59 8.54E − 08	ni60 2.41E − 07	ni61 7.31E − 11
ni62 4.79E − 11	ni63 4.25E − 16	ni64 5.34E − 16	ni65 9.78E − 22	ni66 2.60E − 21
cu57 1.50E − 19	cu58 1.93E − 13	cu59 1.99E − 10	cu60 2.54E − 11	cu61 2.61E − 11
cu62 1.28E − 13	cu63 5.70E − 13	cu64 9.45E − 17	cu65 5.43E − 16	cu66 3.87E − 20
cu67 3.31E − 19	cu68 2.39E − 24	cu69 3.04E − 24	zn59 3.13E − 22	zn60 1.24E − 11
zn61 1.85E − 12	zn62 5.58E − 11	zn63 3.31E − 14	zn64 7.66E − 13	zn65 5.59E − 16
zn66 3.56E − 15	zn67 3.65E − 19	zn68 5.74E − 18	zn69 5.69E − 23	zn70 1.30E − 21
ga62 4.70E − 22	ga63 3.49E − 19	ga64 2.77E − 19	ga65 9.80E − 19	ga66 1.30E − 20
ga67 5.08E − 19	ga68 9.26E − 22	ga69 1.81E − 19	ga70 2.72E − 22	ga71 1.11E − 20
ga73 2.33E − 23	ge64 7.24E − 20	ge65 2.20E − 21	ge66 1.95E − 18	ge67 1.38E − 21
ge68 2.31E − 19	ge69 5.78E − 22	ge70 2.21E − 19	ge71 3.97E − 22	ge72 3.35E − 20
ge73 8.86E − 24	ge74 5.56E − 22	ge76 9.44E − 25		

Table 8
20 $M_\odot$ – mass cut at incomplete Si-burning

$M/M_\odot$	$M/M_\odot$	$M/M_\odot$	$M/M_\odot$	$M/M_\odot$
d 4.05E − 17	t 6.17E − 20	he3 2.50E − 19	he4 2.09E + 00	li6 6.09E − 19
li7 5.40E − 20	be7 5.56E − 22	be9 8.21E − 18	be10 1.52E − 21	b10 3.24E − 17
b11 1.04E − 14	b12 6.12E − 24	c11 1.25E − 17	c12 1.14E − 01	c13 4.86E − 07
c14 1.00E − 08	c15 1.87E − 14	n13 8.12E − 11	n14 2.71E − 03	n15 5.06E − 08
n16 5.53E − 13	n17 1.38E − 18	o14 3.89E − 19	o15 1.48E − 11	o16 1.48E + 00
o17 1.84E − 08	o18 8.68E − 03	o19 8.07E − 10	o20 1.78E − 13	f17 5.35E − 15
f18 2.37E − 08	f19 3.41E − 10	f20 8.49E − 13	f21 4.50E − 15	ne18 7.25E − 25
ne19 4.56E − 16	ne20 2.28E − 01	ne21 3.11E − 04	ne22 2.93E − 02	ne23 1.83E − 07
ne24 1.85E − 12	ne25 3.26E − 18	na21 9.93E − 13	na22 1.33E − 07	na23 1.16E − 03
na24 8.93E − 08	na25 6.21E − 11	na26 2.52E − 18	mg22 1.82E − 17	mg23 3.48E − 07
mg24 1.46E − 01	mg25 1.86E − 02	mg26 1.73E − 02	mg27 7.64E − 08	mg28 9.24E − 11
al24 1.91E − 22	al25 2.72E − 11	al26 6.77E − 06	al27 1.59E − 02	al28 1.24E − 05
al29 5.21E − 08	al30 8.83E − 13	si26 1.31E − 15	si27 2.64E − 07	si28 8.32E − 02
si29 1.00E − 02	si30 7.71E − 03	si31 4.29E − 06	si32 1.24E − 08	si33 3.51E − 16
p28 3.34E − 25	p29 2.71E − 12	p30 4.90E − 05	p31 1.18E − 03	p32 1.03E − 06
p33 5.80E − 07	p34 6.39E − 11	p35 6.29E − 13	s30 2.62E − 16	s31 2.30E − 08
s32 2.40E − 02	s33 1.20E − 04	s34 1.26E − 03	s35 4.89E − 07	s36 4.65E − 07
s37 9.15E − 16	s38 7.00E − 17	cl32 8.81E − 24	cl33 2.60E − 14	cl34 1.13E − 09
cl35 4.94E − 05	cl36 6.63E − 07	cl37 8.10E − 07	cl38 2.95E − 11	cl39 5.73E − 13
cl40 8.50E − 17	ar34 4.37E − 17	ar35 1.65E − 10	ar36 4.11E − 03	ar37 6.07E − 06
ar38 3.70E − 04	ar39 2.57E − 09	ar40 3.39E − 09	ar41 1.20E − 12	ar42 2.79E − 14
ar43 5.88E − 18	ar44 1.05E − 19	k36 5.09E − 21	k37 2.40E − 16	k38 7.02E − 09
k39 1.82E − 05	k40 8.08E − 09	k41 2.62E − 09	k42 2.83E − 11	k43 1.86E − 12
k44 6.51E − 14	k45 5.86E − 15	k46 5.89E − 17	ca38 2.81E − 20	ca39 3.08E − 12
ca40 3.66E − 03	ca41 1.39E − 06	ca42 9.49E − 06	ca43 8.97E − 09	ca44 6.13E − 09
ca45 8.25E − 12	ca46 9.00E − 12	ca47 4.35E − 14	ca48 8.56E − 16	ca49 8.96E − 22
sc40 1.41E − 24	sc41 5.56E − 17	sc42 3.30E − 13	sc43 2.42E − 09	sc44 4.29E − 10
sc45 2.80E − 09	sc46 6.52E − 11	sc47 1.37E − 11	sc48 3.31E − 13	sc49 9.21E − 15
sc50 5.53E − 19	ti43 2.62E − 15	ti44 1.59E − 06	ti45 4.03E − 08	ti46 3.73E − 06
ti47 6.61E − 08	ti48 3.38E − 08	ti49 1.36E − 10	ti50 1.39E − 10	ti51 3.75E − 16
ti52 1.81E − 17	v44 3.30E − 26	v45 2.60E − 16	v46 6.94E − 19	v47 2.12E − 08
v48 1.15E − 08	v49 3.44E − 08	v50 3.40E − 10	v51 2.54E − 09	v52 6.49E − 14
v53 9.30E − 16	v54 2.58E − 20	cr46 2.48E − 23	cr47 2.85E − 13	cr48 4.41E − 05
cr49 4.06E − 06	cr50 3.53E − 05	cr51 5.05E − 07	cr52 5.61E − 06	cr53 1.41E − 09
cr54 6.23E − 11	cr55 1.07E − 17	cr56 4.20E − 19	mn48 7.61E − 26	mn49 8.20E − 18
mn50 7.20E − 16	mn51 6.36E − 06	mn52 2.83E − 07	mn53 3.78E − 06	mn54 1.50E − 08
mn55 5.46E − 09	mn56 2.37E − 14	mn57 5.33E − 17	mn58 9.77E − 22	fe51 4.51E − 19
fe52 7.22E − 04	fe53 8.27E − 05	fe54 3.29E − 03	fe55 1.25E − 05	fe56 4.03E − 05
fe57 4.83E − 09	fe58 2.84E − 10	fe59 1.21E − 16	fe60 8.16E − 19	fe61 1.81E − 25
co53 7.99E − 21	co54 2.76E − 16	co55 2.99E − 04	co56 1.35E − 06	co57 1.54E − 06
co58 4.69E − 09	co59 2.12E − 09	co60 3.62E − 14	co61 5.09E − 16	co62 3.76E − 22
co63 2.06E − 22	ni55 1.56E − 21	ni56 1.86E − 02	ni57 3.51E − 04	ni58 4.81E − 04
ni59 6.59E − 07	ni60 1.50E − 06	ni61 4.09E − 10	ni62 1.83E − 10	ni63 4.19E − 16
ni64 4.66E − 17	ni65 9.06E − 24	ni66 1.82E − 24	cu57 2.21E − 13	cu58 7.66E − 10
cu59 2.72E − 06	cu60 2.99E − 06	cu61 1.52E − 07	cu62 2.82E − 09	cu63 1.54E − 11
cu64 4.23E − 16	cu65 8.17E − 17	cu66 3.36E − 22	cu67 2.10E − 22	zn59 5.64E − 23
zn60 6.33E − 05	zn61 1.92E − 06	zn62 1.34E − 05	zn63 4.23E − 09	zn64 3.02E − 10
zn65 3.44E − 12	zn66 1.71E − 14	zn67 3.28E − 18	zn68 1.06E − 19	zn70 1.58E − 25
ga61 1.91E − 19	ga62 1.36E − 20	ga63 2.30E − 09	ga64 1.12E − 08	ga65 8.36E − 10
ga66 6.27E − 11	ga67 2.55E − 13	ga68 6.43E − 18	ga69 2.29E − 20	ga70 6.70E − 26
ga71 6.10E − 24	ge64 9.87E − 08	ge65 3.33E − 09	ge66 7.49E − 08	ge67 4.15E − 11
ge68 2.33E − 11	ge69 3.48E − 16	ge70 1.45E − 17	ge71 4.93E − 23	ge72 2.69E − 21
ge73 1.09E − 25	ge74 3.65E − 24			

Table 9
25 $M_{\odot}$ – mass cut at incomplete Si-burning

$M/M_{\odot}$	$M/M_{\odot}$	$M/M_{\odot}$	$M/M_{\odot}$	$M/M_{\odot}$
t 3.62E − 19	he3 7.32E − 19	he4 1.94E + 00	be10 5.76E − 24	b10 2.91E − 23
b11 5.29E − 14	b12 9.02E − 25	c11 1.71E − 17	c12 1.48E − 01	c13 1.03E − 08
c14 9.15E − 09	n13 3.00E − 15	n14 9.53E − 04	n15 1.04E − 08	n16 2.31E − 21
n17 3.54E − 23	o14 5.51E − 20	o15 2.55E − 11	o16 2.99E + 00	o17 7.86E − 08
o18 6.69E − 03	o19 1.80E − 16	o20 1.60E − 18	f17 6.58E − 17	f18 3.50E − 10
f19 8.17E − 10	f20 6.20E − 12	f21 4.36E − 13	ne18 2.29E − 24	ne19 9.33E − 16
ne20 5.94E − 01	ne21 3.22E − 03	ne22 3.39E − 02	ne23 8.37E − 10	ne24 2.05E − 13
ne25 7.92E − 21	na21 1.77E − 13	na22 2.56E − 07	na23 1.81E − 02	na24 2.73E − 06
na25 6.64E − 09	na26 7.14E − 13	mg22 1.34E − 16	mg23 1.92E − 06	mg24 1.59E − 01
mg25 3.92E − 02	mg26 3.17E − 02	mg27 4.72E − 07	mg28 1.56E − 09	al24 3.63E − 19
al25 4.15E − 13	al26 9.73E − 06	al27 1.95E − 02	al28 3.79E − 05	al29 3.38E − 07
al30 1.08E − 10	si26 1.61E − 13	si27 1.98E − 06	si28 1.02E − 01	si29 6.97E − 03
si30 6.81E − 03	si31 8.57E − 06	si32 4.77E − 08	si33 1.38E − 14	p28 1.15E − 18
p29 4.07E − 11	p30 3.89E − 06	p31 8.93E − 04	p32 1.71E − 06	p33 9.61E − 07
p34 3.96E − 10	p35 5.59E − 12	s30 6.94E − 14	s31 1.44E − 07	s32 3.79E − 02
s33 2.19E − 04	s34 2.76E − 03	s35 7.67E − 07	s36 7.28E − 07	s37 2.81E − 15
s38 2.14E − 16	cl32 2.53E − 20	cl33 1.89E − 12	cl34 2.87E − 08	cl35 6.61E − 05
cl36 1.19E − 06	cl37 1.56E − 06	cl38 5.52E − 11	cl39 1.98E − 12	cl40 6.14E − 16
ar34 7.90E − 15	ar35 9.49E − 09	ar36 6.47E − 03	ar37 1.17E − 05	ar38 7.24E − 04
ar39 5.08E − 09	ar40 7.06E − 09	ar41 2.66E − 12	ar42 1.16E − 13	ar43 5.46E − 17
ar44 2.68E − 18	k36 3.67E − 21	k37 1.77E − 14	k38 1.11E − 08	k39 3.37E − 05
k40 1.68E − 08	k41 5.71E − 09	k42 6.91E − 11	k43 6.75E − 12	k44 5.45E − 13
k45 1.13E − 13	k46 2.88E − 15	ca38 4.51E − 17	ca39 1.50E − 09	ca40 5.66E − 03
ca41 2.72E − 06	ca42 1.77E − 05	ca43 1.90E − 08	ca44 1.96E − 08	ca45 2.98E − 11
ca46 3.56E − 11	ca47 5.30E − 13	ca48 1.70E − 14	ca49 5.68E − 20	sc40 1.49E − 25
sc41 1.26E − 16	sc42 7.29E − 13	sc43 7.96E − 10	sc44 7.93E − 10	sc45 6.10E − 09
sc46 2.24E − 10	sc47 5.26E − 11	sc48 2.62E − 12	sc49 1.27E − 13	sc50 3.01E − 17
ti42 6.80E − 23	ti43 2.20E − 15	ti44 1.82E − 06	ti45 7.81E − 08	ti46 6.83E − 06
ti47 1.22E − 07	ti48 8.08E − 08	ti49 5.12E − 10	ti50 5.90E − 10	ti51 9.21E − 15
ti52 1.60E − 15	v45 3.89E − 18	v46 4.58E − 11	v47 2.18E − 08	v48 1.68E − 08
v49 3.81E − 08	v50 7.99E − 10	v51 5.84E − 09	v52 3.56E − 13	v53 5.93E − 14
v54 4.56E − 18	cr46 4.25E − 20	cr47 1.09E − 12	cr48 5.44E − 05	cr49 5.00E − 06
cr50 4.81E − 05	cr51 8.94E − 07	cr52 9.20E − 06	cr53 2.30E − 09	cr54 1.19E − 10
cr55 1.26E − 16	cr56 1.16E − 16	mn48 3.10E − 24	mn49 2.19E − 15	mn50 1.84E − 09
mn51 7.50E − 06	mn52 2.04E − 07	mn53 4.74E − 06	mn54 2.40E − 08	mn55 8.95E − 09
mn56 4.28E − 14	mn57 5.01E − 15	mn58 1.26E − 18	fe50 2.64E − 20	fe51 8.21E − 12
fe52 8.71E − 04	fe53 1.01E − 04	fe54 4.27E − 03	fe55 2.33E − 05	fe56 6.92E − 05
fe57 7.79E − 09	fe58 4.70E − 10	fe59 2.26E − 16	fe60 4.17E − 16	fe61 1.07E − 21
fe62 3.51E − 21	co52 3.31E − 25	co53 1.19E − 15	co54 9.86E − 09	co55 3.53E − 04
co56 1.62E − 06	co57 2.81E − 06	co58 7.86E − 09	co59 3.76E − 09	co60 6.25E − 14
co61 6.24E − 15	co62 4.47E − 19	co63 6.91E − 18	ni54 2.02E − 21	ni55 7.03E − 12
ni56 1.71E − 02	ni57 2.35E − 04	ni58 3.76E − 04	ni59 7.34E − 07	ni60 2.53E − 06
ni61 6.26E − 10	ni62 2.97E − 10	ni63 8.81E − 16	ni64 5.10E − 15	ni65 3.26E − 20
ni66 2.58E − 18	ni67 8.11E − 24	cu57 2.82E − 17	cu58 4.00E − 13	cu59 2.57E − 10
cu60 4.60E − 11	cu61 1.05E − 10	cu62 1.44E − 12	cu63 5.99E − 12	cu64 7.46E − 16
cu65 5.68E − 15	cu66 6.21E − 19	cu67 4.64E − 17	cu68 8.32E − 22	cu69 1.27E − 20
zn59 1.17E − 21	zn60 1.33E − 11	zn61 2.91E − 12	zn62 1.06E − 10	zn63 2.19E − 13
zn64 1.01E − 11	zn65 6.68E − 15	zn66 5.21E − 14	zn67 4.66E − 18	zn68 1.88E − 16
zn69 5.13E − 21	zn70 2.44E − 18	zn71 1.40E − 23	zn72 1.88E − 21	ga62 5.04E − 21
ga63 5.52E − 19	ga64 4.93E − 19	ga65 3.25E − 18	ga66 1.84E − 19	ga67 7.57E − 18
ga68 2.97E − 20	ga69 1.91E − 17	ga70 5.00E − 20	ga71 3.65E − 18	ga72 3.23E − 22
ga73 9.45E − 20	ga74 2.50E − 23	ge64 7.80E − 20	ge65 2.98E − 21	ge66 3.73E − 18
ge67 7.43E − 21	ge68 3.99E − 18	ge69 2.83E − 20	ge70 2.57E − 17	ge71 4.23E − 20
ge72 4.78E − 18	ge73 1.65E − 21	ge74 3.22E − 19	ge75 3.18E − 23	ge76 2.94E − 20
ge77 1.32E − 24	ge78 5.90E − 23			

Table 10
Major nucleosynthesis yields

Element	13 $M_\odot$		15 $M_\odot$		20 $M_\odot$	25 $M_\odot$	
C	0.060	0.062	0.083	0.084	0.115	0.148	0.152
O	0.218	0.188	0.433	0.359	1.480	3.000	2.816
Ne	0.028	0.017	0.039	0.044	0.257	0.631	0.467
Mg	0.012	0.018	0.046	0.039	0.182	0.219	0.342
Si	0.047	0.053	0.071	0.058	0.095	0.116	0.142
S	0.026	0.027	0.023	0.025	0.025	0.040	0.029
Ar	5.5 − 3	5.1 − 3	4.0 − 3	4.8 − 3	4.5 − 3	7.2 − 3	5.4 − 3
Ca	5.3 − 3	4.2 − 3	3.3 − 3	4.0 − 3	3.7 − 3	6.2 − 3	4.4 − 3
Fe	?0.150?		?0.150?		0.075	?0.050?	

6. Averaged SN II abundance yields

Galactic chemical evolution calculations take into account the continuous enrichment of the interstellar medium by SNe I and SNe II, stellar winds (planetary nebulae), etc. In the very early evolution of the galaxy, only the most massive stars could contribute because of their short lifetime. At time t only those stars with $\tau_{MS}(M) < t$ can be considered (using the main sequence lifetime as an approximate measure for the lifetime until the onset of a supernova event in massive stars). If we have varying nucleosynthesis yields with stellar mass, this will lead to varying abundance ratios [x/Fe] in the ISM as a function of time or metallicity [Fe/H]=$\log_{10}[(\text{Fe/H})/(\text{Fe/H})_\odot]$, which can also be taken as a time indicator.

Matteuchi (1987), Matteuchi and Francois (1989) and Mathews, Bazan and Cowan (1991) find that for a typical star formation rate in the solar neighborhood, 30 $M_\odot$ stars will contribute for the first time at [Fe/H] ≈ -3.9, 12 $M_\odot$ stars at -3 and the least massive SNe II somewhere between -3 and -2. Intermediate mass stars will enrich the interstellar medium for [Fe/H] ≥ -2 via planetary nebula ejection. SNe Ia, which come from binary systems of intermediate mass stars, are further delayed in time and appear at [Fe/H] ≈ -1. The elements listed in tables 10 and 11 can only derive from supernovae (with the exception of C) and therefore can be contributed solely by SNe II for [Fe/H]< -1. In the range $-2.5 \leq$ [Fe/H] ≤ -1 we will expect averaged values for [x/Fe], because SNe II of the whole progenitor mass range contribute. Only below -3 do we expect deviations due to selection effects, singling out more and more massive SNe II with decreasing [Fe/H] which could evolve fast enough to undergo already SN II events at such low metallicities. Therefore it is not surprising that observations show a constant [x/Fe], x being O, Mg, Si, S, Ca, Ti, Cr, Ni between -2.5 and -1. The integrated yields of SNe II should therefore result in an abundance pattern as found in low metallicity stars.

In a first attempt we have tried a crude method to test whether these considerations are consistent with the results from our explosion calculations. We utilized the coarse grid given by a set conisisting of 13, 15, 20, and 25 $M_\odot$ stars – neglecting the contribution from stars less massive than 13 $M_\odot$ – and performed an integration over the abundance yields of the individual elements $M_{ej,x}(M)$ from table 10, weighted with a Salpeter initial mass function (IMF)

$$M_x \propto \int_8^{100} M_{ej,x}(M) M^{-2.35} dM. \tag{6.1}$$

We extrapolated the yields smoothly up to M=40 $M_\odot$, from where they were kept constant. This relates to the fact that more massive stars will lose large amounts of envelope mass, in the form of stellar winds, during their early evolution, so that their later evolution resembles that of less massive stars. The procedure differed only for Fe, which was kept constant for M>25 $M_\odot$.

The integration over an IMF gives the same abundance ratios as full scale galactic chemical evolution calculations, provided that the IMF and the star formation rate (SFR) are constant in time. The resulting [x/Fe] ratios and the average mass ejected for the elements are given in table 11, and compared to the [x/Fe] values observed in low metallicity stars. The latter are taken from reviews by Gehren (1988); Wheeler, Sneden, and Truran (1989); and Lambert (1989).

The results are encouraging, considering the crude method and the fact that the observations probably have errors of 0.1–0.2 dex. They agree within

Table 11
Integrated abundance yields

Element	[x/Fe]	$< M_x >$	[x/Fe] for [Fe/H]<-1
C	−0.13	0.067	0.0
O	0.68	1.369	0.5
Ne	0.76	0.295	-
Mg	0.63	0.082	0.4
Si	0.40	0.052	0.4
S	0.21	0.020	0.5
Ar	0.13	0.004	-
Ca	0.25	0.003	0.3
Fe	0.00	0.038	0.0

the observational errors for all elements, with the exception of S. The detailed calculations show an increase for the yields of S, Ar, and Ca from 20 to 25 $M_\odot$ (see table 10), which is then extrapolated up to 40 $M_\odot$ in the integration of eq. (6.1). It is very important to obtain results for another stellar model in the range 30–40 $M_\odot$ to find out whether this behavior can be extrapolated or was just a local scatter. To obtain results for the Fe-yields it was also necessary to assume mass cuts for the 13, 15, and 25 $M_\odot$ stars. These were taken from papers explaining SN Ib/c light curves for stars of initial main sequence masses of 13 and 15 $M_\odot$ (Shigeyama et al. 1990, Nomoto et al. 1990, Hachisu et al. 1990), and require the ejection of 0.15 $M_\odot$ of ^{56}Ni for the 13 and 15 $M_\odot$ stars, respectively. If one wants to obtain a [Si/Fe] value of 0.4 and believes in the given Si yields, where no mass cut uncertainty enters, then the average Fe-mass produced in SN II+Ib events has to be 0.038 $M_\odot$. We were only able to achieve this goal when downscaling the values listed above and assuming for 25 $M_\odot$ and more massive stars the ejection of only 0.02 $M_\odot$, thus changing the respective value given in table 10. A possible interpretation of the statistically still-insignificant sample of bolometric Type II plateau supernova light curves (Young and Branch 1989, Phillips et al. 1990), is that it is an indication that the average Type II-P supernova (being less massive than 20 $M_\odot$) produces more Fe than SN 1987A, which has the dimmest tail by about a factor of 2. Because of the very small sample, a more massive Type II plateau supernova (which would have an even dimmer tail according to our prediction) was not observed. This is a still unsettled question. Other researchers even predict the opposite trend, Fe-ejecta increasing with stellar mass (Woosley and Weaver 1991). If, however, our predictions for Si are correct and results do not change drastically when using an initial mass function different from a Salpeter IMF, the average ejected Fe-mass for SNe II has to be 0.038 $M_\odot$ when we neglect contributions from 8–13 $M_\odot$ (for any progenitor mass dependence, whether rising or declining with M). This value is small by any standards and less than previously expected.

We neglected contributions by SNe II in the mass range 8–10 $M_\odot$, which will undergo collapse to neutron star densities, as well as C- through Si-burning in one continuous burning stage initiated by e-capture in a strongly degenerate core. 10–13 $M_\odot$ stars are also strongly affected by core degeneracy and have a very steep density gradient at the edge of the Fe-core. In both cases minor amounts of explosive nucleosynthesis ejecta are expected (e.g. the Crab nebula), although it is not completely clear whether these are negligible. But the C/O ratio in hydrostatic C-cores will be larger than for more massive stars, and with the strong statistical weight of the lower mass stars (IMF) the [C/Fe] ratio will increase and the [O/Fe] ratio decrease towards the observed value. When this happens, one obtains a picture which is consistent with observations. This is not a direct proof for our correct choice; Ni(Fe)-ejecta increasing with mass of the progenitor star but giving the same IMF-integrated yield, would produce the same result.

Observational evidence for the correct behavior can only come from [x/Fe]-ratios for stars with [Fe/H] ≤ -2.5, where (in time) the lower-mass core-collapse supernovae could not have exploded yet, and only more and more massive stars are contributing with decreasing [Fe/H]. At [Fe/H] ≈ -4 one would expect [x/Fe]-ratios which are only affected by stars with masses M>30 $M_\odot$ and dominated by the least massive ones, because of the steep slope of the IMF. Our list in table 10 does not yet include such massive stars, so we take the yields of the 25 $M_\odot$ star as a close estimate. Some values would be [Mg/Fe] $\approx$ 1.11 and [Ca/Fe] $\approx$ 0.37 for the masses of ejected Fe as listed in table 10. This seems to coincide with recent observations by Molaro and Bonifacio (1990), and would be a very encouraging result. However, with ejected Fe masses of 0.02 $M_\odot$ these values would change to 1.51 and 0.77, which is larger than the observed ratios. Whether this is a clear contradiction has still to be evaluated, because the corresponding [Fe/H] values were calculated by Matteucci (1987) and Mathews, Bazan, Cowan (1991) with different Fe yields, and the time at which [Fe/H] = -4 is obtained, would be later, when stars smaller than a 30 $M_\odot$ are exploding. Thus, a comparison awaits a reevaluation of [Fe/H] and a complete galactical evolution calculation with these new yields. A complete survey over more such low metallicity objects (hopefully forthcoming, Beers et al. 1990) can give final evidence for the correct choice of the neutron star mass cut.

We want to stress the point that the results of this chapter are highly dependent on the extrapolation towards larger progenitor masses between 25 and 40 $M_\odot$, and neglect of stars in the range 8-13 $M_\odot$. The more massive stars burn He at higher temperatures, which enhances the $^{12}C(\alpha,\gamma)^{16}O$ rate (independent of nuclear uncertainties), and essentially only ^{16}O is left after He burning. Thus, core C and Ne burning do not take place, and larger Fe cores with higher entropies are expected, which will have a decisive influence on the final outcome in a supernova explosion. A different behavior of the nucleosynthesis yields could cause important changes in the average ejected masses of SNe II, given in tables 11 and 12. This in turn would have consequences with respect to the allowed amount of Fe ejection for more massive stars and stars in the 8–13 $M_\odot$ range. *In a preliminary evaluation of a 40 $M_\odot$ star (16 $M_\odot$ He-core), with the aid of the analytical model discussed in section 5.1, we obtained yields for Si, S, Ar, and Ca more than twice as large as the*

Table 12
Masses in SNe Ia and SNe II

	SNI (TNY 1986)	SNII average
C	0.020	0.067
O	0.130	1.369
Ne	0.004	0.295
Mg	0.016	0.082
Si	0.150	0.052
S	0.083	0.020
Ar	0.018	0.004
Ca	0.015	0.003
Fe	0.742	0.038

linear extrapolation beyond 25 $M_\odot$. This results in a value for the average ejected mass of SNe II for these elements, which is almost twice as large, while C, O, and Ne are not much affected. This in turn allows an average ejected mass of Fe of 0.07 $M_\odot$ (still neglecting 8–13 $M_\odot$ stars) and reduces the [O/Fe] ratio to 0.5. Therefore, the results of table 11 should be taken as preliminary and subject to a further exploration of explosion calculations beyond the presently discussed mass range.

7. SN I and SN II contributions to nucleosynthesis

To compare the different contributions of SNe Ia and SNe II to the interstellar medium, we display in table 12 masses resulting from the standard model of SNe Ia (W7) and an average SNe II (taken from table 11). The main difference is seen in the vastly differing amounts of Fe-peak elements. However, one also finds that for all elements beyond Si, SNe Ia produce larger quantities in a single event than the average SN II. This factor is much larger for Fe than for Si-Ca. Therefore, the relative frequency of both events determines which one is the dominant source for individual elements. Another difference is given by the fact that only SNe Ia seem to eject matter which experienced a normal freeze-out in complete Si-burning. This also ensures that the dominant abundances of ^{54}Fe and ^{55}Mn (from ^{55}Co-decay) come from SNe Ia, to cite one example, while their counterparts ^{58}Ni and ^{59}Co (from ^{59}Cu-decay) stem from a distorted Fe-peak composition in an alpha-rich freeze-out.

The innermost matter of SNe Ia experiences strong electron captures and attains values of Y_e=0.46-0.47 while a 20 $M_\odot$ star only ejects matter as neutron-rich as $Y_e = 0.498$, the only stable ^{56}Fe – not being a decay product of ^{56}Ni – comes from SNe Ia. Similarly the contributions to ^{54}Fe and ^{55}Co, both nuclei with $N/Z > 1$, are enhanced. This statement is very tentative, however, as we assume that less massive SNe II can actually eject more neutron-rich material and even r-process nuclei; and the Y_e-values in SNe Ia depend strongly on the propagation speed of the deflagration front, which governs the amount of electron captures and is still somewhat uncertain.

Zones further out in SNe Ia and SNe II have a Y_e determined by the original metallicity in the form of ^{22}Ne, which is produced in hydrostatic He-burning from CNO-nuclei. Thus for the same metallicities the burning conditions barely differ, but the masses involved vary. While SNe Ia, consisting initially only of C and O, eject only products of *explosive* Ne and C-burning, SNe II can have extended convective shells of C and Ne-burning which will only be partially processed explosively (see discussion in section 5.1–5.3), and thus a large amount of hydrostatic C and Ne-burning material will also be contributed from SNe II.

Relying on the still very tentative results for average ejecta of SNe II from table 11, one can try to derive a ratio of SN Ia to SN II events, which is necessary to produce a solar Si/Fe ratio in total

$$\frac{M(Si)}{M(Fe)_\odot} = \frac{R_\mathrm{I} M_\mathrm{I}(Si) + R_\mathrm{II} M_\mathrm{II}(Si)}{R_\mathrm{I} M_\mathrm{I}(Fe) + R_\mathrm{II} M_\mathrm{II}(Fe)}. \tag{7.1}$$

Here M denotes the mass involved, R the supernova rate, I and II the types of supernovae. From here we can derive a ratio

$$\frac{R_\mathrm{I}}{R_\mathrm{II}} = -\frac{M_\mathrm{II}(Si) - M(Si)/M(Fe)_\odot M_\mathrm{II}(Fe)}{M_\mathrm{I}(Si) - M(Si)/M(Fe)_\odot M_\mathrm{I}(Fe)} = 0.16 \pm 0.04, \tag{7.2}$$

if we adopt the appropriate values for M_I and M_II from table 12, as well as $M(Si)/M(Fe)_\odot$ from Anders and Grevesse (1989). The error range comes from using either all Si and Fe isotopes, or only ^{28}Si and ^{56}Fe (the neutron-rich isotopic yields will vary with the metallicity evolution in time). Such a ratio is quite uncertain, due to the fact that small differences of large uncertain numbers are involved. However, the results for SNe Ia seem quite reliable, since a number of tests comparing theoretical and observational light curves and spectra have been performed. $R_\mathrm{I}/R_\mathrm{II}$ reflects the ratio of SNe Ia to all core collapse events. If SNe Ib/c are interpreted as core collapse events of massive Wolf-Rayet stars (e.g. Wheeler and Levreault 1985; Ensman and Woosley 1988; Shigeyama et al. 1990; Nomoto et al. 1990; Hachisu et al. 1990) and one uses the respective observational rates for SNe Ia, SNe Ib/c, and SNe II (van den Bergh and Tammann 1991), a remarkable agreement is obtained ($R_{Ia}=.\,R_{Ib}+R_{II}/\ =0:151$).

When we take the value for $R_I=R_{II}$ from eq. (7.2), we obtain that the intermediate mass elements from Si to Ca (Si being representative) are produced to roughly 30% in SNe Ia, while Fe, i.e. ^{56}Fe, is produced to 75% in SNe Ia. This means that 70% of Si and 25% of Fe originates from SNe II. It will be interesting to test similar predictions for other elements in the future. However, to obtain really reliable results, one has to extend explosive nucleosynthesis predictions for SNe II to the progenitor mass ranges $M<13\ M_\odot$ and $M>25\ M_\odot$.

Acknowledgements

We want to thank our collaborators M. Aufderheide, E. Baron, M. Hashimoto, T. Shigeyama, and T. Tsujimoto, who contributed to the material presented here. This research was supported in part by NSF grant AST 89-13799, NASA grant NGR 22-007-272; Grants-in-Aid for Scientific Research of the Ministry of Education, Science, and Culture in Japan (01540216, 01652503,02234202, 02302024); and the U.S.-Japan Cooperative Science Program (INT 88-15999/ EPAR-071) operated by the NSF and JSPS. The computations were performed at the National Center for Supercomputer Applications at the University of Illinois (AST 890009N).

References

Alastuey, A. and B. Jancovici 1978. *Astron. Astrophys.* **266**, 1034.

Anders, E. and N. Grevesse 1989. *Geochim. Cosmochim. Acta* **53**, 197.

Arnett, W.D., J.N. Bahcall, R.P. Kirshner and S.E. Woosley 1989. *Ann. Rev. Astron. Astrophys.* **27**, p. 629.

Arnett, W.D. and F.-K. Thielemann 1985. *Ap. J.* **295**, 589.

Aufderheide, M., E. Baron and F.-K. Thielemann 1991. *Ap. J.* **370**, 630.

Aufderheide, M.B., G.E. Brown, T.T.S. Kuo, D.B. Stout and P. Vogel 1990. *Ap. J.* **362**, 241.

Bao, Z.Y. and F. Käppeler 1987. *At. Nucl. Data Tables* **36**, 411.

Baron, E. and J. Cooperstein 1990. in Supernovae, ed. S.E. Woosley, (Springer-Verlag, New York), p. 342.

Beers, T., G.W. Preston and S.A. Shectman 1991. in Elements and the Cosmos, ed. R. Terlevich (Cambridge Univ. Press), in press.

Bethe, H.A. 1990. *Rev. Mod. Phys.* **62**, 801.

Blake, J.B., S.E. Woosley, T.A. Weaver and D.N. Schramm 1981. *Ap. J.* **248**, 315.

Bouchet, P., I.J. Danziger and L. Lucy 1991. in SN1987A and Other Supernovae, ed. I.J. Danziger (ESO, Garching), in press.

Bruenn, S.W. 1989. *Ap. J.* **340**, 955.

Bruenn, S.W. 1989. *Ap. J.* **341**, 385.

Cameron, A.G.W. 1989. in Cosmic Abundances of Matter, ed. C.J. Waddington, AIP Conf. Proc. 183, p. 349.
Canal, R., J. Isern, J. Labay and R. Lopez 1990. in Supernovae, ed. S.E. Woosley, (Springer-Verlag, New York), p. 535.
Caughlan, G.R., W.A. Fowler, M.J. Harris and G.E. Zimmerman 1985. *At. Nucl. Data Tables* **32**, 197.
Caughlan, G.R. and W.A. Fowler 1988. *At. Nucl. Data Tables* **40**, 283.
Clayton, D.D. 1968. Principles of Stellar Evolution and Nucleosynthesis, (McGraw Hill, New York).
Cooperstein, J. and E. Baron 1989. in Supernovae, ed. A. Petschek, (Springer-Verlag, New York), p. 213.
Cowan, J.J., A.G.W. Cameron and J.W. Truran 1983. *Ap. J.* **265**, 429
Cowan, J.J., F.-K. Thielemann and J.W. Truran. 1991. *Phys. Rep.*, in press.
Danziger, I.J., P. Bouchet, C. Gouiffes and L. Lucy 1990. in Supernovae, ed. S.E. Woosley, (Springer-Verlag, New York), p. 69.
Domogatsky, G.V. and D.K. Nadyozhin 1977. *M.N.R.A.S.* **178**, 33p.
Elias, J.H. et. al. 1991. in SN1987A and Other Supernovae, ed. I.J. Danziger (ESO, Garching), in press.
Ensman, L. and S.E. Woosley 1988. *Ap. J.* **333**, 754.
Epstein, R.I., S.A. Colgate and W.C. Haxton 1988. *Phys. Rev. Lett.* **61**, 2038.
Filippone, B.W. 1987. *Ann. Rev. Nucl. Part. Sci* **36**, 717.
Filippone, B.W., J. Humblet and K. Langanke 1989. *Phys. Rev. C*, **40**, 515.
Fowler, W.A., G.E. Caughlan and B.A. Zimmerman 1967. *Ann. Rev. Astron. Astrophys.* **5**, 525.
Fuller, G.M., W.A. Fowler, M. Newman 1980. *Ap. J. Suppl.* **42**, 447.
Fuller, G.M., W.A. Fowler and M. Newman 1982. *Ap. J. Suppl.* **48**, 279.
Fuller, G.M., W.A. Fowler and M. Newman 1985. *Ap. J.* **293**, 1.
Fushiki, I. and D.Q. Lamb 1987. *Ap. J.* **317**, 368.
Gehren. T. 1988. in Rev. in Mod. Astronomy **1**, p. 52.
Graham, J.R. 1987. *Ap. J.* **315**, 558.
Hansen, J.P., G.M. Torrie and P. Veillefosse 1977. *Phys. Rev.* **A16**, 2153.
Hashimoto, M., K. Nomoto and T. Shigeyama 1989. *Astron. Astrophys.* **210**, L5.
Haxton, W.C. 1988. *Phys. Rev. Lett.* **60**, 1999.
Henry, R.B.C. and R.A. Fesen 1988. *Ap. J.* **329**, 693.
Holmes, J.A., S.E. Woosley, W.A. Fowler and B.A. Zimmerman 1976. *At. Data Nucl. Data Tables* **18**, 306.
Ichimaru, S., S. Tanaka and H. Iyetomi 1984. *Phys. Rev.* **A29**, 2033.
Ichimaru, S. and K. Utsumi 1984. *Ap. J.* **286**, 363.
Itoh, N., F. Kuwashima and H. Munakatu 1990. *Ap. J.* **362**, 620.
Itoh, N., H. Totsuji and S. Ichimaru 1977. *Ap. J.* **218**, 477; *Ap. J.* **220**, 742.
Itoh, N., H. Totsuji, S. Ichimaru and H.E. DeWitt 1979. *Ap. J.* **234**, 1079; *Ap. J.* **239**, 415.
Khoklov, A.M. 1991. *Astron. Astrophys.*, in press.
Khoklov, A.M. 1991. *Astron. Astrophys.*, in press.
Klapdor, H.V., J. Metzinger and T. Oda 1981. *At Nucl. Data Tables*, **31**, 81.
Kratz, K.-L., F.-K. Thielemann, W. Hillebrandt, P. Möller, V. Harms, A. Wöhr and J.W. Truran 1988. *J. Phys. G.* **24**, S331.
Lambert, D.L. 1989. in Cosmic Abundances of Matter, ed. C.J. Waddington, AIP Conf. Proc. 183, p. 168.
LeBlanc, J.M. and J.R. Wilson 1970. *Ap. J.* **161**, 541.

Malaney, R.A. and W.A. Fowler 1988. *Ap. J.*, **333**, 14.
Malaney, R.A. and W.A. Fowler 1989. *Ap. J. Lett.*, **345**, L5.
Mathews, G.J., G. Bazan and J.J. Cowan, submitted to *Ap. J.*.
Mathews, G.J. and J.J. Cowan 1990. *Nature* **345**, 491.
Matteucci, F. 1987. in Stellar Evolution and Dynamics of the Outer Halo of the Galaxy, eds. M. Azzopardi, F. Matteucci, *ESO Conf. Proc.* **27**, p. 609.
Matteucci, F. and P. Francois 1989. *M.N.R.A.S.*, **239**, 885.
Mayle, R.W. and J.R. Wilson 1988. *Ap. J.* **334**, 909.
Mayle, R.W. and J.R. Wilson 1990. in Supernovae, ed. S.E. Woosley, (Springer-Verlag, New York), p. 333.
Möller, P. and J. Randrup 1990. *Nucl. Phys. A*, in press.
Mönchmeyer, R. and E. Müller 1989. in Timing Neutron Stars, eds. H. Ögelman, E. van den Heuvel (Kluwer, Dordrecht), p. 549.
Mönchmeyer, R. and E. Müller 1989. *Astron. Astrophys.* **217**, 351.
Molaro, P. and P. Bonifacio 1990. *Astron. Astrophys.*, submitted.
Müller, E. and W.D. Arnett 1986. *Ap. J.* **307**, 619.
Myra, E.S. and S. Bludman 1989. *Ap. J.* **340**, 384.
Nomoto, K. and M. Hashimoto 1988. *Phys. Rep.* **163**, 13.
Nomoto, K., A.V. Filippenko and T. Shigeyama 1990. *Astron. Astrophys.* **240**, L1.
Nomoto, K. and T. Shigeyama 1990. in Supernovae, ed. S.E. Woosley, (Springer-Verlag, New York), p. 572.
Nomoto, K., F.-K. Thielemann and K. Yokoi 1984. *Ap. J.*, **286**, 644.
Nomoto, K., F.-K. Thielemann and S. Myaji 1985. *Astron. Astrophys.*, **149**, 239.
Phillips, M.M., M. Hamuy, J. Maza, M.T. Ruiz, B.W. Carney and J.A. Graham 1990. *Publ. Astron. Soc. Pac.* **102**, 299.
Pinto, P.A. and J. Spyromilio 1991. private communication.
Press, W.H., B.P. Flannery, S.A. Teukolsky and W.T. Vetterling 1986. Numerical Recipes (Cambridge Univ. Press).
Rolfs, C. and W.S. Rodney 1988. Cauldrons in the Cosmos, (Univ. of Chicago Press).
Rolfs, C., H.P. Trautvetter and W.S. Rodney 1987. *Rep. Prog. Phys.* **50**, 233.
Salpeter, E.E. and H.M. van Horn 1969. *Ap. J.* **155**, 183.
Schramm, S. and S.E. Koonin 1990. *Ap. J.* **365**, 296.
Shigeyama, T., K. Nomoto and M. Hashimoto 1988. *Astron. Astrophys.* **196**, 141.
Shigeyama, T., K. Nomoto, T. Tsujimoto and M. Hashimoto 1990. *Ap. J. Lett.* **361**, L23.
Staudt, A., E. Bender, K. Muto and H.V. Klapdor 1989. *Z. Phys.*, **A334**, 47.
Staudt, A., E. Bender, K. Muto and H.V. Klapdor 1990. *Atomic and Nucl. Data Tables.*, **44**, 79.
Symbalisty, E.M.D., D.N. Schramm and J.R. Wilson 1985. *Ap. J. Lett.* **291**, L11.
Taam, R.E. 1985. *Ann. Rev. Nucl. Part. Sci* **35**, 1.
Takahara, M., M. Nino, T. Oda, K. Muto, A.A. Wolters, P.W.M. Claudemans and K. Sato 1989. *Nucl. Phys.* **A504**, 167.
Takahashi, K., M. Yamada and Z. Kondo 1973. *At. Data Nucl. Data Tables* **12**, 101.
Takahashi, K. and K. Yokoi 1988. *At. Data Nucl. Data Tables* **36**, 375.
Thielemann, F.-K. and W.D. Arnett 1985. *Ap. J.* **295**, 604.
Thielemann, F.-K., M. Arnould and W. Hillebrandt 1979. *Astron. Astrophys.*, **74**, 175.
Thielemann, F.-K., M. Arnould and J.W. Truran 1987. in Advances in Nuclear Astrophysics, eds. E. Vangioni-Flam et al., (éditions frontières: Gif sur Yvette), p. 525.
Thielemann, F.-K., M. Hashimoto and K. Nomoto 1990. *Ap. J.* **349**, 222.

Thielemann, F.-K., K. Nomoto and M. Hashimoto 1990. in Chemical and Dynamical Evolution of Galaxies, eds. F. Ferrini, J. Franco, F. Matteucci (Giardini, Pisa-Lugano), in press.
Thielemann, F.-K., K. Nomoto and K. Yokoi 1986. *Astron. Astrophys.*, **158**, 17.
Thielemann, F.-K., K. Nomoto, T. Shigeyama, T. Tsujimoto and M. Hashimoto 1991. in Elements and the Cosmos, ed. R. Terlevich (Cambridge Univ. Press), in press.
Thielemann, F.-K. and J.W. Truran 1987. in *Advances in Nuclear Astrophysics*, eds. E. Vangioni-Flam *et al.*, éditions frontières: Gif sur Yvette, p. 541.
Thielemann, F.-K. and M. Wiescher 1990. in Primordial Nucleosynthesis, eds. W. Thompson and B. Carney, (World Scientific, Singapore), p. 92.
Truran, J.W. 1985. *Ann. Rev. Nucl. Part. Sci.* **34**, 53.
Truran, J.W., J.J. Cowan and A.G.W. Cameron 1978. *Ap. J. Lett.* **222**, L63.
Unno, W. 1967. *Publ. Astron. Soc. Japan* **19**, 140.
van den Bergh, S. and G.A. Tammann 1991. *Ann. Rev. Astron. Astrophys.* **29**, in press.
Varani, G.-F., W.P.S. Meikle, J. Spyromilio and D.A. Allen 1990. *MNRAS* **245**, 570
Wallace, R.A. and S.E. Woosley 1981. *Ap. J. Suppl.* **45**, 389.
Wapstra, A.H., G. Audi and R. Hoekstra 1988. *At. Nucl. Data Tables* **39**, 281.
Weaver, T.A. and S.E. Woosley 1980. *Ann. N.Y. Acad. Sci.* **366**, 335.
Wheeler, J.C., C. Sneden and J.W. Truran 1989. *Ann. Rev. Astron. Astrophys.*, **27**, 279.
Wheeler, J.C. and R. Levreault 1985. *Ap. J. Lett.* **294**, L17.
Wiescher, M., J. Görres, F.-K. Thielemann and H. Ritter 1986. *Astron. Astrophys.* **160**, 56.
Wiescher, M., V. Harms, J. Görres, F.-K. Thielemann and L.J. Rybarcyk 1987. *Ap. J.* **316**, 162.
Wiescher, M. and J. Görres 1988. *Z. Phys.* **A329**, 121.
Wiescher, M., J. Görres and F.-K. Thielemann 1988. *Ap. J.* **326**, 384.
Wiescher, M., J. Görres and F.-K. Thielemann 1990. *Ap. J.* **363**, 340.
Wiescher, M., J. Görres, S. Graaf, L. Buchmann and F.-K. Thielemann 1989. *Ap. J.*, in press.
Wilson, J.R. and R.W. Mayle 1988. *Phys. Rep.* **163**, 63.
Witteborn, F.C., D. Rank, J.D. Bregman, P.A. Pinto, D. Wooden and T.S. Axelrod *Ap. J. Lett.*, in press.
Woosley, S.E. 1988. *Ap. J.* **330**, 218.
Woosley, S.E., W.D. Arnett and D.D. Clayton 1973. *Ap. J. Suppl.* **26**, 231.
Woosley, S.E., W.A. Fowler, J.A. Holmes and B.A. Zimmerman 1978. *At. Nucl. Data Tables* **22**, 371.
Woosley, S.E., D. Hartmann, R.B. Hoffman and W.C. Haxton 1990. *Ap. J.*, in press.
Woosley, S.E. and W.C. Haxton 1988. *Nature* **334**, 45.
Woosley, S.E., P.A. Pinto and T.A. Weaver 1988. *Proc. Astron. Soc. Australia* **7**, 355.
Woosley, S.E. and T.A. Weaver 1986. *Ann. Rev. Astron. Astrophys.* **24**, 205.
Woosley, S.E. and T.A. Weaver 1986. *in* Radiation Hydrodynamics, IAU Colloq. No. 89, eds., D. Mihalas, K.H. Winkler, (Reidel, Dordrecht), p. 91.
Woosley, S.E. and T.A. Weaver 1991. in Les Houches, Session LIV, Supernovae, eds. S.R. Bludman, R. Mochkovitch, J. Zinn-Justin (Elsevier Science Publ.), in press.
Young, T.R. and D. Branch 1989. *Ap. J. Lett.* **342**, L79.
Zeldovich, Ya.B., G.I. Baerenblatt, V.B. Librovich and G.M. Makhviladze 1985. *The Mathematical Theory of Combustion and Explosions*, (Plenum, New York).

COURSE XIV

THE LATE EMISSION FROM SUPERNOVAE

CLAES FRANSSON

Stockholm Observatory
S-133 36 Saltsjöbaden, Sweden

S. Bludman, R. Mochkovitch and J. Zinn-Justin, eds.
Les Houches, Session LIV, 1990
Supernovae

Contents

1. Introduction 680
2. Hydrodynamical and chemical structure 681
3. Gamma-ray thermalization 685
   3.1. Radioactive input 685
   3.2. The gamma-ray spectrum 685
   3.3. Gamma-ray thermalization 686
   3.4. Electron thermalization 688
   3.5. Positrons 695
4. Thermal and ionization equilibrium 696
5. Line formation 700
6. Plasma diagnostics 707
7. The spectra of Type II supernovae 710
   7.1. The hydrogen envelope 710
   7.2. The helium mantle 716
   7.3. The oxygen core 717
   7.4. The iron core 724
8. Type Ia supernovae 726
9. Mixing 726
10. Formation of molecules 727
11. Dust formation in supernovae 729
12. Effects of a neutron star 731
13. Circumstellar excitation 734
14. Conclusions 738
References 739

1. Introduction

Observations of supernovae in the late stage are likely to give the most interesting information about nucleosynthesis, hydrodynamics of the explosion, and the formation of a compact remnant. Both in connection with SN 1987A and other supernovae, there has recently been an impressive increase in the observational input to our knowledge of this stage (see the lectures by Bob Kirshner). For these reasons there is a strong motivation to understand the physics of this phase.

The energy input in core collapse supernovae is, during the first phase after the explosion, dominated by the internal energy of the remnant produced by the passage of the shock. For an extended progenitor, where adiabatic losses are of less importance, this phase may last up to a hundred days (e.g. Chevalier 1976; Weaver and Woosley 1980). For a compact progenitor, like that of SN 1987A, the internal energy decreases by a factor of 10–100 in the expansion, and this phase only lasts for a week or so. If there were no other source of energy, the emission from the remnant would then decay rapidly. However, from studies of SN 1987A and other supernovae we know that the production of ^{56}Ni in the explosion, and the subsequent radioactive decay, is enough to power the remnant for a long period of time after the thermal energy has been radiated away. This has been for a long time, the generally accepted model for Type Ia supernovae, and most of the early work on late spectra concentrated on this class of supernovae (Axelrod 1980b; Meyerott 1980). Also, at very late phases, the energy due to a newly born neutron star, or circumstellar interaction, may become important for the excitation of line emission in Type II's.

Late phases are in general understood to mean epochs later than about 200 days, when the core region becomes visible. This is sometimes known as the nebular phase, which is somewhat misleading since its physics differs greatly from that of ordinary gaseous nebulae. In these lectures I review different excitation mechanisms, and their implications for the observed emission. The emphasis will be on the basic physics, rather than detailed applications. Although most of the review deals with applications to core collapse supernovae, the physics is the same for Type Ia's. Related reviews and applications can be found in Fransson (1987b; 1988), Fransson and Chevalier (1989), Axelrod (1988), Xu (1989), and McCray (1990).

2. Hydrodynamical and chemical structure

Figure 1 shows the result of a one-dimensional, hydrodynamical calculation of an explosion of a $20M_\odot$ ZAMS star. This particular model, 11E1 of Shigeyama et al. (1988), has a $6M_\odot$ helium core, and is chosen to reproduce the parameters of SN 1987A. The explosive nucleosynthesis of this model is discussed by Hashimoto et al. (1989). The structure can be divided into four distinct regions. In the center we have the neutron star with a mass of $\sim 1.6M_\odot$. For most of our discussion this unfortunately has little observational influence (however, see section 12). The oxygen core between $1.6M_\odot$ and $3.76M_\odot$, includes elements from the carbon burning stages and later. The inner part of this zone, from $1.6M_\odot$ to $1.8M_\odot$, is the result of explosive nucleosynthesis in the explosion, and is shown in more detail in the lower frame of fig. 1a. The structure outside of this mass is determined by the progenitor's evolution. The relative abundances between oxygen, carbon, neon etc. are sensitive to both the $^{12}C(\alpha,\gamma)^{16}O$ rate and the convective treatment. The 11E1 model with a high $^{12}C(\alpha,\gamma)^{16}O$ rate, resulted in large O/Ne and O/C ratios. A lower rate of this reaction leads to a substantial decrease of both these ratios (Woosley et al. 1988). Woosley et al. estimate that the uncertainty in the mass of ^{16}O is a factor of ~ 6. The helium mantle between 3.76 and $6.0M_\odot$ is dominated by helium, and less than 0.02 by number is in heavier elements, mainly carbon. The mass of the exterior hydrogen envelope depends on the amount of mass loss in the progenitor. In this particular case $7.5M_\odot$ has been lost, and only $6.5M_\odot$ remains. Mixing of CNO products can alter the main sequence composition of the envelope substantially, mainly increasing the N/C ratio. This has been observed in both SN 1979C and SN 1987A (Fransson et al. 1984, 1989).

The velocity at the base of the hydrogen envelope is $\sim 1900\,\mathrm{km\,s^{-1}}$, and extends to several times $10,000\,\mathrm{km\,s^{-1}}$. Only a small fraction, less than $0.5M_\odot$, has a velocity of more than $5000\,\mathrm{km\,s^{-1}}$. The helium mantle extends over a velocity range of only 1470 to $1900\,\mathrm{km\,s^{-1}}$, while the oxygen core spans an even narrower range, from 1320 to $1470\,\mathrm{km\,s^{-1}}$. There is no matter at lower velocities in these models; this is the result of the ^{56}Ni-bubble in the center. The heat input from radioactive decay during the first weeks

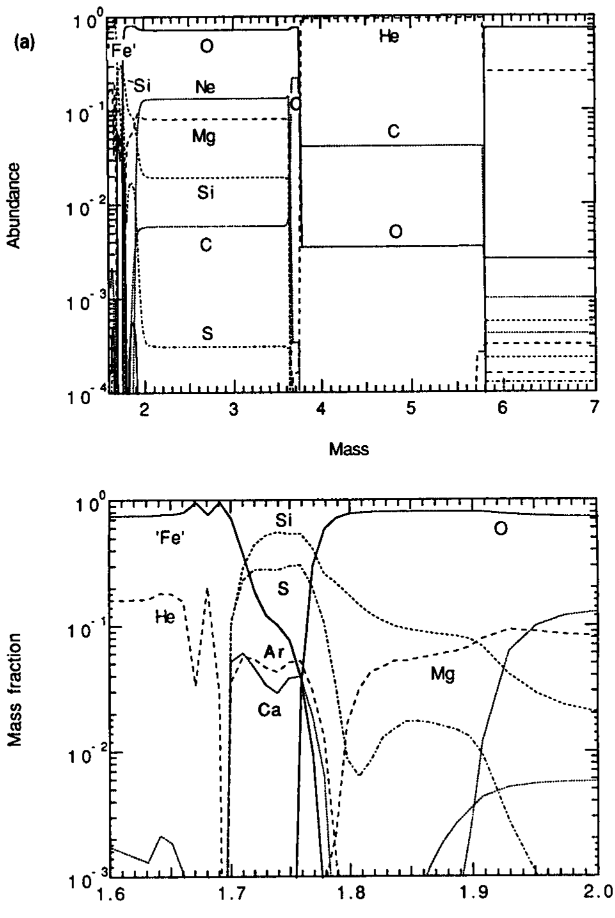

Fig. 1a. Elemental composition as a function of the mass from the center, for model 11E1 ($6M_{\odot}$ He-core) after explosive nucleosynthesis. (From Shigeyama et al. 1988; and Hashimoto et al. 1989). The mass of the neutron star is $\sim 1.8M_{\odot}$. The region inside $\sim 1.5M_{\odot}$ has undergone explosive nucleosynthesis.

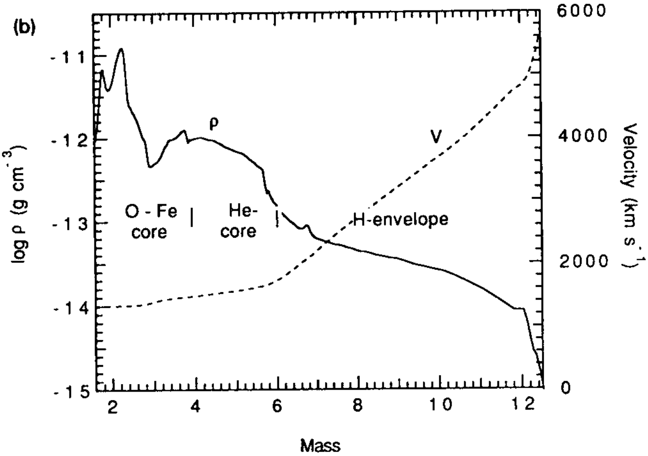

Fig. 1b. Density and velocity for the model in fig. 1a. Note the sharp density peak and nearly constant velocity in the oxygen core.

accelerates the gas in the center to higher velocities, creating a central cavity (Shigeyama et al. 1988; Woosley 1988).

An important result is that after a few weeks the remnant expands homologously, with $V(r) \propto r$. This simplifies the dynamics greatly, since the density is basically set by the early evolution, and after this scales with $\rho \propto t^{-3}$, while the radius of a given mass coordinate, m, expands as $r(m) = V(m)t$. In section 5 this is exploited in the analysis of the line profiles in order to extract information about the structure of the remnant.

The density graph (fig. 1b) has a sharp peak in the oxygen core, resulting from the reverse shock and the Ni-bubble. At the transition to the hydrogen envelope, the density decreases by a factor ~ 10. The outer $\sim 0.5 M_\odot$ has a steep density gradient, close to $\rho \propto r^{-9.7}$. This part is of interest mainly in the very early phase, and for the interaction with the circumstellar medium (section 13).

These models are the result of one-dimensional calculations. As will be discussed in section 8, the structure is subject to strong instabilities, which mix the abundances and smooth the density structure.

For much of the subsequent discussion, density is an important parameter. For a core of uniform density its number density can be estimated from

$$n = \frac{3 M_{\rm core}}{4\pi m_p A R_{\rm core}^3},$$

or

$$n = 5.1 \times 10^8 \left(\frac{A}{16}\right)^{-1} \left(\frac{M_{\rm core}}{4M_\odot}\right) \left(\frac{V_{\rm core}}{2000\,{\rm km\,s^{-1}}}\right)^{-3} \left(\frac{t}{300\,{\rm days}}\right)^{-3} \,{\rm cm}^{-3}, \tag{2.1}$$

where A is the mean atomic weight, $M_{\rm core}$ and $V_{\rm core}$ the core mass and expansion velocity, and t the time in days. The 1-D model by Shigeyama et al. has a somewhat higher density in the oxygen-core, where A $\sim$ 16

$$\rho = 6.3 \times 10^{-14} \left(\frac{t}{300\,{\rm days}}\right)^{-3} \,{\rm g\,cm}^{-3}, \tag{2.2a}$$

$$n = 2.3 \times 10^9 \left(\frac{t}{300\,{\rm days}}\right)^{-3} \,{\rm cm}^{-3}, \tag{2.2b}$$

and in the helium-core, where A$\sim$ 4

$$\rho = 3.0 \times 10^{-14} \left(\frac{t}{300\,{\rm days}}\right)^{-3} \,{\rm g\,cm}^{-3}, \tag{2.3a}$$

$$n = 4.5 \times 10^9 \left(\frac{t}{300\,{\rm days}}\right)^{-3} \,{\rm cm}^{-3}. \tag{2.3b}$$

The mass density of the hydrogen envelope can be approximated by

$$\rho = 5.7 \times 10^{-15} \left(\frac{R_{\rm core}}{r}\right) \left(\frac{t}{300\,{\rm days}}\right)^{-3} \,{\rm g\,cm}^{-3}, \tag{2.4a}$$

Using $A \sim 1.6$

$$n = 1.2 \times 10^9 \left(\frac{R_{\rm core}}{r}\right) \left(\frac{t}{300\,{\rm days}}\right)^{-3} \,{\rm cm}^{-3}. \tag{2.4b}$$

When mixing is taken into account, it is expected that the density within a given region varies by a large factor (see section 8).

While the core mass is a function mainly of the total main sequence mass, the core velocity is highly dependent on the explosion energy and the mass of the hydrogen envelope at the time of the explosion. If most of the envelope is retained, a low velocity of 1500 to 2000 km s^{-1} results. If a large fraction is lost, as may occur due to a stellar wind, for example, the core velocity can reach $\sim$ 6000 km s^{-1} (Ensman and Woosley 1988). This is likely to correspond to a Type Ib supernova.

3. Gamma-ray thermalization

3.1. Radioactive input

After core bounce, the passage of the shock through the region immediately outside the neutron star results in explosive nucleosynthesis in the silicon shell and inner part of the oxygen shell. Since nuclear statistical equilibrium is established, the most abundant isotope is ^{56}Ni. This isotope is unstable, and decays first to $^{56}\mathrm{Co} + \gamma$, on a time scale of 8.8 days. ^{56}Co decays to $^{56}\mathrm{Fe}+\gamma$ (or in 19% of the cases to $^{56}\mathrm{Fe}+e^{+}$), on a time scale of 111.26 days.

Calculations show that for explosion energies less than $\sim 2 \times 10^{51}\,\mathrm{erg\,s^{-1}}$, 0.05–0.3$M_{\odot}$ of ^{56}Ni is produced in core collapse supernovae (Ensman and Woosley 1988). The exact amount is sensitive to where the mass cut between the neutron star and ejecta occurs, which is unfortunately not very well determined. Another uncertain aspect is the radial distribution of radioactive material. One-dimensional models have the ^{56}Ni at the boundary of the Ni-bubble, but 2-D and 3-D hydrodynamic simulations show significant mixing of the different burning zones (section 8). This is also indicated by analysis of the optical and x-ray light curves (e.g. Woosley 1988; Shigeyama and Nomoto 1990). Therefore, the γ-ray source is distributed radially, and the deposition is more uniform than for a point source (section 3.3).

Type Ia supernovae produce from 0.3 to 1.4 $M_{\odot}$ of ^{56}Ni (Arnett et al. 1985). The lower figure is that needed to unbind the white dwarf. The uncertainty here is mainly due to the physics of the burning front, which can be either a detonation or a deflagration (see lectures by Woosley). Also, in this case, the radioactive material is distributed rather uniformly.

3.2. The gamma-ray spectrum

For the late spectrum we are mainly interested in the ^{56}Co to ^{56}Fe decay. In this, 96.5% of the energy emerges as γ-rays, and only 3.5% as positrons. The strongest γ-ray lines have energies of 0.846 MeV and 1.24 MeV, while the average photon energy is 1.24 MeV. The positrons are injected with a mean kinetic energy of 0.658 MeV. The gamma ray release per decay is 3.57 MeV, and the total energy input is therefore given by

$$L_{\gamma} = 1.27 \times 10^{42} \left(\frac{M(^{56}\mathrm{Ni})}{0.1 M_{\odot}} \right) e^{-t/111\,\mathrm{d}} \mathrm{erg\,s^{-1}}. \qquad (3.1)$$

There are also other sources of radioactivity in the supernova debris (Woosley et al. 1989; Kumagai et al. 1989). Hashimoto et al. (1989) find for SN 1987A that $4.3 \times 10^{-3} M_\odot$ of ^{57}Ni is produced, which first decays to ^{57}Co and then to ^{57}Fe, on a time scale of 391.2 days, emitting γ-rays. In addition, $1.2 \times 10^{-4} M_\odot$ of ^{44}Ti is produced, which decays to ^{44}Sc and ^{44}Ca on a time scale of 78.2 years. Woosley et al. find for the energy generation rate from ^{57}Co

$$L_\gamma = 5.9 \times 10^{38} \left(\frac{M(^{57}\mathrm{Co})}{4.3 \times 10^{-3} M_\odot} \right) e^{-t/391\,\mathrm{d}} \mathrm{erg\,s^{-1}}, \tag{3.2}$$

and from ^{44}Ti

$$L_\gamma = 4.1 \times 10^{36} \left(\frac{M(^{44}\mathrm{Ti})}{10^{-4} M_\odot} \right) e^{-t/78.2\,\mathrm{yr}} \mathrm{erg\,s^{-1}}. \tag{3.3}$$

^{44}Ti also has an important positron channel (section 3.5). For SN 1987A the input from ^{57}Co is comparable to the ^{56}Co decay around day 1200. After $\sim$ 1500 days ^{44}Ti dominates ^{57}Co.

3.3. Gamma-ray thermalization

The first step in the thermalization of γ-rays from the radioactive decay is Compton scattering by electrons. The γ-ray energies are much higher than the binding energies of the electrons in the atoms (at most 7.1 keV for iron), and both free and bound electrons contribute in the same way. The photon energy, E', after a scattering is given by the Compton formula

$$E' = \frac{E}{1 + \frac{E}{m_e c^2}(1 - \cos\theta)}, \tag{3.4}$$

where θ is the scattering angle, and the cross section, σ_{KN}, is given by the Klein-Nishina formula. This reduces to the Thompson cross section at low energy, $\sigma_T = (8\pi e^4)/(3m^2c^4) = 0.665 \times 10^{-24}\mathrm{cm}^2$. At 1 MeV σ_{KN} is approximately $\sigma_T/3$, with a marked forward peaking of the scattering. The optical depth of the γ-rays is given by

$$\tau_\gamma = \int \langle \sigma_{\mathrm{KN}} \rangle n_e dr = \int \kappa_\gamma \rho \, dr, \tag{3.5}$$

where n_e is the number density of free and bound electrons, $n_e = \langle (Z\rho)/(Am_p) \rangle$. $\langle \sigma_{\mathrm{KN}} \rangle$ is the cross section averaged over energy and scattering angle. From Monte-Carlo simulations, Fransson and Chevalier (1989) find that $\langle\sigma_{\rm KN}\rangle \approx \sigma_T/6$. In the core A/Z ≈ 2 and $\tau_\gamma \approx (1/12)(\sigma_T/m_u)\int \rho\, dr = 0.03\int \rho\, dr$. In general, $\kappa_\gamma = 0.06\frac{Z}{A}$. For a core of uniform density we get

$$\tau_\gamma = 2.1\left(\frac{M_{\rm core}}{4M_\odot}\right)\left(\frac{V_{\rm core}}{2000\,{\rm km\,s^{-1}}}\right)^{-2}\left(\frac{t}{300\,{\rm days}}\right)^{-2}. \tag{3.6}$$

This assumes a central source of ^{56}Ni. As is evident by the x-ray light curves of SN 1987 A (see Nomoto and Müller in this volume), mixing of ^{56}Ni to high velocities is important. The expression above will overestimate the time of γ-ray transparency. For a more accurate determination of γ-ray escape and deposition, the equation of transfer and the energy loss equation have to be solved. This can be done in several ways, either by direct integrations, or by Monte Carlo technique (e.g. Xu 1989).

A simple discussion of the basic physics is given by Shull and Xu (1988), which we follow. In each scattering the photon loses on the average an energy $\Delta E = -E^2/m_{\rm e}c^2$, if $E \ll m_{\rm e}c^2$, as is the case after the first scattering. Considering this as a continuous process with small changes in energy, we can replace $\Delta E/\Delta N$ by dE/dN, and obtain for the energy E after N scatterings

$$N = \int dN = \int_{E_0}^{E} \frac{dE}{-E^2/m_{\rm e}c^2} \approx \frac{m_{\rm e}c^2}{E}, \tag{3.7}$$

if $E \ll E_0$, the initial energy. The number of scatterings a photon undergoes on its way out is $N \sim \tau^2$, so the energy is $E \sim m_{\rm e}c^2/\tau^2$.

A photon is destroyed by photoelectric absorption when $\tau_{\rm abs} = N\lambda_{\rm scatt}\rho\kappa_{\rm abs} \approx 1$ (assuming $\kappa_{\rm abs} \ll \kappa_{\rm scatt}$). Here $\lambda_{\rm scatt} = 1/n_{\rm e}\sigma_{\rm scatt}$ is the mean free path for the γ-rays. Above 7.11 keV, the K-shell of iron dominates absorption both in the envelope and in the core (e.g. Fransson and Chevalier 1987), with a cross section given by $\sigma_{\rm abs} = 3.8\times10^{-20}(E/7.1\,{\rm keV})^{-3}\,{\rm cm}^{-2}$. In SN 1987A the $4M_\odot$ core contains $\sim 0.075M_\odot$ Fe, so if this is uniformly mixed the Fe abundance by number is 2.2×10^{-3} (compared to 1.3×10^{-5} in the envelope), and the opacity $\kappa_{\rm abs} = \xi(7.1\,{\rm keV}/E)^3\kappa_{\rm scatt}$, where $\xi \sim 130$ in the core and $\xi \sim 1$ in the envelope. Thus $\tau_{\rm abs} \sim \tau_{\rm scatt}^2\kappa_{\rm abs}\kappa_{\rm scatt}^{-1} \sim \xi\tau_{\rm scatt}^2(7.1\,{\rm keV}/E)^3 \sim \xi(7.1\,{\rm keV}/511\,{\rm keV})^3\tau_{\rm scatt}^8 \sim 2.7\times10^{-6}\xi\tau_{\rm scatt}^8$. Therefore, photons will be absorbed after traversing a *radial* optical depth of $\tau_0 \sim 5.0\xi^{-1/8}$ at an energy $E_{\rm abs} \sim 22\xi^{1/4}$keV. We therefore expect a continuum of hard photons with energy from more than 1 MeV down to $E_{\rm abs}$, a few tens of keV's. Monte

Carlo simulations show that the spectrum is fairly flat between these energies (e.g. Xu 1989). Most of the scatterings take place in the envelope, and a photon will be scattered ~ 25 times before being absorbed. If τ_0 is larger than the actual scattering depth of the remnant, $\kappa_\gamma \int \rho \, dr$, the down-scattered photons leave the remnant before absorption. The time corresponding to τ_0 marks the turn-on of the x-ray emission from the remnant. Since $E_{\rm abs}$ is much less than the initial energy, $\sim 1\,{\rm MeV}$, we can neglect photoelectric absorption to the energy input of the remnant.

As a fair approximation we assume that the γ-ray photon loses most of its energy in the first scattering. For a central point source, the energy deposition per unit radius is then given by $L_\gamma \kappa_\gamma \rho e^{-\tau_\gamma}$, or per unit mass $L_\gamma \kappa_\gamma e^{-\tau_\gamma}/4\pi r^2$. It is likely that the ^{56}Ni source is distributed more uniformly within the core. If the core is also optically thin to γ-rays, the energy input is given by $D_\gamma L_\gamma \kappa_\gamma/(4\pi R_{\rm core}^2)$, where

$$D_\gamma(r) = \frac{3}{2}\left[1 + \frac{1-x^2}{2x}\ln\left(\frac{1+x}{|1-x|}\right)\right], \tag{3.8}$$

and $x = r/R_{\rm core}$. This is a fairly flat distribution, peaking at the center with $D_\gamma = 3$ and decreasing to $D_\gamma = 3/2$ at $r = R_{\rm core}$. At large distances $D_\gamma = 1/x^2$, as expected. For more complicated situations the deposition has to be calculated by Monte-Carlo methods. As a rough approximation for energy deposition per volume we can use

$$\frac{dE_\gamma}{dV} = 4\pi J_\gamma \kappa_\gamma \rho \approx \frac{D_\gamma L_\gamma \kappa_\gamma \rho e^{-\tau_\gamma}}{4\pi R_{\rm core}^2}, \tag{3.9}$$

where J_γ is the mean γ-ray intensity. In some situations, we are only interested in the total γ-ray input to the remnant, approximately given by $(1 - e^{-\tau_\gamma})L_\gamma$. This is the case when discussing the bolometric light curve.

3.4. Electron thermalization

The γ-rays give rise to a population of highly non-thermal electrons with energies 0.01–1 MeV. These lose their energy in ionization and excitation of neutral and singly ionized atoms, as well as in Coulomb scattering by free, thermal electrons. The slowing down of a fast particle is an old problem, which has occupied some of the most prominent physicists of our century, like Niels Bohr and Hans Bethe. These pioneers were mainly interested in the fate of the primary electron. Here we need to know how the particle distributes

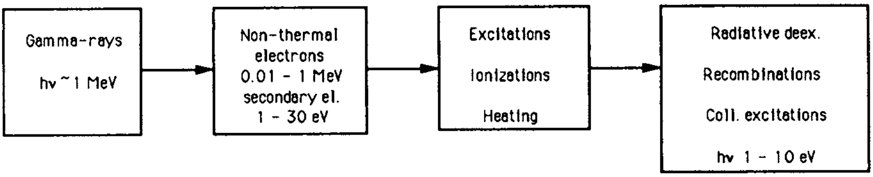

Fig. 2. Schematic representation of the thermalization of the γ-rays resulting from the radioactive decay. (deex. $\equiv$ deexcitations)

its energy among the various possible channels. Thus, it is required to keep track of not only the primary particle, but also of the secondary electrons produced in each ionization, which can undergo the same processes as the primaries. Each primary therefore gives rise to a whole cascade of secondary electrons (fig. 2). The calculation of this thermalization requires a solution of the Boltzmann equation, which was first done by Spencer and Fano (1954).

The energy loss due to excitations and ionizations in a gas with atomic number Z is given by the classical Bethe (1930) formula

$$-\frac{dE}{dx} = n\frac{2\pi e^4 Z}{E}\left(\ln\left(\frac{E}{I_0}\right) + \frac{1}{2}(1-\ln 2)\right), \qquad (3.10)$$

where E is the kinetic energy. I_0 is the mean excitation energy given in terms of the oscillator strengths, f_i, of the levels and continuum by

$$\ln I_0 = \frac{\sum_i f_i \ln E_i}{Z}. \qquad (3.11)$$

This expression shows that most of the excitations go to levels with large f values, that is, the resonance lines and the continuum. In practice I_0 is determined experimentally for complex ions. Examples of I_0 are for H I, 15.0 eV, He I, 42.3 eV, and for O I, 91 eV (Ahlen 1980). At relativistic energies the bracket is modified and causes dE/dx to increase with energy (Bethe 1933).

The stopping distance, d_e, for a fast electron in a neutral medium is for $v/c \ll 1$ given by

$$d_e \equiv \frac{E}{-\frac{dE}{dx}} \approx \frac{3.36}{\rho}\left(\frac{E}{m_e c^2}\right)^2 \frac{A}{Z}\left(\ln\left(\frac{E}{I_0}\right) + 0.15\right)^{-1} \text{cm}. \qquad (3.12)$$

Thus, d_e decreases rapidly with energy, and is always much less than the γ-ray mean free path, corresponding to $\sim 33\,\rho^{-1}$cm. Only if the γ-ray optical depth is less than 0.02 will the energetic electrons escape the remnant. If there is a non-radial magnetic field, the stopping distance will be even smaller (Colgate and McKee 1969; Axelrod 1980a). In contrast to the γ-rays, we can therefore consider the non-thermal electron energy deposition as a local process and neglect spatial diffusion.

For the scattering by the *free*, thermal electrons in the gas, collective effects in the form of plasma waves must be taken into account. In the non-relativistic limit the continuous energy loss is given by (Schunk and Heyes 1971)

$$-\frac{dE}{dx} = n_e \frac{2\pi e^4}{E} \ln\left(\frac{2E}{\zeta}\right), \tag{3.13}$$

where

$$\zeta = \frac{h}{2\pi}\omega_p = \frac{h}{2\pi}\left(\frac{4\pi n_e e^2}{m_e}\right)^{1/2} = 3.7 \times 10^{-11} n_e^{1/2} \mathrm{eV}. \tag{3.14}$$

for E greater than 14 eV. For lower energies the logaritmic factor changes to $\left(\ln(v^3/n_e^{1/2}) - 29.7\right)$, where v is the electron velocity.

The formulae above are sufficient for estimating the slowing down of the primary electrons. As mentioned above, to also include the deposition from the secondary electrons we have to solve the Boltzmann equation. One approach is to calculate the secondary cascade by a Monte Carlo procedure, which is well suited for this purpose. A limitation of this is that a very large number of experiments have to be followed, if information is wanted on rare excitation channels and elements of low abundance. Examples of these types of calculations can be found in Shull and van Steenberg (1985) for a H/He plasma, and in Fransson and Chevalier (1989) for metal-dominated plasmas.

A more efficient technique is a direct numerical solution of the Boltzmann equation (for a good review see Xu 1989). If $y(E)\,dE$ is the flux of electrons from E to $E+dE$, it takes the form (Spencer and Fano 1953; Douthat 1975; Xu 1989)

$$\begin{aligned} &y(E)\left[\sum_n \sigma_n(E) + \int_I^{(I+E)/2} \sigma(E,E')dE'\right] \\ &= \sum_n y(E+E_n)\sigma_n(E+E_n) + \int_I^{\lambda} y(E+E')\sigma(E+E',E')dE' \\ &+ \int_{2E+I}^{E_{\max}} y(E')\sigma(E',E+I)dE' + \frac{d}{dE}\left(y(E)\frac{dE}{dx}\right) + S(E), \end{aligned} \tag{3.15}$$

where $\lambda = \min(E_{\max} - E, E + I)$. $\sigma(E, \Delta E)$ is the ionization cross section for the production in an ionization of one electron with energy $E_1 = E - \Delta E$, and one with $E_2 = \Delta E - I$ from an initial energy E. The term involving dE/dx is the continuous loss to the free electrons given by eq. (3.13). The left hand side of the Boltzmann equation represents the total loss of electrons with energy E, due to excitations of the n levels and to ionizations. The first term on the right hand side is the input at E due to losses by electrons having a higher energy $E + E_n$. The next term is a similar term due to ionizations. The third term represents the input of secondary electrons. The secondary is defined as the less energetic electron of the two outgoing in the ionization. It is left to the reader to explain the origin of the different integration limits, where the definition of primary and secondary electrons is crucial. The source of non-thermal, primary electrons, $S(E)$, is given by the calculation of the Compton scattered γ-rays.

The similar dependence on energy for all cross sections, $\ln(E/\chi)/E$, makes the results only weakly dependent on the primary electron energy, as long as this is above $\sim 1\,\mathrm{keV}$. Since an electron can only be scattered down in energy, the electron spectrum from high energies to lower can be directly solved for. Knowing the electron distribution, the energy going into the different channels can be calculated. This has been done by Xu (1989) for a hydrogen plasma. For more complicated compositions and for higher initial primary energy, this becomes an uneconomical method, like Monte-Carlo. The reason is that the energy resolution has to be such that the different excitation and ionization thresholds are well resolved, i.e. of order of eV. A more economical method results if eq. (3.15) is integrated over energy. The advantage of this is that the cross section for the energy transfer can be integrated analytically, and that this is an integral equation, which can be solved by standard matrix techniques with good accuracy (Kozma and Fransson 1991).

In fig. 3 the result of the thermalization in a pure oxygen gas is shown. Figure 3a shows the electron distribution for an electron fraction $X_e = 10^{-2}$, and an initial primary electron energy of 3 keV. We also show the fraction of the energy going into the different channels as a function of energy in fig. 3b. At high energy, most the energy loss is due to ionizations and excitations, while at low energy Coulomb scattering on electrons dominates. At low energy, the population of non-thermal electrons builds up, due to the secondary electrons formed by the ionization of primary electrons. The distribution of these as a function of primary E_p and secondary E_s energy is

$$S(E_p, E_s) = \frac{1}{J \tan^{-1}\left(\frac{E_p - I}{2J}\right)\left(1 + \left(\frac{E_s}{J}\right)^2\right)}, \tag{3.16}$$

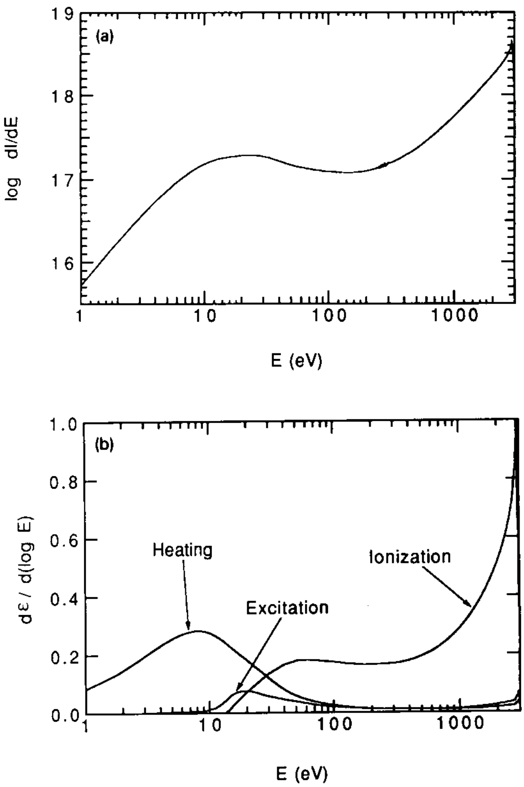

Fig. 3a. Non-thermal electron distribution in a pure oxygen gas at $X_e = 10^{-2}$, for an initial primary electron energy of 3 keV.
Fig. 3b. The relative fraction of the energy per decade, $d\varepsilon/d\,\log E$, going into heating, ionizations, and excitations for the case in fig. 3a.

where J is an experimentally determined parameter varying with the element (Opal et al. 1971), but in general somewhat lower than the ionization potential. For He I, $J = 15.8\,\mathrm{eV}$. Therefore most secondary electrons are created with energies less than $\sim 30\,\mathrm{eV}$, independent of the primary energy. The lowest excitation threshold can be many eV above the ground state. Below this energy, only Coulomb scattering on the free electrons takes place, and a large fraction of the energy of the secondary electrons therefore goes into heating. This means that even for $X_e \ll 1$, there is an appreciable heating of the gas.

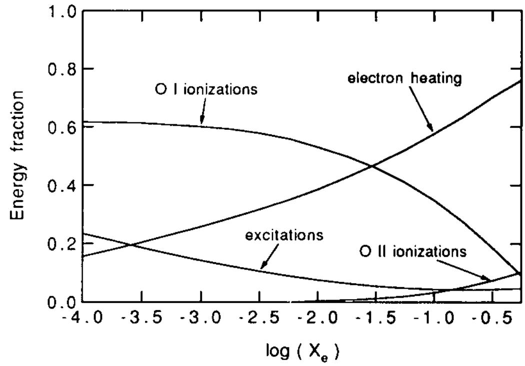

Fig. 4. Fractional deposition of the non-thermal electron energy for a pure oxygen gas.

Fig. 4 shows the total deposition in the different modes for oxygen. Above $X_e \sim 10^{-2}$, heating of the thermal electrons dominates, with ionization as the second most important channel. Most of the non-thermal excitation goes to the lowest allowed levels; for O I the 3s ^{3}S level at 9.5 eV. At $X_e = 10^{-2}$, $\sim$ 2% of the total energy goes into this level. This is in contrast to *thermal* excitation, which is dominated by the lowest forbidden ^{1}D and ^{1}S levels at 1.96 eV and 4.17 eV. In addition, the non-thermal ionizations give rise to a number of high excitation, recombination lines.

Since only a fraction ε, less than 50%, of the energy goes into ionization, one can define an effective ionization potential

$$\chi_{\mathrm{eff},i} = \frac{\chi_{\mathrm{ion},i}}{\varepsilon(X_e)/X_i}. \tag{3.17}$$

where X_i is the abundance (by number of the ion), and $\chi_{\mathrm{ion},i}$ the real ionization potential of the ion. For O I, $\chi_{\mathrm{eff}} \sim 25.4\,\mathrm{eV}$ at $X_e \sim 0.01$.

The ionization rate per volume of an ion i is

$$\Gamma_{c,i}\, n_i = \frac{4\pi\sigma_{\gamma,i} J_\gamma}{\chi_{\mathrm{eff},i}(X_e)} n_i, \tag{3.18}$$

where $\sigma_{\gamma,i} = 0.06 Z_i m_p = 1.0 \times 10^{-25} Z_i\,\mathrm{cm}^2$ for an ion with nuclear charge Z_i.

The ionization potentials and energies of the lowest levels, as well as the cross sections, differ from element to element, and the efficiencies for

Table 1.
Effective ionization potentials, $\chi_{\rm eff}$ (eV), at two values of $X_{\rm e}$ for pure compositions. $\chi_{\rm ion}$ is the real ionization potential, and $\varepsilon_{\rm ex}$ the fraction of the total energy going into excitation. From Kozma and Fransson (1991).

	X_e	H I	He I	C I	O I	Mg I	Si I	Ca II	Fe I
$\chi_{\rm ion}$ (eV)		13.6	24.6	11.9	13.6	7.7	8.2	11.9	7.9
$\chi_{\rm eff}$ (eV)	0.1	59.0	76.5	30.2	35.4	39.5	24.0	64.8	36.0
	0.01	37.1	51.4	23.6	25.4	31.3	15.6	57.8	19.7
$\varepsilon_{\rm ex}$	0.01	0.33	0.17	0.20	0.08	0.61	0.17	0.50	0.27

Table 2.
Effective ionization potentials, $\chi_{\rm eff}$ in eV, at $X_e = 0.01$, for different mass zones of a $6M_\odot$ helium-core (Woosley 1988). The upper row gives the abundances by number for each shell (2.7–4 stands for $2.7 \cdot 10^{-4}$, etc.). From Kozma and Fransson (1991).

Zone	He I	C I	O I	Ne I	Mg I	Si I	S I	Ca II	Fe I
Fe core	5.5–1	2.7–4				1.1–5	3.4–4	1.9–4	4.4–1
$\chi_{\rm eff}$ (eV)	52.6	10.8				7.6	6.9	14.7	17.3
O core		1.7–2	8.5–1	9.2–3	1.1–2	6.4–2	3.8–2	5.4–4	
$\chi_{\rm eff}$ (eV)		20.4	26.8	44.1	12.1	10.9	12.5	27.4	
He shell	9.7–1	1.8–2	2.0–3	3.9–3	1.3–4	1.0–4	5.1–5	7.7–6	
$\chi_{\rm eff}$ (eV)	53.0	10.1	13.1	21.4	6.9	6.1	6.3	13.6	

ionization and excitation therefore also vary considerably. In table 1 $\chi_{\rm eff}$ is given at $X_{\rm e} = 10^{-2}$ and 10^{-1} for a number of elements. The variation with $X_{\rm e}$ can within $\sim 25\%$ be described by

$$\chi_{{\rm eff},i}(X_{\rm e}) = 1.46\chi_{{\rm eff},i}(X_{\rm e} = 10^{-2})X_{\rm e}^{-0.55}. \qquad (3.19)$$

In reality, the situation is more complex, since $\chi_{\rm eff}$ depends on both $X_{\rm e}$ and on the presence of other elements. A mixed composition can change the values of $\chi_{\rm eff}$ of the various elements by a large factor. In table 2 the results are given at $X_{\rm e} = 10^{-2}$ for compositions characteristic of the iron core, the oxygen core and the helium shell. These mixtures are taken from the 10H model by Woosley (1988). Especially for trace elements there is no obvious correlation between the effective ionization potentials and the real ionization potential. Both Mg I, Si I, and S I have very low effective potentials in both the helium shell and the iron core, much less than the values in table 1. The reason for this is the comparatively large ionization cross sections for these elements, which lead to an ionization rate *per atom* that is larger than for the more abundant elements. Detailed results for other compositions and electron fractions are given in Kozma and Fransson (1991).

High excitation levels can be populated either by non-thermal ionizations followed by recombination, or by direct excitation. The former gives a standard recombination spectrum, while the latter may give a more preferential excitation. We find that the levels with largest excitation rates in the helium shell are 2p ^{1}P (11% of the total energy at $X_e = 0.01$) and 3p ^{1}P (3%). In the oxygen core the most populated are the O I 3s ^{3}S and 3s$'$ ^{3}D levels. Most Ca is likely to be in the form of Ca II (see section 7.3), and the Ca II 4p ^{2}P level is responsible for most of the excitation in the Si-Ca shell.

Nearly all of the most populated levels are resonance levels. Low energy levels, like the Ca II 4p ^{2}P level, can also be populated by thermal excitations, while higher levels are populated by recombinations. It is therefore difficult to distinguish levels directly populated by non-thermal excitations.

3.5. Positrons

In ^{56}Co decay, 3.5% of the energy is in kinetic energy of the positrons, and the positron input is

$$L_{+} = 4.44 \times 10^{41} \left(\frac{M(^{56}\mathrm{Ni})}{1 M_{\odot}} \right) e^{-t/111\,\mathrm{d}} \mathrm{erg\,s^{-1}}. \tag{3.20}$$

These have a stopping distance close to that of the electrons (eq. 3.12), much less than the γ-rays. The positron input is important when the γ-ray optical depth is less than ~ 0.1. In Type Ia supernovae this occurs quite early because of the large expansion velocity and low mass of the remnant. With $M = 1.4 M_{\odot}$ and a typical expansion velocity of $\sim 10^4\,\mathrm{km\,s^{-1}}$ (e.g. Nomoto et al. 1984), we get from eq. (3.6) $\tau_{\gamma} \sim 2.9 \times 10^{-2} (t/300\,\mathrm{days})^{-2}$. Type II supernovae have lower expansion velocities of the core and larger core masses, so the γ-ray input of even ^{44}Ti dominates the positron input (Woosley et al. 1989). For remnants more than 1000 days old, the positron channel in the ^{44}Ti decay may be important. Woosley et al. find for this a luminosity of

$$L_{+} = 1.3 \times 10^{36} \left(\frac{M(^{44}\mathrm{Ti})}{10^{-4} M_{\odot}} \right) e^{-t/78.2\,\mathrm{yr}} \mathrm{erg\,s^{-1}}. \tag{3.21}$$

The thermalization of the positrons proceeds in the same way as for the non-thermal primary electrons created by the γ-rays.

4. Thermal and ionization equilibrium

The thermalization of γ-rays results in ionizations, excitations of discrete levels, and heating of thermal electrons. The ionizations are balanced by recombinations, while the non-thermal excitations in general give rise to one or more line photons. The heating of free electrons is balanced by thermal collisional excitations of low excitation levels, which decay with the emission of line photons, or in high density environments by collisional de-excitations. Therefore, the energy of the MeV γ-rays finally escapes as photons with energy on the order of an eV or less (fig. 2).

To calculate the emerging spectrum from the supernova, one has to know the temperature and populations of the various energy levels and ionization stages at each point. The ionization balance for an ion i is given by

$$\left\{4\pi \frac{J_\gamma \sigma_{\gamma,i}}{\chi_{\mathrm{eff},i}} + 4\pi \int_{\nu_0}^{\infty} \frac{J_\nu \sigma_{\nu,i}}{h\nu} d\nu + C_i n_{\mathrm{e}} + \sum_k \zeta_{k+1,i} n_k \right\} n_i = \left\{\alpha_{i+1} n_e + \sum_k \zeta_{k,i+1} n_k \right\} n_{i+1}. \quad (4.1)$$

The first term is the γ-ray ionization given by eq. (3.18), while the second term describes photoionizations by diffuse emission from line and continuum photons in the remnant. Collisional ionization, $C_i n_{\mathrm{e}}$, is usually negligible at the low tempertures of interest here. The fourth term represents ionizations due to charge transfer between ions i and k. On the right hand side are inverse processes due to recombination and charge transfer.

Examples of important charge transfer reactions are the interstellar medium process

$$\mathrm{H\,I}(^2\mathrm{S}_{1/2}) + \mathrm{O\,II}(^4\mathrm{S}_{3/2}) \longleftrightarrow \mathrm{H\,II} + \mathrm{O\,I}(^3\mathrm{P}_{0,1,2}) + \Delta E, \quad (4.2)$$

taking place in the envelope, and in the core the less familiar

$$\mathrm{Ca\,I}(^1\mathrm{S}_0) + \mathrm{O\,II}(^4\mathrm{S}^0) \longleftrightarrow \mathrm{Ca\,II}(5\mathrm{p}^2\mathrm{P}_{1/2}) + \mathrm{O\,I}(^3\mathrm{P}) + \Delta E. \quad (4.3)$$

For this type of process to be likely, the difference of the total energy of the system before and after the collision (i.e. the separated ions) has to be positive, or within $\sim kT$. This is satisfied by the first reaction, which is nearly resonant, $\Delta E = -0.02$ to $0.01\,\mathrm{eV}$ for the different ^{3}P levels, and which therefore takes place in both directions (e.g., Osterbrock 1989). The second reaction proceeds via the excited 5p $^2P_{1/2}$ state of Ca II, and $\Delta E = 0.001$ eV, and is therefore also nearly resonant. Since the 5p $^2P_{1/2}$ level is 7.504 eV above the ground state, the inverse reaction (i.e., recombination of Ca II), is unimportant at thermal energies, and the reaction acts mainly as an ionization process for Ca I and recombination of O II.

In the calculation of these cross sections, the nuclei are usually treated as classical particles, while the electrons are described by molecular orbitals. The potential curves of the two states (the final and initial systems) as a function of separation is then calculated, and the transition occurs close to the crossing of the two potentials. Turner-Smith et al. (1973) find that as a rough general rule, rates are expected to be highest ($\sim 10^{-9}\,\mathrm{cm\,s^{-1}}$) for systems where the resulting ion is 0.1 to 0.4 eV below the exact resonance. For non-resonant reactions the rates are usually considerably lower, $\sim 10^{-13}\,\mathrm{cm^3\,s^{-1}}$. Examples of the latter are O II + Mg I $\leftrightarrow$ O I + Mg II, and O II + Na I $\leftrightarrow$ O I + Na II. These rules are by no means without exceptions, and in general, accurate calculations should be performed to evaluate the importance of a particular reaction. Except for reactions with hydrogen and helium, unfortunately few are available.

Charge transfer is for many ions the dominant mode of both ionization and recombination. In resonance situations, the rates, ζ_{ik}, may be on the order of $10^{-9}\mathrm{cm^{-3}s^{-1}}$. Comparing ordinary recombination with charge transfer one finds

$$\frac{\mathrm{rec}}{\mathrm{CT}} = \frac{\alpha_{i+1}n_e}{\zeta_{ik}n_k} \approx 10^{-3}\left(\frac{\alpha}{10^{-12}\mathrm{cm^{-3}s^{-1}}}\right)\left(\frac{\zeta_{ik}}{10^{-9}\mathrm{cm^{-3}s^{-1}}}\right)\frac{n_e}{n_k}. \quad (4.4)$$

If $n_k > 10^{-3}n_e$, charge transfer may dominate recombination. In section 7.3 the dramatic effect of charge transfer is illustrated for the ionization of calcium in the core.

The photoionization term may in some cases be more important than γ-ray ionization. In particular, for an element whose ionization threshold is below that of important emission lines, these may provide a strong source of photoionization. Examples of such lines are He I λ584, Lyα, O I $\lambda\lambda$1302, 1356, Mg II λ2800; and the H I and He I two-photon continua. The He I emission can ionize H I and most neutral elements, e.g., C I, while the others may ionize Na I (with an ionization threshold at 2425 Å), Mg I (1622 Å), Si I (1521 Å), Ca I (2028 Å) and Fe I (1575 Å). Another important case is hydrogen, where the $n = 2$ level may have a sufficient population to absorb this emission. This is further discussed in section 7.1. Also, in these cases the primary energy source is, of course, the γ-rays. The flux of the recombination lines from these ions is therefore expected to follow the exponential decay.

If we for the moment consider the simple case where γ-rays dominate the ionization, and radiative recombination dominates the recombination, the state of ionization is characterized by the parameter

$$\xi = \frac{4\pi J_\gamma}{n}, \tag{4.5}$$

which is the equivalent of the photoionization parameter in QSO emission line calculations. The scaling of ξ with time is

$$\xi = \frac{L_\gamma D_\gamma}{4\pi R^2 n} \propto t e^{-t/111\,\mathrm{d}}. \tag{4.6}$$

The degree of ionization and excitation is therefore expected to decrease with time in spite of the density decrease.

The heat input to the thermal balance is dominated by γ-ray heating of the thermal electrons. Cooling of the gas is controlled by a large number of processes, where collisional excitation dominates. Since the temperature is in general less than $\sim$ 7000 K, low excitation lines with $h\nu \lesssim 4\,\mathrm{eV}$ are the most important. Of the most abundant ions, only Na I, Mg II, Ca II, and Fe II have permitted transitions with low enough energies (at 5890–96 Å, 2800 Å, 3934–68 Å, and between 2300–3000 Å, respectively). Most other neutral and singly ionized elements only have forbidden or semi-forbidden transitions in this energy range. Likely electron densities are above $\sim 10^5\,\mathrm{cm}^{-3}$, so the forbidden lines may be heavily quenched by collisional deexcitation. Despite this, since there are few other lines available, forbidden and semi-forbidden are still responsible for most of the cooling. This explains why lines like [O I] λλ6300–64, [Ca II] λ7300 and Mg I] λ4571 are so strong in the observed spectra.

The rate of collisional excitations per atom is given by $n_e C_{12}$, and that of de-excitation by $n_e C_{21}$, where

$$C_{21} = \frac{8.63\times 10^{-6}\Omega_{21}}{g_2 T_e^{1/2}} = \frac{g_1 e^{h\nu/kT}}{g_2} C_{12}. \tag{4.7}$$

where Ω_{21} is the usual collision strength.

The high density means that both optical depth effects and collisional de-excitation have to be included when calculating the cooling and emission from the remnant. The situation is in this respect more similar to that of a QSO BLR, than to an H II region. For a two-level atom, the mean intensity, J, of a line is given by (e.g., Mihalas p. 481)

$$J = (1 - \beta)S + W\beta I_c, \tag{4.8}$$

where β is the escape probability, $(1 - e^{-\tau})/\tau$ (section 5), and W the dilution factor of the photospheric background intensity, I_c. The first term is a local contribution, while the second is the background intensity at the point. The source function, S, defined by

$$S = \frac{2h\nu^3}{c^2\left(\frac{g_2}{g_1}\frac{n_1}{n_2} - 1\right)^{-1}}, \tag{4.9}$$

is for a two-level atom

$$S = \frac{W\beta I_c + \varepsilon B}{\beta + \varepsilon}, \tag{4.10}$$

where $\varepsilon = C_{21}n_e/A_{21} = n_e/n_{\rm crit}$ is the de-excitation probability from the upper level *if* the line is thin, and B is the Planck function. For supernovae at late times, when the photosphere has receded to low velocities, $WI_c \approx 0$ is a good approximation, and consequently radiative excitations are unimportant. Therefore,

$$S = \frac{\varepsilon}{\beta + \varepsilon}B, \tag{4.11}$$

and

$$J = \frac{(1 - \beta)\varepsilon}{\beta + \varepsilon}B. \tag{4.12}$$

If $\varepsilon \ll \beta$, $S \approx (C_{21}n_e/\beta A_{21})B$, while if $\varepsilon \gg \beta$, $S = B$. Thus, the lines are thermalized and in LTE at an electron density

$$n_{\rm crit} = \frac{\beta A_{21}}{C_{21}}. \tag{4.13}$$

If in addition, $\beta \ll 1$, then $J = B$, and the intensity is that of a black body. For this, *both* $\tau \gg 1$ and $n_e \gg n_{\rm crit}$ are required.

The energy loss can be written

$$\Gamma = \frac{h\nu C_{12}}{(1 + n_e/n_{\rm crit})}. \tag{4.14}$$

If $n_e \gg n_{\rm crit}$

$$\Gamma = \frac{h\nu\beta A_{21} C_{12}}{n_{\rm e} C_{21}} = h\nu\beta A_{21} \frac{g_2 e^{-h\nu/kT}}{g_1 n_{\rm e}}, \tag{4.15}$$

implying that the levels are in LTE. If $\tau \gg 1$, $\beta \approx 1/\tau$, and stimulated effects are important

$$\Gamma = \frac{4\pi h B_\nu}{\lambda t}. \tag{4.16}$$

In the opposite case when $n_{\rm e} \ll n_{\rm crit}$, the familiar expression is recovered

$$\Gamma = h\nu C_{12} = 8.63 \times 10^{-6} \frac{h\nu\,\Omega_{21}}{g_1 T_{\rm e}^{1/2}} e^{-h\nu/kT}. \tag{4.17}$$

Finally, consider the validity of the steady state assumption. The relevant time scale for equilibrium is the recombination time scale, $t_{\rm rec} = 1/\alpha_r n_{\rm e}$. In the oxygen core $\alpha_{\rm r} \sim 2.4 \times 10^{-13} T_4^{-0.8}$, so if $T_{\rm e} \sim 3000\,{\rm K}$, n_e must be larger than $\sim 5 \times 10^4/t_{\rm yr}\,{\rm cm}^{-3}$. Estimating n from eq. (2.1), the degree of ionization must be larger than $\sim 1.8 \times 10^{-4} t_{\rm yr}^2$. This is satisfied in most cases of interest during the first years.

5. Line formation

The homologous expansion of the ejecta offers a unique possibility to probe the conditions in the envelope from observations of spectral line profiles. The expansion introduces both complications and simplifications for line formation (see Rybicki and Hummer 1978 for a clear discussion).

An important concept for high velocity flows is the surface of constant velocity along the line of sight (SCV). This is defined by

$$\frac{\nu - \nu_0}{\nu_0} = \frac{V_z}{c} = \frac{z}{r}\frac{V(r)}{c}, \tag{5.1}$$

where z is the coordinate along the line of sight, and V_z the corresponding velocity (fig. 5). For a homologously expanding ejecta $V(r) = V_0(r/R_0) = r/t$, where V_0 is the velocity at a reference radius R_0, and one obtains

$$\frac{z}{R_0} = \frac{ct}{R_0}\frac{(\nu - \nu_0)}{\nu_0} \equiv x. \tag{5.2}$$

Therefore, the SCV's are surfaces of constant z, perpendicular to the line of sight (fig. 5). As frequency shifts from red to blue in the line, the ejecta are probed from the back in towards the center and out to the front.

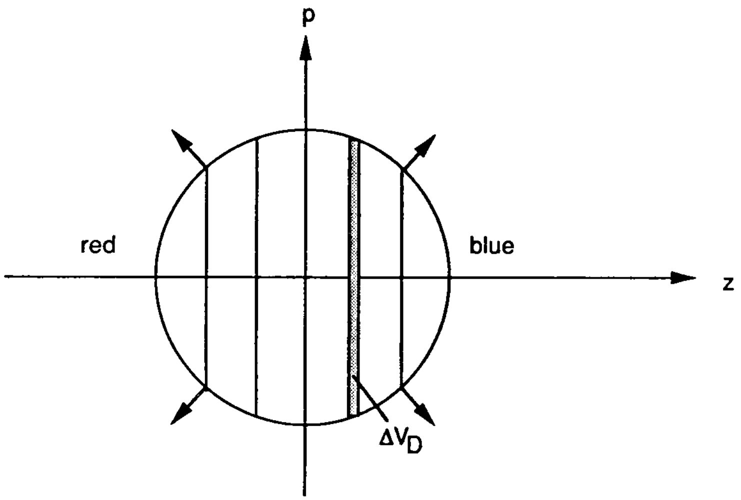

Fig. 5. Surfaces of constant frequency along the line of sight, for a velocity $v(r) \propto r$. The shaded area indicates schematically the region within which a photon emitted at a given frequency interacts.

An important simplification is possible because when the expansion velocity is much larger than the thermal width of the line, only a narrow interval in depth contributes to a given frequency (fig. 5). This is the basis of the Sobolev approximation. A simple derivation of the optical depth in this approximation starts with

$$\tau_\nu = \sigma_\nu n_1 \, \delta l, \tag{5.3}$$

where σ_ν is the cross section at frequency ν, n_1 the population in the lower state and δl the thickness of the layer with which the photon interacts. For a box line profile,

$$\sigma_\nu = \frac{\pi e^2}{mc} \frac{f_{12}}{\Delta \nu_D} = \frac{A_{21} g_2 \lambda^2}{8\pi g_1 \Delta \nu_D}, \tag{5.4}$$

where f_{12} is the absorption oscillator strength of the line, and A_{21} the transition probability. A photon emitted at a radius r interacts with the surrounding gas within a region corresponding to one Doppler width of the line. Regions further away are redshifted too much to come within the line width. As in an expanding universe with velocity proportional to radius, this corresponds to a spherical region with velocity radius Δv_D. The escape probability is therefore the same in all directions, and can be evaluated in the radial direction.

The radius of the interaction region is then

$$\delta l = \frac{\partial r}{\partial V}\Delta v_D = \left[\frac{\partial}{\partial r}\left(\frac{V_0}{R_0}r\right)\right]^{-1} \Delta v_D = \frac{R_0}{V_0}\Delta v_D = \frac{\Delta \nu_D}{\nu}ct. \quad (5.5)$$

Including the usual stimulated emission factor we get

$$\tau = \frac{A_{21}\lambda^3 g_2}{8\pi g_1}\left(n_1 - \frac{g_1}{g_2}n_2\right)t. \quad (5.6)$$

Since τ is isotropic, the escape probability averaged over the region is given by

$$\beta = \frac{1}{2\tau}\int_0^{\tau}\int_{-1}^{1} e^{-\tau'}d\mu\, d\tau' = \frac{1-e^{-\tau}}{\tau}. \quad (5.7)$$

Knowing the optical depth and escape probability, the line profile can be calculated for a given source function (eq. 4.10). For simplicity, assume that there is no background continuum. This is a good approximation for supernovae at late times, but is of course not valid in the early stages. For a more general treatment see Fransson (1984a). Using cylindrical coordinates, with p perpendicular to the line of sight (fig. 5), the intensity is given by

$$I_x = 2\pi \int_{p_{\rm min}}^{p_{\rm max}} S(p, z = xR)(1 - e^{-\tau})p\, dp, \quad (5.8)$$

Using $p\,dp = r\,dr$ for constant z (constant x), this can be written

$$I_x = 2\pi \int_{r_{\rm min}}^{R} S(r)(1 - e^{-\tau})r\, dr, \quad (5.9)$$

where $r_{\rm min} = xR$, and x is given by eq. (5.2). If the level populations are known, the line profile can now be calculated.

An interesting case for supernovae is that of a geometrically thin shell at a radius r_s. In this case, $S(r) = S_0\delta(r - r_s)$ and obtain

$$I_x = 2\pi S_0(1 - e^{-\tau_s})r_s \qquad \text{if } |x| \le \frac{r_s}{R}, \quad (5.10)$$

and zero otherwise, which means that the resulting line profile is flat out to a velocity corresponding to the shell velocity.

Another important case is that of an optically thin line. In this case

$$I_x = 2\pi \int_{r=xR}^{R} j(r) r\, dr. \tag{5.11}$$

From an observational point of view, it is of more interest to invert this relation.

$$j(r = xR) = \frac{-1}{2\pi x R} \frac{dI_x}{dx}. \tag{5.12}$$

The line profile therefore directly gives the emissivity as a function of radius in the remnant. This result assumes spherical symmetry of the ejecta. If the contributions from the different lines as a function of velocity are added, the total energy loss is obtained as a function of radius. This must be balanced by the energy input from the γ-rays, so the line profiles also map this quantity. In the simple, but important, case of one line dominating the total energy loss (e.g. [O I] λλ6300–64 Å) and an optically thin ($\tau_\gamma < 1$) source of γ-rays, the energy equation is

$$j(r) = H(r) \approx \frac{L_\gamma \kappa_\gamma D_\gamma \rho}{4\pi R_{\rm core}^2}, \tag{5.13}$$

so

$$D_\gamma(xR)\rho(xR) \propto \frac{1}{x} \frac{dI(x)}{dx}. \tag{5.14}$$

Therefore in this simple case, the total density distribution times the energy deposition function of the supernova can be obtained directly from the derivative of the line profile (Fransson 1986b). For a central ^{56}Ni source $D_\gamma \propto r^{-2} \propto x^{-2}$, while a uniform source has $D_\gamma \sim$ constant (section 3.3).

In some cases in addition to the line opacity there may also be a continuous source of opacity in the remnant. This can be dust (see section 10), or continuous bound-free absorption (section 7.1). The profile is then given by

$$I_x = 2\pi \int_{0}^{(R^2-x^2)^{1/2}} S(p, z = xR)(1 - e^{-\tau_\ell}) e^{-\tau_c(p,x)} p\, dp, \tag{5.15}$$

where

$$\tau_c(p, x) = \int_{xR}^{(R^2-p^2)^{1/2}} \kappa_c \rho\, dz, \tag{5.16}$$

is the continuous optical depth at frequency x, along a ray of constant p, and τ_ℓ the line optical depth. In this case only the source function is local, while the continuous opacity is integrated along the ray along a ray parallell to the line of sight.

For dust absorption, Lucy et al. (1991a) discuss the case of an optically thin line of constant emissivity and dust opacity within the remnant. In this case

$$I_x = 2\pi R^2 j \frac{(1+\tau_{\mathrm{d}}x) - (1+\tau_{\mathrm{d}})e^{-\tau_{\mathrm{d}}(1-x)}}{\tau_{\mathrm{d}}^2}, \tag{5.17}$$

where $\tau_d = \kappa_c \rho R$ is the total optical depth to the center of the supernova. The peak of the line is at a frequency

$$x_{\mathrm{peak}} = 1 - \frac{\ln(1+\tau_{\mathrm{d}})}{\tau_{\mathrm{d}}}. \tag{5.18}$$

For $\tau \ll 1, x_{\mathrm{peak}} \approx \tau_{\mathrm{d}}/2$. Therefore, the peak velocity gives the optical depth in the continuum. This assumes that the emissivity is spherically symmetric.

A special feature of supernova spectra is the large probability of line blending, which is a result of the large expansion velocity. At early times the velocity can be up to $3 \times 10^4\,\mathrm{km\,s^{-1}}$, and the probability for flouresence between various transitions is very large. Examples of this has been discussed by Lucy et al. (1991b). The most extreme case is the ultraviolet part of the spectrum. Here a large number of ions, like C I, O I, Si I, Fe I, Fe II, have strong transitions from low excitation levels, and the spacing between the lines is small. Using eqs. (2.4*b*) and (5.6), we can estimate the optical depth of a typical resonance line from an ion with relative abundance X_i in the envelope

$$\tau_{21} = 2.7 \times 10^3 \left(\frac{\lambda}{2500\,\text{Å}}\right)^3 \left(\frac{A_{21}}{10^7 \mathrm{s}^{-1}}\right) \left(\frac{X_i}{10^{-5}}\right) \left(\frac{t}{300\,\mathrm{days}}\right)^{-2}. \tag{5.19}$$

Even low abundance elements in the envelope and core can therefore have large optical depths in the UV.

Now, consider two lines with wavelengths λ_1 and λ_2, with $\lambda_1 < \lambda_2$. If a photon is re-emitted from a point with wavelength λ_1, relative to another point it is redshifted to $\lambda_1' = (1 + v_r/c)\lambda_1$, where v_r is the *relative* velocity between two points. As already discussed, v_{r} is constant on a sphere with radius $d = Rv_{\mathrm{r}}/V$, so that $\lambda_1' = \lambda_2$ for

$$\frac{d}{R} = \frac{c}{V}\frac{(\lambda_2 - \lambda_1)}{\lambda_1}. \tag{5.20}$$

The requirement for scattering is that $d < R$, and that the optical depth is larger than one. After the absorption, the photon is emitted isotropically from the resonance point. Consequently it performs a random walk from line to line with step length d, and at the same time be redshifted. This continues until either there is a wavelength gap between the optically thick lines larger than $\lambda V/c$, the photon escapes in a transition to an intermediate excited level in the optical range, it is destroyed by continuum absorption, or escapes from the optically thick region of the supernova. If for simplicity, we assume that there is a constant velocity spacing, $\Delta v = c\Delta\lambda/\lambda$ between the optically thick lines, the total number of scatterings for a photon until it reaches the boundary is $N \sim (R/d)^2 \sim (V/\Delta v)^2$. The Doppler shift after N scatterings is $N\Delta v \sim V^2/\Delta v$, which can be much larger than V, if $\Delta\lambda$ is small.

In fig. 6a we show the distribution of lines with optical depth larger than one at an age of 500 days, for typical core abundances and a velocity of $3000\,\mathrm{km\,s^{-1}}$. The lines have been selected from the line list by Kurucz and Peytremann (1975) and Kurucz (1981), and an equal mixture of neutral and singly ionized ions is assumed. This is a very rough approximation, but because of the large depths, this is not expected to introduce errors which are too large in the fluxes. More serious are any incomplete entries in the line list. The most interesting feature is that most of the UV (up to $\sim$ 3000 Å) is covered by a forest of optically thick lines. Above $\sim$ 3000 Å there are increasingly wide gaps between the lines. Also at shorter wavelengths, there are some important gaps in the line distribution, the most obvious at $\sim$ 1200 Å, $\sim$ 1500 Å and at $\sim$ 2900 Å.

Schematically to see the scattering effects of these lines, it is assumed that the UV flux from the core is emitted in four emission lines, at 912 Å, 1356 Å, 1640 Å, and 2335 Å, with equal fluxes. The line emissivities are in an actual case determined by the γ-ray input to the core, and the resulting recombination cascade (section 7.2). We then calculate the scattering process with a Monte-Carlo code. Although not very realistic for the resulting spectrum, it illustrates the random walk aspect well, and the result of this experiment is shown in fig. 6b. As expected, there is an inverse correlation between the gaps in the line distribution and the emission from the supernova. The photons emitted (e.g., in the O I λ1302–56 lines) scatter $\sim$ 10 times until they escape in the gap at $\sim$ 1500 Å. The photons emitted at 2335 Å (corresponding to either C II] or Si II]) do not find any gaps before $\sim$ 3300 Å, so most photons emitted between $\sim$ 2000 Å and $\sim$ 3300 Å emerge in this gap, if they have not been destroyed by continuum absorption or photon splitting, before escaping.

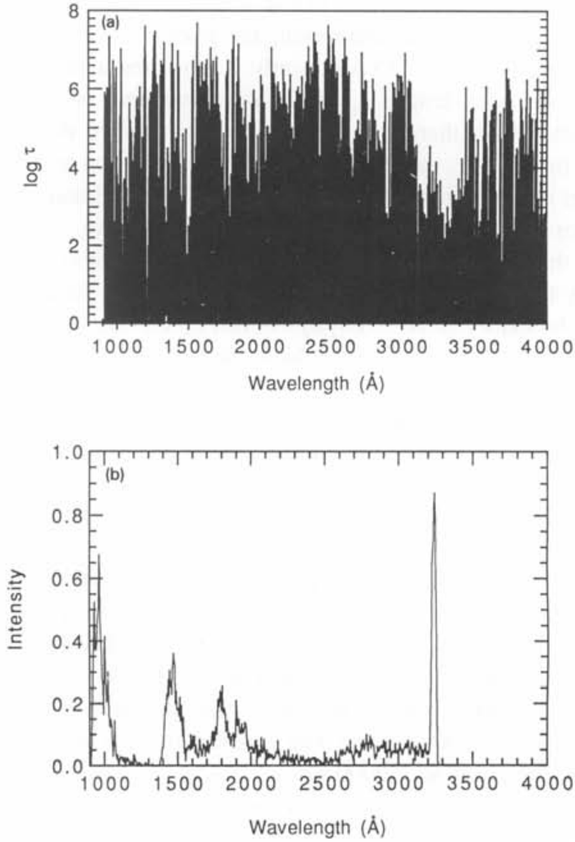

Fig. 6a. Distribution of lines with optical depth larger than one, for an expansion velocity of $3000\,\mathrm{km\,s^{-1}}$, and for a typical core composition, at 500 days. Note the gaps at $\sim$ 1200, 1500, and above 3000 Å.
Fig. 6b. Emerging spectrum for the same parameters as in fig. 6a. The emitting lines are at 912, 1302, 1640, and 2335 Å. The radiation escapes preferentially in the opacity gaps in the line distribution.

Resonance scattering is probably the most important factor for the strong UV deficiency in both SN 1987A and Type I supernovae (Branch and Venkatakrishna 1981; Wheeler et al. 1986; Fransson et al. 1987; Fransson 1987b; Lucy 1987). Because of the high optical depths, solar abundances are sufficient to give this effect (eq. 5.19), especially at early times when the velocities are higher, making blanketing even more efficient. It is interesting to note that the IUE spectra of SN 1987A even after a year showed a residual continuum flux below ~ 2500 Å, with the strongest features at 1300–1400 Å and 1800–2000 Å (Fransson et al. 1989). These are very broad, without any obvious correspondance to emission lines. It is likely that they corresponded to line emission from the core, e.g. [O I]$\lambda\lambda$1302, 1356, which managed to escape in the wavelength regions where the number of optically thick lines is a minimum.

The total path length for the photon is $Nd \sim R^2/d \sim RV/\Delta v$, where d was defined in eq. (5.20). This can be much larger than R, so that continuum absorption may be effective, even if the radial optical depth in the continuum is considerably less than one. The photons in fig. 6*b* have on the average been scattered a total distance corresponding to 10–30 times the radial distance. This is important for both the Balmer continuum, discussed in section 7.1, and for dust absorption (see section 10).

Also, continuum scattering can be important. If a photon is scattered coherently in the rest frame of the scattering particle, as for Thompson scattering, it is as is the case with resonance scattering, redshifted for an observer at rest, it will be redshifted for an observer at rest, as is the case with resonance scattering. If the scattering optical depth is τ_s, the probability to be scattered N times is τ_s^N, if $\tau_s < 1$, and there is a red extension of the line profile to $\Delta\lambda_{tot} \sim N\lambda V/c$. Fransson and Chevalier (1989) have made Monte Carlo calculations to study this effect quantitatively. Electron scattering has been proposed as an explanation for the observed line asymmetries at early epochs in SN 1987A by Witteborn et al. (1989). Based on the lack of expected time development in the [Fe II] 1.257μ line profile, Spyromilio et al. (1990) argue against this interpretation, and instead ascribe the asymmetries to fragmentation and non-spherical effects.

6. Plasma diagnostics

For H II regions and planetary nebulae, the most important quantities can often be inferred without any detailed modeling by using line ratios among the forbidden lines. To a limited extent this is useful also for supernovae.

In the optical region, the most important ratios are [O I] $\lambda\lambda\, 5577/(6300 + 6364)$, and [C I] $\lambda\lambda\, (9824 + 9850)/8727$. In fig. 7 we present these as a function of electron density and temperature. The presence of recombination lines can also be useful for putting constraints on temperature and electron density. An example is the O I recombination lines at 7774 Å and 8446

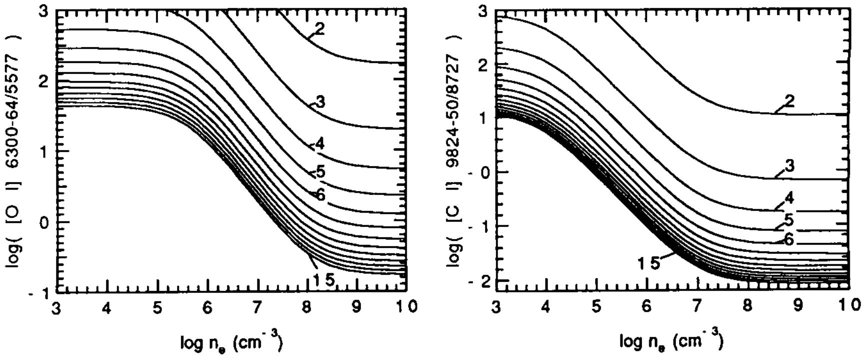

Fig. 7. Line ratios of [O I] λλ5577/(6300 + 6364) and [C I] λλ(9824 + 9850)/8727, as a function of electron density and temperature. The numbers in the figure give the the electron temperature in 10^3 K.

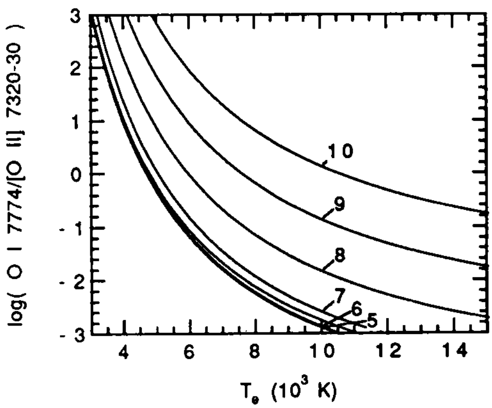

Fig. 8. Ratio of the O I recombination lines at 7774 Å and [O II] λλ7320, 7330 as a function of temperature and electron density. The different curves are labeled with the logaritm of the electron density.

Å. These are rather insensitive to the temperature, typically proportional to $T_e^{-0.7}$. The ratio of these lines to the forbidden [O II] λλ3726 or 7320–7330 lines is independent of the O I/O II ratio, and a function of only the temperature and electron density. This is shown in fig. 8.

Begelman and Sarazin (1986) and Fransson and Chevalier (1989) have used these lines, and the total luminosity of the [O I] λλ6300–64 lines to estimate parameters in the Type Ib SN 1985F. If $n_e \gg n_{\rm crit} \approx 2.8 \times 10^6\,{\rm cm}^{-3}$ and $\tau < 1$

$$L([{\rm O\,I}]\,\lambda\lambda 6300\text{–}64) = 1.1 \times 10^{42} \left(\frac{M({\rm O\,I})}{M_\odot}\right) e^{-2.272\times 10^4/T_e}\,{\rm erg\,s^{-1}}. \quad (6.1)$$

Based on this, Begelman and Sarazin argued for an O I mass of at least $5.6 M_\odot$. The main limitation of this approach is that one effectively considers the whole supernova as one uniform zone. From both 1-D and 2-D calculations of the hydrodynamic and abundance structure, this is known to be a poor approximation. The error becomes especially severe if lines of different elements or ionization stages are compared. Fransson and Chevalier showed that this can give an error of an order of magnitude for the derived oxygen mass, which makes any firm conclusions impossible.

Also, the Ca II H and K lines, the IR-triplet at 8600 Å, and the forbidden lines at 7300 Å can be used as density and temperature indicators (Fransson and Chevalier 1989).

A nice example of a nebular analysis applied to SN 1987A is provided by Varani et al. (1990). From observations of the IR [Fe II] 1.547μ/[Co II] 1.533μ ratio, they determine the relative Co II/Fe II ratio. The temperature is derived from the [Co II] $1.547\mu/10.52\mu$ ratio, and is between 3620 K on day 284 and 2950 K on day 576. The ionization correction is derived from the [Fe II] 1.535μ/[Fe I]1.533μ or [Fe I]1.44μ ratios. In this way Varani et al. obtain an M(Co)/M(Fe) ratio from day 255 to day 576, and find that it changes consistently with the decay of $\sim 0.07 M_\odot\,^{56}$Co to ^{56}Fe. The time scale agrees well with the radioactive decay time scale. On the final days, the time evolution is best fitted with an additional contribution of radioactive ^{57}Fe decaying on a longer time scale (section 3.2).

In the far-IR, Moseley et al. (1989) have used the [Fe II] $25.98\mu/17.93\mu$ ratio in SN 1987A to estimate the temperature. At densities above $10^5\,{\rm cm}^{-3}$, and at temperatures less than $\sim$ 7000K, the populations are given by the LTE value, and the line ratio is only a function of temperature. The same is true for the [Fe II] $24.5\mu/25.98\mu$ ratio and [Ni II] $18.24\mu/6.64\mu$ ratio. Moseley et al. find a temperature in the line forming layer of $(5 \text{ to } 8)\times 10^3$ K on day 265, considerably higher than Varani et al. for day 284.

An interesting variation on plasma diagnostics is given by Spyromilio and Pinto (1991). They exploit the fact that the [O I] $\lambda\lambda$6300–64 doublet is optically thick during the first year after the explosion (Fransson 1987b). Since the density is above critical, the doublet lines emit at the black body rate, and thus are equally intense. In the optically thin case, the lines instead have a ratio of $A_{6300}/A_{6363} = 3.0$. The optical depth is given by

$$\tau(6300) = 3\tau(6364) = 9.0 \times 10^{-10} n(\mathrm{O\,I}) \left(\frac{t}{300\,\mathrm{days}}\right). \tag{6.2}$$

If the time of unity optical depth for the lines can be estimated, the O I density at this epoch can be determined. Spyromilio and Pinto find for SN 1987A an oxygen density of $1.6 \times 10^{10}\,\mathrm{cm}^{-3}$ on day 173. This is considerably more than that of eq. (2.2*b*). The most likely reason for this is that the filling factor is only $\sim 10\%$, due to instabilities.

7. The spectra of Type II supernovae

In previous sections we have discussed the general physics and associated principles determining the conditions in the remnant and the emission from it. These results are now applied to the various regions in the supernova. Since they differ considerably, especially in composition, we discuss them one by one, starting with the hydrogen envelope. Except for the hydrogen envelope, our results are applicable to both Type II and Type Ib supernovae.

7.1. The hydrogen envelope

The Hα line is (along with [Ca II] and [O I] lines), the most prominent in the late spectra of Type II supernovae. While the excitation of the [Ca II] and [O I] lines is thermal, collisional excitation from the ground state, the Hα line is formed by a more complicated mechanism. This is immediately seen from the excitation temperature, 1.4×10^5 K, of the $n = 3$ level. Therefore thermal excitations as well as collisional ionizations from $n = 1$, followed by recombination, are negligible at temperatures below 10^4 K. Direct *non-thermal* excitations are also unimportant since only $\sim 3\%$ of the energy goes to $n = 3$, even at $X_e = 0.01$ (Kozma and Fransson 1991). Instead, Kirshner and Kwan (1975) suggested that the line arises as a result of photoionizations from the $n = 2$ level, followed by recombination. Because of the trapping of the Lyman α line, the population of the $n = 2$ level may be significant, and the opacity in the Balmer continuum may be sufficient to absorb the energy at shorter wavelengths. The energy may then be supplied by UV lines from the core and helium-mantle, which are excited by the γ-rays (Fransson 1987a; Fransson and Chevalier 1989; Chugai 1987; Xu and McCray 1991). The discussion here follows mainly Kozma and Fransson (1991). The advantage with this mechanism is that a large fraction (more than $\sim 75\%$) of the γ-rays are absorbed in this region. A clear discussion of this scenario for SN 1987A is given by McCray (1990).

If the optical depth in the Balmer continuum is larger than unity, the Balmer lines will also be thick. An electron which recombines to a level n' higher than $n = 3$ then gives rise to one or more photons from n' to n'' and a Balmer photon in the transition n'' to 2. Since the Balmer lines are thick, the photon is scattered a large number of times, until it decays as an Hα photon plus a member of the Paschen, Brackett, [etc.] series. Consequently, all optically thick Balmer lines higher than Hα are suppressed, and the Balmer decrement is very steep, in accordance with the observations. This explanation of the Balmer decrement was proposed by Kirshner and Kwan (1975), and is further discussed by McCray (1990), who termed it "Case C recombination," in analogy to Case B, where the Lyman lines are thick. If the Balmer continuum is thick, the total recombination rate is given by

$$\alpha_C = \sum_{k=3}^{\infty} \alpha_k \approx 1.82 \times 10^{-13} (T/10^4\,\mathrm{K})^{-0.88}\,\mathrm{cm^3 s^{-1}}$$

(Osterbrock 1989). In general, we have $\alpha_C = \alpha_B - (1 - \beta_B)\alpha_2$, where $\beta_B \approx e^{-\tau_B}$ is the average escape probability in the Balmer continuum.

Assuming that only recombinations populate the $n = 2$ level from above, the population of this level is determined by

$$(A_{2\gamma} + A_{21}\beta_{21} + C_{21}n_e + P_2)n_2 = n_e n_+ \alpha_C + (\Gamma_2 + C_{12}n_e)n_1, \tag{7.1}$$

and the ionization by

$$\left(\Gamma_c + P_1 + \sum_k \zeta_{k,H}\, n_k\right) n_1 + P_2 n_2 = \left(n_e \alpha_C + \sum_k \zeta_{H,k}\, n_k\right) n_+, \tag{7.2}$$

where β_{21} is the Lyman α escape probability, P_1 and P_2 are the photoionization rates from the $n = 1$ and $n = 2$ levels, and Γ_2 and Γ_c are the non-thermal excitation rate to $n = 2$ and the continuum, respectively. $\zeta_{k,H}$ is the charge transfer rate of H I + k II $\rightarrow$ H II + k I, and $\zeta_{H,k}$ is the inverse rate.

Neglecting the charge transfer for the moment, we can solve for $n_+ n_e$

$$n_+ n_e = \frac{\Gamma_2 + C_{12}n_e + \left(\dfrac{A_{2\gamma} + A_{21}\beta_{21} + C_{21}n_e}{P_2} + 1\right)(\Gamma_c + P_1)}{\left(\dfrac{A_{2\gamma} + A_{21}\beta_{21} + C_{21}n_e}{P_2}\right)\alpha_C} n_1. \tag{7.3}$$

For most cases of interest we can neglect the thermal collisions. We can now distinguish two separate cases. If $(A_{2\gamma} + A_{21}\beta_{21}) \ll P_2$, we have

$$n_+ n_e = \frac{P_2(\Gamma_2 + \Gamma_c + P_1)}{(A_{2\gamma} + A_{21}\beta_{21})\alpha_C} n_1, \tag{7.4}$$

while if $(A_{2\gamma} + A_{21}\beta_{21}) \gg P_2$

$$n_+ n_e = \frac{\Gamma_c + P_1}{\alpha_C} n_1, \tag{7.5}$$

since $\Gamma_2 < \Gamma_c$ (section 3.4). Consequently, if photoionizations from $n = 2$ are important, $n_e n_+$ is boosted by a factor $P_2/(A_{2\gamma} + A_{21}\beta_{21})$. The optical depth in the Balmer continuum for a shell of thickness Δr is

$$\tau_B = \sigma_B \int n_2 dr \approx n_2 \sigma_B \Delta r = \sigma_B \Delta r \, n_1 \frac{(\Gamma_2 + \Gamma_c + P_1)}{(A_{2\gamma} + A_{21}\beta_{21})}, \tag{7.6}$$

independent of P_2. Here $\sigma_B \approx 1.5 \times 10^{-17} (\nu/\nu_0)^{-2.9}\,\mathrm{cm}^2$.

The intensity in the Hα line is given by

$$I_\nu = 2\pi \int_{xR}^{R} S(1 - e^{-\tau}) r \, dr, \tag{7.7}$$

where the source function between levels $n = 2$ and $n = 3$ is given by eq. (4.9). Using

$$(A_{32}\beta_{32} + n_e C_{32}) n_3 = \alpha_{3\mathrm{eff}} n_e n_+ + C_{23} n_e n_2, \tag{7.8}$$

and assuming, as is reasonable in most cases, that collisional terms are small, induced emission unimportant, and that $\tau_{32} \gg 1$, so that $\beta_{32} \sim 1/\tau_{32}$, one obtains for the source function

$$S = \frac{hc n_e n_+ \alpha_{3\mathrm{eff}} t}{4\pi}, \tag{7.9}$$

and for the intensity

$$I_\nu = \frac{hct}{2} \int_{xR}^{R} n_e n_+ \alpha_{3\mathrm{eff}} r \, dr. \tag{7.10}$$

where $n_e n_+$ is given by eq. (7.3). This result is true also if τ_{32} is less than one, and has a straightforward interpretation in terms of recombinations.

Observationally, the electron density can be determined in several ways. In SN 1987A the continuum intensity was nearly flat with a flux $\sim$ 10 Jy from 16.6 to 65μ, 267 days after the explosion (Moseley et al. 1989). Assuming that most of this is due to free-free emission, and using

$$L_\nu = 6.8 \times 10^{-38} T^{-1/2} e^{-h\nu/kT} \sum_i (g_{ff} Z_i^2 n_i) n_e V \ \text{erg s}^{-1}, \qquad (7.11)$$

one derives an emission measure, $n_e V \sum_i (Z_i^2 n_i) \sim 2.8 \times 10^{64} T_4^{1/2}\,\text{cm}^{-3}$, where $T_4 = T/10^4$ K. Here g_{ff} is the gaunt factor, and Z is the charge of the ion i. A value of $n_e n(\text{H II})V = 3.2 \times 10^{64} T_4^{-1.23}\,\text{cm}^{-3}$ can also be derived from the H I 7–8 recombination line at 19.06μ (Moseley et al. 1989). The approximate agreement between these two determinations does not necessarily mean that this radiation comes from the same region, since the free-free emission can have an important contribution from metals. With a hydrogen envelope of uniform density expanding at 5000 km s^{-1}, the electron density on day 267 is

$$n_e = 7.1 \times 10^7\, T_4^{-0.62} \left(\frac{V_{\text{env}}}{5000\,\text{km s}^{-1}}\right)^{-3/2} \text{cm}^{-3}. \qquad (7.12)$$

Further, assuming an envelope mass of $10 M_\odot$, the total density on this day is $1.85 \times 10^9\,\text{cm}^{-3}$ and the electron fraction

$$X_e = 3.8 \times 10^{-2} T_4^{-0.62} \left(\frac{V_{\text{env}}}{5000\,\text{km s}^{-1}}\right)^{3/2} \left(\frac{M_{\text{env}}}{10 M_\odot}\right)^{-1}. \qquad (7.13)$$

Xu and McCray (1991) have discussed the ionization equilibrium, and find that the non-thermal ionization from the ground state alone is too small by an order of magnitude to account for the observed ionization as determined from the IR free-free continuum. The likely explanation, discussed above, is that photoionizations in the Balmer continuum provide most of the observed ionization. As Xu and McCray point out, this is a more economical way of ionizing, because of the smaller ionization potential of $n = 2$, 3.4 eV instead of 13.6 eV. Because of the leakage to $n = 1$ by collisions and radiative decays, non-thermal excitations from $n = 1$ to the continuum and from $n = 2$ are also necessary for this mechanism to work. This is evident from eq. (7.4).

To estimate the electron density, we assume that a fraction η of the total γ-ray energy absorbed in the helium and oxygen core, $(1-e^{-\tau_{\gamma,c}})L_\gamma$, results in emission with $E > 3.4\,\mathrm{eV}$. Here $\tau_{\gamma,c}$ is the γ-ray optical depth of the core inside of the hydrogen envelope. The Balmer ionization rate, P_2, is then

$$\begin{aligned} P_2 &= 4\pi \int_{3.4\,\mathrm{eV}} \frac{J_\nu \sigma_B(\nu) d\nu}{h\nu} = \frac{\eta(1-e^{-\tau_{\gamma,c}})L_\gamma \sigma_B}{4\pi r^2 \chi_2} \\ &= 5.2 \times 10^3 \eta (1-e^{-\tau_{\gamma,c}}) \left(\frac{V_{\mathrm{core}}}{2000\,\mathrm{km\,s^{-1}}}\right)^{-2} \left(\frac{R_{\mathrm{core}}}{r}\right)^2 \frac{e^{-t/111\,\mathrm{d}}}{t_{\mathrm{yr}}^2}, \end{aligned} \tag{7.14}$$

interior of $\tau_B < 1$. We estimate that $\beta_{21} A_{21} \sim 0.3 t_{\mathrm{yr}}^2 \ll A_{2\gamma} = 8.3/4 = 2.1$ (assuming equipartition of 2s and 2p), and since $A_{2\gamma} \ll P_2$, we are justified in using eq. (7.4) , so

$$n_+ n_{\mathrm{e}} \approx {n_{\mathrm{e}}}^2 \approx \frac{P_2 \Gamma_c}{A_{2\gamma}\alpha_C} n_1. \tag{7.15}$$

Γ_c is given by

$$\Gamma_c = \frac{L_\gamma \sigma_\gamma e^{-\tau_{\gamma,c}}}{4\pi r^2 \chi_{\mathrm{eff}}(\mathrm{H\,I})}, \tag{7.16}$$

where $\chi_{\mathrm{eff}}(\mathrm{H\,I}) \approx 30\,\mathrm{eV}$ and $\sigma_\gamma \approx 1.0 \times 10^{-25}\,\mathrm{cm^{-2}}$. To estimate the hydrogen envelope density we use eq. (2.4*b*). The electron fraction is then given by

$$\begin{aligned} X_{\mathrm{e}} &= 6.7\, \eta^{1/2} (1-e^{-\tau_{\gamma,c}})^{1/2} e^{-\tau_{\gamma,c}/2} \left(\frac{V_{\mathrm{core}}}{2000\,\mathrm{km\,s^{-1}}}\right)^{-2} \left(\frac{R_{\mathrm{core}}}{r}\right)^{3/2} \\ &\times \left(\frac{n(R_{\mathrm{core}}, 1\,\mathrm{yr})}{6.7 \times 10^8\,\mathrm{cm^{-3}}}\right)^{-1/2} \left(\frac{T_{\mathrm{e}}}{5000\,\mathrm{K}}\right)^{0.44} \left(\frac{M(^{56}\mathrm{Ni})}{0.075 M_\odot}\right) \frac{e^{-t/111\,\mathrm{d}}}{t_{\mathrm{yr}}^{1/2}}, \end{aligned} \tag{7.17}$$

which is valid interior of $\tau_{\mathrm{B}} < 1$. $n(R_{\mathrm{core}}, 1\,\mathrm{yr})$ is the density at $r = R_{\mathrm{core}}$ and $t = 1\,\mathrm{yr}$, normalized to the value given by eq. (2.4*b*). Below and in section 7.2 we argue that $\eta \approx 0.3$. The next two factors in eq. (7.17) are together between 0.3–0.6 for $0.1 < \tau_c < 2$, so we estimate the coefficient to be ~ 1.5. Most of the time dependence is therefore in the $t_{\mathrm{yr}}^{-1/2} e^{-t/111\,\mathrm{d}}$ factor. At 300 days we get $X_{\mathrm{e}} \sim 0.11$, which is in good agreement with eq. (7.13). At 400 days one gets $X_\epsilon \sim 0.04$, and at 500 days $X_e \sim 0.01$. If there is a substantial mixing of hydrogen into the core, as is indicated by observations and numerical simulations, the ionization can increase by a substantial amount. The similar metal and hydrogen line profiles in SN 1987A indicate that most of the Hα emission probably comes from this region, and gives little information about the total hydrogen mass.

As discussed by Xu and McCray (1991), charge transfer may decrease the ionization, especially if there is a *microscopic* mixing of metals into the hydrogen-rich gas. In fact, they argue that only a small amount of such mixing is allowed, since the ionization would otherwise be decreased by an order of magnitude.

The Balmer continuum optical depth is, assuming $P_1 \ll \Gamma_c$

$$\tau_{\rm B} \approx \frac{\sigma_{\rm B}}{A_{2\gamma}} \int_{R_{\rm core}}^{r} \Gamma_c n_1 dr. \tag{7.18}$$

For n given by eq. (2.4*b*) the integrand behaves as r^{-3}, and most of the contribution comes from near the core. Inserting numerical values,

$$\tau_{\rm B} \approx 59 \left(\frac{V_{\rm core}}{2000\,{\rm km\,s^{-1}}}\right)^{-1} \left(\frac{n(R_{\rm core}, 1\,{\rm yr})}{6.7 \times 10^8\,{\rm cm^{-3}}}\right) \left(\frac{M(^{56}{\rm Ni})}{0.075 M_\odot}\right) \frac{e^{-t/111\,{\rm d}}}{t_{\rm yr}^4}. \tag{7.19}$$

Therefore, the optical depth is larger than one up to ~ 400 days. In addition, resonance scattering in the UV can increase the optical depth by an order of magnitude (section 5). Therefore, we expect that Hα emission will follow the exponential decay closely up to at least 600 days. This is indeed observed for SN 1987A (Phillips and Williams, 1991). We note that the estimate is sensitive to the hydrogen density, and mixing increases the Balmer depth. This may be needed to explain the exponential decline after approximately day 700.

Estimating the emitting thickness in eq. (7.10) from $\tau_{\rm B} \sim 1$, and using eq. (7.14) for P_2, the luminosity in the Hα line becomes

$$L({\rm H}\alpha) \approx \eta(1 - e^{-\tau_{\gamma,c}}) \frac{h\nu_{{\rm H}\alpha}}{\chi_2} \frac{\alpha_{3{\rm eff}}}{\alpha_C} L_\gamma, \tag{7.20}$$

as expected. If $\tau_{\rm B} > 1$, $\alpha_{3{\rm eff}} \approx \alpha_C$, so

$$L({\rm H}\alpha) \approx \frac{5}{9} \eta(1 - e^{-\tau_{\gamma,c}}) L_\gamma. \tag{7.21}$$

To estimate the Hα luminosity we need to know the efficiency of the UV emission from the core, η. The UV resonance lines of Fe II at 2300–2700 Å have been proposed as a likely source of excitation. These, however, all have large optical depths, making branching to intermediate levels efficient, and essentially all the energy emerges as optical, forbidden lines. A similar example in the optical is Ca II, where nearly all resonance excitations in the H and K lines result in emission in the IR triplet and [Ca II] λ7300. Only elements where there are no intermediate levels between the ground state and resonance level are likely to have large UV fluxes. In the core, the strongest UV emission is expected from C I $\lambda\lambda$1140, 1993, C II λ2326, O I $\lambda\lambda$1302, 1356, Mg II λ2800, as well as the H I and He I two-photon continua.

An important ionizing source is radiation from the helium mantle. In 1-D models the column density of this is 30% of the total, which is also the fraction of the energy deposited if $\tau_\gamma < 1$. In next section we show that of this energy a fraction (~ 0.35) can ionize hydrogen from $n = 2$. The column density of the helium plus metal core is $\sim 75\%$ of the total. Assuming the same γ-ray to UV conversion in the rest of the core as in the helium mantle (~ 0.35), the total Hα efficiency is then $0.75 \times 0.35 \times 5/9 \sim 0.15$. This agrees well with that observed for SN 1987A (Phillips and Williams, 1991).

A possible problem for this mechanism is that the Hα line is strong and also very late for SN 1987A, even at 900 days. At this epoch it is difficult to have a sufficient population at the $n = 2$ level to keep the Balmer continuum optically thick. Apart from this, Hα is seen in several supernovae at an age of several years. In this case it is unlikely that radioactive excitation is important. Instead, circumstellar or pulsar excitation are more probable (see sections 12 and 13).

7.2. *The helium mantle*

In the helium shell the most abundant metals are carbon, nitrogen, and oxygen, all with abundances less than 0.02 by number. Therefore, helium dominates the absorption and thermalization of the γ-rays. At $X_e \sim 10^{-2}$, $\sim 35\%$ of the total non-thermal energy input goes into heating of the free electrons, $\sim 17\%$ leads to excitation of He I 2p ^{1}P, and $\sim 48\%$ to ionization (table 1). Most of the recombinations and non-thermal excitations of He I result in emission in the two-photon continuum from 2s ^{1}S (with a total energy of 20.6 eV). If the continuum below the He I edge at 24.5 eV were transparent, these photons could in principle, ionize hydrogen from the ground state in the envelope, as in H II regions (Osterbrock 1989). The small fraction of carbon in the helium shell ($\sim 1.5 \times 10^{-2}$ by number), however, is sufficient to make the continuum above 11.26 eV opaque. At this energy, the optical depth to C I is $\tau \sim 4.4 \times 10^6 (V_{core}/2000\,\mathrm{km\,s^{-1}})^{-2} (t/300\,\mathrm{days})^{-2}$. Therefore, most of the ionizing radiation from the He II recombinations results in ionization of C I. Of the two-photon emission, a fraction (0.64) of the energy has $h\nu \geq 11.26\ eV$. At least $\sim (0.17 + 0.48 \times \frac{20.2}{24.5}) \times 0.64 = 0.36$ of the absorbed γ-ray energy in the helium mantle is capable of ionizing C I. From Escalante and Victor (1990) we estimate that $\sim$ 60% of the energy in the recombination radiation of C II is above the Balmer limit, the strongest lines being C I $\lambda\lambda$1140, 1993. In addition, the two-photon emission between 3.4 eV and 11.26 eV ($\sim$ 0.13 of the energy) can ionize hydrogen directly from $n = 2$. A fraction ($0.6 \times 0.36 + 0.13 = 0.35$) of the energy absorbed in the helium shell can ionize the surrounding hydrogen (Kozma and Fransson 1991). To summarize the He I photons with $h\nu \sim$ 11–20 eV are degraded first to C I UV recombination photons, ionizing H I, and finally to Ha photons.

While the metals in this region are not important for the heating, they are important for cooling. Because of the high excitation potential of the first levels of He I (19.8 eV), thermal collision excitation from the ground state is negligible. Due to the metastable character of the 2 ^{3}S level, the population of this level can be large. Collisional excitation from 2 ^{3}S to 2 ^{3}P in the 10,830 Å transition may therefore be important for cooling. The strength of this line is consequently expected to depart considerably from the intensity calculated from pure recombination, as was observed in SN 1987A (Elias et al. 1988; Meikle et al. 1989). Most of the cooling in this region is, however, done by the metals. The strongest lines are [C I] λ8727, C I λ2966, C II] λ2326, Mg II λ2800, and [Ca II] λ7300 (Fransson and Chevalier 1989). The strong carbon lines are mainly a result of the high carbon abundance, in comparison to other elements. The low abundances of the metals result in a much higher temperature in this shell than in the metal rich core, typically 5000–7000 K.

7.3. The oxygen core

The region of greatest interest for nucleosynthesis is the metal rich core. To illustrate the physics and the general behaviour here, we discuss a simplified model with only a few of the most interesting processes included. We assume that the core has a uniform density given by eq. (2.1), an expansion speed of 2000 km s^{-1}, and a composition with oxygen dominating. For reasons which will become clear, we also include a trace amount of calcium, $X(\mathrm{Ca})$. We allow for the fact that the γ-ray source may be distributed. The γ-ray intensity is then

$$J_\gamma = \frac{L_\gamma D_\gamma e^{-\tau_\gamma}}{16\pi^2 r^2} = 3.0 \times 10^8 D_\gamma e^{-\tau_\gamma} \left(\frac{M(^{56}\mathrm{Ni})}{0.1 M_\odot}\right)$$
$$\times \left(\frac{V_{\mathrm{core}}}{2000\,\mathrm{km\,s^{-1}}}\right)^{-2} \left(\frac{t}{300\,\mathrm{d}}\right)^{-2} e^{-t/111\,\mathrm{d}} \mathrm{erg\,cm^{-2}s^{-1}}. \quad (7.22)$$

For a central source, D_γ is replaced by $(R_{\mathrm{core}}/r)^2$. The statistical equations describing the ionization equilibrium are

$$4\pi \frac{J_\gamma \sigma_\gamma}{\chi_{\mathrm{O\,I}}} n_{\mathrm{O\,I}} = (\alpha_{\mathrm{O\,II}} n_\mathrm{e} + \zeta n_{\mathrm{Ca\,I}}) n_{\mathrm{O\,II}}, \quad (7.23)$$

$$\left(4\pi \frac{J_\gamma \sigma_\gamma}{\chi_{\mathrm{Ca\,I}}} + \zeta n_{\mathrm{O\,II}}\right) n_{\mathrm{Ca\,I}} = \alpha_{\mathrm{Ca\,II}} n_\mathrm{e} n_{\mathrm{Ca\,II}}. \quad (7.24)$$

Here $\sigma_\gamma \sim 0.06 Z m_\mathrm{p} \sim 0.8 \times 10^{-24}\,\mathrm{cm}^2$. The effective ionization potentials, χ_i, are for O I $\sim$ 30 eV and for Ca I 4–8 eV, between $X_\mathrm{e} = 0.01$–0.1. The charge transfer rate of

$$\mathrm{Ca\,I}(^1\mathrm{S}_0) + \mathrm{O\,II}(^4\mathrm{S}^0) \rightarrow \mathrm{Ca\,II}(5p\ ^2\mathrm{P}_{1/2}) + \mathrm{O\,I}(^3\mathrm{P})$$

is

$$\zeta = 3.8 \times 10^{-9} (T_e/10^3\,\mathrm{K})^{1/2}\,\mathrm{cm^3 s^{-1}}$$

(Rutherford et al. 1972). The inverse process is negligible (section 4). The radiative recombination rate of O II is $\alpha_{\mathrm{O\,II}} = 2.0 \times 10^{-13} (T_\mathrm{e}/10^4\,\mathrm{K})^{-0.7}\,\mathrm{cm^3 s^{-1}}$, and of Ca II $\alpha_{\mathrm{Ca\,II}} = 1.12 \times 10^{-13} (T_\mathrm{e}/10^4\,\mathrm{K})^{-0.9}\,\mathrm{cm^3 s^{-1}}$. Above 4000 K, dielectronic recombination is important for Ca II, with a rate of $3.28 \times 10^{-10} (T_\mathrm{e}/10^4\,\mathrm{K})^{-1.5} e^{-36400/T}$. We assume that photoionization is not important for these ions.

Since $n_\mathrm{O} \gg n_{\mathrm{Ca}}$, the electron density is determined by

$$n_\mathrm{e} \approx n_{\mathrm{O\,II}} = n_\mathrm{O} - n_{\mathrm{O\,I}}. \quad (7.25)$$

Consider first the oxygen equilibrium. If we for the moment neglect recombination due to charge transfer for O II, we can solve these equations for $n_{\mathrm{O\,II}}$, and thus n_e.

$$X_\mathrm{e} \approx \frac{n_{\mathrm{O\,II}}}{n_\mathrm{O}} = \left(q + \frac{q^2}{4}\right)^{1/2} - \frac{q}{2}, \quad (7.26)$$

where

$$q = \frac{4\pi J_\gamma \sigma_\gamma}{n \chi_{\mathrm{O\,I}} \alpha_{\mathrm{O\,II}}}. \tag{7.27}$$

Usually $q \ll 1$, in which case we get

$$X_{\mathrm{e}} \approx q^{1/2} = \left(\frac{L_\gamma \sigma_\gamma D_\gamma}{4\pi R_{\mathrm{core}}^2 n \chi_{\mathrm{O\,I}} \alpha_{\mathrm{O\,II}}} \right)^{1/2}. \tag{7.28}$$

Inserting the expressions for J_γ, R_{core}, and n, we find

$$X_{\mathrm{e}} = 0.62 \left(\frac{M(^{56}\mathrm{Ni})}{0.1 M_\odot} \right)^{1/2} \left(\frac{V_{\mathrm{core}}}{2000\,\mathrm{km\,s^{-1}}} \right)^{1/2} \left(\frac{t}{300\,\mathrm{d}} \right)^{1/2} \times \left(\frac{M_{\mathrm{core}}}{4 M_\odot} \right)^{-1/2} \left(\frac{T_{\mathrm{e}}}{5000\,\mathrm{K}} \right)^{0.35} D_\gamma^{1/2} e^{-t/222\,\mathrm{d}} \tag{7.29}$$

In the case of a uniform ^{56}Ni distribution, $D_\gamma^{1/2} \sim 1.2$–1.7, while for a point source $D_\gamma^{1/2}$ is replaced by $(r/R_{\mathrm{core}})^{-1}$. We can now estimate the relative importance of the charge transfer terms in the recombination of O II and in the ionization of Ca I. For Ca I, the charge transfer ionization is given by $\zeta n_{\mathrm{O\,II}} \approx \zeta n_{\mathrm{e}}$, and the ratio of the two ionization terms on the left hand side is

$$4\pi \frac{J_\gamma \sigma_\gamma}{\chi_{\mathrm{Ca\,I}} \zeta n_{\mathrm{e}}} = 5.8 \times 10^{-5} \left(\frac{M(^{56}\mathrm{Ni})}{0.1 M_\odot} \right)^{1/2} \left(\frac{V_{\mathrm{core}}}{2000\,\mathrm{km\,s^{-1}}} \right)^{1/2} \left(\frac{t}{300\,\mathrm{d}} \right)^{1/2} \times \left(\frac{M_{\mathrm{core}}}{4 M_\odot} \right)^{-1/2} \left(\frac{\chi_{\mathrm{Ca\,I}}}{12\,\mathrm{eV}} \right)^{-1} \left(\frac{T_{\mathrm{e}}}{5000\,\mathrm{K}} \right)^{-1.2} e^{-t/222\,\mathrm{d}}. \tag{7.30}$$

Therefore, charge transfer dominates the ionization of Ca I by a large factor, and the equilibrium of Ca is reduced to

$$\frac{n_{\mathrm{Ca\,I}}}{n_{\mathrm{Ca\,II}}} \approx \frac{\alpha_{\mathrm{Ca\,II}} n_e}{\zeta n_{\mathrm{O\,II}}} \approx \frac{\alpha_{\mathrm{Ca\,II}}}{\zeta} \approx 1.9 \times 10^{-5} \left(\frac{T_{\mathrm{e}}}{5000\,\mathrm{K}} \right)^{0.4}, \tag{7.31}$$

so calcium is nearly completely ionized. The ratio of the two O II recombination terms is

$$\frac{\alpha_{\mathrm{O\,II}} n_{\mathrm{e}}}{\zeta n_{\mathrm{Ca\,I}}} \approx \frac{\alpha_{\mathrm{O\,II}}}{\alpha_{\mathrm{Ca\,II}}} \frac{n_{\mathrm{e}}}{n_{\mathrm{Ca\,II}}} \approx 1.5 \left(\frac{T_e}{5000\,\mathrm{K}} \right)^{0.22} \frac{n_{\mathrm{e}}}{n_{\mathrm{Ca\,II}}}. \tag{7.32}$$

Table 3.
Parameters for the cooling rates defined by eq. (7.34), and optical depth parameter τ_0 (eq. 7.38).

Transition	B erg cm^{3}s^{-1}	γ	$T_{\rm ex}$ K	$n_{\rm crit}$(5000 K) cm^{-3}	τ_0
[O I] $\lambda\lambda$ 6300–64	$5.3 \cdot 10^{-21}$	0.6	$2.272 \cdot 10^4$	$2.8 \cdot 10^6$	0.62
[Ca II] λ7300	$2.3 \cdot 10^{-18}$	−0.5	$1.974 \cdot 10^4$	$7.6 \cdot 10^6$	$1.3 \cdot 10^3$
[O I] λ63.18μ	$2.3 \cdot 10^{-24}$	0.87	$2.277 \cdot 10^2$	$1.8 \cdot 10^5$	$0.8 \cdot 10^3 T_4^{-1}$

Since $n_{\rm Ca\,II} \approx n_{\rm Ca} \ll n_{\rm e}$, charge transfer is not important for the recombination of O II. This illustrates a general rule that charge transfer mainly affects elements with small abundance, while the most abundant are less affected.

The temperature is determined from a balance between the γ-ray input per particle, H, and the cooling, C. A fraction ε, where $\varepsilon \sim 0.5$ (section 3.4), of the absorbed γ-rays goes into heating, so

$$H \approx 4\pi \varepsilon J_\gamma \sigma_\gamma. \tag{7.33}$$

The cooling is less straightforward to calculate, since a large number of lines contribute. In general, $C = n_{\rm e} \sum_i X_i \Gamma_i$. Here we include only three of the most important lines, [O I] $\lambda\lambda$6300–64, [Ca II] λ7300, and the fine structure transition [O I] λ63.18μ. The rate for these for low temperatures (less than $\sim$ 5000 K) can be approximated by

$$\Gamma = B \left(\frac{T_{\rm e}}{5000\,{\rm K}}\right)^{\gamma} \frac{e^{-T_{\rm ex}/T}}{1 + \frac{n_{\rm e}}{n_{\rm crit}}}\ {\rm erg\,cm^3 s^{-1}}, \tag{7.34}$$

where

$$n_{\rm crit} = n_{\rm crit}(5000\,{\rm K}) \left(\frac{T_{\rm e}}{5000\,{\rm K}}\right)^{-\gamma}\ {\rm cm^{-3}}, \tag{7.35}$$

is the electron density where collisional de-excitation sets in. Above this density, the levels are in thermal equilibrium. B, γ, $T_{\rm ex}$, and $n_{\rm crit}$(5000 K) are given in table 3.

An additional complication is that although these lines are forbidden, they may be optically thick (Fransson 1988). Using eqs. (2.1) and (5.6) we find

$$\tau_i = \tau_0 X_i \left(\frac{A}{16}\right)^{-1} \left(\frac{M_{\rm core}}{4M_\odot}\right) \left(\frac{V_{\rm core}}{2000\,{\rm km\,s^{-1}}}\right)^{-3} \left(\frac{t}{300\,{\rm d}}\right)^{-2}, \tag{7.36}$$

where X_i is the abundance by number in the shell, and τ_0 is given in table 3 for our lines.

[O I] $\lambda\lambda$6300–64, [Ca II] λ7300 may be optically thick for approximately the first year, while the [O I] 63.18μ line is thick for all times of interest in the oxygen core. The large depth of the 63.18μ line decreases the cooling by the factor $\beta = 1/\tau_i$. Since n_e is likely to be higher than n_{crit} $(\sim 10^6\,\mathrm{cm}^{-3})$, optically thick transitions will also be in LTE, and the line radiates at the black body rate, $J \sim S \sim B$. The emitting volume is $dV = 2\pi p\,dp\,dz = 2\pi p\,dp\,\lambda t\,dv$ (fig. 5), and the cooling per volume, L, is

$$L = \frac{4\pi B_\nu}{\lambda t} = \frac{8\pi hc}{\lambda^4 t(e^{h\nu/kT} - 1)}. \tag{7.37}$$

In general, for [O I] 63.18μ $h\nu \ll kT$, and using $L = \Gamma n n_e$, we find

$$\Gamma = \frac{8\pi kT}{\lambda^3 t n n_e}, \tag{7.38}$$

or, inserting relevant parameters,

$$\Gamma_{63.18\mu} = \frac{5.31 \times 10^{-13}}{n n_e}\left(\frac{T_e}{1000\,\mathrm{K}}\right)\left(\frac{t}{300\,\mathrm{d}}\right)^{-1} \mathrm{erg\,cm^3\,s^{-1}}. \tag{7.39}$$

In contrast to the optical lines, $\Gamma_{63.18\mu}$ depends on both the density and electron fraction.

As we have seen, oxygen is neutral in most cases of interest and due to charge transfer, calcium is singly ionized. The equation of thermal equilibrium is then

$$X_e[X(\mathrm{O})(\Gamma_{6300} + \Gamma_{63.18}) + X(\mathrm{Ca})\Gamma_{7300}] = \frac{\varepsilon L_\gamma D_\gamma \sigma_\gamma}{4\pi n R_{core}^2}. \tag{7.40}$$

For a given epoch this equation, together with eq. (7.28), is a function of the temperature only, and can easily be solved by iteration.

In fig. 9 we show the temperature, electron fraction, and individual contributions to the cooling as functions of time for $X(\mathrm{Ca}) = 5 \times 10^{-4}$; the core parameters are $M_{core} = 2M_\odot$, $V_{core} = 2000\,\mathrm{km\,s^{-1}}$; $A = 16$; and $M(^{56}\mathrm{Ni}) = 0.075M_\odot$. The most interesting evolution is seen in the temperature. At 300 days $T_e \sim 4200\,\mathrm{K}$ and decreases slowly to 1700 K by day 1000. It then suddenly drops to $\sim 300\,\mathrm{K}$ in just ~ 200 days, and then continues to decrease more slowly to $\sim 100\,\mathrm{K}$ at 1500 days. The reason for this is easy to understand if we plot the cooling function (i.e. the left hand side of eq. (7.40)) for a few dates (fig. 10).

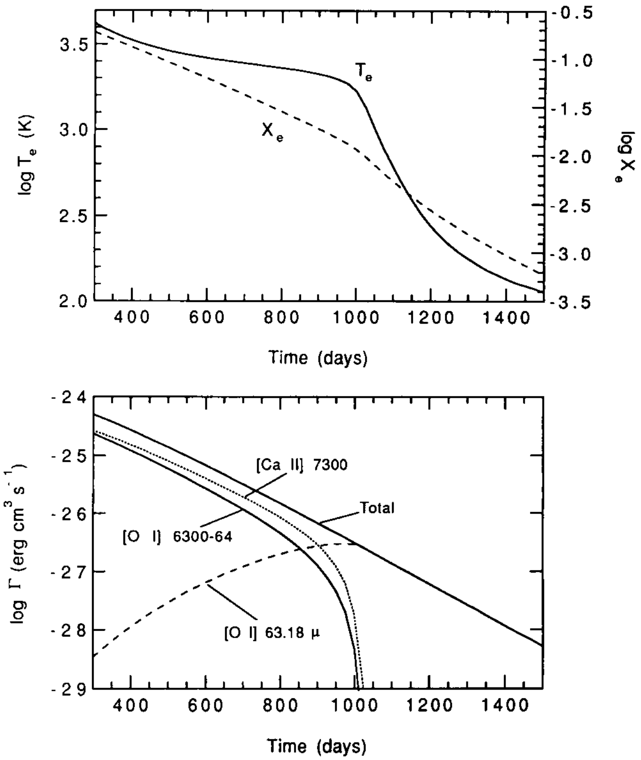

Fig. 9. Temperature, electron fraction, and individual contributions to cooling as a function of time for an oxygen core (see text for parameters). The core is assumed to have a mass of $2M_{\odot}$, and an expansion velocity of $2000\,\mathrm{km\,s^{-1}}$. The thermal instability sets in at ~ 1000 days.

Since γ-ray heating is nearly independent of temperature and decreases with time as $te^{-t/111\,\mathrm{d}}$, the temperature first follows the steep branch of the cooling curve, due to excitation of [O I] λλ6300–64 and [Ca II] λ7300. A decrease in the heating therefore results in only a small decrease in the temperature. At ~ 2000 K, the cooling curve flattens due to the nearly linear dependence of the fine structure cooling with temperature (eq. 7.41). A decrease in the heating now has a dramatic effect, and the temperature falls to only a few hundred K, where the Boltzmann factor again becomes important.

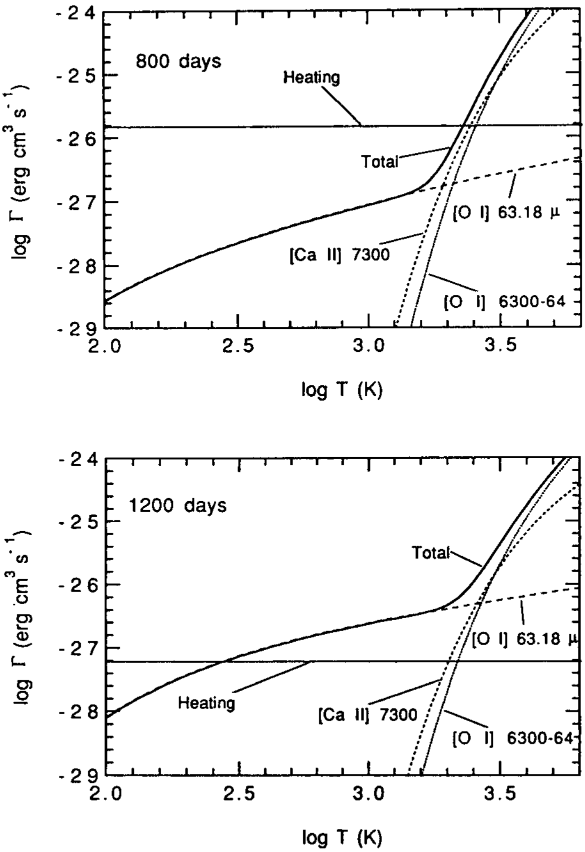

Fig. 10. Cooling and heating functions for 800 and 1200 days calculated for the model in fig. 9.

We can estimate the temperature evolution during the instability, if we neglect processes other than fine structure cooling. Balancing heating and cooling, we find

$$T_e = 1.6 \times 10^3 \left(\frac{M_{\rm core}}{4M_\odot}\right)\left(\frac{V_{\rm core}}{2000\,{\rm km\,s^{-1}}}\right)^{-5} \times \left(\frac{t}{1000\,{\rm days}}\right)^{-4} e^{-(t-1000^{\rm d})/111^{\rm d}}\ {\rm K}. \quad (7.41)$$

Once fine structure cooling dominates below $\sim$ 2000 K, the temperature drops exponentially. The time when the instability sets in, $\sim$ 1000 days, is therefore fairly insensitive to the exact density distribution.

The cooling efficiencies of the different elements can vary by several orders of magnitude. Of particular importance are the [O I] $\lambda\lambda$6300–64 and the [Ca II] λ7300 lines. At low temperatures the ratio is given by

$$\frac{\Gamma(7300)}{\Gamma(6300-64)} = 4.3 \times 10^2 \left(\frac{T}{5000\mathrm{K}}\right)^{-1.1} e^{2980/T} \times \frac{1 + \frac{n_e}{2.8\times10^6\mathrm{cm}^3}\left(\frac{T}{5000\mathrm{K}}\right)^{0.6}}{1 + \frac{n_e}{7.6\times10^6\mathrm{cm}^3}\left(\frac{T}{5000\mathrm{K}}\right)^{-0.5}} \frac{n(\mathrm{Ca\,II})}{n(\mathrm{O\,I})}. \quad (7.42)$$

For $n_e \gg 10^7\,\mathrm{cm}^{-3}$

$$\frac{\Gamma(7300)}{\Gamma(6300-64)} = 1.2 \times 10^3 e^{2980/T} \frac{n(\mathrm{Ca\,II})}{n(\mathrm{O\,I})}. \quad (7.43)$$

At 3000 K, the cooling efficiency per Ca II ion is $\sim 3.3 \times 10^3$ times higher than that of O I. Therefore, only a small fraction of calcium mixed with the oxygen causes the [Ca II] emission to dominate the [O I] emission. For the 10H model of SN 1987A, Woosley (1988) finds a calcium abundance of 6×10^{-4} by number in the oxygen shell, while the 11E1 model by Hashimoto et al. (1989) has no calcium in this region. The difference is presumably due to different treatments of convection during silicon burning in the progenitor. Although appearing unimportant at first sight, thus uncertainty in composition makes an accurate determination of the oxygen mass difficult. Conversely, it shows the potential of late time spectra as a diagnostic of the progenitor.

7.4. The iron core

The mass of the innermost region of the core is dominated by iron group nuclei, initially ^{56}Ni, which decay to ^{56}Co and finally to ^{56}Fe. After 300 days, 93% of these nuclei have decayed to iron, and in the following we will neglect the remaining cobalt and nickel. An important constituent in this region is helium, formed by photodissociation. Hashimoto et al. (1989) find an abundance of 0.18, by mass. More relevant for the cooling, the proportion by number of He : Fe is 0.70 : 0.23. The same numbers for the 10H model are He : Fe = 0.55 : 0.44. The cooling of an Fe-dominated plasma was first discussed in detail by Axelrod (1980b) in connection with Type Ia supernovae (section 8), and shows many similarities with the oxygen core in section 7.3.

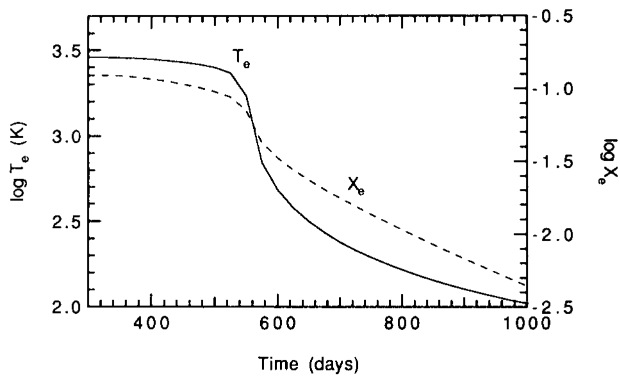

Fig. 11. Temperature evolution for the iron core. The thermal instability sets in at ~ 600 days; considerably earlier than in the oxygen core (fig. 9).

The Fe I and Fe II atomic spectra are similar in nature. The ground state is split up into five fine-structure levels, with a separation of ~ 0.05 eV. Between 1–2 eV above the ground state there are a number of metastable levels, connected to the ground state by forbidden lines in optical and near-IR regions of the spectrum. Finally, there are a large number of resonance levels above ~ 3 eV for Fe I and ~ 4.8 eV for Fe II, with transitions in the UV.

The Fe II resonance lines are important for the UV radiation field, since they can block out a large fraction of this region of the spectrum (section 5). The optical depths are very large, and although the branching ratio to the metastable levels are only on the order of 10^{-3}, most of the flux in the UV lines escapes as optical radiation. The metastable levels dominate collisional cooling above ~ 2000 K, while fine-structure cooling dominates below.

Because of the many levels with low excitation potential, cooling of the iron core is more efficient than cooling of the oxygen core, making the temperature considerably lower in this region. Fransson and Chevalier (1989) find an iron core temperature of ~ 3500 K, compared to an oxygen core temperature of ~ 5000 K at 300 days.

Figure 11 shows the temperature evolution of an iron core element expanding at $1000\,\mathrm{km\,s^{-1}}$, containing 50% Fe, and having the same mass density as the oxygen core in section 7.2. (given by eq. (2.1), with A ~ 30 and $M_{\rm core} \sim 2M_{\odot}$). As long as metastable lines dominate the cooling, the temperature is fairly constant (~ 3000 K). Close to day 600, thermal instability sets in and quickly cools the gas to only a few hundred K. The emission above the thermal instability is dominated by the $^6D_{9/2}$–$^4F_{7/2}$ 1.257μ and

${}^6D_{9/2}$–${}^4F_{9/2}$ 5.34μ lines between the ground state and first two metastable levels. Below the instability only far-IR fine structure lines contribute, the strongest being the ${}^6D_{9/2}$–${}^6D_{7/2}$ 26.0μ and ${}^4F_{9/2}$–${}^4F_{7/2}$ 17.94μ lines.

8. Type Ia supernovae

The emission from Type Ia supernovae has a similar character to the iron core at late times (Meyerott 1980; Axelrod 1980a,1980b). Because of the much higher expansion velocity for Type Ia supernovae, the density is considerably smaller; at the same time they get transparent earlier. Together with a strong density gradient, this results in a considerably higher state of ionization for Type I than for Type II supernovae. Axelrod finds that a wide range of ions from Fe II to Fe V are present. The spectrum is dominated by lines of [Fe II] and [Fe III]; but lines of [Fe V] and even [Fe VII] are present. A problem with some of these models is that they predict overly strong lines (e.g., of Fe V) arising in the outer density gradient (Pinto, priv. comm.).

The higher expansion velocity in Type Ia supernovae makes line blending very severe, and what in the observations seems like a non-Planckian continuum, is in reality a large number of overlapping lines. Of particlar interest is the spectral region 5700 Å–6400 Å, which in Axelrod's models is dominated by emission from the forbidden [Co III] a^4P and a^2G multiplets to the ground state. Both observations and models show a decrease of this feature with time, which is due to the radioactive decay of ^{56}Co. Although this needs to be confirmed (both by more detailed modeling and by observation), it is a strong indication that the ^{56}Ni model is correct also for Type Ia supernovae.

A severe problem for the modeling of Type Ia supernovae is the lack of accurate atomic data. In particular, collision strengths for the first three ionization stages of Fe, Co and Ni are badly needed.

9. Mixing

For line formation, the spatial distribution of elements is of fundamental importance. One dimensional calculations of the hydrodynamics show a stratified element distribution, with most of the metals moving at essentially one velocity in a thin shell, with a helium core outside of this, and finally a hydrogen envelope (fig. 1b). However, from line profiles it is immediately seen that this cannot be the case, since this would result in flat line profiles in conflict with observations (Fransson 1986b; Fransson and Chevalier 1989;

section 5). This is a very robust result, since it is only a consequence of the geometry and not of the excitation conditions. A direct inversion of the [O I] $\lambda6300$ profile for the Type Ib SN 1985F also indicates a wide velocity-distribution in the emitting oxygen mass, as well as small-scale irregularities (Fransson and Chevalier 1989; Schlegel and Kirshner 1989; Filippenko and Sargent 1990).

Mixing has several consequences for the observed spectrum. The most straightforward is the previously mentioned distribution of emitting material in velocity space. Another effect is that since the line profiles are a reflection of total energy input as a function of velocity, a more extended distribution of the radioactive material leads to less peaked lines (see section 5). Finally, the cooling of a given mass element is sensitive to the relative abundances in the region. This effect was discussed for the particular case of calcium in the oxygen shell. In that case, the microscopic mixing is a result of convection in the final burning phases of the progenitor. Analogous effects result for a *microscopic* mixing in the explosion, which may drastically change the relative strengths of the lines. Mixing of metal rich gas with the hydrogen envelope essentially kills the hydrogen emission.

Arnett et al. (1990) and Hachisu et al. (1990) (see the lectures by Müller and Nomoto) have made 2-D and 3-D calculations of the hydrodynamics of the explosion, and find that Rayleigh-Taylor instabilities develop at the O/He core interface and at the He/H interface, leading to fingers of oxygen-rich material penetrating into the hydrogen envelope, and also hydrogen-rich material penetrating into the oxygen core. The helium shell is completely distorted into a corrugated shape, separating the hydrogen and oxygen layers. While very impressive, these calculations should probably be considered as only indicative, since they have several shortcomings, as acknowledged by the authors. The primary ones are the unknown size of the initial perturbations, and the neglecting of radioactive heat input on the dynamics ("the Ni-bubble"). Arnett et al. also find that microscopic mixing in the explosion is very inefficient, in agreement with what is found from spectral synthesis models (Fransson and Chevalier 1989). However some microscopic mixing may take place in the interfaces of the "fingers" due to Kelvin-Helmhotz instabilities.

10. Formation of molecules

After day 112, infrared emission from CO and SiO was observed in the spectrum of SN 1987A (Oliva et al. 1987; Spyromilio et al. 1988). The chemistry of molecule formation in SN 1987A has been discussed by Petuchowski et al. (1989) and by Lepp et al. (1990). Petuchowski et al. (1989) suggest that CO may be formed by radiative association

$$C^+ + O \longrightarrow CO^+ + h\nu, \tag{10.1}$$

followed by charge transfer

$$CO^+ + O \longrightarrow CO + O^+. \tag{10.2}$$

Accurate calculations by Dalgarno et al. (1990) decreased the rate of this reaction by several orders of magnitude, but Lepp et al. still find it important, especially at low temperatures, where the neutral reaction

$$C + O \longrightarrow CO + h\nu, \tag{10.3}$$

is slow. Petuchowski et al. and Lepp et al. discuss a large number of other reactions that may contribute to the formation of CO.

The radiation field in the core limits the CO abundance by photodissociation, the reverse of eq. (10.3),

$$CO + h\nu \longrightarrow C + O, \tag{10.4}$$

with $h\nu > 11.1$ eV for CO and $h\nu > 8.3$ eV for CO^+. The intensity of the far UV flux is highly uncertain. Petuchowski et al. (1989) suggest that the major sources of hard photons are He I 2 ^{1}P–1 ^{1}S at 19.8 eV and He I two-photon emission. Photoelectric absorption by C and O, however, is very important at these energies (section 7.2), and a realistic estimate of the dissociation and ionization rates is only possible with a detailed model taking these effects into account.

The chemistry is sensitive to the abundance structure in the ejecta. As discussed in section 8, there is strong evidence for mixing in the supernova. For the chemistry to be affected by this, mixing must be on a microscopic scale and not just large groups of different shells mixed with each other. Petuchowski et al. (1989) assume complete mixing of the helium-oxygen core, while Lepp et al. use a mixed model as their standard model but include discussion of the effects of less complete mixing. In particular, if helium is mixed into the C/O rich gas, neutralizing reactions like

$$He^+ + CO \longrightarrow He + C^+ + O, \tag{10.5}$$

are important for the destruction of CO. Lepp et al. find that an overabundance of He^+ in fact leads to such rapid destruction of the molecules that it is difficult to reproduce the observations. The abundance of He^+ is sensitive to unknown rates of charge exchange, especially with C,

$$He^+ + C \longrightarrow He + C^+. \tag{10.6}$$

In a blob with no helium mixed into it, these types of reactions do not occur, in which case photodissociation is probably the most important destruction process.

While models discussed by the authors mentioned above are useful for identifying the important processes, a quantitative comparison with observations depends on a large number of assumptions, such as mixing, the UV-field, the assumed temperature, and effects of other molecules, for example SiO, etc.

11. Dust formation in supernovae

Danziger et al. (1989) found that after being red shifted up to day 400, the peaks of the line profiles of Mg I] λ4571, [O I] λ6300, Hα, and [C I] λ9844 changed to blue shifted after day 530. At the same time, the fluxes of the lines started to decrease more rapidly than at earlier epochs. Based on an analysis similar to that in section 5 (especially eq. 5.18), Lucy et al. (1989, 1991b) have convincingly interpreted this as a result of dust formation in the envelope of the supernova. Requiring the dust extinction derived from the line profiles to be the same as that needed to correct the observed V light curve to agree with model predictions, they also argued that most of the dust was in small silicate grains, rather than graphite. The rapid decay of the 1.09μ [Si I] line was suggested to be the result of an actual depletion of silicon into dust. This is not an entirely clear signature, since such a decay in fact was predicted as just a result of temperature evolution by Fransson and Chevalier (1987). In fact, dust condensation is expected to correlate with the cooling of the ejecta. From the absence of any spectral features of dust in the IR, the blue shift of the IR lines, and on the apparent small condensation efficiency, Lucy et. al. found that most of the dust was probably in opaque clouds, in addition to a uniform component of small dust particles. The latter was needed to explain the selective extinction at short wavelengths.

Since dust absorption is found to be important for optical lines, which have a maximum path length of $2R$, it must be even more important in the

UV, since the path length there is much larger, due to resonance scattering (section 5). It is likely that a large fraction of the far UV emission from radioactive excitation is thermalized, and emerges as far-IR radiation.

Dust formation in SN 1987A was predicted by several groups. Dwek (1988) found that this might have dramatic effects, and even black out the supernova completely. A weakness of his calculation is the assumption of adiabatic cooling, which is not very realistic (e.g., Fransson and Chevalier 1989).

Kozasa et al. (1989) made detailed calculations of the condensation, using the theory of homogeneous nucleation. They found that nucleation is sensitive both to the temperature evolution, and to the chemical composition, and in particular the degree of mixing, which here is meant in a microscopic sense. If mixing is not important, graphite would form at a temperature of $\sim 1810\,K$ in the carbon-rich regions of the inner helium layer. Kozasa et al. also considered a mixed core, where oxygen consequently dominated. This resulted in a dominance of "silicates," like Mg_2SiO_4, Al_2O_3, and Fe_3O_4, which formed at $\sim$ 1400 K, 1590 K, and 1140 K, respectively. This probably also characterizes the situation in an unmixed oxygen core. Since Mg, Al, and Si occur together in most of the oxygen shell, the formation of Mg_2SiO_4 and Al_2O_3 occurs here. Of these three elements, Si has the smallest abundance, ~ 0.02 by mass, so the dust mass in the $\sim 2M_\odot$ oxygen shell is $\sim (4 \times 16 + 2 \times 24 + 28) / 28 \times 0.02 \times 2 \sim 0.2\,M_\odot$. This estimate is sensitive to the $^{12}C(\alpha, \gamma)^{16}O$ rate, and assumes that all Si goes into grains. It is difficult to see how Fe_3O_4 would form if there is no microscopic mixing. To some extent this could possibly take place at the interfaces between the iron fingers and the oxygen shell.

The temperature evolution with time was not directly computed but only parameterized, and since dust formation is mainly controlled by this parameter, this is the primary uncertainty in the calculation. For their preferred temperature evolution, Kozasa et al. predicted that dust would form between 400 and 600 days, agreeing with the models by Fransson and Chevalier (1989). An additional uncertain factor is the degree of latent heating, as well as the effects of the radiation field. UV-trapping can increase the radiation density (section 5), and this may have important effects on the formation.

For both graphite and Mg_2SiO_4, Kozasa et al. found that the optical depth due to dust absorption would be very large. Thus, the epoch for dust formation is approximately correct, but the lack of strong dust absorption is probably a result of clumpy distribution of the dust, in agreement with the picture suggested by observations.

12. Effects of a neutron star

It has long been recognized that the presence of a neutron star may be important for the emission from supernovae at late stages (e.g., Chevalier 1976). The radiation from the neutron star can be either that characteristic of a pulsar or that of an accreting x-ray source, depending on the gas density close to the neutron star. If the pressure from the magnetic field, $B^2/8\pi$, is larger than the ram pressure from the accreting gas, ρV^2 (here V is the infall velocity, $V \sim (GM/r)^{1/2}$), the magnetic field may sweep the surroundings of the neutron star free of gas, and the system can act like an isolated pulsar (Illiarionov and Sunyaev 1975). If, on the other hand, the accretion rate is high, the pulsar mechanism is quenched, and the situation is closer to that of an accreting x-ray binary. This is discussed in the lectures by Chevalier. Here we consider only the consequences for the emitted spectrum from the supernova at late times (Fransson and Chevalier 1987; Fransson 1987b).

In the pulsar scenario, most of the emission comes from accelerated particles close to the neutron star. The magnetic field and relativistic particles from the pulsar exert a pressure on the remnant and form a bubble in the center, which expands relative to the rest of the supernova remnant. Chevalier (1977) found that for a uniform density of the ejecta, and with $\gamma = 4/3$, the radius of the bubble-remnant interface expands as

$$R_{\rm b} \sim 1.1 \times 10^{15} \left(\frac{L_{\rm p}}{10^{39}\,{\rm erg\,s^{-1}}}\right)^{1/5} \left(\frac{V_{\rm core}}{2000\,{\rm km\,s^{-1}}}\right)^{3/5} \times \left(\frac{M_{\rm core}}{4M_\odot}\right)^{-1/5} \left(\frac{t}{\rm years}\right)^{6/5} {\rm cm}, \quad (12.1)$$

where $L_{\rm p}$ is the particle and field "luminosity." The velocity of the bubble is $V_{\rm b} = (6/5)(R_{\rm b}/t)$, and that of the ejecta just outside the bubble, $V_{\rm ej} = R_{\rm b}/t$, is

$$V_{\rm ej} = 370 \left(\frac{L_{\rm p}}{10^{39}\,{\rm erg\,s^{-1}}}\right)^{1/5} \left(\frac{V_{\rm core}}{2000\,{\rm km\,s^{-1}}}\right)^{3/5} \times \left(\frac{M_{\rm core}}{4M_\odot}\right)^{-1/5} \left(\frac{t}{\rm years}\right)^{1/5} {\rm km\,s^{-1}}. \quad (12.2)$$

This is the minimum velocity expected in the ejecta, and line profiles from the ejecta are expected to be flat for velocities less than this. The bubble sweeps up the ejecta in a thin shell of shocked gas. The shock velocity is

$$V_s = V_b - \frac{R_b}{t} = \frac{V_{ej}}{5} \sim 62 \left(\frac{L_p}{10^{39}\,\mathrm{erg\,s^{-1}}}\right)^{1/5} \left(\frac{V_{core}}{2000\,\mathrm{km\,s^{-1}}}\right)^{3/5} \times \left(\frac{M_{core}}{4M_\odot}\right)^{-1/5} \left(\frac{t}{\mathrm{years}}\right)^{1/5} \mathrm{km\,s^{-1}}. \quad (12.3)$$

The temperature behind the shock depends on the composition and state of ionization, but is in the range of 10^5–10^6 K. Because of the low temperature and high metalicity, this shock is radiative, and therefore the resulting compression behind the shock is large. In reality this shell is likely to be unstable (Chevalier 1977), and will probably break up into filaments. This may fill the interior with filaments of gas, giving more peaked line profiles. While a stable shell absorbs all hard radiation, a filamentary allows some of the ionizing radiation to penetrate into the unshocked ejecta. The luminosity from the shock is

$$L_s \sim 2.3 \times 10^{37} (L_p/10^{39}\,\mathrm{erg\,s^{-1}}) t_{yr}\,\mathrm{erg\,s^{-1}}.$$

In discussing the evolution and the extent of ionization of the ejecta, a simple power law spectrum $\nu^{-\alpha}$ with total luminosity L_i between ν_{min} and ν_{max}, from the relativistic electrons is assumed. This corresponds to a total number of ionizing photons per unit time, S_i, above the thresholds of the various ions, i. Neglecting the empty bubble, we find that the radius of the ionized gas is given by

$$\frac{R_i}{R_{core}} = \left(\frac{Am_p}{M_{core}}\right)^{2/3} \left(\frac{4\pi S_i}{3\alpha_r(T_e) X_e}\right)^{1/3} R_{core}. \quad (12.4)$$

For an enriched, highly ionized gas, the electron fraction, X_e, can be considerably larger than one. The time when the whole core is ionized is given by

$$t_i = \left(\frac{M_{core}}{Am_p}\right)^{2/3} \left(\frac{3\alpha_r(T_e) X_e}{4\pi S_i}\right)^{1/3} V_{core}^{-1}, \quad (12.5)$$

which depends on both the density structure and the composition. The shell close to the bubble can delay the ionization considerably, since the ionized mass is proportional to S/n, where n is the shell density. Once the shell is ionized, the rest of the core is progressively ionized, with the outer boundary at $V_i = t V_{\rm core}/t_i$. Since $t_i \propto A^{-2/3}$, metal-rich regions are ionized faster than those dominated by helium.

To be specific, consider a core consisting of either pure helium or oxygen. Taking a luminosity of $10^{39} L_{39}\,{\rm erg\,s^{-1}}$ between $\nu_{\rm min} = 13.6$ eV and $\nu_{\rm max} = 10$ keV, and $\alpha = 1.5$, we obtain $S_{49}({\rm O\,I}) = 1.59 L_{39}\ {\rm s^{-1}}$, $S_{49}({\rm O\,II}) = 0.38 L_{39}\ {\rm s^{-1}}$, $S_{49}({\rm He\,I}) = 0.46 L_{39}\ {\rm s^{-1}}$, and $S_{49}({\rm He\,II}) = 0.20 L_{39}\ {\rm s^{-1}}$ for He II, where $S_{49} = S/10^{49}\,{\rm s}{-1}$. Setting $\alpha_r = 2.4 \times 10^{-13} \zeta (T_e/10^4\,{\rm K})^{3/4}\,{\rm cm^3\,s^{-1}}$, where $\zeta = 1$ for O II, 5.6 for O III, 1.1 for He II, and 6.4 for He III, we obtain

$$t_i = 81 S_{49} \left(\frac{V_{\rm core}}{2000\,{\rm km\,s^{-1}}}\right)^{-1} \left(\frac{M_{\rm core}}{4 M_\odot}\right)^{2/3} \times \left(\frac{T_e}{10^4 {\rm K}}\right)^{1/4} A^{-2/3} X_{\rm e}^{1/3} \zeta^{1/3} {\rm years}. \quad (12.6)$$

Therefore, the oxygen core is ionized up to O II after $11\,L_{39}^{-1/3}$ years and to O III after $39\,L_{39}^{-1/3}$ years, while the helium core takes $43\,L_{39}^{-1/3}$ years to get ionized up to He II, and $130\,L_{39}^{-1/3}$ years to be ionized to He III. During the first decades, the ionized region is probably contained in the shell outside the bubble, so the velocity of the lines will only be $\sim$ 500–1000 km s^{-1}. Once the core is ionized, the hydrogen envelope quickly follows because of its lower density. The general characteristic of a pulsar excited remnant is lines of high ionization (Fransson 1987b; Fransson and Chevalier 1987; Colgan and Hollenbach 1988), such as [O III], increasing in width with time. *In contrast to excitation by circumstellar interaction, we expect that the lines should have widths less than the core velocity ($\sim$ 1000–2000 km s^{-1}) during the first decades.*

If accretion dominates, most of the emission can be thermalized (Chevalier, these lectures), and the radiation temperature only is approximately $\sim$ 4000 K. However, absorption decreases with energy as E^{-3}, so some of the hard x-rays from the accretion can penetrate to the core and envelope. If these have energies higher than $\sim$ 5 keV they contribute to the ionization in roughly the same way as the radiation from reverse shock (see next section). Fransson (1987b) and Fransson and Chevalier (1987) calculated the optical depth, τ_x, for models of SN 1987A, and found that the remnant becomes transparent at an energy, E, after a time

$$t(\tau_x = 1) = 28 \left(\frac{E}{10\,\mathrm{keV}} \right)^{-1.4} \text{ years.} \tag{12.7}$$

This time scale is sensitive to instabilities as well as to the density distribution close to the center of the remnant. If the spectrum continues above $\sim$ 10 keV, a large fraction of the ejecta is ionized. In a manner similar to γ-ray excitation, the degree of ionization is expected to be low, with strong lines such as [O I] $\lambda\lambda$6300–64, in contrast to the lines of pulsar excitation. In the latter case, we expect high ionized UV lines and lines like [O III] $\lambda\lambda$4949–5007.

13. Circumstellar excitation

From radio and UV observations of supernovae during the first years after the explosion, it is clear that the interaction between the supernova and the surrounding circumstellar medium can be very important. The physics of this is not treated in any detail here, since several reviews already exist (e.g. Chevalier 1990; Fransson 1986a). Here we concentrate on those aspects which have direct implications for the observed optical spectrum, and which can compete with radioactive and pulsar excitation at late stages.

That circumstellar excitation may be important for optical emission is suggested from observations of narrow emission line component especially in Hα. Examples of this are SN 1979C (Branch et al. 1981), SN 1984E (Dopita et al. 1984), SN 1986J (Rupen et al. 1987; Leibundgut et al. 1990) and SN 1988Z (Filippenko 1990; Stathakis and Sadler 1990). A clear example of circumstellar excitation is the ring around SN 1987A (Fransson et al. 1989; Wampler et al. 1990). The narrow emission lines are due to circumstellar gas expelled by the progenitor and excited by the burst of hard radiation accompanying the outbreak of the shock (Fransson and Lundqvist 1989; Lundqvist and Fransson 1991). In this section we concentrate on the broad emission lines from the ejecta itself.

Radio observations provide the strongest evidence that most Type II and Type Ib supernovae are surrounded by a dense circumstellar medium, presumably due to the stellar wind from the progenitor star (Weiler et al. 1986). The epoch of the turn-on of radio emission at a certain frequency signals the time when the gas becomes optically thin with respect to free-free absorption, and provides a tool to determine the emission (or more correctly, absorption) measure, $\int n_e^2\, dr$ (see Lundqvist and Fransson (1988) for the various assumptions going into this determination). The electron density as a function of radius is given by

$$
\begin{aligned}
n_{\rm e} &= \frac{\dot{M}}{4\pi \mu m_{\rm p} u r^2} \\
&= 2.6 \times 10^7 \left(\frac{\dot{M}/u}{10^{-6} M_\odot \,{\rm yr}^{-1}\,{\rm km}^{-1}\,{\rm s}} \right) \left(\frac{r}{10^{15}{\rm cm}} \right)^{-2} {\rm cm}^{-3},
\end{aligned} \tag{13.1}
$$

where $\dot{M}$ is the mass loss rate, u the wind velocity, and μ the mean molecular weight of the electrons, is approximately 1.15 for a cosmic, fully ionized gas. Therefore, the mass loss rate, or rather $\dot{M}/u$, can be determined. Typical wind velocities for red supergiants are $\sim$ 10 km s^{-1}, and derived mass loss rates for the two well-observed Type II supernovae, SN 1979C and SN 1980K, are $1 \times 10^{-4} M_\odot\,{\rm yr}^{-1}$ and $3 \times 10^{-5} M_\odot\,{\rm yr}^{-1}$, respectively (Lundqvist and Fransson 1988). Type Ib's have considerably lower values of $\dot{M}/u$, presumably due to higher wind velocities from their assumed hot progenitor stars (e.g. Chevalier 1990).

The interaction between the supernova and the circumstellar medium produces an outward propagating fast shock into the circumstellar medium, and a reverse shock into the ejecta. The velocity of the former is at least 5×10^3 km s^{-1} and for SN 1987A was more than 3×10^4 km s^{-1}. The reverse shock velocity is sensitive to the density gradient of the ejecta, but on the order of 10^3 km s^{-1}. Chevalier (1982) found a very useful similarity solution for the case where the density of the ejecta can be described by a power law, $\rho \propto r^{-n}$, with n typically in the range 7–12. Since there are no scales in either the density of the ejecta or circumstellar medium, a similarity solution can be found, and one finds that the radius of the shock scales with time as $R_{\rm s} \propto t^{(n-3)/(n-2)}$. From this result, most properties can be derived. Of special interest is the velocity of the reverse shock,

$$
V_{\rm r} = V_{\rm ej} - \frac{dR_{\rm s}}{dt} = \frac{R_{\rm s}}{t} - \frac{(n-3)}{(n-2)}\frac{R_{\rm s}}{t} = \frac{1}{(n-2)}\frac{R_{\rm s}}{t} = \frac{1}{(n-3)} V_{\rm s}. \tag{13.2}
$$

The temperature of the shocked gas is given by

$$
T_{\rm e} = \frac{3}{16}\frac{\mu m_{\rm p} V_{\rm s}^2}{k} = 1.36 \times 10^9 \left(\frac{V_s}{10^4\,{\rm km\,s}^{-1}} \right)^2 {\rm K}, \tag{13.3}
$$

resulting in $\sim 10^9$ K for the outer shock, while the reverse has a temperature lower by a factor of $(n-3)^{-2}$, or 10^7–10^8 K. The density behind the reverse is a factor of $(n-4)(n-3)/2$ higher, in comparison to the wind shock.

In general, the outer shock is adiabatic except during the first weeks when it cools by Compton scattering of photospheric photons (Chevalier 1981; Fransson 1982). Most of the ionizing radiation comes from the reverse shock, where cooling is important and the energy is emitted as soft x-rays. For mass loss rates of more than $\sim 10^{-4} M_{\odot}\,\mathrm{yr}^{-1}$ the reverse shock can be radiative for several years, and the luminosity is roughly given by

$$L_{\mathrm{r}} = 1.6 \times 10^{42} \frac{(n-4)}{(n-3)^2} \left(\frac{\dot{M}/u}{10^{-5} M_{\odot}\,\mathrm{yr}^{-1} \mathrm{km}^{-1} \mathrm{s}} \right) \left(\frac{V_s}{10^4 \mathrm{km\,s}^{-1}} \right)^3 \mathrm{erg\,s}^{-1}. \tag{13.4}$$

Thus, L_{r} decays as $t^{-3/(n-2)}$. For $n = 12$, the coefficient in eq. (13.4) is $1.6 \times 10^{41}\,\mathrm{erg\,s}^{-1}$, and for $n = 7$, $3.0 \times 10^{41}\,\mathrm{erg\,s}^{-1}$. As the shock becomes adiabatic the luminosity decays as $t^{-\alpha}$, where $\alpha \sim 1$.

Because of the lower temperature and higher luminosity at late epochs, it is mainly the reverse shock which is contributes to the excitation of the the ejecta, and it has been suggested that the Hα line in some supernovae may be excited by radiation from the circumstellar interaction (Chevalier and Fransson 1985, 1990; Fransson 1986; Chugai 1988). While a detailed comparison with observations requires a calculation of both the radiation from the shock and the excitation of the ejecta, some of the characteristics can be obtained from simpler considerations. Chevalier and Fransson (1990) have calculated the dynamics of the interaction, for both power law distributions and for realistic, hydrodynamic calculations of the ejecta–assuming that the interaction shell is geometrically thin, and that the shock spectrum can be assumed to have a *bremsstrahlung* shape. The cooling is determined from a fit to the steady state cooling of a cosmic plasma. The hydrodynamic structure of the ejecta is taken from a $20 M_{\odot}$ ZAMS model of SN 1987A by Woosley (1988).

The structure of an exploding red supergiant can differ substantially from that of the blue progenitor in SN 1987A, especially at early stages. Our results should therefore be taken with some caution. However, most of the structure inside the power law region is fairly similar to that of the $15 M_{\odot}$ red supergiant model by Weaver and Woosley (1980).

In fig. 12 we show the result of a calculation for $\dot{M}/u = 5 \times 10^{-6} M_{\odot}\,\mathrm{yr}^{-1} \mathrm{km}^{-1} \mathrm{s}$. For this mass loss rate, the shock luminosity is more than $10^{39}\,\mathrm{erg\,s}^{-1}$, even up to ~ 10 years after the explosion, while the reverse shock temperature is 5×10^6 to 10^7 K. The reverse shock is radiative for ~ 3 years. This luminosity is the maximum that can emerge in the Hα line. Half of this is emitted towards the ejecta, where it can ionize the high velocity gas close to the shock, and half is emitted outward, where it may

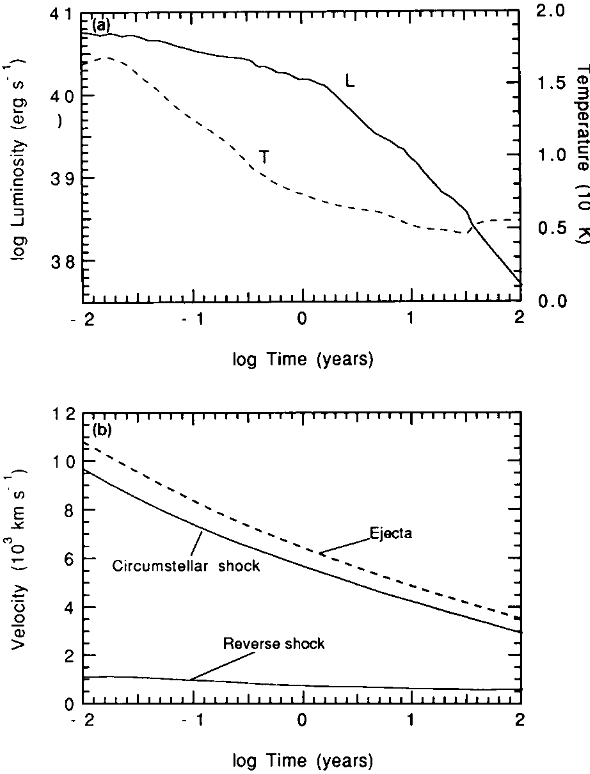

Fig. 12a. Luminosity and temperature of the reverse shock into the supernova ejecta for $\dot{M}/u = 5 \times 10^{-6} M_{\odot}\,\mathrm{yr}^{-1}\,\mathrm{km}^{-1}\mathrm{s}$.

Fig. 12b. Velocity of the circumstellar shock, the reverse shock and the maximum velocity in the ejecta. The latter is the highest velocity expected from the line profiles.

be absorbed by the dense, cool gas behind the reverse shock. Exactly how much is re-emitted in Hα remains to be determined, but it is clear that the necessary energy is there. In fig. 12b we show the velocity of the ejecta close to the reverse shock. This is the maximum velocity of the ionized ejecta, and thus represents the width of the line. The velocity of the cooling shell is a factor $(n-3)/(n-2) \approx$ 0.8–0.9 smaller. While the absolute value of the velocity is sensitive to the explosion model, Fig. 12b illustrates the slow decrease of the velocity width with time. During the first decades, only a small region close to the shock is ionized, and it takes several hundred years until the whole remnant is ionized. Therefore, *a characteristic of this type of excitation is that the spectral lines should have a high expansion velocity, more than* $\sim 4000 km\ s^{-1}$, *have flat line profiles, and a luminosity only slowly decreasing with time.*

In view of these conclusions, the observations of SN 1980K nearly ten years after the explosion (Long et al. 1989; Leibundgut et al. 1990) are of special interest, because they show just the mentioned characteristics. After decaying on an exponential time scale for about two years (Uomoto and Kirshner 1986), the luminosity levels off at $\sim 3 \times 10^{37}\,\mathrm{erg\,s^{-1}}$, and remains approximately constant for $\sim$ 10 years. Also, the line profile extending to $\sim 5700\,\mathrm{km\,s^{-1}}$, although noisy, is consistent with being flat. The velocity is not very different from that of the observations in 1980.

Although both observations and models are rather crude, it clearly shows that circumstellar excitation may be a very important ingredient at very late phases.

14. Conclusions

While radioactive excitation is well established as the primary source of emission during the first years after the explosion, much of the detailed physics is yet to be understood. This includes both the microphysics and the macroscopic structure. A major problem is uncertainty in the density and chemical distribution in the ejecta. For reliable determinations of abundances, for example, these multidimensional effects must be included. Conversely, since the observed spectrum is sensitive to these parameters, they contain, for example, a large amount of information about mixing. Only a small fraction of this has yet been exploited. It is therefore a safe prediction that this field will continue to evolve rapidly, both observationally and theoretically. This applies especially to the very late phases, when circumstellar and neutron star effects become important.

Acknowledgements

Many of the results in this paper have been obtained in collaboration with Roger Chevalier and Cecilia Kozma, and I am grateful to them for many discussions and comments. Mats Löfdahl has struggled with translating this paper to TEX, and guiding me through all pitfalls. Finally, I thank all participants in the school for discussions, and for making the stay at Les Houches a pleasant memory, in particular for our son Tobias.

References

Ahlen, S.P. 1980. Rev. Mod. Phys. **52**, 121.

Arnett, W.D., D. Branch, and J.C. Wheeler. 1985. Nature **314**, 337.

Arnett, W.D., B.A. Fryxell, and E. Müller. 1991. Ap. J. in press.

Axelrod, T.S. 1980a. *In*: Type I Supernovae, ed. J.C. Wheeler, Univ. of Texas, p. 80.

Axelrod, T.S. 1980b. Ph.D. thesis, Univ. of California, Santa Cruz.

Axelrod, T.S. 1988. *In*: Proceedings of IAU Colloquium No. 108, Atmospheric Diagnostics of Stellar Evolution: Chemical Peculiarity, Mass Loss, and Explosion, ed. K. Nomoto, Springer Lecture Notes in Physics, p. 375.

Bethe, H. A. 1930. Ann. Phys. **5**, 325.

Bethe, H. A. 1933. *In*: Handbuch der Physik, vol. **24** (2), p. 273.

Begelman, M.C., and Sarazin, C.L. 1986. Ap. J. (Letters) **302**, L59.

Branch, D., and Nomoto, K. 1986. Astr. Ap. **164**, L13.

Branch, D., and Venkatakrishna, K.L. 1981. Ap. J. (Letters) **306**, L21.

Branch, D., Falk, S.W., McCall, M.L., Rybski, P., Uomoto, A.K., and Wills, B.J. 1981. Ap. J. **258**, 790.

Chevalier, R.A. 1976. Ap. J. **207**, 872.

Chevalier, R.A. 1977. *In*: Supernovae, ed. D.N. Schramm, (D. Reidel: Dordrecht) p. 53.

Chevalier, R.A. 1981. Ap. J. **251**, 259.

Chevalier, R.A. 1982. Ap. J. **258**, 790.

Chevalier, R.A. 1990. *In*: Supernovae, ed. A. G. Petschek, Springer, New York.

Chevalier, R.A., and Fransson, C. 1985. *In*: Supernovae as Distance Indicators, Ed. N. Bartel, Springer, p. 123.

Chevalier, R.A., and Fransson, C. 1991. *In* preparation.

Chugai, N.N. 1987. Sov. Astron. Lett. **13**, 282.

Chugai, N.N. 1988. Astrophys. Space Sci. **146**, 375.

Colgan, S.W.J., and Hollenbach, D.J. 1988. Ap. J. (Letters) **329**, L25.

Colgate, S.A., and McKee, C. 1969. Ap. J. **157**, 623.

Dalgarno, A., Du, M.L., and You, J.H. 1990. Ap. J. **349**, 675.

Danziger, I.J., Gouiffes, C., Bouchet, and P. Lucy, L.B. 1989. IAU Circ. No. 4746.

Dopita, M., Evans, R., Cohen, M., and Schwartz, R. 1984. Ap. J. (Letters) **287**, L69.

Douthat, D. A. 1975. Radiation Research **64**, 141.

Dwek, E. 1988. Ap. J. **329**, 814.

Elias, J.H., Gregory, B., Philips, M.M., Williams, R.E., Graham, J.R., Schwartz, R.D., and Wilking, B. 1988. Ap. J. (Letters) **331**, L9.

Ensman, L.M., and Woosley, S.E. 1988. Ap. J. **333**, 754.

Escalante, V. and Victor, G.A. 1990. Ap. J. Suppl. **73**, 513.

Filippenko, A.V. 1990. *In*: Supernovae, Proc. of the Tenth Santa Cruz Summer Workshop in Astronomy and Astrophysics, ed. S.E. Woosley (Springer Verlag).

Filippenko, A.V., and Sargent, W.L.W. 1990. Ap. J. (Letters) **345**, L43.

Fransson, C. 1982. Astr. Ap. **111**, 140.

Fransson, C. 1984a. Astr. Ap. **132**, 115.

Fransson, C. 1984b. Astr. Ap. **133**, 264 (1984).

Fransson, C. 1986a. *In*: IAU Coll. No. 89, Radiation Hydrodynamics of Stars and Compact Objects, ed. D. Mihalas and K.H. Winkler, p. 141.

Fransson, C. 1986b. *In*: Highlights of Astronomy, ed. J.P. Swings, (D. Reidel: Dordrecht) p. 611.

Fransson, C. 1987a. *In*: Cargese Advanced Study Institute on High Energy Phenomena Around Collapsed Stars, ed. F. Pacini, p. 51.

Fransson, C. 1987b. *In*: ESO Workshop on SN 1987A, ed. I.J. Danziger, p. 467.

Fransson, C. 1988. *In*: Proceedings of IAU Colloquium No. 108, Atmospheric Diagnostics of Stellar Evolution: Chemical Peculiarity, Mass Loss, and Explosion, ed. K. Nomoto, Springer Lecture Notes in Physics, p. 383.

Fransson, C., and Chevalier, R.A. 1987. Ap. J., (Letters) **322**, L15.

Fransson, C., and Chevalier, R.A. 1989. Ap. J. **343**, 323.

Fransson, C., and Lundqvist, P. 1989. Ap. J. (Letters) **341**, L59.

Fransson, C., Benvenuti, P., Gordon, C., Hempe, K., Palumbo, G.G.C., Panagia, N., Reimers, D., and Wamsteker, W. 1984. Astr. Ap. **132**, 1.

Fransson, C., Grewing, M., Cassatella, A., Panagia, N., and Wamsteker, W. 1987. Astr. Ap. **177**, L33.

Fransson, C., Cassatella, A., Gilmozzi, R., Kirshner, R.P., Panagia, N., Sonneborn, G., and Wamsteker, W. 1989. Ap. J. **336**, 429.

Hachisu, I., Matsuda, T., Nomoto, K., and Shigeyama, T. 1990. Ap. J. (Letters) **358**, L57.

Hashimoto, M., Nomoto, K., and Shigeyama, T. 1989. Astr. Ap. **210**, L5.

Illiarionov, A.F., and Sunyaev, R.A. 1975. Astr. Ap. **39**, 195.

Kirshner, R.P., and Kwan, J. 1975. Ap. J. **197**, 415.

Kozasa, T., Hasegawa, H., and Nomoto, K. 1989. Ap. J. **344**, 325.

Kozma, C., and Fransson, C. 1991. Preprint.

Kumagai, S., Shigeyama, T., Nomoto, K., Itoh, M., Nishimura, J., and Tsuruta, S. 1989. Ap. J. **345**, 412.

Kurucz, R.L. 1981. SAO Special Report No. 390.

Kurucz, R.L., and Peytremann, E. 1975. SAO Special Report No. 362.

Leibundgut, B., Kirshner, R.P., Pinto, P.A., Rupen, M.P., Smith, R.C., Gunn, J.E., and Schneider, D.P. 1990. Ap. J. in press.

Lepp, S., Dalgarno, A., and McCray, R. 1990. Ap. J., **358**, 262.

Long, K.S., Blair, W.P., and Krzeminski, W. 1989. Ap. J. (Letters), **340**, L25.

Lucy, L.B. 1987. Astr. Ap. **182**, L31.

Lucy, L.B., Danziger, I.J., Gouiffes, C., and Bouchet, P. 1989. *In*: IAU Colloquium No. 120, Structure and Dynamics of the Interstellar Medium, eds. G. Tenorio-Tagle, M. Moles, and J. Melnick, Lecture Notes in Physics (Springer Verlag), p. 82.

Lucy, L.B., Danziger, I.J., Gouiffes, C., and Bouchet, P. 1990. *In*: Supernovae, Proc. of the Tenth Santa Cruz Summer Workshop in Astronomy and Astrophysics, ed. S.E. Woosley (Springer Verlag), p. 82.

Lucy, L.B., Danziger, I.J., Gouiffes, C. 1991. Astr. Ap. in press.

Lundqvist, P. and Fransson, C. 1988. Astr. Ap. **192**, 221.

Lundqvist, P., and Fransson, C., 1991. Ap. J., in press.

McCray, R. 1990. *In*: Molecular Astrophysics, ed. T. Hartquist, Cambridge University Press, p. 439.

Meikle, W.P.S., Allen, D.A., Spyromilio, J., and Varani, G.-F. 1989. MNRAS **238**, 193.

Meyerott, R.E. 1980. Ap. J. **239**, 257.

Mihalas, D. 1978. Stellar Atmospheres, W.H. Freeman and Company.

Moseley, S.H., Dwek, E., Glaccum, W., Graham, J.R., Loewenstein, R.F., and Silverberg, R.F. 1989. Ap. J. **347**, 1119.

Nomoto, K., Thielemann, F.-K., and Yokoi, K. 1984. Ap. J. **286**, 644.

Oliva, E., Morwood, A. F. M., and Danziger, I. J. 1987. Messenger **50**, 18.

Opal, C.B., Peterson, W.K., and Beaty, E.C. 1971. J. of Chemical Phys. **55**, 4100.
Osterbrock, D.E. 1989. Astrophysics of Gaseous Nebulae and Active Galactic Nuclei, University Science Books.
Petuchowski, S.J., Dwek, E., Allen, J.E., and Nuth, J.A. 1989. Ap. J. **342**, 406.
Phillips, M.M., and Williams, R.E. 1990. *In*: Supernovae, Proc. of the Tenth Santa Cruz Summer Workshop in Astronomy and Astrophysics, Ed. S.E. Woosley (Springer Verlag), p. 36.
Pinto, P., and Spyromilio, J. 1990. Preprint.
Rupen, M.P., van Gorkom, J.H., Knapp, G.R., Gunn, J.E., and Schneider, D.P. 1987. Astron. J. **94**, 61.
Rutherford, J.A., Mathis, R.F., Turner, B.R., and Vroom, D.A. 1972b. J. Chem. Phys. **57**, 3087.
Rybicki, G.R., and Hummer, D.G. 1978. Ap. J. **219**, 654.
Shigeyama, T., Nomoto, K., and Hashimoto, M. 1988. Astr. Ap. **196**, 141.
Shigeyama, T., and Nomoto, K. 1990. Ap. J. **360**, 242.
Schlegel, E.M., and Kirshner, R.P. 1989. Astron. J. **98**, 577.
Schunk, R.W., and Heyes, P.B. 1971. Plan. Sp. Sc. **19**, 113.
Shull, J.M., and Xu, Y 1988. *In*: SN 1987A in the Large Magellanic Cloud, eds. M. Kafatos and A. Michalitsianos, Cambridge University Press (Cambridge), p. 371.
Shull, J.M., and van Steenberg, M. 1985. Ap. J. **298**, 268
Spencer, L.V., and Fano, U. 1954. Phys. Rev. **93**, 1172.
Spyromilio, J., Meikle, W. P. S., Learner, R. C. M., and Allen, D. A. 1988. Nature **334**, 327.
Spyromilio, J., Meikle, W.P.S., and Allen, D.A. 1990. MNRAS **242**, 669.
Stathakis, R.A, and Sadler, E.M. 1990. Preprint.
Turner-Smith, A.R., Green, J.M., and Webb, C.E. 1973. J. Phys. B **6**, 114.
Xu, Y. 1989. Ph. D. thesis, University of Colorado.
Xu, Y., and McCray, R. 1991. *In*: Supernovae, Proc. of the Tenth Santa Cruz Summer Workshop in Astronomy and Astrophysics, ed. S.E. Woosley (Springer Verlag), p. 444.
Uomoto, A.K., and Kirshner, R.P. 1986. Ap. J. **308**, 685.
Varani, G.-F., Meikle, W.P.S., Spyromilio, J., and Allen, D.A. 1990. MNRAS **245**, 570.
Wampler, E.J., Wang, L., Baade, D., Banse, K., D'Odorico, S., Goiffes, C., and Tarenghi, M. 1990. Ap. J. (Letters) **362**, L13.
Weaver, T.A., and Woosley, S.E. 1980. *In*: Supernova Spectra, ed. R. Meyerott and G.H. Gillespie, American Institute of Physics, p. 15.
Wheeler, J.C., Harkness, R.P., Barkat, Z., and Schwatz, D. 1986. PASP **98**, 1018.
Witteborn, F.C., Bregman, J.D., Wooden, D.H., Pinto, P., Rank, D.M., and Cohen M. 1989. Ap. J. (Letters) **338**, L9.
Woosley, S.E. 1988. Ap. J. **330**, 218.
Woosley, S.E., and Weaver, T.A. 1986. *In*: Radiation Hydrodynamics in Stars and Compact Objects, eds. D. Mihalas and K.H. Winkler, Springer, p. 91.
Woosley, S.E., Pinto, P.A., and Weaver, T.A. 1988. Proc. Astron. Soc. Australia **7**, 355.
Woosley, S.E., Pinto, P.A., and Hartmann, D. 1989. Ap. J. **346**, 395.

COURSE XV

SUPERNOVAE AND THE INTERSTELLAR MEDIUM

ROGER A. CHEVALIER

Department of Astronomy, University of Virginia
Charlottesville, VA 22903, USA

S. Bludman, R. Mochkovitch and J. Zinn-Justin, eds.
Les Houches, Session LIV, 1990
Supernovae

Contents

1. Introduction 746
2. Supernovae 746
3. The interstellar medium 748
4. Circumstellar environments 750
5. Hydrodynamic evolution 752
6. Circumstellar interaction 756
7. X-ray and infrared emission from hot gas 759
8. Shock wave emission and stability 762
9. Future prospects 764

References 765

1. Introduction

The interaction of supernovae with their surroundings involves several areas, each of which has large uncertainties: the physical processes involved in the interaction, as well as the nature of supernovae and their surroundings. There has been considerable progress on the nature of supernovae in the past decade, but the structure of the interstellar medium and the influence of supernovae on that structure remain uncertain. Recent research on supernova remnants has shown that, in many cases, their properties are closely related to the nature of the progenitor stars and their presupernova evolution. The progenitor star affects its surroundings through mass loss and photoionizing radiation; the region thus affected is called the circumstellar medium. The physical processes involved in circumstellar interaction are similar to those in interstellar interaction and both will be covered in this review. The proceedings of IAU Colloquium 101 (Roger and Landecker 1988) give a detailed overview of supernova remnants and the interstellar medium.

2. Supernovae

The interaction with the surrounding medium is expected to become important after the supernova has expanded by many times its initial radius, so that pressure forces within the exploded star are small. In this situation, an element of gas moves with constant velocity, and the velocity field is given by

$$\mathbf{v} = \mathbf{r}/t$$

where t is the time since the explosion. The velocity vector is radial. The density of an element of gas drops due to the volume expansion as t^{-3}, so that the density profile is described by

$$\rho = f(\mathbf{v})t^{-3}.$$

The function f is determined by the initial explosion and is crucial for supernova remnant evolution.

Early studies of remnant evolution (e.g., Gull 1973) made the simple assumption that the density is constant out to particular velocity, v_m, beyond which the density vanishes. The velocity v_m is related to the energy and mass in the explosion by $E = 0.3 M v_m^2$. This form for the density profile is still used in some studies, although supernova computations are now available that give more accurate density distributions. This is particularly true for SN 1987A, for which Arnett (1988) and Shigeyama and Nomoto (1990) give the function $f(v)$ for spherically symmetric models. In the outer parts of the supernova, f has a power law form v^{-n}, where n is in the range 9 to 10. Some understanding of this property can be obtained from the self-similar solution for a shock front accelerating down a density gradient that is a power law from the edge of the star (Sakurai 1960). When this solution is expanded into a vacuum, a steep power law in radius is obtained of about the correct slope (Chevalier and Soker 1989; Imshennik and Nadëzhin 1989). The density profile flattens in the interior to approximately v^{-1}, although there is considerable structure in the density profile, especially in that of Shigeyama and Nomoto. This structure is probably due to the pressure waves that travel through the interior during the early phases and to the later energy input from radioactivity.

While SN 1987A was a Type II supernova (SNII), its density profile may not be representative of the more typical SNII, which have red supergiant progenitors. Diffusion of radiation can lead to the formation of a dense shell in the outer parts of the supernova (Grasberg et al. 1971; Chevalier 1976) and this effect is more important for a more extended initial star. Grasberg and Nadëzhin (1987) have considered an extreme case of dense presupernova mass loss in which much of the stellar mass goes into an outer shell. In addition to the diffusion effects, the envelope of a red supergiant is likely to have a flatter density profile than that of the SN 1987A progenitor, which can lead to the ejection of a shell-like structure.

While the standard models for SNII explosions are spherically symmetric, the evidence for mixing in SN 1987A has stimulated great interest in the development of nonspherical structure. The two-dimensional calculations of Fryxell et al. (1990) demonstrate the plausibility of mixing as a result of hydrodynamic instabilities at composition interfaces where there is a sharp change in the density. The mixing occurs in a inhomogeneous fashion and can give rise to clumping of the ejected gas.

We do not yet have a complete theory for SNIa, but the carbon deflagration of a white dwarf is currently a leading contender. The models of Nomoto et al. (1984) are particularly detailed with regard to the composition and density structure and their model W7 has been used to model the observed spectra of SNIa (Branch et al. 1985). The result of this work is that mixing of intermediate element layers with velocities above 8000 km · s^{-1} significantly improves the spectral fit. The density structure of the gas in the free expansion phase is complex because of the partial incineration of the gas. The process that mixes the gas may also smooth some of the dense features in the density profile.

The observational evidence on SNIb points to massive stars that have lost their hydrogen envelopes as progenitors. Shigeyama et al. (1990) have recently argued for low mass helium core progenitors that have presumably lost their envelopes in a close binary system. The density structure is subject to hydrodynamic instabilities during the explosion so that mixing is expected to take place, as in SN 1987A. The mixing makes it possible to fit the observed light curves and is also indicated by the late time line profiles (Fransson and Chevalier 1989).

The overall result on the density structure of supernovae is that they have a steep outer gradient of an approximately power law form with radius, inside of which is a relatively flat density gradient. Hydrodynamic instabilities that can give rise to mixing and clumping are expected over a wide range of cases. These effects are probably most important for the denser layers; while the shock acceleration that gives rise to the steep outer layers is subject to hydrodynamic instability (Chevalier 1990a), the growth rate is slow so that large initial perturbations are required for significant effects.

3. The interstellar medium

The interstellar medium contains components that are studied by a variety of techniques and are understood to varying degrees. For the present purposes, the important properties are the filling factor of each component and the pressure attributed to each. The pressure here is given in terms of p/k, where k is Boltzmann's constant; for a thermal gas, this quantity is simply the total density times the temperature. In considering the various components, I will start with high densities and go to more diffuse media. A general reference on the properties of the interstellar medium is Spitzer (1978), which is the source of many of the numerical estimates given here. A more recent survey, with an emphasis on HI observations, is Kulkarni and Heiles (1988).

Dense molecular clouds are observed primarily through molecular line emission, especially lines of CO. The molecular hydrogen density is typically $\geq 10^3$ cm^{-3} and the density in cloud cores can reach 10^6 cm^{-3}. The temperature is about 10 K, so that the pressure is $p/k \geq 10^4$ cm^{-3} K. Dense clouds need not be in pressure equilibrium with their surroundings because they are normally self-gravitating. Masses of individual clouds are in the range $10^3 - 10^4 M_\odot$ and the total molecular mass is about $3 \times 10^9 M_\odot$. The volume filling factor of the molecular clouds is thus about 10^{-3}, so the probability of a supernova remnant interacting with such a cloud over much of its surface area is small. The fact that massive stars are probably born in such clouds increases the probability, although the supernova progenitor stars may be able to move away from their birthplace before they explode.

Diffuse clouds are observed by HI 21 cm line emission, by optical and ultraviolet line absorption, and by dust extinction. A typical density is 20 cm^{-3}, temperature 100 K, and size 5 pc, although there is a considerable range in these parameters. The corresponding pressure is $p/k \approx 2000$ cm^{-3} K. Although many theoretical models assume that clouds are spherical, HI maps have indicated filamentary structure for some time (Kulkarni and Heiles 1988). This structure has been confirmed by the IRAS satellite observations of the infrared "cirrus."

The warm neutral medium is a more pervasive medium that can be observed in 21 cm line emission. It has a typical density of 0.2 cm^{-3} and temperature of 8000 K, giving a pressure of 1600 cm^{-3} K. The column density of warm neutral medium through the Galactic disk is comparable to that of the diffuse clouds. The volume-filling factor is at least 0.2 and it is possible that the warm neutral medium fills most of the volume. The vertical structure of neutral hydrogen is described by (Lockman et al. 1986)

$$n(z) = 0.32\, e^{-(z/190 \text{ pc})^2} + 0.11\, e^{-(z/500 \text{ pc})} \text{cm}^{-3}$$

where z is the distance from the galactic plane. The first component includes both the diffuse clouds and the warm neutral medium, while the second, extended component was found in the inner Galaxy by Lockman (1984). The height of the hydrogen layer is relatively constant in the inner Galaxy, but increases in the outer Galaxy, beyond 10 kpc from the Galactic center.

The warm ionized medium has been studied by low frequency radio absorption, pulsar dispersion measures, and diffuse Hα emission. While early pulsar dispersion studies showed the scale height for this component to be large, the discovery of a number of pulsars in globular clusters and in the LMC has shown that the scale height is 1 to 1.5 kpc (Reynolds 1989). The volume averaged electron density in the Galactic disk is 0.03 cm^{-3} and the actual density is 0.2 cm^{-3}, so that the volume-filling factor is 0.1–0.2. It is plausible that the filling factor of this component rises with height in the Galaxy because of its large-scale height. The pressure of the warm ionized medium is about 3200 cm^{-3} K.

The hot ionized medium can be observed by ultraviolet absorption lines and soft X-ray emission. Collisional ionization of the OVI that is observed suggests that it is formed in a region with a temperature of about 3×10^5 K. Line widths imply a temperature $\geq 2 \times 10^5$ K and the volume-filling factor of this gas is ≤ 0.2 (Jenkins 1978). A soft X-ray background is observed around the Sun, presumably from a hot gas with a temperature of order 10^6 K. However, it appears that this emission is primarily from a region within 100 pc of the Sun and does not give us information on the large-scale interstellar medium. The filling factor of the hot gas is poorly determined at present.

This summarizes the components of the interstellar medium that occupy separate volumes of the medium. In addition, there are two nonthermal components that interpenetrate the thermal gas. The galactic magnetic field is best studied through pulsar rotation measures. Rand and Kulkarni (1989) find an average magnetic field strength of 5×10^{-6} Gauss, corresponding to a magnetic pressure of 7200 cm^{-3} K. Cosmic rays are relativistic particles that also interpenetrate the thermal gas. They can be directly detected at Earth and by their gamma ray and synchrotron radio emission in the interstellar medium. The energy density of cosmic rays is dominated by mildly relativistic protons and their effective pressure is about 3600 cm^{-3} K.

The sum of the thermal, magnetic, and cosmic ray pressure is 14 000 cm^{-3} K and is dominated by the nonthermal component. This central disk pressure can be compared with the pressure needed to support the vertical disk structure against the galactic gravitational field, assuming hydrostatic equilibrium. An estimate by Cox (1988) yields a required pressure of 16 000 cm^{-3} K, which is close to the observed pressure. An additional nonthermal pressure that is likely to contribute to the vertical extent of the gas is the velocity dispersion of clouds. In fact, Lockman (1991) finds that the broad HI component in the solar neighborhood can be supported by its velocity dispersion.

A final component of the interstellar medium is dust grains, which have radii $\leq 10^{-4}$ cm. The grain component is observed by absorption and scattering of starlight and by the depletion of heavy elements from the gas. The ratio of dust to gas is 0.006 by mass along a typical line of sight, with a factor 5 scatter. The depletion is measured by comparing abundances in cold clouds with those in the solar system. It is found that 3/4 of the C, N, and O, and all but $\leq 1\%$ of refractory elements like Al, Ca, and Fe are condensed onto grains.

4. Circumstellar environments

Our understanding of the progenitors of SNIa is not sufficiently well developed to be able to predict their circumstellar environment. Iben and Tutukov

(1984) have considered a number of paths that potentially lead to a SN Ia explosion through the evolution of binary stellar systems. Many of the paths involve mass loss from the binary at some point in the evolution, but the evolution timescale is sufficiently long and the progenitor velocities are likely to be sufficiently high that the exploding star may expand into the ambient interstellar medium. An exception is if the progenitor is a white dwarf accreting mass from the wind of a companion star.

The SNII and SNIb have massive star progenitors which are known to lose mass during their evolution and to emit ionizing radiation. For the main sequence evolution, the mass 15 $M_\odot$ is a critical stellar mass above which the circumstellar effects are large and below which they decrease rapidly because the rate of emission of ionizing photons drops dramatically for stars later than type B0 (e.g. Panagia 1973). For the massive stars, values of $r_s n_H^{2/3}$, where r_s is the radius of the Stromgren sphere and n_H is the density, are in the 10's of pc $\cdot$ cm^{-2}, while for the later-type stars the values drop to a few pc $\cdot$ cm^{-2}. For O-type main sequence stars strong winds are clearly present, while for the B stars, effects of a wind are usually unobservable (Abbott 1982). An exception is the Be stars, which are observed to have winds with velocities 600 to 1100 km $\cdot$ s^{-1} and mass loss rates of 10^{-11} to $3 \times 10^{-9} M_\odot \mathrm{yr}^{-1}$ (Snow 1981). The wind luminosity is much lower than that of the O-type stars. The radii of the bubbles created by the winds in a uniform medium can be many 10's of pc (Weaver et al. 1977). McKee et al. (1984) have examined the propagation of a wind bubble in a cloudy medium. They find that during the main sequence lifetime of an O4 to B0 star, a region of radius $R_h = 53 n_m^{-0.3}$ pc, where n_m is the average density, is made homogeneous by the photoionizing radiation. A wind bubble expands adiabatically out to this radius, but suffers radiative losses at larger radii so that R_h may characterize the final bubble radius.

The mass range for SNII ($\geq 8\ M_\odot$) covers both O4–B0 stars with large bubbles and the early B stars which are likely to have smaller regions affected by winds. The nature of the interstellar medium is likely to be important for the early B stars. If SNIb have very massive progenitors that evolve to a Wolf–Rayet phase, they are expected to be in large bubbles created by the main sequence wind and photoionizing radiation. If they result from the binary evolution of lower-mass stars, an extended cavity may not be present.

During the next evolutionary phase for a massive star, the red giant or supergiant phase, the star has a slow wind with velocity 5–50 km $\cdot$ s^{-1} and a mass loss rate of $10^{-7} - 10^{-4} M_\odot \mathrm{yr}^{-1}$ (Zuckerman 1980). The total duration of the red giant phase is about 10% of the main sequence lifetime. The rate of mass loss may evolve during this phase; the highest rates of mass loss have been observed in OH/IR stars at the tip of the red giant branch with absolute magnitudes M < −6. The duration of the OH/IR phase may be about 5×10^5 yr and the wind velocity is about 15 km · s^{-1} (e.g. Herman 1985). However, most OH/IR stars may have initial masses in the range 2−5 $M_\odot$, which is below the range of interest for supernovae.

Most Type II supernovae are expected to explode at this point, but extreme mass loss can complicate the evolution. Loops can occur in the HR diagram (Chiosi and Maeder 1986); while the star is relatively blue, a faster, lower density wind is expected. Loss of the hydrogen envelope leads to a blue Wolf–Rayet star; these stars have typical mass loss rates of $10^{-5} - 10^{-4} M_\odot \mathrm{yr}^{-1}$ and wind velocities of 1000–2000 km · s^{-1} (Chiosi and Maeder 1986). While these stars are expected to become supernovae, it is unclear whether they should be identified with SNIb. Massive stars with their hydrogen envelopes but low metallicity may also explode as blue stars (e.g. SN 1987A).

The interaction of the fast wind from the blue star with the red supergiant wind creates a shocked, cool shell of the dense wind and a hot shell of shocked fast wind (McCray 1983; Chevalier and Imamura 1983). Ring nebulae have been observed around Wolf–Rayet stars. These typically have radii of 3–10 pc, velocities of 30–100 km · s^{-1}, and densities of 300–1000 cm^{-3} (Chu et al. 1983). Some of the nebulae show evidence for abundance enhancements of N and He (Kwitter 1984). Many of the wind blown nebulae are asymmetrically distributed about the Wolf–Rayet star (Chu et al. 1983). A model in which this is due to stellar motion is attractive, but is not tenable if the fast wind only interacts with the red supergiant wind because both winds have the same space motion. Interaction with the interstellar medium is needed (e.g. Bandiera, 1987). Asymmetries in the winds may also be a factor.

5. Hydrodynamic evolution

The result of the supernova explosion is a radial flow in free expansion. The pressure in the expanding gas is negligible because of adiabatic expansion. The pressure and velocity of the ambient medium can generally be neglected because of the high initial supernova velocities and only the density distribution is relevant. Because of these simplifications, self-similar solutions can be very useful in delineating the major features of the interaction. These solutions are calculated for one-dimensional flows. Although two-dimensional flows are expected to be self-similar when the ambient or supernova den-

1982). In the limits of either saturated heat conduction or an isothermal shocked layer, no new dimensional parameters are introduced so that self-similar flow might be expected. However, such solutions do not appear to exist (Band 1988). Bedogni and d'Ercole (1988) have carried out numerical computations of the above case with heat conduction included and two-fluid flow. They find that the flow becomes complex with reverse shocks forming close to the contact discontinuity and thermal conduction driving a broad inner-shocked region.

The reverse shock solutions do assume that the expanding supernova gas is smoothly distributed. Some remnants, like Cas A, indicate that the ejecta may be clumpy. Hamilton (1985) has investigated the interaction of clumpy ejecta with an ambient gas for cases similar to the reverse shock solutions discussed above. In order to preserve self-similar flow, certain assumptions, such as undecelerated clump motion, were necessary. Ablation of the clumps was allowed. If the clumps interacted strongly with the ambient medium, the solution for smooth flow was recovered. For weaker interaction, the clumps moved out ahead of the shock front in the ambient medium. This type of behavior is qualitatively expected.

The above reverse shock solutions assume a relatively steep power law density profile. Hamilton and Sarazin (1984a) have found self-similar solutions for the initial phases of a reverse shock in a medium with a flat density profile ($n < 1$). The solutions apply to the time when the distance between the reverse shock wave and the edge of the "freely expanding" ejecta is much less than the radius so that the flow is approximately planar. For uniform ejecta, the reverse shock propagates as $z \propto t^{(5-s)/2}$, where z is the distance to the edge of the ejecta if it continued in free expansion. As opposed to the steep power law case, the shocked supernova ejecta have a density peak at the contact discontinuity for both $s = 0$ and $s = 2$. The solutions for the shocked ambient medium resemble those for the steep power law case, although the flow is not exactly self-similar.

For the transition from the early reverse shock flow and for more general density distributions than power-laws in radius, numerical hydrodynamic calculations are needed. Because of the steep density profiles present in the early flows, many computational zones are needed in the one-dimensional calculations to reproduce the self-similar solutions (Jones and Smith 1983; Hamilton and Sarazin 1984a). A number of computations have been carried out on the interaction with circumstellar matter (Fabian et al. 1983; Itoh and Fabian 1984; Dickel and Jones 1985; Band and Liang 1988). The general expectations for the expansion of a massive star are that it will first interact with the dense wind ejected in the red supergiant phase, it will then approach free expansion in the bubble created by the fast wind lost in the main sequence phase, and will finally interact with the swept-up wind bubble shell. The interaction with the interstellar medium takes place in a late evolutionary phase. In supernovae with Wolf–Rayet star progenitors and in SN 1987A, the dense wind does not occur close to the stellar surface, but may be present further out from an earlier evolutionary phase. In this case, there is likely to be interaction with a shell of swept-up red supergiant wind. SNIa may interact more directly with the interstellar medium.

The interaction of a supernova with a circumstellar bubble has been the subject of analytical (Chevalier and Liang 1989) and numerical (Dickel and Jones 1985; Ciotti and D'Ercole 1989; Tenorio-Tagle et al. 1990) studies. If the supernova has an outer steep power law density profile and if the bubble interior can be described by an approximately constant density shocked wind, the propagation of the shock front inside the bubble is described by the self-similar solution mentioned above. Once the interaction region reaches the shell, a reflected shock moves back through the interaction region and a transmitted shock moves into the shell. The initial propagation of the transmitted shock can be described using the pressure evolution at the shell interface. In the case where the transmitted shock does not move the shell, the evolution tends toward another self-similar solution in which the steep supernova density structure interacts directly with the shell. In this case, a stand-off shock is present at a constant radius inside the shell. Eventually, the supernova energy is largely thermalized if the shell is massive, or the remnant evolves in the region surrounding the shell.

Multidimensional calculations are needed for studying the supernova remnant interaction with clouds (see McKee 1988 for a recent review). Although it was not intended to represent supernova expansion, Woodward's (1976) calculation of flow past a cloud has a particularly accurate treatment of the cloud boundary. His calculation ,which included radiative cooling, demonstrated the growth of Rayleigh–Taylor and Kevin–Helmholtz instabilities along the cloud boundary. The calculation stopped before the shock wave in the cloud had completely traversed the cloud. Bedogni and Woodward (1990) have recently computed the evolution of cloud interaction for both the adiabatic and isothermal cases. They followed the complete shock compression of the cloud and its subsequent small re-expansion. Instabilities at the sides of the cloud are particularly important for the adiabatic case and there is some shredding of the cloud. The isothermal case, on the other hand, shows dominant instability growth at the front interface with the flow. After the initial phases, the ram pressure of the flow continues to accelerate the cloud. McKee et al. (1978) calculated cloud motion in this phase on the assumption of a constant cloud cross section and found that accelerated clouds could move outside of the blast wave. Instabilities are likely to modify the cross section and may break up the cloud (Nittman et al. 1982). The final evolution of clouds is still not known.

The overall evolution of supernova remnants in their late radiative phases in a uniform medium has been described by numerical computations. Cioffi et al. (1988) have recently obtained an analytic description of the remnant evolution in these late phases. The numerical calculations show a complex evolution, including the development of secondary shocks. Slavin and Cox (1990) have followed remnant evolution to very late times and showed that heat conduction and the interstellar magnetic field can have a significant effect on the evolution. Heat conduction lowers the temperature and raises the density of the hot interior bubble so that radiative cooling becomes important and leads to the collapse of the bubble. A 5×10^{-6} Gauss magnetic field gives pressure support for a very broad cool shell. For typical parameters, the hot bubble reaches a maximum radius of about 50 pc and then collapses. This behavior is important for the generation of the hot ionized component of the interstellar medium.

6. Circumstellar interaction

There is excellent evidence for interaction with a dense circumstellar wind for the Type II supernovae SN 1979C and SN 1980K (see reviews by Fransson 1986 and Chevalier 1990b). The evidence includes radio emission from the interaction region for both supernovae, infrared dust echoes for both supernovae, thermal X-ray emission from the interaction region in SN 1980K, and the ultraviolet line emission from highly ionized atoms in SN 1979C. The radio emission is a particularly good diagnostic because the early absorption of the radio emission can be interpreted as free-free absorption by the preshock gas and an estimate of the circumstellar density is obtained. Lundqvist and Fransson (1988) have made a detailed study of the temperature and ionization of the circumstellar gas in the radiation field of the supernova and have been able to reproduce detailed features of the radio light curves. They derive mass loss rates of $12 \times 10^{-5} M_\odot yr^{-1}$ and $3 \times 10^{-5} M_\odot \cdot yr^{-1}$ for a wind velocity $v_w = 10\ km \cdot s^{-1}$ for SN 1979C and SN 1980K respectively.

There are presently 5 radio supernovae with fairly extensive data, including the rising part of the radio light curve. They are SN 1979C, SN 1980K (Weiler et al. 1986), SN 1983N (Sramek et al. 1984), SN 1986J (Rupen et al. 1987; Weiler et al. 1990), and SN 1987A (Turtle et al. 1987). Table 1

Table 1
Radio supernovae

SN	Type	Ratio to Cas A at 6 cm	t_{20} (days)	$\dot{M}/v_w$ $(M_\odot/\mathrm{yr})/(\mathrm{km/s})$
1979C	II	~ 250	950	1×10^{-5}
1980K	II	~ 15	190	3×10^{-6}
1983N	Ib	~ 125	30	5×10^{-7}
1986J	II	~ 700	1600	2×10^{-5}
1987A	II	~ 0.02	2	1×10^{-8}

lists the supernova type, the radio luminosity ratio to Cas A, the time of optical depth unity at 20 cm, t_{20}, and the circumstellar density given in terms of the presupernova mass loss rate divided by the wind velocity. SN 1986J was probably not observed near maximum light and the Type II designation given here is based solely on the presence of hydrogen line emission. Of the 5 supernovae, only SN 1979C and SN 1980K show clear evidence for circumstellar interaction outside of radio wavelengths. For SN 1983N and SN 1987A this is attributable to the low circumstellar density and for SN 1986J to the late discovery.

The results show that the winds around SN 1979C 1980K, and 1986J are consistent with the dense slow winds expected around red supergiant stars. The density around the Type Ib event SN 1983N is considerably lower, but is higher than the value expected for a typical Wolf–Rayet star. A wind velocity of 1000 km $\cdot$ s^{-1} and $\dot{M} = 10^{-4} M_\odot \mathrm{yr}^{-1}$ leads to a value of $\dot{M}/v_w$ that is a factor of 5 below the estimated value. SN 1987A had an even earlier turn-on and was a faint radio supernova, but the estimated value of $\dot{M}/v_w$ is roughly consistent with the density expected around a B3 I star like the Sk-69 202 progenitor star (Chevalier and Fransson 1987). The observational estimate is a factor of a few larger than the expected value. If there is clumping in the circumstellar wind, the observational estimates are reduced.

In the circumstellar interaction model for the radio emission, the radio luminosity at a given age should be correlated with the density of circumstellar material; this is observed. It appears that the circumstellar interaction does give information on the properties of the supernova progenitor.

An exciting development is the possibility of resolving radio supernovae with very long baseline interferometry (VLBI) techniques. The expansion of SN 1979C has been measured and Bartel (1988) has estimated that if the expansion follows $R \propto t^m$, then $m = 1.03 \pm 0.15$. The radius and the expansion law are consistent with circumstellar interaction. SN 1986J, which is currently the brightest radio supernova, has also been resolved by VLBI observations (Bartel et al. 1989). Measurements of the expansion of the radio source should allow the age of the supernova to be estimated.

During the next phase of evolution the supernova may approach free expansion in a low density wind bubble. When SN 1979C enters this phase, an accelerated rate of decline of the radio emission is expected. One way to identify supernova remnants in this evolutionary stage would be to search for pulsar nebulae which show little or no evidence for interaction with a surrounding medium. This may be the explanation for "Crabs without shells" which are about equal in number to the Crabs with shells (Helfand and Becker 1987). Of course the Crab Nebula itself is lacking a shell.

Of the young supernova remnants, Cassiopeia A is the most likely to be related to Wolf–Rayet stars and possibly to SNIb. It has fast-moving oxygen-rich gas and is interacting with dense nitrogen-rich circumstellar gas; Fesen et al. (1987) have suggested that the progenitor was a Wolf–Rayet WN star. The problems with the Type Ib identification are that Cas A has recently been found to have fast-moving hydrogen-rich gas (Fesen et al. 1987) and the supernova was probably too faint to be a typical Type Ib event, even if it was observed by Flamsteed in 1680 (Ashworth 1980). Although the presence of hydrogen would appear to rule out a Type I supernova, it is perhaps possible that the hydrogen would not have been detectable spectroscopically near maximum light. If the progenitor was a Wolf–Rayet star, it is likely that the slow-moving nitrogen-rich gas is in a shell.

A remnant with oxygen-rich ejecta, which is likely to be interacting with circumstellar gas, is N 132D in the Large Magellanic Cloud. Optical studies of this remnant show a faint outer shell of radius 40 pc, an inner disk of radius 16 pc, and a ring of expanding oxygen-rich ejecta at a radius of 3 pc (Lasker, 1978 1980). X-ray emission from the remnant has approximately a 16 pc radius (Mathewson et al. 1983). The inner oxygen knots give an age of only 1300 years, which implies that the X-ray emitting gas has been expanding in a low density medium if it is a normal supernova (Hughes 1987). Hughes (1987) suggests that the cavity was created by an HII region. A fast stellar wind may also play a role. The present X-ray remnant is then the result of interaction with the swept-up red supergiant wind. The faint outer shell may be a remnant of the stellar wind and photoionizing radiation while the progenitor star was on the main sequence.

An interesting recent suggestion is that Kepler's supernova remnant is the result of a Type Ib supernova. An analysis of the X-ray emission indicates that the initial stellar mass was $> 7M_{\odot}$ (Hughes and Helfand 1985), although this is rather uncertain. Bandiera (1987) has argued that the progenitor star was a runaway Wolf–Rayet star from the galactic plane. Proper motion studies of the dense optical knots do imply a high space velocity (van den Bergh and Kamper 1977) and the asymmetry of the supernova remnant may be due to the interaction of presupernova mass loss with an ambient medium (Bandiera 1987).

There is evidence that some larger supernova remnants are interacting with circumstellar gas. The Cygnus Loop, with a radius of 20 pc, is interacting with gas density ≥ 5 cm^{-3} over much of its surface area, yet the appearance of the remnant shows circular symmetry. The X-ray properties imply that the remnant has been expanding in a low density medium until recently (Charles et al. 1985). The implication is that the remnant is interacting with a spherical shell of radius 20 pc. Since this radius is smaller than the bubbles expected around O stars, Charles et al. (1985) suggest that the progenitor star was an early B star.

Although circumstellar interaction around SN 1987A did not give large effects during its initial evolution, there is evidence for dense gas close to the supernova (Fransson et al. 1989) and brightening of the supernova at radio and X-ray wavelengths is expected. Chevalier and Liang (1989) estimated that shell interaction could lead to a 1 GHz radio flux of 10 Jy at an age of about 18 years. A rising radio flux has been observed already in July 1990 (Turtle et al. 1990); this could be due to interaction with a small amount of dense gas that is closer to the supernova than is the well-observed line emitting region. It has recently been possible to spatially resolve the line emitting gas with the ESO New Technology Telescope (Wampler et al. 1990) and with the Hubble Space Telescope, and the observations suggest that the emitting gas is in a ring around the supernova. The interaction of the supernova with the ring may eventually give rise to the appearance of ejecta in a ring, as is observed in N132D.

7. X-ray and infrared emission from hot gas

The physical properties of young supernova remnants are probably best studied by X-ray spectroscopy and there have been a number of recent theoretical studies in this area. The first case to be examined in detail was the X-ray emission from a self-similar Sedov blast wave (Gronenschild and Mewe 1982; Hamilton et al. 1983). The properties of the emission are determined by two parameters, e.g. n_o^2E and t where n_o is the ambient density, E is the total energy, and t is the age. The most important property of the flow is that the gas is underionized compared to equilibrium values because ionization timescales can be longer than the hydrodynamic timescales. Since underionization can favor line emission, the X-ray luminosity from a nonequilibrium flow may be a factor of 10 higher than that from an equivalent flow assumed to be in ionization equilibrium.

It is not known to what extent electrons are heated in collisionless shock fronts so that the amount of heating is often a parameter in theoretical studies (e.g. Hamilton et al. 1983). Even if collisionless heating does take place in the shock, electrons may be released by ionization in the postshock flow which have not been subject to this heating. Itoh (1984) noted that some fast shocks appear to be moving into a partially neutral medium and that the electrons released from the neutrals in the postshock flow are only subject to Coulomb heating. Hamilton and Sarazin (1984c) noted a similar process for the postshock ionization and heating of a heavy element gas. In either case, it is necessary to take into account two populations of electrons.

Hamilton and Sarazin (1984b) found that the X-ray emission from a variety of self-similar flows can be estimated without carrying out detailed calculations for each case. Two important parameters are an ionization time τ, which is weighted by a Boltzmann factor and an emissivity parameter ϵ, which is a function of radius. Two supernova remnants that have similar values of τ versus ϵ through the remnant belong to the same structural type. The two basic types are the Sedov type, which approaches a hot, low density medium in the postshock flow, and a type which approaches a cold, high density medium in the postshock flow. The interaction of a steep power law density profile with an $s = 0$ medium is of the first type. The interaction of a steep profile with an $s = 2$ medium and the reverse shock wave for uniform ejecta are of the second type. Two remnants of the same type that have similar values of average τ, average temperature, and total emissivity are expected to produce similar X-ray spectra. The fact that detailed spectra have been calculated for Sedov blast waves makes this method quite useful.

A more general way to calculate X-ray spectra is to solve the time dependent ionization equations along with a numerical hydrodynamic computation (Itoh and Fabian 1984; Nugent et al. 1984, Hughes and Helfand 1985). Hughes and Helfand (1985) have developed a useful matrix method that speeds up the calculation of the ionization equations.

As discussed in the previous section, the explosions of massive stars are likely to interact with circumstellar matter during their early phases. Direct interaction with the interstellar medium is most likely for Type Ia supernovae and Tycho's supernova (SN 1572) and SN 1006 may belong to this class. Detailed modeling of the X-ray spectra of these remnants has been carried out by Hamilton et al. (1986a,b). They find that in both cases, the spectra are best fit by models of the second type discussed above, i.e., models with cool dense ejecta. A range of temperatures is needed to give an approximate power law continuum and to produce emission that approximates ionization equilibrium. The fact that observations with the *Tenma* satellite (Hughes 1990 and references therein) found lower high energy fluxes than was assumed by Hamilton et al. (1986a,b) based on *HEAO–1* data casts doubt on the details of their models. Hamilton et al. (1986a,b) concentrate on models in which constant density ejecta with a sharp edge expand into the interstellar medium. For both supernova remnants, the models can accommodate $\geq 0.5 M_{\odot}$ of Fe as expected in a Type Ia supernova because the Fe is either unshocked or is at low density. The presence of cold Fe in SN 1006 appears to be confirmed by the presence of broad ultraviolet Fe absorption in the direction of the Schweizer–Middleditch star (Wu et al. 1983; Fesen et al. 1988).

The X-ray spectra of Tycho and of SN 1006 are very different in that Tycho shows strong line emission while SN 1006 does not. Hamilton et al. (1986a,b) attribute this to a low density surrounding SN 1006 so that its "ionization age" is less than that of Tycho and the ionization has not yet proceeded to the stage which gives X-ray line emission. Kirshner et al. (1987) have recently confirmed this hypothesis by measuring the Balmer line emission from two remnants and using it to estimate shock velocities. SN 1006 has a higher shock velocity even though it is an older remnant, which implies it is expanding into a low density medium.

The models of Hamilton et al. (1986a,b) appear to be promising but they do not allow for the presence of a steep outer power law component to the density profile that is expected from supernova modeling. A related problem may be that the expansion rate of the supernova remnants in the models are larger than is indicated by optical and radio observations. A power law region with n somewhat greater than 5 would lead to greater deceleration of the outer shock front. Possible resolutions of these problems are that there is an outer power law region but with a relatively small amount of mass or that clumping of the ejecta plays an important role. Seward et al. (1983) in fact found that the X-ray emission from Tycho's remnant is clumped.

The best approach to modeling X-ray spectra is to take a realistic model for the supernova explosion, compute its interaction with a surrounding medium, and calculate the resulting X-ray spectrum. Itoh et al. (1988) have done this for Tycho's remnant, using the W7 model for a SNIa explosion. They were able to adequately fit the *Tenma* spectrum by assuming inner mixing over the velocity range 0 to 13 300 km $\cdot$ s^{-1} and by taking an ambient density of 1

cm^{-3}. While the *Tenma* data cover a wide energy range, The spectrum has relatively low resolution so that further checks of this model are desirable. One difference with the model of Hamilton et al. (1986a,b) is that the emission is primarily from the reverse shock wave over the entire velocity range, while in the Hamilton et al. (1986a,b) model, the blast wave plays an important role at higher energies. This difference is at least in part due to the difference in the observational data.

The future of X-ray spectroscopy of supernova remnants is promising because high spectral resolution experiments are planned for the late 1990s. Such experiments hold promise for determining ionization, temperature, composition, and velocities (from line profiles) for the X-ray emitting gas. High resolution studies of the remnant Puppis A with the *Einstein Observatory* were able to establish that the gas was in ionization equilibrium and thus had a density ≥ 3 cm^{-3} (Winkler et al. 1981).

While X-ray emission provides many diagnostics for hot gas, the gas emissivity is actually higher for infrared emission from dust grains. While this type of emission had been predicted long ago (Ostriker and Silk, 1973), it took the IRAS satellite in the 1980s to make observations of the infrared emission (Dwek 1988 and references therein). The grain emissivity climbs as $T^{3/2}$ up to $T \approx 10^7$ K, at which temperature the efficiency of grain heating by fast electrons is reduced and the emissivity flattens. This property of the emissivity curve makes it possible to obtain density estimates for the hotter remnants. The IRAS observations confirmed the expectation of high infrared emissivity, with the infrared luminosity of young remnants being up to 100 times the X-ray luminosity (Dwek 1988).

8. Shock wave emission and stability

The general agreement between radiative shock wave models and the optical emission from most supernova remnants strongly argues that we are observing emission from shock waves (Shull 1988 and references therein). The shock wave emission can then be used to determine basic physical properties such as the shock velocity, the preshock density, and the elemental abundances. For example, Blair, Kirshner et al. (1981) used optical observations of the supernova remnants in M31 to determine the abundance gradient in the galaxy. The basic observational properties of radiative shock emission at optical wavelengths are: underionized species strong relative to Hβ (e.g. [OI] $\lambda6300$, [NI] $\lambda5200$, [OII] $\lambda3726-29$); high excitation temperature

($\geq$ 20 000 K) from the [OIII] line ratio $\lambda 4363/(\lambda 5007 + \lambda 4959)$; and a range of ionization stages (e.g. [OI], [OII], [OIII], [NeIII], [NeV]).

Prior to the radiative phase, optical emission is observable from a fast shock front if it is moving into a partially neutral medium (Chevalier et al. 1980). Neutral H atoms penetrate the collisionless shock front and can undergo collisional excitation directly, or charge exchange with a fast proton. The result is a H line profile with both narrow and broad components. The width of the broad component and the ratio of broad to narrow line intensity both give an estimate of the shock velocity which, when combined with proper motion observations of the supernova remnant, yield a distance estimate. Hydrogen Balmer lines dominate the optical spectrum, as observed, because of the large hydrogen abundance; the hydrogen lines are easily excited in the hot, postshock medium. While initially identified in Tycho's remnant, Balmer-dominated filaments have been identified in a growing number of remnants, most recently Kepler's remnant (Fesen et al. 1989) and RCW86 (Long and Blair 1990).

Raymond et al. (1988) have extensively examined an optical filament in the Cygnus Loop and deduced that the shock velocity varies from 80 km $\cdot$ s^{-1} at one end of the filament to 140 km $\cdot$ s^{-1} at the other end. Steady shock-wave models give a good fit to the lower shock velocity emission, but at high velocity, the recombination zone appears to be incomplete. The implication is that the shock front is just now entering the radiative phase because of interaction with higher density gas. Even at the lower shock velocities, the shock emission is not well modeled by the assumption of steady-state ionization of the preshock medium, because the timescale for the preshock gas to recombine is longer than the timescale for the shock front to decelerate. The preshock medium is fully ionized in the velocity range 80–100 km $\cdot$ s^{-1} because of shock ionization in an earlier phase. Raymond et al. also found that the postshock thermal pressure was substantially less than the total shock ram pressure $\rho_o v_{sh}^2$, which suggests that some form of nonthermal pressure comes to dominate in the postshock flow.

The striking morphology of optical supernova remnants has been interpreted in a number of ways including sheets, rope-like filaments, and cloudlets. Detailed studies of the surface brightness variations around a filament together with high-resolution spectra of individual lines have shown that the emission is from a wavy sheet that is observed edge-on in places (Hester et al. 1983; Hester 1987). The presence of a wavy sheet suggests the operation of an instability. In fact, the shell built up by a radiative shock wave with an internal pressure is overstable (Chevalier and Theys 1975; Vishniac 1983). The properties of the instability may be modified if magnetic pressure dominates in the cool layer. An argument against the instability is that the Hα, nonradiative shock emission from the Cygnus Loop also appears to be from a wavy sheet.

Another instability can operate in the cooling region of a shock front. Chevalier and Imamura (1982) showed that a radiative shock front with a cooling function of the form $\Lambda \propto T^{\alpha}$ is overstable to planar perturbations if $\alpha \leq 0.5$. For a realistic model of an interstellar shock wave, it is necessary to put together time-dependent hydrodynamic and non-ionization equilibrium codes. Innes et al. (1987a,b) and Gaetz et al. (1988) have done this and found that instability occurs for $v_{sh} \geq 140$. While this is larger than the values of v_{sh} generally inferred from observations of radiative shock waves, the instability can cause the shock velocity to vary over a range of velocities that overlaps with the observed range. There are some shock emission regions where the steady-state shock models do not provide a good fit to the relative line intensities and some type of time-dependent behavior is likely (Raymond et al. 1980, 1988; Fesen et al. 1982). As discussed above, in some instances this can be attributed to a recent onset of cooling, but the cooling instability could also play a role. Regions where a cooling shock wave is just forming are the most likely to show the instability; the numerical calculations of Falle (1981) did show oscillations at just this time.

While shock wave models have been successful in describing the characteristics of emission from gas with normal cosmic abundances, this is not true for emission from a heavy element gas, as is observed in the Cas A supernova remnant. Attempts to model heavy element emission have concentrated on the O lines because they are generally the most prominent (Dopita et al. 1984; Borkowski and Shull 1990). Problems are that the observed [OIII] line ratio $\lambda4363/(\lambda5007 + \lambda4959)$ implies a temperature of 20 000 K, which is too low compared to the models and that the [OI] $\lambda6300$ line is too weak in the models. Possible alternatives to shocks to give the emission are photoionization, conductive heating, and the action of suprathermal ions (Dopita et al. 1984), but none of these mechanisms has been shown to yield detailed agreement with the observations. Reliable abundances in heavy element ejecta would be very useful for comparison with supernova models.

9. Future prospects

The study of supernova remnants is now a well developed field. With regard to hydrodynamic evolution, many aspects of spherically symmetric expansion are now understood. However, much work remains to be done on multidimensional evolution, particularly on the development of hydrodynamic instabilities. The work of Fryxell et al. (1990) has shown the complex structure resulting from instabilities during the supernova explosion. Similar instabilities are likely to develop due to the deceleration of the supernova ejecta by the surrounding medium. Progress has also been made on the theory of shock emission; a remaining gap is an understanding of the optical emission from heavy element ejecta. On the side of observations, the most promising advance is the development of the next generation of X-ray telescopes, such as *AXAF*. The combination of high spatial and spectral resolution will revolutionize the study of the hot gas produced by the interaction of a supernova with its surroundings.

The author's research on hot gas in supernovae and their remnants is supported in part by NASA grant NAGW-764.

References

Abbott, D.C. 1982, Ap. J., 263, 723.
Arnett, W.D. 1988, Ap. J., 331, 377.
Ashworth, W.B. 1980, J. Hist. Astr., 11, 1.
Band, D.L. 1988, Ap. J., 332, 842.
Band, D.L. and E.P. Liang 1988, Ap. J., 334, 266.
Bandiera, R. 1987, Ap. J., 319, 885.
Bartel, N. 1988, in IAU Symp. 129, The Impact of VLBI on Astrophysics and Geophysics, M.J. Reid and J.M. Moran, eds. (Dordrecht: Reidel), p. 175.
Bartel, N., M. Rupen, and I.I. Shapiro 1989, Ap J. (Letters), 337, L85.
Bedogni, R., and A. d'Ercole 1988, Astr. Ap., 190, 320.
Bedogni, R. and P. Woodward 1990, Astr. Ap., 231, 481.
Blair, W.P., R.P. Kirshner, and R.A. Chevalier 1981, Ap. J., 254, 50.
Borkowski, K.J., and J.M. Shull 1990, Ap. J., 348, 169.
Branch, D., J.B. Doggett, K. Nomoto, and F.K. Thielemann 1985, Ap. J., 294, 619.
Charles, P.A., S.M. Kahn, and C.F. McKee 1985, Ap. J., 295, 456.
Chevalier, R.A. 1976, Ap. J., 207, 872.
Chevalier, R.A. 1982, Ap. J., 258, 790.
Chevalier, R.A. 1990a, Ap. J., 359, 463.
Chevalier, R.A. 1990b, in Supernovae, A.G. Petschek, ed. (New York: Springer), p. 91.
Chevalier, R.A., and C. Fransson 1987, Nature, 328, 44.
Chevalier, R.A., and J.N. Imamura 1982, Ap. J., 261, 543.
Chevalier, R.A., and J.N. Imamura 1983, Ap. J., 270, 554.
Chevalier, R.A., and E.P. Liang 1989, Ap. J., 344, 332.
Chevalier, R.A., and N. Soker 1989, Ap. J., 341, 867.
Chevalier, R.A., and J.C. Theys 1975, Ap. J., 195, 53.
Chevalier, R.A., R.P. Kirshner, and J. C. Raymond, 1980, Ap. J., 235, 186.

Chiosi, C., and A. Maeder, 1986, Ann. Revs. Astr. Ap., 24, 329.
Chu, Y.-H., R.R. Treffers, and K.B. Kwitter, 1983, Ap. J. Suppl., 53, 937.
Cioffi, D.F., C.F. McKee, and E. Bertschinger, 1988, Ap. J., 334, 252.
Ciotti, L., and A. D'Ercole, 1989, Astr. Ap., 215, 347.
Cox, D.P. 1988, in Roger and Landecker 1988, p. 73.
Cox, D.P., and R.J. Edgar, 1983, Ap. J., 265, 443.
Dickel, J.R., and E.M. Jones, 1985, Ap. J., 288, 707.
Dopita, M.A., L. Binette, and I.R. Tuohy, 1984, Ap. J., 282, 142.
Dwek, E. 1988, in Roger and Landecker 1988, p. 363.
Fabian, A.C., W. Brinkmann, and G.C. Stewart, 1983, in IAU Symposium 101, Supernova Remnants and Their X-Ray Emission, I. J. Danziger and P. Gorenstein, eds. (Dordrecht: Reidel), p. 83.
Falle, S.A.E.G. 1981, M.N.R.A.S., 195, 1011.
Fesen, R.A., R.H. Becker, and W.P. Blair, 1987, Ap. J., 313, 378.
Fesen, R.A., R.H. Becker, W.P. Blair, and K.S. Long, 1989, Ap. J. (Letters), 338, L13.
Fesen, R.A., W.P. Blair, and R.P. Kirshner, 1982, Ap. J., 262, 171.
Fesen, R.A., C.-C. Wu, M. Leventhal, and A.J.S. Hamilton, 1988, Ap. J., 327, 164.
Fransson, C. 1986, in Radiation Hydrodynamics in Stars and Compact Objects, D. Mihalas and K.H.A. Winkler, eds. (Berling: Springer), p. 141.
Fransson, C., and R.A. Chevalier, 1989, Ap. J., 343, 323.
Fransson, C., A. Cassatella, R. Gilmozzi, R.P. Kirshner, N. Panagia, G. Sonneborn, and W. Wamsteker, 1989, Ap. J., 336, 429.
Fryxell, B.A., E. Müller, and W.D. Arnett 1991, Ap. J., 367, 619.
Gaetz, T.J., R.J. Edgar, and R.A. Chevalier, 1988, Ap. J., 329, 927.
Gronenschild, E.H.B.M. and R. Mewe, 1982, Astr. Ap. Suppl., 48, 305.
Grasberg, E.K., and D.K. Nadëzhin, 1987, Sov. Astr. AJ, 31, 629.
Grasberg, E.K., V.S. Imshennik, and D.K. Nadëzhin, 1971, Ap. Space Sci., 10, 28.
Gull, S.F. 1973, M.N.R.A.S., 161, 47.
Hamilton, A.J.S. 1985, Ap. J., 291, 523.
Hamilton, A.J.S., and C.L. Sarazin, 1984a, Ap. J., 281, 682.
Hamilton, A.J.S., and C.L. Sarazin, 1984b, Ap. J., 284, 601.
Hamilton, A.J.S., and C.L. Sarazin, 1984c, Ap. J., 287, 282.
Hamilton, A.J.S., C.L. Sarazin, and R.A. Chevalier, 1983, Ap. J. Suppl., 51, 115.
Hamilton, A.J.S., C.L. Sarazin, and A.E. Symkowiak, 1986a, Ap. J., 300, 698.
Hamilton, A.J.S., C.L. Sarazin, and A.E. Symkowiak, 1986b, Ap. J., 300, 713.
Helfand, D.J., and R.H. Becker, 1987, Ap. J., 314, 203.
Herman, J. 1985, in Mass Loss from Red Giants, eds. M. Morris and B. Zuckerman (Dordrecht: Reidel), p. 215.
Hester, J.J., 1987, Ap. J., 314, 187.
Hester, J.J., R.A.R. Parker, and R.J. Dufour, 1983, Ap. J., 273, 219.
Hughes, J.P., 1987, Ap. J., 314, 103.
Hughes, J.P. 1990, in Supernovae, S.E. Woosley, ed. (Berlin: Springer) p. 661.
Hughes, J.P., and D.J. Helfand, 1985, Ap. J., 219, 544.
Iben, I., and A.V. Tutukov, 1984, Ap. J. Suppl., 32, 351.
Imshennik, V.S., and D.K. Nadëzhin, 1989, Sov. Scientific Reviews, 8, 1.
Innes, D.E., J.R. Giddings, and S.A.E.G. Falle, 1987a, M.N.R.A.S., 224, 179.
Innes, D.E., J.R. Giddings, and S.A.E.G. Falle, 1987b, M.N.R.A.S., 226, 67.
Itoh, H. 1984, Ap. J., 285, 601.

Itoh, H., and A.C. Fabian, 1984, M.N.R.A.S., 208, 645.
Itoh, H., K. Masai, and K. Nomoto, 1988, Ap. J., 334, 279.
Jenkins, E.B., 1978, Ap. J., 220, 107.
Jones, E.M., and B.W. Smith, 1983, in IAU Symposium 101, Supernova Remnants and Their X-Ray Emission, I.J. Danziger and P. Gorenstein, eds. (Dordrecht: Reidel), p. 83.
Kirshner, R.P., P.F. Winkler, and R.A. Chevalier, 1987, Ap. J. (Letters), 315, L135.
Korobeinikov, B.P., 1956, J. Acad. Sci. Soviet Union, 109, 271.
Kulkarni, S.R., and C. Heiles, 1988, in Galactic and Extragalactic Radio Astronomy, G.L. Verschuur and K.I. Kellermann, eds. (Berlin: Springer), p. 95.
Kwitter, K.B. 1984, Ap. J., 287, 840.
Lasker, B.M. 1978, Ap. J., 223, 109.
Lasker, B.M. 1980, Ap. J., 237, 765.
Lockman, F.J., 1984, Ap. J., 283, 90.
Lockman, F.J. 1991, in IAU Symp. 144, The Disk-Halo Connection in Galaxies, H. Bloemen, ed. (Dordrecht: Kluwer), p. 15.
Lockman, F.J., L.M. Hobbs, and J.M. Shull, 1986, Ap. J., 307, 380.
Long, K.S., and W.P. Blair, 1990, Ap. J. (Letters), 358, L13.
Lundqvist, P., and C. Fransson, 1988, Astr. Ap., 192, 221.
Mathewson, D.S., V.L. Ford, M.A. Dopita, I.R. Tuohy, K.S. Long, and D.J. Helfand, 1983, Ap. J. Suppl., 51, 345.
McCray, R.A. 1983, Highlights of Astr., 6, 565.
McKee, C.F. 1988, in Roger and Landecker 1988, p. 205.
McKee, C.F., L.L. Cowie and J.P. Ostriker, 1978, Ap. J. (Letters), 219, L23.
McKee, C.F., D. Van Buren, and B. Lazareff, 1984, Ap. J. (Letters), 278, L115.
Nadyozhin, D.K. 1985, Ap. and Sp. Sci., 112, 225.
Nittman, J., S. Falle, and P. Gaskell, 1982, M.N.R.A.S., 201, 833.
Nomoto, K., F.-K. Thielemann, and K. Yokoi, 1984, Ap. J., 286, 644.
Nugent, J.J., S.H. Pravdo, G.P. Garmire, R.H. Becker, I.R. Tuohy, and P.F. Winkler, 1984, Ap. J., 284, 612.
Ostriker, J.P., and J. Silk, 1973, Ap. J. (Letters), 184, L113.
Panagia, N. 1973, A. J., 78, 929.
Rand, R.J., and S.R. Kulkarni, 1989, Ap. J., 343, 760.
Raymond, J.C., J.H. Black, A.K. Dupree, L. Hartmann, and R.S. Wolff, 1980, Ap. J., 238, 881.
Raymond, J.C., J.J. Hester, D. Cox, W.P. Blair, R.A. Fesen, and T.R. Gull, 1988, Ap. J., 324, 869.
Reynolds, R.J. 1989, Ap. J. (Letters), 339, L29.
Roger, R., and T. Landecker, 1988, eds. IAU Colloquium 101, The Interaction of Supernova Remnants with the Interstellar Medium (Cambridge: Cambridge Univ. Press).
Rupen, M.P., J.H. van Gorkom, G.R. Knapp, J.E. Gunn, and D.P. Schneider, 1987, A. J., 94, 61.
Sakurai, A., 1960, Comm, Pure Appl. Math., 13, 353.
Sedov, L. 1959, Similarity and Dimensional Methods in Mechanics (New York: Academic).
Seward, F.D., P. Gorenstein, and W. Tucker, 1983, Ap. J., 266, 287.
Shigeyama, T., and K. Nomoto, 1990, Ap. J., 360, 242.
Shigeyama, T., K. Nomoto, T. Tsujimoto, and M. Hashimoto, 1990, Ap. J. (Letters), 361, L23.
Shull, J.M. 1988, in Roger and Landecker 1988, p. 161.
Slavin, J.D., and D.P. Cox 1992, Ap. J. 392, 131.
Snow, T.P. 1981, Ap. J., 251, 139.

Solinger, A., S. Rappaport, and J. Buff, 1975, Ap. J., 201, 381.
Spitzer, L., Jr. 1978, Physical Processes in the Interstellar Medium (New York: Wiley).
Sramek, R.A., N. Panagia, and K.W. Weiler, 1984, Ap. J. (Letters), 285, L59.
Tenorio-Tagle, G., P. Bodenheimer, J. Franco, and M. Różyczka, 1990, M.N.R.A.S., 244, 563.
Turtle, A.J., et al. 1987, Nature, 327, 38.
Turtle, A.J., D. Campbell-Wilson, R.N. Manchester, L. Staveley-Smith, and M.J. Kesteven, 1990, IAU Circ. No. 5086.
van den Bergh, S., and K.W. Kamper, 1977, Ap. J., 218, 617.
Vishniac, E.T. 1983, Ap. J., 274, 152.
Wampler, E.J., L. Wang, D. Baade, K. Banse, S. D'Odorico, C. Gouiffes, and M. Tarenghi, 1990, Ap. J. (Letters), 362, L13.
Weaver, R., R. McCray, J. Castor, P.R. Shapiro and R.T. Moore, 1977, Ap. J., 218, 377.
Weiler, K.W., N. Panagia, and R.A. Sramek 1990, Ap. J. 364, 611.
Weiler, K.W., R.A. Sramek, N. Panagia, van der J.M. Hulst, and M. Salvati, 1986, Ap. J., 301, 790.
Winkler, P.F., C.R. Canizares, G.W. Clark, T.H. Markert, K. Kalata, and H.W. Schnopper, 1981, Ap. J. (Letters), 246, L27.
Woodward, P.R., 1976, Ap. J., 207, 484.
Wu, C.-C., M. Leventhal, C.L. Sarazin, and T.R. Gull, 1983, Ap. J. (Letters), 269, L5.
Zuckerman, B. 1980, Ann. Rev. Astr. Ap., 18, 263.

SEMINAR 1

THE SEARCH FOR SUPERNOVAE AT THE OBSERVATOIRE DE LA CÔTE D'AZUR

CHRISTIAN POLLAS

Observatoire de Calern, OCA
Caussols 06470, FRANCE

S. Bludman, R. Mochkovitch and J. Zinn-Justin, eds.
Les Houches, Session LIV, 1990
Supernovae

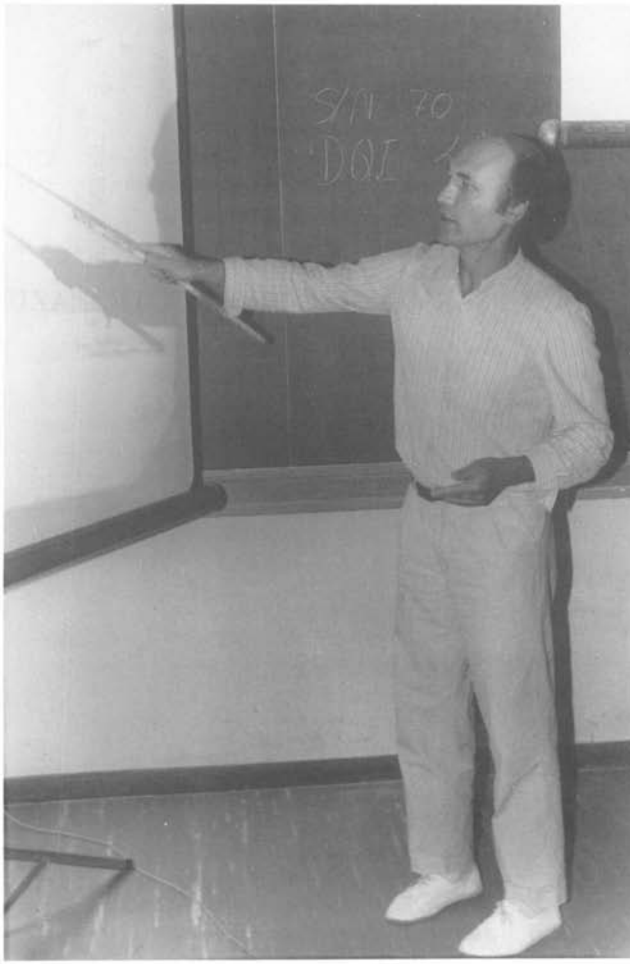

Contents

1. Presentation 772
2. The SN search 772
3. The OCA Schmidt results 776
   3.1. What is my method? 776
   3.2. Some advice 779
4. Must we continue? 784
References 786

1. Presentation

A search for SNe is being conducted at the Observatoire de la Côte d'Azur (OCA) in France with a 90/152/316 cm Schmidt telescope. The staff members are D. Albanese, C. Labeyrie, A. Maury and C. Pollas. A local Scientific Commitee manages external and internal programs, including the SN search being conducted under the responsibility of the author.

The station is at an altitude of 1270 m in the hinterland of Grasse. Our photographic detector covers a $5°15' \times 5°15'$ field, roughly up to the 22nd magnitude in a 1 h exposure. The plate scale is $1''/15.3\mu$, and the faintest stellar images are smaller than $2''$.

We have recently started to use unfiltered Kodak technical panchromatic films, reaching a detection limit of 22, a S/N of 70%, and a DQE of 4%. Classical UBVR images are obtained on hypersensitized glass plate emulsions (now with hydrogen), between magnitude 20 and 22.

A Schmidt telescope provides good images of extended areas for astrometric, statistical, and morphological studies, and is used for the search of rare objects. It currently provides the best memory support for such a large volume of data.

My SN search is not an exhaustive survey in a particular direction, but rather makes use of plates obtained for many other astronomical purposes. At the present time, I have just begun some specific SN tracking on inexpensive films.

2. The SN search

Statistical considerations on the observational work are provided in the four next diagrams.

Figure 1 is an interpretation of the second figure in the Asiago Catalogue of SNe [Barbon et al.] giving the number of discoveries obtained annually to date. It shows an increase in the number of discoveries since 1987, along

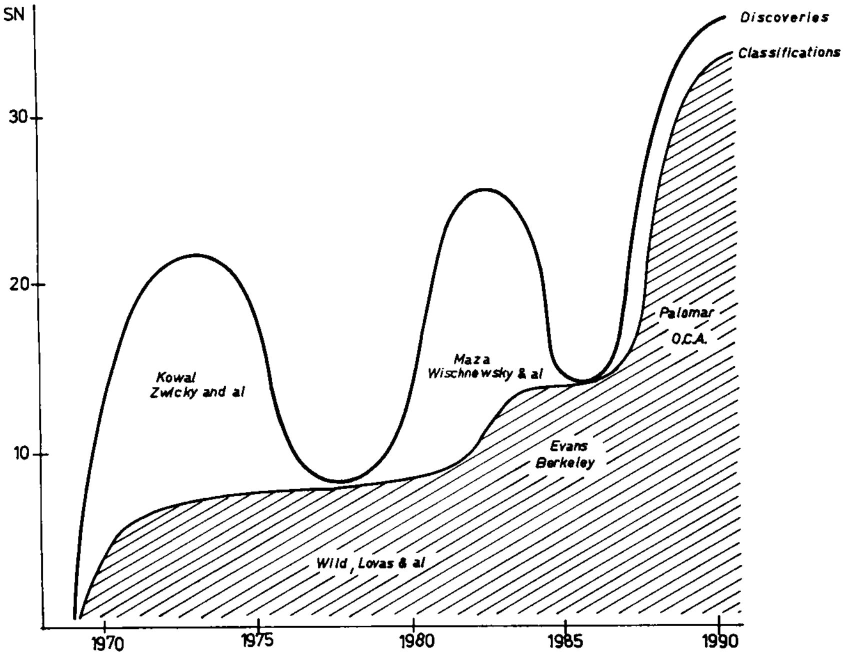

Fig. 1. Evolution of a number of new SNe and their classification.

with an increase of classified SNe and allows us to identify the main contributors. In the seventies these were F. Zwicky, C. Kowal et al.; before 1985, M. Wischnewsky, J. Maza et al.; the Palomar and OCA Schmidt telescopes contributions began in 1987; during the eighties, the discoveries were by R. Evans and the Berkeley automatical SN search along with the continuous development from P. Wild, M. Lovas, and several other hardworking observers.

Classification of supernovae is made possible by access to large telescopes with modern detectors, under the supervision of different people including A. Filippenko, R. Kirshner, R. Lopez, M. Philipps, and teams at the AAT and ESO.

Figure 2 shows that a few teams (approximately three) have produced many new objects (approximately twenty) in the last four years, whereas many discoverers (approximately twenty) obtained an average production of a few SNe (approximately three).

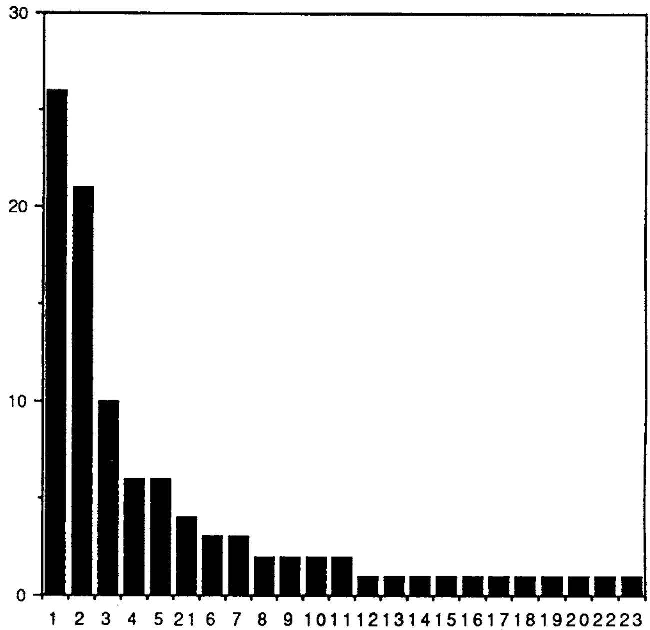

Fig. 2. SN production per team from 1987 to November 1990.

Figure 3 shows the magnitude at discovery in the recent SN surveys including the two brightness extrema, that is, SN 1987 A and the Danish attempt to high redshift SNe [Norgaard, Neilson et al., 1989].

Several kinds of prospections clearly appear. An obvious contribution of faint objects from magnitude 18 to 20 is provided by the "big Schmidts" (i.e, 1m-aperture Schmidt telescopes with high S/N photographic detectors). These include the Oschein Schmidt at Palomar (J. Mueller), the OCA Schmidt, and the Anglo-Australian Schmidt (R. McNaught).

R. Evans' watch and the Berkeley automatical survey are located in the magnitude range 15 to 16 and are complementary. Recall that they are, respectively, a famous visual work by an amateur in the southern hemisphere, and a highly elaborate search made by a professional team in California.

The groundbase is provided by an extended watch with small Schmidt telescopes devoted to SN patrols. Included are the Bern, Konkoly, and Asiago

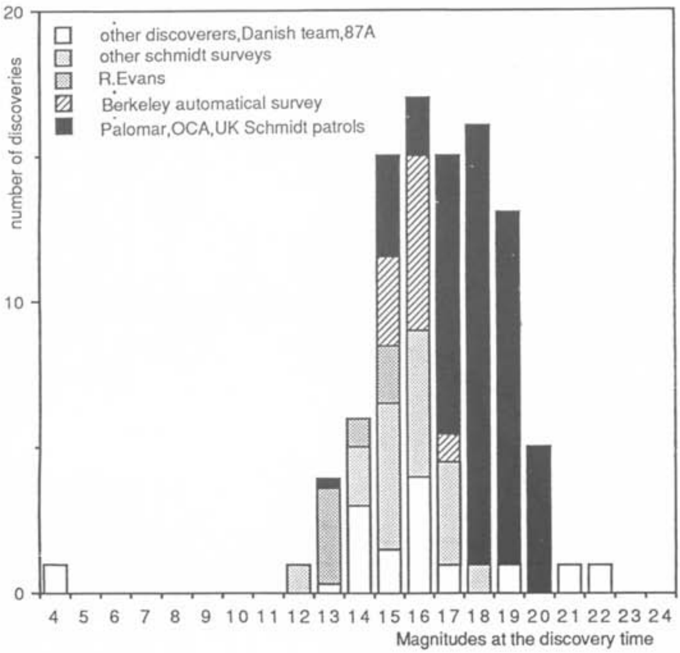

Fig. 3. Magnitudes at the time of discovery for the SNe discovered since 1987.

Schmidts, the different Soviet teams, and the Curtis Schmidt at the CTI Observatory. Occasional discoveries result from various professional telescopes (large and small) and amateur searches.

The filters used are not specified in fig. 3, mixing B, V, R, and "panchromatic" magnitudes. Most discoveries up to magnitude 17, and part of the others are made near the maximum where B–V is faint or null. Red discoveries provide objects essentially of magnitude 18 to 19. This does not change the general aspect of the diagram's left wing. It appears that it is much more probable (and easier) to find a faint SN than a bright one. But the latter are of greater importance since they allow extended observations.

Figure 4 shows the discoveries since the beginning of 1980, and the evolution of this work, especially the recent increase of new events found on Schmidt plates.

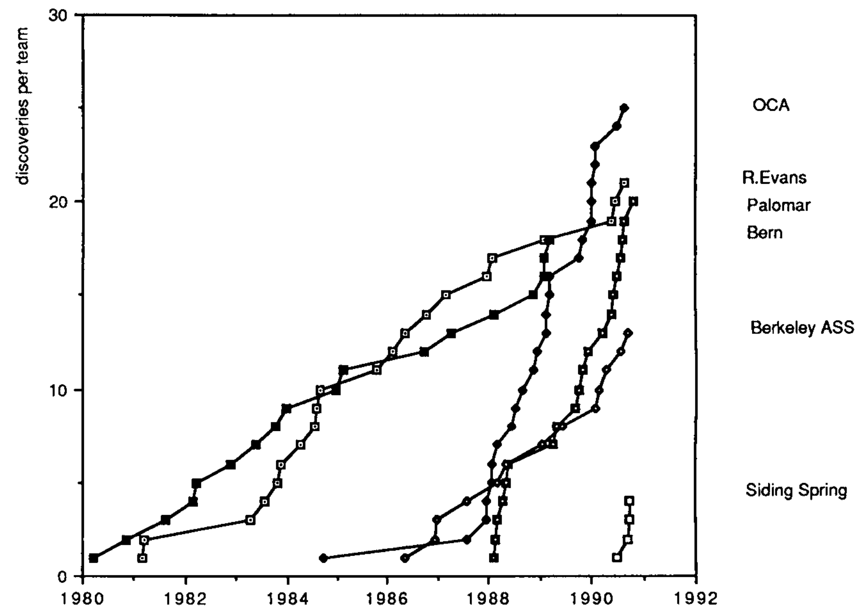

Fig. 4. Increase (and trends) of the SN production since 1980.

3. The OCA Schmidt results

In the interval from 1987 to the present, I found 25 SNe as shown in fig. 5 (except for the first one which I discovered in 1984).

3.1. What is my method?

If you want to find a SN candidate, each star can be examined and checked to see if it was present before.

Then, "false stars" must be eliminated, that is, defects including those of photographic cosmetic, accidental secondary images, isolated lights of satellites or airplanes, slow moving objects and also: from the solar system and stars with strong proper motion, very red or very blue quasistellar condensations, variable stars, especially VVO and cataclysmic stars (flare stars for short exposures), and ... already known SNe!

Another way is to examine each star that looks like a SN, that is, a star inside 2 times the radius of the apparent extension of a galaxy corrected from the angle of sight, and not brighter than 2 times the nucleus.

	SN	Host galaxy		inclination	mag	z	constellation	mag		type	from maximum
1	1984P	UGC	Sc:		15.4		Cet-Tau	18.			
2	1987J	Eso	Scd:		15.7		Aqr	17.2 V		II	+2m
3	1987O	UGC-IR	Sc:		15	.015	Gem-Cnc	17.6		Ia	+1m
4	1987P	ZW	Sp?		15.4		Gem-Cnc	19 ->18		Ia	pMx
5	1988A*	M58-IR	Sab LII		11	.01		15.5		IIp	Mx+
6	1988C	UGC	Sbc		15.1	.02	Pup	17		Ia	+1m
7	1988I		Sc:	Side-on?	17?	.038	Leo	19	(HII?)	IIpe-n?	+1m
8	1988P		Sp?		18		Ser small group	18.5	HII	I?	
9	1988Q		Sp?		17	.022	Her	18		II	+1m-
10	1988S	MCG	Sp		15.5	.043	Psc	19	external arm	II	+1m
11	1988W				18.5		Leo	20.2	far	...(CFA obs.)...	
12	1988Z*	MCG	Sc:very diffuse f-on		15	.030	Leo	17.4		IIp-pe n?	
13	1989E	H530A-B	(Scd:)	complex	15.6	.026	CVn	18.6	complex	Ib	+1m
14	1989H	MCG	Sb	face-on	15		CVn	20	HII		
15	1989I				16		Boo-Vir	19			
16	1989J		Sp?		16		CVn	18.5			
17	1989Q		Sp?		17	.059	Psc	19.5		Ia	+1m
18	1989T		Sp? face-on		18		Psc-Cet	20			
19	1989V		compact asp.		18	.061	Psc	18.5		Ia	Mx
20	1989W						CVn	18 R			
21	1990A	NGC 500	E -------> type I?		15.2		Psc	19.3		(I)	
22	1990D		compact asp.		18.5		CVn small group	20.			
23	1990F	KUG	Scd:		15.7		CVn	19.2	condens.	Ia	...(Mx+)
24	1990Q	Arp254	Sab:		14.5	.005	Lib	18.		II	
25	1990X	UGC 12565	Sb-Sc	face-on	15.4		Peg	19. B	far	II	+1.5m

without classification: 9/25 ~1/3 (including 1990A)

type II	8/17	~44%	II	5
			IIp-pe-n	3
I	9/17 (with 1990A)	56%	Ia	6
			Ib	1
			I?	2

Fig. 5. Data about SNe discovered with the OCA Schmidt telescope.

What is the difference between these two methods of search? It is the time spent! On a 5 degree Schmidt plate, I must examine about 3×10^5 stars with the first method and with the second method, it is only necessary to screen 10^3 galaxies with 4 stars in each of them. To check the previous presence of a star by means of an earlier comparison image (on an old plate for example) I need several seconds. But for the second step, the elimination of false stars

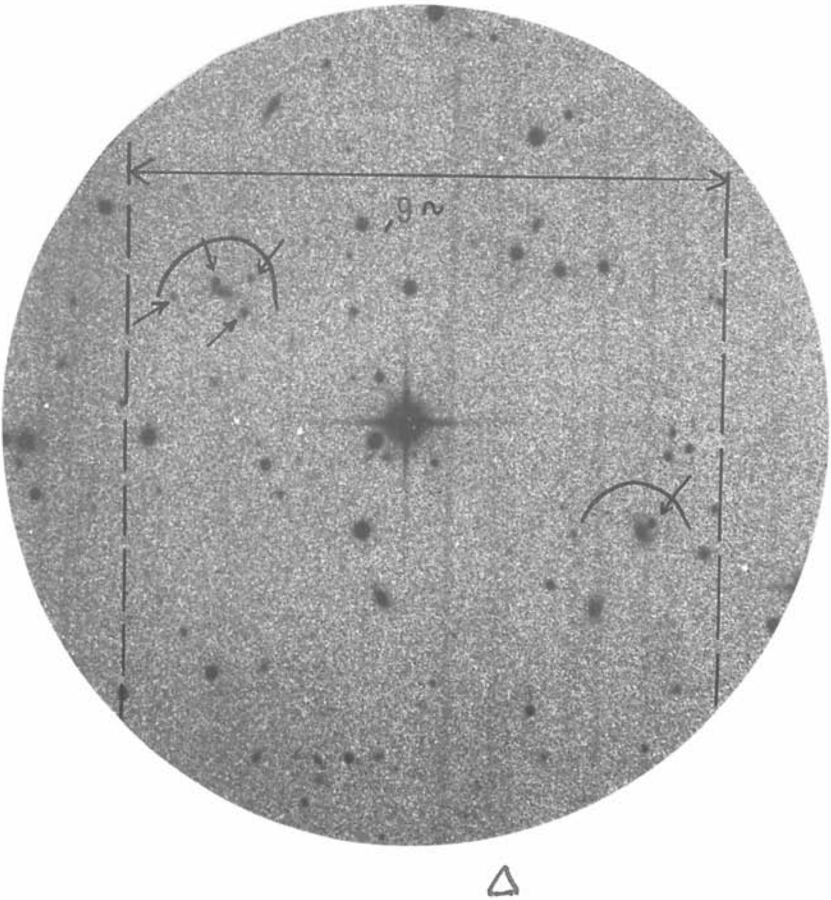

Fig. 6. A field scanned through a binocular. Only marked galaxies will be checked. Their stars are shown here with an arrow, and will be taken into account.

requires several minutes (approximately 60 times longer). The first method also increases the number of "false SNe," and thus requires as much as 300 times more time. For up to five hours per plate, a production of 200 plates at our telescope provides 7 SNe per year. The game seems worth playing, and accounts for about 25% of my professional work.

The first step in the analysis is a whole-plate scan with a binocular, marking the host galaxies as candidates for a further examination. Then I quickly count and estimate the number of galaxies to be looked at (with varying magnitudes).

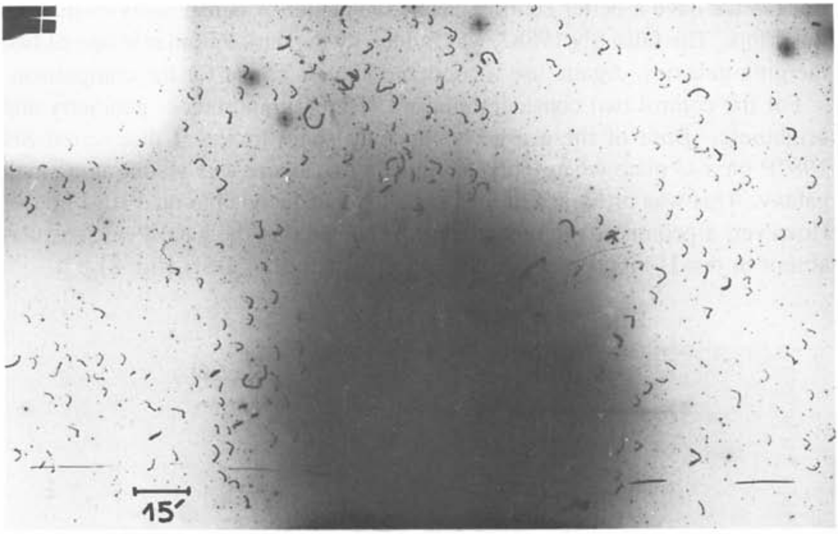

Fig. 7. Part of a plate prepared for SN checking. This peculiar overexposed field was obtained for a program on the satellites of Jupiter.

The second step is to check each galaxy with a comparison image using two oculars, one for the left eye (on the new image) and the other ocular for the right eye (on the comparison image). On the left, I memorize the stars present near or superimposed on the galaxy. After a quick motion of my body I verify the similar presence or disposition of these stars in my right ocular. Each mark is erased after examination.

3.2. Some advice

In choosing a comparison image, the choice of a similar image is the best. Be careful about color effects between two spectroscopically different images. Be sure to note scale and resolution differences.

At the OCA Schmidt I often use a panchromatic emulsion without a filter and the red and blue first Palomar Observatory Sky Survey prints. The Kodak Tech Pan panchromatic emulsion on glass plate and 4415 on film is especially sensitive in H-alpha. Many condensations appear stronger on our plates with a more pronounced stellar aspect than the POSS prints. The false SN 1985 H was one of these. Sometimes only one of the blue and red counterparts of the same object is visible on the Palomar prints; moreover some very faint objects appear only on our emulsion, like the false SN 1990C. On our images we have a better contrast inside the center of dense galaxies than on the prints. The false SN 1988X was hidden by the dark Palomar image of two merging galaxies. Again, use a good and similar image for the comparison.

For the control two considerations are of great importance: geometry and brightness. Both of these aspects can play some tricks. I discovered SN 1987P on a U plate where only a bright stellar image was visible in a small galaxy. This was presumed at first to be the nucleus visible on a IIIaJ image. However, a geometric alignment control showed that the galaxy nucleus was absent in our U image and that the object was indeed a SN (fig. 8).

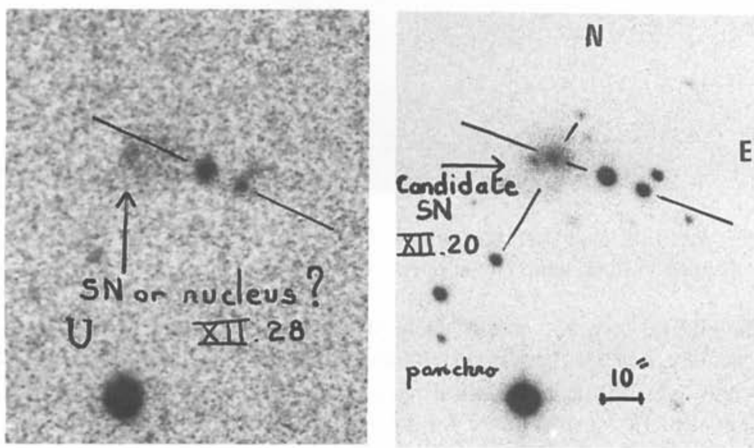

Fig. 8. The discovery of SN 1987P.

Another trick was uncovered during the discovery of SN 1990Q where a geometrical figure appeared on the Palomar print as well as on our short exposure image. However, a better observation allowed us to identify a bright new object and another very faint star on this plate (fig. 9).

In fact, before the first step, I perform a quick examination of the brighter galaxies (magnitude 14 or 15) immediately visible on the image, but for not more than 15 to 20 minutes. This short work, which is possible in all observatories, yielded 7 SNe: 1984P, 1987J, 1988A, 1988Z, 1989J (fig. 10), 1990F and 1990Q, that is, one to two SNe/year.

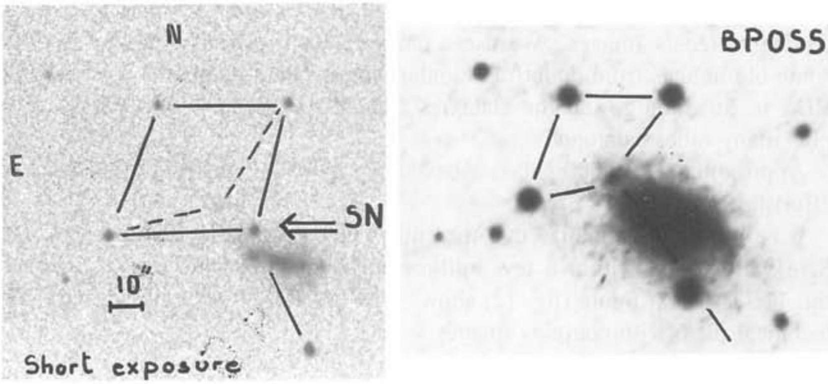

Fig. 9. The discovery of SN 1990Q.

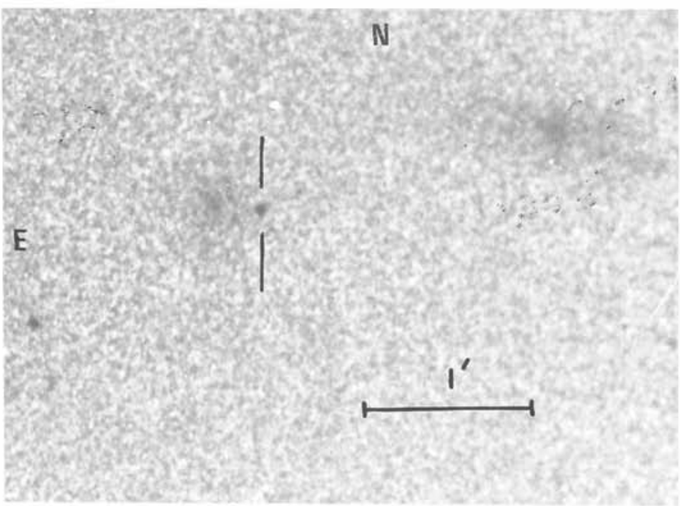

Fig. 10. SN 1987J was discovered after a quick examination of this plate.

For the final step of rejecting a false SNe, it is always better to have a couple of recent images. We use a database bank of our plates to recover some old images from doubtful Palomar plates. Other databases used are the CDS in Strasbourg, and the Galaxies Data Base of the Lyon Observatory, plus many other catalogues.

Approximately 30,000 galaxies have been looked at since July 1988. This effort has provided 16 SNe.

It is important to realize that the entire plate must be examined. Several SNe were found within a few millimeters from the plate edge as seen in fig. 11. The next figure (fig. 12) shows how SN 1988Q was discovered on a technical plate with complex images.

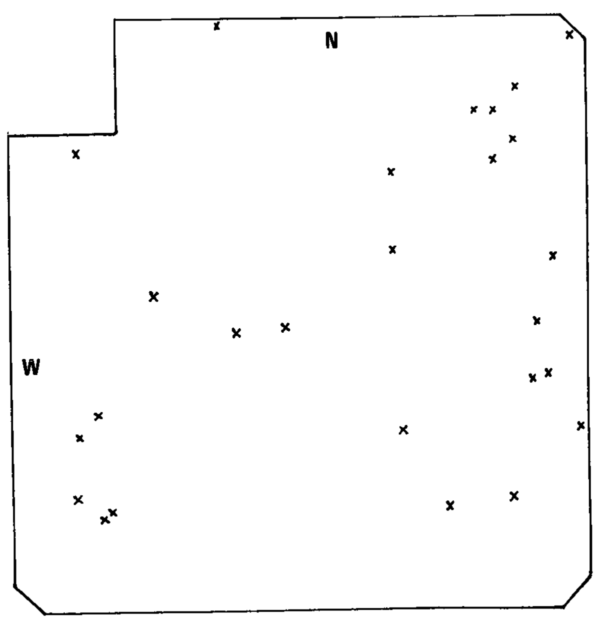

Fig. 11. Distribution of the discovery images on the plate.

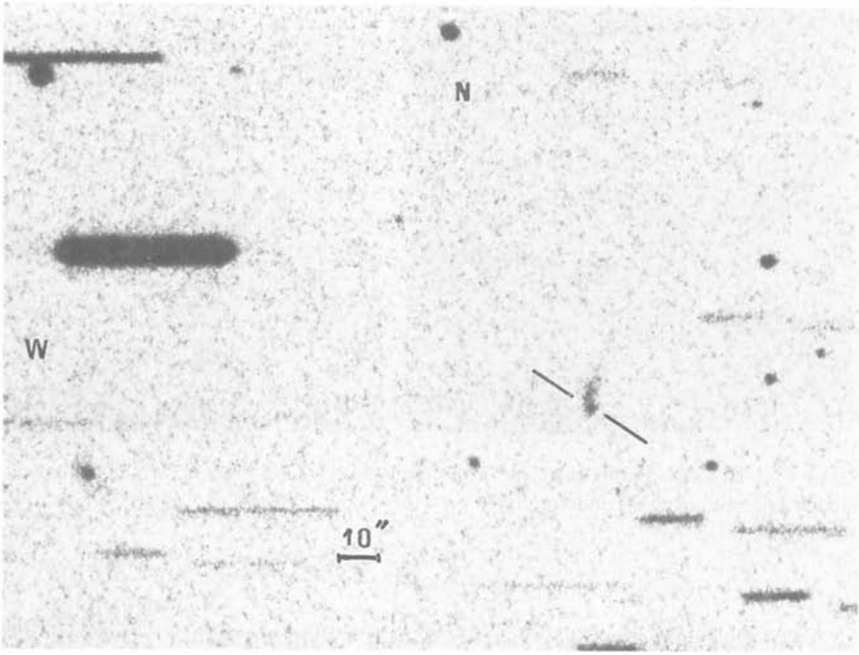

Fig. 12. Multi-exposure with different driving motions.

The data in fig. 5 require several comments. Many SNe are found in face-on spiral galaxies and many apparently compact galaxies in the Palomar survey reveal evidence of some spiral structure on better images. On the contrary, the SN Ib 1989E appeared in a galaxy classified as spiral, which turned out to be a more complex system on our plate as was already noticed by Holmberg.

Many of the SNe in fig. 5 would not be visible with a larger inclination. Several are superimposed with HII regions or condensations. When the SN fades out, it becomes difficult to extract the SN signal from the small surrounding nebulosity (see figs. 13 and 14).

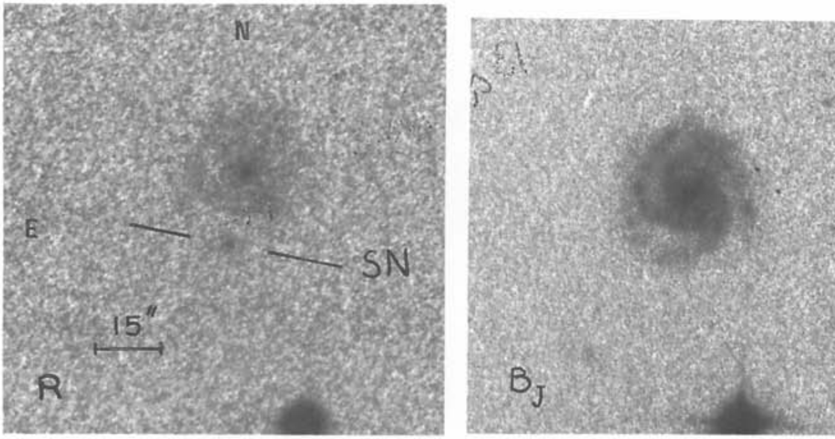

Fig. 13. This SN 1989H occurred in a spiral galaxy seen face-on, which revealed many absorptions and condensations.

Faint SNe are generally discovered near maximum light. However, in some cases such as SN 1990F, there is a discrepancy between the maximum deduced from spectroscopy and from our photographic estimates based on plates obtained one month before discovery. In December 1987, a multidiscovery occured with 2 new objects on the same plate. Also, in a period of two years, I found six new objects in the same $2^\circ \times 4^\circ$ field, showing some directions to be very prolific! Several of these SNe appeared in small groups of galaxies.

4. Must we continue?

In many observatories and with most old astronomical image collections work of this type is possible. The more galaxies we observe (or the same galaxies with an observational frequency compatible with the time constant) the better it is. Keep in mind the improvement obtained with the high S/N on big Schmidt telescopes. This allows us to populate an incomplete but large sample of new data on SNe.

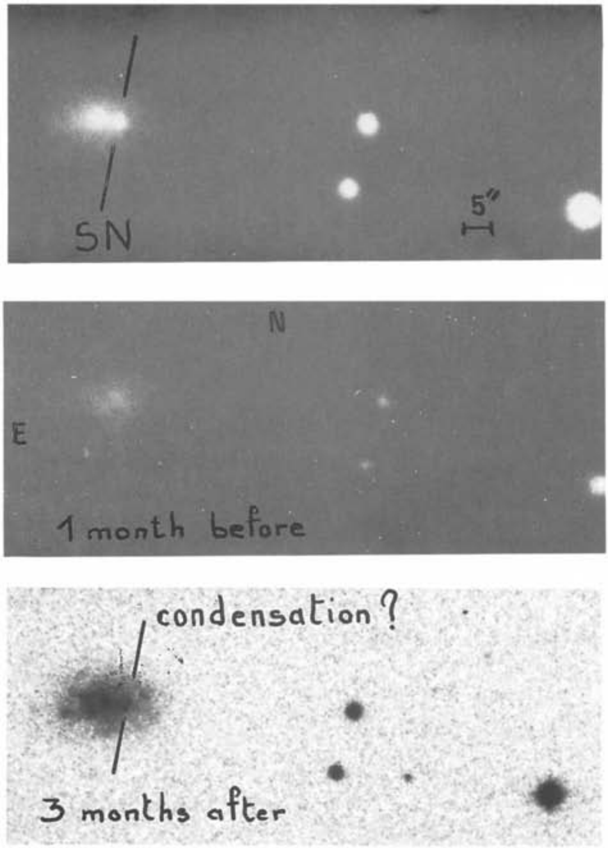

Fig. 14. Screen displays of SNe 1990F and an image of improved resolution of the host spiral galaxy.

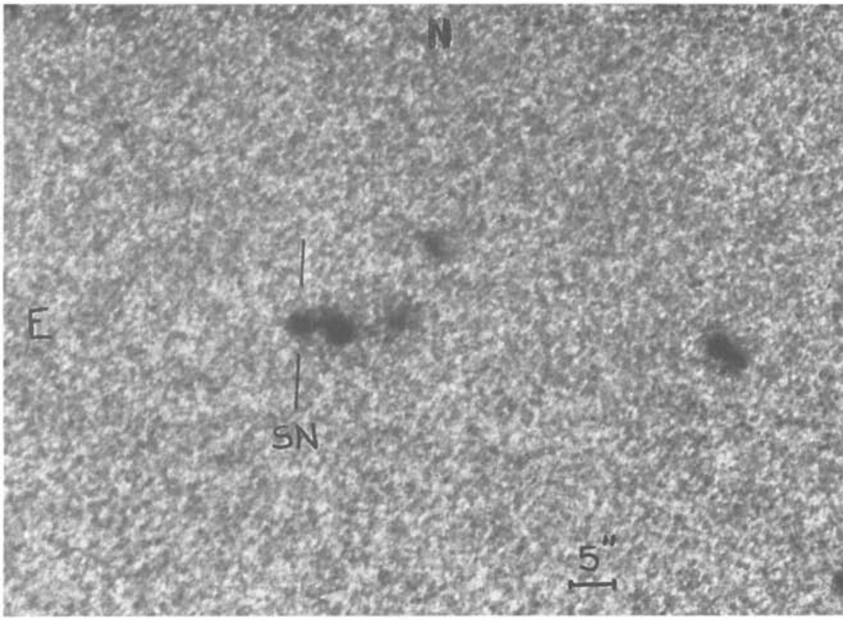

Fig. 15. SN 1990 D among a group of four galaxies.

References

Barbon, R., E. Cappellaro, and M. Turatto, 1989 *Astron. Astrophys. Suppl.* **81**, 421.
Norgaard-Nielsen, H.U., L. Hansen, H.E. Jorgensen, A.A. Salamanca, R.S. Ellis, and W.J. Couch, 1989 *Nature* **339**, 523.

SEMINAR 2

GENERAL RELATIVISTIC NEUTRINO HYDRODYNAMICS: THE PHYSICS OF AND NUMERICAL TECHNIQUES FOR MODELING STELLAR COLLAPSE AND THE EARLY COOLING OF NEUTRON STARS

PAUL J. SCHINDER

Department of Astronomy, Cornell University
Ithaca NY 14853, USA
[schinder@astrosun.tn.cornell.edu]

S. Bludman, R. Mochkovitch and J. Zinn-Justin, eds.
Les Houches, Session LIV 1990
Supernovae

Contents

1. Introduction 789
2. General relativistic hydrodynamics 791
   2.1. Preliminaries 792
   2.2. The equations of polar sliced neutrino hydrodynamics 793
   2.3. Numerical techniques 795
   2.4. Summary 796
3. General relativistic neutrino transport 796
   3.1. The role of neutrinos 796
   3.2. The neutrino transport equations 798
   3.3. The variable Eddington factor method 800
   3.4. Other transport treatments 802
4. Neutrino interactions with the gas 803
   4.1. The basic neutrino interactions 803
   4.2. The interaction functions G and L 805
5. Conclusion 806
References 806

1. Introduction

In this paper, I will give an overview of the physics and numerical techniques Sid Bludman and I will be using to model the collapse of the core of a massive star and the first 20 seconds or so of its life as a neutron star. After completing a statistical analysis of the 19 $\bar{\nu}_e$ detected by Kamiokande and IMB from SN1987A[1], we decided to begin work on a code to compute accurate neutrino spectra for all six "types" of neutrinos (neutrinos and antineutrinos of the electron, μ, and τ flavors). We also made the decision to first model early cooling of neutron stars, starting with a post-collapse hot nascent neutron star, rather than attempting right away to do the more difficult core collapse problem. Since the neutrino signal from SN1987A was, almost certainly, entirely due to the neutron star cooling phases rather than the collapse phase, we feel this is a useful approach that will allow us to refine our physics and numerics for stellar collapse while enabling us to compute neutrino signals from newly born neutron stars. *Our goal is to compute accurately, for 10–20 seconds, the spectra of neutrinos emitted by collapsing stellar cores to infinity which are potentially observable by both existing and proposed neutrino detectors.*

Our choice of techniques is unique. We do fully general relativistic neutrino transport and hydrodynamics in comoving (Lagrangian) coordinates. We use *polar slicing* of space-time, which enables us to compute in situations where a black hole forms. We use the *variable Eddington factor* method to solve neutrino Boltzmann (transport) equations. I feel the variable Eddington factor method is the simplest technique (with built in error checks) which will give accurate spectra *and which can reproduce accurately simple test problems with analytic solutions.* (To my knowledge, no neutrino transport technique currently used in Type II supernova codes has been demonstrated to reproduce accurately *any* test problem; the few tests that I have seen in the literature show, in my opinion, that these techniques are not working very well.)

Both hydrodynamics and neutrino transport equations are differenced and solved *implicitly*, so the timesteps we take are limited only by considerations of accuracy. In particular, the Courant time, the limiting timestep for an explicit hydrodynamics code, can be safely ignored. Because the speed of sound in a neutron star is a significant fraction of the speed of light, the Courant time is much smaller than the neutrino diffusion timescales relevant to neutron star cooling. Neutrino processes such as neutrino-electron scattering and ν-$\bar{\nu}$ production-absorption are treated as realistically as possible, since the physics of these processes is well known and can be calculated straightforwardly using the Weinberg-Salam-Glashow theory of weak interactions. We use a new high-density, high-temperature equation of state constructed by Swesty and Lattimer [2], and try to keep the number of free parameters to a minimum. There are enough uncertainties in the physics of stellar core collapse and neutron star cooling that I feel anything that can be modeled correctly, for which we know the correct physics, should be modeled as exactly as possible.

One reason for telling you up front about the techniques we use is that these are the techniques I'm most familiar with and expert at. In some cases, I am also very familiar with the techniques used in other codes. I have, for example, written and used a May and White type general relativistic hydrodynamics code. In other cases, I'm familiar with the basics of the technique but have never used it. For example, I've never used a flux-limited diffusion code (and most likely never will, since I think that flux-limited diffusion is a poor transport approximation). I will nevertheless attempt to outline below other techniques which are used in core collapse and neutron star cooling codes, along with the reasons we are not using them.

While constructing the code, I was strongly influenced by lessons I learned at a numerical relativity conference at the University of Illinois [3], which I attended two years ago. Workers in the field of numerical relativity construct and use codes to model events which are, in most cases not now subject to comparison with observations, and which in many cases, never will be. Workers in relativity are very sensitive to the fact that their codes must, under these conditions, be tested and verified before the results are to be believed. They strongly emphasize that codes must be compared with both test-problems which have known analytic solutions, and with other codes using different numerical techniques (a major effort is made to identify suitable test problems [4]). Results computed with codes which are successfully tested are accepted. Results computed with codes which are not validated are not believed, and are not published.

In many respects, modelers of stellar core collapse and nascent neutron star cooling are in the same situation. Only one observation of neutrinos from a core collapse has ever been made, and with only 19 $\bar{\nu}_e$, very little more can be said about details of the collapse or the neutron star cooling phase, except that they really did occur. Under these circumstances, it is very important to demonstrate that codes intended to model this process can accurately reproduce the solutions for simple test problems. Codes using different numerical techniques can also be compared with each other when used to solve more difficult and realistic problems to give confidence that the solutions obtained are correct.

The remainder of this paper is divided into three sections, corresponding to three of the four major pieces of physics needed in a stellar collapse/neutron star cooling code. These four pieces are (*a*) general relativistic hydrodynamics, (*b*) general relativistic neutrino transport for all six types of neutrinos, (*c*) neutrino interaction functions ("opacities") for all six types of neutrinos, which describe the interaction of neutrinos with various components of the gas, and (*d*) the equation of state of high density, high temperature matter. Of these four pieces of physics, our expertise is in the first three. Those wishing to learn more about the Swesty-Lattimer equation of state should consult [2]. To learn about the equation of state in general, one can consult the article by Vautherin in this volume.

There are excellent descriptions in the literature of the two major possibilities for the Type II supernovae mechanism (many in this volume), so I will not go over it again. Instead, I want you to keep in mind a third possibility, namely, that Nature has almost as much trouble exploding stars as numerical core-collapse codes do. It's possible that a significant fraction of all core collapses never produce an outgoing shock (by whatever mechanism) that is powerful enough to unbind the exterior layers of the star. Instead, a black hole forms, but *a strong neutrino signal is still observed until the hole swallows most of the mass of the star*. Neutrino signals from core-collapse, then, might occur at a significantly greater rate than Type II supernovae.

2. General relativistic hydrodynamics

The necessity for using general relativistic hydrodynamics was demonstrated in [5]. As Cooperstein and Baron [6] emphasize in a recent article, general relativity does two things: 1) "gravity is stronger," and more energy is released from the deeper potential well. This gives the shock more energy initially. However, 2) the size of the homologous core is reduced; the shock has to pass through more nuclear matter and dissociate more nuclei, and this hurts the shock as it moves out.

In any event, simply by computing the relevant dimensionless quantity for parameters typical of neutron stars, $GM/Rc^2 \gtrsim 0.1$, we find that relativity is obviously necessary once the core becomes a neutron star.

2.1. Preliminaries

I begin by writing a spherically symmetric metric in the form

$$\begin{aligned} ds^2 = &- (\alpha^2 - \beta^r \beta_r)dt^2 + 2\beta_r dr dt + \left(\frac{R'}{\Gamma}\right)^2 dr^2 \\ &+ R^2(d\theta^2 + \sin\theta^2 d\phi^2). \end{aligned} \tag{2.1}$$

Throughout we will assume spherical symmetry and use gravitational units ($G = c = 1$). Here r is any comoving coordinate (for example, the enclosed baryon number), α is the *lapse function*, β^r is the *shift vector*, and R is the *areal radius*, or the Schwartzschild radius such that the surface area of a sphere of radius R is $4\pi R^2$. The notation $' \equiv \partial/\partial r$ and, for future use, $\dot{} \equiv \partial/\partial t$.

Since the equations of general relativity are covariant, there is great freedom in the choice of both spatial and time coordinates to describe the physical process under investigation. We use, as does almost every relativistic code, the 3+1 formalism of Arnowitt, Deser, and Misner [7]. Spacetime is "sliced" into a set of spacelike hypersurfaces (upon which a computational coordinate grid will be placed), each labeled by a coordinate time t.

There are three choices of slicing which have been used in relativistic hydrodynamics codes. The most common, May and White slicing [8, 9], sets $\beta^r = 0$. (We sometimes call these "synchronous" coordinates, meaning that the metric has no off-diagonal $dr\,dt$ term.) This is the type of slicing used in all relativistic hydrodynamics codes which have been used to date to model core collapse and neutron star cooling calculations. For our purposes, however, this is an unacceptable choice, for as soon as a black hole and its enclosed singularity forms, the spacelike hypersurfaces "hit" the singularity and computation must cease.

The other two types of slicing avoid this problem. The one we use, polar slicing [10], sets $K^\theta_\theta + K^\phi_\phi = 0$, where K is the *extrinsic curvature tensor* and is essentially a measure of the curvature of the spacelike hypersurfaces (for more details, see [9], chapter 21). This slicing condition leads to the simple condition $\beta^r = \dot{R}/R'$, and has *strong singularity avoidance*. Nevertheless, the hydrodynamic (a subset of $T^{\mu\nu}_{;\nu} = 0$) plus geometric (a subset of $G_{\mu\nu} = 8\pi T_{\mu\nu}$) equations are all first order equations and are no more complicated to solve than the May and White equations. The region of space-time avoided is the entire region inside the event horizon, while all of space-time outside the horizon is covered.

The third major slicing condition, maximal slicing [11], sets $\mathrm{Tr}(K) = 0$. This also has the property of strong singularity avoidance, but the limit surface (the hypersurface with $t = \infty$) lies in part inside the event horizon. All of space-time outside the horizon is covered. Some of the equations are second order PDE's.

The choice of slicing is arbitrary so long as a black hole never forms. May and White slicing is entirely adequate for the stellar collapse problem and neutron star cooling, so long as a singularity never occurs. It was our desire to compute the neutrino signal from black hole formation that led us to use polar slicing. As I will now show, the set of equations we have to solve is no more complicated than the May and White equations.

2.2. The equations of polar sliced neutrino hydrodynamics

I will now briefly describe the specific equations of general relativistic polar sliced hydrodynamics (with neutrino transport terms included), which our code solves. Several of the quantities appearing in this section refer to neutrinos; these will be more fully described in section 3. These equations have already been published elsewhere [12, 13]. My purpose is to show those of you with experience in Newtonian hydrodynamics that the basic physics of these equations is the same; they're just the conservation laws (with conservation of baryon number replacing conservation of mass), plus some gravitational equations. For those of you who have seen the May and White equations, you will see how very similar the polar sliced equations are to those of May and White.

The lapse function α satisfies the equation

$$\frac{\alpha'}{\alpha} = \frac{R'}{\Gamma^2}\left[\frac{M}{R^2} + 4\pi R\left(\frac{\Gamma^2(P + P_\nu) + 2U\Gamma F_\nu + U^2(\rho + E_\nu)}{\Omega^2}\right)\right], \quad (2.2)$$

where $U \equiv \dot{R}/\alpha$, $\Omega^2 \equiv \Gamma^2 - U^2$ (Ω is just a generalization of the special relativistic γ), $M \equiv \frac{1}{2}R(1 - \Gamma^2)$ is the gravitational mass, P is the gas pressure, and ρ is the total energy density of the gas. The quantities P_ν, F_ν, and E_ν are the total neutrino pressure, flux, and energy density, respectively, due to all six types of neutrinos.

The field equations may be separated into evolution and constraint equations. The constraint equations must be satisfied on every spacelike hypersurface, and in particular, this means that initial data must satisfy the constraint equations. We use one constraint equation, the Hamiltonian constraint

$$M' = 4\pi R^2 R' \left(\frac{\Gamma^2(\rho + E_\nu) + 2U\Gamma F_\nu + U^2(P + P_\nu)}{\Omega^2} \right). \tag{2.3}$$

(Another constraint equation, known as the momentum constraint, may be written $\dot{M} = -4\pi\alpha R^2 R'(U(P + P_\nu) + \Gamma F_\nu)$, and is used as a numerical check on the solution. Note that at the surface of the star $P = 0$; this equation means that the star radiates mass as neutrinos leave the surface.)

The internal energy equation is

$$\dot{e} + P\dot{v} = -\frac{2\pi}{h^3}\frac{\alpha\Omega v}{\Gamma} \int dE \int d\mu E^3 \sum_{i=\nu_e,\bar{\nu}_e,\nu_\mu,\bar{\nu}_\mu,\nu_\tau,\bar{\nu}_\tau} (G_i - L_i f_i). \tag{2.4}$$

Here e is the internal energy density, $v = 1/\rho_0$ where ρ_0 is the baryon rest mass density (the baryon number density n_B multiplied by a constant baryon rest mass m_B). The total energy density $\rho = (1 + e)\rho_0$. The right hand side of (2.4) is the net rate at which energy is exchanged by the gas and neutrinos. The quantity E is the comoving neutrino energy; μ is a direction cosine with respect to the radial direction; G is a function describing the total rate at which neutrinos enter the small region of phase space around energy E and direction μ due to all processes; L describes all losses out of this element of phase space; and f is the neutrino phase space distribution function. G and L will be described in more detail in section 4.

Baryon number conservation requires

$$\frac{\partial}{\partial t}\left(\frac{\rho_0 R^2 R'}{\Omega}\right) = 0. \tag{2.5}$$

The momentum equation is

$$\begin{aligned} &\frac{P'}{R'} + \frac{\dot{P}U}{\alpha\Omega^2} + \frac{(\rho + P)\Gamma^2}{\alpha\Omega^4}\left(\dot{U} - U\frac{\dot{\Gamma}}{\Gamma}\right) \\ &\quad + \frac{(\rho + P)}{\Omega^2}\left(\frac{M + 4\pi R^3\left[P + P_\nu + \frac{U}{\Gamma}F_\nu\right]}{R^2}\right) \\ &= -\frac{2\pi}{h^3}\frac{1}{\Omega}\int\int dE d\mu\, E^3\mu \sum_{\text{types}}(G_i - L_i f_i), \end{aligned} \tag{2.6}$$

where the right hand side expresses the rate of exchange of momentum between the neutrinos and the gas. Note that in a static situation ($\partial/\partial t = 0$) with no neutrinos ($P_\nu = F_\nu = 0$, r.h.s. $= 0$), this reduces to the Tolman-Oppenheimer-Volkoff equation of hydrostatic equilibrium.

Electron lepton number conservation requires

$$n_B \frac{\partial Y_e}{\partial t} = -\frac{2\pi}{h^3}\frac{\alpha\Omega}{\Gamma} \int dE \int d\mu \, E^2 (G_{\nu_e} - L_{\nu_e} f_{\nu_e} - \bar{G}_{\nu_e} + \bar{L}_{\nu_e} \bar{f}_{\nu_e}). \quad (2.7)$$

The quantity $Y_e = (n_{e^-} - n_{e^+})/n_B$ is the net electron lepton number carried by electrons and positrons per baryon. Note that only ν_e and $\bar{\nu}_e$ occur in the exchange term on the right hand side. Because conditions during core collapse and neutron star cooling are such that heavy particles such as muons and tauons do not occur in significant numbers, μ and τ lepton numbers are identically zero, and ν_μ (ν_τ) is only emitted and absorbed paired with $\bar{\nu}_\mu$ ($\bar{\nu}_\tau$). The corresponding chemical potentials can always be described as $\mu_{\nu_\mu} = \mu_{\nu_\tau} = 0$.

2.3. Numerical techniques

I will now briefly describe the numerical technique we use to solve (2.2–2.7). Equations (2.4), (2.5), (2.6), and (2.7) are differenced fully implicitly [14]. Equations (2.2) and (2.3), which have no time derivatives, play the role of constraint equations, and are always evaluated at the current timestep. A staggered mesh is used, with geometric quantities (R, U, α, Γ, Ω) evaluated on zone boundaries; gas quantities (ρ, ρ_0, P) are evaluated on zone centers, F_ν is evaluated on the zone boundaries; and E_ν and P_ν on the zone centers. Neutrino quantities are assumed to be known and are not changed while the hydrodynamics equations are solved; this permits us to easily change the neutrino transport scheme if desired (in principle one should solve both the neutrino transport and hydrodynamics equations simultaneously, but we suspect, and will verify by numerical tests, that no significant error occurs in the quasi-static cooling of a neutron star because of this approximation). An artificial viscosity is added to the pressure ($P \to P + Q$ in (2.2–2.7)); it is only needed to prevent numerical instability if shocks occur. Q is zero if there are no shocks. We use the pseudo-tensor form of the artificial viscosity Q presented in [15]. The equations are non-linear, and for this reason the equations are linearized and iterated until a solution is found for the dependent variables P, ρ_0, U, R, α, Γ, and e. Because the equations are linearized, derivatives of equations (2.2–2.7) are needed with respect to all of the dependent variables. We take these derivatives numerically. In this way, differencing schemes for the equations may be changed with a minimum of fuss. An example of a "mock supernova" computed with our code may be found in [3]; this example shows the power of implicit differencing to compute accurately both the very dynamic core collapse phase and the quasi-static evolution which occurs afterward.

2.4. Summary

If the Type II supernova mechanism were purely or even largely hydrodynamic, we would now have detailed complete solutions for Type II supernovae. General relativistic hydrodynamics is a straightforward numerical task. It is only a little more difficult than Newtonian hydrodynamics, which is a mature, robust field of computational physics. Every group doing stellar core collapse computations has used numerical techniques which can compute the hydrodynamics accurately.

However, as Myra and Bludman [16] show, neutrino transport is of vital importance, even during the collapse phase. They further show that the details of the dynamics are sensitive to a process, neutrino-electron scattering, which is a minor part of the total neutrino interaction with the gas. The reason this sensitivity occurs is that (*a*) the change caused by neutrino-electron scattering is *secular*; once lepton number escapes from the star, it never returns, and (*b*) the core size is a *non-linear* function of the lepton number fraction Y_ℓ. Minor processes have potentially big effects, because these effects can be amplified by the non-linearity of the problem. Neutrino transport is even more vital for the delayed shock mechanism, because a tiny fraction of the total neutrino luminosity, preferentially taken from the high-energy part of the spectrum at energies above the luminosity peak, is captured to revive the shock. When one remembers that 99% of the total energy of collapse is eventually carried away by neutrinos, the importance of neutrino transport for the core-collapse/neutron star cooling process is obvious. I discuss neutrino transport equations in the following section.

3. General relativistic neutrino transport

3.1. The role of neutrinos

For those of you who have done photon transport, much of what I'm about to present will be familiar, at least in part. The essence of the problem of neutrino transport in supernovae and neutron stars is the same as photon transport in a star or a planetary atmosphere. We must transport massless particles which have mean free paths much longer than the mean free paths of constituent particles in the gas; long enough, in fact, that the mean free path near the surface is a significant fraction of the radius of the star. Because of the long mean free paths, the distribution functions (intensities) of those particles are anisotropic. Nevertheless, they interact with the gas frequently enough that they don't just escape to infinity from the point at which they are produced.

However, there *are* significant differences between photon transport and neutrino transport, and those differences have to do with both the physical differences between neutrinos and photons, and the conditions under which neutrinos find themselves in a core collapse or neutron star. Neutrinos are fermions (spin $\frac{1}{2}$ particles). Because of the Pauli exclusion principle, neutrinos cannot simultaneously occupy the same states in phase space. This causes phase space blocking, sometimes called "stimulated absorption" in analogy with the stimulated emission which bosons undergo. Since neutrinos in stellar cores can and do become degenerate, phase space blocking must be built into the interaction terms on the right-hand side of the transport equation; the transport equation becomes non-linear. Neutrinos do not interact electromagnetically, but only via the weak interaction. Not only are their cross-sections different in detail than photon cross-sections, but they are much smaller as well. A typical neutrino cross-section goes something like $\sigma \sim 10^{-44}(E/m_e)^2$ cm^2, where E is the neutrino energy and m_e is the mass of the electron. There are six "types" of neutrinos: ν_e, $\bar{\nu}_e$, ν_μ, $\bar{\nu}_\mu$, ν_τ, $\bar{\nu}_\tau$, all of which must be included in the calculation of neutron star cooling. Each of these neutrinos carries a conserved lepton number. Electron, μ, and τ lepton numbers are separately conserved. ν_e and $\bar{\nu}_e$ can exchange lepton numbers with electrons and positrons in the gas, while $\nu_{\mu,\tau}$ and $\bar{\nu}_{\mu,\tau}$ are only produced paired together, because there are no μ's or τ's in the gas ($m_{\mu,\tau} > T$). The net μ and τ lepton numbers are always zero.

Why do neutrinos play such an important role in stellar collapse? Photons are produced in stellar collapse as well, but they quickly reach thermal equilibrium distributions because they are very effectively trapped, have an extremely high optical depth, and cannot carry energy away from the star on dynamic (millisecond) timescales. Neutrinos have cross-sections small enough to leave the star rapidly (they diffuse out on timescales of seconds), but large enough to be produced in abundance. In fact, in the interior of the collapsing core the neutrinos reach thermal and chemical equilibrium.

3.2. The neutrino transport equations

I have derived the relativistic neutrino transport (Boltzmann) equations in polar sliced space-time in [13]. In this section I present the key equations from that paper.

The neutrino transport results in polar sliced comoving coordinates are

$$
\begin{aligned}
&\left\{ \left[\frac{\Gamma}{\alpha \Omega} \left(1 + \mu \frac{U}{\Gamma} \right) \right] \frac{\partial}{\partial t} \right. \\
&+ \frac{\Omega}{R'} \mu \frac{\partial}{\partial r} \\
&- \frac{E \Gamma}{\alpha \Omega} \left[\mu A + \mu^2 B + \frac{\alpha U}{R} (1 - \mu^2) \right] \frac{\partial}{\partial E} \\
&\left. - (1 - \mu^2) \frac{\Gamma}{\alpha \Omega} \left[A - C + \mu B - \mu \frac{\alpha U}{R} \right] \frac{\partial}{\partial \mu} \right\} f(E, \mu) \\
&= G(E, \mu; f, \bar{f}) - L(E, \mu; f, \bar{f}) f(E, \mu),
\end{aligned} \tag{3.1}
$$

where μ is the direction cosine to the radial direction as seen by an observer comoving with the gas, E is the neutrino energy as seen by a comoving observer, and f is the neutrino phase space distribution function,

$$
\begin{aligned}
A &\equiv \Gamma \frac{\alpha'}{R'} - \frac{U}{\Gamma} \left(\frac{\dot{\Gamma}}{\Gamma} - \frac{\alpha U}{R'} \frac{\Gamma'}{\Gamma} \right) + \frac{U \Gamma}{\Omega^2} \left(\frac{\dot{U}}{U} - \frac{\dot{\Gamma}}{\Gamma} \right), \\
B &\equiv - \frac{\dot{\rho}_0}{\rho_0} - \frac{2 \alpha U}{R}, \\
C &\equiv \frac{\Gamma \alpha}{R}.
\end{aligned} \tag{3.2}
$$

What does eq. (3.1) mean physically? Much of the apparent complexity is due to effects that have a simple physical explanation. The coefficient of $\partial / \partial t$ includes effects of both motion of the fluid and gravitation. The coefficient of $\partial / \partial r$ includes both length contraction and the static flat space result that the path length traveled by the neutrino $\Delta s = \Delta r / \mu$. The coefficient of $\partial / \partial \mu$ would be simply $(1 - \mu^2)/R$ in static flat space due entirely to the spherical geometry, for the direction cosine μ changes automatically as the neutrino follows its geodesic (which is straight in flat space). The additional terms are aberration effects due to both gravitation and fluid motion. The coefficient of $\partial/\partial E$ describes change in the energy of the neutrino due to the relative motion of comoving observers and due to gravitational effects.

The use of comoving coordinates here is deliberate. One reason is simply that these are the coordinates we use to solve the hydrodynamics, and using the same coordinates allows us to avoid doing constant coordinate transformations; it also allows us to avoid maintaining two different grids, difficult even in flat space. The other, more fundamental, reason for the use of comoving coordinates is that the collision term on the right-hand side of eq. (3.1) is simplest in the comoving frame, because the functions G and L involve integrals over the distribution functions of gas components which are isotropic *only* in the comoving frame.

I now define the angular moments

$$\{J, H, K, M\} = 2\pi \int_{-1}^{1} d\mu \{1, \mu, \mu^2, \mu^3\} E^3 f. \tag{3.3}$$

The first two moments of (3.1) may be written

$$\begin{aligned} &\frac{\partial R^2 J}{\partial t} + \frac{\Omega}{R'}\left[\frac{\partial}{\partial t}\left(\frac{U R^2 R' H}{\Omega \Gamma}\right) + \frac{\partial}{\partial r}\left(\frac{\alpha \Omega R^2 H}{\Gamma}\right)\right] \\ &\quad - E R^2 \left[\frac{\alpha U}{R}\frac{\partial J}{\partial E} + A\frac{\partial H}{\partial E} + \left(B - \frac{\alpha U}{R}\right)\frac{\partial K}{\partial E}\right] \\ &\quad + B R^2 J = \frac{2\pi R^2 \alpha \Omega}{\Gamma}\int_{-1}^{1} d\mu E^3 (G - Lf), \end{aligned} \tag{3.4}$$

$$\begin{aligned} &\frac{\partial R^2 H}{\partial t} + \frac{\Omega}{R'}\left[\frac{\partial}{\partial t}\left(\frac{U R^2 R' K}{\Omega \Gamma}\right) + \frac{\partial}{\partial r}\left(\frac{\alpha \Omega R^2 K}{\Gamma}\right)\right] \\ &\quad - E R^2 \left[\frac{\alpha U}{R}\frac{\partial H}{\partial E} + A\frac{\partial K}{\partial E} + \left(B - \frac{\alpha U}{R}\right)\frac{\partial M}{\partial E}\right] \\ &\quad + (A - C) R^2 (J - K) + \left(2B - \frac{\alpha U}{R}\right) R^2 H \\ &\quad - \left(B - \frac{\alpha U}{R}\right) R^2 M \\ &= \frac{2\pi R^2 \alpha \Omega}{\Gamma}\int_{-1}^{1} d\mu\, \mu E^3 (G - Lf). \end{aligned} \tag{3.5}$$

Note that integrating (3.1) over any power μ^n always produces the moment with μ^{n+2}. Therefore, the process of constructing moment equations can go on endlessly; the transport equation can never be replaced by a finite set of moment equations. However, we can *formally* close the moment equations by defining the *Eddington factors* $f_H = H/J$, $f_K = K/J$, $f_M = M/J$. Because we will be using the two moment equations, (3.4) and (3.5), we will need f_H only at the surface of the star, where it is needed for the boundary condition ($H = 0$ at $r = 0$ and at the surface $H = f_H J$).

3.3. The variable Eddington factor method

The transfer equation (3.1) is a formidable equation to solve. Even with spherical symmetry, it is a three dimensional (E, μ, r) time-dependent non-linear integro-differential equation. The moment equations (3.4) and (3.5) are easier to solve, since one dimension (μ) is integrated away. Furthermore, we find everything we need to solve the neutrino hydrodynamics equations (2.2–2.7) by solving the moment equations

$$E_\nu = \sum_{\text{types}} J_i,\ F_\nu = \sum_{\text{types}} H_i,\ P_\nu = \sum_{\text{types}} (f_K J)_i,$$

and the right-hand sides that appear in eqs. (3.4) and (3.5) also appear in (2.4) and (2.6). However, there are two problems: first, we don't know the Eddington factors necessary to form a closed set from (3.4) and (3.5), and second, we need to know the distribution function f in any event to find the source/sink terms on the right-hand sides of eqs. (3.4) and (3.5).

There are two ways we can find the Eddington factors. One is to "guess"; choose by some prescription functions $f_K(H, J)$, $f_M(H, J)$ (and at the surface f_H). Now the moment equations are closed, and although non-linear, they may be solved provided the r.h.s. are known. Such functions have been proposed, ranging from simple linear interpolations between free streaming ($f_K = f_M = 1$) and diffusion ($f_K = 1/3$, $f_M = 0$) limits [17], to more sophisticated formulae based on the "maximum entropy" method [18,19]; Fu's work [19] is particularly intriguing. However, as we discovered [20], these formulae are not all that accurate when compared with exact analytic or numerical solutions, and in any event the physical basis for the choice of angular distribution functions in maximum entropy derivations is obscure.

For this reason, although we plan to try several of these guesses, we desire a more reliable prescription for finding f_K and f_M.

The *most* reliable technique is, of course, to solve (3.1) with no approximations. Then one simply takes the moments of the distribution function f and has the Eddington factors directly. Of course, there is no reason to solve (3.4) and (3.5) once the solution to (3.1) is known, since all moments are also known once $f(E, \mu)$ is known. Solving (3.1) directly is, in my opinion, at the very limit of what can be done by current supercomputers, when the equation is solved dynamically coupled with the hydrodynamics equations. This work is currently being done by Mezzacappa [21]. His work will provide rigorous, realistic solutions which can be used to finally find out how well the transport approximations used until now have actually succeeded, and whether or not they have missed any interesting, and possibly dynamically important, subtleties of the physics of neutrino transport during core collapse.

The method that we have chosen, the *variable Eddington factor* [15] method, does not have the rigor of a full transport solution but avoids the uncertainties of more common methods of approximation used in stellar collapse and neutron star cooling codes, and has error checks built into the technique. It is not a full solution of equation (3.1); an approximation to (3.1) (with only the right-hand side approximated) is used to find the variable Eddington factors. These factors are used in eqs. (3.4) and (3.5) to find trial solutions J and H, and the entire set (3.1) (with the approximate r.h.s.), (3.4) and (3.5) is iterated until a self-consistent solution is found. Justifications for this technique are sometimes based on the fact that only a ratio of moments is needed to find f_K and f_M, and such ratios are unchanged by, for example, a scaling error in the distribution function f. Thus one expects that the errors in f_K and f_M are not as large as errors in the distribution function f itself. However, I feel the most compelling justification is that accurate solutions to test problems with both known analytic and numerical solutions can be obtained with this technique. The numerical technique *works*, at least for these test problems, and the errors can be quantified. In the end, of course, we would like to compare our solution with real neutrino physics – and with Mezzacappa's Boltzmann equation solution.

The reason (3.1) is so numerically time-consuming is that the integrals on the right-hand side couple all energy and angular bins at a given radius. The transport equations must be solved implicitly. A timestep limit analogous to the hydrodynamic Courant time also exists for the neutrino transport equation. If the equations were solved explicitly, enormously small timesteps capable of accurately tracking the evolution of the highest energy neutrinos would have to be used. Since nothing of interest occurs on these timescales (the energy density of neutrinos as a whole evolves on much longer timescales, similar to the timescales which are typical of a neutrino at the average energy) we must be able to exceed this timestep restriction. This means, however, that a large matrix equation must be solved at each timestep. Efficient techniques [21] can be found to solve this matrix equation, but it is still time consuming.

If we somehow knew the right-hand side of (3.1), then this difficulty disappears. The left-hand side of (3.1) contains only derivatives and couples together adjacent bins only, so an implicit solution with a known right-hand side is much less time consuming. In addition, by making coordinate transformations in *momentum* space and using the constants of the motion of neutrinos [20], the left-hand side can be simplified. So the first approximation I make is to expand G and L in low order Legendre expansions $G = \sum_{j=0}^{2} G_j(E)P^j(\mu)$, $L = \sum_{j=0}^{2} L_j(E)P^j(\mu)$, where P^j is the jth Legendre polynomial. (I find that this is an excellent approximation for all neutrino processes except neutrino electron scattering, where it can occasionally be seriously in error.) The r.h.s. is now a known function, using currently known values of J, H, and f_K; and it becomes comparatively very easy to solve (3.1) for f. The functions L_j and G_j, which are integral functions of f, are evaluated using a similar low-order Legendre expansion of the scattering and pair production-absorption kernels (see section 4). Once f is known, the Eddington factors may be found by quadrature. Then eqs. (3.4) and (3.5) are solved for the moments J and H. The algorithm is repeated, and eqs. (3.1), (3.4), and (3.5) are iterated until a converged solution is obtained.

In order to make the computation of (3.1) even simpler for a neutron star, we will initially make the approximation that neutron star cooling is quasi-static, and we make the approximation in (3.1) that the background space-time is *static*. Details of this approximation, along with simple analytic transport test problems for relativistic spherically static space-times may be found in [20]. In that paper we show that the variable Eddington factor technique works extremely well for these test problems.

3.4. Other transport treatments

A variety of approximate treatments of neutrino transport have been used in stellar collapse and neutron star cooling codes. Of all these approximations, only one, the multi-group flux limited diffusion approximation, allows calculation of neutrino spectra at infinity. In this section, then, I will briefly describe the flux-limited diffusion approximation (FLDA), which is the current "industry standard," and give you the reasons why we do not use it in our code.

A good description of the FLDA along with a critique, can be found in [15]. In its most common form, the FLDA is a single diffusion-like equation for the neutrino flux H. The diffusion coefficient is chosen to make this equation look like the diffusion approximation for large optical depths $\tau \gg 1$, and the free streaming approximation ($H \propto r^{-2}$) for small optical depths $\tau \ll 1$. In some sense, this equation "interpolates" between the diffusion equation and the free streaming equation.

I've often heard it said of the flux-limited diffusion approximation that it is "correct in both limits." However, while it is true that the flux-limited diffusion *equation* is correct in both limits, *this is not necessarily true of the solution.* In particular, imagine you are solving the free streaming equation in the optically-thin region of the star. You will quickly realize that you need an inner boundary condition. In flux-limited diffusion, this boundary condition is provided by the solution to the diffusion approximation in the interior, which must first pass through a transition region where the FLDA is neither the diffusion equation, the free streaming equation, or a good approximation to the Boltzmann equation. Errors of unknown size will occur in the transition region. These errors are then (correctly) propagated by the free streaming equation in the exterior. No "healing" can occur, since the free streaming equation has no way of knowing what the correct interior boundary condition should be; the best that can be said is that the error will not get any worse. In neutrino transport, this failure is complicated by the fact that different neutrino energies can potentially have transition regions in different parts of the star.

In short, the flux-limited diffusion approximation (*a*) cannot be derived as an approximation to the Boltzmann equation, (*b*) produces errors of unknown size. The few attempts to test the FLDA that I've seen [22, 23, 24], show, in my opinion, that it does not work very well. Of particular interest with respect to neutrino transport are the tests shown in [23, 24], where the deviations are, to my eye, large.

4. Neutrino interactions with the gas

4.1. The basic neutrino interactions

Neutrino interactions may be divided into three basic types. These three different types of interactions have fundamentally different effects on neutrino transport. The first type, neutrino scattering reactions, are those reactions where one neutrino is in both the initial and final state. These reactions can be further subdivided. In the "elastic" scattering reactions (ν scattering off of n (neutrons), p (protons), or A (nuclei)), the change in energy of the neutrino $\Delta E/E \propto E/m$, where m is the mass of the scattering particle. Since m is at least 1 GeV, the change in energy is typically quite small. ν-e, scattering, however, is characterized by large energy transfers in a single scattering, since $m_e = 0.511$ MeV $< E$ typically. Thus, while ν-nucleon scattering basically serves as a source of opacity, keeping the neutrinos trapped (ν-A scattering is the dominant reaction, since the interaction is coherent and is $\propto A^2$ [25]), ν-e scattering plays an active and important [16] role in exchanging energy with the gas, and so helps drive the neutrinos toward thermal equilibrium.

The β processes are those in which a neutrino is only on one leg of the Feynman diagram, and only ν_e and $\bar{\nu}_e$ participate. The basic processes are $n+\nu_e \leftrightarrow p+e^-$ and $n+e^+ \leftrightarrow p+\bar{\nu}_e$. These reactions exchange both energy and electron lepton number between neutrinos and the gas, and so are important factors in establishing both thermal and *chemical* equilibrium. These processes can occur either on free nucleons or nucleons in nuclei; however, shell-blocking effects usually significantly alter the interaction rates in nuclei. Neutrino capture on protons in nuclei is effectively shut off once $N > 40$ [26]. More exotic processes, for example, the URCA processes, which play an important role in neutron star cooling once the neutrons become degenerate, are unimportant here because nucleons are at most mildly degenerate in a hot neutron star.

The third class of neutrino interactions are those in which two neutrinos occur in either the initial or final state, the pair production-absorption processes. These are sometimes called "thermal" processes, but this means *only* that this process becomes important at high temperature, when significant numbers of pairs are found. It does *not* mean that the neutrino pairs are emitted with thermal (Fermi-Dirac) distributions. Only $e^+ - e_-$pairs occur in significant numbers in the gas, because of their low mass, and so only electron pairs are created and annihilated; they, however, produce all three flavors of neutrino pairs. Because electrons can become degenerate, a more exotic pair process can also be important. This process, the *plasmon* process [27], is due to the decay of plasmons (collective excitations of the electron gas). A plasmon to good approximation behaves just like a massive photon. Although it is ordinarily down by roughly a factor of $1/137$ from the $e^+ - e^-$ pair process, the plasmon process does operate when electrons are degenerate. The plasmon process is, in any event, usually only a minor interaction.

4.2. The interaction functions G and L

Quite generally, G and L may be written for a given flavor of neutrino

$$G = \mathcal{E} + \frac{1}{\hbar^3}\int_0^\infty dE' \int_{-1}^{1} d\mu' E'^2 \{R_s(E, E', \mu, \mu') f(E', \mu') + R_e(E, E', \mu, \mu')(1 - \bar{f}(E', \mu'))\}, \tag{4.1}$$

$$\begin{aligned} L = \mathcal{A} + \mathcal{E} + \frac{1}{\hbar^3}\int_0^\infty dE' \int_{-1}^{1} d\mu' E'^2 \{ & \\ & [R_s(E', E, \mu', \mu) - R_s(E, E', \mu, \mu')] f(E', \mu') \\ & + R_s(E, E', \mu, \mu') \\ & + [R_a(E, E', \mu, \mu') - R_e(E, E', \mu, \mu')]\bar{f}(E', \mu') \\ & + R_e(E, E', \mu, \mu')\}. \end{aligned} \tag{4.2}$$

Similar expressions exist for the antineutrinos. In eqs. (4.1) and (4.2), $\mathcal{E}$ is the emissivity and $\mathcal{A}$ is the absorptivity which describe all processes which inject or extract net lepton number into or from the gas (the β processes). R_s describes all scattering processes. R_e is the pair emission function, and R_a the pair absorption function.

It can be shown that several Kirchoff type relations connect these functions. $\mathcal{E} = \exp[-(E - \mu_\nu)/T]\mathcal{A}$, where $\mu_\nu \equiv \mu_p + \mu_e - \mu_n$ and the μ's are chemical potentials including rest masses. This means that the β processes drive the neutrinos to an equilibrium Fermi-Dirac distribution at the local temperature and neutrino chemical potential. For scattering, $R_s(E, E', \mu, \mu') = \exp[(E - E')/T]R_s(E', E, \mu', \mu)$; from this it is easy to show that the scattering pieces of the right-hand side of equation (3.1) vanish whenever f and $\bar{f}$ are Fermi-Dirac distributions with any neutrino chemical potential. Scattering (exclusively electron scattering since the energy exchanged by neutrino-nucleon scattering is negligible) will drive neutrinos and antineutrinos into thermal, but not chemical, equilibrium. The pair absorption and emission functions are related by $R_e = \exp[-(E + E')/T]R_a$, and this is all that is necessary for the pair emission-absorption functions to vanish when the neutrino and antineutrino distribution functions are Fermi-Dirac distributions at *zero* chemical potential. Pair processes, then, also help thermalize the neutrinos, but in addition to drive the neutrino chemical potential to zero, in competition with the β processes.

Detailed expressions for the interaction functions may be found in the literature [24, 28, 29, 30].

5. Conclusion

The code which implements the physics described above has been built; barring unanticipated difficulties, we should have several neutron star cooling models within the next six months.

The reader may wonder by now why insistence on numerically verified codes and accurate neutrino physics in this paper, with consequent need for large amounts of computer time to obtain a solution. The answer is simple: twenty-five years after Colgate and White, we still don't know the mechanism for Type II supernovae, although much of importance has been learned. One of the major contenders has died (the prompt mechanism), at least for now; and the other (the delayed mechanism) is, at this date, still seen by only one code and has not been verified by any others. Indications are that the delayed mechanism is sensitive to numerical details and minor changes in the physics. In these circumstances, without useful observational checks or constraints on the codes, codes *must* be shown to be reliable, and physics must be done as accurately and realistically as possible. Approximations that are known to be poor, for instance, the FLDA, or the common use of a Fokker-Planck approximation for electron scattering [31], must be discarded. It is only in this way that real uncertainties in the physics of Type II supernovae can be separated from purely numerical inaccuracies or the consequences of poor approximations. There is enough uncertain physics in this problem (for example, the high density EOS) that adding any unnecessary approximations may well obscure or cover completely the essential physics of the Type II supernova mechanism.

References

[1] Bludman, S.A. and P.J. Schinder, *Ap. J.*, 326: 265.

[2] Swesty, F.D. and J. Lattimer, in preparation.

[3] Frontiers in Numerical Relativity, 1989. C.R. Evans, L.S. Finn, and D.W. Hobill, eds. Cambridge University Press.

[4] Centrella, J.M., S.L. Shapiro, C.R. Evans, J.F. Hawley, and S.A. Teukolsky, 1986. Dynamical Spacetimes and Numerical Relativity, J.M. Centrella, eds. Cambridge University Press.

[5] E. Baron, Ph.D. thesis, State University of New York at Stony Brook, 1985; E. Baron, J. Cooperstein, and S. Kahana, *Nucl. Phys.*, A440, 744; *Phys. Rev. Lett.*, 55, 126.

[6] Cooperstein, J. and E.A. Baron. 1990. Supernovae, A.G. Petscheck, ed. Springer-Verlag.

[7] Arnowitt, R., S. Deser, and C.W. Misner. 1962. Gravitation: An Introduction to Current Research, L. Witten, ed. Wiley.

[8] May, M., and R.H. White, *Phys. Rev.*, 141, 1232; *Methods Comput. Phys.*, 7, 219.

[9] Misner, C.W., K.S. Thorne, and J.A. Wheeler. 1973. Gravitation. W. H. Freeman and Co.

[10] Bardeen, J.M., and T. Piran, *Phys. Rep.*, 96, 205.

[11] Recent works using maximal slicing include C.R. Evans, Ph.D. thesis, University of Texas at Austin, 1980; A. Mezzacappa and R.A. Matzner, *Ap. J.*, 343: 853.

[12] Schinder, P.J., S.A. Bludman, and T. Piran, *Phys. Rev. D*, 37, 2722.

[13] Schinder, P.J., *Phys. Rev. D*, 38: 1673.

[14] Press, W.H., B.P. Flannery, S.A. Teukolsky, and W.T. Vetterling. 1986. Numerical Recipes: The Art of Scientific Computing. Cambridge University Press.

[15] Mihalas, D. and B.W. Mihalas. 1984. Foundations of Radiation Hydrodynamics. Oxford University Press.

[16] Myra, E. and S.A. Bludman, *Ap. J.*, 340: 384.

[17] Auer, L.H. 1984. Methods in Radiative Transfer, W. Kalkofen, ed. Cambridge University Press.

[18] Minerbo, G.N., *J. Quant. Spectrosc. Rad. Transf.*, 20: 541.

[19] Fu, A., *Ap. J.*, 323: 211; A. Fu, *Ap. J.*, 323: 227.

[20] Schinder, P.J. and S.A. Bludman, *Ap. J.*, 346: 350.

[21] Mezzacappa, A., in preparation.

[22] Levermore, C.D. and G.C. Pomraning, *Ap. J.*, 248: 321.

[23] Mayle, R., J.R. Wilson, and D.N. Schramm, *Ap. J.*, 318: 288.

[24] Bruenn, S.W., *Ap. J.*, Suppl. 58: 771.

[25] Freedman, D.Z., *Phys. Rev. D*, 9: 1389.

[26] Fuller, G.M., W.A. Fowler, and M.J. Newman, *Ap. J.*, 252: 715; G.M. Fuller, *Ap. J.*, 252: 741.

[27] Adams, J.B., M.A. Ruderman, and C.H. Woo, *Phys. Rev.*, 129: 1383; M.H. Zaidi, *Nuovo Cimento*, 40a: 502.

[28] Bond, J.R., Ph.D. thesis, California Institute of Technology, 1978. This is, in my opinion, the best single reference because Bond considered all processes and all aspects of neutrino interactions with matter, including the effects of nucleon-nucleon interactions and other collective effects.

[29] Schinder, P.J. and S.L. Shapiro, *Ap. J.*, Suppl. 50: 23.

[30] Schinder, P.J., *Ap. J.*, Suppl. 74: 249.

[31] Tubbs, D.L., T.A. Weaver, R.L. Bowers, J.R. Wilson, and D.N. Schramm, *Ap. J.*, 239: 271; this paper is often cited in support of using a Fokker-Planck approximation for electron scattering, but, in fact, concludes that Fokker-Planck cannot be fit to the exact results.

SEMINAR 3

THE CHEMICAL EVOLUTION OF THE GALAXY

R. SCHAEFFER

Service de Physique Théorique
CEN Saclay, F-91191 Gif-sur-Yvette Cedex, France

S. Bludman, R. Mochkovitch and J. Zinn-Justin, eds.
Les Houches, Session LIV, 1990
Supernovae

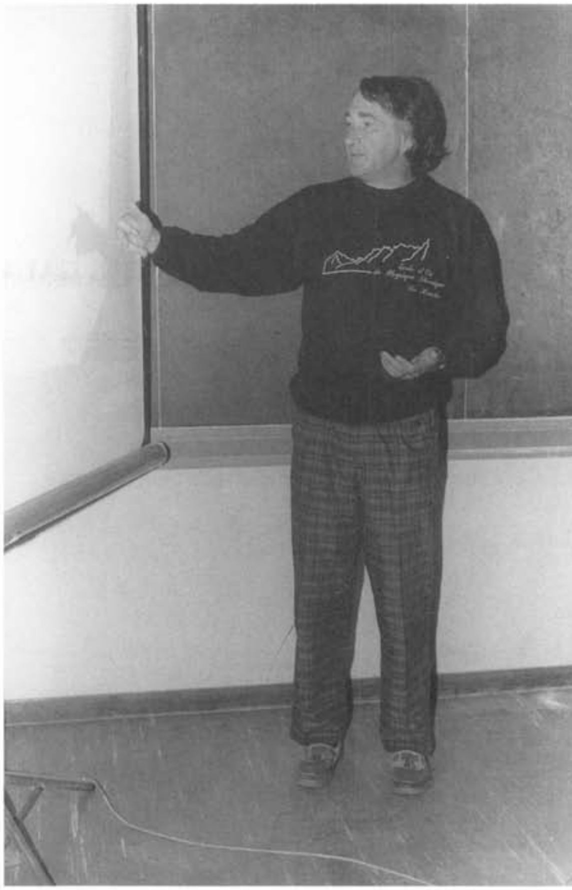

Contents

1. Introduction 812
2. Modelling galactic chemical evolution 814
   2.1. Star formation 814
   2.2. Supernova rate 814
   2.3. Evolution equation 815
3. The sources of metals 816
   3.1. Mass ejection by winds 816
   3.2. Type I supernovae 816
   3.3. Type II supernovae 817
   3.4. Peculiar types of supernovae 817
4. History of galactic evolution modelling. Role of the supernovae. 820
References 823

1. Introduction

Chemical evolution is not independent of the history and formation process of our galaxy (e.g. see the reviews by Trimble 1975, Audouze and Tinsley 1976, Truran 1984, Gilmore 1989). It is generally agreed that galaxies formed from the collapse of chemically unprocessed gas (except for the elements D, He, Li made during the Big Bang) at an epoch when the universe was much younger ($\sim 10^8 - 10^9$y) than present (a few 10^{10}y). Star formation is expected to occur between the collapse epoch and now. For our galaxy, this process is quite slow: a sizeable fraction of gas is still observed in our neighbourhood, and stars of all ages are seen to populate the disk of our galaxy. These stars evolve and synthesize all elements, from helium up to iron. The elements eventually are recycled by stellar winds and by supernovae, enriching the remaining gas. The evolution of "metallicity" (which in principle is the relative abundance of carbon and all heavier elements but is often taken — as we shall do here — to be the iron abundance $[\mathrm{Fe/H}] = \log \frac{(\mathrm{Fe}/H)}{(\mathrm{Fe}/H)_{\odot}}$) thus plays the role of a clock that traces time evolution.

Two major phases are to be distinguished in the evolution of a spiral galaxy. Just after collapse, the galaxy is spheroidal. There is some time for stellar evolution to process the gas before a disk forms. Whereas the enriched gas in which dissipative processes occur eventually ends up in the disk, stars made during this period stay in the halo. Some of these halo stars (the less massive ones, whose lifetime is quite long) still exist nowadays and form the population of the globular clusters. This scenario heavily hinges on the observation of systematically low metallicity of globular cluster stars, ($[\mathrm{Fe}/\ H] < -1$), whereas there are no low-metallicity stars in the disk (Zinn 1985). This can be explained by a halo-disk scenario, in which the halo stars were made at an early epoch from gas that was only partially enriched, whereas the disk stars were made subsequently. For simplicity, the halo phase is usually ignored. Early models (Searle and Sargent 1972) treat the disk as a closed box. In more recent calculations, the need of some influx of gas during the evolution of the disk is recognized (Mayor and Vigroux 1981, Chiosi and Matteucci 1982, Lacey and Fall 1985). This avoids modelling the disk formation and allows some freedom in the initial conditions. It should be considered as the standard procedure in these matters. Some authors (Hartwick 1976, Searle and Zinn 1985, Rocca-Volmerange and Schaeffer 1990, see also Pagel 1991) model the whole galactic evolution. This is one illustration of how important an accurate chemical evolution model will be in pinning down the history of our galaxy.

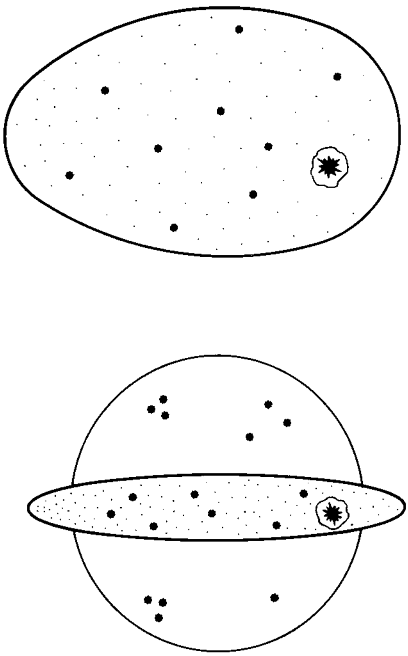

Fig. 1. Schematic evolution of our galaxy. In a first phase (top), star formation and SN recycling occurs in a nearly spheroidal mass condensation. The enriched gas settles eventually (bottom) in the disk, while the stars made during this first period remain in the halo. In the second phase, star formation and gas processing are restricted to the disk. There are thus only poor metallicity stars in the halo, and only enriched stars in the disk. The metallicity at which the transition occurs measures the epoch of the formation of the disk.

Separate consideration of the major elements C, O, Si, Fe brings in much richer constraints, provided their evolution can be sufficiently well modelled. Apart from the important calculation of the yield of these elements as a function of star mass and the rate of supernova explosions, a major step in the understanding of galactic chemical evolution is the knowledge, for each type of supernovae, of the explosion mechanism and kind of star the SN event is associated with.

2. Modelling galactic chemical evolution

2.1. Star formation

The number of stars with mass between m and $m + dm$ born during the time dt can be written

$$dN(m) = \quad (m)\,{}_*(t)\; d\log m\; dt. \qquad (1)$$

The "initial mass function" (m) gives the relative proportions of the stars of various masses made in that process. In principle (m) may depend on time. For simplicity, this is usually ignored. The second factor ${}_*(t)$ is the star formation rate. The latter obviously is expected to grow with the gas fraction that is available. Since the latter depends on time, ${}_*$ is also time-dependent. It is usually parametrized as

$${}_*(t) = \quad {}^{n}(t), \qquad (2)$$

where the "astration rate" is a constant, is the gas fraction which is available at time t and n (usually equal to unity) a parameter that reflects our prejudice on how star formation occurs.

The initial mass function has been the object of numerous studies. It may be derived from the observed star counts (Salpeter 1955, Miller and Scalo 1979, Scalo 1986) and is usually parametrized (fig. 2) by several power-laws with different exponents for low, intermediate and large masses.

2.2. Supernova rate

The theoretical study of stellar evolution provides for a mass-dependent lifetime t_m for each star.

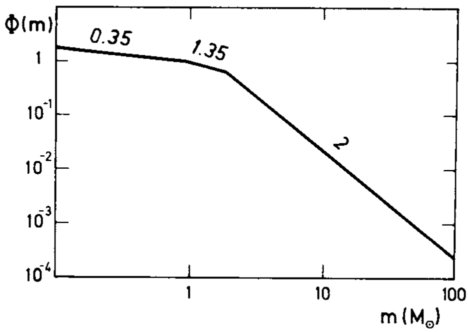

Fig. 2. Distribution of newly born stars as a function of mass ("Initial Mass Function"). This function is usually parametrized by successive power-laws in various mass intervals. Here $\Phi(m) \propto m^{-0.35}$ for the lower masses, $\Phi(m) \propto m^{-1.35}$ for ~ 1 $M_\odot$ stars and $\Phi(m) \propto m^{-2}$ for the larger masses.

The rate of (Type II) supernova explosions is then

$$\mathrm{SNR}(t) = \int \Phi(m)\tau_*(t - t_m)\, d\log m. \tag{3}$$

The present frequency of supernovae explosions determines the astration rate ν. Then, eq. (3) can be used to determine the rate of explosions in the past.

The modelling of Type I supernovae can be done in a similar way, but is somewhat more complicated since it involves, as discussed below, the counts of binary stars. Again the presently observed frequency of events is sufficient to determine counts in the past (Greggio and Renzini 1983, Matteucci and Greggio 1986).

2.3. Evolution equation

The gas fraction is readily estimated to be a balance between the fraction that disappears due to star formation and the one that is recycled by supernovae:

$$\frac{d\sigma}{dt} = -\tau_*(t) + \int E(m)\Phi(m)\tau_*(t - t_m) d\log m, \tag{4}$$

where $E(m)$ is the mass ejected by a star of initial mass m. It is typically taken to be

$$E(m) = m - 1.4\ M_\odot \qquad m > 5\ M_\odot,$$

to account for the 1.4 $M_\odot$ white dwarf or the neutron star left over by these stars, and

$$E(m) = 0.83m - 0.55\ M_\odot \qquad m < 5\ M_\odot,$$

since, due to winds and instabilities, the white-dwarf remnant has less than 1.4 $M_\odot$ in this case.

The chemical abundance X_i of element i is then seen to evolve as

$$\frac{d\ X_i\sigma}{dt} = -X_i\tau_*(t) + \int E_i(m)\Phi(m)\tau_*(t - t_m)d\log m.$$

Again, the yield of element i by a star of mass m is estimated as a result of a stellar evolution calculation. Estimates for yields according to stellar masses have been made by various authors, and will be discussed in the next section.

3. The sources of metals

3.1. Mass ejection by winds

Stars with initial mass below, say, 8 $M_\odot$ end up their life as 1.4 $M_\odot$ white dwarfs. During their red giant phase, they develop a large envelope that, at the He($\longrightarrow C$) burning stage is ejected due to instabilities. This is the major source of elements such as C, O (Iben and Truran 1978, Renzini and Voli 1981).

3.2. Type I supernovae

Type I supernovae are recognized by the absence of hydrogen in the ejecta. For this reason, the progenitors are believed to be white dwarfs. Although other models have been proposed, the standard explanation is that a white dwarf in a binary accretes matter from its younger companion and collapses when its mass reaches the Chandrasekhar limit. There is only a small fraction of close binaries where this process is effective, explaining why only a very small fraction of white dwarfs explode as supernovae.

Explosion models have been made by Nomoto, Thieleman and Yokoi (1984), who give convincing arguments why nearly all the matter in the exploding C,O white dwarf is converted into Fe, the most stable element in Nature. Elements such as O, Mg, Si are also produced. The radioactive decay of Ni into Fe provides a light curve which yields very accurate measurements of the mass of Fe ejected by an SN I.

3.3. Type II supernovae

Stars above 8 $M_\odot$ are believed to develop a $\sim 1\ M_\odot$ degenerate core that eventually becomes unstable and collapses to a neutron star. The remainder of the star is expelled by a shock wave generated by this collapse. The arguments given by Bethe et al. (1979) in favor of this scenario are still not backed by numerical simulations (see the discussion by S. Bludman), which indeed follow the above scenario but do not produce a strong enough shock wave. The observation of a neutron star in the Crab nebula; the probable formation of a neutron star in SN1987A (detected via the neutrino emission associated to the event); and the appearance of an early spike in UV emission of Type II supernovae detected at their early stage of explosion (including SN1987A), make the above scenario appear to be the most likely one, despite the difficulties encountered by the numerical simulations.

Yields of the ejected elements as a function of the star's initial mass have been calculated by Arnet 1978, Woosley 1986, Thieleman and Arnett 1985, Nomoto and Hashimoto 1986, and Maeder 1991. These yields are regularly updated. Type II supernovae appear to be a major source of elements such as O, Ne, Mg, Si, and Fe.

3.4. Peculiar types of supernovae

In the late 1980's, people became aware that Type I supernovae did not form a unique class. Various attempts to change this classification were made by introducing new subclasses such as SN Ib or SN Ip. The problem was that some of the SN I's had very peculiar spectra, as discovered by Filipenko and Sargent (1985) with unusually high abundances of heavy elements such as

O, Ca, Mg, etc. Simultaneously it was noted (Wheeler and Levrault 1985, Begelman and Sarazin 1985) that the light curve of some of the SN I's was quite underluminous. Also, these events exhibit a temperature near maximum close to 5000 K, the temperature of recombination of electrons, rather than the quite standard 10000 K, an indication that very different physical processes are at work (Uomoto and Kishner 1985). In a very different line of thought, Cahen, Schaeffer and Cassé (1985), following Chevalier (1976), worked out the salient features of the explosion of quite massive .> 20 $M_\odot$/ Wolf-Rayet stars (Maeder 1981), which explode by core collapse, neutron star formation and shock ejection of the outer layers. Originally, the shape of the light curve seemed not to be consistent with the explosion of massive stars (Wheeler and Levrault 1985). The latter authors thus argued against such an identification, whereas Begelman and Sarazin (1985), argue in favor of it on the basis of the oxygen content of the ejecta, despite the problem of the light curve. However, since stellar winds had already ejected the hydrogen envelope prior to the explosion, C, O layers were apparent in these compact stars, and the light curve turned out quite precisely to have all the properties seen for the peculiar SN I's (Schaeffer, Cassé, Cahen 1987, Ensman and Woosley 1988). This led to the identification of these peculiar events as the new SN Ib subclass, which explode as SN II's do, but look like SN I's. The normal SN I's with white dwarf progenitors were then by contrast called SN Ia's (table 1).

SN 1987A, which was an SN II with a 15 $M_\odot$ progenitor, had many of the characteristics of the SN Ib's and should be viewed as in between the 8 $M_\odot$ stars that produce ordinary SN II's and the 20 $M_\odot$ stars that explode as SN Ib's. It is sometimes called an SN IIb for this reason. This leads to the classification presented in fig. 3, which has two important modifications as compared to the old SN I-SN II picture.

Firstly, when adjusting the astration parameter which determines the star formation rate and the rate of massive star explosions, one should not only count the SN II's, but add the SN Ib's. For determining the frequency of white dwarf explosions, only the SN Ia's should be counted. Second, the light curve of SN 1987A and the SN Ib's provides an estimate of the amount of Fe ejected by supernovae with massive progenitors: 0.1 to 0:3 $M_\odot$ rather than the 0:5 $M_\odot$ assumed in the old calculations. Since only the SN Ia rate is to be taken into account, taken together with the reduction of the white dwarf explosion rate, this reduces considerably the amount of Fe produced during the galactic evolution (table 2).

Table 1
Salient properties of the various supernova types. Massive stars explode as the standard SNII does, but the progenitor as well as the light curve are different. The supernovae due to these massive progenitors may be identified as those of the new type Ib.

Supernova type	SN I[a)]	SN II[a)]	Massive progenitors[b)]	SN 1987A
Initial mass $M_\odot$	<8	8 – 15	15 – 50?	15 – 20
Final mass $M_\odot$	1	8 – 10	10 – 20	10 – 12
Radius (cm)	10^9	10^{14}	10^{10} – 10^{12}	3 10^{12}
Nature	white dwarf	red giant	stripped star Wolf Rayet	blue stripped star
Cause of explosion	thermonuclear	gravitational collapse	gravitational collapse	gravitational collapse
Remnant	–	neutron star	neutron star	neutron star
Composition	no H	H	little or no H, He, O	H, He, O
Energy source of light curve	Ni, Co decay	shock due to collapse	Ni, Co recombination of electrons	Ni, Co
Luminosity $erg.s^{-1}$	10^{44} – 10^{43}	10^{43} – 10^{42}	10^{42} – 10^{41}	10^{42}
Photospheric temperature at maximum	hot (10000 K)	hot (10000 K)	cold (5000 K)	cold (5000 K)

[a)] from Trimble (1982); [b)] from Schaeffer et al. (1987)

Table 2
Relative supernova rates.

	I_a	I_b	II
Tammann (1981) Branch (1986)	0.18 – 0.43	0.37 – 0.11	0.45
van den Bergh et al. (1987)	0.17	0.22	0.61
Evans et al. (1989)	0.10	0.19	0.71
van den Bergh and Tammann (1991)	0.08	0.14	0.72
Ev. model (RVS90)	0.25	0.75	

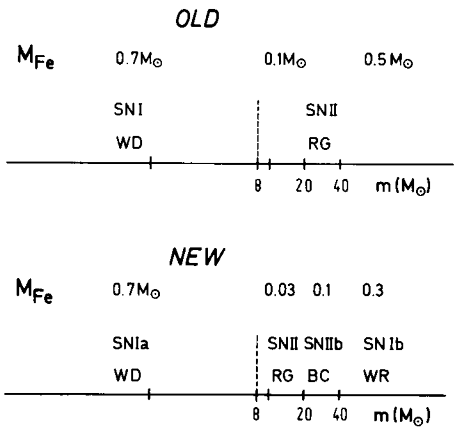

Fig. 3. Mass of iron ejected by various supernova events, according to the initial mass of the progenitor star. Above: standard view, where stars of less than 8 $M_\odot$ end as white dwarfs and possibly SNe I, and more massive stars become red giants and explode as SNe II, with iron yields determined from theory. Below: new view, in which 8 – 20 $M_\odot$ stars become red giants, the 20 – 40 $M_\odot$ stars become blue compact stars, and the more massive ones become Wolf-Rayet stars. The mass of iron corresponds to observed masses for the SN types associated with these progenitors.

4. History of galactic evolution modelling. Role of the supernovae.

In the early 1980's, the role of Type I supernovae was very difficult to establish. No convincing explosion model was available to decide which white dwarfs exploded and which ones did not. The role of SN I's was ignored. With a strong caveat based on this simplification, Twarog and Wheeler (1982) model galactic evolution using the yields of the 12 $M_\odot$ star of Arnett (1978) as typically representative of massive stars. The short lifetime of these massive stars allows use of the instant recycling approximation (t_m in eqs. 3.4 can be neglected in comparison to the time of galactic evolution); *the relative abundances are then independent of the SN rates,* and simply reflect the yields. The agreement with the measured abundances of Cameron (1973) is impressive (table 3).

Table 3
Relative (solar) abundances from type II SN alone.

	C/O	Ne/O	Mg/O	Fe+Si/O
Theory (TW82)	0.52	0.25	0.09	0.27
Obs. (C73)	0.42	0.20	0.08	0.22

But we now know that this agreement is quite misleading. Arnett (1978) used the $^{12}C(\alpha, \gamma)^{16}O$ cross-section measured by Fowler, Caughlan and Zimmerman (1973). Later measurements (Kettner et al. 1982) showed that this cross-section is larger by a factor of 3 to 5. This has the consequence that nearly all the carbon is transformed into oxygen, and that the theoretical ratio C/O calculated in table 3 is grossly overtimated. Also, the contribution of SN I's to the iron yield would considerably enhance the ratio Fe + Si/O.

In the mid 1980's, the role of SN I's as a source of Fe became obvious. Observation showed that there are about as many SN I's as SN II's, each SN I producing nearly 1 $M_{\odot}$ of Fe, whereas an SN II produces 0.1 to 0.5 $M_{\odot}$ of Fe. This results in a considerable enhancement of iron production (table 4), in a calculation where *the relative abundances depend on the relative* SN I/SN II *rates* (Matteucci and Greggio 1986, Matteucci 1986, Twarog and Wheeler 1987).

Table 4
Relative (solar) abundances from type I+II SN.

	C/O	Ne/O	Mg/O	Fe+Si/O
Theory (M86)	0.25	0.09	0.05	0.48
Obs. (C82)	0.45	0.15	0.07	0.15

It is straightforward to see that the relative abundances are too low, reflecting an abundance of O which is too large by a factor of two. This increases because of the new $C(\alpha, \gamma)O$ reaction rate. Despite this increase in O, the ratio Fe + Si/O is 3 times too large. Would the O abundance be the observed one, it would be too large by a factor of 6. Note also the mild evolution of the observed abundances.

In the late 1980's, separation of the SN Ia's from the SN Ib's reduced (table 5) the Fe abundance quite drastically (table 5), and also reduced the contribution of SN I's to O abundance (Rocca-Volmerange and Schaeffer 1990; but see also Schaeffer et al. 1987. The former work was started before the explosion of SN 1987A, but then delayed by this event, which focused interest toward other topics).

Table 5
Relative (solar) abundances from type Ia, Ib and II SN.

	C/O	Ne/O	Mg/O	Fe+Si/O
Theory (RVS90)	0.53	0.20	0.20	0.24
Obs. (C82)	0.45	0.15	0.07	0.15

Since in these calculations halo evolution also is modelled, predictions for the halo abundances, that we take more specifically as the abundances at [Fe/H] $= -2.5$, are an output of the theory and compare very well to the observations (table 6). These abundances are totally dominated by the yield of massive star explosions. But since we normalize them, as usual, to the calculated solar abundances, the results actually depend on all SN rates.

Table 6
Halo abundances at [Fe/H]= −2.5.

	[C/Fe]	[N/Fe]	[O/Fe]	[Mg/Fe]
SN Ib = white dwarfs	0.30	−0.20	0.83	0.83
SN Ib = massive stars	−0.44	−0.70	0.49	0.40
Obs.	−0.14	−0.60	0.60	0.50
	(1)	(1)	(2)	(3)

(1) Laird (1985); (2) Clegg et al., (1988); Barbuy (1988); (3) Tomkin et al., (1985), François (1985)

A few problems remain, however, in this calculation. The absolute supernova rate has been chosen in accordance with photometric evolution models (Guiderdoni and Rocca-Volmerange 1987), which reproduce the evolution of deep galaxy counts. This rate, 0.3 SNU (SN/10^{10} $L_\odot$/100y) turns out to give approximately correct *absolute* solar abundances (table 7), and is consistent with the latest determination from observations at the time of the calculation: 0.4 SNU (v. den Bergh et al. 1987). It is however smaller than the older rate, 1.4 SNU, given by Tamman 1984 and is smaller than the newer one, 0.9 SNU determined by v. den Bergh and Tamman 1991.

Table 7
Absolute predictions for the solar abundances.

Abundances ($\odot$ x 10^3)	C	N	O	Ne	Mg	Si+Fe
Theory (RVS90)	4.6	0.9	8.7	1.7	1.6	1.4
Obs. (C82)	3.9	0.9	8.5	1.5	0.6	1.5

A second problem is that the calculation gives star counts in the halo which are somewhat too large when compared to observed ones (Gilmore and Wyse 1985, Sandage 1987, Crézé and Robin 1989). This has been used by François et al. (1990), following Pagel (1991), to conclude that such a model is inadequate. Rocca-Volmerange and Schaeffer (1990) on the other hand, argue that a slightly larger yield in the low metallicity halo, or an halo IMF slightly more heavily weighted towards larger masses, would be sufficient to resolve this difficulty.

References

Arnett, D. 1978. *Ap. J.* **219**, 1008.
Audouze, J. and B. Tinsley. 1976. *Ann. Rev. Astr. Ap.* **14**, 43.
Barbuy, E. 1988. *A. A.* **123**, 1.
Begelman, M. C. and C. L. Sarazin. 1985. *Ap. J.* **302**, L59.
Bethe, M. and G. E. Brown, J. Applegate, J. Lattimer. 1979. *Nucl. Phys.* **A324**, 487.
Branch, D. 1986. *Ap. J.* **300**, L51.
Cahen, S. and R. Schaeffer, M. Cassé. 1985. 5th Astrophysics Moriond Meeting, Audouze and Matthieu eds, Reidel.
Cameron, A. G. W. 1982. Essays in Nuclear Astrophysics, Cambridge University Press.
Chevalier, R. A. 1976. *Ap. J.* **208**, 826.
Chiosi, C. and F. Matteucci. 1982. *A. A.* **105**, 140.
Clegg, R. E. S. and D. L. Lambert, J. Tomkin. 1981. *Ap. J.* **287**, 745.
Crézé, M. and A. M. Robin. 1989. *A.A.* **211**, 1.
Ensman, L. M. and S. E. Woosley. 1988. *Ap. J.* **333**, 754.
Evans, R. and S. van den Bergh, R. E. McClure. 1989. *Ap. J.* **345**, 752.
Filipenko, A. V. and W. L. W. Sargent. 1985. *Nat.* **316**, 407.
Fowler, W. A. and G. R. Caughlan, B. A. Zimmerman. 1975. *Ann. Rev. Astr. Ap.* **13**, 69.
François, P. 1986. *A. A.* **160**, 264.
François, P. and E. Vangoni-Flam, J. Audouze. 1990. *Ap. J.* **361**, 487.
Gilmore, G. and R. Wyse. 1985. *Astr. J.* **90**, 2015.
Gilmore, G. and R. Wyse, K. Kuijken. 1989. *Ann. Rev. Astron. Astrophys.* **27**, 555.
Greggio, L. and A. Renzini. 1983. *A. A.* **118**, 217.
Guiderdoni, B. and B. Rocca-Volmerange. 1987. *A. A.* **186**, 1.
Hartwick, F. D. A. 1976. *Ap. J.* **225**, 357.
Iben, I., Jr. and J. B. Truran. 1978. *Ap. J.*, **220**, 980.
Kettner, K. U. et al. 1982. *Z. Phys.* **A308**, 73.
Lacey, C. and M. Fall. 1985. *Ap. J.* **290**, 154.
Laird, J. B. 1985. *Ap. J.* **289**, 556.
Maeder, A. 1981. *A. A.* **102**, 401.
Maeder, A. 1991. *A. A.* to be published
Matteucci, F. 1986. *Ap. J.* **305**, L81.
Matteucci, F. and L. Greggio. 1986. *A. A.* **154**, 279.
Mayor, M. and L. Vigroux. 1981. *A. A.* **98**, 1.
Miller, C. and J. Scalo. 1979. *Ap. J. Sup.* **41**, 13.
Nomoto, K. and M. Hashimoto. 1986. *Prog. Part. Nucl. Phys.* **17**, 267.

Nomoto, K. and F. Thieleman, K. Yokoi. 1984. *Ap. J.* **286**, 644.
Pagel, B. E. J. 1991. Dynamical and Chemical Evolution of Galaxies, Elba, Franco and Matteucci eds, Kluwer.
Pagel, B. E. J. and B. E. Patchett. 1975. *MNRAS* **176**, 13.
Renzini A. and M. Voli. 1981. *A. A.* **94**, 175.
Rocca-Volmerange, B. and R. Schaeffer. 1990. *A. A.* **233**, 427.
Salpeter, E. E. 1955. *Ap. J.* **121**, 161.
Sandage, A. 1987. The Galaxy, Gilmore, Carswell eds, NATO ASI series, p. 321.
Scalo, J. 1986. Fundamental Cosmic Physics II, 1.
Scarle, L. and W. L. W. Sargent. 1972. *Ap. J.* **173**, 25.
Scarle, L. and R. Zinn. 1985. *Ap. J.* **225**, 357.
Schaeffer, R. and M. Cassé, S. Cahen. 1987. 2nd IAP Astrophysics Workshop, ed. Frontières.
Schaeffer, R. and M. Cassé, S. Cahen. 1987. *Ap. J.* **316**, L31.
Tamman, G. A. 1982. Supernovae, Rees, Stoneham eds, Reidel, p.371.
Thieleman, F. and D. Arnett. 1985. *Ap. J.* **295**, 604.
Tomkin, J. and D. L. Lambert. 1984. *Ap. J.* **279**, 220.
Trimble, V. 1975. *Rev. Mod. Phys.* **47**, 877.
Truran, J. W. 1984. *Ann. Rev. Nucl. Part. Sci.* **34**, 53.
Twarog, B. A. and J. C. Wheeler. 1987. *Ap. J.* **316**, 153.
Uomoto, A. and R. P. Kirshner. 1985. *A. A.* **149**, L7.
van den Bergh, S. and R. D. McClure, R. Evans. 1987. *Ap. J.* **323**, 44.
van den Bergh, S. and G. Tamman. 1991. *Ann. Rev. Astr. Ap.* in press.
Wheeler, J. C. and R. Levrault. 1985. *Ap. J.* **294**, L17.
Wheeler, J. C. and C. Sneden, J. W. Truran. 1989. *Ann. Rev. Astr. Ap.* **27**, 279.
Woosley, J. C. 1986. Nucleosynthesis and Chemical Evolution, 16th Saas-Fee Course, Hauck et al eds., Geneva Obs.
Zinn, R. 1985. *Ap. J.* **293**, 424.

SEMINAR 4

SOLAR NEUTRINOS: PHYSICS BEYOND THE STANDARD MODEL?

SIDNEY A. BLUDMAN

Center for Particle Astrophysics, University of California
Berkeley, CA 94720, USA

S. Bludman, R. Mochkovitch and J. Zinn-Justin, eds.
Les Houches, Session LIV, 1990
Supernovae

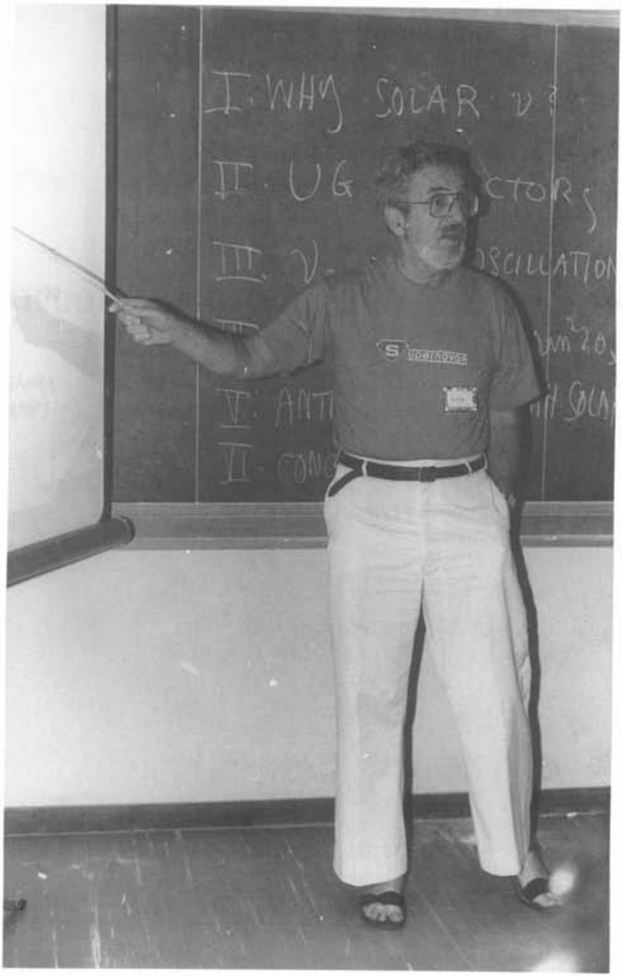
I. WHY SOLAR ν?

Contents

1. Standard solar models: is there a solar neutrino problem? 826
   1.1. Predicted solar neutrino detection rates 826
   1.2. Time variation? 827
2. Distinguishing new neutrino physics from solar model questions 828
   2.1. Neutrino oscillations 828
   2.2. Parke formula for ν_e persistence probability 831
   2.3. Neutrino spectral shape observed at Kamiokande II 833
   2.4. Total rates observed at Kamiokande II, Homestake and Sage 834
3. Physics beyond the standard model [20, 21, 22] 834
   3.1. Neutrino flavor mixing 835
   3.2. See-Saw formula for light neutrino masses 836
   3.3. Extrapolation for the τ neutrino mass 837
4. Terrestrial searches for neutrino oscillations 837
5. Conclusions 838

References 839

1. Standard solar models: is there a solar neutrino problem?

In this paper, we review the spectral shape and total rates of solar neutrinos observed at Kamiokande II and at Homestake, along with uncertainties in the Standard Solar Model (SSM). We interpret the apparent deficit of solar neutrinos in terms of matter-amplified neutrino oscillations, since almost any extension of the standard model of electroweak unification leads to masses and flavor-mixings for the light neutrinos. At present, this interpretation still admits either large-angle ($\sin^2 2\theta > 0.5$), large-mass ($\delta m^2 \sim 10^{-4}\mathrm{eV}^2$) adiabatic oscillations, or semi-adiabatic oscillations with $\delta m^2 \sin^2 2\theta = (4 \pm 2) \times 10^{-8}\mathrm{eV}^2$. The present analysis rests only on the Kamiokande II and Homestake experiments. Within a year the preliminary gallium experiments should decide whether neutrino oscillations are indeed taking place in the Sun and, if so, should allow us to choose between large-mass adiabatic and small-mass semi-adiabatic neutrino oscillations.

Assuming that neutrino oscillations are indeed taking place, we interpret the neutrino parameters, δm^2 and $\sin^2 2\theta$, in terms of the See-Saw Model, the only grand unification theory (GUTS) that naturally predicts small masses for the light neutrinos. The oscillations in the Sun must be $\nu_e \to \nu_\mu$ with $m_{\nu_\mu} = 10^{-3\pm 1}$ eV induced by GUTS at the intermediary scale 10^{11}–10^{13} GeV. Applying the See-Saw Formula to the third family implies $m_{\nu_\tau} = 2\times 10^{\pm 2}$ eV. Proposed neutrino oscillation experiments at accelerators can observe $\nu_\mu \to \nu_\tau$ oscillations if the τ neutrino mass falls in the cosmologically important region > 2 eV, and may observe $\bar{\nu}_e \to \bar{\nu}_\mu$ at reactors if $m_{\nu_\mu} = 10^{-2}$ eV.

1.1. Predicted solar neutrino detection rates

The total solar neutrino flux on Earth, $\phi(\nu) = 6.0 \times 10^{10}\ \nu\ \mathrm{cm}^{-2}\ \mathrm{s}^{-1}$, follows directly from the solar luminosity, $L_\odot = 3.83 \times 10^{33}\mathrm{ergs}^{-1}$, and the fact that each proton fusion reaction produces 26.7 MeV along with two electron neutrinos. However, the energy distribution of these neutrinos depends on the solar production of various β-decaying nuclei and on the spectrum of neutrinos characteristic of each parent nucleus. The total neutrino flux from each parent depends on nuclear cross-sections and ambient conditions in the Sun. But, within each neutrino group, the neutrino spectral shape depends only on weak interactions.

There are by now at least four [1, 2, 3, 4] "Standard" Solar Models (SSM) whose results agree within 3%, when the same input physics (opacities, nuclear cross-sections) are used. The small differences in radiative opacities and in the $^7\mathrm{Be}(p, \gamma)^8$ B cross-section used by Bahcall and Ulrich [1] and by Turck-Chièze et al [2], lead to 11% and 50% differences in their computed flux of neutrinos ϕ from the ^{7}Be and ^{8}B parent nuclei. This is shown in the first two lines of table 1. When, as in fig. 1(a), the flux is folded into the ^{37}Cl absorption cross section and integrated over neutrino energies, this leads to correspondingly large differences for the predicted detection rates, $N(i) = \Sigma\phi(i)\sigma_i$, given in the middle of table 1.

The rates observed in the ^{37}Cl detector [5] and also in the Kamiokande II detector [6], each relative to the Bahcall-Ulrich and to the Turck-Chièze SSM predictions, are shown in the last two lines of table 1. The errors shown are only the statistical and systematic errors of the two experiments. The range of theoretical uncertainty is indicated by comparison of the two columns. Apparently, two different experiments detect total neutrino rates only 30-70% of that predicted.

Table 1
Neutrino Fluxes, Counting Rates, Predicted and Observed

	B-U	T-C	T-C/B-U
$\phi(^7\mathrm{Be})$	0.47×10^{10}	0.42×10^{10}	0.89
$\phi(^8\mathrm{B})$	5.8×10^6	3.8×10^6	0.66
N(^{8}B)	6.1	4.0	
N(^{7}B)	1.1	1.0	
N(others)	0.7	0.8	
	7.9 ± 2.4 SNU	5.8 ± 1.2 SNU	
KAM/SSM	$0.46 \pm 0.05 \pm 0.06$	$0.69 \pm 0.08 \pm 0.09$	
^{37}Cl/SSM	0.27 ± 0.04	0.39 ± 0.06	

1.2. Time variation?

The Homestake ^{37}C1 observations have been running for twenty years, through two solar sunspot cycles. The rate detected at solar minimum was 4.1 ± 0.9 SNU in 1977 and 4.2 ± 0.8 SNU in 1986-88, just consistent with the

Turck-Chièze calculations. While a statistically significant anticorrelation has been established between the Homestake solar neutrino flux and sunspots [7, 8, 9], no time variation greater than 30% appears in the 1987–90 Kamiokande II data. A greater than 30% effect is not expected theoretically [10]. In this paper, we assume no significant time-variation and do not consider any magnetic effects.

2. Distinguishing new neutrino physics from solar model questions

In fig. 1 we show the fraction of the total solar neutrino rate in each energy group expected at the ^{37}Cl, KAM-II, and ^{71}Ga detectors as calculated on the Bahcall-Ulrich SSM. The rates for different neutrino groups ($\phi(^8\mathrm{B})$ of high energy, $\phi(^7\mathrm{Be})$ of intermediate energy, ϕ(others) of low energy) depend on solar conditions, but for each individual group, the spectral shape depends only on neutrino microphysics. Therefore, independent of SSM, the distortion of the electron neutrino spectrum within a given group, say $\nu(^8\mathrm{B})$, implies new neutrino physics.

In the Standard Model of lepton and quark interactions (SM), there are three massless Weyl (two-component) neutrinos ν_i $(i = e, \mu, \tau)$, with each neutrino flavor separately conserved. In almost every extension of the SM, the neutrinos acquire masses m_i $(i = 1, 2, 3)$ and mixing takes place among the flavor eigenstates, producing neutrino flavor oscillations. We therefore consider only this minimal extension of the SM.

In this chapter, we present a simple treatment of two-flavor neutrino oscillations based on our own derivation of the Parke formula for the survival probability $P(E)$ of $\nu_e \to \nu_e$ in the Sun. Observations at Kamiokande II, Homestake, and Sage then imply $\nu_e \to \nu_\mu$ with mixing angle $\sin\theta \approx 0.01$ to 1.0, and squared mass difference $\delta m^2 = 10^{-6\pm2}$ eV^2. This evidence, (from the Sun) is the first evidence for new particle physics beyond the Standard Model (SM) and the test evidence that thus far, has not been found in terrestrial laboratories.

2.1. Neutrino oscillations

We restrict ourself to grand unification theories in which neutrinos and charged fermions occur in the same GUTS multiplet, since only these GUTS naturally predict light neutrino masses. In these theories, nearly the same neutrino and quark mixing matrices are generated and generally neutrino masses follow the normal hierarchy, $m_e \ll m_\mu \ll m_\tau$. Because in the quark

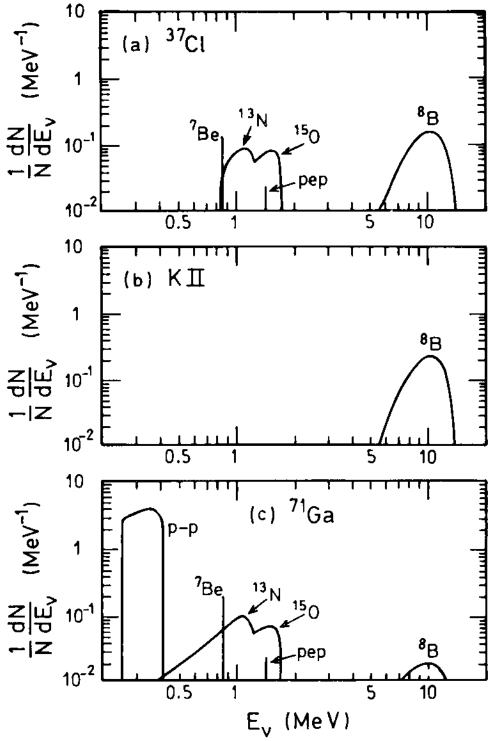

Fig. 1. Neutrino detection rates predicted by the SSM at (a)^{37}CI, (b) KAM-II and (c) ^{71}Ga detectors, each normalized to unity [ref. 14]. While the total rate for $\nu(^8\mathrm{B})$ and for $\nu(^7\mathrm{Be})$ depends on the SSM, the spectral shape within each group depends only on the β-spectrum.

mixing (CKM) matrix, the mixing between the first and third families and $\sin\theta_{13} = (0.001-0.007)$, the $\nu_e-\nu_\tau$ mixing, $\sin^2 2\theta_{e\tau}$ approximately 6×10^{-5} in the quark mixing (CKM) matrix, is too small for perceptible $\nu_e - \nu_\tau$ oscillations anywhere in the Sun or on Earth.

We therefore consider only $\nu_e - \nu_\mu$ mixing in which, in vacuum, the flavor eigenstates are related to the mass eigenstates by

$$\begin{pmatrix} \nu_e \\ \nu_\mu \end{pmatrix} = \begin{pmatrix} c & s \\ -s & c \end{pmatrix} \begin{pmatrix} \nu_1 \\ \nu_2 \end{pmatrix}, \tag{1}$$

where $c \equiv \cos\theta, s \equiv \sin\theta$. Because at distance r from ν, momentum eigentstates differ in vacuum energy by $\Delta \equiv \delta m^2/2p$, the production the

ν_μ probability is

$$|\langle\nu_\mu|\nu_e\rangle_r|^2 = \sin^2 2\theta \cdot \sin^2 \Delta r/2. \tag{2}$$

Hereafter, δm^2 is measured in eV^2, energies and momenta in MeV, so that $\Delta = 2.53(\delta m^2/E)$ meters^{-1}.

In matter, ν_e and ν_μ have different interactions with the electrons, so that, in the flavor basis, the mass matrix is

$$H_M = \frac{1}{2} \begin{array}{cc} \nu_{eL} & \nu_{\mu L} \\ \end{array} \begin{pmatrix} 2a_e - \Delta c_2 & \Delta s_2 \\ \Delta s_2 & 2a_\mu + \Delta c_2 \end{pmatrix}, \tag{3}$$

where a_e, a_μ are the different potential energies of ν_e, ν_μ and $s_2 \equiv \sin 2\theta$, $c_2 \equiv \cos 2\theta$. Diagonalization of this matrix requires a mixing angle in matter

$$\tan 2\theta_M = \frac{\Delta \sin 2\theta}{\Delta \cos 2\theta - \Delta_e(r)}, \tag{4}$$

where $\Delta_e(r) \equiv a_e(r) - a_\mu(r) = \sqrt{2} G_F N_e(r)$; $N_e(r) \equiv$ the electron number density at radius r in units of Avogadro's constant. The mass eigenstates have energy difference in matter

$$\Delta_M(r) = \{[\Delta c_2 - \Delta_e(r)]^2 + (\Delta s_2)^2\}^{1/2}, \tag{5}$$

where $c_2 \equiv \cos 2\theta, s_2 \equiv \sin 2\theta$.

We can write $\tan 2\theta_M(r) = \tan 2\theta/(1 - f(r))$, where $f(r) \equiv \Delta_e(r)/\Delta c_2 = (N_e(r)/N_{ec})(E/E_A)$, which shows that neutrinos above a minimum energy $E_A \equiv c_2 \delta m^2/2\Delta_{ec} = 6.7 \times 10^4\ \delta m^2 c_2$ have their mixing angle resonantly amplified at a radius determined by the level-crossing, $\Delta_e(r) = \Delta c_2$, at $N_e(r) = N_{ec}(E/E_A)$.

In the Sun, $N_{ec}/N_A = 98.6$ g $\cdot$ cm^{-3}, and the electron number density varies, for $r > 2h$, exponentially as $N_e(r)/N_{ec} = 2.48 e^{-r/h}$ with density scale height $h \equiv (-d \ln N_e/dr)^{-1} = 0.096 R_\odot$. Therefore, neutrinos of energy $E > E_A$ resonantly convert at a distance $r = h \log(2.48 E/E_A)$ from where they are produced. For $E > 7$ MeV $\nu(^8B)$, resonance falls outside the neutrino production region $r < h$, if $\delta m^2 < 10^{-4}$ eV^2. For the lowest energy (0.23 MeV $\nu(pp)$) neutrinos to be detected in gallium detectors, resonance overlaps the neutrino production region $r < 2.5h$ if $\delta m^2 c_2 > 7 \times 10^{-7}$ eV^2.

The resonance full-width in radius is $\delta r = 2h\ \tan 2\theta$ and resonance matter oscillation length is $2\pi/\Delta s_2$. The ratio of these two lengths defines the adiabaticity, $\xi = h \Delta s_2^2/c_2 \pi$.

2.2. *Parke formula for ν_e persistence probability*

The neutrinos are produced and detected in ν_e flavor eigenstates, but propagate inside the Sun and onto the Earth in mass eigenstates $m_{1,2}$. Whether or not a resonance is encountered, each mass state changes its flavor composition as it propagates from high density at the center of the Sun to near vacuum. A ν_e created inside the Sun can arrive as a ν_e at the detector from either energy eigenstate, by persisting with probability $(1 - P_j)$ adiabatically in one mass eigenstate or by a sudden transition with probability P_j between different mass eigenstates.

Because an average is taken over production and detection sites, quantum-mechanical phase information disappears, and the $\nu_e \to \nu_e$ persistence probablility depends only on the probabilities c^2, s^2 of states 1, 2 at production and at detection. The ν_e persistence probability is therefore

$$\begin{aligned} P &= (c^2 \quad s^2) \begin{pmatrix} 1 - P_j & P_j \\ P_j & 1 - P_j \end{pmatrix} \begin{pmatrix} c_M^2 \\ s_M^2 \end{pmatrix} \\ &= A(1 - P_j) + B P_j \\ &= \frac{1}{2}[1 + (1 - 2P_j)\cos 2\theta \cdot \cos 2\theta_M], \end{aligned} \tag{6}$$

where $A \equiv c^2 c_M^2 + s^2 s_M^2$, $B \equiv c^2 s_M^2 + s^2 c_M^2$. In this formula the matter mixing angle θ_M is to be evaluated where the neutrinos are produced. As E passes through E_A from below, $\cos 2\theta_M$ changes abruptly from $+1$ to -1 and $P(E)$ changes from $\cos^2\theta - P_j \cos 2\theta$ to $\sin^2\theta + P_j \cos 2\theta$.

The Parke formula (6) [11] is a classical formula which depends only on probabilities. On the other hand, the jump probability P_j requires a quantum mechanical calculation which leads to an exponential tunnelling probability $P_j = \exp(-\chi)$, $\chi \equiv (\pi^2/2)\xi(1 - \tan^2\theta)$. (This tunnelling formula is derived in the simplest way [12] from the energy level crossing ($\Delta_M(r) = 0$) which takes place at complex time r/c). If a sudden transition were to take place deep in the Sun, where the neutrino resonance and production regions overlap, the exponential formula would not apply and the neutrino evolution equations would have to be integrated numerically [13]. For the experimentally preferred $\delta m^2 < 10^{-5}\ eV^2$, this rarely happens, except for $E < 0.67$ MeV neutrinos that are detected in gallium.

Thus, we can write

$$\chi \equiv E_{NA}/E,$$

where

$$E_{NA} \equiv \pi h \delta m^2 \sin^2\theta = 1.0 \times 10^9\ \delta m^2 \sin^2\theta = 1.5 \times 10^4\ (\sin^2\theta/c_2)\ E_A$$

is the maximum energy for which appreciable conversion takes place ($P_j < e^{-1}$). If $\sin^2\theta > 6.7 \times 10^{-5}$, a band of energies, $E_A < E < E_{NA}$ undergoes adiabataic or semi-adiabatic conversion leading to appreciable ν_e suppression in the Sun. Since 7 to 14 MeV $\nu(^8B)$ are appreciably suppressed in the Kamiokande II and ^{37}Cl experiments, we conclude that $E_A < 7$ MeV, $E_{NA} >$ 14 MeV or $\delta m^2 < 10^{-4}$ eV^2; $5 \times 10^{-4} < \sin^2 2\theta < 0.5$.

Therefore, we write for the ν_e persistence probability as function of neutrino energy,

$$P(E) = \begin{cases} \cos^2\theta - P_j \cos 2\theta, & E < E_A \\ \sin^2\theta + P_j \cos 2\theta, & E_A < E, \end{cases} \tag{7}$$

where $P_j = \exp(-E_{NA}/E)$ and E_A is nearly independent of θ, E_{NA} is proportional to the combination $\delta m^2 \sin^2\theta$. The total neutrino detection rate is obtained by integrating over neutrino production sites and energies. Suppressing the spatial integration, the observed ν_e rate is

$$\int P(E)\phi\sigma dE \equiv \langle P(E)\rangle \int \phi\sigma dE$$

This defines the energy-averaged ν_e persistence probability $\langle P(E)\rangle$.

In fig. 2 (after [14]), $P(E)$ is plotted for five choices of the neutrino parameters (δm^2, $\sin^2 2\theta$), all chosen to realize the same total (energy-averaged) survival probability $\langle P(E)\rangle = 0.29$ either because the oscillations are adiabatic, with large-mixing ($\sin^2 2\theta = 0.29$) or with large mass ($\delta m^2 = 10^{-4}$eV^2), or because the oscillations are semiadiabatic ($\delta m^2 \sin^2\theta = 10^{-8}$eV^2, $\chi = 10$ MeV/E). In any experiment, the measurement of $\langle P(E)\rangle$ alone cannot determine the two separate parameters E_A, E_{NA} or δm^2, $\sin^2\theta$. Instead an entire right triangle is determined in parameter space (MSW isoSNU diagram). The same $P(E)$ is possible if either $\sin^2 2\theta$ is large or if $\delta m^2 \sin^2 2\theta$ is small. Large-angle neutrino oscillations lead to an energy-independent reduction in solar neutrino flux, as does a Sun that is cooler than theoretically predicted. Small-angle neutrino oscillations preferentially suppress high-energy ($E > E_A$) neutrinos if $\delta m^2 \sim 10^{-4}$eV^2 (large-mass fit) and suppress low-energy ($E < E_{NA}$) neutrinos if $\delta m^2 \ll 10^{-4}$eV^2 (semi-adiabatic fit).

An apparently low energy-integrated detection rate or $\langle P(E)\rangle$ can be attributed to either a non-standard solar model, large-mixing neutrino oscillations, or to small mixing neutrino adiabatic or semi-adiabatic neutrino oscillations. Only precise neutrino spectroscopy can distinguish between these two posssibilities.

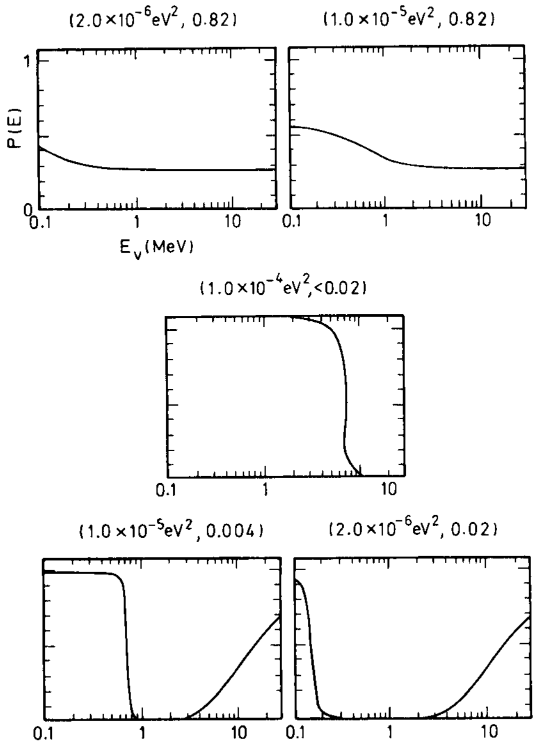

Fig. 2. The MSW ν_e survival probability $P(E)$ as function of energy for five choices of neutrino parameters ($\delta m^2, \sin^2 2\theta$), all chosen to give 71% suppression of solar neutrinos (based on [14]). The two large-angle fits suppress neutrinos at all energies equally. The small-angle fits suppress high-energy neutrinos in the large-mass case (adiabatic oscillations), and suppress low-energy neutrinos in the two small-mass cases (semi-adiabatic oscillations).

2.3. Neutrino spectral shape observed at Kamiokande II

Compared with radiochemical detectors, Kamiokande II has the advantages of real-time observations, directionality, and (limited) spectral information. The threshold, originally 9 MeV (now 7.5 MeV), allows observation of $\nu(^8B)$ from the Sun. The spectrum of recoil electrons observed (fig. 3) is consistent with the upper three-fourths of the ^8B neutrino spectrum, and rules out, at confidence limit, 90%. E_A >8.7 MeV. This rules out adiabatic neutrino oscillations in the core of the Sun, with large mass $\delta m^2 \sim 1.3 \times 10^{-4} eV^2$,

$7.2 \times 10^{-4} < \sin^2 2\theta < 6.3 \times 10^{-3}$. The spectral shape observed is therefore consistent with semi-adiabatic neutrino oscillations with either a cool Sun or with large-angle adiabatic oscillations.

2.4. Total rates observed at Kamiokande II, Homestake and Sage

A comparison of daytime and nightime neutrino fluxes observed at Kamiokande II [17] sets limits on neutrino regeneration in the Earth and excludes the mid-portion ($2 \times 10^{-6} < \delta m^2 < 10^{-5}$) of the large-angle solution in fig. 4. The total rates observed at Kamiokande II and at Homestake [15, 16] are consistent with each other and permit (*a*) large-angle adiabatic oscillations with $\delta m^2 \sim 10^{-4}\text{eV}^2, \sin^2 2\theta > 0.5$ or (*b*) semi-adiabatic oscillations with $E_{NA} = 10 \pm 5$ MeV ($\delta m^2 \sin^2 2\theta = (4 \pm 2) \times 10^{-8}\text{eV}^2$) [18].

Since a cool Sun is spectroscopically indistinguishable from the large-angle fit, we cannot be certain that neutrino oscillations are taking place in the Sun until this large-angle solution is excluded. These two possibilities will be realized as soon as Ga detectors determine whether or not low-energy neutrinos are being filtered out in the Sun. If the Ga detectors ultimately observe greater than 90 SNU, then either the SSM has overestimated the expected neutrino flux or vacuum-like large-angle neutrino oscillations are taking place in the Sun. If the Ga detectors observe less than 40 SNU, the semi-adiabatic fit is selected. Preliminary results from SAGE [19] find no neutrino flux, but are also consistent with the SSM at 95% confidence limit.

We hereafter assume that the Sun is not unexpectedly cool, and that the apparent deficit of solar neutrinos does imply neutrino oscillations in the Sun.

3. Physics beyond the standard model [20, 21, 22]

The Standard Model of electroweak unification, until now consistent with all terrestial measurements, contains three massless Weyl neutrinos whose flavor is conserved. Grand unification theories unify leptons and quarks, and almost inevitably allow neutrino masses, flavor mixing, and (usually) proton decay. We now consider the only available theoretical mechanism that naturally leads to small neutrino masses, the See-Saw Model [23].

In See-Saw Models, charged fermions, neutrinos, and a new *superheavy* right-handed Majorana neutrino N_R belong to the same group representation and therefore are subject to a common mixing in each family. (We do not consider GUTS such as minimal SU(5) which, because quarks, and leptons appear in more than one representation, do not predict small neutrino masses

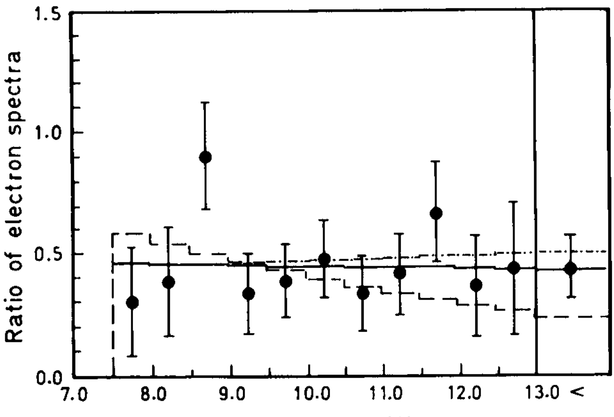

Fig. 3. The ratio of the KAM–II differential recoil-electron energy spectrum to the expected spectrum as a function of the observed recoil-electron energy. The lines are the spectra distorted electron due to neutrino oscillations with representative parameters of ($\sin^2 2\theta, \delta m^2$): ($6.3 \times 10^{-4}$) for the solid line, ($10^{-2}, 3.2 \times 10^{-6}$) for the dotted-dashed line, and (2×10^{-3}, 1.4×10^{-4}) for the dashed line[15].

in a natural way. Minimal SU(5) is, in any case, ruled out because it predicts proton decay at a rate that has not been observed.)

We will show that, if neutrino oscillations are indeed taking place in the Sun, the GUTS See-Saw Formula for light neutrino masses implies that $m_{\nu_\mu} \sim 10^{-3\pm1}$ eV, that symmetry breaking is at the intermediate scale 10^{11} to 10^{13} GeV, and that the τ neutrino mass extrapolates to $2 \times 10^{\pm 2}$ eV, which may be cosmologically significant.

3.1. Neutrino flavor mixing

In the quark mixing (CKM) matrix, first-second family mixings are of order $\sin\theta_c = 0.22$ (the Cabbibo angle) second-third family mixings of order $\sin^2\theta_c$ and first-third family mixings of order $\sin^3\theta_c$. More precisely [23], $\sin\theta_{13} = (0.001 - 0.007) \ll \sin\theta_{23} = (0.03 \text{ to } 0.06) \ll \sin\theta_{12} = 0.22$. For the neutrino mixings, we therefore expect $\sin^2 2\theta_{e\tau} \sim 6 \times 10^{-5}$, a value too small for detectable oscillations in the Sun or anywhere else. We expect $\nu_e \leftrightarrow \nu_\mu$ and $\nu_\mu \leftrightarrow \nu_\tau$ mixings with $\sin^2 2\theta \sim 0.2, 0.01$ respectively.

Barring accidental mass degeneracies, δm^2 measures the squared mass of the more massive neutrino. Therefore we interpret solar neutrino oscillations with $\delta m^2 = 10^{-6\pm2}\text{eV}^2$ as evidence for $m_{\nu_\mu} = 10^{-3\pm1}$ eV. This small value for δm^2 in the Sun prevents any direct laboratory measurement of the μ neutrino mass. If new reactor neutrino oscillation experiments can reach down to $\delta m^2 \sim 10^{-4}$ eV^2, they can test on Earth the large-mass, large-angle solution to the solar neutrino problem. This solution will, however, already be tested by gallium solar neutrino experiments in the next year or two.

3.2. See-Saw formula for light neutrino masses

The See-Saw Model [25] invokes a superheavy right-handed Majoran neutrino N_R, which can form a (Majorana) mass $M_N \overline{N}_L^c N_R$ with itself and a (Dirac) mass $m_D \overline{\nu}_L N_R$ with the ν_{iL} of the Standard Model, i.e. a mass term

$$m_D \overline{\nu}_L N_R + M_N \overline{N}_L^c N_R = \frac{1}{2} (\, \overline{\nu}_L \quad \overline{N}_L^c \,) \begin{pmatrix} 0 & m_D \\ m_D^T & M_N \end{pmatrix} \begin{pmatrix} \nu_R^c \\ N_R \end{pmatrix}, \tag{8}$$

in the Lagrangian. Allowing for three flavors for both the R- and L- neutrinos, m_D and M_N are each 3×3 matrixes. Diagonalizing the Lagrangian leads to three (unobserved) superheavy neutrinos, and three light neutrinos whose masses are $m_l = m_D M^{-1} m_D^T$. All of these masses are evaluated at the GUTS scale X, so that for each family we obtain $m_{\nu_i}(X) = m_D^2(X)/M_{Ni}(X)$.

There are large uncertainties in the numerator and the denominator of the See-Saw Formula. It is unclear whether m_D should be identified with the actual lepton and quark masses which differ by a factor of approximately 10 in the second family or by a factor of approximately 100 in the third family. In addition, the superheavy neutrino mass in the denominator $M_N(X)$ is expected to be family-dependent.

Allowing for masses running from 1 GeV to the X scale [20], the neutrino masses are $m_{\nu_i}(X) = (0.953) m_{\nu_i}$; the up-quark masses, $m_u(X) = (.23)(5.6$ MeV$)$, $m_c(X) = (0.29)(1.35$ GeV$)$, $m_t(X) = (0.72)(135$ GeV$)$. For the second family superheavy Majorana neutrino, we therefore obtain $M_{N2}(X) = (5$ to $50) \times 10^{10}$ GeV if quark masses are used, and $M_{N2}(X) = (3$ to $30) \times 10^9$ GeV, if charged lepton masses are used in the numerator of the See-Saw Formula. Although the Ga solar neutrino experiments will soon reduce the uncertainty in m_m, by distinguishing between the two MSW fits to the solar neutrino flux , M_{N2} remains uncertain by a factor of 200 because of the ambiguity about which fermion mass is to be associated with m_D.

The superheavy neutrino mass M_{N2} is less than the GUTS scale M_X by a coupling constant squared $\sim 10^{-2}$. Therefore, applying the See-Saw Formula only to the second family, the existence of neutrino oscillations in the Sun leads to the important conclusion that the GUTS scale is intermediate (10^{11} to 10^{13} GeV), rather than about 10^{16} GeV, as suggested by SUSY symmetry-breaking. Such an intermediate scale GUTS may arise naturally from the breakdown of Peccei-Quinn symmetry at a scale $\sim 10^{11}$ to 10^{12} GeV needed to close the Universe by invisible axions, or can arise from gravitinos involved in supergravity symmetry-breaking.

3.3. Extrapolation for the τ neutrino mass

If we naively assume that $M_N(X)$ is family-independent, then $m_{\nu_\tau} = m_{\nu_\mu}(m_{D3}/m_{D2})^2 = (1 \text{ to } 100)$ eV, if, in the numerator of the See-Saw Formula, quark masses are used; or (0.3 to 30) eV, if charged lepton masses are used. If we allow for a factor of 10 uncertainty in the family-dependence of $M_N(X)$, then we conclude that $m_{\nu_\tau} = 2 \times 10^{\pm 2}$ eV. If $m_{\nu_\tau} > 2$ eV, then neutrinos dominate over baryons cosmologically. If $m_{\nu_\tau} > 92h^2 > 20$ eV, where 100h is the Hubble constant, then neutrinos will close the Universe.

4. Terrestrial searches for neutrino oscillations

Equation (2) tells us that the oscillation length for neutrinos in a vacuum or on Earth is $2\pi/\Delta = 2.5(E/\delta m^2)$ meters, so that accelerator neutrinos ($E >$ GeV, distances approximately 100 to 1000 meters) are sensitive to $\delta m^2 > 1$ eV^2; reactor antineutrinos can be sensitive to $\delta m^2 \geq 10^{-4}$ eV^2, and atmospheric neutrinos ($E \sim$ GeV, for distances to 10^7 km) are sensitive to δm^2 approximately 10^{-4}eV^2.

Figure 5 shows that existing accelerator, reactor, and atmospheric neutrino oscillation experiments are not sensistive enough to probe the region of parameter space for which $\nu_e - \nu_\mu$ oscillations have apparently been observed in the Sun. These terrestrial experiments can never test the low-mass, δm^2 approximately $10^{-6\pm 1}$ MSW solution, whose presence would establish neutrino oscillations in the Sun. Atmospheric neutrino oscillation experiments [25] probe the mass region δm^2 approximately 10^{-4} eV^2 but are difficult to perform and to interpret. Proposed reactor neutrino experiments may reach this region, but not before it will have been already tested in the Sun by the gallium experiments.

In the preceeding chapter, we saw that the CKM matrix implies $\nu_\mu \leftrightarrow \nu_\tau$ mixing with $\sin^2 2\theta_{\mu\tau}$ approximately 0.04 and that the See-Saw Formula suggests, with much less precision, that $\delta m^2_{\mu\tau}$ approximates $4 \times 10^{\pm 4}$. The right-half of fig. 5 shows that existing accelerator experiments already exclude any cosmologically important $m_{\nu_\tau} > 3$ eV for $\sin^2 2\theta_{\mu\tau} \geq 0.008$. Nevertheless, it is important to check and extend the sensitivity of these accelerator limits down to the cosmologically important $\delta m^2_{\mu\tau} \geq 4$ eV^2.

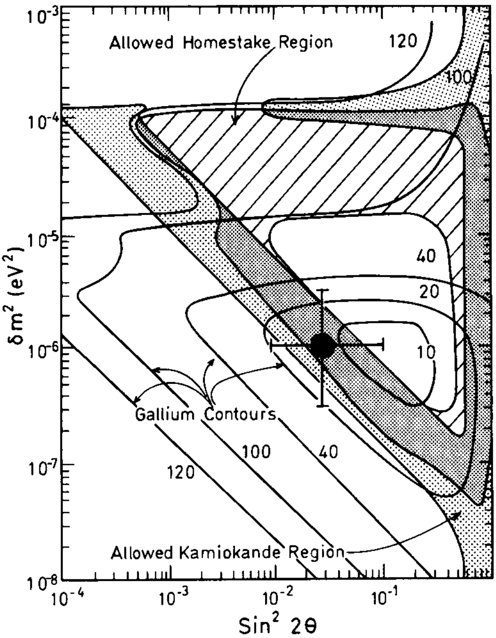

Fig. 4. Neutrino oscillations: the regions in mass-difference-mixing-angle space allowed by all experimental results. The shaded region is the area permitted (with 95 per cent confidence) by Kamiokande II; the cross-hatched area, that is allowed by Homestake. The overlap between both experiments is heavily shaded, and shows that the large-angle, large-mass solution cannot be excluded by these experiments. The solid lines correspond to gallium counting rates of 10 to 120 SNU (based on ref. [16]).

5. Conclusions

We believe that unless radiative opacities or the ^{7}Be$(p, \gamma)^8$B cross section have been seriously overestimated, there is a deficit of solor neutrinos that must involve neutrino physics beyond the Standard Model of electroweak unification. Minimal extension of the Standard Model leads to neutrino masses and mixings, and to neutrino flavor oscillations in the Sun. The Kamiokande II and Homestake observations of solar neutrinos, together with the approximate equality of lepton and quark mixing angles in See-Saw Models, tell us then that the μ neutrino mass $m_{\nu_\mu} = 10^{-3\pm1}$ eV and that, in the second family, the symmetry-breaking is at an intermediate scale $M_X = 10^{11}$ to 10^{13}

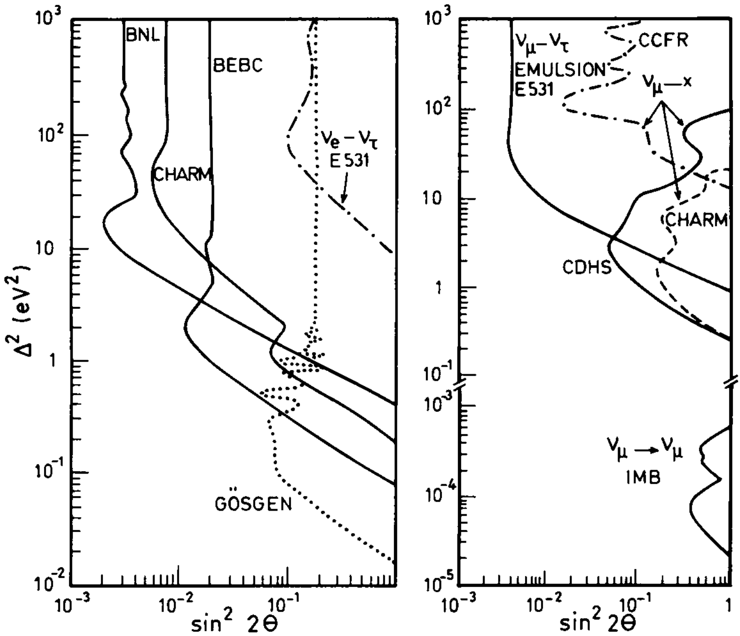

Fig. 5. Limits (90% confidence limits) on $\nu_\mu \rightarrow \nu_e$, $\nu_e \rightarrow \nu_\tau$, and $\nu_e \rightarrow x$ (left); and $\nu_\mu \rightarrow x$ and $\nu_\mu \rightarrow \nu_\tau$ (right). The allowed areas are to the left of the curves [25].

GeV. The uncertainties can be reduced if the gallium detectors or reactor neutrino oscillation experiments exclude $\delta m^2 = 10^{-4}$ eV^2.

Extrapolating the See-Saw Formula to the third family can only be approximate which leads to $m_{\nu_\tau} = 2 \times 10^{\pm 2}$ eV. Accelerator $\nu_\mu \leftrightarrow \nu_\tau$ oscillation experiments merit refinement to the cosmologically interesting limit of $\delta m^2_{\mu\tau} = 4$ eV^2.

References

[1] Bahcall, J. N., and R. K. Ulrich, Rev. Mod. Phys. **60**, 297, 1988.
[2] Turck-Chieże, S., S. Cahen, M. Cassé and C. Doom, Ap. J. **335**, 415, 1988.
[3] Sienkiewicz, R., J. N. Bahcall and B. Paczynski, Ap. J., **349**, 641, 1990.
[4] Dearborn, D. S., and G. M. Fuller, Phys. Rev. D **39**, 3543, 1989.
[5] Davis, R., Jr., *Proceedings Twenty-first International Cosmic Ray Conference*, Adelaide, Australia.
[6] Hirata, K. S. et al., Phys. Rev. Lett. **65**, 1297, 1990.
[7] Bahcall, J. N., and W. H. Press, Ap. J. 1990.
[8] Bieber, J. W., D. Seckel, T. Stanev and G. Steisman, Nature, Dec. 1990.

[9] Fillipone, B. W. and P. Vogel, Phys. Lett. B **246**, 546, 1990.
[10] Bludman, S. A., *Proceedings First International Symposium on Particles, Strings and Cosmology*, Northwestern University, 1990.
[11] Parke, S. J., Phys. Rev. Lett. **57**, 1275, 1986.
[12] Pizzochero, P., Phys. Rev. D **36**, 2293, 1987.
[13] Haxton, W. C., Phys. Rev. Lett. **57**, 1271, 1986.
[14] Barger, V., R. J. N. Phillips, K. Whisnant, University of Wisconsin preprint MAD/PH/587/IS-J4076, 1990.
[15] Hirata, K. S., et al., Phys. Rev. Lett. **65**, 1301.
[16] Cherry, M., Nature **347**, 708, 1990.
[17] Hirata, K. S., et al., Phys. Rev. Lett., **63**, 16, 1989.
[18] Bahcall, J. N., and H. A. Bethe, Phys. Rev. Lett. **65**, 2233, 1990.
[19] Abazov, A. I., et al., *Proceedings XIII International Conference Neutrino 1990*, in press.
[20] Bludman, S. A., D. C. Kennedy, and P. G. Langacker, Pennsylvania preprint UPR–0443T and Center for Particle Astrophysics preprint CfPA–TH–91-002.
[21] Langacker, P., R. D. Peccei, and T. Yamagida, Mod. Phys. Lett. **A1**, 541 (1986).
[22] Langacker, P., S. T., Petcov, G. Steigman, and S. Toshev, Nucl. Phys. **B282**, 589 (1987).
[23] Gell-Mann, M., P. Ramonds and R. Slansky, *Supergravity*, eds. F. van Nieuwenhuizen and D. Freedman, North-Holland, Amsterdam, 1979; T. Yanigida, Prog. Th. Phys. **B135**, 66, 1978.
[24] Review of Particle Properties, Phys. Lett. **B239**, III.61, 1990.
[25] Eichler, D., *Lepton and Photon Interactions*, Proc. Intl. Symp on Photon Interactions at High Energies, Hamburg; [Nucl. Phys. B (Proc. Suppl.) **3**, 389].